UNIVERSIDADE D
COIMBRA

Ricardo José Novo Azeiteiro

NUMERICAL SIMULATION OF LIQUEFACTION-RELATED PHENOMENA

Thesis for the degree of Doctor of Philosophy in Civil Engineering, specialisation in Geotechnics, supervised by Professor Doctor Paulo Alexandre Lopes de Figueiredo Coelho, Professor Doctor José Carlos Duarte Grazina and Professor Doctor David Martins Geraldo Taborda and submitted to the Department of Civil Engineering of the Faculty of Sciences and Technology of the University of Coimbra.

July 2020

Department of Civil Engineering of the Faculty of Sciences and Technology of the University of Coimbra

NUMERICAL SIMULATION OF LIQUEFACTION-RELATED PHENOMENA

Ricardo José Novo Azeiteiro

A thesis supervised by Dr. Paulo Alexandre Lopes de Figueiredo Coelho, Dr. José Carlos Duarte Grazina and Dr. David Martins Geraldo Taborda and submitted to the Department of Civil Engineering of the Faculty of Sciences and Technology of the University of Coimbra for the degree of Doctor of Philosophy.

July 2020

À memória do meu pai:

"O homem de esperança é o que se abandona absolutamente na certeza de que encontrará segurança no ser, contrariamente à insegurança do ter."

Fernando Azeiteiro (1992)
em "Gabriel Marcel: da angústia à esperança. Fundamentação ontológica."

[*In memory of my father:*

"The person of hope is the one who completely abandons oneself to the certainty of finding safety in being, as opposed to the unsafety of having."

Fernando Azeiteiro (1992)
in "Gabriel Marcel: from distress to hope. Ontological arguments."]

ABSTRACT

Liquefaction-related phenomena are a major concern for modern societies, at least in seismically active zones, due to their massive destructive potential, capable of causing great economic losses, social disruption and loss of life. Although the great development of numerical tools in recent years has extended the possibilities of performance-based design, it has also revealed the need for more reliable constitutive models, capable of simulating the mechanisms involved in these complex phenomena. In this thesis, a bounding surface plasticity model is implemented into the finite element code FEMEPDYN, developed at the University of Coimbra, and applied to the simulation of liquefaction-related phenomena induced by cyclic loading and observed in element laboratory tests and centrifuge experiments.

In the first part of this thesis, the outcome of an extensive laboratory testing programme performed on Hostun sand is presented, including results of bender element tests, as well as of drained and undrained monotonic triaxial compression and extension tests, allowing for the characterisation of the monotonic response of Hostun sand within the very small to large strain range. The effects of the void ratio, consolidation stress state and stress path on the measured response are discussed. Moreover, a state-parameter approach is used in conjunction with critical state soil mechanics concepts to characterise the distinctive states of the response of sand, namely the undrained instability, phase transformation, peak stress ratio, and critical states. The stress-dilatancy characteristics of sand are also investigated. In addition, results of a series of drained and undrained cyclic triaxial tests carried out on Hostun sand are used to assess the key aspects of its cyclic response, including the reduction of the secant shear stiffness and concurrent increase in damping ratio with strain amplitude, the generation of excess pore water pressure with cyclic loading and the undrained cyclic resistance.

The second part of this thesis includes a comprehensive description of a bounding surface plasticity model proposed in the literature and adopted in the present study. To increase the overall flexibility and expand the modelling capabilities of the constitutive model, two modifications are introduced to its formulation. Attention is subsequently given to its implementation into the finite element code FEMEPDYN. The operations required in each step of the stress integration scheme are thoroughly described, giving particular emphasis to the operations required by the co-existence of the two yield surfaces of the constitutive model. Validation exercises comprising the simulation of both element laboratory tests and centrifuge experiments and the comparison of the obtained results with those reported in the literature are presented afterwards.

The third and final part of this thesis starts with the calibration of the constitutive model against the results of element laboratory tests performed on Hostun sand during the first stage of the research. Subsequently, the ability of the constitutive model to reproduce the response of Hostun sand measured in the laboratory is explored in detail, enabling to characterise the merits and pitfalls of the constitutive model. Its performance is further evaluated by simulating two dynamic centrifuge experiments presented in the literature concerning the performance of shallow foundations resting on saturated deposits of Hostun sand subjected to dynamic loading causing liquefaction. The obtained results suggest that the numerical tool is able to capture accurately important aspects of the sand-structure interaction observed in the centrifuge experiments, such as the generation of large excess pore pressures in sand induced by the applied dynamic loading and consequent alteration of the input motion due to the reduction of sand's stiffness and increase in material damping, as well as the progressive accumulation of large structural settlement with dynamic loading. Furthermore, the impacts of both densification and closely spaced high-capacity vertical drains on the mitigation of liquefaction effects seem also adequately captured in the numerical analysis.

RESUMO

Os fenómenos associados a liquefação são uma preocupação para as sociedades modernas, nomeadamente quando localizadas em zonas sísmicas ativas, devido ao seu enorme potencial de destruição, capaz de provocar elevados prejuízos económicos, alteração ao normal funcionamento da sociedade e perda de vidas humanas. Apesar do grande desenvolvimento de ferramentas numéricas verificado nos últimos anos ter aumentado as possibilidades do uso do dimensionamento baseado no desempenho das estruturas na prática, este progresso também evidenciou a necessidade do desenvolvimento de modelos constitutivos mais robustos, capazes de simular os mecanismos envolvidos neste tipo de fenómenos. Nesta tese, um modelo baseado na teoria *bounding surface plasticity* é implementado no código de elementos finitos FEMEPDYN, desenvolvido na Universidade de Coimbra, e utilizado para a simulação de fenómenos associados a liquefação induzida por carregamentos cíclicos e observada ensaios elementares de laboratório e ensaios de centrifugadora.

Na primeira parte desta tese, são apresentados os resultados obtidos num extenso programa de ensaios elementares realizados sobre a areia de Hostun, incluindo ensaios de *bender elements* e ensaios triaxiais de compressão e de extensão drenados e não drenados, os quais permitem a caracterização da resposta monotónica da areia de Hostun no domínio das muito pequenas a grandes deformações. Os efeitos do índice de vazios, do estado de tensão na consolidação das amostras e da trajectória de tensão na resposta medida no laboratório são aí discutidos. Para além disso, é utilizada uma metodologia com um parâmetro de estado em conjunto com conceitos de mecânica dos solos de estado crítico para caracterizar estados distintos da resposta de areias, nomeadamente os relativos a instabilidade em condições não drenadas, a transformação de fase, ao valor de pico do rácio de tensão e ao estado crítico. As características da relação entre o estado de tensão e a dilatância de areias são também investigadas. Para complementar, são utilizados resultados obtidos em ensaios triaxiais cíclicos em condições drenadas e não drenadas sobre a areia de Hostun para caraterizar os aspectos principais da sua resposta cíclica, incluindo a redução da rigidez secante ao corte acompanhada do aumento do amortecimento com o nível de extensão, a geração de pressões de água nos poros com o carregamento cíclico e a resistência cíclica não drenada.

A segunda parte da tese inclui uma descrição detalhada do modelo baseado na teoria *bounding surface plasticity* proposto na bibliografia e adotado neste estudo. Para aumentar a versatilidade do modelo, assim como as suas capacidades de modelação, são introduzidas duas modificações na sua formulação. De seguida, apresenta-se a implementação do modelo no código de elementos finitos FEMEPDYN. As operações necessárias em cada passo do método de integração são descritas em detalhe, dando especial atenção às operações requeridas pela coexistência de duas superfícies de cedência no modelo constitutivo. São

finalmente apresentados exemplos de validação, incluindo a simulação de ensaios de laboratório elementares e de centrifugadora, comparando-se os resultados obtidos neste estudo com os que estão descritos na bibliografia.

A terceira e última parte da tese começa por descrever a calibração do modelo constitutivo utilizando os resultados dos ensaios de laboratório elementares realizados sobre a areia de Hostun durante a primeira fase do trabalho de investigação. De seguida, a capacidade do modelo para reproduzir a resposta medida no laboratório é explorada em detalhe, permitindo a caracterização das capacidades e limitações do modelo constitutivo. O seu desempenho é posteriormente avaliado através da simulação de dois ensaios dinâmicos de centrifugadora, cujos resultados são apresentados na bibliografia, acerca do desempenho de fundações superficiais assentes em depósitos saturados de areia de Hostun quando sujeitas a ações dinâmicas causando liquefação. Os resultados obtidos sugerem que a ferramenta numérica é capaz de prever, de forma adequada, aspectos importantes da interação solo-estrutura observados nos ensaios de centrifugadora, tais como a geração de pressões de água nos poros elevadas no depósito de areia devido ao carregamento dinâmico e a consequente alteração da acção dinâmica aplicada na base do modelo devido à redução da rigidez ao corte da areia e aumento do amortecimento material, bem como a progressiva acumulação de elevados assentamentos estruturais com o carregamento dinâmico. Para além disso, os impactos da densificação da areia e da introdução de uma malha densa de drenos verticais de alta capacidade na mitigação dos efeitos de liquefação também parecem ser adequadamente simulados na análise numérica.

ACKNOWLEDGMENTS

First and foremost, I would like to thank my three supervisors Dr. Paulo Coelho, Dr. José Grazina and Dr. David Taborda for their guidance, constant support and availability to discuss every detail of this work. From my perspective, they are great examples of dedicated Professors and I feel very fortunate for the opportunity I had to be supervised by them.

I would also like to express my gratitude to other people, who contributed to the research presented in this thesis. First, I would like to thank my PhD colleague Andreia Silva Marques for allowing the use in this research of results of dynamic centrifuge experiments performed in the Turner Beam Centrifuge facility at the Schofield Centre, University of Cambridge, United Kingdom. Additionally, I would like to thank our laboratory technician, Mr. José António, who assisted me constantly during the laboratory testing phase, Vania Marques, who helped me in getting familiar with the triaxial testing facilities, and all the colleagues with whom I had the opportunity to share many (sometimes unforeseen) great moments during the time I spent in the laboratory, namely Rui Silveira, Cristina Danisi and Dr. Luís Araújo Santos. Still regarding laboratory testing, I would like to highlight the support of Dr. António Pedro in the performance of the bender element tests, by helping me setting up the required equipment and connections, getting me familiar with bender element testing and available methods for the interpretation of the obtained results. His availability to discuss the obtained results is also deeply appreciated.

I would also like to acknowledge the access to biaxial and triaxial test data on Hostun sand obtained as part of the research programme undertaken in Grenoble Institute of Technology, France, kindly granted by Professor Jacques Desrues. Moreover, I would like to thank Dr. João Camões, who helped me with literature review on experimental data on Hostun sand obtained at French Institutions. His availability to discuss geomechanics, his interest in my research and his friendship are also highly appreciated.

In addition, I would like to acknowledge the financial support provided by FCT – *Fundação para a Ciência e Tecnologia*, Portugal (grant SFRH/BD/84656/2012), as part of the financial *Programa Operacional Potencial Humano* (POPH).

Being part of the Geotechnical group of the department of Civil Engineering of the University of Coimbra was undoubtedly an enormous privilege. I am extremely grateful to Professor Jorge Almeida e Sousa, who fostered, in first place, my interest in Soil Mechanics and has always been fully supportive to me. Similarly, I would like to thank Prof. António Alberto, Professor Luís Lemos, Prof. Paulo Pinto and Professor Paulo da Venda Oliveira for their friendship and interest in my research.

I am also grateful for the work experiences that I have had so far in my life. In particular, I would like to thank my former manager Ana Quintela, who gave me invaluable insight into Soil Mechanics. My former colleagues at Tetraplano also have a special place in my heart. In addition, I would like to thank Fredrik Clifford and Vedran Skopal for their encouragement and discussions on geotechnical design practices during the time I worked at WSP. More recently, I had the opportunity to join Plaxis and I am very grateful for the friendship and incentive to finish this thesis received from my managers Dennis Waterman, Erwin Beernink, Micha van der Sloot and Stefanos Papavasileiou, as well as my colleagues, particularly Dimitris Kargias, Ferdinando Marinelli, Georgia Paterianaki, Ilaria Del Brocco, Pedro Reis and Vasileios Basas. In addition, I would like to thank Professor Ronald Brinkgreve, Dr. Richard Witasse, Dr. Sandro Brasile and, particularly, Dr. Paul Bonnier for the availability to discuss aspects of finite element method, numerical algorithms and constitutive modelling.

It would be difficult to name, and properly acknowledge, the contribution of all my friends and family members. I hope that they all know how thankful I feel for having them in my life. I believe, nevertheless, that I cannot finish this section without expressing my immense gratitude to my closest family. To my mother Berta and my father Fernando for their unconditional and warm care, trust and inspiration. To my sister Ana and my brother-in-law Alex, my nephew Miguel and niece Marta, my brother João, my sister- and brother-in-law Teresinha and Pedro, the little niece on her way Gabriela, my brother- and sister-in-law Zé Manel and Joana, and my parents-in-law Álvaro and Lola, I would like to thank them all for the happiness and affection that we genuinely share. Finally, I am hugely thankful to my wife, Ana Laura, for her love, care, companionship and faith. Indeed, the greatest personal achievement of my research consisted of meeting Ana Laura at the university in the course of this research. Perhaps, I can mention that I put all my love in this research.

TABLE OF CONTENTS

LIST OF FIGURES

LIST OF TABLES

LIST OF SYMBOLS

Abbreviations and acronyms

ALERT	Alliance of laboratories in Europe for education, research and technology
ASTM	American society for testing and materials
BE	Bender element
BSP	Bounding surface plasticity
BSPM	Bounding surface plasticity model
B&W SPC	Bishop and Wesley (1975)'s stress path cell
CANLEX	Canadian liquefaction experiment
CFL	Courant–Friedrichs–Lewy condition
CRR	Cyclic resistance ratio
CRSP	Constant rate of strain pump
CS	Critical state
CSL	Critical state line
CSR	Cyclic stress ratio
CSSM	Critical state soil mechanics
CWRU	Case Western Reserve University
DCT	Drained cyclic triaxial
DMTC	Drained monotonic triaxial compression
DMTE	Drained monotonic triaxial extension
DOF	Degree of freedom
EMTS	Electro-mechanical triaxial system
ENPC	*École Nationale des Ponts et Chaussées*
ENTPE	*École Nationale des Travaux Publics de l'État*
FD	Frequency domain
FE	Finite element
FEMEPDYN	Finite element code developed at the University of Coimbra (Almeida e Sousa, 1999; Grazina, 2009)
HS	Hostun sand
IC	Isotropic consolidation; isotropically consolidated
ICFEP	Imperial College Finite Element Program (Potts and Zdravković, 1999; Taborda, 2011)
INPG	Grenoble Institute of Technology
K0C	Anisotropic (i.e. K_0) consolidation; anisotropically consolidated

LBS	Leighton Buzzard sand
LVDT	Linear variable displacement transducer
MC	Mohr-Coulomb
MEMS	Microelectromechanical system measuring acceleration
NS	Nevada sand
OS	Ottawa sand
p↓	Decreasing mean stress
p↑	Increasing mean stress
PSD	Particle size distribution
PSRS	Peak stress ratio state
PT	Phase transformation
PTL	Phase transformation line
PTS	Phase transformation state
QSS	Quasi-steady state
RTOL	Reversal tolerance
SAM	Stored angular momentum
SDOF	Single degree of freedom
SERIES	Seismic engineering research infrastructures for European synergies
SR	Shear reversal
SSTOL	Sub-stepping tolerance
TA	Transnational access
TC	Triaxial compression
TD	Time domain
TE	Triaxial extension
TS	Toyoura sand
TUD	Technical University of Dresden
UC	University of Coimbra
UCam	University of Cambridge
UCT	Undrained cyclic triaxial
UIS	Undrained instability state
UMTC	Undrained monotonic triaxial compression
UMTE	Undrained monotonic triaxial extension
US	University of Stuttgart
USCS	Unified soil classification system
VELACS	Verification of liquefaction analysis by centrifuge studies
YTOL	Yield tolerance

Greek alphabet

α	Angle of the major principal effective stress to the axis of the sample; parameter defining the contribution of the tangent elastic shear modulus to the plastic hardening modulus associated with the primary yield surface for the present BSPM; parameter of the excess pore water pressure models proposed by Seed *et al.* (1975b), Booker *et al.* (1976), Nemat-Nasser and Shokooh (1979) and Berrill and Davis (1985); parameter of the Newmark and α-generalised time-integration schemes
α_f	Parameter of the α-generalised time-integration scheme defining the instant within the time increment for which damping and stiffness terms are evaluated
α_m	Parameter of the α-generalised time-integration scheme defining the instant within the time increment for which inertia term is evaluated
$\boldsymbol{\alpha}$	Back-stress tensor (i.e. tensor defining the axis of the primary yield surface) for the present BSPM
β	Parameter defining the non-linearity of the function introducing the influence of the distance from the current effective stress point to the boundary surface on the plastic hardening modulus associated with the primary yield surface for the present BSPM; parameter of the Newmark and α-generalised time-integration schemes; parameter of the excess pore water pressure models proposed by Nemat-Nasser and Shokooh (1979) and Berrill and Davis (1985)
γ	Unit weight; shear strain; shear strain amplitude; parameter defining the influence of the void ratio on the plastic hardening modulus for the present BSPM
γ_1	Parameter defining the shear strain limit for the reduction of the elastic tangent shear modulus of the present BSPM
γ_{max}	Maximum shear strain amplitude
γ_{sat}	Saturated unit weight
γ_{tl}	Linear cyclic threshold shear strain (Vucetic, 1994)
γ_w	Unit weight of water (considered equal to 9.81 kN/m^3 for 1 g conditions)
δ	Increment
δW	Energy dissipated per unit value per loading cycle
Δ	Variation
ΔL	Element size
Δq	Deviatoric stress oscillation
Δt	Time step
Δu	Evolution of excess pore (water) pressure
ΔW	Energy dissipated per unit volume during a given stress-strain loop
ε	Strain, strain amplitude
$\boldsymbol{\varepsilon}$	Strain tensor

ζ	Parameter defining the influence of the initial principal effective stress on the shearing-induced fabric index for the present BSPM; reduction factor of the modified forward Euler integration scheme
η	Stress ratio for triaxial loading conditions: $\eta = q/p'$
θ	Lode's angle (third invariant of the stress tensor)
κ	Parameter defining the non-linearity of the elastic tangent shear modulus for the present BSPM
μ	Non-linearity of the effect of the current mean effective stress on the plastic hardening modulus associated with the primary yield surface
ν	Poisson's ratio
λ	Slope of the CSL in the void ratio – mean effective stress space; wavelength
λ_{min}	Minimum wavelength
μ	Parameter defining the non-linearity of the function introducing the effect of the current mean effective stress on the plastic hardening modulus associated with the primary yield surface for the present BSPM
ν	Poisson's ratio
ξ	Parameter defining the curvature of CSL in the $e - p'$ space for the present BSPM; damping ratio; reduction factor
ρ	Mass density
ρ_∞	Spectral radius at infinity
σ	Total stress
σ'	Effective stress
$\boldsymbol{\sigma'}$	Effective stress tensor
τ	Shear stress
τ	Shear stress
ϕ	Friction angle (i.e. slope of the Mohr-Coulomb failure criterion)
ϕ'^{c}_{c}	Critical-state friction angle in TC
ϕ'^{c}_{e}	Critical-state friction angle in TE
χ	Parameter of the excess pore water pressure models proposed by Nemat-Nasser and Shokooh (1979)
χ^{e}_{ref}	Distance between the current deviatoric strain and the deviatoric strain at last shear reversal point for the present BSPM
ψ	State parameter (Been and Jefferies, 1985)

Roman alphabet

a	Acceleration; Scalar defining the inherent fabric anisotropy tensor for the present BSPM
a_1	Parameter defining the maximum reduction of the elastic tangent shear modulus for the present BSPM

$\boldsymbol{a}$	General tensor
A	Plastic hardening modulus for the present BSPM; Cross-sectional area
A_0	Dilatancy coefficient for the present BSPM
A_F	Scalar-valued anisotropic state variable for the present BSPM
b	Intermediate principal effective stress ratio
c	Ratio between the value of a quantity in triaxial extension to its value in triaxial compression
c'	Apparent cohesion (i.e. intercept at the origin of the Mohr-Coulomb failure criterion)
C	Parameter defining the rate of evolution of the deviatoric component of the shearing-induced fabric tensor for the present BSPM
C_c	Coefficient of curvature
C_g	Parameter defining the elastic shear modulus at small strains for the present BSPM
C_u	Coefficient of uniformity
d	Derivative; displacement
d^b	Distance from the current effective stress point to the bounding surface for the present BSPM
d^b_{ref}	Diameter of the bounding surface along the direction of the deviatoric loading direction tensor in the deviatoric plane for the present BSPM
d^c	Distance from the current effective stress point to the critical surface for the present BSPM
d^c_{ref}	Diameter of the critical surface along the direction of the deviatoric loading direction tensor in the deviatoric plane for the present BSPM
d^d	Distance from the current effective stress point to the dilatancy surface for the present BSPM
D	Dilatancy coefficient for the present BSPM
D_{10}	Grain sizes corresponding to 10 % of material passing through sieves of ASTM series
D_{30}	Grain sizes corresponding to 30 % of material passing through sieves of ASTM series
D_{50}	Grain sizes corresponding to 50 % of material passing through sieves of ASTM series (i.e. mean grain size)
D_{60}	Grain sizes corresponding to 60 % of material passing through sieves of ASTM series
D_r	Relative density
$\boldsymbol{D}$	elastic stiffness tensor (also referred to as elastic constitutive matrix)
$\boldsymbol{D^{ep}}$	Elasto-plastic stiffness tensor (also referred to as elastic-plastic constitutive matrix)
e	Void ratio
e_{cs}	Void ratio at critical state
$(e_{cs})_A$	Interception of the CSL with the p'-axis in the void ratio – mean effective stress space as a function of the scalar-valued anisotropic state variable for the present BSPM
$(e_{cs})_{ref}$	Interception of the CSL with the p'-axis in the $e - p'$ space for the present BSPM

e_{lim}	Lower limit of the void ratio influence on the plastic hardening modulus associated with the primary yield surface
$\boldsymbol{e}$	Deviatoric strain tensor
E	Error
f	Frequency; function
f_g	Coefficient of interaction (i.e. ratio of the maximum shear stress developed in a soil–geosynthetic interface to the maximum shear stress developed in soil)
f_p	Isotropic component of the shearing-induced fabric tensor
$f(e)$	Function defining the influence of the void ratio on the small-strain shear modulus
$\boldsymbol{f}$	Deviatoric component of the shearing-induced fabric tensor for the present BSPM
F	Yield function
$\boldsymbol{F}$	Shearing-induced fabric tensor for the present BSPM
$\boldsymbol{F_A}$	Inherent fabric anisotropy tensor for the present BSPM
g	Acceleration of gravity (considered equal to 9.81 m/s^2); interpolation function in the deviatoric plane for the present BSPM
G	Shear modulus
G_{max}	Maximum (i.e. small-strain) shear modulus
G_{min}	Lower limit for the tangent shear modulus for the present BSPM
G_s	Density of solid particles
h	Plastic hardening modulus multiplier
h_0	Plastic hardening modulus constant for the present BSPM
h_A	Component of the plastic hardening modulus related to the inherent fabric anisotropy tensor for the present BSPM
h_b	Component of the plastic hardening modulus related to the inherent fabric anisotropy tensor for the present BSPM
h_e	Component of the plastic hardening modulus related to the void ratio for the present BSPM
h_f	Component of the plastic hardening modulus related to the shearing-induced fabric tensor for the present BSPM
$h_{f,min}$	Lower limit for h_f for the present BSPM
$h_{f,max}$	Upper limit for h_f for the present BSPM
h_g	Component of the plastic hardening modulus related to the elastic tangent shear modulus for the present BSPM
H	Thickness of a deposit; height; shearing-induced fabric index for the present BSPM
H_0	Shearing-induced fabric index constant for the present BSPM
H_{max}	Upper limit for the fabric index
i	Hydraulic gradient
$\boldsymbol{I}$	Identity tensor

$\boldsymbol{j}$	Generic set of elastic state parameters
k	General integer; hydraulic conductivity; parameter defining the non-linearity of the evolution of the small-strain shear modulus with OCR;
k_A	Parameter defining the influence of inherent fabric anisotropy on the plastic hardening modulus for the present BSPM
k_c^b	Effect of the state parameter on the peak stress ratio in triaxial compression
k_c^d	Effect of the state parameter on the stress ratio at phase transformation in triaxial compression
k_e^b	Effect of the state parameter on the peak stress ratio in triaxial extension
k_e^d	Effect of the state parameter on the stress ratio at phase transformation in triaxial extension
$\boldsymbol{k}$	Generic set of state parameters related to the yield function (i.e. hardening parameters)
K	Bulk modulus
K_0	Coefficient of earth pressure at rest (i.e. ratio of the horizontal to the vertical effective stress)
K_n	Normal stiffness of the interface element
K_s	Shear stiffness of the interface element
L	Length; travel distance of a body wave
L_{BE}	Bender element protrusions into the sample
m	Opening of the primary yield surface
m_g	Parameter defining the function of the void ratio to the evolution of the small-strain shear modulus with the mean effective stress
$\boldsymbol{m}$	Generic set of state parameters related to the gradient of the plastic potential
M_c^c	Critical state strength in triaxial compression for the present BSPM
M_e^c	Critical state strength in triaxial extension
n	General integer
n_{elem}	Number of elements
n_g	Parameter defining the non-linearity of the evolution of the small-strain shear modulus with the mean effective stress
n_{inc}	Number of increments
n_k	Parameter of the non-linear hydraulic model defining the non-linearity of the evolution of the hydraulic conductivity with the excess pore pressure ratio
n_{steps}	Number of steps
$\boldsymbol{n}$	Unit radial stress tensor (also termed as deviatoric loading direction tensor) for the present BSPM
N	Number of loading cycles
N_{liq}	Number of loading cycles required to the onset of liquefaction
OCR	Overconsolidation ratio

p	Mean stress (first invariant of the stress tensor)
p'	Mean effective stress (first invariant of the effective stress tensor)
p'_{min}	Lower limit for the mean effective stress for the present BSPM
p'_{ref}	Reference pressure (typically assumed as equal to the atmospheric pressure, with a value of about 101.3 kPa)
p'_{YS}	Parameter defining the position of the secondary yield surface (i.e. lower limit value for the mean effective stress) for the present BSPM
PI	Plastic index
$\boldsymbol{P}$	Plastic potential
q	Deviatoric stress under triaxial loading conditions; uniformly distributed load magnitude discharge capacity
r_u	Excess pore (water) pressure ratio
r_u^*	Parameter of the non-linear hydraulic model defining the value of r_u corresponding to the maximum permeability
$\boldsymbol{r}$	Deviatoric stress ratio tensor for the present BSPM
$\bar{\boldsymbol{r}}$	Radial tensor for the present BSPM
R	Relative error; reduction to the sub-step strain increment
$\boldsymbol{s}$	Deviatoric stress tensor
t	Time; thickness
t_{arr}	Time of arrival
t_{lag}	Time lag
T	Pseudo time; period
u	Pore pressure
v	Velocity
v_p	Compression wave velocity
v_s	Shear wave velocity
V	Volume
W	Energy
$W_{e,max}$	Maximum elastic stored energy

Subscripts

0	Initial value
1	Along the major principal direction; related to the primary yield surface of the present BSPM
2	Along the intermediate principal direction; related to the secondary yield surface of the present BSPM
3	Along the minor principal direction

a	Along the axial direction
av	Average value
c	In triaxial compression
cell	Related to the triaxial cell (laboratory testing)
cons	Value immediately after consolidation
cs	Critical state value
da	Double amplitude
e	In triaxial extension; elastic
eq	Equivalent
f	Fluid phase
i	Related to an interface element (numerical modelling)
init	Initial (i.e. immediately after sample preparation)
liq	Value corresponding to the onset of liquefaction
lim	Limit value
m	Related to the membrane
max	Maximum value
min	Minimum value
n	General integer; normal
p	Peak value
q	Deviatoric value
r	Along the radial direction
red	Reduced value
ref	Reference value
res	Residual value (i.e. corresponding to a null shear stress)
s	Solid phase; shear
sa	Single amplitude
sec	Secant value
ss	Sub-step
tan	Tangent value
v	Volumetric; vertical
w	Related to water
x	Along the x-axis
y	Along the y-axis
z	Along the z-axis

Superscripts

‘	Effective stress
*	Modified value
b	Related to the bounding surface of the present BSPM
c	Related to the critical surface of the present BSPM
d	Related to the dilatancy surface of the present BSPM
e	Elastic
ep	Elasto-plastic
new	New value (to be used in the following sub-step increment)
p	Plastic
SR	Value at the last shear reversal for the present BSPM
UI	Related to undrained instability state

Chapter 1 INTRODUCTION

1.1 Background

The term “liquefaction” has been employed to designate a variety of distinctive, though related phenomena, involving the generation of excess pore water pressure in saturated soils under undrained or partially undrained conditions, either due to static and/or dynamic loading.

According to Kramer (1996), liquefaction-related phenomena can be essentially categorised into “flow liquefaction” and “cyclic mobility”. The former phenomenon occurs when a static or dynamic solicitation brings the soil to an unstable state, from which its shear strength suddenly reduces to a magnitude smaller than that required to maintain static equilibrium. Once triggered, the produced flow failure is driven by static shear stresses, with a rapid development of large deformations. Figure 1.1a illustrates the occurrence of this phenomenon during an undrained element laboratory test. It is apparent that, although the unstable state may be induced by either monotonic or cyclic loading (point B or D, respectively), once such point is reached, a monotonic decrease of the deviatoric stress is observed (up to point C), concurrently with a rapid development of large deformations. Since failure is induced by monotonic shear stresses, this phenomenon has been also termed as “static liquefaction” by some authors (e.g. Jefferies and Been, 2006). As highlighted by these authors, although failures induced by this phenomenon are typically catastrophic, not only due to its sudden initiation, but also due to the high speed at which failure progresses and large distances over which liquefied soil often moves, its occurrence has been only observed for soils in very loose states.

Conversely, cyclic mobility (often also referred to as “cyclic softening”, “cyclic liquefaction” or simply “liquefaction”) is characterised by static shear stresses that are lower than the shear strength of the liquefied soil. Eventual periods of instability, characterised by effective stresses close to zero, and continuous accumulation of permanent deformations caused by both static and cyclic shear stresses are typically observed during the occurrence of this type of phenomenon (Kramer, 1996). This is illustrated in Figure 1.1b, where the application of cyclic loading results in a gradual increase in excess pore water pressures and, consequently, reduction of soil’s strength and stiffness to very low values and accumulation of large deformations.

On gently sloping ground or flat ground adjacent to water, cyclic mobility may result in “lateral spreading”, which may severely damage embankments, bridges, buried lifelines and waterfront structures (e.g. Okamura *et al.*, 2001). In level ground deposits of saturated sand, due to the absence of static horizontal shear stresses, which could induce significant lateral

deformations, a chaotic ground movement is typically observed (Kramer, 1996). Moreover, in such case (often termed as "level-ground liquefaction"), large surface settlements are commonly observed concurrently with the application of cyclic loading (typically seismically-induced), as well as after its cessation, as a result of the upwards flow of water resulting from the migration and/or dissipation of excess pore water pressures (Coelho, 2007). Note that, although effects of brittle failures associated with flow liquefaction are usually far more severe – as illustrated by the flow-liquefaction type of failure of Fort Peck Dam, in Canada, in 1938 (e.g. Jefferies and Been, 2006), and more recently in 2016 and 2019, respectively, of Fundão and Brumadinho tailing dams, in Brazil (Morgenstern *et al.*, 2016; Robertson *et al.*, 2019) – , cyclic mobility can occur in a wider range of soils and site conditions than flow liquefaction. Moreover, note that, in the present thesis, the term liquefaction will be used to include both flow liquefaction and cyclic mobility.

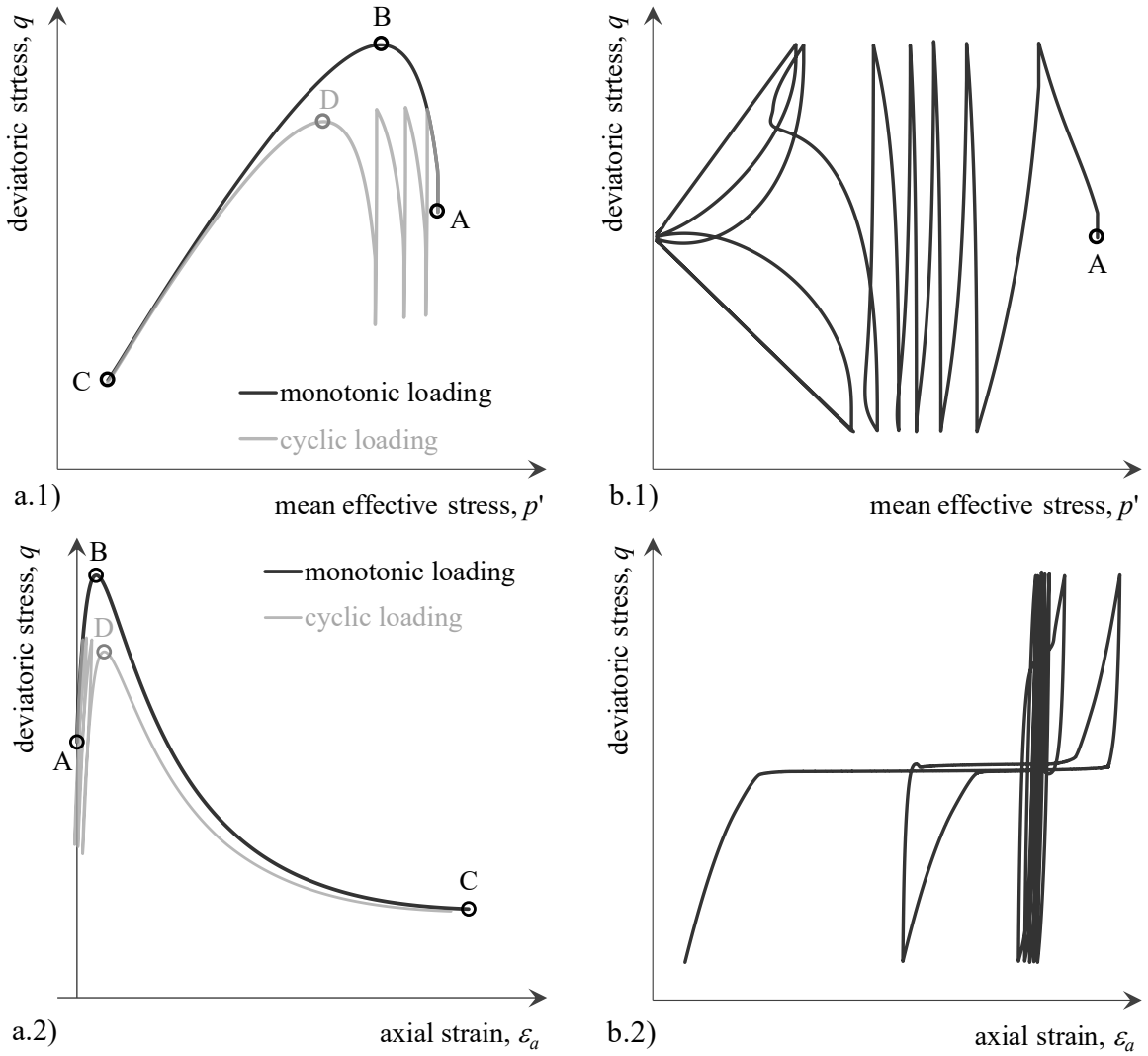

Figure 1.1 – Illustration of liquefaction-related phenomena (adapted from Kramer, 1996): (a) flow liquefaction and (b) cyclic mobility.

Awareness of the severe damaging nature of liquefaction-related phenomena has mainly developed from earthquake-induced failures developed during the major events occurred in

March of 1964 in Alaska, U.S., and June of 1964 in Niigata, Japan (Ishihara, 1993; Towhata, 2008). As a consequence of these strong motion events, formation of sand boils, subsidence of wide areas and tilting and collapse of structures built-on shallow foundations (Figure 1.2), among other occurrences, were observed, resulting in great economic losses and causing long-term disruption of society.

(a) (b)

Figure 1.2 – Illustration of liquefaction-induced damage during the 1964 Niigata earthquake (photos from National Geophysical Data Centre, U.S. Department of Commerce): (a) collapse of the Showa Bridge and (b) tilting of Kawagishi-Cho apartment buildings.

Despite the research effort made since the occurrence of those events to understand the fundamental mechanisms of liquefaction-related phenomena, to develop tools to evaluate the liquefaction potential of a given site and to enhance the use of different techniques to mitigate the risk and consequences of the phenomena, liquefaction-induced damage has been recurrently observed in major earthquakes around the world in the last decades. Remarkable examples of liquefaction-induced damage include post-earthquake failure of Lower San Fernando Dam in 1971, as well as many other earthquake-induced liquefaction events, such as: the 1983 Nihonkai-Chubu earthquake, the 1989 Loma Prieta earthquake, the 1995 Kobe earthquake, the 1999 Izmit earthquake, the 1999 Chi-Chi earthquake, the 2010 Canterbury earthquake, the 2011 Christchurch earthquake and the 2011 Great East Japan (or Tōhoku) earthquake. As highlighted by Coelho (2007), this may indicate that understanding of liquefaction is still limited and/or design procedures and mitigation technique are not properly applied.

Scientific understanding on the conditions required to the onset of flow liquefaction and cyclic mobility, their development and effects, as well as mitigation, was initially developed based on undrained element laboratory tests (e.g. Seed and Lee, 1966; Peacock and Seed, 1968; Castro, 1969; Seed and Idriss, 1970a; Finn *et al.*, 1971; Ishihara and Li, 1972; Lee and Albaisa, 1974; De Alba *et al.*, 1975; Ishihara and Yasuda, 1975; Sladen *et al.*, 1985; Tatsuoka *et al.*, 1986a; Toki *et al.*, 1986; Nagase and Ishihara, 1988; Alarcon-Guzman *et al.*, 1988). More recently, dynamic centrifuge experiments have contributed to the understanding of mechanisms governing the field performance, while also providing data to the calibration, verification and further development of numerical tools. In particular, it is worth mentioning the several large international collaborative research projects using this modelling technique

undertaken during the last three decades, such as the VErification of Liquefaction Analysis by Centrifuge Studies (VELACS) (Arulanandan and Scott, 1993) and the CANadian Liquefaction EXperiment (CANLEX) (Byrne *et al.*, 2000; Robertson *et al.*, 2000), among others. Moreover, it is of particular relevance for the present study the research projects undertaken at the University of Cambridge, United Kingdom (U.K.), where dynamic centrifuge experiments were performed to assess the performance of shallow foundations built on liquefiable sand deposits when subjected to earthquake loading (Coelho, 2007; Marques *et al.*, 2014a). As detailed later, the results of two of these dynamic centrifuge experiments were employed as benchmark for the evaluation of the modelling capabilities of an advanced constitutive model implemented into a Finite Element (FE) code during the research study presented in this thesis.

Naturally, the adequate simulation of complex dynamic phenomena, such as those involving liquefaction, requires the use of advanced constitutive models capable of simulating the highly non-linear soil response observed under such situations. Among the several frameworks existing in the literature, two-surface plasticity is certainly noteworthy, given the great number of models based on this framework recently proposed in the literature (e.g. Manzari and Dafalias, 1997; Papadimitriou and Bouckovalas, 2002; Dafalias and Manzari, 2004; Dafalias *et al.*, 2004; Taiebat and Dafalias, 2008; Loukidis and Salgado, 2009; Taborda *et al.*, 2014; Woo and Salgado, 2015). This framework uses the distance from the current stress point to its projection on the so-called bounding and dilatancy surfaces to quantify the plastic modulus and the flow rule, respectively. Moreover, the concept of the state parameter (Been and Jefferies, 1985) is explicitly used in conjunction with the principles of Critical State Soil Mechanics (CSSM), as established by Schofield and Wroth (1968), to predict accurately the occurrence of key features of the response of soil using a single set of model parameters. Indeed, these constitutive models have been successfully applied to the simulation of cyclic soil response under general loading conditions (e.g. Taiebat *et al.*, 2007; Andrianopoulos *et al.*, 2010; Taborda, 2011; Tsaparli *et al.*, 2016).

1.2 Finite element code FEMEPDYN

The main numerical tool used during the research presented in this thesis was the finite element (FE) code FEMEPDYN, which has been continuously developed at the University of Coimbra over the last two decades (Almeida e Sousa, 1999; Venda Oliveira, 2000; Grazina, 2009). In particular, the last author developed a dynamic (DYN) module, which, in conjunction with the main code (FEMEP), allows for the simulation of dynamic response of both dry (one-phase) and saturated (two-phase) materials, in the latter case considering a fully coupled flow-deformation response. More specifically, a complete formulation "$d^s - d^f - u$" (where "d" and "u" designate displacement and pore pressure degrees of freedom, respectively, while the superscripts "s" and "f" designates solid and fluid phases, respectively) of the equation of motion is implemented into the FE code, meaning that the displacement of both

solid and fluid phases and pore pressure are computed concurrently (Zienkiewicz *et al.*, 1999; Grazina, 2009). Note that this formulation is often referred to as "*u – w – p*" (Zienkiewicz *et al.*, 1980). Moreover, several robust time-integration schemes are implemented into the FE code, including the generalised-α algorithm (Chung and Hulbert, 1993), which is capable of filtering the high-frequencies modes of vibration without affecting significantly the low frequency response (Grazina, 2009). The fundamental aspects behind the formulation implemented into FEMEPDYN, as well as the basic aspects concerning the validation of the formulation to the simulation of dynamic soil response are comprehensively presented in Grazina (2009) and, therefore, omitted from this thesis. In addition, a detailed description about the structure of the code and its integration with other tools (such as pre- and post-processors) can also be found in Grazina (2009). Therefore, only alterations performed to the code will be presented in this thesis.

The dynamic capabilities added by Grazina (2009) were applied to the simulation of the performance of retaining structures built on sand deposits under dynamic loading. While highlighting the potential of the code to replicate the response of saturated porous media under dynamic loading, the obtained results revealed that the elasto-plastic constitutive models available in FEMEPDYN could not capture accurately key aspects of the response of sand under dynamic loading, such as the generation of large excess pore water pressures with dynamic loading, the strong reduction in stiffness and concurrent increase in hysteretic damping, the occurrence of phase transformation and onset of liquefaction.

1.3 Main objective and scope of research

The main objective of the research was to expand the modelling capabilities of a finite element (FE) code developed at the University of Coimbra in order to reproduce accurately liquefaction-related phenomena observed in centrifuge experiments.

With this main objective, the research programme was essentially divided into three parts. In the first part, an extensive element laboratory testing programme was carried out on Hostun sand. Besides the identification of the key aspects of both monotonic and cyclic responses of sand, this experimental programme intended to provide reliable data for the calibration of the constitutive model subsequently employed in the numerical simulation of the dynamic centrifuge experiments. In fact, as explained in more detail in the following section, a series of dynamic centrifuge experiments concerning the response of shallow foundations built on saturated deposits of Hostun sand when subjected to dynamic loading causing liquefaction were performed at the Schofield Centre, University of Cambridge, U.K., as part of a collaboration between the University of Cambridge and the University of Coimbra. Given the lack of field monitoring data concerning liquefaction-related phenomena, as well as difficulties inherent to the characterisation of natural/intact sandy soils, the availability of centrifuge test data was considered particularly valuable for the present research work. Therefore, a significant effort was made to obtain a large amount of reliable element

laboratory test data, which was used as reference for the calibration of the constitutive model and, consequently, bridged the gap between centrifuge and numerical modelling.

The second part of the research consisted of the identification of an advanced constitutive model capable of simulating key aspects of cyclic sand response. Among the vast number of constitutive models available in the literature, a two-surface bounding surface plasticity model (BSPM) initially formulated by Manzari and Dafalias (1997) and later extended by Papadimitriou and Bouckovalas (2002) and Taborda *et al.* (2014) was chosen, due to its extensive ability to simulate cyclic sand response under a wide range of strain amplitudes. Moreover, this constitutive model is characterised by a great flexibility and by having a modular structure (Taborda *et al.*, 2014), allowing for its extension with relatively low effort. In effect, this aspect was considered important in the present work, since an inherent fabric anisotropy formulation proposed in the literature (Williams, 2014) was added to the formulation of the constitutive model to improve its ability to simulate the response of sand under loading conditions other than triaxial compression. Having selected the constitutive model, the following task comprised its implementation into FEMEPDYN. A robust explicit integration scheme with automatic sub-stepping and error control was selected, due to its ability to deal with the integration of the highly non-linear elasto-plastic constitutive models. Subsequently, the implementation was extensively validated by comparing the results of simulations of element laboratory tests and centrifuge experiments obtained by the newly implemented constitutive model with those published in the literature (Taborda, 2011; Williams, 2014).

The third part of the research work focused on the characterisation of the ability of the constitutive model to replicate important aspects of the monotonic and cyclic response of Hostun sand. Specifically, after calibration of the constitutive model for Hostun sand against the element laboratory test data obtained in the first part of this research, its ability to replicate element laboratory test results was firstly examined. Subsequently, the performance of the constitutive model was investigated in the context of boundary-value problems. This included the numerical simulation of two dynamic centrifuge experiments concerning sand-structure interaction and the occurrence of liquefaction-related phenomena under dynamic loading.

1.4 Synergies with other research programmes

As part of a Seismic Engineering Research Infrastructures for European Synergies (SERIES) Transnational Access Use Agreement, a dynamic centrifuge testing programme was undertaken by the PhD candidate Andreia Silva Marques using the Turner Beam Centrifuge facility at the Schofield Centre, University of Cambridge, U.K. More specifically, following the previous research work developed by Coelho (2007) in this field, this study was designed to assess the influence of the bearing pressure induced by the shallow foundation in the underlying Hostun sand deposit on the performance of the sand-structure system, the

potential interaction effects between neighbouring shallow foundations and the efficiency of different techniques to the mitigation of liquefaction effects: narrow densified zones and their combination with high-capacity vertical drains. As detailed in Coelho *et al.* (2010) and Marques *et al.* (2014a), the research project aimed at enhancing the understanding of the fundamental mechanisms governing the performance of neighbouring shallow foundations resting on sand deposits under dynamic loading causing liquefaction, providing insight into the most effective liquefaction measures and assisting in the development of numerical tools capable of reproducing the phenomena observed in this type of problems. This last point is undoubtedly of great importance, since the development of robust numerical tools can contribute to broaden the use of a performance-based design and risk analysis in current geotechnical engineering practice and, therefore, to reduce the vulnerability of the society to this type of phenomena (Coelho *et al.*, 2017). Furthermore, after properly validated and calibrated, numerical tools can be used to extend the experimental findings and, therefore, to study the applicability and efficiency of innovative solutions.

The accurate numerical simulation of the response observed in centrifuge experiments requires, however, the availability of reliable experimental data on the materials used in those experiments. This means that, by providing reliable data for the calibration of constitutive models, element laboratory testing is a fundamental tool to bridge the gap between centrifuge and numerical data. With this objective, and given the time and funding limitations, a collaboration was established between the present PhD research programme and the PhD research programme undertaken by Andreia Silva Marques. While an extensive element laboratory testing programme on Hostun sand was carried out by the author, centrifuge experiments were performed at the University of Cambridge by Andreia Silva Marques (Marques *et al.*, 2012a, 2012b, 2012c, 2014a, 2014b, 2014c, 2015). The obtained sets of experimental data were subsequently shared between both authors, with different numerical tools being subsequently used by the authors to simulate the dynamic centrifuge experiments.

1.5 Layout of the thesis

This thesis is essentially composed of three different parts, each one describing different stages of the research programme. The first part comprises Chapter 2 and Chapter 3, which present, respectively, the results of the element laboratory tests performed to characterise the monotonic and cyclic responses of Hostun sand. The second part, consisting of Chapter 4 and Chapter 5, includes a comprehensive description of the selected constitutive model, as well as of the numerical algorithms required to implement the constitutive model into the FE code. This part concludes with validation exercises. Finally, the third (and last) part, which includes Chapter 6, Chapter 7 and Chapter 8, details the calibration of the constitutive model against the results of element laboratory tests performed in the first part of this research

programme, followed by the application of the constitutive model to the simulation of both element laboratory tests and centrifuge experiments.

In more detail, Chapter 2 presents the results of bender element tests, as well as of drained and undrained monotonic triaxial compression and extension tests performed on Hostun sand. The tested material, used equipment, experimental procedures and main principles used for the interpretation of the response measured in the laboratory are firstly described. Afterwards, the results of bender element tests are presented, allowing for the characterisation of the maximum (i.e. at very small strains) shear modulus of Hostun sand. The results of the monotonic triaxial compression and extension tests are subsequently presented. A state parameter approach, in conjunction with CSSM concepts, is used to characterise the distinctive states of the monotonic response of Hostun sand within the medium to large strain range are assessed, namely the undrained instability, phase transformation, peak stress ratio and critical states. Furthermore, the experimental data is used to examine a stress-dilatancy relationship often incorporated in constitutive models.

Chapter 3 presents the results of drained and undrained cyclic triaxial tests on Hostun sand. After describing the main patterns of the undrained cyclic response of sand, emphasis is given to the evaluation of the influence of the void ratio, isotropic consolidation stress and cyclic stress ratio on the measured undrained response. The experimental data is subsequently used to evaluate key aspects of the undrained cyclic response of Hostun sand, such as excess pore water pressure build-up with cyclic loading, evolution of both normalised secant shear modulus and damping ratio with strain amplitude, as well as the occurrence of cyclic mobility. Lastly, the results of drained cyclic triaxial tests are presented, allowing for the characterisation of the main patterns of the volumetric strain evolution with cyclic loading.

Chapter 4 describes the two-surface bounding surface plasticity model (BSPM) implemented into FEMEPDYN and used for the simulation of the dynamic centrifuge experiments performed on deposits of Hostun sand. Particular attention is firstly given to the fundamental aspects of the two-surface plasticity framework. Subsequently, the complete set of constitutive equations are presented in the three-dimensional stress space. With the purpose of enhancing the ability of the constitutive model to replicate anisotropic response of sand, an inherent fabric anisotropy formulation proposed in the literature is described and its incorporation into the formulation of the constitutive model is discussed.

Chapter 5 describes the explicit stress point algorithm with automatic sub-stepping and error control used to integrate the constitutive model. After providing an overview of the integration scheme, the operations required in each step of the integration process are detailed, including: the initialisation of the state parameters, the detection of a shear reversal, the computation of an elastic trial, the intersection of the elastic trial effective stress path with one or the two yield surfaces of the constitutive model, the detection of an elasto-plastic unloading, the computation of elasto-plastic response, the activation of an additional yield

surface and the correction of yield surface drift. Subsequently, attention is given to the validation of the implementation. Given the lack of theoretical or analytical solutions, the strategy consists of comparing the results obtained when using FEMEPDYN with those obtained by a validated finite element code. This includes the simulation of different types of element laboratory tests, as well as of two different dynamic centrifuge experiments involving liquefaction-related phenomena, to provide evidence on the successful implementation of the constitutive model and, therefore, to ensure the reliability of the results obtained in the subsequent stages of this research.

Chapter 6 presents the calibration of the constitutive model for Hostun sand against the vast amount of element laboratory test results obtained in the first part of this research. After describing the main aspects of the calibration strategy, its application to Hostun sand is detailed. The model parameters defining clear features of the response of sand, such as stiffness at very small strains and the critical state, are firstly calibrated. Subsequently, the calibration process focuses on the model parameters that, despite having a numerical nature, control known physical features of the response of sand, including the phase transformation state, the peak stress ratio state, the stress-dilatancy relationship and the reduction of shear modulus under shearing. Lastly, trial-and-error procedures are employed to calibrate the model parameters lacking physical meaning, including model parameters related to the plastic hardening modulus, as well as to the shearing-induced fabric and inherent fabric anisotropy components of the constitutive model. Having completed the calibration process, the values obtained for the several model parameters are compared with those proposed in the literature for other sands (Taborda, 2011; Williams, 2014), with the main differences between the sets of model parameters being discussed.

Chapter 7 focuses on the evaluation of the ability of the constitutive model to replicate key aspects of the monotonic and cyclic response of Hostun sand observed in the element laboratory tests. Starting with the application of the constitutive model to the simulation of drained and undrained monotonic triaxial compression and extension tests, the ability of the model to capture the effects of the initial void ratio, effective stress state at consolidation and stress path direction on the modelled monotonic response of sand are firstly assessed. Subsequently, the results of the simulations of undrained and drained cyclic triaxial tests are compared with those registered in the laboratory. Due to its relevance to the study of liquefaction-related phenomena, particular emphasis is given to the evaluation of the ability of constitutive model to reproduce adequately the evolutions of excess pore water pressure, secant shear stiffness and hysteretic damping with cyclic loading observed in the laboratory, as well as to the ability to replicate the undrained cyclic resistance curves inferred from experimental data. In addition, a detailed investigation of the impact of the alterations introduced to the formulation of the constitutive model originally proposed by Taborda (2011) and Taborda *et al.* (2014) on its modelling capabilities is undertaken.

Chapter 8 is dedicated to the characterisation of the performance of the constitutive model in the context of boundary-value problems involving liquefaction-related phenomena. More specifically, the results of two dynamic centrifuge experiments concerning the performance of adjacent shallow foundations resting on saturated deposits of Hostun sand subjected to dynamic loading causing liquefaction are used as benchmark for finite element analyses. An overview of the centrifuge testing programme, including its background, main objectives and most relevant characteristics of the experiments, is firstly provided. Subsequently, focus is given to the first centrifuge experiment. After describing the experimental results, the main aspects of the numerical analysis are detailed and the results of the performed FE analysis are compared with those measured in the experiment. The ability of the numerical tool to replicate the main mechanisms identified in the experiment, including the key aspects of sand-structure interaction under dynamic loading, are assessed. The impact of the hydraulic conductivity of the deposit of Hostun sand on the obtained settlements, particularly in the zone of the model in between the two adjacent foundations, is explored by performing an additional FE analysis considering a simple hydraulic model proposed in the literature, which describes the evolution of the hydraulic conductivity with the excess pore pressure ratio. The second part of this chapter is dedicated to the numerical reproduction of the second centrifuge experiment, which, contrary to the first one, included measures to mitigate the effects of liquefaction. After providing an overview of the experimental results and describing the main aspects of the FE analysis, the numerical results are compared with those registered in the experiment. In this case, particular emphasis is given to the ability of the numerical tool to predict accurately the impact of the liquefaction measures on the performance of the sand-structure system under dynamic loading.

Finally, Chapter 9 summarises the main results and conclusions of the research study presented in the previous chapters and provides guidelines for future research on the numerical simulation of liquefaction-related phenomena.

Two additional aspects are noteworthy. Firstly, given the broad range of topics discussed in this thesis, ranging from laboratory testing to constitutive modelling and finite element simulations of centrifuge experiments, rather than condensing the literature review in an inevitably eclectic chapter, it is introduced at the start of each chapter of this thesis (or during the discussion of the methodologies and results obtained in the present research). When compared to the perhaps more conventional structure of having an introductory chapter solely dedicated to literature review, the adopted strategy tends to make the topics under discussion easier to follow, avoiding the need for jumping from a given chapter to another to get insight into the topic under discussion. In addition, it is hoped that this structure improves the consistency of each chapter, by making it as complete as possible. Secondly, it is important to note that part of the element laboratory test results on Hostun sand presented in this thesis have already been published in a scientific journal (Azeiteiro *et al.*, 2017a). Although further details on the adopted experimental procedures and obtained results are provided in this

thesis, the most relevant experimental findings are similar to those presented in Azeiteiro *et al.* (2017a). Nevertheless, note that, since the work was developed as part of the present research, citation to this paper is considered unnecessary.

Chapter 2 LABORATORY CHARACTERISATION OF THE MONOTONIC RESPONSE OF HOSTUN SAND

2.1 Introduction

In recent years, state-parameter approaches (Been and Jefferies, 1985) have been increasingly used in conjunction with critical state soil mechanics (CSSM) concepts (Roscoe *et al.*, 1958; Schofield and Wroth, 1968) to establish constitutive models capable of reproducing the response of sand under general loading conditions (Manzari and Dafalias, 1997; Papadimitriou and Bouckovalas, 2002; Ling and Yang, 2006; Manzanal *et al.*, 2011; Taborda *et al.*, 2014), as well as for the interpretation of site investigation data in sand (e.g. Been *et al.*, 1986, 1987; Carriglio *et al.*, 1990; Yu, 1994; Konrad, 1998). Indeed, the state-parameter concept appears to be an effective form of predicting the occurrence of relevant features of the response of sand, such as phase transformation and strain softening after a peak-stress-ratio state, for a wide range of densities and stress states (e.g. Been and Jefferies, 1985; Ishihara, 1993; Klotz and Coop, 2001; Murthy *et al.*, 2007; Stamatopoulos, 2010). Furthermore, it has been suggested that the capabilities of a model to reproduce the response of sand can be improved by considering a state-dependent dilatancy (e.g. Manzari and Dafalias, 1997; Gajo and Wood, 1999; Li and Dafalias, 2000; Yang and Li, 2004).

In this chapter, the key features of the monotonic response of air-pluviated Hostun sand are assessed by employing a state-parameter approach – i.e. by using the difference between the current void ratio and void ratio at critical state (CS) corresponding to the current mean effective stress (Been and Jefferies, 1985). With this purpose, results of an extensive laboratory testing programme performed on air-pluviated Hostun sand are firstly presented. This includes both bender element (BE) and triaxial testing on samples prepared to different initial void ratios and consolidated under various isotropic and anisotropic stress states, allowing for the characterisation of the response of Hostun sand within the small to large strain range. After the prediction of the critical state (CS), the occurrences of distinctive states of the response of Hostun sand, such as the undrained instability state (UIS), phase transformation state (PTS) and peak stress ratio state (PSRS), are examined as a function of the state parameter. In addition, the stress-dilatancy response of Hostun sand is investigated.

It is important to note that the vast majority of the experimental results presented in this chapter has already been published by the author and his supervisors in a scientific journal (Azeiteiro *et al.*, 2017a). While further details on the experimental results are provided in this thesis, the outline of this chapter and most relevant findings are similar to those presented in Azeiteiro *et al.* (2017a). Note, however, that the work published in this paper was developed

as part of the present PhD research. As such, it is considered as original work in the present thesis and, therefore, citation to the paper is considered unnecessary.

In addition, it should be noted that, although involving the propagation of shear waves through a sample and, therefore, cyclic loading, it was decided to include the results of BE tests in this chapter (rather than in the following chapter, which focus on the cyclic response of Hostun sand). The main reason for this choice is related to the importance of these results to the characterisation of the distinctive states of the response of Hostun sand, as detailed later.

In terms of structure, the first part of this chapter focuses on the characterisation of the tested material. After presenting the main physical properties of Hostun sand, assessed by identification tests, a literature review on the experimental studies previously performed on this sand is provided. Subsequently, in Section 2.3, attention is given to the laboratory test apparatus and experimental procedures, while the methods used for the interpretation of the obtained experimental results are described in Section 2.4. The experimental results are presented in the following two sections. Specifically, Section 2.5 is dedicated to the presentation of the bender element test results, which allow for the characterisation of the shear modulus of Hostun sand at small-strains. Complementary, Section 2.6 focuses on the response of Hostun sand within the medium to large strain range. Besides the presentation of the drained and undrained triaxial compression (TC) and triaxial extension (TE) test results, the key features of the response of sand are assessed. Finally, Section 2.7 summarises the main results and conclusions concerning the monotonic response of Hostun sand.

2.2 Hostun sand

2.2.1 Physical properties

All tests in this experimental programme were performed on a washed and selected fraction of Hostun sand, which is a fine-grained, sub-angular to angular, siliceous sand (Flavigny *et al.*, 1990). This sand is obtained by sieving the material extracted from a natural deposit in Hostun, Drôme, Rhône-Alpes, Southeast of France (Desrues, 1998). The particle size distribution (PSD) of Hostun sand used in the present study, which was evaluated by the traditional sieving method, is depicted in Figure 2.1, along with those used in other experimental research programmes, which will be described in the following section. It can be observed that slightly different gradations have been used in different experimental programmes.

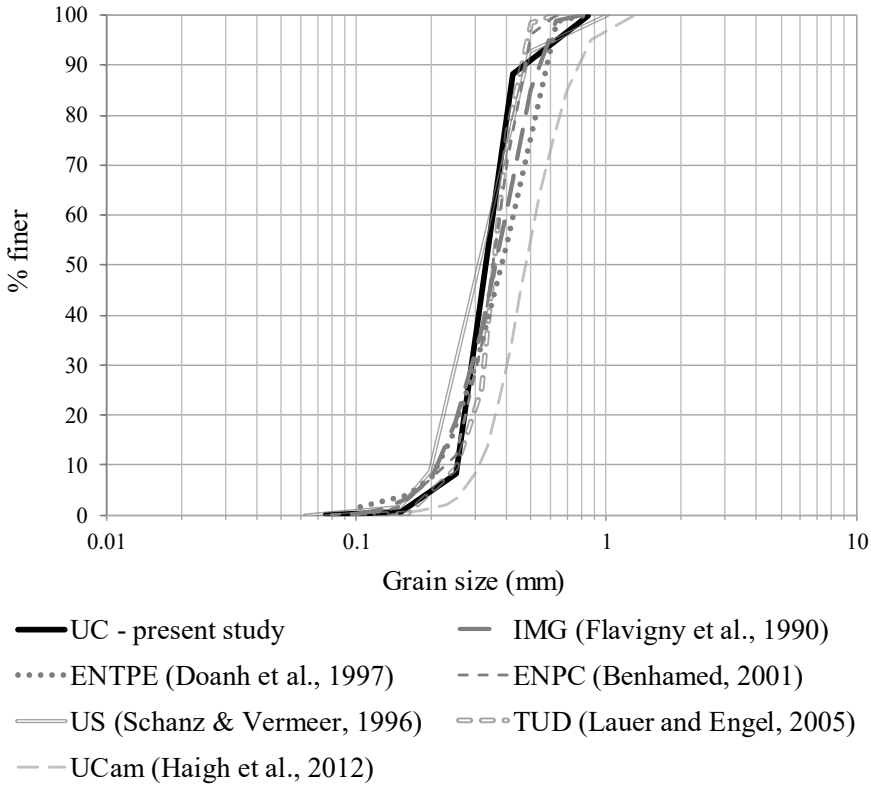

Figure 2.1 – Particle-size distribution curve of Hostun sand.

In the present study, Hostun sand is uniformly graded between sieve no. 20 (0.850 mm) and sieve no. 200 (0.075 mm) of American Society for Testing and Materials (ASTM) series, with more than 50 % of the material passing through the ASTM sieve no. 40 (0.425 mm), while being retained by the ASTM sieve no. 60 (0.250 mm). The mean grain size, D_{50}, is about 0.34 mm, the coefficient of uniformity, C_u, is approximately 1.43 (Equation 2.1) and the coefficient of curvature, C_c, is close to 0.96 (Equation 2.2), enabling to classify the material as poorly graded sand (SP), according to Unified Soil Classification System (USCS), proposed by ASTM.

$$C_u = \frac{D_{60}}{D_{10}} \approx \frac{0.362}{0.253} \approx 1.43 \tag{2.1}$$

$$C_c = \frac{(D_{30})^2}{D_{10} \times D_{60}} \approx \frac{(0.297)^2}{0.253 \times 0.362} \approx 0.96 \tag{2.2}$$

where D_{10}, D_{30} and D_{60} are the grain sizes corresponding to 10 %, 30 % and 60 % of material passing through sieves of ASTM series, respectively.

Moreover, by applying the water pycnometer test method described in ASTM D854-02 (ASTM, 2002), it was concluded that the density of soil particles, G_s, is 2.64. In addition, the standard test methods defined in ASTM D4253-00 (ASTM, 2006a) and ASTM D4254-00 (ASTM, 2006b) were applied to determine the minimum and maximum void ratios, with values of $e_{min} \approx 0.66$ and $e_{max} \approx 1.00$ being obtained, respectively. It should be noted that, by using the multiple sieving pluviation technique, introduced by Miura and Toki (1982) and described

in Section 2.3.1.2, smaller values for the void ratio than that obtained by applying ASTM D4253-00 (ASTM, 2006a) were measured. Furthermore, it was observed that, by tapping the mould after sand pluviation, it would be possible to compact even more the sand and, therefore, to obtain smaller void ratios. In particular, by performing a series of tests where sand was pluviated in a mould with known dimensions by using the multiple sieving pluviation technique and subsequently subjected to vibration by tapping the mould, void ratios as low as 0.61 were obtained. Nevertheless, in order to use a standard as reference and, consequently, enable comparisons with other experimental programmes on this sand reported in the literature, the minimum void ratio of $e_{min} \approx 0.66$, determined according to ASTM D4253-00 (ASTM, 2006a), is adopted.

Table 2.1 compares the physical properties of Hostun sand used in the present study with those reported in the literature for other experimental programmes. As expected, due to the use of slightly different gradations, some discrepancies can be observed between the values reported in the literature and those obtained in the present study. Nevertheless, the observed discrepancies seem small enough to allow for comparisons between experimental results obtained by different researchers.

Table 2.1 – Physical properties of Hostun sand.

Institution [a]	Grain size	PSD			Density	
	D_{50} (mm)	C_u ( )	C_c ( )	G_s ( )	e_{min} ( )	e_{max} ( )
UC (present study)	0.34	1.43	0.96	2.64	0.66	1.00
INPG	0.32[c]–0.36[b]	1.70[c]–1.88[b]	1.00[b]	2.65[b],[c]	0.63[c]	0.96[c]
ENTPE	0.38[d],[e]	1.90[d],[e]	0.97[d],[e]	2.65[d]	0.62[e]	0.96[e]
ENPC	0.35[f]–0.38[g]	1.57[f]	1.06[f]	2.65[f],[g]	0.66[f],[g]	1.00[f],[g]
US	0.34[h]	1.87[h]	0.97[h]	2.65[h]	0.65[h]	1.04[h]
TUD	0.36[i]	1.43[i]	1.11[i],[*]	2.64[i]	0.65[i]	1.03[i]
UCam	0.35[j]–0.42[k]	1.59[k]–1.90[j]	1.00[k]–1.11[j]	2.65[j],[k]	0.55[j]	1.01[j]–1.07[k]

[a] UC: University of Coimbra; INPG: Grenoble Institute of Technology; ENTPE: *École Nationale des Travaux Publics de l'État*; ENPC: *École Nationale des Ponts et Chaussées*; US: University of Stuttgart; TUD: Technical University of Dresden; UCam: University of Cambridge.
[b] Flavigny *et al.* (1990); [c] Desrues *et al.* (1996); [d] Doanh (1997); [e] Doanh *et al.* (2012); [f] Benahmed (2001); [g] De Gennaro *et al.* (2004); [h] Schanz and Vermeer (1996); [i] Lauer and Engel (2005); [j] Mitrani (2006); [k] Stringer (2008).
[*] Estimated from the PSD curve presented in the reference.

It is also interesting to compare the physical properties of Hostun sand with those exhibited by other reference sands, which have been used in liquefaction research projects over the past few decades. With that purpose, Figure 2.2 compares the PSD of Hostun sand with those exhibited by Leighton Buzzard sand (Been *et al.*, 1991), Nevada sand (Arulmoli *et al.*, 1992), Ottawa sand (Murthy *et al.*, 2007) and Toyoura sand (Verdugo and Ishihara, 1996), while Table 2.2 summarises their main physical characteristics. It can be observed that, although Hostun sand has a similar PSD to that exhibited by Ottawa sand, the grain shapes of those sands are different, resulting in completely different minimum and maximum void ratios. Conversely,

the minimum and maximum void ratios of Hostun sand are similar to those obtained for Leighton Buzzard and Toyoura sands, despite the slightly coarser gradation of Hostun sand. Possible impacts of these differences on the main features of the response of sand will be discussed later.

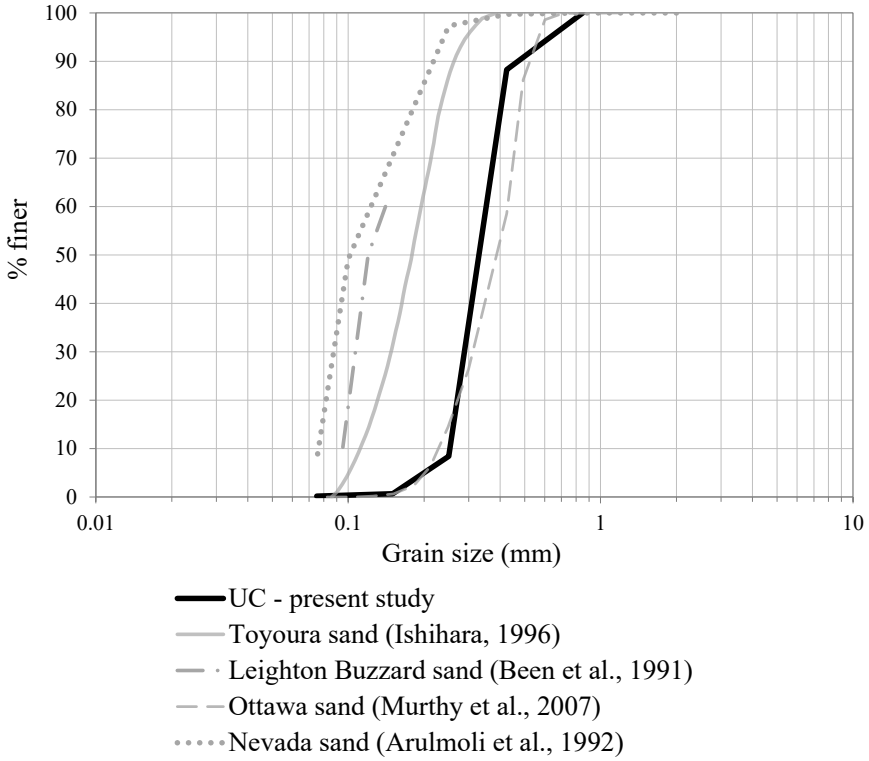

Figure 2.2 – Comparison of the particle-size distribution curve of Hostun, Leighton Buzzard, Nevada, Ottawa and Toyoura sands.

Table 2.2 – Comparison of the physical properties of Hostun, Leighton Buzzard, Nevada, Ottawa and Toyoura sands.

Sand	Reference	Grain size		Grain shape	Density		
		D_{50} (mm)	C_u ( )		G_s ( )	e_{min} ( )	e_{max} ( )
Hostun	Present study	0.34	1.43	Subangular to angular	2.64	0.66	1.00
Leighton Buzzard	Been *et al.* (1991)	0.12	1.50	Subangular to angular	2.65	0.66	1.01
Nevada	Arulmoli *et al.* (1992)	0.17	2.00	Rounded to subrounded	2.67	0.51	0.89
Ottawa	Murthy *et al.* (2007)	0.39	1.40	Rounded	2.65 [(b)]	0.48	0.78
Toyoura	Verdugo and Ishihara (1996)	0.17	1.70	Subangular to angular	2.65	0.6	0.98

[(a)] Okamura *et al.* (2001); [(b)] Yamamuro and Lade (1997).

2.2.2 Overview of previous experimental studies on Hostun sand

Hostun sand has been extensively used in research projects conducted at French institutions since the early 1980's, with its use being broadened to other European institutions during the

last two decades. In particular, due its close location to the natural deposit, this sand was originally used as a reference material at the Grenoble Institute of Technology (INPG), France. As part of an international workshop held at Case Western Reserve University (CWRU), Cleveland, Ohio, United States, in late 80's, which aimed at assessing the predictive capability of constitutive models for sand, Hostun sand was tested both in a cubic cell device at INPG and in a hollow cylinder torsional apparatus at CWRU (e.g. Bianchini *et al.*, 1989; Lanier *et al.*, 1989; Bianchini *et al.*, 1991). In addition, a large amount of drained and undrained biaxial and triaxial tests were carried out by the non-profit association Alliance of Laboratories in Europe for Education, Research and Technology (ALERT) "Geomaterials", hosted and financially supported by INPG, for the study of strain localisation during shearing (e.g. Desrues *et al.*, 1996; Desrues, 1998; Mokni and Desrues, 1999; Desrues and Viggiani, 2004; Desrues and Georgopoulos, 2006). It is also noteworthy the study of the response of very loose Hostun sand, conducted as part of a collaboration between the Laval University, Quebec, Canada, and INPG, intending to establish the undrained instability line for Hostun sand (e.g. Konrad *et al.*, 1991; Konrad, 1993).

Further research on the undrained response of very loose sand was carried out at *École Nationale des Travaux Publics de l'État* (ENTPE), Lyon, France. In particular, the influence of the type of consolidation and previous strain history on the undrained instability state and minimum undrained strength of Hostun sand under monotonic triaxial compression and extension loading was assessed (e.g. Doanh *et al.*, 1997; Doanh and Ibraim, 2000; Finge *et al.*, 2006; Doanh *et al.*, 2012). Other experimental studies undertaken at this French university included the anisotropy of Hostun sand at small strains (e.g. Ezaoui *et al.*, 2007).

Hostun sand was also used at *École Nationale des Ponts et Chaussée*s (ENPC), Paris, France, for studying the influence of the inherent anisotropy created by different methods of sample preparation on its monotonic response (e.g. Benahmed, 2001; Benahmed *et al.*, 2004), as well as the influence of different loading paths (e.g. De Gennaro *et al.*, 2004).

Since the 1990's, Hostun sand has also been used as a reference material in other well-known European universities out of France. For instance, the monotonic response of Hostun sand was examined at the University of Stuttgart, Germany (e.g. Schanz and Vermeer, 1996), and used for the validation of constitutive models, such as Hardening Soil model (Schanz *et al.*, 1999) and Hardening Soil Small Strain model (Benz, 2007). Similarly, true triaxial test data (e.g. Wood *et al.*, 2007) and hollow cylinder torsional test data (e.g. Ibraim *et al.*, 2011) on Hostun sand obtained at the University of Bristol, United Kingdom (U.K.), were used for the verification of critical state models (Gajo and Wood, 1999; Jafarzadeh *et al.*, 2008; Russell and Muir Wood, 2010). Additionally, bender element tests have also been performed at the University of Bristol to study the inherent and stress-induced anisotropy of Hostun sand (Sadek and Lings, 2007; Escribano and Nash, 2015).

In terms of hydro-mechanical response of Hostun sand, two experimental programmes on the capillary pressure-saturation relationship (also known as soil-water characteristic curves) are of particular relevance: one undertaken at the University of Weimar, Weimar, Germany, using a modified pressure plate apparatus and large scale column tests (e.g. Lins and Schanz, 2005; Lins *et al.*, 2007; Lins, 2009) and another one carried out at the Technical University of Dresden (TUD) using a newly-developed triaxial device (e.g. Lauer and Engel, 2005).

Hostun sand has also been recently adopted as model sand in centrifuge experiments at the University of Cambridge (UCam), U.K. (e.g. Mitrani, 2006; Stringer and Madabhushi, 2013a, 2013b; Chian *et al.*, 2014; Li and Bolton, 2014; Marques *et al.*, 2014a, 2014b; Tsinidis *et al.*, 2015; Adamidis and Madabhushi, 2018). These studies highlighted the need for high quality element laboratory testing on this material to assist the interpretation of the obtained centrifuge test results and to be used for the calibration of advanced constitutive models and subsequent numerical simulation of the centrifuge experiments.

In the next sections, the experimental results obtained in the present study will be presented. This includes a large set of drained and undrained element laboratory tests on samples of Hostun sand prepared using a single method of sample reconstitution and covering a wide range of initial density and stress conditions. Whenever relevant, results obtained in other research programmes mentioned in this section will be presented with the purpose of corroborating or extending the experimental findings.

2.3 Laboratory test apparatuses and experimental procedures

2.3.1 Triaxial tests

2.3.1.1 Apparatuses

Conventional monotonic triaxial compression tests with increasing mean stress (MTC $p\uparrow$) were conducted using an electro-mechanical triaxial system manufactured by ELE International using 100-mm-diameter cylindrical samples with a height/diameter ratio close to 2 (Figure 2.3a). Conversely, monotonic compression tests with decreasing mean stress (MTC $p\downarrow$), as well as monotonic extension tests with decreasing and increasing mean stress (MTE $p\downarrow$ and MTE $p\uparrow$, respectively) were performed using a more versatile and fully computer-controlled hydraulically operated triaxial apparatus of the type developed by Bishop and Wesley (1975), designed for 38-mm-diameter specimens with a height/diameter ratio close to 2 (Figure 2.3b). Both triaxial cells were designed for a maximum working cell pressure of 1000 kPa.

a) b)

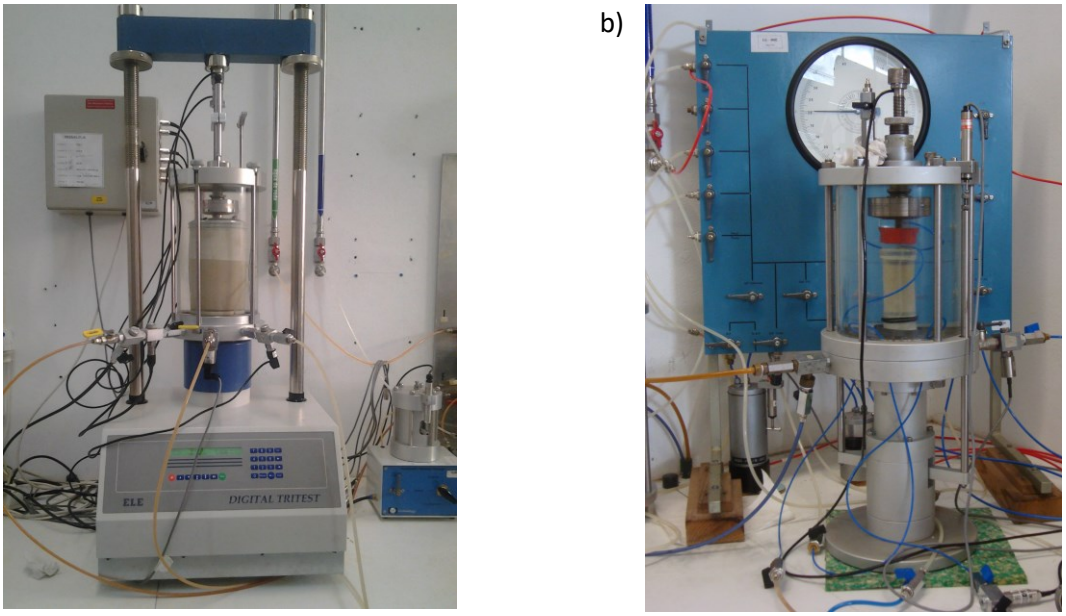

Figure 2.3 – Triaxial apparatuses used in the present study: (a) electro-mechanical triaxial cell and (b) hydraulically operated Bishop and Wesley (1975)'s stress path cell.

In the electro-mechanical triaxial system, the constant-rate axial motion of the pedestal of the triaxial cell, imposing the axial load on the sample, was controlled by a motorised system, which was run manually using a digital keypad installed in the front panel of the load frame. Moreover, bladder-type air-water interchange cylinders connected to manual air pressure regulators were used to establish the cell pressure, as well as back pressure (i.e. sample's internal pore water pressure, measured and controlled at the base) up to about 700 kPa. Note that this maximum working pressure of 700 kPa was dictated by the capacity of the compressed air system (rather than by the capacity of the triaxial cell). Note also that an additional water line connection to the top of the sample, whose pressure was also applied by an air-water interchange cylinder connected to a manual air pressure regulator, was used during the saturation stage to establish a differential sample's internal pore water pressure between the base and top of the sample and, consequently, to induce water flow through the sample. This saturation strategy facilitated the removal of air bubbles from voids of the tested sample. Moreover, standard instrumentation was used, including a submersible 10 kN-range load cell, a 1000 kPa-range cell pressure transducer and two 1000 kPa-range pore pressure transducers, one of which connected to the base pedestal and the other one connected to the top cap. In addition, a 100 cm^3-capacity volume gauge and an externally mounted 50 mm-range linear variable displacement transducer (LVDT) were used to measure changes in sample's volume and axial displacement, respectively. The data provided by the different instruments was acquired by a data acquisition system and subsequently transferred to a computer.

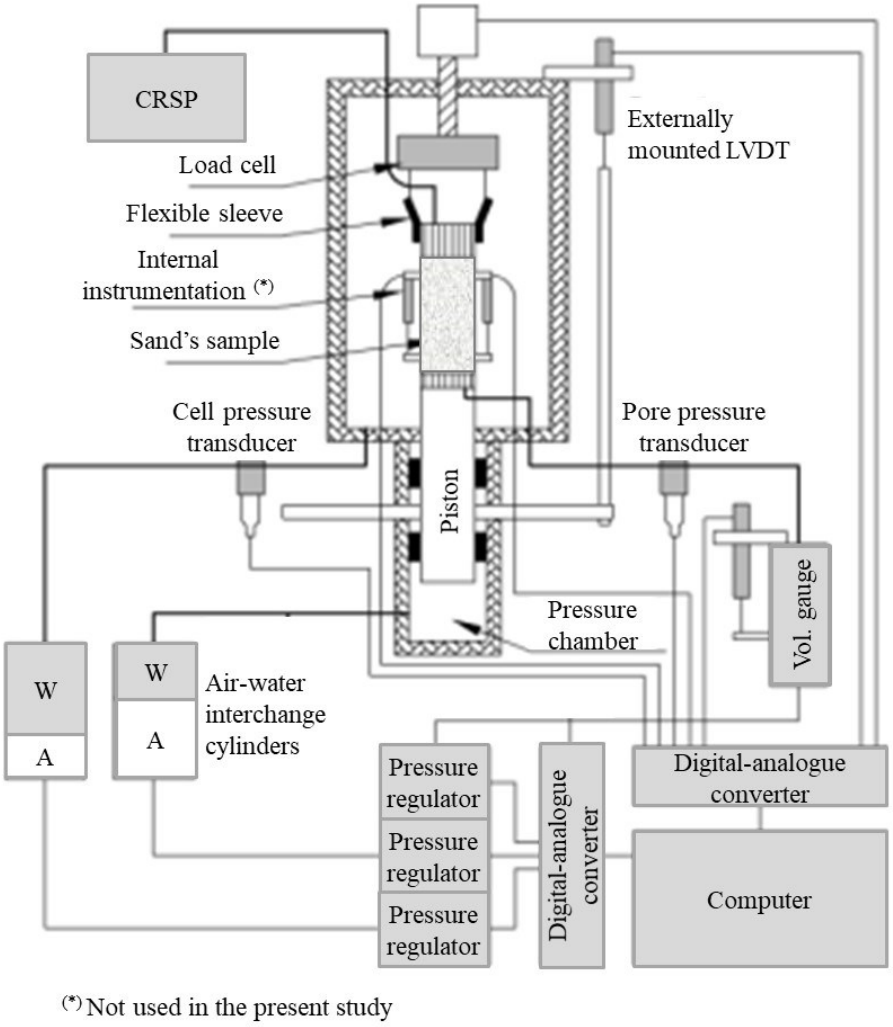

Figure 2.4 – Schematic illustration of the hydraulically operated Bishop and Wesley (1975)'s stress path cell (adapted from Pedro, 2013).

With respect to the hydraulically-actuated stress path cell, the pedestal was mounted at the top of a loading ram, which was connected to a piston and to a water pressure chamber at its bottom (Figure 2.4). By changing the pressure in the water pressure chamber, a vertical movement of the loading ram was induced allowing for the application of axial load to the sample. Two alternative systems were used to control the ram line. For strain-controlled tests, a constant rate of strain pump (CRSP) was used to apply a constant flow of water to the pressure chamber and, therefore, to induce a constant-rate axial motion of the pedestal. Conversely, for stress-controlled tests, a bladder-type air-water interchange cylinder connected to an air pressure regulator was used to control the ram pressure. In both cases, an automated data acquisition and control system enabled a computer control of the rate of axial displacement or load applied to the sample. Moreover, in order to allow for extension testing, a flexible sleeve was used to connect the top cap to an adjustable reaction head. The remaining equipment was similar to that used in the electro-mechanical triaxial cell system, with air-water interchange cylinders connected to air pressure regulators being used to control independently the cell and the internal pore water pressure at the base and top of

the sample. The only difference consisted of the use of the automated data acquisition and control system to control the air pressure regulators through a computer, rather than manually control them. The instrumentation consisted of 1000 kPa-range pore pressure transducers, a submersible 5 kN-range load cell, an externally mounted 25 mm-range LVDT and a 50 cm^3-capacity volume gauge. The software TRIAX, developed at the University of Durham (Toll, 1993), was used to record and monitor all devices, as well as to control the different stages of the tests. This software offers a very large flexibility, with the user being allowed to define up to 100 test stages, as well as conditional equations, which trigger specific actions (such as to move from a given test stage to another or to stop the test when a given condition is reached). Furthermore, it includes calibration facilities, assisting a frequent calibration of the instruments.

Further details on these two type of triaxial apparatuses and their operations can be found in Bishop and Henkel (1962), Bishop and Wesley (1975) and Head (1994), while a discussion about the role of triaxial testing in the characterisation of the stiffness and strength of soil can be found, for example, in Head (1998).

2.3.1.2 Experimental procedures

Air-pluviation of dry sand was used to prepare all samples. This technique usually results in homogeneous samples in clean uniform sands (as it is the case of Hostun sand), with relatively uniform void ratio distribution, at least when compared with compaction techniques, such as moist tamping (e.g. Vaid and Negussey, 1988; Benahmed *et al.*, 2004). Moreover, this technique is well-known for its good repeatability, which ensures that results obtained for different tests can be compared (e.g. De Gennaro *et al.*, 2004; Coelho, 2007). In addition, since one of the main objectives of the present experimental study was to produce reliable data to be used in the calibration of constitutive models and, subsequently, in the numerical simulation of centrifuge experiments, it was considered to be fundamental to use the same technique applied in centrifuge modelling, which was air-pluviation, as described, for example, in Marques *et al.* (2014a, 2014b, 2015).

At this point, it is perhaps important to note that, apart from brief references, the evaluation of the effect of the method of sample preparation on the monotonic and cyclic response of sand is beyond the scope of the present study. Vast information on this topic can be found in the literature (e.g. Oda, 1972; Mulilis *et al.*, 1977; Tatsuoka *et al.*, 1979; Miura and Toki, 1982; Tatsuoka *et al.*, 1986c; Ishihara, 1993; Zlatovic and Ishihara, 1997; Vaid and Sivathayalan, 2000; Papadimitriou *et al.*, 2005).

Different initial relative densities can be obtained by varying the rate and/or the height of pouring. The former aspect is typically seen as the most influential, with higher rates of pouring resulting in looser arrangements. According to Miura and Toki (1982), this can be explained by larger number of collisions between falling particles (interference effects), which result in larger energy dissipation and, therefore, inhibit particles from finding the most stable

(and, therefore, most compact) arrangement. Conversely, when grains fall apart from each other, the number of collisions decrease and, consequently, the stored energy is used to find a more stable position for the grains. In relation to the height of pouring, Vaid and Negussey (1984) observed that larger kinematic impact energies during air pluviation are generally associated with higher fall heights, leading to compaction and, therefore, denser arrangements.

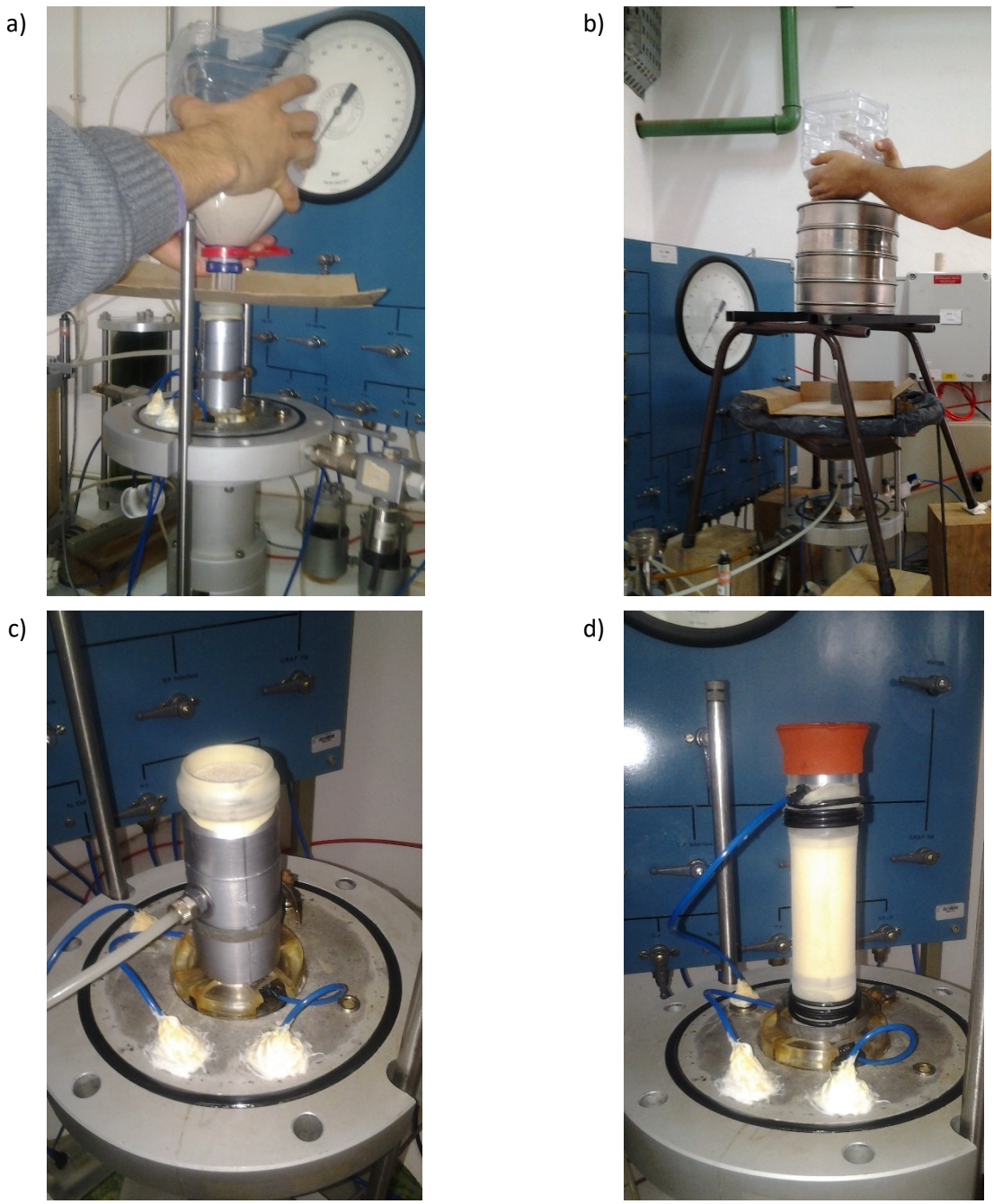

Figure 2.5 – Sample set-up: (a) air-pluviation of loose sand using a miniature container; (b) air-pluviation of dense sand by applying the multiple sieve technique; (c) detachable mould supporting the sample; and (d) application of vacuum after disassembly the mould.

To prepare loose and moderately loose sand samples, the rate of pouring was controlled by the size and number of openings of a miniature container (Figure 2.5a). Moreover, in order to ensure homogeneity of samples, the height of pouring (corresponding to the height of the mould) was kept as constant as possible by raising the container during pluviation of sand. Regarding dense sand samples, the multiple sieving pluviation technique, described in Miura and Toki (1982), was employed (Figure 2.5b). In this case, the height of pouring was observed to have little impact on the obtained density of the sample. Both techniques were regularly tested to ensure reproducibility. The density of the produced samples was methodically confirmed from mass and volume measurements after preparation.

In order to sustain the sample during air-pluviation, a detachable mould was used (Figure 2.5c). Moreover, a small suction of about 5 to 10 kPa was used to extract the air existing between the membrane and the internal walls of the mould and, therefore, to prevent sample's shape imperfections. Once the top porous stone and top cap were carefully placed and the membrane ends sealed with o-rings, a small suction (once more, of about 5 to 10 kPa) was applied to the sample through the top cap (Figure 2.5d). This value was deemed sufficiently low to avoid disturbance of the samples, while ensuring stability of the sample during the subsequent preparation stages. The perspex cylinder was finally placed and the triaxial cell filled with water. Note that, although Figure 2.5 refers to sample's set-up in the Bishop and Wesley (1975)'s stress path cell, similar procedures were employed to prepare samples to be tested in the electro-mechanical triaxial cell. Naturally, the containers used in the air-pluviation procedures and their openings had to be specifically designed for each sample size.

After reducing the suction of the sample to zero, while simultaneously increasing the cell pressure to about 15 kPa, water was allowed to flow through the sample, by prescribing a small differential pressure between the top and base of the sample of about 5 kPa. At least 250 cm^3 (corresponding approximately to ten times the capacity of the volume gauge of the stress path cell) of de-aired water was circulated at this stage. Subsequently, the back and cell pressures were concurrently increased at a very slow rate until desired values were obtained. At this stage, water was allowed to percolate through the sample once more, by prescribing a differential pressure between its bottom and its top of about 5 kPa. This procedure was undertaken until a Skempton's *B*-value (i.e. the ratio of the induced pore water pressure due to the change of cell pressure under undrained condition) typically above 0.98 was measured, which usually took about 1 day.

The samples were subsequently consolidated, typically by increasing the cell pressure, while maintaining the back pressure constant. This stage was considered finished when stabilisation of the volume change occurred. Afterwards, the piston was slowly raised, while maintaining the cell and back pressures constant. As the contact between the top cap and the adjustable

reaction head was established, typically observed by a very small deviatoric stress, the shearing phase was performed.

As mentioned before and illustrated in Figure 2.6, samples were sheared by applying different total stress paths. Specifically, a first series of ten drained and nine undrained monotonic triaxial compression tests with increasing mean stress (DMTC $p\uparrow$ and UMTC $p\uparrow$, respectively) were performed on samples isotropically consolidated (IC) to 25, 50, 80, 135, 200, and 500 kPa in the electro-mechanical triaxial cell. In this case, a constant axial strain increment of about 6% per hour, which was slow enough to allow pore water pressure changes to equalise throughout the sample, was applied. To evaluate the impact of the effective stress at consolidation and stress path on the measured response, a second series of four drained monotonic triaxial compression tests with decreasing mean stress (DMTC $p\downarrow$) were performed on either isotropically consolidated (IC) or anisotropically consolidated (K0C) samples to a mean effective stress of 80 kPa by using the Bishop and Wesley (1975)'s stress path cell. In this series of tests, the radial effective stress was reduced while maintaining the effective axial stress constant, which implied increasing the ram pressure at a similar rate at which the cell pressure was decreased and maintaining the back pressure constant (as required in a drained test). A smaller axial strain rate of about 0.5% per hour was required in these tests to control adequately the concurrent variations of ram and cell pressures.

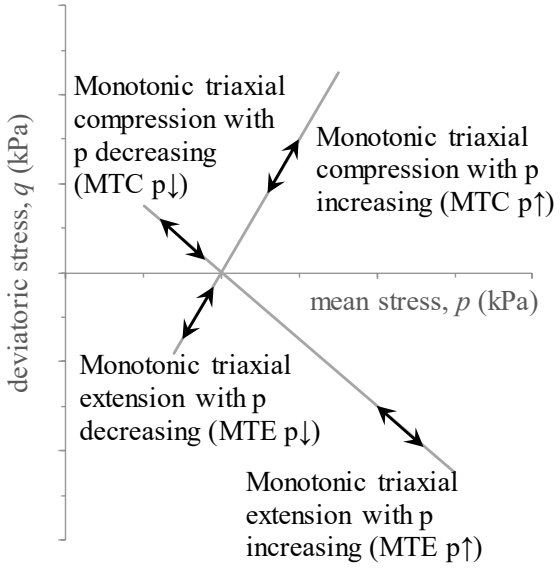

Figure 2.6 – Illustration of the total stress paths followed in each type of monotonic triaxial test performed.

By using once more the Bishop and Wesley (1975)'s stress path cell, a complementary series of four drained monotonic triaxial extension tests with increasing mean stress (DMTE $p\uparrow$) and one drained monotonic triaxial extension tests with decreasing mean stress (DMTE $p\downarrow$) were performed on samples either IC or K0C to a mean effective stress of 80 kPa. Finally, a series of four undrained monotonic triaxial extension tests with decreasing mean stress (UMTE $p\downarrow$) were performed on samples isotropically consolidated to an effective stress of 25

and 80 kPa. An axial strain rate of approximately 2% per hour was deemed adequate to control the test and obtain accurate instrument measurements.

In all cases, tests were stopped when the piston reached its maximum displacement, pore-water pressure dropped sufficiently for cavitation to occur, or a visible shear band developed in the sample. Further details on the laboratory testing programme are provided in Section 2.6.2.

2.3.1.3 Main advantages and limitations of triaxial testing

Although hollow cylinder torsional shear testing is becoming more popular (Nakata *et al.*, 1998; Yoshimine *et al.*, 1998; O'Kelly and Naughton, 2009; Araújo Santos, 2015), triaxial testing still remains the reference type of test used to obtain data for the calibration of advanced constitutive models, usually supplemented with bender element or resonant column testing (e.g. Papadimitriou and Bouckovalas, 2002; Loukidis and Salgado, 2009). When compared to the former type of test, triaxial tests are usually preferred due to their low cost, widespread availability of this equipment in geotechnical laboratories, simpler procedures to prepare samples and to control the equipment and monitoring system, as well as due to the very large past experience. Furthermore, although a large number of experimental studies have been performed since 1960's using this equipment, including to study liquefaction-related phenomena, it is still possible to conduct innovative experimental studies, as demonstrated, for instance, by the triaxial testing programme conducted by Azeiteiro *et al.* (2012), Coelho *et al.* (2013) and Azeiteiro *et al.* (2017b) on the effect of a singular large-amplitude peak cycle within uniform cyclic loading on the cyclic mobility resistance of sand. However, on the contrary to hollow cylinder torsional shear testing, triaxial testing cannot be used to investigate independently the effect of the magnitude of the intermediate principal effective stress, σ'_2, and the effect of the direction of the principal effective stresses on the response of soil, the latter aspect typically characterised by the orientation of the direction of the maximum principal effective stress to the direction of deposition (e.g. Yoshimine *et al.*, 1998). Note that the influence of these aspects is discussed in Section 4.3.3.

Furthermore, even if cyclic direct simple shear tests may reproduce more accurately the seismic loading occurring in the field than cyclic triaxial tests, at least for level ground deposits with no soil-structure interaction, which would make the former type of test attractive to study liquefaction-related phenomena, the fact that the strains imposed on the sample in direct simple shear tests are usually highly non-uniform and that lateral stresses are unknown hampers a more generalised use of direct simple shear tests (Ishihara, 1996). It does not mean, however, that stresses and strains are uniform in samples subjected to triaxial tests. In fact, formation of shear bands and stress concentration zones are commonly observed in triaxial tests. An interesting study on strain localisation on Hostun sand during triaxial shearing was carried out by Professor Jacques Desrues and his co-workers (e.g. Desrues *et al.*, 1996; Desrues and Georgopoulos, 2006) by using computed tomography. Moreover, an

overview of the currently available test apparatus and procedures particularly suitable for studying liquefaction-related phenomena is provided by Ishihara (1996).

2.3.2 Bender element tests

Bender element (BE) tests were firstly introduced to soil testing by Shirley and Hampton (1978) and Shirley (1978). Later, Dyvik and Madshus (1985) compared values of the maximum (i.e. at very small strains) shear modulus, G_{max}, estimated from results of bender elements and resonant column tests on clay under a wide range of stress states, concluding that a remarkable agreement between both sets of data was obtained. Although it has become clear that the interpretation of BE elements is not straightforward (e.g. Viggiani and Atkinson, 1995; Jovicic *et al.*, 1996; Santamarina and Fam, 1997; Lee and Santamarina, 2005; Alvarado and Coop, 2012), due to its simplicity, relatively low cost and potential for determining stiffness anisotropy, the use of bender element testing to characterise the small-strain response of soil has become increasingly popular over the last decades (Clayton, 2011).

The bender element consists of two thin piezo-ceramic plates, bonded rigidly together, with a conductive metal between them and electrodes on their outer surfaces, typically coated with an epoxy resin to allow operations in the presence of water (Figure 2.7). As a voltage is applied to this element, it tends to bender, generating a shear wave in the soil in which the element is embedded. Moreover, when subjected to distortion, this type of element generates voltage, which can also be recorded. Therefore, by using a pair of bender elements and adequate devices to generate the input signal and record the transmitted and received signals, it is possible to estimate the travel time of the generated shear wave, t, and, given that the distance between the tips of bender elements, L, is known, to compute the velocity of the shear wave, $v_s = L/t$, and, by knowing the mass density of the material, ρ, the shear modulus, $G = \rho v_s^2$, corresponding to the direction of wave propagation and particle vibration under analysis. Note that, according to Dyvik and Madshus (1985), shear strains imposed by bender element testing are below 10^{-5} and, therefore, the estimated shear modulus is relevant for the very small strains (Clayton, 2011). Note also that, although other configurations are possible (e.g. Pennington *et al.*, 1997; Alvarado, 2007; Clayton, 2011), the typical set-up for triaxial testing consists of having the BE installed at the top and bottom of the sample, resulting in vertically propagated waves with horizontal polarisation.

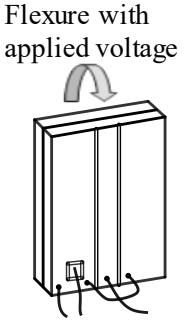

Figure 2.7 – Illustration of a bender element (Clayton, 2011).

In the present study, bender elements of the Dyvik and Madshus (1985)'s type, with a width of about 7.5 mm, a thickness of about 1.5 mm and protruding about 4.0 mm in height into the sample, were installed in the Bishop and Wesley (1975)'s stress path cell, simply by replacing the pedestal and the top cap by similar pieces modified at Imperial College London to incorporate the elements (Figure 2.8a). A TTi TG1010 function generator was used to generate the input signal. Specifically, a single sine pulse was adopted for the input signal, since it has been shown to give reliable time measurements, while enabling a good control of the input frequency and, therefore, wavelength (e.g. Blewett *et al.*, 2000; Viana da Fonseca *et al.*, 2009; Clayton, 2011). This signal was sent to the transmitter bender element, mounted at the top cap, as well as to a Tektronix TDS220 digital storage oscilloscope, to be recorded. The vertically propagated wave with horizontal polarisation was then detected by the receiver bender element, which was mounted at the pedestal and connected to the oscilloscope. Both transmitted and received signals were displayed simultaneously by the oscilloscope and then transferred to a computer for interpretation. The software WaveStar™, also developed by Tektronix (Tektronix, 1998), was used to visualise and store the signals in digital format. The data was subsequently post-processed by the author, as detailed in Section 2.4.2. It should be noted that, as recommended by Lee and Santamarina (2005), adequate shielding and grounding of electronic cables, leak-free connections and, as much as possible, noise-free equipment (which included turning off the air conditioning during the performance of the bender element measurements) were used to prevent electromagnetic coupling and minimise electrical noise.

a) **b)**

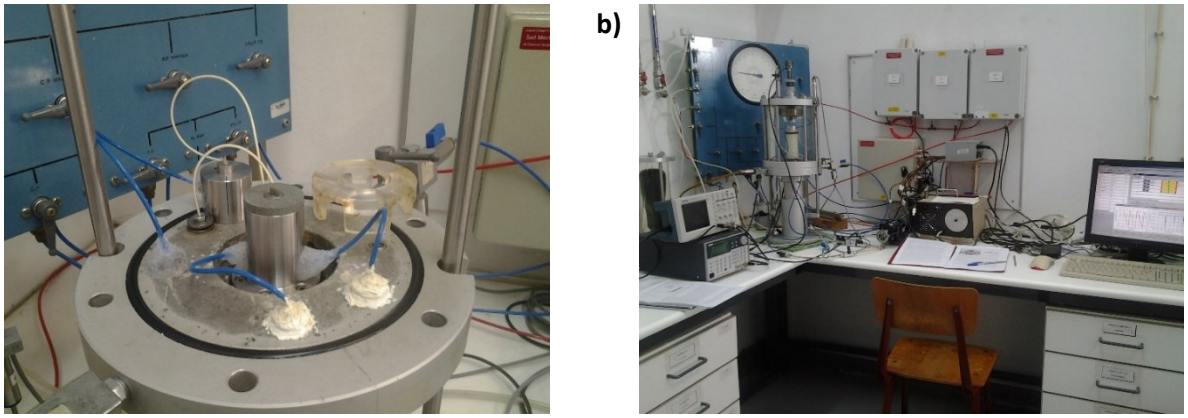

Figure 2.8 – Bender elements testing: (a) pedestal and top cap of the stress path cell incorporating the bender elements and (b) overview of all devices used to perform the bender element tests.

Before testing Hostun sand, a preliminary test was performed to determine the time lag of the system. With that objective, the tips of the transmitter and the receiver bender elements were placed in direct contact, with the elements perfectly aligned, and a sine pulse was generated. By testing sequentially frequencies of the input signal varying from 1 to 10 Hz, it was concluded that the maximum time lag was as low as 0.012 ms. As shown by Pedro (2013), the time lag increases significantly as the alignment of the bender elements diverges from 0° (i.e. from the correct alignment), with this author registering a time lag increase greater than

50% when bender elements were positioned with their axes at 30°. Similar observations were made by Lee and Santamarina (2005). Therefore, to minimise this source of error, guidelines were drawn in the pedestal, mould and top cap to ensure an adequate positioning of the top cap after sand pluviation (i.e. to ensure a correct alignment of the top bender element in relation to the bottom one). Apart from this detail, moderately loose and dense specimens of Hostun sand were prepared and saturated using exactly the same procedures described in the previous section for triaxial tests. In this case, a back pressure of 200 kPa was used during the saturation stage, as well as during the subsequent drained isotropic compression (DIC) stage, which, providing the maximum working pressure of about 700 kPa, enabled the application of a maximum isotropic effective stress to the samples of 500 kPa, as detailed below.

The samples were gradually consolidated to several different isotropic effective stresses (as detailed later), with a loading rate of 3 kPa per minute. At each effective stress level, the increase in stress was temporarily paused and single sine pulses with a peak-to-peak amplitude of 20 V and varying frequencies (from 1 to 10 kHz) were transmitted to the probes, with all responses being recorded. Note that the performance of readings of several signals having different frequencies assisted the identification of near field effects, generally recognised by a deflection of the received waveform before the effective arrival of the shear wave (e.g. Sanchez-Salinero *et al.*, 1986; Jovicic *et al.*, 1996). Note also that, as recommended by Sanchez-Salinero *et al.* (1986) and Alvarado and Coop (2012), at least one of the applied frequencies resulted in a wavelength, λ, smaller than half of the travel distance of the shear wave, in order to minimise near field effects. For instance, for the densest sample subjected to the highest confining stress of 500 kPa, a shear wave velocity of $v_s \approx 324.0$ m/s was estimated from the bender element measurements. Since a frequency of $f = 10$ kHz was applied, then $\lambda = v_s/f \approx 324.0/10000.0 \approx 32.4$ mm. Assuming that the travel distance of the shear wave can be estimated by the initial height of the sample subtracted by its height reduction during DIC loading and by the protrusion of the bender elements, a value of about 76.5 mm is obtained, which is, indeed, greater than twice the wavelength ($2\,\lambda \approx 2 \times 32.4$ mm ≈ 64.8 mm).

After first loading, a first unloading, a reloading and a second unloading phases were applied, with a similar loading rate to that used during first loading. During these phases, bender element measurements were also conducted at several different isotropic effective stresses, as detailed later.

2.4 Principles used in the interpretation of laboratory test results

2.4.1 Triaxial tests

Triaxial test results were interpreted in terms of the conventional invariants of stress – mean effective stress, $p' = (\sigma'_a + 2\,\sigma'_r)/3$, and deviatoric stress, $q = \sigma'_a - \sigma'_r$ (where σ'_a and σ'_r

are, respectively, the axial and radial effective stresses) – and conventional strain invariants – volumetric strain, $\varepsilon_v = \varepsilon_a + 2\,\varepsilon_r$, and deviatoric strain, $\varepsilon_q = 2\,(\varepsilon_a - \varepsilon_r)/3$ (where ε_a and ε_r are, respectively, the axial and radial strains).

As suggested by Been and Jefferies (2004), to improve the accuracy of the estimation of relevant features of sand (such as the critical state, which is typically only mobilised for very large deformations of the samples), strains were computed using the current dimensions of the sample, rather than its initial dimensions (i.e. the large-strain definition was used). This means that, for each instant of time, axial strain increment was calculating by employing $\delta\varepsilon_a = -\delta H/H_i$, where H_i is the current height of the sample and δH is its variation, measured by the LVDT, while volumetric strain increment was estimated by using $\delta\varepsilon_v = -\delta V/V_i$, where V_i is the current volume of the sample and δV is its variation, measured by the volume gauge. The axial strain, ε_a, and volumetric strain, ε_v, at a given instant of time were obtained by integrating all previous $\delta\varepsilon_a$ and $\delta\varepsilon_v$, respectively.

In addition, assumptions about the evolution of the cross-sectional area of the sample over which axial load acts during triaxial testing are required to compute axial stresses from axial load measurements. As often suggested in the literature (e.g. Been and Jefferies, 2004), in the present study, it was assumed that the sample deforms as a right-circular cylinder throughout loading (i.e. it was assumed that the cross-section perpendicular to the vertical axis of the sample remains constant through its height). Based on this assumption, the change in the cross-sectional area of the sample can be estimated using Equation 2.3.

$$\begin{aligned} &V_{i+1} = V_i + \delta V \Leftrightarrow \frac{V_{i+1}}{V_i} = \frac{V_i}{V_i} + \frac{\delta V}{V_i} \Leftrightarrow \frac{A_{i+1}\,H_{i+1}}{A_i\,H_i} = 1 - \delta\varepsilon_v \Leftrightarrow \\ &\frac{A_{i+1}(H_i + \delta H)}{A_i\,H_i} = 1 - \delta\varepsilon_v \Leftrightarrow \frac{A_{i+1}}{A_i}(1 - \delta\varepsilon_a) = 1 - \delta\varepsilon_v \Leftrightarrow A_{i+1} = A_i\,\frac{1 - \delta\varepsilon_v}{1 - \delta\varepsilon_a} \end{aligned} \tag{2.3}$$

where A_i and A_{i+1} are the cross-sectional areas of the sample at two consecutive instants of time, at which measurements were registered.

As highlighted in the literature (e.g. La Rochelle *et al.*, 1988; Klotz and Coop, 2002; Been and Jefferies, 2004), even when lubricated pedestal and top plate are used to reduce the friction between the ends of the sample and the equipment, samples are often observed to barrel/bulge and, consequently, the cross-sectional area in the middle of the sample is often greater than given by Equation 2.3. In addition, as pointed out by Desrues *et al.*(1996), even if it cannot be observed from the outside, strain localisation (also termed as shear band) is often observed to develop within the sample and, therefore, the proposed area correction is seldom accurate, particularly at large strains. Nevertheless, as also highlighted by the previous group of authors, unless sophisticated techniques are used (as, for example, computed tomography), it is difficult to find a consistent deformation pattern that can provide a more accurate area correction. Therefore, Equation 2.3 is, in general, considered satisfactory.

Particular evidence of non-uniform strain conditions are observed in triaxial extension tests, where strain localisation inevitably occurs in the form of sample necking (e.g. Roscoe *et al.*, 1964; Lam and Tatsuoka, 1988; Yamamuro and Lade, 1995). Under such conditions, test results seem to be unreliable at large strains, even when more sophisticated area corrections than that given by Equation 2.3 are applied (Yamamuro and Lade, 1995). In fact, in the present experimental testing programme, regardless of the drainage conditions, sample necking was recurrently observed in all performed triaxial extension tests, as axial strains reached 8 to 10 % (Figure 2.9). It was, therefore, decided to disregard test data obtained for axial strains larger than 10 %. As detailed later, although it prevents the use of triaxial extension test data for the characterisation of the critical state of Hostun sand in triaxial extension, the obtained results were employed to the characterisation of the phase transformation state and peak stress ratio state, which were generally observed to occur before axial strains reached 10 %.

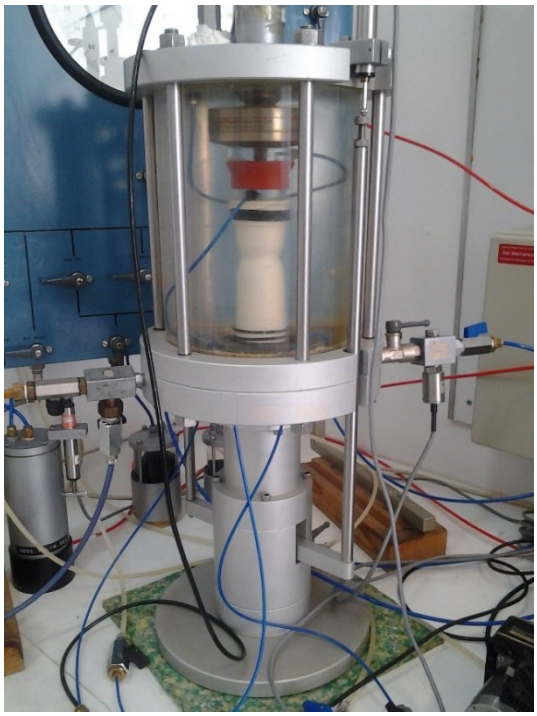

Figure 2.9 – Sample necking in triaxial extension.

To evaluate the impact of membrane penetration on the obtained triaxial test results, the methodology proposed by Baldi and Nova (1984) was employed. According to these authors, in a drained triaxial test conducted on a saturated sample with initial volume V_0 and initial diameter D_0, the volume change due to uniquely membrane penetration, ΔV_m, can be estimated by Equation 2.4.

$$\Delta V_m = \frac{1}{2}\frac{d_{50}}{D_0} V_0 \left(\frac{\sigma'_r \, d_{50}}{E_m \, t_m}\right)^{1/3} \tag{2.4}$$

where d_{50} is the mean diameter of the sand grains (which is about 0.34 mm, as described in Section 2.2.1), σ'_r is the radial effective stress applied to the sample and E_m and t_m are the Young modulus and thickness of the membrane, respectively.

Furthermore, by using a small-strain approach, the authors suggested that the volumetric strain uniquely associated with membrane penetration, ΔV_m, and the corresponding change in the void ratio, Δe_m, can be estimated by Equation 2.5 and Equation 2.6, respectively. In these equations, it is particularly interesting to observe that Δe_m is inversely proportional to D_0, which means that an effective form of reducing undesirable membrane penetration effects consists of testing samples with larger diameters.

$$\varepsilon_{v,m} = \frac{\Delta V_m}{V_0} = \frac{1}{2}\frac{d_{50}}{D_0}\left(\frac{\sigma'_r\, d_{50}}{E_m\, t_m}\right)^{1/3} \tag{2.5}$$

$$\Delta e_m = -(e_0 + 1)\, \varepsilon_{v,m} = -(e_0 + 1)\, \frac{1}{2}\frac{d_{50}}{D_0}\left(\frac{\sigma'_r\, d_{50}}{E_m\, t_m}\right)^{1/3} \tag{2.6}$$

Given that membranes characterised by a Young modulus of $E_m = 1.4$ MPa and having a thickness of $t_m = 0.35$ mm were used in the present testing programme, and considering the loosest sample tested under drained conditions (having a void ratio after preparation of $e_0 = 0.89$), the maximum changes in void ratio associated with membrane penetration, Δe_m, as a function of radial effective stress, σ'_r, were estimated from Equation 2.6. The obtained results are depicted in Figure 2.10, where the grey curve refers to 100 mm-diameter samples tested in the electro-mechanical triaxial cell, while the black curve refers to 38 mm-diameter samples tested in the Bishop and Wesley (1975)'s stress path cell. As expected, it can be seen that, for a given value of σ'_r, the smaller the diameter of the sample, the larger the value of Δe_m. Nevertheless, it is apparent that the computed values are very small. Specifically, given that samples tested in the Bishop and Wesley (1975)'s stress path cell were consolidated to radial effective stresses ranging from 60 to 80 kPa, a maximum value of $\Delta e_m = 0.0025$ is expected to have occurred according to Baldi and Nova (1984)'s methodology, which is well within the range of experimental uncertainty. Similarly, given that samples tested in the electro-mechanical triaxial cell were consolidated under radial effective stresses ranging from 25 to 500 kPa, any correction to the void ratio would not exceed $\Delta e_m = 0.0020$. As detailed later, changes in the void ratio ranging from 0.037 to 0.124 were measured in the drained triaxial tests conducted in the electro-mechanical triaxial cell and, therefore, due to its small relevance (smaller than 5%), it was decided to disregard the effect of membrane penetration. Note that, according to Lade and Hernandez (1977) and Baldi and Nova (1984), the membrane penetration may also affect the pore water pressures measured in undrained triaxial compression tests. However, since the initial conditions of the undrained triaxial tests performed in the present experimental programme were similar to those of the drained triaxial tests, negligible effects of membrane penetration on the registered excess pore water pressures are also believed to have occurred under undrained conditions.

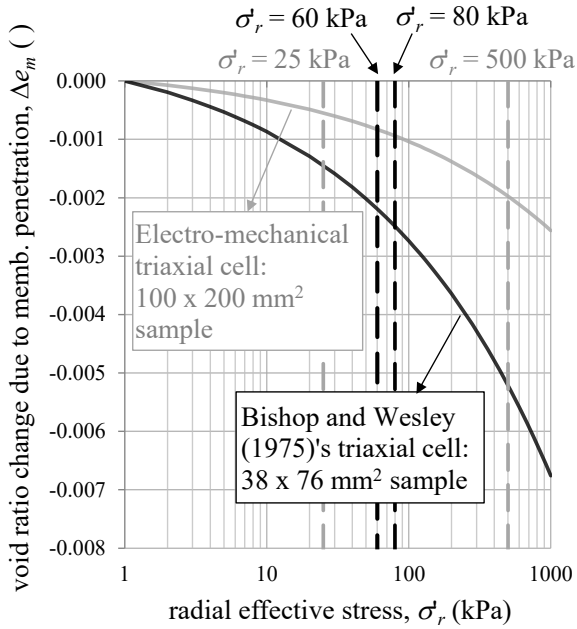

Figure 2.10 – Maximum change in void ratio due to membrane penetration as a function of the radial effective stress estimated from Baldi and Nova (1984)'s methodology for the present experimental programme.

Similarly, other factors affecting triaxial test data, such as volume changes due to the water compressibility or triaxial cell expansion, were considered sufficiently small to be neglected. Note that a comprehensive description of these factors is provided in Head (1998).

2.4.2 Bender element tests

Having determined the travel time, *t*, of the shear wave vertically propagating through the sample from bender element (BE) measurements, the small-strain (or maximum) shear modulus, G_{max}, of Hostun sand was computed based on Equation 2.7.

$$G_{max} = \rho v_s^2 = \rho \frac{L^2}{t^2} \tag{2.7}$$

where ρ is the density of the sample, v_s is the shear wave velocity and *L* is the travel distance, which should be taken as the distance between the tips of the BE, according to Viggiani and Atkinson (1995). Note that the tip-to-tip distance was determined by subtracting the protrusion of the bender elements from the sample's initial height, along with the changes in sample height during triaxial compression registered by the LVDT mounted on the stress path cell.

Although conceptually simple, the determination of the travel time can be challenging. In particular, it is generally argue that distortions in the signal caused by near-field effects (e.g. Sanchez-Salinero *et al.*, 1986; Jovicic *et al.*, 1996; Arroyo *et al.*, 2003) and/or electrical noise (e.g. Lee and Santamarina, 2005) often mask the arrival of the shear wave, resulting in some degree of subjectivity when analysing the obtained BE results. Other factors such as sample size effects due to reflections of shear waves at lateral boundaries (Arroyo *et al.*, 2006;

Camacho-Tauta *et al.*, 2015) may also contribute to misinterpretation of the obtained results. In effect, many authors have reported difficulties in the interpretation of BE results (Viggiani and Atkinson, 1995; Jovicic *et al.*, 1996; Arroyo *et al.*, 2003; Clayton *et al.*, 2004; Arroyo *et al.*, 2006; Yamashita *et al.*, 2009; Clayton, 2011; Camacho-Tauta *et al.*, 2015), with several methodologies being proposed in the literature, from simple observation of the shear wave waveforms and identification of the instant of arrival of the received wave to more elaborate methods involving signal processing. An overview of the available interpretation methods, their merits and drawbacks, is presented, for example, in Viana da Fonseca *et al.* (2009) and Yamashita *et al.* (2009). Indeed, according to these authors, there seems to be no consensus about the most appropriate method to be used.

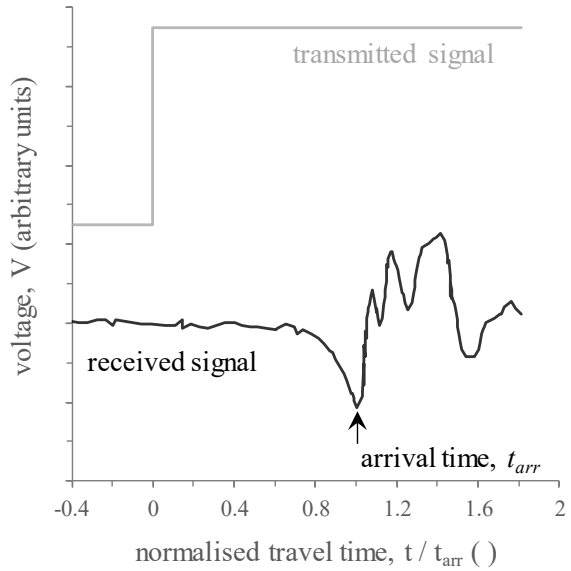

Figure 2.11 – Detection of the arrival time of a shear wave by considering the first significant reversal of polarity of the received signal (adapted from Jovicic et al., 1996).

As suggested by Alvarado (2007) and Viana da Fonseca *et al.* (2009), in the present study, with the objective of minimise subjectivity and increase reliability, two different methods – one of them belonging to the time domain (TD), while the other one included in the frequency domain (FD) – were employed to analyse BE test data, with the travel times estimated by both methods being compared. More specifically, within the TD, the "first arrival" (FA) method (also known as "start to start" method), which is characterised by its simplicity and widespread use, was employed. By assuming plane waves transmission between transducers and no reflected or refracted waves (Arroyo *et al.*, 2006), the method consists on the identification of the instant at which the transmitted excitation first arrives to the receiver (henceforth referred to as "arrival time"), t_{arr}, which, according to Dyvik and Madshus (1985), Viggiani and Atkinson (1995) and Jovicic *et al.* (1996) corresponds to the first significant reversal of polarity of the received signal, identified with an arrow in Figure 2.11. Perhaps, it should be noted that different points were considered by other authors (for instance, Yamashita *et al.* (2009) suggested that arrival time should be identified by the point where

the received signal crosses the zero voltage line, after the initial deflection). Moreover, it should be noted that the arrival time was subsequently subtracted by the time lag, t_{lag}, to give the travel time, t, as indicated by Equation 2.8. As mentioned before, t_{lag} was estimated by performing a preliminary test, where the tips of the transmitter and the receiver bender elements were placed in direct contact, with a value of 0.012 ms being obtained.

$$t = t_{arr} - t_{lag} \tag{2.8}$$

In the frequency domain (FD), the "phase velocity" method, originally proposed by Mancuso *et al.* (1989) for the interpretation of crosshole test results and later applied by Viggiani and Atkinson (1995) to the interpretation of BE test results was selected. Noteworthy, this method was comprehensively explored by Alvarado (2007) and Alvarado and Coop (2012), with the sole difference that the arrival time was estimated from the phase of the transfer function (as detailed below), rather than from the phase of the cross-power spectrum, as originally proposed by Mancuso *et al.* (1989). In the present study, the methodology proposed by Alvarado (2007) and Alvarado and Coop (2012) was followed and, therefore, the method is described in terms of the transfer function. Specifically, after the transformation of domain by using a fast Fourier transform (FFT), the received signal, $L_y(f) = FFT(Y(t))$, is related to the transmitted signal, $L_x(f) = FFT(X(t))$, through a transfer function, $H(f)$ (Equation 2.9), which is assumed to be unique and independent of the type of transmitted signal (Alvarado and Coop, 2012). While the gain factor of the transfer function, $|H(f)|$, given by the ratio of the amplitudes of the received to the transmitted signals (Equation 2.10), can be used to identify the modes of vibration of the system, the phase of the transfer function, $\phi(f)$ (Equation 2.11), indicates the phase delay between the transmitted and received signals across the frequency spectrum (Alvarado and Coop, 2012).

$$L_y(f) = H(f)\, L_x(f) \Leftrightarrow H(f) = \frac{L_y(f)}{L_x(f)} \tag{2.9}$$

$$|H(f)| = \sqrt{[\mathrm{Re}(H(f))]^2 + [\mathrm{Im}(H(f))]^2} = \frac{|L_y(f)|}{|L_x(f)|} = \frac{\sqrt{\left[\mathrm{Re}(L_y(f))\right]^2 + \left[\mathrm{Im}(L_y(f))\right]^2}}{\sqrt{[\mathrm{Re}(L_x(f))]^2 + [\mathrm{Im}(L_x(f))]^2}} \tag{2.10}$$

$$\phi(f) = \begin{cases} \mathrm{atan}\left[\dfrac{\mathrm{Im}\left(H(f)\right)}{\mathrm{Re}\left(H(f)\right)}\right] & , \quad \mathrm{Re}\left(H(f)\right) > 0 \\ \mathrm{atan}\left[\dfrac{\mathrm{Im}\left(H(f)\right)}{\mathrm{Re}\left(H(f)\right)}\right] + \pi & , \quad \mathrm{Re}\left(H(f)\right) < 0 \text{ and } \mathrm{Im}(H(f)) \geq 0 \\ \mathrm{atan}\left[\dfrac{\mathrm{Im}\left(H(f)\right)}{\mathrm{Re}\left(H(f)\right)}\right] - \pi & , \quad \mathrm{Re}\left(H(f)\right) < 0 \text{ and } \mathrm{Im}\left(H(f)\right) < 0 \\ \dfrac{\pi}{2} & , \quad \mathrm{Re}\left(H(f)\right) = 0 \text{ and } \mathrm{Im}\left(H(f)\right) > 0 \\ -\dfrac{\pi}{2} & , \quad \mathrm{Re}\left(H(f)\right) = 0 \text{ and } \mathrm{Im}\left(H(f)\right) < 0 \\ \text{undetermined} & , \quad \mathrm{Re}\left(H(f)\right) = 0 \text{ and } \mathrm{Im}\left(H(f)\right) = 0 \end{cases} \tag{2.11}$$

where $\mathrm{Re}(H(f))$ and $\mathrm{Im}(H(f))$ are, respectively, the real and imaginary components of the complex number defining the transfer function for a discrete frequency, f (i.e. $H(f) = \mathrm{Re}(H(f)) + \mathrm{Im}(H(f))\,i$, with i being the imaginary number). Similarly, $\mathrm{Re}(L_x(f))$ and $\mathrm{Im}(L_x(f))$ are, respectively, the real and imaginary parts of the transmitted signal, while $\mathrm{Re}(L_y(f))$ and $\mathrm{Im}(L_y(f))$ are, respectively, the real and imaginary parts of the received signal. For further information on the use of complex numbers in the context of soil dynamics refer to Kramer (1996).

Note that, although by definition $\phi(f)$ varies between $-\pi$ and $+\pi$, a stacking (also termed as unwrapping) algorithm is used to obtain values varying between zero and infinity. In the present case, the stacking algorithm suggested by Alvarado (2007) was employed, involving the following two steps:

1. verification that the value of the phase, $\phi(f)$, belongs to the interval $[0, 2\pi]$ by adding 2π to the obtained value (Equation 2.11) whenever necessary;
2. verification that the value of $\phi(f)$ obtained for the discrete frequency under analysis is greater than that obtained for the previously analysed discrete frequency by increasing $\phi(f)$ by an integer multiple of 2π whenever necessary.

For an ideal unimodal and non-dispersive system, the stacked phase of the transfer function, $\phi(f)$, when plotted against the frequency content, would be a straight line passing through the origin, with slope (termed as "phase velocity") being directly proportional to the arrival time of the shear wave, t_{arr}, as given by Equation 2.12 (Alvarado and Coop, 2012).

$$t_{arr} = \frac{1}{2\pi}\frac{\partial\phi(f)}{\partial f} \tag{2.12}$$

According to these authors, in reality, bender element systems have, in general, a multimodal and dispersive nature, which may lead to slope variations and phase reversals. In fact, as pointed out by the authors, the system is not perfect and comprises not only the medium (which may have several modes of vibration), but also its boundaries and the bender elements themselves. Nevertheless, as illustrated in Figure 2.12, for the confining stresses typically encountered in geotechnical engineering (typically below 1000 kPa), it is, in general, possible to approximate the phase of the transfer function (or, similarly, the phase of the cross-power spectrum) by a straight line, at least over a selected frequency interval around the resonant frequency (e.g. Viggiani and Atkinson, 1995; Alvarado and Coop, 2012). To distinguish from the slope that would be obtained for an ideal unimodal and non-dispersive system, the slope of the fitting line is typically termed as "group velocity" and can be employed to estimate t_{arr} (Equation 2.12), which, in this case, is typically referred to as "group arrival time" (e.g. Viggiani and Atkinson, 1995; Alvarado and Coop, 2012). Note, nevertheless, that, since values of t_{arr} obtained when using this method will be compared to those obtained when using the "first arrival" method in the present study, the term "group" will be omitted henceforth (i.e. the term "arrival time" will be simply used).

As also illustrated in Figure 2.12, singularities typically appear at frequencies where gain approaches a local minimum. This is typically the case at low frequencies (below 5 kHz), resulting in a poor definition of the stacked phase within this frequency range and, consequently, in an offset of the stacked curve in relation to the origin (Alvarado and Coop, 2007, 2012). Nevertheless, as pointed out by these authors, providing that this part of the curve is disregarded, this offset from origin should have no influence on the estimated arrival time, which is solely a function of the slope of the stacked phase curve, as explained before.

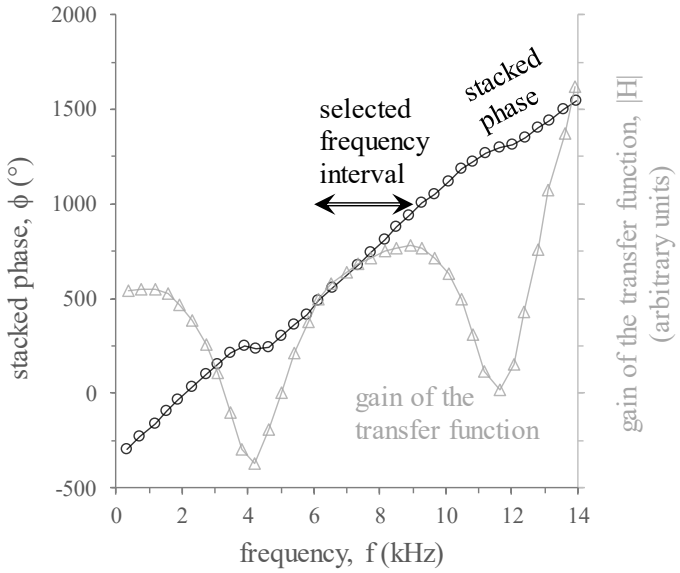

Figure 2.12 – Illustration of the evolutions of the stacked phase and gain of the transfer function with frequency obtained from bender element measurements (Alvarado and Coop, 2012).

2.5 Monotonic response of Hostun sand at small strains

2.5.1 General aspects

Although it has been observed that, even at very small strains, the response of soil is typically non-linear, for practical purposes and below a strain level of about 10^{-5} to 10^{-6}, stress-strain non-linearity is typically considered small enough to be disregarded (e.g. Clayton and Heymann, 2001; Clayton, 2011; Oztoprak and Bolton, 2012). Moreover, despite the fact that typical strain range of liquefaction-related phenomena are, in general, well above that elastic threshold, as illustrated in Figure 2.13, the characterisation of the shear modulus at very small strains, G_{max}, is considered very important, since it defines the starting point of the stiffness-strain curve. This parameter has been often measured by dynamic methods, either by *in-situ* seismic wave tests (such as seismic refraction and crosshole tests) or by laboratory tests (such as bender element and resonant column tests).

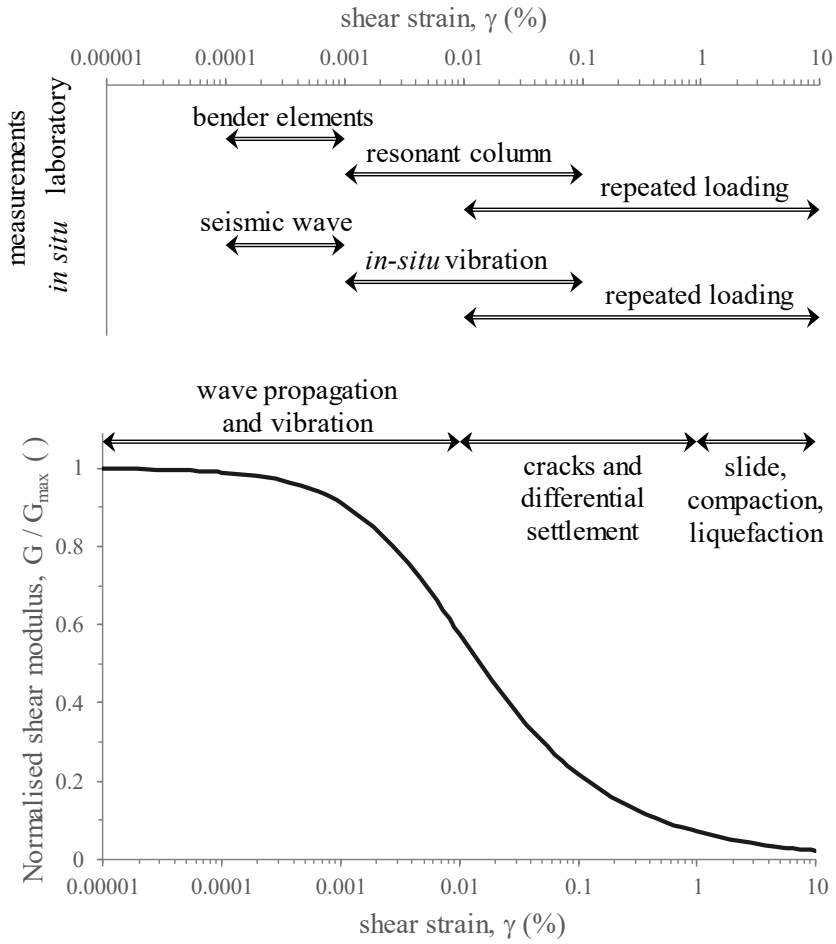

Figure 2.13 – Reduction of stiffness with strain and typical ranges of different dynamic phenomena, laboratory and field measurements (adapted from Ishihara, 1996; Clayton, 2011).

The small-strain shear stiffness of soil has typically been defined as a function of the void ratio, *f(e)*, the overconsolidation ratio, *OCR*, and the mean effective stress, *p'*, as shown by Equation 2.13 (Hardin and Black, 1968).

$$G_{max} = C_g \, p'_{ref} \, f(e) \, OCR^k \left(\frac{p'}{p'_{ref}} \right)^{n_g} \tag{2.13}$$

where C_g, k and n_g are soil-dependent parameters and p'_{ref} is the reference pressure (typically considered equal to the atmospheric pressure, i.e. $p'_{ref} \approx 101.3$ kPa). For sands, several experimental studies (e.g. Hardin and Drnevich, 1972a, 1972b; Lo Presti *et al.*, 1997; Zhou and Chen, 2005) have shown that *OCR* has minor influence on G_{max}. Therefore, its contribution to G_{max} is usually neglected by setting k to zero in Equation 2.13, with G_{max} being essentially related to e and p'. Moreover, for air-pluviated sands, the exponent n_g have been found to have a small variation, between approximately 0.4 and 0.6 (see, for example, Benz (2007)), with a value of 0.50 being employed by many researchers to characterise small-stiffness data (Hardin and Black, 1966a, 1968; Oztoprak and Bolton, 2012). With respect to the function of the void ratio, *f(e)*, based on the resonant column test results obtained by Hardin and Richart (1963) and Hardin and Black (1966) on two materials having very different particle shape –

Ottawa sand no. 20-30 having round particles and crushed quartz consisting of angular particles – Hardin (1965) and Hardin and Black (1966) proposed the use of Equation 2.14 for round-grained sand and Equation 2.15 for angular-grained sand. In the present study, due to the sub-angular to angular shape of Hostun sand's particles (Section 2.2.1), Equation 2.15 was adopted. Note that other expressions for *f(e)* can be found in the literature – refer, for example, to Hardin (1978) and Lo Presti *et al.* (1993).

For round-grained sand: $f(e) = \frac{(2.17 - e)^2}{1.0 + e}$ (2.14)

For angular-grained sand: $f(e) = \frac{(2.97 - e)^2}{1.0 + e}$ (2.15)

2.5.2 Bender element testing programme

Two isotropically consolidated drained isotropic compression (ICDIC) tests, termed as ICDIC 0.787/25 and ICDIC 0.653/25, were performed on a moderately loose sample ($e_0 = 0.787$) and on a dense sample ($e_0 = 0.653$), respectively. These tests were used to perform BE measurements at different effective stress levels, as detailed below. Table 2.3 summarises the initial conditions of both tests, including: the dimensions of each sample after its preparation (i.e. initial diameter, D_{init}, and initial height, H_{init}), as well as the initial travel distance of the shear wave, $L_{BE,init}$ (obtained by subtracting the bender element protrusions into the sample from the sample's initial height), and the dry mass after sample's preparation, M_{init}; the void ratio, e_0, and corresponding relative density, $D_{r,0}$, the cell and back pressures, $\sigma_{cell,0}$ and u_0, respectively, and corresponding isotropic effective stress, σ'_0, before drained isotropic compression loading was applied.

Table 2.3 – Initial conditions of the drained isotropic compression tests during which bender element measurements were undertaken.

Test ID [(a)]	Sample's preparation [(b)]				Soil's state and stress conditions before drained isotropic compression loading				
	D_{init}	H_{init}	$L_{BE,init}$	M_{init}	e_0	$D_{r,0}$	$\sigma_{cell,0}$	u_0	σ'_0
	(mm)	(mm)	(mm)	(g)	( )	(%)	(kPa)	(kPa)	(kPa)
ICDIC 0.787/25	37.4	80.5	72.6	129.8	0.787	62.5	225.0	200.0	25.0
ICDIC 0.653/25	37.3	84.7	76.8	147.7	0.653	102.1	225.0	200.0	25.0

[(a)] The designation identifies: (1) type of consolidation: isotropic consolidation (IC); (2) type of drainage: drained (D); (3) type of loading: isotropic compression (IC); (4) initial void ratio, e_0; and (5) initial isotropic effective stress, σ'_0 (i.e. first isotropic effective stress level at which BE measurements were undertaken).
[(b)] Volume and mass measurements were performed after sample's preparation.

In both tests, samples were gradually consolidated to isotropic effective stresses of 25, 55, 80, 110, 135, 165, 200, 300, 400 and 500 kPa. For each of these effective stress levels, single sine pulses with a peak-to-peak amplitude of 20 V and varying frequencies (from 1 to 10 kHz) were transmitted to the probes and the obtained responses were recorded. A first unloading phase was subsequently performed with bender element measurements being conducted at isotropic effective stresses of 500, 400, 300, 200, 135, 80 and 25 kPa. In order to evaluate the

effect of overconsolidation, sample was subjected to reloading and a second phase of unloading with bender element measurements being once more taken at isotropic effective stresses of 25, 80, 135, 200, 300, 400 and 500 kPa.

2.5.3 Time-domain analysis of the measured waves

Figure 2.14 depicts the waveforms corresponding to the transmitted and received signals at the selected effective stress levels during the first loading of test ICDIC 0.787/25. More specifically, for each effective stress level, two sets of transmitted and received signals are presented: one set of signals corresponding to $f = 4$ kHz (represented by dashed curves) and the other set of signals corresponding to a selected frequency (represented by solid curves) – i.e. the frequency, among those applied to the probes, that seems to have resulted in a received signal less affected by near field effects, identified by an initial deflection of the waveform before the arrival of the shear wave (Sanchez-Salinero *et al.*, 1986; Jovicic *et al.*, 1996; Lee and Santamarina, 2005). For clarity of the presentation, the remaining eight recorded waveforms (for other input frequencies) are omitted from the figure. Three aspects are particularly noteworthy. Firstly, the presentation of signals corresponding to $f = 4$ kHz for all effective stress levels intends to illustrate the modification of the waveforms with isotropic effective stress. Other value than 4 kHz could have been selected. Secondly, it is apparent that, as the effective stress level increases, higher frequencies are required to minimise near field effects (i.e. the selected frequency has a higher value). This could, in fact, be expected, since the increase in isotropic effective stress, σ'_0, likely leads to an increase in the maximum shear modulus, G_{max}, and, consequently, to an increase in the shear wave velocity, v_s (which, according to the theory of wave propagation in an isotropic elastic medium, is given by $v_s = \sqrt{G/\rho}$, where G is the elastic shear modulus – in this case, assumed equal to G_{max} – and ρ is the density of the material). This means that the wavelength, λ (which is given by $\lambda = v_s/f$, according to the theory of wave propagation in an isotropic elastic medium), is expected to increase with the isotropic effective stress, likely increasing near field effects, unless the frequency is also increased to counterbalance it (Sanchez-Salinero *et al.*, 1986; Alvarado and Coop, 2012). Thirdly, it should be noted that the received signals are displayed in the figure with reversed polarity (i.e. sine-type received signals appear inverted in relation to the transmitted single sine pulses). Moreover, note that, since the received signal is typically strongly attenuated in relation to the transmitted signal, its amplitude is multiplied by a constant for clarity of presentation and, consequently, the units of the waveforms are arbitrary.

In general, the first arrival could be identified with a good degree of confidence by the first downward deflection of the received signal, as indicated in the figure. As expected, earlier arrival times are obtained for higher effective stress levels.

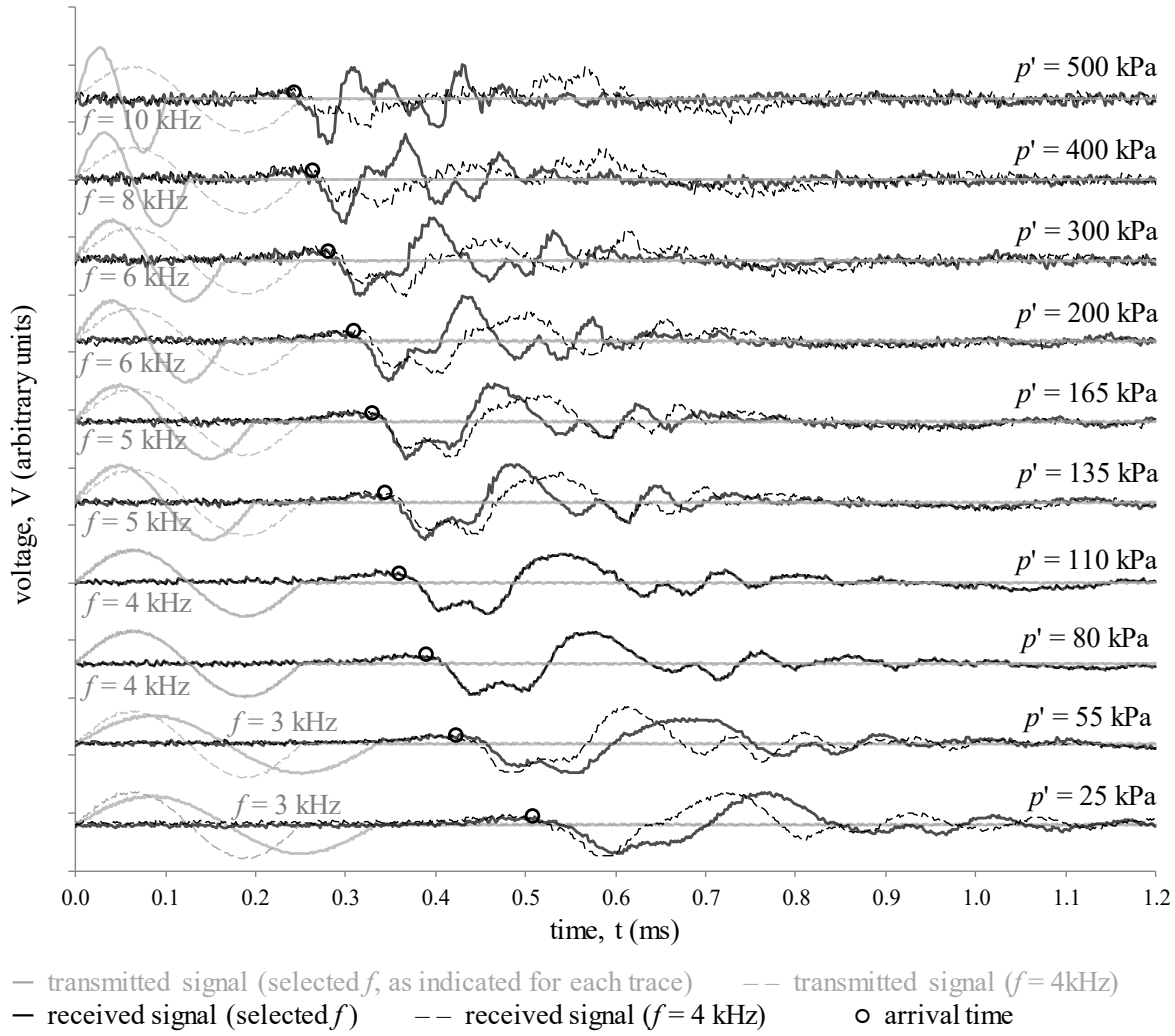

Figure 2.14 – Selected first arrivals in time domain during the first loading of test ICDIC 0.787/25.

Complementary, the waveforms registered during the first loading (black solid curves) are compared with those recorded during the first unloading (dashed dark grey curves) for identical effective stress levels (25, 80, 135, 200, 300, 400 and 500 kPa) of test ICDIC 0.787/25 in Figure 2.15. Note that, in the case, only the waveforms corresponding to a selected frequency are shown in the figure to ease the presentation. The waveforms registered during the first unloading can barely be distinguished from those recorded during the first loading, suggesting that, at least for this type of loading, the previous stress history has little influence on the shear wave velocity and, consequently, on the maximum shear modulus of sand, as expected (see Section 2.5.1). This conclusion seems to be further strengthened by comparing the waveforms registered during the first loading and reloading phases of test ICDIC 0.787/25, represented, respectively, by black solid curves and dashed dark grey curves in Figure 2.16. Once again, it is apparent that very similar waveforms were obtained for these two different phases of the DIC test. Similarly, the waveforms recorded during second unloading (not shown here for brevity of the presentation) were observed to be very similar to those registered during the previous phases of the test (i.e. first loading, first unloading and reloading phases). Note that similar results showing minor influence of the previous DIC

loading history on the shear wave velocity propagation in sand have been reported in the literature (e.g. Hardin and Drnevich, 1972a, 1972b; Lo Presti *et al.*, 1997; Zhou and Chen, 2005).

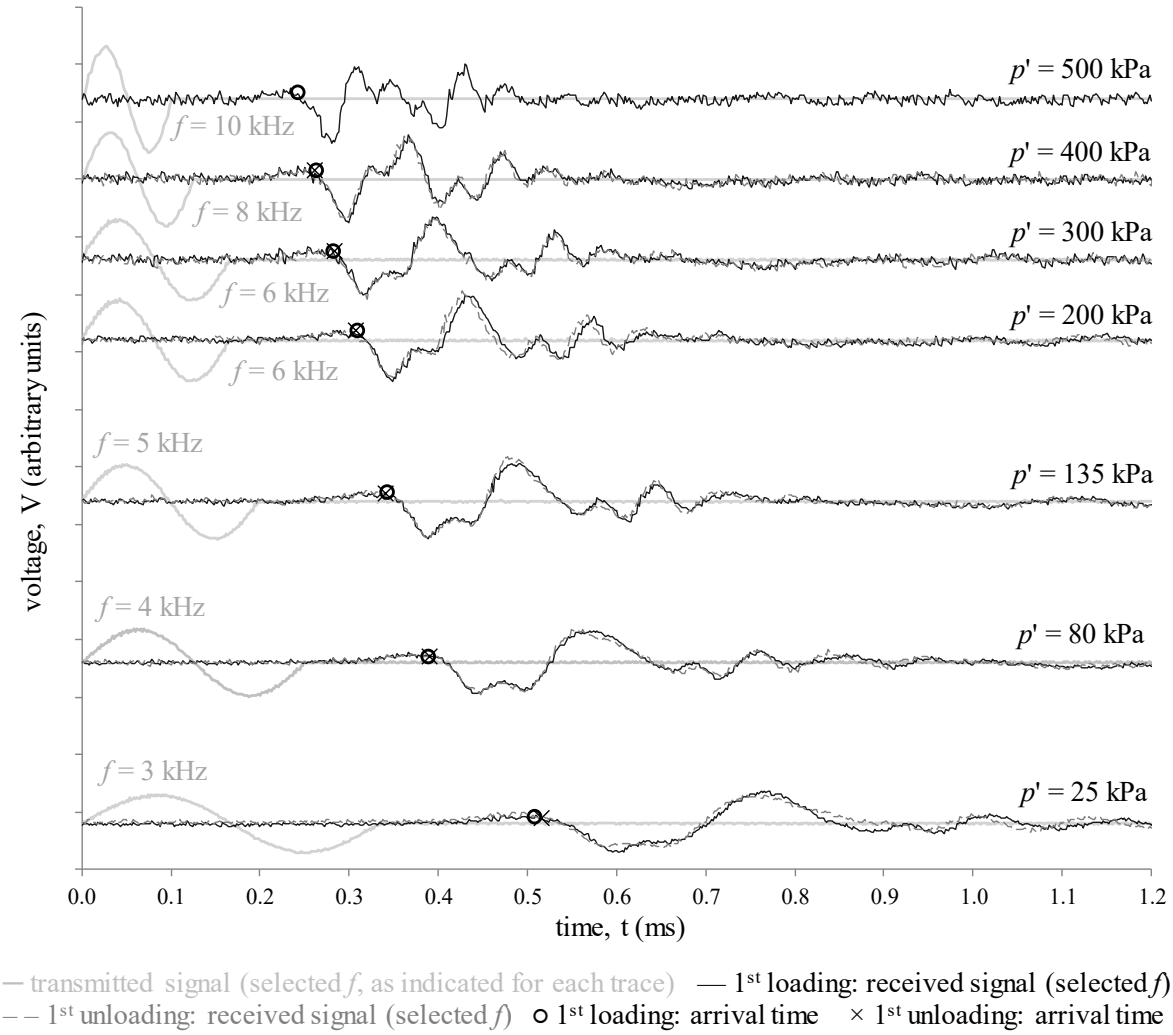

Figure 2.15 – Comparison of the waveforms recorded during the first loading with those registered during the first unloading of test ICDIC 0.787/25.

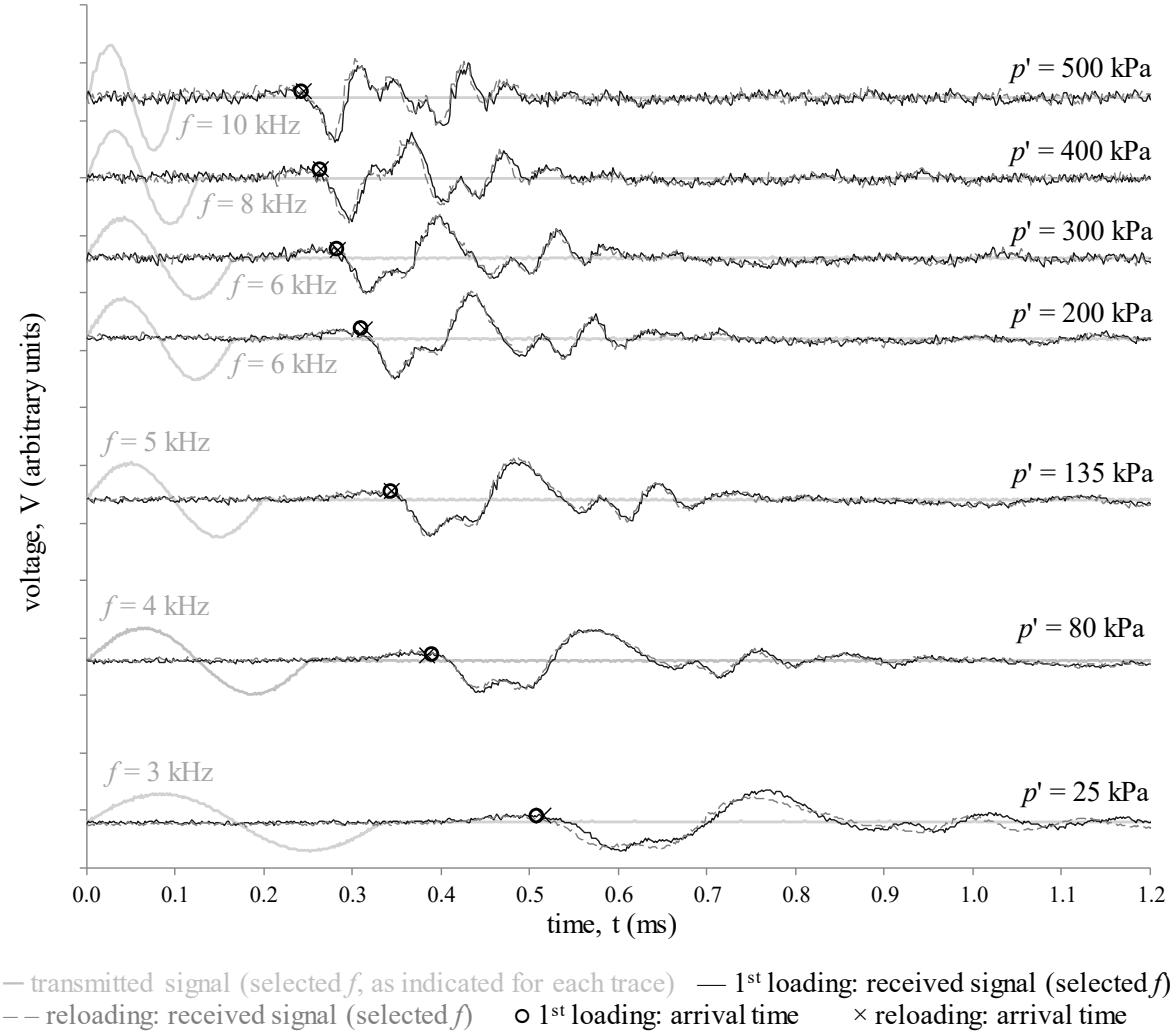

Figure 2.16 – Comparison of the waveforms recorded during the first loading with those registered during reloading of test ICDIC 0.787/25.

In addition, the waveforms registered during the first loading of test ICDIC 0.653/25 conducted on a dense sample are depicted in Figure 2.17, along with the selected arrival times. Once again, for each effective stress level, two sets of transmitted and received signals are presented: one set of signals corresponding to $f = 4$ kHz (dashed curves) and another set of signals corresponding to a selected frequency (solid curves), with the remaining eight recorded waveforms (for other input frequencies) being omitted from the presentation. Note, nevertheless, that, as for the previous test, to pick up the time instant likely corresponding to the arrival of the shear wave for a given effective stress level, all recorded waveforms (with frequencies varying from 1 to 10 kHz, as mentioned before) were inspected simultaneously. The inferred arrival times are also shown in Figure 2.17. Similar to the previously analysed test, it can be seen that the higher the stress level, the earlier the shear-wave arrival takes place, as expected. Moreover, as also observed for test ICDIC 0.787/25, the waveforms seem to be little affected by the previous stress history, meaning that, for each effective stress level, similar waveforms were recorded during first loading, first unloading, reloading and second unloading. Although the comparison of the waveforms corresponding to these different

phases of this test is omitted from the presentation, the values of the maximum shear modulus obtained for the different phases are compared in Section 2.5.5.

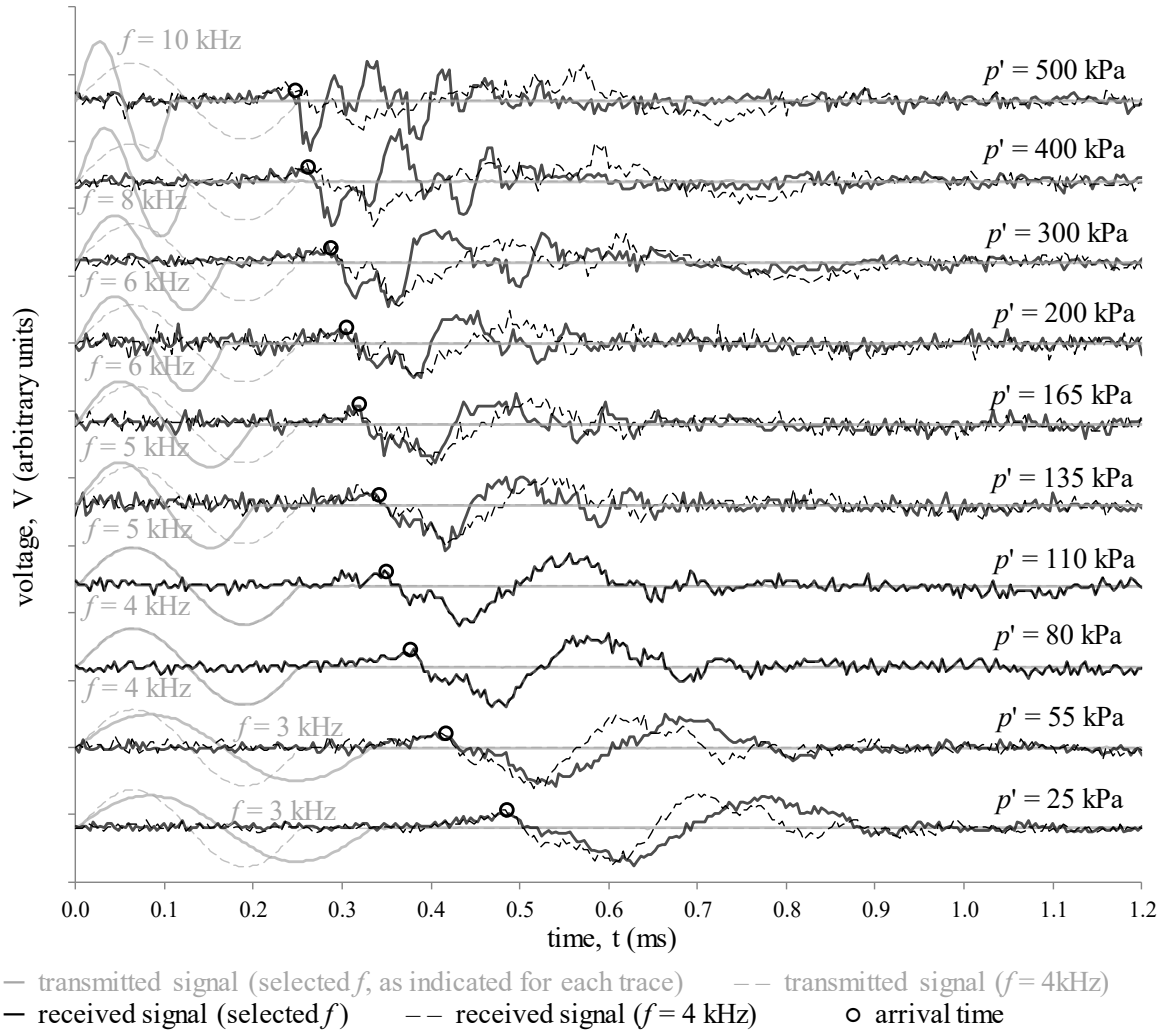

Figure 2.17 – Selected first arrivals in time domain during the first loading of ICDIC 0.653/25 test.

2.5.4 Frequency-domain analysis of the measured waves

Figure 2.18 illustrates the application of the phase velocity method to the estimation of the arrival time of the shear wave for a bender element measurement performed during the first loading of test ICDIC 0.787/25 at an isotropic effective stress level of 200 kPa and using an input frequency of $f = 6$ kHz. It can be seen that, although the transmitted signal exhibits more than a single frequency of vibration, its predominant frequency is close to the intended value ($f = 6$ kHz). Moreover, it is apparent that the shape of the received signal is similar, in terms of frequency content, to that of the transmitted signal. In particular, it can be seen that the resonant frequencies of the system (i.e. frequencies at which the Fourier amplitude of the received signal reaches a local maximum) seem close to the predominant frequencies of the input (i.e. frequencies at which the Fourier amplitude of the transmitted signal reaches a local maximum). In terms of stacked phase (Figure 2.18), as discussed in Alvarado and Coop (2012), it is apparent that discontinuities occur at frequencies where the gain of the transfer function,

$|H|$, reaches low values (particularly evident, in this case, for $f \approx 3$ kHz and $f \approx 11$ kHz). Furthermore, it can be seen that, due to the poor definition of the received signal at low frequencies, the obtained points do not align towards the origin of the plot – an aspect also observed by Alvarado and Coop(2007) and Alvarado and Coop (2012) for other sands. Nevertheless, as pointed out by these authors, linear trends appear to be observed for sections of the stacked phase curve around the resonant frequencies. Following the methodology suggested by these authors, a frequency interval around the first resonant frequency (in this particular case, the interval defined by $f \approx 4.2$ and 9.3 kHz) was selected and the arrival time, t_{arr}, was estimated from the slope of the stacked phase curve over that interval (which, in the present study, was obtained by performing a linear regression over the selected data).

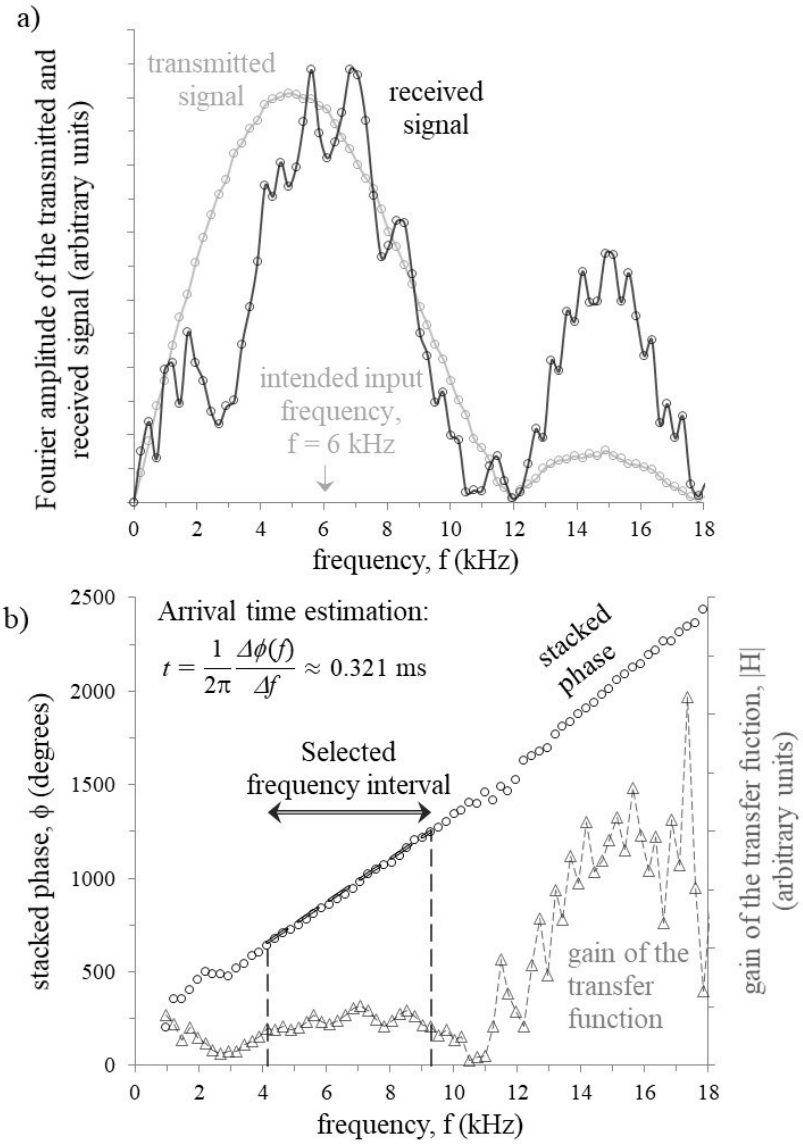

Figure 2.18 – Illustration of the application of the phase velocity method to the estimation of the arrival time for test ICDIC 0.787/25 at *p'* = 200 kPa: (a) Fourier spectra of the transmitted and received signals and (b) stacked phase and gain of the transfer function.

The above described methodology was applied to all bender element measurements performed during tests ICDIC 0.787/25 and ICDIC 0.653/25. Starting by analysing the results obtained during the first loading of the former test, Figure 2.19 depicts the computed stacked phase evolutions with frequency for various effective stress levels (25, 80, 135, 200, 300, 400 and 500 kPa), together with the lines considered for the estimation of the arrival times. Note that, for clarity of the presentation, only the results obtained for selected frequencies (indicated in the figure for each case) are shown. Moreover, with the purpose of comparing the stacked phase evolutions obtained for different effective stress levels, the curves are offset to point to the origin of the plot (note that this offset has no impact on the estimation of the time arrival, since it is solely related to the slope the curve). It can be seen that, as expected, the higher the effective stress level, the milder the slope of the stacked phase evolutions with frequency (over the considered interval) and, therefore, the earlier the arrival time.

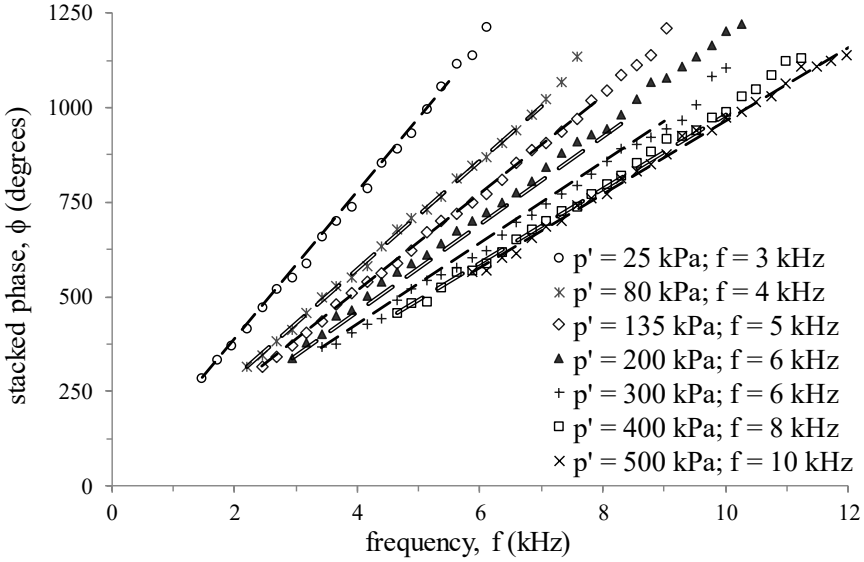

Figure 2.19 – Stacked phase as a function of the frequency for bender element measurements performed during the first loading of test ICDIC 0.787/25.

Similarly, Figure 2.20 depicts the computed evolutions of the stacked phase with frequency for several stress levels at which bender element measurements where undertaken during the first loading of test ICDIC 0.653/25. Once more, it is apparent that, the higher the effective stress level, the higher the frequency required as input to obtain a clean (as possible) signal, as well as the higher the resonant frequency of the system and, therefore, the higher the frequency interval used for the estimation of the slope of the stacked phase curve. Moreover, as observed for test ICDIC 0.787/25, milder slope inclinations are obtained for higher effective stress levels.

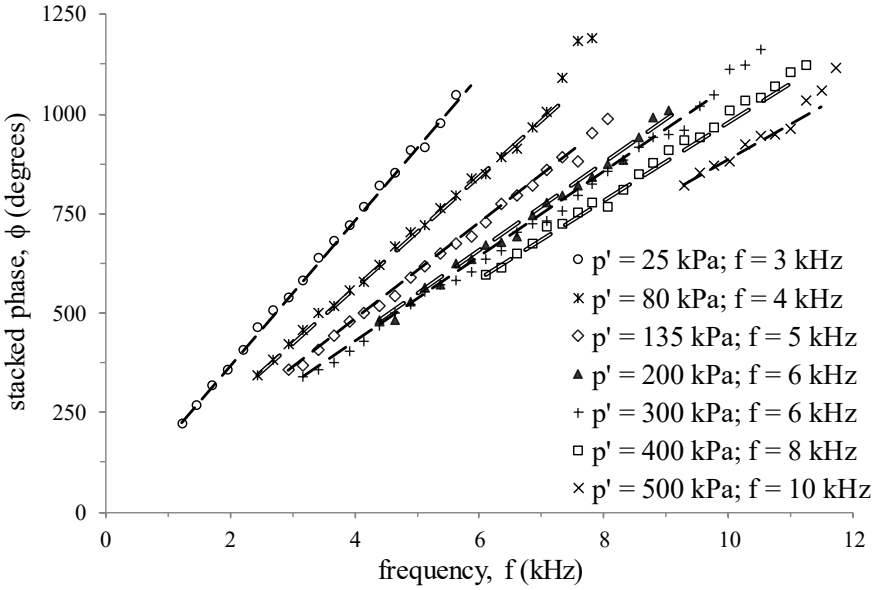

Figure 2.20 – Stacked phase of the transfer function as a function of the frequency for bender element measurements performed during the first loading of test ICDIC 0.653/25.

The arrival times computed using this frequency-domain (FD) method for the first loading of test ICDIC 0.787/25 are compared with those previously selected in the time domain (TD) in Figure 2.21. As reported in the literature (e.g. Viggiani and Atkinson, 1995; Greening and Nash, 2004; Alvarado and Coop, 2012), it can be observed that consistently larger values for the arrival time were estimated from the FD method than those computed from the TD method. Furthermore, it can be seen that, in some cases (e.g. for effective stresses of 300, 400 and 500 kPa), the arrival times computed by the FD method are located within the middle part of the received sine-type signal, after the crossing of the zero voltage line, and, therefore, seem to represent less accurately the arrival time of the shear wave than the values estimated from the TD method.

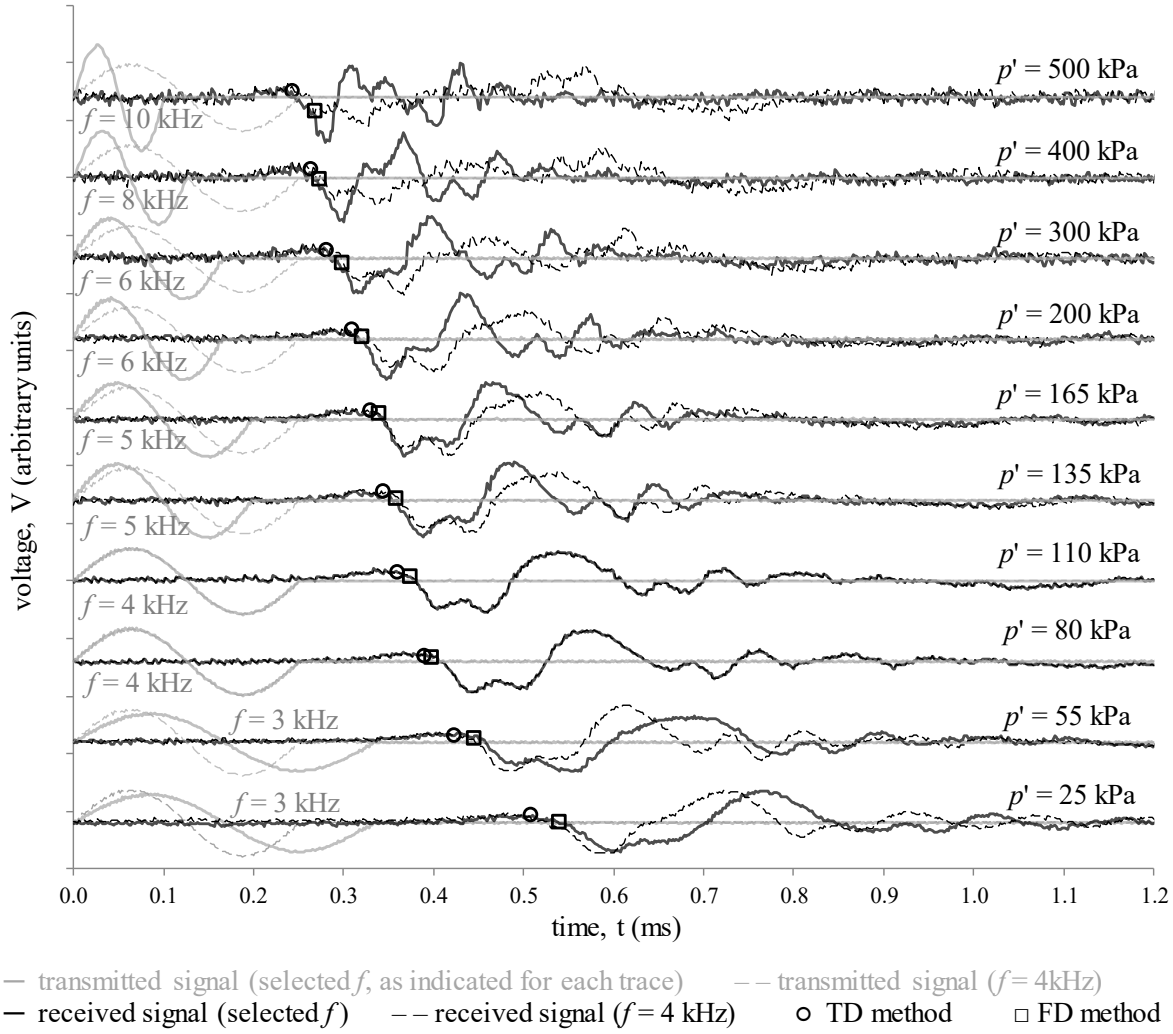

Figure 2.21 – First arrivals in time domain (TD) and frequency domain (FD) at the selected stress levels, during the first loading of test ICDIC 0.787/25.

Similarly, the arrival times estimated by applying the TD and FD methods to the interpretation of the bender element measurements undertaken during the first loading of test ICDIC 0.653/25 test are compared in Figure 2.22. In this case, closer results were obtained by the two different interpretation methods, even if a tendency for obtaining later arrival times when applying the FD method can be generally observed.

Since not all results obtained from the FD method seem to accurately represent the arrival time of the shear wave, it was decided to adopt the arrival times selected by the TD method to compute the shear modulus of Hostun sand at small strains, as detailed in the following section.

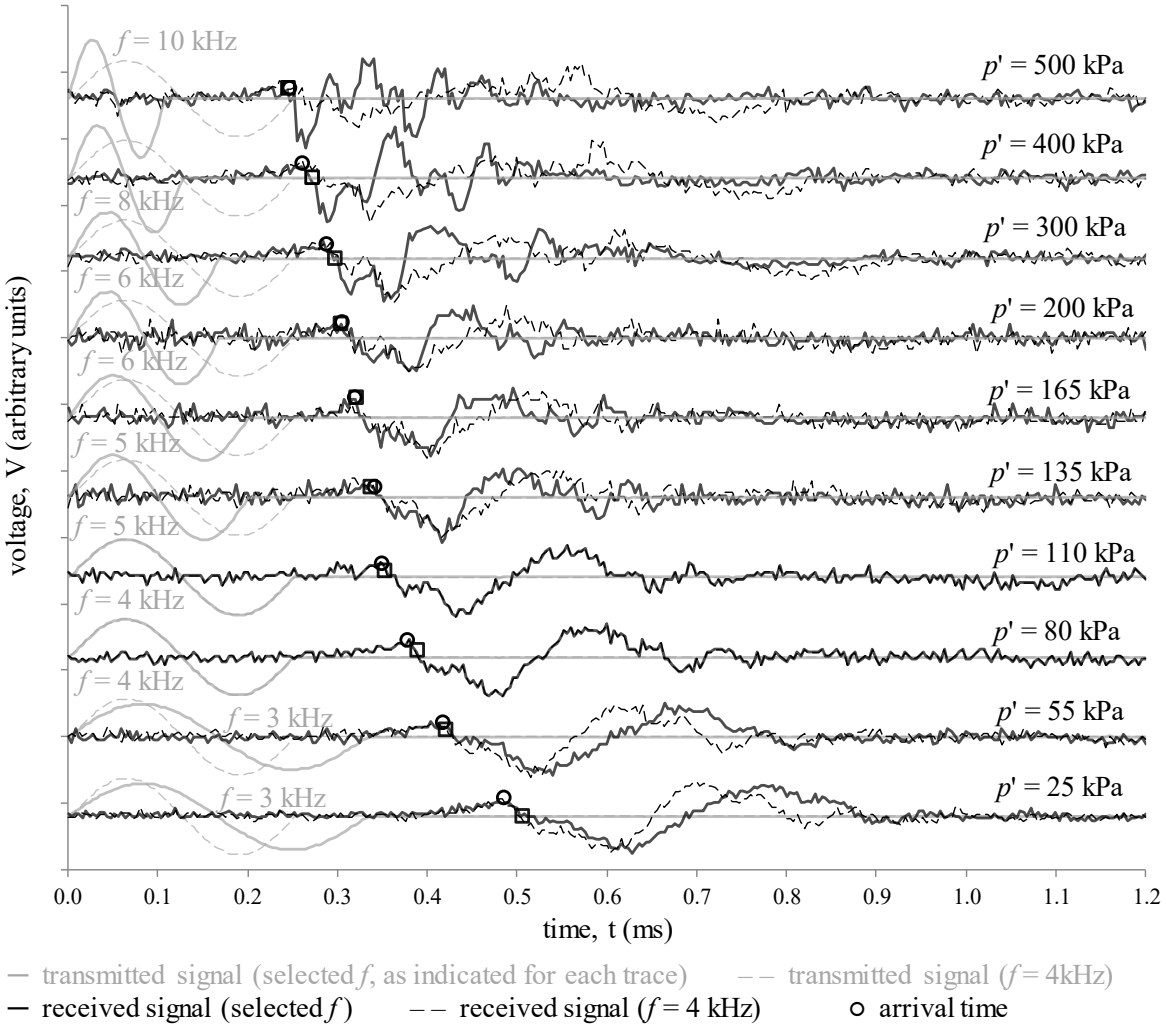

Figure 2.22 – First arrivals in time domain (TD) and frequency domain (FD) at the selected stress levels, during the first loading of the ICDIC 0.653/25 test.

2.5.5 Shear modulus at small strains

The values of the small-strain shear modulus, G_{max}, obtained for the ICDIC 0.787/25 and ICDIC 0.653/25 tests during the first loading (1L), the first unloading (1UL), the reloading (2L) and the second unloading (2UL) phases are depicted in Figure 2.23. As expected, the estimated values of G_{max} are higher for the denser sample (ICDIC 0.653/25 test) and increase with mean effective stress. Moreover, as mentioned before, for these loading conditions, it seems that previous stress history (or, in other words, overconsolidation) has little influence on the small-strain response of Hostun sand, and, therefore, G_{max} can be essentially related to the mean effective stress, p', and the void ratio, e. Taking that into account, the obtained results were used to calibrate the parameters C_g and n_g of Equation 2.16, obtained from Equation 2.13 (Hardin and Black, 1968) and Equation 2.15 (Hardin, 1965; Hardin and Black, 1966a).

$$G_{max} = C_g \, p'_{ref} \, \frac{(2.97 - e)^2}{1 + e} \left(\frac{p'}{p'_{ref}} \right)^{n_g} \tag{2.16}$$

As shown in Figure 2.24, the obtained results present little scatter with a simple least square fitting over the bender element data points leading to $C_g \approx 293.0$ and $n_g \approx 0.49$. Indeed, the present results are close to those obtained by Hoque and Tatsuoka (2000) when using small-amplitude cyclic triaxial loading on dry samples of Hostun sand locally instrumented by strain gauges, as also shown in the figure.

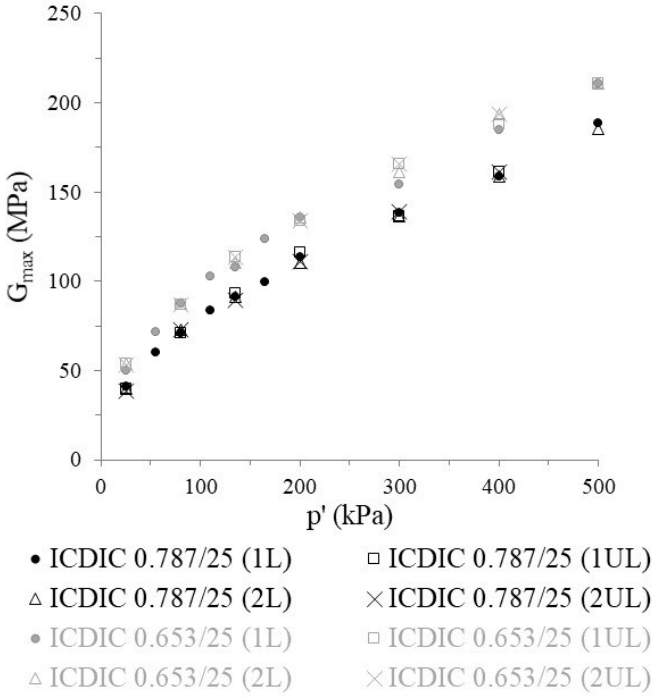

Figure 2.23 – Values of the small-strain shear modulus estimated by employing the first arrival method for tests ICDIC 0.787/25 and ICDIC 0.653/25.

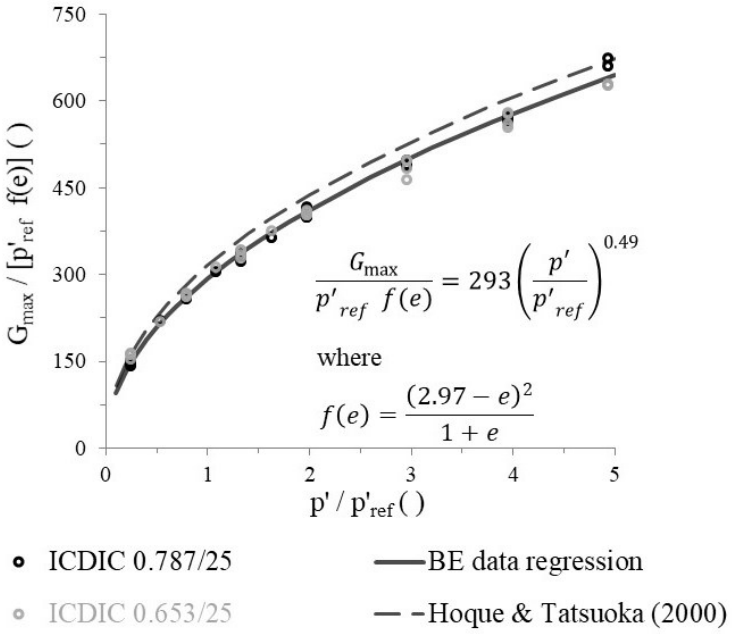

Figure 2.24 – Small-strain shear modulus for Hostun sand.

2.6 Monotonic response of Hostun sand at medium to large strains

2.6.1 General aspects

Over the last decades, the critical-state soil mechanics (CSSM) framework, established by Schofield and Wroth (1968), has been recurrently used as a conceptual framework for modelling the response of sand (e.g. Nova and Wood, 1979a; Mróz *et al.*, 1979; Zienkiewicz *et al.*, 1985; Pastor *et al.*, 1990; Manzari and Dafalias, 1997; Papadimitriou and Bouckovalas, 2002; Ling and Yang, 2006; Taborda *et al.*, 2014). The fundamental principle of the CSSM framework is that, when sheared, soil reaches a final state, termed as "critical state" (CS), at large strains characterised by a unique relationship between void ratio, *e*, and mean effective stress, *p*'. Moreover, as this state is reached, "soil continues to deform at constant stress and constant void ratio", as defined by Roscoe *et al.* (1958). While it is well established that the critical state line (CSL) is independent of *e* and *p*' (Been *et al.*, 1991; Ishihara, 1993; Verdugo and Ishihara, 1996; Riemer and Seed, 1997; Klotz and Coop, 2002; Murthy *et al.*, 2007), its independence in relation to the following aspects has been the subject of much discussion:

- drainage conditions (e.g. Casagrande, 1975; Poulos, 1981), with a large number of recent studies showing that a unique CSL can be obtained under drained or undrained test conditions (e.g. Been *et al.*, 1991; Verdugo and Ishihara, 1996; Riemer and Seed, 1997; Li and Wang, 1998; Murthy *et al.*, 2007); therefore, although the term "steady state" has often been employed to designate the final state of sand response under undrained conditions, rather than "critical state", in the present study, for consistency reasons, the term "critical state" (CS) is exclusively used for that purpose;
- stress path, with a number of experimental studies suggesting that the CSL depends on the direction of the major principal effective stress in relation to the direction of soil deposition and/or on the magnitude of the intermediate principal effective stress and, therefore, different CSL are reached, for example, in triaxial extension and triaxial compression (Vaid *et al.*, 1990a; Riemer and Seed, 1997; Yoshimine *et al.*, 1998; Mooney *et al.*, 1998), while other studies supporting the opposite (Been *et al.*, 1991; Yoshimine and Kataoka, 2007);
- initial soil fabric, commonly obtained by using different methods of sample preparation, with a number of experimental studies suggesting that, at large strains, the effect of the fabric is negligible and, therefore, a unique CSL is reached for samples prepared by different methods (Ishihara, 1993; Zlatovic and Ishihara, 1997; Papadimitriou *et al.*, 2005; Murthy *et al.*, 2007; Sadrekarimi and Olson, 2012).

Although the lack of consensus on its uniqueness, the CSL is undoubtedly a very efficient and useful form of predicting soil response (Murthy *et al.*, 2007). Therefore, in the present study, significant effort was dedicated to its adequate characterisation, based on the results of drained and undrained triaxial compression and extension tests.

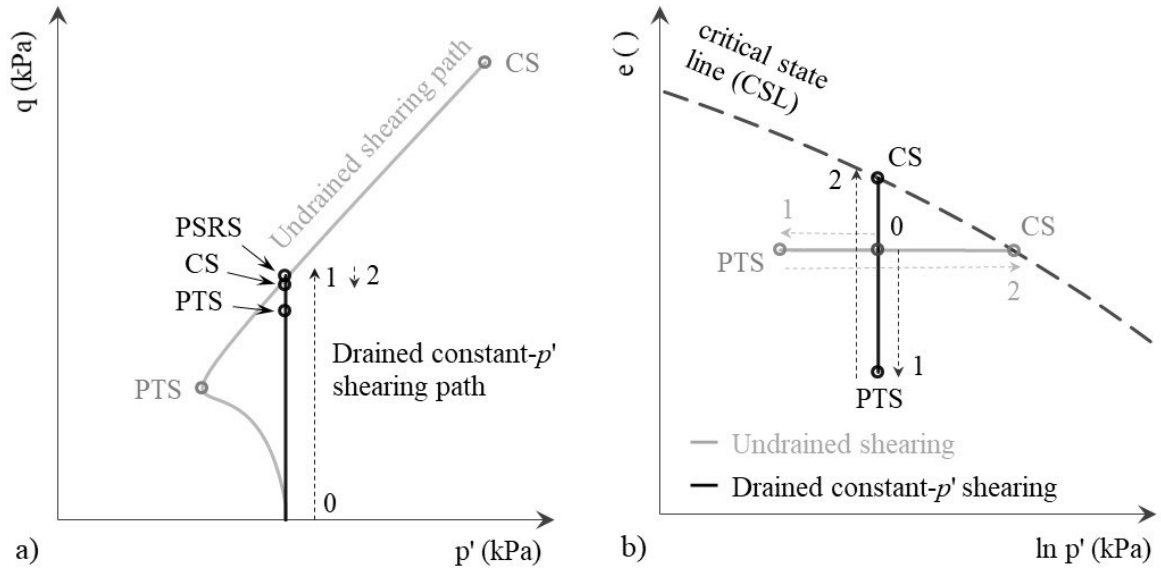

Figure 2.25 – Phase transformation, peak stress ratio and critical states identified from undrained shearing and drained constant-*p*' shearing in the (a) deviatoric stress – mean effective stress and (b) void ratio – mean effective stress (adapted from Manzari and Dafalias, 1997).

Prior to the CS, at moderate or large strains, two transitory states, termed as phase transformation state (PTS) and peak stress-ratio state (PSRS) have been identified as distinctive features of the response of sand (Been and Jefferies, 1985; Manzari and Dafalias, 1997; Murthy *et al.*, 2007; Jefferies and Been, 2006). While the PTS is the state at which the response of sand changes from plastic contraction to plastic dilation (i.e. dilatancy is temporarily null), the PSRS is related to the mobilisation of the maximum angle of shearing resistance (or, equivalently, the maximum stress ratio). These distinctive states are illustrated in Figure 2.25, which depicts a typical response of an initially denser-than-critical sample when subjected to a drained monotonic constant-*p*' triaxial compression test, as well as to an undrained monotonic triaxial compression test with increasing mean stress.

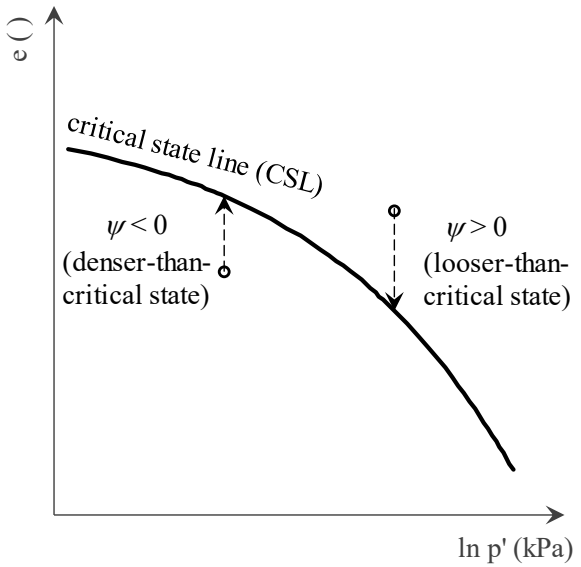

Figure 2.26 – Definition of the state parameter, as proposed by Been and Jefferies (1985).

As proposed by Been and Jefferies (1985) and later experimentally supported by several authors (e.g. Ishihara, 1993; Klotz and Coop, 2001; Jefferies and Been, 2006; Stamatopoulos, 2010), the occurrence of both states can be basically related to the density and mean effective stress through the use of the state-parameter, ψ, which is given by the difference between the current void ratio, e, and the void ratio at critical state, e_{cs}, corresponding to the current mean effective stress (Equation 2.17 and Figure 2.26).

$$\psi = e - e_{cs} \tag{2.17}$$

It is perhaps important to note that some authors (e.g. Ishihara, 1993; Murthy *et al.*, 2007) distinguish between the occurrence of the PTS and another state, termed as quasi-steady state (QSS), although differences in shear strengths and mean effective stresses generally do not exceed 10 % (Murthy *et al.*, 2007). This latter state is defined as the state at which the deviatoric stress, q, reaches a local minimum in undrained shearing (Alarcon-Guzman *et al.*, 1988). In addition, there is another transitory state of the undrained monotonic response of loose sand, termed as undrained instability state (UIS), which is of practical interest. This state is characterised by a local maximum of the deviatoric stress and has been associated with the onset of "flow liquefaction" (e.g. Sladen *et al.*, 1985; Ishihara, 1993). As mentioned before, this liquefaction-related phenomenon is characterised by a sharp reduction of soil's strength to levels below those required to maintain static equilibrium, therefore implying a type of failure induced by static shear stresses and rapid development of large deformations (Kramer, 1996). These distinctive states are schematically illustrated in Figure 2.27.

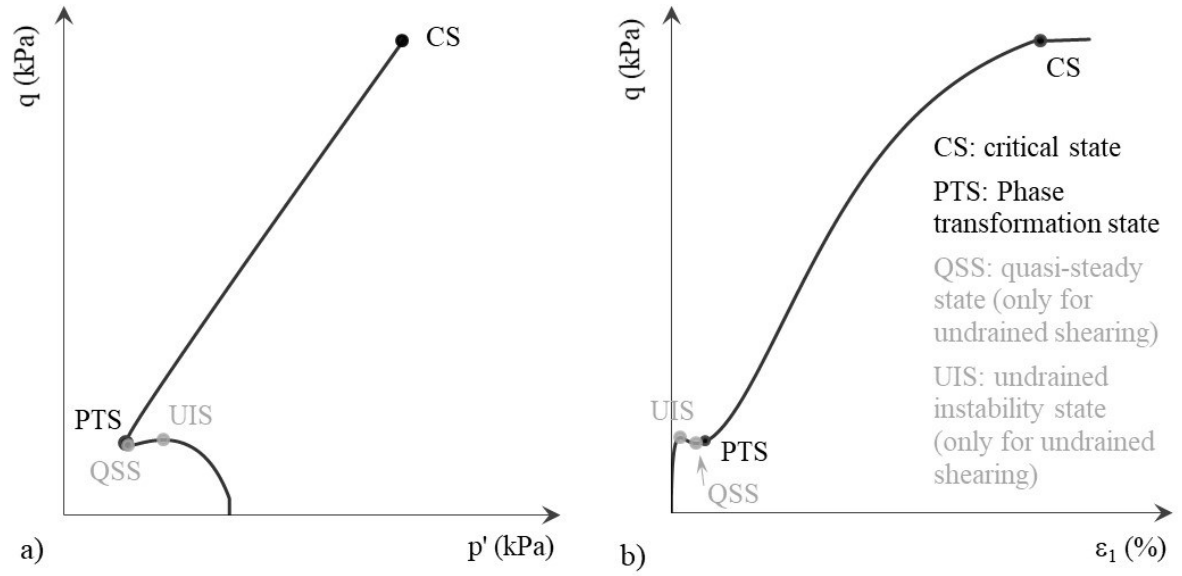

Figure 2.27 – Distinctive states of the undrained response of sand identified in the (a) deviatoric stress – mean effective stress space and (b) deviatoric stress – major principal strain space (adapted from Murthy *et al.*, 2007).

As pointed out by Murthy *et al.* (2007), both QSS and UIS vanish for tests conducted on samples whose initial states are located well below the CSL. As detailed later, due to the use of air-pluviation as the method of sample's preparation, the initial states of all samples tested

in the present experimental programme were located below the CSL (i.e. $\psi_0 < 0$ as shown in Figure 2.26). Consequently, both QSS and UIS were solely observed to occur for three samples, hampering an extensive analysis of the occurrence of these two states for Hostun sand. For information on the occurrence of these two distinctive states for Hostun sand samples prepared by using the moist tamping technique, please refer, for example, to Konrad *et al.* (1991), Konrad (1993), Doanh *et al.* (1997) and Benahmed (2001).

Complementary, the stress-dilatancy response of Hostun sand is investigated, since its reliable characterisation has been identified as crucial for accurately modelling the stress-strain response of sand (e.g. Rowe, 1962; Nova and Wood, 1979a; Li and Dafalias, 2000; Jefferies and Been, 2006). As detailed later, the obtained experimental data is used to investigate the stress-dilatancy relationship proposed by Manzari and Dafalias (1997) and incorporated in the constitutive model implemented into the finite element code and used for the numerical simulation of the dynamic centrifuge experiments.

In the following sections, the main characteristics of the triaxial testing programme on Hostun sand are firstly presented (Section 2.6.2) and the obtained experimental results are reported (Sections 2.6.3 and 2.6.4). Subsequently, the occurrence of the each of the aforementioned distinctive states for Hostun sand is examined (Section 2.6.5), followed by the characterisation of its stress-dilatancy response (Section 2.6.6).

Note that, while in this chapter the results of the conducted monotonic triaxial tests are, in general, presented together to provide an overall assessment of the monotonic response of Hostun sand, the results obtained in each test are individually presented in Appendix A.

2.6.2 Monotonic triaxial testing programme

Overall, thirty-two monotonic triaxial compression (TC) and triaxial extension (TE) tests were carried out, including:

- fourteen drained monotonic triaxial compression (DMTC) tests, ten of them with increasing mean stress (p↑), while the remaining four with decreasing mean stress (p↓);
- nine undrained monotonic triaxial compression tests with increasing mean stress (UMTC p↑ tests);
- five drained monotonic triaxial extension (DMTE) tests, one of them with decreasing mean stress (p↓) and the remaining four with increasing mean stress (p↑);
- four undrained monotonic triaxial extension tests with decreasing mean stress (UMTE p↓ tests).

Table 2.4 – Initial conditions of the monotonic triaxial compression tests performed.

Test ID [a]	Apparatus [b]	Sample's preparation [c]				Soil's state and stress conditions after consolidation									Loading [d]
		D_{init} (mm)	H_{init} (mm)	M_{init} (g)	ΔV_{cons} (cm^3)	e_0 ( )	$D_{r,0}$ (%)	$\sigma_{cell,0}$ (kPa)	u_0 (kPa)	q_0 (kPa)	$\sigma'_{r,0}$ (kPa)	$\sigma'_{a,0}$ (kPa)	K_0 ( )	p'_0 (kPa)	
ICDMTCp↑ 0.875/50	EMTS	99.6	203.7	2230.4	3.46	0.875	36.9	650.0	600.0	0.0	50.0	50.0	1.0	50.0	DMTCp↑
ICDMTCp↑ 0.885/80	EMTS	99.6	202.7	2203.2	6.15	0.885	33.8	650.0	570.0	0.0	80.0	80.0	1.0	80.0	DMTCp↑
ICDMTCp↑ 0.846/200	EMTS	99.6	200.8	2220.3	11.98	0.846	45.2	700.0	500.0	0.0	200.0	200.0	1.0	200.0	DMTCp↑
ICDMTCp↑ 0.835/500	EMTS	99.6	200.7	2216.4	23.18	0.835	48.5	680.0	180.0	0.0	500.0	500.0	1.0	500.0	DMTCp↑
ICDMTCp↑ 0.829/25	EMTS	99.9	199.1	2250.6	1.55	0.829	50.4	650.0	625.0	0.0	25.0	25.0	1.0	25.0	DMTCp↑
ICDMTCp↑ 0.798/80	EMTS	99.9	200.4	2299.4	5.20	0.798	59.5	650.0	570.0	0.0	80.0	80.0	1.0	80.0	DMTCp↑
ICDMTCp↑ 0.804/135	EMTS	99.9	197.5	2252.3	9.04	0.804	57.6	650.0	515.0	0.0	135.0	135.0	1.0	135.0	DMTCp↑
ICDMTCp↑ 0.667/25	EMTS	99.9	198.9	2467.4	1.17	0.667	97.9	650.0	625.0	0.0	25.0	25.0	1.0	25.0	DMTCp↑
ICDMTCp↑ 0.725/80	EMTS	99.9	202.8	2423.6	6.40	0.725	81.0	650.0	570.0	0.0	80.0	80.0	1.0	80.0	DMTCp↑
ICDMTCp↑ 0.728/135	EMTS	99.9	198.5	2364.4	8.72	0.728	80.1	650.0	515.0	0.0	135.0	135.0	1.0	135.0	DMTCp↑
ICDMTCp↓ 0.826/80	B&W SPC	37.0	84.5	130.6	0.61	0.826	51.1	650.0	570.0	0.0	80.0	80.0	1.0	80.0	DMTCp↓
K0CDMTCp↓ 0.797/80	B&W SPC	37.0	78.9	124.2	0.40	0.797	59.8	700.0	640.0	60.0	60.0	120.0	0.5	80.0	DMTCp↓
ICDMTCp↓ 0.650/80	B&W SPC	37.0	74.1	127.1	0.33	0.650	103.0	650.0	570.0	0.0	80.0	80.0	1.0	80.0	DMTCp↓
K0CDMTCp↓ 0.672/80	B&W SPC	37.0	77.3	130.9	0.32	0.672	96.6	700.0	640.0	60.0	60.0	120.0	0.5	80.0	DMTCp↓
ICUMTCp↑ 0.876/80	EMTS	99.6	200.2	2195.8	5.90	0.876	36.4	650.0	570.0	0.0	80.0	80.0	1.0	80.0	UMTCp↑
ICUMTCp↑ 0.868/80	EMTS	99.6	202.7	2212.1	7.07	0.868	38.7	680.0	600.0	0.0	80.0	80.0	1.0	80.0	UMTCp↑
ICUMTCp↑ 0.843/135	EMTS	99.6	201.0	2230.5	8.63	0.843	46.1	685.0	550.0	0.0	135.0	135.0	1.0	135.0	UMTCp↑
ICUMTCp↑ 0.783/25	EMTS	99.9	202.0	2342.9	1.53	0.783	64.0	650.0	625.0	0.0	25.0	25.0	1.0	25.0	UMTCp↑
ICUMTCp↑ 0.801/80	EMTS	99.9	202.3	2315.2	6.33	0.801	58.5	650.0	570.0	0.0	80.0	80.0	1.0	80.0	UMTCp↑
ICUMTCp↑ 0.815/135	EMTS	99.9	202.4	2296.5	8.17	0.815	54.5	650.0	515.0	0.0	135.0	135.0	1.0	135.0	UMTCp↑
ICUMTCp↑ 0.686/25	EMTS	99.9	204.1	2502.9	1.49	0.686	92.3	650.0	625.0	0.0	25.0	25.0	1.0	25.0	UMTCp↑
ICUMTCp↑ 0.751/80	EMTS	99.9	201.1	2369.3	5.31	0.751	73.3	650.0	570.0	0.0	80.0	80.0	1.0	80.0	UMTCp↑
ICUMTCp↑ 0.694/135	EMTS	99.9	197.6	2402.5	7.75	0.694	90.1	650.0	515.0	0.0	135.0	135.0	1.0	135.0	UMTCp↑

[a] The designation identifies: 1) the type of consolidation – IC or K0 for isotropic or anisotropic consolidation, respectively; 2) the type of drainage – D or U for drained or undrained test, respectively; 3) the type of loading – IC for isotropic compression, MTCp↑ for monotonic triaxial compression with increasing mean stress, MTCp↓ for monotonic triaxial compression with decreasing mean stress, MTEp↓ for monotonic triaxial extension with decreasing mean stress and MTEp↑ for monotonic triaxial extension with increasing mean stress; 4) the void ratio immediately after consolidation; 5) the mean effective stress immediately after consolidation.
[b] As described in Section 2.3, two different apparatuses were used: B&W SPC refers to Bishop and Wesley (1975)'s stress path cell, while EMTS refers to the electro-mechanical triaxial system. [c] Volume and mass measurements were performed after sample's preparation. [d] See Figure 2.6.

Table 2.5 – Initial conditions of the monotonic triaxial extension tests performed.

Test ID [a]	Apparatus [b]	Sample's preparation [c]				Soil's state and stress conditions after consolidation									Loading[d]
		D_{init} (mm)	H_{init} (mm)	M_{init} (g)	ΔV_{cons} (cm^3)	e_0 ( )	$D_{r,0}$ (%)	$\sigma_{cell,0}$ (kPa)	u_0 (kPa)	q_0 (kPa)	$\sigma'_{r,0}$ (kPa)	$\sigma'_{a,0}$ (kPa)	K_0 ( )	p'_0 (kPa)	
ICDMTEp↑ 0.798/80	B&W SPC	36.6	76.4	117.4	0.54	0.798	59.5	250.0	170.0	0.0	80.0	80.0	1.0	80.0	DMTEp↑
K0CDMTEp↑ 0.801/80	B&W SPC	36.6	76.0	116.8	0.40	0.801	58.5	250.0	190.0	60.0	60.0	120.0	0.5	80.0	DMTEp↑
ICDMTEp↑ 0.652/80	B&W SPC	36.6	76.2	127.6	0.41	0.652	102.5	250.0	170.0	0.0	80.0	80.0	1.0	80.0	DMTEp↑
K0CDMTEp↑ 0.652/80	B&W SPC	36.6	78.1	130.8	0.39	0.652	102.3	150.0	90.0	60.0	60.0	120.0	0.5	80.0	DMTEp↑
ICDMTEp↓ 0.793/80	B&W SPC	36.6	74.8	115.3	0.48	0.793	60.9	650.0	570.0	0.0	80.0	80.0	1.0	80.0	DMTEp↓
ICUMTEp↓ 0.790/25	B&W SPC	36.9	74.9	118.0	0.08	0.790	61.7	650.0	25.0	0.0	25.0	25.0	1.0	25.0	UMTEp↓
ICUMTEp↓ 0.799/80	B&W SPC	36.9	75.2	117.3	0.47	0.799	59.0	650.0	80.0	0.0	80.0	80.0	1.0	80.0	UMTEp↓
ICUMTEp↓ 0.658/25	B&W SPC	36.9	76.8	130.6	0.09	0.658	100.5	650.0	25.0	0.0	25.0	25.0	1.0	25.0	UMTEp↓
ICUMTEp↓ 0.650/80	B&W SPC	36.9	72.3	123.0	0.46	0.650	102.9	650.0	80.0	0.0	80.0	80.0	1.0	80.0	UMTEp↓

[a], [b], [c], [d] See notes below Table 2.4.

The initial conditions of the TC and TE tests are summarised in Table 2.4 and Table 2.5, respectively, where D_{init}, H_{init} and M_{init} are, respectively, the diameter, height and dry mass of the sample after preparation; ΔV_{cons} is the volume change during consolidation; e_0 and $D_{r,0}$ are, respectively, the void ratio and the corresponding relative density immediately after consolidation (and, therefore, immediately before shearing); $\sigma_{cell,0}$, u_0 and q_0 are, respectively, the cell pressure, the back pressure and the deviatoric stress after consolidation; $\sigma'_{r,0}$ are $\sigma'_{a,0}$ are, respectively, the radial and axial stresses after consolidation; K_0 is the ratio of $\sigma'_{r,0}$ to $\sigma'_{a,0}$ (equivalent, in the field, to the coefficient of earth pressure at rest); and, finally, p'_0 is the mean effective stress immediately after consolidation. It can be observed that samples were prepared to very different void ratios, ranging from $e_0 = 0.650$ to $e_0 = 0.885$, and consolidated under various isotropic stress states, characterised by $p'_0 =$ 25, 50, 80, 135, 200 and 500 kPa, as well as under an anisotropic (i.e. K_0) stress state, characterised by $\sigma'_{r,0} = 60$ kPa and $\sigma'_{a,0} = 120$ kPa (which correspond to $p'_0 = 80$ kPa and $q_0 = 60$ kPa).

To aid the presentation of the experimental results, it is important to identify which samples are considered "loose", "moderately loose" and "dense". Although other criteria could have been devised, in the present study, the target void ratio (i.e. planned to be achieved during sample preparation), $e_{init,target}$, is employed, as indicated in Table 2.6. Note that the target void ratios, as well as the effective stresses at consolidation were particularly selected to cover the initial state of the Hostun sand deposits tested in centrifuge experiments, as detailed later. It can be observed that loose samples have relative densities before shearing, $D_{r,0}$, below 50 %, while dense samples are characterised by values of $D_{r,0}$ above 70 %. Moderately loose samples are considered those having values of $D_{r,0}$ in the range of 50 to 70 %. Note that these criteria are also used for samples subjected to cyclic loading (Chapter 3).

Table 2.6 – Distinction between loose, moderately loose and dense samples adopted in the present experimental testing programme.

Designation	Target initial density		Density after consolidation [a]		
	$e_{init,target}$	$D_{r,init,target}$	$e_{0,min}$	$e_{0,max}$	$D_{r,0}$
	( )	(%)	( )	( )	(%)
Loose	0.90	29.4	0.835	0.885	33.8 – 48.5
Moderately loose	0.81	55.9	0.797	0.829	50.3 – 59.7
Dense	0.66[1] – 0.69[2]	91.2 – 100	0.650	0.751[3]	73.2 – 102.9

[a] Minimum and maximum void ratios determined in the laboratory after sample's preparation, saturation and consolidation – see Table 2.4 and Table 2.5.

[1] Target void ratio for samples tested in the Bishop and Wesley (1975)'s stress path cell; [2] target void ratio for samples tested in the electro-mechanical triaxial system; [3] sample corresponding to test ICUMTCp↑ 0.751/80; if this sample would be disregarded, $e_{cons,max}$ would be equal to 0.728, which corresponds to $D_{r,0}$ of about 80 %.

2.6.3 Monotonic triaxial compression test results

2.6.3.1 Drained monotonic triaxial compression with increasing mean stress

Figure 2.28 presents the results of the isotropically consolidated drained monotonic triaxial compression tests with increasing mean stress (ICDMTC p↑ tests, which correspond to the conventional triaxial compression tests). To ease the interpretation of the obtained results, the curves corresponding to tests conducted on loose samples (i.e. tests ICDMTCp↑ 0.875/50, ICDMTCp↑ 0.885/80, ICDMTCp↑ 0.846/200 and ICDMTCp↑ 0.835/500) are represented in black, the curves corresponding to tests conducted on moderately loose samples (i.e. tests ICDMTCp↑ 0.829/25, ICDMTCp↑ 0.798/80 and ICDMTCp↑ 0.804/135) are represented in dark grey, while the curves corresponding to tests conducted on dense samples (i.e. tests ICDMTCp↑ 0.667/25, ICDMTCp↑ 0.725/80, ICDMTCp↑ 0.728/135) are represented in light grey. Moreover, similar line types are adopted for samples consolidated to similar stresses (e.g. dashed line type is used for tests performed on samples consolidated to $p'_0 = 25$ kPa, namely tests ICDMTCp↑ 0.829/25 and ICDMTCp↑ 0.667/25). Note also that the adopted sign convention implies that compressive strains and stresses are positive, while extensive strains and stresses are negative; in addition, volumetric contraction is positive, while volumetric expansion/dilation is negative.

The strong effect of the initial (i.e. immediately after consolidation) void ratio and isotropic consolidation stress on the monotonic response of sand can be clearly observed in Figure 2.28. Starting by comparing the responses of samples consolidated to the same effective stresses (e.g. tests ICDMTCp↑ 0.885/80, ICDMTCp↑ 0.798/80 and ICDMTCp↑ 0.725/80), it is clear that, as expected, higher peak deviatoric stresses are mobilised during shearing by the initially denser samples at lower axial strains (Figure 2.28a). Specifically, a peak deviatoric stress of $q_{max} \approx 304.2$ kPa was mobilised by the sample having $e_0 = 0.725$ (i.e. test ICDMTCp↑ 0.725/80) at an axial strain of $\varepsilon_a \approx 7.0$ %, while a smaller value of $q_{max} \approx 255.1$ kPa was reached at $\varepsilon_a \approx 9.5$ % by the sample having $e_0 = 0.798$ (i.e. test ICDMTCp↑ 0.798/80) and an even smaller value of $q_{max} \approx 237.9$ kPa at $\varepsilon_a \approx 13.1$ % was registered for the sample having $e_0 = 0.885$ (i.e. test ICDMTCp↑ 0.885/80). Indeed, initially denser samples not only tend to mobilise larger deviatoric stresses during shearing, but also larger stress ratios, η (i.e. larger ratios of the deviatoric stress, q, to the mean effective stress, p'), as clearly observed in Figure 2.28b. Interestingly, when the tests were stopped, the stress ratios measured in tests ICDMTCp↑ 0.885/80, ICDMTCp↑ 0.798/80 and ICDMTCp↑ 0.725/80 were fairly similar ($\eta \approx 1.36 - 1.38$), suggesting that, irrespective of the initial density of the samples, similar stress conditions tend to be reached at the end of the tests, as stated by the CSSM framework.

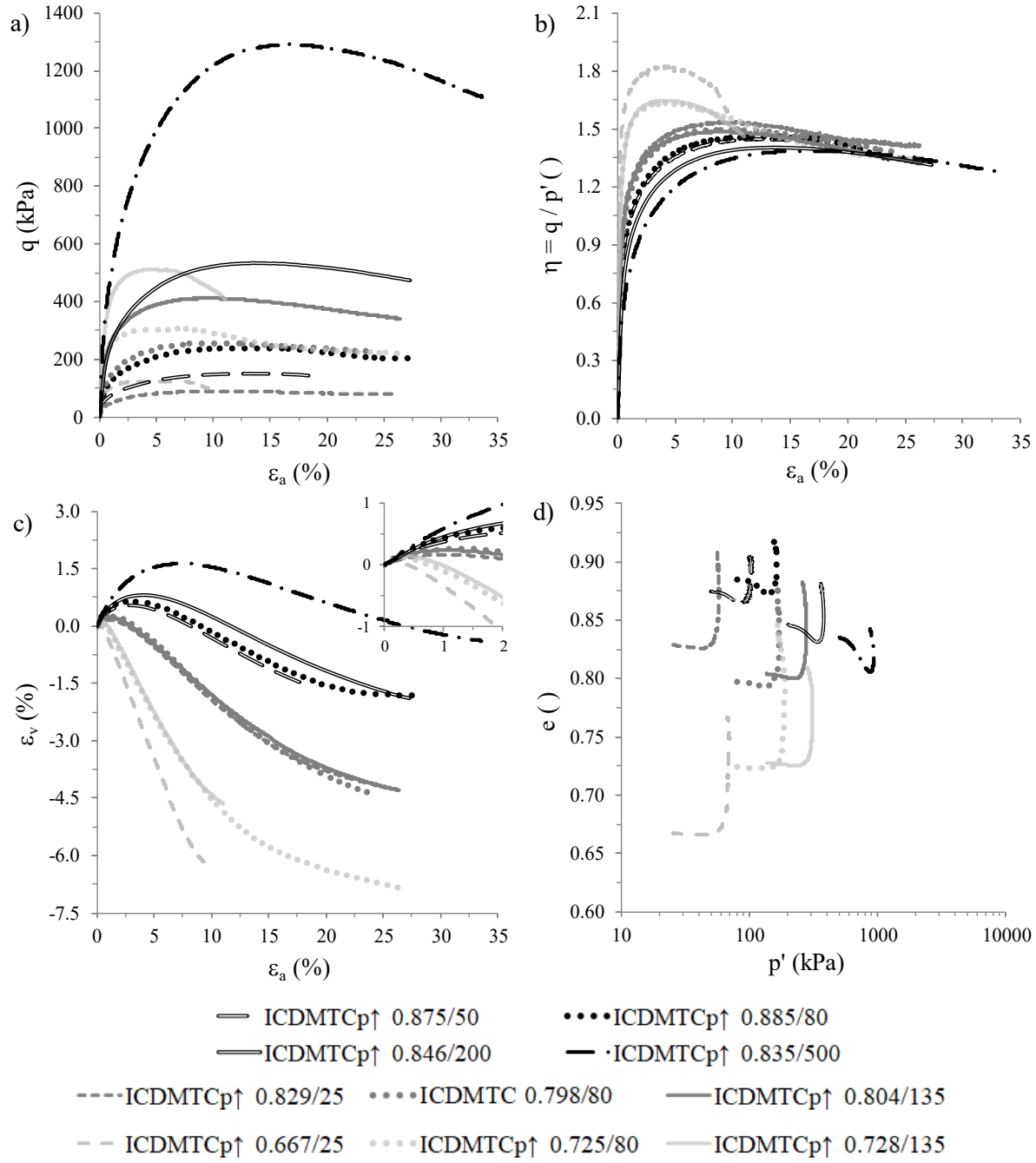

Figure 2.28 – ICDMTC p↑ test results: (a) stress-strain response; (b) stress ratio evolution with axial strain; (c) volumetric strain evolution with axial strain; and (d) void ratio evolution with mean effective stress.

Furthermore, by observing Figure 2.28b, it can be concluded that initially denser samples tend to exhibit stiffer stress-strain responses (e.g. for $\varepsilon_a \approx 2.5$ %, it can be observed that $\eta \approx 1.61$ for test ICDMTCp↑ 0.725/80, while smaller values of $\eta \approx 1.34$ and $\eta \approx 1.24$ were mobilised, respectively, in tests ICDMTCp↑ 0.798/80 and ICDMTCp↑ 0.885/80). It is also interesting to observe that samples prepared to higher densities (or, equivalently, to lower void ratios) tend to exhibit a more dilatant response during shearing (Figure 2.28c). More specifically, initially denser samples are observed to contract less than initially looser samples during the earlier stages of loading and to start dilating at lower strain levels (as observed in the detail of Figure

2.28c). Moreover, the rate at which the volumetric strain, ε_v, evolves with axial strain at the later stages of loading is also higher for initially denser samples than for initially looser samples. Finally, it is apparent in Figure 2.28d that larger variations of the void ratio, Δe, during shearing were obtained for the initially denser samples (i.e. Δe is larger for test ICDMTCp↑ 0.725/80 than for test ICDMTCp↑ 0.798/80 and much larger than for test ICDMTCp↑ 0.885/80). This aspect also seems to agree well with the CSSM framework, according to which samples closer to the CSL (which, in this case, are the loosest samples, since all samples show dilative response after initial contraction), when subjected to the same confining stress, need to contract less to reach a CS condition.

Insight into the influence of the initial effective stress state on the monotonic response of sand is provided by comparing the results of tests ICDMTCp↑ 0.875/50 (where $p'_0 = 50$ kPa), ICDMTCp↑ 0.885/80 (where $p'_0 = 80$ kPa), ICDMTCp↑ 0.846/200 (where $p'_0 = 200$ kPa) and ICDMTCp↑ 0.835/500 (where $p'_0 = 500$ kPa), even if the initial void ratios of these samples were slightly different. As it can be seen in Figure 2.28a, considerably larger deviatoric stresses were mobilised by samples consolidated to higher effective stresses. This does not mean, however, that these samples mobilise larger stress ratios. In effect, the analysis of Figure 2.28b suggests that samples consolidated to higher effective stresses (namely, those corresponding to tests ICDMTCp↑ 0.835/500 and ICDMTCp↑ 0.846/200) tend to mobilise slightly smaller stress ratios than those consolidated to lower effective stresses (specifically, tests ICDMTCp↑ 0.885/80 and ICDMTCp↑ 0.875/50). Similar experimental findings were, for example, reported by Verdugo and Ishihara (1996). In addition, samples consolidated to higher effective stresses tend to contract more during the earlier stages of loading, as it can be seen in Figure 2.28c. During the later stages of loading, however, it seems that the influence of the confining stresses on the volumetric response is less important than the effect of the initial density. In fact, for the initial conditions tested in the present experimental programme, the effect of the initial mean effective stress on volumetric response of sand response seems to be more limited than the effect of the initial density of the sample.

In relation to the characterisation of the CS, two aspects are particularly noteworthy. First, as pointed out before, even the initially loosest samples (i.e. tests ICDMTCp↑ 0.875/50, ICDMTCp↑ 0.885/80, ICDMTCp↑ 0.846/200 and ICDMTCp↑ 0.835/500) are observed to dilate after an initial contraction, with their $e - p'$ path moving upwards after an initial deflection to the right downwards side (Figure 2.28d). Therefore, the CSL in the $e - p'$ path is located above the initial state of all samples (i.e. all samples are initially denser-than-critical, as further detailed later). The second aspect worth highlighting is that, despite the large axial strains achieved in these tests, a complete stabilisation of both $q - \varepsilon_a$ and $\varepsilon_v - \varepsilon_a$ responses seems to have been only attained for the loosest sample (i.e. test ICDMTCp↑ 0.885/80). For the sample submitted to the largest confining stress (i.e. test ICDMTCp↑ 0.835/500), the variation of ε_v at the final stages of the test seems to be negligible (i.e. it seems practically

stabilised). However, *q* seems to be still evolving. As pointed out by Been and Jefferies (2004), this variation of *q* despite constant volume conditions may be a detrimental consequence of the approximate nature of the expression used to correct the cross-sectional area of the sample during loading (Equation 2.3) and, therefore, to estimate the axial stress from the measured load. As shown later, conditions close to CS seem also to have been attained at the end of test ICDMTCp↑ 0.835/500.

2.6.3.2 Drained monotonic triaxial compression with decreasing mean stress

Figure 2.29 compares the results of two isotropically consolidated drained monotonic triaxial compression tests with decreasing mean stress (ICDMTC p↓ tests, represented by dotted lines) – one of them conducted on a moderately loose sample (i.e. test ICDMTCp↓ 0.826/80, in dark grey) and the other one conducted on a dense sample (i.e. test ICDMTCp↓ 0.650/80, in light grey) – with the results obtained in two tests of the same type conducted on anisotropically consolidated samples (K0CDMTC p↓ tests, represented by solid lines) – one of them conducted on a moderately loose sample (i.e. test K0CDMTCp↓ 0.797/80, in dark grey) and the other one conducted on a dense sample (i.e. test K0CDMTCp↓ 0.672/80, in light grey). Additionally, the results obtained for test ICDMTCp↑ 0.798/80 test (represented by a very dark grey dashed line) are also shown in the figure, to gain insight into the effect of the stress path on the monotonic response of Hostun sand, as discussed below.

Similar to what was observed for the ICDMTC p↑ tests, denser samples (compare, for instance, the results of test ICDMTCp↓ 0.650/80 with those of test ICDMTCp↓ 0.826/80 or, alternatively, results of test K0CDMTCp↓ 0.672/80 with those of test K0CDMTCp↓ 0.797/80) tend to mobilise larger deviatoric strains and stress ratios during shearing, as well as to exhibit stiffer and more dilatant responses. Nevertheless, at large strains, the responses of both sets of samples seem to be characterised by similar deviatoric stresses, as also observed for the ICDMTC p↑ tests.

Regarding the effect of the type of consolidation (isotropic or anisotropic), the responses registered for the initially denser samples (i.e. tests ICDMTCp↓ 0.650/80 and K0CDMTCp↓ 0.672/80), can be compared, since their initial void ratios are very similar. It is clear in Figure 2.29a that significantly larger deviatoric stresses were mobilised during shearing by the anisotropically consolidated sample (i.e. test K0CDMTCp↓ 0.672/80), even though similar-shaped curves seem to have been obtained for both tests. In terms of stress ratio evolution with axial strain (Figure 2.29b), similar responses were measured up to an axial strain level of about 12 %. From that point, the responses are observed to deviate, with the stress ratio – axial strain response measured in test ICDMTCp↓ 0.650/80 approaching that registered in test ICDMTCp↓ 0.826/80 and, at greater axial strains, the response measured in test ICDMTCp↑ 0.798/80. In addition, it can be observed in Figure 2.29c that very similar volumetric strain – axial strain responses were measured in both ICDMTCp↓ 0.650/80 and K0CDMTCp↓ 0.672/80 tests, suggesting that the type of consolidation has little effect on this

aspect of sand response. Interestingly, the void ratio – mean effective stress paths (Figure 2.29b) registered in both tests seem also to have a similar shape. To sum up, it seems that the type of consolidation has little effect on the stress ratio – axial strain path, as well as on the volumetric response, while affecting the maximum deviatoric shear stress that can be mobilised.

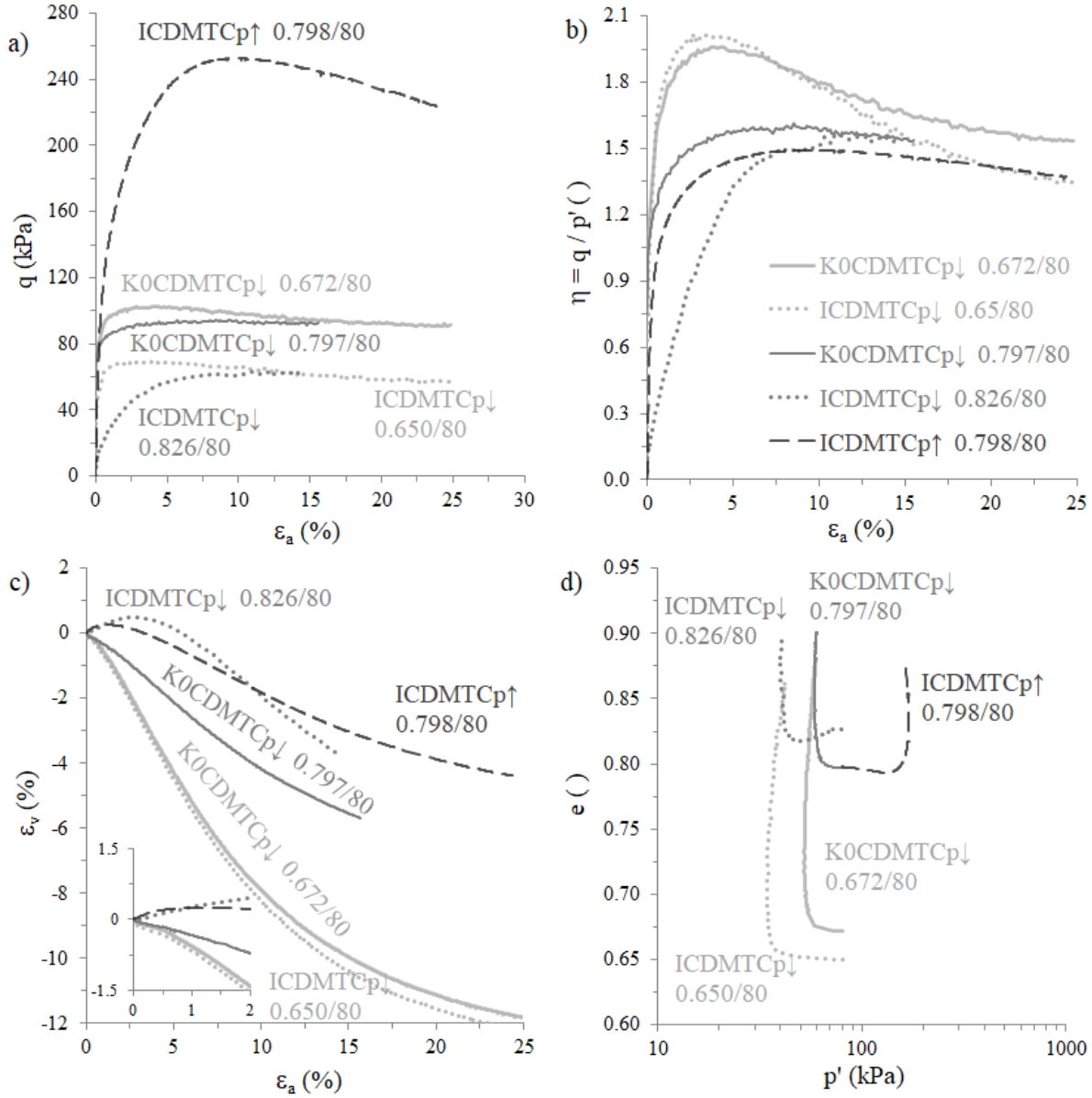

Figure 2.29 – ICDMTC p↓, K0CDMTC p↓ and ICDMTC p↑ test results: (a) stress-strain response; (b) stress ratio evolution with axial strain; (c) volumetric strain evolution with axial strain; and (d) void ratio evolution with mean effective stress.

Finally, it is interesting to compare the response obtained for samples tested under different stress paths (i.e. tests ICDMTCp↓ 0.826/80 and ICDMTCp↑ 0.798/80), even if the initial void ratios of these samples were not exactly identical and sizes of the samples were different. In relation to the latter aspect, according to a series of ICDMTCp↑ test results reported by Jefferies and Been (2006) on dry-pluviated Ticino sand, samples with smaller sizes tend to

exhibit slightly stiffer responses from the start of shearing up to the peak stress than those exhibited by samples with larger sizes and, consequently, a smaller tendency to contract during the early stages of loading. In this case, however, it can be observed that a considerably softer response was measured in test ICDMTCp↓ 0.826/80 in relation to that registered in test ICDMTCp↑ 0.798/80(Figure 2.29a and b), which is likely the consequence of the larger initial void ratio of sample subjected to the former test, as well as different stress path applied in these two tests. Moreover, as expected, it can be seen that the strength mobilised in the former test is substantially smaller than mobilised in the latter test. Although these conclusions have been drawn based on very limited experimental data (only two tests), it is noteworthy that similar findings were reported by Vaid and Sasitharan (1992) on water-pluviated Erksak sand.

2.6.3.3 Undrained monotonic triaxial compression with increasing mean stress

Figure 2.30 presents the results of the isotropically consolidated undrained monotonic triaxial compression tests with increasing mean stress (ICUMTC p↑ tests). Once again, the curves corresponding to loose samples (i.e. tests ICUMTCp↑ 0.876/80, ICUMTCp↑ 0.868/80 and ICUMTCp↑ 0.843/135) are represented in black, the curves corresponding to moderately loose samples (i.e. tests ICUMTCp↑ 0.783/25, ICUMTCp↑ 0.801/80 and ICUMTCp↑ 0.815/135) are represented in dark grey and, finally, the curves corresponding to dense samples (i.e. tests ICUMTCp↑ 0.686/25, ICUMTCp↑ 0.751/80 and ICUMTCp↑ 0.694/135) are represented in light grey.

Similar to what was observed when analysing the results of ICDMTC p↑ tests, Figure 2.30 show that both void ratio and isotropic effective stress at consolidation have a clear effect on the measured response. In relation to the former aspect, it can be observed in the detail of Figure 2.30e (by comparing, for example, the results obtained for tests ICUMTCp↑ 0.868/80, ICUMTCp↑ 0.801/80 and ICUMTCp↑ 0.751/80) that denser samples tend to generate smaller positive excess pore water pressures, Δu, during the earlier stages of loading, when compared to looser samples. In fact, this is in a remarkably good agreement with the results obtained under drained conditions, where initially denser samples are observed to contract less than initially looser samples during the earlier stages of loading. As a result, the reduction of the mean effective stress during this initial stage is more limited for denser samples, with their effective stress path in $q - p'$ space showing a lesser tendency to bend to the left (i.e. to the direction of $p' = 0$) than the stress paths corresponding to looser samples (detail of Figure 2.30a). Note that, in tests ICUMTCp↑ 0.686/25, ICUMTCp↑ 0.751/80 test and ICUMTCp↑ 0.783/25, p' increased from the start until the end of loading, meaning that the increase in the total mean stress, p, was constantly greater than the increase in pore water pressure, u. Conversely, for all remaining tests, a decrease in p' was observed in the earlier stages of loading, followed by an increase until the end of the test (Figure 2.30a). As suggested by Ishihara *et al.* (1975), the point at which the effective stress path is reversed can be

associated with the occurrence of the phase transformation phase (PTS), as discussed later in more detail.

In addition, it can be seen that denser samples tend to exhibit significantly stiffer stress-strain responses (Figure 2.30b), as well as to mobilise higher stress ratios during shearing than those mobilised by looser samples (Figure 2.30d), as also observed under drained conditions.

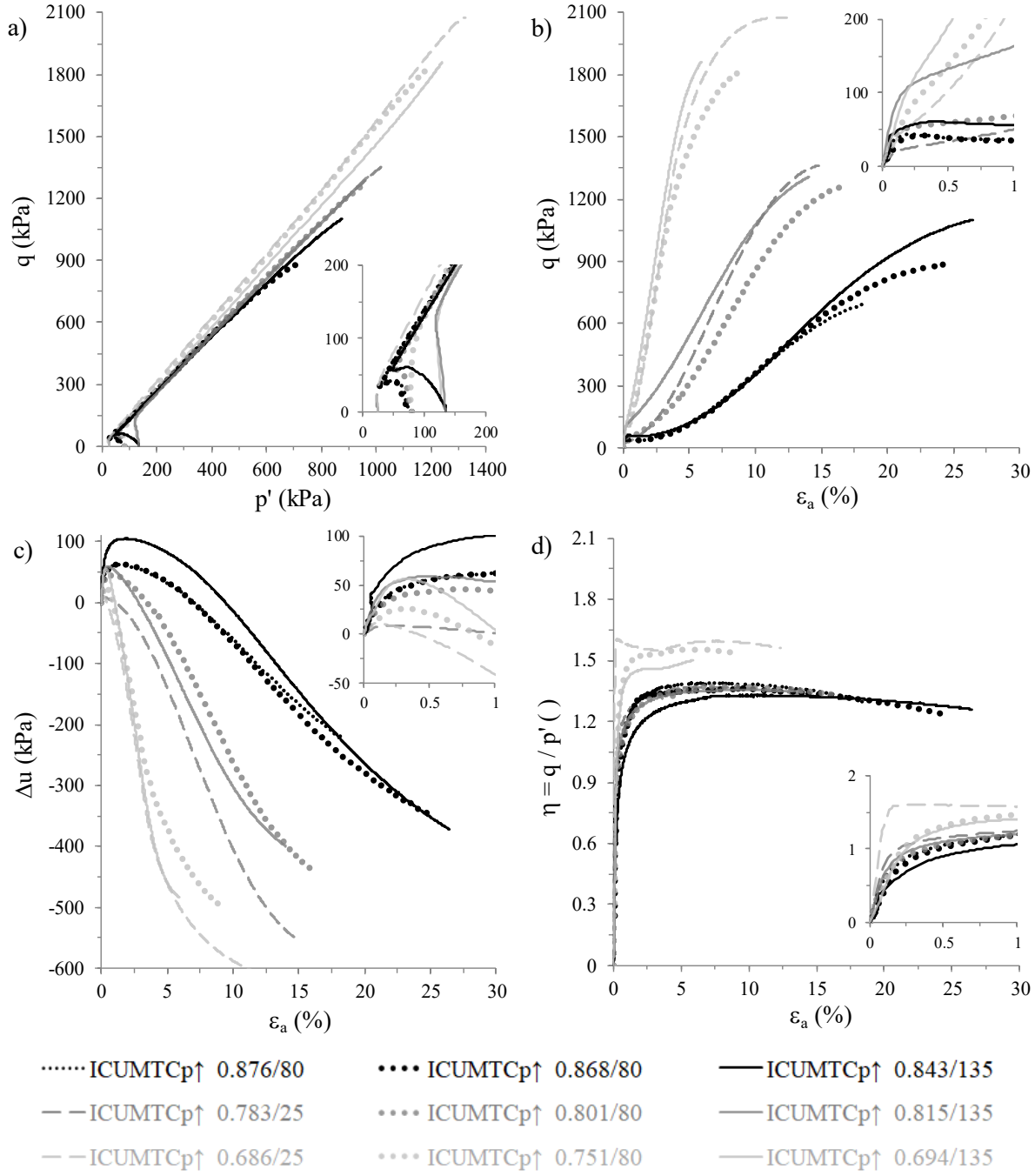

Figure 2.30 – ICUMTC p↑ test results: (a) effective stress path; (b) stress-strain response; (c) excess pore water pressure build-up; and (d) stress ratio evolution with axial strain.

In order to assess the effect of the isotropic consolidation stress, the response exhibited, for instance, by the moderately loose samples (ICUMTCp↑ 0.783/25, ICUMTCp↑ 0.801/80 and ICUMTCp↑ 0.815/135 tests) can be compared, even if the void ratios immediately after

consolidation are slightly different. In the earlier stages of loading, samples subjected to higher confining stresses seem to show stiffer stress-strain responses (detail of Figure 2.30b), while generating greater positive excess pore water pressures (detail of Figure 2.30c). These effects seem, however, to vanish at large strain levels.

Moreover, it is interesting to observe that the loosest samples (ICUMTCp↑ 0.876/80, ICUMTCp↑ 0.868/80 and ICUMTCp↑ 0.843/135 tests) exhibit stress-strain responses termed as "flow liquefaction with limited deformation" (Ishihara, 1993), which are characterised by a temporary drop in the deviatoric shear stress accompanied by a considerable accumulation of axial strain, a tendency reverted as response of sand changes from contractive to dilative. As mentioned before, the state at which the local maximum of deviatoric stress occurs is termed as undrained instability state (UIS), with its characterisation being performed later.

Lastly, although excess pore water pressures do not appear to stabilise completely in any test, the variations of excess pore water pressure measured at the end of the ICUMTCp↑ 0.876/80 and ICUMTCp↑ 0.868/80 tests seem fairly modest. Indeed, their $q - \varepsilon_a$ responses seem practically stabilised and, therefore, the conditions at the end of these tests are considered representative of the CS. Although slightly larger variations of stresses and excess pore water pressure seem to occur at the end of the other test performed on a loose sample (i.e. ICUMTCp↑ 0.843/135 test), the conditions at the end of this test do not seem far from CS, as also explored in more detail later.

2.6.4 Monotonic triaxial extension test results

2.6.4.1 Drained monotonic triaxial extension with increasing and decreasing mean stress

Figure 2.31 compares the results of two isotropically consolidated drained monotonic triaxial extension tests with increasing mean stress (ICDMTE p↑ tests, represented by dotted lines) – one of them performed on a moderately loose sample (i.e. test ICDMTEp↑ 0.798/80, in dark grey) and the other one performed on a dense sample (i.e. test ICDMTEp↑ 0.652/80, in light grey) – with the results obtained in two tests of the same type conducted on anisotropically consolidated samples (K0CDMTEp↑ tests, represented by solid lines) – one of them conducted on a moderately loose sample (i.e. test K0CDMTEp↑ 0.801/80, in dark grey) and the other one conducted on a dense sample (i.e. test K0CDMTEp↑ 0.652/80, in light grey). Note that the adopted sign convention means that the deviatoric stress, q, and, hence, the stress ratio, η, are, in this case, negative, as well as the axial strain, ε_a. In relation to the volumetric strains, similar to the monotonic triaxial compression tests, a positive sign means volumetric contraction of the sample, while a negative sign means volumetric expansion/dilation. Note that, as mentioned before, although samples have been generally tested until larger strain levels, sample's necking was observed to occur at $\varepsilon_a \approx -10.0$ % and, therefore, obtained test data is only presented up to that point. The only exception consists of test K0CDMTEp↑ 0.652/80, which had to be stopped earlier (at $\varepsilon_a \approx -4.3$ %), due to the

development of negative (i.e. suction-type) pore water pressures, which could not be accurately measured.

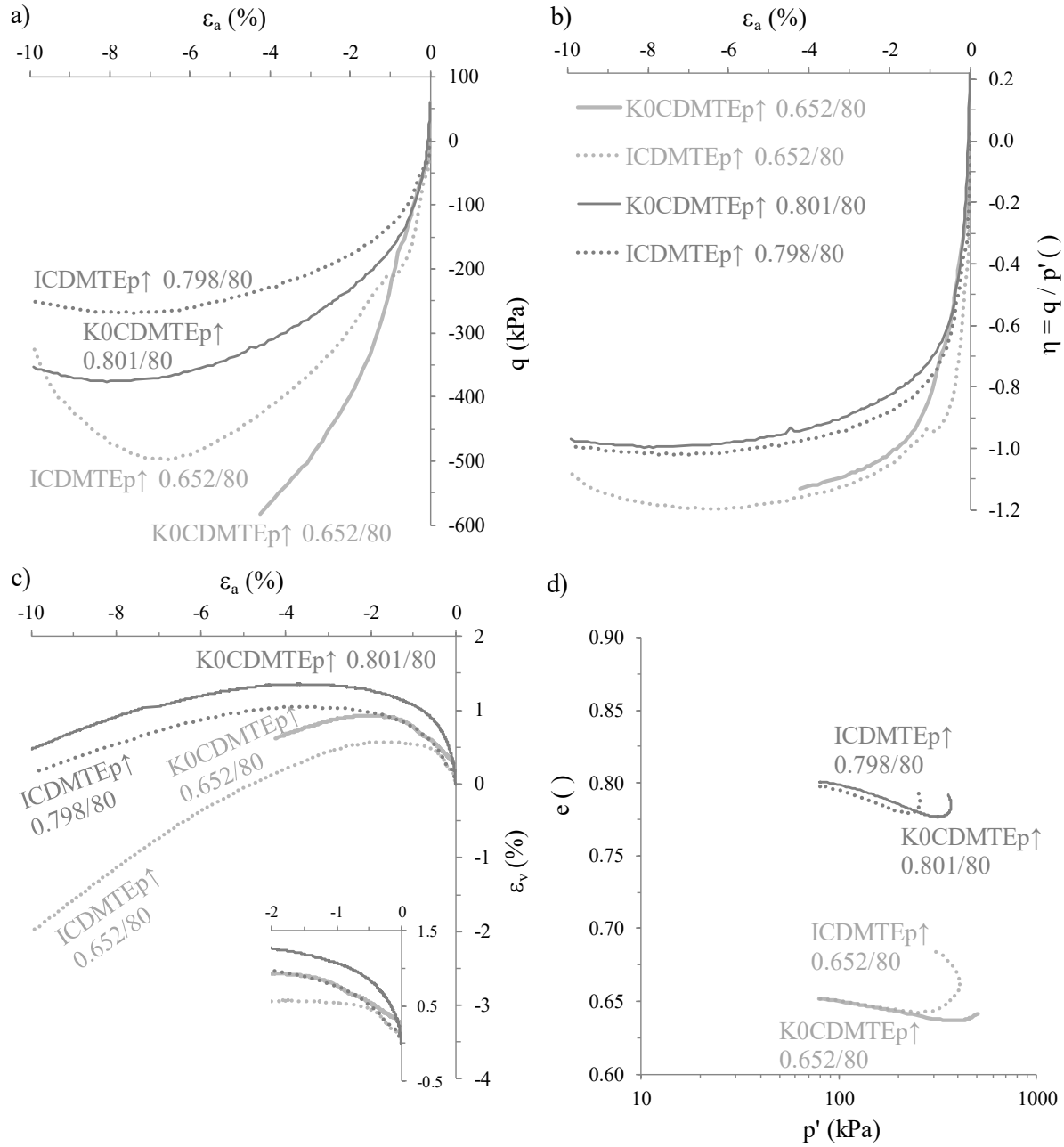

Figure 2.31 – ICDMTE p↑ and K0CDMTE p↑ test results: (a) stress-strain response; (b) stress ratio evolution with axial strain; (c) volumetric strain evolution with axial strain; and (d) void ratio evolution with mean effective stress.

Comparing, for example, the results obtained in tests ICDMTEp↑ 0.652/80 and ICDMTEp↑ 0.798/80, it can be seen that, as observed in TC, the initially denser sampler (i.e. subjected to the former test) tends to mobilise a larger peak deviatoric stress (Figure 2.31a), as well as a larger stress ratio (Figure 2.31b) than that mobilised by the initially looser sample (i.e. subjected to the former test). Nevertheless, at large strains, both deviatoric stress and stress ratio measured in test ICDMTEp↑ 0.652/80 tend to approach those measured in test ICDMTEp↑ 0.798/80, suggesting that a similar stress state would have likely been reached if

TE loading would have continued (and measurements would be reliable for such large strains induced by this type of loading). Moreover, as also observed in TC, initially denser samples tend to contract less during the earlier stages of loading and to show a higher rate of volumetric dilation during the later stages of loading (Figure 2.31c).

When comparing the responses of isotropically and anisotropically consolidated samples (e.g. those measured in tests ICDMTEp↑ 0.798/80 and K0CDMTEp↑ 0.801/80), it is observed that larger peak deviatoric stresses are exhibited by the anisotropically consolidated samples, although similar stress ratios seem to be mobilised throughout loading. Furthermore, it is apparent that, although anisotropically consolidated samples tend to contract more during the earlier stages of loading, the rate at which dilation occurs in the subsequent stages of loading is similar.

In addition, Figure 2.32 compares results of four tests performed on samples prepared to similar void ratios and consolidated under the same isotropic effective stress ($\sigma'_0 = 80$ kPa), however, each of them subjected to a different total stress path (namely, DMTCp↑, DMTCp↓, DMTEp↑ or DMTEp↓). Note that, since drained conditions were imposed in these tests (i.e. $\Delta u = 0$), the effective stress path is identical to the total stress path imposed. Note also that, to ease the comparison between the results, the axial strains, deviatoric stresses and stress ratios obtained for DMTEp↑ and DMTEp↓ tests are, in this case, considered positive.

In Figure 2.32a, it can be seen that, regardless of applying TC or TE loading to the sample, much higher deviatoric stresses were mobilised in the tests with increasing mean stress (i.e. tests ICDMTCp↑ 0.798/80 and ICDMTEp↑ 0.798/80) than in the tests with decreasing mean stress (i.e. test ICDMTCp↓ 0.826/80 and ICDMTEp↓ 0.793/80). Taking into account that the stress ratios, $\eta \approx q/p'$, mobilised in these four tests, although not exactly similar, are not very different (Figure 2.32b), it could be, in fact, expected that samples sheared with continuously decreasing *p*' mobilise smaller values of *q* than those sheared with continuously increasing *p*', as observed in Figure 2.32a. These results agree well with those reported by Bianchini *et al.* (1991) for dense Hostun sand. By comparing results obtained in a hollow cylinder torsional apparatus and in a cubic cell device, these authors concluded that samples subjected to stress paths similar to DMTEp↓ tend to exhibit less-resistant responses than samples subjected to stress paths similar to DMTCp↑, as observed here. Moreover, in terms of stress ratio evolution with axial strain (Figure 2.32b), the obtained results suggest that the stress ratios mobilised by samples submitted to TE are smaller than those exhibited by samples under TC. A similar trend is reported in the literature for other sands (e.g. Vaid *et al.*, 1990; Lade, 2006; Loukidis and Salgado, 2009). Note that, as detailed later, the fact that smaller values of η are mobilised in TE than in TC does not imply, however, that the critical state friction angle, ϕ'_{CS}, in TE is lower than in TC. In effect, some experimental studies on pluviated sands (e.g. Vaid *et*

al., 1990; Lade, 2006) suggest that the critical state friction angle, ϕ'_{CS}, in TE is similar to that mobilised in TC. This topic is further discussed in Section 2.6.5.1.

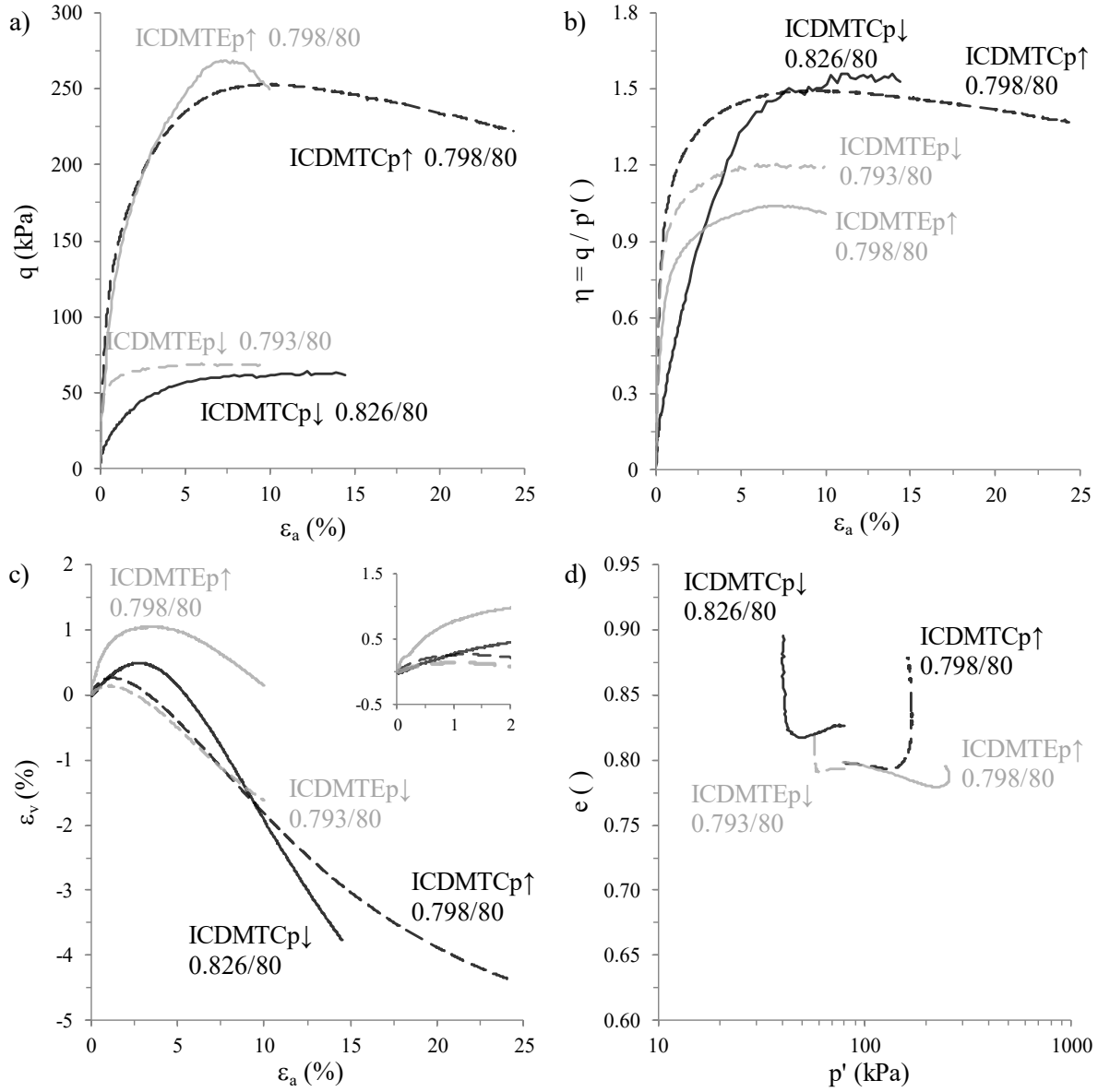

Figure 2.32 – Influence of the stress path on moderately loose samples tested under drained conditions: (a) stress-strain response; (b) stress ratio evolution with axial strain; (c) volumetric strain evolution with axial strain; and (d) void ratio evolution with mean effective stress.

With respect to the volumetric strain evolution with axial strain (Figure 2.32c), as it could also be expected due to the influence of the mean effective stress evolution on the volumetric response, it can be seen that samples subjected to stress paths with increasing mean stress (i.e. ICDMTCp↑ 0.798/80 and ICDMTEp↑ 0.798/80 tests) tend to contract more during the earlier stages of loading than those submitted to stress paths with decreasing mean stress (i.e. ICDMTCp↓ 0.826/80 and ICDMTEp↓ 0.793/80 tests).

2.6.4.2 Undrained monotonic triaxial extension with decreasing mean stress

The final series of monotonic tests performed consisted of isotropically consolidated undrained monotonic triaxial extension with decreasing mean stress (ICUMTE p↓ tests), with the obtained results being depicted in Figure 2.33.

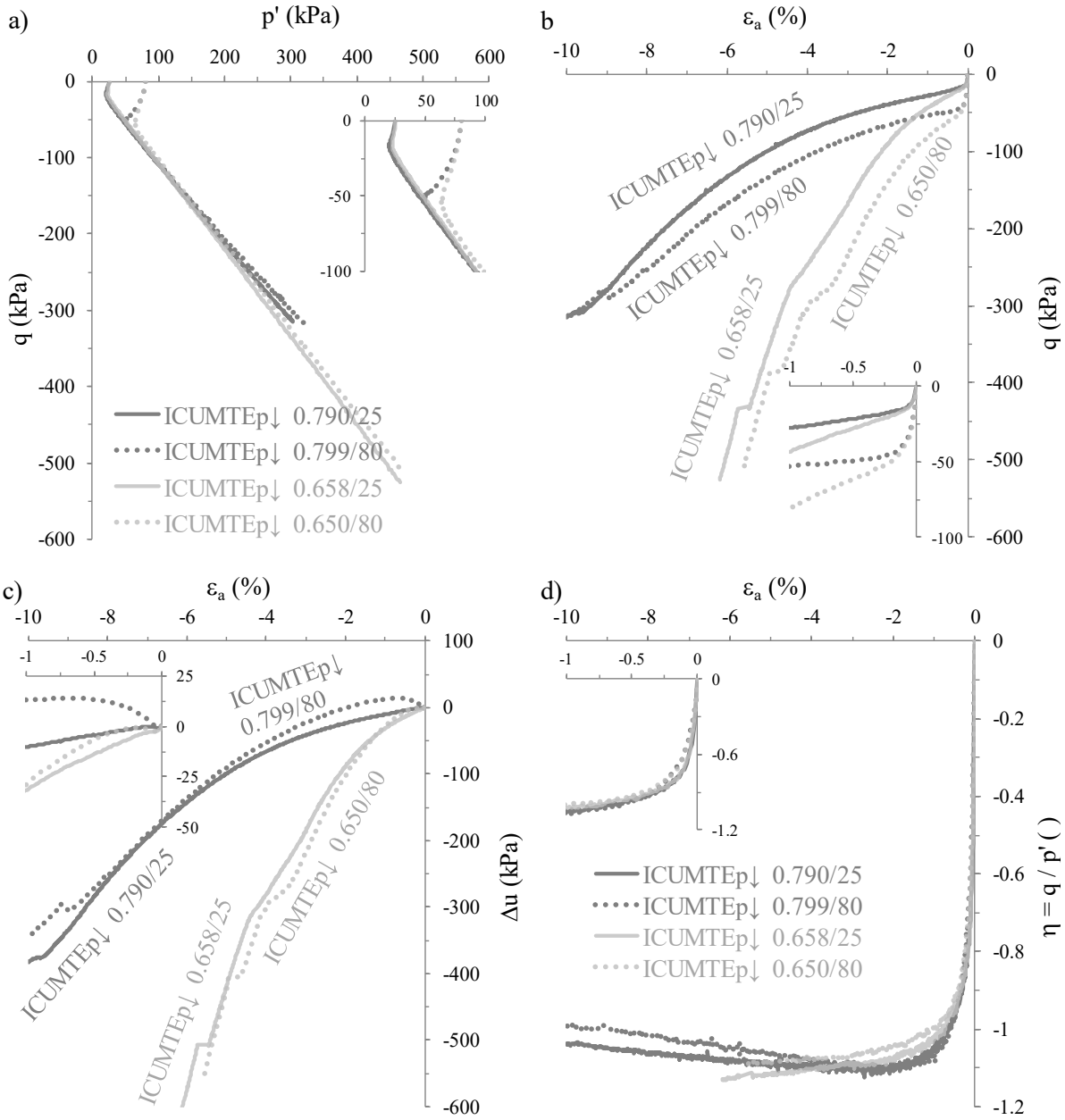

Figure 2.33 – ICUMTE p↓ test results: (a) effective stress path; (b) stress-strain response; (c) excess pore water pressure build-up; and (d) stress ratio evolution with axial strain.

Similar to UMTCp↑, it can be observed (particularly in the detail of Figure 2.33c) that looser samples consolidated under higher effective stresses (in this case, sample corresponding to test ICUMTEp↓ 0.799/80) tend to generate greater positive excess pore water pressures, Δu, during the earlier stages of loading than those prepared to denser states (i.e. corresponding to test ICUMTEp↓ 0.650/80), as well as to those consolidated under smaller effective stress (i.e. corresponding to test ICUMTEp↓ 0.658/25). Moreover, it can be observed in Figure 2.33c

that looser samples tend to start developing negative excess pore water pressures at higher strain levels (in terms of absolute magnitude) and at lower rates than those measured for denser samples. Still regarding Figure 2.33c, it is apparent that, as discussed before, the density of the samples appear to have a stronger impact on their volumetric response (which, under undrained conditions, its reflected on the generation of excess pore water pressures) than the effective stress at consolidation (for instance, the discrepancies between the responses measured in tests ICUMTEp↓ 0.790/25 and ICUMTEp↓ 0.799/80 seem much smaller than those observed between results of test ICUMTEp↓ 0.799/80 and test ICUMTEp↓ 0.650/80). Furthermore, as observed for TC, looser samples tend to exhibit softer stress-strain responses (Figure 2.33b).

As a consequence of its greater tendency to generate positive excess pore water pressures (or, at least, smaller negative excess pore water pressures) during the earlier stages of loading, the effective stress path of looser samples (i.e. corresponding to tests ICUMTEp↓ 0.790/25 and ICUMTEp↓ 0.799/80) are observed to bend more to the left (i.e. to the direction of $p' = 0$) than those corresponding to denser samples (i.e. those corresponding to tests ICUMTEp↓ 0.658/25 and ICUMTEp↓ 0.650/80), as shown in the detail of Figure 2.33a. Furthermore, as expected, looser samples tend to exhibit softer stress-strain responses than those exhibited by denser samples (Figure 2.33b). As also expected, the effective stresses at consolidation also affect the stress-strain response, particularly during the earlier stages of loading, with stiffer responses being observed for samples consolidated to higher stresses, as it is apparent in the detail of Figure 2.33b.

To further extend the interpretation of the experimental results, Figure 2.34 compares results of tests performed on similarly prepared moderately loose samples consolidated to a mean effective stress of 25 or 80 kPa, two of them subjected to ICUMTCp↑ (namely, tests ICUMTCp↑ 0.783/25 and ICUMTCp↑ 0.801/80), while the remaining two subjected to ICUMTEp↓ (namely, tests ICUMTEp↓ 0.790/25 and ICDMTEp↓ 0.793/80). Note that the total stress paths imposed in these tests (MTCp↑ and MTEp↓) are the most conventional in triaxial testing (involving only the variation of the axial stress, while keeping the radial stress constant).

When comparing the results obtained for TC and TE tests performed on samples consolidated to the same effective stress (e.g. tests ICUMTCp↑ 0.801/80 and ICUMTEp↓ 0.799/80), it is apparent that, although smaller positive excess pore water pressures were generated in the TE test (Figure 2.34e), when compared with that developed in the TC test, a higher reduction of the mean effective stress was obtained for the TE test (Figure 2.34a), as expected due to the reduction of mean stress applied during shearing and observed for other sands in other experimental testing programmes (e.g. Miura and Toki, 1982; Yoshimine *et al.*, 1998). Moreover, a softer response can be observed for the TE test (Figure 2.34b), with similar results being also reported for very loose Hostun sand by Doanh *et al.* (1997). Finally, in a

good agreement with the results obtained under drained conditions (Figure 2.32b), smaller stress ratios were mobilised in TE than in TC, as reported for other sands (e.g. Vaid *et al.*, 1990; Lade, 2006; Loukidis and Salgado, 2009).

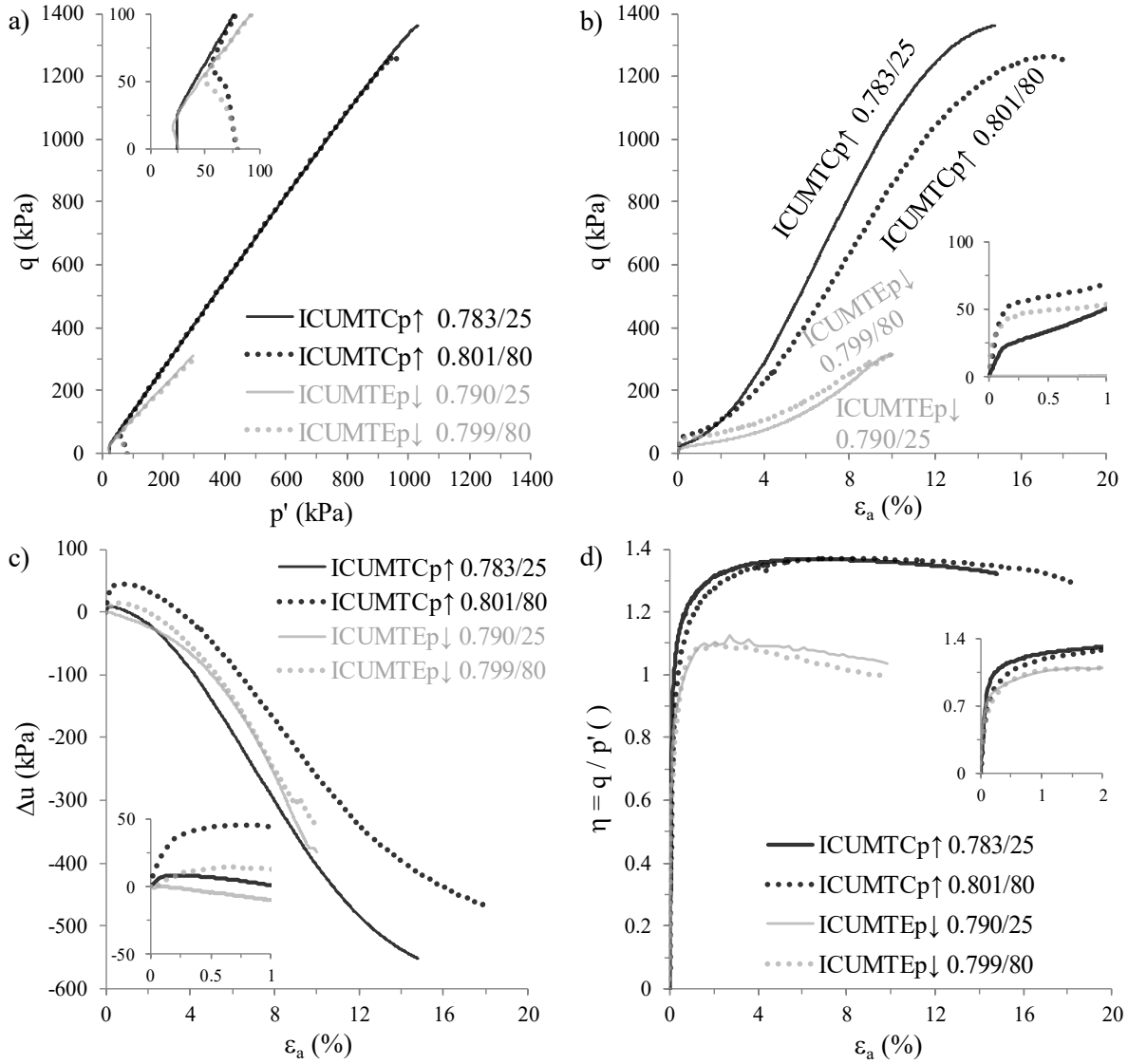

Figure 2.34 – Influence of the stress path on moderately loose samples tested under undrained conditions: (a) effective stress path; (b) stress-strain response; (c) excess pore water pressure build-up; and (d) stress ratio evolution with axial strain.

2.6.5 Distinctive states of the response of sand

2.6.5.1 Critical state

Although a significant number of tests were conducted, critical state conditions appear to be only attained in four tests, specifically for tests ICDMTCp↑ 0.885/80, ICDMTCp↑ 0.835/500, ICUMTCp↑ 0.876/80 and ICUMTCp↑ 0.868/80. For the remaining tests, clear signs of stresses and volumetric strain stabilisation – for drained shearing – or stresses and pore water pressure stabilisation – for undrained shearing – are not visible and, consequently, the conditions at the end of those tests cannot be considered representative of CS.

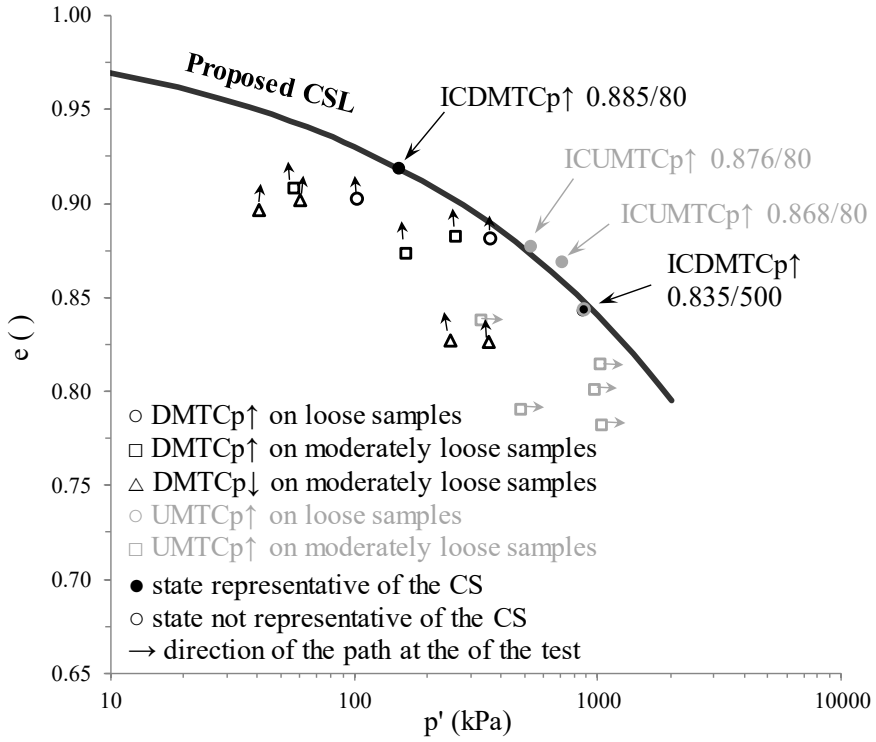

Figure 2.35 – Prediction of the critical state line for Hostun sand.

The void ratio, e, – mean effective stress, p', data at the end of all drained and undrained triaxial compression (TC) tests conducted on initially loose and moderately loose specimens are summarised in Table 2.10 (presented at the end of this chapter for convenience) and illustrated in Figure 2.35. For those tests where CS conditions were not attained (unfilled markers), arrows indicate the directions of the paths at the instant when those tests were stopped. It can be observed that, although TC tests were performed on samples consolidated to stress as low as 25 kPa, it was not possible to obtain data representative of CS at stresses below 100 kPa. According to Klotz and Coop (2002), this difficulty may arise from the incompleteness of tests, as a consequence of the premature occurrence of barrelling and strain localisation when samples are sheared under lower confining stresses. This problem seems to be particularly evident when pluviation is used to prepare samples, since it is practically impossible to prepare initially looser than critical state samples at stress levels in the range of 0 – 1000 kPa (as it was the case of the present study) and, consequently, the critical state line in this range can only be reached by drained triaxial tests on dilatant samples (Been *et al.*, 1991).

As proposed by Li and Wang (1998), a power law was used to define the critical state line (CSL):

$$e_{cs} = (e_{cs})_{ref} - \lambda \ln\left(\frac{p'}{p'_{ref}}\right)^{\xi} \tag{2.18}$$

where $(e_{cs})_{ref}$, λ and ξ are fitting parameters, which were estimated by a least-square regression. Due to the aforementioned difficulty in obtaining CS data at low stresses, the void

ratio under zero effective stress, $(e_{cs})_{ref}$, was constrained by the maximum void ratio, e_{max}, as proposed by Riemer *et al.* (1990) and also assumed in subsequent studies (e.g. Klotz and Coop, 2002; Murthy *et al.*, 2007). By employing this approach, values of 1.00, 0.07 and 0.36 were estimated for $(e_{cs})_{ref}$, λ and ξ, respectively, with the resulting critical state line (CSL) being depicted in Figure 2.35.

The obtained CS data were subsequently compared with other results of TC tests on Hostun sand presented in the literature (Table 2.7, where $e_{end\ test}$ and $p'_{end\ test}$ are, respectively, the void ratio and mean effective stress obtained at the end of each test). It can be seen in Figure 2.36 that the additional data found in the literature plot very close to the CSL proposed in this paper, independently of the sample preparation method and drainage conditions. Additionally, Figure 2.36 presents the CSL proposed for Toyoura sand (Verdugo and Ishihara, 1996), Leighton Buzzard sand (Been *et al.*, 1991) and Ottawa sand (Murthy *et al.*, 2007). Interestingly, as previously discussed by Klotz and Coop (2002b), it was found that the CSL proposed for sands with identical particle shape (namely, Hostun, Toyoura and Leighton Buzzard sands, as indicated in Table 2.2) plot very close to each other for values of p' within the range of 100 to 1000 kPa, despite having different particle size distributions (Figure 2.2). Conversely, although presenting similar particle size distributions, the CSL proposed for Ottawa sand is located far below that suggested for Hostun sand. This suggests that particle shape has a major influence on the CSL of sand (particularly on the value of $(e_{cs})_{ref}$), at least for uniformly graded fine to medium fine sands, as suggested by Cho *et al.* (2006).

Table 2.7 – Characteristics of TC tests performed on Hostun sand at other institutions and used for comparing with the critical state data obtained in the present experimental programme.

Test ID [a]	*Method of prep.*[b]	e_0 ( )	p'_0 (kPa)	ψ_0 [c] ( )	$e_{end\ test}$ ( )	$p'_{end\ test}$ (kPa)	*Institution*	Reference
ICDMTCp↑ 0.867/600	AP	0.867	600.0	-0.030	0.820	933.4	INPG [*]	Mokni and Desrues (2013)
ICUMTCp↑ 0.895/300	AP	0.895	300.0	0.000	0.895	205.3	INPG [*]	Mokni and Desrues (2013)
ICUMTCp↑ 0.970/279	MT	0.970	279.0	0.072	0.970	22.0	INPG [*]	Konrad (1993)
ICUMTCp↑ 0.922/772	MT	0.922	772.0	0.063	0.922	60.1	INPG [*]	Konrad (1993)
ICDMTCp↑ 0.918/100	MT	0.918	100.0	-0.009	0.908	173.5	ENPC [**]	Benahmed (2001)
ICDMTCp↑ 0.910/200	MT	0.910	200.0	0.001	0.887	345.1	ENPC [**]	Benahmed (2001)
ICDMTCp↑ 0.899/400	MT	0.899	400.0	0.013	0.859	682.3	ENPC [**]	Benahmed (2001)
ICUMTCp↑ 0.919/100	MT	0.919	100.0	-0.008	0.919	103.9	ENPC [**]	Benahmed (2001)
ICUMTCp↑ 0.910/200	MT	0.910	200.0	0.001	0.910	154.1	ENPC [**]	Benahmed (2001)
ICUMTCp↑ 0.898/400	MT	0.898	400.0	0.012	0.898	216.3	ENPC [**]	Benahmed (2001)

[a] The designation is identical to that presented in Table 2.4 (see note below that table).
[b] Method of sample preparation: air pluviation (AP) or moist tamping (MT)
[c] $\psi_0 = e_0 - e_{cs}$, as defined by Been and Jefferies (1985).
[*] Grenoble Institute of Technology (INPG); [**] *École Nationale des Ponts et Chaussées* (ENPC).

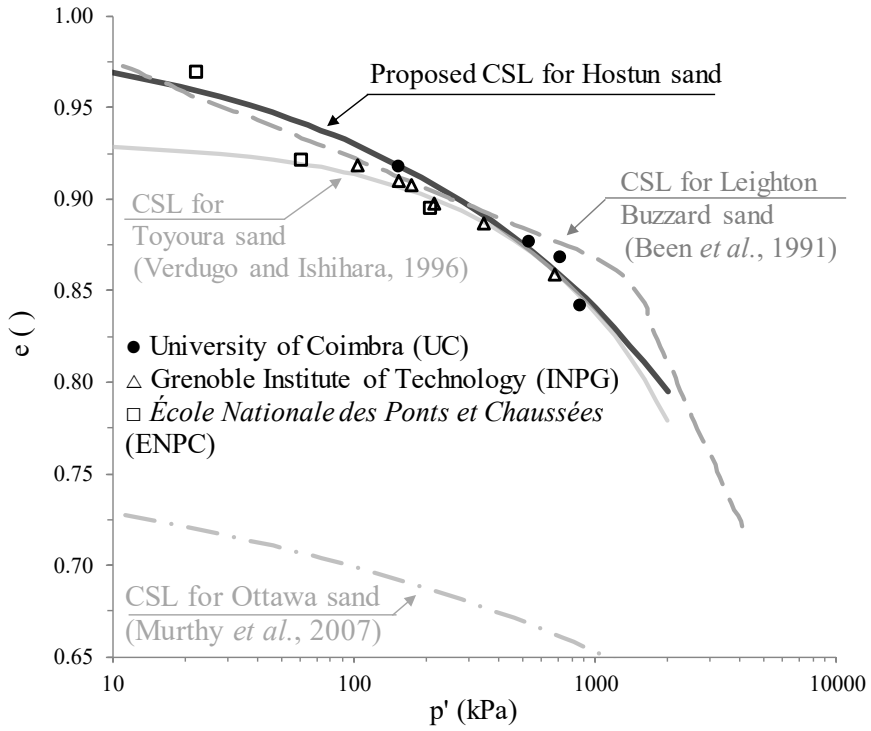

Figure 2.36 – Comparison of the proposed critical state line (CSL) with results presented in the literature.

The CS strength in TC and in TE, identified, respectively, by subscripts "c" and "e", is quantified by the corresponding stress ratio $M_{c,e}^{c} = q_{cs}/p'_{cs}$, where q_{cs} and p'_{cs} are, respectively, the deviatoric stress and mean effective stress at critical state. Figure 2.37 presents the $q - p'$ data obtained at the end of shearing for loose and moderately loose specimens. The four data points, which were considered representative of the CS, are distinguished by using filled markers. Based on these CS points, the critical strength in TC, M_c^c, was estimated as 1.265, which corresponds to a CS friction angle, ϕ'^c_c, of approximately 31.5°. With respect to the CS in TE, it is difficult to obtain a reliable estimation from the obtained results, since test data measured after the occurrence of necking were disregarded. Several experimental studies have shown that the friction angle in TE, ϕ'^c_e , is close to that in TC, ϕ'^c_c, or slightly greater (typically up to a maximum of $\phi'^c_e = \phi'^c_c + 2°$) for pluviated sands (Vaid *et al.*, 1990a; Lade, 2006). In the present study, a stress ratio of $M_e^{cs} \approx 0.911$ was considered, corresponding to $\phi'^c_e = \phi'^c_c + 1° \approx 31.5° + 1° \approx 32.5°$ and to a ratio of M_e^c/M_c^c of about 0.72, which is within the typical 0.67 – 0.75 range for silica sands (Loukidis and Salgado, 2009). Note that, although $q_{cs} - p'_{cs}$ data in TE is defined by a negative slope, which means that, to be formally correct, $M_e^c = q_{cs}/p'_{cs}$ should take a negative value, M_e^c is taken here as positive to comply with the constitutive equations presented in Chapter 4. In constitutive modelling, a tensor typically introduces the effect of the loading direction on the modelled response and, therefore, these model parameters are considered positive. Note also that the $q - p'$ data points corresponding to the end of TE tests (limited to an axial stress of -10 %, due to sample's necking, as

mentioned before) are also plotted in Figure 2.37. It can be seen that these points do not plot far from the adopted CS strength line in extension.

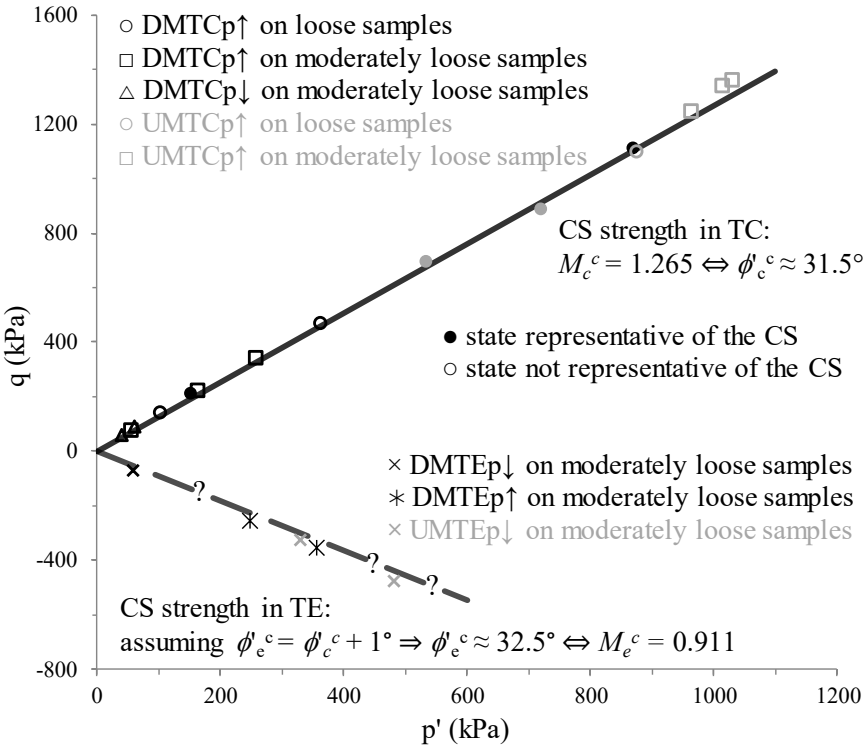

Figure 2.37 – Critical state strength of Hostun sand in compression and in extension.

2.6.5.2 Peak stress ratio state

The occurrence of a peak (or bounding) stress ratio either in TC or in TE, $M_{c,e}^b$, can be related to the current value of the state parameter, ψ^b, through the following equation (Wood *et al.*, 1994):

$$M_{c,e}^b = M_{c,e}^c - k_{c,e}^b \, \psi^b \tag{2.19}$$

where $k_{c,e}^b$ is a set of positive material parameters (one value for TC and another for TE). Note that this relationship has been incorporated in several constitutive models for sand, including in that described in Chapter 4, which was proposed by Manzari and Dafalias (1997) and extended by Papadimitriou and Bouckovalas (2002) and Taborda *et al.* (2014). Note also that, to comply with the terminology used in the constitutive model, the superscript "b" is preferred to "PSRS". Additionally, note that, with the purpose of improving the modelling response, some authors have replaced the linear dependency on the state parameter by an exponential dependency (e.g. Li and Dafalias, 2000). The results obtained in the present study, however, do not suggest that there could be any substantial gain in accuracy by introducing a modification of that type to Equation 2.19.

For each monotonic triaxial test conducted in this experimental programme, η_c^b (or η_e^b) was identified from test data, as well as the corresponding mean effective stress, p'^b, and void ratio, e^b. Subsequently, based on Equation 2.18, the void ratio at critical state, e_{cs},

corresponding to the same mean effective stress (i.e. for $p' = p'^{b}$) was computed, allowing for the calculation of $\psi^b = e^b - e_{cs}$. The $\eta^b_{c,e} - \psi^b$ data obtained from the results of all monotonic triaxial tests performed in this experimental programme are presented in Figure 2.38. It can be observed that, irrespective of the type of consolidation, of the drainage conditions and of the stress path followed in each test, the experimental results are well represented by an equation of the form of Equation 2.19. By employing the least square method, the fitting parameters of Equation 2.19 were estimated as $k^b_c \approx 2.81$ for TC and $k^b_e \approx 1.44$ for TE, as also indicated in the figure. Note that, in TE, the slope obtained by linear regression is slightly lower than that commonly assumed in constitutive modelling $k^b_e = (M^{cs}_e / M^{cs}_c)\, k^b_c \approx (0.911/1.265) \times 2.81 \approx 2.02$ (Papadimitriou and Bouckovalas, 2002). Note also that, rather than $M^b_{c,e}$ and $M^c_{c,e}$, which represent positive model parameters (as detailed in Chapter 4), the experimental results are presented in the figure in terms of $\eta^b_{c,e}$ and $\eta^c_{c,e}$ to comply with the adopted sign convention, where stress ratio in triaxial compression takes negative value (i.e. η^b_e and η^c_e are negative).

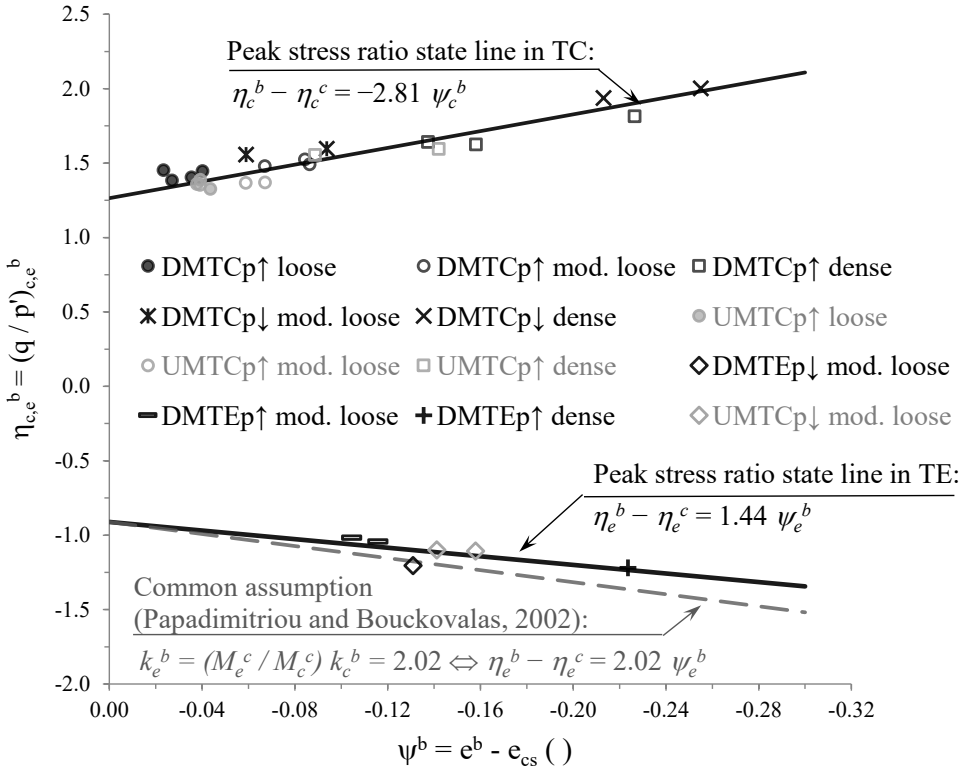

Figure 2.38 – Peak stress ratio as a function of the state parameter.

2.6.5.3 Phase transformation state

Under undrained conditions, the state at which the response of sand changes from plastic contraction to plastic dilation, termed as phase transformation state (PTS), can be identified by a local minimum of the mean effective stress, *p'* (Ishihara *et al.*, 1975). In the case of drained shearing, the identification of the PTS is much more complex, since it involves the estimation of the dilatancy coefficient, *D*, and, consequently, of the increment of plastic

volumetric strain, $\delta\varepsilon_v^p$, and increment of plastic deviatoric strain, $\delta\varepsilon_q^p$, as indicated by Equation 2.20.

$$D = \frac{d\varepsilon_v^p}{d\varepsilon_q^p} \approx \frac{\delta\varepsilon_v^p}{\delta\varepsilon_q^p} \tag{2.20}$$

Assuming that the soil response can be decoupled into elastic and plastic components, D can be expressed by Equation 2.21.

$$D \approx \frac{\delta\varepsilon_v^p}{\delta\varepsilon_q^p} \approx \frac{\delta\varepsilon_v - \delta\varepsilon_v^e}{\delta\varepsilon_q - \delta\varepsilon_q^e} \tag{2.21}$$

where $\delta\varepsilon_v$ and $\delta\varepsilon_q$ are, respectively, the total volumetric and total deviatoric strain increments, while $\delta\varepsilon_v^e$ and $\delta\varepsilon_q^e$, are their respective elastic components.

Moreover, by employing an isotropic hypoelastic formulation to describe the elastic response of soil and assuming that the deviatoric and volumetric responses are independent from each other, Equation 2.21 can be further developed, as shown by Equation 2.22, where triaxial conditions are assumed.

$$D \approx \frac{\delta\varepsilon_v - \delta\varepsilon_v^e}{\delta\varepsilon_q - \delta\varepsilon_q^e} \approx \frac{\delta\varepsilon_v - \dfrac{\delta p'}{K_{tan}}}{\delta\varepsilon_q - \dfrac{\delta q}{3\,G_{tan}}} \tag{2.22}$$

where $\delta p'$ and δq are the mean effective stress and deviatoric stress increments, respectively, while G_{tan} and K_{tan} are the tangent shear and bulk moduli, respectively.

Further assuming that G_{tan} and K_{tan} can be approximated by their respective small-strain values, G_{max} and K_{max}, Equation 2.23 can be written.

$$D \approx \frac{\delta\varepsilon_v - \dfrac{\delta p'}{K_{tan}}}{\delta\varepsilon_q - \dfrac{\delta q}{3\,G_{tan}}} \approx \frac{\delta\varepsilon_v - \dfrac{\delta p'}{K_{max}}}{\delta\varepsilon_q - \dfrac{\delta q}{3\,G_{max}}} \tag{2.23}$$

Note that, as discussed by Loukidis and Salgado (2009), this simplification is acceptable when results from drained tests are used. According to these authors, since strains induced in sand during triaxial loading are mostly of plastic nature, the value of D is expected to be primarily affected by the total volumetric and deviatoric strain increments, $\delta\varepsilon_v$ and $\delta\varepsilon_q$, respectively, and, therefore, to depend only to a limited extent on the elastic volumetric and deviatoric strain components, $\delta\varepsilon_v^e$ and $\delta\varepsilon_q^e$, respectively. Conversely, under undrained conditions, since $\delta\varepsilon_v \approx 0.0$, D is more dependent on $\delta\varepsilon_v^e \approx (p'_{j+1} - p'_j)/K_{tan} \approx (p'_{j+1} - p'_j)/K_{max}$ and, therefore, inaccurate values of D can be obtained when adopting this simplification. This undesirable situation is avoided, in the present study, by using solely drained triaxial compression test data to estimate the dilatancy coefficient, D (and, therefore, to characterise the stress-dilatancy response of Hostun sand, as detailed in Section 2.6.6). Note that a similar approach was followed by Been and Jefferies (2004) when examining the stress-dilatancy

response of Erksak sand, as well as by Loukidis and Salgado (2009) when characterising the stress-dilatancy responses of both Toyoura and Ottawa sands.

Given that only G_{max} was calibrated against bender element test results, the value of K_{max} was obtained using Equation 2.24, derived from the theory of isotropic elasticity.

$$K_{max} = \frac{2\,(1+\nu)}{3\,(1-2\nu)}\,G_{max} \tag{2.24}$$

where a constant Poisson's ratio, ν, equal to 0.18, as proposed by Hoque and Tatsuoka (2000) for Hostun sand, was assumed. Note, however, that this does mean that K_{max} remains constant during shearing. In effect, since G_{max} (Equation 2.16) depends on the current values of the void ratio, e, and mean effective stress, p', K_{max} is expected to evolve throughout loading.

Lastly, in order to compute Equation 2.23, a forward-difference first-order approach, similar to that outlined by Been and Jefferies (2004), was employed. In this approach, both G_{max} and K_{max} are assumed to remain constant over each time step (i.e. from a given instant j to the subsequent instant $j+1$), as shown by Equation 2.25.

$$D \approx \frac{\Delta\varepsilon_v - \frac{\Delta p'}{K_{max}}}{\Delta\varepsilon_q - \frac{\Delta q}{3\,G_{max}}} \approx \frac{\left(\varepsilon_{v_{j+1}} - \varepsilon_{v_j}\right) - \frac{p'_{j+1} - p'_j}{K_{max}}}{\left(\varepsilon_{q_{j+1}} - \varepsilon_{q_j}\right) - \frac{q_{j+1} - q_j}{3\,G_{max}}} \tag{2.25}$$

It is perhaps important to note that, while frequently used for the numerical modelling of response of sand, the use of an isotropic hypoelastic formulation, where both shear and bulk moduli are a function of the mean effective stress (see Equation 2.16), implies the laws of thermodynamics are not observed and non-conservative results may be obtained. Please refer to Houlsby *et al.* (2005) for further details on this topic.

Having identified the PTS from the local minimum of p' for undrained test data and from the point at which $D \approx 0$ for drained test data, the stress ratio at PTS (also termed as dilatancy stress ratio) and represented by $M^d_{c,e}$ (where the subscripts "c" and "e" refer to TC and TE, respectively, and the superscript "d" is preferred to "PTS" to comply with the terminology used in the constitutive model described in Chapter 4) was plotted against the corresponding value of the state parameter, ψ^d, as shown in Figure 2.39. Note also that, rather than $M^d_{c,e}$ and $M^c_{c,e}$, which represent positive model parameters, the experimental results are presented in the figure in terms of $\eta^d_{c,e}$ and $\eta^c_{c,e}$ to comply with the adopted sign convention, where stress ratio in triaxial compression takes negative value (i.e. η^d_e and η^c_e are negative). Although some scatter exists, particularly in TE, the obtained results suggest that, irrespective of the type of consolidation, of the drainage conditions and of the stress path followed in each test, the stress ratio at PTS can be satisfactorily described by Equation 2.26, proposed by Manzari and Dafalias (1997) and incorporated in the constitutive model used in the present study (Chapter 4).

$$M_{c,e}^{d} = M_{c,e}^{c} + k_{c,e}^{d}\ \psi^{d} \tag{2.26}$$

where $k_{c,e}^{d}$ is a set of positive material parameters (one value for TC and another for TE). Having applied least square regressions over available test data, $k_{c}^{d} = 0.94$ and $k_{e}^{d} = 0.20$ were obtained for TC and TE, respectively. Note that, as observed for the PSRS, in TE, a value lower than that commonly assumed in constitutive modelling $k_{e}^{d} \approx (M_{e}^{c}/M_{c}^{c})\ k_{c}^{d} = (0.911/1.265) \times 0.94 \approx 0.67$ (Papadimitriou and Bouckovalas, 2002) was found.

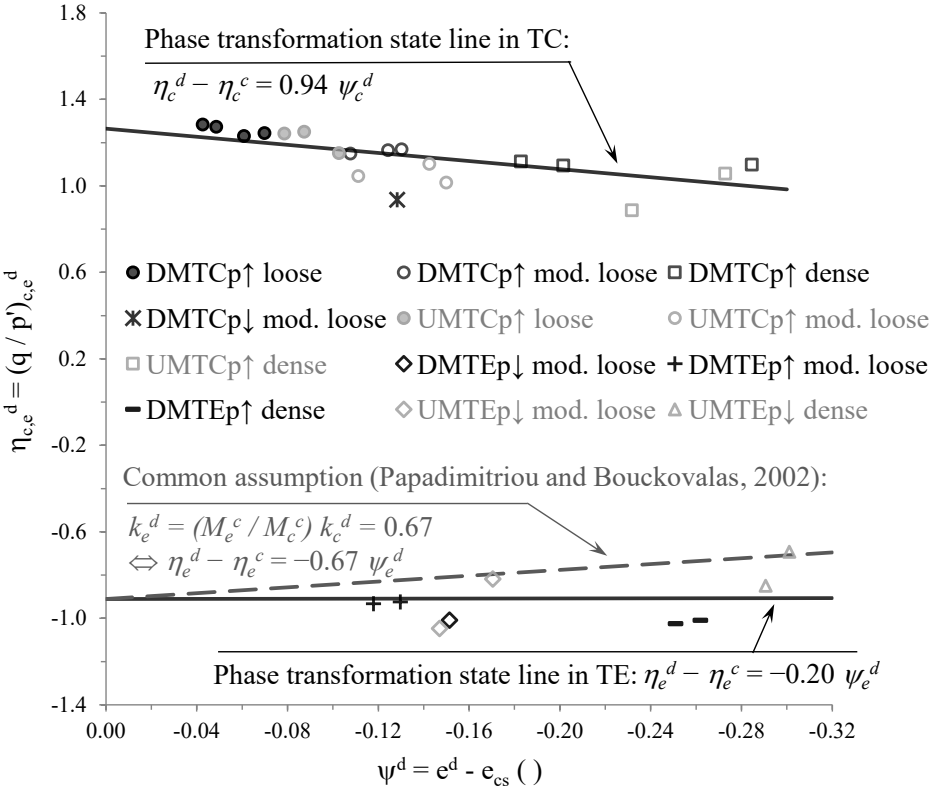

Figure 2.39 – Stress ratio at phase-transformation state as a function of the state parameter.

2.6.5.4 Undrained instability state and quasi-steady state

The characterisation of the undrained instability state (UIS) and quasi-steady state (QSS) are of particular interest for design practice, since these states correspond, respectively, to temporarily maximum and minimum values of undrained shear strength at relatively small-strains (Murthy *et al.*, 2007).

In the present study, the UIS was only observed to occur in three of the thirteen undrained monotonic tests performed, specifically in tests ICUMTCp↑ 0.876/80, ICUMTCp↑ 0.868/80 and ICUMTCp↑ 0.843/135, which were conducted on loose samples. The outcome of these tests is depicted in Figure 2.40, together with the points at which the UIS occurred. Complementary, the points corresponding to the occurrence of both QSS and PTS are also identified in the figure. As anticipated, it can be seen that, in terms of stress path (Figure 2.40a), the points corresponding to the occurrence of the QSS and PTS are practically coincident. In effect, the major differences between the occurrences of these states are

observed in terms of axial strains (Figure 2.40b). Specifically, the PTS is observed to occur at axial strains of about 0.2 – 0.4 % greater than those corresponding to the occurrence of the QSS. With respect to the UIS, it is apparent in Figure 2.40 that it occurs during the earlier stages of loading (i.e. at axial strain levels smaller than those corresponding to the QSS and PTS). In particular, the UIS is observed to occur at axial strains of 0.23, 0.30 and 0.37%, respectively for tests ICUMTCp↑ 0.876/80, ICUMTCp↑ 0.868/80 and ICUMTCp↑ 0.843/135.

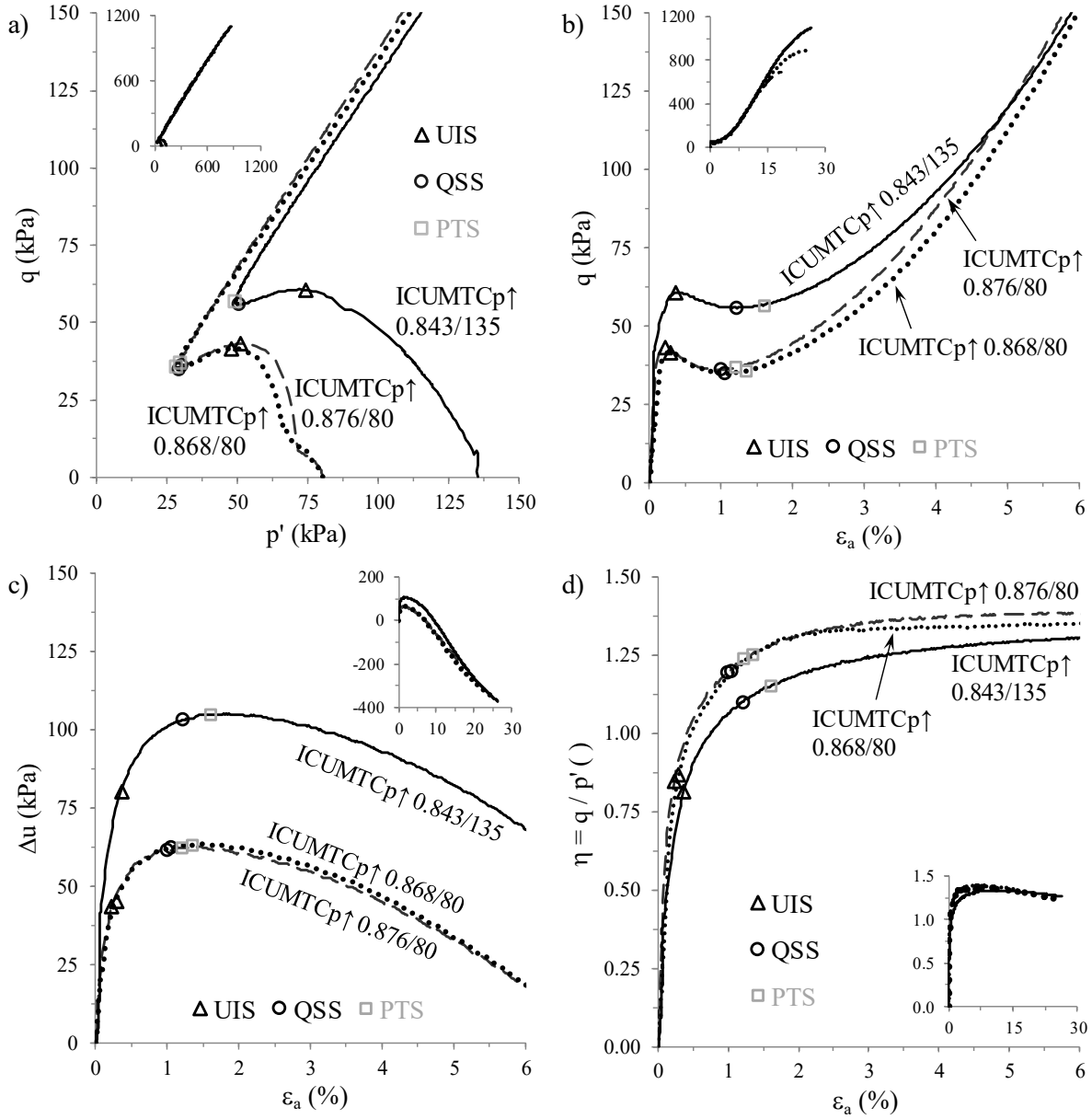

Figure 2.40 – Occurrence of the undrained instability, quasi-steady and phase transformation states in undrained shearing: (a) effective stress path; (b) stress-strain response; (c) excess pore water pressure build-up; and (d) stress ratio evolution with axial strain.

According to Ishihara (1993), the mean effective stress at UIS, p'^{UI}, is strongly correlated with the mean effective stress immediately after consolidation, p'_0. In the present study, a p'^{UI}/p'_0 ratio of about 0.57 was obtained (Figure 2.41). Although the number of points used for the estimation of this ratio is very limited (only three points, with two of them plotting very close),

it is interesting to note that the obtained value is similar to that reported by Ishihara (1993) for moist-tamped Toyoura sand ($p'^{UI}/p'_0 = 0.61$) and by Murthy *et al.* (2007) for slurry-deposited Ottawa sand ($p'^{UI}/p'_0 = 0.60$). This does not mean, however, that the UIS is either independent of the material tested or independent of the method of sample preparation. In effect, Murthy *et al.* (2007) obtained a higher ratio for moist-tamped Ottawa sand ($p'^{UI}/p'_0 = 0.66$). In order to evaluate the influence of the method of preparation on the occurrence of the UIS for Hostun sand, the ICUMTCp↑ tests performed on moist-tamped samples at the Grenoble Institute of Technology (INPG) and at the *École Nationale des Ponts et Chaussées* (ENPC) and used to confirm the position of the CSL in the $e - p'$ space (Section 2.6.5.1) were examined once more, with the obtained $p'^{UI} - p'_0$ points being indicated in Table 2.8 and plotted in Figure 2.41.

Table 2.8 – Characteristics of ICUMTC p↑ tests performed on Hostun sand at other institutions and used for comparing with the results obtained in the present experimental programme.

Test ID [a]	*Method of prep.*[b]	e_0 ( )	p'_0 (kPa)	ψ_0 [c] ( )	$e_{end\ test}$ ( )	$p'_{end\ test}$ (kPa)	*Institution*	Reference
ICUMTCp↑ 0.970/279	MT	0.970	279.0	0.072	0.970	22.0	INPG [*]	Konrad (1993)
ICUMTCp↑ 0.922/772	MT	0.922	772.0	0.063	0.922	60.1	INPG [*]	Konrad (1993)
ICUMTCp↑ 0.919/100	MT	0.919	100.0	-0.008	0.919	103.9	ENPC [**]	Benahmed (2001)
ICUMTCp↑ 0.910/200	MT	0.910	200.0	0.001	0.910	154.1	ENPC [**]	Benahmed (2001)
ICUMTCp↑ 0.898/400	MT	0.898	400.0	0.012	0.898	216.3	ENPC [**]	Benahmed (2001)

[a] The designation is identical to that presented in Table 2.4 (see note below that table).
[b] Method of sample preparation: air-pluviation (AP) or moist tamping (MT)
[c] $\psi_0 = e_0 - e_{cs}$, as defined by Been and Jefferies (1985).
[*] Grenoble Institute of Technology (INPG); [**] *École Nationale des Ponts et Chaussées* (ENPC).

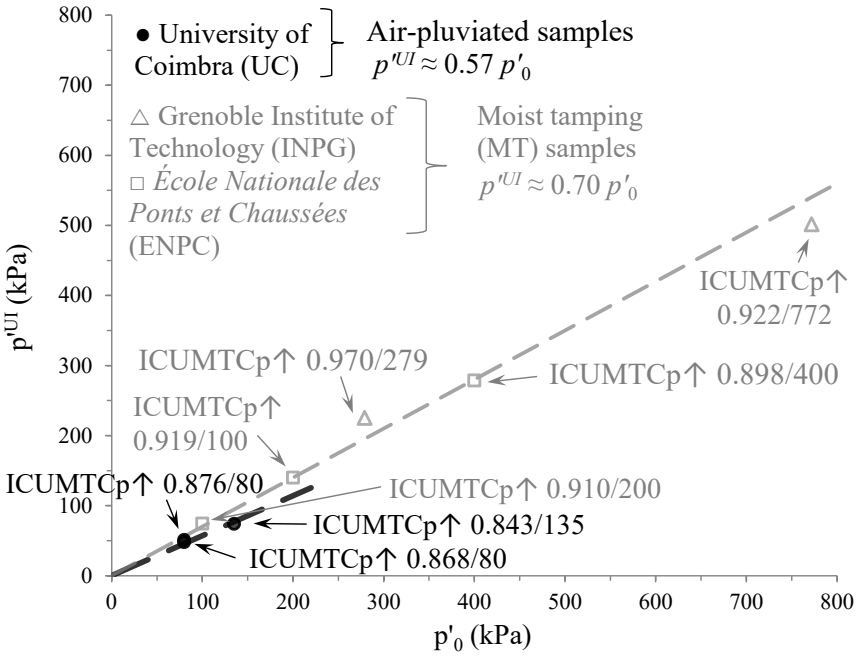

Figure 2.41 – Mean effective stress at the undrained instability state as a function of the mean effective stress at consolidation.

As indicated in the figure, a higher p'^{UI}/p'_0 ratio of about 0.70 (rather than 0.57) was obtained for moist-tamped samples of Hostun sand, suggesting that, contrarily to what was observed within the large strain range, the method of sample preparation influences the response of sand within small to medium strain range.

2.6.5.5 Summary of the results of the monotonic triaxial tests performed

Table 2.9 summarises the initial conditions and main results in terms of distinctive states of the response of Hostun sand obtained for all monotonic triaxial compression tests performed. Similarly, Table 2.10 indicates the initial conditions and main results of all monotonic triaxial extension tests performed. In these tables, the quantities e, p', q, η and ψ are, respectively, the void ratio, mean effective stress, deviatoric stress, stress ratio and state parameter; the subscripts "0" and "end" refer to test data values at the start and at the end of the test, while the superscripts "UI", "d" and "b" refer to values registered at the undrained instability state, at the phase transformation state and at peak stress ratio state, respectively.

Table 2.9 – Summary of the initial conditions and results obtained for all monotonic triaxial compression tests performed.

Test ID [(a)]	Consolidation			UIS		PTS				PSRS				End of the test			
	e_0 ( )	p'_0 (kPa)	ψ_0 ( )	p'^{UI} (kPa)	q^{UI} (kPa)	p'^{d} (kPa)	q^{d} (kPa)	η^{d} ( )	ψ^{d} ( )	p'^{b} (kPa)	q^{b} (kPa)	η^{b} ( )	ψ^{b} ( )	e_{end} ( )	p'_{end} (kPa)	q_{end} (kPa)	η_{end} ( )
ICDMTCp↑ 0.875/50	0.875	50.0	-0.071	–	–	84.6	105.3	1.244	-0.070	102.9	149.2	1.447	-0.040	0.902	102.3	145.9	1.426
ICDMTCp↑ 0.885/80	0.885	80.0	-0.050	–	–	138.9	176.9	1.273	-0.049	162.8	237.6	1.458	-0.023	0.918	154.2	210.0	1.362
ICDMTCp↑ 0.846/200	0.846	200.0	-0.064	–	–	336.4	414.0	1.231	-0.061	379.5	533.1	1.404	-0.035	0.881	360.3	473.2	1.313
ICDMTCp↑ 0.835/500	0.835	500.0	-0.040	–	–	867.7	1109.2	1.278	-0.043	927.8	1284.0	1.383	-0.027	0.842	871.2	1109.6	1.274
ICDMTCp↑ 0.829/25	0.829	25.0	-0.129	–	–	40.3	47.6	1.181	-0.124	57.3	87.7	1.528	-0.084	0.909	56.1	79.0	1.409
ICDMTCp↑ 0.798/80	0.798	80.0	-0.138	–	–	130.4	152.4	1.169	-0.130	169.3	253.0	1.493	-0.086	0.874	162.7	224.1	1.377
ICDMTCp↑ 0.804/135	0.804	135.0	-0.118	–	–	218.1	250.6	1.149	-0.108	275.6	407.8	1.479	-0.067	0.883	258.0	340.1	1.318
ICDMTCp↑ 0.667/25	0.667	25.0	-0.291	–	–	37.9	41.6	1.098	-0.285	67.5	122.8	1.816	-0.227	0.774	61.2	97.0	1.586
ICDMTCp↑ 0.725/80	0.725	80.0	-0.211	–	–	125.4	137.3	1.095	-0.202	183.3	298.2	1.626	-0.158	0.847	164.5	220.1	1.338
ICDMTCp↑ 0.728/135	0.728	135.0	-0.195	–	–	216.4	245.5	1.135	-0.183	308.1	506.3	1.642	-0.137	0.813	265.7	364.2	1.370
ICDMTCp↓ 0.826/80	0.826	80.0	-0.109	–	–	49.3	47.8	0.970	-0.129	40.5	63.1	1.557	-0.059	0.896	40.7	63.0	1.549
K0CDMTCp↓ 0.797/80	0.797	80.0	-0.139	–	–	–	–	–	–	58.6	93.6	1.597	-0.094	0.902	59.8	91.5	1.530
ICDMTCp↓ 0.650/80	0.650	80.0	-0.286	–	–	–	–	–	–	34.4	69.7	2.002	-0.255	0.864	42.0	54.7	1.303
K0CDMTCp↓ 0.672/80	0.672	80.0	-0.264	–	–	–	–	–	–	51.9	102.4	1.938	-0.213	0.881	59.1	90.2	1.526
ICUMTCp↑ 0.876/80	0.876	80.0	-0.059	51.0	43.2	29.7	36.9	1.241	-0.079	170.4	236.5	1.387	-0.039	0.876	535.1	694.1	1.297
ICUMTCp↑ 0.868/80	0.868	80.0	-0.067	47.8	41.6	28.5	35.6	1.251	-0.087	229.6	312.3	1.360	-0.038	0.868	721.8	888.1	1.230
ICUMTCp↑ 0.843/135	0.843	135.0	-0.079	74.2	60.5	49.2	56.6	1.151	-0.103	288.9	383.7	1.328	-0.055	0.843	874.1	1101.6	1.260
ICUMTCp↑ 0.783/25	0.783	25.0	-0.175	–	–	23.9	17.7	0.742	-0.176	550.3	753.3	1.368	-0.089	0.783	1030.0	1361.4	1.322
ICUMTCp↑ 0.801/80	0.801	80.0	-0.135	–	–	55.5	61.1	1.101	-0.143	494.1	677.4	1.371	-0.075	0.801	962.7	1246.8	1.295
ICUMTCp↑ 0.815/135	0.815	135.0	-0.108	–	–	118.6	120.5	1.016	-0.111	785.4	1063.4	1.354	-0.039	0.815	1014.5	1340.7	1.322
ICUMTCp↑ 0.686/25	0.686	25.0	-0.272	–	–	23.1	24.4	1.056	-0.273	1228.5	1959.7	1.595	-0.142	0.686	1326.9	2075.0	1.564
ICUMTCp↑ 0.751/80	0.751	80.0	-0.185	–	–	78.8	18.4	0.234	-0.185	1018.1	1582.4	1.554	-0.089	0.751	1223.4	1789.6	1.463
ICUMTCp↑ 0.694/135	0.694	135.0	-0.229	–	–	121.0	107.3	0.887	-0.232	1305.6	1980.2	1.516	-0.131	0.694	1306.0	1979.9	1.516

[(a)] See note below Table 2.4.

Table 2.10 – Summary of the initial conditions and results obtained for all monotonic triaxial extension tests performed.

Test ID [a]	Consolidation			PTS				PSRS				End of the test			
	e_0 ( )	p'_0 (kPa)	ψ_0 ( )	p'^d (kPa)	q^d (kPa)	η^d ( )	ψ^d ( )	p'^b (kPa)	q^b (kPa)	η^b ( )	ψ^b ( )	e_{end} ( )	p'_{end} (kPa)	q_{end} (kPa)	η_{end} ( )
ICDMTEp↑ 0.798/80	0.798	80.0	-0.138	205.8	-190.2	-0.924	-0.130	257.6	-269.1	-1.039	-0.116	0.796	246.1	-249.0	-1.012
K0CDMTEp↑ 0.801/80	0.801	80.0	-0.135	314.3	-293.1	-0.933	-0.118	369.3	-376.1	-1.002	-0.105	0.793	355.5	-352.2	-0.991
ICDMTEp↑ 0.652/80	0.652	80.0	-0.284	238.6	-240.7	-1.009	-0.262	407.5	-497.1	-1.210	-0.224	0.681	341.2	-392.7	-1.151
K0CDMTEp↑ 0.652/80	0.652	80.0	-0.284	375.3	-384.9	-1.026	-0.251	(*)	(*)	(*)	(*)	0.642	505.9	-581.6	-1.150
ICDMTEp↓ 0.793/80	0.793	80.0	-0.143	60.1	-60.6	-1.008	-0.151	57.0	-69.0	-1.204	-0.131	0.822	57.2	-68.4	-1.196
ICUMTEp↓ 0.790/25	0.790	25.0	-0.167	20.3	-16.6	-0.819	-0.170	43.9	-49.3	-1.125	-0.158	0.790	289.0	-301.0	-1.041
ICUMTEp↓ 0.799/80	0.799	80.0	-0.137	49.3	-51.6	-1.047	-0.147	65.5	-72.7	-1.110	-0.141	0.799	283.9	-284.7	-1.003
ICUMTEp↓ 0.658/25	0.658	25.0	-0.300	22.7	-15.7	-0.692	-0.301	(*)	(*)	(*)	(*)	0.658	241.1	-267.4	-1.109
ICUMTEp↓ 0.650/80	0.650	80.0	-0.286	63.9	-54.3	-0.849	-0.291	(*)	(*)	(*)	(*)	0.650	253.4	-271.7	-1.072

[a] See note below Table 2.4. (*) When the test was stopped, the stress ratio was still increasing.

2.6.6 Stress-dilatancy characteristics

A fundamental aspect of soil response is its well-known tendency to change volume when sheared, a characteristic termed as "dilatancy". Based on the postulate of Rowe (1962) that, for soil, the mobilised stress ratio is strongly dependent on the plastic strain increments (or, in other words, on the dilatancy, *D*), several expressions have been proposed in the literature to describe the stress-dilatancy relationship for soils. Among them, it is of particular interest in the present work to examine the stress-dilatancy relationship introduced by Manzari and Dafalias (1997) – Equation 2.27, which is incorporated in the constitutive model used in the present study (described in Chapter 4).

$$D = A_0 \left(\eta_{c,e}^{d} - \eta \right) \tag{2.27}$$

where A_0 is a model parameter. This equation states a direct dependence of the dilatancy, *D*, on the difference between the current stress ratio, η, and the stress ratio at the phase transformation state (PTS), $\eta_{c,e}^{d}$ (Section 2.6.5.3). Since this latter parameter depends on the current state of sand, as suggested by Equation 2.26 and clearly corroborated by the experimental data presented in Figure 2.39, it can be concluded that Equation 2.27 introduces *D* as a state-dependent quantity.

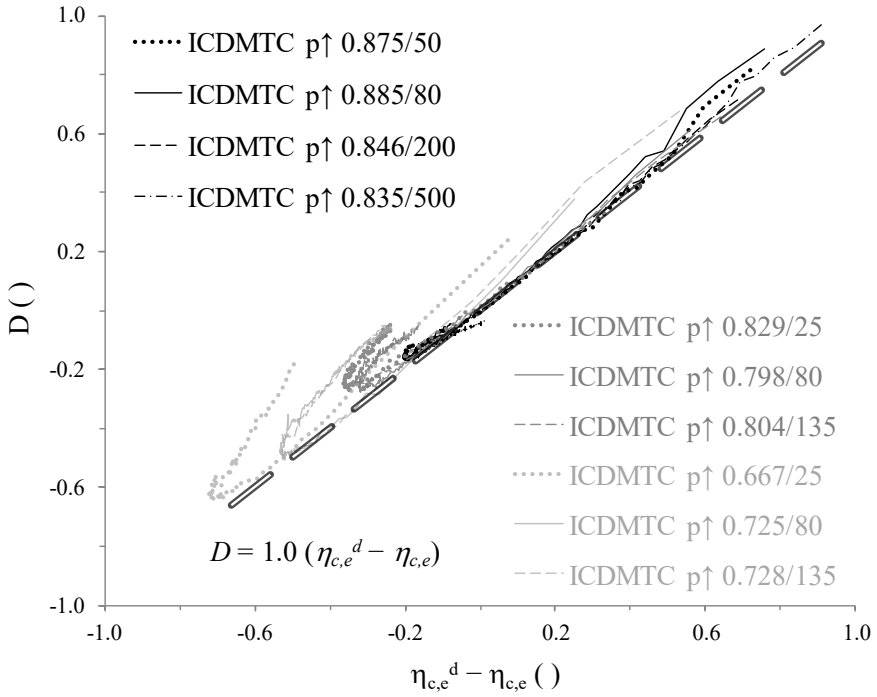

Figure 2.42 – Stress-dilatancy relationship computed from ICDMTCp↑ tests.

Figure 2.42 shows the stress-dilatancy curves obtained from the available ICDMTCp↑ data. It seems that Equation 2.27 can be used to describe adequately the stress-dilatancy response of both loose and dense samples when considering $A_0 = 1.0$, at least until η_c^b (i.e. the inversion point of the curve) is reached.

2.7 Summary and conclusions

An extensive laboratory testing programme was performed on air-pluviated samples of Hostun sand to assess its monotonic response under a wide range of strains. In particular, a series of bender element tests were performed on moderately loose and dense samples subjected to drained isotropic compression to estimate the shear modulus of Hostun sand at very small strains. Two different methods of interpretation, one in the time domain (TD) and the other in the frequency domain (FD), were described in detail and employed to estimate the arrival time of the shear wave. The obtained results seem to indicate that, when sand is subjected to this type of loading, the previous stress history has little influence on the estimated arrival time, with similar results being obtained for first loading, unloading and reloading, for a given stress level. This suggests that the shear modulus of sand can be primarily related to the void ratio and mean effective stress. The results computed by both methods were subsequently compared. It was concluded that, in general, larger values for the arrival time were estimated from the FD method than those computed from the TD method, as typically reported in the literature (e.g. Viggiani and Atkinson, 1995; Greening and Nash, 2004; Alvarado and Coop, 2012). In some cases, however, the results obtained by the FD method seem excessively large, with the computed arrival times being located within the middle part of the received sine-type signal, after the crossing of the zero voltage line. Due to this, the results computed by the TD method were preferred to those estimated from the FD method and used to calibrate a well-known expression proposed in the literature, where the shear modulus at very small strains is related to the current values of the void ratio and mean effective stress.

Within the medium to large strain range, a series of drained and undrained monotonic triaxial compression (TC) and triaxial extension (TE) tests were conducted on samples prepared to different initial void ratios, consolidated under various isotropic and anisotropic stress states and sheared under the four different stress paths commonly applied in a stress-path cell. The obtained results were firstly presented and the impacts of the initial density, effective stress state at consolidation and stress path on the measured response were assessed. Starting with tests conducted under drained conditions, it was concluded that, as expected, initially denser samples tend to mobilise larger peak deviatoric stresses during the earlier stages of loading. At later stages of loading, however, the mobilised deviatoric stress tends to be solely influenced by the mean effective stress at consolidation and, therefore, independent of the initial density, as postulated by the critical state soil mechanics (CSSM) framework. Indeed, in a good agreement with this framework, similar stress ratios were measured at large strains irrespective of the initial density of the sample and effective stresses at consolidation. Furthermore, it was noted that initially denser samples consolidated under lower effective stresses tend to contract less during the earlier stages of loading, as well as to start dilating at lower strain levels, as also expected. During the later stages of loading, it appears that the effect of the initial density on the volumetric response of sand is significantly more important

than the effect of the effective stresses at consolidation, with initially denser samples tending to exhibit higher rates of dilation.

With respect to the influence of the stress path, and still in terms of drained conditions, it was concluded that, as expected, samples subjected to stress paths with decreasing mean stress (MTCp↓ or MTEp↓) tend to exhibit considerably lower strength than those tested under increasing mean stress (MTCp↑ or MTEp↑). Interestingly, in terms of stress ratio mobilised at large strains, small differences were observed between values obtained in MTCp↓ and MTCp↑ tests, as well as between MTEp↑ and MTEp↓ tests. In effect, the most significant differences in terms of stress ratio were observed when comparing results of TC (either MTCp↑ or MTEp↑) with TE (either MTEp↑ or MTEp↓), with samples subjected to TC tending to mobilise larger stress ratios than those subjected to TE, as reported in the literature for other sands (e.g. Vaid *et al.*, 1990; Lade, 2006; Loukidis and Salgado, 2009). Regarding the volumetric response, it was apparent that samples subjected to stress paths with increasing mean stress tend to contract more during the earlier stages of loading and start dilating at greater axial strains than those submitted to stress paths with decreasing mean stress.

In terms of undrained response, the experimental results suggest that, as expected, denser samples and/or samples consolidated under lower effective stresses tend to generate lesser positive excess pore water pressures during the earlier stages of loading and, therefore, to exhibit lesser compliant effective stress paths than those exhibited by looser samples and/or samples consolidated under higher effective stresses. In addition, denser sample tend to exhibit stiffer stress-strain responses, as well as to mobilise higher peak stress ratios during shearing than those mobilised by looser samples, as also observed under drained conditions. Regarding the effect of the effective stress at consolidation on the stress-strain response, it was observed that samples subjected to higher confining stresses exhibit stiffer stress-strain responses during the earlier stages of loading. This effect seemed, however, to vanish during the later stages of loading.

Further insight into the response of Hostun sand was obtained by using a state parameter approach in conjunction with the critical state framework to assess the distinctive states of its monotonic response, with particular focus being placed on the critical state (CS), the peak stress ratio state (PSRS), the phase transformation state (PTS), as well as on the undrained instability state (UIS) and quasi-steady state (QQS). In particular, results of DMTCp↑ and UMTCp↑ on loose samples were used for the prediction of the critical state line (CSL). Additional test data found in the literature was used to corroborate the proposed CSL, which appears to be independent of the sample preparation method and drainage conditions. Moreover, as suggested by some authors (e.g. Verdugo and Ishihara, 1996; Li and Wang, 1998), a curved shape for the CSL in the e – ln p' space seems to describe more accurately the experimental data than a linear shape.

In addition, it was concluded that, irrespective of the initial void ratio of the samples, effective stresses at consolidation, drainage conditions and stress-path direction, the PSRS and the PTS of Hostun sand, identified from the experimental results, appear to be very well described by simple linear state-dependent relationships. Interestingly, despite the complexity associated with the estimation of the PTS under drained conditions, involving a significant number of assumptions to estimate the dilatancy, the results of the PTS under drained conditions are remarkably similar to those obtained under undrained conditions, particularly in TC. In relation to the UIS, it was highlighted that this state was only observed to occur in three of the thirteen undrained monotonic triaxial compression (UMTC) tests performed and, therefore, further investigation on this aspect may be require in the future. Nevertheless, having correlated the mean effective stress at UIS, p'_{UI}, with the mean effective stress immediately after consolidation, p'_0, for the available UMTC test data, and compare it with other UMTC test results obtained for moist-tamped Hostun sand published in the literature, it was concluded that the occurrence of this state may depend on the method of sample preparation, as observed for other sands in other studies published in the literature (Murthy *et al.*, 2007). In relation to the QSS, it was observed that its occurrence in the $q - p'$ space is practically coincident with that of the PTS, with only slightly differences being observed in terms of strains at which these two states occur.

Lastly, it was found that the dilatancy deduced from drained triaxial compression (DMTC) tests conducted on both loose and dense samples can be adequately related to the difference between the current stress ratio and that at the PTS, as proposed in the literature (Manzari and Dafalias, 1997). This is a particularly important conclusion, since the equation used to describe the stress-dilatancy response is incorporated in the constitutive model used in the present study (Chapter 4).

In conclusion, the results obtained in this first stage of the research work seem to highlight the importance of characterising the response of sand over the full strain range. In particular, it appears that accurate predictions of the small-strain stiffness and of the critical state are crucial to assess other aspects of the response of sand. Moreover, it is noteworthy that the extensive experimental programme presented here provides not only a solid framework for interpreting the response of sand under general loading conditions (as observed, for instance, in centrifuge experiments presented in Chapter 8), but also reliable data for the calibration of the constitutive model used in the present research (Chapter 6) and for the assessment of its performance (Chapter 7).

Chapter 3 LABORATORY CHARACTERISATION OF THE CYCLIC RESPONSE OF HOSTUN SAND

3.1 Introduction

An extensive laboratory testing programme using a stress-path cell was carried out to characterise the cyclic response of air-pluviated Hostun sand. Samples were prepared to different initial void ratios, consolidated under various isotropic effective stress states and subjected to several different deviatoric stress oscillations, to evaluate the impact of these aspects on the measured response. Particular relevance was given to the characterisation of main aspects of the cyclic response of Hostun sand under undrained conditions, in particular of its resistance to cyclic mobility. In addition, drained test data were used to inspect aspects of the evolution of volumetric strain with cyclic loading.

As mentioned before, the element laboratory tests carried out as part of this thesis intended to: (1) assist the interpretation of centrifuge experiments performed on loose and dense deposits of air-pluviated Hostun sand; (2) provide data for the calibration of advanced constitutive models, capable of simulating liquefaction-related phenomena; (3) provide data for the characterisation of the ability of those constitutive models to reproduce the main features of the cyclic response of sand.

In the first part of this chapter, a literature review on previous element laboratory testing programmes designed to study cyclic mobility of sand is provided. Subsequently, the main characteristics of the material and equipment used in the present experimental programme are briefly described, as well as the procedures employed to prepare and perform the laboratory tests. Particular emphasis is given to the description of the additional procedures required to carry out cyclic triaxial tests in relation to those employed in the monotonic triaxial compression and extension tests. The main characteristics of the performed tests are summarised in the following section.

The undrained cyclic response of Hostun sand is comprehensively characterised in Section 3.5. Specifically, the experimental results are firstly presented in Section 3.5.1, given particular attention to the characterisation of the main patterns of the undrained cyclic response of sand, as well as to the evaluation of the influence of the void ratio, isotropic confining stress and magnitude of cyclic loading on the measured response. The experimental data is subsequently used to evaluate important aspects of the undrained cyclic response of sand, namely the evolution of the secant shear modulus and damping ratio with strain amplitude (Section 3.5.3), the resistance to cyclic mobility (Section 3.5.2), and the excess pore water pressure generation with cyclic loading (Section 3.5.4).

The drained cyclic response of Hostun sand is discussed in Section 3.6. In particular, the results of three drained cyclic triaxial tests are presented and the main trends of the response of Hostun sand are analysed. Finally, Section 3.7 summarises the main experimental results and present some conclusions regarding the cyclic response of Hostun sand.

Note that, while in this chapter the results of the cyclic triaxial tests are, in general, presented together to provide an overall assessment of the cyclic response of Hostun sand, the results obtained in each cyclic triaxial test are individually presented in Appendix B.

3.2 Use of triaxial testing to investigate cyclic mobility

One of the first triaxial testing programmes designed to study the mechanisms and factors influencing the onset of cyclic mobility was carried out by Seed and Lee (1966). As discussed by the authors, although a pure shear stress oscillation cannot be imposed in a horizontal plane of a sample during an undrained cyclic triaxial test, as typically idealised for a level ground deposit subjected to earthquake-induced loading (Figure 3.1), this condition seems to be applied in a 45° plane of the sample, providing that isotropic consolidation is used. This aspect is illustrated in Figure 3.2, where it can be observed that the shear stresses acting on a 45° plane of the sample are equal to half of the deviatoric stress oscillation applied to the sample (i.e. Δq / 2). Moreover, since loading is applied under undrained conditions, the authors argued that the effective stress changes occurring during cyclic loading are mainly the result of the excess pore water pressure build-up, as typically observed in centrifuge experiments. Based on these arguments, Seed and Lee (1966) concluded that undrained cyclic triaxial tests could be employed to study cyclic mobility.

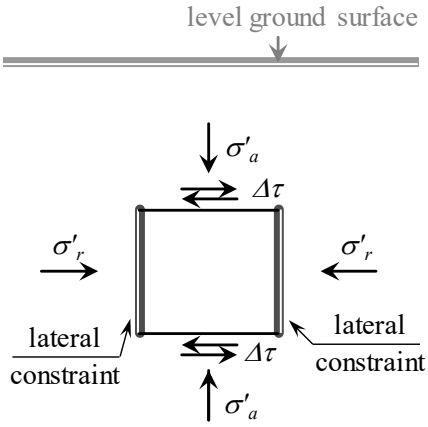

Figure 3.1 – Idealised stress conditions in a level ground deposit subjected to earthquake loading (adapted from Ishihara, 1996).

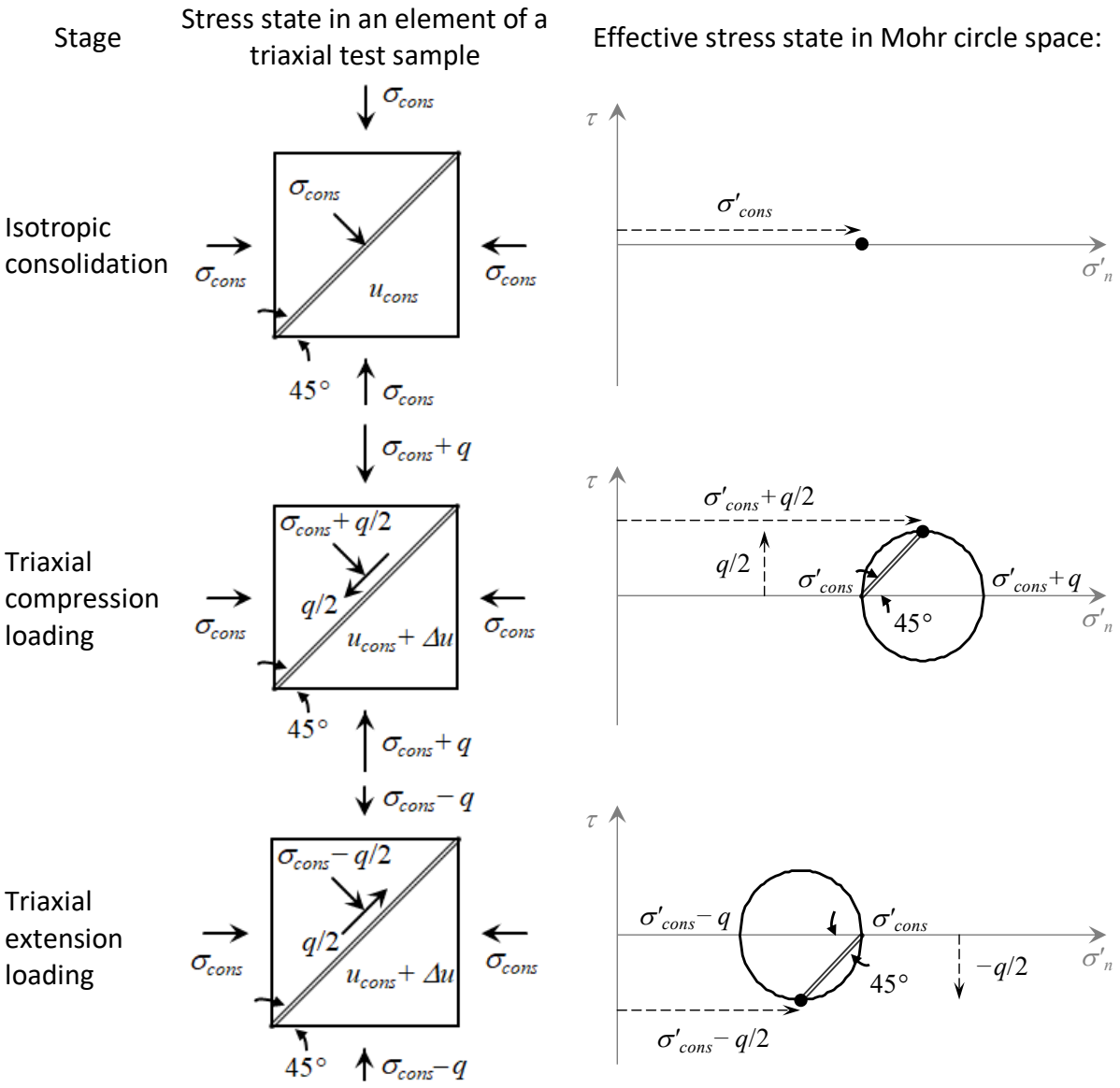

Figure 3.2 – Stress conditions imposed in a 45° plane in an isotropically consolidated undrained cyclic triaxial test (adapted from Ishihara, 1996).

Although it was not mentioned by Seed and Lee (1966), it is important to note that the use of isotropic consolidation, rather than anisotropic consolidation (which typically characterises more accurately the field conditions), is not very problematic when studying liquefaction-related phenomena. In fact, results of dynamic centrifuge experiments on level ground deposits of sand suggest that the total horizontal stresses within the sand deposit tend to increase concurrently with the application of dynamic loading, with total isotropic stress conditions being typically observed as liquefaction approaches (e.g. Ishihara and Li, 1972; Ishihara, 1996; Coelho, 2007). As discussed by this latter author, what seems more questionable is the use of non-confined lateral boundaries in cyclic triaxial tests, which do not seem to represent accurately the conditions in the field (Figure 3.1). Furthermore, it has been also observed in dynamic centrifuge experiments that volumetric deformations occur during dynamic excitation of the level ground deposit and, therefore, fully undrained conditions do

not seem to represent accurately the conditions observed in this type of problems. According to Coelho (2007), partially drained conditions seem more appropriate to characterise the response of level ground deposits of sand under dynamic loading, at least when there is no sand-structure interaction. Indeed, although attempts have been made to simulate partially drained conditions in triaxial testing, the available techniques do not seem to provide satisfactory results (Yamamoto *et al.*, 2010) and, therefore, fully-undrained conditions are typically employed to study cyclic mobility of sand.

The outcome of the pioneer work of Seed and Lee (1966) suggested that the number of loading cycles required to the onset of cyclic mobility was mainly affected by the relative density of the sample, the confining pressure and the magnitude of the deviatoric stress oscillation. More specifically, the authors concluded that fewer loading cycles to the onset of cyclic mobility were required as samples were initially looser, consolidated under higher effective stresses and subjected to larger deviatoric stress oscillations.

Further research on the fundamental aspects of cyclic mobility by means of triaxial testing was undertaken in the following years by several authors (e.g. Castro, 1969; Finn *et al.*, 1971). Concurrently, simple shear testing programmes designed to study this phenomenon were also undertaken (e.g. Peacock and Seed, 1968; Finn *et al.*, 1971), also contributing to the understanding of the phenomenon. In an attempt to summarise the findings derived from these laboratory testing programmes, as well as from observations provided by case histories, and to make these findings useful for design practice, Seed and Idriss (1970a) and Seed and Idriss (1971) proposed a simplified (i.e. semi-empirical) procedure to evaluate the earthquake-induced liquefaction potential of a site. In this approach, the earthquake-induced loading, characterised by an equivalent uniform cyclic stress ratio (CSR), is compared against the liquefaction resistance of sand, defined by the uniform cyclic stress ratio required to cause liquefaction in a given number of loading cycles (termed as “cyclic resistance ratio” (CRR) by the authors). According to the initial proposal (Seed and Idriss, 1970a), this latter quantity can be inferred from results of cyclic triaxial tests or simple shear tests performed using uniform loading conditions.

For clarity, in the present study, the designation “cyclic stress ratio” (CSR) is used to define the applied uniform cyclic solicitation, which, under triaxial loading conditions, can be determined as (e.g. Ishihara, 1996):

$$CSR = \frac{|\Delta q|}{2\,p'_0} \tag{3.1}$$

where $|\Delta q|$ is the applied deviatoric stress oscillation, while p'_0 is the mean effective stress before the start of shearing (i.e. immediately after consolidation). Conversely, the designation “cyclic resistance ratio” (CRR) is used to characterise the cyclic stress ratio inducing cyclic mobility in a given number of loading cycles, N_{liq}. The curves obtained when plotting *CRR* against N_{liq} are designated as undrained cyclic resistance curves.

A critical step in stress-based approaches to evaluate liquefaction potential consists of the estimation of a uniform shear stress time-history (characterised by a uniform shear stress oscillation and a given number of loading cycles) causing an effect in sand similar to that resulting from the irregular time-history pattern of the earthquake-induced shear stresses. Based on laboratory test data on Monterey sand, a weighting procedure defining the equivalent effects of different shear stress levels was developed by Seed *et al.* (1975a). Alternatively, the authors proposed to estimate the equivalent number of uniform stress cycles based on the earthquake magnitude. Although the proposed methodology had been developed based on a limited number of observations and involved a considerable number of simplifications that may not represent reality accurately (e.g. Ishihara and Yasuda, 1972, 1975; Azeiteiro *et al.*, 2017b), it represented a great effort to summarise the main aspects influencing the occurrence of cyclic mobility. Specifically, it stated the liquefaction potential of a deposit as a function of the physical characteristics of sand, the state of sand (typically characterised by the relative density and effective stresses) and the intensity and duration of the earthquake motion. This procedure has been refined over the past decades to incorporate later experimental findings and to enable the use of field test data to predict liquefaction resistance (e.g. Youd *et al.*, 2001; Idriss and Boulanger, 2004, 2006; Boulanger and Idriss, 2014).

Recognising that the liquefaction resistance of sand is also affected by other factors not included in the original Seed and Idriss (1970) and Seed and Idriss (1971)'s procedure (such as the method of sample preparation, prestraining, overconsolidation and time effects), and assuming that those factors are likely to have similar influences on both cyclic strength and stiffness and, consequently, only slight influence on cyclic strain, Dobry *et al.* (1982) proposed a cyclic strain approach as an alternative to the cyclic stress approach. Along the same lines of the earlier proposed methodology, the earthquake-induced loading, characterised, in this case, by an equivalent uniform cyclic shear strain loading, is compared with the liquefaction resistance of sand, evaluated by the cyclic shear strain required to cause liquefaction in a given number of loading cycles. According to the authors, the great advantage of the strain-based approach over the stress-based approach consists of circumventing the need for characterising the influence of some of the abovementioned factors, which require detailed knowledge of the geological and seismic history of the site (e.g. sand's fabric and prestraining) by characterising adequately the shear modulus of sand. Specifically, the authors pointed out that the shear modulus of sand at small strains, G_{max}, which can be directly measured in the field through shear-wave velocity measurements (e.g. crosshole tests) and is included in the estimation of the earthquake-induced shear strain, would already incorporated many aspects that influence excess pore water pressure build-up with cyclic loading (e.g. density of the deposit of sand, mean effective stress at a given depth, sand's fabric and prestraining, among other factors). Moreover, the authors suggested that, by performing cyclic triaxial tests with constant cyclic strain amplitude (i.e. where shear reversals are controlled by a strain

condition), rather than cyclic triaxial tests with constant cyclic stress amplitude (i.e. where load reversals are controlled by a stress condition), it would be possible to evaluate the ratio of excess pore water pressure build-up as a function of the cyclic shear strain applied in the test irrespective of the method of sample preparation and isotropic effective stress at consolidation, as observed in the laboratory. This approach, however, also implies the decomposition of the irregular shear strain time-history of a given earthquake in order to find an equivalent uniform loading.

Based on the assumption made by Nemat-Nasser and Shokooh (1979) that pore water pressure generation can be uniquely related to the cumulative energy dissipated per unit volume of soil up to the onset of liquefaction, energy-based procedures for the evaluation of liquefaction potential of sand have been developed (e.g. Davis and Berrill, 1982; Berrill and Davis, 1985; Law *et al.*, 1990; Figueroa *et al.*, 1994; Kokusho, 2013). According to Liang *et al.* (1995), when compared to alternative stress- and strain-based approaches, energy-based methods have the strong advantage of accounting for both induced shear stress and strain, thus avoiding the need to decompose the irregular shear stress (or strain) time histories to find an equivalent uniform loading. The first laboratory testing programme particularly designed to assess the suitability of the energy concept to the evaluation of liquefaction potential was undertaken by Simcock *et al.* (1983). By performing a series of undrained cyclic triaxial tests, the authors observed that energy dissipation continuously increased as excess pore water pressure were generated. Further evidence on the satisfactory relationship between these quantities was presented by Towhata and Ishihara (1985). Based on results of torsional shear tests using different loading patterns, the authors concluded that the relationship between the excess pore water pressure build-up and dissipated energy per unit volume is unique throughout the entire test, being independent of the stress path followed in each test. A similar conclusion was drawn by Baziar and Sharafi (2011) and Kokusho (2013) when analysing results of undrained hollow cylinder cyclic torsional tests and undrained cyclic triaxial tests, respectively. The laboratory testing programme performed by Figueroa and his co-workers (Figueroa *et al.*, 1994; Liang *et al.*, 1995; Dief and Figueroa, 2007) is also noteworthy. These authors concluded that the energy required to the onset of liquefaction – known as capacity energy – was practically independent of the loading pattern used (uniform and non-uniform) and type of test performed (torsional cyclic shearing and centrifuge experiments). These results seemed to be confirmed by a study undertaken by Polito *et al.* (2013), where cyclic triaxial tests using three different uniform loading shapes (sinusoidal, triangular and rectangular), as well as two irregular patterns where performed. More recently, Azeiteiro *et al.* (2017b) extended the experimental findings by comparing the results of undrained cyclic triaxial tests including a large-amplitude singular peak loading cycle – a type of loading characteristic of shock-type earthquakes (Ishihara and Yasuda, 1975) – with those obtained using uniform loading conditions. Although sand samples were subjected to loading patterns that would have been deemed equivalent by conventional stress-based

methods, the authors observed that the number of cycles required to trigger liquefaction strongly depended on the amplitude and location of the peak cycle within the loading history. Conversely, the obtained experimental results suggested that, irrespective of the loading conditions, a unique relationship existed between the accumulation of dissipated energy per unit volume, computed using stress and strain measurements, and the observed residual pore water pressure build-up for all tests, throughout the entire cyclic loading application. Therefore, the authors concluded that conventional laboratory tests using uniform loading conditions can be employed to the evaluation of liquefaction resistance, providing that energy principles are used to interpret the laboratory test results.

It is perhaps important to clarify that the use of these semi-empirical methodologies is beyond the scope of the present study. The main intention of the cyclic triaxial testing programme on Hostun sand is to characterise important aspects affecting its cyclic response, such as the initial relative density of the specimens and the effective stresses at consolidation, and to provide reliable data for the calibration of a bounding surface plasticity model to be used in the numerical modelling of liquefaction-related phenomena observed in centrifuge experiments.

It is also important to note that, although cyclic simple shear tests may represent more accurately the field conditions observed in level ground deposits subjected to earthquake loading causing cyclic mobility, concerns about non-uniformity of strain distribution – with several authors attempting to minimise the influence of the rigid boundary conditions on the obtained results by developing new plane-strain apparatus (e.g. Desrues *et al.*, 1985; Tatsuoka *et al.*, 1986b; Alshibli *et al.*, 2004) – and the impossibility of measuring the lateral stresses developed during the test have made triaxial testing a preferable tool for the experimental characterisation of the cyclic response of sand. Moreover, although the advantages of cyclic torsional shearing on hollow cylinder samples are becoming widely recognised (Nakata *et al.*, 1998; Yoshimine *et al.*, 1998; O'Kelly and Naughton, 2009; Araújo Santos, 2015), enabling to assess important aspects of the response of sand which cannot be investigated in triaxial testing, such as the independent influence of the value of the intermediate principal effective stress and the direction of the principal effective stress directions on the soil response, triaxial testing still remains the reference type of test used to obtain data for the calibration of advanced constitutive models, namely when supplemented with bender element and/or resonant column testing (e.g. Papadimitriou and Bouckovalas, 2002; Loukidis and Salgado, 2009). The main reasons for this comprise the low cost of triaxial tests in relation to hollow cylinder torsional shear tests, widespread availability of this equipment in geotechnical laboratories, simpler procedures to prepare samples and to control the equipment and monitoring system, as well as due to the very large past experience.

Two additional aspects are noteworthy. First, there seems to exist a lack of consensus in the literature about the most appropriate criterion used to define the onset of cyclic mobility. The moment at which the ratio of the excess pore water pressure to the initial effective vertical stress reaches 1.0 was initially proposed by Seed and Lee (1966). However, as pointed out by Ishihara (1996), in some cases (e.g. in dense sand), the excess pore water pressure is observed to stop building-up for values close, yet not equal, to the initial effective confining stress, which invalidates the use of the criterion introduced by Seed and Lee (1966). Therefore, the authors refer to the development of 5 % double amplitude axial strain as the most appropriate criterion to define the onset of liquefaction. Still according to Ishihara (1996), more important than the specific criterion selected in a given experimental study is to clearly state it, to enable the appropriate comparison with other experimental studies. Secondly, although modern apparatus enable the use of high-frequency loading, as those typically observed in the field during an earthquake event, the possible development of highly non-uniform pore water pressures in the sample under such fast loading conditions and the ability to measure these at the sample boundaries raises concerns over its use (Coelho, 2007). Therefore, lower loading frequencies have been commonly used in triaxial testing, with the effect of the changing of frequency on the obtained results being generally negligible (Tatsuoka *et al.*, 1986a).

3.3 Laboratory test apparatus and experimental procedures

3.3.1 Material and equipment used

All tests included in this laboratory testing programme were performed on Hostun sand, whose main physical characteristics were previously described in Section 2.2.1. Indeed, the distinctive aspects of its monotonic response were comprehensively characterised in the previous chapter.

Similar to the monotonic triaxial compression tests with increasing mean stress, as well as to the triaxial extension tests with increasing or decreasing mean stress, cyclic triaxial tests were performed using a fully computer-controlled hydraulic triaxial apparatus of the Bishop and Wesley (1975) type, designed for 38 mm diameter specimens. The main characteristics of the equipment were described in Section 2.3.1.1. It is perhaps important to highlight that, by using either a constant rate of strain pump (CRSP) or a bladder-type air-water interchange cylinder connected to an air pressure regulator, it was possible to induce, respectively, strain-controlled or stress-controlled loading. The former type of control was particularly important during the later stages of the undrained cyclic triaxial tests, where samples typically exhibited a highly non-linear hysteretic response, which would be difficult to register with adequate definition when imposing stress-controlled loading (particularly at very low stresses, where the slope of the stress-strain response is typically very flat). This does not mean, however, that load reversals were controlled by a strain condition. In fact, load reversals were, in general, dictated by a stress condition, as detailed later. In addition, it is also important to

note that, in order to apply extension loading conditions, a flexible sleeve was used to connect the top cap to an adjustable reaction head.

Standard instrumentation was also used in this series of tests, comprising pore-water pressure transducers, a submersible load cell, an externally mounted linear variable displacement transducer (LVDT) and a volume gauge. The software TRIAX, developed at the University of Durham (Toll, 1993), was used to record and monitor all devices, as well as control the different stages of the tests. This software enables a full-automatic control of the test, with different stages being triggered by control equations that are continuously updated through data acquisition (e.g. axial strain is continuously updated based on displacement measured by the LVDT mounted on the stress path cell).

3.3.2 Experimental procedures

Air-pluviation of dry sand was used once more to prepare samples with a height/diameter ratio close to 2. As pointed out in Section 2.3.1.2, besides the advantages generally recognised for this technique, such as producing samples with relatively uniform void ratio distribution in depth and having a good repeatability, its selection was also dictated by the fact that this same technique was employed in centrifuge tests used as benchmark in the present work (Chapter 8). Moreover, as also described in detail in Section 2.3.1.2, different relative densities were attained by varying the rate and height of pouring. Specifically, for moderately loose samples, a miniature container was used, with the rate of pouring depending on the number and size of the openings. The height of pouring, which also affects the obtained relative density, was kept approximately constant during sample preparation by raising the container while pouring the sand, ensuring the uniformity of the specimens in height. In relation to dense samples, the multiple sieving pluviation technique described by Miura and Toki (1982) was used. Mass and volume measurements after sample's preparation were undertaken to determine the density of the produced samples.

After preparation, samples were saturated by flowing de-aired water through the sample, always at very small effective stresses, until a Skempton's B-value above 0.98 was measured in all tests. Subsequently, samples were isotropically consolidated to effective stresses of 25, 80 or 135 kPa, before drained or undrained cyclic loading was applied. The choice of these three different effective stress levels was related to the initial effective stress state of the centrifuge models, where Hostun sand was employed as model material. More specifically, these effective stresses intended to replicate the mean effective stresses of shallow, middle and deep levels of the deposits of Hostun sand subjected to centrifuge tests, as discussed in detail in Chapter 8.

In the case of undrained shearing, two different loading stages were defined. In the earlier stage of the test, a stress-controlled loading was imposed by varying the deviatoric stress between desired minimum and maximum values at a constant rate. More specifically, the deviatoric stress variation with time was determined in forehand to result in a loading

frequency of 1.5 cycles/h. For instance, in order to impose a deviatoric stress oscillation of ±40 kPa, a deviatoric stress rate of $1.5 \times 4 \times 40 = 240$ kPa/h was specified. Note that data registered by the different instruments were continuously acquired by a data logger and transferred to the computer, enabling a control of the test based on updated values of stress and strain quantities. In addition, it should be noted that, in order to estimate the axial stress from the measured axial force, the software employed a cross-sectional area correction identical to that previously defined by Equation 2.3 (in which the sample is assumed to deform as a right-circular cylinder throughout loading). As the axial strain reached 0.3 %, the control of the test was switched from stress- to strain-control. As mentioned before, this alteration intended to enable a well-defined depiction of the response of sand at relatively large strains, typically characterised by a highly nonlinear hysteretic stress-strain response as sample approached liquefaction. The value of 0.3 % was established based on the results of earlier experimental studies on the response of sand performed by Coelho (2007), as well as by the author (e.g. Azeiteiro *et al.*, 2017b). Note, nevertheless, that, in these tests, load reversals were always controlled by a stress condition (namely, loading was reversed as the maximum deviatoric stress amplitude was reached either in triaxial compression or in triaxial extension). The tests were stopped when large values of double axial strain amplitude, $\varepsilon_{a,da}$ (i.e. the sum of the axial strain amplitude in triaxial compression and in triaxial extension), were measured, typically 5 % for moderately loose samples and 2 % for dense sands.

With respect to the drained cyclic triaxial testing, all performed tests were conducted on moderately loose samples. Moreover, although these tests were stress-controlled, the criterion used for triggering load reversals differ from one of the tests to the remaining ones. Specifically, while, in one of these tests, the load reversals were triggered when reaching a given axial strain amplitude, in the remaining tests the load reversals were dictated by a given deviatoric stress amplitude, as detailed later. These tests were stopped when a given number of loading cycles were completed.

Note that both undrained and drained cyclic tests were performed by applying conventional cyclic triaxial loading with increasing mean stress in triaxial compression and decreasing mean stress in triaxial extension (Figure 2.6). A study on the effect of other types of cyclic triaxial loading on the response of sand was reported by Coelho *et al.* (2013).

3.4 Testing programme

Overall, thirteen isotropically consolidated undrained cyclic triaxial (ICUCT) tests were performed on moderately loose ($e_0 = 0.77 - 0.83$, corresponding to $D_{r,0} \approx 50 - 67\%$) and dense ($e_0 \approx 0.65$, corresponding to $D_{r,0} \approx 102$ %) samples of Hostun sand consolidated under effective stresses of 25, 80 and 135 kPa.

Table 3.1 – Main characteristics of the undrained cyclic triaxial tests performed.

Test ID [a]	Sample's preparation [b]			Sample's state and stress conditions after consolidation								Applied cyclic loading		
	D_{init} (mm)	H_{init} (mm)	M_{init} (g)	ΔV_{cons} (cm^3)	e_0 ( )	$D_{r,0}$ (%)	$\sigma_{cell,0}$ (kPa)	u_0 (kPa)	q_0 (kPa)	p'_0 (kPa)	ψ_0 ( )	$\lvert\Delta q\rvert$ (kPa)	CSR ( )	N_{liq} [c] ( )
ICUCT 0.821/25/13	36.6	76.4	116.5	0.09	0.821	52.5	550.0	525.0	0.0	25.0	-0.136	13.0	0.260	27.0
ICUCT 0.777/25/18	36.6	77.3	120.8	0.09	0.777	65.5	550.0	525.0	0.0	25.0	-0.181	18.0	0.360	8.0
ICUCT 0.771/80/32	36.9	76.2	120.6	0.49	0.771	67.3	650.0	570.0	0.0	80.0	-0.165	32.0	0.200	57.0
ICUCT 0.803/80/36	36.6	73.8	113.1	0.50	0.803	58.0	650.0	570.0	0.0	80.0	-0.133	36.0	0.225	43.0
ICUCT 0.832/80/42	36.6	77.0	116.0	0.61	0.832	49.5	550.0	470.0	0.0	80.0	-0.104	42.0	0.263	8.0
ICUCT 0.804/80/48	36.6	76.4	117.1	0.46	0.804	57.7	650.0	570.0	0.0	80.0	-0.132	48.0	0.300	4.0
ICUCT 0.773/80/56	36.6	75.5	117.6	0.52	0.773	66.6	650.0	570.0	0.0	80.0	-0.162	56.0	0.350	2.0
ICUCT 0.805/135/40	36.6	86.5	131.9	0.86	0.805	57.0	650.0	515.0	0.0	135.0	-0.117	40.0	0.148	66.0
ICUCT 0.830/135/54	36.6	75.1	113.1	0.70	0.830	50.0	650.0	515.0	0.0	135.0	-0.092	54.0	0.200	32.0
ICUCT 0.793/135/67.5	36.6	72.5	111.4	0.68	0.793	60.7	650.0	515.0	0.0	135.0	-0.129	67.5	0.250	3.0
ICUCT 0.651/80/43	36.6	75.6	126.6	0.42	0.651	102.4	650.0	570.0	0.0	80.0	-0.285	43.0	0.269	78.0
ICUCT 0.652/80/72	36.6	74.9	125.5	0.39	0.652	102.6	650.0	570.0	0.0	80.0	-0.284	72.0	0.450	21.0
ICUCT 0.652/80/88	36.8	73.5	124.3	0.37	0.652	102.7	650.0	570.0	0.0	80.0	-0.284	88.0	0.550	45.0

[a] The designation identifies: 1) the type of consolidation – IC for isotropic consolidation; 2) the type of drainage –U for undrained conditions; 3) the type of loading – CT for cyclic triaxial; 4) the void ratio immediately after consolidation, e_0; 5) the mean effective stress immediately after consolidation, p'_0; (6) the deviatoric stress oscillation, $\lvert\Delta q\rvert$, applied in the test.

[b] Volume and mass measurements were performed after sample's preparation.

[c] In the present study, cyclic mobility was considered to be initiated as $r_{u,res} = \Delta u_{res}/\sigma'_{v,0} \geq 0.95$, as detailed later.

Table 3.2 – Main characteristics of the drained cyclic triaxial tests performed.

Test ID [a]	Sample's preparation [b]			Sample's state and stress conditions after consolidation								Load reversal		Test stop
	D_{init} (mm)	H_{init} (mm)	M_{init} (g)	ΔV_{cons} (cm^3)	e_0 ( )	$D_{r,0}$ (%)	$\sigma_{cell,0}$ (kPa)	u_0 (kPa)	q_0 (kPa)	p'_0 (kPa)	ψ_0 ( )	$\lvert\Delta\varepsilon_a\rvert$ (%)	$\lvert\Delta q\rvert$ (kPa)	N_{tot} ( )
ICDCT 0.773/80/1	36.8	79.7	125.7	0.52	0.773	64.7	650.0	570.0	0.0	80.0	-0.163	1.0	–	100.0
K0CDCT 0.811/80/30	36.6	75.7	115.7	0.38	0.811	54.1	250.0	190.0	60.0[(*)]	80.0[(*)]	-0.125	–	30.0[(**)]	10.0
ICDCT 0.820/135/81	36.7	72.4	110.2	0.69	0.794	51.4	650.0	515.0	0.0	135.0	-0.102	–	81.0	10.0

[a] The designation identifies: 1) the type of consolidation – IC or K0 for isotropic or anisotropic consolidation, respectively; 2) the type of drainage – D for drained conditions; 3) the type of loading – CT for cyclic triaxial; 4) the void ratio immediately after consolidation; 5) the mean effective stress immediately after consolidation; (6) the axial strain oscillation, $\lvert\Delta\varepsilon_a\rvert$, or deviatoric stress oscillation, $\lvert\Delta q\rvert$, applied in the test (in any case, an identical absolute value was imposed in triaxial compression and in triaxial extension, meaning that two-way symmetric cyclic loading conditions were used).

[b] Volume and mass measurements were performed after sample's preparation.

[(*)] The radial and axial effective stresses at consolidation were $\sigma'_{r,0} = 60.0$ kPa and $\sigma'_{a,0} = 120.0$ kPa, respectively, resulting in a mean effective stress and in a deviatoric stress at consolidation of $p'_0 = 80.0$ kPa and $q_0 = 60.0$ kPa, respectively.

[(**)] In this test, a deviatoric stress oscillation from $q_{min} = q_0 - \Delta q = 60.0 - 30.0 = 30.0$ kPa to $q_{max} = q_0 + \Delta q = 60.0 + 30.0 = 90.0$ kPa, and vice-versa, was applied.

The main characteristics of these tests are summarised in Table 3.1, including: the initial diameter, D_{init}, height, H_{init}, and dry mass, M_{init}, of the sample measured after preparation; the volume change during consolidation, ΔV_{cons}; the void ratio, e_0 and the corresponding relative density, $D_{r,0}$, the cell pressure, $\sigma_{cell,0}$, the back pressure, u_0, the deviatoric stress, q_0, and the mean effective stress, p'_0, before the start of shearing (i.e. immediately after consolidation); the state parameter, $\psi_0 = e_0 - e_{cs}$ (according to the critical state line proposed for Hostun sand in Chapter 2); the deviatoric stress oscillation, $|\Delta q|$, the applied cyclic stress ratio (CSR) – as defined by Equation 3.1 – and the number of loading cycles required to the onset of cyclic mobility, N_{liq}.

Similarly, Table 3.2 summarises the main characteristics of the three drained cyclic triaxial (DCT) tests performed on moderately loose samples, two of them isotropically consolidated (IC) and remaining one anisotropically consolidated (K0C).

Still regarding Table 3.1 and Table 3.2, note that:

- the Bishop and Wesley (1975)'s stress path cell was used to test all samples and, therefore, this information is omitted from both tables;
- with the exceptions of test ICDCT 0.773/80/1, where the load reversal was triggered as an axial strain amplitude of 1 % was reached, and test K0CDCT 0.811/80/30, where the deviatoric stress was varied in between 30 and 90 kPa, in all remaining tests, symmetric deviatoric stress oscillations (i.e. identical deviatoric stress amplitude in triaxial compression and in triaxial extension) were imposed.

3.5 Undrained cyclic response

3.5.1 Overview of obtained results

3.5.1.1 Main patterns of the undrained cyclic response of Hostun sand

Figure 3.3 presents the results of test ICUCT 0.832/80/42, which illustrates the typical undrained cyclic response of Hostun sand observed in the present laboratory testing programme. It can be seen that, as expected, there is an increase in excess pore water pressure, Δu, in each loading cycle, N (Figure 3.3c), which results in a progressive reduction of the mean effective stress, p', with cyclic loading (Figure 3.3a), as well as softening of the (average) deviatoric stress, q, – axial strain, ε_a, response in each loading cycle (Figure 3.3b). As the phase transformation line is crossed and the effective stress path approaches zero (Figure 3.3a), a significant accumulation of axial strains occur (Figure 3.3d), leading to a degraded hysteresis type stress-strain response (Figure 3.3b). This suggests that Hostun sand is effectively susceptible to cyclic mobility.

It is also interesting to observe that, during the first five cycles of loading, excess pore water pressure increases during triaxial compression (TC) loading, with the opposite trend being observed during unloading and, subsequently, during triaxial extension (TE) loading (Figure

3.3c). A tendency for positive excess pore water pressure generation is, once more, observed as stress reversal occurs and unloading and TC loading is applied. Note, however, that, from the 5th loading cycle onwards, a different excess pore water pressure evolution pattern is observed. In effect, during this loading cycle, the effective stress path is observed to reverse during triaxial extension (point P1 in Figure 3.3a), which, as established by Ishihara *et al.* (1975), suggests that the phase transformation (PT) line has been crossed and, therefore, the response of sand changes from plastic contraction to plastic dilation. Once it occurs, excess pore water pressures and axial strains are observed to decrease at a higher rate until the effective stress path is reversed (point P2). Subsequently, as unloading is applied, significant positive excess pore water pressure develops, with the mean effective stress being observed to reduce at a higher rate than in the previous loading cycles (i.e. a more compliant effective stress path is observed in Figure 3.3a). This tendency is, however, reverted once the PT line is crossed in triaxial compression (point P3), with excess pore water pressures being observed to decrease until the temporarily maximum deviatoric stress is reached (point P4). As unloading and, subsequently, TE loading is applied, pore water pressure starts increasing once again, with the mean effective stress strongly reducing, until the PT line is crossed in triaxial extension (point P5). A strong decrease in the excess pore water pressure is observed with further triaxial extension loading until the temporarily minimum deviatoric stress is reached (point P6). This double-frequency phenomenon of the transient excess pore water pressures – as termed by Coelho (2007) – was firstly explained by Ishihara *et al.* (1975) and has been shown to occur also in other element laboratory tests, such as torsional shear tests (Ishihara, 1985, 1996).

It is worth mentioning that some authors (e.g. Nemat-Nasser and Tobita, 1982) suggest that the strong change in sand response after crossing the PT line is due to significant changes in fabric occurring during plastic dilation. Based on that, some constitutive models, including those based on bounding surface plasticity framework (e.g. Papadimitriou and Bouckovalas, 2002; Dafalias and Manzari, 2004; Taborda *et al.*, 2014), incorporate a fabric tensor, which allows for the replication of the change in the response of sand observed once the PT line is crossed and stress path is reversed. This topic is further explored in Chapter 4.

In addition, it should be noted that the fact that PT line was firstly crossed in TE is consistent with the smaller stress ratio amplitudes characterising the location of the PT line in TE than in TC, as observed for monotonic loading conditions and as discussed in Chapter 2.

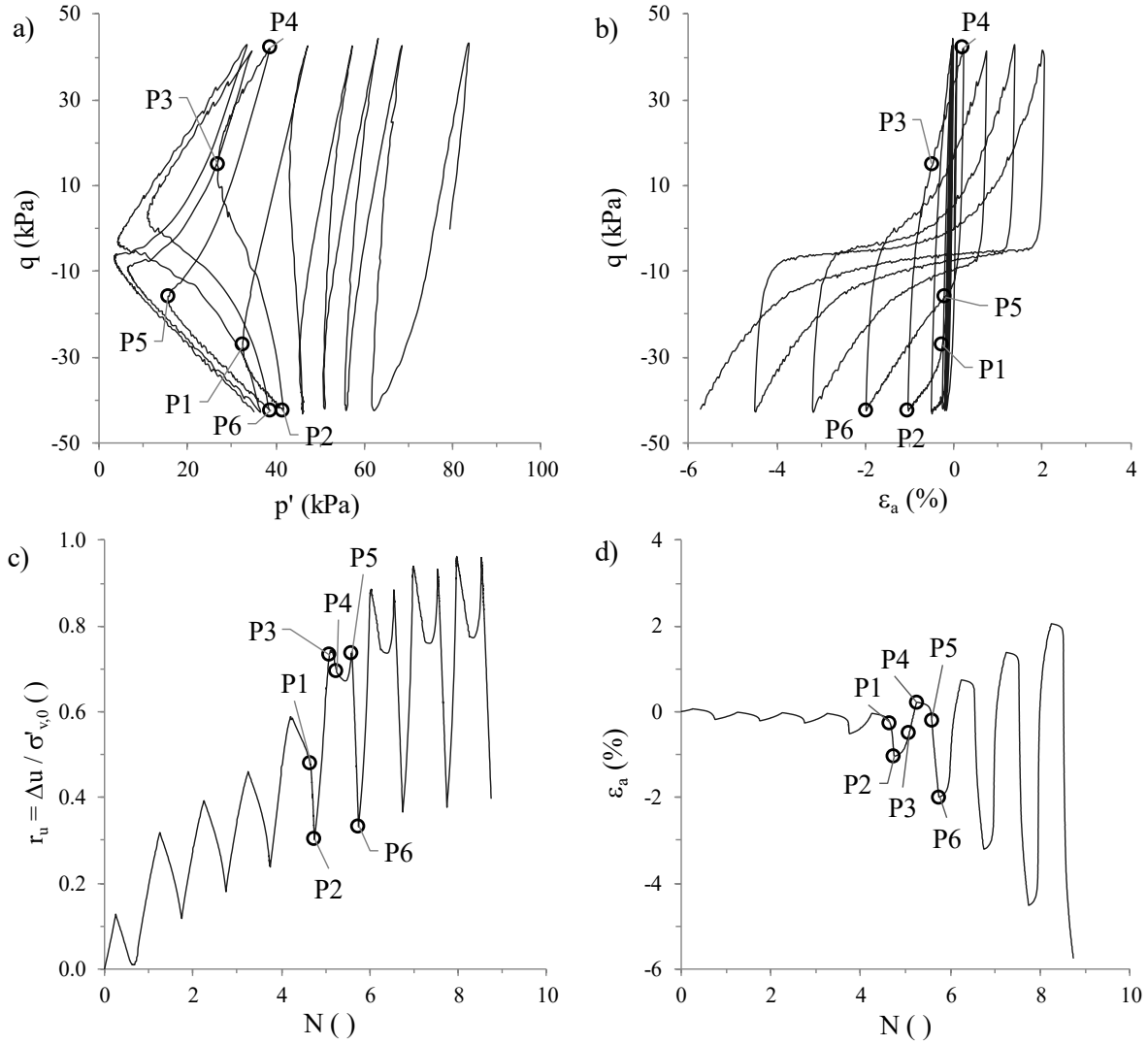

Figure 3.3 – Test ICUCT 0.832/80/42: (a) effective stress path; (b) stress-strain response; (c) excess pore water pressure build-up; and (d) axial strain evolution with the number of loading cycles.

3.5.1.2 Influence of the void ratio

Figure 3.4 compares the results of tests ICUCT 0.832/80/42 and ICUCT 0.651/80/43, which were conducted on moderately loose ($e = 0.832$) and dense ($e = 0.651$) samples. In these tests, samples were consolidated under the same isotropic effective stress ($\sigma'_0 = 80$ kPa) and sheared under similar deviatoric stress oscillations ($|\Delta q| = 42$ kPa and $|\Delta q| = 43$ kPa, respectively), meaning that similar cyclic stress ratios were applied to these samples. It is apparent that the void ratio has a strong influence on the undrained cyclic response of sand. While the looser sample (i.e. subjected to test ICUCT 0.832/80/42) required only about 8 loading cycles to the onset of cyclic mobility, characterised by temporarily very low effective stresses and accumulation of large axial strains, a much larger number of loading cycles (of about 78) were required to initiate cyclic mobility in test ICUCT 0.651/80/43, conducted on the denser sample (note that the number of loading, *N*, axis is presented in logarithmic scale, to aid the visualisation of both looser and denser samples responses in the same plot). In effect, it can be seen that the excess pore water pressure generated in each loading cycle is

significantly smaller in the latter test, when compared with that developed in the former test, therefore, resulting in smaller rates of average effective stress reduction and axial strain accumulation in each loading cycle. Nevertheless, it is perhaps important to highlight that, as observed in centrifuge experiments (e.g. Coelho, 2007), as well as in the field (e.g. Youd *et al.*, 2001, 2004), both loose and dense sand samples may be subjected to cyclic mobility, although its effects (particularly in terms of axial strain accumulation) appear to have a clearly different magnitude in moderately loose and dense sand. This topic is further explored in Chapter 8.

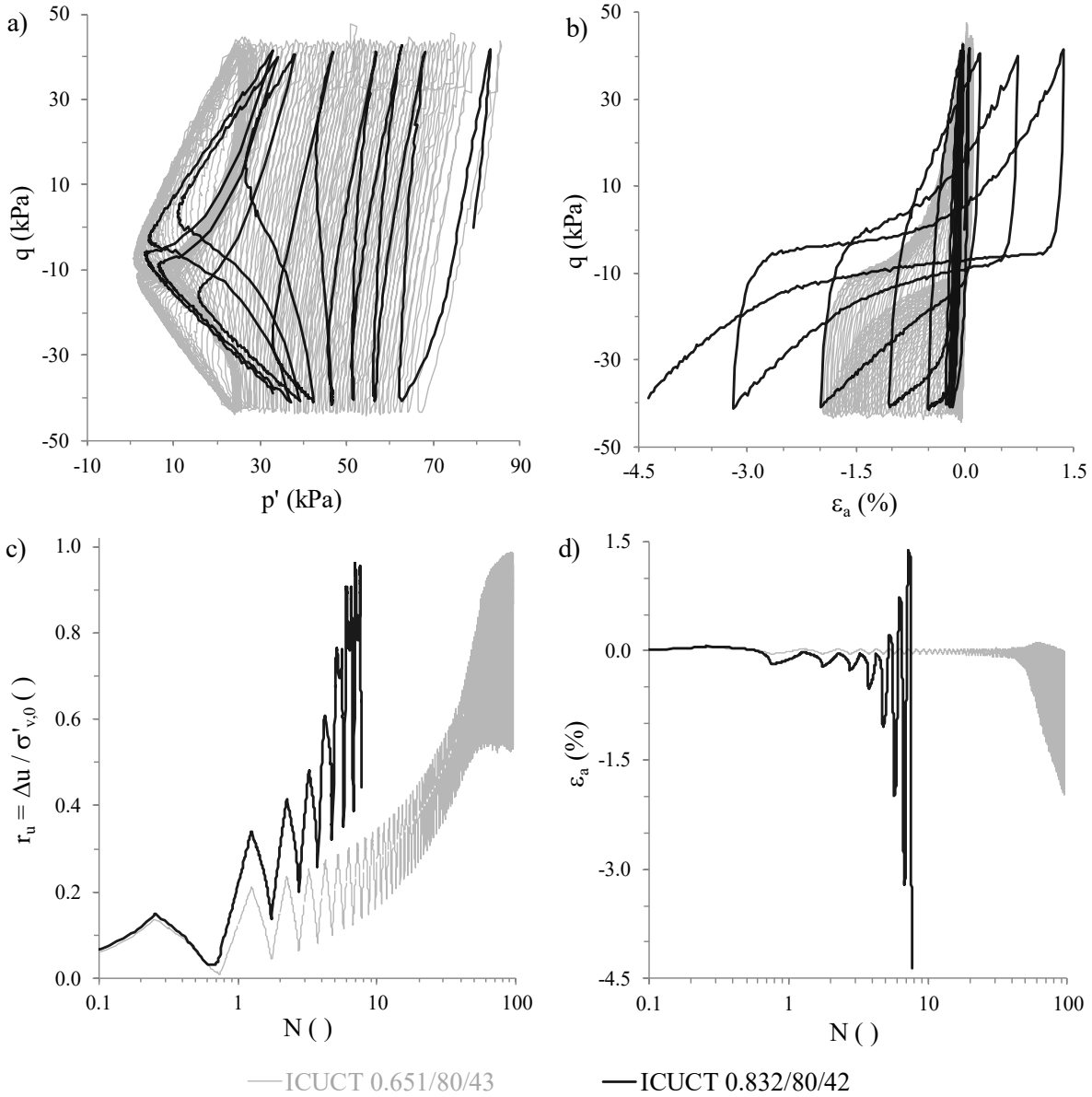

Figure 3.4 – Influence of the void ratio on the undrained cyclic response of Hostun sand: (a) effective stress path; (b) stress-strain response; (c) excess pore water pressure build-up; and (d) axial strain evolution with the number of loading cycles.

3.5.1.3 Influence of the isotropic effective stress at consolidation

Figure 3.5 compares the results of tests ICUCT 0.821/25/13, ICUCT 0.832/80/42 and ICUCT 0.793/135/67.5. In these tests, samples were prepared to similar void ratios

($e = 0.793 - 0.832$), though consolidated under different isotropic effective stress states ($\sigma'_0 = 25$, 80 and 135 kPa, respectively) and subjected to different deviatoric stress oscillations ($|\Delta q| \approx 13$, 42 and 67.5 kPa, respectively). Note, nevertheless, that similar cyclic stress ratios ($|\Delta q|/(2\,p'_0) \approx 0.250 - 0.263$) were used in these tests and, therefore, the influence of the isotropic confining stress on the undrained cyclic response of sand can be examined. It is apparent in the figure that the lower the isotropic effective stress at consolidation, the greater the number of loading cycles required to the onset of cyclic mobility (i.e. to generate large excess pore water pressures in the sample and, consequently, periods of instability characterised by very low effective stresses and rapid accumulation of large strains).

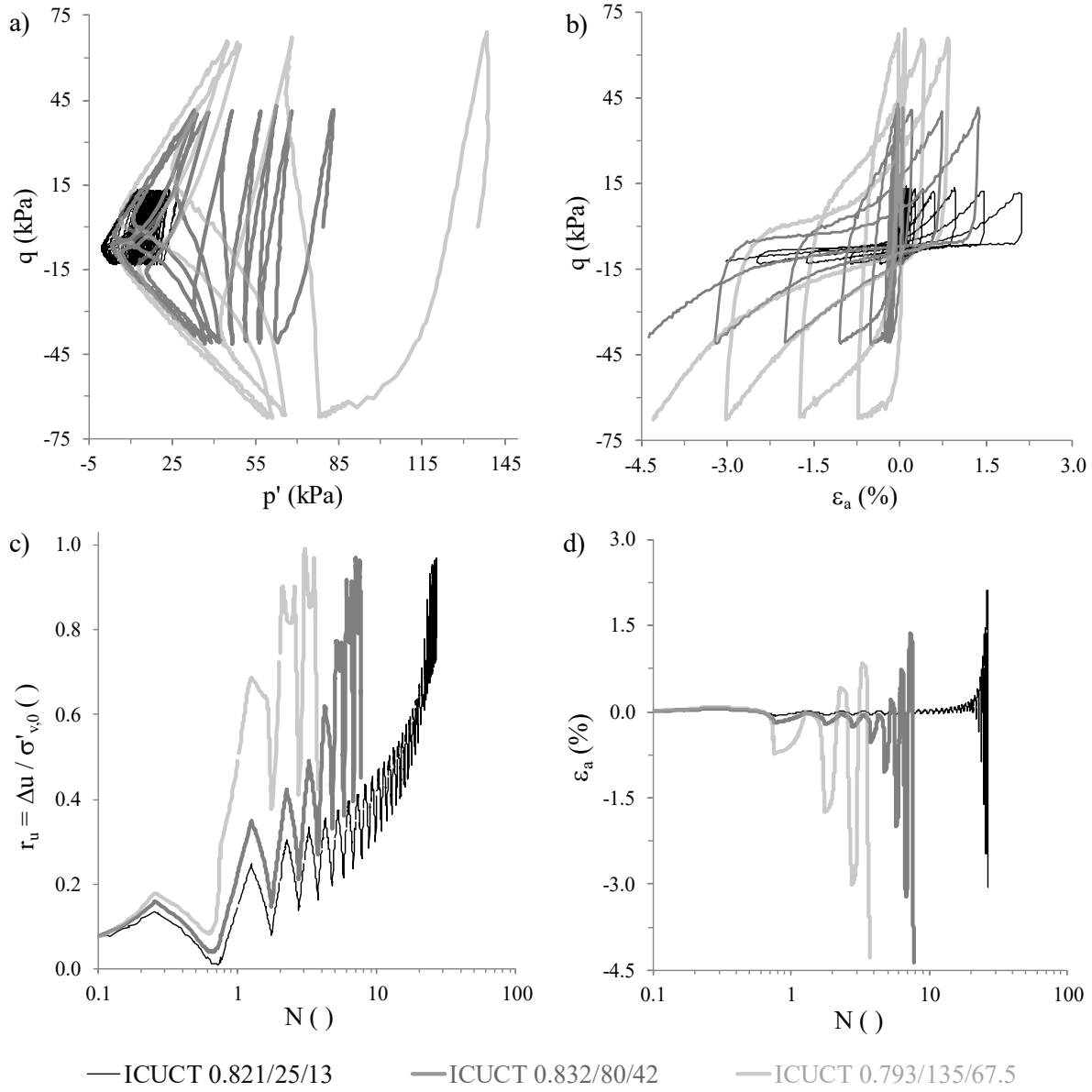

Figure 3.5 – Influence of the isotropic consolidation stress on the undrained cyclic response of Hostun sand: (a) effective stress path; (b) stress-strain response; (c) excess pore water pressure build-up; and (d) axial strain evolution with the number of loading cycles.

Interestingly, in the ICUCT 0.793/135/67.5 test, a very soft response in triaxial extension was measured during the first loading cycle, resulting in a severe mean effective stress reduction of more than 40 % of the initial value. A similar response was observed in other tests (specifically, tests ICUCT 0.804/80/48 and ICUCT 0.773/80/56), suggesting that the cyclic response of Hostun is highly anisotropic, with much softer response being observed in triaxial extension than in triaxial compression. Similar experimental observations were reported by Coelho (2007), when analysing the results of ICUCT tests on Leighton Buzzard sand.

3.5.1.4 Influence of the cyclic stress ratio

Figure 3.6 compares the results of tests ICUCT 0.771/80/32, ICUCT 0.832/80/42 and ICUCT 0.773/80/56, performed on samples prepared to similar void ratios ($e = 0.771 - 0.832$) and consolidated to the same isotropic effective stress state ($\sigma'_0 = 80$ kPa). Different deviatoric stress oscillations were, however, used in these tests and, therefore, the cyclic stress ratios applied to the samples were different: $|\Delta q|/(2\,p'_0) \approx 0.20$ for test ICUCT 0.771/80/32, $|\Delta q|/(2\,p'_0) \approx 0.263$ for test ICUCT 0.832/80/42 and, lastly, $|\Delta q|/(2\,p'_0) \approx 0.35$ for test ICUCT 0.773/80/56.

A very strong influence of applied cyclic stress ratio on undrained cyclic resistance of sand can be observed. In particular, it is apparent that the higher the cyclic stress ratio, the lesser the number of loading cycles required to the onset of cyclic mobility, as expected. In the case of test ICUCT 0.773/80/56, the PT line was crossed during the first loading cycle in triaxial extension, resulting in a strong reduction of the mean effective stress once the effective stress path was reversed. In this test, at the end of the first loading cycle, excess pore water pressures close to the initial effective stress and, therefore, effective stresses close to zero were measured. Conversely, in tests ICUCT 0.771/80/32 and ICUCT 0.832/80/42, a greater number of loading cycles were required to reach such low effective stresses (57 and 8 loading cycles, respectively).

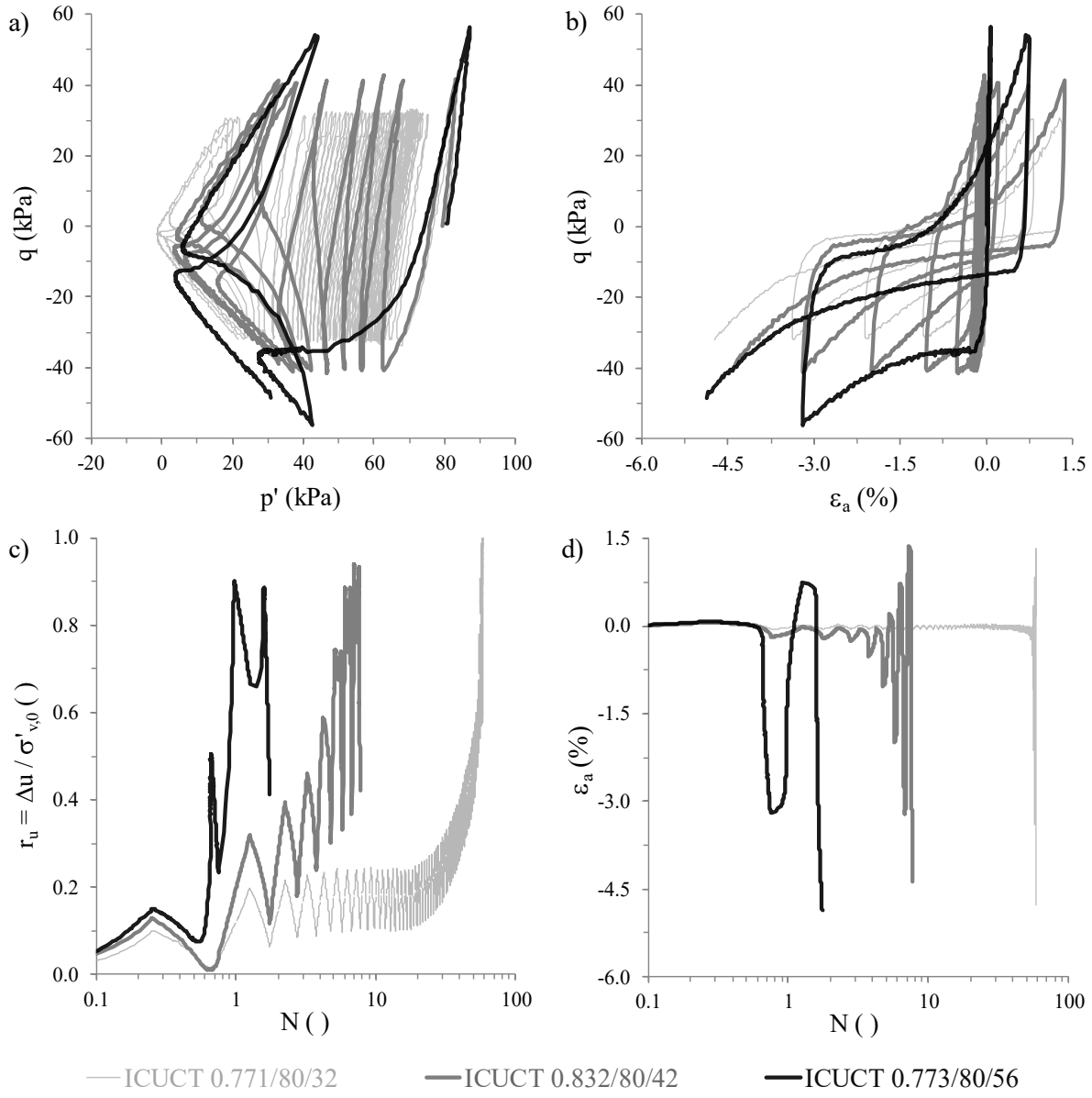

Figure 3.6 – Influence of the applied cyclic stress ratio on the undrained cyclic response of Hostun sand: (a) effective stress path; (b) stress-strain response; (c) excess pore water pressure build-up; and (d) axial strain evolution with the number of loading cycles.

3.5.2 Undrained cyclic resistance

As described in Section 3.2, the undrained cyclic resistance of sand has been defined by the number of loading cycles of constant cyclic stress ratio amplitude required to trigger cyclic mobility. With that purpose, a suitable criterion defining the onset of cyclic mobility is required. As discussed before, although the development of unit excess pore water pressure ratio (i.e. $r_u = \Delta u / \sigma'_{v,0} = 1.0$) has been initially proposed by Seed and Lee (1966) as an appropriate criterion, the fact that such high value is not always observed in some laboratory tests conducted on dense to very dense sand has led to the selection of other criteria in several other experimental studies. In particular, the development of 5 % double amplitude (i.e. between two consecutive stress reversals) axial strain (i.e. $\varepsilon_{a,da} = 5.0$ %) has been often

used to define the onset of cyclic mobility (e.g. Ishihara, 1996). The major drawback of this criterion consists of the fact that cyclic tests conducted on dense samples are often stopped before such large value of $\varepsilon_{a,da}$ is reached (as it was the case of some tests carried out in the present laboratory testing programme, as discussed later) and, therefore, two different criteria (one for moderately loose and another for dense sand) are, in such case, required to define the onset of cyclic mobility. In addition, it should be noted that, when test results are interpreted using energy principles (as it will be performed later), a criterion based on excess pore water pressures is considered more adequate, since this quantity (more specifically, its residual value, which corresponds to a null shear stress) seems to be strongly correlated to the accumulation of dissipated energy per unit volume, regardless of the initial state of the samples, as well as shape of applied cyclic load (Figueroa *et al.*, 1994; Liang *et al.*, 1995; Polito *et al.*, 2013; Kokusho, 2013; Azeiteiro *et al.*, 2015, 2017b).

Figure 3.7 illustrates the application of two different criteria to define the onset of cyclic mobility for test ICUCT 0.832/80/42. Specifically, one of the criteria assumes that cyclic mobility occurs as $\varepsilon_{a,da} \geq 5.0\,\%$ is firstly observed (Figure 3.7d), while the other criterion considers the generation of $r_{u,res} \geq 0.95$ as threshold (Figure 3.7c). Note that the use of $r_{u,res} \geq 0.95$, rather than $r_{u,res} = 1.0$, is justified by the fact that the latter was not observed in all undrained cyclic triaxial (UCT) tests performed in the present experimental study and, therefore, could not be employed to all test data. In fact, it is apparent that, even for very large values of $\varepsilon_{a,da}$, of about 7.7 %, the maximum value of $r_{u,res}$ registered during this test was approximately 0.95. Moreover, note that, due to the difficulty in reaching $r_{u,res} = 1.0$, values slightly below unit has been employed in other experimental studies reported in the literature (e.g. Okada and Nemat-Nasser, 1994).

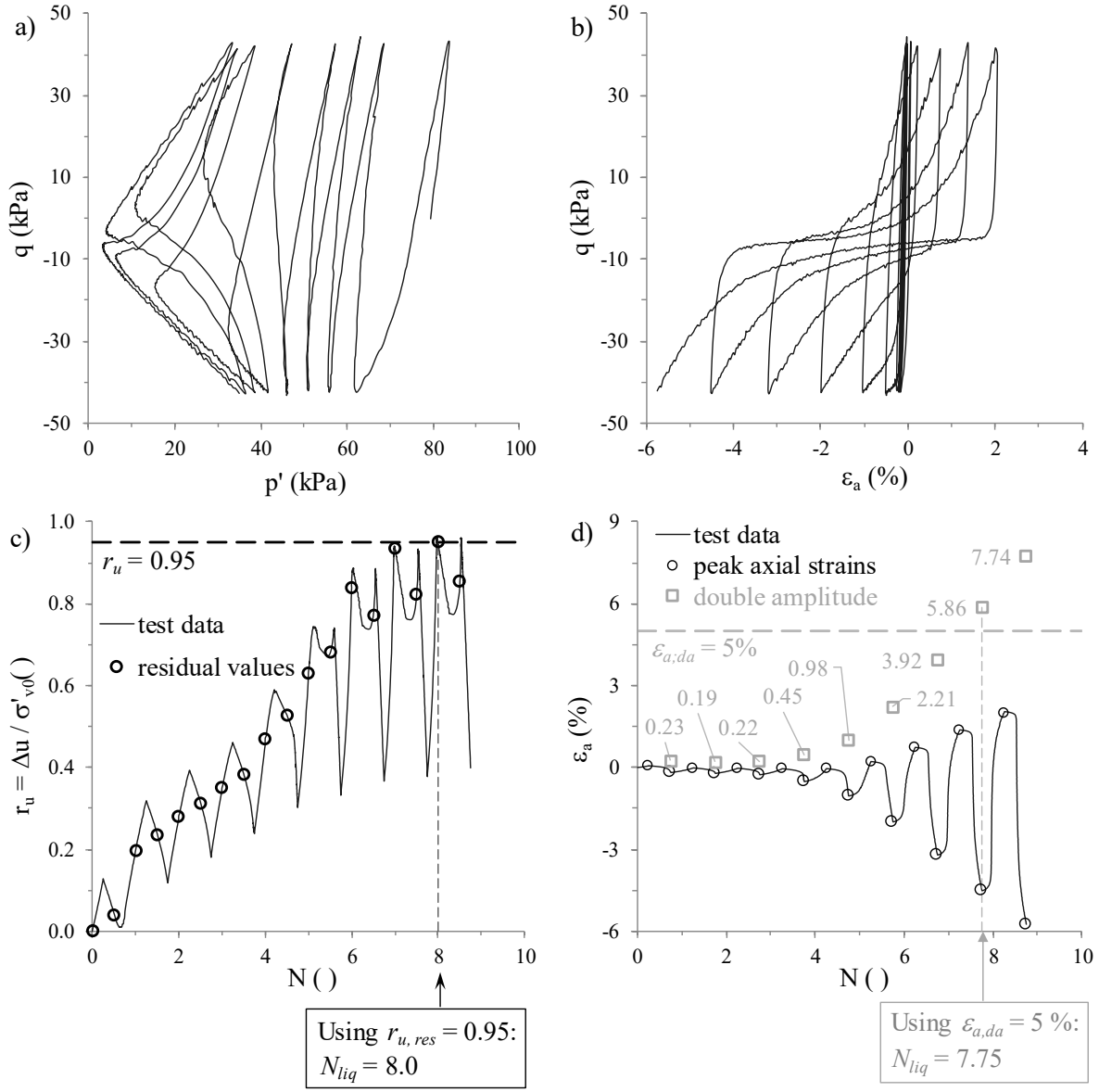

Figure 3.7 – Illustration of the application of two different criteria to define the onset of cyclic mobility for test ICUCT 0.832/80/42: (a) effective stress path; (b) stress-strain response; (c) excess pore water pressure build-up; and (d) axial strain evolution with the number of loading cycles.

Further insight into the impact of these two different criteria on the evaluation of the undrained cyclic resistance of Hostun sand is provided in Figure 3.8. In this figure, the cyclic resistance ratio (*CRR*), as defined by Equation 3.1, is plotted against the number of loading cycles to the onset of cyclic mobility, N_{liq}, obtained for all tests performed on moderately loose samples consolidated under an isotropic effective stress of 80 kPa (i.e. samples subjected to tests ICUCT 0.771/80/32, ICUCT 0.803/80/36, ICUCT 0.832/80/42, ICUCT 0.804/80/48 and ICUCT 0.773/80/56 – see Table 3.1). The data points obtained when employing the criterion $\varepsilon_{a,da} = 5.0\,\%$ are displayed in grey, while the data points obtained when using $r_{u,res} = 0.95$ are represented in black. It is apparent that very similar results were obtained when using both criteria. The only slight discrepancies are observed for tests where cyclic mobility was induced in very few loading cycles (i.e. tests ICUCT 0.804/80/48 and ICUCT 0.773/80/56).

Moreover, as also shown in Figure 3.8, both sets of data may be satisfactorily approximated by power relationships of the form of that given by Equation 3.2 (e.g. Idriss and Boulanger, 2006):

$$CRR = a \ N_{liq}^{-b} \tag{3.2}$$

where *a* and *b* are material parameters. It can be seen that the resulting curves are practically coincident, at least within the range of $10 \leq N_{liq} \leq 100$.

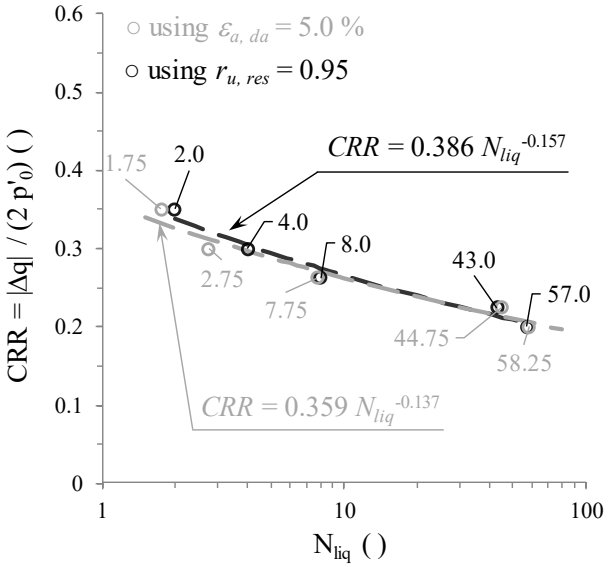

Figure 3.8 – Impact of the application of two different criteria to the prediction of the undrained cyclic resistance of moderately loose samples of Hostun sand consolidated to $p'_0 = 80$ kPa.

In terms of dense Hostun sand, Figure 3.9 depicts the results of test ICUCT 0.651/80/43, conducted on a sample having $e_0 = 0.651$ and consolidated to $p'_0 = 80.0$ kPa. The application of the criterion $r_{u,res} = 0.95$ is illustrated in Figure 3.9c, with $N_{liq} = 78.0$ being obtained. With respect to the criterion $\varepsilon_{a,da} = 5.0\%$, it can be observed that such level of double amplitude axial strain was not measured, even though about 62 additional loading cycles have been applied after $r_{u,res} = 0.95$ was registered, with large excess pore water pressures remaining to be registered. In effect, the increase in double amplitude axial strain occurs at a much smaller rate than that observed for moderately loose Hostun sand, with $\varepsilon_{a,da}$ being only about 3.5 % after more than 140 loading cycles. This means that, if a criterion based on $\varepsilon_{a,da}$ would be used in the present experimental programme to define the onset of cyclic mobility, different thresholds would have to be used for moderately loose and dense Hostun sand. Conversely, the criterion $r_{u,res} = 0.95$ can be applied to both moderately loose and dense Hostun sand and, therefore, was preferred in the present study.

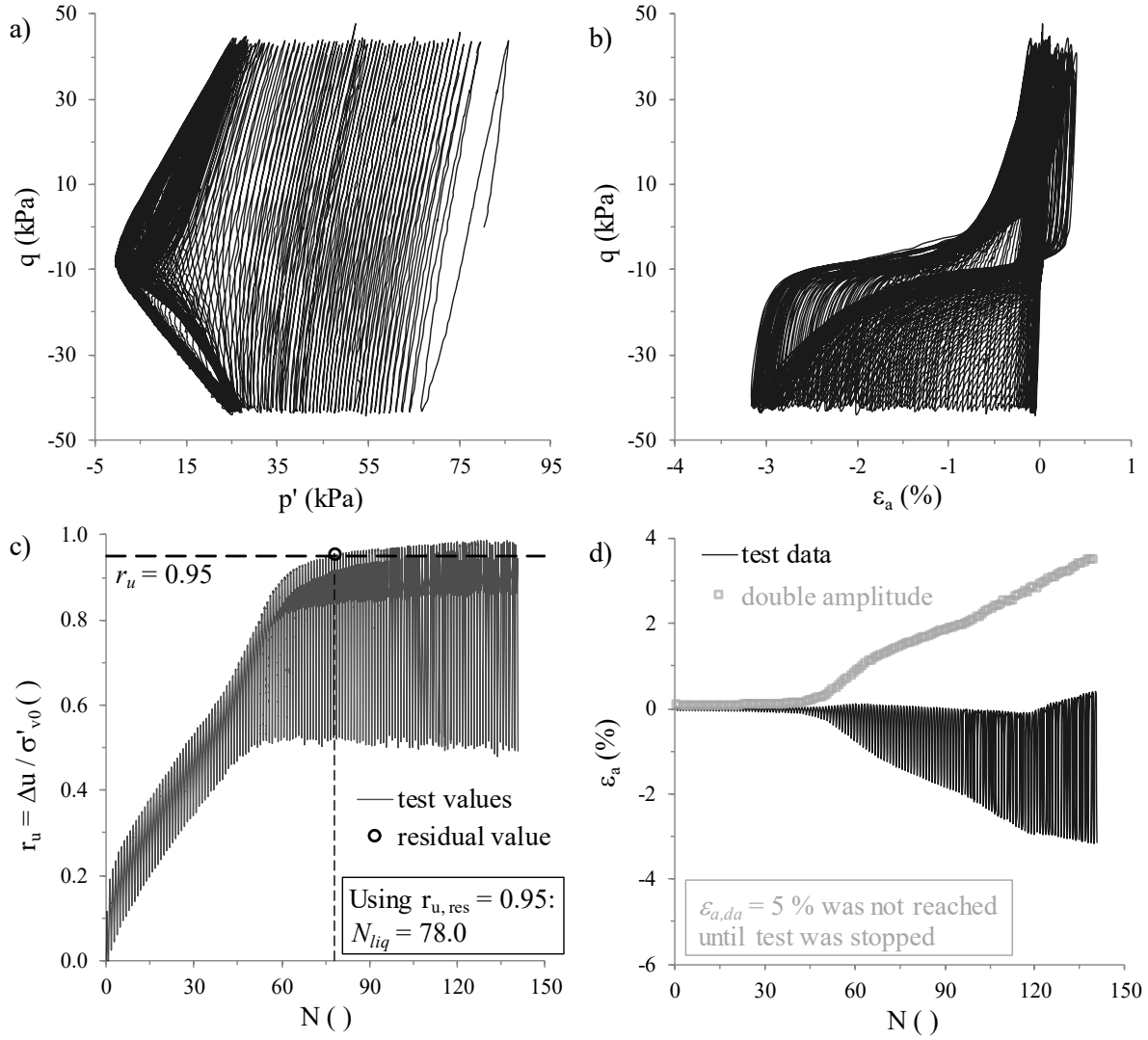

Figure 3.9 – Illustration of the application of two different criteria to define the onset of cyclic mobility for test ICUCT 0.651/80/43: (a) effective stress path; (b) stress-strain response; (c) excess pore water pressure build-up; and (d) axial strain evolution with the number of loading cycles.

Having defined the criterion employed to define the onset of cyclic mobility, Figure 3.10 depicts the values of the cyclic resistance ratio (*CRR*) against the number of loading cycles, N_{liq}, obtained for all ICUCT tests conducted in the present experimental programme. Note that these values are also indicated in Table 3.1. As widely reported in the literature (e.g. Seed and Idriss, 1970a; Tatsuoka *et al.*, 1986c; Ishihara, 1996; Jefferies and Been, 2006; Idriss and Boulanger, 2006), for a given cyclic stress ratio, the looser the sample and the higher the effective stress at consolidation, the lesser the number of loading cycles required to induce cyclic mobility. Moreover, the larger the cyclic stress ratio applied in the test, the lesser the number of loading cycles required to the onset of cyclic mobility.

Additionally, power relationships of the form of Equation 3.2 were employed to approximate the four different sets of data, namely: (1) moderately loose samples consolidated to $p'_0 = 25$ kPa; (2) moderately loose samples consolidated to $p'_0 = 80$ kPa; (3) moderately loose samples consolidated to $p'_0 = 135$ kPa and (4) dense samples consolidated to $p'_0 = 80$ kPa.

The obtained curves are also depicted in Figure 3.10. Naturally, the robustness of the proposed relationships is expected to increase with the number of points available for the regression, which means that the curve obtained for moderately loose samples consolidated to $p'_0 = 80$ kPa is probably the most reliable, since five data points were used for the regression. For moderately loose samples consolidated to either $p'_0 = 25$ or 135 kPa, only two data points were available. Moreover, although three data points were available for dense samples consolidated to $p'_0 = 80$ kPa, only two of these were considered for the regression. As it can be seen in the figure, the values of CRR inferred from tests ICUCT 0.652/80/72 and ICUCT 0.652/80/88 do not appear to be consistent. In particular, it is apparent that the value obtained for the latter test would result in an unlikely very steep regression curve and, therefore, it was decided to remove it from the regression. In fact, as discussed later, the rate of excess pore water pressure increase observed in this test for values of $r_{u,res}$ above 0.80 is significantly smaller than those registered for the other two tests conducted on dense samples (i.e. tests ICUCT 0.651/80/43 and ICUCT 0.652/80/72).

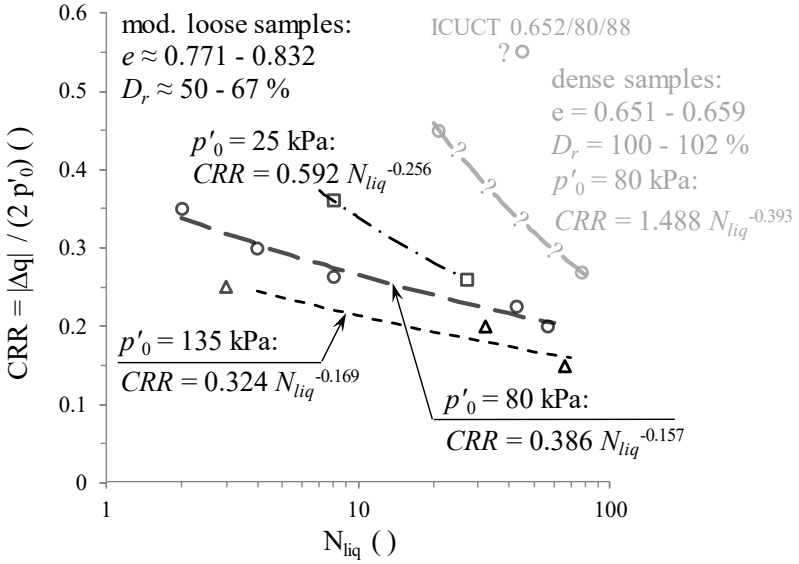

Figure 3.10 – Undrained cyclic resistance of Hostun sand inferred from ICUCT test data.

Although it would be interesting to compare the undrained cyclic resistance curves obtained in the present experimental programme with those obtained in other research programmes on Hostun sand, there seems to exist scarcity of published data on this aspect of the response of Hostun sand. The most relevant experimental study on this aspect is probably that reported by De Gennaro *et al.* (2004). Similar to the present laboratory testing programme, these authors presented results of UCT tests conducted on air-pluviated Hostun sand. In the study reported by De Gennaro *et al.* (2004), however, samples prepared to higher void ratios, specifically in the range of 0.866 – 0.910, and isotropically consolidated to $p'_0 = 400$ kPa were tested. Moreover, although results of tests using one-way deviatoric stress oscillations (i.e. applying cyclic loading only in triaxial compression or only in triaxial extension) are presented by De Gennaro *et al.* (2004), only the test results obtained using cyclic two-way symmetric

deviatoric stress reversals are presented here, to allow for a direct comparison with the results obtained in the present laboratory testing programme. In addition, note that, although the criterion used to define the onset of cyclic mobility by De Gennaro *et al.* (2004) was the observation of $\varepsilon_{a,da} = 5.0\,\%$, this seems to have little impact when analysing the undrained cyclic resistance of moderately loose Hostun sand (and likely of loose Hostun sand), as discussed before. The results obtained by De Gennaro *et al.* (2004) are compared with those obtained in the experimental programme in Figure 3.11. Consistently, the curve obtained by De Gennaro *et al.* (2004), obtained for looser samples consolidated under an higher mean effective stress, plots below those obtained in the present study.

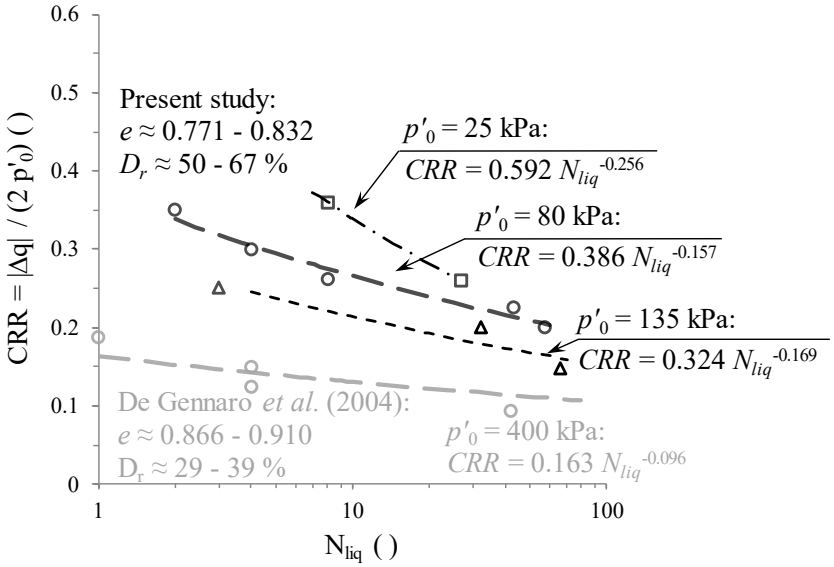

Figure 3.11 – Comparison of the undrained cyclic resistance of Hostun obtained in the present experimental programme with that reported by De Gennaro *et al.* (2004).

In addition, the undrained cyclic resistance of Hostun sand was compared to those exhibited by two other reference sands, namely Toyoura and Ottawa sands. Note that the main physical properties of these sands were described in Section 2.2.1. Moreover, critical state lines (CSL) proposed in the literature for Toyoura sand and Ottawa sands were compared to that proposed in the present study for Hostun sand in Section 2.6.5.1. As a brief summary, it was found that, despite having noticeable differences in their particle size distributions, the CSL proposed for sands having similar particle shape (namely, Hostun and Toyoura sands) plot close to each other. Conversely, although presenting similar particle size distributions, the CSL proposed for Ottawa sand is located far below that suggested for Hostun sand. It is perhaps also important to note that, when comparing the undrained cyclic resistance of sand, additional difficulties arise from the fact that, contrarily to the critical state (as per definition), it depends on the initial state of the sample (i.e. on the void ratio and mean effective stress at consolidation), as well as on the technique used to prepare the samples and type of loading (e.g. Ishihara, 1996). Some criteria were, therefore, establish to ensure the comparison of the undrained cyclic resistances inferred from test data performed under similar conditions. In

particular, based on the data obtained in the present experimental programme and data available in the literature, the following criteria were considered in this comparative study:

- method of sample preparation: air pluviated sand samples;
- relative density of the sample: between 45 and 70 %;
- consolidation: isotropic effective stress of 100 kPa;
- cyclic loading conditions: undrained cyclic triaxial loading with two-way symmetric deviatoric stress reversals.

For the reason explained before, the criterion employed to define the onset of cyclic mobility was not considered relevant. Nevertheless, it should be clarified that in both experimental studies on Toyoura sand (Toki *et al.*, 1986) and Ottawa sand (Shen *et al.*, 1978), $\varepsilon_{a,da} = 5.0\%$ was adopted as criterion. In relation to the choice of comparing resistance curves obtained for $p'_0 = 100$ kPa, it might seem inconsistent, since the present experimental testing programme do not contemplate tests performed on samples consolidated under such mean effective stress (rather to 25, 80 and 135 kPa). However, reliable data found in the literature for both Toyoura and Ottawa sands verifying the three remaining criteria listed above were only obtained from tests performed on samples consolidated to $p'_0 = 100$ kPa. Due to the qualitative nature of this comparative study, it was considered preferable to use data on Toyoura and Ottawa sands obtained for $p'_0 = 100$ kPa and estimate an undrained cyclic resistance curve corresponding to $p'_0 = 100$ kPa for Hostun sand. As illustrated in Figure 3.12, by simply employing a weighted average procedure, a resistance curve corresponding $p'_0 = 100$ kPa was obtained from those corresponding to $p'_0 = 80$ kPa and $p'_0 = 135$ kPa.

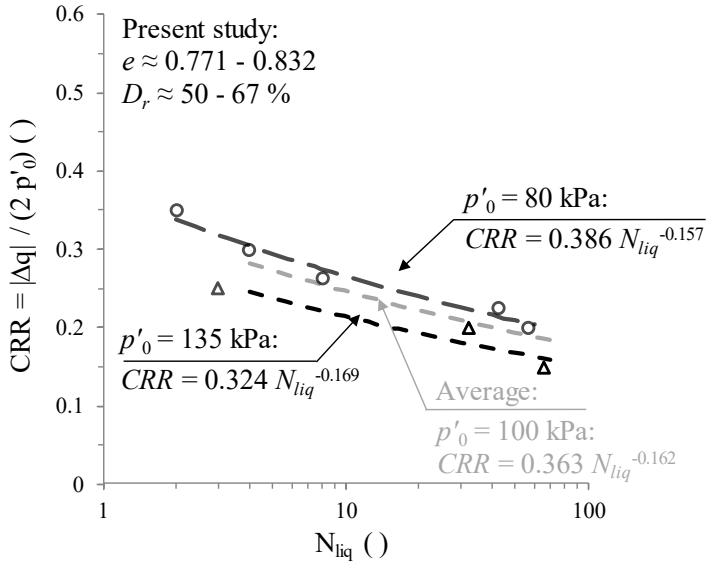

Figure 3.12 – Estimation of the undrained cyclic resistance of loose Hostun sand corresponding to $p'_0 = 100$ kPa.

The comparison between the undrained cyclic resistance of Hostun, Ottawa and Toyoura sands is provided in Figure 3.13. Note that neither the curve proposed for Ottawa sand (Shen *et al.*, 1978), not that proposed for Toyoura sand (Toki *et al.*, 1986) is accompanied by an

equation and, therefore, it is not possible to ascertain whether a power law (Equation 3.2) was used to define the proposed curves by the authors. It can be observed that, among the three sands, Hostun sand appears to be the most resistant, at least for loading histories comprising five to thirty loading cycles. Note that, as highlighted by Ishihara (1996) and investigated by Azeiteiro *et al.* (2012) and Azeiteiro *et al.* (2017b), the majority of the earthquakes is likely to have a significant number of cycles within this range (of five to thirty loading cycles). Providing that the undrained cyclic resistance of sand can be defined as the cyclic stress ratio producing cyclic mobility in twenty loading cycles, as suggested by Ishihara (1996), a value of 0.222 is obtained for Hostun sand, a value in between 0.209 and 0.168 for Ottawa sand, depending on its relative density (45 or 65%, respectively) and, finally, a value of 0.128 is obtained for Toyoura sand (which is almost half of that obtained for Hostun sand), as also shown in the figure. Note that, although the particle size distribution of Toyoura sand is finer than those corresponding to Hostun and Ottawa sands, any particular conclusion on possible correlations between these aspects based solely on these results would be merely speculative.

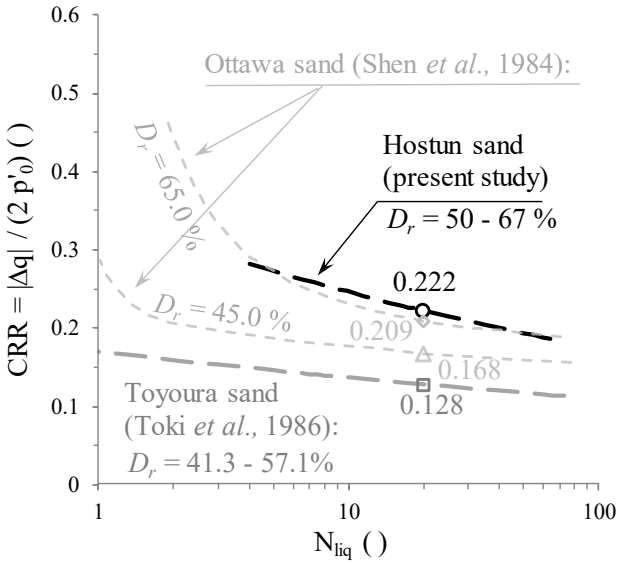

Figure 3.13 – Comparison of the undrained cyclic resistance of Hostun, Ottawa and Toyoura sands.

Finally, it is important to note that many other factors not considered in the present experimental programme have been shown to influence the undrained cyclic resistance of sand, particularly:

- Sample preparation method: air-pluviated samples are typically less resistant than moist-tamped samples (e.g. Tatsuoka *et al.*, 1986a; Ishihara, 1996); the discrepancies between the resistance of moist-tamped and air-pluviated samples seem, however, more appreciable under undrained cyclic triaxial loading than under undrained cyclic torsional shear loading (Tatsuoka *et al.*, 1986a).
- Initial shear stress ratio (typically denoted by the quantity $\alpha = \tau_0 / \sigma'_{v,0}$): a large number of researchers (e.g. Seed and Lee, 1966; Vaid and Chern, 1983) have dedicated

significant effort to study this aspect, by using either the simple shear or triaxial apparatus. The experimental results were summarised by Seed (1981) and Rollins and Seed (1990), suggesting that the effect of $\alpha = \tau_0/\sigma'_{v,0}$ on the cyclic resistance varies with the relative density of the material, with larger number of loading cycles being typically required to produce cyclic mobility on relatively loose to dense sand, while the opposite trend being observed for very loose sands, particularly when $\alpha > 0.2 - 0.3$. Further investigation on this topic has been performed more recently (e.g. Hosono and Yoshimine, 2004; Pan and Yang, 2017). While confirming that compressional static shear stress applied in the triaxial apparatus (i.e. $\tau_0 = (\sigma'_{a,0} - \sigma'_{r,0})/2$ with $\sigma'_{a,0} > \sigma'_{r,0}$) and in the simple shear apparatus has typically a beneficial impact on cyclic mobility (apart from very loose sands subjected to $\alpha > 0.2 - 0.3$), these studies have also revealed that extensional static shear stress applied in the triaxial apparatus (i.e. $\tau_0 = (\sigma'_{a,0} - \sigma'_{r,0})/2$ with $\sigma'_{a,0} < \sigma'_{r,0}$) tend to reduce cyclic mobility resistance. As highlighted by Hosono and Yoshimine (2004), these results may, however, depend on the degree of anisotropy of the material and, therefore, further investigation seems to be required.

- Overconsolidation: several authors (e.g. Ishihara and Takatsu, 1979) have suggested that overconsolidated sands tend to exhibit larger undrained cyclic resistance than normally-consolidated sands.
- Stress paths applied by different laboratory equipment: early studies undertaken by Peacock and Seed (1968) suggested that the undrained cyclic resistance of sand is smaller under simple shear loading than under triaxial loading. These results seem to be confirmed by Vaid and Sivathayalan (1996). On the contrary, experimental results reported by Finn *et al.* (1971) suggested that similar undrained cyclic resistances are obtained by both tests. More recently, Hosono and Yoshimine (2004) conducted a series of tests to investigate the undrained cyclic resistance of dry-deposited Toyoura sand under simple shear conditions using a hollow cylinder torsional shear apparatus and compare it with that predicted when using a triaxial test device. According to the authors, the use of the hollow cylinder equipment allows for the accurate application of a constant volume condition, while also enabling stress and strain measurements in the lateral boundaries of the specimen. The obtained results indicate that the undrained cyclic resistance of isotropically-consolidated samples under triaxial conditions is slightly smaller than that of anisotropically-consolidated ($K_0 = 0.5$) samples under simple shear conditions, providing that no initial shear stress ratio is applied (i.e. $\alpha = 0.0$). The apparent inconsistent results of the aforementioned research studies suggest that further investigation on this topic is required.
- Non-uniform versus uniform loading conditions: experimental results on Coimbra sand carried out by Azeiteiro *et al.* (2012) and Azeiteiro *et al.* (2017b) suggest that the number of cycles to the onset of cyclic mobility is strongly dependent on both the

magnitude and location of the peak load cycles; therefore, the cyclic resistance of sand is strongly dependent on the loading pattern, with an evaluation being required in each case.

- Multidirectional loading versus unidirectional loading: experimental studies reported by Nagase and Ishihara (1988) using the simple shear test apparatus and Coelho *et al.* (2013) using a triaxial stress-path cell suggest that lesser number of loading cycles are required to the onset of cyclic mobility when multidirectional loading is applied.

3.5.3 Secant shear modulus and damping ratio evolutions with strain amplitude

3.5.3.1 Basic concepts

Due to their importance to the interpretation and analysis of wave propagation phenomena, the characterisation of the evolution of both secant shear modulus and damping ratio with strain amplitude has been the subject of many research studies. In effect, while the shear modulus can be related to the velocity at which shear waves propagate through a given deposit, the damping ratio is a measure of the energy dissipated through hysteresis.

Starting with the shear modulus, several experimental studies have shown that, within the very small strains (typically below 10^{-5} to 10^{-6}), this property can be considered independent of the shear strain level for most practical applications (e.g. Vucetic, 1994; Clayton and Heymann, 2001; Clayton, 2011; Oztoprak and Bolton, 2012). As presented in Chapter 2, results of bender element tests were used in the present study to characterise the maximum (i.e. at small strains) shear modulus, G_{max}, of Hostun sand, as a function of the void ratio and mean effective stress.

Conversely, as the shear strain amplitude increases above that limit, which was termed as "linear cyclic threshold shear strain" and denoted as γ_{tl} by Vucetic (1994), sand typically exhibits a non-linear hysteretic response, with the shear modulus being highly depend on the applied shear strain level (e.g. Seed and Idriss, 1970b; Hardin and Drnevich, 1972b; Iwasaki *et al.*, 1978; Kokusho, 1980; Lo Presti *et al.*, 1997; Darendeli, 2001; Benz, 2007). Within such strain range, it has been customary to use the secant shear modulus, G_{sec}, to characterise the evolution of stiffness of sand during cyclic loading. As schematically illustrated in Figure 3.14, G_{sec} corresponds to the slope of the line connecting the two tips of a given stress-strain loop, providing an indication of the average stiffness exhibited by the material during a given loading cycle.

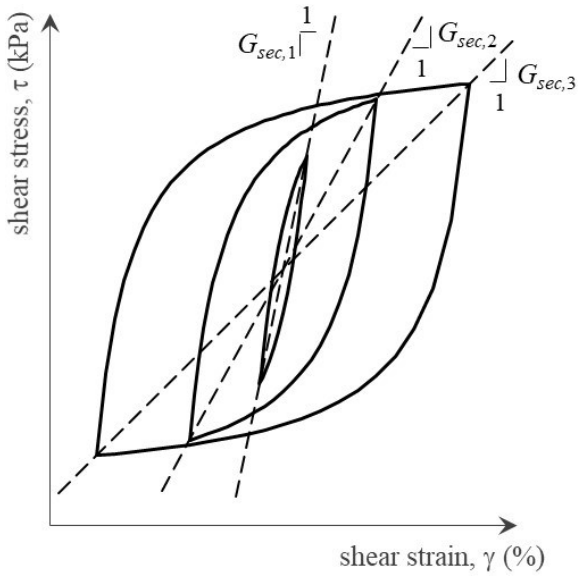

Figure 3.14 – Schematic representation of the strain-dependency of the secant shear stiffness modulus under cyclic loading exceeding the very small strain domain for three distinct strain amplitudes (adapted from Taborda, 2011).

As also illustrated in Figure 3.14, flatter stress-strain loops are typically obtained as larger shear strain amplitudes are applied, meaning that the magnitude of G_{sec} is typically observed to reduce with shear strain amplitude, γ. To illustrate such strain-dependency, $G_{sec} - \gamma$ curves characterising different types of materials (such as sand, clay, gravel) have been proposed in early studies on this subject. It was later acknowledged that it would be preferable to present G_{sec} as a percentage of the value of G_{max}, as illustrated in Figure 3.15. In fact, as highlighted by Taborda (2011), this normalisation allows for an independent evaluation of the aspects influencing the magnitude of the shear modulus at very small strains, G_{max}, and those influencing its reduction with further straining (i.e. G_{sec} / G_{max}).

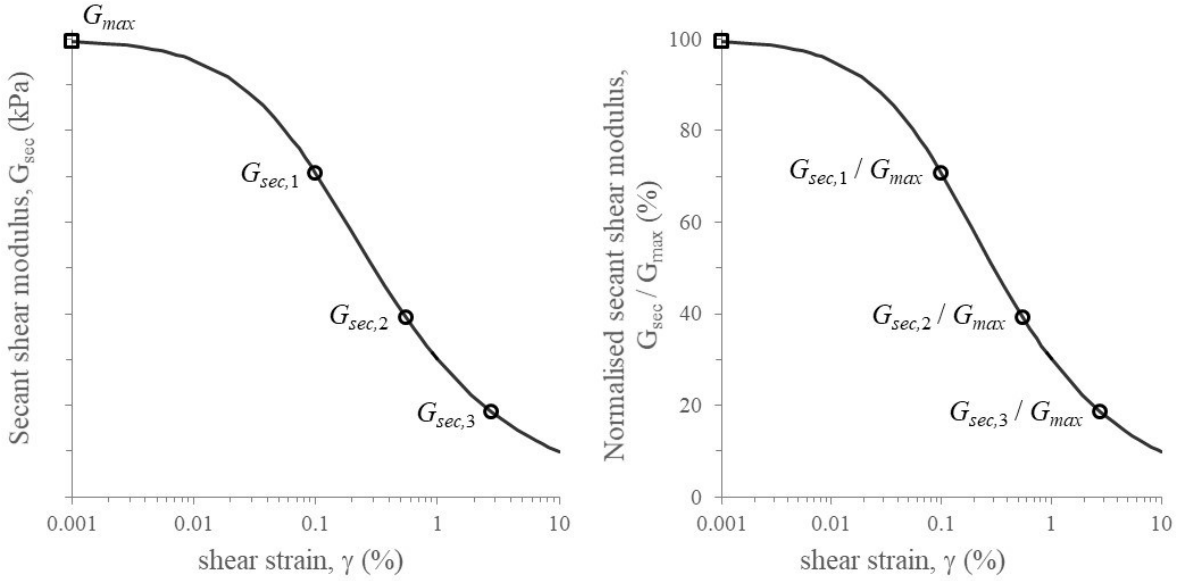

Figure 3.15 – Stiffness reduction curves: (a) secant shear modulus with shear strain amplitude and (b) normalised secant shear modulus with shear strain amplitude (adapted from Taborda, 2011).

Another crucial aspect of the response of sand within the small to large strain range is the capacity to dissipate energy when sheared, which has been typically quantified by the damping ratio, ξ – Equation 3.3 (Kramer, 1996).

$$\xi = \frac{1}{4\,\pi}\,\frac{\delta W}{W_{e,max}} \tag{3.3}$$

where δW and $W_{e,max}$ are, respectively, the energy dissipated and maximum elastic stored energy during a given loading cycle. As illustrated in Figure 3.16, the former quantity corresponds to the area enclosed by the stress-strain loop and is defined by Equation 3.4. Conversely, the latter quantity is associated with the shaded area in Figure 3.16a, defined by the undeformed state, the point of shear reversal (γ_p, τ_p) and its corresponding image on the horizontal axis (γ_p, 0), as mathematically described by Equation 3.5.

$$\delta W = \int \sigma'\, d\varepsilon = \int \tau\, d\gamma \tag{3.4}$$

$$W_{e,max} = \frac{1}{2}\,\tau_p\,\gamma_p = \frac{1}{2}\,G_{sec}\,\gamma_p^2 \tag{3.5}$$

where γ and τ are, respectively, the shear strain and shear stress.

Note that, contrary to the secant shear modulus, the damping ratio tends to increase with the shear strain level.

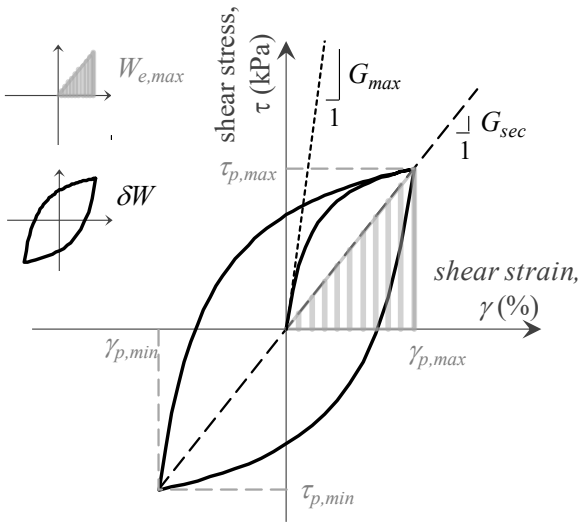

Figure 3.16 – Definition of damping ratio using concepts of energy dissipated and maximum elastic stored energy during a given stress-strain loop.

Several experimental studies focused on obtaining representative secant shear stiffness and damping ratio curves for different materials. For sand, the works of Seed and Idriss (1970b), Vucetic and Dobry (1991), Ishibashi and Zhang (1993) and Darendeli (2001) are particularly noteworthy. The outcome of these four different proposals is provided in Figure 3.17. It should be pointed out that Seed and Idriss (1970b) proposed lower, mean and upper bounds for both normalised secant shear modulus and damping ratio, to account for the scatter observed in the extensive experimental data collected and analysed by the authors, including

results from different laboratory tests (specifically, resonant column, cyclic triaxial, cyclic simple shear and cyclic torsional shear tests) performed on samples consolidated under mean effective stresses ranging from about 20 to 400 kPa, as well as results from *in situ* wave velocity tests. Note, nevertheless, that, to ease the visualisation, only the mean bound is depicted in the figure. Regarding the curves proposed by Vucetic and Dobry (1991), which were inferred from simple shear, triaxial and resonant column test data and described solely as a function of the plastic index, *PI*, those depicted in Figure 3.17 correspond to $PI = 0$ %, as typically observed for clean sands. In terms of the curves proposed by Ishibashi and Zhang (1993) and Darendeli (2001), for comparison purposes and following the strategy adopted by Taborda (2011) when reviewing and comparing these different proposals, the following characteristics were assumed: mean effective stress of $p' = 100$ kPa, a plasticity index of $PI = 0$ %, an overconsolidation ratio of $OCR = 1.0$, a frequency of loading of $f = 1$ Hz and a number of loading cycles of $N = 10$ (note that these three last characteristics are only required when plotting the curves proposed by Darendeli (2001)). It can be observed that, apart from the normalised secant shear stiffness reduction curve proposed by Ishibashi and Zhang (1993), which plots above the remaining curves, similar curves are obtained from all remaining proposals (Figure 3.17a). In terms of damping ratio (Figure 3.17b), curves are observed to plot in a narrow band for shear strain levels below 1 %. Perhaps more importantly, these studies suggest that the normalised secant shear modulus reduction and damping ratio curves for sand are primarily affected by the mean effective stress at consolidation, even though the overconsolidation ratio, the frequency of loading and the number of loading cycles may also have influence on the obtained relationships.

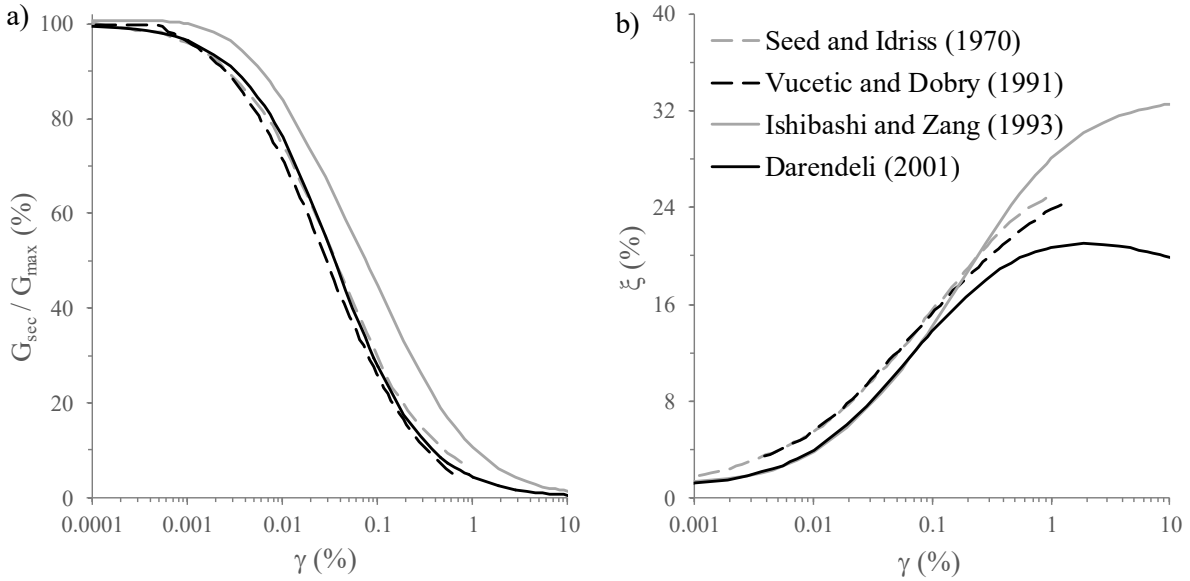

Figure 3.17 – Comparison of: (a) stiffness reduction curves and (b) damping ratio curves proposed in the literature for sand (adapted from Taborda, 2011).

3.5.3.2 Methodology adopted to compute the secant shear modulus and damping ratio

Although both secant shear modulus, G_{sec}, and damping ratio, ξ, evolutions with shear strain amplitude, γ, can be computed from results of undrained cyclic triaxial tests with stress-controlled shear reversals (as those performed in the present study), difficulties arise from the fact that the measured stress-strain loops are rarely closed, as shown in Figure 3.18a. A numerical procedure is, therefore, required to compute these quantities for each stress-strain loop. In the present study, the following approach, which is similar to that outlined by Taborda *et al.* (2016) and Azeiteiro *et al.* (2017b), was employed:

1) Isolate each half-cycle stress-strain loop, as shown in Figure 3.18a.
2) Create a symmetric image of each half-cycle stress-strain loop about its centre.
3) Centre each half-cycle stress-strain loop and its corresponding mirror image at the origin of the stress-strain space (i.e. move each half-loop in such a way that its two tips are located at equal horizontal and vertical distances to the origin); at this point, two closed stress-strain loops are defined by original and mirrored half-cycle stress-strain loops (Figure 3.18b).
4) For each closed stress-strain loop:
   4.1) estimate the area enclosed by each loop using a trapezoidal approximation – Equation 3.6, which assumes undrained triaxial loading conditions and gives the energy dissipated per unit volume per loading cycle, δW; divide the obtained value by two, in order to account for only half stress-strain loop;
   4.2) estimate the area of the triangle defined by the undeformed state, the peak deviatoric stress and axial strain and its corresponding image on the horizontal axis, which corresponds to the maximum elastic stored energy, $W_{e,max}$ (Equation 3.7, which also assumes undrained triaxial loading conditions);
   4.3) determine the damping ratio corresponding to each closed stress-strain loop, ξ (Equation 3.3).
5) Sum the two values of ξ corresponding to each of the two half loops in order to obtain a measure of the damping ratio per loading cycle.

$$\delta W = \int \sigma \, \mathrm{d}\varepsilon = \int_k q \, \mathrm{d}\varepsilon_a \approx \sum_{i=1}^{k-1} \frac{1}{2}\left(q^{(i)} + q^{(i+1)}\right)\left(\varepsilon_a^{(i+1)} - \varepsilon_a^{(i)}\right) \tag{3.6}$$

$$W_{e,max} = \frac{1}{2} q_p \, \varepsilon_{a,p} \tag{3.7}$$

Note that in Equations 3.6 and 3.7, ε_a and q are, respectively, the axial strain and deviatoric stress, with the subscript "p" referring to a peak value of these quantities; k is the total number of points in which the stress-strain loop is discretised (only in Equations 3.6).

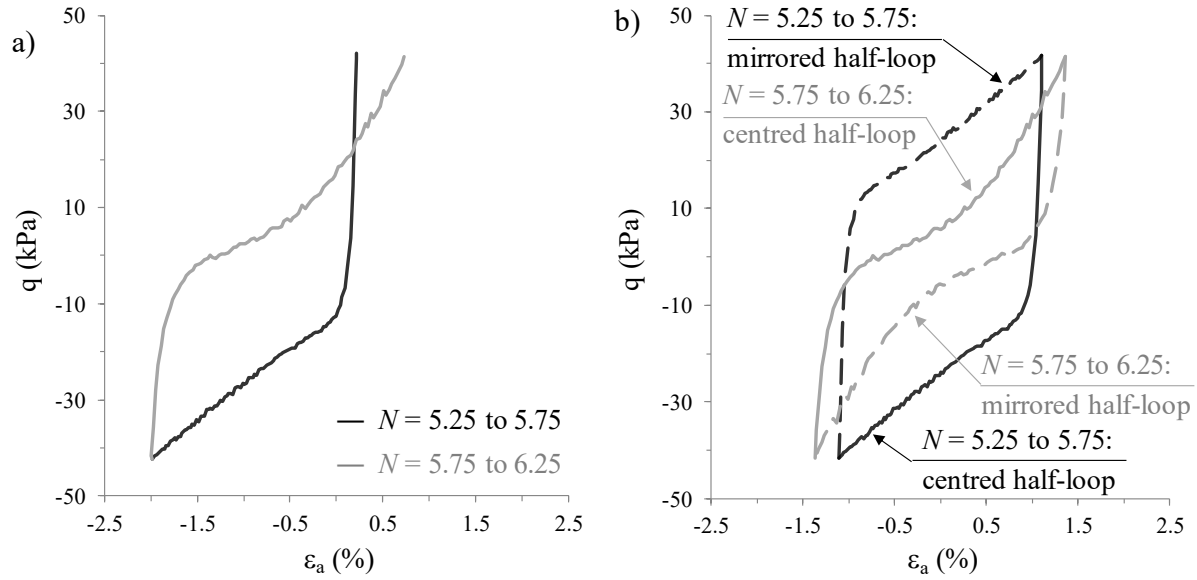

Figure 3.18 – Example of application of the methodology used to estimate the damping ratio for ICUCT 0.832/80/42 test: (a) original deviatoric stress – axial strain loop, (b) closed deviatoric stress – axial strain loops using mirror centred images of the original half-loops.

Moreover, the secant shear modulus, G_{sec}, was estimated for each half stress-strain loop by computing the slope of the line connecting the two tips of the half loop, which, under triaxial loading conditions can be described by Equation 3.8.

$$G_{sec} = \frac{\Delta q}{3\,\Delta\varepsilon_q} = \frac{\Delta q}{2\,(\Delta\varepsilon_a - \Delta\varepsilon_r)} \tag{3.8}$$

where Δq defines the deviatoric stress change (i.e. from peak in triaxial extension to peak in triaxial compression or vice-versa), while $\Delta\varepsilon_q$, $\Delta\varepsilon_a$ and $\Delta\varepsilon_r$ define the corresponding change in deviatoric, axial and radial strains.

For convenience, the computed secant shear modulus is normalised by the maximum (i.e. small-strain) shear modulus, G_{max}. As discussed in Chapter 2, for sand, this quantity can be essentially related to the current value of the void ratio, e, and mean effective stress, p', with Equation 3.9 being proposed for Hostun sand based on results of bender element tests (see Section 2.5.5). Under undrained shearing, while e remains constant (providing that water can be considered incompressible), p' is evolving throughout loading and, consequently, G_{max} does not remain constant during a given loading cycle. A consistent approach is, therefore, required to compute a value for G_{max} that can be considered representative of each half stress-strain loop. Although other strategies could have been devised, in the present study, the residual mean effective stress (i.e. corresponding to zero deviatoric stress) measured in each half stress-strain loop was used for the computation of G_{max}.

$$G_{max} = C_g\, p'_{ref}\, f(e) \left(\frac{p'}{p'_{ref}}\right)^{n_g} \approx 293 \times 101.3 \times \frac{(2.97 - e)^2}{1 + e} \times \left(\frac{p'}{101.3}\right)^{0.49} \tag{3.9}$$

Furthermore, it should be noted that, in the present study, rather than as a function of single amplitude shear strain, γ, the evolutions of both G_{sec} / G_{max} and ξ are examined as a function of single amplitude axial strain, $\varepsilon_{a,sa}$, which was estimated as half of double amplitude axial strain $\varepsilon_{a,da}$, measured in each loading cycle. Note, nevertheless, that, since under undrained triaxial loading conditions the volumetric strain increment, $\Delta\varepsilon_v$, remains practically null, deviatoric strain increment, $\Delta\varepsilon_q$, is approximately equal to axial strain increment, $\Delta\varepsilon_a$, as shown in Equations 3.10 and 3.11, and, therefore, it follows that $\gamma \approx 3/2\ \varepsilon_{a,sa}$.

$$\Delta\varepsilon_v \approx 0 \Leftrightarrow \Delta\varepsilon_a + 2\ \Delta\varepsilon_r \approx 0 \Leftrightarrow \Delta\varepsilon_r \approx -1/2\ \Delta\varepsilon_a \tag{3.10}$$

$$\Delta\varepsilon_q = 2/3\ \Delta\gamma = 2/3(\Delta\varepsilon_a - \Delta\varepsilon_r) \Leftrightarrow \Delta\varepsilon_q \approx 2/3(\Delta\varepsilon_a + 1/2\ \Delta\varepsilon_a) \approx \Delta\varepsilon_a \tag{3.11}$$

3.5.3.3 Main patterns under undrained cyclic triaxial loading

Figure 3.19 depicts the deviatoric stress, q, – axial strain, ε_a, loops measured in each loading cycle, N, of test ICUCT 0.832/80/42. The corresponding normalised secant shear modulus, G_{sec} / G_{max}, and damping ratio, ξ, evolutions with single amplitude axial strain, $\varepsilon_{a,sa}$, are presented in Figure 3.20. The following aspects are particularly noteworthy:

- the $q - \varepsilon_a$ loops registered during the three initial loading cycles are not fully closed (Figure 3.19); the opening is particularly evident for the first loading cycle and, according to Matasović and Vucetic (1993), may explain the tendency to obtain a greater value for ξ during the first loading cycle than during the subsequent ones (Figure 3.20b); these authors suggested to disregard the value of ξ obtained for the first loading cycle – a strategy also adopted in the study presented in the following section; note that, even under drained conditions, the number of loading cycles has been observed to have an important impact on ξ (e.g. Kokusho, 1980; Vucetic and Dobry, 1991; Darendeli, 2001), with $N = 10$ being often adopted to establish damping ratio curves; in terms of G_{sec} / G_{max}, it is apparent that the value of this quantity increases from the first loading cycle to the subsequent two loading cycles; this seems consistent with the tendency of sand to exhibit a stiffening unloading-reloading response under effective stress paths below the phase transformation line (Papadimitriou and Bouckovalas, 2002);
- as expected, the axial strain amplitude induced in the samples in this type of test are relatively large from the start of loading (at least, much larger than those imposed in small-strain measurements); as a result, relatively low values of G_{sec} / G_{max} (in this case, below 30 %) and relatively large values of ξ (in this case, above 20 %) are obtained from the start of the test;
- as observed in other experimental studies involving undrained cyclic shearing (e.g. Matasović and Vucetic, 1993; Wang and Kuwano, 1999; Elgamal *et al.*, 2005), ξ tends to drop substantially during the later stages of loading (in this test, after reaching a value for $\varepsilon_{a,sa}$ of about 0.5 %); according to Matasović and Vucetic (1993), this

tendency arises from the so-called "S-shaping" of the stress-strain curve, which develops as a result of dilative response of sand, once the phase transformation line is crossed; as also pointed out by these authors, although the concepts of dissipated energy per unit volume per loading cycle, δW (Equation 3.4), and of maximum elastic stored energy per loading cycle, $W_{e,max}$ (Equation 3.5), remain valid under such circumstances, the concept of damping ratio, as defined by Equation 3.3, might not retain its validity, since it was derived under the assumption that the hysteresis stress-strain loop is elliptical, as implied by viscous damping and detailed in Kramer (1996); due to this, in what follows, the values of ξ obtained after reaching the peak (which corresponds approximately to the moment at which S-shaping of the stress-strain loop starts to become evident) are disregarded.

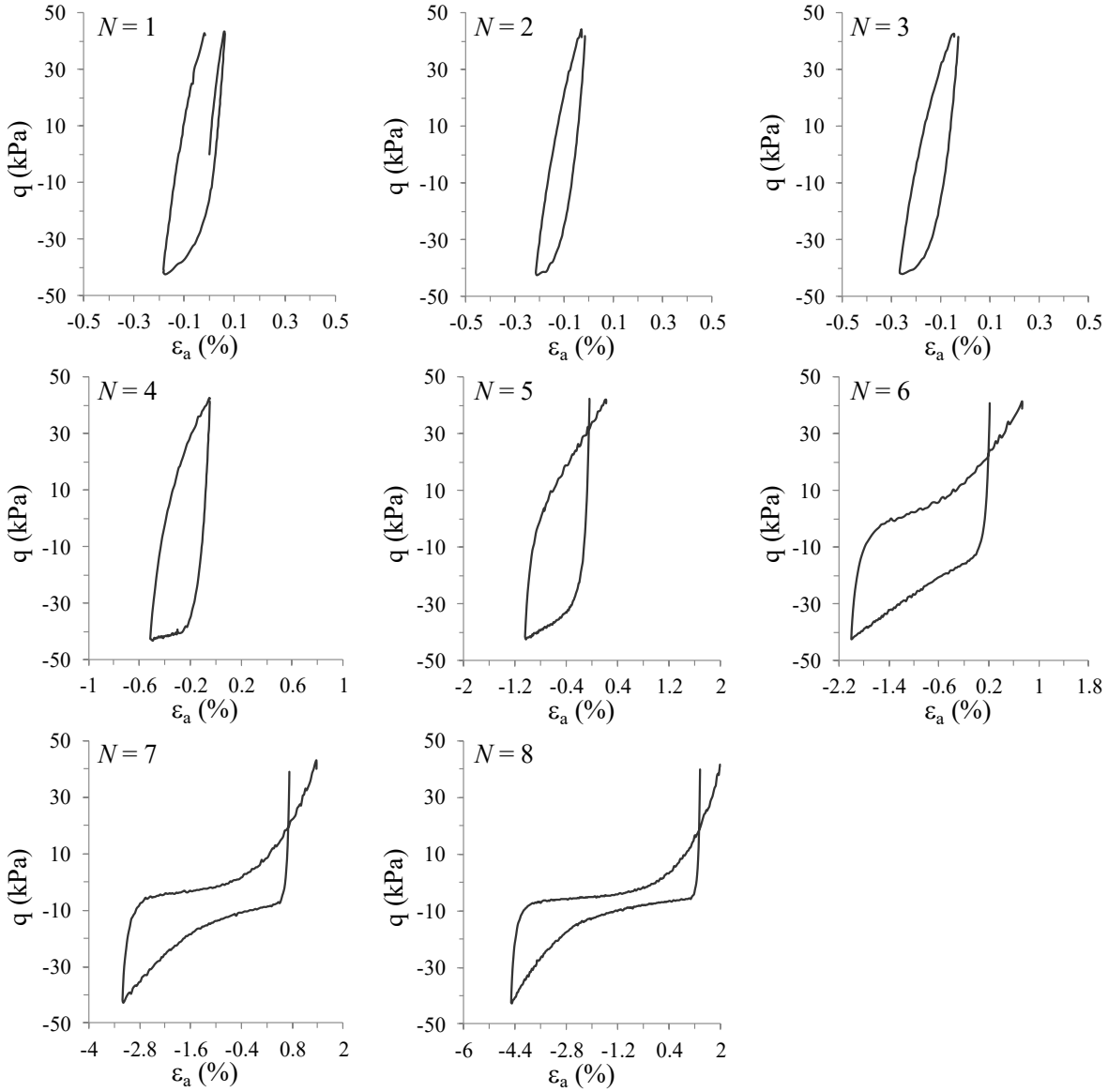

Figure 3.19 – Test ICUCT 0.832/80/42: stress –strain response measured in each loading cycle.

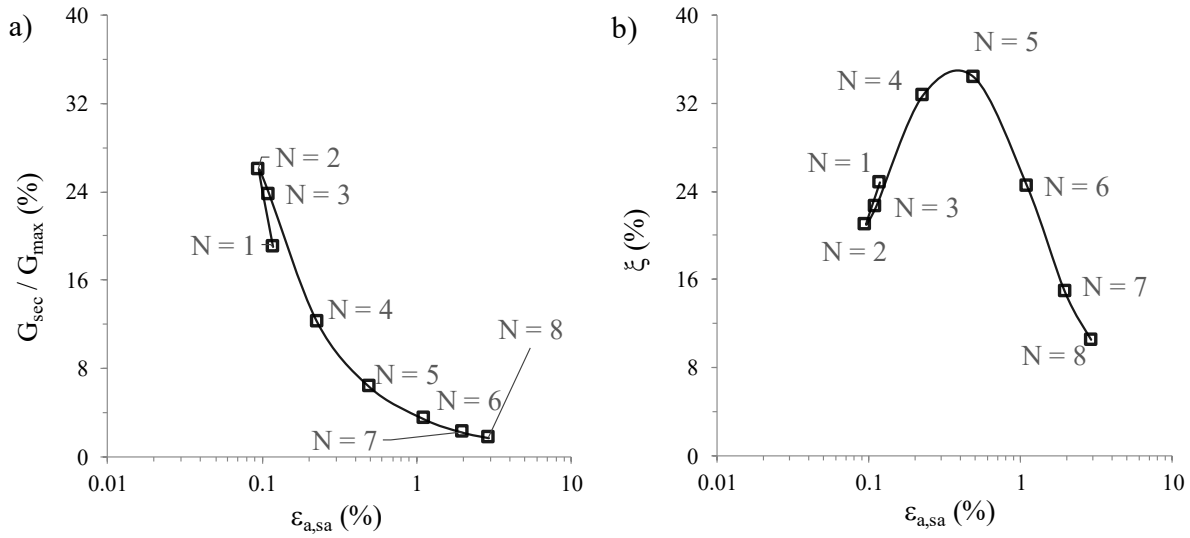

Figure 3.20 – Test ICUCT 0.832/80/42: evolution of the (a) normalised secant shear modulus and (b) damping ratio with single amplitude axial strain inferred from laboratory test results.

3.5.3.4 Influence of the initial state on the evolution of the normalised secant shear stiffness and damping ratio with strain amplitude

Figure 3.21 depicts the evolution of both G_{sec} / G_{max} and ξ with $\varepsilon_{a,sa}$ computed from the results of tests ICUCT 0.821/25/13 and ICUCT 0.832/80/42. Note that, in these tests, samples prepared to similar void ratios were consolidated under different mean effective stresses, respectively of 25 and 80 kPa, while being sheared under similar cyclic stress ratios (CSRs), as indicated in the figure.

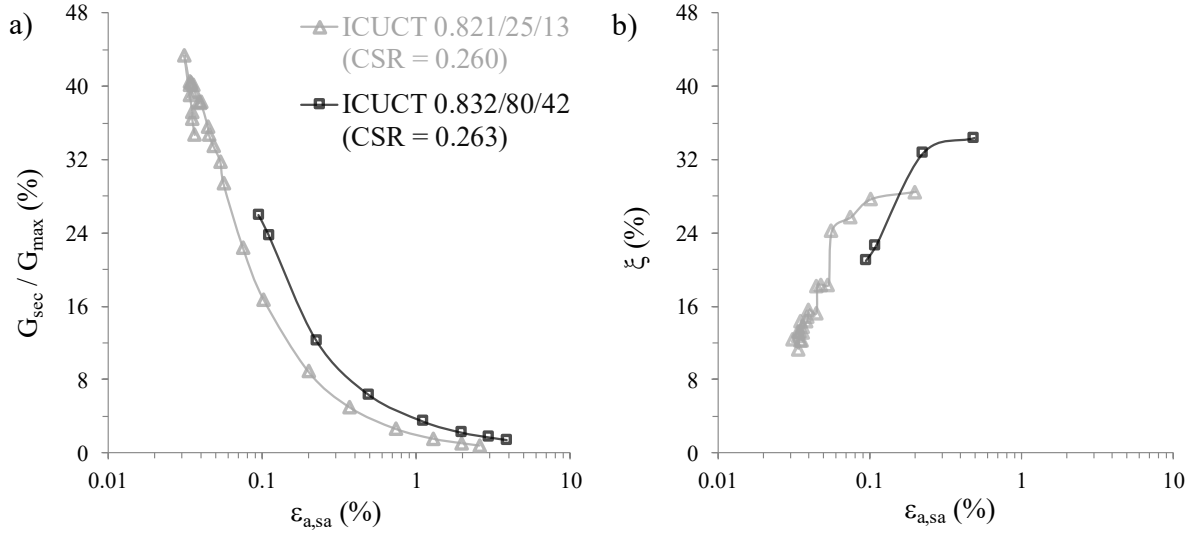

Figure 3.21 – Impact of the mean effective stress at consolidation on the evolution of: (a) normalised secant shear modulus and (b) damping ratio with single amplitude axial strain.

It can be seen that, for a given single amplitude axial strain, the higher the mean effective stress at consolidation, the larger the normalised secant shear modulus – a trend also observed in other experimental studies (e.g. Ishibashi and Zhang, 1993; Darendeli, 2001). With respect to damping ratio, it can be seen that slightly larger peak values of this quantity

were obtained in test ICUCT 0.832/80/42 than in test ICUCT 0.821/25/13. Moreover, it is apparent that the peak value was mobilised at a larger axial strain amplitude in the former test. Note, however, that, during the early stages of loading, it seems that, for a given axial strain amplitude, larger values of damping ratio were mobilised in the test where the sample was consolidated under the smaller mean effective stress (i.e. in test ICUCT 0.821/25/13), with similar observations being reported in the literature (e.g. Ishibashi and Zhang, 1993; Darendeli, 2001).

With the purpose of evaluating the impact of the void ratio on the evolution of both G_{sec} / G_{max} and ξ with $\varepsilon_{a,sa}$, Figure 3.22 compares the results obtained for tests ICUCT 0.832/80/42 and ICUCT 0.651/80/43, where a moderately loose sample and a dense sample, respectively, were consolidated under the same isotropic effective stress of 80 kPa and sheared under similar deviatoric stress oscillations (and, therefore, similar CSRs). It can be observed that similar reductions of normalised secant shear stiffness with strain amplitude were obtained for both tests, suggesting that the influence of the void ratio on this aspect of cyclic sand response is negligible, as reported in the literature (e.g. Darendeli, 2001). With respect to the evolution of ξ with $\varepsilon_{a,sa}$, it can be observed that the magnitudes of ξ obtained during the early stages of test ICUCT 0.832/80/42 (particularly for the second and third loading cycles) are similar to those obtained for test ICUCT 0.651/80/43 (for values of $\varepsilon_{a,sa}$ of about 0.1 %). At larger strains, larger peak values are mobilised in the later stages of the former test, conducted on the looser sample. Note, however, that this might arise from the inappropriateness of using viscous damping concepts to describe the cyclic response of sand under such large strains (as discussed before). In fact, the void ratio has been generally reported to have a very limited impact on the damping ratio of sand (e.g. Darendeli, 2001). Therefore, the results presented herein need to be considered carefully and further testing would be advisable.

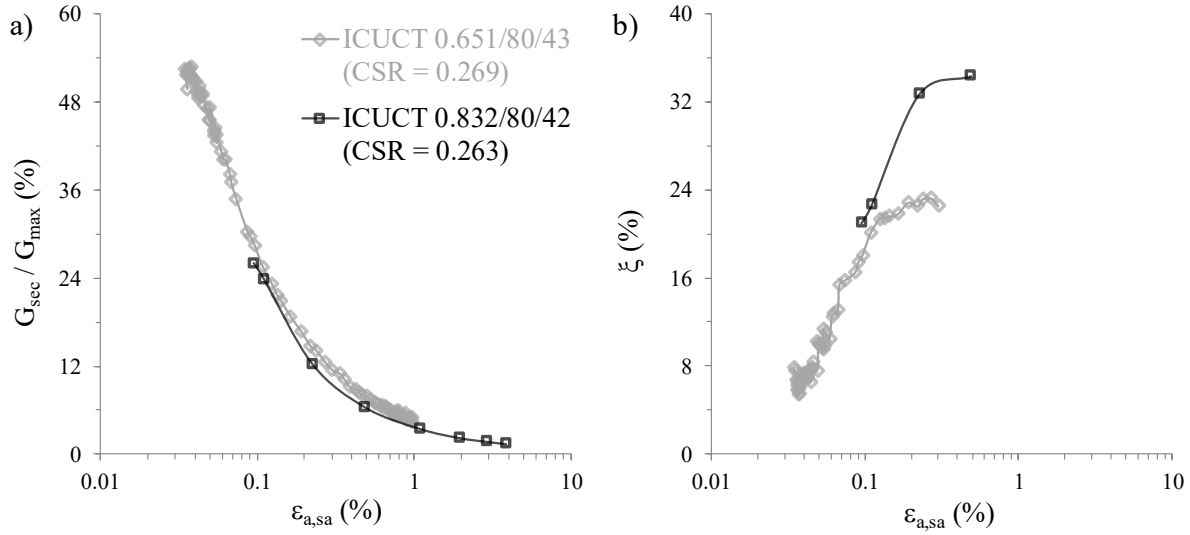

Figure 3.22 – Impact of the void ratio on the evolution of: (a) normalised secant shear modulus and (b) damping ratio with single amplitude axial strain.

In conclusion, among the aspects analysed, it seems that the evolution of both G_{sec} / G_{max} and ξ with $\varepsilon_{a,sa}$ is considerably affected by the mean effective stress at consolidation. The influence of the void ratio on these aspects of the cyclic response of sand seems to be negligible.

3.5.3.5 Comparison with curves proposed in the literature for sand

Figure 3.23 compares the G_{sec} / G_{max} and ξ data points inferred from the results of tests ICUCT 0.771/80/32, ICUCT 0.832/80/42 and ICUCT 0.651/80/43 with reference curves proposed in the literature for sand (Seed and Idriss, 1970b; Ishibashi and Zhang, 1993; Darendeli, 2001). Note that, in this case, the evolutions of both G_{sec} / G_{max} and ξ are presented as a function of single amplitude shear strain, γ, rather than single amplitude axial strain, $\varepsilon_{a,sa}$, as in the previous section. Note also that, for completeness, the lower, mean and upper bounds proposed by Seed and Idriss (1970b) are shown in the figure.

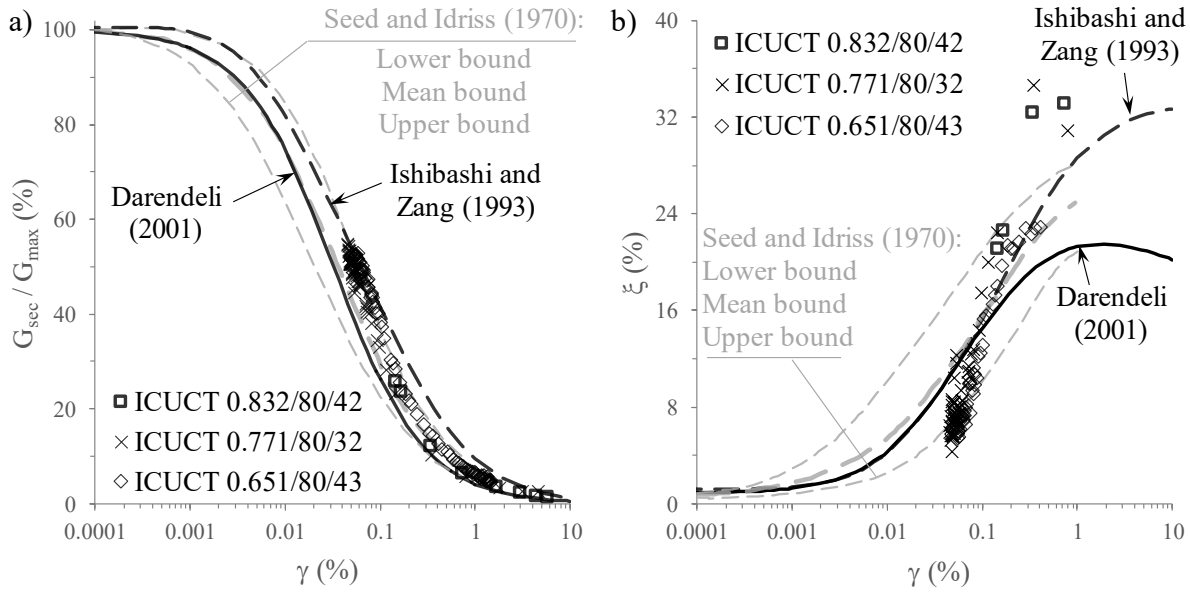

Figure 3.23 – Evolution of: (a) normalised secant shear modulus and (b) damping ratio with single amplitude shear strain inferred from UCT tests performed on samples consolidated to $p' = 80$ kPa. Comparison with curves proposed in the literature.

It is interesting to observe that, despite the fact that the mean effective stress, p', varies significantly in each cycle under undrained shearing and, consequently, G_{max} is also expected to vary in each cycle, as defined by Equation 3.9, G_{sec} / G_{max} – γ data points obtained from the present laboratory testing plot very close to the curves proposed in the literature. In terms of ξ – γ data points, the agreement is less satisfactory, particularly at large shear strains (close to 1 %), likely due to the "S-shaping" of the stress-strain curve, as explained before. Other aspects, such as the large plasticity induced in this type of tests from the start of loading and the fact that the strain rate was not kept constant during the test (as described in Section 3.3.2), might have also contributed to the less satisfactory agreement. Moreover, it is important to highlight that the curves proposed in the literature have been, in general, established based on wave measurements and data from strain -controlled element

laboratory tests (cyclic triaxial, cyclic simple shear and cyclic torsional shear tests) under drained conditions.

3.5.4 Excess pore water pressure build-up with cyclic loading

3.5.4.1 General aspects

When studying liquefaction-related phenomena, one of the fundamental aspects requiring proper characterisation is the generation of excess pore water pressure with cyclic loading, which affects the effective stresses and, consequently, the stiffness and resistance of sand. For convenience, it is usual to normalise the excess pore water pressure, Δu, by the vertical effective stress before the start of cyclic loading, $\sigma'_{v,0}$, which is commonly defined as the excess pore water pressure ratio, $r_u = \Delta u / \sigma'_{v,0}$, (Ishihara, 1996).

One of the first attempts to characterise the evolution of r_u with cyclic loading was performed by Seed *et al.* (1975b). Based on results of cyclic triaxial tests reported by Lee and Albaisa (1974), as well as results of simple shear tests reported by De Alba *et al.* (1975), Seed *et al.* (1975b) observed that the rate of excess pore water pressure build-up generally falls within a narrow band when plotted as a function of normalised number of loading cycles (i.e. ratio of the number of loading cycles to that required to the onset of cyclic mobility, N / N_{liq}), as illustrated in Figure 3.24.

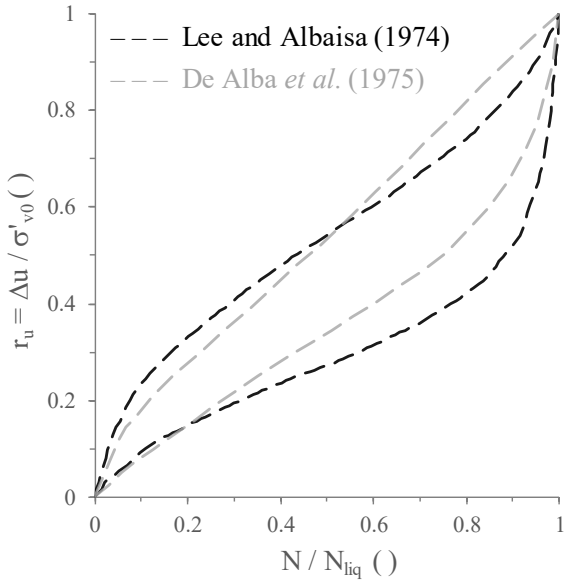

Figure 3.24 – Bounds of excess pore water pressure ratio build-up as a function of the normalised number of loading cycles obtained from cyclic triaxial tests (Lee and Albaisa, 1974) and from cyclic simple shear tests (De Alba *et al.*, 1975).

To describe the observed experimental trends, Seed *et al.* (1975b) proposed Equation 3.12.

$$r_u = \frac{1}{2} + \frac{1}{\pi}\, asin\left(2\left(\frac{N}{N_{liq}}\right)^{1/\alpha} - 1\right) \tag{3.12}$$

where α is a parameter, for which a value of 0.70 was found to provide an average value of the upper and lower bounds of the element laboratory test results by the authors.

This expression was later altered by Booker *et al.* (1976), as given by Equation 3.13.

$$r_u = \frac{2}{\pi} asin\left(\frac{N}{N_{liq}}\right)^{1/2\alpha} \tag{3.13}$$

As pointed out by Polito *et al.* (2008) and Taborda (2011), although the presence of N_{liq} in Equations 3.12 and 3.13 enable to include the effect of important factors on the evolution of r_u, such as the effect of the void ratio, initial effective stress state and magnitude of cyclic loading (as discussed before), it may result in some ambiguities. For instance, it has been observed that, for sands with plastic fines, the excess pore water pressure may stop increasing when values of r_u close to 0.9 are reached, even if very large deformations are measured (Ishihara, 1996). Similarly, for dense and very dense sands, large values of r_u (close to 1.0), as well as of $\varepsilon_{a,da}$, may not be observed (or require a very large number of loading cycles), particularly when samples are consolidated under small confining stresses. This suggests that it may be difficult to use a single criterion to define N_{liq} for different materials, and, therefore, to establish equations which may represent accurately the evolution of r_u with N for different materials. In addition, it should be noted that, since data used to derive Equations 3.12 and 3.13 were obtained from laboratory tests using uniform loading conditions and it has been shown that the response of sand is highly dependent on the stress path, the range of application of these equations for non-uniform loading histories may be severely restricted. This topic is discussed in Azeiteiro *et al.* (2017b).

To overcome these difficulties, several studies have attempted to characterise the evolution of excess pore water pressure as a function of the accumulation of energy dissipated per unit volume of soil, denoted as ΔW. In effect, since both shear stress and strain are employed in the estimation of the energy dissipated per unit volume of soil (Equation 3.6), this quantity seems to be independent of the stress path imposed to the soil, as experimentally observed in element laboratory tests (Towhata and Ishihara, 1985; Figueroa *et al.*, 1994; Liang *et al.*, 1995; Baziar and Sharafi, 2011; Kokusho, 2013; Polito *et al.*, 2013; Azeiteiro *et al.*, 2017b), as well as centrifuge experiments (Dief and Figueroa, 2007). It seems, therefore, possible to predict the generation of excess pore water pressure without the need for converting the earthquake-induced irregular shear stress (or strain) time histories into an equivalent uniform loading.

One of the first mathematical models proposed to describe the evolution of the excess pore water pressure ratio, r_u, with the accumulation of dissipated energy per unit volume, ΔW, was proposed by Nemat-Nasser and Shokooh (1979) – Equation 3.14 – in their comprehensive paper on the interrelation between both densification and liquefaction with the

rearrangement of grains in microscale and, therefore, dissipation of energy. Note that, in this equation, α, β and χ are model parameters, while K_w is the bulk modulus of the water.

$$r_u = \left(\frac{1 - \Delta W\,(e_0 - e_{max})^{\beta})}{\frac{\chi}{(\alpha - 1)} K_w\, e_0} \right)^{1/(1-\alpha)} - 1 \tag{3.14}$$

A much simpler power law-type equation was later proposed by Berrill and Davis (1985), when introducing an empirical energy-based approach to evaluate liquefaction potential:

$$r_u = \alpha \left(\frac{\Delta W}{\sigma'_0} \right)^{\beta} \tag{3.15}$$

where α and β are model parameters and σ'_0 is the isotropic effective stress at consolidation (note that nothing is mentioned by the authors about how to account for an anisotropic consolidation stress state).

Note that similar equations relating r_u to $\Delta W/\sigma'_0$ or ΔW were proposed by many other authors (e.g. Yamazaki *et al.*, 1985; Law *et al.*, 1990; Figueroa *et al.*, 1994; Liang *et al.*, 1995; Davis and Berrill, 2001; Polito *et al.*, 2008; Kokusho, 2013). However, in most cases, additional dependencies of the model parameters α and β on the relative density, effective stresses at consolidation and cyclic stress ratio were introduced to improve the replication of the laboratory results.

At this point, it is perhaps important to note that the main purpose of the present study is presenting data obtained from the performed undrained cyclic triaxial tests and, based on the available data, assessing the dependency of the relationship between r_u and N / N_{liq}, as well as r_u and $\Delta W/\sigma'_0$ on void ratio, mean effective stress and applied stress ratio. The intention is neither to evaluate the most accurate expressions proposed in the literature nor to propose new expressions. With such objective, a larger amount of experimental data would likely be required.

Moreover, it should be highlighted that, as proposed in several studies (e.g. Towhata and Ishihara, 1985; Law *et al.*, 1990; Figueroa *et al.*, 1994; Kokusho, 2013; Azeiteiro *et al.*, 2017b), rather than r_u, its residual component, $r_{u,res} = \Delta u_{res}/\sigma'_{v,0}$, is considered in the present study. As mentioned before, this component corresponds to the excess pore water pressure when no deviatoric loading is applied (i.e. $q = 0$) and, therefore, reflect the permanent alterations to the effective stresses acting in the soil (Dobry *et al.*, 1982; Law *et al.*, 1990; Polito *et al.*, 2008). Conversely, the other component of r_u (typically termed as "transitory") reflects the changes in the mean total stress during dynamic loading (Polito *et al.*, 2008) and, therefore, is considered less important. As illustrated in Figure 3.25, non-monotonic evolution of $r_{u,res}$ with N is obtained once the phase transformation (PT) line (Ishihara *et al.*, 1975) is firstly crossed. In particular, it can be observed that, once it occurs, larger values of $r_{u,res}$ are consistently measured at the start of each loading cycle (i.e. when starting reloading in triaxial

compression) than at the middle of the middle of each loading cycle (i.e. when starting reloading in triaxial extension). To smooth the variation of $r_{u,res}$ values during this stage and, consequently, to ease the comparison between data obtained from different tests, it was decided to use average values of $r_{u,res}$ for each loading cycle – denoted henceforth as $r_{u,res,av}$ and represented in the figure by solid black squares. Note that this strategy has been used in other studies reported in the literature (e.g. Simcock *et al.*, 1983) and does not seem to affect the trends exhibited by the experimental results.

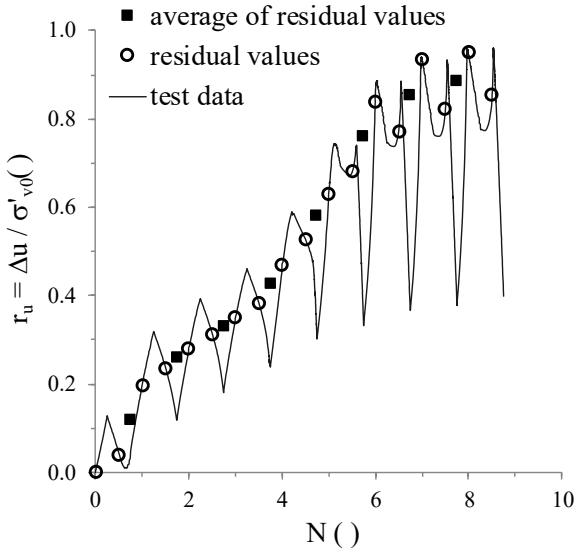

Figure 3.25 – Illustration of the computation of the average values of the residual excess pore water pressure ratio evolution with the number of loading cycles for test ICUCT 0.832/80/42.

3.5.4.2 Residual excess pore water pressure ratio evolution as a function of the normalised number of loading cycles

Figure 3.26a compares the evolution of $r_{u,res,av}$ with N / N_{liq} inferred from tests ICUCT 0.821/25/13, ICUCT 0.832/80/42 and ICUCT 0.793/135/67.5, where samples prepared to similar void ratios ($e = 0.793 - 0.832$) were consolidated to different isotropic confining stresses, respectively: $\sigma'_0 = 25$, 80 and 135 kPa. Complementary, Figure 3.26b depicts $r_{u,res,av} - N / N_{liq}$ data obtained from tests ICUCT 0.832/80/42 and ICUCT 0.651/80/43, respectively performed on a moderately loose and on a dense sample, both of them consolidated to $\sigma'_0 = 80$ kPa. Note that similar cyclic stress ratios ($CSR = |\Delta q| / \left(2\, p'_0\right) \approx 0.250 - 0.269$) were used in all these tests (Table 3.1). Note also that, to provide a reference, Equation 3.12 proposed by Seed *et al.* (1975b) is plotted in the figure with $\alpha = 0.90$ (which provides the best possible approximation of the available experimental data). It can be seen that the evolutions of $r_{u,res,av}$ with N / N_{liq} obtained from these tests do not differ much from each other, regardless of the mean effective stress at consolidation and void ratio of the samples. Furthermore, Equation 3.12 proposed by Seed *et al.* (1975b) seems to describe reasonably well the experimental data (particularly during the early stages of loading). This suggests that the normalisation of N by N_{liq} produces the desired objective of obtaining an

equation independent of both isotropic effective stress and void ratio at consolidation, as also observed by Polito *et al.* (2008) and Taborda (2011).

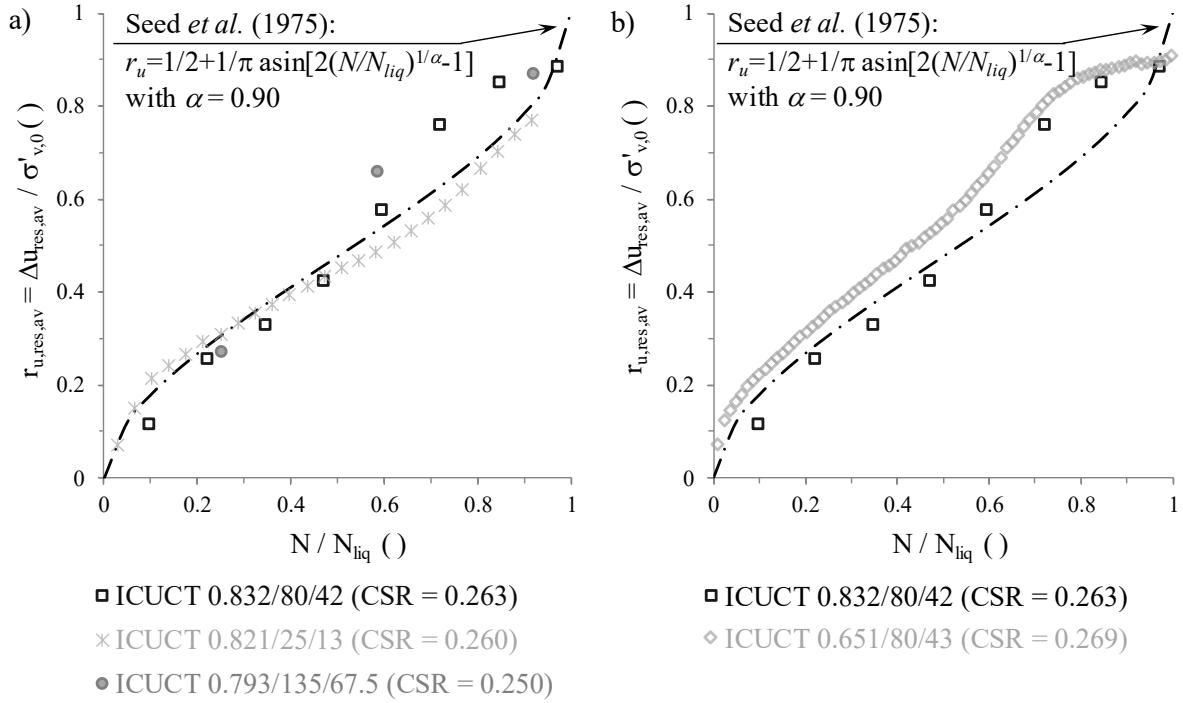

Figure 3.26 –Influence of (a) the isotropic effective stress at consolidation and of (b) the void ratio on the evolution of the average residual excess pore water pressure ratio with the normalised number of loading cycles inferred from ICUCT test results.

In addition, Figure 3.27a compares $r_{u,res,av} - N / N_{liq}$ data inferred from three UCT tests performed on moderately loose samples ($e = 0.771 - 0.832$), which were isotropically consolidated to $\sigma'_0 = 80$ kPa and, subsequently, sheared under different cyclic stress ratios: $CSR \approx 0.200$ for test ICUCT 0.771/80/32, $CSR \approx 0.225$ for test ICUCT 0.803/80/36 and $CSR \approx 0.263$ for test ICUCT 0.832/80/42. Complementary, Figure 3.27b depicts the results inferred from three other UCT tests conducted on dense samples ($e = 0.651 - 0.652$), also consolidated to $\sigma'_0 = 80$ kPa and sheared under different cyclic stress ratios. Note that, in this second series of tests, larger cyclic stress ratios were imposed, namely: $CSR \approx 0.269$ for test ICUCT 0.651/80/43, $CSR \approx 0.450$ for test ICUCT 0.652/80/72 and $CSR \approx 0.550$ for test ICUCT 0.652/80/88. By observing both figures, it is apparent that very different $r_{u,res,av} - N / N_{liq}$ curves were obtained for all tests, suggesting that the evolution of $r_{u,res,av}$ with N / N_{liq} is strongly dependent on the CSR imposed in each test. In general, it seems that the higher the cyclic stress ratio, the larger the rate of $r_{u,res,av}$ increase with N / N_{liq} during the early stages of loading, while the opposite trend appears to be observed when cyclic mobility approaches (i.e. when N / N_{liq} approaches 1.0). This aspect can be more clearly observed in Figure 3.27b than in Figure 3.27a, possibly due to the greater differences in terms of cyclic stress ratios applied to the dense samples (within the range of 0.269 to 0.550, as mentioned before). Indeed, it seems evident that it is not possible to describe accurately the evolution of $r_{u,res,av}$

with N / N_{liq} inferred from all tests using Equation 3.12 Seed *et al.* (1975b) with a single value for α. This aspect is illustrated in both figures by plotting Equation 3.12 with $\alpha = 0.90$.

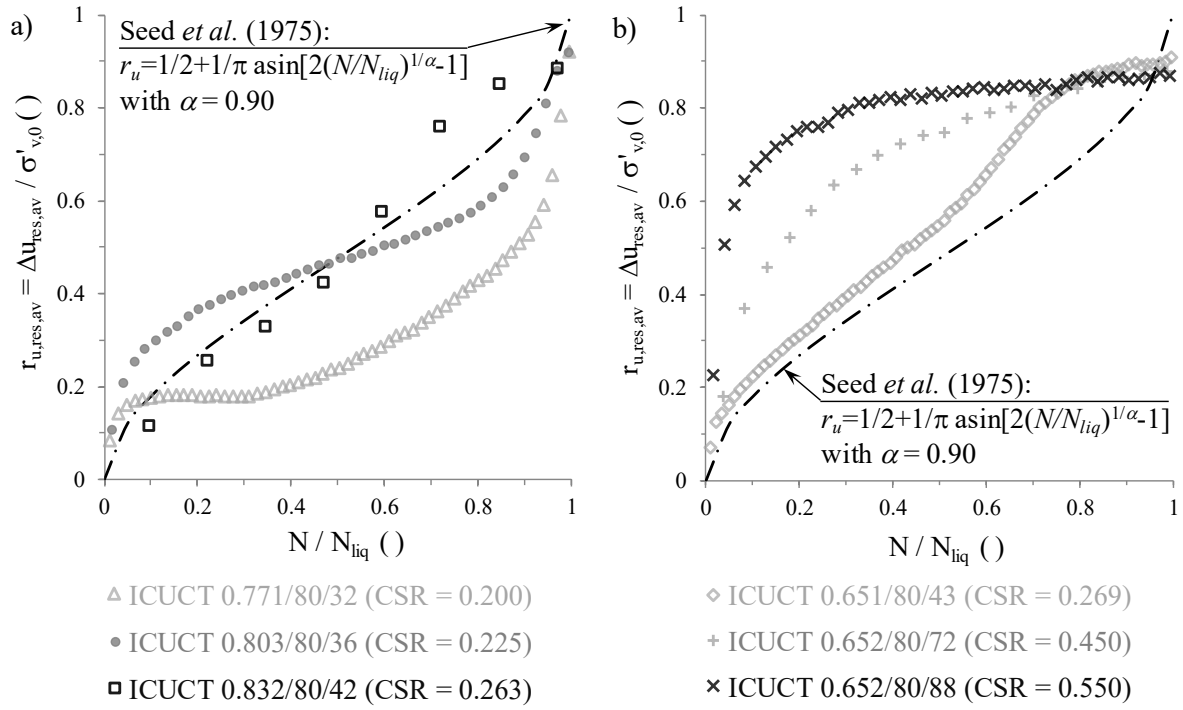

Figure 3.27 – Influence of the applied cyclic stress ratio on the evolution of the average residual excess pore water pressure ratio with the normalised number of loading inferred from ICUCT test results performed on a) moderately loose and b) dense samples consolidated to $\sigma'_0 = 80$ kPa.

Similar conclusions are obtained when analysing $r_{u,res,av} - N$ / N_{liq} data obtained from UCT tests conducted on samples prepared to similar void ratios ($e = 0.777 - 0.830$) and isotropically consolidated to 25 kPa and 135 kPa, respectively shown in Figure 3.28a and b. This is particular evident when comparing results obtained for tests having larger differences in terms of applied cyclic stress ratios (i.e. results of test ICUCT 0.821/25/13 with those of test ICUCT 0.777/25/18 and results of test ICUCT 0.805/135/40 with those of test ICUCT 0.793/135/67.5). Once again, it is apparent that Equation 3.12 (Seed *et al.*, 1975b) when used with a single value for α is not able to describe accurately the available experimental data.

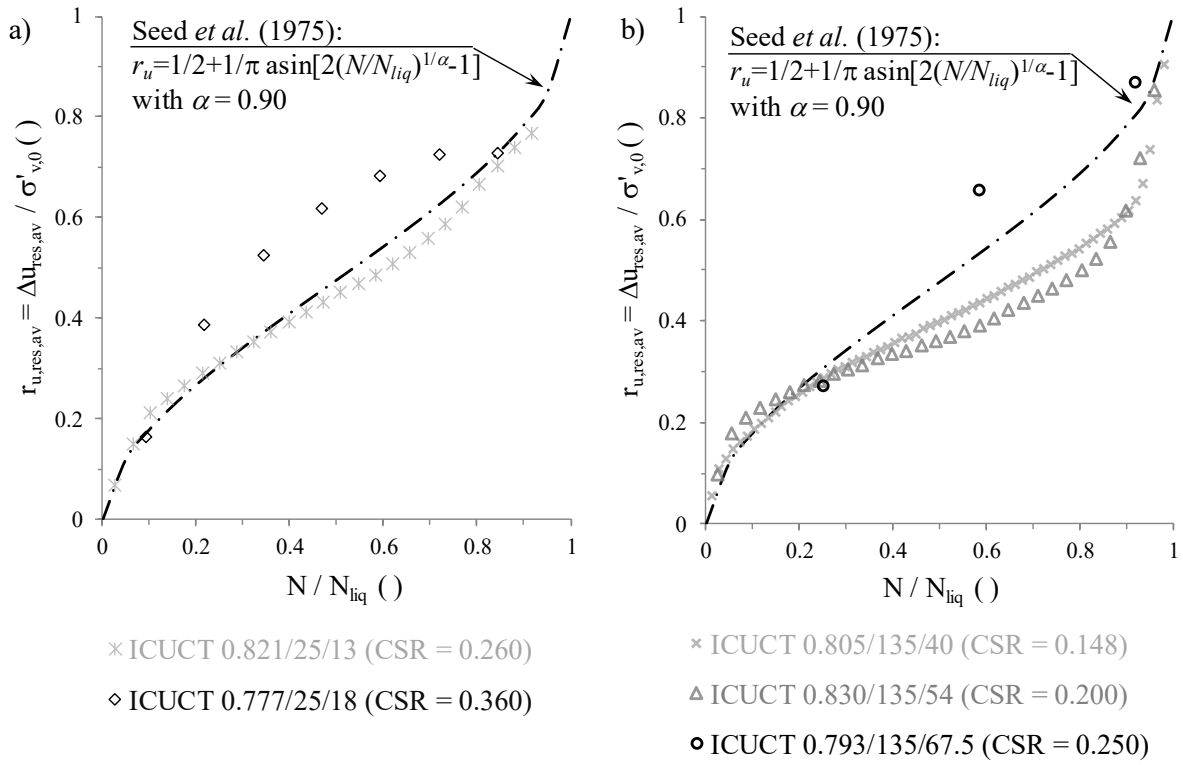

Figure 3.28 – Influence of the applied cyclic stress ratio on the evolution of the average residual excess pore water pressure ratio with the normalised number of loading cycles inferred from ICUCT tests performed on moderately loose samples consolidated to: a) σ'_0 = 25 kPa and b) σ'_0 = 135 kPa.

3.5.4.3 Residual excess pore water pressure ratio evolution as a function of the energy dissipated per unit volume

Having applied the methodology described in Section 3.5.3.2, the accumulation of dissipated energy per unit volume, ΔW, during cyclic loading was estimated from the stress-strain histories measured in the laboratory. The obtained values were, subsequently, normalised by the isotropic effective stress at consolidation, σ'_0, and plotted against $r_{u,res,av}$. Starting by analysing the effect of the isotropic stress at consolidation and void ratio of the samples on the relationship of $r_{u,res,av} - \Delta W/\sigma'_0$, Figure 3.29 shows that this relationship seems to be practically independent of the initial state of the soil. Therefore, a single curve, in this case computed from Equation 3.15 (Berrill and Davis, 1985), appears to describe reasonably well the available experimental data. Similar findings were reported by Kokusho (2013) when examining results of stress-reversal-controlled undrained cyclic triaxial tests conducted on moist-tamped Futtsu beach sand samples prepared to three different initial relative densities (30, 50 and 70%).

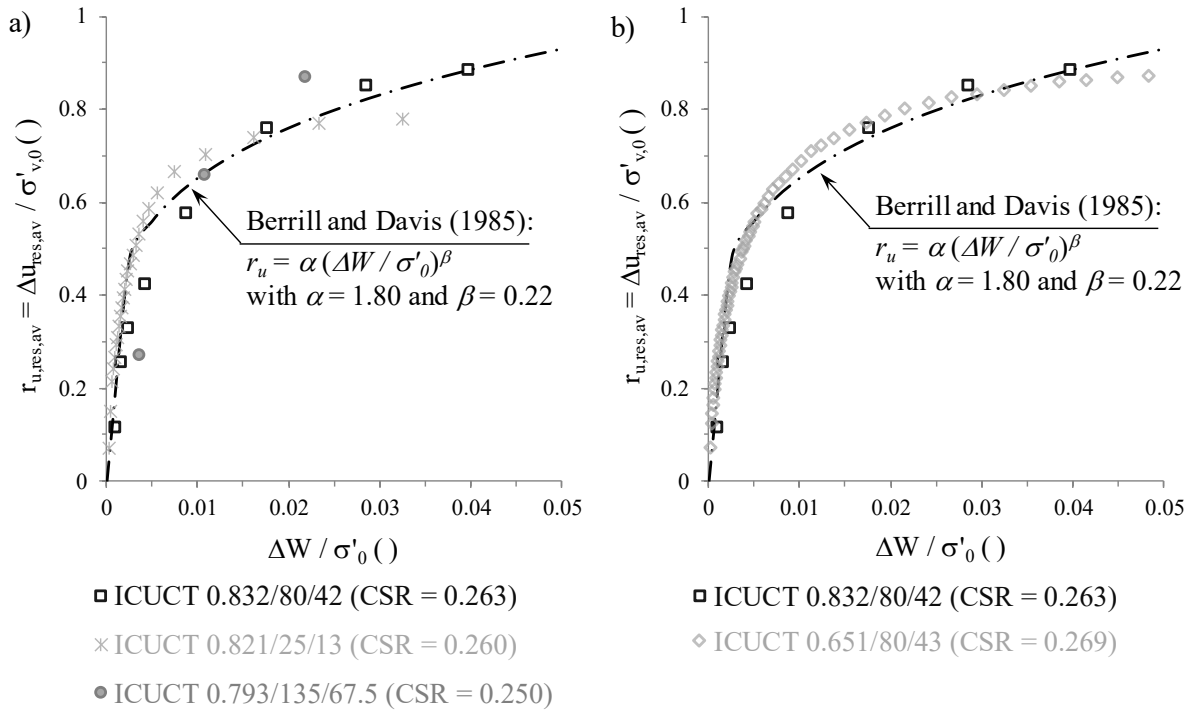

Figure 3.29 – Influence of (a) the isotropic effective stress at consolidation and of (b) the void ratio on the evolution of the average residual excess pore water pressure ratio with the normalised accumulation of dissipated energy per unit volume inferred from ICUCT test results.

Conversely, as shown in Figure 3.30 and , it seems that the CSR applied in each test has a considerable influence on the obtained evolution of $r_{u,res,av}$ with $\Delta W/\sigma'_0$. In particular, it seems that the larger the stress ratio, the smaller the rate of $r_{u,res}$ generation with $\Delta W/\sigma'_0$. Consequently, the experimental data cannot be accurately described by a single curve, as also illustrated in the figure. Similar observations are obtained when inspecting the results of tests where samples were isotropically consolidated to 25 kPa and 135 kPa (not shown here for brevity). As suggested in the literature (e.g. Figueroa *et al.*, 1994), a better description of the results would likely be obtained by making one of the model parameters dependent on CSR.

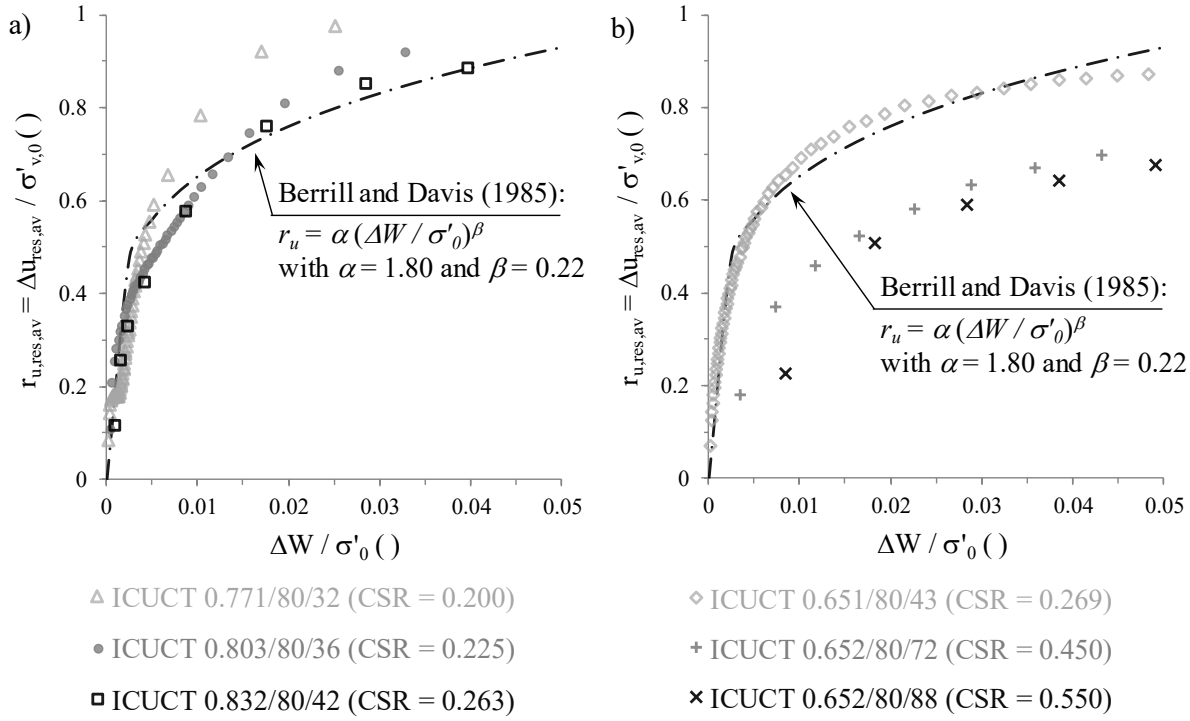

Figure 3.30 – Influence of the applied cyclic stress ratio on the evolution of the average residual excess pore water pressure ratio with the normalised accumulation of dissipated energy per unit volume inferred from ICUCT test results performed on a) moderately loose and b) dense samples consolidated to σ'_0 = 80 kPa.

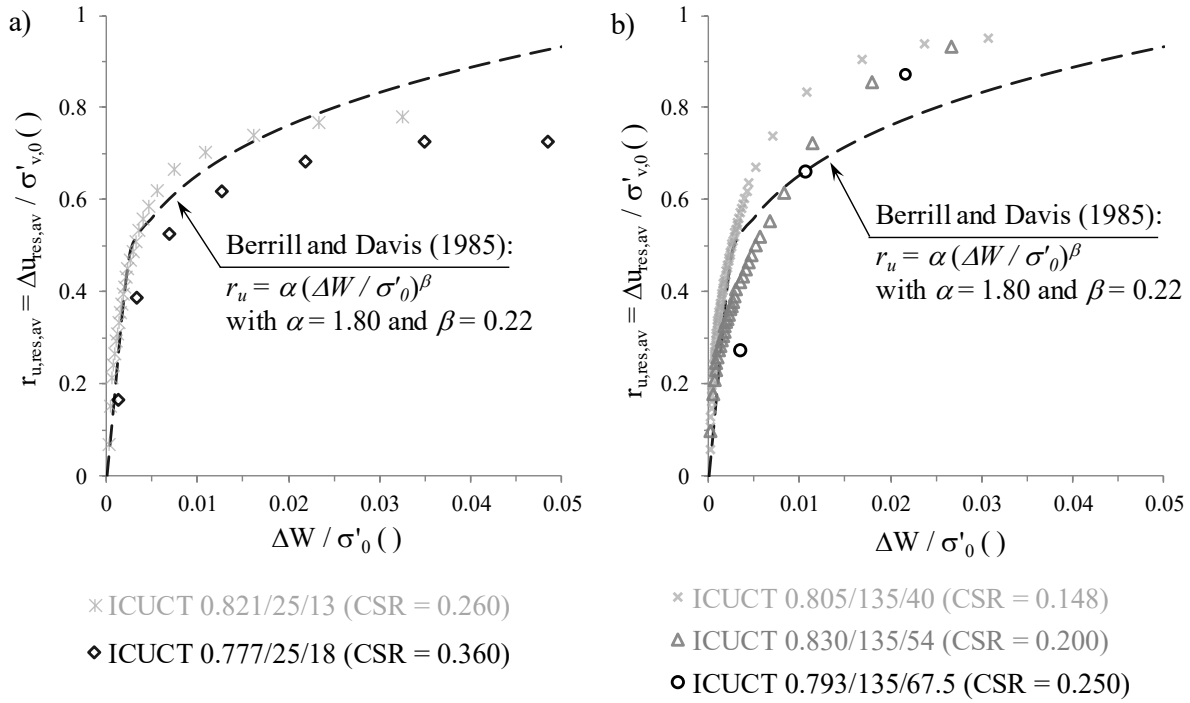

Figure 3.31 – Influence of the applied cyclic stress ratio on the evolution of the average residual excess pore water pressure ratio with the normalised accumulation of dissipated energy per unit volume inferred from ICUCT test results performed on moderately loose samples consolidated to: a) σ'_0 = 25 kPa and b) σ'_0 = 135 kPa.

3.6 Drained cyclic response

Three drained cyclic triaxial (DCT) tests were performed on moderately loose samples of Hostun sand ($e = 0.773 - 0.820$), with the main objective of obtaining experimental data relevant to the characterisation of the ability of the constitutive model to replicate the volumetric strain response of Hostun sand under drained cyclic loading. In two of these tests, the loading reversals were controlled by maximum and minimum values of the deviatoric stress, namely a deviatoric stress oscillation of $\Delta q = \pm 81$ kPa was specified for test ICDCT 0.820/135/81 test, while $\Delta q = \pm 30$ kPa was used for test K0CDCT 0.811/80/30 (which implied that, in this test, q was varied in between 60 and 90 kPa). Both tests were stopped when 10 loading cycles were completed. Conversely, in the third test, identified as test ICDCT 0.773/80/1, an axial strain oscillation of $\Delta \varepsilon_a = \pm 1.0$ % was imposed, with 100 loading cycles being applied.

The results of tests K0CDCT 0.811/80/30 and ICDCT 0.820/135/81 tests are shown in Figure 3.32. Note that, in the former test, the sample was anisotropically consolidated to an axial effective stress of $\sigma'_{a,0} = 120$ kPa and a radial effective stress of $\sigma'_{r,0} = 60$ kPa, which correspond to a mean effective stress of $p'_0 = 80$ kPa and a deviatoric stress of $q_0 = 60$ kPa. Conversely, in the latter test, the sample was consolidated under an isotropic confining stress state characterised by $p'_0 = 135$ kPa. It can be seen that, in both tests, a much larger axial and contractive volumetric strain accumulation was measured during the first loading cycle than during the remaining ones. Moreover, in the case of test ICDCT 0.820/135/81, where two-way symmetric deviatoric loading conditions were applied, the accumulation of both axial and volumetric strains during the first loading cycle in triaxial extension are significantly greater than those measured in triaxial compression. These aspects seem to agree well with the experimental observations under undrained conditions, where larger excess pore water pressures and, consequently, larger mean effective stress reductions were typically measured during the first loading cycle, especially in triaxial extension, than during the subsequent loading cycles.

Furthermore, it is apparent that contractive volumetric strain accumulation with a progressive smaller rate was measured in test ICDCT 0.820/135/81 until the end of the 5th loading cycle. During the subsequent loading cycles, the volumetric strain practically stabilises or reduces slightly. This aspect is particularly evident in Figure 3.32d, which depicts the evolution of the residual volumetric strain (i.e. the volumetric strain corresponding to a null deviatoric stress) with the number of loading cycles. Similar experimental observations were reported by López-Querol and Coop (2012) when testing air-pluviated Dogs Bay sand. With respect to the axial strains, after reaching a double amplitude axial strain of about $\varepsilon_{a,da} \approx 0.36\%$ during the first loading cycle, the axial strain accumulation seems to be slightly reduced during the subsequent loading cycles (Figure 3.32b).

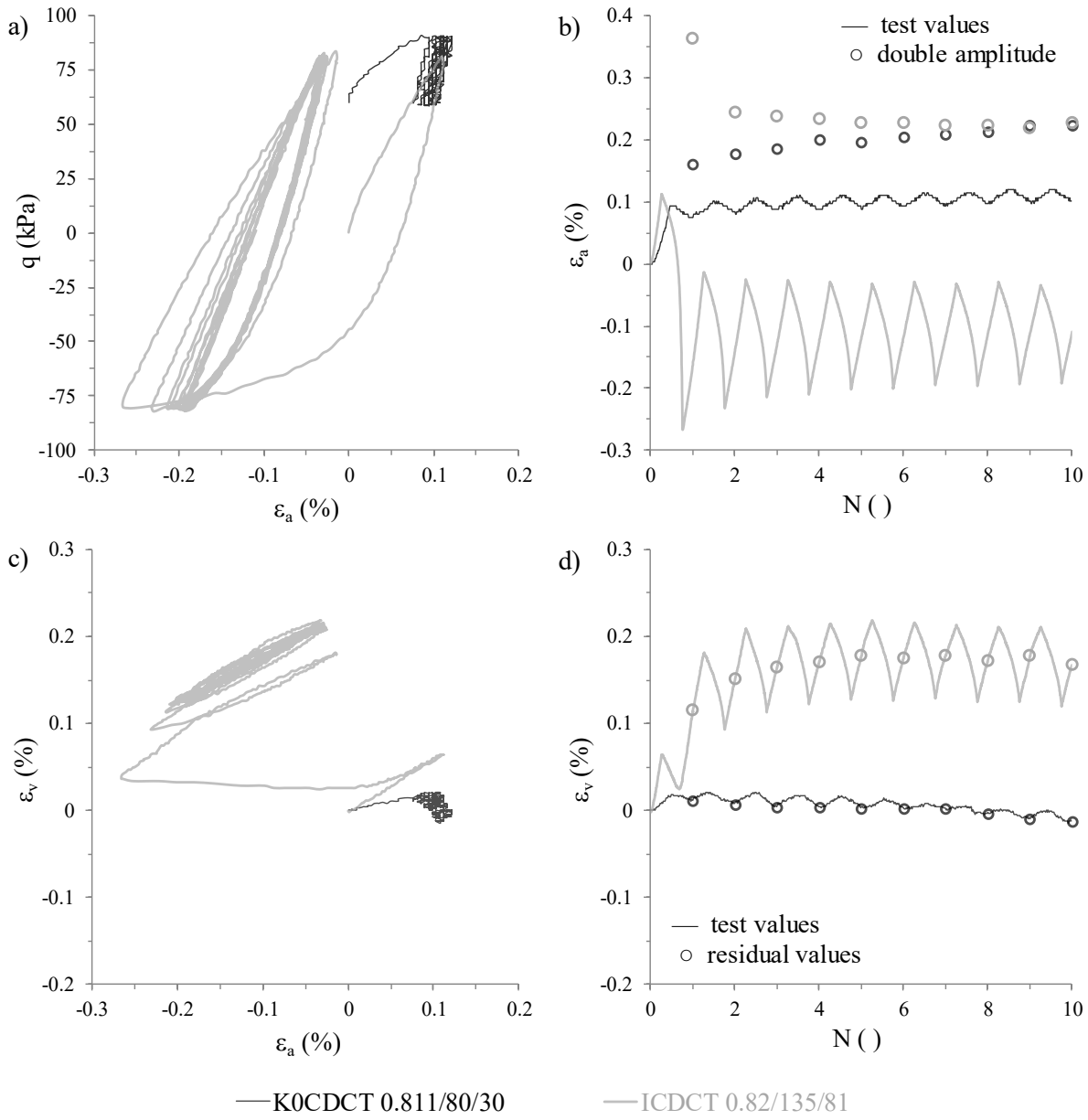

Figure 3.32 – Tests K0CDCT 0.811/80/30 and ICDCT 0.820/135/81: (a) stress-strain response; (b) axial strain evolution with the number of loading cycles; (c) volumetric strain evolution with the axial strain; and (d) volumetric strain evolution with the number of loading cycles.

Regarding test K0CDCT 0.811/80/30, due to the application of a large initial deviatoric stress and one-way cyclic loading in triaxial compression, the response seems to be characterised by different patterns from that observed in test ICDCT 0.820/135/81. In particular, it can be observed that, as expected, the response is much softer during the first quarter of the first loading cycle (i.e. during primary loading in triaxial compression), than during the remaining part of the test, simply characterised by a set of unloading and reloading cycles. Consequently, a larger accumulation of axial strains occurs during the first loading cycle than during the remaining loading cycles.

In addition, Figure 3.33 presents the results obtained for test ICDCT 0.773/80/1, where an axial strain oscillation of ±1.0 % was imposed during 100 loading cycles. It is interesting to

observe that the response in triaxial extension is much softer than that in triaxial compression. More specifically, it can be seen that, while the maximum deviatoric stress measured in triaxial compression reaches 184 kPa during the first loading, gradually increasing up to 313 kPa during the subsequent loading cycles, the deviatoric stress in triaxial extension never reaches a value smaller than -58 kPa. This strong anisotropic soil response has also been observed under undrained conditions, being particularly evident in tests ICUCT 0.804/80/48, ICUCT 0.773/80/56 and ICUCT 0.793/135/67.5, where cyclic mobility was triggered in few loading cycles after a very strong reduction of effective mean stress in triaxial extension (Figure 3.5 and Figure 3.6).

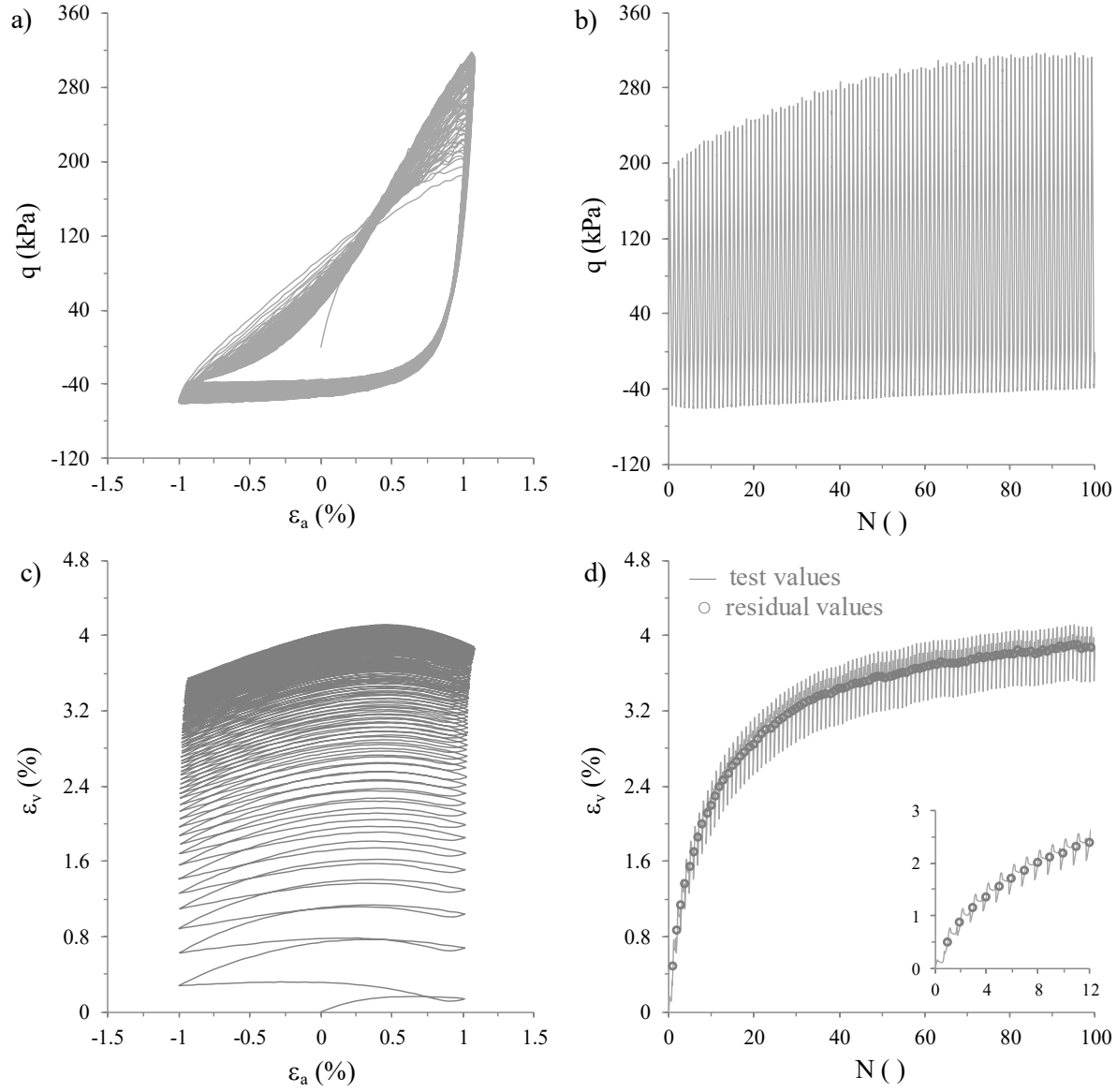

Figure 3.33 – Test ICDCT 0.773/80/1: (a) stress-strain response; (b) deviatoric stress evolution with the number of loading cycles; (c) volumetric strain evolution with the axial strain; and (d) volumetric strain evolution with the number of loading cycles.

Moreover, similar to the previous DCT tests, the volumetric strain accumulation registered during the first loading cycle is larger than during the remaining ones. However, in this case,

two different aspects of the volumetric strain response can be observed: (1) the sample exhibits a monotonic increase in the residual volumetric strain and (2) a double frequency phenomenon (similar to that observed for the excess pore water pressure when samples approach cyclic mobility) is observed for volumetric strain (which is particularly evident in the detail of Figure 3.33d). In relation to the former aspect, a plausible explanation resides on the fact that the shear reversals were governed by reaching 1 % of axial strain, rather than by a given value of deviatoric stress, implying a gradual increase in deviatoric stress oscillation (and, therefore, in mean effective stress oscillation) with loading. With respect to the double frequency phenomenon of the volumetric strains, it is likely to occur as a result of the crossing of the phase transformation line, which defines the change from plastic contraction to plastic dilation. Figure 3.34 seems to confirm this aspect, with test ICDCT 0.773/80/1 test being the only one where the phase transformation state line appears to be crossed. Note that, although both the phase transformation state (PTS) and the peak stress ratio state (PSRS) lines depicted in Figure 3.34 were characterised based on monotonic test data (Sections 2.6.5.2 and 2.6.5.3), they should retain their validity for cyclic loading.

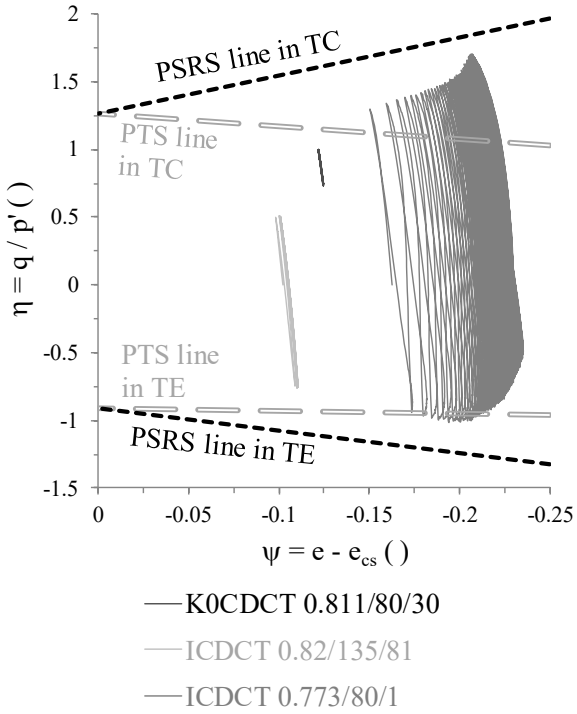

Figure 3.34 – Drained cyclic triaxial tests: stress ratio as a function of the state parameter.

3.7 Summary and conclusions

A series of drained and undrained cyclic triaxial tests were used to investigate the cyclic response of air-pluviated Hostun sand. Samples were prepared to different initial void ratios, consolidated under various effective stress states and sheared using different deviatoric stress amplitudes to characterise the effect of these aspects on the cyclic response of Hostun sand. Particular focus was given to the response under undrained conditions, due to its

relevance to the characterisation of main features of sand observed in liquefaction-related phenomena, such as the generation of excess pore water pressure with cyclic loading, the consequent reduction in stiffness and increase in hysteretic damping, the occurrence of phase transformation and the onset of cyclic mobility. Complementary, a set of three drained cyclic triaxial tests was used to inspect some aspects of the volumetric strain response of Hostun sand under drained cyclic loading and to provide additional valuable data for model calibration.

The results of undrained cyclic triaxial (UCT) tests confirmed that air-pluviated Hostun sand (having the physical characteristics identified in the present laboratory testing programme) is effectively susceptible to cyclic mobility. Specifically, it was observed that, irrespective of the relative density, initial effective stress state and applied cyclic stress ratio, all samples exhibited a more or less pronounced tendency to generate excess pore water pressure when subjected to undrained cyclic shearing, resulting in a progressive reduction of the mean effective stress in each cycle, as well as significant softening of their stress-strain response. Eventually, effective stresses close to zero were reached in all tests, leading to a degraded stress-strain response, with large strain accumulation being measured. Moreover, as suggested in previous investigations on the undrained cyclic response of sand (Ishihara *et al.*, 1975; Nemat-Nasser and Tobita, 1982; Papadimitriou *et al.*, 2001), the experimental results suggest that the response of sand is significantly affected by the first crossing of the phase transformation (PT) line and subsequent loading reversal. Once it occurs, a more compliant response of Hostun sand (i.e. a greater reduction in mean effective stress than that measured in the previous loading cycles) is typically observed.

In addition, due to the relatively large number of laboratory tests performed, it was possible to examine independently the effect of the initial void ratio, isotropic confining stress and cyclic stress ratio (CSR) on the undrained cyclic response of Hostun sand. As expected, it was concluded that the looser the sample, the higher the effective stress at consolidation and the higher the CSR applied, the greater the tendency to generate large excess pore water pressures in each loading cycle and, therefore, the lesser the number of loading cycles required to the onset of cyclic mobility. The accumulation of axial strains seems to be particularly affected by the void ratio of the samples, with a higher rate of accumulation of double amplitude axial strains being observed for looser samples.

Subsequently, important aspects of the undrained cyclic response of sand were characterised, including the evolution of excess pore water pressure with cyclic loading, the reduction in secant shear stiffness and concurrent increase in damping ratio with strain amplitude, as well as the undrained cyclic resistance. Particular emphasis was given to the characterisation of the impact of the initial void ratio, isotropic confining stress and cyclic stress ratio on these aspects of the cyclic response. Starting with the undrained cyclic resistance, the impact of using different criteria to define the onset of cyclic mobility proposed in the literature was

firstly assessed. Based on the available experimental data, it was shown that similar undrained cyclic resistance curves – i.e. cyclic resistance ratio, CRR, – number of loading cycles to the onset of cyclic mobility, N_{liq}, curves – were obtained for moderately loose samples ($e = 0.771 - 0.832$) of Hostun sand when considering a double amplitude axial strain of 5 % or a residual excess pore water pressure ratio of 0.95. However, given the slow rate of axial strain accumulation observed in tests performed on dense samples ($e = 0.651 - 0.652$) of Hostun sand, the former criterion was not suitable for defining the onset of liquefaction in those tests. Therefore, it was decided to adopt the observation of a residual excess pore water pressure ratio of 0.95 as a cyclic mobility criterion. Having established that, the undrained cyclic resistance of Hostun sand was characterised. More specifically, undrained cyclic resistance curves were proposed for moderately loose Hostun sand samples consolidated under isotropic effective stresses of 25, 80 and 135 kPa, as well as for dense samples consolidated under isotropic effective stress of 80 kPa. As widely reported in the literature (Seed and Idriss, 1970a; Tatsuoka *et al.*, 1986c; Ishihara, 1996; Jefferies and Been, 2006; Idriss and Boulanger, 2006), the undrained cyclic resistance curve of dense Hostun sand plots above and is characterised by a steeper (average) slope than that of moderately loose Hostun sand. Moreover, the smaller the isotropic effective stress at consolidation, the greater the undrained cyclic resistance, meaning that the curve corresponding to moderately loose Hostun sand consolidated under an isotropic effective stress of 25 kPa, plots above the curve corresponding to 80 kPa and even more above than that corresponding to 135 kPa. Further insight into the undrained cyclic resistance of Hostun sand was provided by comparing the curves obtained in the present laboratory testing programme with those proposed in the literature for Ottawa sand (Shen *et al.*, 1978) and Toyoura sand (Toki *et al.*, 1986). It was shown that undrained cyclic resistance of Hostun sand appears to be greater than those exhibited by both Ottawa and Toyoura sands.

Subsequently, the evolution of the secant shear stiffness, normalised by the maximum (i.e. at very small strains) shear modulus, as well as of damping ratio with axial strain amplitude were examined. After describing the methodology used to compute these quantities for each stress-strain loop, the curves obtained from each test were compared. Starting with the normalised secant shear stiffness, it was observed that the void ratio has a minor influence on this aspect of cyclic response of Hostun sand. Conversely, the experimental data suggests that the mean effective stress at consolidation has an important effect on the stiffness degradation with strain. In particular, it was observed that the larger the effective mean stress at consolidation, the larger the secant shear modulus, for a given strain level. These findings seem to agree well with those obtained in previous studies on this topic (Seed and Idriss, 1970b; Vucetic and Dobry, 1991; Ishibashi and Zhang, 1993; Darendeli, 2001). With respect to the evolution of damping ratio with strain, the obtained results suggest that the relationship between these quantities is mainly affected by the mean effective stress under

which samples were consolidated, with larger values being mobilised for samples consolidated under smaller mean effective stresses.

The final aspect of the undrained cyclic response of Hostun sand studied was the evolution of the average residual excess pore water pressure ratio, $r_{u,res,av}$, with the normalised number of loading cycles, N / N_{liq}, as well as with the normalised energy dissipated per unit, $\Delta W/\sigma'_0$. In relation to the $r_{u,res,av} - N / N_{liq}$ relationship, it seems to be practically independent of the void ratio of the samples and isotropic effective stress at consolidation. However, a strong dependency on the CSR seems to exist. In particular, it was observed that, the larger CSR applied to the sample, the higher the rate of generation of $r_{u,res,av}$ during the early stages of loading, while the opposite trend appears to be observed as cyclic mobility approaches (i.e. as N / N_{liq} approaches 1.0). Similarly, the relationship between $r_{u,res,av}$ and $\Delta W/\sigma'_0$ seems to be practically independent of the void ratio and isotropic confining stress, though dependent on the CSR applied.

Lastly, the results of three drained cyclic triaxial tests on moderately loose samples of Hostun sand ($e = 0.773 - 0.820$) were used to investigate the volumetric strain response of Hostun sand under cyclic loading. As expected, samples exhibit a tendency to contract (i.e. to develop contractive volumetric strains) when subjected to cyclic loading. Moreover, it was observed that the volumetric strains measured during the first loading cycle were consistently larger than those registered during the subsequent loading cycles. In effect, a similar tendency was observed under undrained conditions, with samples tending to generate larger excess pore water pressures during the first loading cycle than during the subsequent ones. Interestingly, in one of the tests, the stress path seemed to cross temporarily the phase transformation line – as identified in the previous chapter – both in triaxial compression and triaxial extension, resulting in a double frequency phenomenon of volumetric strains. This resembled the pattern of the excess pore water pressure evolution with undrained cyclic loading, where a double frequency phenomenon was also observed after the crossing of the phase transformation line. Finally, the results of the drained cyclic triaxial tests seemed to indicate that the response of Hostun sand is significantly softer in triaxial extension than in triaxial compression, as also observed in undrained cyclic triaxial tests.

Chapter 4 A BOUNDING SURFACE PLASTICITY MODEL FOR SAND

4.1 Introduction

To simulate adequately the highly non-linear monotonic and cyclic responses of sand, several advanced elasto-plastic constitutive models have been proposed in the literature, such as those based on nested yield surfaces (e.g. Prévost, 1977; Yang and Elgamal, 2007), generalised plasticity (e.g. Pastor *et al*., 1990; Ling and Yang, 2006), and bounding surface plasticity (e.g. Manzari and Dafalias, 1997; Papadimitriou and Bouckovalas, 2002; Dafalias and Manzari, 2004; Dafalias *et al.*, 2004; Taiebat and Dafalias, 2008; Loukidis and Salgado, 2009; Taborda *et al.*, 2014; Woo and Salgado, 2015). In particular, the latter ones have known the greatest development in recent years (Taborda, 2011).

Bounding surface plasticity was first developed for metal plasticity (Dafalias and Popov, 1975; Krieg, 1975), being later introduced to soil mechanics by Mróz *et al.* (1979) and Dafalias (1986). While retaining the basic elements of classical plasticity (such as a conventional yield surface, a plastic potential function and hardening/softening rules), bounding surface plasticity models relate the plastic hardening modulus to the distance from the current stress point to its projection on the bounding surface (Dafalias, 1986). This allows for a better reproduction of the highly non-linear pre-failure response of soil (Loukidis and Salgado, 2009).

A two-surface bounding surface plasticity model for sand using explicitly concepts from critical state soil mechanics (CSSM), as established by Schofield and Wroth (1968), was firstly proposed by Manzari and Dafalias (1997). This model employs a small kinematic yield surface to determine the onset of plasticity, as well as three other surfaces, termed dilatancy, bounding and critical, which model the occurrence of three distinctive states of the response of sand. More specifically, the dilatancy surface determines the change from plastic contraction to plastic dilation – i.e. the phase transformation state, as defined by Ishihara *et al.* (1975). The bounding surface is related to the occurrence of a maximum peak stress ratio. Finally, the critical surface determines the onset of failure – i.e. the point from which sand deforms under constant volume and stress, according to the principles of CSSM. Furthermore, the positions of the dilatancy and bounding surfaces are associated with the state parameter, ψ (Been and Jefferies, 1985), enabling the model to capture the effect of sand's initial state (characterised by the mean effective stress and void ratio) on its shear response using a single set of model parameters (Manzari and Dafalias, 1997).

Due to its flexibility and modular structure, the original model proposed by Manzari and Dafalias (1997) has been modified and extended over the last two decades (Papadimitriou and Bouckovalas, 2002; Dafalias and Manzari, 2004; Dafalias *et al.*, 2004; Taiebat and Dafalias, 2008; Loukidis and Salgado, 2009; Andrianopoulos *et al.*, 2010a; Li and Dafalias, 2012;

Taborda *et al.*, 2014; Woo and Salgado, 2015). Unfortunately, not all newly developed versions of the constitutive model have incorporated alterations and/or additional components included in earlier versions and, therefore, the constitutive model did not progress steadily towards a more complete constitutive relationship capable of simulating the response of sand under general loading conditions. Therefore, as pointed out by Taborda (2011), each version of the model may be a better option for a specific boundary value problem to be analysed.

With the objective of simulating the cyclic response of sand over a wide range of strains, Taborda (2011) selected the model proposed by Papadimitriou and Bouckovalas (2002) as a starting point and extended that model. In particular, three alterations were introduced by Taborda (2011): 1) a modification in the shape of the critical state line (CSL) in the void ratio – mean effective stress space; 2) a more sophisticated formulation of the plastic hardening modulus with additional dependences on the void ratio and elastic stiffness; and 3) an additional low-stress yield surface, which limits the detrimental effects of the numerical integration of the constitutive model on the computation time when effective stresses are very low. As detailed in Taborda (2011) and Taborda *et al.* (2014), these alterations resulted in an inherently more versatile model than the original version of Papadimitriou and Bouckovalas (2002), with the prediction of liquefaction-related phenomena for a wide range of densities being improved. Due to its great modelling capabilities, flexibility and numerical stability, the version of the model proposed by Taborda (2011) and summarised by Taborda *et al.* (2014) was a natural choice for a starting point. Indeed, this version has been used to replicate not only laboratory tests, as the most of the remaining versions, but also to model centrifuge experiments, meaning that there is a large availability and diversity of numerical data which can be used to validate the implementation of the constitutive model into a Finite Element (FE) code.

The formulation proposed by Taborda *et al.* (2014) is presented in Section 4.2. Particular attention is given firstly to the fundamental aspects related to the two-surface bounding surface plasticity framework (Section 4.2.1), with the constitutive equations being presented afterwards in multiaxial stress space (Section 4.2.2 to 4.2.6). In order to increase further the ability of the model to reproduce the response of sand under general loading conditions, a series of alterations to the original formulation are discussed in Section 4.3.

4.2 Original formulation

4.2.1 Fundamental concepts

The constitutive model proposed by Taborda *et al.* (2014) is an extended version of the model proposed by Papadimitriou and Bouckovalas (2002), which followed an early version of Manzari and Dafalias (1997). These models use concepts of both bounding surface plasticity (Dafalias, 1986) and CSSM (Schofield and Wroth, 1968) frameworks to describe the

mechanical response of sand under general loading conditions. In accordance with CSSM, a unique CSL in the void ratio, *e*, – mean effective stress, *p'*, space is employed by these models. A linear expression in the *e* – ln *p*' space (Equation 4.1) was initially proposed by Manzari and Dafalias (1997) and also adopted by Papadimitriou and Bouckovalas (2002).

$$e_{CS} = (e_{CS})_{ref} - \lambda \ln\left(\frac{p'}{p'_{ref}}\right) \tag{4.1}$$

where p'_{ref} is a reference pressure (usually taken as the atmospheric pressure, i.e. $p'_{ref} \approx$ 101.3 kPa), $(e_{CS})_{ref}$ is the void ratio at critical state (CS) when $p' = p'_{ref}$ and λ is the slope of the CSL in the *e* – ln *p*' space.

However, based on experimental evidence demonstrating that such form does not reproduce satisfactorily the observed CSL for a wide range of stresses (e.g. Been *et al.*, 1991; Verdugo and Ishihara, 1996), Taborda *et al.* (2014) adopted a power law (Equation 4.2), as originally proposed by Li and Wang (1998). According to Taborda *et al.* (2014), the power law form improves the prediction of the deformation level required for very dense sand to reach the critical state.

$$e_{CS} = (e_{CS})_{ref} - \lambda \left(\frac{p'}{p'_{ref}}\right)^{\xi} \tag{4.2}$$

where $(e_{CS})_{ref}$ is now the void ratio at critical state when $p' = 0$ and ξ is an additional model parameter defining the curvature of the CSL.

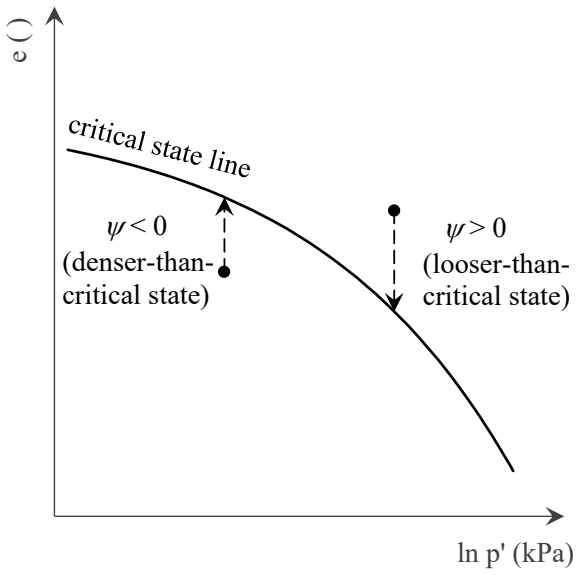

Figure 4.1 – Definition of the state parameter, ψ, as proposed by Been and Jefferies (1985).

Moreover, these models use explicitly the uniqueness of a CSL through the use of the state parameter, ψ (Been and Jefferies, 1985), which is given by the distance between the current void ratio, *e*, and void ratio at critical state, e_{cs}, corresponding to the current mean effective stress, *p'* (Equation 4.3).

$$\psi = e - e_{CS} = e - (e_{CS})_{ref} + \lambda \left(\frac{p'}{p'_{ref}} \right)^{\xi} \tag{4.3}$$

As illustrated in Figure 4.1, the sign of the state parameter indicates whether the material is in a denser-than-critical state ($\psi < 0$) or in a looser-than-critical state ($\psi > 0$), with its magnitude providing a measure of how far the material's state is from the critical state. Indeed, as discussed before (Section 2.6.5), the use of the state parameter concept seems to provide an efficient form of predicting distinctive states of the response of sand (e.g. phase transformation and peak stress ratio states) for a wide range of initial void ratios and effective stress states. Based on this experimental observation, this concept has been extensively used in constitutive modelling to efficiently address the simulation of the effect of the initial state of sand on its response under both monotonic and cyclic loading by using a single set of model parameters (e.g. Jefferies, 1993; Manzari and Dafalias, 1997; Gajo and Wood, 1999; Manzanal *et al.*, 2011).

The main principles behind the incorporation of the state parameter concept in the formulation of a bounding surface plasticity model (BSPM) were explained by Manzari and Dafalias (1997) by considering the typical response of an initially denser-than-critical sample ($\psi_0 < 0$) when subjected to drained monotonic constant-*p*' triaxial compression test, as well as to an undrained monotonic triaxial compression test with increasing mean stress. As schematically illustrated in Figure 4.2, under drained constant-*p*' shearing, the sample tends to exhibit an initially contractive response, meaning that the void ratio will move downwards from point A_0 (initial state) to point A_d (path represented by a grey line in Figure 4.2a). From this point, and as shearing progresses, a dilative response will be observed, with the void ratio moving upwards, from point A_d towards point A_c, located on the CSL, where $e = e_{CS}$ and, therefore, $\psi = 0$. According to the CSSM, from this point onwards the sample will deform under constant volume and effective stress. Analysing now the effective stress path in the deviatoric stress, *q*, – mean effective stress, *p'*, space (represented, once more, by a grey line in Figure 4.2b), it can be observed that the point moves initially upwards, passes point A_d, where $\eta = q/p' = M_c^d$ and the response changes from contractive to dilative, and reaches a peak position at point A_b, where $\eta = M_c^b$. With further shearing, the point eventually moves downwards to the critical state point A_c, where $\eta = M_c^c$. Conversely, under undrained shearing, since the volume of the sample remains constant throughout loading, the path in the *e* – ln *p'* space is horizontal (represented by a black line in Figure 4.2a). In this case, due to the initial tendency of the initially denser-than-critical sample to contract under shearing, an initial reduction of *p'* is observed, with the path in the *e* – ln *p'* space moving to the left from point A_0 (initial state) to point A'_d. With further undrained shearing, the path in the *e* – ln *p'* space will be reverted, eventually reaching the CSL at point A'_c. Regarding the effective stress path in the *q* – *p'* space (which is represented by a black curve in Figure 4.2b), a qualitatively similar response to that observed under drained conditions is obtained: after

reaching point A'_d, where $\eta = M_c^d$ and a minimum in the mean effective stress is observed, the stress path will tend to reach a peak position, characterised by $\eta = M_c^b$, eventually experiencing softening until critical state (characterised by $\eta = M_c^c$) is reached.

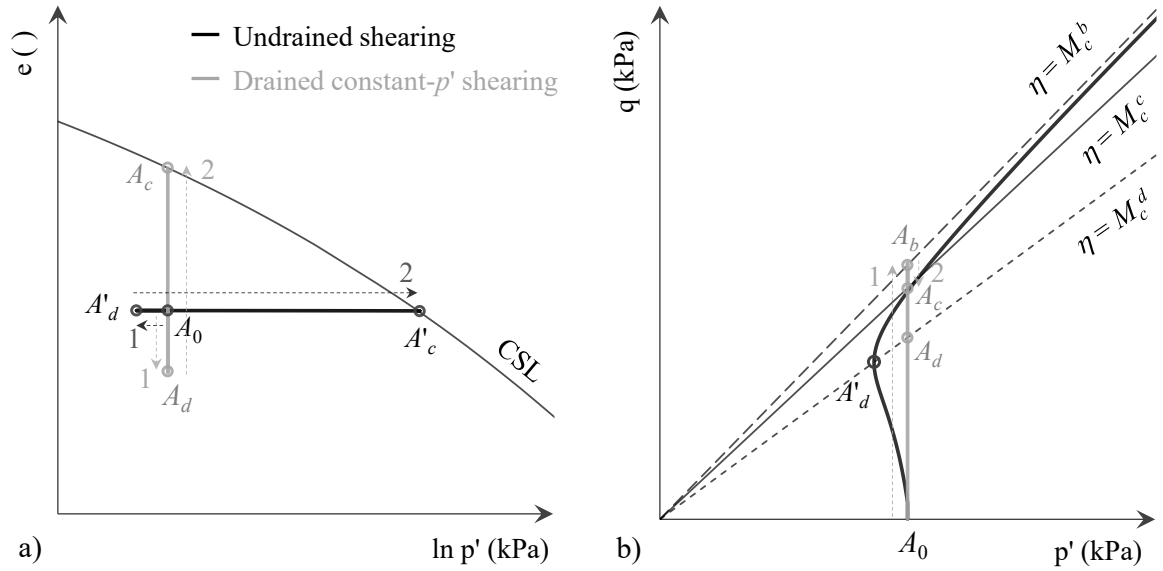

Figure 4.2 – Idealised response of an initially denser-than-critical sample when subjected to a drained monotonic constant-*p*' triaxial compression test and to an undrained monotonic triaxial compression test: (a) in the *e* – ln *p*' space and (b) in the *q* – *p*' space.

Qualitatively different responses are usually observed for an initially looser-than-critical sample ($\psi_0 > 0$). Specifically, as illustrated in Figure 4.3, when subjected to a drained constant-*p'* triaxial compression test, the sample tends to exhibit a contractive response throughout loading, in which case no reversal point is observed in the *e* – ln *p'* path (Figure 4.3a). Moreover, initially looser-than-critical samples usually do not experience softening, meaning that the deviatoric stress typically increases until CS conditions are reached, as illustrated in Figure 4.3b. Similarly, when subjected to an undrained triaxial compression test with increasing mean stress, a continuous reduction of mean effective stress is commonly observed until CS conditions are reached (black curve in Figure 4.3b).

According to Manzari and Dafalias (1997), this typical response of an initially looser-than-critical sample may, however, not be observed in every case. In particular, the authors suggested that, when the initial state of the sample is very close to the CSL (i.e. the value of ψ at the start of the test, although positive, is very small), the initial contraction may be large enough for the path in the *e* – ln *p*' path to cross the CSL, either under drained or undrained shearing (Figure 4.4a). In such case, a dilative response is subsequently observed to bring the state back to the CSL. In the *q* – *p*' plane (Figure 4.4b), the undrained response is characterised by a substantial reduction of the mean effective stress in the earlier stages of loading until a minimum value is reached (where $\eta = M_c^d$). A subsequent increase of the mean effective stress is observed until critical state conditions are reached (where $\eta = M_c^c$.). Under drained

constant-*p*' shearing, the effective stress path is typically observed to increase until reaching the CS.

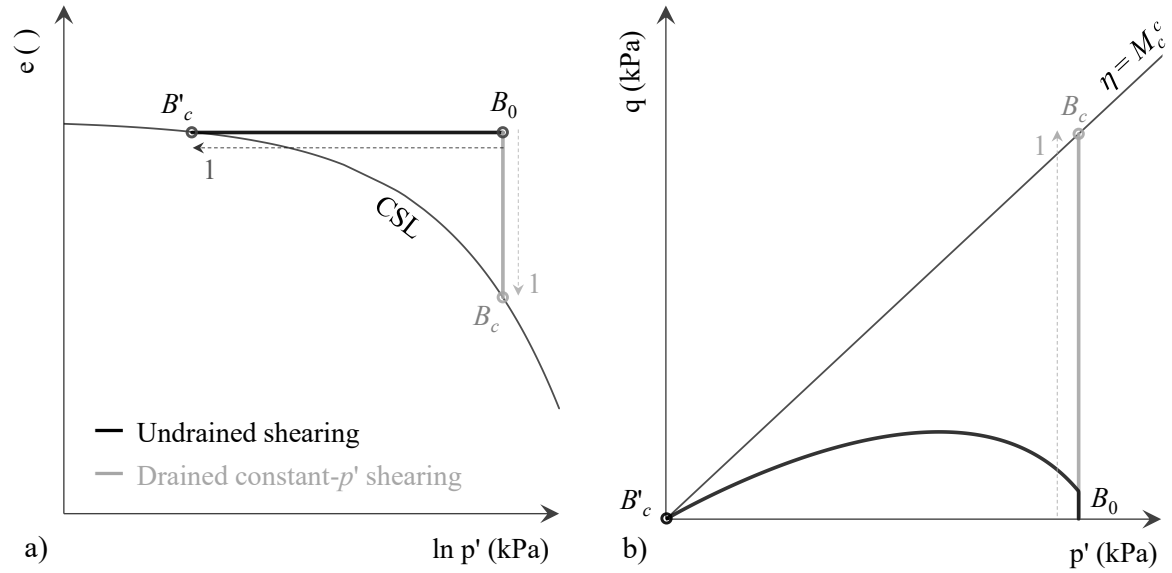

Figure 4.3 – Idealised response of an initially much-looser-than-critical sample when subjected to a drained monotonic constant-*p*' triaxial compression test and to an undrained monotonic triaxial compression test: (a) in the *e* – ln *p*' space and (b) in the *q* – *p*' space.

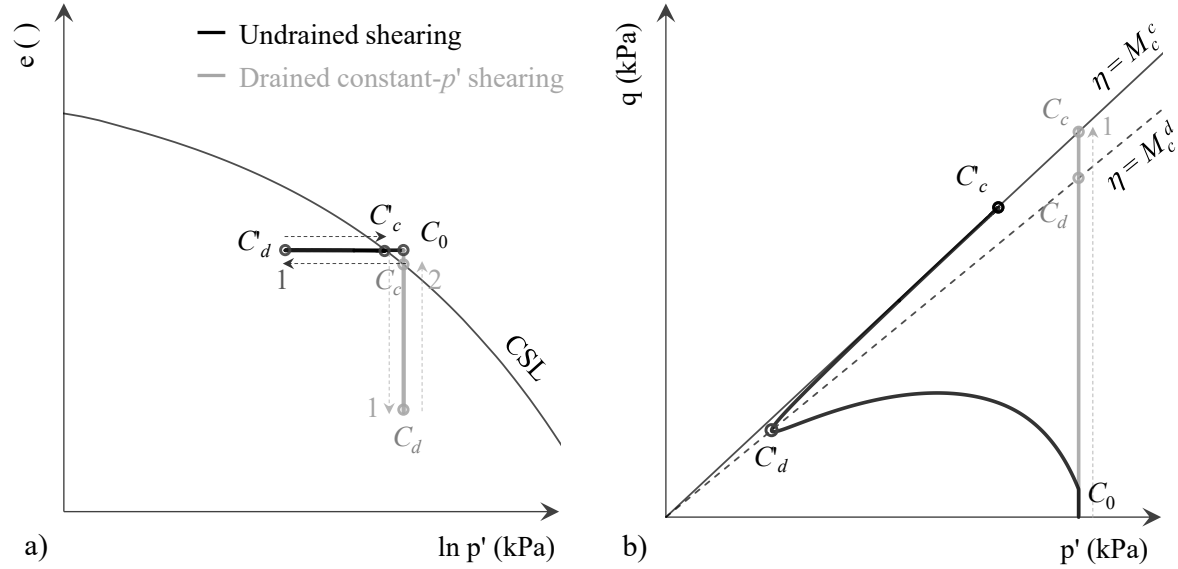

Figure 4.4 – Idealised response of an initially slightly-looser-than-critical sample when subjected to a drained monotonic constant-*p*' triaxial compression test and to an undrained monotonic triaxial compression test: (a) in the *e* – ln *p*' space and (b) in the *q* – *p*' space.

To capture these typical responses of sand, three particular surfaces (whose projections on the $q - p'$ plane are straight lines) were proposed by Manzari and Dafalias (1997): the dilatancy surface (where the stress ratio is given by $\eta = M_c^d$), the bounding surface (characterised by $\eta = M_c^b$) and the critical surface (where $\eta = M_c^c$). While the superscripts are related to the name of the surfaces – "*d*" for dilatancy, "*b*" for bounding and "*c*" for critical – the subscript "*c*" refers to triaxial compression. Along the same lines, a subscript "*e*" is used

to characterise the stress ratio in triaxial extension. As it can be concluded from what was previously described, the dilatancy surface is associated with the phase transformation state – i.e. state at which the response of sand changes from plastic contraction to plastic dilation and, therefore, dilatancy is temporarily null. Regarding the bounding surface, it is related to the mobilisation of a maximum stress ratio (or, in other words, a maximum angle of shear resistance), marking a change from strain-hardening to strain-softening response. Finally, the critical surface is associated with the mobilisation of critical state conditions. Apart from the critical surface, which is basically characterised by a set of positive model parameters, M_c^c for triaxial compression and M_e^c for triaxial extension, or, in a compact notation, $M_{c,e}^c$, the positions of the dilatancy and bounding surfaces are not fixed in the stress space. In effect, these surfaces depend on the state parameter (as mathematically described below), which is continuously evolving during shearing. According to Manzari and Dafalias (1997), this dependency enables an adequate simulation of the main features of sand response using a single set of model parameters for a wide range of initial void ratios and stress states.

Based on a proposition made by Wood *et al.* (1994) (see also Section 2.6.5.2), Manzari and Dafalias (1997) proposed a linear dependency of the position of the bounding surface, $M_{c,e}^b$, on the position of the critical state surface, characterised by $M_{c,e}^c$, through the state parameter, ψ, as indicated by Equation 4.4.

$$M_{c,e}^b = M_{c,e}^c + k_{c,e}^b \langle -\psi \rangle \tag{4.4}$$

where $k_{c,e}^b$ is a set of positive model parameters (one value for compression, k_c^b, and one value for extension, k_e^b) and the Macaulay brackets $\langle\ \rangle$ define the mathematical operation: $\langle A \rangle = A$ when $A > 0$, while $\langle A \rangle = 0$ when $A \leq 0$. The introduction of this operation is the main difference to the initial proposal of Wood *et al.* (1994). Essentially, it is used to prevent the occurrence of $M_{c,e}^b < M_{c,e}^c$ (i.e. to prevent the bounding surface to be located below the critical state surface) for looser-than-critical samples ($\psi > 0$), which, according to Manzari and Dafalias (1997), could potentially result in an unrealistic change in the stress-strain response from hardening to softening. Note, however, that the introduction of the Macaulay brackets is not consensual, since not all subsequent versions of the constitutive model use them to restrict the position of the bounding surface to one side of the critical state surface (e.g. Li and Dafalias, 2000; Dafalias and Manzari, 2004; Loukidis and Salgado, 2009).

An interesting aspect of this formulation, which distinguishes this constitutive model from others based on the same framework (e.g. from that proposed by (Li, 2002)), is that the stress state can momentarily step outside the bounding surface (even though this surface is termed "bounding"), since no persistence condition is imposed. As this happens, a negative plastic hardening modulus – which is proportional to the distance between the current stress state and the bounding surface, as detailed later – will be obtained, triggering softening response and eventually moving the stress state back to the bounding surface. According to Manzari

and Dafalias (1997), this is an efficient form of simulating the softening response observed for denser-than-critical samples.

Similarly, the position of the dilatancy surface, $M^d_{c,e}$, is also linearly dependent on the position of the critical surface, $M^c_{c,e}$, through the state parameter, ψ (Equation 4.5). This dependency ensures that the constitutive model conforms to the principles of the CSSM. In fact, since dilatancy is proportional to the distance between the current effective stress state and its projection on the dilatancy surface, as mathematically detailed later, it is crucial that the position of the dilatancy surface coincides with the position of the critical surface when critical state conditions are reached, as defined by Equation 4.5, where $M^d_{c,e} = M^c_{c,e}$ when $\psi = 0$ and, therefore, $e = e_{CS}$.

$$M^d_{c,e} = M^c_{c,e} + k^d_{c,e}\ \psi \tag{4.5}$$

where $k^d_{c,e}$ is a new set of positive model parameters.

Contrary to the formulation proposed for the bounding surface, the equation governing the position of the dilatancy surface, as introduced by Manzari and Dafalias (1997), does not make use of the Macaulay brackets. Consequently, the dilatancy surface can occupy either a lower position than critical surface when the sample is denser than critical ($\psi < 0$) or a higher position when the sample is looser than critical ($\psi > 0$).

Moreover, as also pointed out by Manzari and Dafalias (1997), it is interesting to note that the projection of the dilatancy surface on the $q - p'$ plane can be associated with the phase transformation line (PTL), as proposed by Ishihara *et al.* (1975). In fact, since dilatancy is proportional to the distance between the current effective stress state and its projection on the dilatancy surface, as already mentioned before, the dilatancy and, consequently, the incremental plastic volumetric strain is null when the current effective stress point is on that surface (i.e. $\Delta\varepsilon^p_v = 0$). Under undrained conditions, since the total volumetric strain remains null throughout loading (i.e. $\Delta\varepsilon_v = 0$), it follows that the incremental elastic volumetric strain is also null when the effective stress point is on the dilatancy surface (i.e. $\Delta\varepsilon_v = \Delta\varepsilon^e_v + \Delta\varepsilon^p_v = 0 \Leftrightarrow \Delta\varepsilon^e_v = 0$). Assuming that the volumetric and distortional responses can be analysed independently of each other, it follows that the mean effective stress increment ($\Delta p' = K\,\Delta\varepsilon^e_v$, where K is the bulk modulus) is also null for an effective stress point lying on the dilatancy surface. Moreover, due to the change in the modelled response from plastic contraction to plastic dilation as the dilatancy surface is crossed, the effective stress path is reversed with further loading, meaning that a point of minimum mean effective stress is therefore observed when the dilatancy surface is crossed in undrained shearing, as defined by the PTL (Ishihara *et al.*, 1975).

It is perhaps important to note that an exponential form has been used by other authors to describe the dependence of the dilatancy and bounding surfaces on critical surface through the state parameter (e.g. Li and Dafalias, 2000; Dafalias and Manzari, 2004; Li and Dafalias,

2004; Loukidis and Salgado, 2009). Based on the large amount of experimental data obtained in the present study, the potential benefits of using a more elaborated form for Equations 4.4 and 4.5 are discussed in Chapter 6, where the calibration of the present constitutive model for Hostun sand is presented.

According to the principles of classical plasticity, the model also employs a yield surface, which defines a small elastic region within the stress space (or, in other words, which separates purely elastic from elasto-plastic response). As shown in Figure 4.5, Manzari and Dafalias (1997) proposed an open wedge-type yield surface in the $q - p'$ space, with its apex at the origin (Equation 4.6).

$$F = \eta - \alpha \pm m = q - \alpha p' \pm m p' = 0 \tag{4.6}$$

where α and m are both stress ratios, the former locating the slope of the bisector of the wedge and the latter controlling the opening of the wedge. The sign ± is used to characterise the top and bottom limits of the wedge, as illustrated in Figure 4.5, meaning that the total opening of the wedge is $2\,m\,p'$.

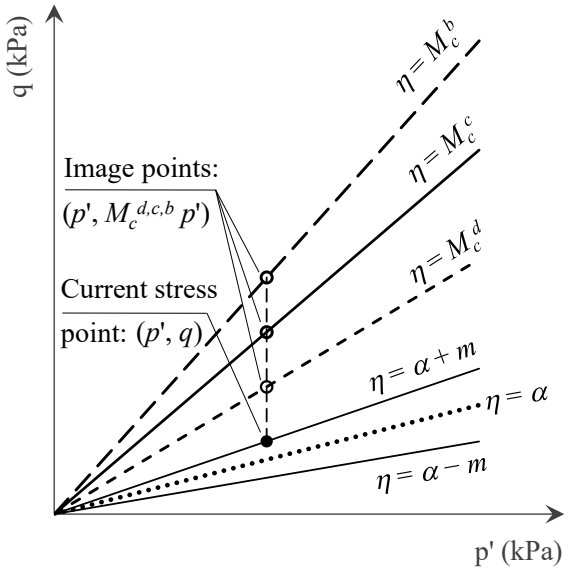

Figure 4.5 – Overview of the surfaces employed by the model in the q – p' space.

It is perhaps noteworthy that, according to the classical plasticity terminology, the term "back-stress ratio" is used to designate α, since it is basically a state parameter associated with the recent loading history (Manzari and Dafalias, 1997). This term is recurrently adopted in the present study. In addition, it should be noted that, although the initial version of the model proposed by Manzari and Dafalias (1997) assumed the existence of both kinematic and isotropic hardening of the yield surface, associated with α and m, respectively, it was acknowledged by the authors that a constant and small value for m (in the order of 0.01 $M_{c,e}^c$ to 0.05 $M_{c,e}^c$) can be used in most practical situations. Consequently, the isotropic hardening has been, in general, disregarded in the majority of the more recent versions of this

constitutive model, including in the version proposed by Papadimitriou and Bouckovalas (2002) and further elaborated by Taborda (2011) and Taborda *et al.* (2014).

As recognised by Manzari and Dafalias (1997), due to the open shape of the yield surface, the model predicts only elastic response when a constant stress ratio loading is applied (e.g. when simulating a drained isotropic compression test). However, as added by the authors, under confining pressures within the range of practical interest for Geotechnical engineering (i.e. not causing crushing of particles), this type of loading usually results in relatively small strains. Therefore, the authors suggested that the additional complexity associated with the introduction of a cap to the yield surface, as proposed for example by Li (2002), or a more elaborated shape for the yield surface, as proposed for example by Taiebat and Dafalias (2008), does not compensate the little improvement that it would bring to the model. Along the same lines, the version of the model proposed by Papadimitriou and Bouckovalas (2002) and further extended by Taborda (2011) and Taborda *et al.* (2014) also uses the open wedge-type yield surface described by Equation 4.6.

It is perhaps important to note that, to reduce the complexity of the stress integration process (e.g. to avoid the need for a *drift* correction, whose concept is explained in detail in the next chapter), the constitutive model proposed by Andrianopoulos *et al.* (2010b) adopts a vanished elastic region, meaning that the yield surface is reduced to a line (rather than being a wedge) intercepting the origin of the $q - p'$ space. This simplification implies, however, that the constitutive model does not include a back-stress ratio, which, as highlighted before, has the important role of characterising the recent loading history. Moreover, the inexistence of a yield surface has the additional inconvenience of requiring the definition of a mapping rule of the current effective stress point on the model surfaces different from that originally proposed by Manzari and Dafalias (1997), which has been shown to be simple and numerically stable, as recognised by Andrianopoulos *et al.* (2010b).

In the next sections, the constitutive model proposed by Taborda *et al.* (2014) will be detailed. Note that, although triaxial conditions were used here to present the fundamental concepts of the constitutive model, a multiaxial (3D) formulation is required to solve general boundary-value problems and, therefore, the following section will describe the constitutive model in this form. In 3D stress-strain space, all components of the effective stress tensor, $\boldsymbol{\sigma}'$, need to be considered (Equation 4.7). Note that this tensor can be decomposed into its volumetric and deviatoric components, termed as mean effective stress, p' (Equation 4.8), and deviatoric stress, $\boldsymbol{s}$ (Equation 4.9), respectively.

$$\boldsymbol{\sigma}' = \begin{bmatrix} \sigma'_{xx} & \tau_{xy} & \tau_{xz} \\ \tau_{yx} & \sigma'_{yy} & \tau_{yz} \\ \tau_{zx} & \tau_{zy} & \sigma'_{zz} \end{bmatrix} = \frac{1}{3}\mathrm{tr}\boldsymbol{\sigma}'\,\boldsymbol{I} + \mathrm{dev}\boldsymbol{\sigma}' = p'\,\boldsymbol{I} + \boldsymbol{s} \tag{4.7}$$

where:

$$p' = \frac{1}{3}\mathrm{tr}\boldsymbol{\sigma}' = \frac{\sigma'_{xx} + \sigma'_{yy} + \sigma'_{zz}}{3} \tag{4.8}$$

$$\boldsymbol{s} = \mathrm{dev}\boldsymbol{\sigma}' = \boldsymbol{\sigma}' - \frac{1}{3}\mathrm{tr}\boldsymbol{\sigma}' = \boldsymbol{\sigma}' - p'\boldsymbol{I} = \begin{bmatrix} \sigma'_{xx} - p' & \tau_{xy} & \tau_{xz} \\ \tau_{yx} & \sigma'_{yy} - p' & \tau_{yz} \\ \tau_{zx} & \tau_{zy} & \sigma'_{zz} - p' \end{bmatrix} \tag{4.9}$$

where "tr" denotes the trace of a tensor (see definition below) and "dev" the deviatoric part of a tensor (characterised by a null trace). The second-order identity tensor, $\boldsymbol{I}$, is given by:

$$\boldsymbol{I} = \begin{bmatrix} 1 & 0 & 0 \\ 0 & 1 & 0 \\ 0 & 0 & 1 \end{bmatrix} \tag{4.10}$$

Furthermore, as shown in Figure 4.5 and indicated by Equation 4.4 to 4.6, the present model is formulated in terms of stress-ratio-related quantities. In the multiaxial formulation, the stress ratio tensor, $\boldsymbol{r}$ (Equation 4.11), replaces the triaxial quantity η, while the back-stress ratio tensor, $\boldsymbol{\alpha}$ (Equation 4.12), replaces the scalar α.

$$\boldsymbol{r} = \frac{\boldsymbol{s}}{p'} = \begin{bmatrix} \dfrac{\sigma'_{xx} - p'}{p'} & \dfrac{\tau_{xy}}{p'} & \dfrac{\tau_{xz}}{p'} \\ \dfrac{\tau_{yx}}{p'} & \dfrac{\sigma'_{yy} - p'}{p'} & \dfrac{\tau_{yz}}{p'} \\ \dfrac{\tau_{zx}}{p'} & \dfrac{\tau_{zy}}{p'} & \dfrac{\sigma'_{zz} - p'}{p'} \end{bmatrix} \tag{4.11}$$

$$\boldsymbol{\alpha} = \begin{bmatrix} \alpha_{xx} & \alpha_{xy} & \alpha_{xz} \\ \alpha_{yx} & \alpha_{yy} & \alpha_{yz} \\ \alpha_{zx} & \alpha_{zy} & \alpha_{zz} \end{bmatrix} \tag{4.12}$$

In addition, due to its frequent use, it is important to introduce at this point the tensorial operation termed as the trace product between two second-order tensors, which is denoted by "**:**" and defined as:

$$\boldsymbol{a} : \boldsymbol{b} = \mathrm{tr}(\boldsymbol{a}\,\boldsymbol{b}) = \sum_{i,\,j} a_{ij}\, b_{ij} \tag{4.13}$$

Moreover, the Euclidian norm, $\| \|_2$, of a second-order tensor $\boldsymbol{a}$ is defined by Equation 4.14.

$$\|\boldsymbol{a}\|_2 = \sqrt{\boldsymbol{a} : \boldsymbol{a}} = \sqrt{\mathrm{tr}(\boldsymbol{a}\,\boldsymbol{a})} \tag{4.14}$$

Note that, since all second-order tensors used in the constitutive model are symmetric (i.e. $a_{xy} = a_{yx}$, $a_{xz} = a_{zx}$ and $a_{yz} = a_{zy}$ for a second-order tensor $\boldsymbol{a}$), only six components need to be defined and, therefore, it is usual to represent the tensors as arrays (i.e. $\boldsymbol{a} = \left\{a_{xx} \;\; a_{yy} \;\; a_{xy} \;\; a_{zz} \;\; a_{xz} \;\; a_{yz}\right\}^{\mathrm{T}}$).

4.2.2 Non-linear elastic response

For the elastic part of the model, an isotropic hypoelastic formulation is adopted. The elastic strain increment, $\Delta\boldsymbol{\varepsilon}^{\boldsymbol{e}}$, is decoupled into its volumetric, $\Delta\varepsilon_v^e$, and deviatoric, $\Delta\boldsymbol{e}^{\boldsymbol{e}}$, components

(Equation 4.15), which can be related to the mean effective stress increment, $\Delta p'$ (Equation 4.16), and to the deviatoric stress increment, $\Delta \boldsymbol{s}$ (Equation 4.17), respectively.

$$\Delta \boldsymbol{\varepsilon^e} = \begin{bmatrix} \Delta\varepsilon^e_{xx} & \Delta\gamma^e_{xy} & \Delta\gamma^e_{xz} \\ \Delta\gamma^e_{yx} & \Delta\varepsilon^e_{yy} & \Delta\gamma^e_{yz} \\ \Delta\gamma^e_{zx} & \Delta\gamma^e_{zy} & \Delta\varepsilon^e_{zz} \end{bmatrix} = \frac{1}{3}\mathrm{tr}\Delta\boldsymbol{\varepsilon^e}\,\boldsymbol{I} + \mathrm{dev}\,\Delta\boldsymbol{\varepsilon^e} = \frac{1}{3}\Delta\varepsilon^e_v\,\boldsymbol{I} + \Delta\boldsymbol{e^e} \tag{4.15}$$

where:

$$\Delta\varepsilon^e_v = \mathrm{tr}\Delta\boldsymbol{\varepsilon^e} = \Delta\varepsilon^e_{xx} + \Delta\varepsilon^e_{yy} + \Delta\varepsilon^e_{zz} = \frac{\Delta p'}{K_{tan}} \tag{4.16}$$

$$\Delta\boldsymbol{e^e} = \begin{bmatrix} \Delta\varepsilon^e_{xx} - \frac{1}{3}\Delta\varepsilon^e_v & \Delta\gamma^e_{xy} & \Delta\gamma^e_{xz} \\ \Delta\gamma^e_{yx} & \Delta\varepsilon^e_{yy} - \frac{1}{3}\Delta\varepsilon^e_v & \Delta\gamma^e_{yz} \\ \Delta\gamma^e_{zx} & \Delta\gamma^e_{zy} & \Delta\varepsilon^e_{zz} - \frac{1}{3}\Delta\varepsilon^e_v \end{bmatrix} = \frac{\Delta\boldsymbol{s}}{2\,G_{tan}} \tag{4.17}$$

where K_{tan} and G_{tan} are the tangent bulk and tangent shear moduli, respectively.

In the early version of Manzari and Dafalias (1997), a power law was employed to obtain variations of K_{tan} and G_{tan} with p'. However, all subsequent versions of the model have used different expressions for the calculation of the elastic moduli, in order to include the recognised influence of other properties in the small strain response of sand, such as the void ratio (e.g. Richart *et al.*, 1970; Hardin, 1978). In particular, based on the well-established hysteretic model of Ramberg and Osgood (1943), Papadimitriou and Bouckovalas (2002) introduced a non-linear hysteretic response, where G_{tan} is obtained by applying a reduction, T, to the maximum shear modulus, G_{max}, as indicated by Equation 4.18.

$$G_{tan} = \frac{G_{max}}{T} \tag{4.18}$$

with G_{max} being given by Equation 4.19 (Hardin, 1978):

$$G_{max} = C_g\,p'_{ref}\,\frac{1}{0.3 + 0.7\,e^2}\sqrt{\frac{p'}{p'_{ref}}} \tag{4.19}$$

where C_g is a model parameter and p'_{ref} is the reference pressure, which was already introduced when defining the CSL (Equation 4.2).

The scalar reduction factor, T (Equation 4.20), depends on the distance, χ^r_{ref} (Equation 4.21), in the deviatoric stress ratio plane between the current stress ratio, $\boldsymbol{r}$, and that corresponding to the last shear reversal point, $\boldsymbol{r^{SR}}$.

$$T = 1 + \kappa\left(\frac{1}{a_1} - 1\right)\left(\frac{\chi^r_{ref}}{N\,\eta_1}\right)^{\kappa-1} \leq 1 + \kappa\left(\frac{1}{a_1} - 1\right) \tag{4.20}$$

with:

$$\chi_{ref}^{r} = \sqrt{\frac{1}{2}}\,\|\boldsymbol{r} - \boldsymbol{r}^{SR}\|_2 = \sqrt{\frac{1}{2}}\sqrt{(\boldsymbol{r} - \boldsymbol{r}^{SR}):(\boldsymbol{r} - \boldsymbol{r}^{SR})} \tag{4.21}$$

where a_1 and η_1 are positive scalars, whose physical meaning will be described later, and κ is a model parameter having a value greater than 1, with $\kappa = 2$ being employed by Papadimitriou and Bouckovalas (2002), as well as by Taborda (2011) and Taborda *et al.* (2014) in all numerical simulations. Additionally, *N* is a state parameter, which takes initially the value of 1.0 but changes to 2.0 when a shear reversal is firstly detected, as originally proposed by Masing (1926).

According to Papadimitriou and Bouckovalas (2002), shear reversals (SR) occur whenever the distance, χ_{ref}^{e} (Equation 4.22), in deviatoric shear strain plane between the current deviatoric strain, $\boldsymbol{e}$, and that corresponding to the last shear reversal point, $\boldsymbol{e}^{SR}$, is observed to decrease during a given solicitation – i.e. whenever $\chi_{ref}^{e_0} > \chi_{ref}^{e_0+\Delta e}$ is detected, where $\chi_{ref}^{e_0}$ is the distance corresponding to the deviatoric strain before the solicitation, $\boldsymbol{e_0}$, and $\chi_{ref}^{e_0+\Delta e}$ is the distance corresponding to the deviatoric strain after the solicitation, $\boldsymbol{e_0} + \Delta\boldsymbol{e}$. As noted by Papadimitriou and Bouckovalas (2002), a shear reversal point can be different from a loading reversal point, which is often characterised by the trace product between the gradient of the yield surface, $\partial F/\partial\boldsymbol{\sigma}'$, and the effective stress increment that would occur if the response would be elastic, $\Delta\boldsymbol{\sigma}'^{\boldsymbol{e}}$, as detailed later.

$$\chi_{ref}^{e} = \sqrt{\frac{1}{2}}\,\|\boldsymbol{e} - \boldsymbol{e}^{SR}\|_2 = \sqrt{\frac{1}{2}}\sqrt{(\boldsymbol{e} - \boldsymbol{e}^{SR}):(\boldsymbol{e} - \boldsymbol{e}^{SR})} \tag{4.22}$$

By assuming $\kappa = 2$, it is apparent that the upper limit of T (Equation 4.20) is reached when $\chi_{ref}^{r} = N\,\eta_1$, remaining constant with further loading (i.e. with further increase of χ_{ref}^{r}). According to Papadimitriou and Bouckovalas (2002), this means that the positive scalar η_1 can be essentially interpreted as a threshold stress ratio above which any further reduction of the overall shear stiffness of the material is predominantly related to plasticity. Therefore, the authors suggested evaluating η_1 by Equation 4.23.

$$\eta_1 = a_1 \left(\frac{G_{max}^{SR}}{p'^{SR}}\right) \gamma_1 \tag{4.23}$$

where p'^{SR} and G_{max}^{SR} are, respectively, the mean effective stress and maximum shear modulus at last shear reversal (SR), a_1 is a model parameter also used in Equation 4.20 and γ_1 is a model parameter, which can be physically associated with the cyclic threshold shear strain, γ_{tc}, found by Vucetic (1994), above which irreversible strains become dominant, typically in the range of 6.5×10^{-5} to 2.5×10^{-4} for non-plastic sands and silts (Papadimitriou and Bouckovalas, 2002).

To gain further insight into the role of the positive scalars a_1 and γ_1, the non-linear elastic formulation proposed by Papadimitriou and Bouckovalas (2002) is applied to the numerical simulation of two drained cyclic constant-*p*' triaxial tests on samples having identical initial void ratio, $e_0 = 0.80$, and consolidated under the same mean effective stress of $p'_0 = 100.0$ kPa (Figure 4.6). Note that, in these simulations, G_{max} (Equation 4.18) remains constant troughout loading, since *p'* is kept constant during this type of test and, providing that a small-strain approach is considered, the void ratio, *e*, is also kept constant (i.e. $\Delta e = (1.0 + e_0)\,\Delta\varepsilon_v^e = (1.0 + e_0)\;\Delta p'/K_{tan} = 0$). Consequently, the variation of the tangent shear modulus, G_{tan}, during loading is solely a function of the evolution of the scalar reduction factor, *T* (Equation 4.20). In relation to the model parameters, values of 7000.0, 1.5×10^{-4} and 2.0 are adopted for *B*, γ_1 and κ, respectively, with the only difference between the two simulations consisting of the value adopted for the model parameter a_1: while $a_1 = 0.40$ is used in one of the simulations, $a_1 = 0.80$ is employed in the other simulation. Before presenting the obtained numerical results, it should be noted that, for triaxial conditions, the amplitude of the deviatoric stress is given by $|q| = \sqrt{3/2}\,\|\boldsymbol{s}\|_2 = \sqrt{3/2}\,\sqrt{\boldsymbol{s}:\boldsymbol{s}} = |\sigma'_a - \sigma'_r|$, where σ'_a and σ'_r are, respectively, the axial and radial effective stresses registered in the test. Similarly, the deviatoric strain amplitude is given by $|\varepsilon_q| = \sqrt{2/3}\,\|\boldsymbol{e}\|_2 = \sqrt{2/3}\,\sqrt{\boldsymbol{e}:\boldsymbol{e}} = 2/3\,|\varepsilon_a - \varepsilon_r| = 2/3\,|\gamma|$, where ε_a and ε_r are, respectively, the axial and radial strains registered in the test and γ is the shear strain amplitude.

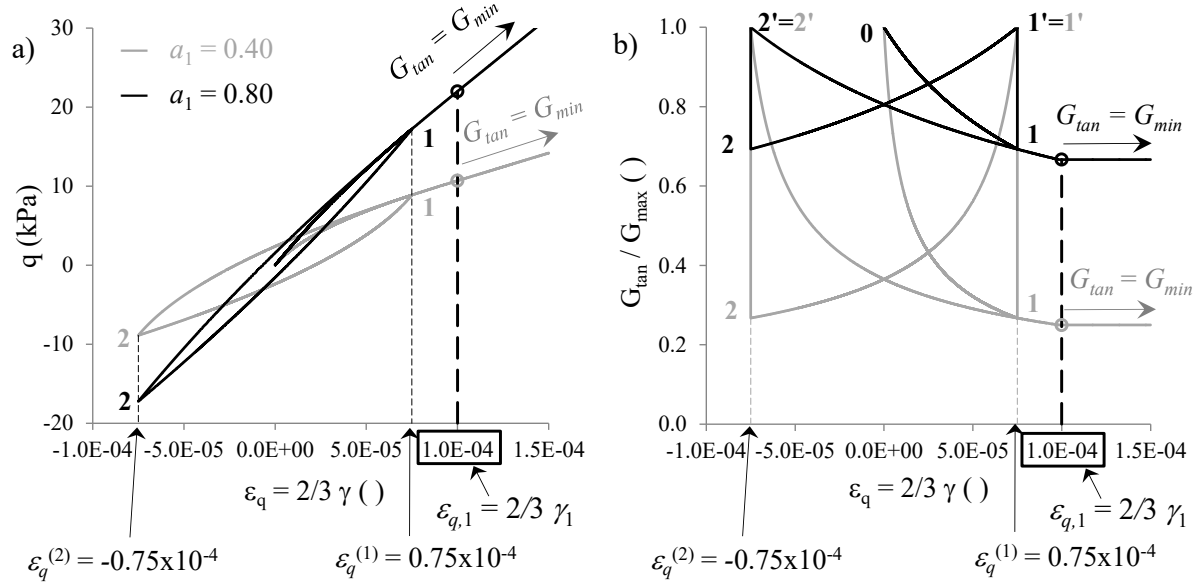

Figure 4.6 – Numerical simulation of two drained cyclic constant-*p*' triaxial tests using the small-strain non-linear hysteretic model: (a) stress-strain response and (b) reduction of the tangent shear modulus with shear strain.

Figure 4.6a depicts the stress-strain response of both samples, while Figure 4.6b presents the corresponding evolution of the tangent shear modulus reduction, $G_{tan}/G_{max} = 1/T$, with deviatoric strain. It can be observed that both samples are initially sheared until a deviatoric strain of $\varepsilon_q^{(1)} = 0.75 \times 10^{-4}$ is obtained – point 1 in the figure. A shear reversal is applied at

that point, with both samples being subsequently sheared until a similar amplitude of deviatoric strain in triaxial extension, $\varepsilon_q^{(2)} = -0.75 \times 10^{-4}$, is registered – point 2 in the figure. At this point, an additional shear reversal is applied, with the samples being eventually sheared beyond $\varepsilon_{q,1} = 2/3\ \gamma_1 = 1.0 \times 10^{-4}$ in triaxial compression. Overall, it is apparent that the larger the value of the model parameter a_1, the stiffer the stress-strain response registered in the test. In fact, Figure 4.6b shows that a_1 controls the rate of the tangent shear modulus reduction up to the point at which the amplitude of the deviatoric strains reaches $\varepsilon_{q,1} = 2/3\ \gamma_1$. From that point, it can be observed that the tangent shear modulus ceases to degrade, with a constant tangent shear modulus equal to its minimum value (i.e. $G_{tan} = G_{max}/[1 + \kappa(1/a_1 - 1)]$, according to Equations 4.18 and 4.20) being registered for further shearing. It can, therefore, be concluded that γ_1 defines a threshold strain amplitude, above which no further reduction of the tangent shear modulus occurs, as highlighted by Papadimitriou and Bouckovalas (2002).

In Figure 4.6a, it is also interesting to note that deviatoric strains are not completely recovered when loading is removed (i.e. when $q = 0$), meaning that irreversible strains may be obtained when no plasticity occurs. As pointed out by Papadimitriou and Bouckovalas (2002) and Taborda (2011), this means that the constitutive model does not include a region of true elastic response, although the term *elastic* has been used for this component of the constitutive model and will be also adopted in the present study. As also mentioned by the aforementioned authors, when non-linear cyclic elasticity is used, as in the present constitutive model, the term *paraelastic* would be more appropriate, as originally suggested by Hueckel and Nova (1979). In addition, it is perhaps important to note that, contrary to what Figure 4.6a may suggest, due to the hypoelastic form of G_{max} (Equation 4.19), the proposed formulation may also produce small irreversible strains in closed shear stress cycles. This aspect is not observed in Figure 4.6a, since G_{max} is kept constant during the simulations, as explained before.

Assuming a constant Poisson's ratio, ν, the tangent bulk modulus, K_{tan}, is obtained from the theory of elasticity (Equation 4.24).

$$K_{tan} = \frac{2\ (1 + \nu)}{3\ (1 - 2\ \nu)} G_{tan} \tag{4.24}$$

Finally, it is important to note that, although the present formulation was adopted by Taborda (2011) without any particular modification, the author mentioned that small values may be obtained for G_{tan} when the mean effective stress is very low (e.g. when simulating liquefaction-related phenomena), which may potentially affect the stability of the numerical analysis. Indeed, due to the dependence of the plastic hardening modulus on G_{tan}, as detailed in Section 4.2.3.6, this aspect may be even more problematic. To alleviate this problem, Taborda (2011) suggested to lower limit G_{max} by using an additional model parameter, defining a minimum value for the mean effective stress, p'_{min}, as indicated by Equation 4.25.

Alternatively, it is possible to apply a lower limit directly the tangent shear modulus, G_{tan}, by using a model parameter with such purpose, G_{min}, as shown by Equation 4.26.

$$G_{max} = C_g\, p'_{ref}\, \frac{1}{0.3 + 0.7\, e^2} \sqrt{\frac{p'}{p'_{ref}}} \geq C_g\, p'_{ref}\, \frac{1}{0.3 + 0.7\, e^2} \sqrt{\frac{p'_{min}}{p'_{ref}}} \tag{4.25}$$

$$G_{tan} = \frac{G_{max}}{T} \geq G_{min} \tag{4.26}$$

4.2.3 Plastic response

4.2.3.1 Introduction

According to the plasticity theory – refer, for example, to Potts and Zdravkovic (1999) for further details –, the plastic strain increment, $\Delta\boldsymbol{\varepsilon}^{\boldsymbol{p}}$, is given by the so-called *flow rule* (Equation 4.27):

$$\Delta\boldsymbol{\varepsilon}^{\boldsymbol{p}} = \begin{bmatrix} \Delta\varepsilon^p_{xx} & \Delta\gamma^p_{xy} & \Delta\gamma^p_{xz} \\ \Delta\gamma^p_{yx} & \Delta\varepsilon^p_{yy} & \Delta\gamma^p_{yz} \\ \Delta\gamma^p_{zx} & \Delta\gamma^p_{zy} & \Delta\varepsilon^p_{zz} \end{bmatrix} = \lambda\, \frac{\partial \boldsymbol{P}}{\partial \boldsymbol{\sigma}'} \tag{4.27}$$

where λ is the plastic multiplier, which controls the magnitude of the increment of the plastic strains, and $\partial \boldsymbol{P}/\partial \boldsymbol{\sigma}'$ is the gradient of the plastic potential, which defines the direction of the plastic strain increment in the multiaxial strain space.

Moreover, according to the general principles of plasticity, during plastic straining, the effective stress point must remain on the yield surface – i.e. the so-called "consistency condition" must be satisfied (Equation 4.28):

$$\Delta F = \frac{\partial F}{\partial \boldsymbol{\sigma}'} : \Delta\boldsymbol{\sigma}' + \frac{\partial F}{\partial \boldsymbol{k}} : \Delta\boldsymbol{k} = 0 \tag{4.28}$$

where $\partial F/\partial \boldsymbol{\sigma}'$ is the gradient of the yield surface to the effective stress state and $\partial F/\partial \boldsymbol{k}$ is the gradient of the yield surface to the state parameters. Note that, to keep the presentation general, the state parameters controlling the size and/or position of the yield surface are, at this point, generally represented by $\boldsymbol{k}$. Moreover, note that, in this thesis, the term "state parameter" is used to designate any internal variable responsible for the evolution of the yield surface (which is often referred to as "hardening parameter" in the literature), as well as any other internal variable controlling the evolution of the elastic moduli and plastic potential.

Complementary, taking into account that the incremental effective stresses, $\Delta\boldsymbol{\sigma}'$, are related to the incremental elastic strains, $\Delta\boldsymbol{\varepsilon}^{\boldsymbol{e}}$, by the elastic constitutive matrix, $\boldsymbol{D}$, and assuming that the incremental total strains, $\Delta\boldsymbol{\varepsilon}$, can be decomposed into its elastic and plastic components, it can be written (Equation 4.29):

$$\Delta\boldsymbol{\sigma}' = \begin{bmatrix} \sigma'_{xx} & \tau_{xy} & \tau_{xz} \\ \tau_{yx} & \sigma'_{yy} & \tau_{yz} \\ \tau_{zx} & \tau_{zy} & \sigma'_{zz} \end{bmatrix} = \boldsymbol{D} : \Delta\boldsymbol{\varepsilon}^{\boldsymbol{e}} = \boldsymbol{D} : (\Delta\boldsymbol{\varepsilon} - \Delta\boldsymbol{\varepsilon}^{\boldsymbol{p}}) = \boldsymbol{D} : \Delta\boldsymbol{\varepsilon} - \lambda\ \boldsymbol{D} : \frac{\partial \boldsymbol{P}}{\partial \boldsymbol{\sigma}'} \tag{4.29}$$

By using Equation 4.28 in conjunction with Equation 4.29, it is possible to define explicitly the plastic multiplier, λ, as given by Equation 4.30.

$$\frac{\partial F}{\partial \boldsymbol{\sigma}'} : \boldsymbol{D} : \Delta\boldsymbol{\varepsilon} - \lambda \frac{\partial F}{\partial \boldsymbol{\sigma}'} : \boldsymbol{D} : \frac{\partial \boldsymbol{P}}{\partial \boldsymbol{\sigma}'} + \frac{\partial F}{\partial \boldsymbol{k}} : \Delta\boldsymbol{k} = 0 \Leftrightarrow$$
$$\lambda = \frac{\frac{\partial F}{\partial \boldsymbol{\sigma}'} : \boldsymbol{D} : \Delta\boldsymbol{\varepsilon}}{\frac{\partial F}{\partial \boldsymbol{\sigma}'} : \boldsymbol{D} : \frac{\partial \boldsymbol{P}}{\partial \boldsymbol{\sigma}'} + A} \tag{4.30}$$

where A is the plastic hardening modulus, which depends on the state parameters affecting the yield surface, $\boldsymbol{k}$, and their particular evolution, $\Delta\boldsymbol{k}$, during plastic loading (Equation 4.31).

$$A = -\frac{1}{\lambda} \frac{\partial F}{\partial \boldsymbol{k}} : \Delta\boldsymbol{k} \tag{4.31}$$

Moreover, as detailed later, the present model assumes strain hardening/softening plasticity, meaning that $\Delta\boldsymbol{k}$ is related to $\Delta\boldsymbol{\varepsilon}^{\boldsymbol{p}}$. In such case, Equation 4.31 can be written as Equation 4.32 (Potts and Zdravkovic, 1999).

$$A = -\frac{1}{\lambda} \frac{\partial F}{\partial \boldsymbol{k}} : \frac{\partial \boldsymbol{k}}{\partial \boldsymbol{\varepsilon}^{\boldsymbol{p}}} : \Delta\boldsymbol{\varepsilon}^{\boldsymbol{p}} \tag{4.32}$$

Moreover, similar to the majority of strain hardening/softening constitutive models, there is a linear relationship between $\boldsymbol{k}$ and $\boldsymbol{\varepsilon}^{\boldsymbol{p}}$ (i.e. $\partial\boldsymbol{k}/\partial\boldsymbol{\varepsilon}^{\boldsymbol{p}} = C_k = \text{constant}$), allowing for A to become independent of the unknown plastic multiplier, λ, and, therefore, determinant when Equation 4.27 is substituted in Equation 4.32, as shown by Equation 4.33 (Potts and Zdravkovic, 1999).

$$A = -\frac{\partial F}{\partial \boldsymbol{k}} : \frac{\partial \boldsymbol{k}}{\partial \boldsymbol{\varepsilon}^{\boldsymbol{p}}} : \frac{\partial \boldsymbol{P}}{\partial \boldsymbol{\sigma}'} = -C_k \frac{\partial F}{\partial \boldsymbol{k}} : \frac{\partial \boldsymbol{P}}{\partial \boldsymbol{\sigma}'} \tag{4.33}$$

Along the lines of two-surface plasticity framework introduced by Krieg (1975) and later adapted by Manzari and Dafalias (1997), the gradient of the plastic potential, $\partial\boldsymbol{P}/\partial\boldsymbol{\sigma}'$, and the plastic hardening modulus, A, depend on the distances between the current effective stress point and its projection on the dilatancy and bounding surfaces, respectively. Therefore, it is necessary to extend the formulation of these model surfaces to the multiaxial (3D) stress space (Section 4.2.3.2), before introducing the procedure (termed as *mapping rule*) used to estimate the projection of the current effective stress point on those surfaces (Section 4.2.3.3). After defining the gradient of the yield surface (Section 4.2.3.4), as well as the gradient of the plastic potential (Section 4.2.3.5), the plastic hardening modulus is defined (Section 4.2.3.6).

4.2.3.2 Model surfaces in the multiaxial stress space

In Section 4.2.1, it was explained how the constitutive model employs three particular surfaces (dilatancy, critical and bounding surfaces) to predict the distinctive states of sand response, as well as a yield surface to define a small elastic region within the stress space. To ease the understanding of their particular role in the model, these surfaces were presented

in the $q - p'$ space in Section 4.2.1. In order to use the constitutive model in boundary value problems, it is, however, necessary to extend their formulation to the multiaxial (3D) stress state, as presented in this section.

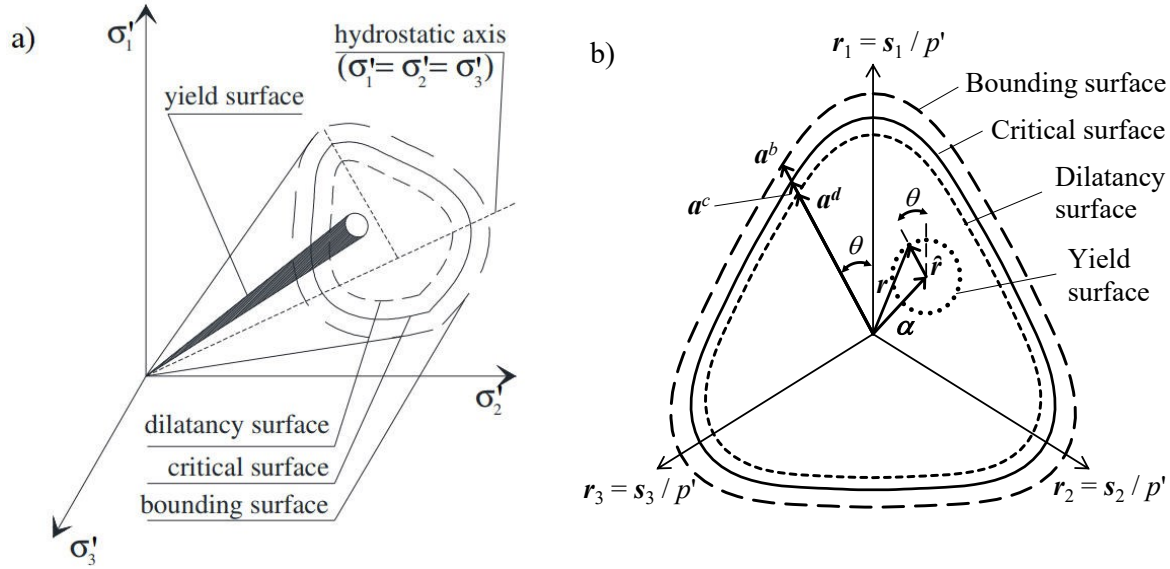

Figure 4.7 – Schematic representation of model surfaces and mapping rule in (a) the multiaxial stress space and in (b) the normalised deviatoric stress ratio plane.

The shapes of all model surfaces in multiaxial stress space are schematically presented in Figure 4.7a. Starting with the yield surface, it can be seen that its previous open wedge-type shape in the $q - p'$ plane is replaced by an open cone in multiaxial space, also having its apex at the origin of the stress space. The intersection of the yield surface with a normalised deviatoric stress ratio plane (i.e. a normalised plane perpendicular to the hydrostatic axis) is a circle with centre defined by $\boldsymbol{\alpha}$ (Figure 4.7b). As in the $q - p'$ space, its opening (i.e. its radius in multiaxial stress space) depends on the parameter m and increases with the mean effective stress, p'. Equation 4.34 defines the yield surface in the multiaxial stress space.

$$F = \|\boldsymbol{s} - p'\,\boldsymbol{\alpha}\|_2 - \sqrt{\frac{2}{3}}\, m\, p' = \sqrt{(\boldsymbol{s} - p'\,\boldsymbol{\alpha}) : (\boldsymbol{s} - p'\,\boldsymbol{\alpha})} - \sqrt{\frac{2}{3}}\, m\, p' = 0 \tag{4.34}$$

Unlike the yield surface, as shown in Figure 4.7b, the intersections of the dilatancy, critical and bounding surfaces with a normalised deviatoric stress ratio plane are generally non-circular. The positions of these three surfaces in the generalised stress space, $M^{d,c,b}$ (Equation 4.35), are determined based on their positions in triaxial compression, $M_c^{d,c,b}$ (Equations 4.4 and 4.5), as well as on an interpolation function g (Equation 4.36), which was proposed by Papadimitriou and Bouckovalas (2002). The interpolation function g is a function of the modified Lode's angle, θ (Equation 4.37), as well as of $c^{d,c,b}$, defining the ratio between the stress ratios in triaxial extension and in triaxial compression (Equation 4.38).

$$M^{d,c,b} = g(\theta, c^{d,c,b})\, M_c^{d,c,b} \tag{4.35}$$

$$g(\theta, c^{d,c,b}) = \frac{2\,c^{d,c,b}}{\frac{1+c^{d,c,b}}{2} - \frac{1-c^{d,c,b}}{2}\cos(3\theta)} - \left[\frac{1+c^{d,c,b}}{2} + \frac{1-c^{d,c,b}}{2}\cos(3\theta)\right] \tag{4.36}$$

$$\cos(3\theta) = \left(\frac{3\sqrt{3}}{2}\frac{\overline{J_3}}{\left(\overline{J_2}\right)^{3/2}}\right) \tag{4.37}$$

$$c^{d,c,b} = \frac{M_e^{d,c,b}}{M_c^{d,c,b}} \tag{4.38}$$

where $\overline{J_2} = 1/2\,\bar{\boldsymbol{r}} : \bar{\boldsymbol{r}}$ and $\overline{J_3} = 1/3\,\bar{\boldsymbol{r}} : \bar{\boldsymbol{r}} : \bar{\boldsymbol{r}} = det\,\bar{\boldsymbol{r}}$ are, respectively, the modified second and third invariants of the effective stress. Note that the term *modified* is used to emphasise the use of the radial tensor, $\bar{\boldsymbol{r}} = \boldsymbol{r} - \boldsymbol{\alpha}$., in the definition of the Lode's angle, θ, rather than the more conventional use of the current deviatoric stress tensor, $\boldsymbol{s}$ (see, for example, Potts and Zdravkovic, 1999). Moreover, note that the present formulation results in a modified Lode's angle of $\theta = 0$ for triaxial compression and $\theta = \pi/3$ for triaxial extension. As expected, when $\theta = 0$, it follows that $g(\theta, c^{d,c,b}) = 1$ and, consequently, $M^{d,c,b} = M_c^{d,c,b}$. As also expected, when $\theta = \pi/3$, it follows that $g(\theta, c^{d,c,b}) = c^{d,c,b}$, guaranteeing that $M^{d,c,b} = M_e^{d,c,b}$. For any other loading conditions (e.g. plane strain), intermediate values of θ are obtained, meaning that $c^{d,c,b} < g(\theta, c^{d,c,b}) < 1$ and $M_e^{d,c,b} < M^{d,c,b} < M_c^{d,c,b}$. Indeed, it is noteworthy that, to ensure the convexity of the model surfaces (i.e. that any line connecting two points located inside any of the surfaces does not intersect its boundary), $c^{d,c,b} \geq 0.717$ should be employed in the numerical analysis (Loukidis and Salgado, 2009).

By comparing the several different constitutive models originating from the Manzari and Dafalias (1997)'s proposal, it can be concluded that the interpolation function is one of the components registering a larger number of different formulations (e.g. Manzari and Dafalias, 1997; Li, 2002; Papadimitriou and Bouckovalas, 2002; Loukidis and Salgado, 2009). In relation to the original proposal of Manzari and Dafalias (1997), which makes use of the well-known Argyris surface (Argyris *et al.*, 1974), it is argued by Papadimitriou and Bouckovalas (2002) that Equation 4.36 allows for a better prediction of the friction angle for non-triaxial conditions. As suggested by Taborda (2011), the variation of the critical-state friction angle, ϕ^c, for intermediate values of θ, may be analysed by using Equations 4.36 together with Equations 4.39 (Potts and Zdravkovic, 1999), which is derived from the well-known Mohr-Coulomb failure criterion.

$$\phi^c = \phi^c(\theta, c^c) = \sin^{-1}\left(\frac{2\sqrt{3}\,\sin(\phi_c^c)\,g(\theta, c^c)\cos(\theta - \frac{\pi}{6})}{3 - \sin(\phi_c^c) - 2\sin(\phi_c^c)\,g(\theta, c^c)\sin(\theta - \frac{\pi}{6})}\right) \tag{4.39}$$

where $\phi_c^c = \phi^c(0, c^c)$ is the critical-state friction angle in triaxial compression, which can be related to $M_c^{d,c,b}$, as given by Equation 4.40.

$$M_c^{d,c,b} = \frac{6\sin(\phi_c^c)}{3 - \sin(\phi_c^c)} \tag{4.40}$$

Figure 4.8 depicts the evolution of the critical-state friction angle, ϕ^c, with the value of θ, predicted by the present constitutive model, for three different critical-state friction angles in triaxial compression ($\phi_c^c = 30°$, 33° and 36° in Figure 4.8a, b and c, respectively), as well as for three different values of c^c: 0.70, 0.75 and 0.80. Note that the selected values for ϕ^c, as well as for c^c belong to the typical range of values typically observed for silica sands (Loukidis and Salgado, 2009). For these values, it can be observed that the present formulation generally predicts critical-state friction angles under plane strain conditions, ϕ_{PS}^c, – for which θ is typically close to 15°, according to Loukidis and Salgado (2009) – about 4 to 8° greater than the value obtained for triaxial compression, which is reasonably consistent with values typically measured in the laboratory, e.g. Pradhan *et al.* (1988) obtained $\phi_{PS}^c - \phi_c^c \approx 5°$ for Toyoura sand. Indeed, it is apparent in Figure 4.8 that the critical-state friction angle in triaxial extension, ϕ_e^c, is highly dependent on the value selected for c^c, with a range of values $\phi_e^c - \phi_c^c \approx -1$ to 11° being obtained for the values for ϕ^c and c^c under analysis.

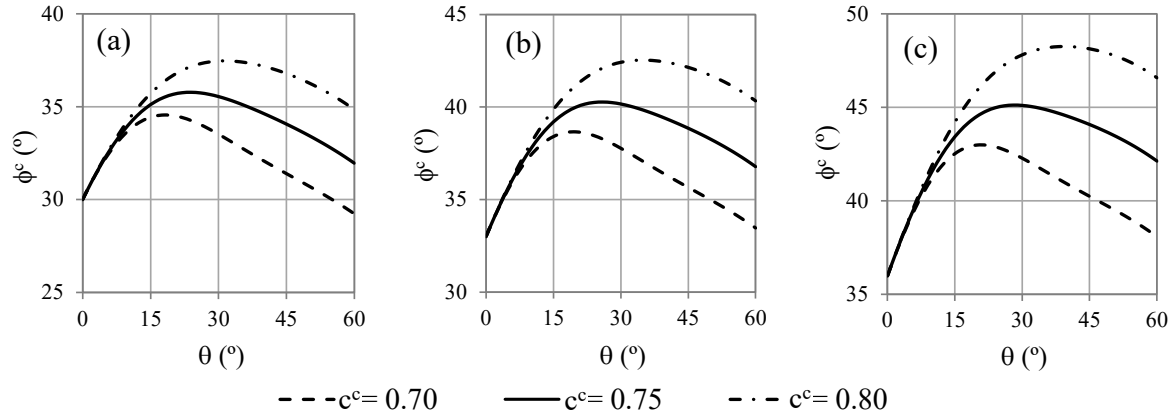

Figure 4.8 – Evolution of the critical-state friction angle with the modified Lode's angle for (a) $\phi_c^c = 30°$, (b) $\phi_c^c = 33°$ and (c) $\phi_c^c = 36°$.

4.2.3.3 Distances from the current effective stress point to its projections on the model surfaces

Although other possibilities exist (e.g. Andrianopoulos *et al.*, 2010; Woo and Salgado, 2015), a radial projection rule (i.e. using a straight line, which passes through the origin of the stress space and has the direction defined by the radial stress tensor, $\bar{\boldsymbol{r}}$), as originally proposed by Manzari and Dafalias (1997), is used to obtain the projections (also termed as "images" by the authors) of the current effective stress point on the dilatancy, $\boldsymbol{\alpha}^d$, critical, $\boldsymbol{\alpha}^c$, and bounding, $\boldsymbol{\alpha}^b$, surfaces, as illustrated in Figure 4.7. Mathematically, these image stress ratio tensors, $\boldsymbol{\alpha}^{d,c,b}$, are described by Equation 4.41.

$$\boldsymbol{\alpha}^{\boldsymbol{d,c,b}} = \sqrt{\frac{2}{3}}\ \alpha_{\theta}^{d,c,b}\ \boldsymbol{n} = \sqrt{\frac{2}{3}}\left(g(\theta, c^{d,c,b})\ M_c^{d,c,b} - m\right)\boldsymbol{n} \tag{4.41}$$

where $\boldsymbol{n}$ is a traceless (i.e. tr $\boldsymbol{n} = 0$) and unitary (tr $\boldsymbol{n}^{\boldsymbol{2}} = \boldsymbol{n} : \boldsymbol{n} = 1$) stress ratio tensor obtained by normalising the radial tensor, $\bar{\boldsymbol{r}}$ (Equation 4.42). Note that, since tensor $\boldsymbol{n}$ has the same direction of tensor $\bar{\boldsymbol{r}}$, it can be alternatively used it in the definition of the modified Lode's angle, θ, in which case $\overline{J_2} = 1/2\ \boldsymbol{n} : \boldsymbol{n}$ and $\overline{J_3} = det\ \boldsymbol{n}$.

$$\boldsymbol{n} = \frac{\bar{\boldsymbol{r}}}{\|\bar{\boldsymbol{r}}\|_2} = \frac{\boldsymbol{r} - \boldsymbol{\alpha}}{\sqrt{(\boldsymbol{r} - \boldsymbol{\alpha}) : (\boldsymbol{r} - \boldsymbol{\alpha})}} = \frac{\boldsymbol{r} - \boldsymbol{\alpha}}{\sqrt{2/3}\ m} = \frac{\boldsymbol{s} - p'\,\boldsymbol{\alpha}}{\sqrt{2/3}\ m\,p'} \tag{4.42}$$

Having determined $\boldsymbol{\alpha}^{\boldsymbol{d,c,b}}$, the distances in the normalised deviatoric stress ratio plane from the current effective stress point to the image points can be obtained from Equation 4.43.

$$d^{d,c,b} = (\boldsymbol{\alpha}^{\boldsymbol{d,c,b}} - \boldsymbol{\alpha}) : \boldsymbol{n} = \sqrt{\frac{2}{3}}\ \alpha_{\theta}^{d,c,b} - \boldsymbol{\alpha} : \boldsymbol{n} = \sqrt{\frac{2}{3}}\left(g(\theta, c^{d,c,b})\ M_c^{d,c,b} - m\right) - \boldsymbol{\alpha} : \boldsymbol{n} \tag{4.43}$$

Note that, for convenience, these distances are expressed in terms of back-stress ratio tensors, $\boldsymbol{\alpha}^{\boldsymbol{d,c,b}}$. Nevertheless, since $\bar{\boldsymbol{r}} = \boldsymbol{r} - \boldsymbol{\alpha}$, it would have been possible to write Equation 4.43 as a function of the stress ratio tensors, $\boldsymbol{r}^{\boldsymbol{d,c,b}}$, instead. Note also that $d^{d,c,b}$ can take either a positive value when the current effective stress point is inside a given surface or a negative value when it is outside that surface.

4.2.3.4 Gradient of the yield surface

The gradient of the yield surface, which defines the direction of loading, is given by Equation 4.44:

$$\frac{\partial F}{\partial \boldsymbol{\sigma}'} = \frac{1}{3}\ \frac{\partial F}{\partial p'}\ \boldsymbol{I} + \frac{\partial F}{\partial \boldsymbol{s}} = \frac{1}{3}\left(-\boldsymbol{\alpha} : \frac{\boldsymbol{s} - p'\,\boldsymbol{\alpha}}{\|\boldsymbol{s} - p'\,\boldsymbol{\alpha}\|_2}\right)\boldsymbol{I} + \frac{\boldsymbol{s} - p'\,\boldsymbol{\alpha}}{\|\boldsymbol{s} - p'\,\boldsymbol{\alpha}\|_2} \tag{4.44}$$

which, by using the unit stress ratio tensor, $\boldsymbol{n}$ (Equation 4.42), can be simplified to Equation 4.45:

$$\frac{\partial F}{\partial \boldsymbol{\sigma}'} = -\frac{1}{3}\left(\boldsymbol{\alpha} : \boldsymbol{n} + \sqrt{\frac{2}{3}}\ m\right)\boldsymbol{I} + \boldsymbol{n} \tag{4.45}$$

From Equation 4.45, it can be observed that the loading direction in the deviatoric stress plane is solely defined by tensor $\boldsymbol{n}$. Therefore, tensor $\boldsymbol{n}$ is often termed "deviatoric loading direction".

4.2.3.5 Gradient of the plastic potential

As proposed by Manzari and Dafalias (1997), the gradient of plastic potential, which defines the direction of the plastic strain increment, is defined by Equation 4.46:

$$\frac{\partial \boldsymbol{P}}{\partial \boldsymbol{\sigma'}} = \frac{1}{3} D \boldsymbol{I} + \boldsymbol{n} \tag{4.46}$$

where D is the dilatancy coefficient.

By comparing Equation 4.45 and 4.46, it can be promptly concluded that this version of the model assumes the existence of associated plasticity on the deviatoric plane, since the deviatoric components of both $\partial F/\partial \boldsymbol{\sigma'}$ and $\partial \boldsymbol{P}/\partial \boldsymbol{\sigma'}$ are defined by tensor $\boldsymbol{n}$. Although alternative expressions have been proposed for the deviatoric component of the plastic potential in the literature (e.g. Dafalias and Manzari, 2004; Loukidis and Salgado, 2009) with the objective of improving the prediction of the intermediate principal effective stress ratio at critical state under plane strain conditions, the constitutive models proposed by Papadimitriou and Bouckovalas (2002) and Taborda (2011) retained the original equation (Equation 4.46).

Regarding the volumetric component, following the general principle of Rowe's stress-dilatancy theory (Rowe, 1962) and work done by Roscoe *et al.* (1958), (Nova and Wood (1979) and Nova (1982), Manzari and Dafalias (1997) proposed Equation 4.47 to define D, which essentially postulates that the dilatancy coefficient is proportional to the distance from the current stress ratio to the dilatancy stress ratio.

$$\begin{aligned} D = A_0\, d^d = A_0\, (\boldsymbol{\alpha^d} - \boldsymbol{\alpha}) : \boldsymbol{n} &= A_0 \left(\sqrt{\frac{2}{3}}\, \alpha_\theta^d - \boldsymbol{\alpha} : \boldsymbol{n} \right) \\ &= A_0 \left(\sqrt{\frac{2}{3}} \left(g(\theta, c^d)\, M_c^d - m \right) - \boldsymbol{\alpha} : \boldsymbol{n} \right) \end{aligned} \tag{4.47}$$

where A_0 is a positive model parameter and $d^d = (\boldsymbol{\alpha^d} - \boldsymbol{\alpha}) : \boldsymbol{n}$ defines the distance from the current effective stress point to the dilatancy surface (Equation 4.43). By comparing Equation 4.45 to 4.47, it can be concluded that, unless the condition $A_0 \left(\sqrt{2/3}\ \alpha_\theta^d - \boldsymbol{\alpha} : \boldsymbol{n} \right) = \boldsymbol{\alpha} : \boldsymbol{n} + \sqrt{2/3}\ m$ is verified, the model assumes a non-associated flow rule.

Moreover, due to the positive value of A_0, it can be observed that, as conceptually explained before (Section 4.2.1), the present formulation guarantees that contractive plastic volumetric strains ($D > 0$) occur when the current effective stress point lies inside the dilatancy surface (i.e. $d^d > 0$), changing to dilatant plastic volumetric strains ($D < 0$) as the dilatancy surface is crossed and the effective stress point lies outside that surface (i.e. $d^d < 0$). In order to ensure that no plastic dilation occurs in looser-than-critical-state sand (i.e. when $\psi > 0$), a restriction of $D = 0$ is introduced when both $D < 0$ and $\psi > 0$ hold true (Manzari and Dafalias, 1997).

4.2.3.6 Plastic hardening modulus

The plastic hardening modulus, A, is associated with the distance from the current effective stress point to the bounding surface, d^b, as indicated by Equation 4.48. As pointed out by

Manzari and Dafalias (1997), the dependence of A on d^b is the main underlying concept of bounding surface plasticity theory, as introduced by Dafalias and Popov (1975) and Krieg (1975) and later applied to soil mechanics by Dafalias (1986).

$$A = p'\,h\,d^b = p'\,h(\boldsymbol{\alpha^b} - \boldsymbol{\alpha}) : \boldsymbol{n} = p'\,h\left(\sqrt{\frac{2}{3}}\;\alpha_\theta^b - \boldsymbol{\alpha} : \boldsymbol{n}\right) = A_0\left(\sqrt{\frac{2}{3}}\left(g(\theta, c^b)\,M_c^b - m\right) - \boldsymbol{\alpha} : \boldsymbol{n}\right) \tag{4.48}$$

where h is a positive scalar parameter, function of state parameters. Since the mean effective stress, p', is also positive (for the present case of a compression-positive sign convention), the sign of the plastic hardening modulus is solely related to the sign of d^b. Specifically, when the effective stress point is inside the bounding surface (i.e. $d^b > 0$), strain hardening response is simulated, changing to strain softening response once the effective stress point lies outside the bounding surface (i.e. $d^b < 0$).

Several different formulations have been proposed in the literature to define the scalar h. In particular, the original version of the constitutive model proposed by Manzari and Dafalias (1997) presents h as a simple function of the distance to the bounding surface, d^b, in relation to a reference distance, d_{ref}^b, scaled by a model parameter, h_0, as given by Equations 4.49, 4.50 and 4.51. Note that d_{ref}^b corresponds roughly to the "diameter" of the bounding surface along the direction of the tensor $\boldsymbol{n}$ (Manzari and Dafalias, 1997).

$$h = h_0\,h_b \tag{4.49}$$

$$h_b = \frac{\left|\,d^b\,\right|}{\left|d_{ref}^b - \left|d^b\right|\,\right|} \tag{4.50}$$

$$d_{ref}^b = \sqrt{\frac{2}{3}}\left(\alpha_\theta^b + \alpha_{\theta+\pi}^b\right) = \sqrt{\frac{2}{3}}\left(g(\theta, c^b)\,M_c^b + g(\theta+\pi, c^b)\,M_c^b - 2\,m\right) \tag{4.51}$$

The formulation of h was extended by Papadimitriou and Bouckovalas (2002) – Equation 4.52 – to incorporate the effect of the mean effective stress, p', on the plastic hardening modulus, through the term h_b (Equation 4.53), as well as the effect of the fabric evolution of sand during shearing, described by the term h_f (Equation 4.54).

$$h = h_0\,h_b\,h_f \tag{4.52}$$

$$h_b = \left(\frac{p'}{p'_{ref}}\right)^{\mu-1}\frac{\left|\,d^b\,\right|}{\langle d_{ref}^b - \left|d^b\right|\rangle} \tag{4.53}$$

$$h_f = \frac{1 + \langle \boldsymbol{F} : \boldsymbol{I}\rangle^2}{1 + \langle \boldsymbol{F} : \boldsymbol{n}\rangle} \tag{4.54}$$

where the exponent μ is a model parameter taking values between 0.5 and 1.0 (Papadimitriou and Bouckovalas, 2002) and $\boldsymbol{F}$ is a second-order fabric tensor, which can be decomposed into

its volumetric, f_p, and deviatoric, $\boldsymbol{f}$, components, as given by Equation 4.55. The term h_f can, therefore, be rewritten as indicated by Equation 4.56. Note that, to avoid confusion with the "inherent fabric tensor", $\boldsymbol{F_A}$, which will be introduced later, the "fabric tensor" $\boldsymbol{F}$ will be henceforth termed as "shearing-induced fabric tensor".

$$\boldsymbol{F} = \frac{1}{3}\text{tr}\,\boldsymbol{F}\;\boldsymbol{I} + \text{dev}\,\boldsymbol{F} = \frac{1}{3}f_p\,\boldsymbol{I} + \boldsymbol{f} \tag{4.55}$$

$$h_f = \frac{1 + \left\langle f_p \right\rangle^2}{1 + \langle \boldsymbol{f} : \boldsymbol{n} \rangle} \tag{4.56}$$

As mentioned by Papadimitriou and Bouckovalas (2002), due to the use of the Macaulay brackets both in the numerator and in the denominator of Equation 4.56, h_f can only take positive values, meaning that the sign of the plastic hardening modulus is, in effect, solely dictated by the sign of d^b, as mentioned before. Furthermore, the Macaulay brackets in the denominator implies that the deviatoric part of the shearing-induced fabric tensor $\boldsymbol{f}$ only affects h_f when it has a similar direction to the deviatoric loading tensor, $\boldsymbol{n}$. Since $\boldsymbol{f}$ will only evolve during plastic dilation and in the opposite direction of the tensor $\boldsymbol{n}$, as detailed later (Section 4.2.4), it means that $\boldsymbol{f}$ only affects h_f when a loading reversal is triggered after a dilative phase of plastic deformation. This is particularly intended to replicate the faster decrease of the mean effective stress upon shear reversal in undrained cyclic shearing once phase transformation line is crossed, observed in the laboratory (Chapter 3). Moreover, as highlighted by Papadimitriou and Bouckovalas (2002) and Taborda (2011), the relative magnitude of the volumetric and deviatoric components plays an important role in determining the value of h_f: when it increases (e.g. f_p increases and $\boldsymbol{f}$ remains constant), A increases (Equation 4.56, 4.52 and 4.48), leading to a decrease in the plastic strain increment (Equation 4.30 and 4.27); on the contrary, when the relative magnitude of the volumetric and deviatoric components is such that h_f reduces (e.g. f_p remains constant, while $\boldsymbol{f}$ increases), the plastic strain increment is expected to increase. According to Taborda (2011), the magnitude of h_f can be extremely variable when small values of p' are reached (which is likely to occur when simulating liquefaction-related phenomena). This can result in large oscillations of the value of h_f, which may affect the stability of the numerical analysis. In order to limit this undesirable situation, the author suggested the adoption of lower, $h_{f,min}$, and upper, $h_{f,max}$, limits to h_f:

$$h_{f,min} \leq h_f \leq h_{f,max} \tag{4.57}$$

The formulation of h was further extended by Taborda (2011) and Taborda *et al.* (2014) – Equation 4.58 – to account for the effects of the void ratio and elastic stiffness of the material on the plastic hardening modulus – terms h_e (Equation 4.60) and h_g (Equation 4.62), respectively. Moreover, the authors proposed a modification to the expression defining the influence of the distance from the current effective stress point to the bounding surface (Equation 4.59 replaces Equation 4.53). According to the authors, the adoption of a power

law increases the flexibility of the model, by enabling the reduction rate of the plastic hardening modulus during shearing to be adjusted, which may be particularly important when simulating flow liquefaction. Note that, in this formulation, h_0 remains a model parameter and the formulation of the scalar multiplier h_f (Equation 4.61) remains equal to that introduced by Papadimitriou and Bouckovalas (2002).

$$h = h_b\, h_e\, h_f\, h_g \tag{4.58}$$

$$h_b = \left(\frac{p'}{p'_{ref}}\right)^{\mu-1} \left(\frac{\left|d^b\right|}{\langle d^b_{ref} - \left|d^b\right|\rangle}\right)^{\beta+1} \tag{4.59}$$

$$h_e = h_0\,(1 - \gamma e) \geq h_0\,(1 - \gamma e_{lim}) \tag{4.60}$$

$$h_{f,min} \leq h_f = \frac{1 + \left\langle f_p \right\rangle^2}{1 + \langle \boldsymbol{f} : \boldsymbol{n} \rangle} \leq h_{f,max} \tag{4.61}$$

$$h_g = G^{\alpha}_{tan} \tag{4.62}$$

where α, β, γ and e_{lim} are new model parameters, with the latter one introducing a minimum value to the scalar multiplier h_e to avoid eventual negative values for very loose sand (Taborda *et al.*, 2014). It is also important to observe that, when the new model parameters α, β and γ are set to 0.0, the formulation proposed by Papadimitriou and Bouckovalas (2002) is recovered (Equations 4.52 to 4.56). As highlighted by Taborda *et al.* (2014), this allows for any new feature to be deactivated whenever there is not sufficient experimental evidence to use it (i.e. the calibration procedure reveals that the overall performance of the model is not sufficiently improved when considering, for example, the effect of the elastic stiffness and/or the void ratio on the plastic hardening modulus). Further details on the impact of each of these quantities on the magnitude of the plastic hardening modulus can be found in Taborda (2011) and Taborda *et al.* (2014).

Still regarding the multitude of formulations proposed for the plastic hardening modulus, it is perhaps important to note that a slightly different equation for the scalar multiplier h_b was introduced by Dafalias and Manzari (2004), in relation to those proposed by Manzari and Dafalias (1997), Papadimitriou and Bouckovalas (2002) and Taborda *et al.* (2014) – Equations 4.50, 4.53 and 4.59, respectively – , which, in fact, have a similar form. Specifically, based on earlier propositions made by Dafalias (1986), the scalar multiplier h_b proposed by Dafalias and Manzari (2004) is inversely proportional to the difference between the current back-stress ratio tensor, $\boldsymbol{\alpha}$, and a discrete memory tensor, denoted as $\boldsymbol{\alpha_{in}}$. (Equation 4.63). The latter quantity takes the value of $\boldsymbol{\alpha}$ at the start of the loading process, as well as once a stress reversal is detected. As this occurs, the distance $(\boldsymbol{\alpha} - \boldsymbol{\alpha_{in}}) : \boldsymbol{n}$ becomes null, rendering an infinite scalar multiplier h_b and, consequently, an infinite plastic hardening modulus, A. Although the authors argued that this particular form allows for more accurate simulations of experimental data, they also acknowledged that overshooting issues may occur when simulating boundary-value problems, mainly due to the occurrence of small loading cycles in

a general loading path. It is perhaps unsurprising that more recent versions proposed by Dafalias and his co-authors (e.g. Taiebat and Dafalias, 2008) had abandoned this form and reverted to a form similar to that included in the original Manzari and Dafalias (1997)'s proposal.

$$h_b = \left(\frac{p'}{p'_{ref}}\right)^{-1/2} \frac{1}{(\boldsymbol{\alpha} - \boldsymbol{\alpha_{in}}) : \boldsymbol{n}} \tag{4.63}$$

4.2.4 State parameter evolution laws

For both non-linear elastic and plastic components of the model, state parameters (besides the effective stress state, $\boldsymbol{\sigma'}$, and the void ratio, e) are required to define the constitutive relationship. Since these internal variables evolve, in general, with straining, it is necessary to prescribe particular evolution laws for each variable, termed "hardening laws" (Potts and Zdravkovic, 1999).

For the non-linear elastic part of the model (Section 4.2.2), the stress state, the strain state and the void ratio at last shear reversal, $\boldsymbol{\sigma'^{SR}}$, $\boldsymbol{\varepsilon^{SR}}$ and e^{SR}, respectively, as well as the scaling factor N are required to identify eventual shear reversals (Equation 4.22) and to determine the scalar reduction factor T (Equation 4.20). Note that e^{SR} is not directly included in Equation 4.20, however it is necessary to determine the maximum shear modulus at last shear reversal, G_{max}^{SR}, affecting the value of the scalar quantity η_1 (Equation 4.23). The hardening laws for all these state parameters consist solely of updating their values whenever a shear reversal is detected.

Regarding the plastic component of the formulation (Section 4.2.3), there are two state parameters: the back-stress ratio tensor, $\boldsymbol{\alpha}$, which defines the location of axis of the yield surface in the multiaxial stress space (Equation 4.34), and the shearing-induced fabric tensor, $\boldsymbol{F}$, which introduces the effect of the evolution of sand's fabric during shearing on the plastic hardening modulus through the plastic multiplier h_f (Equation 4.61). Starting with $\boldsymbol{\alpha}$, according to the general principles of plasticity, its hardening law must ensure that the consistency condition (Equation 4.28) is satisfied. It is, therefore, necessary to determine the partial derivative of the yield function to the back-stress ratio tensor, $\partial F/\partial \boldsymbol{\alpha}$, as given by Equation 4.64. Using Equations 4.31, 4.48, 4.58 and 4.64, the evolution of the axis of the yield surface, $\Delta\boldsymbol{\alpha}$, can be explicitly presented as indicated by Equation 4.65.

$$\frac{\partial F}{\partial \boldsymbol{\alpha}} = \frac{\partial}{\partial \boldsymbol{\alpha}}\left(\|\boldsymbol{s} - p'\,\boldsymbol{\alpha}\|_2 - \sqrt{\frac{2}{3}}\, m\, p'\right) = -p' \frac{\boldsymbol{s} - p'\,\boldsymbol{\alpha}}{\|\boldsymbol{s} - p'\,\boldsymbol{\alpha}\|_2} = -p'\,\boldsymbol{n} \tag{4.64}$$

$$\Delta\boldsymbol{\alpha} = -\frac{\lambda\, A}{\dfrac{\partial F}{\partial \boldsymbol{\alpha}}} = \lambda\, h(\boldsymbol{\alpha^b} - \boldsymbol{\alpha}) = \lambda\, h_b\, h_e\, h_f\, h_g\, (\boldsymbol{\alpha^b} - \boldsymbol{\alpha}) \tag{4.65}$$

For the shearing-induced fabric tensor, two independent hardening rules were established by Papadimitriou and Bouckovalas (2002) for the evolution of the isotropic, Δf_p (Equation 4.66), and deviatoric, $\Delta \boldsymbol{f}$ (Equation 4.67), components of the tensor.

$$\Delta f_p = H\,\Delta \varepsilon_v^p \tag{4.66}$$

$$\Delta \boldsymbol{f} = -H\,\langle -\Delta \varepsilon_v^p \rangle\,[C\,\boldsymbol{n} + \boldsymbol{f}] \tag{4.67}$$

where C and H are model parameters. As pointed out by the Papadimitriou and Bouckovalas (2002), although both components depend on the incremental plastic volumetric strain, $\Delta \varepsilon_v^p$, the use of the Macaulay brackets in Equation 4.67 implies that $\boldsymbol{f}$ only changes when plastic dilation (i.e. $\Delta \varepsilon_v^p < 0$) occurs. Moreover, due to the negative sign used in Equation 4.67 (before the model parameter H), it can be concluded that, when $\boldsymbol{f}$ evolves, it occurs in the opposite direction of the tensor defined by $[C\,\boldsymbol{n} + \boldsymbol{f}]$. Therefore, at a given moment of loading history, if the magnitude of $\boldsymbol{f}$ is non-zero and $\boldsymbol{f}$ starts evolving due to the occurrence of plastic dilation, then $\boldsymbol{f}$ and, consequently, $[C\,\boldsymbol{n} + \boldsymbol{f}]$ will be reduced until $\boldsymbol{f} = -C\,\boldsymbol{n}$ is obtained and, therefore, $\Delta \boldsymbol{f} = 0$, or until a change in the loading direction, $\boldsymbol{n}$, occurs. It can, therefore, be concluded that C establishes a maximum value for the norm of $\boldsymbol{f}$.

According to Papadimitriou and Bouckovalas (2002), an appropriate value for C is given by the maximum value ever recorded by f_p (Equation 4.68).

$$C = \max \left| f_p \right|^2 \tag{4.68}$$

Since C defines the maximum norm of $\boldsymbol{f}$, as previously explained, this means that the denominator in Equation 4.61, defining the scalar of h_f, is limited to $1 + \max \left| f_p \right|^2$, which corresponds to the maximum value ever obtained by the numerator. As pointed out by Taborda (2011), although Equation 4.68 eliminates the need for an additional model parameter, it introduces a new state parameter in the analysis. In effect, whenever f_p changes, it is necessary to check whether the newly computed value of $\left| f_p \right|^2$ is larger than the current value of C and, if true, update the parameter C.

In relation to the model parameter H, which controls the rate of the evolution of both isotropic and deviatoric components of the shearing-induced fabric tensor and is often referred to as shearing-induced "fabric index", Papadimitriou and Bouckovalas (2002) suggested that it can be related to sand's initial conditions through Equation 4.69.

$$H = H_0 \left(\frac{\sigma'_{1,0}}{p'_{ref}} \right)^{-\xi} \langle -\psi_0 \rangle \tag{4.69}$$

where H_0 and ζ are new positive model parameters, while $\sigma'_{1,0}$ and ψ_0 are the initial values of the major principal effective stress and state parameter, respectively. It is interesting to note that the use of the Macaulay brackets in this equation implies that the effect of fabric evolution during shearing is only simulated when sand is initially in a denser-than-critical state

(i.e. when $\psi_0 < 0$); otherwise, H is null and, consequently, $\boldsymbol{f}$ and f_p do not evolve during loading. Furthermore, this equation states that, for a given sand, the initially denser it is (i.e. the larger the negative value of ψ_0) and the lower the initial major principal effective stress applied to it, the greater the value of H and, consequently, the faster the rate at which f_p and $\boldsymbol{f}$ develop (Equation 4.66 and 4.67, respectively) with the plastic volumetric strain increment, $\Delta\varepsilon_v^p$. Indeed, as mentioned by Papadimitriou and Bouckovalas (2002), the fact that H depends on $\sigma'_{1,0}$ and not on the initial mean effective stress, p', intends to account for the dependency of fabric evolution on both initial confinement and initial stress anisotropy.

As pointed out by Taborda (2011), under low effective stresses (e.g. close to the ground surface), Equation 4.69 may result in very large values for H, which may have a detrimental impact on the computation. To prevent this from happening, Taborda (2011) suggested the introduction of a upper limit for H (Equation 4.70).

$$H \leq H_{max} \tag{4.70}$$

4.2.5 Additional low-stress yield surface

In the present constitutive model, both non-linear elastic and plastic response depend on the current stress ratio, $\boldsymbol{r}$. Specifically, the distance between $\boldsymbol{r}$ and its value at last shear reversal, $\boldsymbol{r}^{SR}$, in the deviatoric stress ratio plane is employed to determine the scalar reduction, T (Equation 4.20), of the tangent shear modulus. Similarly, the dilatancy coefficient and plastic hardening modulus depend on the distance from $\boldsymbol{r}$ to its projection on the dilatancy and bounding surfaces (Equation 4.47 and 4.48, respectively). As mentioned by Taborda *et al.* (2014), while being useful, this normalisation of the deviatoric stress tensor, $\boldsymbol{s}$, by the mean effective stress, p', can result in a loss of accuracy in situations where effective stresses are very low, e.g. when simulating liquefaction-related phenomena. To prevent this from happening, the authors introduced an additional yield surface, termed as *secondary yield surface*, which establishes a lower limit value for the mean effective stress, p'_{YS} (Equation 4.71). Note that the subscript "2" is used to distinguish this secondary yield surface from the original yield surface (henceforth termed *primary yield surface*), which was previously defined by Equation 4.34.

$$F_2 = p'_{YS} - p' = 0 \tag{4.71}$$

In order to keep the formulation of the secondary yield surface as simple as possible, p'_{YS}, is considered a model parameter, rather than a state parameter. Therefore, the plastic hardening modulus associated with this additional surface is null (i.e. $\partial F_2/\partial \boldsymbol{k_2} = 0 \Longrightarrow A_2 = 0$, where $\boldsymbol{k_2}$ represents generically a set of state parameters associated with the secondary yield surface), meaning that perfect plasticity is assumed (Potts and Zdravkovic, 1999). Moreover, an associated flow rule is adopted, which means that the gradient of the plastic potential, $\partial \boldsymbol{P_2}/\partial \boldsymbol{\sigma'}$, coincides with the gradient of the yield function $\partial F_2/\partial \boldsymbol{\sigma'}$, as indicated by Equation 4.72.

$$\frac{\partial \boldsymbol{P_2}}{\partial \boldsymbol{\sigma'}} = \frac{\partial F_2}{\partial \boldsymbol{\sigma'}} = \frac{1}{3}\,\frac{\partial F_2}{\partial p'}\,\boldsymbol{I} + \frac{\partial F_2}{\partial \boldsymbol{s}} = -\frac{1}{3}\,\boldsymbol{I} \tag{4.72}$$

where $\boldsymbol{I}$ is the second-order identity tensor.

Similar to what was previously presented for the primary yield surface, when the current effective stress point activates the secondary yield surface, the plastic strain increment associated with that plastic mechanism, $\Delta\boldsymbol{\varepsilon_2^p}$, is given by Equation 4.73.

$$\Delta\boldsymbol{\varepsilon_2^p} = \begin{bmatrix} \Delta\varepsilon^p_{2,xx} & \Delta\gamma^p_{2,xy} & \Delta\gamma^p_{2,xz} \\ \Delta\gamma^p_{2,yx} & \Delta\varepsilon^p_{2,yy} & \Delta\gamma^p_{2,yz} \\ \Delta\gamma^p_{2,zx} & \Delta\gamma^p_{2,zy} & \Delta\varepsilon^p_{2,zz} \end{bmatrix} = \lambda_2\,\frac{\partial \boldsymbol{P_2}}{\partial \boldsymbol{\sigma'}} \tag{4.73}$$

where λ_2 is now the plastic multiplier associated with the secondary yield surface, which is given by Equation 4.74 when only this surface is active.

$$\lambda_2 = \frac{\dfrac{\partial F_2}{\partial \boldsymbol{\sigma'}} : \boldsymbol{D} : \Delta\boldsymbol{\varepsilon}}{\dfrac{\partial F_2}{\partial \boldsymbol{\sigma'}} : \boldsymbol{D} : \dfrac{\partial \boldsymbol{P_2}}{\partial \boldsymbol{\sigma'}} + A_2} \tag{4.74}$$

with $\boldsymbol{D}$ being the elastic constitutive matrix and $A_2 = 0$, as explained before.

Note, however, that, for models having two yield surfaces, the effective stress point may activate individually any of the yield surfaces or both simultaneously. In the latter situation, the equations employed to determine the incremental plastic strains need to be modified (Potts and Zdravkovic, 1999; Taborda *et al.*, 2014). Specifically, the plastic strain increment, $\Delta\boldsymbol{\varepsilon^p}$, and effective stress increment, $\Delta\boldsymbol{\sigma'}$, are given by Equation 4.75 and 4.76, respectively.

$$\Delta\boldsymbol{\varepsilon^p} = \Delta\boldsymbol{\varepsilon_1^p} + \Delta\boldsymbol{\varepsilon_2^p} = \lambda_1\,\frac{\partial \boldsymbol{P_1}}{\partial \boldsymbol{\sigma'}} + \lambda_2\,\frac{\partial \boldsymbol{P_2}}{\partial \boldsymbol{\sigma'}} \tag{4.75}$$

$$\Delta\boldsymbol{\sigma'} = \boldsymbol{D} : \Delta\boldsymbol{\varepsilon^e} = \boldsymbol{D} : (\Delta\boldsymbol{\varepsilon} - \Delta\boldsymbol{\varepsilon^p}) = \boldsymbol{D} : \Delta\boldsymbol{\varepsilon} - \lambda_1\ \boldsymbol{D} : \frac{\partial \boldsymbol{P_1}}{\partial \boldsymbol{\sigma'}} - \lambda_2\ \boldsymbol{D} : \frac{\partial \boldsymbol{P_2}}{\partial \boldsymbol{\sigma'}} \tag{4.76}$$

where all quantities associated with the primary yield surface are now denoted by the subscript "1", while those associated with the secondary yield surface are denoted by the subscript "2".

Furthermore, when both plastic mechanisms are active, the stress state must remain on both yield surfaces, meaning that Equations 4.77 and 4.78 need to be satisfied simultaneously.

$$\begin{aligned} \Delta F_1 &= \frac{\partial F_1}{\partial \boldsymbol{\sigma'}} : \Delta\boldsymbol{\sigma'} + \frac{\partial F_1}{\partial \boldsymbol{k_1}} : \Delta\boldsymbol{k_1} = 0 \\ &\Leftrightarrow \frac{\partial F_1}{\partial \boldsymbol{\sigma'}} : \boldsymbol{D} : \Delta\boldsymbol{\varepsilon} - \lambda_1\,\frac{\partial F_1}{\partial \boldsymbol{\sigma'}} : \boldsymbol{D} : \frac{\partial \boldsymbol{P_1}}{\partial \boldsymbol{\sigma'}} - \lambda_2\,\frac{\partial F_1}{\partial \boldsymbol{\sigma'}} : \boldsymbol{D} : \frac{\partial \boldsymbol{P_2}}{\partial \boldsymbol{\sigma'}} - \lambda_1 A_1 = 0 \end{aligned} \tag{4.77}$$

$$\begin{aligned} \Delta F_2 &= \frac{\partial F_2}{\partial \boldsymbol{\sigma'}} : \Delta\boldsymbol{\sigma'} + \frac{\partial F_2}{\partial \boldsymbol{k_2}} : \Delta\boldsymbol{k_2} = 0 \\ &\Leftrightarrow \frac{\partial F_2}{\partial \boldsymbol{\sigma'}} : \boldsymbol{D} : \Delta\boldsymbol{\varepsilon} - \lambda_1\,\frac{\partial F_2}{\partial \boldsymbol{\sigma'}} : \boldsymbol{D} : \frac{\partial \boldsymbol{P_1}}{\partial \boldsymbol{\sigma'}} - \lambda_2\,\frac{\partial F_2}{\partial \boldsymbol{\sigma'}} : \boldsymbol{D} : \frac{\partial \boldsymbol{P_2}}{\partial \boldsymbol{\sigma'}} - \lambda_2 A_2 = 0 \end{aligned} \tag{4.78}$$

where:

$$A_1 = -\frac{1}{\lambda_1}\frac{\partial F_1}{\partial \boldsymbol{k_1}} : \Delta \boldsymbol{k_1} \tag{4.79}$$

$$A_2 = -\frac{1}{\lambda_2}\frac{\partial F_2}{\partial \boldsymbol{k_2}} : \Delta \boldsymbol{k_2} \tag{4.80}$$

It can be observed that Equations 4.77 and 4.78 depend linearly on the plastic multipliers λ_1 and λ_2. (Equations 4.81 and 4.82). Therefore, it can be written as:

$$\lambda_1 L_{11} + \lambda_2 L_{12} = T_1 \tag{4.81}$$

$$\lambda_1 L_{21} + \lambda_2 L_{22} = T_2 \tag{4.82}$$

where:

$$L_{11} = \frac{\partial F_1}{\partial \boldsymbol{\sigma'}} : \boldsymbol{D} : \frac{\partial \boldsymbol{P_1}}{\partial \boldsymbol{\sigma'}} + A_1 \tag{4.83}$$

$$L_{12} = \frac{\partial F_1}{\partial \boldsymbol{\sigma'}} : \boldsymbol{D} : \frac{\partial \boldsymbol{P_2}}{\partial \boldsymbol{\sigma'}} \tag{4.84}$$

$$L_{21} = \frac{\partial F_2}{\partial \boldsymbol{\sigma'}} : \boldsymbol{D} : \frac{\partial \boldsymbol{P_1}}{\partial \boldsymbol{\sigma'}} \tag{4.85}$$

$$L_{22} = \frac{\partial F_2}{\partial \boldsymbol{\sigma'}} : \boldsymbol{D} : \frac{\partial \boldsymbol{P_2}}{\partial \boldsymbol{\sigma'}} + A_2 \tag{4.86}$$

$$T_1 = \frac{\partial F_1}{\partial \boldsymbol{\sigma'}} : \boldsymbol{D} : \Delta \boldsymbol{\varepsilon} \tag{4.87}$$

$$T_2 = \frac{\partial F_2}{\partial \boldsymbol{\sigma'}} : \boldsymbol{D} : \Delta \boldsymbol{\varepsilon} \tag{4.88}$$

It is possible to solve this system of linear equations by substitution, resulting in Equations 4.89 and 4.90.

$$\lambda_1 = \frac{L_{22}\, T_1 - L_{12}\, T_2}{L_{11}\, L_{22} - L_{12}\, L_{21}} \tag{4.89}$$

$$\lambda_2 = \frac{L_{11}\, T_2 - L_{21}\, T_1}{L_{11}\, L_{22} - L_{12}\, L_{21}} \tag{4.90}$$

Since this secondary yield surface does not make use of any state parameter, there is no need to specify any additional hardening law for the constitutive model. Nevertheless, as pointed out by Taborda (2011) and Taborda *et al.* (2014), when the secondary yield surface is active, the resulting plastic volumetric strain increment, $\Delta\varepsilon^p_{2,v} = \Delta\varepsilon^p_{2,xx} + \Delta\varepsilon^p_{2,yy} + \Delta\varepsilon^p_{2,zz}$, should be employed in the computation of the evolutions of the isotropic, Δf_p, and deviatoric, $\Delta \boldsymbol{f}$, components of the shearing-induced fabric tensor. In general, it can be written:

$$\Delta f_p = H\left(\Delta\varepsilon^p_{1,v} + \Delta\varepsilon^p_{2,v}\right) \tag{4.91}$$

$$\Delta \boldsymbol{f} = -H\left\langle -\Delta\varepsilon^p_{1,v} - \Delta\varepsilon^p_{2,v}\right\rangle \left[C\,\boldsymbol{n} + \boldsymbol{f}\right] \tag{4.92}$$

where $\Delta\varepsilon^{p}_{1,v}$ and $\Delta\varepsilon^{p}_{2,v}$ are the plastic strain increment associated with the primary and secondary yield surfaces, respectively, and *C* and *H* are given by Equations 4.68 and 4.69, respectively.

In relation to the back-stress tensor α, as it is uniquely related to the primary yield surface, its evolution is solely associated with the plastic multiplier associated with the primary yield surface, as given by Equation 4.93 (which is identical to Equation 4.65).

$$\Delta\alpha = \lambda_1 \, h_b \, h_e \, h_f \, h_g \, (\alpha^b - \alpha) \tag{4.93}$$

4.2.6 Summary of the original model formulation and parameters

The key ingredients of the present constitutive model include:

- non-linear cyclic elasticity, which has been shown to play a crucial role on the accurate simulation of the response of sand at relatively small amplitudes (Papadimitriou and Bouckovalas, 2002);
- dependence of the stress ratio at phase transformation (i.e. dilatancy stress ratio), as well as peak (or bounding) stress ratio on the state parameter, ψ, proposed by Been and Jefferies (1985), allowing for a satisfactory prediction of the response of sand for a wide range of initial void ratios and effective stress states using a single set of model parameters (Manzari and Dafalias, 1997); in addition, the use of the state parameter concept ensures compatibility with CSSM, as established by Schofield and Wroth (1968), since both dilatancy and bounding stress ratios coincide with the critical state ratio when $\psi = 0$ at critical state (Manzari and Dafalias, 1997; Dafalias *et al.*, 2006);
- as postulated by the bounding surface plasticity framework (Dafalias, 1986), the plastic hardening modulus is related to the distance from the current effective stress point to its projection on the bounding surface, allowing for a better prediction of the highly non-linear pre-failure response of sand (Loukidis and Salgado, 2009); moreover, when used in conjunction with a small yield surface and kinematic hardening plasticity (as it is the case), it allows for an accurate prediction of the accumulation of irrecoverable strains during cyclic loading, which would be difficult to capture when using a constitutive model formulated within the classical elasto-plasticity framework (Potts and Zdravkovic, 1999);
- the dilatancy coefficient is proportional to the distance from the current effective stress point to its projection on the dilatancy surface;
- dependence of the plastic modulus on an empirical index describing the effect of fabric evolution during shearing; as pointed out by Papadimitriou and Bouckovalas (2002), due to this dependency, the constitutive model is able to replicate the continuously stiffening unloading-reloading response observed in drained and undrained shearing under successive loading cycles of relatively small amplitude; more importantly, as highlighted by the authors, the introduction of this fabric-related

index allows for the simulation of a more compliant (i.e. softer) response of sand once the phase transformation line is crossed and the stress path is reversed, as observed in the laboratory (Ishihara *et al.*, 1975).

The equations of the constitutive model proposed by Taborda *et al.* (2014), as well as its model parameters are summarised in Table 4.1. Note that the numbering of the equations indicated in the table refer to those previously presented in this chapter.

Table 4.1 – Summary of the formulation of the model and its parameters.

Description		Constitutive equation	Parameters
Non-linear cyclic elasticity			
Small-strain shear modulus at small strains	(4.25)	$G_{max} = C_g\, p'_{ref}\, \frac{1}{0.3 + 0.7\, e^2} \sqrt{\frac{p'}{p'_{ref}}} \geq C_g\, p'_{ref}\, \frac{1}{0.3 + 0.7\, e^2} \sqrt{\frac{p'_{min}}{p'_{ref}}}$	C_g, p'_{ref}, p'_{min}
Tangent shear modulus	(4.26)	$G_{tan} = \frac{G_{max}}{T} \geq G_{min}$	G_{min}
		where:	
	(4.20)	$T = 1 + \kappa \left(\frac{1}{a_1} - 1\right) \left(\frac{\chi^r_{ref}}{N\, \eta_1}\right)^{\kappa - 1} \leq 1 + \kappa \left(\frac{1}{a_1} - 1\right)$	κ
	(4.21)	$\chi^r_{ref} = \sqrt{1/2}\, \sqrt{(\boldsymbol{r} - \boldsymbol{r}^{SR}) : (\boldsymbol{r} - \boldsymbol{r}^{SR})}$	
	(4.23)	$\eta_1 = a_1 \left(\frac{G^{SR}_{max}}{p'^{SR}}\right) \gamma_1$	a_1, γ_1
Tangent bulk modulus	(4.24)	$K_{tan} = \frac{2\,(1 + \nu)}{3\,(1 - 2\,\nu)} G_{tan}$	ν
Model surfaces			
Critical state line in the $e - p'$ space	(4.2)	$e_{CS} = (e_{CS})_{ref} - \lambda \left(\frac{p'}{p'_{ref}}\right)^{\xi}$	$(e_{CS})_{ref}$, λ, ξ
Critical state ratio	(4.35, 4.38)	$M^c = g(\theta, c^c)\, M^c_c$ with $c^c = M^c_e / M^c_c$	M^c_c, M^c_e
Dilatancy stress ratio	(4.5, 4.35, 4.38)	$M^d = g\left(\theta, c^d\right) M^d_c$ with $c^d = M^d_e / M^d_c$ and $M^d_c = M^c_c + k^d_c\, \psi$ and $M^d_e = M^c_e + k^d_e\, \psi$	k^d_c, k^d_e
Bounding stress ratio	(4.4, 4.35, 4.38)	$M^b = g\left(\theta, c^b\right) M^b_c$ with $c^b = M^b_e / M^b_c$ and $M^b_c = M^c_c + k^b_c\, \langle -\psi \rangle$ and $M^b_e = M^c_e + k^b_e\, \langle -\psi \rangle$	k^b_c, k^b_e

Table 4.1 – Summary of the formulation of the model and its parameters.

Description		Constitutive equation	Parameters
Interpolation function	(4.36)	$g(\theta, c^{d,c,b}) = \dfrac{2\, c^{d,c,b}}{\dfrac{1+c^{d,c,b}}{2} - \dfrac{1-c^{d,c,b}}{2}\cos(3\theta)} - \left[\dfrac{1+c^{d,c,b}}{2} + \dfrac{1-c^{d,c,b}}{2}\cos(3\theta)\right]$	
Modified Lode's angle	(4.37)	$\cos(3\theta) = \left(\dfrac{3\sqrt{3}}{2}\dfrac{\overline{J_3}}{\left(\overline{J_2}\right)^{3/2}}\right)$	
Primary YS	(4.34)	$F_1 = \sqrt{(\boldsymbol{s}-p'\,\boldsymbol{\alpha}) : (\boldsymbol{s}-p'\,\boldsymbol{\alpha})} - \sqrt{2/3}\; m\, p' = 0$	m
Secondary YS	(4.71)	$F_2 = p'_{YS} - p' = 0$	p'_{YS}
Gradients of the yield surfaces (YS)			
Associated with the primary YS	(4.45)	$\dfrac{\partial F_1}{\partial \boldsymbol{\sigma}'} = -\dfrac{1}{3}\left(\boldsymbol{\alpha} : \boldsymbol{n} + \sqrt{\dfrac{2}{3}}\, m\right)\boldsymbol{I} + \boldsymbol{n}$	
		where:	
	(4.42)	$\boldsymbol{n} = \dfrac{\boldsymbol{r}-\boldsymbol{\alpha}}{\sqrt{2/3}\; m} = \dfrac{\boldsymbol{s}-p'\,\boldsymbol{\alpha}}{\sqrt{2/3}\; m\, p'}$	
Associated with the secondary YS	(4.72)	$\dfrac{\partial F_2}{\partial \boldsymbol{\sigma}'} = -\dfrac{1}{3}\,\boldsymbol{I}$	
Gradients of the plastic potentials			
Associated with the primary YS	(4.46)	$\dfrac{\partial \boldsymbol{P}}{\partial \boldsymbol{\sigma}'} = \dfrac{1}{3}\, D\, \boldsymbol{I} + \boldsymbol{n}$	
		where:	
	(4.47)	$D = A_0\, d^d$	A_0
	(4.43)	$d^d = \left(\boldsymbol{\alpha^d} - \boldsymbol{\alpha}\right) : \boldsymbol{n} = \sqrt{2/3}\,\alpha_\theta^d - \boldsymbol{\alpha} : \boldsymbol{n} = \sqrt{2/3}\left(g(\theta, c^d)\, M_c^d - m\right) - \boldsymbol{\alpha} : \boldsymbol{n}$	
Associated with the secondary YS	(4.72)	$\dfrac{\partial \boldsymbol{P_2}}{\partial \boldsymbol{\sigma}'} = -\dfrac{1}{3}\,\boldsymbol{I}$	
Plastic hardening modulus			
Associated with the primary YS	(4.48, 4.58)	$A_1 = p'\, h_b\, h_e\, h_f\, h_g\, d^b$	
		where:	
	(4.59)	$h_b = \left(\dfrac{p'}{p'_{ref}}\right)^{\mu-1}\left(\dfrac{\left\lvert d^b\right\rvert}{\langle d^b_{ref} - \left\lvert d^b\right\rvert\rangle}\right)^{\beta+1}$	μ, β
	(4.60)	$h_e = h_0\,(1-\gamma e) \geq h_0\,(1-\gamma e_{lim})$	h_0, γ, e_{lim}

Table 4.1 – Summary of the formulation of the model and its parameters.

Description		Constitutive equation	Parameters
	(4.61)	$h_{f,min} \leq h_f = \dfrac{1+\langle f_p \rangle^2}{1+\langle \boldsymbol{f}:\boldsymbol{n} \rangle} \leq h_{f,max}$	$h_{f,min}$, $h_{f,max}$
	(4.62)	$h_g = G_{tan}^{\alpha}$	α
		with:	
	(4.43)	$d^b = (\boldsymbol{\alpha^b} - \boldsymbol{\alpha}) : \boldsymbol{n} = \sqrt{2/3}\,\alpha_\theta^b - \boldsymbol{\alpha}:\boldsymbol{n} = \sqrt{2/3}\,(g(\theta,c^b)\,M_c^b - m) - \boldsymbol{\alpha}:\boldsymbol{n}$	
	(4.51)	$d_{ref}^b = \sqrt{2/3}\,\left(g(\theta,c^b)\,M_c^b + g(\theta+\pi,c^b)\,M_c^b - 2\,m\right)$	
Associated with the secondary YS		$A_2 = 0$	
Hardening rules			
Back-stress ratio evolution	(4.65)	$\Delta\boldsymbol{\alpha} = \lambda_1\, h_b\, h_e\, h_f\, h_g\, (\boldsymbol{\alpha^b} - \boldsymbol{\alpha})$	
Shearing -induced fabric tensor evolution	(4.66)	$\Delta f_p = H\,\Delta\varepsilon_v^p$	
	(4.67)	$\Delta\boldsymbol{f} = -H\,\langle -\Delta\varepsilon_v^p \rangle\,[C\,\boldsymbol{n} + \boldsymbol{f}]$	
		where	
	(4.69, 4.70)	$H = H_0 \left(\dfrac{\sigma'_{1,0}}{p'_{ref}}\right)^{-\xi} \langle -\psi_0 \rangle \leq H_{max}$	H_0, ζ, H_{max}
	(4.68)	$C = \max \left\lvert f_p \right\rvert^2$	

It can be observed that the constitutive model requires a total of twenty-five parameters and six optional parameters (p'_{min}, G_{min}, e_{min}, $h_{f,min}$, $h_{f,max}$ and H_{max} represented in grey in Table 4.1), which were introduced by Taborda (2011) to increase the numerical stability of the constitutive model when simulating boundary-value problems. As discussed in Chapter 6, reference values may be used for these six additional model parameters. In addition, as proposed by Papadimitriou and Bouckovalas (2002), the number of model parameter may be reduced by considering the following two simplifications: $k_e^d = k_c^d\,(M_e^c/M_c^c)$ and $k_e^b = k_c^b\,(M_e^c/M_c^c)$. Note that these simplifications imply that $c^d = c^b = c^c$. The suitability of these simplifications are also discussed in Chapter 6, based on experimental data obtained for Hostun sand.

In addition, Table 4.2 presents the meaning of each model parameter. Once more, note that the optional model parameters (p'_{min}, G_{min}, e_{min}, $h_{f,min}$, $h_{f,max}$ and H_{max}), defining either lower

or upper limits to the values of constitutive parameters, are represented in grey. Moreover, note that values that have been proposed in the literature for the model parameters are discussed in Chapter 6, where the calibration of the constitutive model for Hostun sand is presented.

Table 4.2 – Model parameters: meaning and typical range for sand (after Papadimitriou and Bouckovalas, 2002; Taborda, 2011).

Parameter	Meaning
C_g	Constant of the elastic shear modulus at small strains
p'_{ref}	Reference pressure (typically assumed as equal to the atmospheric pressure, with a value of 101.3 kPa)
p'_{min}	Lower limit for the mean effective stress
κ a_1	Non-linearity of the elastic shear modulus
γ_1	Strain limit for the reduction of the elastic shear modulus
G_{min}	Lower limit for the tangent shear modulus
ν	Poisson's ratio
$(e_{CS})_{ref}$	Interception of the CSL with the p'-axis in the $e - p'$ space
λ	Slope of the CSL in the $e - p'$ space
ξ	Curvature of CSL in the $e - p'$ space
M_c^c	Critical state strength in triaxial compression
M_e^c	Critical state strength in triaxial extension
k_c^d	Effect of the state parameter on the stress ratio at phase transformation in triaxial compression
k_e^d	Effect of the state parameter on the stress ratio at phase transformation in triaxial extension
k_c^b	Effect of the state parameter on the peak stress ratio in triaxial compression
k_e^b	Effect of the state parameter on the peak stress ratio in triaxial extension
m	Opening of the primary yield surface
p'_{YS}	Lower limit value for the mean effective stress
A_0	Dilatancy coefficient
μ	Non-linearity of the effect of the current mean effective stress on the plastic hardening modulus associated with the primary yield surface
β	Non-linearity of the effect of the distance from the current effective stress point to the boundary surface on the plastic hardening modulus associated with the primary yield surface
h_0	Constant of the plastic hardening modulus associated with the primary yield surface
γ	Effect of the void ratio on the plastic hardening modulus associated with the primary yield surface

Table 4.2 – Model parameters: meaning and typical range for sand (after Papadimitriou and Bouckovalas, 2002; Taborda, 2011).

Parameter	Meaning
e_{lim}	Lower limit of the void ratio influence on the plastic hardening modulus associated with the primary yield surface
α	Effect of the tangent elastic shear modulus on the plastic hardening modulus associated with the primary yield surface
$h_{f,min}$	Lower limit for the influence of the shearing-induced fabric tensor on the plastic hardening modulus associated with the primary yield surface
$h_{f,max}$	Upper limit for the influence of the shearing-induced fabric tensor on the plastic hardening modulus associated with the primary yield surface
H_0	Shearing-induced fabric index constant
ζ	Effect of the major principal effective stress on the shearing-induced fabric index
H_{max}	Upper limit for the shearing-induced fabric index

4.3 Modifications to the formulation proposed by Taborda et al. (2014)

4.3.1 Introduction

As mentioned before, a large number of extended versions of the original model proposed by Manzari and Dafalias (1997) can be found in the literature (e.g. Papadimitriou and Bouckovalas, 2002; Dafalias and Manzari, 2004; Dafalias *et al.*, 2004; Taiebat and Dafalias, 2008; Loukidis and Salgado, 2009; Andrianopoulos *et al.*, 2010; Li and Dafalias, 2012; Taborda *et al.*, 2014; Woo and Salgado, 2015). A review of those proposals suggests that the ability of the model to simulate the response of sand for loading conditions other than triaxial compression seems greatly improved when an inherent fabric anisotropy component is introduced to the constitutive relationship (Dafalias *et al.*, 2004; Loukidis and Salgado, 2009; Woo and Salgado, 2015). In particular, and as detailed later, this component allows for the replication of different sand's responses as the direction of the major principal effective stress to the vertical axis of the sample is changed – a feature of sand's response widely observed in the laboratory, which is not captured by the constitutive model proposed by Taborda (2011) and Taborda *et al.* (2014). In effect, a research project aiming at extending the version of the constitutive model proposed by Taborda *et al.* (2014) to incorporate an inherent fabric anisotropy component was recently carried out at Imperial College London (Williams, 2014). As part of that project, it was concluded that the ability of the constitutive model to replicate hollow cylinder torsional shear test results on sand is greatly improved when this additional component is used, as also detailed later. Due to the short duration of the research project, it was, unfortunately, not possible to further explore the impact of the inherent fabric anisotropy component on the simulation of the response of sand under general loading conditions, such as those found in boundary value problems. It was, therefore, considered

important to introduce an inherent fabric anisotropy component in the present constitutive model and further evaluate its impact on the modelled response. In Section 4.3.3, three particular formulations proposed in the literature (Dafalias *et al.*, 2004; Loukidis and Salgado, 2009; Williams, 2014) are presented. As explained in detail, although the three formulations make use of similar concepts, the formulation proposed by Williams (2014) is the only one among them which complies with the principles of CSSM and, therefore, it was selected to be incorporated in the present version of the model. Note that, due to the modular structure of the constitutive model, it is relatively simple to introduce new components to the formulation without the need to reformulate, at least completely, other components, as highlighted by Taborda *et al.* (2014).

In addition, as detailed in Section 4.3.2, it was deemed important to introduce a more general constitutive equation for the computation of the shear modulus at small strains, G_{max}, allowing for the use of the vast majority of the equations reported in the literature for sands.

The new equations and required model parameters are summarised in Section 4.3.4.

4.3.2 Small-strain shear modulus

The small-strain shear stiffness, G_{max}, of a given material is generally defined as a function of the void ratio, *f(e)*, the overconsolidation ratio, *OCR*, and the mean effective stress, *p'*, as shown by Equation 4.94 (Hardin and Black, 1968).

$$G_{max} = C_g \, p'_{ref} f(e) \, OCR^k \left(\frac{p'}{p'_{ref}} \right)^{n_g} \tag{4.94}$$

where C_g, k and n_g are model parameters. For sands, several experimental studies (e.g. Hardin and Drnevich, 1972; Lo Presti *et al.*, 1997; Zhou and Chen, 2005; Azeiteiro *et al.*, 2017) have shown that *OCR* has a minor influence on G_{max} (as discussed in more detail in Section 2.5.5). Therefore, its effect is usually neglected, with G_{max} being essentially related to e and *p'*. Regarding the function of the void ratio, *f(e)*, based on the experimental results performed by Hardin and Richart (1963) and Hardin and Black (1966) on a round-grained sand (Ottawa sand no. 20-30) and on an angular-grained sand (crushed quartz), Equation 4.95 and Equation 4.96 were proposed by Hardin (1965) and Hardin and Black (1966).

Round-grained sand:

$$f(e) = \frac{(2.17 - e)^2}{1.0 + e} \tag{4.95}$$

Angular-grained sand:

$$f(e) = \frac{(2.97 - e)^2}{1.0 + e} \tag{4.96}$$

An alternative expression for Equation 4.96 was later presented by Hardin (1978) – Equation 4.97. According to this author, Equations 4.96 and 4.97 give very similar results when the void ratio is in the range of 0.4 to 1.2, with the solely advantage of the latter equation being its

simplicity. Note that Equation 4.97 was included in the version of the constitutive model proposed by Papadimitriou and Bouckovalas (2002) and also adopted by Taborda *et al.* (2014) to introduce the effect of the void ratio on shear modulus at small strains (Equation 4.25).

$$f(e) = \frac{1.0}{0.3 + 0.7\,e^2} \tag{4.97}$$

More recently, Lo Presti *et al.* (1993) also suggested an alternative form for this function (Equation 4.98).

$$f(e) = e^{-x} \tag{4.98}$$

where the exponent *x* is a material constant. Note that different values for *x* can be found in the literature, such as 0.8 for Kenya carbonate and Ticino sands (Fioravante, 2000) and 1.3 for Toyoura sand and Quiou carbonate sand (Lo Presti *et al.*, 1993, 1997). A relation between the value of *x* and the shape of the sand particles was not established in any of these references.

Table 4.3, which is mostly extracted from Benz (2007), presents the outcome of several experimental studies on the characterisation of the shear modulus of sand at small strains, where Equation 4.94 was used to describe the experimental data.

Table 4.3 – Parameters for the evaluation of the shear modulus of sand at small strains using Equation 4.94 (after Benz, 2007).

Sand tested and reference	D_{50} (1) (mm)	U_C (2) ( )	C_g ( )	$f(e)$ ( )	n_g ( )
Ham river sand (sub-angular) (Kuwano and Jardine, 2002)	0.27	1.67	720 - 810	$\frac{(2.17-e)^2}{1.0+e}$	0.50
Hostun sand (sub-angular) (Hoque and Tatsuoka, 2000)	0.31	1.94	800	$\frac{(2.17-e)^2}{1.0+e}$	0.47
Hostun sand (sub-angular) (Azeiteiro *et al.*, 2017a) (3)	0.33	1.40	293	$\frac{(2.97-e)^2}{1.0+e}$	0.49
Kenya carbonate sand (sub-rounded) (Fioravante, 2000)	0.13	1.86	1010 - 1290	$e^{-0.8}$	0.45 - 0.52
Ottawa sand (rounded to sub-rounded) (Carraro *et al.*, 2003) (3)	0.38	1.43	611	$\frac{(2.17-e)^2}{1.0+e}$	0.44
Ottawa sand no.20-30 (rounded) (Hardin, 1965; Hardin and Black, 1966a)	0.72	1.20	690	$\frac{(2.17-e)^2}{1.0+e}$	0.50
Quiou carbonate sand (Lo Presti *et al.*, 1997)	0.75	4.40	710	$e^{-1.3}$	0.62
Silica sand (angular) (Zhou and Chen, 2005) (3)	0.14	1.6	206	$\frac{(2.97-e)^2}{1.0+e}$	0.51
	0.34	3.1	211	$\frac{(2.97-e)^2}{1.0+e}$	0.505
Silica sand (sub-angular) (Tika *et al.*, 2003)	0.20	1.10	800	$\frac{(2.17-e)^2}{1.0+e}$	0.50
	0.20	1.70	620	$\frac{(2.17-e)^2}{1.0+e}$	0.50

Table 4.3 – Parameters for the evaluation of the shear modulus of sand at small strains using Equation 4.94 (after Benz, 2007).

Sand tested and reference	D_{50} [1] (mm)	U_C [2] ( )	C_g ( )	$f(e)$ ( )	n_g ( )
	0.32	2.80	480	$\frac{(2.17-e)^2}{1.0+e}$	0.50
Silica sand (Wichtmann and Triantafyllidis, 2004)	0.55	1.80	275	$\frac{(1.46-e)^2}{1.0+e}$	0.42
Silver Leighton Buzzard sand (sub-rounded)	0.62	1.11	820 - 1300	$\frac{(2.17-e)^2}{1.0+e}$	0.44 - 0.53
Ticino sand (sub-angular) (Tatsuoka and Hoque, 2004)	0.50	1.33	610 - 640	$\frac{(2.17-e)^2}{1.0+e}$	0.44 - 0.53
Ticino sand (sub-angular) (Lo Presti *et al.*, 1993)	0.54	1.50	710	$\frac{(2.27-e)^2}{1.0+e}$	0.43
Toyoura sand (sub-angular) (Iwasaki *et al.*, 1978) [3]	0.16	1.46	900	$\frac{(2.17-e)^2}{1.0+e}$	0.40
Toyoura sand (sub-angular) (Tatsuoka and Hoque, 2004)	0.16	1.46	710 - 870	$\frac{(2.17-e)^2}{1.0+e}$	0.41 - 0.51
Toyoura sand (sub-angular) (Kokusho, 1980)	0.19	1.30	840	$\frac{(2.17-e)^2}{1.0+e}$	0.41 - 0.51
Toyoura sand (sub-angular) (Chaudhary *et al.*, 2004)	0.19	1.56	840 - 1040	$\frac{(2.17-e)^2}{1.0+e}$	0.50
Toyoura sand (sub-angular) (Lo Presti *et al.*, 1997)	0.22	1.35	720	$e^{-1.3}$	0.45

[1] D_{50}: mean diameter of the particles; [2] U_C: coefficient of uniformity; [3] Not presented in Benz (2007).

It is interesting to note that, in most published studies, either Equation 4.95 or Equation 4.96 was employed to characterise $f(e)$. Moreover, it can be observed that not only the values of 2.17 (included in the numerator of Equations 4.95) and of 2.97 (included in the numerator of Equation 4.96) have been employed to describe $f(e)$; for instance, Lo Presti *et al.* (1993) adopted a value of 2.27 for Ticino sand, while Wichtmann and Triantafyllidis (2004) used 1.46 to characterise the influence of the void ratio on G_{max} for Silica sand. In addition, it is apparent that, although $n_g = 0.50$ has been adopted in the majority of the studies, values in the range of 0.41 to 0.62 have also been reported in the literature. Therefore, to increase the flexibility of the constitutive model, it was decided to replace Equation 4.19 by a more general equation for G_{max}, consisting of Equation 4.94 with $k = 0.0$, as shown by Equation 4.99, together with Equation 4.100. Note that the adoption of $k = 0.0$ (i.e. the disregard for the effect of OCR) is justified by the fact that the constitutive model has been essentially developed to address the simulation of the response of sand under cyclic loading. Note also that two additional model parameters are introduced: the exponent n_g, which replaces the previously constant value of 0.50, and the model parameter m_g, which usually takes the value 2.17 or 2.97, according to most data published in the literature (Table 4.3). Finally, it is noteworthy that Loukidis and Salgado (2009) also adopted Equations 4.99 and 4.100 to describe G_{max}, with the only

difference residing on the fact that these authors considered $m_g = 2.17$ (i.e. m_g was considered a model constant, rather than a model parameter).

$$G_{max} = C_g \, p'_{ref} f(e) \left(\frac{p'}{p'_{ref}} \right)^{n_g} \tag{4.99}$$

with:

$$f(e) = \frac{\left(m_g - e\right)^2}{1.0 + e} \tag{4.100}$$

4.3.3 Inherent fabric anisotropy

4.3.3.1 Experimental evidence on anisotropic sand response

There is experimental evidence that the response of sand depends on the angle α of the major principal effective stress, σ'_1, to the axis of the sample (Figure 4.9), as well as on the magnitude of the intermediate principal effective stress, σ'_2, in relation to the magnitudes of the major and minor principal effective stresses, σ'_1 and σ'_3, respectively, which is typically characterised by the intermediate principal effective stress ratio $b = (\sigma'_2 - \sigma'_3)/(\sigma'_1 - \sigma'_3)$.

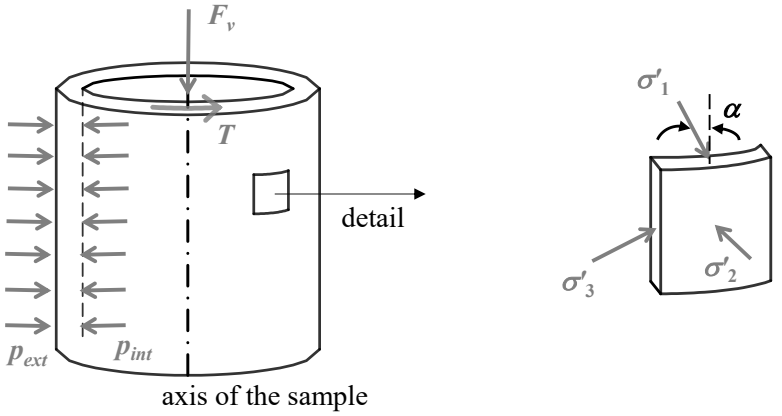

Figure 4.9 – Definition of the direction of the major principal effective stress to the axis of the sample in hollow cylinder torsional shear tests (adapted from Yoshimine *et al.*, 1998).

Figure 4.10 compares the results of two isotropically consolidated undrained monotonic triaxial compression tests with increasing mean stress (ICUMTC p↑) – characterised by $\alpha = 0.0°$ and $b = 0.0$ – with those obtained in two isotropically consolidated undrained monotonic triaxial extension tests with decreasing mean stress (ICUMTE p↓) – characterised by $\alpha = 90.0°$ and $b = 1.0$ – performed by Yoshimine *et al.* (1998) on samples of dry-deposited Toyoura sand prepared to similar initial void ratios ($e_0 = 0.861 - 0.866$) and consolidated under isotropic effective stresses of $\sigma'_0 = 100.0$ or 500 kPa.

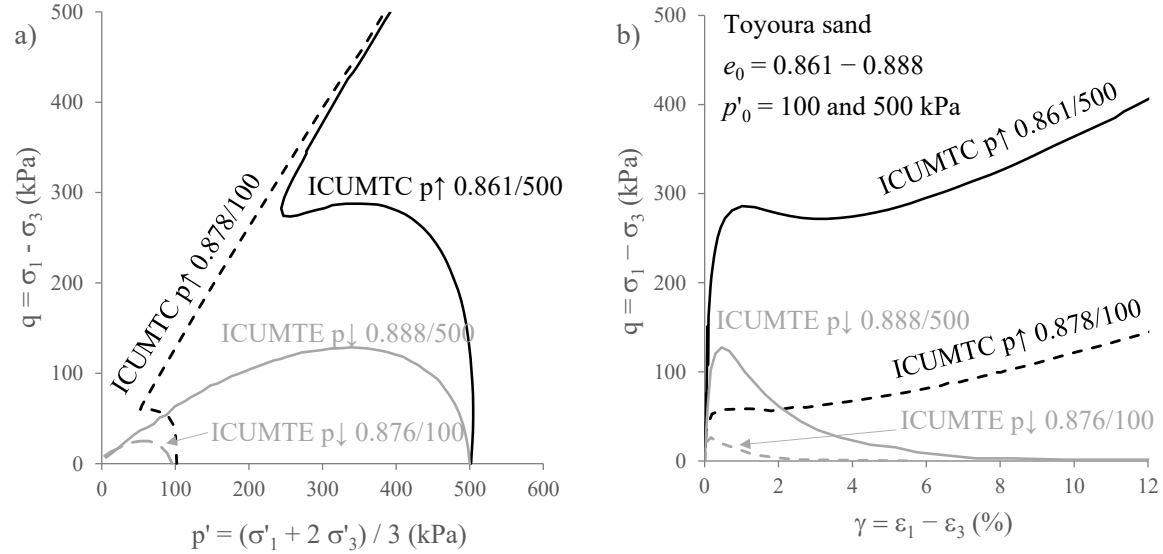

Figure 4.10 – Isotropically consolidated undrained monotonic triaxial compression and extension tests on Toyoura sand samples having similar initial conditions: (a) effective stress path and (b) stress-strain response (Yoshimine *et al.*, 1998).

It can be observed that, irrespective of the initial effective stress, more compliant effective stress paths were registered in the ICUMTE p↓ tests than in the ICUMTC p↑ tests (Figure 4.10a). Furthermore, it is apparent that significantly softer stress-strain responses were measured in triaxial extension than those exhibited in triaxial compression (Figure 4.10b). Similar results were reported by other authors, such as Vaid *et al.* (1990) on water-pluviated Ottawa sand, Vaid and Thomas (1995) on water-pluviated Fraser River sand and Riemer and Seed (1997) on moist-tamped samples of Monterey sand.

Further experimental evidence on the effect of α and b on the undrained response of sand has been collected by performing torsional shear tests using the hollow cylinder apparatus. Note that, contrary to the triaxial equipment, the hollow cylinder apparatus allows for an independent control of α and b, which means that the influence of each of these aspects on the material response can be individually investigated. One of the most comprehensive experimental studies on this topic was undertaken by Yoshimine *et al.* (1998) on dry-deposited Toyoura sand. Figure 4.11 depicts the results of three different torsional shear tests performed by those authors on samples prepared to similar void ratios ($e_0 = 0.821 - 0.825$) and consolidated under an isotropic effective stress of $\sigma'_0 = 100.0$ kPa. In these three tests, the intermediate principal effective stress ratio was kept constant, with a value of $b = 0.5$, while the direction α of the major principal effective stress to the vertical axis of the sample was varied from 15 to 75°. It can be seen that more compliant effective stress paths (Figure 4.11a) and softer stress-strain responses (Figure 4.11b) are registered as value of α is increased from 15 to 75° (i.e. as the direction of the major principal effective stress tended to the horizontal plane, which corresponds to the bedding plane of the reconstituted sample).

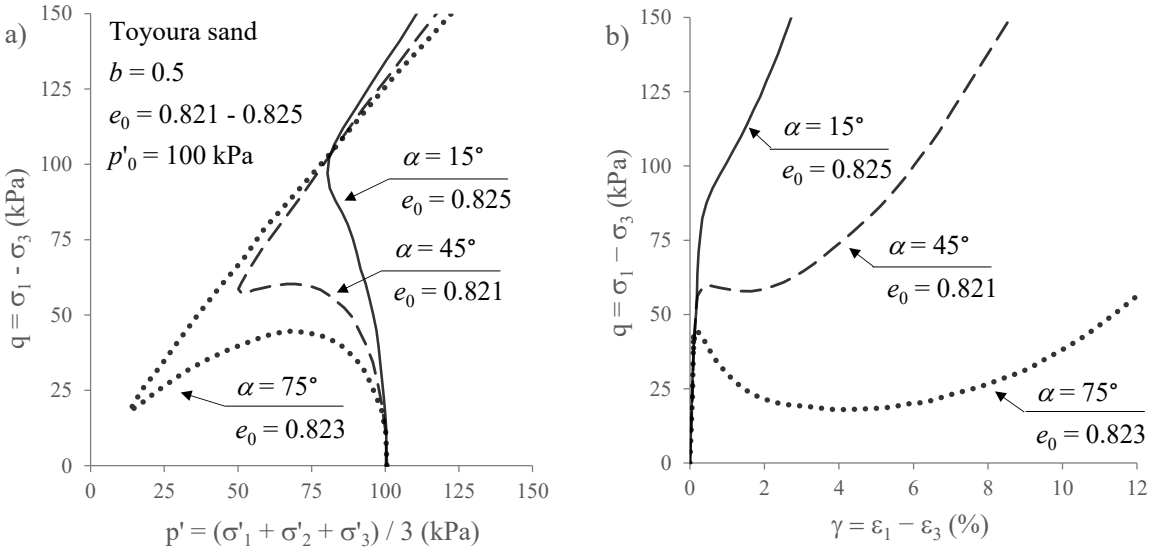

Figure 4.11 – Undrained hollow cylinder torsional shear tests with constant *b* = 0.5 on Toyoura sand samples having similar initial conditions: (a) effective stress path and (b) stress-strain response (Yoshimine *et al.*, 1998).

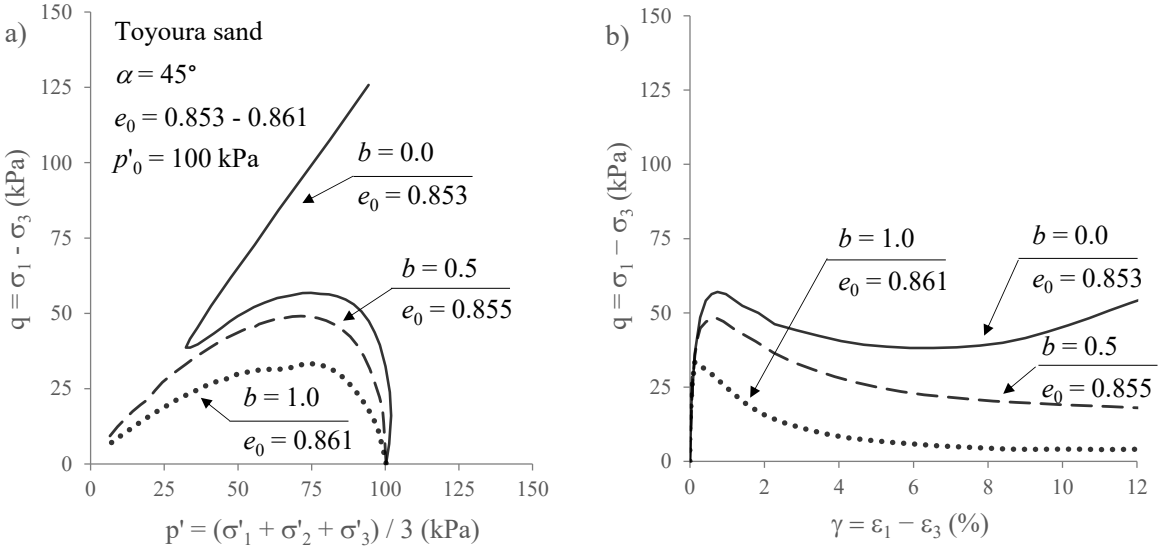

Figure 4.12 – Undrained hollow cylinder torsional shear tests with constant α = 45° on Toyoura sand samples having similar initial conditions: (a) effective stress path; (b) stress-strain response (Yoshimine *et al.*, 1998).

In addition, the authors performed a series of undrained torsional shear tests where the value of *b* was varied, while keeping $\alpha = 45°$. The results of three of these tests performed on samples prepared to similar void ratios ($e_0 = 0.853 - 0.861$) and consolidated to $\sigma'_0 =$ 100.0 kPa are presented in Figure 4.12. It can be observed that the larger the value of *b*, the higher the reduction of the mean effective stress with shearing, as well as the lower the shear stress mobilised in the test. These results seem to agree well with those obtained by the same authors when using the triaxial cell (Figure 4.10). In effect, as the values of α and *b* are increased, as it happens when changing from triaxial compression ($\alpha = 0.0°$ and $b = 0.0$) to triaxial extension ($\alpha = 90.0°$ and $b = 1.0$), a more compliant and softer response was exhibited by the samples, with the results of the hollow cylinder torsional shear tests enabling

to extend the findings and conclude that both α and *b* play a role in the observed response. Note that similar experimental results were reported, for example, by Nakata *et al.* (1998) on air-pluviated Toyoura sand and Uthayakumar and Vaid (1998) on Fraser River sand.

According to Yoshimine *et al.* (1998), the different responses obtained when varying α and/or *b* may be attributed to the anisotropic nature of the sample. In fact, as highlighted by the authors, both in the laboratory and in the field, the gravitational field under which sand structure is formed tends to induce an anisotropic sand fabric, with particles preferentially orientated towards horizontal directions (i.e. to form a horizontal bending plane). Therefore, the mechanical response of sand tends to be stiffer and more resistant when the direction of loading is perpendicular to the bedding plane of the sand particles than when a similar loading is applied parallel to the bedding plane.

4.3.3.2 Motivation for incorporating an inherent fabric anisotropy component in the formulation of the bounding surface plasticity model

The original formulation of the model accounts for anisotropic sand response by defining different dilatancy, bounding and critical stress ratios in triaxial compression, M_c^d, M_c^b and M_c^c, respectively, and in triaxial extension, M_e^d, M_e^b and M_e^c, respectively, and interpolating their values for other loading conditions through the use of the interpolation function *g* (Equation 4.36), which depends on the modified Lode's angle, θ (Equation 4.37). Therefore, the constitutive model has been shown to capture satisfactorily the response of sand under different loading conditions, such as in triaxial compression, in triaxial extension and in direct simple shearing (Papadimitriou *et al.*, 2001; Papadimitriou and Bouckovalas, 2002; Taborda, 2011; Williams, 2014).

Further insight into the ability of the constitutive model to predict the response of sand under other loading conditions than triaxial shearing and direct shearing was provided by Williams (2014). This author carried out a series of simulations of undrained hollow cylinder torsional shear tests using the version of the BSPM implemented by Taborda (2011) into the Imperial College Finite Element Program (ICFEP), which was chosen as a starting point in the present study. Based on the obtained results, Williams (2014) concluded that the constitutive model was unable to capture the effect of the direction of the major principal effective stress to the vertical axis of the sample, characterised by the quantity α, on the modelled response, contradicting the experimental evidence. This is illustrated in Figure 4.13, which compares the results of numerical simulations performed by Williams (2014) with the experimental data obtained by Uthayakumar and Vaid (1998) on water-pluviated samples of Fraser river sand prepared to similar initial void ratios ($e_0 \approx 0.905$) and subjected to the isotropic confining stress of $\sigma'_0 = 200.0$ kPa. While the experimental data suggests that the response of sand changes drastically when α is increased from 0 to 90°, with larger excess pore water pressures being generated and softer stress-strain response being registered, identical responses were

modelled, irrespectively of the value of α. Note that, in these tests, $b = 0.5$ was kept constant throughout loading.

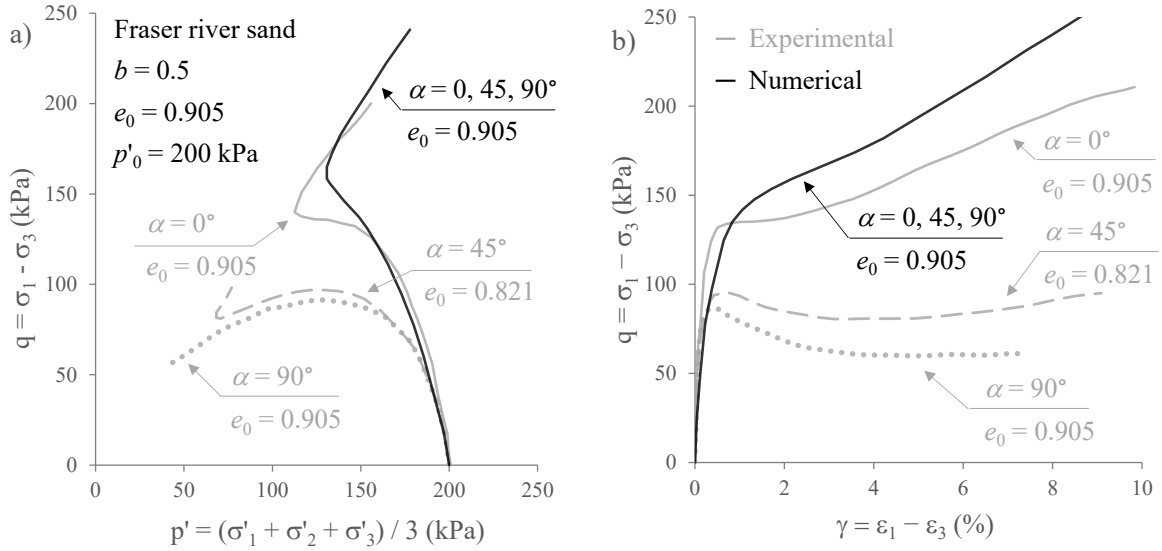

Figure 4.13 – Numerical simulation of undrained hollow cylinder torsional shear tests with constant *b* = 0.5 on Fraser River sand using the original version of the model (Williams, 2014).

A significant improvement on the modelled response was obtained when an inherent fabric anisotropy formulation was incorporated in the constitutive model. This is illustrated in Figure 4.14, which compares the results of a new series of numerical simulations performed by Williams (2014) using the modified version of the constitutive model with those obtained in the laboratory (Uthayakumar and Vaid, 1998). It is noticeable that, by having an inherent fabric anisotropy component, the constitutive model is able to predict the main trends observed in the laboratory. Note that details on the proposed formulation are provided later.

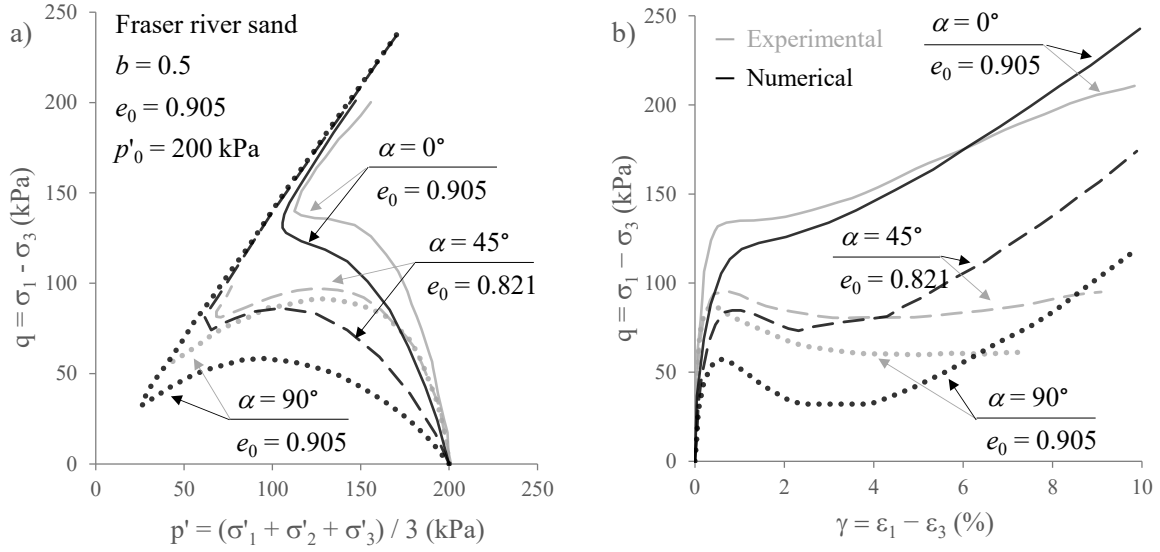

Figure 4.14 – Numerical simulation of undrained hollow cylinder torsional shear tests with constant *b* = 0.5 on Fraser River sand using a modified version of the model incorporating an inherent fabric anisotropy component (Williams, 2014).

A further motivation for incorporating an inherent fabric anisotropy component in the formulation of the constitutive model is related to its inability to predict accurately highly anisotropic sand response observed in some undrained cyclic triaxial tests (Taborda, 2011). This is illustrated in Figure 4.15, which compares the results of a numerical simulation of an undrained cyclic triaxial test on a dense sample Leighton Buzzard Fraction-E sand sample carried out by Taborda (2011) with those obtained in the laboratory by Coelho (2007). It is apparent that the constitutive model is unable to replicate the very soft response in triaxial extension observed during the first loading cycle. As a result, the constitutive model noticeably overpredicts the number of loading cycles required to the onset of cyclic mobility. According to Taborda (2011), the introduction of an inherent fabric anisotropy component may significantly improve the ability of the constitutive model to reproduce this considerably more compliant response in triaxial extension than that observed in triaxial compression. In fact, at least under monotonic loading conditions, the incorporation of an inherent fabric anisotropy component has been shown to improve the accuracy of bounding surface plasticity models to replicate anisotropic sand response (e.g. Dafalias *et al.*, 2004; Loukidis and Salgado, 2009; Li and Dafalias, 2012; Papadimitriou *et al.*, 2014).

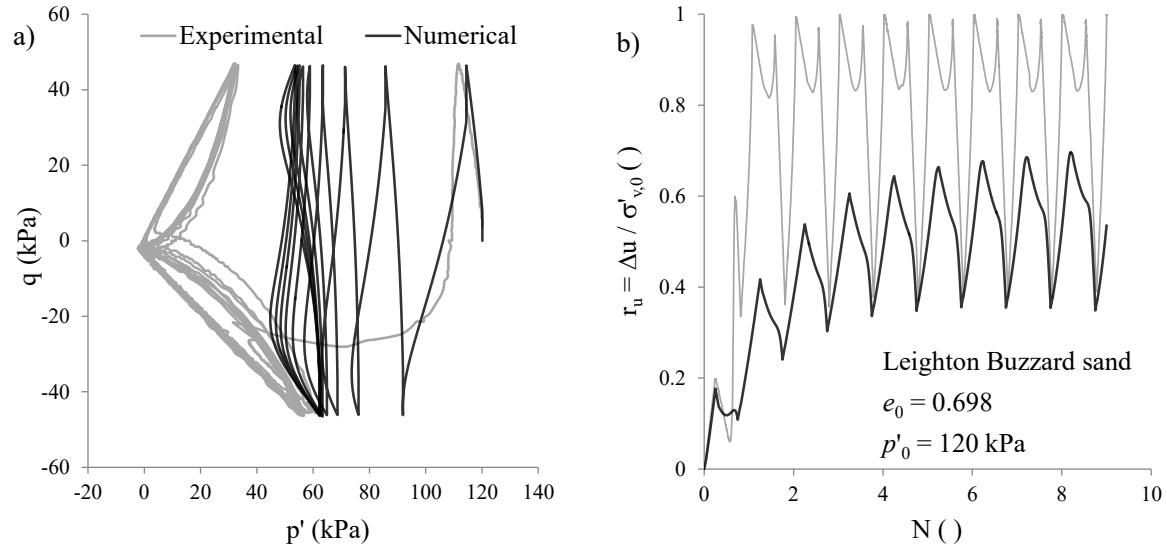

Figure 4.15 – Simulation of an undrained cyclic triaxial test on a dense sample of Leighton Buzzard Fraction-E sand using the original version of the model (Taborda, 2011).

Taking into account that a similar highly anisotropic response was also exhibited by samples of Hostun sand when subjected to undrained cyclic shearing (Chapter 3) and that the constitutive model will be applied to the simulation of dynamic centrifuge experiments performed on Hostun sand (Chapter 8), it was deemed important to include this additional component in the constitutive relationship.

4.3.3.3 *Inherent fabric anisotropy formulations proposed in the literature for constitutive models based on the bounding surface plasticity framework*

A bounding surface plasticity model explicitly accounting for the effect of inherent fabric anisotropy on the response of sand was proposed by Dafalias *et al.* (2004). These authors introduced a second-order symmetric inherent fabric tensor $\boldsymbol{F_A}$, which analytically describes the orientation of sand particle distribution in the 3D stress space. By assuming transverse isotropy on the horizontal *xz* plane (which coincides with the plane of the deposition of the particles), the authors defined $\boldsymbol{F_A}$ in the form of Equation 4.101.

$$\boldsymbol{F_A} = \begin{bmatrix} F_{xx} & F_{xy} & F_{xz} \\ F_{yx} & F_{yy} & F_{yz} \\ F_{zx} & F_{zy} & F_{zz} \end{bmatrix} = \begin{bmatrix} 1/2\,(1-a) & 0 & 0 \\ 0 & a & 0 \\ 0 & 0 & 1/2\,(1-a) \end{bmatrix} \tag{4.101}$$

where the scalar a is a measure of the orientation of particle distribution and varies from 0.0 to 1.0. As described by the authors, $a = 0.0$ corresponds to the case where particles "lie" entirely on the horizontal plane, while the other extreme value, $a = 1.0$, represents a fabric formation where particles are oriented parallel to the vertical y-direction and tightly packed along xx- and zz-direction. Furthermore, $a = 1/3$ corresponds to a statistically isotropic orientation of particles (i.e. there is no preferred orientation of particle distribution). According to the authors, due to the existence of the gravitational field, the most common case corresponds to a preferential orientation of particles towards horizontal directions, meaning that, typically, $0.0 < a < 1/3$.

In order to introduce the effect of the inherent fabric anisotropy on the mechanical response of sand, the inherent fabric tensor, $\boldsymbol{F_A}$, was related to the deviatoric loading direction tensor, $\boldsymbol{n}$, defining the scalar-valued anisotropic state parameter, A_F (Equation 4.102).

$$A_F = g(\theta, c^a)\, \boldsymbol{F_A} : \boldsymbol{n} \tag{4.102}$$

where g is the interpolation function (Equation 4.36), which is a function of the modified Lode's angle, θ (Equation 4.37), and of c^a, which is given by $c^a = \left|A_{F,e}/A_{F,c}\right|$ (i.e. the absolute ratio of the value of A_F in triaxial extension, $A_{F,e}$, to its value in triaxial compression, $A_{F,c}$).

It is perhaps important to note that, while $\boldsymbol{F_A}$ remains constant throughout loading, A_F may vary due to changes in the deviatoric loading direction tensor, $\boldsymbol{n}$, and, consequently, also in the modified Lode's angle, θ. This aspect is illustrated in Figure 4.16, which depicts a typical variation of A_F with α and b for radial monotonic loading (i.e. loading starting from $\boldsymbol{r} = \boldsymbol{0}$ and at constant θ, such as monotonic TC or TE). Note that, under such loading conditions, Equation 4.102 (which has a tensorial form) can be written solely as a function of scalar quantities, as given by Equation 4.103 (Dafalias *et al.*, 2004). Moreover, note that to elaborate Figure 4.16, it was assumed that $c^a = c^c = 0.72$ and $a = 0.29$, a set of values that will be used for the numerical simulation of the response of Hostun sand, as detailed in Chapter 6.

$$A_F = g(\theta, c^a)\frac{3}{2}\sqrt{\frac{3}{2}}\frac{cos^2 a - \frac{1}{3}(1+b)}{\left(b^2 - b + 1\right)^{1/2}}\left(a - \frac{1}{3}\right) \tag{4.103}$$

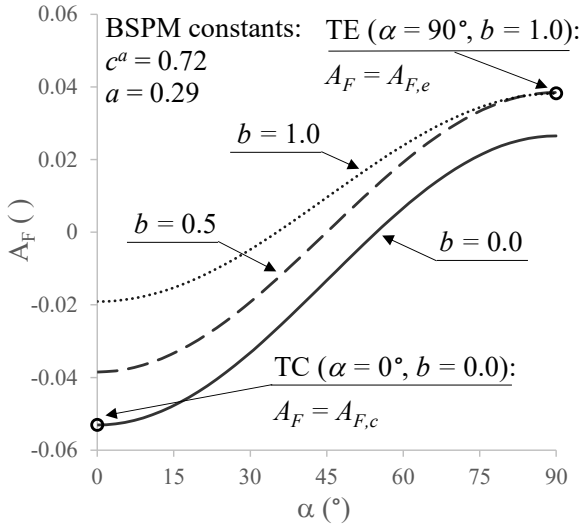

Figure 4.16 – Variation of the anisotropic state parameter A_F with α and b for radial monotonic loading (adapted from Dafalias *et al.*, 2004).

In this figure, it is interesting to observe that A_F increases with both α and b, from its minimum value in TC (characterised by $\alpha = 0.0°$ and $b = 0.0$) to its maximum value in TE (characterised by $\alpha = 90.0°$ and $b = 1.0$).

Having defined the anisotropic state parameter A_F, Dafalias *et al.* (2004) proposed a relocation of the critical state line (CSL) in the $e - p'$ space as a function of A_F. Specifically, rather than being a model parameter, the interception of the critical state line (CSL) with the e-axis is now a function of A_F, as indicated by Equations 4.104 and 4.105.

$$e_{CS} = (e_{CS})_A - \lambda\left(\frac{p'}{p'_{ref}}\right)^{\xi} \tag{4.104}$$

$$(e_{CS})_A = (e_{CS})_{ref}\, exp\,(-A_F) \tag{4.105}$$

where $(e_{CS})_{ref}$ defines now the CSL at $p' = 0.0$ and $A_F = 0.0$. Note that, since A_F is expected to increase from TC to TE, as shown in Figure 4.16, the minus sign of A_F in Equation 4.105 implies that the CSL in TC is, in general, located above the CSL in TE (i.e. the value of $(e_{CS})_{ref}$ is expected to be larger for the former case).

This relocation of the CSL affects the value of the state parameter ψ (Equation 4.3) and, consequently, the positions of the bounding and dilatancy surfaces (given by Equation 4.4 and Equation 4.5, respectively). Therefore, both the dilatancy coefficient (Equation 4.47) and the plastic hardening modulus (Equation 4.48) are altered by the shift of the CSL, addressing the change in the contractiveness and stiffness, as observed experimentally. For instance, for an initially looser-than-critical sample (i.e. $\psi > 0$), when A_F increases (due to an increase of α and/or b – Figure 4.16), a downward relocation of the CSL occurs (Equation 4.105) and a larger

value of ψ is obtained. Since the position of the dilatancy surface is directly proportional to ψ (Equation 4.5), the larger value of ψ results in a larger value of $M_{c,e}^{d}$ (i.e. in an upwards relocation of the dilatancy surface) and, consequently, a more contractive response is simulated under drained conditions (or, similarly, a higher tendency to generate excess pore water pressures is simulated under undrained conditions), as typically observed in the laboratory. Furthermore, since the position of the bounding surface is proportional to -ψ (Equation 4.4), a smaller value of $M_{c,e}^{b}$ (i.e. a lower position for the bounding surface) is obtained when A_F is increased and, consequently, a softer stress-strain response is simulated, as typically observed in laboratory.

It is important to note that, despite allowing for a more accurate simulation of the intended response, this relocation of the CSL implies a departure from CSSM principles, according to which the CSL is unique and independent of loading mode and direction. Even though there seems to be a lack of consensus on this subject, with some experimental studies suggesting that the CSL depends on the loading direction and mode (e.g. Vaid *et al.*, 1990b; Riemer and Seed, 1997; Mooney *et al.*, 1998; Loukidis and Salgado, 2009), while other studies suggesting that the CSL is unique (Been *et al.*, 1991; Yoshimine and Kataoka, 2007), this relocation of the CSL undoubtedly involves a profound alteration to the fundamentals of the constitutive model, as originally established by Manzari and Dafalias (1997).

Moreover, having concluded that the effect of the relocation of the CSL on the plastic hardening modulus, A, was not sufficiently effective, Dafalias *et al.* (2004) decided to introduce an additional dependency of the plastic hardening modulus, A, on the scalar-valued anisotropic state parameter, A_F. Specifically, as shown by Equation 4.106, a new scalar multiplier, h_A, which is a function of the current value of A_F, as well as of its value in TC and TE, was proposed by Dafalias *et al.* (2004).

$$h_A = 1 + k_A - k_A^{(A_{F,e} - A_F)/(A_{F,e} - A_{F,c})} \tag{4.106}$$

where k_A is a new positive model parameter. Note that, since $A_F = A_{F,c}$ in TC, it follows that $h_A = 1.0$, meaning that no influence of h_A on A is simulated under such loading conditions. On the contrary, in TE, since $A_F = A_{F,e}$, it follows that $h_A = k_A$. Since, in general, the response of sand is softer in TE than in TC, the model parameter k_A is expected to take a value smaller than 1.0 (Dafalias *et al.*, 2004). Moreover, for other loading conditions than TC and TE, intermediate values of h_A are obtained by Equation 4.106, as typically observed in the laboratory.

A similar inherent fabric anisotropy formulation was proposed by Loukidis and Salgado (2009). In particular, it makes use of the inherent fabric descriptor (Equation 4.101) introduced by Dafalias *et al.* (2004), as well as the same definition for the anisotropic state parameter A_F (Equation 4.102). A modification was, however, introduced by the authors to the equation

defining the interception of the CSL with the void ratio-axis, in order to set TC as the reference loading condition (Equation 4.107 replaces Equation 4.105).

$$(e_{CS})_A = (e_{CS})_{ref}\, exp\left(A_{F,c} - A_F\right) \tag{4.107}$$

where $(e_{CS})_{ref}$ defines now the CSL at $p' = 0.0$ and $A_F = A_{F,c}$ (i.e. the interception of the CSL in TC).

In addition, the authors modified the expression defining the additional influence of A_F on the plastic hardening modulus through the plastic multiplier h_A (Equation 4.108 replaces Equation 4.106).

$$h_A = exp\left[\left(\frac{A_{F,c} - A_F}{A_{F,c} - A_{F,e}}\right)^{1.25} ln(k_A)\right] \tag{4.108}$$

where k_A is a model parameter, which, as mentioned before, takes values in the range of $0.0 < k_A \leq 1.0$.

Figure 4.17 compares the variation of h_A with A_F obtained when using the formulation proposed by Dafalias *et al.* (2004) – Equation 4.106 – and the one proposed by Loukidis and Salgado (2009) – Equation 4.108 – , assuming, once more, radial monotonic loading and using $c^a = c^c = 0.72$, $a = 0.29$ and $k_A = 0.8$. It can be seen that very similar variations of the value of h_A with A_F are indeed obtained by the two formulations.

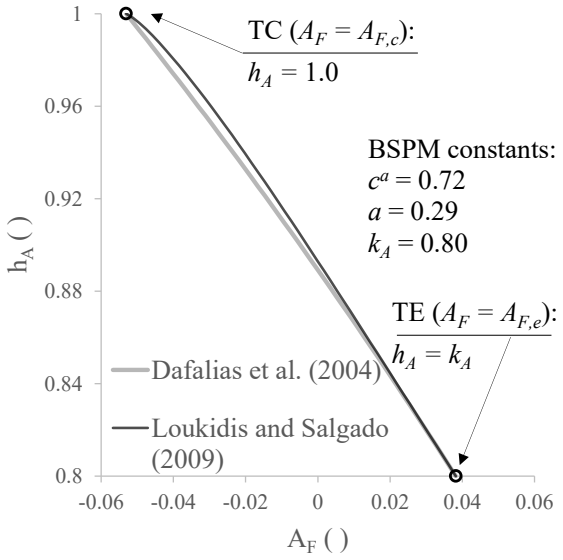

Figure 4.17 – Plastic multiplier h_A as a function of the anisotropic state parameter A_F for radial monotonic loading.

Conversely, Figure 4.18 shows that the variation of h_A with k_A, for a given value of A_F, obtained from Equations 4.106, proposed by Dafalias *et al.* (2004), is very different from that given by Equations 4.108, introduced by Loukidis and Salgado (2009). The former formulation results in identical values for h_A either when $k_A = 0.0$ or $k_A = 1.0$ and, in general, a non-monotonic variation between these extreme values of k_A. Conversely, the formulation proposed by

Loukidis and Salgado (2009) defines a monotonic increase of h_A with k_A, which brings more flexibility to the calibration process, as discussed in more detail by Williams (2014).

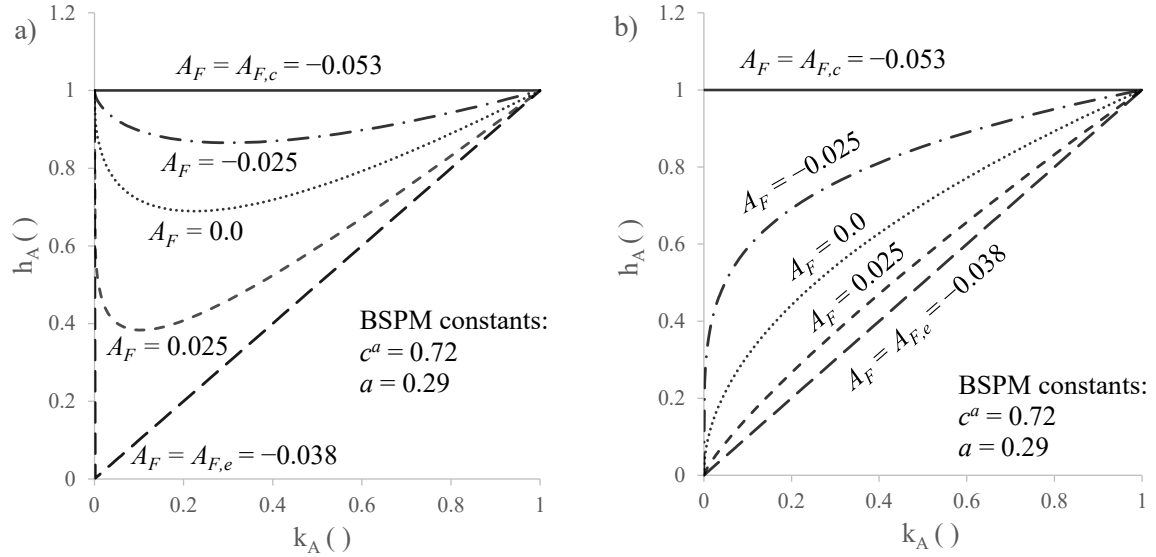

Figure 4.18 – Evolution of the plastic multiplier h_A with the model parameter k_A for several values of the anisotropic state parameter A_F and for radial monotonic loading, according to the formulations proposed by (a) Dafalias *et al.* (2004) and (b) Loukidis and Salgado (2009).

Further insight into the ability of both formulations to simulate anisotropic response of sand was provided by Williams (2014). The author integrated each of the aforementioned formulations with the constitutive model proposed by Taborda *et al.* (2014) and carried out simulations of undrained hollow cylinder torsional shear tests, whose experimental results were reported by Uthayakumar and Vaid (1998). Based on the obtained results, Williams (2014) concluded that a reasonable match between numerical and experimental results is, in general, possible when using any of the formulations, with slightly better results being typically obtained when using the formulation proposed by Loukidis and Salgado (2009), in relation to that proposed by Dafalias *et al.* (2004). The author noticed, however, that, in some situations, due to the relocation of the CSL, a monotonic reduction of the mean effective stress throughout loading is obtained for initially denser-than-critical samples. This modelled response seems to contradict experimental observations and one of the fundamental concepts of the constitutive framework, according to which this type of response is only predicted for initially looser-than-critical samples (Section 4.2.1). To overcome this limitation, the author decided to replace Equation 4.107 by Equation 4.109. This latter equation specifies a continuously evolution of the CSL position with the distance in the normalised deviatoric plane from the current effective stress point to the critical state line, d^c.

$$(e_{CS})_A = (e_{CS})_{ref}\, exp\left(v_A\, \frac{\langle d^c \rangle}{d^c_{ref}} \left(A_{F,c} - A_F\right)\right) \tag{4.109}$$

where d^c_{ref} is a reference distance to the CSL (Equation 4.110) and v_A is a new model parameter, which controls the magnitude of the effect of the anisotropic state parameter on the CSL.

$$d^c_{ref} = \sqrt{\frac{2}{3}}\,(\alpha^c_\theta + \alpha^c_{\theta+\pi}) = \sqrt{\frac{2}{3}}\,(g(\theta, c^c)\,M^c_c + g(\theta+\pi, c^c)\,M^c_c - 2\,m) \tag{4.110}$$

Note that the use of the Macaulay brackets in Equation 4.109 guarantees that the relocation of the CSL is only performed when the effective stress point is inside the critical surface. As the effective stress point moves beyond that surface (i.e. $d^c < 0.0$), the CSL remains fixed in the $e - p'$ space (i.e. $(e_{CS})_A = (e_{CS})_{ref}$ is set to persist until CS conditions are reached). More important, this new formulation ensures that a unique CSL exists (i.e. that the final position of the CSL is independent of the inherent fabric and loading direction), as postulated by CSSM.

As detailed by Williams (2014), the proposed alteration (Equation 4.109) appears to overcome the aforementioned limitation of predicting a continuous reduction of the mean effective stress with shearing for initially denser-than-critical samples subjected to undrained torsional shear loading. Indeed, the author concluded that this new formulation, when coupled with the additional influence of A_F on the plastic hardening modulus proposed by Loukidis and Salgado (2009) – Equation 4.108 –, improves the ability of the model to reproduce the effect of α and b on the modelled response of sand, particularly observed in hollow cylinder torsional shear tests.

Interestingly, updated inherent fabric anisotropy formulations have been recently proposed by Dafalias and his co-workers (Li and Dafalias, 2012) and by Salgado and his co-workers (Woo and Salgado, 2015). In both proposals, the uniqueness of the critical state is reassumed. This is performed by specifying an evolution to the inherent fabric anisotropy towards a critical state value. As this critical state value is attained, the effect of the anisotropic state parameter, A_F, on the position of the critical state line vanishes (i.e. the final position of the critical state line is obtained). These principles seem to be similar to those introduced by Williams (2014). It should, however, be noted that, rather than having a CSL moving in the $e - p'$ space, in these latest formulations proposed by Li and Dafalias (2012) and Woo and Salgado (2015), its position is fixed in that space, as in the original model of Manzari and Dafalias (1997), as well as subsequent versions of Papadimitriou and Bouckovalas (2002) and Taborda *et al.* (2014). A new line, termed "dilatancy state line" (DSL), whose position depends on the anisotropic state parameter, A_F, is introduced in the formulations proposed by Li and Dafalias (2012) and Woo and Salgado (2015) to define the value of the state parameter, ψ, and, consequently, to define the positions of the dilatancy and bounding surfaces (i.e. the DSL replaces the CSL in its role of defining the value of ψ). Therefore, in practice, the strategy used by Li and Dafalias (2012) and Woo and Salgado (2015) is similar to that employed by Williams (2014), consisting of relocating the line against which ψ is determined as A_F evolves.

4.3.3.4 Adopted formulation

In the present study, the inherent fabric anisotropy formulation proposed by Williams (2014) was chosen to be added to the bounding surface plasticity model proposed by Taborda *et al.* (2014) and implemented into FEMEPDYN . While noticeable advantages over this formulation have not been found in the most recent formulations proposed by Li and Dafalias (2012) and Woo and Salgado (2015), the fact that the formulation proposed by Williams (2014) was implemented into the Imperial College Finite Element Code (ICFEP), using the model proposed by Taborda *et al.* (2014) as the main constitutive platform, presents a major advantage for the implementation validation process, since results obtained by the two different finite element codes can be directly compared.

The new constitutive equations are summarised in the following section. Nevertheless, for future reference, it is important to clarify at this stage that the introduction of a new plastic multiplier h_A in the definition of the plastic hardening modulus, A, implies that Equation 4.58 is replaced by Equation 4.111.

$$h = h_A \, h_b \, h_e \, h_f \, h_g \tag{4.111}$$

where h_b, h_e, h_f and h_g have been previously defined by Equations 4.59, 4.60, 4.56 and 4.62, respectively, while h_A is given by Equation 4.108 (re-written below for clarity).

$$h_A = exp\left[\left(\frac{A_{F,c} - A_F}{A_{F,c} - A_{F,e}}\right)^{1.25} ln(k_A)\right] \tag{4.112}$$

Moreover, note that the influence of the scalar-valued anisotropic state parameter, A_F (Equation 4.102), on the position of the CSL is given by Equation 4.109 (also re-written below for clarity).

$$(e_{CS})_A = (e_{CS})_{ref} \, exp\left(v_A \, \frac{\langle d^c \rangle}{d^c_{ref}} \left(A_{F,c} - A_F\right)\right) \tag{4.113}$$

4.3.4 Summary of the new constitutive equations and model parameters required

Table 4.4 summarises the new constitutive equations introduced by the alteration to the computation of the shear modulus at small strains (Section 4.3.2) and by the incorporation of an inherent fabric anisotropy formulation (Section 4.3.3). To assist the presentation of these newly introduced equations, some equations already included in the original formulation are also presented in the table. The grey colour is used to distinguish these equations from the newly introduced equations. Similarly, the model parameters already included in the original version of the model are also shown in grey, while the new model parameters are presented in black. It can be observed that five new model parameters are required in the modified version, two of these to characterise the shear modulus at small strains while the remaining are used to introduce the inherent fabric tensor and its effect on the CSL and on the plastic hardening modulus. It should be highlighted that the inherent fabric anisotropy formulation

can be deactivated by adopting $a = 1.0/3.0$ (i.e. by considering an isotropic inherent fabric tensor) or, alternatively, by cancelling the effect of the anisotropic state parameter A_F on the CSL ($v_A = 0.0$) and on the plastic hardening modulus ($k_A = 1.0$).

Table 4.4 – Summary of the new equations introduced to the formulation of the constitutive model and new model parameters required.

Description		Equation	Parameters
Non-linear cyclic elasticity			
Small-strain shear modulus at small strains	(4.99, 4.100)	$G_{max} = C_g\, p'_{ref} \frac{(m_g - e)^2}{1+e} \left(\frac{p'}{p'_{ref}}\right)^{n_g} \geq C_g\, p'_{ref} \frac{(m_g - e)^2}{1+e} \left(\frac{p'_{min}}{p'_{ref}}\right)^{n_g}$	C_g, m_g, n_g, p'_{ref}, p'_{min}
Model surfaces			
Critical state line in the $e - p'$ space	(4.104)	$e_{CS} = (e_{CS})_A - \lambda \left(\frac{p'}{p'_{ref}}\right)^{\xi}$	λ, ξ
		where:	
	(4.109)	$(e_{CS})_A = (e_{CS})_{ref}\, exp\left(v_A \frac{\langle d^c \rangle}{d^c_{ref}} (A_{F,c} - A_F)\right)$	$(e_{CS})_{ref}$, v_A
	(4.43)	$d^c = (\alpha^c - \alpha) : \boldsymbol{n} = \sqrt{\frac{2}{3}}\, \alpha^c_\theta - \alpha : \boldsymbol{n} = \sqrt{\frac{2}{3}} (g(\theta, c^c)\, M^c_c - m) - \alpha : \boldsymbol{n}$	
	(4.110)	$d^c_{ref} = \sqrt{\frac{2}{3}}\, (\alpha^c_\theta + \alpha^c_{\theta+\pi}) = \sqrt{\frac{2}{3}}\, (g(\theta, c^c)\, M^c_c + g(\theta+\pi, c^c)\, M^c_c - 2\, m)$	
Plastic hardening modulus			
Associated with the primary YS	(4.48, 4.111)	$A_1 = p'\, h_A\, h_b\, h_e\, h_f\, h_g\, d^b$	
		where:	
	(4.108)	$h_A = exp\left[\left(\frac{A_{F,c} - A_F}{A_{F,c} - A_{F,e}}\right)^{1.25} ln(k_A)\right]$	k_A
	(4.59)	$h_b = \left(\frac{p'}{p'_{ref}}\right)^{\mu-1} \left(\frac{\lvert d^b \rvert}{\langle d^b_{ref} - \lvert d^b \rvert \rangle}\right)^{\beta+1}$	μ, β
	(4.60)	$h_e = h_0\, (1 - \gamma e) \geq h_0\, (1 - \gamma e_{lim})$	h_0, γ, e_{lim}
	(4.61)	$h_{f,min} \leq h_f = \frac{1 + \langle f_p \rangle^2}{1 + \langle \boldsymbol{f} : \boldsymbol{n} \rangle} \leq h_{f,max}$	

Table 4.4 – Summary of the new equations introduced to the formulation of the constitutive model and new model parameters required.

Description		Equation	Parameters
	(4.62)	$h_g = G^{\alpha}_{tan}$	α
	(4.43)	$d^b = \left(\boldsymbol{\alpha^b} - \boldsymbol{\alpha}\right) : \boldsymbol{n} = \sqrt{2/3}\,\alpha^b_\theta - \boldsymbol{\alpha} : \boldsymbol{n} = \sqrt{2/3}\left(g(\theta, c^b)\, M^b_c - m\right) - \boldsymbol{\alpha} : \boldsymbol{n}$	
	(4.51)	$d^b_{ref} = \sqrt{2/3}\,\left(g(\theta, c^b)\, M^b_c + g(\theta + \pi, c^b)\, M^b_c - 2\, m\right)$	
Inherent fabric anisotropy			
Inherent fabric tensor	(4.101)	$\boldsymbol{F_A} = \begin{bmatrix} 1/2\,(1-a) & 0 & 0 \\ 0 & a & 0 \\ 0 & 0 & 1/2\,(1-a) \end{bmatrix}$	a
Anisotropic state parameter	(4.102)	$A_F = g(\theta, c^a)\, \boldsymbol{F_A} : \boldsymbol{n}$	

4.4 Summary and conclusions

In this first part of this chapter, the formulation of a bounding surface plasticity model (BSPM), as proposed by Taborda *et al.* (2014), was presented. Particular emphasis was firstly given to the fundamental concepts of the framework. Subsequently, and given the modularity of the constitutive model, each component of the model was comprehensively described, with differences between the constitutive equations of the model proposed by Taborda *et al.* (2014) and those included in other models based on the same framework (e.g. Manzari and Dafalias, 1997; Papadimitriou and Bouckovalas, 2002; Dafalias and Manzari, 2004; Taiebat and Dafalias, 2008; Loukidis and Salgado, 2009; Andrianopoulos *et al.*, 2010b) being outlined.

The second part of this chapter focused on the expansion of the formulation proposed by Taborda *et al.* (2014). A more general constitutive equation for the shear modulus at small strains was introduced to encompass the vast majority of the equations reported in the literature for sands, including that proposed for Hostun sand (Chapter 2). In addition, with the objective of improving the ability of the constitutive model to simulate the response of sand for loading conditions other than triaxial compression, an inherent fabric anisotropy component was added to the constitutive model. In particular, it was shown that this component brings additional flexibility to the model, by enabling the replication of different sand response as the angle α of the major principal effective stress, σ'_1, to the axis of the sample is changed – a feature of sand response widely observed in the laboratory, which is not captured by the constitutive model proposed by Taborda *et al.* (2014). Among several other similar formulations proposed in the literature for constitutive models based on the two-surface plasticity framework (Dafalias *et al.*, 2004; Loukidis and Salgado, 2009; Li and Dafalias, 2012; Woo and Salgado, 2015), the formulation proposed by Williams (2014) was selected to be incorporated in the present constitutive model, due to its compliance with the

principles of CSSM and the fact that it does not imply profound alterations to the formulation proposed by Taborda *et al.* (2014).

Chapter 5 IMPLEMENTATION OF A BOUNDING SURFACE PLASTICITY MODEL INTO A FINITE ELEMENT CODE AND ITS VALIDATION

5.1 Introduction

In finite element analysis (FEA), the constitutive model holds a key role in two different moments (Potts and Zdravkovic, 1999; Taborda, 2011): (1) the determination of the tangent stiffness matrix of each element of the mesh, given the current stress and strain states, which is subsequently assembled into a global tangent stiffness matrix; and (2) the determination of the stress change corresponding to a given strain increment for each Gauss point. While the first operation consists essentially of implementing the equations of the constitutive model, as presented in the previous chapter, the second operation requires the use of a stress integration scheme.

Both implicit and explicit stress integration schemes can be found in the literature. As detailed by Potts and Zdravkovic (1999), the main difference between these two types of integration schemes consists of the strategy used to compute the plastic strains. In explicit schemes, the strain increment is divided into small sub-step strain increments, which are assumed proportional to the total strain increment. The ordinary differential constitutive equations are numerical integrated over each sub-step strain increment, typically using either a Euler, a modified Euler or a Runge-Kutta method. By following this approach, the plastic strains are estimated based on the stress state evaluated at the beginning of each sub-increment and at a temporary updated stress state. The size of each sub-step can be automatically chosen to restrain the integration error to a value smaller than a given tolerance. Conversely, when an implicit scheme is used, the plastic strains are calculated based on the stress state corresponding to the end of the increment. Since the stress state at the end of the increment is not known in advance, an elastic predictor is firstly used to give an estimation of the final stress state. An iterative algorithm is subsequently used to relocate the stress state back to the yield surface, ensuring that, as convergence is achieved, the plastic strains over the increment are calculated from the plastic potential and plastic multiplier corresponding to the end of the increment.

Implicit integration schemes, such as the return mapping algorithm (e.g. Borja and Lee, 1990; Borja, 1991; Zhang, 1995; Rouainia and Wood, 2001), have become popular due to its unconditionally stable integration of elastoplastic models employed in the simulation of monotonic loading and appreciable convergence. However, their application to highly non-linear constitutive laws used in conjunction with the simulation of cyclic loading has been proven very difficult, since the iterative process inherent to this type of methods may not

converge (e.g. Büttner and Simeon, 2002; Luccioni *et al.*, 2001). Furthermore, these methods typically require the use of a consistent tangent operator and second-order derivatives of the yield function and plastic potential with respect to the state parameters, which might be difficult to obtain analytically for complex models (Luccioni *et al.*, 2001; Hiley and Rouainia, 2008). Consequently, simplifications of the constitutive relationship might be required, with a detrimental impact on the ability of the constitutive model (e.g. Manzari and Nour, 1997). Alternatively, explicit schemes, such as the forward Euler or Runge-Kutta methods (Sloan, 1987; Sloan *et al.*, 2001), have been shown to be robust and efficient, especially when using an automatic sub-stepping procedure and including a drift correction procedure (e.g. Potts and Ganendra, 1994; Potts and Zdravkovic, 1999; Luccioni *et al.*, 2001). Moreover, these methods have the main advantage of being much more straightforward to implement into a FE code and can easily be applied to the integration of constitutive models having a highly non-linear elastic component and more than one active yield surface (Potts and Zdravkovic, 1999; Hong *et al.*, 2012), which is the case of the present constitutive model. Indeed, most of the operations required by an explicit integration scheme are common to any constitutive model. Therefore, once implemented, the integration scheme can be used for any other constitutive model that may be implemented into the FE code in the future. Due to these advantages, Potts and Zdravkovic (1999) highlighted that a robust approach is to use a sub-stepping scheme with automatic error control. The bounding surface plasticity model (BSPM) proposed by Taborda (2011) and Taborda *et al.* (2014) is also integrated using this methodology within the Imperial College Finite Element Program (ICFEP). Additional reports in the literature seem to indicate that explicit integration schemes with automatic sub-stepping and error control have been typically preferred over semi-explicit and implicit schemes for bounding surface plasticity models (Zhao *et al.*, 2005; Andrianopoulos *et al.*, 2010b; E-Kan and Taiebat, 2014; Xu and Zhang, 2015; Vilhar *et al.*, 2018).

Although very attractive due to the abovementioned advantages, it should be noted that explicit integration schemes are only conditionally stable. In fact, due to the assumption that strains vary proportionally during a given increment, small strain increments may be required to keep the error within a negligible magnitude. This aspect seems, however, to be greatly enhanced by the introduction of a sub-stepping technique with automatic error control, such as that proposed by Sloan (1987) and Sloan *et al.* (2001). In addition, it is noteworthy that the use of an explicit scheme requires additional operations when compared to those typically required by an implicit scheme. Specifically, it is necessary to find the intersection of the stress path with the yield surface, when the stress path moves from a purely elastic state (i.e. from the elastic region) to an elasto-plastic state (i.e. on the yield surface). Furthermore, a drift of the effective stress point from the yield surface may be observed at the end of an elasto-plastic increment. A drift correction scheme is, therefore, required to bring the stress back to the yield surface. Nevertheless, some methods have been proposed in the literature to

overcome these drawbacks of the explicit integration schemes, allowing for a robust integration of the constitutive relationship (e.g. Sloan, 1987; Potts and Gens, 1985; Potts and Zdravkovic, 1999; Sloan *et al.*, 2001).

Given the above, it was decided to adopt the explicit modified forward Euler scheme with automatic sub-stepping and error control introduced by Sloan (1987) and Sloan *et al.* (2001) to integrate the present BSPM into FEMEPDYN. The operations required by this scheme are described in Section 5.2. Similar to the structure adopted in the finite element code, the presentation of the integration scheme is kept as comprehensive as possible, to allow its general application to any other constitutive model. Note, however, that the particular application of the integration scheme to the BSPM developed in Chapter 4 is detailed in Appendix C. In addition, note that implicit schemes will not be further elaborated in this thesis. For details on algorithms included in this class of integration schemes, refer, for example, to Ortiz and Simo (1985), Ortiz and Simo (1986), Borja and Lee (1990), Borja (1991), Manzari and Nour (1997), Rouainia and Wood (2001), Borja *et al.* (2001), Borja *et al.* (2003).

The second part of this chapter, comprising Section 5.3, focuses on the validation of the implementation. Due to its importance in ensuring the reliability of the developed numerical tool, a significant effort was placed on this task. A large number of numerical simulations was performed, with the obtained results being subsequently compared with reference data. This included numerical simulations of different element laboratory tests, as well as the simulation of dynamic centrifuge experiments, one of them considering the response of a level deposit of fully saturated deposit of loose sand subjected to cyclic mobility and a second one including soil-structure interaction under dynamic loading.

Once the validation routine is completed, a brief summary and some conclusions are presented in Section 5.4.

Note that, in what follows, the conventional finite element representation for tensors is adopted. In particular, due to their symmetrical form, second-order tensors are represented by an array, as shown by Equation 5.1, 5.2 and 5.3 for the effective stress state, $\{\boldsymbol{\sigma'}\}$, strain state, $\{\boldsymbol{\varepsilon}\}$, and identity tensor, $\{\boldsymbol{I}\}$, respectively. Note that the same applies to all stress- and strain-related tensors (such as the deviatoric stress, $\{\boldsymbol{s}\}$, stress ratio, $\{\boldsymbol{r}\}$, and deviatoric strain, $\{\boldsymbol{e}\}$, tensors), incremental stress and strain tensors (such as the effective stress increment, $\{\Delta\boldsymbol{\sigma'}\}$, and strain increment, $\{\Delta\boldsymbol{\varepsilon}\}$, tensors), state parameter tensors (such as the back-stress ratio tensor, $\{\boldsymbol{\alpha}\}$, and deviatoric component of the shearing-induced fabric tensor, $\{\boldsymbol{f}\}$), gradients of the yield and plastic potential, $\{\partial F/\partial\boldsymbol{\sigma'}\}$ and $\{\partial\boldsymbol{P}/\partial\boldsymbol{\sigma'}\}$, respectively, as well as other tensorial quantities of the constitutive model (such as the deviatoric loading direction tensor, $\{\boldsymbol{n}\}$). Moreover, for computational convenience, fourth-order tensors, such as the elastic stiffness tensor, $[\boldsymbol{D}]$, are represented by a matrix (Equation 5.4). Note that, when adopting this form of representation, $[\boldsymbol{D}]$ is usually referred to as elastic constitutive matrix.

$$\{\boldsymbol{\sigma'}\} = \left\{\sigma'_{xx} \quad \sigma'_{yy} \quad \sigma_{xy} \quad \sigma'_{zz} \quad \sigma_{xz} \quad \sigma_{yz}\right\}^{\mathrm{T}} \tag{5.1}$$

$$\{\boldsymbol{\varepsilon}\} = \left\{\varepsilon_{xx} \quad \varepsilon_{yy} \quad \varepsilon_{xy} \quad \varepsilon_{zz} \quad \varepsilon_{xz} \quad \varepsilon_{yz}\right\}^{\mathrm{T}} \tag{5.2}$$

$$\{\boldsymbol{I}\} = \{1.0 \quad 1.0 \quad 0.0 \quad 1.0 \quad 0.0 \quad 0.0\}^{\mathrm{T}} \tag{5.3}$$

$$[\boldsymbol{D}] = \begin{bmatrix} D_{xxxx} & D_{xxyy} & D_{xxxy} & D_{xxxz} & D_{xxxz} & D_{xxyz} \\ D_{yyxx} & D_{yyyy} & D_{yyxy} & D_{yyzz} & D_{yyxz} & D_{yyyz} \\ D_{xyxx} & D_{xyyy} & D_{xyxy} & D_{xyzz} & D_{xyxz} & D_{xyyz} \\ D_{zzxx} & D_{zzyy} & D_{zzxy} & D_{zzzz} & D_{zzxz} & D_{zzyz} \\ D_{xzxx} & D_{xzyy} & D_{xzxy} & D_{xzzz} & D_{xzxz} & D_{xzyz} \\ D_{yzxx} & D_{yzyy} & D_{yzxy} & D_{yzzz} & D_{yzxz} & D_{yzyz} \end{bmatrix} \tag{5.4}$$

Finally, note that the conventional soil mechanics sign convention is used in the present thesis, meaning that compressive stresses and strains are taken as positive.

5.2 Explicit stress integration

5.2.1 Overview of an explicit stress integration scheme

Having computed the total strain increment, $\{\Delta\boldsymbol{\varepsilon}\}$, for each Gauss point, the stress integration algorithm is used to estimate the corresponding effective stress increment, $\{\Delta\boldsymbol{\sigma'}\}$. With such objective, it is initially assumed that the material behaves elastically and, consequently, the effective stress increment, $\{\Delta\boldsymbol{\sigma'}\} = \{\Delta\boldsymbol{\sigma'^{e}}\}$, can be determined by integrating the elastic constitutive matrix, $[\boldsymbol{D}]$, over $\{\Delta\boldsymbol{\varepsilon}\}$ (Equation 5.5).

$$\{\Delta\boldsymbol{\sigma'}\} = [\boldsymbol{D}]\,\{\Delta\boldsymbol{\varepsilon}\} \tag{5.5}$$

For the present constitutive model, since $[\boldsymbol{D}]$ is not constant, rather a function of the current effective stress state, $\{\boldsymbol{\sigma'}\}$, among other state parameters, an integration procedure is required to calculate $\{\Delta\boldsymbol{\sigma'}\}$ using Equation 5.5. Among other possibilities – see, for example, Sloan *et al.* (2001) – , the modified forward Euler scheme with automatic sub-stepping and error control is selected, as suggested for example by Potts and Zdravkovic (1999). As detailed in Section 5.2.2, this scheme involves the division of the total strain increment, $\{\Delta\boldsymbol{\varepsilon}\}$, into sub-step strain increments, $\{\Delta\boldsymbol{\varepsilon_{ss}}\}$, which have the same direction of the former, yet may have smaller magnitude. Furthermore, the magnitude of each $\{\Delta\boldsymbol{\varepsilon_{ss}}\}$ is automatically controlled to keep the error resulting from the approximations required by the integration procedure below a user-defined tolerance. By using this approach, Equation 5.5 is replaced by Equation 5.6. Note that, in this equation, $[\boldsymbol{D}\{\boldsymbol{\sigma'_{n-1}}\}]$ is used instead of $[\boldsymbol{D}]$, to highlight its dependency on the current (i.e. at the beginning of the sub-step) effective stress state, $\{\boldsymbol{\sigma'_{n-1}}\}$, and, consequently, the implicit nature of the stress-strain relation. Moreover, note that, for the present constitutive model, $[\boldsymbol{D}(\{\boldsymbol{\sigma'_{n-1}}\})]$ is also a function of the current void ratio, e, as well as of the following set of elastic state parameters: effective stresses and void ratio at last shear reversal, $\{\boldsymbol{\sigma'^{SR}}\}$ and e^{SR}, respectively, as well as scaling factor N. With respect to the void ratio, its evolution is a function of the total volumetric strain, which is assumed to be known at the start of each sub-step increment. Due to this, and to simplify the presentation, the

dependency of $[\boldsymbol{D}]$ on e is not represented (although considered in the algorithm, as detailed in Section 5.2.7). Regarding $\{\boldsymbol{\sigma}'^{SR}\}$, e^{SR} and N, these quantities are assumed to remain constant over a given sub-step increment, being only updated, if necessary, at the start of it, as detailed in Section 5.2.4.

$$\{\Delta\boldsymbol{\sigma}'_{\boldsymbol{n}}\} = [\boldsymbol{D}(\{\boldsymbol{\sigma}'_{\boldsymbol{n-1}}\})]\ \{\Delta\boldsymbol{\varepsilon}_{\boldsymbol{ss}}\} \tag{5.6}$$

Having determined effective stress increment for the current sub-step increment, $\{\Delta\boldsymbol{\sigma}'_{\boldsymbol{n}}\}$, an estimation of the current stress state, $\{\boldsymbol{\sigma}'_{\boldsymbol{n}}\}$, can be obtained by adding $\{\Delta\boldsymbol{\sigma}'_{\boldsymbol{n}}\}$ to the stress state at the beginning of the sub-step, $\{\boldsymbol{\sigma}'_{\boldsymbol{n-1}}\}$, as indicated by Equation 5.7.

$$\{\boldsymbol{\sigma}'_{\boldsymbol{n}}\} = \{\boldsymbol{\sigma}'_{\boldsymbol{n-1}}\} + \{\Delta\boldsymbol{\sigma}'_{\boldsymbol{n}}\} \tag{5.7}$$

At this point, the initial assumption of purely elastic response (also known as "elastic trial") should be checked. If the recently determined effective stress point, $\{\boldsymbol{\sigma}'_{\boldsymbol{n}}\}$, lies within both the primary and secondary yield surfaces of the constitutive model (i.e. if both $F_1(\{\boldsymbol{\sigma}'_{\boldsymbol{n}}\},\{\boldsymbol{\alpha}_{\boldsymbol{n}}\}) \leq YTOL$ and $F_2\left(\{\boldsymbol{\sigma}'_{\boldsymbol{n}}\},\ p'_{ys}\right) \leq YTOL$ conditions hold true, where $\{\boldsymbol{\alpha}_{\boldsymbol{n}}\}$ is current the back-stress tensor (which remains constant during elastic trial), p'_{YS} is the lower limit of the mean effective stress and *YTOL* is a very small positive user-defined yield function tolerance, usually in the range of 10^{-6} to 10^{-12}), then $\{\boldsymbol{\sigma}'_{\boldsymbol{n}}\}$ is accepted. On the contrary, when $F_1(\{\boldsymbol{\sigma}'_{\boldsymbol{n}}\},\{\boldsymbol{\alpha}_{\boldsymbol{n}}\}) > YTOL$ and/or $F_2\left(\{\boldsymbol{\sigma}'_{\boldsymbol{n}}\},\ p'_{ys}\right) > YTOL$, then elasto-plastic response should be considered, meaning that the initial assumption of purely elastic response is not acceptable. In such case, additional operations are required to compute $\{\boldsymbol{\sigma}'_{\boldsymbol{n}}\}$, as detailed below.

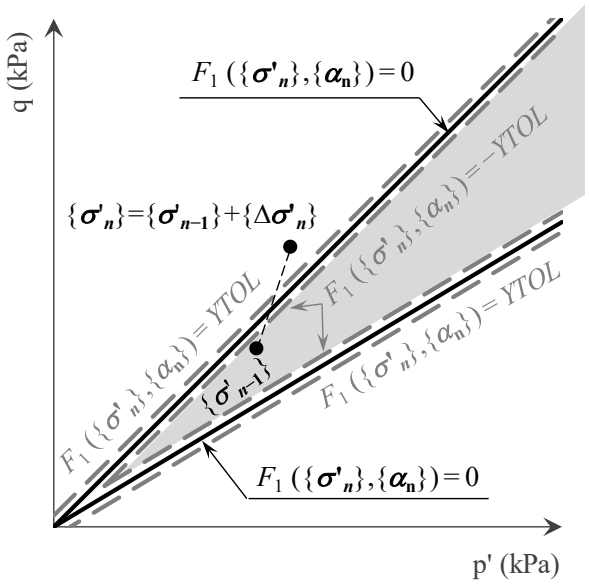

Figure 5.1 – Transition from purely elastic to elasto-plastic response (adapted from Potts and Zdravkovic, 1999). Note that the yield surface adopted in the present constitutive model plots as an open wedge in *q* – *p'* plane.

A typical situation where the effective stress point at the beginning of the sub-step, $\{\boldsymbol{\sigma}'_{\boldsymbol{n-1}}\}$, is located inside the primary and secondary yield surfaces (i.e. $F_1(\{\boldsymbol{\sigma}'_{\boldsymbol{n-1}}\},\{\boldsymbol{\alpha}\}) < -YTOL$ and

$F_2(\{\sigma'_{n-1}\},\ p'_{ys}) < -YTOL$), but lies outside the primary yield surface at the end of the sub-step increment (i.e. $F_1(\{\sigma'_n\},\{\alpha_n\}) > YTOL$) is illustrated in Figure 5.1, where, as presented in Chapter 4, the primary yield surface is plotted as an open wedge (i.e. the elastic region is the shaded area within the two dashed dark grey lines corresponding to $F_1(\{\sigma'_n\},\{\alpha_n\}) = -YTOL$). When this situation happens, it is necessary to determine the effective stress state corresponding to the intersection of the stress path with the primary yield surface. In other words, it is necessary to find the portion β of the sub-step strain increment, $\{\Delta\varepsilon_{ss}\}$, which moves the initial stress state, $\{\sigma'_{n-1}\}$, to the primary yield surface, as given by Equation 5.8. Note that, in this equation, a more generic notation is employed. Specifically, since a similar situation where the effective stress point moves outside the yield surface may involve the secondary yield surface, the active yield surface condition is generically denoted as *F* (rather than by F_1 or F_2) and the set of state parameters is generically denoted as $\{k_n\}$ (rather than by $\{\alpha_n\}$ or p'_{ys}). In addition, it is noteworthy that, in this equation, a value of $\beta = 0.0$ would indicate that the initial stress state would be already on the yield surface (primary or secondary) at the beginning of the sub-step increment, meaning that the response would be elasto-plastic from the beginning of the sub-step increment. Conversely, $\beta = 1.0$ would mean that, after the elastic trial, the effective stress state, $\{\sigma'_n\}$ would lie on the active yield surface (i.e. the response would be purely elastic over the entire sub-step increment). In effect, when a transition from purely elastic to elasto-plastic response occurs during a given sub-step increment, as illustrated in Figure 5.1, the value of β should belong to the range]0.0, 1.0[.

$$F(\{\sigma'_{n-1}\} + \beta[D\{\sigma'_n\}]\{\Delta\varepsilon_{ss}\},\{k_n\}) = 0.0 \tag{5.8}$$

Among other algorithms that have been proposed in the literature to solve Equation 5.8 (Sloan, 1987; Potts and Zdravkovic, 1999), which is non-linear, Sloan *et al.* (2001) suggested the use of the Pegasus method introduced by Dowell and Jarratt (1972). As pointed out by Sloan *et al.* (2001), this algorithm is unconditionally convergent and does not required the use of second-order derivatives. Moreover, it is possible to accelerate its convergence rate by reducing the initial search interval of β, as suggested by Hong *et al.* (2012), resulting in a very efficient method. Due to these advantages, this method was selected to implement into FEMEPDYN, with its formulation being described in Section 5.2.5.1.

It may happen that one or both yield surfaces are already active at the beginning of the sub-stress increment (i.e. $F(\{\sigma'_{n-1}\},\{k_{n-1}\}) \leq YTOL$), and the yield tolerance is exceeded at the end of the sub-step increment (i.e. $F(\{\sigma'_{n-1}\} + \{\Delta\sigma'_n\},\{k_n\}) > YTOL$). In such case, two alternative situations may have occurred: (a) the response is elasto-plastic over the entire sub-step increment (Figure 5.2a); or (b) unloading occurred first and, with further straining, the effective stress point has crossed the elastic region and has moved beyond the other projection of the yield surface (Figure 5.2b).

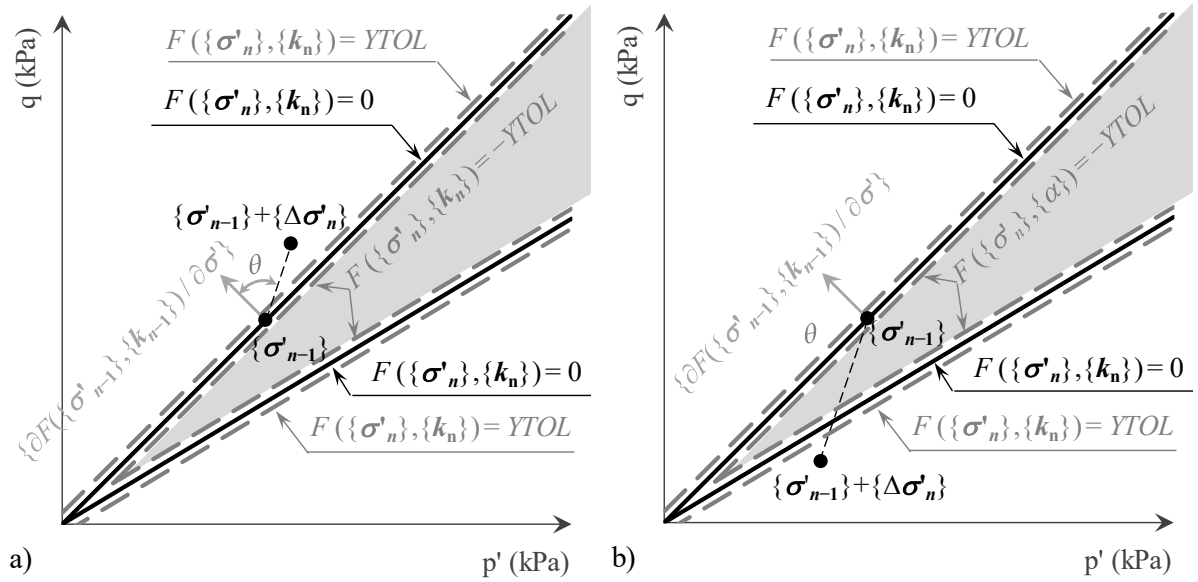

Figure 5.2 – Elasto-plastic loading (a) without a loading reversal and (b) with a loading reversal (adapted from Potts and Zdravkovic, 1999).

While β is null in situation (a), its value is different from 0.0 in the situation (b). Therefore, it is necessary to identify which situation (a) or (b) has occurred. This can be done by checking whether an elasto-plastic unloading occurred during the sub-step increment. With that purpose, the strategy proposed by Potts and Zdravkovic (1999) and Sloan *et al.* (2001) was adopted. Note that, although other strategies to distinguish loading from unloading exist, the adopted methodology has been shown to be consistent with the sub-stepping stress integration scheme (Papadopoulos and Taylor, 1995; Luccioni *et al.*, 2001). In this approach, the angle θ between the active yield surface gradient, $\{\partial F(\{\boldsymbol{\sigma'}_{n-1}\},\{\boldsymbol{k}_{n-1}\})/\partial \boldsymbol{\sigma'}\}$, and the trial effective stress increment, $\{\Delta \boldsymbol{\sigma'}_n\} = \{\Delta \boldsymbol{\sigma'}^{e}_n\}$, as given by Equation 5.9, is firstly computed.

$$\cos\theta = \frac{\left\{\dfrac{\partial F(\{\boldsymbol{\sigma'}_{n-1}\},\{\boldsymbol{k}_{n-1}\})}{\partial \boldsymbol{\sigma'}}\right\} : \{\Delta \boldsymbol{\sigma'}_n\}}{\left\|\left\{\dfrac{\partial F(\{\boldsymbol{\sigma'}_{n-1}\},\{\boldsymbol{k}_{n-1}\})}{\partial \boldsymbol{\sigma'}}\right\}\right\|_2 \|\{\Delta \boldsymbol{\sigma'}_n\}\|_2} \tag{5.9}$$

where $\| \|_2$ refers to the Euclidian norm of a second-order tensor, defined as $\|\{\boldsymbol{a}\}\|_2 = \sqrt{\{\boldsymbol{a}\}:\{\boldsymbol{a}\}} = \sqrt{a_{xx}^2 + a_{yy}^2 + a_{zz}^2 + 2\,a_{xy}^2 + 2\,a_{xz}^2 + 2\,a_{yz}^2}$ for a second-order tensor $\{\boldsymbol{a}\} = \{a_{xx} \quad a_{yy} \quad a_{xy} \quad a_{zz} \quad a_{xz} \quad a_{yz}\}^T$.

Based on the obtained value for θ, the occurrence of elasto-plastic unloading is evaluated. Specifically, when θ is smaller or equal to 90.0° (and, therefore, $\cos\theta \geq 0.0$), it is assumed that elastic-plastic unloading has not occurred. In such case, the response is elasto-plastic over the entire sub-step increment, with β being set to 0.0. On the contrary, when θ is greater than 90.0° (and, therefore, $\cos\theta < 0.0$), elasto-plastic unloading has occurred. A strategy is subsequently required to determine the value of β. As pointed out by Potts and Zdravkovic (1999), when a sub-stepping scheme is employed, a simple approach would consist of

restarting the sub-step increment with a successive smaller sub-step strain increment until an effective stress point lying inside both yield surfaces would be found (i.e. until a purely elastic response would be obtained). Having found this point, the calculation would proceed as usual, until an effective stress point lying outside of the yield surface being eventually found. At this point, however, the stress path would depart from the elastic domain and, therefore, the problem would be analogous to that described before (Figure 5.1), with several possible numerical algorithms being used to solve Equation 5.8, as mentioned before. In the present study, this strategy was deemed unnecessary. In fact, providing that the initial search interval of β is properly computed, the Pegasus method can be applied to unambiguously compute β, without the need for reducing the sub-step strain increment, as detailed in Section 5.2.5.2.

Having determined β, the purely elastic portion of the sub-step strain increment is given by $\{\Delta\boldsymbol{\varepsilon}_{\boldsymbol{n}}^{\boldsymbol{e}}\} = \beta\{\Delta\boldsymbol{\varepsilon}_{\boldsymbol{ss}}\}$. The remaining portion of the sub-step strain increment, $(1.0 - \beta)\ \{\Delta\boldsymbol{\varepsilon}_{\boldsymbol{ss}}\}$, is associated with elasto-plastic response. It is, therefore, necessary to integrate the elasto-plastic constitutive matrix, $[\boldsymbol{D}^{\boldsymbol{ep}}]$, over that portion of the sub-step strain increment, as well as over the remaining portion of the total strain increment that has not yet been integrated, together denoted by $\{\Delta\boldsymbol{\varepsilon}^{\boldsymbol{ep}}\}$ in Equation 5.10. Note that $[\boldsymbol{D}^{\boldsymbol{ep}}]$ is a function of the effective stress state, $\{\boldsymbol{\sigma}'\}$, as well as of all elastic and plastic state parameters of the constitutive model. Moreover, note that, contrary to the elastic state parameters (i.e. $\{\boldsymbol{\sigma}'^{SR}\}$, e^{SR} and N), the plastic state parameters of the present constitutive model (i.e. the back-stress ratio tensor, $\{\boldsymbol{\alpha}\}$, the isotropic and deviatoric components of the shearing-induced fabric tensor, f_p and $\{\boldsymbol{f}\}$, respectively, as described in Chapter 4) – may vary during an elasto-plastic sub-step increment. Therefore, as shown in Equation 5.10, it is convenient to represent the dependency of $[\boldsymbol{D}^{\boldsymbol{ep}}]$ on the effective stress state, $\{\boldsymbol{\sigma}'\}$, as well as on the state parameters associated with the yield surfaces and with the gradients of the plastic potentials, generically represented as $\{\boldsymbol{k}\}$ and $\{\boldsymbol{m}\}$, respectively.

$$\{\Delta\boldsymbol{\sigma}'\} = [\boldsymbol{D}^{\boldsymbol{ep}}(\{\boldsymbol{\sigma}'\},\{\boldsymbol{k}\},\{\boldsymbol{m}\})]\ \{\Delta\boldsymbol{\varepsilon}^{\boldsymbol{ep}}\} \tag{5.10}$$

Similar to the integration of the elastic constitutive matrix (Equation 5.5), a sub-stepping modified forward Euler scheme is used to solve Equation 5.10, which should, in such case, be written as Equation 5.11 (where $\{\Delta\boldsymbol{\varepsilon}_{\boldsymbol{ss}}^{\boldsymbol{ep}}\}$ is the elasto-plastic sub-step strain increment). This scheme guarantees that the errors resulting from the approximations made during the evaluation of the effective stress increment and evolution of state parameters remain below a user-defined tolerance, as detailed in Section 5.2.2.

$$\{\Delta\boldsymbol{\sigma}'_{\boldsymbol{n}}\} = [\boldsymbol{D}^{\boldsymbol{ep}}(\{\boldsymbol{\sigma}'_{\boldsymbol{n-1}}\},\{\boldsymbol{k}_{\boldsymbol{n-1}}\},\{\boldsymbol{m}_{\boldsymbol{n-1}}\})]\ \{\Delta\boldsymbol{\varepsilon}_{\boldsymbol{ss}}^{\boldsymbol{ep}}\} \tag{5.11}$$

As the integration of the elasto-plastic constitutive matrix is concluded, the effective stresses, plastic strains and sets of state parameters are updated, as given by Equation 5.12 to 5.15, respectively.

$$\{\boldsymbol{\sigma}'_{\boldsymbol{n}}\} = \{\boldsymbol{\sigma}'_{\boldsymbol{n-1}}\} + \{\Delta\boldsymbol{\sigma}'_{\boldsymbol{n}}\} \tag{5.12}$$

$$\{\boldsymbol{\varepsilon}_{\boldsymbol{n}}^{\boldsymbol{p}}\} = \{\boldsymbol{\varepsilon}_{\boldsymbol{n-1}}^{\boldsymbol{p}}\} + \{\Delta\boldsymbol{\varepsilon}_{\boldsymbol{n}}^{\boldsymbol{p}}\} \quad (5.13)$$

$$\{\boldsymbol{k}_{\boldsymbol{n}}\} = \{\boldsymbol{k}_{\boldsymbol{n-1}}\} + \{\Delta\boldsymbol{k}_{\boldsymbol{n}}\} \quad (5.14)$$

$$\{\boldsymbol{m}_{\boldsymbol{n}}\} = \{\boldsymbol{m}_{\boldsymbol{n-1}}\} + \{\Delta\boldsymbol{m}_{\boldsymbol{n}}\} \quad (5.15)$$

where $\{\boldsymbol{\sigma'}_{\boldsymbol{n-1}}\}$ and $\{\boldsymbol{\varepsilon}_{\boldsymbol{n-1}}^{\boldsymbol{p}}\}$, $\{\boldsymbol{k}_{\boldsymbol{n-1}}\}$ and $\{\boldsymbol{m}_{\boldsymbol{n-1}}\}$ represent, respectively, the effective stresses, plastic strains and state parameters associated with the yield surfaces and with the gradients of the plastic potentials at the beginning of a given sub-step increment.

At this point, two additional verifications are required. Firstly, if a single yield surface was active at the beginning of the sub-step increment, it is necessary to check whether the effective stress point did not move outside of the initially non-active yield surface. If that happens, then it is necessary to estimate the portion of the sub-step strain increment that results in an effective stress point lying on the newly activated yield surface. This problem is similar to that occurring during the elastic trial, when the stress path intersects one yield surface. Therefore, the Pegasus method (Dowell and Jarratt, 1972) is also employed to solve this problem, as detailed in Section 5.2.6.2. In addition, it is necessary to verify that the effective stress point does not lie outside of the active yield surface(s) at the end of the sub-step increment. In fact, due to the approximate nature of the integration scheme used to solve Equation 5.10, it may happen that the combination of final stresses and state parameters does not satisfy one (or both) yield condition(s) (i.e. $F_1(\{\boldsymbol{\sigma'}_{\boldsymbol{n}}\}, \{\boldsymbol{\alpha}_{\boldsymbol{n}}\}) > YTOL$ and/or $F_2\left(\{\boldsymbol{\sigma'}_{\boldsymbol{n}}\}, p'_{ys}\right) > YTOL$ may occur). This situation is usually referred to as "yield surface drift" (Potts and Zdravkovic, 1999; Sloan *et al.*, 2001). In this case, a correction should be applied to bring the effective stress point back to the yield surface. Among the several different iterative methods proposed in the literature (e.g. Potts and Gens, 1985; Crisfield, 1991; Potts and Zdravkovic, 1999; Sloan *et al.*, 2001; Hong *et al.*, 2012), an extension of the one proposed by Sloan *et al.* (2001) was implemented into FEMEPDYN, as presented in Section 5.2.6.3.

Having finally obtained the correct effective stresses, plastic strains and state parameters, a new sub-step increment is applied until the total strain increment, $\{\Delta\boldsymbol{\varepsilon}\}$, is fully applied.

5.2.2 A modified forward Euler integration scheme with automatic sub-stepping and error control

The application of the well-known modified forward Euler approximation to the explicit stress integration of elasto-plastic constitutive relationships was originally proposed by Sloan (1987). An updated version of that approach was presented by Sloan *et al.* (2001). As mentioned by the authors, this scheme is very attractive, since it attempts to control the errors arising from the estimation of the effective stress change and state parameter evolution by using a measure of those errors to automatically divide the strain increment into smaller or greater sub-steps. More specifically, in this scheme, a pseudo time, T_n, belonging to the range $0.0 \leq T_n \leq 1.0$, is defined, with $T_n = 0.0$ and $T_n = 1.0$ denoting the beginning

and the end of the integration process, respectively. The evolution of T_n is controlled by the pseudo-time step, ΔT_n, which belongs to the range $0.0 < \Delta T_n \leq 1.0$. This quantity is used to divide the strain increment, $\{\Delta\boldsymbol{\varepsilon}\}$, into a series of smaller sub-step strain increments, $\{\Delta\boldsymbol{\varepsilon_{ss}}\}$, as given by Equation 5.16. This means that the integration is performed between the pseudo time T_{n-1} and $T_n = T_{n-1} + \Delta T_n$, where the subscripts "$n$ – 1" and "n" denote the start and the end of sub-step n, respectively. It is initially assumed that a single sub-step increment is sufficient to perform the integration and, therefore, ΔT_n is initially set to 1.0. As detailed later, accurate integration of the stress-strain relationship may require more than a single sub-step increment and, in such case, the integration process may need to be repeated using a reduced value of ΔT_n, determined based on the error obtained in a rejected sub-step.

$$\{\Delta\boldsymbol{\varepsilon_{ss}}\} = \Delta T_n \{\Delta\boldsymbol{\varepsilon}\} \tag{5.16}$$

Since, in the present study, this method was employed during both elastic trial and elasto-plastic response (i.e. to solve both Equation 5.5 and 5.10), a distinction is subsequently made between the sub-step strain increment used during elastic trial, $\{\Delta\boldsymbol{\varepsilon_{ss}}\}$, and the sub-step strain increment used during elasto-plastic response, $\{\Delta\boldsymbol{\varepsilon_{ss}^{ep}}\}$, which is given by Equation 5.17. Note, nevertheless, that the same principle applies: the initial increment is sub-divided into smaller sub-step strain increments, $\{\Delta\boldsymbol{\varepsilon_{ss}^{ep}}\}$, by using a pseudo-time step, $\Delta T_n{}^{ep}$ (where the superscript "ep" refers to elasto-plastic). Note also that, since sub-stepping in the plastic region should not move the effective stress point back to the elastic region, the strain increment associated with elasto-plastic response, $\{\Delta\boldsymbol{\varepsilon^{ep}}\}$, is given by the sum of the portion of the total strain increment that has not yet been integrated (i.e. $(1.0 - T_{n-1})\{\Delta\boldsymbol{\varepsilon}\}$) with the remaining portion of the current sub-step strain increment, $(1.0 - \beta)\{\Delta\boldsymbol{\varepsilon_{ss}}\} = (1.0 - \beta)\Delta T_n \{\Delta\boldsymbol{\varepsilon}\}$.

$$\{\Delta\boldsymbol{\varepsilon_{ss}^{ep}}\} = \Delta T_n{}^{ep}\{\Delta\boldsymbol{\varepsilon^{ep}}\} = \Delta T_n{}^{ep}\left[(1.0 - T_{n-1}) + (1.0 - \beta)\,\Delta T_n\right]\{\Delta\boldsymbol{\varepsilon}\} \tag{5.17}$$

Given the effective stress state at the beginning of a given sub-step increment, $\{\boldsymbol{\sigma'_{n-1}}\}$, as well as sets of state parameters associated with the yield surfaces and with the gradients of the plastic potentials at the beginning of that sub-step increment, denoted as $\{\boldsymbol{k_{n-1}}\}$ and $\{\boldsymbol{m_{n-1}}\}$, respectively, a first-order approximation of the effective stress change, $\left\{\Delta\boldsymbol{\sigma'^{(1)}_n}\right\}$, can be obtained by Equation 5.18a for purely elastic response (i.e. during elastic trial), or, similarly, by Equation 5.18b for elasto-plastic response. Furthermore, in the latter case, a first order estimation of the plastic strain change, $\left\{\Delta\boldsymbol{\varepsilon_n^{p\,(1)}}\right\}$, can be computed by Equation 5.19 and the evolution of the set of state parameters associated with the yield surfaces, $\left\{\Delta\boldsymbol{k_n^{(1)}}\right\}$, by Equation 5.20. Note that, to keep the presentation general, it is assumed that the evolution of $\left\{\Delta\boldsymbol{k_n^{(1)}}\right\}$ depends on $\left\{\Delta\boldsymbol{\varepsilon_n^{p\,(1)}}\right\}$. This is not the case of perfect plasticity (as considered for the secondary yield surface of the present constitutive model), where the set of state parameters remains constant. It is, however, the case of strain hardening/softening plasticity (which is the case of the primary yield surface of the present constitutive model) and work hardening/softening plasticity, which depend on the accumulated plastic work and,

therefore, on the plastic strains. Further details on this topic are discussed in Potts and Zdravkovic (1999). In addition, note that, although the set of parameters associated with the gradients of the plastic potentials, $\{\boldsymbol{m}\}$, also evolves during sub-stepping, for simplicity of the presentation, its evolution is omitted from the set of equations shown below. In effect, as detailed later, $\{\boldsymbol{m}\}$ is not required by the "consistency condition" (according to which the effective stress point should remain on, at least, one of the yield surfaces during elasto-plastic response) and, therefore, can be considered less important to the presentation of this integration scheme.

$$\left\{\Delta\sigma'^{(1)}_n\right\} = [\boldsymbol{D}(\{\sigma'_{n-1}\})]\,\{\Delta\varepsilon_{ss}\} \tag{5.18a}$$

$$\left\{\Delta\sigma'^{(1)}_n\right\} = [\boldsymbol{D}^{ep}(\{\sigma'_{n-1}\},\{\boldsymbol{k}_{n-1}\},\{\boldsymbol{m}_{n-1}\})]\,\{\Delta\varepsilon^{ep}_{ss}\} \tag{5.18b}$$

$$\left\{\Delta\boldsymbol{\varepsilon}^{p\,(1)}_n\right\} = \lambda(\{\sigma'_{n-1}\},\{\boldsymbol{k}_{n-1}\},\{\boldsymbol{m}_{n-1}\},\{\Delta\varepsilon^{ep}_{ss}\})\left\{\frac{\partial \boldsymbol{P}(\{\sigma'_{n-1}\},\{\boldsymbol{m}_{n-1}\})}{\partial\sigma'}\right\} \tag{5.19}$$

$$\left\{\Delta\boldsymbol{k}^{(1)}_n\right\} = \left\{\Delta\boldsymbol{k}\left(\left\{\Delta\boldsymbol{\varepsilon}^{p\,(1)}_n\right\}\right)\right\} \tag{5.20}$$

where $\lambda(\{\sigma'_{n-1}\},\{\boldsymbol{k}_{n-1}\},\{\boldsymbol{m}_{n-1}\},\{\Delta\varepsilon^{ep}_{ss}\})$ and $\{\partial\boldsymbol{P}(\{\sigma'_{n-1}\},\{\boldsymbol{m}_{n-1}\})/\partial\sigma'\}$ are, respectively, the plastic multiplier and gradient of the plastic potential.

Using the above quantities, the effective stress state, $\left\{\boldsymbol{\sigma}'^{(1)}_n\right\}$ (Equation 5.21), as well as plastic strains, $\left\{\boldsymbol{\varepsilon}^{p\,(1)}_n\right\}$ (Equation 5.22), and set of state parameters, $\left\{\boldsymbol{k}^{(1)}_n\right\}$ (Equation 5.23), during elasto-plastic response, are temporarily updated.

$$\left\{\boldsymbol{\sigma}'^{(1)}_n\right\} = \{\sigma'_{n-1}\} + \left\{\Delta\sigma'^{(1)}_n\right\} \tag{5.21}$$

$$\left\{\boldsymbol{\varepsilon}^{p\,(1)}_n\right\} = \{\boldsymbol{\varepsilon}^{p}_{n-1}\} + \left\{\Delta\boldsymbol{\varepsilon}^{p\,(1)}_n\right\} \tag{5.22}$$

$$\left\{\boldsymbol{k}^{(1)}_n\right\} = \{\boldsymbol{k}_{n-1}\} + \left\{\Delta\boldsymbol{k}^{(1)}_n\right\} \tag{5.23}$$

Additionally, the newly-computed effective stress state, $\left\{\boldsymbol{\sigma}'^{(1)}_n\right\}$, is used to update the elastic constitutive matrix, $\left[\boldsymbol{D}\left(\left\{\boldsymbol{\sigma}'^{(1)}_n\right\}\right)\right]$. Similarly, during elasto-plastic response, the elasto-plastic constitutive matrix, $\left[\boldsymbol{D}^{ep}\left(\left\{\boldsymbol{\sigma}'^{(1)}_n\right\},\left\{\boldsymbol{k}^{(1)}_n\right\},\left\{\boldsymbol{m}^{(1)}_n\right\}\right)\right]$, is updated using $\left\{\boldsymbol{\sigma}'^{(1)}_n\right\}$, $\left\{\boldsymbol{k}^{(1)}_n\right\}$ and $\left\{\boldsymbol{m}^{(1)}_n\right\}$.

A second-order forward Euler approximation is subsequently obtained using the updated quantities, as indicated by Equation 5.24 to 5.26.

$$\left\{\Delta\sigma'^{(2)}_n\right\} = \left[\boldsymbol{D}\left(\left\{\boldsymbol{\sigma}'^{(1)}_n\right\}\right)\right]\{\Delta\varepsilon_{ss}\} \tag{5.24a}$$

$$\left\{\Delta\sigma'^{(2)}_n\right\} = \left[\boldsymbol{D}^{ep}\left(\left\{\boldsymbol{\sigma}'^{(1)}_n\right\},\left\{\boldsymbol{m}^{(1)}_n\right\},\left\{\boldsymbol{k}^{(1)}_n\right\}\right)\right]\{\Delta\varepsilon^{ep}_{ss}\} \tag{5.24b}$$

$$\left\{\Delta\boldsymbol{\varepsilon}^{p\,(2)}_n\right\} = \lambda\left(\left\{\boldsymbol{\sigma}'^{(1)}_n\right\},\left\{\boldsymbol{k}^{(1)}_n\right\},\left\{\boldsymbol{m}^{(1)}_n\right\},\{\Delta\varepsilon^{ep}_{ss}\}\right)\left\{\frac{\partial \boldsymbol{P}\left(\left\{\boldsymbol{\sigma}'^{(1)}_n\right\},\left\{\boldsymbol{m}^{(1)}_n\right\}\right)}{\partial\sigma'}\right\} \tag{5.25}$$

$$\left\{\Delta\boldsymbol{k}^{(2)}_n\right\} = \left\{\Delta\boldsymbol{k}\left(\left\{\Delta\boldsymbol{\varepsilon}^{p\,(2)}_n\right\}\right)\right\} \tag{5.26}$$

A more accurate modified forward Euler approximation of the effective stress change, $\{\Delta\boldsymbol{\sigma'}_n\}$, plastic strain evolution, $\{\Delta\boldsymbol{\varepsilon}_n^p\}$, and state parameter evolution, $\{\Delta\boldsymbol{k}_n\}$ for the current sub-step increment can now be obtained by Equation 5.27 to 5.29.

$$\{\Delta\boldsymbol{\sigma'}_n\} = \frac{\left\{\Delta\boldsymbol{\sigma'}_n^{(1)}\right\} + \left\{\Delta\boldsymbol{\sigma'}_n^{(2)}\right\}}{2} \tag{5.27}$$

$$\{\Delta\boldsymbol{\varepsilon}_n^p\} = \frac{\left\{\Delta\boldsymbol{\varepsilon}_n^{p\,(1)}\right\} + \left\{\Delta\boldsymbol{\varepsilon}_n^{p\,(2)}\right\}}{2} \tag{5.28}$$

$$\{\Delta\boldsymbol{k}_n\} = \frac{\left\{\Delta\boldsymbol{k}_n^{(1)}\right\} + \left\{\Delta\boldsymbol{k}_n^{(2)}\right\}}{2} \tag{5.29}$$

Furthermore, as discussed by Sloan (1987) and Sloan *et al.* (2001), since the local truncation error associated with the first-order forward Euler approximation (i.e. Equations 5.21 to 5.23) and modified second-order forward Euler approximation (i.e. Equations 5.27 to 5.29) are of order $O\left(\Delta T_n{}^2\right)$ and $O\left(\Delta T_n{}^3\right)$, respectively, the local error in effective stress change, E_σ, can be estimated from Equation 5.30, while the local error in computation of the state parameter evolution, E_k, can be approximated by Equation 5.31.

$$E_\sigma \approx \frac{1}{2}\left(\left\{\Delta\boldsymbol{\sigma'}_n^{(2)}\right\} - \left\{\Delta\boldsymbol{\sigma'}_n^{(1)}\right\}\right) \tag{5.30}$$

$$E_k \approx \frac{1}{2}\left(\left\{\Delta\boldsymbol{k}_n^{(2)}\right\} - \left\{\Delta\boldsymbol{k}_n^{(1)}\right\}\right) \tag{5.31}$$

Thus, the relative error in the modified forward Euler approximation of the effective stresses, R_σ, and set of state parameters, R_k, can be obtained from Equations 5.32 and 5.33, respectively. A maximum relative error, R, can, therefore, be computed using Equation 5.34.

$$R_\sigma \approx \frac{1}{2}\frac{\left\|\left(\left\{\Delta\boldsymbol{\sigma'}_n^{(2)}\right\} - \left\{\Delta\boldsymbol{\sigma'}_n^{(1)}\right\}\right)\right\|_2}{\|\{\boldsymbol{\sigma'}_{n-1}\} + \{\Delta\boldsymbol{\sigma'}_n\}\|_2} \tag{5.32}$$

$$R_k \approx \frac{1}{2}\frac{\left\|\left(\left\{\Delta\boldsymbol{k}_n^{(2)}\right\} - \left\{\Delta\boldsymbol{k}_n^{(1)}\right\}\right)\right\|_2}{\|\{\boldsymbol{k}_{n-1}\} + \{\Delta\boldsymbol{k}_n\}\|_2} \tag{5.33}$$

$$R = max\{R_\sigma, R_k\} \tag{5.34}$$

where $\|\ \|_2$ refers to the Euclidian norm of a second-order tensor, as defined before.

This error is used to decide whether the current sub-step increment is accepted or not. Specifically, this error is checked against a user-defined tolerance, *SSTOL*, which is typically in the range of 10^{-2} to 10^{-5}, according to Sloan (1987) and Potts and Zdravkovic (1999). If $R = max\{R_\sigma, R_k\} > SSTOL$, then the current sub-step increment is rejected and a new iteration is performed using a reduced pseudo-time step, $\Delta T_n{}^{new}$ (Equation 5.35).

$$\Delta T_n{}^{new} = \zeta \Delta T_n \tag{5.35}$$

Note, however, that the choice of the $\Delta T_n{}^{new}$ is not arbitrary. On the contrary, the reduction factor ζ can be related to the maximum relative error obtained in the present iteration, R,

and the one expected to be obtained in the next iteration, R^{new}, as indicated by Equation 5.36. Moreover, considering that R^{new} should be smaller or equal to *SSTOL*, an upper limit for ζ can be defined (Equation 5.37).

$$R^{new} \approx \zeta^2 R \tag{5.36}$$

$$\zeta \leq \sqrt{\frac{SSTOL}{R}} \tag{5.37}$$

Although it would be possible to use this upper limit to determine the value of ζ and, therefore, the value of ΔT_n^{new} to be used in the following sub-step increment, a conservative choice for this value has been proposed by several authors (Sloan, 1987; Potts and Zdravkovic, 1999; Sloan *et al.*, 2001), to minimise the number of rejected sub-step increments. In particular, the latter authors proposed to reduce the value computed by Equation 5.37 by a value of 0.9. In addition, to avoid excessive the oscillations in the pseudo-time step, the authors suggested limiting its reduction to 0.1. Both conditions are indicated in Equation 5.38.

$$\zeta = max\left\{0.9\sqrt{\frac{SSTOL}{R}}, 0.1\right\} \tag{5.38}$$

Finally, to add extra control to the procedure, a minimum pseudo-time step, $\Delta T_{n,min}$, can be used, as indicated by Equation 5.39. This condition enforces that the integration of the constitutive model is performed, even when an error smaller than *SSTOL* is not attained. A value of $\Delta T_{n,min} = 10^{-4}$ was suggested by Sloan *et al.* (2001), while a less conservative value of $\Delta T_{n,min} = 10^{-3}$ was used by Andrianopoulos *et al.* (2010a) when applying this procedure to integrate a bounding surface plasticity model. It should be mentioned that, in general, this condition is very rarely invoked. In fact, it was added essentially for robustness of the algorithm (Sloan *et al.*, 2001).

$$\Delta T_{n+1} = max\left\{\zeta \Delta T_n, \Delta T_{n,min}\right\} \tag{5.39}$$

Having defined ΔT_{n+1}, the integration procedure is repeated from Equation 5.16, now using $\Delta T_n = \Delta T_{n+1}$.

When the current sub-step increment is accepted (which, in general, means that $R = max\{R_\sigma, R_k\} \leq SSTOL$), the effective stresses, plastic strains, and state parameters are updated, as given by Equation 5.40 to 5.42, respectively.

$$\{\boldsymbol{\sigma'}_n\} = \{\boldsymbol{\sigma'}_{n-1}\} + \{\Delta\boldsymbol{\sigma'}_n\} \tag{5.40}$$

$$\{\boldsymbol{\varepsilon}^p_n\} = \{\boldsymbol{\varepsilon}^p_{n-1}\} + \{\Delta\boldsymbol{\varepsilon}^p_n\} \tag{5.41}$$

$$\{\boldsymbol{k}_n\} = \{\boldsymbol{k}_{n-1}\} + \{\Delta\boldsymbol{k}_n\} \tag{5.42}$$

As mentioned before, at this point of the stress integration, some additional verifications are required. Specifically, when this procedure is applied to the initial estimation of purely elastic

response (i.e. to integrate the elastic constitutive matrix, $[\boldsymbol{D}(\{\boldsymbol{\sigma'}\})]$), it is necessary to verify whether the updated effective stress state, $\{\boldsymbol{\sigma'_n}\}$ (Equation 5.40) in conjunction with the set of state parameters, $\{\boldsymbol{k_n}\}$ (which do not change during purely elastic loading), is located inside or on the yield surfaces of the constitutive model – i.e. for a two-yield surface model, whether both $F_1\left(\{\boldsymbol{\sigma'_n}\},\{\boldsymbol{k_{1,n}}\}\right) \leq YTOL$ and $F_2\left(\{\boldsymbol{\sigma'_n}\},\{\boldsymbol{k_{2,n}}\}\right) \leq YTOL$ conditions hold true. If that is not the case, then the intersection with yield surface(s) need to be determined. Conversely, when this procedure is applied to the estimation of the elasto-plastic response (i.e. to integrate the elasto-plastic constitutive matrix, $[\boldsymbol{D^{ep}}(\{\boldsymbol{\sigma'}\},\{\boldsymbol{k}\},\{\boldsymbol{m}\})]$), two additional verifications should be performed. Firstly, supposing that only the primary yield surface is active during a given sub-step increment, which is typically the case of the present constitutive model, it should be checked whether the updated effective stress state, $\{\boldsymbol{\sigma'_n}\}$, remains inside the secondary yield surface (i.e. $F_2\left(\{\boldsymbol{\sigma'_n}\},\{\boldsymbol{k_{2,n}}\}\right) \leq YTOL$). If that is not the case, then a procedure is necessary to estimate a reduction to the pseudo-time step, ΔT_n, which results in an effective stress point located at the intersection between both yield surfaces. The second verification to be performed during elasto-plastic response concerns the possible occurrence of yield surface drift. In fact, due to the approximations inherent to the numerical algorithm, it can happen that the updated effective stress state, $\{\boldsymbol{\sigma'_n}\}$, is located outside of the active yield surface(s), violating one of the fundamental principles of the elasto-plasticity theory (i.e. the consistency condition). In such case, a procedure is required to bring the effective stress point back to the active yield surface(s).

Having performed the aforementioned verifications, the pseudo time can be finally updated (Equation 5.43).

$$T_n = T_{n-1} + \Delta T_n \tag{5.43}$$

If $T_n = 1.0$, then the integration is complete. Otherwise, the integration must proceed with a new sub-step increment. Similar to the situation where the sub-step increment fails, the size of the new pseudo-time step, ΔT_{n+1}, can be defined by Equation 5.38 and 5.39. However, in this case, an upper limit to this quantity should be set to allow for a better control of the numerical procedure. Specifically, as proposed by Sloan *et al.* (2001), when the previous sub-step increment failed, no increase of ΔT_{n+1}in relation to ΔT_n should be permitted. On the contrary, when the previous sub-step increment was successful, ΔT_{n+1} is allowed to be greater than ΔT_n. Nevertheless, the growth in ΔT_{n+1} is limited to a value 10% greater than ΔT_n. These conditions are indicated by Equation 5.44a and 5.44b, respectively. In addition, it should be guaranteed that the new pseudo-time step does not exceed 1.0 at the end of the following sub-step increment (i.e. $T_n + \Delta T_{n+1} \leq 1.0$, as indicated by Equation 5.45).

If the previous sub-step increment or the one before the previous failed, then:

$$\zeta = min\left\{0.9\sqrt{\frac{SSTOL}{R}}, 1.0\right\} \tag{5.44a}$$

otherwise:

$$\zeta = min\left\{0.9\sqrt{\frac{SSTOL}{R}}, 1.1\right\} \tag{5.44b}$$

$$\Delta T_{n+1} = min\{\zeta \Delta T_n,\ 1.0 - T_n\} \tag{5.45}$$

5.2.3 Initialisation of the elastic and plastic state parameters

Before starting the integration procedure, it is necessary to initialise the elastic and plastic state parameters of the constitutive model. For the present bounding surface plasticity model, the non-linear elastic component depends on the effective stress state, strain state and void ratio at a reference state, respectively $\{\boldsymbol{\sigma'^{SR}}\}$, $\{\boldsymbol{\varepsilon^{SR}}\}$ and e^{SR}. As suggested by Papadimitriou and Bouckovalas (2002), this reference state is initially set to coincide with the initial state, as indicated by Equation 5.46, 5.47 and 5.48. Moreover, as detailed in the following section, it is updated whenever a shear strain reversal occurs. The subscript "SR" is, therefore, used to refer to "last shear reversal". In addition, the elastic component of the model uses a scaling factor, *N*. This value is initially set to 1.0. Once the first shear strain reversal is detected, the value of this scalar quantity is changed to 2.0, remaining constant thereafter.

$$\{\boldsymbol{\sigma'^{SR}_0}\} = \{\boldsymbol{\sigma'_0}\} = \left\{\sigma'_{xx,0} \quad \sigma'_{yy,0} \quad \tau_{xy,0} \quad \sigma'_{zz,0} \quad \tau_{xz,0} \quad \tau_{yz,0}\right\}^{\mathrm{T}} \tag{5.46}$$

$$\{\boldsymbol{\varepsilon^{SR}_0}\} = \{\boldsymbol{\varepsilon_0}\} = \{0.0 \quad 0.0 \quad 0.0 \quad 0.0 \quad 0.0 \quad 0.0\}^{\mathrm{T}} \tag{5.47}$$

$$e^{SR}_0 = e_0 \tag{5.48}$$

Regarding the plastic state parameters of the bounding surface plasticity model, the back-stress tensor, $\{\boldsymbol{\alpha}\}$, which defines the axis of the primary yield surface, is set to coincide with the initial stress ratio tensor, as given by Equation 5.49.

$$\{\boldsymbol{\alpha_0}\} = \{\boldsymbol{r_0}\} = \left\{\frac{\sigma'_{xx,0} - p'_0}{p'_0} \quad \frac{\sigma'_{yy,0} - p'_0}{p'_0} \quad \frac{\tau_{xy,0}}{p'_0} \quad \frac{\sigma'_{zz,0} - p'_0}{p'_0} \quad \frac{\tau_{xz,0}}{p'_0} \quad \frac{\tau_{yz,0}}{p'_0}\right\}^{\mathrm{T}} \tag{5.49}$$

Furthermore, since the previous cyclic shearing history is unknown at the start of the analysis, both isotropic and deviatoric components of shearing-induced fabric tensor, as well as the constant *C*, required to determine the evolution of its deviatoric component, are initially set to be null, as given by Equation 5.50, 5.51 and 5.52, respectively.

$$f_{p,0} = 0.0 \tag{5.50}$$

$$\{\boldsymbol{f_0}\} = \{0.0 \quad 0.0 \quad 0.0 \quad 0.0 \quad 0.0 \quad 0.0\}^{\mathrm{T}} \tag{5.51}$$

$$C_0 = 0.0 \tag{5.52}$$

Although the shearing-induced fabric index, *H*, is constant throughout the analysis, it needs to be set independently to each Gauss point, since it depends on the material's initial state, as indicated by Equation 5.53:

$$H = H_0 \left(\frac{\sigma'_{1,0}}{p'_{ref}} \right)^{-\zeta} \langle -\psi_0 \rangle \leq H_{max} \tag{5.53}$$

where $\sigma'_{1,0}$ is the initial major principal effective stress and ψ_0 is the initial value of the state parameter.

In relation to the inherent fabric tensor, $\boldsymbol{F_A}$, which quantifies the anisotropy related to the orientation of sand particle distribution in 3D stress space, it is considered a material constant, rather than a state parameter. Consequently, similar to the shearing-induced fabric index, *H*, it is only required to set its value at the start of the analysis, based on the value of the model parameter *a* (Equation 5.54).

$$\{\boldsymbol{F_A}\} = \left\{ \frac{1}{2}(1-a) \quad a \quad 0.0 \quad \frac{1}{2}(1-a) \quad 0.0 \quad 0.0 \right\}^{\mathrm{T}} \tag{5.54}$$

5.2.4 Detection of a shear strain reversal and update of the elastic state parameters

Since the present model includes a non-linear cyclic (i.e. hysteretic) component, a check for the occurrence of a shear strain reversal is performed in every sub-step increment, before determining the tangent elastic shear and bulk moduli, G_{tan} and K_{tan}, respectively. Note that these quantities are used to compute the elastic constitutive matrix, $[\boldsymbol{D}(\{\boldsymbol{\sigma'}\})]$, during elastic trial, as well as the the elasto-plastic constitutive matrix, $[\boldsymbol{D^{ep}}(\{\boldsymbol{\sigma'}\},\{\boldsymbol{k}\})]$, during elasto-plastic response.

According to the methodology proposed by Papadimitriou and Bouckovalas (2002), the distance χ^e_{ref} (Equation 5.55) between the current deviatoric strain, $\{\boldsymbol{e}\} = \{\boldsymbol{\varepsilon}\} - 1.0/3.0\ \varepsilon_v\{\boldsymbol{I}\}$, and the deviatoric strain at last shear reversal point, $\{\boldsymbol{e^{SR}}\} = \{\boldsymbol{\varepsilon^{SR}}\} - 1.0/3.0\ \varepsilon_v\{\boldsymbol{I}\}$, measured in the deviatoric strain plane, is used to detect the occurrence of a shear strain reversal.

$$\begin{aligned} \chi^e_{ref} &= \sqrt{\frac{1}{2}} \|\{\boldsymbol{e}\} - \{\boldsymbol{e^{SR}}\}\|_2 = \sqrt{\frac{1}{2}} \sqrt{(\{\boldsymbol{e}\} - \{\boldsymbol{e^{SR}}\}) : (\{\boldsymbol{e}\} - \{\boldsymbol{e^{SR}}\})} \\ &= \sqrt{\frac{1}{2}} \sqrt{\begin{array}{c} \left[\left(\varepsilon_{xx} - \frac{1}{3}\varepsilon_v \right) - \left(\varepsilon_{xx}{}^{SR} - \frac{1}{3}\varepsilon_v{}^{SR} \right) \right]^2 + \\ \left[\left(\varepsilon_{yy} - \frac{1}{3}\varepsilon_v \right) - \left(\varepsilon_{yy}{}^{SR} - \frac{1}{3}\varepsilon_v{}^{SR} \right) \right]^2 + \\ \left[\left(\varepsilon_{zz} - \frac{1}{3}\varepsilon_v \right) - \left(\varepsilon_{zz}{}^{SR} - \frac{1}{3}\varepsilon_v{}^{SR} \right) \right]^2 + \\ 2\left[\varepsilon_{xy} - \varepsilon_{xy}{}^{SR} \right]^2 + 2[\varepsilon_{xz} - \varepsilon_{xz}{}^{SR}]^2 + 2\left[\varepsilon_{yz} - \varepsilon_{yz}{}^{SR} \right]^2 \end{array}} \end{aligned} \tag{5.55}$$

where:

$$\varepsilon_v = \varepsilon_{xx} + \varepsilon_{yy} + \varepsilon_{zz} \tag{5.56}$$

$$\varepsilon_v{}^{SR} = \varepsilon_{xx}{}^{SR} + \varepsilon_{yy}{}^{SR} + \varepsilon_{zz}{}^{SR} \tag{5.57}$$

More specifically, this distance is evaluated using both the strain state at the beginning of the sub-step increment, $\{\boldsymbol{\varepsilon_n}\}$, and the strain state at the end of that sub-step increment, $\{\boldsymbol{\varepsilon_{n-1}}\} + \{\Delta\boldsymbol{\varepsilon_{ss}}\} = \{\boldsymbol{\varepsilon_{n-1}}\} + \Delta T_n \{\Delta\boldsymbol{\varepsilon}\}$, with the values of $\chi^e_{ref} = \sqrt{\frac{1}{2}}\|\{\boldsymbol{e_{n-1}}\} - \{\boldsymbol{e^{SR}}\}\|_2$ and $\chi^{e+\Delta e}_{ref} = \sqrt{\frac{1}{2}}\|\{\boldsymbol{e_{n-1}}\} + \Delta T_n \{\Delta\boldsymbol{e}\} - \{\boldsymbol{e^{SR}}\}\|_2$ being computed, respectively. If $\chi^e_{ref} > \chi^{e+\Delta e}_{ref}$, then the occurrence of a shear strain reversal is flagged and the effective stresses, strains and void ratio at last shear reversal, $\{\boldsymbol{\sigma'^{SR}}\}$, $\{\boldsymbol{\varepsilon^{SR}}\}$ and e^{SR}, respectively, are updated with their values at the beginning of the sub-step increment. In addition, the scaling factor *N* is set to 2.0. Note, however, that in case the current sub-step increment is rejected and, consequently, the sub-stepping needs to be restarted (as detailed in Section 5.2.2), the changes in the values of the elastic state parameters are reverted (i.e. the previous values of these quantities are re-assigned). Naturally, this implies a temporary storage of the values of the elastic state parameters before performing this check.

As pointed out by Taborda (2011), since the value determined by Equation 5.55 is always non-negative, particular attention should be given to the situation in which the norm of the deviatoric part of the strain increment, denoted by $\chi^{\Delta e}$ (Equation 5.58), is larger than χ^e_{ref}. In such situation, a shear reversal may not be detected by using solely the aforementioned methodology.

$$\begin{aligned}\chi^{\Delta e} &= \sqrt{\frac{1}{2}}\|\Delta T_n \{\Delta\boldsymbol{e}\}\|_2 = \sqrt{\frac{1}{2}}\Delta T_n \sqrt{\{\Delta\boldsymbol{e}\}:\{\Delta\boldsymbol{e}\}} \\ &= \sqrt{\frac{1}{2}}\Delta T_n \sqrt{\Delta e_{xx}{}^2 + \Delta e_{yy}{}^2 + \Delta e_{zz}{}^2 + 2\Delta e_{xy}{}^2 + 2\Delta e_{xz}{}^2 + 2\Delta e_{yz}{}^2}\end{aligned} \tag{5.58}$$

For instance, supposing the initial strain state $\{\boldsymbol{\varepsilon_{n-1}}\} = \{0.0 \;\; 0.0 \;\; 0.01 \;\; 0.0 \;\; 0.0 \;\; 0.0\}^T$, the strain state at last shear reversal $\{\boldsymbol{\varepsilon^{SR}}\} = \{0.0 \;\; 0.0 \;\; 0.0 \;\; 0.0 \;\; 0.0 \;\; 0.0\}^T$, the strain increment $\{\Delta\boldsymbol{\varepsilon_{ss}}\} = \{0.0 \;\; 0.0 \;\; -0.03 \;\; 0.0 \;\; 0.0 \;\; 0.0\}^T$ and a pseudo-time step $\Delta T_n = 0.75$, the distances χ^e_{ref} and $\chi^{e+\Delta e}_{ref}$would be, respectively, given by:

$$\chi^e_{ref} = \sqrt{\frac{1}{2}}\|\{\boldsymbol{e_{n-1}}\} - \{\boldsymbol{e^{SR}}\}\|_2 = \sqrt{\frac{1}{2}}\sqrt{2\,(0.01 - 0.0)^2} = 0.01 \tag{5.59}$$

$$\chi_{ref}^{e+\Delta e} = \sqrt{\frac{1}{2}}\|\{\boldsymbol{e_{n-1}}\} + \Delta T_n\{\Delta \boldsymbol{e}\} - \{\boldsymbol{e^{SR}}\}\|_2 = \sqrt{\frac{1}{2}}\sqrt{2\,(0.01 - 0.75 \times 0.03 - 0.0)^2} = 0.0125 \tag{5.60}$$

Since $\chi_{ref}^{e} < \chi_{ref}^{e+\Delta e}$, a shear reversal would not be indicated, even though a purely deviatoric strain increment with the opposite direction of the current purely deviatoric strain state had been applied. Note, however, that, in this case, $\chi^{\Delta e} > \chi_{ref}^{e}$., as shown below:

$$\chi^{\Delta e} = \sqrt{\frac{1}{2}}\|\Delta T_n\{\Delta \boldsymbol{e}\}\|_2 = \sqrt{\frac{1}{2}}\sqrt{2\,(0.75 \times 0.03)^2} = 0.0225 > 0.01 \tag{5.61}$$

It is, therefore, clear that an additional verification is required for these particular situations. In the present study, a methodology similar to that proposed by Taborda (2011) is employed. Specifically, a reduction to the sub-step strain increment, $R\ \Delta T_n\{\Delta \boldsymbol{\varepsilon}\}$, where R is a positive number smaller than 1.0, is applied until a value of $\chi^{R\,\Delta e} = R\,\chi^{\Delta e}$ (Equation 5.62) smaller than χ_{ref}^{e} is found.

$$\chi^{R\,\Delta e} = \sqrt{\frac{1}{2}}\|R\ \Delta T_n\{\Delta \boldsymbol{e}\}\|_2 = \sqrt{\frac{1}{2}}R\ \Delta T_n\sqrt{\{\Delta \boldsymbol{e}\}:\{\Delta \boldsymbol{e}\}} = R\,\chi^{\Delta e} \tag{5.62}$$

As this condition is verified, $\chi_{ref}^{e+R\,\Delta e}$ (Equation 5.63) is used to detect the occurrence of a shear reversal (which occurs if $\chi_{ref}^{e} > \chi_{ref}^{e+R\,\Delta e}$).

$$\chi_{ref}^{e+R\,\Delta e} = \sqrt{\frac{1}{2}}\|\{\boldsymbol{e_{n-1}}\} + R\ \Delta T_n\{\Delta \boldsymbol{e}\} - \{\boldsymbol{e^{SR}}\}\|_2 = \sqrt{\frac{1}{2}}\sqrt{(\{\boldsymbol{e_{n-1}}\} + R\ \Delta T_n\{\Delta \boldsymbol{e}\} - \{\boldsymbol{e^{SR}}\}):(\{\boldsymbol{e_{n-1}}\} + R\ \Delta T_n\{\Delta \boldsymbol{e}\} - \{\boldsymbol{e^{SR}}\})} \tag{5.63}$$

Furthermore, as mentioned by Taborda (2011), care must be taken to prevent the detection of false shear reversals, which may result in overshooting (i.e. in the computation of a stiffer response than the one that should have been registered). To minimise the occurrence of such undesirable phenomenon, the author suggested to introduce a very small tolerance, *RTOL*, which determines whether the shear strain reversal detection is undertaken or not. More specifically, when $\chi^{\Delta e} \leq RTOL$, the algorithm used to detect the occurrence of a shear reversal is not performed. Note that a value of 10^{-7} for *RTOL* was deemed appropriate for all calculations performed in the present study.

5.2.5 Elastic trial

5.2.5.1 Yield surface intersection

As suggested by Sloan *et al.* (2001) and described in Section 5.2.1, during the elastic trial, the Pegasus method (Dowell and Jarratt, 1972) is employed to solve the yield surface intersection (Equation 5.8). As pointed out by the authors, this method is a modification of the well-known "false position" method (also known as "regula falsi" method). While keeping the two main merits of the original method of being unconditionally convergent and non-requiring the use of derivatives, it appears to show a superior rate of convergence. Indeed, as suggested by suggested by Hong *et al.* (2012), the convergence rate can be further enhanced when reducing the size of the search interval of the method. In such case, prior to the application of the Pegasus method, a proper set of values $\beta^{(inf)}$ and $\beta^{(sup)}$, which locate, respectively, the current effective stress state inside the yield surface (i.e. $F\left(\{\boldsymbol{\sigma'}_{n-1}\} + \beta^{(inf)}\,[\boldsymbol{D}(\{\boldsymbol{\sigma'}_{n}\})]\,\{\Delta\boldsymbol{\varepsilon}_{ss}\}, \{\boldsymbol{k}_{n}\}\right) < -YTOL$), and outside of it (i.e. $F\left(\{\boldsymbol{\sigma'}_{n-1}\} + \beta^{(sup)}\,[\boldsymbol{D}(\{\boldsymbol{\sigma'}_{n}\})]\,\{\Delta\boldsymbol{\varepsilon}_{ss}\}, \{\boldsymbol{k}_{n}\}\right) > YTOL$) are defined by using the following procedure, which is similar to that outlined by Hong *et al.* (2012):

1) Enter with the sub-step strain increment, $\{\Delta\boldsymbol{\varepsilon}_{ss}\}$, effective stresses and set of state parameters at the beginning of the increment, $\{\boldsymbol{\sigma'}_{n-1}\}$ and $\{\boldsymbol{k}_{n-1}\}$, respectively. Initialise the lower and upper limits for the Pegasus method to $\beta^{(inf)} = 0.0$ and $\beta^{(sup)} = 1.0$, respectively, as well as the value of an auxiliary variable $\beta_{save} = \beta^{(sup)} = 1.0$.
2) Apply the modified forward Euler scheme to estimate the effective stress change, $\{\Delta\boldsymbol{\sigma'}_{n}\}$, corresponding to $\beta^{(sup)}\,[\boldsymbol{D}(\{\boldsymbol{\sigma'}_{n}\})]\,\{\Delta\boldsymbol{\varepsilon}_{ss}\}$. Note that the plastic state parameters remain constant during the integration of the elastic constitutive matrix (i.e. under purely elastic response) and, therefore, $\{\boldsymbol{k}_{n}\} = \{\boldsymbol{k}_{n-1}\}$ at this stage. Determine the corresponding value of the yield function: $F(\{\boldsymbol{\sigma'}_{n-1}\} + \{\Delta\boldsymbol{\sigma'}_{n}\}, \{\boldsymbol{k}_{n}\})$.
3) If $F(\{\boldsymbol{\sigma'}_{n-1}\} + \{\Delta\boldsymbol{\sigma'}_{n}\}, \{\boldsymbol{k}_{n}\}) > YTOL$, then the effective stress point is located outside the yield surface. In such situation, the search interval can be reduced. Update $\beta_{save} = \beta^{(sup)}$ and reduce the upper limit of the search range to $\beta^{(sup)} = 0.9\,\beta^{(sup)}$. Return to step 2).
   Else, if $F(\{\boldsymbol{\sigma'}_{n-1}\} + \{\Delta\boldsymbol{\sigma'}_{n}\}, \{\boldsymbol{k}_{n}\}) < -YTOL$, then the effective stress point is located inside the yield surface. Therefore, the actual value of $\beta^{(sup)}$ can be used as the lower limit for the search range of the Pegasus method (i.e. $\beta^{(inf)} = \beta^{(sup)}$). The value of β corresponding to the previous iteration defines the upper limit of the input range for the Pegasus method (i.e. $\beta^{(sup)} = \beta_{save}$). Move to step 4).
   Else, if $|F(\{\boldsymbol{\sigma'}_{n-1}\} + \{\Delta\boldsymbol{\sigma'}_{n}\}, \{\boldsymbol{k}_{n}\})| \leq YTOL$, then the yield surface intersection was found. Set $\beta^{(inf)} = \beta^{(sup)}$.
4) Exit with the input range for the Pegasus method: [$\beta^{(inf)}$, $\beta^{(sup)}$].

Having defined its input range, the Pegasus method, originally proposed by Dowell and Jarratt (1972) and adapted by Sloan *et al.* (2001) to the estimation of the yield surface point is applied. This method consists of the following sequence of operations:

1) Enter with the sub-step strain increment, $\{\Delta\boldsymbol{\varepsilon_{ss}}\}$, effective stresses and set of state parameters at the beginning of the increment, $\{\boldsymbol{\sigma'_{n-1}}\}$ and $\{\boldsymbol{k_{n-1}}\}$, respectively, the input range for the Pegasus method, $[\beta^{(inf)}, \beta^{(sup)}]$, and a maximum number of iterations for this scheme, $N_{iter,max}$.
2) Apply the modified forward Euler scheme to estimate the effective stress change, $\{\Delta\boldsymbol{\sigma'_n}\}$, corresponding to $\beta^{(inf)}\ [\boldsymbol{D}(\{\boldsymbol{\sigma'_n}\})]\ \{\Delta\boldsymbol{\varepsilon_{ss}}\}$, as well as to $\beta^{(sup)}\ [\boldsymbol{D}(\{\boldsymbol{\sigma'_n}\})]\ \{\Delta\boldsymbol{\varepsilon_{ss}}\}$. Determine the corresponding values of the yield function: $F^{(inf)} = F\big(\{\boldsymbol{\sigma'_{n-1}}\} + \beta^{(inf)}\ [\boldsymbol{D}(\{\boldsymbol{\sigma'_n}\})]\ \{\Delta\boldsymbol{\varepsilon_{ss}}\}, \{\boldsymbol{k_n}\}\big)$ and $F^{(sup)} = F\big(\{\boldsymbol{\sigma'_{n-1}}\} + \beta^{(sup)}\ [\boldsymbol{D}(\{\boldsymbol{\sigma'_n}\})]\ \{\Delta\boldsymbol{\varepsilon_{ss}}\}, \{\boldsymbol{k_n}\}\big)$.
3) If the number of iterations, N_{iter}, is smaller than the maximum allowed, $N_{iter,max}$, (i.e. $N_{iter} < N_{iter,max}$), then compute a new value for β by linear interpolation: $\beta = \beta^{(sup)} - F^{(sup)}\left(\beta^{(sup)} - \beta^{(inf)}\right)/\left(F^{(sup)} - F^{(inf)}\right)$. Apply, once again, the modified forward Euler scheme to estimate the effective stress change, $\{\Delta\boldsymbol{\sigma'_n}\}$, corresponding to $\beta[\boldsymbol{D}(\{\boldsymbol{\sigma'_n}\})]\ \{\Delta\boldsymbol{\varepsilon_{ss}}\}$, and determine the corresponding value of the yield function: $F = F(\{\boldsymbol{\sigma'_{n-1}}\} + \beta\,[\boldsymbol{D}(\{\boldsymbol{\sigma'_n}\})]\ \{\Delta\boldsymbol{\varepsilon_{ss}}\}, \{\boldsymbol{k_n}\})$.
   Else, if $N_{iter} = N_{iter,max}$, then the maximum number of iterations were reached. Print an error message and stop.
4) If $|F| \leq YTOL$, then the intersection with the yield surface was found. Move to step 5). Otherwise, set new values and proceed to a new iteration:
   a) if $F\,F^{(sup)} < 0.0$, which means that an effective stress point inside the elastic region was found when using $\beta\{\Delta\boldsymbol{\varepsilon_{ss}}\}$, while a point outside the elastic region was found when using $\beta^{(sup)}\ \{\Delta\boldsymbol{\varepsilon_{ss}}\}$, then set $\beta^{(inf)} = \beta$ and $F^{(inf)} = F$; the values of $\beta^{(sup)}$ and $F^{(sup)}$ remain unchanged;
   b) otherwise, set $\beta^{(sup)} = \beta$ and $F^{(sup)} = F$, while scaling down the value of $F^{(inf)}$ by the factor $F^{(sup)}/\left(F^{(sup)} + F\right)$ to prevent the retention of an end-point (Dowell and Jarratt, 1972), note that this strategy is the only difference between the Pegasus method and its precedent false position method (Dowell and Jarratt, 1972); note also that, in this case, $\beta^{(inf)}$ remains unchanged.
5) Exit with the portion of the sub-step strain increment that is purely elastic, β, as well as with the effective stress state lying on the yield surface, $\{\boldsymbol{\sigma'_{n-1}}\} + \beta\ [\boldsymbol{D}(\{\boldsymbol{\sigma'_n}\})]\ \{\Delta\boldsymbol{\varepsilon_{ss}}\}$.

Three additional notes should be provided. Firstly, it should be highlighted that, for a constitutive model employing two yield surfaces, a transition from purely elastic to elasto-plastic response is considered to occur in any of the three different situations listed below:

i) Activation of the primary yield surface:
$F_1(\{\boldsymbol{\sigma'}_{n-1}\},\{\boldsymbol{k}_{1,n-1}\}) < -YTOL$ and $F_1(\{\boldsymbol{\sigma'}_{n-1}\}+\{\Delta\boldsymbol{\sigma'}_n\},\{\boldsymbol{k}_{1,n}\}) > YTOL$ in conjunction with $F_2(\{\boldsymbol{\sigma'}_{n-1}\}+\{\Delta\boldsymbol{\sigma'}_n\},\{\boldsymbol{k}_{2,n}\}) \leq YTOL$.

ii) Activation of the secondary yield surface:
$F_2(\{\boldsymbol{\sigma'}_{n-1}\},\{\boldsymbol{k}_{2,n-1}\}) < -YTOL$ and $F_2(\{\boldsymbol{\sigma'}_{n-1}\}+\{\Delta\boldsymbol{\sigma'}_n\},\{\boldsymbol{k}_{2,n}\}) > YTOL$ in conjunction with $F_1(\{\boldsymbol{\sigma'}_{n-1}\}+\{\Delta\boldsymbol{\sigma'}_n\},\{\boldsymbol{k}_{1,n}\}) \leq YTOL$.

iii) Activation of both yield surfaces:
$F_1(\{\boldsymbol{\sigma'}_{n-1}\},\{\boldsymbol{k}_{1,n-1}\}) < -YTOL$ and $F_1(\{\boldsymbol{\sigma'}_{n-1}\}+\{\Delta\boldsymbol{\sigma'}_n\},\{\boldsymbol{k}_{1,n}\}) > YTOL$ in conjunction with $F_2(\{\boldsymbol{\sigma'}_{n-1}\},\{\boldsymbol{k}_{2,n-1}\}) < -YTOL$ and $F_2(\{\boldsymbol{\sigma'}_{n-1}\}+\{\Delta\boldsymbol{\sigma'}_n\},\{\boldsymbol{k}_{2,n}\}) > YTOL$.

However, note that in any of the three aforementioned cases, the effective stress point is inside both yield surfaces at the beginning of the increment.

Secondly, due to the co-existence of two yield surfaces, it can happen that the trial elastic stress path intersects both primary and secondary yield surfaces. In such a case, two independent computations (one for each yield surface) should be performed. Depending on the positions of the yield surfaces and on the followed stress path, the intersection may occur firstly with the primary yield surface or with the secondary yield surface or, even, with both yield surfaces concurrently. To assess which surface is firstly intersected, the norm of the effective stress increment moving the initial effective stress point to the primary yield surface – i.e. $\left\|\{\Delta\boldsymbol{\sigma'}_{n,1}\}\right\|_2 = \left\|\beta_1\,[\boldsymbol{D}(\{\boldsymbol{\sigma'}_n\})]\,\{\Delta\boldsymbol{\varepsilon}_{ss}\}\right\|_2 = \beta_1\,\|[\boldsymbol{D}(\{\boldsymbol{\sigma'}_n\})]\,\{\Delta\boldsymbol{\varepsilon}_{ss}\}\|_2$ – can be compared with the norm of the effective stress increment moving the initial effective stress point to the secondary yield surface – i.e. $\left\|\{\Delta\boldsymbol{\sigma'}_{n,2}\}\right\|_2 = \beta_2\,\|[\boldsymbol{D}(\{\boldsymbol{\sigma'}_n\})]\,\{\Delta\boldsymbol{\varepsilon}_{ss}\}\|_2$ – where β_1 and β_2 have a similar meaning to that of β. The smallest value indicates which yield surface is intersected first, with the corresponding effective stress increment (i.e. $\{\Delta\boldsymbol{\sigma'}_{n,1}\}$ or $\{\Delta\boldsymbol{\sigma'}_{n,2}\}$) and value of β (i.e. β_1 or β_2) being used in the subsequent stage of the analysis. Naturally, it may also happen that $\left\|\{\Delta\boldsymbol{\sigma'}_{n,1}\}\right\|_2 = \left\|\{\Delta\boldsymbol{\sigma'}_{n,2}\}\right\|_2$, meaning that the trial effective stress path intersects both yield surfaces simultaneously. The computation of the norm of the effective stress increment, $\|\{\Delta\boldsymbol{\sigma'}_n\}\|_2$ is indicated in Equation 5.64.

$$\begin{aligned}\|\{\Delta\boldsymbol{\sigma'}_n\}\|_2 &= \sqrt{\{\Delta\boldsymbol{\sigma'}_n\}:\{\Delta\boldsymbol{\sigma'}_n\}} \\ &= \sqrt{\Delta\sigma'_{xx}{}^2+\Delta\sigma'_{yy}{}^2+\Delta\sigma'_{zz}{}^2+2\Delta\sigma'_{xy}{}^2+2\Delta\sigma'_{xz}{}^2+2\Delta\sigma'_{yz}{}^2}\end{aligned} \tag{5.64}$$

Finally, a third note is related to the convergence of the process. According to the author experience, convergence is usually attained in less than 5 iterations.

5.2.5.2 Detection of an elasto-plastic unloading

As described in Section 5.2.1, a purely-elastic to elasto-plastic transition may also occur when an effective stress point initially lying on one or on both yield surfaces (i.e. $F(\{\boldsymbol{\sigma'}_{n-1}\},\{\boldsymbol{k}\}) \leq$

YTOL) is subjected to an effective stress path that initially moves the point to the interior of the yield surface and, with further straining, moves the point to the exterior of one of the yield surface (i.e. $F(\{\boldsymbol{\sigma'}_{n-1}\}+\{\Delta\boldsymbol{\sigma'}_n\},\{\boldsymbol{k}\}) \leq YTOL$). As also mentioned, following the methodology proposed by Potts and Zdravkovic (1999) and Sloan *et al.* (2001), to identify the occurrence of such situation, the angle θ between the active yield surface gradient, $\{\partial F(\{\boldsymbol{\sigma'}_{n-1}\},\{\boldsymbol{k}\})/\partial\boldsymbol{\sigma'}\}$, and the elastic effective stress increment, $\{\Delta\boldsymbol{\sigma'}^{e}\}$, is computed by Equation 5.9. When θ is greater than 90.0° (and, therefore, $\cos\theta < 0.0$), an elasto-plastic unloading is flagged.

It should be highlighted that, for the present constitutive model, which employs two yield surfaces, an elasto-plastic unloading followed by a transition from purely elastic to elasto-plastic response is considered to occur in any of the situations listed below:

i) elasto-plastic unloading from the primary yield surface: $\left|F_1\left(\{\boldsymbol{\sigma'}_{n-1}\},\{\boldsymbol{k}_{1,n-1}\}\right)\right| \leq YTOL$ and $\cos\theta_1 < 0.0$, with subsequent activation of the primary and/or secondary yield surface, $F_1\left(\{\boldsymbol{\sigma'}_{n-1}\}+\{\Delta\boldsymbol{\sigma'}_n\},\{\boldsymbol{k}_{1,n}\}\right) > YTOL$ and/or $F_2\left(\{\boldsymbol{\sigma'}_{n-1}\}+\{\Delta\boldsymbol{\sigma'}_n\},\{\boldsymbol{k}_{2,n}\}\right) > YTOL$, respectively;

ii) elasto-plastic unloading from the secondary yield surface: $\left|F_2\left(\{\boldsymbol{\sigma'}_{n-1}\},\ \{\boldsymbol{k}_{2,n-1}\}\right)\right| \leq YTOL$ and $\cos\theta_2 < 0.0$, with subsequent activation of the primary and/or secondary yield surface, $F_1\left(\{\boldsymbol{\sigma'}_{n-1}\}+\{\Delta\boldsymbol{\sigma'}_n\},\{\boldsymbol{k}_{1,n}\}\right) > YTOL$ and/or $F_2\left(\{\boldsymbol{\sigma'}_{n-1}\}+\{\Delta\boldsymbol{\sigma'}_n\},\{\boldsymbol{k}_{2,n}\}\right) > YTOL$, respectively;

iii) elasto-plastic unloading from both primary and secondary yield surfaces: $\left|F_1\left(\{\boldsymbol{\sigma'}_{n-1}\},\{\boldsymbol{k}_{1,n-1}\}\right)\right| \leq YTOL$ and $\cos\theta_1 < 0.0$, as well as $\left|F_2\left(\{\boldsymbol{\sigma'}_{n-1}\},\ \{\boldsymbol{k}_{2,n-1}\}\right)\right| \leq YTOL$ and $\cos\theta_2 < 0.0$, with subsequent activation of the primary and/or secondary yield surface, $F_1\left(\{\boldsymbol{\sigma'}_{n-1}\}+\{\Delta\boldsymbol{\sigma'}_n\},\{\boldsymbol{k}_{1,n}\}\right) > YTOL$ and/or $F_2\left(\{\boldsymbol{\sigma'}_{n-1}\}+\{\Delta\boldsymbol{\sigma'}_n\},\{\boldsymbol{k}_{2,n}\}\right) > YTOL$, respectively.

where:

$$\cos\theta_1 = \frac{\left\{\dfrac{\partial F_1\left(\{\boldsymbol{\sigma'}_{n-1}\},\{\boldsymbol{k}_{1,n-1}\}\right)}{\partial\boldsymbol{\sigma'}}\right\} : \{\Delta\boldsymbol{\sigma'}^{e}\}}{\left\|\left\{\dfrac{\partial F_1\left(\{\boldsymbol{\sigma'}_{n-1}\},\{\boldsymbol{k}_{1,n-1}\}\right)}{\partial\boldsymbol{\sigma'}}\right\}\right\|_2 \|\{\Delta\boldsymbol{\sigma'}^{e}\}\|_2} \tag{5.65}$$

$$\cos\theta_2 = \frac{\left\{\dfrac{\partial F_2\left(\{\boldsymbol{\sigma'}_{n-1}\},\ \{\boldsymbol{k}_{2,n-1}\}\right)}{\partial\boldsymbol{\sigma'}}\right\} : \{\Delta\boldsymbol{\sigma'}^{e}\}}{\left\|\left\{\dfrac{\partial F_2\left(\{\boldsymbol{\sigma'}_{n-1}\},\{\boldsymbol{k}_{2,n-1}\}\right)}{\partial\boldsymbol{\sigma'}}\right\}\right\|_2 \|\{\Delta\boldsymbol{\sigma'}^{e}\}\|_2} \tag{5.66}$$

Note that it may happen that an effective stress point lying on the primary yield surface and inside the secondary yield surface at the start of the sub-step increment (i.e. $\left|F_1\left(\{\boldsymbol{\sigma'}_{n-1}\},\{\boldsymbol{k}_{1,n-1}\}\right)\right| \leq YTOL$ and $F_2\left(\{\boldsymbol{\sigma'}_{n-1}\},\{\boldsymbol{k}_{2,n-1}\}\right) < -YTOL$) moves to the outside of

the secondary yield surface during the elastic trial (i.e. $F_1\left(\{\boldsymbol{\sigma'}_{n-1}\} + \{\Delta\boldsymbol{\sigma'}_n\}, \{\boldsymbol{k}_{1,n}\}\right) < -YTOL$ and $F_2\left(\{\boldsymbol{\sigma'}_{n-1}\} + \{\Delta\boldsymbol{\sigma'}_n\}, \{\boldsymbol{k}_{2,n}\}\right) > YTOL$). This does not necessarily mean the occurrence of an elasto-plastic unloading. In effect, to be considered an elasto-plastic unloading, the angle θ_1 between the primary yield surface gradient, $\{\partial F_1\left(\{\boldsymbol{\sigma'}_{n-1}\}, \{\boldsymbol{k}_{1,n-1}\}\right)/\partial\boldsymbol{\sigma'}\}$, and the elastic effective stress increment, $\{\Delta\boldsymbol{\sigma'}^e\}$, should be greater than 90.0 (i.e. $\cos\theta_1 < 0.0$), as described above. The same principles are valid for a similar situation involving a trial effective stress path departing from the secondary yield surface and crossing of the primary one.

Having detected the occurrence of an elasto-plastic unloading, it is necessary to evaluate the portion of the sub-step increment that is purely elastic (i.e. the portion of the strain increment corresponding to a stress path inside both yield surfaces). This situation is similar to that described in the previous section, with the additional complexity that the effective stress point may cross the yield surface(s) more than once, due to the use of a yield surface tolerance, *YTOL*, as illustrated in Figure 5.3. Nevertheless, as pointed out by Sloan *et al.* (2001), to ensure that the Pegasus method finds the correct crossing, it should be sufficient to find an input range [$\beta^{(inf)}$, $\beta^{(sup)}$] which satisfies the following condition: $F_1\left(\{\boldsymbol{\sigma'}_{n-1}\} + \beta^{(inf)}\ [\boldsymbol{D}(\{\boldsymbol{\sigma'}_n\})]\ \{\Delta\boldsymbol{\varepsilon}_{ss}\}, \{\boldsymbol{k}_n\}\right) < -YTOL$ and $F_2\left(\{\boldsymbol{\sigma'}_{n-1}\} + \beta^{(inf)}\ [\boldsymbol{D}(\{\boldsymbol{\sigma'}_n\})]\ \{\Delta\boldsymbol{\varepsilon}_{ss}\}, \{\boldsymbol{k}_n\}\right) < -YTOL$, in conjunction with $F_1\left(\{\boldsymbol{\sigma'}_{n-1}\} + \beta^{(sup)}\ [\boldsymbol{D}(\{\boldsymbol{\sigma'}_n\})]\ \{\Delta\boldsymbol{\varepsilon}_{ss}\}, \{\boldsymbol{k}_n\}\right) > YTOL$ and/or $F_2\left(\{\boldsymbol{\sigma'}_{n-1}\} + \beta^{(sup)}\ [\boldsymbol{D}(\{\boldsymbol{\sigma'}_n\})]\ \{\Delta\boldsymbol{\varepsilon}_{ss}\}, \{\boldsymbol{k}_n\}\right) > YTOL$. As detailed in the previous section, prior to the application of the Pegasus method and following the strategy proposed by Hong *et al.* (2012), a numerical scheme is used to define a proper set of values for $\beta^{(inf)}$ and $\beta^{(sup)}$, which correspond to an effective stress point inside both yield surfaces and outside of at least one of the yield surfaces (i.e. which satisfies the aforementioned condition). Therefore, although other strategies could have been devised (see, e.g., Potts and Zdravkovic, 1999), in the present study, the Pegasus method was also applied to determine the yield surface intersection after the detection of an elasto-plastic unloading.

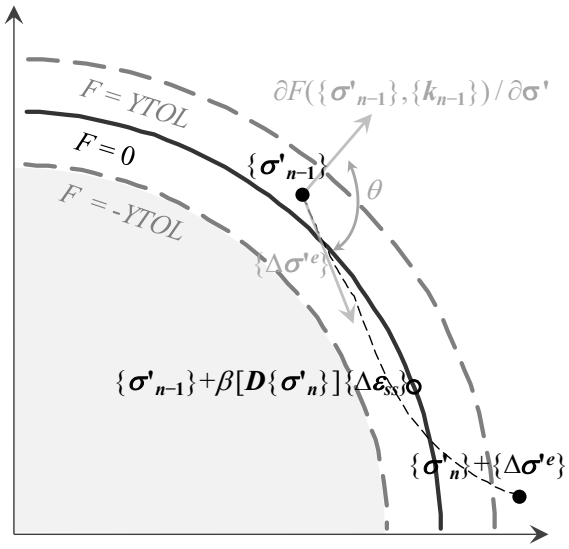

Figure 5.3 – Elasto-plastic unloading (adapted from Sloan et al., 2001).

5.2.6 Elasto-plasticity

5.2.6.1 Elasto-plastic constitutive matrix

The computation of the plastic multipliers associated with the primary and secondary yield surfaces, λ_1 and λ_2, respectively, as well as the computation of the elasto-plastic constitutive matrix, $[\boldsymbol{D^{ep}}]$, depend on the active yield surfaces. Therefore, prior to the computation of these quantities, it is necessary to assess whether a single or both yield surfaces are active at the beginning of each elasto-plastic sub-step increment. Following the strategy described by Hong *et al.* (2012) and given the effective stress state after elastic trial or after a successful elasto-plastic sub-step increment, $\{\boldsymbol{\sigma'}\}$, as well as current values of the sets of plastic state parameters, $\{\boldsymbol{k_1}\}$ and $\{\boldsymbol{k_2}\}$, one of the following three different situations may occur:

1) When $|F_1(\{\boldsymbol{\sigma'}\},\{\boldsymbol{k_1}\})| \leq YTOL$ and $F_2(\{\boldsymbol{\sigma'}\},\{\boldsymbol{k_2}\}) < -YTOL$: only the primary yield surface is active and, therefore, $IYIELD = 1$. Using the current values of the elastic constitutive matrix, $[\boldsymbol{D}(\{\boldsymbol{\sigma'}\})]$, gradient of the primary yield surface, $\{\partial F_1(\{\boldsymbol{\sigma'}\},\{\boldsymbol{k_1}\})/\partial\boldsymbol{\sigma'}\}$, gradient of the plastic potential associated with the primary yield surface, $\{\partial \boldsymbol{P_1}(\{\boldsymbol{\sigma'}\},\{\boldsymbol{m_1}\})/\partial\boldsymbol{\sigma'}\}$, and the current sub-step strain increment associated with elasto-plastic response, $\{\Delta\boldsymbol{\varepsilon_{ss}^{ep}}\}$, the plastic multiplier associated with the primary yield surface, λ_1, can be determined by:

$$\lambda_1 = \frac{\left(\left\{\dfrac{\partial F_1(\{\boldsymbol{\sigma'}\},\{\boldsymbol{k_1}\})}{\partial\boldsymbol{\sigma'}}\right\}\right)^{\mathrm{T}}[\boldsymbol{D}(\{\boldsymbol{\sigma'}\})]\{\Delta\boldsymbol{\varepsilon_{ss}^{ep}}\}}{\left(\left\{\dfrac{\partial F_1(\{\boldsymbol{\sigma'}\},\{\boldsymbol{k_1}\})}{\partial\boldsymbol{\sigma'}}\right\}\right)^{\mathrm{T}}[\boldsymbol{D}(\{\boldsymbol{\sigma'}\})]\left\{\dfrac{\partial \boldsymbol{P_1}(\{\boldsymbol{\sigma'}\},\{\boldsymbol{m_1}\})}{\partial\boldsymbol{\sigma'}}\right\} + A_1} \tag{5.67}$$

where $\{\boldsymbol{m_1}\}$ is a set of state parameters defining the evolution of the plastic potential associated with the primary yield surface and A_1 is the plastic hardening modulus associated with the primary yield surface.

In this case, the plastic multiplier associated with the secondary yield surface, λ_2, is set to 0.0. The elasto-plastic constitutive matrix, $[\boldsymbol{D^{ep}}] = [\boldsymbol{D^{ep}}(\{\boldsymbol{\sigma'}\},\{\boldsymbol{k_1}\},\{\boldsymbol{m_1}\})]$, can be determined by (Potts and Zdravkovic, 1999):

$$[\boldsymbol{D^{ep}}(\{\boldsymbol{\sigma'}\},\{\boldsymbol{k_1}\},\{\boldsymbol{m_1}\})] = [\boldsymbol{D}(\{\boldsymbol{\sigma'}\})] - \frac{[\boldsymbol{D}(\{\boldsymbol{\sigma'}\})]\left\{\frac{\partial \boldsymbol{P_1}(\{\boldsymbol{\sigma'}\},\{\boldsymbol{m_1}\})}{\partial \boldsymbol{\sigma'}}\right\}\left(\left\{\frac{\partial F_1(\{\boldsymbol{\sigma'}\},\{\boldsymbol{k_1}\})}{\partial \boldsymbol{\sigma'}}\right\}\right)^{\mathrm{T}}[\boldsymbol{D}(\{\boldsymbol{\sigma'}\})]}{\left(\left\{\frac{\partial F_1(\{\boldsymbol{\sigma'}\},\{\boldsymbol{k_1}\})}{\partial \boldsymbol{\sigma'}}\right\}\right)^{\mathrm{T}}[\boldsymbol{D}(\{\boldsymbol{\sigma'}\})]\left\{\frac{\partial \boldsymbol{P_1}(\{\boldsymbol{\sigma'}\},\{\boldsymbol{m_1}\})}{\partial \boldsymbol{\sigma'}}\right\} + A_1} \quad (5.68)$$

2) When $F_1(\{\boldsymbol{\sigma'}\},\{\boldsymbol{k_1}\}) < -YTOL$ and $|F_2(\{\boldsymbol{\sigma'}\},\{\boldsymbol{k_2}\})| \leq YTOL$: only the secondary yield surface is active and, therefore, $IYIELD = 2$. Using the current values of $[\boldsymbol{D}(\{\boldsymbol{\sigma'}\})]$, gradient of the secondary yield surface, $\{\partial F_2(\{\boldsymbol{\sigma'}\},\{\boldsymbol{k_2}\})/\partial \boldsymbol{\sigma'}\}$, gradient of the plastic potential associated with the secondary yield surface, $\{\partial \boldsymbol{P_2}(\{\boldsymbol{\sigma'}\},\{\boldsymbol{m_2}\})/\partial \boldsymbol{\sigma'}\}$, and $\{\Delta \boldsymbol{\varepsilon_{ss}^{ep}}\}$, the plastic multiplier associated with the secondary yield surface, λ_2, can be determined by (Potts and Zdravkovic, 1999):

$$\lambda_2 = \frac{\left(\left\{\frac{\partial F_2(\{\boldsymbol{\sigma'}\},\{\boldsymbol{k_2}\})}{\partial \boldsymbol{\sigma'}}\right\}\right)^{\mathrm{T}}[\boldsymbol{D}(\{\boldsymbol{\sigma'}\})]\{\Delta \boldsymbol{\varepsilon_{ss}^{ep}}\}}{\left(\left\{\frac{\partial F_2(\{\boldsymbol{\sigma'}\},\{\boldsymbol{k_2}\})}{\partial \boldsymbol{\sigma'}}\right\}\right)^{\mathrm{T}}[\boldsymbol{D}(\{\boldsymbol{\sigma'}\})]\left\{\frac{\partial \boldsymbol{P_2}(\{\boldsymbol{\sigma'}\},\{\boldsymbol{m_2}\})}{\partial \boldsymbol{\sigma'}}\right\} + A_2} \quad (5.69)$$

where $\{\boldsymbol{m_2}\}$ is a set of state parameters defining the evolution of the plastic potential associated with the secondary yield surface and A_2 is the plastic hardening modulus associated with the secondary yield surface. In this case, the plastic multiplier associated with the primary yield surface, λ_1, is set to 0.0. The elasto-plastic constitutive matrix, $[\boldsymbol{D^{ep}}] = [\boldsymbol{D^{ep}}(\{\boldsymbol{\sigma'}\},\{\boldsymbol{k_2}\},\{\boldsymbol{m_2}\})]$, can be determined by (Potts and Zdravkovic, 1999):

$$[\boldsymbol{D^{ep}}(\{\boldsymbol{\sigma'}\},\{\boldsymbol{k_2}\},\{\boldsymbol{m_2}\})] = [\boldsymbol{D}(\{\boldsymbol{\sigma'}\})] - \frac{[\boldsymbol{D}(\{\boldsymbol{\sigma'}\})]\left\{\frac{\partial \boldsymbol{P_2}(\{\boldsymbol{\sigma'}\},\{\boldsymbol{m_2}\})}{\partial \boldsymbol{\sigma'}}\right\}\left(\left\{\frac{\partial F_2(\{\boldsymbol{\sigma'}\},\{\boldsymbol{k_2}\})}{\partial \boldsymbol{\sigma'}}\right\}\right)^{\mathrm{T}}[\boldsymbol{D}(\{\boldsymbol{\sigma'}\})]}{\left(\left\{\frac{\partial F_2(\{\boldsymbol{\sigma'}\},\{\boldsymbol{k_2}\})}{\partial \boldsymbol{\sigma'}}\right\}\right)^{\mathrm{T}}[\boldsymbol{D}(\{\boldsymbol{\sigma'}\})]\left\{\frac{\partial \boldsymbol{P_2}(\{\boldsymbol{\sigma'}\},\{\boldsymbol{m_2}\})}{\partial \boldsymbol{\sigma'}}\right\} + A_2} \quad (5.70)$$

3) When $|F_1(\{\boldsymbol{\sigma'}\},\{\boldsymbol{k_1}\})| \leq YTOL$ and $|F_2(\{\boldsymbol{\sigma'}\},\{\boldsymbol{k_2}\})| \leq YTOL$: both primary and secondary yield surfaces may be active. Using the current values of $[\boldsymbol{D}(\{\boldsymbol{\sigma'}\})]$, $\{\partial F_1(\{\boldsymbol{\sigma'}\},\{\boldsymbol{k_1}\})/\partial \boldsymbol{\sigma'}\}$, $\{\partial \boldsymbol{P_1}(\{\boldsymbol{\sigma'}\},\{\boldsymbol{m_1}\})/\partial \boldsymbol{\sigma'}\}$, $\{\partial F_2(\{\boldsymbol{\sigma'}\},\{\boldsymbol{k_2}\})/\partial \boldsymbol{\sigma'}\}$, $\{\partial \boldsymbol{P_2}(\{\boldsymbol{\sigma'}\},$

$\{\boldsymbol{m_2}\})/\partial\boldsymbol{\sigma'}\}$ and $\{\Delta\boldsymbol{\varepsilon_{ss}^{ep}}\}$, the plastic multipliers associated with the primary and secondary yield surfaces are determined by (Potts and Zdravkovic, 1999):

$$\lambda_1 = \frac{L_{22}\,T_1 - L_{12}\,T_2}{L_{11}\,L_{22} - L_{12}\,L_{21}} \tag{5.71}$$

$$\lambda_2 = \frac{L_{11}\,T_2 - L_{21}\,T_1}{L_{11}\,L_{22} - L_{12}\,L_{21}} \tag{5.72}$$

where:

$$L_{11} = \left(\left\{\frac{\partial F_1(\{\boldsymbol{\sigma'}\},\{\boldsymbol{k_1}\})}{\partial\boldsymbol{\sigma'}}\right\}\right)^{\mathrm{T}} [\boldsymbol{D}(\{\boldsymbol{\sigma'}\})] \left\{\frac{\partial \boldsymbol{P_1}(\{\boldsymbol{\sigma'}\},\{\boldsymbol{m_1}\})}{\partial\boldsymbol{\sigma'}}\right\} + A_1 \tag{5.73}$$

$$L_{12} = \left(\left\{\frac{\partial F_1(\{\boldsymbol{\sigma'}\},\{\boldsymbol{k_1}\})}{\partial\boldsymbol{\sigma'}}\right\}\right)^{\mathrm{T}} [\boldsymbol{D}(\{\boldsymbol{\sigma'}\})] \left\{\frac{\partial \boldsymbol{P_2}(\{\boldsymbol{\sigma'}\},\{\boldsymbol{m_2}\})}{\partial\boldsymbol{\sigma'}}\right\} \tag{5.74}$$

$$L_{21} = \left(\left\{\frac{\partial F_2(\{\boldsymbol{\sigma'}\},\{\boldsymbol{k_2}\})}{\partial\boldsymbol{\sigma'}}\right\}\right)^{\mathrm{T}} [\boldsymbol{D}(\{\boldsymbol{\sigma'}\})] \left\{\frac{\partial \boldsymbol{P_1}(\{\boldsymbol{\sigma'}\},\{\boldsymbol{m_1}\})}{\partial\boldsymbol{\sigma'}}\right\} \tag{5.75}$$

$$L_{22} = \left(\left\{\frac{\partial F_2(\{\boldsymbol{\sigma'}\},\{\boldsymbol{k_2}\})}{\partial\boldsymbol{\sigma'}}\right\}\right)^{\mathrm{T}} [\boldsymbol{D}(\{\boldsymbol{\sigma'}\})] \left\{\frac{\partial \boldsymbol{P_2}(\{\boldsymbol{\sigma'}\},\{\boldsymbol{m_2}\})}{\partial\boldsymbol{\sigma'}}\right\} + A_2 \tag{5.76}$$

$$T_1 = \left(\left\{\frac{\partial F_1(\{\boldsymbol{\sigma'}\},\{\boldsymbol{k_1}\})}{\partial\boldsymbol{\sigma'}}\right\}\right)^{\mathrm{T}} [\boldsymbol{D}(\{\boldsymbol{\sigma'}\})] \{\Delta\boldsymbol{\varepsilon_{ss}^{ep}}\} \tag{5.77}$$

$$T_2 = \left(\left\{\frac{\partial F_2(\{\boldsymbol{\sigma'}\},\{\boldsymbol{k_2}\})}{\partial\boldsymbol{\sigma'}}\right\}\right)^{\mathrm{T}} [\boldsymbol{D}(\{\boldsymbol{\sigma'}\})] \{\Delta\boldsymbol{\varepsilon_{ss}^{ep}}\} \tag{5.78}$$

In most cases, $\lambda_1 > 0.0$ and $\lambda_2 > 0.0$ are obtained, meaning that both yield surfaces are effectively active. In such case, *IYIELD* $= 3$ and the elasto-plastic constitutive matrix, $[\boldsymbol{D^{ep}}] = [\boldsymbol{D^{ep}}(\{\boldsymbol{\sigma'}\},\{\boldsymbol{k_1}\},\{\boldsymbol{m_1}\},\{\boldsymbol{k_2}\},\{\boldsymbol{m_2}\})]$ is determined by (Potts and Zdravkovic, 1999):

$$\begin{aligned}[\boldsymbol{D^{ep}}(\{\boldsymbol{\sigma'}\},\{\boldsymbol{k_1}\},\{\boldsymbol{m_1}\},\{\boldsymbol{k_2}\},\{\boldsymbol{m_2}\})] \\ = [\boldsymbol{D}(\{\boldsymbol{\sigma'}\})] \\ - \frac{[\boldsymbol{D}(\{\boldsymbol{\sigma'}\})]}{\Omega}\left[\left\{\frac{\partial \boldsymbol{P_1}(\{\boldsymbol{\sigma'}\},\{\boldsymbol{m_1}\})}{\partial\boldsymbol{\sigma'}}\right\}(\{\boldsymbol{b_1}\})^{\mathrm{T}}\right. \\ \left. + \left\{\frac{\partial \boldsymbol{P_2}(\{\boldsymbol{\sigma'}\},\{\boldsymbol{m_2}\})}{\partial\boldsymbol{\sigma'}}\right\}(\{\boldsymbol{b_2}\})^{\mathrm{T}}\right][\boldsymbol{D}(\{\boldsymbol{\sigma'}\})]\end{aligned} \tag{5.79}$$

where:

$$\Omega = L_{11}\,L_{22} - L_{12}\,L_{21} \tag{5.80}$$

$$(\{\boldsymbol{b_1}\})^{\mathrm{T}} = L_{22}\left\{\frac{\partial F_1(\{\boldsymbol{\sigma'}\},\{\boldsymbol{k_1}\})}{\partial\boldsymbol{\sigma'}}\right\} - L_{12}\left\{\frac{\partial F_2(\{\boldsymbol{\sigma'}\},\{\boldsymbol{k_2}\})}{\partial\boldsymbol{\sigma'}}\right\} \tag{5.81}$$

$$(\{\boldsymbol{b_2}\})^{\mathrm{T}} = L_{11}\left\{\frac{\partial F_2(\{\boldsymbol{\sigma'}\},\{\boldsymbol{k_2}\})}{\partial\boldsymbol{\sigma'}}\right\} - L_{21}\left\{\frac{\partial F_1(\{\boldsymbol{\sigma'}\},\{\boldsymbol{k_1}\})}{\partial\boldsymbol{\sigma'}}\right\} \tag{5.82}$$

However, it may happen that either $\lambda_1 > 0.0$ and $\lambda_2 \leq 0.0$ or $\lambda_1 \leq 0.0$ and $\lambda_2 > 0.0$ are obtained from Equation 5.71 and 5.72, respectively, meaning that one of the plastic mechanism is eventually not activated. For instance, this may happen when the secondary yield surface is temporarily activated during a given sub-step increment to prevent the mean effective stress to reach a value smaller than that defined by the model parameter p'_{YS}, with this yield surface being eventually deactivated in a subsequent sub-step increment. As this happens, $IYIELD = 1$ is flagged and Equation 5.67 is used to re-compute λ_1, while λ_2 is set to 0.0. Moreover, in such case, the elasto-plastic constitutive matrix is also re-computed using Equation 5.68. Similarly, if $\lambda_1 \leq 0.0$ and $\lambda_2 > 0.0$ are obtained from Equation 5.71 and 5.72, $IYIELD = 2$ is flagged and Equation 5.69 is used to re-compute λ_2, while λ_1 is set to 0.0. In this case, Equation 5.70 is used to re-compute the elasto-plastic constitutive matrix.

5.2.6.2 Activation of an additional yield surface

As briefly mentioned in Section 5.2.1, when a single yield surface is active during a given elasto-plastic sub-step strain increment, $\{\Delta\boldsymbol{\varepsilon}_{ss}^{ep}\}$, it is necessary to check whether the obtained effective stress state, $\{\boldsymbol{\sigma'}_n\}$, remains inside or on the non-active yield surface at the end of the sub-step increment. If that is not the case, then the sub-step increment should be reduced, $\xi\{\Delta\boldsymbol{\varepsilon}_{ss}^{ep}\}$, with $0.0 < \xi < 1.0$, to bring the effective stress point back to that yield surface. Therefore, the value of ξ should be that resulting in an effective stress point lying on both yield surfaces:

$$\left|F_1\left(\{\boldsymbol{\sigma'}_{n-1}\} + \xi\,[\boldsymbol{D}^{ep}(\{\boldsymbol{\sigma'}_n\},\{\boldsymbol{k}_n\},\{\boldsymbol{m}_n\})]\,\{\Delta\boldsymbol{\varepsilon}_{ss}^{ep}\},\{\boldsymbol{k}_{1,n}\}\right)\right| \leq YTOL \tag{5.83}$$

$$\left|F_2\left(\{\boldsymbol{\sigma'}_{n-1}\} + \xi\,[\boldsymbol{D}^{ep}(\{\boldsymbol{\sigma'}_n\},\{\boldsymbol{k}_n\},\{\boldsymbol{m}_n\})]\,\{\Delta\boldsymbol{\varepsilon}_{ss}^{ep}\},\{\boldsymbol{k}_{2,n}\}\right)\right| \leq YTOL \tag{5.84}$$

Note that, as explained in the previous section, $[\boldsymbol{D}^{ep}] = \left[\boldsymbol{D}^{ep}\left(\{\boldsymbol{\sigma'}_n\},\{\boldsymbol{k}_{1,n}\},\{\boldsymbol{m}_{1,n}\}\right)\right]$ when only the primary yield surface is active during a given sub-step increment, while $[\boldsymbol{D}^{ep}] = \left[\boldsymbol{D}^{ep}\left(\{\boldsymbol{\sigma'}_n\},\{\boldsymbol{k}_{2,n}\},\{\boldsymbol{m}_{2,n}\}\right)\right]$ when only the secondary yield surface is active during the sub-step increment. Nevertheless, to keep the presentation more general, the notation $[\boldsymbol{D}^{ep}] = [\boldsymbol{D}^{ep}(\{\boldsymbol{\sigma'}_n\},\{\boldsymbol{k}_n\},\{\boldsymbol{m}_n\})]$ is used in Equation 5.83 and 5.84. Note also that, apart from the fact that the elasto-plastic constitutive matrix, $[\boldsymbol{D}^{ep}(\{\boldsymbol{\sigma'}_n\},\{\boldsymbol{k}_n\},\{\boldsymbol{m}_n\})]$, is employed here, rather the elastic constitutive matrix, $[\boldsymbol{D}(\{\boldsymbol{\sigma'}_n\})]$, this problem is very similar to the one occurring during elastic trial, when the elastic effective stress path crosses the yield surfaces. Therefore, the Pegasus method (Dowell and Jarratt, 1972) can also be employed to solve this problem, using a methodology similar to that described in Section 5.2.5.1.

5.2.6.3 Correction of yield surface drift

5.2.6.3.1 Initial considerations

At the end of each sub-step increment, the combination of obtained effective stresses, $\{\boldsymbol{\sigma'}_n\}$, and set of state parameters, $\{\boldsymbol{k}_{1,n}\}$ and $\{\boldsymbol{k}_{2,n}\}$, may not verify one or both active yield

conditions, a phenomenon usually referred to as *yield surface drift*. The extent of the violation depends on the non-linearity of the constitutive model, as well as on the accuracy of the integration scheme (Sloan *et al.*, 2001).

According to Potts and Gens (1985), the effects of violating the yield surface are cumulative and should, therefore, be corrected before the application of a new sub-step increment. Moreover, by performing a comparative study on the accuracy of several different methods available in the literature to correct *yield surface drift*, these authors concluded that more accurate predictions are obtained when the total strain increment remains unchanged during the correction process. Based on that assumption, which is consistent with the displacement-based finite element procedure, Potts and Gens (1985) proposed a new method, which has been shown to be robust and accurate (Potts and Zdravkovic, 1999). In Section 5.2.6.3.2, the method introduced by Potts and Gens (1985) is described for the case in which a single yield surface is active. By applying the same principles, an extension of the method to the case in which two yield surfaces are simultaneously active is presented in Section 5.2.6.3.3.

5.2.6.3.2 When a single yield surface is active

Considering $\{\boldsymbol{\sigma'}_{prov}\}$ and $\{\boldsymbol{k}_{prov}\}$ the effective stresses and set of state parameters associated with the active yield surface obtained at the end of a given elasto-plastic sub-step increment, the method seeks a new combination of effective stresses, $\{\boldsymbol{\sigma'}_{cor}\} = \{\boldsymbol{\sigma'}_{prov}\} + \{\Delta\boldsymbol{\sigma'}_{cor}\}$, and state parameters, $\{\boldsymbol{k}_{cor}\} = \{\boldsymbol{k}_{prov}\} + \{\Delta\boldsymbol{k}_{cor}\}$, where $\{\Delta\boldsymbol{\sigma'}_{cor}\}$ and $\{\Delta\boldsymbol{k}_{cor}\}$ are corrections to the values obtained at the end of the elasto-plastic sub-step increment, satisfying the yield condition (Equation 5.85).

$$|F_{cor}(\{\boldsymbol{\sigma'}_{cor}\}, \{\boldsymbol{k}_{cor}\})| \leq YTOL \tag{5.85}$$

Taking into account that any change in effective stresses, $\{\Delta\boldsymbol{\sigma'}_{cor}\}$, results in an associated change in elastic strains, $\{\Delta\boldsymbol{\varepsilon}^{e}_{cor}\}$, Equation 5.86 can be written.

$$\{\Delta\boldsymbol{\varepsilon}^{e}_{cor}\} = [\boldsymbol{D}(\{\boldsymbol{\sigma'}_{cor}\})]^{-1}\{\Delta\boldsymbol{\sigma'}_{cor}\} \tag{5.86}$$

where $[\boldsymbol{D}(\{\boldsymbol{\sigma'}_{cor}\})]$ is the elastic constitutive matrix evaluated at the corrected effective stress state.

In order to keep the sub-step total strain increment unchanged, the change in the elastic strains, $\{\Delta\boldsymbol{\varepsilon}^{e}_{cor}\}$, must be balanced by an equal and opposite change in the plastic strains, $\{\Delta\boldsymbol{\varepsilon}^{p}_{cor}\}$, as shown by Equation 5.87.

$$\{\Delta\boldsymbol{\varepsilon}^{p}_{cor}\} = -\{\Delta\boldsymbol{\varepsilon}^{e}_{cor}\} \Leftrightarrow \{\Delta\boldsymbol{\varepsilon}^{p}_{cor}\} = -[\boldsymbol{D}(\{\boldsymbol{\sigma'}_{cor}\})]^{-1}\{\Delta\boldsymbol{\sigma'}_{cor}\} \tag{5.87}$$

Since $\{\Delta\boldsymbol{\varepsilon}^{p}_{cor}\}$ is proportional to the gradient of plastic potential, $\{\partial\boldsymbol{P}(\{\boldsymbol{\sigma'}_{cor}\}, \{\boldsymbol{m}_{cor}\})/\partial\boldsymbol{\sigma'}\}$, as given by Equation 5.88, it follows that $\{\Delta\boldsymbol{\sigma'}_{cor}\}$ can be written as indicated by Equation 5.89.

$$\{\Delta\boldsymbol{\varepsilon}^{\boldsymbol{p}}_{\boldsymbol{cor}}\} = \lambda_{cor}\left\{\frac{\partial \boldsymbol{P}(\{\boldsymbol{\sigma}'_{\boldsymbol{cor}}\},\{\boldsymbol{m}_{\boldsymbol{cor}}\})}{\partial \boldsymbol{\sigma}'}\right\} \tag{5.88}$$

$$\{\Delta\boldsymbol{\sigma}'_{\boldsymbol{cor}}\} = -\lambda_{cor}\,[\boldsymbol{D}(\{\boldsymbol{\sigma}'_{\boldsymbol{cor}}\})]\left\{\frac{\partial \boldsymbol{P}(\{\boldsymbol{\sigma}'_{\boldsymbol{cor}}\},\{\boldsymbol{m}_{\boldsymbol{cor}}\})}{\partial \boldsymbol{\sigma}'}\right\} \tag{5.89}$$

where λ_{cor} is the correction to be applied to the plastic multiplier and $\{\boldsymbol{m}_{\boldsymbol{cor}}\} = \{\boldsymbol{m}_{\mathbf{prov}}\} + \{\Delta\boldsymbol{m}_{\boldsymbol{cor}}\}$ is the corrected set of state parameters of the gradient of the plastic potential.

Furthermore, for a constitutive model belonging to the category of strain hardening/softening plasticity, as it is the case of the present bounding surface plasticity model, the changes in the state parameters, $\{\Delta\boldsymbol{k}_{\boldsymbol{cor}}\}$, are related to the changes in the plastic strains, $\{\Delta\boldsymbol{\varepsilon}^{\boldsymbol{p}}_{\boldsymbol{cor}}\}$, as given by Equation 5.90.

$$\{\Delta\boldsymbol{k}_{\boldsymbol{cor}}\} = \{\Delta\boldsymbol{k}_{\boldsymbol{cor}}(\{\Delta\boldsymbol{\varepsilon}^{\boldsymbol{p}}_{\boldsymbol{cor}}\})\} = \lambda_{cor}\left\{\Delta\boldsymbol{k}_{\boldsymbol{cor}}\left(\left\{\frac{\partial \boldsymbol{P}(\{\boldsymbol{\sigma}'_{\boldsymbol{cor}}\},\{\boldsymbol{m}_{\boldsymbol{cor}}\})}{\partial \boldsymbol{\sigma}'}\right\}\right)\right\} \tag{5.90}$$

In addition, since the new combination of effective stresses, $\{\boldsymbol{\sigma}'_{\boldsymbol{cor}}\} = \{\boldsymbol{\sigma}'_{\boldsymbol{prov}}\} + \{\Delta\boldsymbol{\sigma}'_{\boldsymbol{cor}}\}$, and state parameters, $\{\boldsymbol{k}_{\boldsymbol{cor}}\} = \{\boldsymbol{k}_{\boldsymbol{prov}}\} + \{\Delta\boldsymbol{k}_{\boldsymbol{cor}}\}$, must verify the yield condition (Equation 5.85), it is possible to expand it as Taylor's series, as shown by Equation 5.91, where the second-order and higher-order terms are neglected. Note that the condition defined by the combination of Equation 5.91 with Equation 5.85, according to which the effective stress must remain on the yield surface during elasto-plastic loading, is typically known as "consistency condition".

$$F_{cor} = F_{prov} + \left\{\frac{\partial F(\{\boldsymbol{\sigma}'_{\boldsymbol{cor}}\},\{\boldsymbol{k}_{\boldsymbol{cor}}\})}{\partial \boldsymbol{\sigma}'}\right\}^{\mathrm{T}}\{\Delta\boldsymbol{\sigma}'_{\boldsymbol{cor}}\} + \left\{\frac{\partial F(\{\boldsymbol{\sigma}'_{\boldsymbol{cor}}\},\{\boldsymbol{k}_{\boldsymbol{cor}}\})}{\partial \boldsymbol{k}}\right\}^{\mathrm{T}}\{\Delta\boldsymbol{k}_{\boldsymbol{cor}}\} \tag{5.91}$$

where F_{prov} and F_{cor} are the values of the yield surface before and after the drift correction, and $\{\partial F(\{\boldsymbol{\sigma}'_{\boldsymbol{cor}}\},\{\boldsymbol{k}_{\boldsymbol{cor}}\})/\partial\boldsymbol{\sigma}'\}$ and $\{\partial F(\{\boldsymbol{\sigma}'_{\boldsymbol{cor}}\},\{\boldsymbol{k}_{\boldsymbol{cor}}\})/\partial\boldsymbol{k}\}$ are the gradients of the yield surface to the effective stresses and plastic state parameters, respectively.

By combining Equation 5.89, 5.90 and 5.91, setting $F_{cor} = 0.0$ and rearranging, Equation 5.92 is obtained.

$$\lambda_{cor} = F_{prov}\Bigg/\left(\begin{array}{l}\left\{\dfrac{\partial F(\{\boldsymbol{\sigma}'_{\boldsymbol{cor}}\},\{\boldsymbol{k}_{\boldsymbol{cor}}\})}{\partial \boldsymbol{\sigma}'}\right\}^{\mathrm{T}}[\boldsymbol{D}(\{\boldsymbol{\sigma}'_{\boldsymbol{cor}}\})]\left\{\dfrac{\partial \boldsymbol{P}(\{\boldsymbol{\sigma}'_{\boldsymbol{cor}}\},\{\boldsymbol{m}_{\boldsymbol{cor}}\})}{\partial \boldsymbol{\sigma}'}\right\} - \\ \left\{\dfrac{\partial F(\{\boldsymbol{\sigma}'_{\boldsymbol{cor}}\},\{\boldsymbol{k}_{\boldsymbol{cor}}\})}{\partial \boldsymbol{k}}\right\}^{\mathrm{T}}\left\{\Delta\boldsymbol{k}_{\boldsymbol{cor}}\left(\left\{\dfrac{\partial \boldsymbol{P}(\{\boldsymbol{\sigma}'_{\boldsymbol{cor}}\},\{\boldsymbol{m}_{\boldsymbol{cor}}\})}{\partial \boldsymbol{\sigma}'}\right\}\right)\right\}\end{array}\right) \tag{5.92}$$

Therefore, to evaluate λ_{cor}, the values of the gradients of the yield surface to the effective stresses and plastic state parameters, $\{\partial F(\{\boldsymbol{\sigma}'_{\boldsymbol{cor}}\},\{\boldsymbol{k}_{\boldsymbol{cor}}\})/\partial\boldsymbol{\sigma}'\}$ and $\{\partial F(\{\boldsymbol{\sigma}'_{\boldsymbol{cor}}\},\{\boldsymbol{k}_{\boldsymbol{cor}}\})/\partial\boldsymbol{k}\}$, respectively, the gradient of the plastic potential to the effective stresses, $\{\partial \boldsymbol{P}(\{\boldsymbol{\sigma}'_{\boldsymbol{cor}}\},\{\boldsymbol{m}_{\boldsymbol{cor}}\})/\partial\boldsymbol{\sigma}'\}$, and the elastic constitutive matrix, $[\boldsymbol{D}(\{\boldsymbol{\sigma}'_{\boldsymbol{cor}}\})]$, are required. Clearly, a problem arises from the dependency of these quantities on the effective stresses,

$\{\boldsymbol{\sigma'_{cor}}\} = \{\boldsymbol{\sigma'_{prov}}\} + \{\Delta\boldsymbol{\sigma'_{cor}}\}$, state parameters, $\{\boldsymbol{k_{cor}}\} = \{\boldsymbol{k_{prov}}\} + \{\Delta\boldsymbol{k_{cor}}\}$, and state parameters of the gradient of the plastic potential, $\{\boldsymbol{m_{cor}}\} = \{\boldsymbol{m_{prov}}\} + \{\Delta\boldsymbol{m_{cor}}\}$, which are being the quantities being pursued, resulting in a complex implicit problem. Nevertheless, according to Potts and Gens (1985), since the sub-stepping tolerance (*SSTOL*) is usually set to a very small value (typically in the range of 10^{-2} to 10^{-5}), yield surface drift is seldom observed and, when it occurs, it is usually very small. Therefore, the authors suggested evaluating, as a first approximation, the gradients of the yield surface and plastic potential, as well as the elastic constitutive matrix using the values of the effective stress state, as well as the sets of state parameters controlling the evolution of the yield surfaces and plastic potential corresponding to the beginning of the elasto-plastic sub-step increment, $\{\boldsymbol{\sigma'_{n-1}}\}$, $\{\boldsymbol{k_{n-1}}\}$.and $\{\boldsymbol{m_{n-1}}\}$, or to its end, $\{\boldsymbol{\sigma'_{n}}\}$, $\{\boldsymbol{k_{n}}\}$ and $\{\boldsymbol{m_{n}}\}$. In this latter case, Equation 5.92 can be replaced by Equation 5.93.

$$\lambda_{cor} = F_{prov} \Bigg/ \left(\begin{array}{l} \left\{\dfrac{\partial F(\{\boldsymbol{\sigma'_{n}}\},\{\boldsymbol{k_{n}}\})}{\partial \boldsymbol{\sigma'}}\right\}^{\mathrm{T}} [\boldsymbol{D}(\{\boldsymbol{\sigma'_{cor}}\})] \left\{\dfrac{\partial \boldsymbol{P}(\{\boldsymbol{\sigma'_{n}}\},\{\boldsymbol{m_{n}}\})}{\partial \boldsymbol{\sigma'}}\right\} - \\ \left\{\dfrac{\partial F(\{\boldsymbol{\sigma'_{n}}\},\{\boldsymbol{k_{n}}\})}{\partial \boldsymbol{k}}\right\}^{\mathrm{T}} \left\{\Delta\boldsymbol{k_{cor}} \left(\left\{\dfrac{\partial \boldsymbol{P}(\{\boldsymbol{\sigma'_{n}}\},\{\boldsymbol{m_{n}}\})}{\partial \boldsymbol{\sigma'}}\right\} \right)\right\} \end{array} \right) \tag{5.93}$$

Having determined λ_{cor} by using Equation 5.93, corrected plastic strains, $\{\boldsymbol{\varepsilon^{p}_{cor}}\}$, the corrected effective stresses, $\{\boldsymbol{\sigma'_{cor}}\}$, and set of state parameters, $\{\boldsymbol{k_{cor}}\}$, can be estimated using Equations 5.88, 5.89 and 5.90, respectively.

Due to the adopted simplifications, it may happen that the new combination of $\{\boldsymbol{\sigma'_{cor}}\}$ and $\{\boldsymbol{k_{cor}}\}$ still does not satisfy the yield condition (Equation 5.85). In this case, the correction process should be repeated using an improved estimation of λ_{cor}, until the yield condition is satisfied (Potts and Gens, 1985). According to Sloan *et al.* (2001), an improved estimation of λ_{cor} can be simply obtained by updating $[\boldsymbol{D}]$, $\{\partial F/\partial \boldsymbol{\sigma'}\}$, $\{\partial F/\partial \boldsymbol{k}\}$, $\{\partial \boldsymbol{P}/\partial \boldsymbol{\sigma'}\}$ using $\{\boldsymbol{\sigma'_{cor}}\}$, $\{\boldsymbol{k_{cor}}\}$ and $\{\boldsymbol{m_{cor}}\}$ and computing again Equation 5.92.

5.2.6.3.3 When two yield surfaces are simultaneously active

When both primary and secondary yield conditions are active, the following conditions should be simultaneously satisfied:

$$\left|F_{1,cor}\left(\{\boldsymbol{\sigma'_{cor}}\},\{\boldsymbol{k_{1,cor}}\}\right)\right| \leq YTOL \tag{5.94}$$

$$\left|F_{2,cor}\left(\{\boldsymbol{\sigma'_{cor}}\},\{\boldsymbol{k_{2,cor}}\}\right)\right| \leq YTOL \tag{5.95}$$

where:

$$\{\boldsymbol{\sigma'_{cor}}\} = \{\boldsymbol{\sigma'_{prov}}\} + \{\Delta\boldsymbol{\sigma'_{cor}}\} \tag{5.96}$$

$$\{\boldsymbol{k_{1,cor}}\} = \{\boldsymbol{k_{1,prov}}\} + \{\Delta\boldsymbol{k_{1,cor}}\} \tag{5.97}$$

$$\{\boldsymbol{k_{2,cor}}\} = \{\boldsymbol{k_{2,prov}}\} + \{\Delta\boldsymbol{k_{2,cor}}\} \tag{5.98}$$

with $\{\Delta\boldsymbol{\sigma'_{cor}}\}$ being the correction to the effective stresses, which should now take into account the contribution of both plastic mechanisms (Equation 5.99); moreover, $\{\Delta\boldsymbol{k_{1,cor}}\}$ and $\{\Delta\boldsymbol{k_{2,cor}}\}$ are the corrections to the sets of state parameters associated with the primary and secondary yield surfaces, given by Equation 5.100 and 5.101, respectively.

$$\begin{aligned}\{\Delta\boldsymbol{\sigma'_{cor}}\} = &-\lambda_{1,cor}\,[\boldsymbol{D}(\{\boldsymbol{\sigma'_{cor}}\})]\left\{\frac{\partial \boldsymbol{P_1}(\{\boldsymbol{\sigma'_{cor}}\},\{\boldsymbol{m_{1,cor}}\})}{\partial\boldsymbol{\sigma'}}\right\}\\ &-\lambda_{2,cor}\,[\boldsymbol{D}(\{\boldsymbol{\sigma'_{cor}}\})]\left\{\frac{\partial \boldsymbol{P_2}(\{\boldsymbol{\sigma'_{cor}}\},\{\boldsymbol{m_{2,cor}}\})}{\partial\boldsymbol{\sigma'}}\right\}\end{aligned} \tag{5.99}$$

$$\{\Delta\boldsymbol{k_{1,cor}}\} = \{\Delta\boldsymbol{k_{1,cor}}(\{\Delta\boldsymbol{\varepsilon^p_{cor}}\})\} = \lambda_{1,cor}\left\{\Delta\boldsymbol{k_{1,cor}}\left(\left\{\frac{\partial \boldsymbol{P_1}(\{\boldsymbol{\sigma'_{cor}}\},\{\boldsymbol{m_{1,cor}}\})}{\partial\boldsymbol{\sigma'}}\right\}\right)\right\} \tag{5.100}$$

$$\{\Delta\boldsymbol{k_{2,cor}}\} = \{\Delta\boldsymbol{k_{2,cor}}(\{\Delta\boldsymbol{\varepsilon^p_{cor}}\})\} = \lambda_{2,cor}\left\{\Delta\boldsymbol{k_{2,cor}}\left(\left\{\frac{\partial \boldsymbol{P_2}(\{\boldsymbol{\sigma'_{cor}}\},\{\boldsymbol{m_{2,cor}}\})}{\partial\boldsymbol{\sigma'}}\right\}\right)\right\} \tag{5.101}$$

Similar to what was done when a single yield surface is active, Equation 5.94 and 5.95 can be expanded as Taylor's series. Ignoring the second-order and higher terms, the following two equations are obtained:

$$\begin{aligned}F_{1,cor} = F_{1,prov} &+ \left\{\frac{\partial F_1(\{\boldsymbol{\sigma'_{cor}}\},\{\boldsymbol{k_{1,cor}}\})}{\partial\boldsymbol{\sigma'}}\right\}^{\mathrm{T}}\{\Delta\boldsymbol{\sigma'_{cor}}\}\\ &+ \left\{\frac{\partial F_1(\{\boldsymbol{\sigma'_{cor}}\},\{\boldsymbol{k_{1,cor}}\})}{\partial\boldsymbol{k}}\right\}^{\mathrm{T}}\{\Delta\boldsymbol{k_{1,cor}}\}\end{aligned} \tag{5.102}$$

$$\begin{aligned}F_{2,cor} = F_{2,prov} &+ \left\{\frac{\partial F_2(\{\boldsymbol{\sigma'_{cor}}\},\{\boldsymbol{k_{2,cor}}\})}{\partial\boldsymbol{\sigma'}}\right\}^{\mathrm{T}}\{\Delta\boldsymbol{\sigma'_{cor}}\}\\ &+ \left\{\frac{\partial F_2(\{\boldsymbol{\sigma'_{cor}}\},\{\boldsymbol{k_{2,cor}}\})}{\partial\boldsymbol{k}}\right\}^{\mathrm{T}}\{\Delta\boldsymbol{k_{2,cor}}\}\end{aligned} \tag{5.103}$$

where $F_{1,prov}$ and $F_{2,prov}$ are the values of the primary and secondary yield surfaces obtained at the end of the sub-step increment. Substituting Equations 5.99, 5.100 and 5.101 into Equations 5.102, 5.103, and setting $F_{1,cor} = 0.0$ and $F_{2,cor} = 0.0$, the two following equations are obtained:

$$\begin{aligned}F_{1,prov} &- \lambda_{1,cor}\left\{\frac{\partial F_1(\{\boldsymbol{\sigma'_{cor}}\},\{\boldsymbol{k_{1,cor}}\})}{\partial\boldsymbol{\sigma'}}\right\}^{\mathrm{T}}[\boldsymbol{D}(\{\boldsymbol{\sigma'_{cor}}\})]\left\{\frac{\partial \boldsymbol{P_1}(\{\boldsymbol{\sigma'_{cor}}\},\{\boldsymbol{m_{1,cor}}\})}{\partial\boldsymbol{\sigma'}}\right\}\\ &- \lambda_{2,cor}\left\{\frac{\partial F_1(\{\boldsymbol{\sigma'_{cor}}\},\{\boldsymbol{k_{1,cor}}\})}{\partial\boldsymbol{\sigma'}}\right\}^{\mathrm{T}}[\boldsymbol{D}(\{\boldsymbol{\sigma'_{cor}}\})]\left\{\frac{\partial \boldsymbol{P_2}(\{\boldsymbol{\sigma'_{cor}}\},\{\boldsymbol{m_{2,cor}}\})}{\partial\boldsymbol{\sigma'}}\right\}\\ &+ \lambda_{1,cor}\left\{\frac{\partial F_1(\{\boldsymbol{\sigma'_{cor}}\},\{\boldsymbol{k_{1,cor}}\})}{\partial\boldsymbol{\sigma'}}\right\}^{\mathrm{T}}\left\{\Delta\boldsymbol{k_{1,cor}}\left(\left\{\frac{\partial \boldsymbol{P_1}(\{\boldsymbol{\sigma'_{cor}}\},\{\boldsymbol{m_{1,cor}}\})}{\partial\boldsymbol{\sigma'}}\right\}\right)\right\}\\ &= 0.0\end{aligned} \tag{5.104}$$

$$\begin{aligned} F_{2,prov} &- \lambda_{1,cor}\left\{\frac{\partial F_2\left(\{\boldsymbol{\sigma'}_{cor}\},\{\boldsymbol{k}_{2,cor}\}\right)}{\partial \boldsymbol{\sigma'}}\right\}^{T}[\boldsymbol{D}(\{\boldsymbol{\sigma'}_{cor}\})]\left\{\frac{\partial \boldsymbol{P}_1\left(\{\boldsymbol{\sigma'}_{cor}\},\{\boldsymbol{m}_{1,cor}\}\right)}{\partial \boldsymbol{\sigma'}}\right\} \\ &- \lambda_{2,cor}\left\{\frac{\partial F_2\left(\{\boldsymbol{\sigma'}_{cor}\},\{\boldsymbol{k}_{2,cor}\}\right)}{\partial \boldsymbol{\sigma'}}\right\}^{T}[\boldsymbol{D}(\{\boldsymbol{\sigma'}_{cor}\})]\left\{\frac{\partial \boldsymbol{P}_2\left(\{\boldsymbol{\sigma'}_{cor}\},\{\boldsymbol{m}_{2,cor}\}\right)}{\partial \boldsymbol{\sigma'}}\right\} \\ &+ \lambda_{2,cor}\left\{\frac{\partial F_2\left(\{\boldsymbol{\sigma'}_{cor}\},\{\boldsymbol{k}_{2,cor}\}\right)}{\partial \boldsymbol{\sigma'}}\right\}^{T}\left\{\Delta \boldsymbol{k}_{2,cor}\left(\left\{\frac{\partial \boldsymbol{P}_2\left(\{\boldsymbol{\sigma'}_{cor}\},\{\boldsymbol{m}_{2,cor}\}\right)}{\partial \boldsymbol{\sigma'}}\right\}\right)\right\} \\ &= 0.0 \end{aligned} \tag{5.105}$$

These equations can be solved simultaneously to give:

$$\begin{cases}\lambda_{1,cor}\,L_{11}+\lambda_{2,cor}\,L_{12}=F_{1,prov}\\ \lambda_{1,cor}\,L_{21}+\lambda_{2,cor}\,L_{22}=F_{1,prov}\end{cases}\Leftrightarrow\begin{cases}\lambda_{1,cor}=\dfrac{L_{22}\,F_{1,prov}-L_{12}\,F_{2,prov}}{L_{11}\,L_{22}-L_{12}\,L_{21}} & (5.106)\\ \lambda_{2,cor}=\dfrac{L_{11}\,F_{2,prov}-L_{21}\,F_{1,prov}}{L_{11}\,L_{22}-L_{12}\,L_{21}} & (5.107)\end{cases}$$

where:

$$\begin{aligned} L_{11} &= \left\{\frac{\partial F_1\left(\{\boldsymbol{\sigma'}_{cor}\},\{\boldsymbol{k}_{1,cor}\}\right)}{\partial \boldsymbol{\sigma'}}\right\}^{T}[\boldsymbol{D}(\{\boldsymbol{\sigma'}_{cor}\})]\left\{\frac{\partial \boldsymbol{P}_1\left(\{\boldsymbol{\sigma'}_{cor}\},\{\boldsymbol{m}_{1,cor}\}\right)}{\partial \boldsymbol{\sigma'}}\right\} \\ &- \left\{\frac{\partial F_1\left(\{\boldsymbol{\sigma'}_{cor}\},\{\boldsymbol{k}_{1,cor}\}\right)}{\partial \boldsymbol{\sigma'}}\right\}^{T}\left\{\Delta \boldsymbol{k}_{1,cor}\left(\left\{\frac{\partial \boldsymbol{P}_1\left(\{\boldsymbol{\sigma'}_{cor}\},\{\boldsymbol{m}_{1,cor}\}\right)}{\partial \boldsymbol{\sigma'}}\right\}\right)\right\} \end{aligned} \tag{5.108}$$

$$L_{12} = \left\{\frac{\partial F_1\left(\{\boldsymbol{\sigma'}_{cor}\},\{\boldsymbol{k}_{1,cor}\}\right)}{\partial \boldsymbol{\sigma'}}\right\}^{T}[\boldsymbol{D}(\{\boldsymbol{\sigma'}_{cor}\})]\left\{\frac{\partial \boldsymbol{P}_2\left(\{\boldsymbol{\sigma'}_{cor}\},\{\boldsymbol{m}_{2,cor}\}\right)}{\partial \boldsymbol{\sigma'}}\right\} \tag{5.109}$$

$$L_{21} = \left\{\frac{\partial F_2\left(\{\boldsymbol{\sigma'}_{cor}\},\{\boldsymbol{k}_{2,cor}\}\right)}{\partial \boldsymbol{\sigma'}}\right\}^{T}[\boldsymbol{D}(\{\boldsymbol{\sigma'}_{cor}\})]\left\{\frac{\partial \boldsymbol{P}_1\left(\{\boldsymbol{\sigma'}_{cor}\},\{\boldsymbol{m}_{1,cor}\}\right)}{\partial \boldsymbol{\sigma'}}\right\} \tag{5.110}$$

$$\begin{aligned} L_{22} &= \left\{\frac{\partial F_2\left(\{\boldsymbol{\sigma'}_{cor}\},\{\boldsymbol{k}_{2,cor}\}\right)}{\partial \boldsymbol{\sigma'}}\right\}^{T}[\boldsymbol{D}(\{\boldsymbol{\sigma'}_{cor}\})]\left\{\frac{\partial \boldsymbol{P}_2\left(\{\boldsymbol{\sigma'}_{cor}\},\{\boldsymbol{m}_{2,cor}\}\right)}{\partial \boldsymbol{\sigma'}}\right\} \\ &- \left\{\frac{\partial F_2\left(\{\boldsymbol{\sigma'}_{cor}\},\{\boldsymbol{k}_{2,cor}\}\right)}{\partial \boldsymbol{\sigma'}}\right\}^{T}\left\{\Delta \boldsymbol{k}_{2,cor}\left(\left\{\frac{\partial \boldsymbol{P}_2\left(\{\boldsymbol{\sigma'}_{cor}\},\{\boldsymbol{m}_{2,cor}\}\right)}{\partial \boldsymbol{\sigma'}}\right\}\right)\right\} \end{aligned} \tag{5.111}$$

As suggested by Potts and Gens (1985), by evaluating all quantities using the stress state and state parameters corresponding to the end of the elasto-plastic sub-step increment, $\{\boldsymbol{\sigma'}_n\}$, $\{\boldsymbol{k}_n\}$.and $\{\boldsymbol{m}_n\}$, an initial estimation of $\lambda_{1,cor}$ and $\lambda_{2,cor}$ is obtained. Subsequently, the corrections to the effective stresses, plastic strains, and sets of state parameters can be computed from Equations 5.99 to 5.101. After updating the effective stresses and state parameters, both yield conditions (Equations 5.94 and 5.95) are checked. If both are satisfied, then the yield surface drift correction is completed. Otherwise, all quantities need to be updated and a new iteration is performed. This sequence is repeated until both yield conditions are satisfied, which, according to the experience of the author, typically requires less than 10 iterations.

5.2.7 Summary

All operations required to integrate an elasto-plastic constitutive model using a modified forward Euler integration scheme with automatic sub-stepping and error control are summarised in Table 5.1.

Table 5.1 – Explicit stress integration scheme for the present bounding surface plasticity model.

Stage	Description
1	**Initialisation of model quantities**
	Given the total strain increment, $\{\Delta\boldsymbol{\varepsilon}\}$; Enter with the initial values of: effective stresses, $\{\boldsymbol{\sigma'_n}\} = \{\boldsymbol{\sigma'_0}\}$; elastic and plastic strains, $\{\boldsymbol{\varepsilon^e_n}\} = \{\boldsymbol{\varepsilon^e_0}\}$ and $\{\boldsymbol{\varepsilon^p_n}\} = \{\boldsymbol{\varepsilon^p_0}\}$, respectively; void ratio, $e_{n-1} = e_0$; elastic state parameters, $\{\boldsymbol{j_n}\} = \{\boldsymbol{j_0}\}$; plastic state parameters associated with the primary and secondary yield surface, $\{\boldsymbol{k_{1,n}}\} = \{\boldsymbol{k_{1,0}}\}$ and $\{\boldsymbol{k_{2,n}}\} = \{\boldsymbol{k_{2,0}}\}$, respectively; plastic state parameters of the gradients of the plastic potential associated with the primary and secondary yield surface, $\{\boldsymbol{m_{1,n}}\} = \{\boldsymbol{m_{1,0}}\}$ and $\{\boldsymbol{m_{2,n}}\} = \{\boldsymbol{m_{2,0}}\}$, respectively. Determine the initial positions of the primary and secondary yield surfaces: $F_{1,n}(\{\boldsymbol{\sigma'_n}\}, \{\boldsymbol{k_{1,n}}\})$ and $F_{2,n}(\{\boldsymbol{\sigma'_n}\}, \{\boldsymbol{k_{2,n}}\})$.
2	**Elastic trial**
2.1	Initialise variables of the modified forward Euler scheme required to the elastic trial: $\Delta T_n = 1.0$ and $T_n = 0.0$. Initialise also the variable informing which yield surface is active: $IYIELD = 0$.
2.2	If $T_n < 1.0$, then: Determine the sub-step strain increment: $\{\Delta\boldsymbol{\varepsilon_{ss}}\} = \Delta T_n \{\Delta\boldsymbol{\varepsilon}\}$. Store the pseudo time at the beginning of the sub-step increment, $T_{n-1} = T_n$. Store the effective stresses, elastic strains, void ratio and elastic state parameters at the beginning of the sub-step increment: $\{\boldsymbol{\sigma'_{n-1}}\} = \{\boldsymbol{\sigma'_n}\}, \{\boldsymbol{\varepsilon^e_{n-1}}\} = \{\boldsymbol{\varepsilon^e_n}\}$, $e_{n-1} = e_n$ and $\{\boldsymbol{j_{mem}}\} = \{\boldsymbol{j_{n-1}}\} = \{\boldsymbol{j_n}\}$, respectively. Store also the positions of the yield surfaces at the beginning of the sub-step increment, $F_{1,n-1} = F_{1,n}$ and $F_{2,n-1} = F_{2,n}$. Continue to step 2.3. Else: Move to step 4. End if.
2.3	Check whether a shear strain reversal occurs. If a shear reversal occurs, then: Update the elastic state parameters, $\{\boldsymbol{j_{n-1}}\} = \{\boldsymbol{j_n}\}$. End if. Compute the elastic constitutive matrix using the current effective stress state, void ratio and state parameters: $[\boldsymbol{D}(\{\boldsymbol{\sigma'_{n-1}}\})]$.
2.4	Compute the first-order approximation of changes in effective stresses: $\{\Delta\boldsymbol{\sigma'^{(1)}_n}\} = [\boldsymbol{D}(\{\boldsymbol{\sigma'_{n-1}}\})] \{\Delta\boldsymbol{\varepsilon_{ss}}\}$.

Table 5.1 – Explicit stress integration scheme for the present bounding surface plasticity model.

Stage	Description
2.5	Update temporarily the effective stress state: $\left\{\boldsymbol{\sigma'}_{\boldsymbol{n}}^{(1)}\right\} = \{\boldsymbol{\sigma'}_{\boldsymbol{n-1}}\} + \left\{\Delta\boldsymbol{\sigma'}_{\boldsymbol{n}}^{(1)}\right\}$. Update temporarily the void ratio using a small-strain formulation: $e_n = e_{n-1} - (1.0 + e_{init})\ \Delta\varepsilon_{ss,v}$, where e_{init} is the void ratio of the material at the beginning of the FE analysis and $\Delta\varepsilon_{ss,v}$ is the volumetric component of the sub-step strain increment. Update the elastic constitutive matrix using the newly updated effective stress state and void ratio, $\left[\boldsymbol{D}\left(\left\{\boldsymbol{\sigma'}_{\boldsymbol{n}}^{(1)}\right\}\right)\right]$.
2.6	Compute the second-order approximation of changes in effective stresses: $\left\{\Delta\boldsymbol{\sigma'}_{\boldsymbol{n}}^{(2)}\right\} = \left[\boldsymbol{D}\left(\left\{\boldsymbol{\sigma'}_{\boldsymbol{n}}^{(1)}\right\}\right)\right]\{\Delta\boldsymbol{\varepsilon}_{\boldsymbol{ss}}\}$.
2.7	Compute the modified forward Euler approximation of changes in effective stresses: $\{\Delta\boldsymbol{\sigma'}_{\boldsymbol{n}}\} = \left(\left\{\Delta\boldsymbol{\sigma'}_{\boldsymbol{n}}^{(1)}\right\} + \left\{\Delta\boldsymbol{\sigma'}_{\boldsymbol{n}}^{(2)}\right\}\right)/2$. Determine the relative error in the modified forward Euler approximation of the effective stresses: $R_\sigma \approx \frac{1}{2}\left\|\left(\left\{\Delta\boldsymbol{\sigma'}_{\boldsymbol{n}}^{(2)}\right\} - \left\{\Delta\boldsymbol{\sigma'}_{\boldsymbol{n}}^{(1)}\right\}\right)\right\|_2 / \|\{\boldsymbol{\sigma'}_{\boldsymbol{n-1}}\} + \{\Delta\boldsymbol{\sigma'}_{\boldsymbol{n}}\}\|_2$.
2.8	Compare the obtained relative error R_σ with the tolerance *SSTOL*. If $R_\sigma > SSTOL$ and $\Delta T_n > \Delta T_{n,min}$, then: The sub-step is not successful and a smaller pseudo-time step needs to be used in the integration process; compute: $\zeta = \max\left\{0.9\sqrt{SSTOL/R_\sigma}, 0.1\right\}$ and $\Delta T_n{}^{new} = \max\left\{\zeta\,\Delta T_n,\ \Delta T_{n,min}\right\}$. Discard changes in effective stresses, void ratio and elastic state parameters: $\{\boldsymbol{\sigma'}_{\boldsymbol{n}}\} = \{\boldsymbol{\sigma'}_{\boldsymbol{n-1}}\}$, $e_n = e_{n-1}$ and $\{\boldsymbol{j}_{\boldsymbol{n}}\} = \{\boldsymbol{j}_{\boldsymbol{n-1}}\} = \{\boldsymbol{j}_{\boldsymbol{mem}}\}$, respectively. Set $\Delta T_n = \Delta T_n{}^{new}$ and return to step 2.2. Else, then: The sub-step is considered successful; update the effective stress state: $\{\boldsymbol{\sigma'}_{\boldsymbol{n}}\} = \{\boldsymbol{\sigma'}_{\boldsymbol{n-1}}\} + \{\Delta\boldsymbol{\sigma'}_{\boldsymbol{n}}\}$; note that, during elastic trial, the plastic state parameters remain unaltered: $\{\boldsymbol{k}_{\boldsymbol{1,n}}\} = \{\boldsymbol{k}_{\boldsymbol{1,\,n-1}}\}$, $\{\boldsymbol{k}_{\boldsymbol{2,n}}\} = \{\boldsymbol{k}_{\boldsymbol{2,\,n-1}}\}$, $\{\boldsymbol{m}_{\boldsymbol{1,n}}\} = \{\boldsymbol{m}_{\boldsymbol{1,n-1}}\}$ and $\{\boldsymbol{m}_{\boldsymbol{2,n}}\} = \{\boldsymbol{m}_{\boldsymbol{2,\,n-1}}\}$. Compute a new pseudo-time step multiplier: if the previous sub-step increment or the one before failed, then: $\zeta = \min\left\{0.9\sqrt{SSTOL/R_\sigma}, 1.0\right\}$; otherwise: $\zeta = \min\left\{0.9\sqrt{SSTOL/R_\sigma}, 1.1\right\}$. Continue to step 2.9. End if
2.9	Update the positions of the primary and secondary yield surfaces: $F_{1,n} = F_1\left(\{\boldsymbol{\sigma'}_{\boldsymbol{n}}\}, \{\boldsymbol{k}_{\boldsymbol{1,n}}\}\right)$ and $F_{2,n} = F_2\left(\{\boldsymbol{\sigma'}_{\boldsymbol{n}}\}, \{\boldsymbol{k}_{\boldsymbol{2,n}}\}\right)$, respectively. Determine the portion β of the sub-step increment, $\{\Delta\boldsymbol{\varepsilon}_{\boldsymbol{ss}}\}$, which is purely elastic: If $F_{1,n} \le YTOL$ and $F_{2,n} \le YTOL$, then: The response is purely elastic over the entire sub-step increment; thus, set $\beta = 1.0$. Update the elastic strain increment, $\{\Delta\boldsymbol{\varepsilon}_{\boldsymbol{n}}^{\boldsymbol{e}}\} = \beta\{\Delta\boldsymbol{\varepsilon}_{\boldsymbol{ss}}\}$, and the elastic strains, $\{\boldsymbol{\varepsilon}_{\boldsymbol{n}}^{\boldsymbol{e}}\} = \{\boldsymbol{\varepsilon}_{\boldsymbol{n-1}}^{\boldsymbol{e}}\} + \{\Delta\boldsymbol{\varepsilon}_{\boldsymbol{n}}^{\boldsymbol{e}}\}$. Update the pseudo time $T_n = T_{n-1} + \Delta T_n$ and determine the new pseudo-time step: $\Delta T_n{}^{new} = \max\left\{\zeta\,\Delta T_n,\ \Delta T_{n,min}\right\}$; check that $T_n + \Delta T_n{}^{new}$ does not exceed 1.0, i.e.: $\Delta T_n{}^{new} = \min\left\{\zeta\,\Delta T_n{}^{new},\ 1.0 - T_n\right\}$. Set $\Delta T_n = \Delta T_n{}^{new}$ and return to step 2.2.

Table 5.1 – Explicit stress integration scheme for the present bounding surface plasticity model.

Stage	Description
	Else:
	If ($F_{1,n-1} < -YTOL$ and $F_{1,n} > YTOL$ and $F_{2,n} \leq YTOL$) or ($F_{1,n} \leq YTOL$ and $F_{2,n-1} < -YTOL$ and $F_{2,n} > YTOL$) or ($F_{1,n-1} < -YTOL$ and $F_{1,n} > YTOL$ and $F_{2,n-1} < -YTOL$ and $F_{2,n} > YTOL$), then:
	A transition from purely elastic to elasto-plastic response occurs; estimate the yield surface intersection by applying the Pegasus method; having computed β and a new effective stress increment, $\{\Delta\boldsymbol{\sigma'_n}\}$, update $\{\boldsymbol{\sigma'_n}\} = \{\boldsymbol{\sigma'_{n-1}}\} + \{\Delta\boldsymbol{\sigma'_n}\}$, $\{\Delta\boldsymbol{\varepsilon^e_n}\} = \beta\{\Delta\boldsymbol{\varepsilon_{ss}}\}$, $\{\boldsymbol{\varepsilon^e_n}\} = \{\boldsymbol{\varepsilon^e_{n-1}}\} + \{\Delta\boldsymbol{\varepsilon^e_n}\}$ and $e_n = e_{n-1} - (1.0 + e_{init})\,\beta\,\Delta\varepsilon_{ss,v}$; update the positions of the primary and secondary yield surfaces: $F_{1,n} = F_1\left(\{\boldsymbol{\sigma'_n}\}, \{\boldsymbol{k_{1,n}}\}\right)$ and $F_{2,n} = F_2\left(\{\boldsymbol{\sigma'_n}\}, \{\boldsymbol{k_{2,n}}\}\right)$; move to step 3.1.
	Else:
	One or both yield surfaces were active from the beginning of the sub-step increment; check whether an elasto-plastic unloading has occurred during the current sub-step strain.
	If an elasto-plastic unloading has occurred, then:
	Estimate the yield surface intersection by applying the Pegasus method; having computed β and a new effective stress increment, $\{\Delta\boldsymbol{\sigma'_n}\}$, update $\{\boldsymbol{\sigma'_n}\} = \{\boldsymbol{\sigma'_{n-1}}\} + \{\Delta\boldsymbol{\sigma'_n}\}$, $\{\Delta\boldsymbol{\varepsilon^e_n}\} = \beta\{\Delta\boldsymbol{\varepsilon_{ss}}\}$, $\{\boldsymbol{\varepsilon^e_n}\} = \{\boldsymbol{\varepsilon^e_{n-1}}\} + \{\Delta\boldsymbol{\varepsilon^e_n}\}$ and $e_n = e_{n-1} - (1.0 + e_{init})\,\beta\,\Delta\varepsilon_{ss,v}$; update the positions of the primary and secondary yield surfaces: $F_{1,n} = F_1\left(\{\boldsymbol{\sigma'_n}\}, \{\boldsymbol{k_{1,n}}\}\right)$ and $F_{2,n} = F_2\left(\{\boldsymbol{\sigma'_n}\}, \{\boldsymbol{k_{2,n}}\}\right)$; move to step 3.1.
	Else:
	The response is elasto-plastic over the entire sub-step increment and, therefore, set $\beta = 0.0$ and reset: $\{\boldsymbol{\sigma'_n}\} = \{\boldsymbol{\sigma'_{n-1}}\}$, $e_n = e_{n-1}$ and $\{\boldsymbol{j_n}\} = \{\boldsymbol{j_{n-1}}\} = \{\boldsymbol{j_{mem}}\}$, $F_{1,n} = F_{1,n-1}$ and $F_{2,n} = F_{2,n-1}$.; move to step 3.1.
	End if.
	End if.
	End if.
3	**Elasto-plasticity**
3.1	Determine the part of the strain increment that has not yet been integrated: $\{\Delta\boldsymbol{\varepsilon^{ep}}\} = [(1.0 - T_{n-1}) + (1.0 - \beta)\,\Delta T_n]\{\Delta\boldsymbol{\varepsilon}\}$.
	Initialise variables of the modified forward Euler scheme required to the elasto-plastic computation: $\Delta {T_n}^{ep} = 1.0$ and ${T_n}^{ep} = 0.0$.
3.2	If ${T_n}^{ep} < 1.0$, then:
	Determine the sub-step strain increment: $\{\Delta\boldsymbol{\varepsilon^{ep}_{ss}}\} = \Delta {T_n}^{ep}\,\{\Delta\boldsymbol{\varepsilon^{ep}}\}$.
	Store the pseudo time at the beginning of the sub-step strain increment, ${T_{n-1}}^{ep} = {T_n}^{ep}$.
	Store the effective stresses, elastic and plastic strains, void ratio and set of elastic and plastic state parameters at the beginning of the sub-step strain increment: $\{\boldsymbol{\sigma'_{n-1}}\} = \{\boldsymbol{\sigma'_n}\}$, $\{\boldsymbol{\varepsilon^e_{n-1}}\} = \{\boldsymbol{\varepsilon^e_n}\}$, $\{\boldsymbol{\varepsilon^p_{n-1}}\} = \{\boldsymbol{\varepsilon^p_n}\}$, $e_{n-1} = e_n$, $\{\boldsymbol{j_{mem}}\} = \{\boldsymbol{j_{n-1}}\} = \{\boldsymbol{j_n}\}$, $\{\boldsymbol{k_{1,n-1}}\} = \{\boldsymbol{k_{1,n}}\}$, $\{\boldsymbol{k_{2,n-1}}\} = \{\boldsymbol{k_{2,n}}\}$, $\{\boldsymbol{m_{1,n-1}}\} = \{\boldsymbol{m_{1,n}}\}$ and $\{\boldsymbol{m_{2,n-1}}\} = \{\boldsymbol{m_{2,n}}\}$, respectively.
	Store also the positions of the yield surfaces: $F_{1,n-1} = F_{1,n}$ and $F_{2,n-1} = F_{2,n}$.
	Continue to step 3.3.
	Else:
	Stress integration is completed. Move to step 4.
	End if.

Table 5.1 – Explicit stress integration scheme for the present bounding surface plasticity model.

Stage	Description
3.3	Check whether a shear strain reversal occurs. If shear reversal occurs, then: Update the elastic state parameters, $\{\boldsymbol{j}_{n-1}\} = \{\boldsymbol{j}_n\}$. End if. Compute the elastic constitutive matrix using the current effective stress state, void ratio and elastic state parameters: $[\boldsymbol{D}(\{\boldsymbol{\sigma'}_{n-1}\})]$. Compute the gradients of the primary and secondary yield surfaces: $\{\partial F_1(\{\boldsymbol{\sigma'}_{n-1}\},\{\boldsymbol{k}_{1,\,n-1}\})/\partial\boldsymbol{\sigma'}\}$ and $\{\partial F_2(\{\boldsymbol{\sigma'}_{n-1}\},\{\boldsymbol{k}_{2,\,n-1}\})/\partial\boldsymbol{\sigma'}\}$. Compute the gradients of the plastic potentials associated with the primary and secondary yield surfaces: $\{\partial \boldsymbol{P_1}(\{\boldsymbol{\sigma'}_{n-1}\},\{\boldsymbol{m}_{1,\,n-1}\})/\partial\boldsymbol{\sigma'}\}$ and $\{\partial \boldsymbol{P_2}(\{\boldsymbol{\sigma'}_{n-1}{}'\},\{\boldsymbol{m}_{2,\,n-1}\})/\partial\boldsymbol{\sigma'}\}$, respectively. Compute the plastic hardening moduli associated with the primary and secondary yield surfaces: A_1 and A_2, respectively.
3.4	Check the active yield surface(s): If $\lvert F_1\rvert \le YTOL$ and $F_2 < -YTOL$, then: Only the primary yield surface is active: $IYIELD = 1$. Else if $F_1 < -YTOL$ and $\lvert F_2\rvert \le YTOL$, then: Only the secondary yield surface is active: $IYIELD = 2$. Else if $\lvert F_1\rvert \le YTOL$ and $\lvert F_2\rvert \le YTOL$, then: The effective stress point is at the intersection of both yield surfaces and the actual active yield surface(s) should be determined, by following the methodology described in Section 5.2.6.1. End if. Compute the plastic multipliers associated with the primary and secondary yield surfaces, λ_1 and λ_2, respectively, and the elasto-plastic constitutive matrix, $\left[\boldsymbol{D^{ep}}(\{\boldsymbol{\sigma'}_{n-1}\},\{\boldsymbol{k}_{1,\,n-1}\},\{\boldsymbol{m}_{1,\,n-1}\},\{\boldsymbol{k}_{2,\,n-1}\},\{\boldsymbol{m}_{2,\,n-1}\})\right]$, according to the methodology presented in Section 5.2.6.1.
3.5	Compute the first-order approximation of changes in effective stresses, changes in plastic strains and changes in the set of state parameters: $\{\Delta\boldsymbol{\sigma'}_n^{(1)}\} = \left[\boldsymbol{D^{ep}}(\{\boldsymbol{\sigma'}_{n-1}\},\{\boldsymbol{k}_{1,\,n-1}\},\{\boldsymbol{m}_{1,\,n-1}\},\{\boldsymbol{k}_{2,\,n-1}\},\{\boldsymbol{m}_{2,\,n-1}\})\right]\{\Delta\boldsymbol{\varepsilon}_{ss}^{ep}\}$; $\{\Delta\boldsymbol{\varepsilon}_n^{p(1)}\} = \lambda_1\{\partial\boldsymbol{P_1}(\{\boldsymbol{\sigma'}_{n-1}\},\{\boldsymbol{m}_{1,\,n-1}\})/\partial\boldsymbol{\sigma'}\} + \lambda_2\{\partial\boldsymbol{P_2}(\{\boldsymbol{\sigma'}_{n-1}\},\{\boldsymbol{m}_{2,\,n-1}\})/\partial\boldsymbol{\sigma'}\}$; $\{\Delta\boldsymbol{k}_{1,n}{}^{(1)}\} = \left\{\Delta\boldsymbol{k}_1\left(\{\Delta\boldsymbol{\varepsilon}_n^{p(1)}\}\right)\right\}$; $\{\Delta\boldsymbol{k}_{2,n}{}^{(1)}\} = \left\{\Delta\boldsymbol{k}_2\left(\{\Delta\boldsymbol{\varepsilon}_n^{p(1)}\}\right)\right\}$.
3.6	Update the effective stresses and the sets of state parameters: $\{\boldsymbol{\sigma'}_n^{(1)}\} = \{\boldsymbol{\sigma'}_{n-1}\} + \{\Delta\boldsymbol{\sigma'}_n^{(1)}\}$; $\{\boldsymbol{k}_{1,n}{}^{(1)}\} = \{\boldsymbol{k}_{1,\,n-1}\} + \{\Delta\boldsymbol{k}_{1,n}{}^{(1)}\}$; $\{\boldsymbol{k}_{2,n}{}^{(1)}\} = \{\boldsymbol{k}_{2,\,n-1}\} + \{\Delta\boldsymbol{k}_{2,n}{}^{(1)}\}$. Update other model quantities: $\{\partial F_1(\{\boldsymbol{\sigma'}_n^{(1)}\},\{\boldsymbol{k}_{1,n}{}^{(1)}\})/\partial\boldsymbol{\sigma'}\}$, $\{\partial F_2(\{\boldsymbol{\sigma'}_n^{(1)}\},\{\boldsymbol{k}_2{}^{(1)}\})/\partial\boldsymbol{\sigma'}\}$, $e_n = e_{n-1} - (1.0 + e_{init})\,\Delta\varepsilon_{ss,v}^{ep}$, $\left[\boldsymbol{D}\left(\{\boldsymbol{\sigma'}_n^{(1)}\}\right)\right]$, $\{\boldsymbol{m}_{1,n}{}^{(1)}\}$, $\{\boldsymbol{m}_{2,n}{}^{(1)}\}$, $\{\partial\boldsymbol{P_1}(\{\boldsymbol{\sigma'}_n^{(1)}\},\{\boldsymbol{m}_{1,n}{}^{(1)}\})/\partial\boldsymbol{\sigma'}\}$, $\{\partial\boldsymbol{P_2}(\{\boldsymbol{\sigma'}_n^{(1)}\},\{\boldsymbol{m}_{2,n}{}^{(1)}\})/\partial\boldsymbol{\sigma'}\}$, λ_1, λ_2 and $\left[\boldsymbol{D^{ep}}(\{\boldsymbol{\sigma'}_n^{(1)}\},\{\boldsymbol{k}_{1,n}{}^{(1)}\},\{\boldsymbol{m}_{1,n}{}^{(1)}\},\{\boldsymbol{k}_{2,n}{}^{(1)}\},\{\boldsymbol{m}_{2,n}{}^{(1)}\})\right]$.

Table 5.1 – Explicit stress integration scheme for the present bounding surface plasticity model.

Stage	Description
3.7	Compute the second-order approximation of changes in effective stresses, changes in plastic strains and changes in the sets of state parameters: $\left\{\Delta\boldsymbol{\sigma'}_n^{(2)}\right\} = \left[\boldsymbol{D}^{ep}\left(\left\{\boldsymbol{\sigma'}_n^{(1)}\right\},\left\{\boldsymbol{k}_{1,n}{}^{(1)}\right\},\left\{\boldsymbol{m}_{1,n}{}^{(1)}\right\},\left\{\boldsymbol{k}_{2,n}{}^{(1)}\right\},\left\{\boldsymbol{m}_{2,n}{}^{(1)}\right\}\right)\right]\{\Delta\boldsymbol{\varepsilon}_{ss}^{ep}\};$ $\left\{\Delta\boldsymbol{\varepsilon}_n^{p(2)}\right\} = \lambda_1\left\{\partial\boldsymbol{P_1}\left(\left\{\boldsymbol{\sigma'}_n^{(1)}\right\},\left\{\boldsymbol{m}_{1,n}{}^{(1)}\right\}\right)/\partial\boldsymbol{\sigma'}\right\} + \lambda_2\left\{\partial\boldsymbol{P_2}\left(\left\{\boldsymbol{\sigma'}_n^{(1)}\right\},\left\{\boldsymbol{m}_{2,n}{}^{(1)}\right\}\right)/\partial\boldsymbol{\sigma'}\right\};$ $\left\{\Delta\boldsymbol{k}_{1,n}{}^{(2)}\right\} = \left\{\Delta\boldsymbol{k_1}\left(\left\{\Delta\boldsymbol{\varepsilon}_n^{p(2)}\right\}\right)\right\};$ $\left\{\Delta\boldsymbol{k}_{2,n}{}^{(2)}\right\} = \left\{\Delta\boldsymbol{k_2}\left(\left\{\Delta\boldsymbol{\varepsilon}_n^{p(2)}\right\}\right)\right\}.$
3.8	Compute the modified forward Euler approximation of changes in effective stresses, changes in plastic strains and changes in the sets of state parameters, respectively: $\{\Delta\boldsymbol{\sigma'}_n\} = \left(\left\{\Delta\boldsymbol{\sigma'}_n^{(1)}\right\} + \left\{\Delta\boldsymbol{\sigma'}_n^{(2)}\right\}\right)/2;$ $\{\Delta\boldsymbol{\varepsilon}_n^{p}\} = \left(\left\{\Delta\boldsymbol{\varepsilon}_n^{p(1)}\right\} + \left\{\Delta\boldsymbol{\varepsilon}_n^{p(2)}\right\}\right)/2;$ $\left\{\Delta\boldsymbol{k}_{1,n}\right\} = \left(\left\{\Delta\boldsymbol{k}_{1,n}{}^{(1)}\right\} + \left\{\Delta\boldsymbol{k}_{1,n}{}^{(2)}\right\}\right)/2;$ $\left\{\Delta\boldsymbol{k}_{2,n}\right\} = \left(\left\{\Delta\boldsymbol{k}_{2,n}{}^{(1)}\right\} + \left\{\Delta\boldsymbol{k}_{2,n}{}^{(2)}\right\}\right)/2.$ Determine the relative error in the modified forward Euler approximation of the effective stresses and set of state parameters: $R_\sigma \approx \left\|\frac{1}{2}\left(\left\{\Delta\boldsymbol{\sigma'}_n^{(2)}\right\} - \left\{\Delta\boldsymbol{\sigma'}_n^{(1)}\right\}\right)\right\| / \|\{\boldsymbol{\sigma'}_{n-1}\} + \{\Delta\boldsymbol{\sigma'}_n\}\|;$ $R_{k,1} \approx \left\|\frac{1}{2}\left(\left\{\Delta\boldsymbol{k}_{1,n}{}^{(2)}\right\} - \left\{\Delta\boldsymbol{k}_{1,n}{}^{(1)}\right\}\right)\right\| / \left\|\left\{\boldsymbol{k}_{1,n-1}\right\} + \left\{\Delta\boldsymbol{k}_{1,n}\right\}\right\|;$ $R_{k,2} \approx \left\|\frac{1}{2}\left(\left\{\Delta\boldsymbol{k}_{2,n}{}^{(2)}\right\} - \left\{\Delta\boldsymbol{k}_{2,n}{}^{(1)}\right\}\right)\right\| / \left\|\left\{\boldsymbol{k}_{2,n-1}\right\} + \left\{\Delta\boldsymbol{k}_{2,n}\right\}\right\|.$ Determine the maximum relative error: $R = max\left\{R_\sigma, R_{k,1}, R_{k,2}\right\}$.
3.9	Compare the obtained error R with the tolerance $SSTOL$. If $R > SSTOL$ and $\Delta T_n{}^{ep} > \Delta T_{n,min}{}^{ep}$, then: The sub-step is not successful and, consequently, a smaller pseudo-time step needs to be used in the integration process; compute: $\zeta = max\left\{0.9\sqrt{SSTOL/R}, 0.1\right\}$ and $\Delta T_n{}^{ep,new} = max\left\{\zeta\Delta T_n{}^{ep}, \Delta T_{n,min}{}^{ep}\right\}$. Discard changes in effective stresses, void ratio and other state parameters: $\{\boldsymbol{\sigma'}_n\} = \{\boldsymbol{\sigma'}_{n-1}\}$, $e_n = e_{n-1}$ and $\left\{\boldsymbol{j}_n\right\} = \left\{\boldsymbol{j}_{n-1}\right\} = \left\{\boldsymbol{j}_{mem}\right\}$, $\left\{\boldsymbol{k}_{1,n}\right\} = \left\{\boldsymbol{k}_{1,n-1}\right\}$, $\left\{\boldsymbol{k}_{2,n}\right\} = \left\{\boldsymbol{k}_{2,n-1}\right\}$, $\left\{\boldsymbol{m}_{1,n}\right\} = \left\{\boldsymbol{m}_{1,n-1}\right\}$ and $\left\{\boldsymbol{m}_{2,n}\right\} = \left\{\boldsymbol{m}_{2,n-1}\right\}$; restore the positions of the yield surfaces corresponding to the beginning of the sub-step increment, $F_{1,n} = F_{1,n-1}$ and $F_{2,n} = F_{2,n-1}$. Set $\Delta T_n{}^{ep} = \Delta T_n{}^{ep,new}$ and return to step 3.2. Else, then: The sub-step is considered successful; update the effective stress state and sets of state parameters, respectively: $\{\boldsymbol{\sigma'}_n\} = \{\boldsymbol{\sigma'}_{n-1}\} + \{\Delta\boldsymbol{\sigma'}_n\}$, $\left\{\boldsymbol{k}_{1,n}\right\} = \left\{\boldsymbol{k}_{1,n-1}\right\} + \left\{\Delta\boldsymbol{k}_{1,n}\right\}$, $\left\{\boldsymbol{k}_{2,n}\right\} = \left\{\boldsymbol{k}_{2,n-1}\right\} + \left\{\Delta\boldsymbol{k}_{2,n}\right\}$, $\left\{\boldsymbol{m}_{1,n}\right\}$ and $\left\{\boldsymbol{m}_{2,n}\right\}$; compute a new pseudo-time step multiplier: if the previous sub-step or the one before failed, then: $\zeta = \min\left\{0.9\sqrt{SSTOL/R_\sigma}, 1.0\right\}$; otherwise: $\zeta = \min\left\{0.9\sqrt{SSTOL/R_\sigma}, 1.1\right\}$; continue to step 3.10. End if.

Table 5.1 – Explicit stress integration scheme for the present bounding surface plasticity model.

Stage	Description
3.10	Update the positions of the primary and secondary yield surfaces: $F_{1,n} = F_1\left(\{\boldsymbol{\sigma'}_n\}, \{\boldsymbol{k_{1,n}}\}\right)$ and $F_{2,n} = F_2\left(\{\boldsymbol{\sigma'}_n\}, \{\boldsymbol{k_{2,n}}\}\right)$. If $IYIELD = 1$ or $IYIELD = 2$, then check whether the recently updated effective stress point lies inside the non-active yield surface. If the effective stress point lies outside, then estimate the reduction, $0.0 < \xi < 1.0$, to be applied to the pseudo-time step to bring the effective stress point to the closest yield surface or to the intersection between both yield surfaces. Based on the newly-computed values of the effective stress increment, $\{\Delta\boldsymbol{\sigma'}_n\}$, as well as changes in the sets of state parameters, $\{\Delta\boldsymbol{k_{1,n}}\}$ and $\{\Delta\boldsymbol{k_{2,n}}\}$, update the effective stress state, plastic strains and sets of state parameters: $\{\boldsymbol{\sigma'}_n\} = \{\boldsymbol{\sigma'}_{n-1}\} + \{\Delta\boldsymbol{\sigma'}_n\}$, $\{\boldsymbol{k_{1,n}}\} = \{\boldsymbol{k_{1,n-1}}\} + \{\Delta\boldsymbol{k_{1,n}}\}$ and $\{\boldsymbol{k_{2,n}}\} = \{\boldsymbol{k_{2,n-1}}\} + \{\Delta\boldsymbol{k_{2,n}}\}$. Update the other state parameters: e_n, $\{\boldsymbol{m_{1,n}}\}$ and $\{\boldsymbol{m_{2,n}}\}$. Re-compute the positions of the primary and secondary yield surfaces: $F_{1,n} = F_1\left(\{\boldsymbol{\sigma'}_n\}, \{\boldsymbol{k_{1,n}}\}\right)$ and $F_{2,n} = F_2\left(\{\boldsymbol{\sigma'}_n\}, \{\boldsymbol{k_{2,n}}\}\right)$ respectively. Conversely, if the effective stress point lies inside the non-active yield surface, set $\xi = 1.0$.
3.11	Check whether *yield surface drift* has occurred. If it has occurred, then find a new combination of effective stresses, $\{\boldsymbol{\sigma'}_n\}$, and state parameters associated with the primary and secondary yield surface, $\{\boldsymbol{k_{1,n}}\}$ and $\{\boldsymbol{k_{2,n}}\}$, respectively, that satisfies the yield conditions, as described in Section 5.2.6.3.
3.12	Update the elastic and plastic strains, respectively: $\{\boldsymbol{\varepsilon^e_n}\} = \{\boldsymbol{\varepsilon^e_{n-1}}\} + \{\Delta\boldsymbol{\varepsilon^{ep}_{ss}}\} - \{\Delta\boldsymbol{\varepsilon^p_n}\}$ and $\{\boldsymbol{\varepsilon^p_n}\} = \{\boldsymbol{\varepsilon^p_{n-1}}\} + \{\Delta\boldsymbol{\varepsilon^p_n}\}$. Update the pseudo time: ${T_n}^{ep} = {T_{n-1}}^{ep} + \xi\,\Delta {T_n}^{ep}$. Determine the new pseudo-time step: $\Delta {T_n}^{ep,new} = max\{\zeta\,\Delta {T_n}^{ep},\ \Delta {T_{n,min}}^{ep}\}$; make sure that ${T_n}^{ep} + \Delta {T_n}^{ep,new}$ does not exceed 1.0, i.e.: $\Delta {T_n}^{ep,new} = min\{\zeta\,\Delta {T_n}^{ep,new},\ 1.0 - {T_n}^{ep}\}$. Set $\Delta {T_n}^{ep} = \Delta {T_n}^{ep,new}$ and return to step 3.2.
4	**Store the final values of the stress and strain tensors, as well as state parameters** Store the final values of the effective stress state, $\{\boldsymbol{\sigma'}_n\}$, elastic and plastic strains, $\{\boldsymbol{\varepsilon^e_n}\}$ and $\{\boldsymbol{\varepsilon^p_n}\}$ respectively, void ratio, e_n, elastic state parameters, $\{\boldsymbol{j_n}\}$, plastic state parameters, $\{\boldsymbol{k_{1,n}}\}$ and $\{\boldsymbol{k_{2,n}}\}$, as well as state parameters of the gradients of the plastic potential $\{\boldsymbol{m_{1,n}}\}$ and $\{\boldsymbol{m_{2,n}}\}$. Exit.

5.3 Validation

5.3.1 Methodology

A very important stage of the implementation of a constitutive model consists of its validation. This can be done by comparing the results obtained in numerical simulations with those obtained from a theoretical or analytical solution or, alternatively, with those obtained by a validated code. In the present case, the second alternative was selected, since the original formulation of the bounding surface plasticity model (Section 4.2) was implemented by Taborda (2011) into the Imperial College Finite Element Program (ICFEP) and a large amount of numerical results are available, including results of simulations of element

laboratory tests and dynamic centrifuge experiments. It is important to note that ICFEP is a well-known code developed at Imperial College London over the last 40 years, with the most relevant features for this research being described in Potts and Zdravkovic (1999), Hardy (2003), Kontoe (2006) and Taborda (2011). Moreover, it should be noted that ICFEP has been successfully applied to the simulation of a large variety of boundary-value problems involving complex dynamic phenomena (e.g. Kontoe, 2006; Kontoe *et al.*, 2011; Taborda, 2011; Tsaparli *et al.*, 2016; Han *et al.*, 2016).

With respect to the alterations performed to the formulation of the model developed by Taborda (2011) and Taborda *et al.* (2014) – termed, in what follows, as "original" formulation – , the most significant one consisted of the introduction of an inherent fabric anisotropy component. As described in Section 4.3.3, the selected inherent fabric anisotropy formulation was implemented into ICFEP by Williams (2014), using the constitutive model developed by Taborda (2011) and Taborda *et al.* (2014) as a starting point. Therefore, the validation of this additional component of the model was performed by comparing the results obtained by FEMEPDYN with those obtained by Williams (2014) when using ICFEP. This includes both undrained triaxial extension tests and cyclic direct simple shear tests.

It is important to note that, at this stage, the main objective of the numerical simulations consisted of the validation of the implementation of the constitutive model into FEMEPDYN. As such, the numerical results obtained by FEMEPDYN are solely compared with those obtained by Taborda (2011) and Williams (2014) when using ICFEP, meaning that no comparison is performed with experimental data. Note that the evaluation of the ability of the constitutive model to replicate results of element laboratory tests and dynamic centrifuge experiments performed on Hostun sand is the main objective of Chapter 7 and Chapter 8, respectively.

5.3.2 Original formulation

5.3.2.1 Simulation of element laboratory tests

5.3.2.1.1 Material properties and testing programme

A wide range of numerical simulations were performed by Taborda (2011) to evaluate the ability of the bounding surface plasticity model to replicate element laboratory tests. These included simulations of monotonic and cyclic triaxial tests on Leighton Buzzard Fraction-E and Nevada sands, as well cyclic direct simple shear tests on Nevada sand. As part of the present validation of the implementation of the constitutive model into FEMEPDYN, the aim is not to replicate all simulations performed by Taborda (2011), rather to select a range of simulations which include: 1) different stress paths (triaxial compression and extension, as well as direct simple shear), 2) different drainage conditions (drained and undrained) and 3) different material's initial state (different initial density and stress state). Having that in mind, a first

set of simulations included two drained isotropic compression (DIC) tests, four drained and four undrained monotonic triaxial compression tests (DMTC and UMTC tests, respectively) on samples of Leighton Buzzard Fraction-E sand having different initial void ratios and consolidated to different initial isotropic stress states (Table 5.2). Additionally, one undrained cyclic triaxial test on Leighton Buzzard Fraction-E sand was simulated, as also indicated in Table 5.2, and the results compared to those available in the literature. In order to complement the validation of the implementation of the original formulation of the constitutive model against element laboratory tests, one undrained cyclic direct simple shear (UCDSS) test on Nevada sand, whose initial conditions are presented in Table 5.3, was also simulated.

Table 5.2 – Designation and initial conditions of the monotonic and cyclic triaxial tests on Leighton Buzzard sand (Taborda, 2011).

Type of test	Designation [1]	e_0 ( )	σ'_0 (kPa)	Δq (kPa)
Drained isotropic compression (DIC)	DIC 0.810/20.0	0.810	20.0	–
	DIC 0.694/20.0	0.694	20.0	–
Drained monotonic triaxial compression (DMTC)	DMTC 0.813/39.3	0.813	39.3	–
	DMTC 0.816/119.6	0.816	119.6	–
	DMTC 0.695/40.7	0.695	40.7	–
	DMTC 0.696/120.5	0.696	120.5	–
Undrained monotonic triaxial compression (UMTC)	UMTC 0.820/40.3	0.820	40.3	–
	UMTC 0.818/118.6	0.818	118.6	–
	UMTC 0.694/40.6	0.694	40.6	–
	UMTC 0.688/119.3	0.688	119.3	–
Undrained cyclic triaxial (UCT)	UCT 0.820/119.2/50.0	0.820	119.2	± 50.0

[1] The designation identifies (1) type of test; (2) void ratio immediately after consolidation, e_0; (3) isotropic effective stress immediately after consolidation, σ'_0, and, when applicable, (4) deviatoric stress oscillation (two-way symmetrical stress reversal loading), Δq.

Table 5.3 – Designation and initial conditions of the undrained cyclic direct simple shear tests on Nevada sand (Taborda, 2011).

Type of test	Designation [1]	e_0 ( )	$\sigma'_{h,0}$ (kPa)	$\sigma'_{v,0}$ (kPa)	τ_0 (kPa)	$\Delta\tau$ (kPa)
Undrained cyclic direct simple shear (UCDSS)	UCDSS 0.715/80.0/0.0/7.4	0.715	28.0	80.0	0.0	± 7.4

[1] The designation identifies (1) type of test; (2) void ratio immediately after consolidation, e_0; (3) vertical effective stress immediately after consolidation, $\sigma'_{v,0}$; (4) shear stress immediately after consolidation, τ_0; and (4) shear stress oscillation, $\Delta\tau$.

The model parameters employed in the present simulations are indicated in Table 5.4. Note that values concerning the new features of the constitutive model are also indicated in the table. However, these values are only indicated for completeness, since their choice ($a =$

0.333, $v_A = 0.0$ and $k_A = 1.0$) imply that the new features of the model are not used in the present simulations.

Table 5.4 – Model parameters for Leighton Buzzard and Nevada sands (Taborda, 2011).

Model parameter	Leighton Buzzard sand	Nevada sand
Non-linear elasticity		
C_g	623.0	164.0
m_g	(1)	(1)
n_g	0.500	0.500
κ	2.000	2.000
a_1	0.500	0.300
γ_1	5.50×10^{-4}	6.50×10^{-4}
p'_{min}	5.0 kPa	10.0 kPa
G_{min}	0.0 kPa	1.0 kPa
ν	0.135	0.310
Model surfaces		
p'_{ref}	101.3 kPa	1000.0 kPa
$(e_{CS})_{ref}$	1.010	0.887
λ	0.080	0.140
ξ	0.350	0.250
v_A	0.000 (2)	0.000 (2)
M_c^c	1.180	1.290
M_e^c	0.850	0.900
k_c^d	2.140	2.350
k_e^d	1.542	
k_c^b	1.920	2.180
k_e^b	1.383	
m	0.065	0.065
p'_{YS}	1.0 kPa	1.0 kPa
Plastic hardening modulus		
A_0	1.050	1.460
h_0	0.047	1.939
γ	0.956	1.214
e_{lim}	0.934	0.818
α	1.000	1.000
μ	0.623	1.500
β	0.750	0.000
k_A	1.000 (2)	1.000 (2)
$h_{f,min}$	0.100	0.100
$h_{f,max}$	100.0	100.0
Shearing-induced fabric component		
H_0	8021.2	314.6
ζ	2.400	1.590
H_{max}	9.0×10^4	2.0×10^6

Table 5.4 – Model parameters for Leighton Buzzard and Nevada sands (Taborda, 2011).

Model parameter	Leighton Buzzard sand	Nevada sand
Inherent fabric anisotropy component a	0.333 (2)	0.333 (2)

(1) For the purpose of validation, Equation 4.25 was employed to the computation of the small-strain shear modulus, as proposed in the original formulation of the model. This means that the model parameter m_g, which is used in Equation 4.99 and 4.100, is not necessary in the present simulations.

(2) Value concerning a new feature of the model. The chosen value imply that this feature is not used in the present simulations.

5.3.2.1.2 General aspects of the numerical simulations

All tests were simulated using a single hybrid eight noded element and nine Gauss points. In the case of the triaxial testing (Figure 5.4a), axisymmetric conditions were considered, with the horizontal displacements, Δd_x, being restricted along the left side of the element (axis of symmetry) and the vertical displacement, Δd_y, being restricted along the bottom boundary of the element. Moreover, the loading was simulated by applying either a vertical displacement or normal stresses to the nodes located on the top boundary of the element (i.e. a given value was assigned either to Δd_y or ΔF_y), depending on the nature of the test.

With respect to direct simple shear testing (Figure 5.4b), a plane strain analysis was performed. The horizontal and vertical displacements, Δd_x and Δd_y, respectively, of the nodes located along the bottom boundary of the element were restricted. Additionally, the vertical displacements of the nodes located along the top boundary of the element were tied (i.e. conditions of equal vertical displacements were applied to these nodes) to ensure the top face of the element remains plane throughout the analysis. Due to the load-controlled nature of the test simulated, uniform tangential stresses were applied to the nodes located on the top boundary of the element (i.e. a given value was assigned to ΔF_x). Naturally, it would have been possible to simulate a strain-controlled test by applying a horizontal displacement (along the xx-direction) instead.

In order to simulate undrained conditions, the displacement, velocity and acceleration degrees of freedom of the pore fluid were tied to the ones corresponding to the solid phase in the direction perpendicular to that defined by a given boundary. For example, to set the left boundary impervious, at each node of this boundary, conditions of equal horizontal displacements, velocities and accelerations in the pore fluid and in the solid phase were specified. In the case of the top boundary, the vertical degrees of freedom of the pore fluid and solid phase were tied. Moreover, as pointed out by Grazina (2009), a very large value was assigned to the time step controlling the time integration of the equation of motion, in order to induce very small accelerations and velocities, as well as to reduce the influence of the inertial forces in the system.

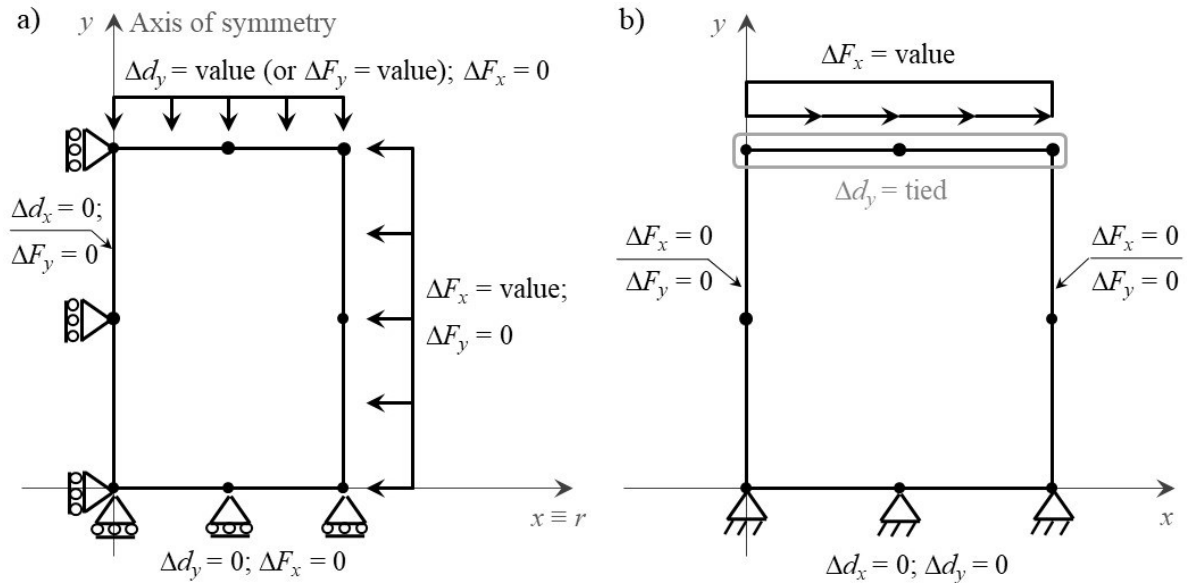

Figure 5.4 – Load and displacement boundary conditions for (a) triaxial tests and (b) direct simple shear tests.

5.3.2.1.3 Drained isotropic compression

In order to simulate drained isotropic compression (DIC) tests, the normal stresses applied to the nodes located along the top boundary of the element were identical to the normal stresses applied to the nodes belonging to the right boundary. These applied stresses started as equal to 20 kPa, being gradually increased up to 1820 kPa. A reduction from 1820 kPa to 20 kPa was applied afterwards. The only difference in the input data of both simulated tests – DIC 0.810/20.0 and DIC 0.694/20.0 (Table 5.2) – consisted of the initial void ratio of the samples, with values of 0.810 and 0.694, respectively in the former and latter tests.

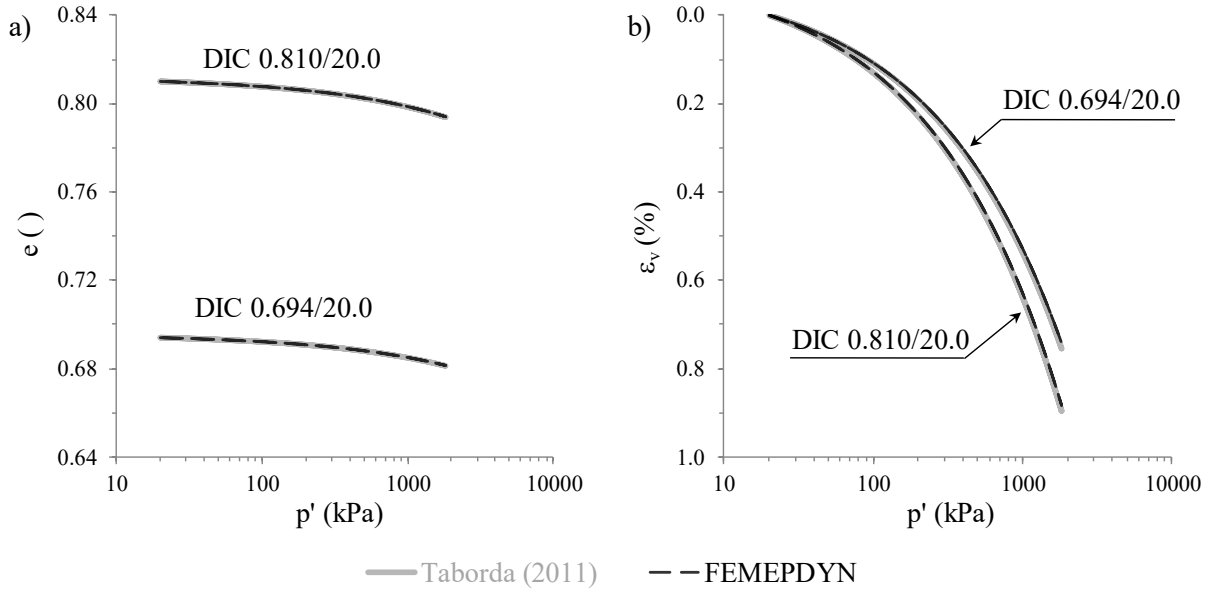

Figure 5.5 – Numerical simulation of DIC tests: evolution of the (a) void ratio and (b) volumetric strain with the mean effective stress.

Figure 5.5 compares the results obtained by FEMEPDYN with data available in Taborda (2011). It can be observed that, in both simulations, the results obtained by the different FE codes agree very well, with the obtained curves being practically coincident. Note that, due to the open shape of the yield surface, the constitutive model predicts only elastic response under constant stress ratio loading. Moreover, since deviatoric stress remains null (and, therefore, $\chi_{ref}^{r} = 0$) throughout loading, the reduction of the shear modulus is not activated. As a result, the same $e - p'$ path is followed during primary loading, unloading and reloading. This topic will be further explored in Chapter 7.

5.3.2.1.4 Drained monotonic triaxial compression tests

Figure 5.6 compares the results of the numerical simulations of four different DMTC tests obtained when using FEMEPDYN with data available in Taborda (2011).

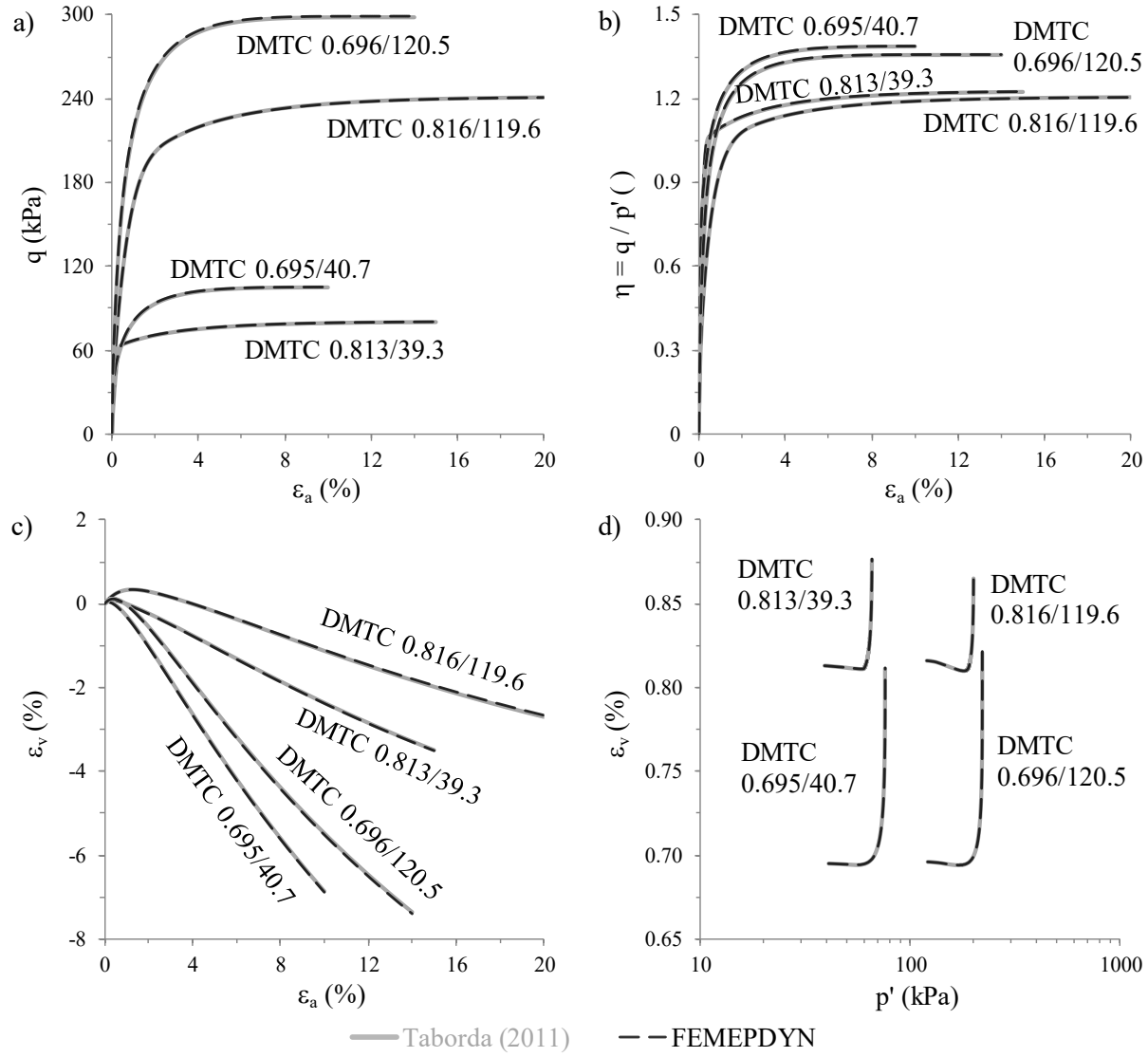

Figure 5.6 – Numerical simulation of DMTC tests: (a) deviatoric stress – axial strain; (b) stress ratio – axial strain; (c) volumetric strain – axial strain; and (d) void ratio – mean effective stress.

Note that, to simulate the strain-controlled nature of the drained monotonic triaxial compression (DTMC) tests, a constant vertical displacement rate was applied to the nodes located along the top boundary of the element. Moreover, observe that a perfect agreement was reached for all conducted simulations.

5.3.2.1.5 Undrained monotonic triaxial compression tests

Similar to the simulation of DMTC, a constant vertical displacement rate was applied to the nodes located along the top boundary of the element, reflecting the strain-controlled nature of the undrained monotonic triaxial compression (UMTC) tests.

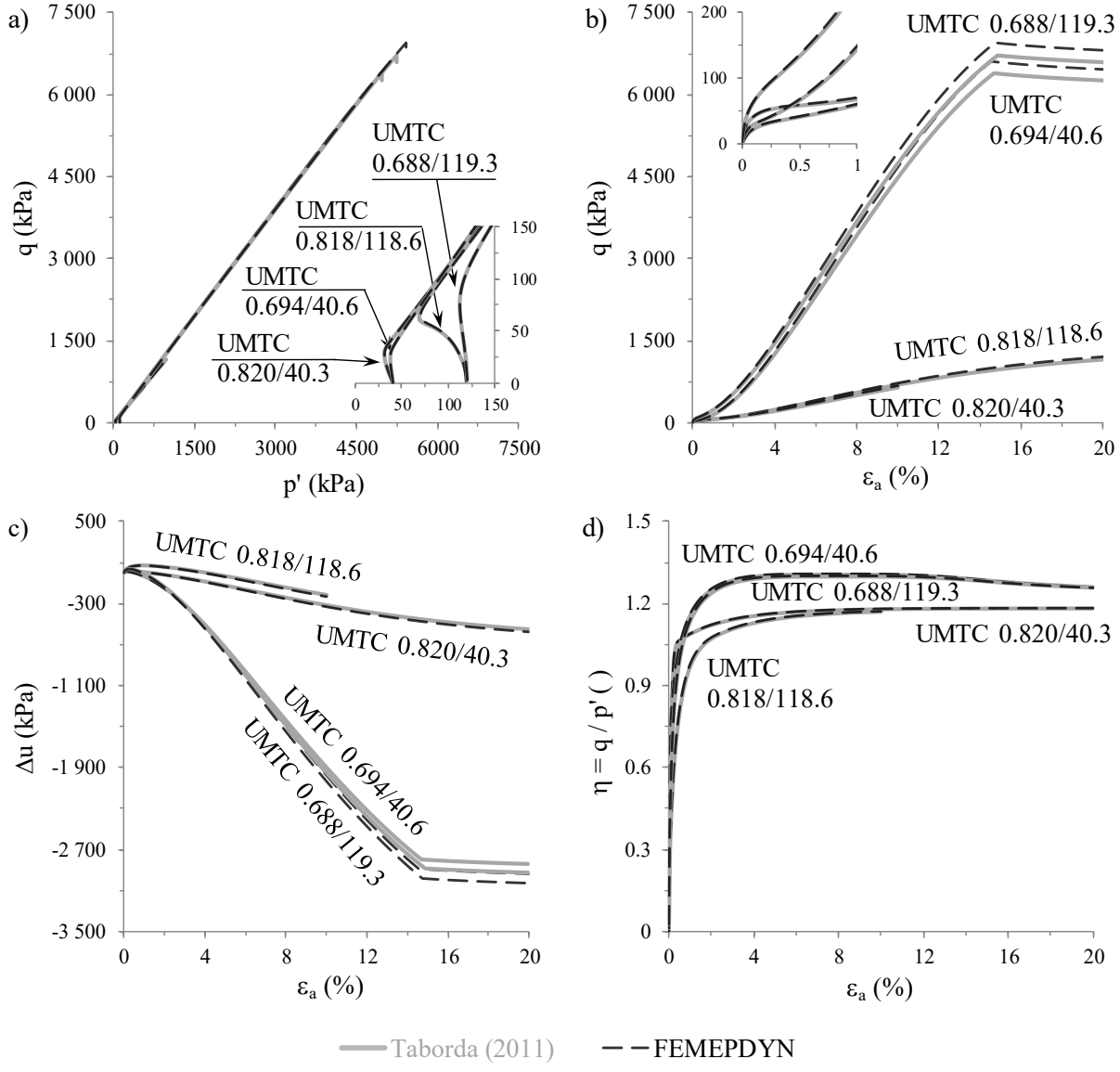

Figure 5.7 – Numerical simulation of UMTC tests: (a) deviatoric stress – mean effective stress; (b) deviatoric stress – axial strain; (c) excess pore water pressure – axial strain and (d) stress ratio – axial strain.

Figure 5.7 depicts the results obtained for all UMTC tests by FEMEPDYN, as well as those obtained by Taborda (2011). It can be seen that a very good match between the two set of

data was obtained for the earlier stages of loading (i.e. within the small to medium strain range). This is particularly noticeable in the details of the stress path and stress-strain response included in Figure 5.7a and Figure 5.7b, respectively. For large strains, some differences between the two set of data can be observed, particularly in terms of obtained deviatoric stress – axial strain response (Figure 5.7b) and excess pore water pressure build-up with strain (Figure 5.7d).

In order to clarify whether these discrepancies would arise from the use of different numerical precisions in the calculations, the simulation of UMTC 0.818/118.6 test was repeated using tighter tolerances in the numerical algorithms used to control the FE analysis. As shown in Figure 5.8, the results obtained in this new computation by FEMEPDYN and by ICFEP (Taborda, 2015) are now in perfect agreement from the beginning to the end of the analysis.

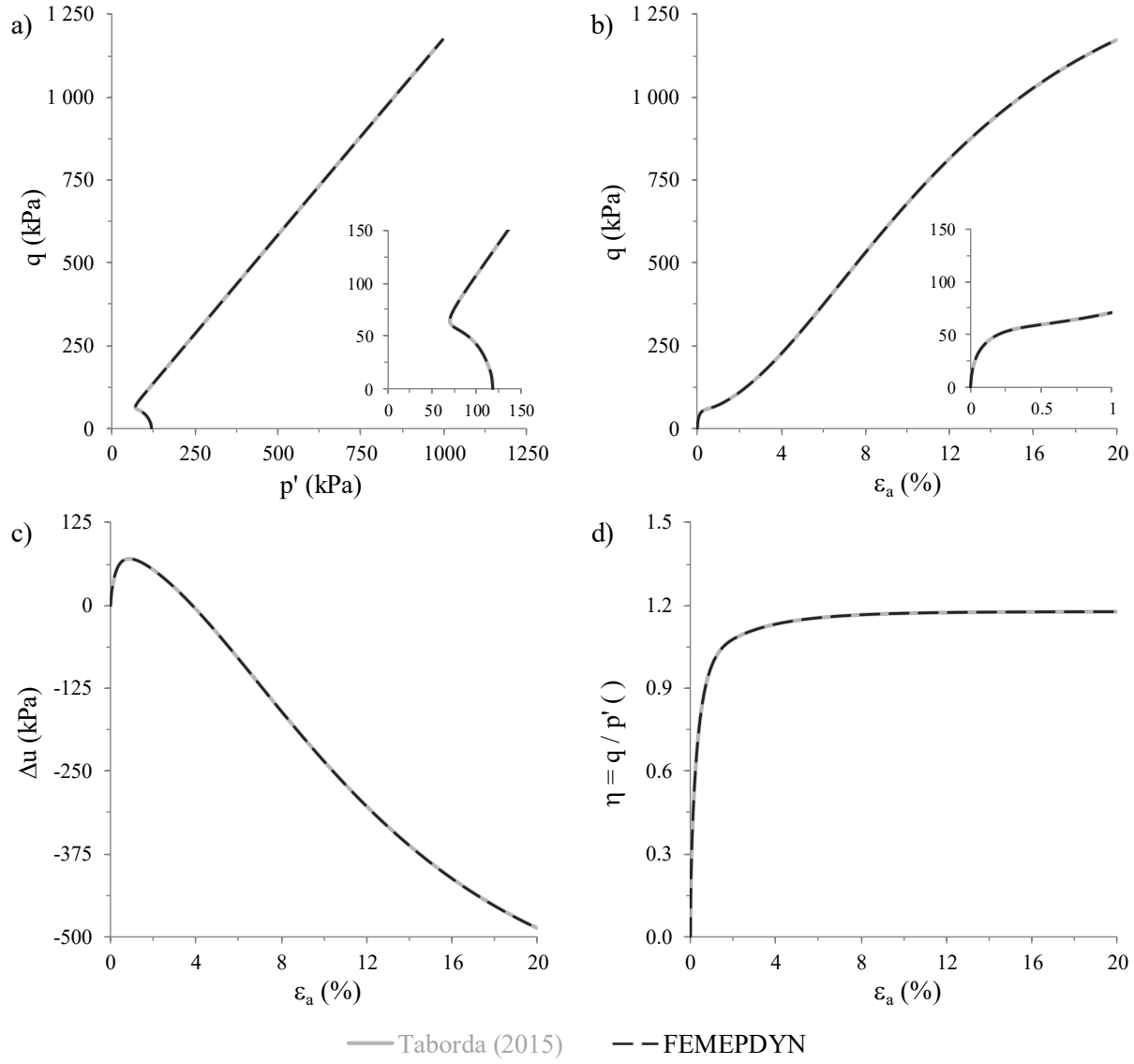

Figure 5.8 – Numerical simulation of UMTC 0.818/118.6 test using tight numerical tolerances: (a) deviatoric stress – mean effective stress; (b) deviatoric stress – axial strain; (c) excess pore water pressure – axial strain and (d) stress ratio – axial strain.

5.3.2.1.6 Undrained cyclic triaxial test

A numerical simulation of an undrained cyclic triaxial (UCT) test using tight numerical tolerances was performed using FEMEPDYN and the obtained results compared to those obtained by ICFEP (Taborda, 2015). In this test, a sample of Leighton Buzzard Fraction-E sand having an initial void ratio of 0.820 and consolidated to an isotropic effective stress of 119.2 kPa was subjected to 4 loading cycles characterised by a deviatoric stress oscillation of ± 50.0 kPa (Table 5.2). The effective stress path, stress-strain response and evolutions of excess pore water pressure ratio and axial strain with the number of loading cycles are shown in Figure 5.9a) to d), respectively. It can be seen that the results obtained in both simulations are in perfect agreement.

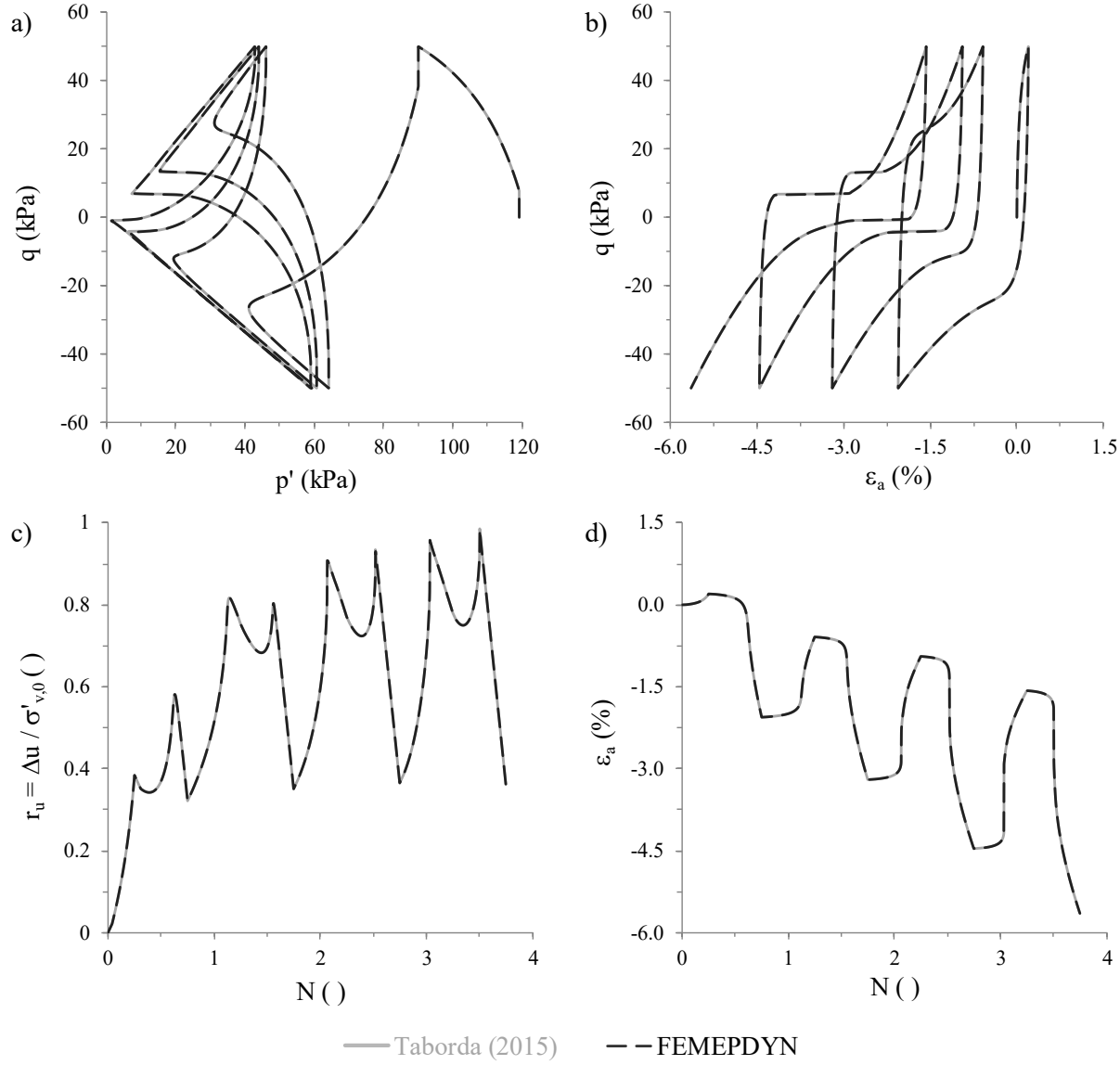

Figure 5.9 – Numerical simulation of test UCT 0.820/119.2/50.0 using tight numerical tolerances: (a) deviatoric stress – mean effective stress; (b) deviatoric stress – axial strain; (c) excess pore water pressure ratio – number of loading cycles; and (d) axial strain – number of loading cycles.

Due to the large availability of data, it was also possible to verify that specific aspects of the formulation of the model were correctly implemented into FEMEPDYN. In particular, it is shown in Figure 5.10 that the evolutions of the elastic moduli with shearing computed by FEMEPDYN and by ICFEP (Taborda, 2015) are in very good agreement.

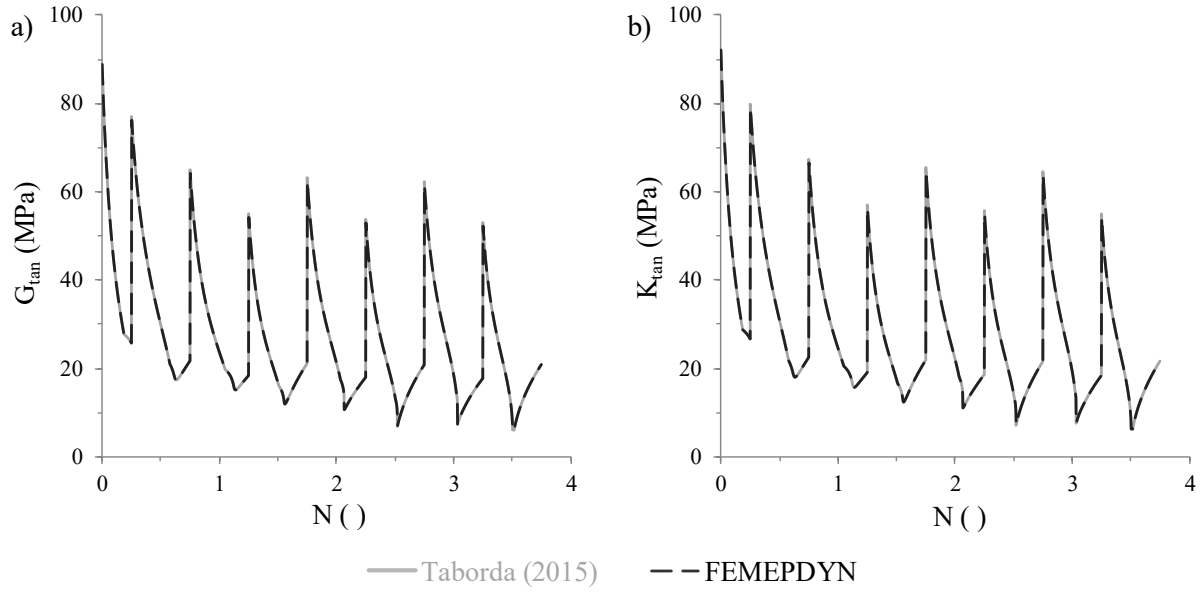

Figure 5.10 – Numerical simulation of test UCT 0.820/119.2/50.0 using tight numerical tolerances: evolution of (a) the tangent shear modulus and of (b) the bulk modulus with the number of loading cycles.

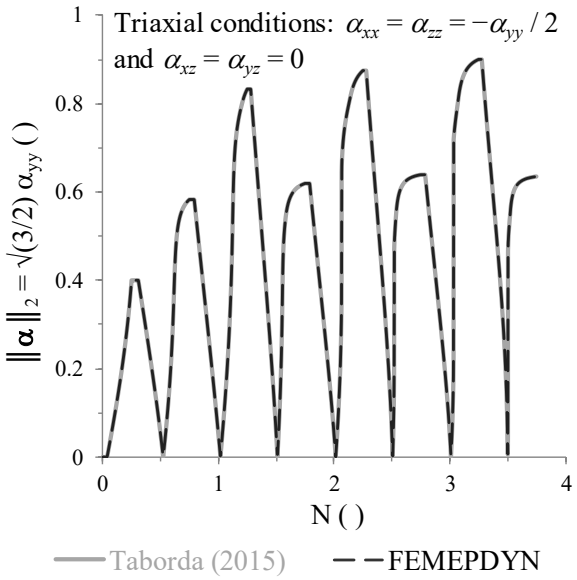

Figure 5.11 – Numerical simulation of test UCT 0.820/119.2/50.0 using tight numerical tolerances: evolution of the norm of the back-stress tensor with the number of loading cycles.

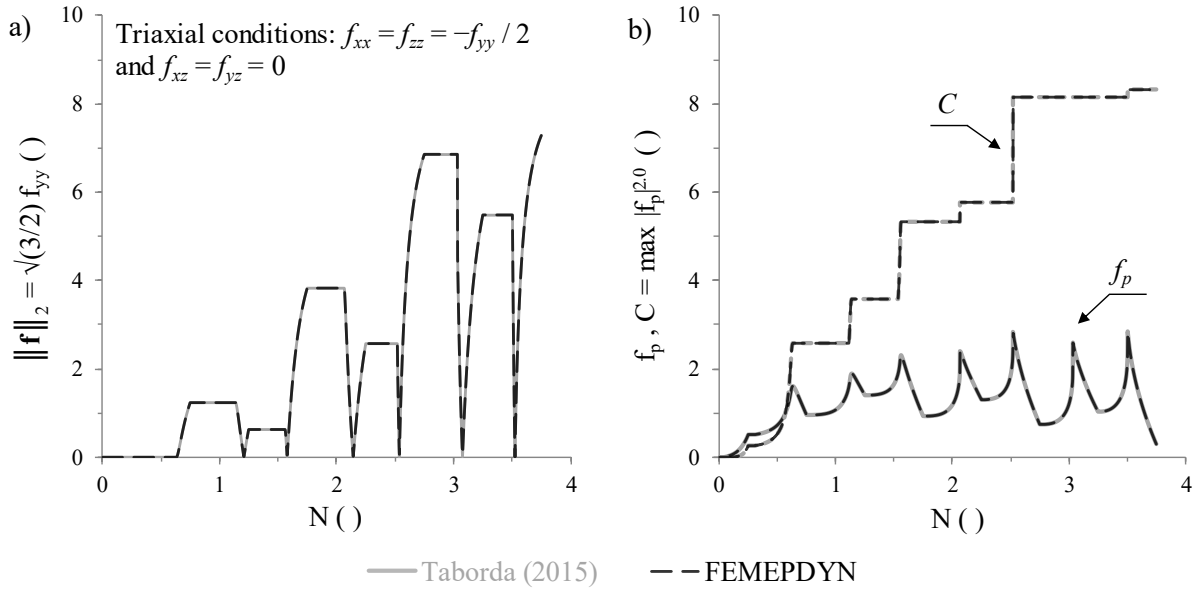

Figure 5.12 – Numerical simulation of test UCT 0.820/119.2/50.0 using tight numerical tolerances: (a) evolution of the norm of the deviatoric component of the shearing-induced fabric tensor with the number of loading cycles; (b) evolution of the volumetric component of the shearing-induced fabric tensor and of parameter *C* with the number of loading cycles.

Similarly, a very good match was obtained for the evolution of the back-stress tensor, $\boldsymbol{\alpha}$ (Figure 5.11), isotropic and deviatoric components of the shearing-induced fabric tensor, f_p and $\boldsymbol{f}$, as well as parameter C (Figure 5.12). Note that, since $\alpha_{xx} = \alpha_{zz} = -1.0/2.0\ \alpha_{yy}$ and $\alpha_{xy} = \alpha_{xz} = \alpha_{yz} = 0.0$ for triaxial conditions, the Euclidian norm of $\boldsymbol{\alpha}$, given, in this case, by $\|\boldsymbol{\alpha}\|_2 = \sqrt{3.0/2.0}\,|\alpha_{yy}|$, provide an indication of the evolution of all components of the tensor. Similar principles apply for $\|\boldsymbol{f}\|_2$.

5.3.2.1.7 Undrained cyclic direct simple shear test

To complement the validation of the implementation of the original formulation of the constitutive model into FEMEPDYN, an undrained cyclic direct simple shear (UCDSS) test on Nevada sand was simulated.

In this test, a sample having initial void ratio $e = 0.715$ and initially submitted to a vertical effective stress of $\sigma'_v = 80.0$ kPa and to a shear stress of $\tau = 0.0$ kPa was subjected to 5 loading cycles characterised by a shear stress oscillation of $\Delta\tau = \pm 7.4$ kPa (Table 5.3).

The numerical results obtained by FEMEPDYN are depicted together with those obtained by ICFEP (Taborda, 2011) in Figure 5.13. It can be observed that, in general, a good agreement was obtained between both sets of data. A slightly higher rate of decrease of the effective vertical stress with shearing was obtained by FEMEPDYN (Figure 5.13a), resulting in a slightly earlier activation of the secondary yield surface (at very low effective stresses). As a consequence, larger shear strains, γ, were obtained by FEMEPDYN for the last loading cycle than those obtained ICFEP (Taborda, 2011), as observed in Figure 5.13b and d. In fact, due to the perfect plasticity associated with the secondary yield surface (Section 4.2.5), strains

quickly accumulate once this yield surface is activated and, therefore, small discrepancies in the rate of effective stress reduction may considerably affect the strains computed at very low effective stresses. Once again, the small discrepancies between both sets of data likely arise from differences in the numerical tolerances used in the analysis.

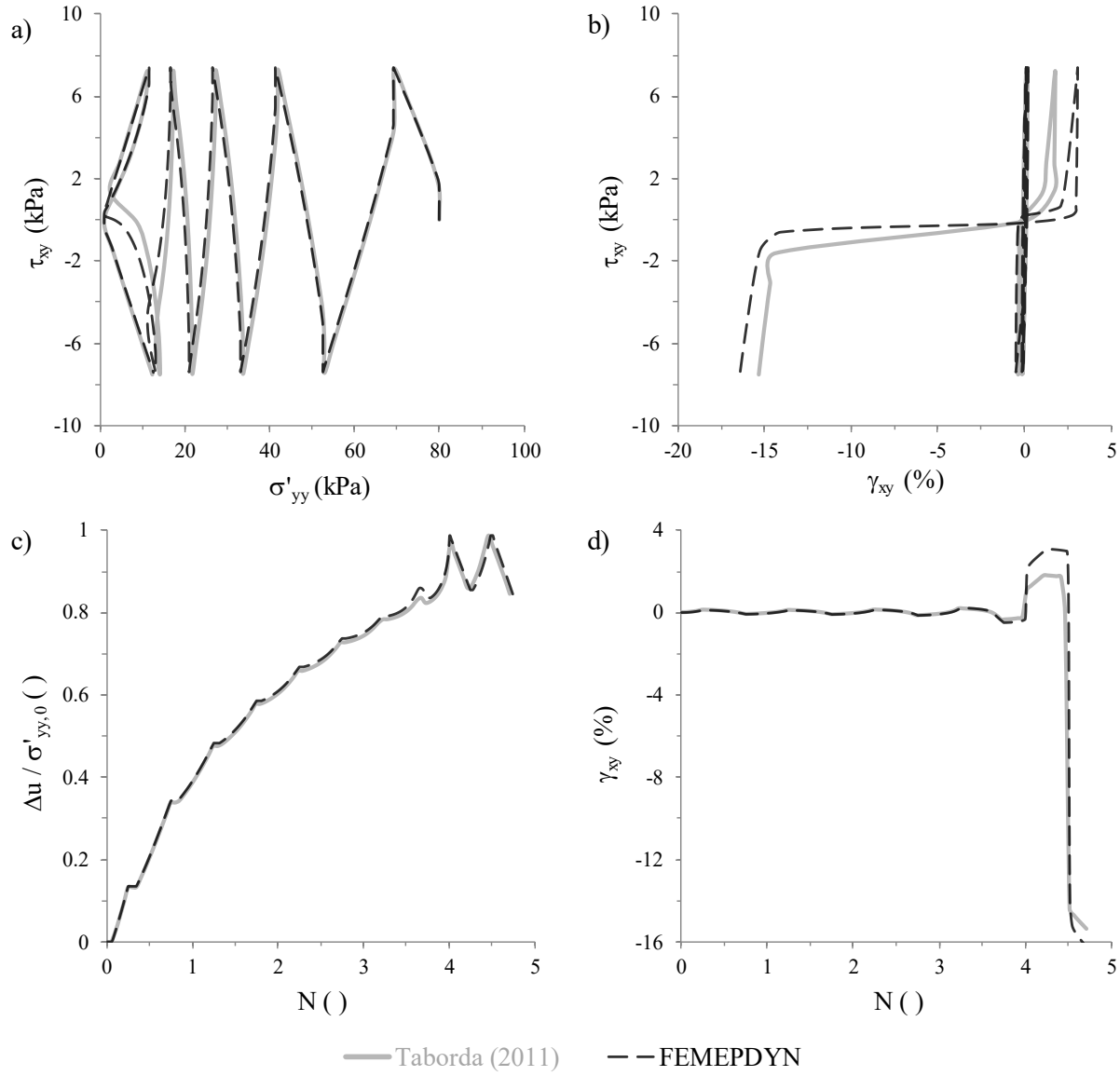

Figure 5.13 – Numerical simulation of test UCDSS 0.715/80.0/0.0/7.4: (a) shear stress – vertical effective stress, (b) shear stress – shear strain, (c) excess pore water pressure ratio – number of loading cycles and (d) shear strain – number of loading cycles.

5.3.2.2 Simulation of dynamic centrifuge experiments

5.3.2.2.1 Brief description of the main aspects of the simulated centrifuge experiments

A series of dynamic centrifuge experiments were performed as part of the large collaborative research project VELACS – VErification of Liquefaction Analysis by Centrifuge Studies, sponsored by the American National Science Foundation (Arulanandan and Scott, 1993). Concurrently, an extensive laboratory testing programme was carried out on the materials

employed in those centrifuge experiments (Arulmoli *et al.*, 1992), assisting the calibration of constitutive models. Therefore, it is unsurprising that the obtained centrifuge results have been extensively used during the last years for the evaluation of the performance of advanced constitutive models, including those based on the bounding surface plasticity framework (e.g. Taiebat *et al.*, 2007; Jeremic *et al.*, 2008; Andrianopoulos *et al.*, 2010b; Taborda, 2011).

Among the twelve available centrifuge experiments, the "VELACS Model 1 – Level ground liquefaction" and the "VELACS Model 12 – Embedded structure in stratified soil layers" were numerically modelled by Taborda (2011). As shown in Figure 5.14, the former model consisted of a level deposit of saturated loose ($D_r = 45$ %) Nevada sand with 10.0 m of thickness (in prototype scale), which was subjected to horizontal accelerations on its base, specified as 10 loading cycles with a frequency of 2 Hz and maximum amplitude of 0.25 *g*. Due to the simple geometry and non-existence of a built-on structure, this model was considered to be crucial to evaluate the ability of the bounding surface plasticity model to predict the occurrence and effects of cyclic mobility in sand (Taborda, 2011).

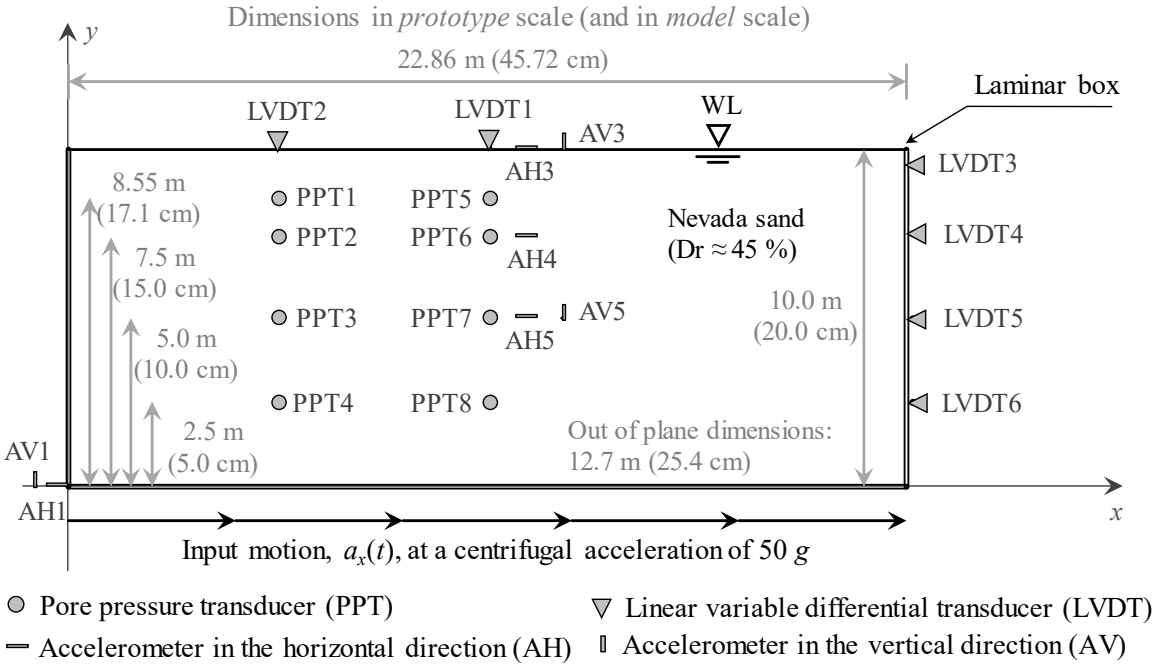

Figure 5.14 – Side view of the centrifuge VELACS model 1 and location of the monitoring instruments (adapted from Taborda, 2011).

With respect to the second centrifuge experiment "*VELACS* Model 12 – Embedded structure in stratified soil layers" simulated by Taborda (2011), it included a compact prismatic structure with 4.0 m of height and 3.0 x 3.0 m^2 of area in plan, centred in the centrifuge model and partially embedded in a 6.0 m-thick deposit of saturated relatively dense ($D_r = 60$ %) Nevada sand, which was overlaid by a 1.0 m-thick low-permeability deposit of Bonnie silt, as illustrated in Figure 5.15. The water level (WL) was located 1.0 m above the surface of the Bonnie silt layer. Moreover, the vertical stress applied by the structure to the underlying

deposit was estimated to be 150 kPa, while the acceleration time-history applied to the base of the centrifuge model was similar to that applied to the VELACS model 1. As pointed out by Taborda (2011), due to the presence of the structure, the observed settlements cease to be solely a result of the dissipation of excess pore water pressures generated during seismic loading (i.e. a result of the consolidation process), as it was the case in VELACS model 1. Indeed, as observed by Coelho (2007), the presence of the structure has a profound impact on the deformation mechanisms observed in this type of dynamic centrifuge experiments, as well as on the pore water pressure build-up and subsequent dissipation.

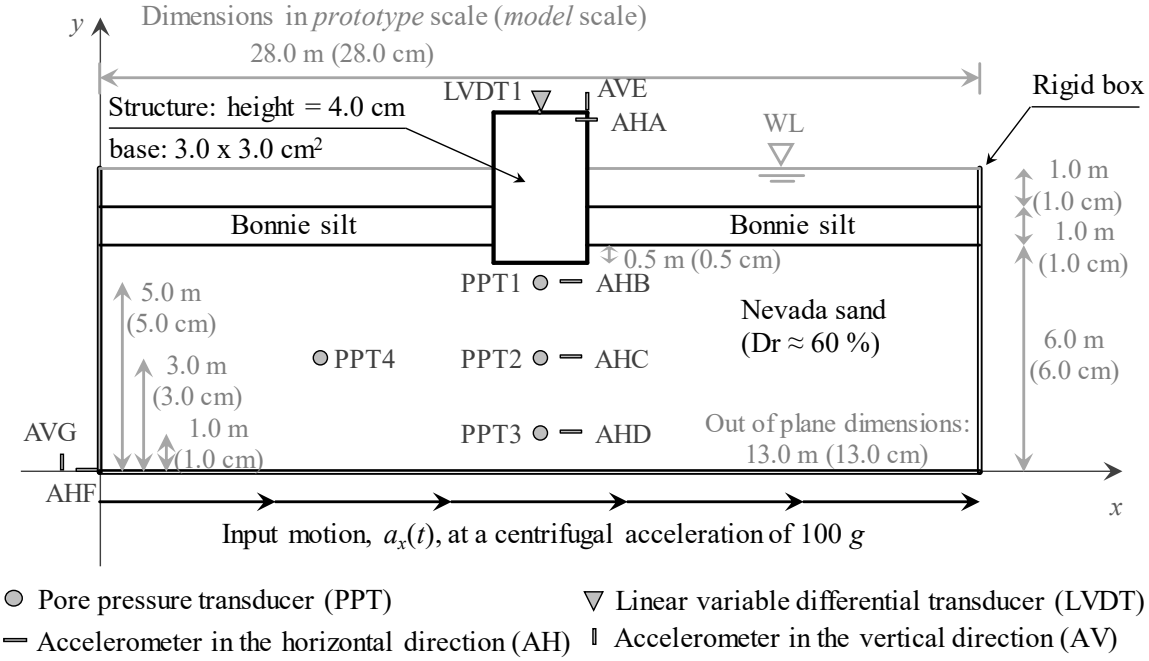

Figure 5.15 – Side view of the centrifuge VELACS model 12 and location of the monitoring instruments (adapted from Taborda, 2011).

A particular aspect of these centrifuge experiments is that water was used as pore fluid. Consequently, a conflict of scaling laws (used to correlate the physical observations in model scale to prototype scale) for time arises: the scaling law is $1 / N^2$ (where N is the ratio of the centrifugal acceleration to the acceleration of gravity) for diffusion/consolidation time, while a scaling law of $1 / N$ applies for dynamic time (Table 5.5). This incompatibility between scaling laws compromises the extrapolation of the observations from model to prototype scale. To prevent this incompatibility from arising, it has been common practice to use a pore fluid N times more viscous than the prototype pore fluid (e.g. Madabhushi, 1994, 2004; Coelho, 2007). In effect, as mathematically detailed in Thusyanthan and Madabhushi (2003), by increasing the viscosity by N, the hydraulic conductivity (often referred to as permeability coefficient) is increased by the same factor N, which, according to the Darcy law, results in a reduction of the seepage velocity by the same factor N. As a result, the scaling laws for seepage velocity and consolidation time become 1 and $1 / N$, respectively, therefore identical to those applicable for velocity and time in a dynamic event (Table 5.5).

Despite compromising the extrapolation of the results from model to prototype scale, the use of water as a pore fluid does not invalidate the numerical reproduction of the centrifuge experiments, providing that the numerical simulations are performed in model scale (i.e. using the dimensions indicated in between parenthesis in Figure 5.14 and Figure 5.15). Particular attention should, however, be given to the scale of the quantities. Specifically, as indicated in Table 5.5, the input accelerations should be *N* times larger than those intended for the prototype, while the duration of the input motion should be *N* times shorter (i.e. the acceleration time-history applied to the centrifuge model should be used in its numerical simulation). Furthermore, in order to adequately replicate the flow of water observed in the model, the hydraulic conductivity of each material should be scaled by *N*, as well as the unit weight of water. Finally, the unit weights of the materials should also be scaled by *N* to properly estimate the initial stress state. All remaining input values, including the model parameters, are independent of the scale at which the centrifuge model is simulated.

Table 5.5 – Scaling laws used in centrifuge modelling to correlate the physical observations in model scale to prototype scale (Madabhushi, 2004).

Quantity	Unit	Scaling law
General scaling laws for slow events		
Length	m	1 / *N*
Area	m^2	1 / N^2
Volume	m^3	1 / N^3
Mass	N m^{-1} s^2	1 / N^3
Mass density	N m^{-4} s^2	1
Force	N	*1* / N^2
Bending moment	N m	1 / N^3
Stress	N m^{-2}	1
Strain	m m^{-1}	1
Work and energy	N m	1 / N^3
Seepage velocity	m s^{-1}	1 / *N*
Diffusion / consolidation time	s	1 / N^2
Scaling laws for dynamic events		
Time	s	1 / *N*
Frequency	s^{-1}	*N*
Displacement	m	1 / *N*
Velocity	m s^{-1}	1
Acceleration	m s^{-2}	*N*

As part of the validation of the implementation of the bounding surface plasticity model into FEMEPDYN, both VELACS model 1 and 12 were numerically simulated, with the obtained results being compared with those obtained by Taborda (2011) when using the original version of the constitutive model in ICFEP. At this point, it is perhaps important to highlight that, although it is expected to obtain overall similar results to those presented in Taborda (2011), it cannot be expected to obtain a perfect match as that obtained when modelling element laboratory tests (particularly when using similar numerical tolerances). In fact, it

should be noted that, although the constitutive equations implemented into FEMEPDYN are expected to be very similar to those implemented into ICFEP, there might exist some discrepancies in the numerical algorithms implemented into both codes to integrate those equations. Moreover, it should be pointed out that different dynamic formulations of the equation of motion are implemented in both codes. Specifically, while a complete formulation "$d^s - d^f - u$" (where "d" and "u" designate displacement and pore pressure degrees of freedom, respectively, while the superscripts "s" and "f" designates solid and fluid phases, respectively) of the equation of the motion is implemented into FEMEPDYN (Grazina, 2009) and is used in the present study, a "$d^s - u$" formulation, which assumes that the acceleration of the pore fluid relative to the soil matrix can be neglected (Zienkiewicz *et al.*, 1980), was used during the simulations performed by Taborda (2011). Note that, in the literature (e.g. Zienkiewicz *et al.*, 1980), the formulation "$d^s - u$" is often designated as "$u - p$" (with "u" being, in this case, the displacement of the solid particles and "p" the pore pressure), while the formulation "$d^s - d^f - u$" is often designated as "$u - w - p$" (where "w" refers to the displacement of the pore fluid). Moreover, note that, although these numerical aspects have typically little influence on the obtained results when simulating problems involving simple, geometry, loading and boundary conditions (e.g. element laboratory tests), they might have a considerable impact on the simulation of dynamic boundary value problems (e.g. Potts and Zdravkovic, 1999; Sloan *et al.*, 2001; Taborda, 2011; Woo and Salgado, 2014; E-Kan and Taiebat, 2014).

5.3.2.2.2 Material properties

In order to characterise the materials employed in these centrifuge experiments (dry-pluviated Nevada sand no. 120 and slurry-deposited Bonnie silt), a very extensive element laboratory testing programme was carried out at The Earth Technology Corporation (Arulmoli *et al.*, 1992). This included characterisation tests to determine physical properties and particle size distribution, constant head-permeameter tests, resonant column tests, oedometer tests, drained and undrained monotonic triaxial compression and extension tests, undrained cyclic triaxial tests, drained and undrained monotonic direct simple shear tests and undrained cyclic simple shear tests. Based on the large amount of experimental data available, the bounding surface plasticity model was calibrated for Nevada sand by Taborda (2011), with the model parameters obtained by the author being indicated in Table 5.4.

With respect to Bonnie silt, a considerable amount of experimental data was available, which would also allow the calibration of the bounding surface plasticity model for this material. This was, however, considered to be unnecessary by Taborda (2011), with a simpler numerical model being selected. In fact, as pointed out by the author, due to the thin thickness of the Bonnie silt layer and the fact that the foundation is not built on it, the mechanical response of this material is expected to have a small influence on the performance of the foundation under dynamic loading, at least when compared with the influence of the deposit of Nevada

sand. A cyclic non-linear elastic model using a hyperbolic backbone curve was, therefore, selected by Taborda (2011). This model was coupled with the Mohr-Coulomb failure criterion in order to limit the shear strength of the material. Unfortunately, a model of this type is not available in FEMEPDYN. Although it would have been possible to use also the BSPM to replicate the response of the Bonnie silt layer, the additional complexity of that option would likely not be offset by an important gain in terms of accuracy. Therefore, it was decided to use a linear isotropic elastic model coupled with the Mohr-Coulomb failure criterion to describe the response of the thin deposit of Bonnie silt. Naturally, the fact that the constitutive model employed in the present study is different from that adopted by Taborda (2011) may lead to some discrepancies in the obtained results (strains, effective stresses and pore water pressures). Nevertheless, these discrepancies are expected to be limited to zones of the model close to or within the Bonnie silt layer.

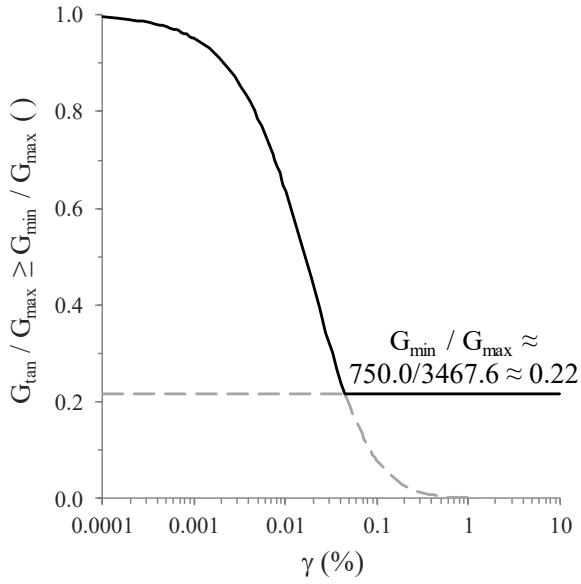

Figure 5.16 – Reduction of the normalised tangent shear modulus with shear strain amplitude under direct simple shear primary loading predicted by the constitutive model employed by Taborda (2011) to model the response of Bonnie silt deposit.

In order to calibrate a linear isotropic elastic model, only two model parameters are required. In the present study, values for the (constant) shear modulus, G, and Poisson's ratio, ν, were defined. Starting with the latter model parameter, since the cyclic non-linear component of the constitutive model employed by Taborda (2011) also makes use of a constant Poisson's ratio, the same value was adopted: $\nu = 0.20$. In relation to the shear modulus, Figure 5.16 depicts the normalised reduction of the tangent shear modulus, G_{tan} / G_{max}, with the shear strain amplitude, γ, defined by the cyclic non-linear elastic model used by Taborda (2011) under direct simple shearing primary loading. Also shown in the figure is the lower limit cut-off adopted by the author for the tangent modulus (i.e. $G_{tan}/G_{max} \geq G_{min}/G_{max}$). It can be observed that the lower limit is activated as the shear strains amplitude exceeds about 0.05 %. Taking into account that significant deformations were observed during the

experiment and reasonably well captured in the numerical simulation performed by Taborda (2011), it was decided to adopt the smallest value of the tangent modulus (i.e. $G = G_{min} =$ 750.0 kPa) in the present study.

With respect to the model parameters required for the Mohr-Coulomb failure criterion, identical values to those adopted by Taborda (2011) were used in the present study: the friction angle was set to $\phi' = 28.0°$, while the apparent cohesion was set to $c' = 5.0$ kPa. Table 5.6 resumes the model parameters adopted for Bonnie silt.

Table 5.6 – Model parameters adopted for Bonnie silt.

Model parameter	Value
Linear isotropic elasticity	
G_{tan} (kPa)	750.0
ν ( )	0.20
Strength (Mohr-Coulomb failure criterion)	
c' (kPa)	5.0
ϕ' (°)	28.0

5.3.2.2.3 VELACS model 1 – Level ground liquefaction

5.3.2.2.3.1 General aspects of the numerical simulation

A fully coupled hydro-mechanical dynamic finite element (FE) analysis of VELACS model 1 was carried out using FEMEPDYN, assuming 2D plane strain conditions. As mentioned before, the numerical simulation was performed in model scale (i.e. considering a 20 cm-thick deposit of Nevada sand), due to the incompatible scaling laws between dynamic time and consolidation time resulting from the use of water as pore fluid in the experiment. An identical mesh to that used by Taborda (2011) was generated in FEMEPDYN, consisting of a single column of 100 hybrid eight-noded isoparametric quadrilateral elements with 0.002 m of size (corresponding to 0.1 m of size in prototype scale). As illustrated in Figure 5.17, each of these hybrid elements has four pore pressure degrees of freedom, located at the corner nodes. Moreover, per element, nine Gauss points were used to estimate the effective stress changes.

Furthermore, to reflect the model scale conditions, a gravitational acceleration of 50.0 $g =$ 490.5 m/s^2 was used in the numerical simulation, increasing the unit weight of the materials (i.e. $\gamma_{sat,50\,g} = 50.0\ \gamma_{sat,1\,g}$) and of water (i.e. $\gamma_{w,50\,g} = 50.0\ \gamma_{w,1\,g}$). In addition, the input motion was also modified, by scaling up the accelerations by a factor of 50.0 and scaling down its duration by the same factor (Figure 5.18).

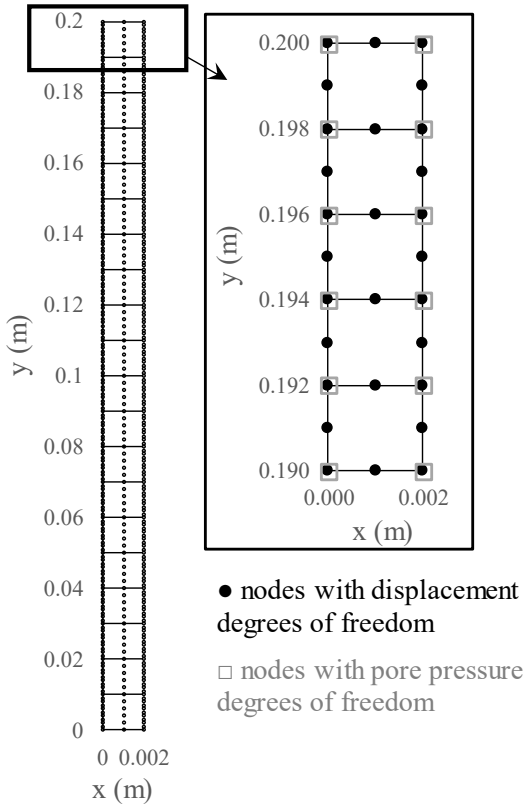

Figure 5.17 – Finite element mesh adopted in the simulation of VELACS model 1.

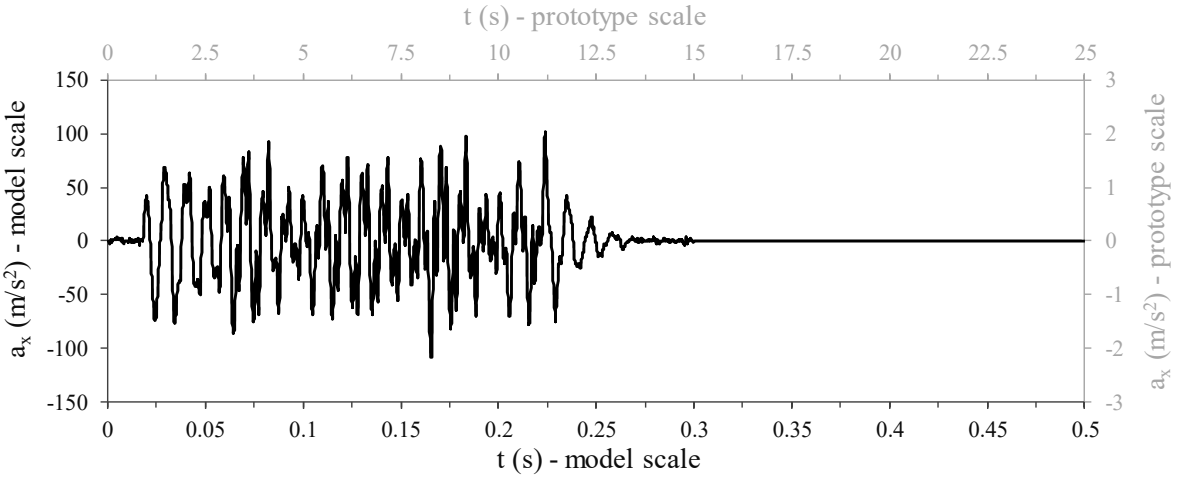

Figure 5.18 – Horizontal acceleration time-history for VELACS model 1.

The numerical analysis included two distinct phases: 1) generation of initial stress state assuming "greenfield" conditions; 2) application of the dynamic loading and subsequent consolidation analysis until the establishment of the hydraulic equilibrium. In relation to the first phase, due to the simple geometry of the problem, a K_0-procedure was employed. As suggested by Taborda (2011), an earth pressure coefficient at rest of $K_0 = 0.5$ was used for the deposit of Nevada sand. Regarding the second phase, as reported by Taborda (2011), a total of 5000 increments of 0.1 ms (corresponding to 0.05 s in prototype scale) were used to simulate the total duration of input signal (0.5 s in model scale, corresponding to 25 s in

prototype scale, as shown in Figure 5.18). Similar to what was performed by Taborda (2011), the dissipative version of the Newmark time-integration scheme ($\alpha = 0.3025$ and $\beta = 0.60$) was used during this phase of the analysis. As detailed by Grazina (2009), these values ensure unconditional stability of the method and result in a spectral radius at infinity of $\rho \approx 0.818$ for a single degree of freedom oscillator.

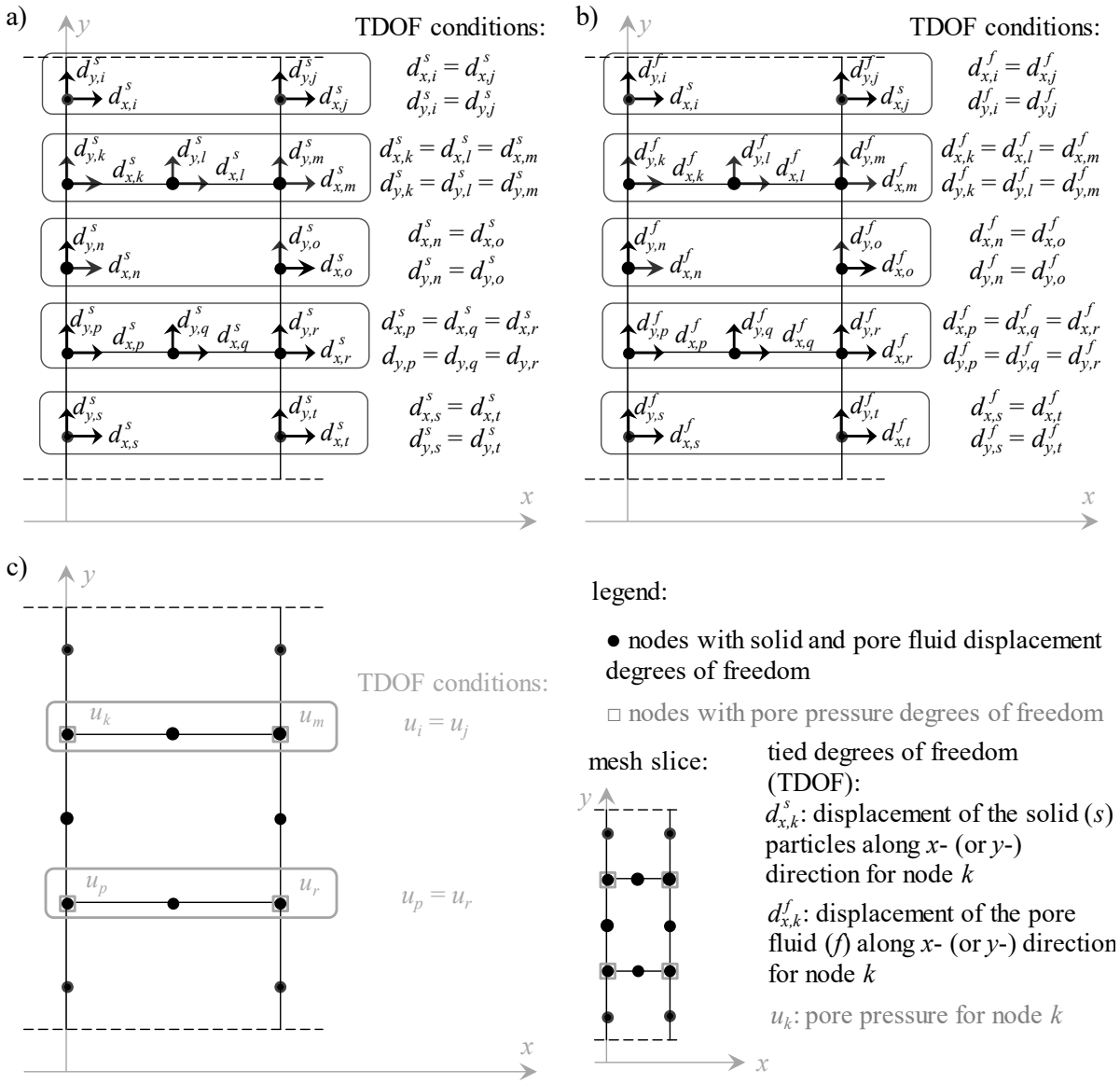

Figure 5.19 – Schematic illustration of tied degrees of freedom for: a) solid displacement degrees of freedom and b) pore fluid displacement degrees of freedom and c) pore pressure degrees of freedom.

In terms of boundary conditions, the horizontal acceleration time-history shown in Figure 5.18, after being appropriately scaled, was applied to the nodes belonging to the bottom boundary of the model, while restricting the vertical displacement degree of freedom at these nodes (i.e. no vertical accelerations were applied to the model). Moreover, as originally proposed by Zienkiewicz *et al.* (1989) and illustrated in Figure 5.19, one-dimensional response

was achieved by tying all degrees of freedom (i.e. displacement of the solid particles in both horizontal and vertical direction, displacement of the pore fluid in both horizontal and vertical directions and pore pressures) at each level of the mesh.

In addition, since drainage was only allowed through the ground surface, two additional boundary conditions were specified: 1) the flow of water through the lateral and bottom boundaries was impeded by tying the displacement degrees of freedom of the pore fluid and solid phase in the direction perpendicular to each boundary; and 2) the pore water pressures at the corner nodes belonging to the top boundary of the mesh were set to remain null throughout the analysis (i.e. a pore water pressure condition was specified for those nodes). It is perhaps important to note that, on the contrary to all remaining boundary conditions, the hydraulic boundary condition applied to the top boundary of the model in the present study (i.e. pore water pressure condition) was different from that used by Taborda (2011). Specifically, this author used a *precipitation* boundary condition, which was characterised by the following dual condition (Potts and Zdravkovic, 1999; Taborda, 2011): when the pore water pressure, u, was larger than a user-defined value (in the case, $u_b = 0.0$ was used), a pore water pressure condition was applied to the node; conversely, when u was smaller than u_b (meaning tensile pore water pressures, since $u_b = 0.0$), a user-defined flow rate, q_b, (in the case, $q_b = 0.0$ was selected) was applied. As shown later, since positive (i.e. compression-type) excess pore water pressures were generated during the application of the dynamic loading in every zone of the deposit, being eventually dissipated during the consolidation phase, the pore water pressure condition was likely applied during the whole analysis carried out by Taborda (2011), meaning that the condition applied to the top boundary condition was, in the end, similar to that used in the present study.

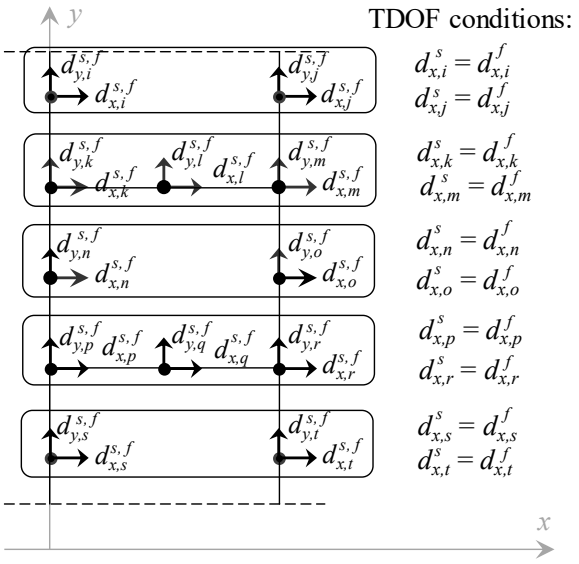

Figure 5.20 – Impervious lateral boundary conditions.

In relation to the characteristics of the Nevada sand deposit, as already mentioned, the original formulation of the bounding surface plasticity model developed by Taborda (2011) was used to simulate its response, with the model parameters listed in Table 5.4 being adopted. Moreover, as reported by Taborda (2011), the state of the deposit was characterised by an initial void ratio of $e_0 = 0.724$ (corresponding to an initial relative density of $D_r \approx 45$ %), as well as by mass density of $G_s = 2.67$, resulting in a saturated unit weight under *1 g* conditions of $\gamma_{sat,\,1\,g} = 19.31$ kN/m^3 (Equation 5.112) and, therefore, in a mass density of $\rho = 1.969$ g/cm^3 (Equation 5.113). Note that, contrary to the unit weight, the mass density is independent of the scale.

$$\gamma_{sat,\,1\,g} = \frac{(G_s + e)\,\gamma_{w,\,1\,g}}{1.0 + e} = \frac{(2.67 + 0.724) \times 9.81}{1.0 + 0.724} = 19.31 \text{ kN/m}^3 \tag{5.112}$$

$$\rho = \frac{\gamma_{sat,\,1\,g}}{g} = 1.969 \text{ g/cm}^3 \tag{5.113}$$

In terms of hydraulic properties, the deposit was characterised by a hydraulic conductivity in both horizontal and vertical directions of $k_{x,\,1\,g} = k_{y\,1\,g} = 6.583 \times 10^{-5}$ m/s for 1 *g* conditions (Taborda, 2011). This value was scaled by *N* to account for the centrifugal acceleration used in this test (i.e. $k_{x,\,50\,g} = k_{y\,50\,g} = 3.291 \times 10^{-3}$ m/s was used in the simulation). These values were assumed to remain constant throughout the analysis.

Finally, it was required to define the bulk modulus of the pore fluid. An identical value to that reported by Taborda (2011) was used: $K_f = 2.2$ GPa. There was no need to scale this value.

5.3.2.2.3.2 Obtained numerical results

The horizontal acceleration time-histories obtained by FEMEPDYN are compared with those reported by Taborda (2011) in Figure 5.21. Note that both sets of results are presented in prototype scale. Moreover, to ease the comparison between them, a bandpass filter with limit frequencies of 0.10 Hz and 25 Hz (in prototype scale) was applied to the raw data by using the software SeismoSignal version 2018 (Seismosoft, 2018). It is apparent that a good match between both sets of data was achieved. In particular, it is noteworthy that, at each level, a good agreement was reached in terms of the instant of time at which the horizontal accelerations are observed to strongly attenuate, suggesting that similar predictions of the moment at which cyclic mobility was initiated was obtained in both FE simulations.

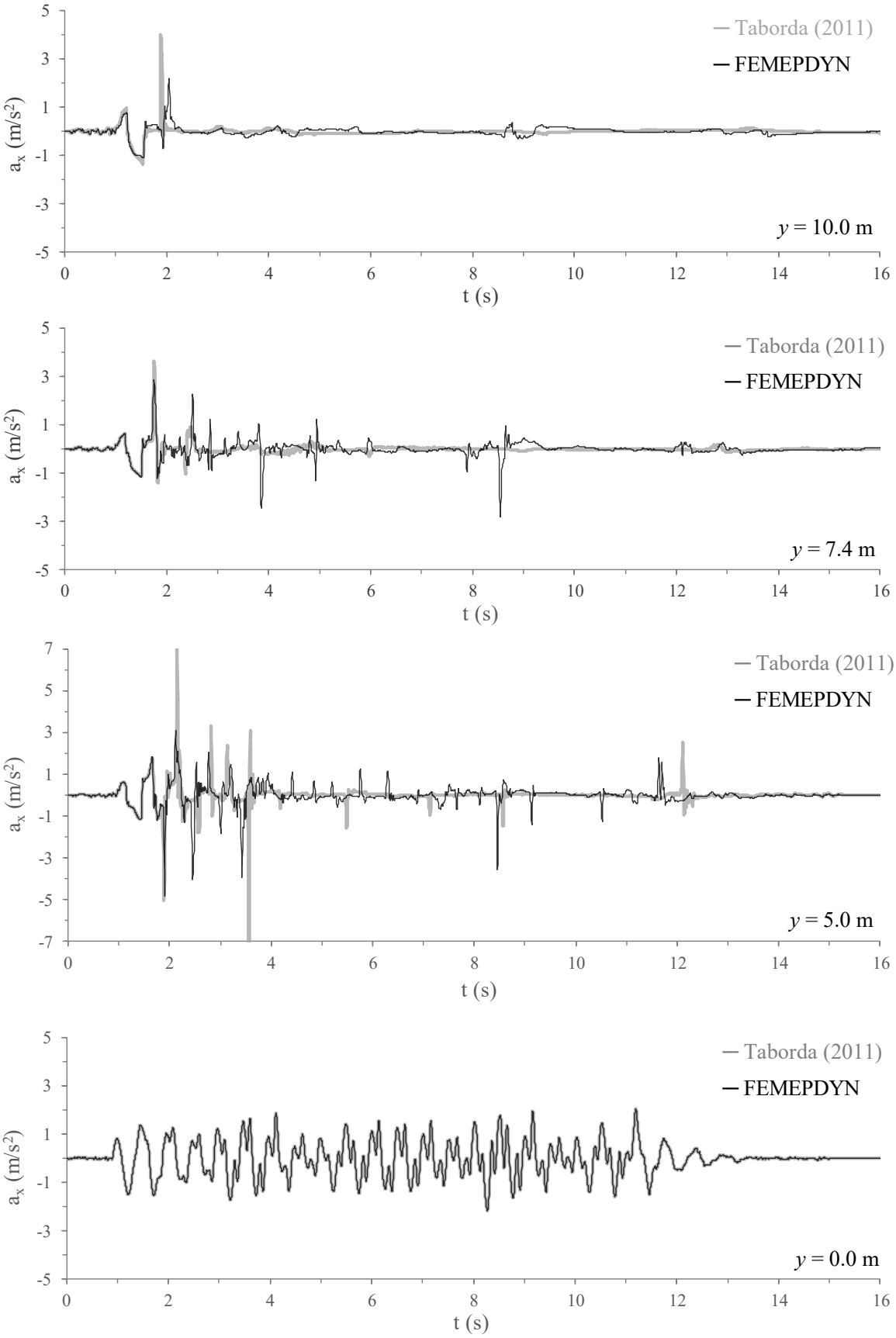

Figure 5.21 – Computed horizontal acceleration time-histories for VELACS model 1.

Furthermore, the evolutions of the excess pore water pressure with time computed by FEMEPDYN are depicted in Figure 5.22, together with those reported by Taborda (2011). Once more, it can be observed that, in general, a very good agreement between both sets of data was reached, with both FE codes predicting a rapid increase of the excess pore water pressure to values close to the initial vertical effective stress at every level of the mesh. The only slight discrepancy seems related to the rate at which the dissipation of the excess pore water pressure occurs after the end of shaking particularly at shallow depths. Nevertheless, both sets of data indicate that post-seismic dissipation of excess pore water pressure starts at the deeper levels of the deposit (at about $t = 13.0$ s for $y = 2.2$ m), being progressively initiated at shallower depths (at about $t = 19.0$ s for $y = 8.8$ m), as typically observed in centrifuge experiments (e.g. Scott, 1986b; Coelho, 2007).

In addition, Figure 5.23 compares the vertical displacements predicted by FEMEPDYN with those registered in the numerical analysis carried out by Taborda (2011) at three different levels of the mesh: at the surface ($y = 10.0$ m), at about one quarter of the total depth of the thickness of the deposit ($y = 7.4$ m) and at a middle depth of the deposit ($y = 5.0$ m). It can be seen that, in general, a very good agreement was reached, with similar rates of settlement being predicted by both FE codes at every level. The small discrepancies observed at ground surface ($y = 10.0$ m) for the later stages of the simulation (final 5 s of the simulations) are likely a direct consequence of the aforementioned differences registered in terms of rate of dissipation of excess pore water pressures during the consolidation phase at shallow depths (Figure 5.22). Nevertheless, considering that different formulations of the equation of motion and different numerical algorithms are implemented into FEMEPDYN and ICFEP, it can be concluded that a remarkably good match between both codes was obtained.

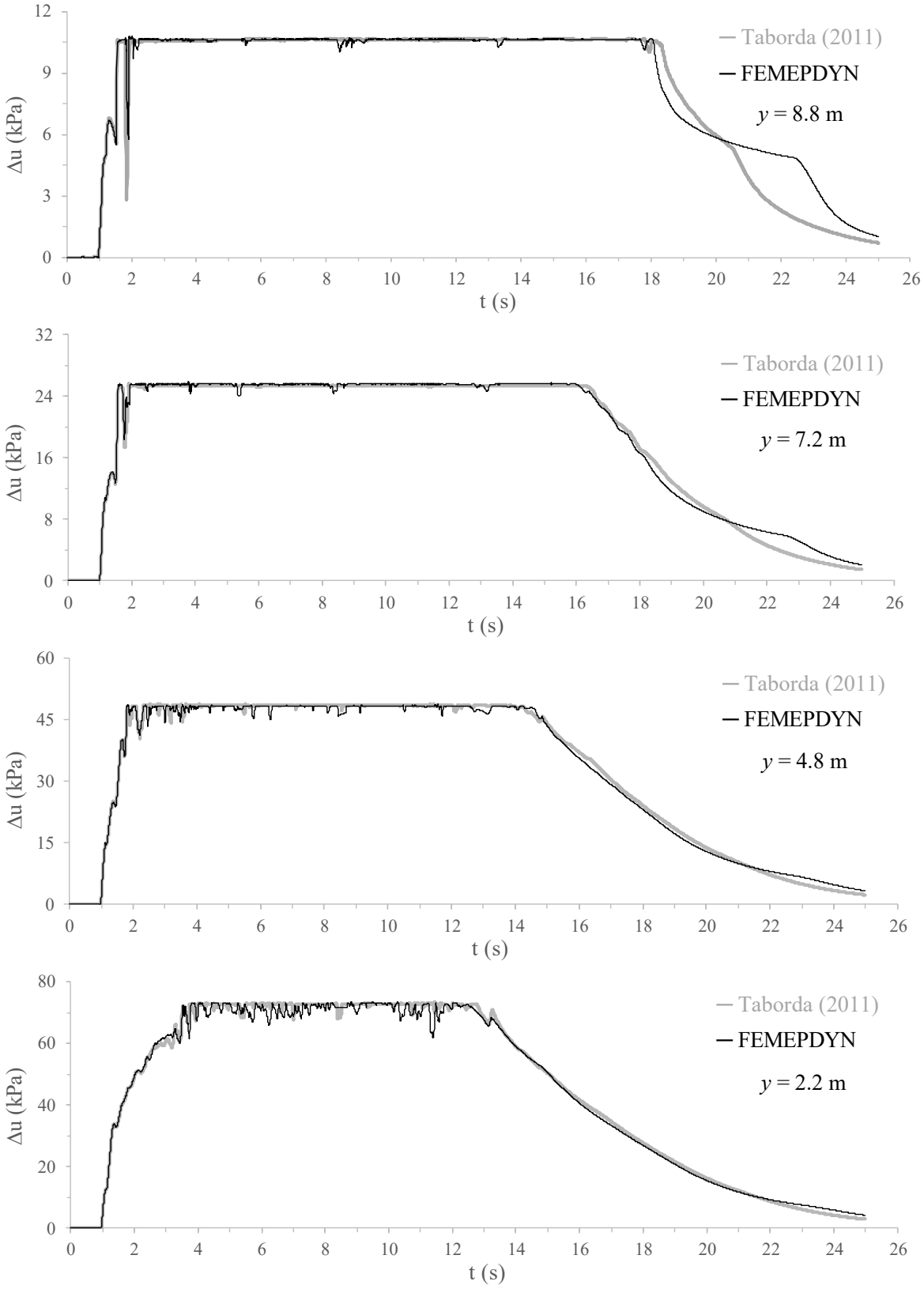

Figure 5.22 – Computed excess pore water pressure evolution with time for VELACS model 1.

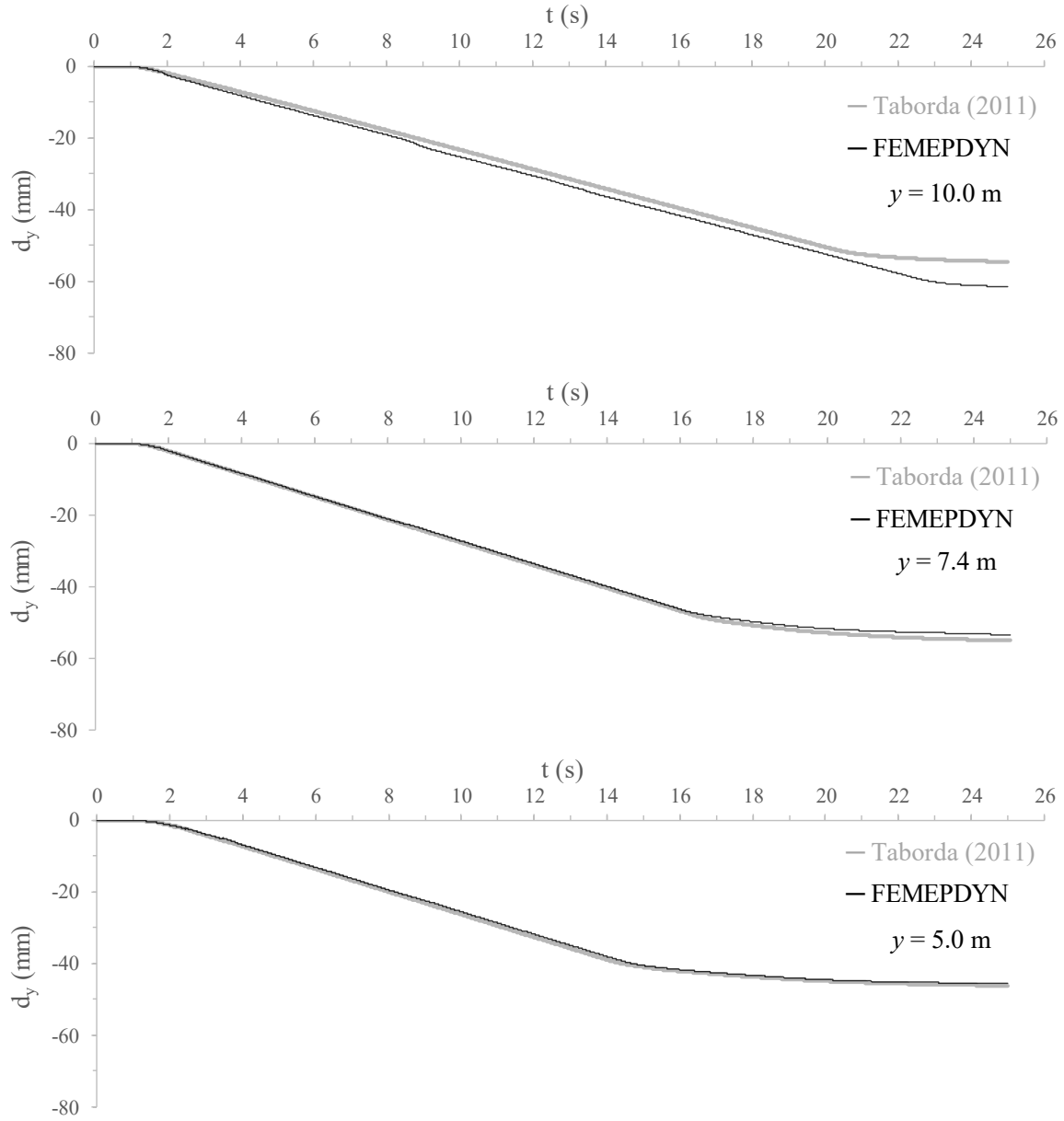

Figure 5.23 – Predicted evolution of vertical displacements with time for VELACS model 1.

5.3.2.2.4 VELACS model 12 – Embedded structure in stratified soil layers

5.3.2.2.4.1 General aspects of the numerical simulation

The second centrifuge experiment was performed at $N = 100.0$ $g = 980.7$ m/s^2 and included a solid structure partially embedded in a thin deposit of Bonnie silt and in an underlying moderately dense ($D_r \approx 60$ %) deposit of Nevada sand (Figure 5.15). Despite the 3D nature of the experiment, due to the significant computational cost that would involve its 3D modelling, a 2D plane strain analysis was carried out by Taborda (2011). This simplification led to the simulation of a strip foundation, rather than a square foundation. As a result, a correction to the contribution of the structure to the initial stress state was applied by the author to better replicate the field stress state (i.e. the stress state measured in the centrifuge experiment),

following the approach outlined by Popescu and Prevost (1993). Specifically, rather than 150 kPa, it was considered that the vertical stress induced by the structure in the underlying deposit of sand was only 63.3 % of this value (i.e. 95.0 kPa). In effect, based on the results of a small parametric study involving a 2D plane strain analysis and a 3D analysis, Popescu and Prevost (1993) observed that, for the problem under analysis, similar settlements were obtained in the two different types of analysis when this correction factor was applied to the self-weight of the structure in the 2D plane strain analysis. This means that the mass density of the structure, ρ, which is independent of the scale (Table 5.5), was estimated based on the weight necessary to apply a vertical stress of 95.0 kPa to the underlying deposit of sand during the generation of initial stresses – Equation 5.114 (Taborda, 2011).

$$\rho = \frac{\gamma_{sat,\,1\,g}}{g} = \frac{\Delta\sigma'}{g\,H} = \frac{95.0}{9.81 \times 4.0} = 2.421 \text{ g/cm}^3 \tag{5.114}$$

Furthermore, it is noteworthy that the structure was simulated as a rigid block, with its response being described by a linear elastic model with typical stiffness properties of aluminium: a shear modulus of $G = 25.9$ GPa and a Poisson's ratio of $\nu = 0.35$ (Taborda, 2011). No interface elements were considered between the structure and the surrounding soil in the numerical analysis.

With respect to the deposit of Nevada sand, the bounding surface plasticity model was employed to simulate its mechanical response, with identical model parameters to those adopted in the previous centrifuge model (Table 5.4). The deposit of Nevada sand was characterised by an initial void ratio of $e_0 = 0.661$, corresponding to an initial relative density of $D_r \approx 60$ %. Thus, the saturated unit weight under *1 g* conditions was, in this case, of $\gamma_{sat,\,1\,g} = 19.67$ kN/m^3 (Equation 5.115), resulting in a mass density of $\rho = 2.005$ g/cm^3 (Equation 5.116). Moreover, since the hydraulic conductivity is also a function of the void ratio (among other parameters), $k_{x,\,1\,g} = k_{y\,1\,g} = 5.6 \times 10^{-5}$ m/s (under *1 g* conditions) was adopted in this simulation. This value was scaled by *N* to account for the centrifugal acceleration used in this test (i.e. $k_{x,\,100\,g} = k_{y\,100\,g} = 5.6 \times 10^{-3}$ m/s was employed in the simulation).

$$\gamma_{sat,\,1\,g} = \frac{(G_s + e)\,\gamma_{w,\,1\,g}}{1.0 + e} = \frac{(2.67 + 0.661) \times 9.81}{1.0 + 0.661} = 19.67 \text{ kN/m}^3 \tag{5.115}$$

$$\rho = \frac{\gamma_{sat,\,1\,g}}{g} = \frac{19.67}{9.81} = 2.005 \text{ g/cm}^3 \tag{5.116}$$

In relation to the Bonnie silt, as justified before, an elastic linear model coupled with a Mohr-Coulomb failure criterion was used to model its response, with the adopted model parameters being listed in Table 5.6. Moreover, taking into account that the material was placed in the centrifuge model with a water content of about 30 % and that the density of the solid particles, G_s, was estimated as 2.67, an initial void ratio of $e_0 = 0.80$ (Equation 5.117),

an unit weight under 1 g conditions of $\gamma_{sat,\,1\,g} = 18.91$ kN/m^3 (Equation 5.118) and a mass density of $\rho = 1.927$ g/cm^3 (Equation 5.119) were considered in the numerical simulation (Taborda, 2011).

$$e = G_s\, w = 2.67 \times 0.30 = 0.80 \tag{5.117}$$

$$\gamma_{sat,\,1\,g} = \frac{(1.0 + w)\, G_s\, \gamma_{w,\,1\,g}}{1.0 + w} = \frac{(2.67 + 0.30) \times 2.67 \times 9.81}{1.0 + 0.30} = 18.91 \text{ kN/m}^3 \tag{5.118}$$

$$\rho = \frac{\gamma_{sat,\,1\,g}}{g} = \frac{18.91}{9.81} = 1.927 \text{ g/cm}^3 \tag{5.119}$$

The hydraulic conductivity of Bonnie silt under 1 g conditions was estimated as $k_{x,\,1\,g} = k_{y\,1\,g} = 1.468 \times 10^{-8}$ m/s, leading to $k_{x,\,100\,g} = k_{y\,100\,g} = 1.468 \times 10^{-6}$ m/s after scaling (Taborda, 2011). Note that, as expected, the permeability of Bonnie silt is significantly smaller than that of Nevada sand (more than three orders of magnitude).

With respect to the pore fluid, it was only required to specify its bulk modulus, with an identical value to that reported by Taborda (2011) being adopted: $K_f = 2.2$ GPa.

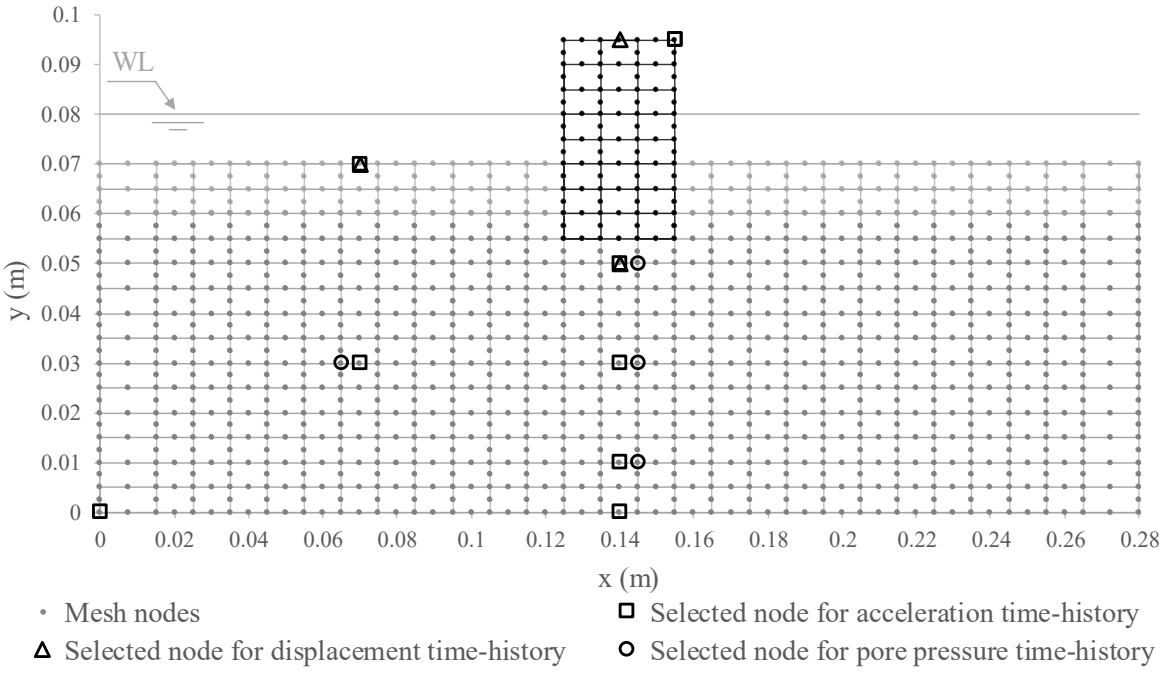

Figure 5.24 – Finite element mesh and selected nodes for plotting results for VELACS model 12.

The FE mesh was also similar to that adopted by Taborda (2011), consisting of 393 hybrid eight-noded isoparametric quadrilateral elements with pore pressure degrees of freedom at the corner nodes. As shown in Figure 5.24, a size of 0.01 x 0.005 m^2 (width x height, in model scale) was adopted for all solid elements, except for those located near the lateral boundaries of the model, which were characterised by a larger width of 0.015 m (in model scale). Although identical meshes are employed, it should be mentioned that the order of Gauss numerical integration employed in the analysis performed by Taborda (2011) was different

from that employed in the present analysis. Specifically, while in the simulation performed by Taborda (2011) a second-order integration was performed by employing 8-noded elements having 4 Gauss points, a third-order integration was carried out in the present analysis by using 8-noded elements with 9 Gauss points, since it has been suggested to lead to more reliable results for isoparametric displacement-based finite element procedures (Bathe, 1996).

The first phase of the numerical simulation comprised the generation of the initial effective stress state. The methodology used to perform this part of the calculation is described in detail in the following section, together with the obtained results. A dynamic FE analysis was subsequently performed, comprising a total of 1550 increments of 0.1 ms, resulting in a total duration of 0.155 s in model scale (i.e. 15.5 s in prototype scale). Following the strategy adopted by Taborda (2011), the dissipative version of the Newmark time-integration scheme ($\alpha = 0.3025$ and $\beta = 0.60$) was used during this phase of the analysis. As pointed out by Taborda (2011), since Rayleigh damping was not employed neither for the soil deposits nor for the structure, the numerical damping introduced by Newmark's method played an important key role in the mitigation of the spurious high-frequency oscillations typically observed in this type of problems.

In terms of dynamic boundary conditions, the horizontal acceleration time-history depicted in Figure 5.25 was applied to the nodes located along the bottom, as well as to the nodes belonging to the lateral boundaries of the FE mesh, in order to replicate the influence of the rigid walls of the centrifuge container used in the experiment (Taborda, 2011). Conversely, no vertical accelerations were applied and, therefore, the vertical displacement of the nodes on the bottom boundary were restricted to achieve equilibrium.

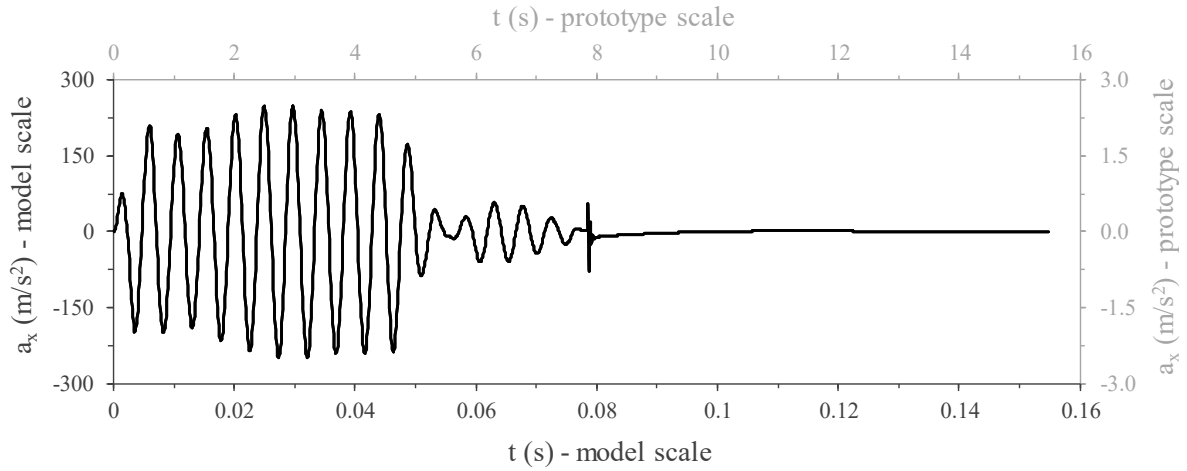

Figure 5.25 – Horizontal acceleration time-history for VELACS model 12.

Regarding the hydraulic boundary conditions, the structure was considered impervious and, therefore, the pore fluid and solid phase degrees of freedom of nodes common to both soil elements and structural elements were tied in the direction perpendicular to that defined by

the soil-structure interface. Similarly, the lateral and bottom boundaries of the model were considered impermeable, meaning that the pore fluid and solid phase nodal degrees of freedom were also tied in the direction perpendicular to each boundary. In addition, to simulate the existence of 1.0 m of water level above the ground surface, a value of 9.81 kPa was prescribed to every node belonging to the top surface of the Bonnie silt layer. Naturally, the position of the water level was also considered during the generation of the initial effective stresses, as discussed in the following section.

5.3.2.2.4.2 Generation of the initial effective stress state

Due to the existence of the structure, the initial effective stress state cannot be simply generated by assuming "greenfield conditions" (Potts and Zdravkovic, 1999), as performed for VELACS model 1. Indeed, the accurate replication of the centrifuge test preparation would involve the simulation of the following six steps: (1) deposition of Nevada sand until the foundation level of the structure (i.e. $y = 0.055$ m in model scale – Figure 5.24); (2) placement of the structure; (3) deposition of the remaining deposit of Nevada sand (i.e. until reaching $y = 0.06$ m in model scale); (4) deposition of the 0.1 m-thick layer of Bonnie silt; (5) saturation of the model and subsequent raising of the water level until reaching the final water level of $y = 0.08$ m in model scale; (6) increasing of the centrifugal acceleration. Although modelling such a detailed process would be possible, the gain in accuracy would probably be very limited, while bringing significant complexity to this phase of the analysis (Taborda, 2011). Therefore, the author decided to adopt a simple gravity loading procedure, involving the incremental application of body forces to the elements of the mesh, considered weightless at the start of the analysis. Concurrently, a hydrostatic pore water pressure profile characterised by a linear variation of the pore water pressures from 9.81 kPa at the top of the Bonnie silt layer to about 78.48 kPa at the bottom of the Nevada sand deposit was gradually introduced in the analysis (Taborda, 2011).

In the present calculation, since a gravity procedure involving the gradual increase of the body forces was not available in FEMEPDYN, it was decided to employ a different strategy, consisting of the following three different stages:

(1) Activation of the elements representing Nevada sand and Bonnie silt deposits; in addition, activation of the elements representing the embedded part of the structure (i.e. elements of the structure below $y = 0.07$ m – Figure 5.24); at this stage, the constitutive model used for Bonnie silt was assigned to this latter set of elements, meaning that a horizontal 1.0 m-thick deposit of Bonnie silt extending from the left to the right boundary of the model was considered at this stage; due to the simple geometry of the model at this stage, the initial stresses were generated using a K_0-procedure (i.e. assuming "greenfield conditions") using $K_0 = 0.5$ for both Nevada sand and Bonnie silt deposits; moreover, a hydrostatic pore water profile characterised by

a linear variation of the pore water pressures from 9.81 kPa at the top of the Bonnie silt layer to about 78.48 kPa at the bottom of the Nevada sand deposit was introduced in the analysis, allowing for the computation of the effective stress state by applying Terzaghi's principle.

(2) Switching of the material used to model the elements comprising the embedded part of the structure from that adopted for Bonnie silt to that selected for the structural elements.

(3) Activation of the remaining elements representing the structure in a total of five increments corresponding to the layers of elements above the ground level (Figure 5.24).

During this phase, drained conditions were prescribed for soil elements, while elements representing the structure were considered non-porous. Moreover, conventional static displacement boundary conditions were adopted during this phase, consisting of the restriction of the horizontal displacements along the lateral boundaries of the model, as well as restriction of both horizontal and vertical displacements along the bottom boundary of the model.

Table 5.7 – Model parameters adopted for the generation of the initial stress state of VELACS Model 12 (Taborda, 2011).

Model parameters	Nevada sand	Bonnie silt	Structure
Linear elasticity			
G_{tan} (in GPa)	26.3	26.3	26.3
ν	0.333	0.333	0.333
Strength (Mohr-Coulomb failure criterion)			
c' (in kPa)	0.0	5.0	–
ϕ' (in °)	30.0	28.0	–

In terms of material properties, a similar strategy to that adopted by Taborda (2011) was followed, consisting of using a linear elastic model coupled with the Mohr-Coulomb failure criterion to describe the response of both Bonnie silt and Nevada sand during this phase of the analysis, rather than the more sophisticated constitutive models adopted in the subsequent dynamic phase (i.e. the BSPM for Nevada sand). Moreover, to prevent the occurrence of large shear stress localisations at the soil-structure interface, which could have a detrimental impact on the subsequent dynamic phase, similar stiffness characteristics were adopted for all materials (Table 5.7), as reported by Taborda (2011). Naturally, at the start of the dynamic phase, the BSPM with the model parameters listed in Table 5.4 was assigned to Nevada sand, with the elastic and plastic state parameters being initialised for each Gauss point according to the methodology described in Section 5.2.3. Similarly, the model parameters assigned to Bonnie silt and to the structure were changed to those indicated in Section 5.3.2.2.2.

Figure 5.26 compares the effective stresses obtained by FEMEPDYN with those reported by Taborda (2011) for three different horizontal alignments: $y = 0.0025$ m (close to the bottom of the model), $y = 0.0325$ m (at about the middle of the deposit of Nevada sand) and $y = 0.0525$ m (close to the top of the deposit of Nevada sand). Note that the dimensions are presented in model scale (to be easily compared with the dimensions of the model – Figure 5.24), while stresses are independent of the scale. Moreover, due to the symmetry of the model (Figure 5.24), the obtained effective stresses are symmetric about the axis of symmetry of the structure ($x = 0.14$ m) and, therefore, only those obtained for the left part of the model are depicted in Figure 5.26.

It can be seen that, although different methodologies were employed during this phase of the analysis, a very good match between the results obtained by both FE codes was observed. Furthermore, the small discrepancies seem essentially limited to the effective stresses obtained for zones of the model close to the structure, with a maximum discrepancy of about 4.1 kPa being registered for the vertical effective stress, σ'_{yy}, at $(x, y) = (0.14, 0.0525)$ m. Note that this value corresponds to a maximum relative difference of about $(78.8 - 74.7)/78.8 \approx 5.2\,\%$. Interestingly, both sets of data seem to suggest that the influence of the structure on the deposit of Nevada sand is particularly noticeable until a distance of about 0.5 *B* to the side of the lateral face of the solid structure (with *B* representing the width of the structure), being practically negligible for distances greater than 2.0 *B*.

Complementarily, Figure 5.27 shows the obtained results for two vertical alignments: $x = 0.07$ m (corresponding half distance from the left boundary to the structure) and $x = 0.14$ m (axis of the structure). Once again, it can be concluded that the differences are very limited, with a slightly smoother increase of the effective stresses being registered in the computation performed using FEMEPDYN.

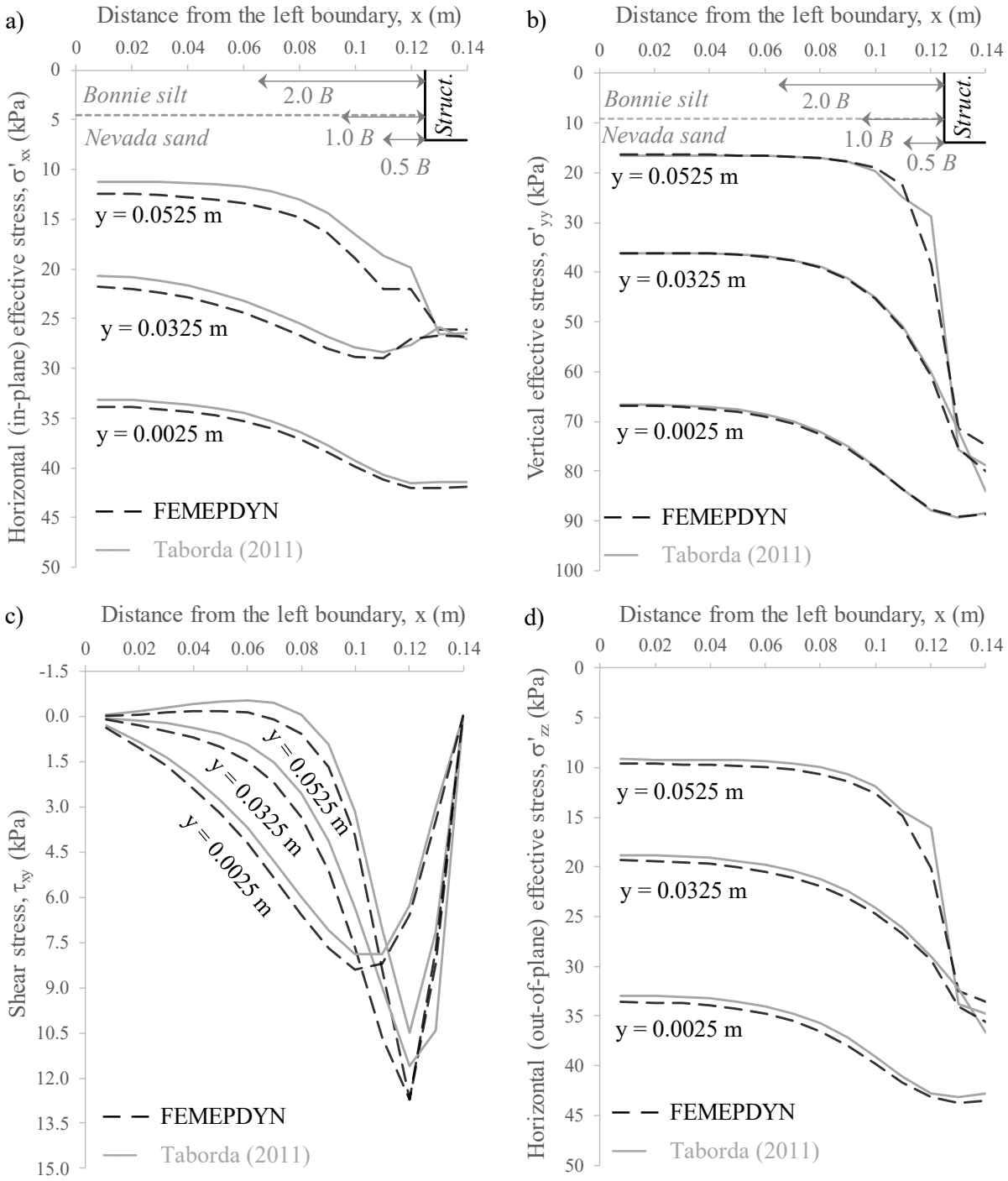

Figure 5.26 – Computed initial effective stresses for three horizontal alignments of VELACS Model 12.

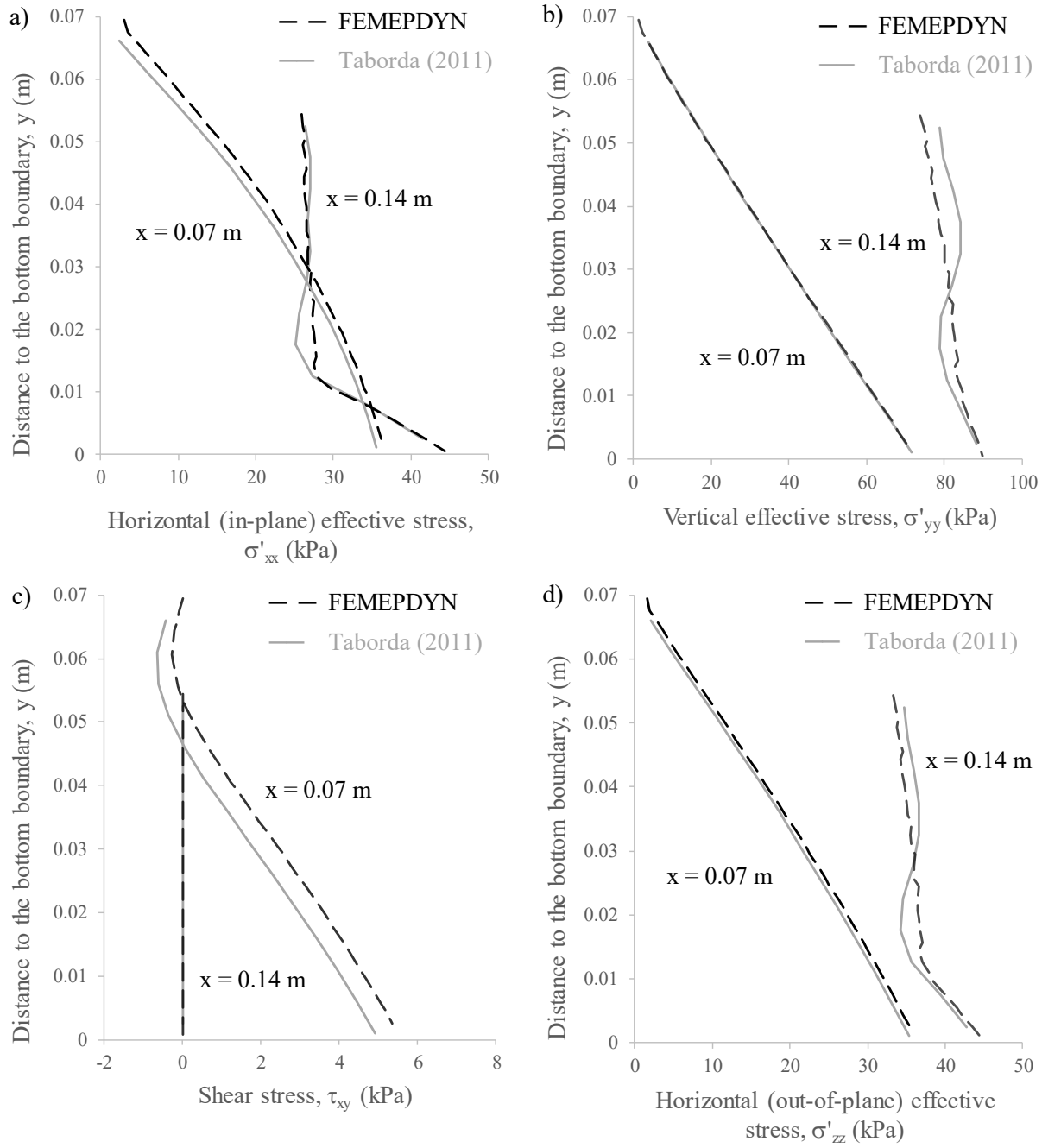

Figure 5.27 – Computed initial effective stresses for two vertical alignments of VELACS Model 12.

5.3.2.2.4.3 Dynamic analysis

Figure 5.28 compares the horizontal acceleration time-histories obtained by FEMEPDYN with those presented in Taborda (2011) for a vertical alignment coincident with the axis of the structure (except for the top horizontal acceleration time-history, which was registered at the top right corner of the structure: $(x, y) = (15.5, 9.5)$ m in prototype scale). Note that all obtained results were converted to prototype scale, by using the relations presented in Table 5.5, to facilitate their interpretation.

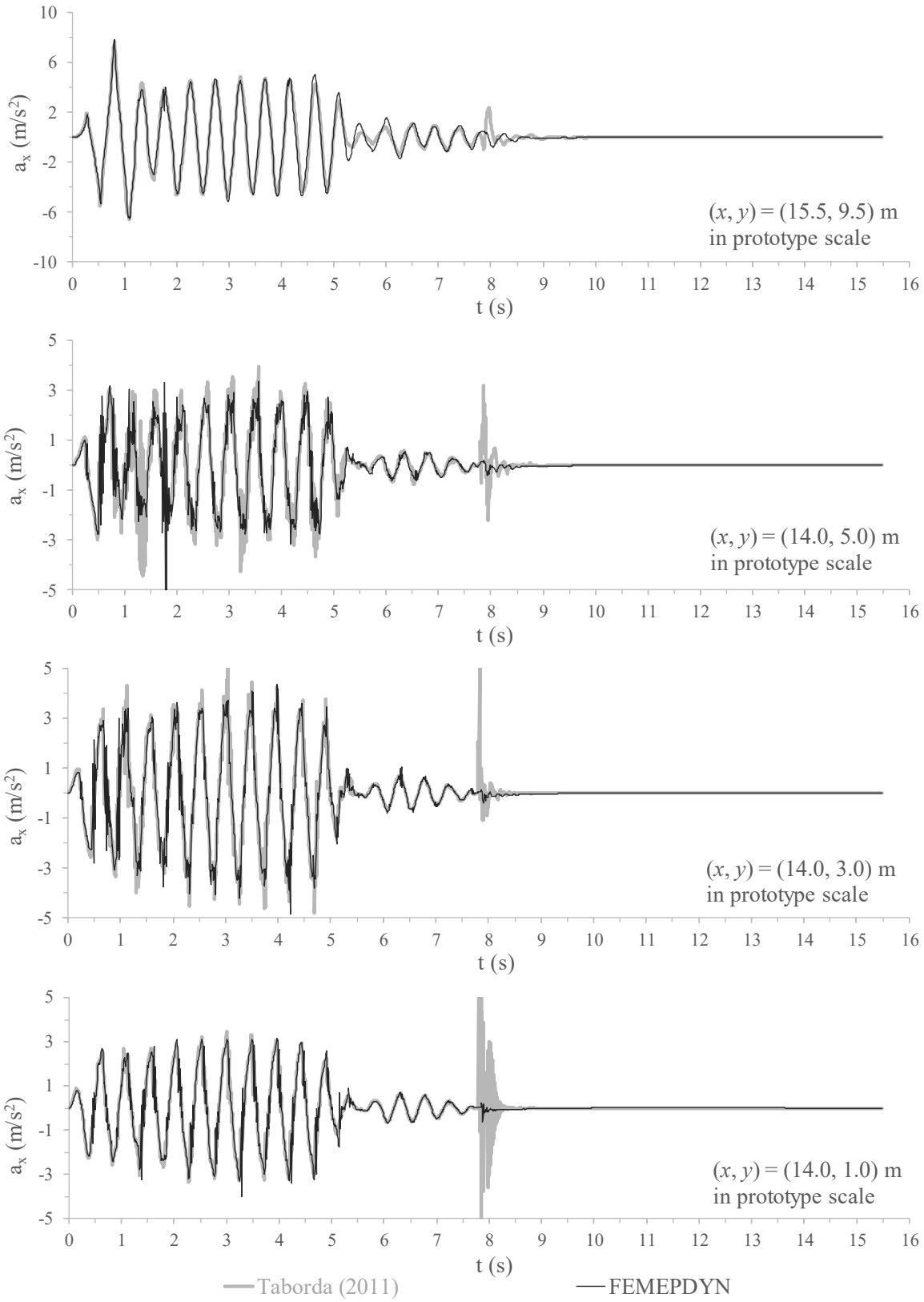

Figure 5.28 – Computed horizontal acceleration time-histories for VELACS model 12 for a vertical alignment coincident with the axis of the structure.

It can be observed that an excellent agreement between both sets of data was obtained, with an increase in the amplitude of the accelerations being observed from the bottom to the top

levels of the sand deposit. As expected, the accelerations at the top corner of the structure are significantly higher than those registered at the base of the structure. In effect, as established by the theory of wave propagation in an isotropic elastic medium (e.g. Kramer, 1996), when a body wave reaches a free surface, due to impossibility of transmitting stresses, the amplitude of the displacement of the boundary is double of that of the incident wave.

Similarly, Figure 5.29 shows that a very good agreement between the horizontal acceleration time-histories computed by FEMEPDYN and those presented in Taborda (2011) was obtained for a vertical alignment corresponding to half distance from the left boundary to the structure (i.e. $x = 7.0$ m, in prototype scale), even though different constitutive relationships were employed for the 1 m-thick deposit of Bonnie silt. This suggests that the constitutive model selected for Bonnie silt has limited impact on this aspect of soil response.

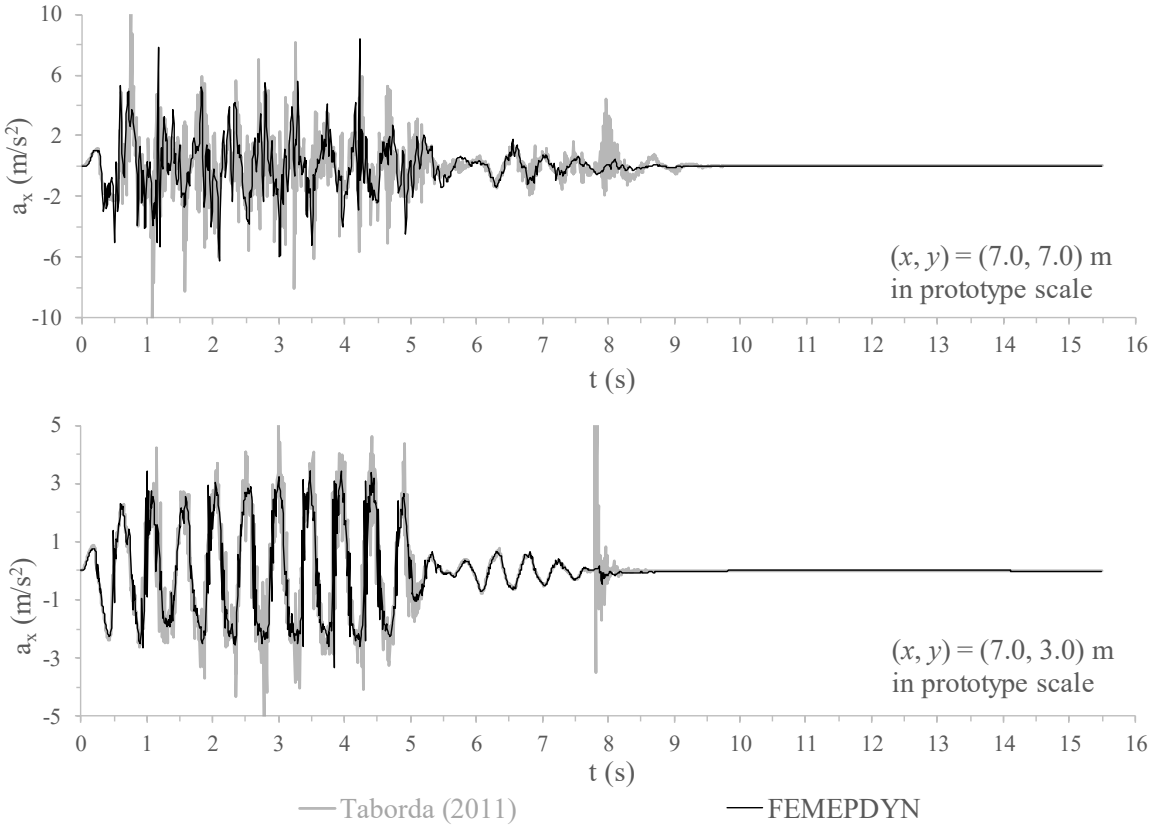

Figure 5.29 – Computed horizontal acceleration time-histories for VELACS model 12 for a vertical alignment corresponding to half distance from the left boundary to the structure.

In addition, Figure 5.30 compares the vertical acceleration time-histories computed by FEMEPDYN with those depicted in Taborda (2011) at the top right corner of the structure ($x = 15.5$ and $y = 9.5$). Once again, it can be observed that a remarkable agreement was obtained between both sets of data. Interestingly, despite null vertical accelerations having been imposed at the bottom boundary of the mesh, large vertical accelerations were computed at the top of the structure. As pointed out by Taborda (2011), this suggests that the structure

exhibited rocking response – i.e. the structure oscillated in the vertical direction due to the generation of unbalanced forces (Coelho, 2007).

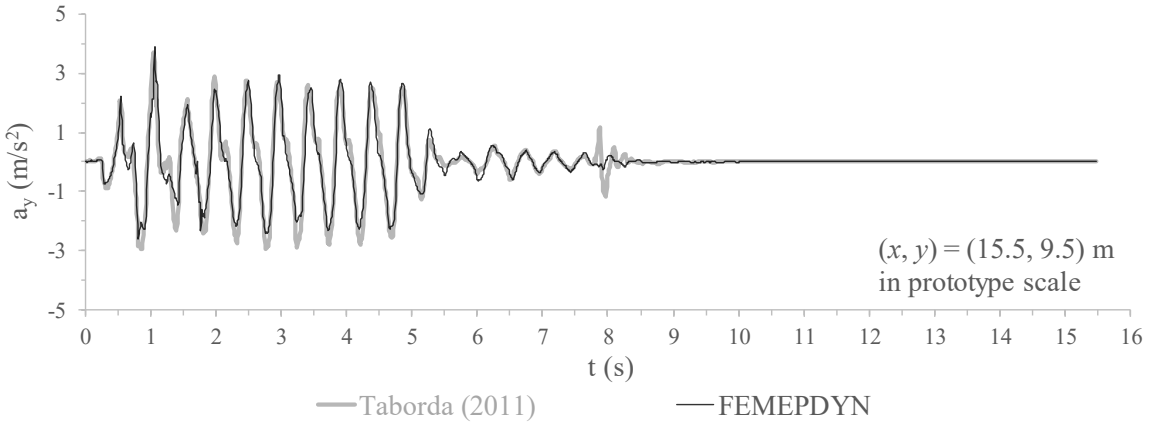

Figure 5.30 – Computed vertical acceleration time-histories at the top right corner of the structure for VELACS model 12.

Figure 5.31 compares the excess pore water pressure computed by FEMEPDYN with those reported by Taborda (2011). It can be observed that, in general, a very good agreement was obtained between both sets of data. This is particularly evident for the results registered at the three positions underneath the structure (i.e. for which $x = 13.75$ m). At the position farthest away from the influence of the structure (i.e. at position $(x, y) = (6.75, 3.0)$ m), small discrepancies between results obtained by FEMEPDYN and those presented in Taborda (2011) can be observed, probably due to the larger influence of the response of Bonnie silt on the overall response of the system at this location.

Finally, Figure 5.32 compares the structure settlement time-history obtained by FEMEPDYN with that reported by Taborda (2011). It can be observed that slightly smaller settlements were registered in the present analysis. However, taking into account the complexity of the present analysis, involving highly non-linear response under very low effective stresses, the different constitutive models used to simulate the response of Bonnie silt and the differences between the algorithms implemented in both FE codes, it can be considered that the results are sufficiently close to conclude that the implementation of the version of the BSPM proposed by Taborda (2011) and Taborda *et al.* (2014) was successful.

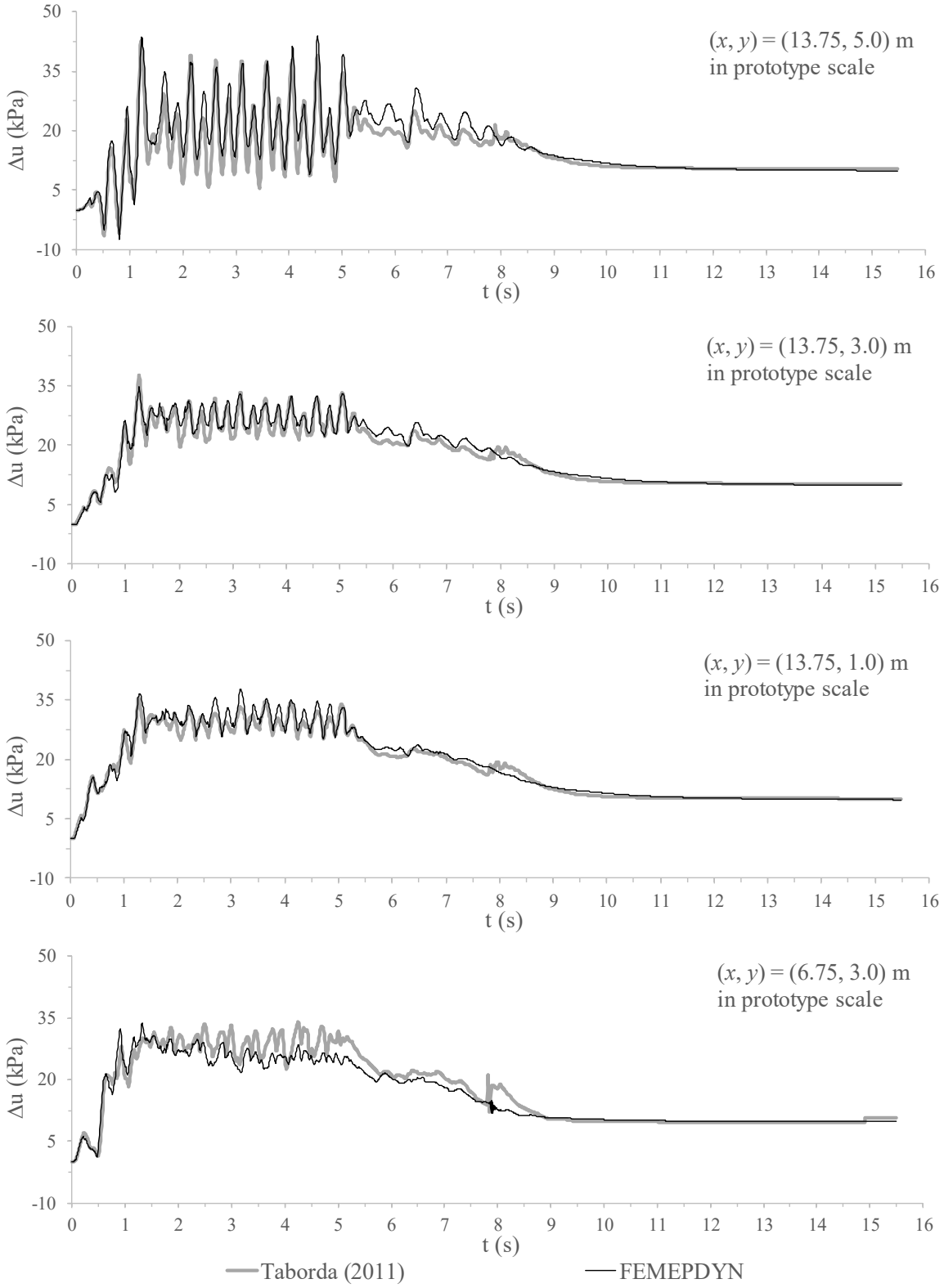

Figure 5.31 – Computed excess pore water pressure evolution with time for VELACS model 12.

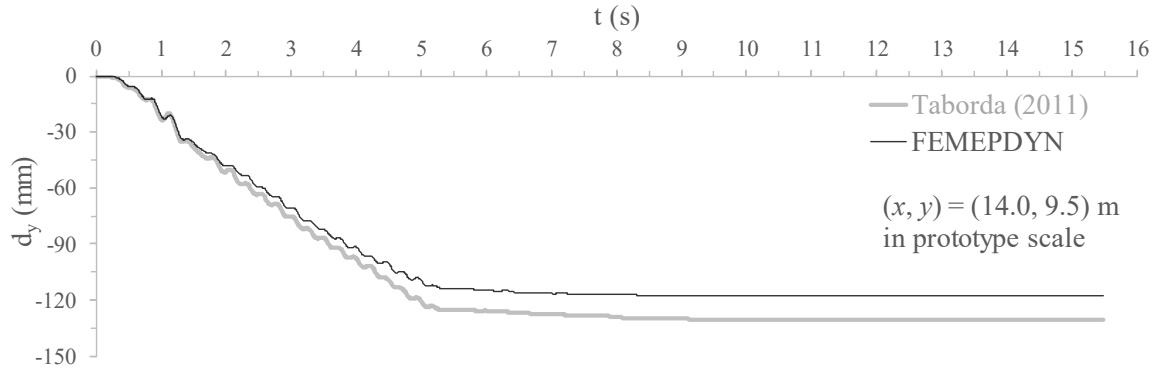

Figure 5.32 – Evolution of structure settlement with time for VELACS model 12.

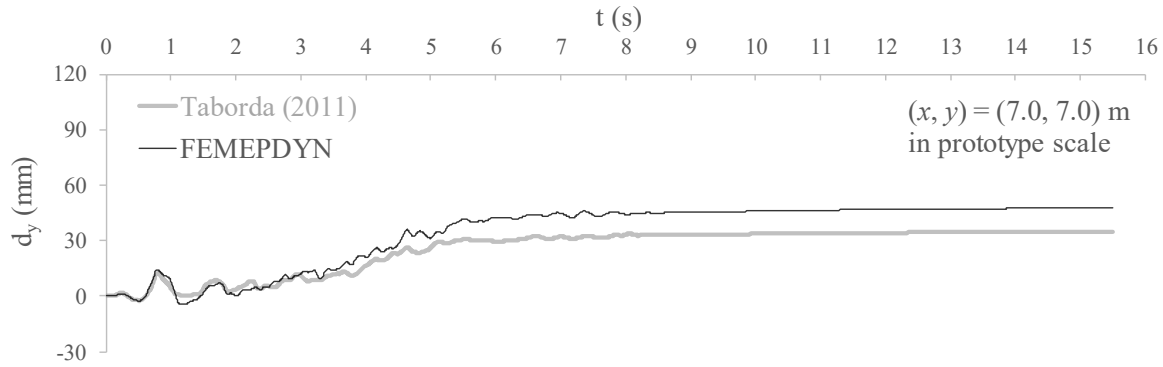

Figure 5.33 – Evolution of settlement with time at the surface of Bonnie silt for VELACS model 12.

5.3.3 Inherent fabric anisotropy formulation

To validate the implementation of the inherent fabric anisotropy component of the model (Section 4.3.3), an undrained cyclic direct simple shear (UCDSS) test on Fraser River sand was simulated, with the obtained results being compared with those presented in Williams (2014). As mentioned before, this author developed an inherent fabric anisotropy formulation, which was coupled with the version of the Bounding Surface Plasticity model proposed by Taborda *et al.* (2014) and implemented into the Imperial College Finite Element Program (ICFEP). It is, therefore, possible to directly compare data presented by Williams (2014) with results obtained by FEMEPDYN.

The available data indicate that a sample of Fraser River sand having an initial void ratio of $e = 0.818$ and subjected to an initial vertical effective stress of $\sigma'_v = 50.0$ kPa and to a shear stress of $\tau = 0.0$ kPa was subjected to 4 loading cycles characterised by a shear stress oscillation of $\Delta\tau = \pm 5.0$ kPa. This solicitation was simulated by applying uniform tangent stresses to the nodes located along the top boundary of the element (Figure 5.4b).

A first simulation was performed using the original version of the model (i.e. by adopting $a = 1.0/3.0$, $v_A = 0.0$ and $k_A = 1.0$). An additional simulation was subsequently performed using the extended version of the model with $a = 0.20$, $v_A = 5.0$ and $k_A = 0.4$. The model parameters employed in both analyses are indicated in Table 5.8.

Table 5.8 – Model parameters for Fraser River sand (Williams, 2014).

Model parameter	Inherent fabric isotropy	Inherent fabric anisotropy
Non-linear elasticity		
C_g	422.0	422.0
m_g	(1)	(1)
n_g	0.500	0.500
κ	2.000	2.000
a_1	0.440	0.440
γ_1	1.60×10^{-3}	1.60×10^{-3}
p'_{min}	Not used	Not used
G_{min}	Not used	Not used
ν	0.200	0.200
Model surfaces		
p'_{ref}	101.3 kPa	101.3 kPa
$(e_{CS})_{ref}$	0.840	0.840
λ	0.030	0.030
ξ	0.660	0.660
$\boldsymbol{v_A}$	**0.000**	**5.000**
M_c^c	1.376	1.376
M_e^c	1.000	1.000
k_c^d	1.670	1.670
k_e^d	1.214	1.214
k_c^b	2.670	2.670
k_e^b	1.940	1.940
m	0.005	0.005
p'_{YS}	1.0 kPa	1.0 kPa
Plastic hardening modulus		
A_0	1.000	1.000
h_0	0.100	0.100
γ	0.650	0.650
e_{lim}	0.946	0.946
α	1.000	1.000
μ	0.000	0.000
β	-0.300	-0.300
$\boldsymbol{k_A}$	**1.000**	**0.400**
$h_{f,min}$	Not used	Not used
$h_{f,max}$	Not used	Not used
Shearing-induced fabric component		
H_0	12 600.0	120 000.0
ζ	2.000	0.600
H_{max}	Not used	Not used
Inherent fabric anisotropy component		
$\boldsymbol{a}$	**0.333**	**0.200**

(1) For the purpose of validation, Equation 4.25 was employed for the calculation of the small-strain shear modulus, as defined in the original formulation of the model. This means that the model parameter m_g, which is used in Equation 4.99 and 4.100, is not necessary in the present simulations.

Figure 5.34 depicts the results obtained when using the original version of the model (i.e. in the first of the two simulations), while Figure 5.35 presents the results obtained when the inherent fabric anisotropy component of the model was activated. In both cases, the results obtained by FEMEPDYN are compared with those presented in Williams (2014).

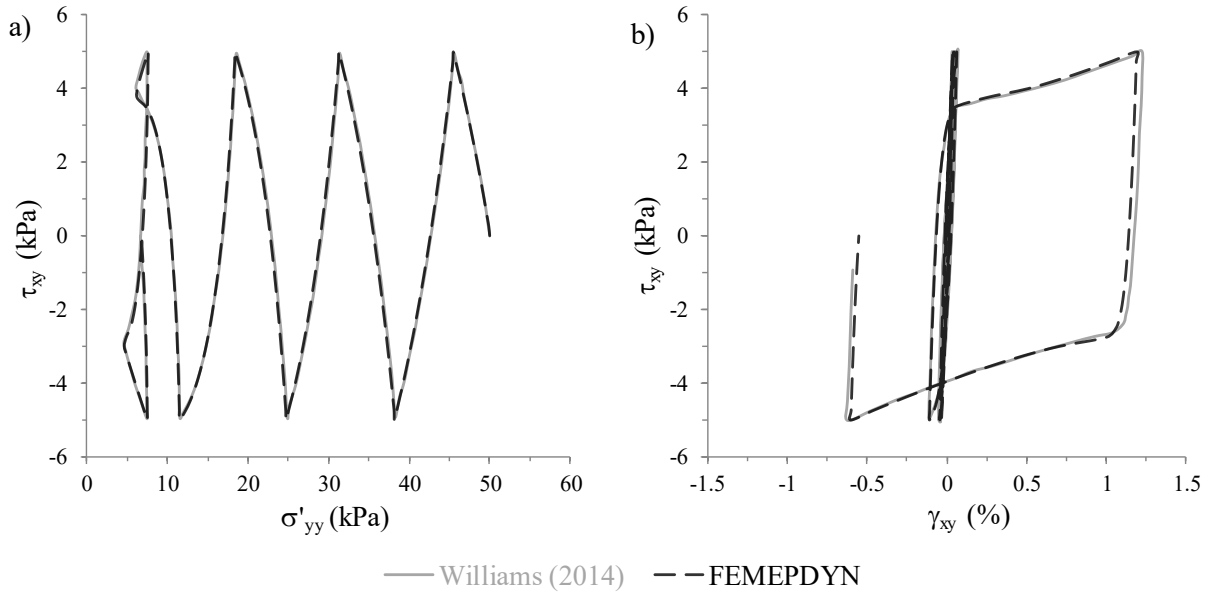

Figure 5.34 – Numerical simulation of an UDSS test using the original version of the model: (a) shear stress – vertical effective stress and (b) shear stress – shear strain.

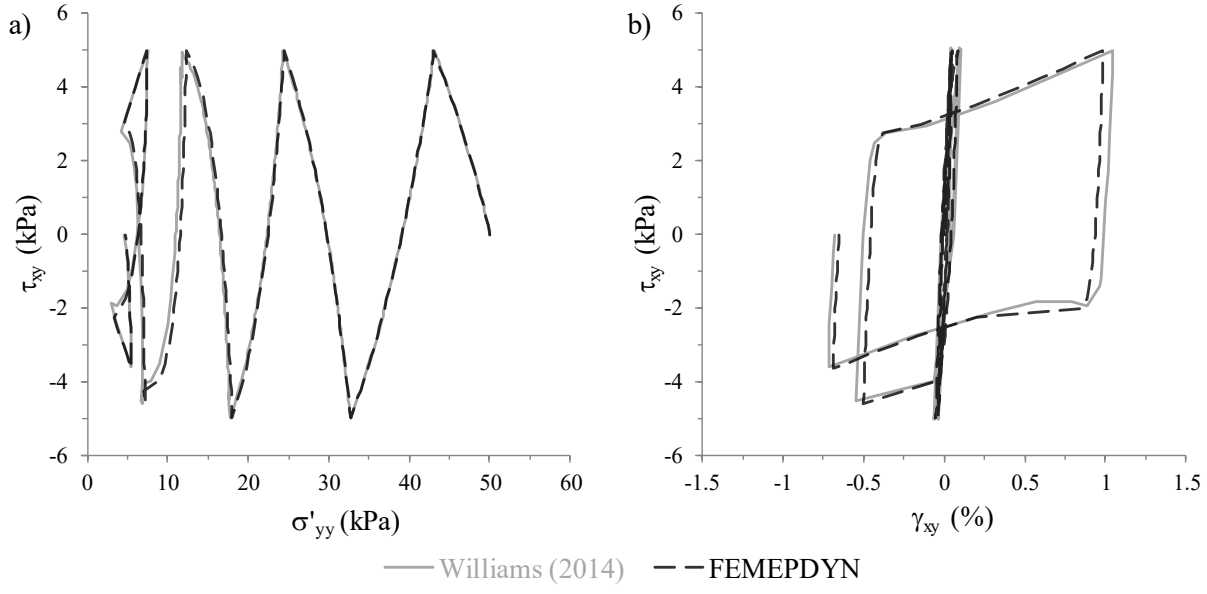

Figure 5.35 – Numerical simulation of an UDSS test using the inherent fabric anisotropy component of the model: (a) shear stress – vertical effective stress and (b) shear stress – shear strain.

It can be seen that a very good agreement was obtained for both simulations. The small discrepancies are believed to arise from the use of different numerical tolerances, as well as from inaccuracies introduced when digitising the results presented in Williams (2014). It is interesting to note that, for these loading conditions and model parameters, the introduction

of the inherent fabric anisotropy led to a faster decrease of the vertical effective stress with loading.

5.4 Summary and conclusions

In the first part of this chapter, the numerical algorithms used for the integration of the bounding surface plasticity model (BSPM) model were comprehensively described. Specifically, due to its robustness and simplicity, a modified forward Euler scheme with automatic sub-stepping and error control, as introduced by Sloan *et al.* (2001), was selected. This scheme involves an initial elastic trial, eventually followed by an elasto-plastic computation once the effective stress point intersects one of the yield surfaces or is located on one of them. The size of the strain step is automatically adapted to the magnitude of the error in computed stresses and plastic state parameters, resulting in a computationally efficient scheme. Moreover, an unconditionally convergent algorithm based on the well-established Pegasus method (Dowell and Jarratt, 1972) is used to find the intersection of the stress path with the yield surface during elastic trial, as proposed by Sloan *et al.* (2001). The rate of convergence of the algorithm is enhanced by reducing the search interval of the algorithm, as suggested by Hong *et al.* (2012). Additionally, a drift correction scheme is employed, when necessary, to prevent the effective stress point from being located out of the yield surface at the end of an elasto-plastic increment (i.e. to ensure that the consistency condition is satisfied, as required by elasto-plasticity theory).

The second part of this chapter focused on the validation of the implementation, by simulating both element laboratory tests and dynamic boundary-value problems. Starting with the former set of simulations, it included the numerical reproduction of drained isotropic compression tests, drained and undrained monotonic triaxial compression tests, undrained cyclic triaxial tests and undrained cyclic direct simple shear tests. It was shown that the numerical precision adopted in the calculations may affect the obtained results, particularly for large strains. Nevertheless, when using similar numerical precisions, it was shown that a remarkably good agreement was obtained between the results obtained by FEMEPDYN and those published in the literature (Taborda, 2011), both in terms of effective stress paths and stress-strain response. The newly developed code was subsequently applied to the simulation of boundary-value problems involving earthquake-induced liquefaction. Specifically, two different dynamic centrifuge experiments, performed as part of the large collaborative research project VErification of Liquefaction Analysis by Centrifuge Studies (VELACS), were reproduced. The first of these centrifuge experiments – VELACS model 1 – comprised a 10 m-thick (in prototype scale), level deposit of saturated loose Nevada sand subjected to horizontal motion on its base. Overall, a very good agreement between the results computed by FEMEPDYN and those presented in the literature (Taborda, 2011) was obtained in terms of horizontal acceleration time histories, as well as evolutions with time of excess pore water

pressures and vertical displacements. It is important to note that very similar results were obtained in terms of the moment at which cyclic mobility was initiated at each level and consequent modification of the horizontal accelerations, as well as initiation of excess pore water pressure dissipation at each level.

To complement the validation of the implementation of the original formulation of the BSPM into FEMEPDYN, a second centrifuge experiment – VELACS model 12 – was simulated. The second centrifuge experiment differed from the previous one by including a 6.0 m-thick (in prototype scale) solid structure partially embedded into a 6.0 m-thick (in prototype scale) deposit of fully-saturated relatively dense Nevada sand and a 1.0 m-thick (in prototype scale) low-permeability deposit of Bonnie silt. Although a different constitutive model had to be employed to characterise the response of Bonnie silt than that used in Taborda (2011), the obtained results were shown to be very similar in terms of simulated horizontal and vertical acceleration time histories, excess pore water pressure and settlements evolution with time. This suggested that FEMEPDYN can be applied to the simulation of boundary-value problems involving liquefaction-related phenomena and soil-structure interaction concurrently.

The final part of the validation routine consisted of simulating an UCDSS test using the extended version of the model (i.e. including the inherent fabric anisotropy component) and compare the obtained results with those presented in Williams (2014). Once again, a remarkable agreement between both sets of numerical data was obtained, suggesting that this additional component of the model was also successfully implemented into FEMEPDYN.

Chapter 6 CALIBRATION OF THE BOUNDING SURFACE PLASTICITY MODEL FOR HOSTUN SAND

6.1 Introduction

The formulation of a bounding surface plasticity model (BSPM) presented in the literature was comprehensively described in Chapter 4 and some alterations to that formulation were proposed. Using an explicit stress integration scheme (Chapter 5), the constitutive model was implemented into the dynamic finite element code FEMEPDYN, with its validation being performed against published results of numerical simulations of element laboratory tests, as well as simulations of centrifuge experiments. A very good agreement was obtained in both cases, suggesting that the implementation of the constitutive model into FEMEPDYN was performed successfully.

In this chapter, the constitutive model is calibrated for Hostun sand against the vast amount of laboratory test results presented in Chapter 2 and Chapter 3. While the majority of the model parameters are calibrated based on well-known features of the response of sand, computational analyses are required to assess the impact of the parameters lacking physical meaning on the modelled response and, based on the obtained results, decide on the best parameters. This is particularly true for the case of the model parameters defining the plastic hardening modulus, as well as the model parameters related to the inherent fabric anisotropy and shearing-induced fabric components, for which small parametric studies are presented to assess the effect of each model parameter on the modelled response in order to assist in the selection of its value. Two different sets of model parameters are obtained, one set for the original formulation of the model (Taborda *et al.*, 2014) and another set for the extended formulation which includes an inherent fabric anisotropy component (Chapter 4). The performance and modelling capabilities of both original and extended constitutive relationships are subsequently evaluated in the context of element laboratory testing (Chapter 7) and centrifuge testing (Chapter 8).

As pointed out in Chapter 2, it should be noted that some results presented in this chapter have already been published by the author and his supervisors in a scientific journal (Azeiteiro *et al.*, 2017a). Note, however, that the work published in this paper was developed as part of the present PhD research. As such, it is considered as original work in the present thesis and, therefore, citation to the paper is considered unnecessary.

6.2 Methodology

The calibration of a constitutive model consists of finding the set of parameters that allows for the best possible reproduction of the available experimental data. The complexity of this

process depends highly on the number of model parameters to be calibrated, as well as on the complexity of the model in itself. An increase in complexity is typically observed when the formulation of the constitutive model requires the calibration of model parameters having no physical meaning or that cannot be directly related to a given distinctive feature of sand response. In such case, optimisation techniques, such as genetic algorithms (e.g. Simpson and Priest, 1993; Pal *et al.*, 1996; Taborda *et al.*, 2008; Azeiteiro, 2008; Azeiteiro *et al.*, 2009; Taborda, 2011; Pedro, 2013) may be a valuable tool. In the present study, an alternative approach, which has been successfully applied to the calibration of BSPMs (e.g. Papadimitriou *et al.*, 2001a; Loukidis and Salgado, 2009; Taborda, 2011; Taborda *et al.*, 2014) was selected. This approach is termed "hierarchical" and consists of calibrating the model parameters sequentially according to a pre-established order of greater physical relevance and independence from other model parameters.

As pointed out by Loukidis and Salgado (2009) and Taborda (2011), the first components of the constitutive model to be calibrated are those defining clear aspects of sand response, namely the Critical state line (CSL) in the $e - p'$ plane, the critical state strength and elastic stiffness at small strains, whose model parameters are simply obtained by curve fitting over experimental data. Subsequently, the calibration process focuses on the quantities that, despite having a numerical nature, control well-known features of the response of sand. This includes the model parameters defining the position of the dilatancy surface, which identifies the phase transformation state (i.e. the state at which the response of sand changes from plastic contraction to plastic dilation), the model parameters controlling the position of the bounding surface, which is related to the occurrence of a maximum angle of shearing resistance, the model parameter defining the stress-dilatancy relationship and those controlling the reduction of the elastic stiffness with shearing. These model parameters can still be obtained by curve fitting over experimental data, with clear instructions on how to do it being provided in this chapter. Finally, trial-and-error procedures are required to calibrate the model parameters having no physical meaning, such as those related to the plastic hardening modulus, as well as to the shearing-induced fabric and inherent fabric anisotropy components. As detailed later, this last step of the calibration process is far more complex than the previous steps, particularly due to the interaction between some model parameters. To overcome this issue, parametric analyses are performed whenever necessary to identify more clearly the impact of each parameter on the computed response.

Table 6.1 summarises the hierarchical order adopted for the calibration of the constitutive model. It can be observed that higher-order components may be influenced by lower-order components. The opposite, however, is generally not true, i.e. lower-order components tend to be independent of higher-order components. For instance, the constitutive model establishes a dependency of the positions of the dilatancy and bounding surfaces on the position of the CSL on $e - p'$ plane and critical state strength, with the attributed orders (3 and 1, respectively) reflecting this aspect. Similarly, it is necessary to calibrate the model

parameters related to small-strain shear modulus (order 2) before those defining the reduction of the tangent shear modulus (order 5). Probably, the only exception consists of orders attributed to the shearing-induced fabric and inherent fabric anisotropy components (orders 7 and 8, respectively). Since the latter component is expected to affect the modelled cyclic response and, therefore, to require a readjustment of the model parameters related to the former component, it would be logical to switch the orders attributed to these components of the constitutive model. However, with the purpose of evaluating the impact of the inherent fabric anisotropy component on the modelled results, it was deemed important to obtain two different sets of model parameters: one of which excluding the inherent fabric anisotropy component (by setting $a = 0.333$, $v_A = 0.0$ and $k_A = 1.0$) and, therefore, implying the use of the formulation originally proposed by Taborda *et al.* (2014), while the second set of model parameters activating the inherent fabric anisotropy component. Apart from the numerical stability-related parameters, whose values are established in a subsequent phase of the process (order 9), the calibration of the set of model parameters compatible with the original version of the model is completed at the end of phase 7, while the calibration of the extended version is only completed at the end of phase 8.

Table 6.1 – Hierarchical order to the calibration of the BSPM parameters (Loukidis and Salgado, 2009).

Order	Component of the model	Parameters
1	Critical state line position on the $e - p'$ plane	$(e_{cs})_{ref}$, λ, ξ, p'_{ref}
	Critical state strength	M_c^c, M_e^c
2	Small-strain shear modulus	C_g, m_g, n_g
	Small-strain Poisson's ratio	ν
3	Position of the dilatancy surface	k_c^d, k_e^d
	Position of the bounding surface	k_c^b, k_e^b
4	Stress-dilatancy relationship	A_0
5	Reduction of the tangent shear modulus	κ, a_1, γ_1
6	Plastic hardening modulus	h_0, α, β, m, γ, e_{lim}, μ
7	Shearing-induced fabric	H_0, ζ
8	Inherent fabric anisotropy	a, v_A, k_A
9	Numerical stability-related parameters	p'_{min}, G_{min}, p'_{ys}, H_{max}, $h_{f,min}$, $h_{f,max}$

The element laboratory test results on Hostun sand, presented in Chapter 2 and Chapter 3, were employed in the calibration of the constitutive model. This includes bender element test results, drained and undrained monotonic triaxial compression and extension tests, as well as undrained cyclic triaxial tests performed on air-pluviated samples prepared to different initial

void ratios and consolidated under various isotropic and anisotropic stress states. Note that, although other strategies would have been possible, all test data were used during the calibration of the constitutive model. This was considered the most appropriate strategy to obtain a set of parameters able to reproduce the response of Hostun sand under different initial and loading conditions, which might be particularly important when using the constitutive model in the context of boundary-value problems (Chapter 8). Note that a similar approach was followed by Loukidis and Salgado (2009).

6.3 Critical state line

The position of the critical state line (CSL) on e – ln p' plane (Equation 4.2) plays a key role in the constitutive model, since it allows the definition of the state parameter, ψ (Equation 4.3), which, in turn, is used to determine the positions of the bounding and dilatancy surfaces (Equation 4.4 and 4.5, respectively) and, consequently, the gradient of the plastic potential and hardening modulus associated with the primary yield surface (Equations 4.46 and 4.48, respectively). Therefore, accurate calibration of the CSL might be crucial for obtaining reliable numerical results with the present model.

The critical state (CS) is defined as the state established at large strains at which soil deforms under constant stress and void ratio (Roscoe *et al.*, 1958). According to this definition, it implies that clear signs of stress and volumetric strain stabilisation are measured for drained shearing, or stress and pore water pressure stabilisation are observed for undrained shearing, not only momentarily (as at the quasi-steady state), rather it should continue in that state with further deformation (Been *et al.*, 1991). Therefore, although a large number of drained and undrained triaxial compression (TC) and triaxial extension (TE) tests were reported in Chapter 2, CS conditions were considered to be only attained in four TC tests, as detailed in Section 2.6.5.1. The e – p' data at the end of shearing for those four tests are presented as solid black circles in Figure 6.1. By considering only those four data points, it can be observed that a lack of representative CS data exists at relatively low stresses ($p' \leq 100$ kPa). As discussed by Klotz and Coop (2002), this seems to be a consequence of the premature occurrence of barrelling and strain localisation when samples are sheared under lower confining stresses, preventing them from reaching critical state conditions. The authors suggested, however, that this lack of experimental data and, consequently, the additional difficulty in estimating the position of the CSL is circumvented by the fact that the CSL tend to the maximum void ratio, e_{max}, of sand at very low stresses, as proposed firstly by Riemer *et al.* (1990). It was, therefore, assumed that $(e_{cs})_{ref} = e_{max} = 1.00$. Having set $p'_{ref} = 101.3$ (i.e. equal to the atmospheric pressure), the remaining two model parameters – λ and ξ, which control the slope and curvature of the CSL, respectively – were subsequently estimated by linear least square fitting over the 4 data points, with the values $\lambda = 0.07$ and $\xi = 0.36$ being obtained.

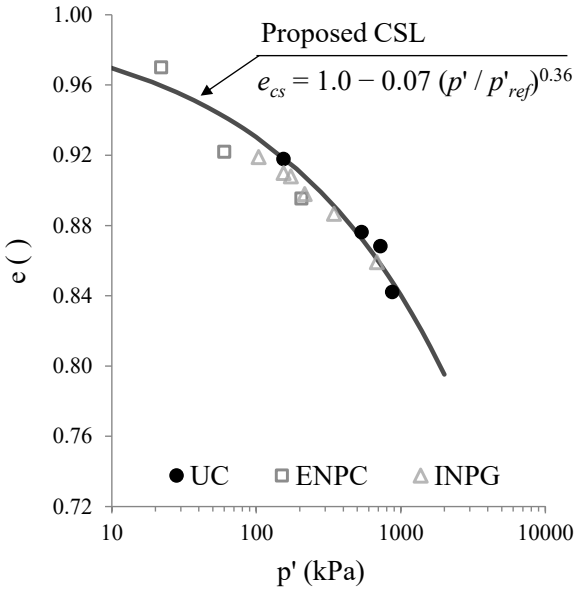

Figure 6.1 – Proposed critical state line for Hostun sand.

As detailed in Section 2.6.5.1, given the few data points used to estimate the position of the CSL, the proposed CSL was compared to critical state test data presented in the literature. In particular, drained and undrained triaxial compression test data obtained in studies carried out at Grenoble Institute of Technology (INPG) and *École National des Ponts et Chaussées* (ENPC) over the last three decades were analysed. The *e – p'* data at the end of tests where CS conditions were considered to be attained are also plotted in Figure 6.1. It can be observed that these additional data points seem to corroborate the adopted CSL.

6.4 Critical state strength

The critical state (CS) strength in triaxial compression (TC) and in triaxial extension (TE) are defined by their corresponding stress ratios M_c^c and M_e^c, respectively. These model parameters define the position of the CS surface in the multiaxial stress space, also influencing the positions of the bounding and dilatancy surfaces (Equation 4.4 and 4.5, as well as 4.35 to 4.38). Therefore, high importance is given to their calibration.

The *q – p'* data obtained at the end of the four TC tests where CS conditions were considered to be attained are shown in Figure 6.2 as solid black circles. By employing a least square fitting over those four data points, M_c^c was estimated as 1.265, which corresponds to a CS friction angle, ϕ'^c_c, of approximately 31.5° (Equation 6.1). Indeed, the additional critical state data obtained from TC tests performed in other institutions seem to be in good agreement with the proposed CSL.

$$\phi'^c_c = asin\left(\frac{3\,M_c^c}{6 + M_c^c}\right) \approx 31.5° \tag{6.1}$$

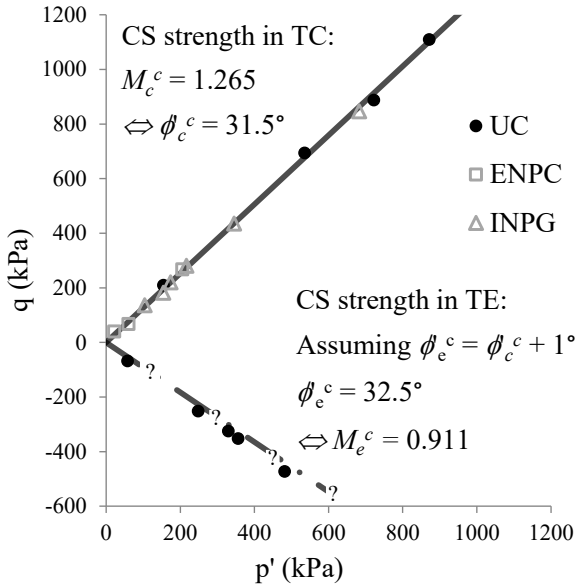

Figure 6.2 – Critical state strength in compression and extension for Hostun sand.

With respect to the CS in TE, it is difficult to obtain a reliable estimation of M_e^c from TE test data due to the inevitable occurrence of necking in those tests, as explained in Chapter 2. Nevertheless, several experimental studies have shown that the CS friction angle in TE, ϕ'^c_e, is close to its counterpart value in TC, ϕ'^c_c, at least for pluviated sands (e.g. Vaid *et al.*, 1990; Lade, 2006). Indeed, Loukidis and Salgado (2009) suggested that ϕ'^c_e for sand is, in general, 0 to 2° greater than ϕ'^c_c. A value in the middle range was adopted, i.e. $\phi'^c_e = \phi'^c_c + 1.0° = 32.5°$, which corresponds to $M_e^c = 0.911$, according to Equation 6.2. Note that, by adopting this value, a CS ratio of $c^c = M_e^c/M_c^c = 0.720$ is obtained, a value within the typical 0.67–0.75 range for silica sands (Loukidis and Salgado, 2009). Furthermore, according to Loukidis and Salgado (2009), this value is greater than the minimum value ensuring a convex shape for the critical surface ($c^c \geq 0.717$), which is a crucial aspect to guarantee numerical stability.

$$\phi'^c_e = asin\left(\frac{3\,M_e^c}{6 - M_e^c}\right) \Leftrightarrow M_e^{cs} = \frac{6\,sin\left(\phi'^c_e\right)}{3 + sin\left(\phi'^c_e\right)} \approx 0.911 \tag{6.2}$$

The obtained CSL in TE is plotted in Figure 6.2 along with the $q - p'$ test data obtained for TE tests performed on moderately loose samples of Hostun sand. As expected, some very slight discrepancies can be observed between the proposed CSL in TE and the obtained experimental data.

6.5 Small-strain shear modulus

As detailed in Section 4.2.2, the present constitutive model makes use of the well-established hysteretic formulation of Ramberg and Osgood (1943) to determine the current tangent shear modulus, G_{tan}, by applying a reduction factor, T, to the maximum shear modulus, G_{max}. (Equation 4.18). The calibration process starts by assessing the model parameters required to

the calculation of G_{max}, focusing at a later stage (Section 6.9) on the calibration of the model parameters required to the computation of T.

Several experimental studies on sand (e.g. Hardin, 1965; Hardin and Black, 1966; Hardin and Drnevich, 1972a; Lo Presti *et al.*, 1997; Zhou and Chen, 2005) have suggested that G_{max} can be essentially related to the current mean effective stress, p', and void ratio, e. The experimental results obtained in the present study (Section 2.5.5) seem also to corroborate this proposition. Moreover, as detailed in Section 4.3.2, a more general expression has been introduced in the present constitutive relationship to define the dependence of G_{max} on p' and e (Equation 4.94, 4.99 and 4.100) than that incorporated in the earlier versions of the model (Equation 4.19). In this updated formulation, the following three model parameters require proper calibration: C_g, m_g and n_g. While the second of these parameters (which define the influence of e on G_{max}) is usually set to 2.17 for round-grained sand or 2.97 for angular-grained sand (Hardin, 1965; Hardin and Black, 1966a), the remaining two parameters are typically calibrated against small-strain measurements (e.g. results of bender element and/or resonant column tests).

In the present case, a value of $m_g = 2.97$ was adopted, due to the sub-angular to angular grain shape of Hostun sand. Moreover, as detailed in Section 2.5.5, results of bender element (BE) tests performed both on moderately loose and dense samples were used to estimate C_g and n_g. As shown again in Figure 6.3, a simple least square fitting over the BE data points led to $C_g = 293.0$ and $n_g = 0.49$.

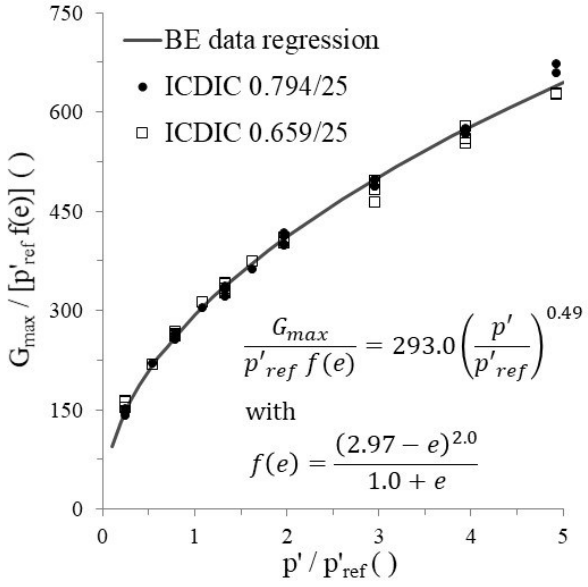

Figure 6.3 – Small-strain shear modulus for Hostun sand.

6.6 Poisson's ratio

The small-strain Poisson's ratio, ν, can be defined by the ratio of the radial strain increment, $\Delta\varepsilon_r$, to the axial strain increment, $\Delta\varepsilon_a$ – Equation 6.3. In the present model, the small-strain Poisson's coefficient is assumed to remain constant throughout loading, relating the current

tangent bulk modulus, K_{tan}, to the current tangent shear modulus, G_{tan}, according to the theory of elasticity (Equation 4.24). Due to this, the *small-strain Poisson's ratio* is often referred to simply as *Poisson's ratio*.

$$\nu = -\frac{\Delta\varepsilon_r}{\Delta\varepsilon_a} \tag{6.3}$$

The value of ν may be obtained from small-strain measurements, providing that wave measurements in two different directions are undertaken. In such case, the shear and compressional wave velocities, v_s and v_p, respectively, may be employed to estimate the small-strain value of ν, as indicated by Equation 6.4.

$$\nu = \frac{1}{2}\,\frac{\left(\frac{v_p}{v_s}\right)^2 - 2}{\left(\frac{v_p}{v_s}\right)^2 - 1} \tag{6.4}$$

Alternatively, it is possible to estimate the small-strain Poisson's ratio, ν, from triaxial tests, providing that high-resolution local-strain transducers are used to measure the deformation of the sample in both axial and radial directions and small cyclic loads are applied.

In the present study, since none of the aforementioned tests was performed, it was necessary to select a value from other studies presented in the literature. Specifically, Hoque and Tatsuoka (2000) and Hoque (2005) present results of small-strain cyclic triaxial loading tests performed on dry samples of air-pluviated Hostun sand, using high-resolution-strain transducers. In these tests, samples were prepared to several different initial void ratio and consolidated under various different confining stresses, with values of ν between 0.14 and 0.23 being measured in the laboratory tests. Since a more reliable source for this parameter was not found, $\nu = 0.18$, corresponding to the average value, was adopted in the present study. Note that the small-strain Poisson's ratio is not expected to vary significantly for different sands (e.g. Loukidis and Salgado, 2009). In fact, based on similar tests, Tatsuoka and Hoque (2004) obtained values in the range 0.16 – 0.18 for Toyoura (Japanese) sand, a value of about 0.16 for Ticino (Italian) sand and values in the range 0.11 – 0.18 for Silver Leighton-Buzzard (U.K.) sand.

6.7 Positions of the bounding and dilatancy surfaces

6.7.1 General aspects

The bounding and dilatancy surfaces are used to model two distinctive states of the response of sand to loading, namely the peak stress ratio state, which is related to the mobilisation of the maximum angle of shearing resistance, and the phase transformation state (Ishihara *et al.*, 1975), which marks the change from plastic contraction to plastic dilation. Contrary to the critical state, which is characterised by stationary conditions, both phase transformation and peak stress ratio states are transitory and can occur either at moderate strains or large strains,

depending on the effective stress state, as well as on the material's state (e.g. Been and Jefferies, 1985; Wood *et al.*, 1994; Li and Dafalias, 2000; Been and Jefferies, 2004; Jefferies and Been, 2006). In order to take into account this dependency in a simple but effective way, a linear dependence of the bounding and dilatancy surface positions (characterised by their respective stress ratios) on the critical state strength and state parameter, ψ (Been and Jefferies, 1985), is considered by the present BSPM – Equation 4.4 and 4.5, respectively. Therefore, the calibration process is very similar for both surface positions. Specifically, providing that results of several triaxial compression and extension tests are available, it involves the computation of stress ratio, η, – state parameter, ψ, data points corresponding to the occurrence of the peak stress ratio (i.e. $\eta^b_{c,e} - \psi^b_{c,e}$ data points) and to the occurrence of phase transformation (i.e. $\eta^d_{c,e} - \psi^d_{c,e}$ data points). Having plotted these points, a simple linear regression can be employed to estimate the slope of straight lines that best describe the available experimental data in triaxial compression and extension (i.e. the set of parameters $k^b_{c,e}$ and $k^d_{c,e}$, respectively for the bounding and dilatancy surfaces). Note that such linear regression must result in $\eta^b_{c,e} = \eta^d_{c,e} = \eta^c_{c,e}$ for $\psi = 0.0$, to ensure compatibility with critical state soil mechanics (CSSM) framework (Roscoe *et al.*, 1958; Schofield and Wroth, 1968), as assumed by the model formulation. Moreover, note that, rather than $M^b_{c,e}$, $M^d_{c,e}$ and $M^c_{c,e}$, which represent positive model parameters, the experimental results are presented in terms of $\eta^b_{c,e}$, $\eta^d_{c,e}$ and $\eta^c_{c,e}$ to comply with the adopted sign convention, where stress ratio in triaxial extension takes negative value (i.e. η^b_e , η^d_e and η^c_e are negative).

Finally, it is important to highlight that, as pointed out by Taborda (2011), to obtain a more accurate estimation of these model parameters, the current value of ψ is used in the calibration process, and not its initial magnitude, as initially suggested by Papadimitriou *et al.* (2001).

6.7.2 Bounding surface

Figure 6.4 presents $\eta^b_{c,e} - \psi^b_{c,e}$ data obtained from triaxial compression and extension tests performed on Hostun sand. As detailed in Section 2.6.5.2, from the thirty-two tests performed, only three undrained triaxial extension tests were excluded, since the stress ratio was still increasing when these tests were stopped. In Figure 6.4, it can be observed that, irrespective of type of consolidation, drainage conditions and stress path direction of tests, the data points seem to align quite well, with a linear trend describing very satisfactorily the experimental data. Moreover, at least for this sand, the exponential form suggested by Li *et al.* (1999) as a replacement for the linear form of Equation 4.4 does not seem to bring any additional gain in accuracy.

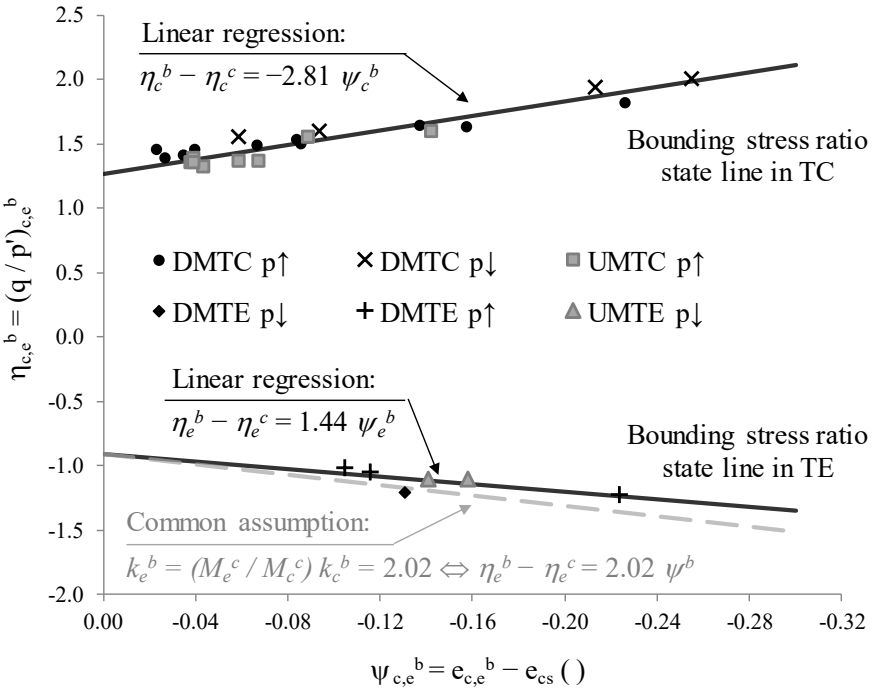

Figure 6.4 – Calibration of the parameters controlling the position of the bounding surface for Hostun sand.

Also shown in the figure is the line obtained when the simplification $k_e^b = k_c^b\ (M_e^c/M_c^c)$, proposed by Papadimitriou and Bouckovalas (2002) and often employed in the literature (e.g. Loukidis and Salgado, 2009; Taborda *et al.*, 2014) is taken into account. It can be observed that this line does not plot far from that obtained when applying a linear regression to the experimental data for most of data points. Moreover, it is apparent that this line approximates better the peak stress state point obtained from DMTE p↓ test than the line obtained by linear regression. Indeed, it was later found that the line considering the simplification $k_e^b = k_c^b\ (M_e^c/M_c^c)$ allows, overall, for a better replication of the available monotonic and cyclic triaxial test data, as well as centrifuge test data. Therefore, in the present study, the model parameters $k_c^b = 2.81$ and $k_e^b = 2.02$ were adopted in all subsequent numerical analyses.

6.7.3 Dilatancy surface

The dilatancy surface is used to model the temporary state at which the volumetric plastic strains change sign (i.e. the plastic dilation is temporarily null). This distinctive state of the response of sand was termed as phase transformation state by Ishihara *et al.* (1975). According to these authors, under undrained conditions, this state can be identified by a local minimum in the mean effective stress, *p'*. Under drained conditions, the identification of this transitory state is much more complex, since it involves the estimation of the volumetric plastic strains, or, more generically, of the dilatancy. For that purpose, the procedure described in Section 2.6.5.3 was applied, with the dilatancy being estimated based on Equation 6.5.

$$D \approx \frac{\Delta\varepsilon_v - \frac{\Delta p'}{K_{max}}}{\Delta\varepsilon_q - \frac{\Delta q}{3\,G_{max}}} \approx \frac{\left(\varepsilon_{v_{j+1}} - \varepsilon_{v_j}\right) - \frac{p'_{j+1} - p'_j}{K_{max}}}{\left(\varepsilon_{q_{j+1}} - \varepsilon_{q_j}\right) - \frac{q_{j+1} - q_j}{3\,G_{max}}} \tag{6.5}$$

where:

$$K_{max} = \frac{2\,(1+\nu)}{3\,(1-2\nu)} G_{max} \tag{6.6}$$

Note that Equation 6.5 assumes that G_{tan} and K_{tan} can be approximated, at this stage of the calibration, by G_{max} and K_{max}, respectively. Furthermore, it assumes that G_{max} and K_{max} remain constant over each time step (i.e. from a given instant j to the subsequent instant j+1). According to Loukidis and Salgado (2009), these simplifications are reasonable provided that data obtained from drained triaxial compression tests are used. In fact, since strains induced in sand during triaxial loading are mostly of plastic nature, the value of D is expected to be primarily affected by the total volumetric and deviatoric strain increments, $\Delta\varepsilon_v$ and $\Delta\varepsilon_q$, respectively, depending only to a limited extent on the elastic volumetric and deviatoric strain components, $\Delta\varepsilon_v^e$ and $\Delta\varepsilon_q^e$, respectively. Conversely, under undrained conditions, since $\Delta\varepsilon_v \approx 0.0$, D is more dependent on $\Delta\varepsilon_v^e \approx (p'_{j+1} - p'_j)/K_{tan} \approx (p'_{j+1} - p'_j)/K_{max}$ and, therefore, inaccurate values of D can be obtained when those simplifications are adopted.

Figure 6.5 presents $\eta_{c,e}^d - \psi_{c,e}^d$ data gather from twenty-eight drained and undrained triaxial compression and extension tests. Note that, as detailed in Section 2.6.5.3, in three drained triaxial compression tests, the samples exhibited dilatant response throughout loading, making it impossible to obtain $\eta_{c,e}^d - \psi_{c,e}^d$ data. In addition, as also described in Section 2.6.5.3, one data point was excluded from the analysis, since it was observed to plot far from the remaining points. In fact, it is apparent that the obtained $\eta_{c,e}^d - \psi_{c,e}^d$ data presented in Figure 6.5 presents more scatter than the obtained $\eta_{c,e}^b - \psi_{c,e}^b$ data presented in Figure 6.4, particularly in triaxial extension. As suggested in the literature (Been and Jefferies, 2004; Loukidis and Salgado, 2009), this greater scatter can be attributed not only to the simplifications adopted for the estimation of the dilatancy, but also to the inherent unreliability of stress-dilatancy data obtained during the early stages of triaxial shearing, at which phase transformation state is typically observed to occur. Indeed, it was found that $k_e^d = 0.20$, obtained by performing a simple linear regression over the $\eta_e^d - \psi_e^d$ data, would be too low to allow for an adequate reproduction of the available monotonic and cyclic triaxial test data, as well as centrifuge test data, with far better results being obtained when using the simplification $k_e^d = k_c^d\,(M_e^c/M_c^c)$ proposed by Papadimitriou and Bouckovalas (2002) and often employed in the literature (e.g. Loukidis and Salgado, 2009; Taborda *et al.*, 2014). Therefore, in the present study, the following values were adopted: $k_c^d = 0.94$ and $k_e^d = 0.67$.

As mentioned for the peak stress state data, the exponential form suggested by Li *et al.* (1999) as a replacement for the linear form of Equation 4.5 does not seem to improve the description of the experimental data in triaxial compression (i.e. $\eta_c^d - \psi_c^d$ data).

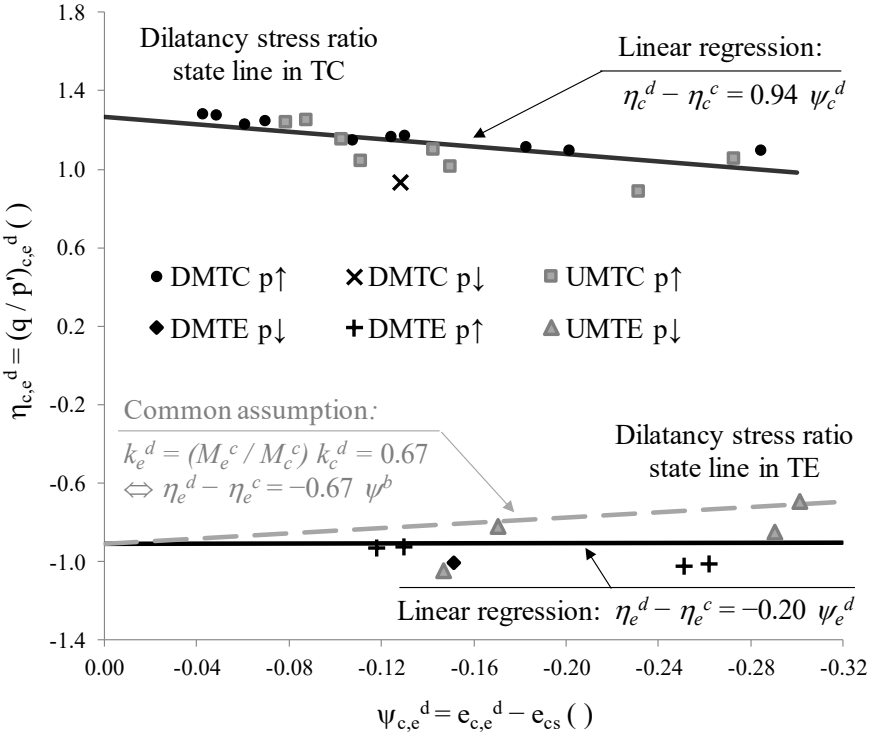

Figure 6.5 – Calibration of the parameters controlling the position of the dilatancy surface for Hostun sand.

6.8 Stress-dilatancy relationship

In this constitutive model, the dilatancy, D, is assumed to be proportional to the distance d^d from the current stress ratio to the dilatancy stress ratio, as expressed by Equation 4.47, where A_0 is the constant of proportionality (i.e. the model parameter characterising the stress-dilatancy relationship). Once more, since the reduction of the shear modulus has yet been calibrated, only drained tests should be employed to assess the stress-dilatancy response (Loukidis and Salgado, 2009). As explained before, when using drained test data, the error introduced by assuming $G_{tan} \approx G_{max}$ and $K_{tan} \approx K_{max}$ in the estimation of the dilatancy, D (Equation 6.5), is expected to be much smaller than that introduced by this simplification when analysing undrained test data.

Figure 6.6 shows the stress-dilatancy curves obtained from drained triaxial compression tests. Note that these curves were smoothed by using an interval of data values to the computation of D greater than the test sampling interval, a procedure also employed by Loukidis and Salgado (2009) and Taborda (2011). A single straight line seems to describe reasonably the stress-dilatancy response of loose, moderately loose and dense samples, at least until the peak stress ratio is reached. Furthermore, by employing a simple linear regression, $A_0 \approx 1.0$ was obtained.

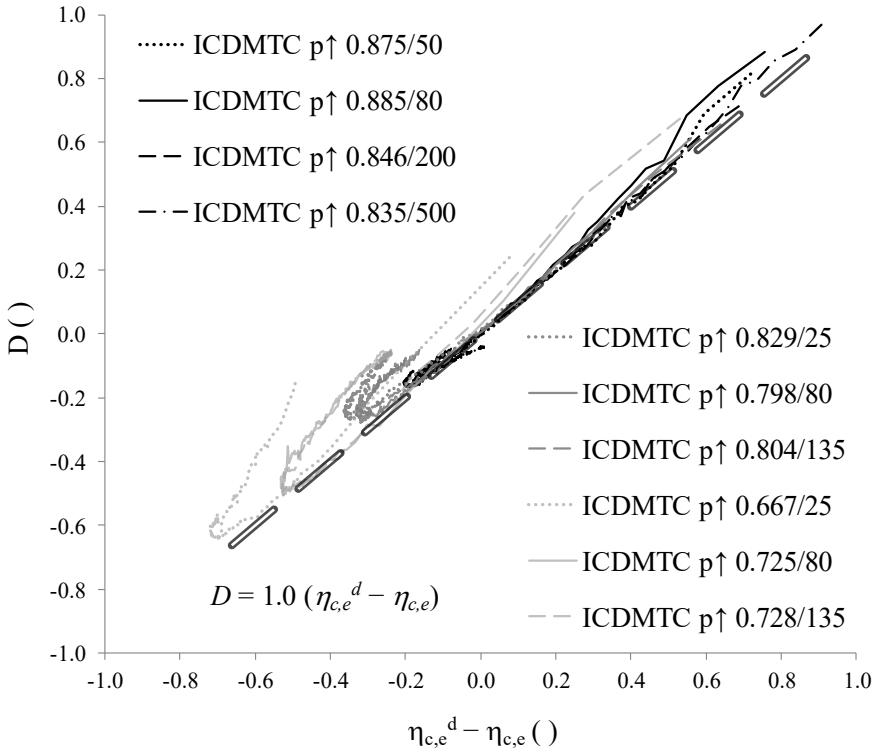

Figure 6.6 – Calibration of the stress-dilatancy relationship for Hostun sand.

6.9 Shear modulus reduction

Figure 6.7 shows the stress-dilatancy response computed from results of undrained triaxial compression tests by using Equation 6.5 in conjunction with $\Delta\varepsilon_v \approx 0.0$. It is apparent that a much smaller value for A_0^* (where the subscript "*" is used to distinguish from the drained case) is obtained for undrained shearing ($A_0^* \approx 0.3$ in comparison with $A_0 \approx 1.0$).

According to Loukidis and Salgado (2009), since dilatancy is considered an intrinsic characteristic of sand, similar stress-dilatancy responses should be obtained in both drained and undrained cases, with eventual discrepancies being likely the result of the use of inappropriate values for elastic stiffness when estimating the dilatancy coefficient, here denoted as D when using drained test data and D^* when using drained test data, to ease the presentation. In fact, as pointed out before, although errors in the estimation of G_{tan} and K_{tan} are likely to affect the estimation of both D and D^*, the impact of the introduced error is predictably larger in the undrained case, where D^* is highly dependent on the value of K_{tan}. In addition, Loukidis and Salgado (2009) pointed out that, due to the inherent unreliability of triaxial test data obtained during the early stage of loading (i.e. for low values of the stress ratio, η), it is usual to discard those data points and use only data obtained during later stages of loading (i.e. for medium to large values of η) to characterise the stress-dilatancy response of sand. Indeed, under such values of η, it is predictable that G_{tan} and K_{tan} have already reached values close to their minimum (i.e. $G_{tan} \approx G_{min}$ and $K_{tan} \approx K_{min}$ are likely observed under such range of values of η).

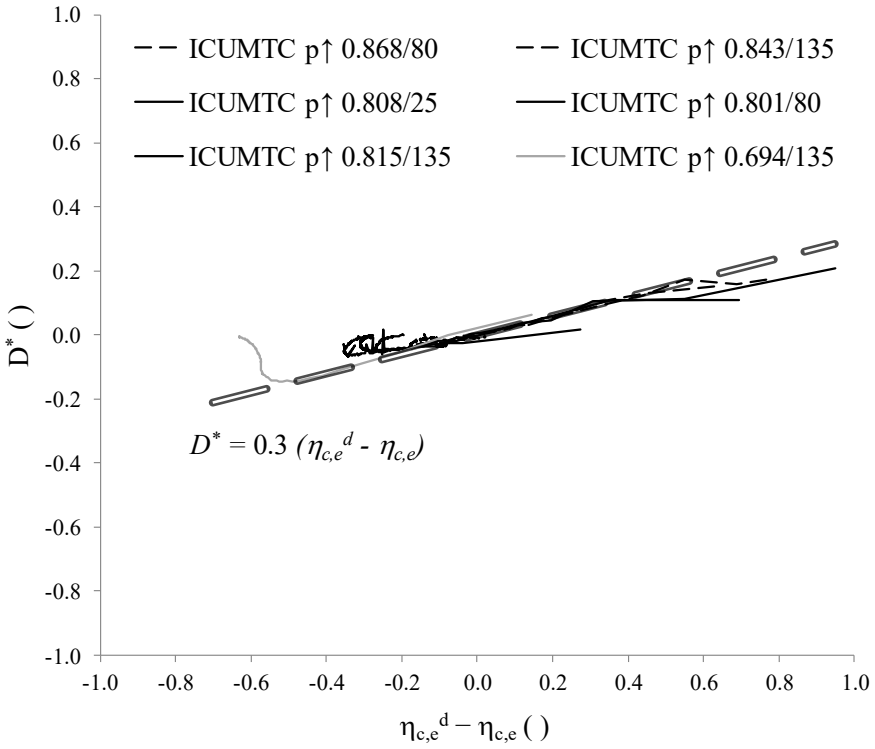

Figure 6.7 – Stress-dilatancy relationship obtained from UMTC test data when constant elastic stiffness is considered.

Taking both aspect into account, Loukidis and Salgado (2009) suggested that similar undrained and drained stress-dilatancy responses (i.e. $A_0^* \approx A_0$) are likely obtained when using $G_{tan} \approx G_{min}$ and $K_{tan} \approx K_{min}$ for the estimation of D^*, rather than using $G_{tan} \approx G_{max}$ and $K_{tan} \approx K_{max}$, as assumed when estimating D, which is less sensitive to the values of G_{tan} and K_{tan}. Therefore, to conciliate the drained and undrained stress-dilatancy responses, Loukidis and Salgado (2009) proposed the adoption of a ratio of the minimum to the maximum tangent shear modulus, K_{min}/K_{max}, equal to the ratio of the undrained to drained stress-dilatancy-related parameters, A_0^*/A_0, – Equation 6.7.

$$\frac{K_{min}}{K_{max}} \approx \frac{A_0^*}{A_0} \tag{6.7}$$

Recalling that, in the present model, the lower limit for the tangent shear modulus is given by $G_{min} = G_{max}/[1 + \kappa(1/a_1 - 1)]$ and that K_{tan} is proportional to G_{tan} via a constant Poisson's ratio ν(Equation 4.24), it is possible to relate the model parameters a_1 and $\kappa$to K_{min}/K_{max}, as given by Equation 6.8.

$$\frac{K_{min}}{K_{max}} = \frac{G_{min}}{G_{max}} = \frac{1}{1 + \kappa\left(\frac{1}{a_1} - 1\right)} \Leftrightarrow a_1 = \frac{\kappa \frac{K_{min}}{K_{max}}}{1 + \frac{K_{min}}{K_{max}}} \tag{6.8}$$

By substituting Equation 6.7 into Equation 6.8 and assuming $\kappa = 2.0$, as proposed by Papadimitriou and Bouckovalas (2002), the following value is obtained for the model parameters a_1:

$$a_1 \approx \frac{\kappa \frac{A_0^*}{A_0}}{1+\frac{A_0^*}{A_0}} \approx \frac{2.0 \times \frac{0.3}{1.0}}{1.0+\frac{0.3}{1.0}} \approx 0.46 \tag{6.9}$$

As highlighted by Taborda (2011), a significant number of assumptions were introduced in the approach proposed by Loukidis and Salgado (2009) for the calibration of the model parameters governing the reduction of the tangent shear modulus. To confirm the reasonability of the approach, Taborda (2011) performed a small parametric study, where values of A_0 and A_0^* were computed for several different values of a_1, considering, as a simplification, a_1 constant in each computation. A similar study was carried out in the present study, with the obtained results being shown in Figure 6.8.

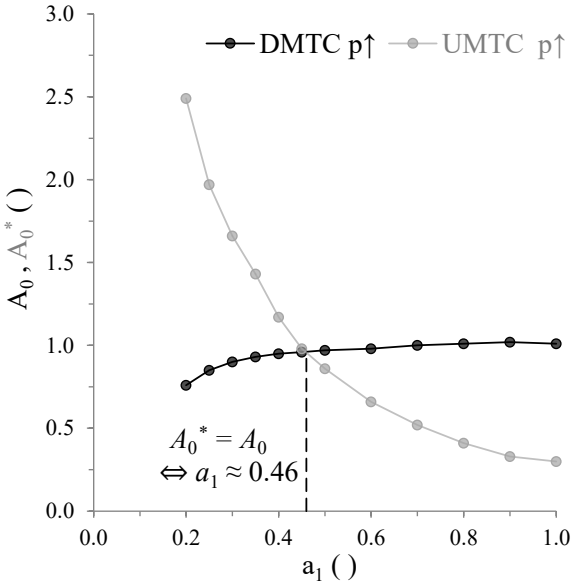

Figure 6.8 – Stress-dilatancy-related parameter A_0 as a function of the parameter a_1 controlling the reduction of the tangent shear modulus with shearing.

It can be observed that the intersection of A_0 and A_0^* curves occurs at a value of a_1 very similar to that obtained when using the approach proposed by Loukidis and Salgado (2009). In addition, Figure 6.8 seems to corroborate the basic assumption of Loukidis and Salgado (2009) that the reduction of stiffness has a much larger impact on the computation of A_0^* (i.e. based on undrained test data) than on that of A_0 (i.e. based on drained test data). Specifically, while values from about 2.5 to 0.3 were obtained for A_0^* when a_1 was varied, respectively, from 0.2 to 1.0, a much more limited variation of A_0, from about 0.75 to 1.0, was obtained for a similar range of values of a_1. Note that similar conclusions were drawn by Taborda (2011) when calibrating a BSPM for Leighton Buzzard Fraction-E sand. It was, therefore, decided to adopt $a_1 = 0.46$. Furthermore, as originally proposed by Papadimitriou and Bouckovalas (2002), $\kappa = 2.0$ was assumed in the present study. Note that this value was also adopted in all numerical analyses performed by Taborda (2011). Moreover, this value is intrinsically employed in the formulation of the numerical relationship proposed by Loukidis and Salgado (2009).

Having defined the model parameters a_1 and κ, it is still necessary to calibrate γ_1. According to Papadimitriou and Bouckovalas (2002), since $G_{tan} \approx G_{min}$ for $\gamma \geq \gamma_1$, the parameter γ_1 can be related to the volumetric cyclic threshold strain, $\gamma_{t,v}$, which defines the limit above which plastic strains become dominant (Vucetic, 1994). This author reported results of cyclic direct simple shear and cyclic triaxial tests performed on several sands indicating values for $\gamma_{t,v}$ in the range of $1.0 \times 10^{-4} - 4.0 \times 10^{-4}$. More recently, an empirical expression (Equation 6.10) has been proposed by Loukidis and Salgado (2009).

$$\gamma_1 = 5.5 \times 10^{-4} \frac{1 - a_1}{2\, {a_1}^2} \tag{6.10}$$

The application of this expression gives a value of $\gamma_1 = 7.0 \times 10^{-4}$, which is slightly above the upper limit of the range indicated by Vucetic *et al.* (1994). Nevertheless, since a more reliable procedure for the calibration of γ_1 was not been found, this value was adopted in the present study. It should be noted, however, that this value might need to be readjusted at a later stage. As shown in Figure 6.9, the parameter γ_1 has a significant impact on the rate at which the reduction of the shear modulus, T, occurs with the distance, χ^r_{ref} (which in monotonic triaxial compression is simply given by $\chi^r_{ref} = |\eta|$), with larger values of γ_1 resulting in slower rates.

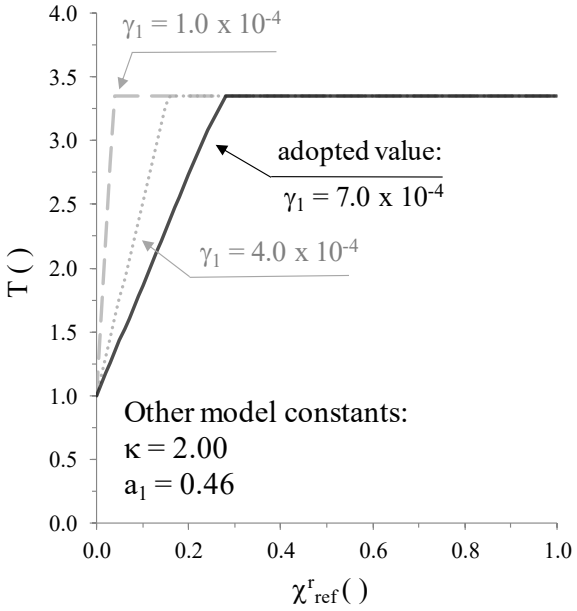

Figure 6.9 – Influence of γ_1 on the reduction of the tangent shear modulus.

A final note concerns the importance of the non-linear elastic formulation on the present model. This formulation was introduced by Papadimitriou and Bouckovalas (2002) to improve the simulation of the reduction of the shear modulus under dynamic loading. Indeed, as shown here, it also plays a key role in guaranteeing the compatibility between the stress-dilatancy response under drained and undrained loading (Loukidis and Salgado, 2009). As discussed by the authors, when a reduction of the shear modulus is not considered – as, for

example, in the original version of the model proposed by Manzari and Dafalias (1997) –either the maximum shear modulus should be set to values much smaller than those measured experimentally (i.e. obtained in bender element or column resonant tests) or, alternatively, unrealistically low values of Poisson's ratio need to be used to simulate adequately both drained and undrained monotonic response of sand.

6.10 Plastic hardening modulus

6.10.1 Initial considerations

Along the lines of the bounding surface plasticity framework, the distance from the current stress point to its projection on the bounding surface is used to determine the plastic hardening modulus associated with the primary yield surface, A_1 (Equation 4.48). That dependency is scaled by the quantity h, which is a function of state parameters. In particular, for the present formulation of the model, the quantity h is given by the product of the following scalar-valued quantities:

1) h_g, introducing the effect of the current tangent elastic shear modulus, G_{tan}, on A_1 – Equation 4.62.
2) h_b, introducing the effect of the current mean effective stress, p', as well as of the current distance to the bounding surface, d^b, in relation to its overall diameter, d^b_{ref}, on A_1 – Equation 4.59;
3) h_e, introducing the effect of the current void ratio, e, on A_1 – Equation 4.60;
4) h_f, introducing the influence of the current characteristics of the shearing-induced fabric tensor, $\boldsymbol{F}$, and its interaction with the deviatoric loading tensor, $\boldsymbol{n}$, on A_1 – Equation 4.54;
5) h_A, introducing the effect of the inherent fabric tensor, $\boldsymbol{F_A}$, and its interaction with $\boldsymbol{n}$ on A_1 – Equation 4.108.

In order to define each of the aforementioned quantities, the following sets of model parameters are required:

1) α defining the non-linearity of the influence of G_{tan} on A_1;
2) μ and β establishing, respectively, the non-linearity of the influence of the normalised mean effective stress, p'/p'_{ref}, and of the normalised distance to the bounding surface, $|d^b|/|d^b_{ref} - d^b|$, on A_1;
3) h_0, γ and e_{max} defining the influence of e on A_1;
4) H_0 and ξ defining the influence of sand's initial conditions on the evolution of $\boldsymbol{F}$ with loading;
5) a characterising $\boldsymbol{F_A}$ and h_A scaling the influence of $\boldsymbol{F_A}$ on A_1.

As mentioned by Loukidis and Salgado (2009) and Taborda (2011), these model parameters cannot be directly associated with any specific aspect of sand response observed in laboratory, resulting in a complex calibration process. Nevertheless, having already determined a considerable number of model parameters, it is possible to carry out simulations of monotonic triaxial tests and assess the impact of these model parameters on the reproduced response. By comparing the obtained numerical results with the available experimental data, it is possible to select appropriate values for the model parameters. This methodology was adopted in the present study, following the abovementioned order 1) to 5), as presented in the following sections. Note that, although affecting solely the plastic hardening modulus, due to its importance for the simulation of the cyclic response of sand, the calibration of the shearing-induced fabric component-related parameters H_0 and ξ is presented in an individual section (Section 6.11). Similarly, the calibration of the model parameters a and h_A, related to the inherent fabric anisotropy component, is presented in an individual section (Section 6.12), since: (1) this component of the model affects not only the plastic hardening modulus, but also the gradient of the plastic potential, due to the relocation of the CSL; and (2) as mentioned before, two sets of model parameters are to be obtained, one set for the original formulation of the model (Taborda *et al.*, 2014) and another set for the extended formulation incorporating the inherent fabric anisotropy component.

6.10.2 Model parameters related to the influence of the tangent shear modulus

According to Taborda (2011), the model parameter α was solely introduced to allow the possibility of reverting to the original formulation proposed by Papadimitriou and Bouckovalas (2002), if desired. More specifically, by adopting $\alpha = 0.0$, the effect of the tangent shear modulus, G_{tan}, on the plastic hardening modulus associated with the primary yield surface, A_1, is removed (i.e. $h_g = 1.0$) and the original formulation of Papadimitriou and Bouckovalas (2002) is retrieved. This is, however, not desirable in the present case. As shown in Taborda *et al.* (2014), the introduction of the effect of G_{tan} on A_1 allows for a more consistent reduction of plastic stiffness throughout loading. Therefore, $\alpha = 1.0$ was adopted in the present study.

6.10.3 Model parameters related to the influence of the normalised distance to the bounding surface

According to Loukidis and Salgado (2009) and Taborda *et al.* (2014), the model parameter β has a strong effect on the shape of the effective stress path obtained in undrained shearing from the start of shearing to the phase transformation state. In particular, when simulating loose samples submitted to undrained triaxial compression loading, it has a strong influence on the stress state at which the temporary peak in deviatoric stress is obtained. Therefore, a proper calibration of β is essential to the accurate prediction of the occurrence of the undrained instability state (Section 2.6.5.4). Similar conclusions were drawn by Loukidis and Salgado (2009), when analysing the effect of a similar model parameter on the plastic

hardening modulus. Given the above, both group of authors performed a small parametric study to calibrate this model parameter, where:

- $\mu = 1.0$ and $\gamma = 0.0$ to deactivate the effect of *p'* and *e* on A_1, respectively;
- $H_0 = 0.0$ and $\zeta = 0.0$ to deactivate the effect of ***F*** on A_1;
- β is varied in each analysis – values of 0.0, 0.3, 0.6 and 0.9 were employed;
- for each value of β, the value of h_0 resulting in a value of p'_{min} similar to that observed in the laboratory test is selected.

A similar procedure was adopted in the present study. Figure 6.10 to Figure 6.12 compare the numerical and experimental results of three ICUMTC p↑ tests performed on loose samples, respectively: ICUMTC p↑ 0.876/80, ICUMTC p↑ 0.868/80 and ICUMTC p↑ 0.843/135 tests. Note that, in these tests, the existence of a temporary peak in deviatoric stress before a minimum value of *p*' is reached is more evident than in tests conducted on samples prepared to denser initial states.

In all three figures, it is apparent that the modelled effective stress paths do not match well the measured effective stress paths. Note, however, that this may be affected by experimental bedding errors (i.e. errors related to the initial adjust of samples to loading) and, therefore, emphasis is given to the matching of the temporary peak in deviatoric stress. For ICUMTC p↑ 0.876/80 test (Figure 6.10) and ICUMTC p↑ 0.868/80 test (Figure 6.11), it seems that, overall, $\beta = 0.3$ allows for a satisfactory reproduction of the measured effective stress paths and stress-strain responses. In fact, it is apparent that higher values of β result in the overprediction of the local maximum peak of the deviatoric stress, while a lower value underestimates that temporarily peak. Moreover, $\beta = 0.3$ seems to result in a very accurate replication of the stress-strain response measured in the first of these tests (i.e. in the ICUMTC p↑ 0.876/80 test, illustrated in Figure 6.10b), although slightly overestimating the stress-strain response measured in the second of these tests (i.e. in the UMTC p↑ 0.868/80 test, illustrated in Figure 6.11b). Regarding the UMTC p↑ 0.843/135 test, while $\beta = 0.0$ seems to simulate more accurately the effective stress path measured in the laboratory, it appears to result in a considerably stiffer stress-strain response that registered in the experiment. This latter aspect seems to be slightly improved when $\beta = 0.3$ is adopted, although a better agreement would require an even higher value for β. Overall, it seems that $\beta = 0.3$ leads to the best possible simulation of these three tests and, therefore, this value was adopted at this stage. Note, however, that the value assigned to this model parameter might be adjusted later if unreasonable modelled response is obtained.

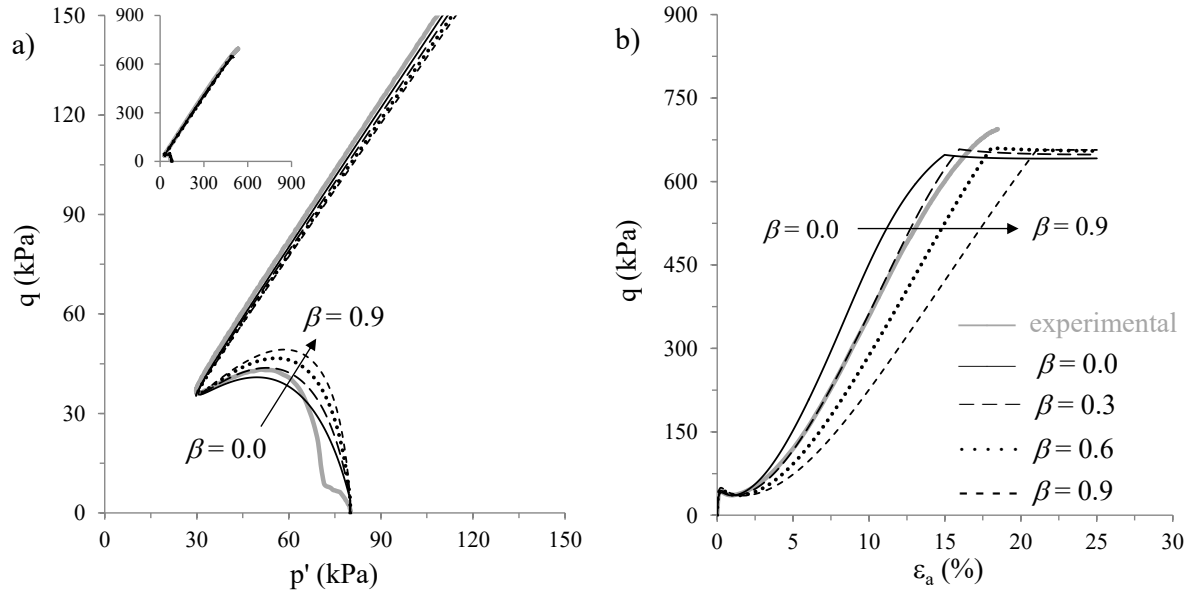

Figure 6.10 – Influence of β on the numerical simulation of test ICUMTC p↑ 0.876/80: (a) effective stress path and (b) stress-strain response.

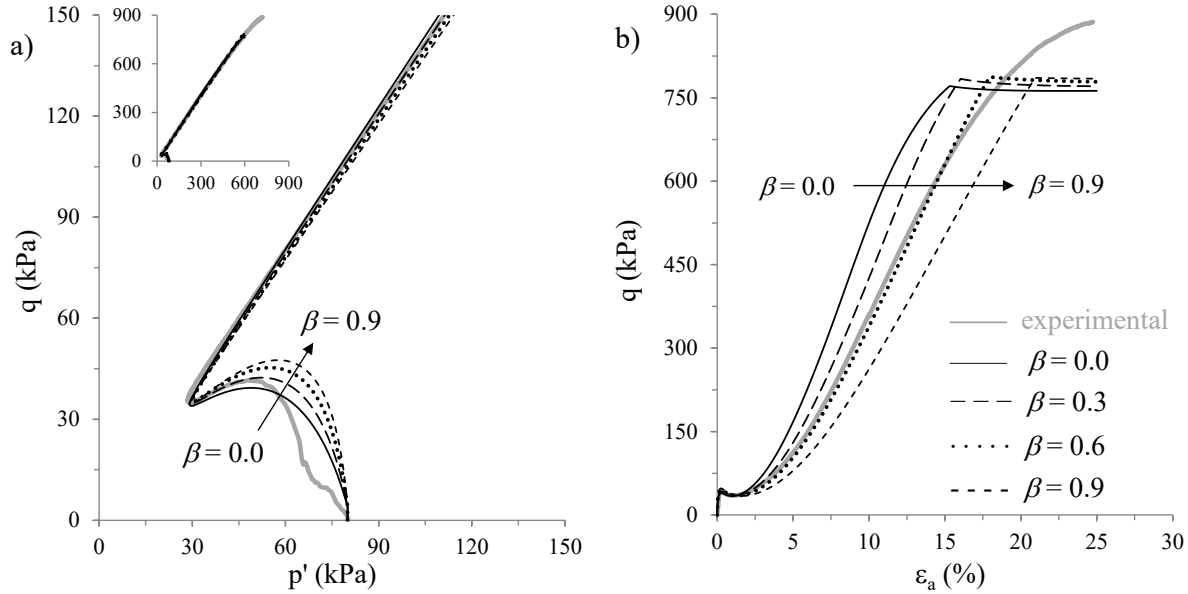

Figure 6.11 – Influence of β on the numerical simulation of test ICUMTC p↑ 0.868/80: (a) effective stress path and (b) stress-strain response.

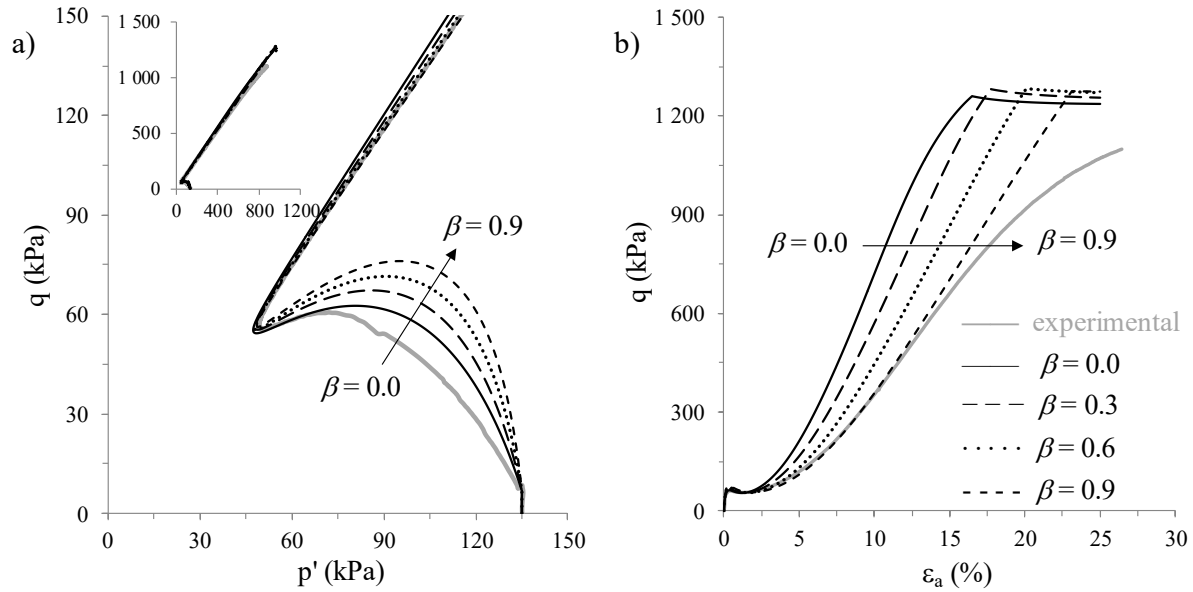

Figure 6.12 – Influence of β on the numerical simulation of test ICUMTC p↑ 0.843/135: (a) effective stress path and (b) stress-strain response.

6.10.4 Model parameters related to the influence of the void ratio and of the mean effective stress

A trial-and-error procedure was employed to calibrate the model parameters h_0, γ and e_{max}, defining the influence of the void ratio, e, (through the plastic multiplier h_e – Equation 4.60) on the plastic hardening modulus associated with the primary yield surface, A_1, as well as the model parameter μ, controlling the influence of the mean effective stress, p', through the plastic multiplier h_b (Equation 4.59), on A_1. Note that, since both p' and e are used to determine the tangent shear modulus, G_{tan}, these state parameters also influence A_1 through the plastic multiplier h_g – Equation 4.62.

As suggested by Taborda (2011), initial simulations of drained and undrained monotonic triaxial compression tests were performed. In these simulations, the effects of e (through the plastic multiplier h_e) and p' (through the plastic multiplier h_b) on A_1 were removed by setting $\gamma = 0.0$ and $\mu = 1.0$, respectively. In addition, $H_0 = 0.0$ and $\zeta = 0.0$ were adopted in the analysis to deactivate the effect of the shearing-induced fabric tensor, $\boldsymbol{F}$, on A_1 (Equations 4.66, 4.67, 4.68, 4.69 and 4.54). By employing a trial-and-error procedure, the value of h_0 resulting in the best possible match between the simulation and the laboratory test data was selected. Note that, to avoid confusion with the final value of the model parameter h_0, the parameter subjected to the trial-and-error optimisation is denoted as h_0^*. Note also that, by neglecting, at this stage, the effect of $\boldsymbol{F}$ (through the plastic multiplier h_f) on A_1, h_0^* is simply defined by Equation 6.11.

$$h_0^* = h_e \left(\frac{p'}{p'_{ref}}\right)^{\mu-1.0} = h_0\,(1.0 - \gamma e)\left(\frac{p'}{p'_{ref}}\right)^{\mu-1.0} \tag{6.11}$$

Table 6.2 – Values of h_0^* obtained by trial and error for each monotonic triaxial compression test.

Test ID [1]	e_0 [2] ( )	p'_0 [2] (kPa)	ψ_0 [2] ( )	h_0^* ( )
ICUMTC 0.876/80/p↑	0.876	80.0	-0.059	0.034
ICUMTC 0.868/80/p↑	0.868	80.0	-0.067	0.030
ICUMTC 0.843/135/p↑	0.843	135.0	-0.079	0.015
ICUMTC 0.783/25/p↑	0.783	25.0	-0.175	0.038
ICUMTC 0.801/80/p↑	0.801	80.0	-0.135	0.033
ICUMTC 0.815/135/p↑	0.815	135.0	-0.108	0.035
ICUMTC 0.686/25/p↑	0.686	25.0	-0.272	0.050
ICUMTC 0.751/80/p↑	0.751	80.0	-0.185	0.040
ICUMTC 0.694/135/p↑	0.694	135.0	-0.229	0.035
ICDMTC 0.875/50/p↑	0.875	50.0	-0.071	0.020
ICDMTC 0.885/80/p↑	0.885	80.0	-0.050	0.022
ICDMTC 0.846/200/p↑	0.846	200.0	-0.064	0.008
ICDMTC 0.835/500/p↑	0.835	500.0	-0.040	0.004
ICDMTC 0.829/25/p↑	0.829	25.0	-0.129	0.036
ICDMTC 0.798/80/p↑	0.798	80.0	-0.138	0.030
ICDMTC 0.804/135/p↑	0.804	135.0	-0.118	0.025
ICDMTC 0.667/25/p↑	0.667	25.0	-0.291	0.044
ICDMTC 0.725/80/p↑	0.725	80.0	-0.211	0.045
ICDMTC 0.728/135/p↑	0.728	135.0	-0.195	0.040
ICDMTC 0.826/80/p↓	0.826	80.0	-0.109	0.008
K0CDMTC 0.797/80/p↓	0.797	80.0	-0.139	0.035
ICDMTC 0.65/80/p↓	0.650	80.0	-0.286	0.055
K0CDMTC 0.672/80/p↓	0.672	80.0	-0.264	0.050

[1] The nomenclature used to designate the laboratory tests is detailed in Chapter 2. [2] Post-consolidation values.

Table 6.2 presents the values of h_0^* selected for each monotonic triaxial compression test simulated, together with the initial conditions of each of those tests (initial void ratio, e_0, initial mean effective stress, p'_0, and initial state parameter, ψ_0). As concluded by Taborda (2011), it is apparent that a single value for h_0^* is not adequate to reproduce accurately all tests, with values within the range of 0.004 – 0.055 being obtained in the present analysis.

By plotting the obtained values of h_0^* against e_0 for tests having $p'_0 = 80.0$ kPa (Figure 6.13), it appears that a fairly linear dependence of h_0^* on e_0 exists, as proposed in the present model (Taborda *et al.*, 2014), as well as in other models based on the same framework (e.g. Dafalias and Manzari, 2004; Taiebat and Dafalias, 2008). Note that, although the void ratio is known to vary significantly during drained shearing, for calibration purposes, the initial value of this state parameter is used, as also assumed by other authors (e.g. Li and Dafalias, 2000; Loukidis and Salgado, 2009; Taborda, 2011).

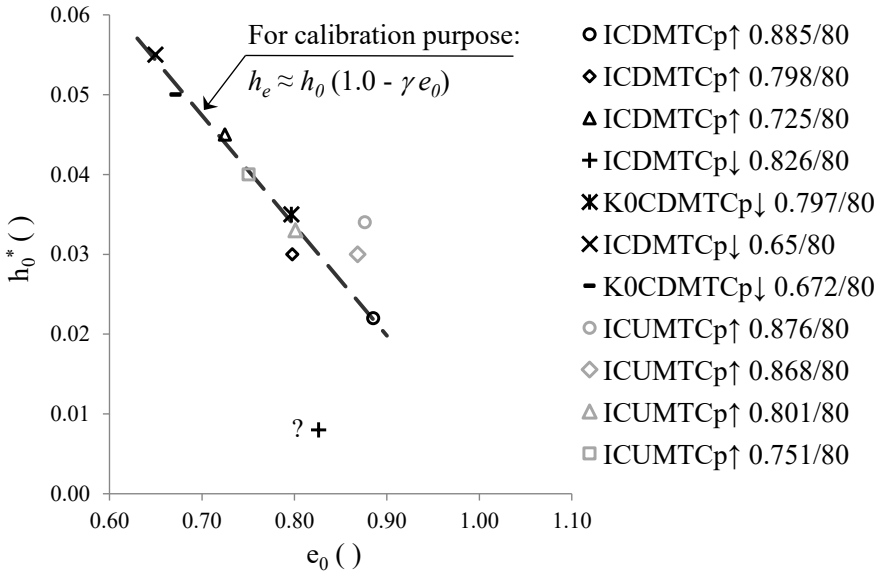

Figure 6.13 – Variation of the obtained values for h_0^* with the initial void ratio for tests having the same initial mean effective stress.

In order to assess the dependence of h_0^* on p'_0, data obtained from tests performed on samples having similar initial void ratio, e_0, though consolidated to different initial mean stress, p'_0, are depicted in Figure 6.14. Although some scatter seems to exist, it seems that, in general, the smaller the value of p'_0, the higher the value of h_0^*. Indeed, it seems that a power law can be used to describe the relationship between those quantities, as proposed in the present constitutive model. Note, however, that, due to the significant variation of p' during the shearing process, care should be taken when extrapolating the conclusions obtained in the present study. Ideally, this relationship should be evaluated based on data obtained from drained constant-p' triaxial tests. Unfortunately, data from that type of tests is not available in the present study and, therefore, future investigation is required. In fact, this may be an interesting topic for future investigation, due to the apparent lack of consensus on whether the expression for the plastic hardening modulus should include a multiplier defining a dependence on p' or not, with several constitutive relationships establishing such dependency (e.g. Papadimitriou and Bouckovalas, 2002; Dafalias and Manzari, 2004; Taiebat and Dafalias, 2008), while others neglect it (e.g. Li, 2002; Loukidis and Salgado, 2009; Andrianopoulos *et al.*, 2010b). In addition, it should be noted that two power curves are displayed in Figure 6.14, one of them corresponding to the best fitting of experimental data (represented in black), with the values of $h_e = 0.018$ and $\mu = 0.126$ being obtained for Equation 6.11, while the other curve (represented in grey) is obtained by restricting $\mu \geq 0.5$, as recommended by Papadimitriou and Bouckovalas (2002). Although no justification was given by these authors, it is believed this restriction intends to prevent strong variations of A_1 under very low values of p' from happening, which could compromise the numerical stability of the constitutive model. This restriction was adopted in the present study.

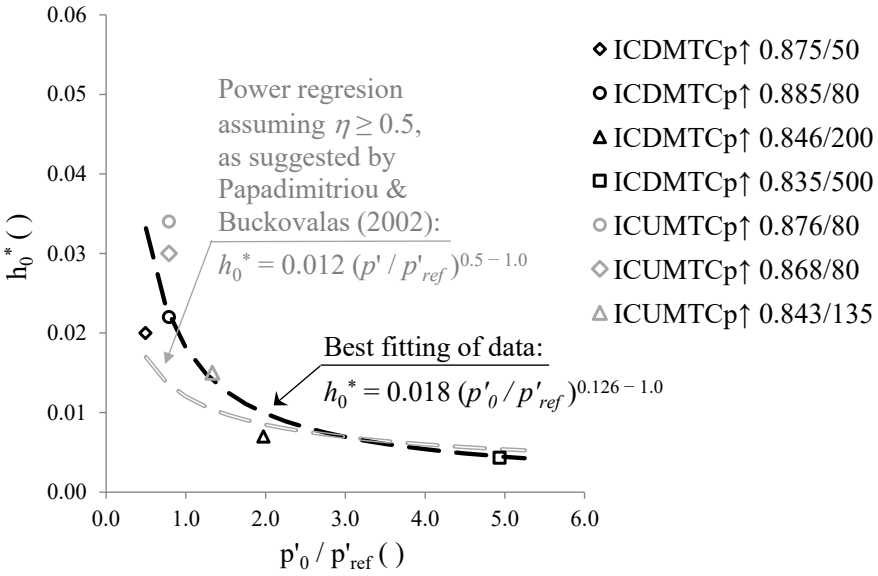

Figure 6.14 – Variation of the obtained values for h_0^* with the initial mean effective stress for tests having similar initial void ratio.

Assuming that the effect of *e* and *p'* on A_1 can be adequately described by their values at the beginning of loading, a multi-variable non-linear regression was performed to estimate the set of model parameters h_0, γ and η that best fit Equation 6.11 and, therefore, better characterise the concurrent effect of both *e* and *p'* on A_1. As explained before, a lower limit of 0.5 was applied to the value of η. The following set of parameters was obtained: $h_0 = 0.132$, $\gamma = 0.999$ and $\mu = 0.500$. Therefore, Equation 6.11 can be re-written as:

$$h_0^* = h_0\,(1.0 - \gamma e)\left(\frac{p'}{p'_{ref}}\right)^{\mu-1.0} = 0.132\,(1.0 - 0.999\,e)\left(\frac{p'}{p'_{ref}}\right)^{0.5-1.0} \quad (6.12)$$

Figure 6.15 compares the values of h_0^* selected when modelling individually each test (Table 6.2) with those computed with Equation 6.12. It can be observed that, in general, satisfactory approximations are obtained for the majority of the tests. Perhaps, the exceptions consist of tests ICDMTC p↓ 0.826/80 and ICDMTC p↑ 0.667/25 (both highlighted in the figure), for which larger values of h_0^* are provided by Equation 6.12 than those leading to the best possible match of experimental data. The opposite trend seems to be observed for tests ICUMTC p↑ 0.876/80 and ICDMTC p↑ 0.843/135 (also highlighted in the figure), with slightly smaller values of h_0^* being provided by Equation 6.12 than those obtaining when modelling individually each test to match experimental data.

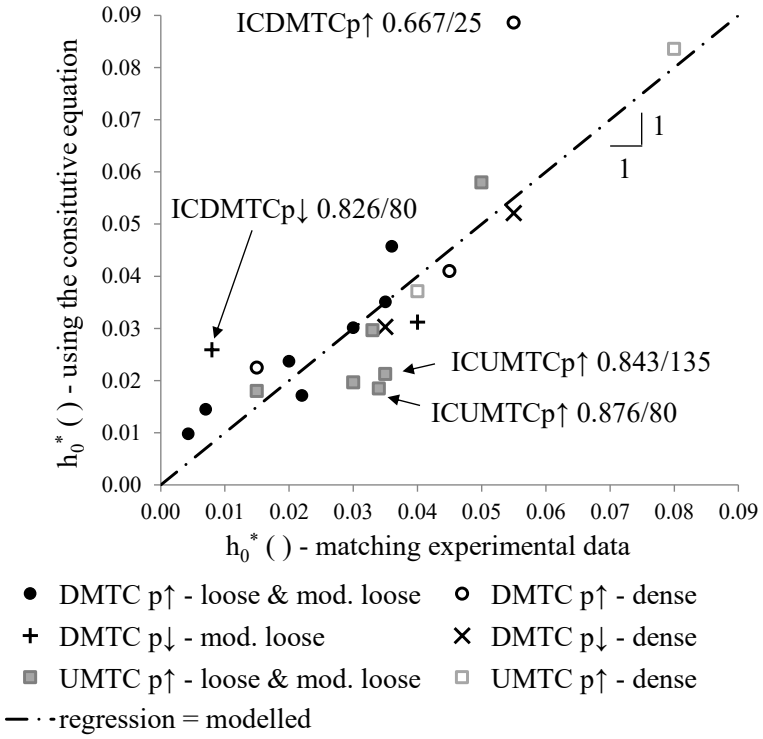

Figure 6.15 – Multi-variable regression analysis. Comparison of the h_0^* values obtained from constitutive equations with those obtained by modelling each test individually.

To avoid the computation of very low (or even negative) values for h_0^*, which could compromise the numerical stability of the analysis, a lower limit for the plastic multiplier h_e is considered, as proposed by Taborda *et al.* (2014):

$$h_e = h_0\,(1.0 - \gamma e) \geq h_0\,(1 - \gamma e_{lim}) \tag{6.13}$$

where e_{lim} is the limit void ratio. At this stage of the calibration process, a value of $e_{lim} = 0.96$ was selected, resulting in a minimum value for h_e of about 0.005.

It is perhaps important to note that, if only monotonic response of Hostun sand would be relevant and the original version of the constitutive model, as proposed by Taborda *et al.* (2014), would be employed, the calibration process could have been terminated at this point. In effect, the shearing-induced fabric component (whose calibration is presented in the following section) was introduced in the formulation of the constitutive model to capture the effect of cyclic history on the modelled response and, therefore, there is, in principle, no need to activate this component when simulating only monotonic response of sand. Regarding the inherent fabric anisotropy component, it intends to improve the simulation of the response of sand for conditions other than triaxial compression. The potential benefits in terms of flexibility and accuracy resulting from the activation of this component are discussed in Section 6.12.

6.11 Shearing-induced fabric

The two model parameters to be calibrated next – H_0 and ζ – concern the evolution of the shearing-induced fabric tensor, $\boldsymbol{F}$, with loading. Specifically, these two parameters are used to relate the evolution of the isotropic and deviatoric components of the shearing-induced fabric tensor, Δf_p and $\Delta \boldsymbol{f}$, respectively, to the initial values of the major principal effective stress, $\sigma'_{1,0}$, and state parameter, ψ_0, through the positive quantity H, as shown by Equations 6.14 to 6.17.

$$\Delta f_p = H\,\Delta\varepsilon_v^p \tag{6.14}$$

$$\Delta \boldsymbol{f} = -H\langle\Delta\varepsilon_v^p\rangle\,(C\,\boldsymbol{n} + \boldsymbol{f}) \tag{6.15}$$

where:

$$H = H_0\left(\frac{\sigma'_{1,0}}{p'_{ref}}\right)^{-\zeta}\langle-\psi_0\rangle \tag{6.16}$$

$$C = max\left|f_p\right|^2 \tag{6.17}$$

As detailed in Chapter 4, the shearing-induced fabric tensor, $\boldsymbol{F} = f_p\,\boldsymbol{I} + \boldsymbol{f}$, determines the plastic multiplier h_f (rewritten below as Equation 6.18) which, in turn, affects the plastic hardening modulus associated with the primary yield surface, A_1.

$$h_f = \frac{1 + \langle f_p\rangle^2}{1 + \langle \boldsymbol{f} : \boldsymbol{n}\rangle} \tag{6.18}$$

As explained before, since $\boldsymbol{f}$ develops only during plastic dilation in the opposite direction of the loading tensor, $\boldsymbol{n}$, and Macaulay brackets are employed in the denominator of Equation 6.18, it can be concluded that $\boldsymbol{f}$ only affects h_f when a shear reversal is triggered after a dilative phase of plastic deformation. Therefore, under monotonic loading, due to the absence of shear reversals, it can be concluded that h_f is solely determined by the value of f_p. In relation to the evolution of this component, since Δf_p has the same sign as $\Delta\varepsilon_v^p$ (Equation 6.14), it follows that f_p increases during plastic contractive sand response (i.e. $\Delta\varepsilon_v^p > 0.0 \Longrightarrow \Delta f_p > 0.0$). The opposite trend is observed as the phase transformation state is reached and, consequently, the response changes from plastic contraction to plastic dilation. Note, however, that, due to the use of the Macaulay brackets in the numerator of Equation 6.18, the value of h_f never becomes less than 1.0 under monotonic loading.

To get insight into the effect of f_p on the monotonic response of Hostun sand, test ICUMTC p↑ 0.876/80 was reproduced using the following three different values for H_0^*: 0.0 (meaning that the shearing-induced fabric component was not activated), 20 000.0 and 45 000.0. Naturally, the previously calibrated model parameters were employed in this small parametric study. Moreover, $\zeta = 0.0$ was used to deactivate the effect of $\sigma'_{1,0}$ on H_0. Note that, similar to the notation adopted before, H_0^* is used to distinguish the values employed in these simulations from that eventually obtained for H_0. The results of the three different

numerical simulations of test ICUMTC p↑ 0.876/80 are depicted in Figure 6.16. As expected, it can be observed that the larger the value of H_0^* the greater the value of h_f (Figure 6.16d) and, consequently, the stiffer the stress-strain response obtained (Figure 6.16b). Moreover, it is apparent that the value of H_0^* affects the evolution of the mean effective stress, p' (Figure 6.16a), as well as the excess pore water pressure build-up, Δu (Figure 6.16c), during the earlier stages of loading. Smaller reductions of p', as well as lesser generation of positive excess pore water pressure are obtained when larger values of H_0^* are employed in the numerical analysis. This clearly illustrates that, although this component of the formulation was introduced to deal with cyclic loading, it affects the modelled monotonic response.

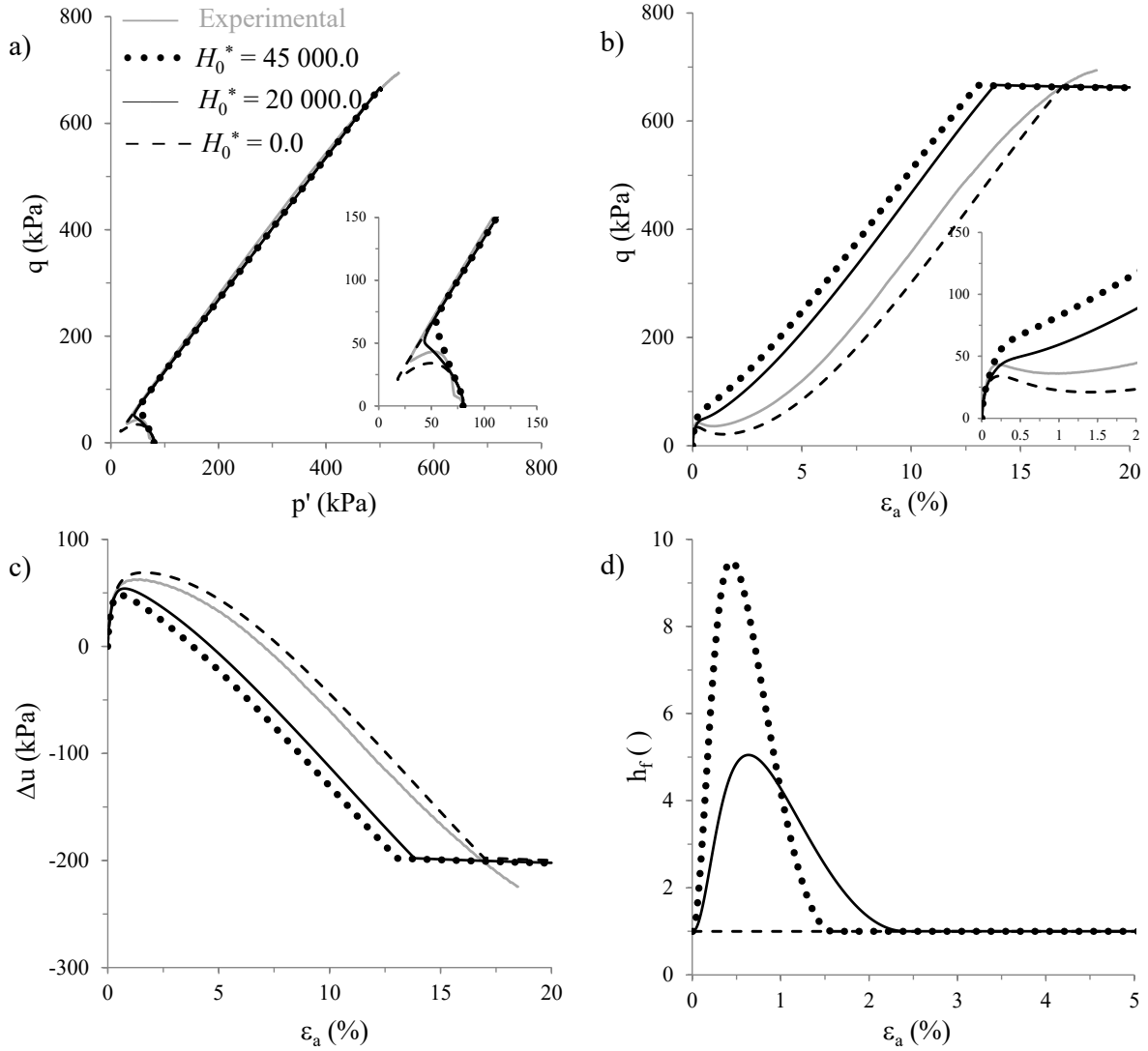

Figure 6.16 – Influence of H_0^* on the numerical simulation of test ICUMTC p↑ 0.876/80: (a) effective stress path, (b) stress-strain response, (c) pore water pressure evolution with axial strain and (d) evolution of h_f with axial strain.

Nevertheless, as expected, a much greater impact of H_0^* on h_f and, therefore, on A_1 is observed when modelling cyclic sand response. Particularly, once a loading reversal occurs after a dilative phase of plastic deformation, a value greater than 0.0 is obtained for $\langle \boldsymbol{f} : \boldsymbol{n} \rangle$ and, consequently, the value of h_f (Equation 6.18) is suddenly reduced. As a result, a softer

response and, consequently, a faster decrease of the mean effective stress upon shear reversal is simulated, as observed experimentally (e.g Ishihara *et al.*, 1975). This aspect is illustrated in Figure 6.17, which depicts the results obtained in the numerical simulation of the undrained cyclic triaxial test ICUCT 0.832/80/42 when using $H_0^* = 35\,000.0$ in conjunction with the previously calibrated model parameters. Note that the exact value of H_0^* employed in this simulation is not important, since the intention is, at this point, to assess the qualitative response. Note also that, to ease the presentation, only the results obtained from the loading cycle $N = 3$ to 5 are included in the figure. Furthermore, observe that, for triaxial conditions, $f_{xx} = f_{zz} = -f_{yy}/2.0$ and $f_{xy} = f_{xz} = f_{yx} = 0.0$.

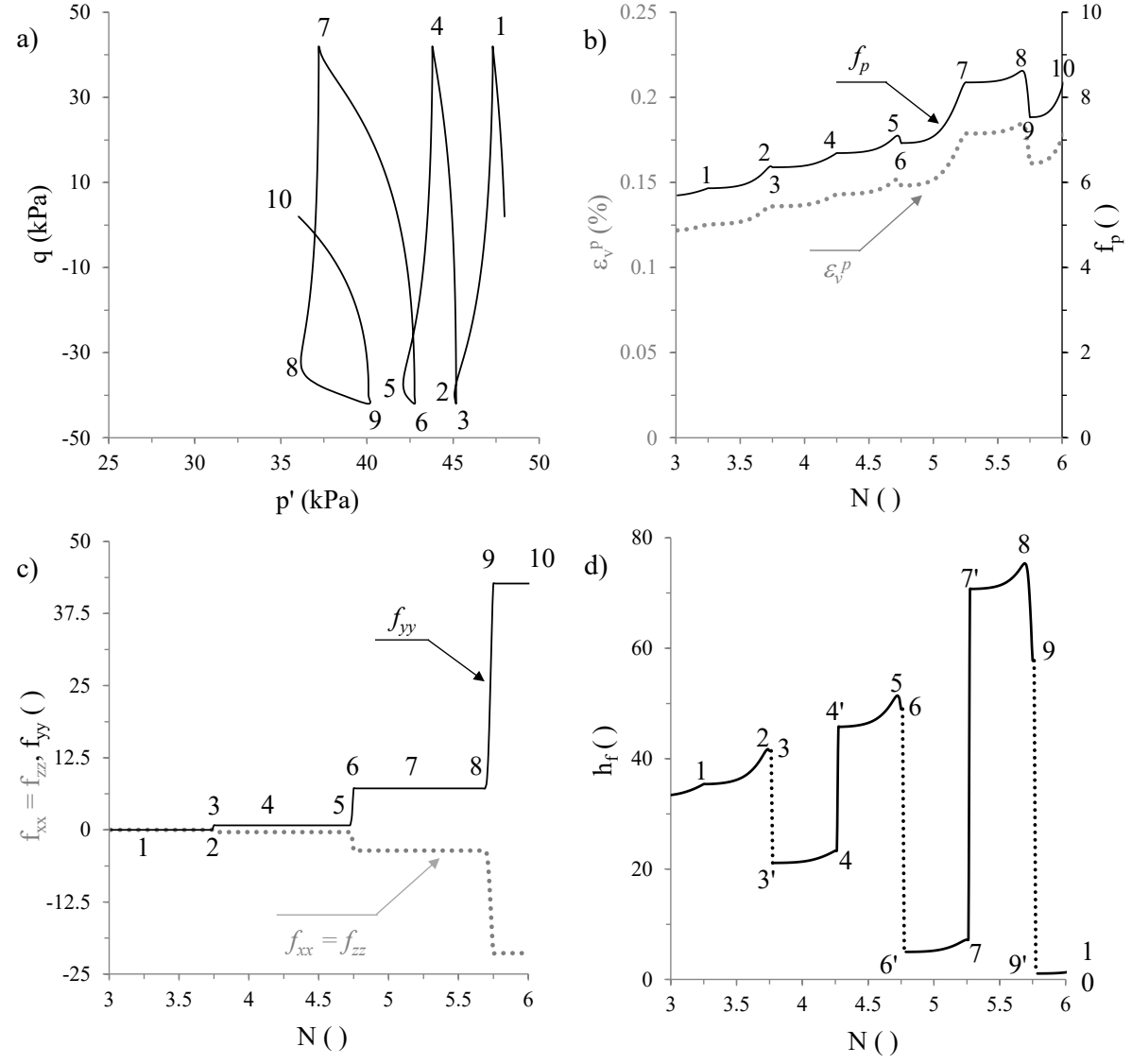

Figure 6.17 – Effect of the shearing-induced fabric component on the numerical simulation of an undrained cyclic triaxial test: (a) effective stress path; (b) and (c) evolutions of the isotropic and deviatoric components of the shearing-induced fabric tensor with the number of loading cycles; (d) evolution of the plastic multiplier h_f with the number of loading cycles.

As pointed out before, Figure 6.17 shows that, while f_p follows the evolution of ε_v^p throughout loading, $\boldsymbol{f}$ develops only during plastic dilation (i.e. during paths 2 – 3, 5 – 6 and 8 – 9). As a

result, the evolution of the plastic multiplier h_f is marked by discontinuities: "jumps" observed in Figure 6.17d from 3 to 3', from 6 to 6' and from 9 to 9', triggered by a positive value of the trace product $\boldsymbol{f} : \boldsymbol{n}$ and consequent activation of the denominator of Equation 6.18; "jumps" from 4 to 4' and from 7 to 7' triggered by a negative value of the trace product $\boldsymbol{f} : \boldsymbol{n}$ and consequent deactivation of the denominator of Equation 6.18.

Furthermore, by comparing, for instance, the effective stress paths 3 – 4 to 6 – 7 (Figure 6.17a), it is apparent that the reduction of p' is more pronounced during the latter than during the former path. This modelled response is primarily controlled by the value of h_f, which is, in fact, lower during the path 6' – 7 than during 3' – 4 (Figure 6.17d). This seems to be a consequence of the larger accumulation of plastic dilation during path 6' – 7, as well as the dependency of the evolution of the deviatoric component of shearing-induced fabric tensor, $\Delta \boldsymbol{f}$, on the previous values of $\boldsymbol{f}$ and f_p (through model quantity C), as indicated by Equation 6.15. Therefore, it can be concluded that the shearing-induced fabric tensor introduces the effect of the cyclic history on the modelled response.

To further illustrate the great effect of H_0^* on the simulated cyclic response of sand, test ICUCT 0.832/80/42 was reproduced using two different values for H_0^*, respectively 20 000 and 35 000. The obtained results are presented in Figure 6.18. It can be observed that the smaller the value of H_0^* the greater the increase in excess pore water pressures and the reduction of the mean effective stress with cyclic loading. Consequently, fewer cycles are required to reach the onset of cyclic mobility when a smaller value for H_0^* is used in the numerical analysis. In this case, it is apparent that $H_0^* = 35\,000.0$ provides a much better reproduction of the experimental data than $H_0^* = 20\,000.0$. However, it is important to note that there is an interdependency between the value to be selected for H_0^* and those used for other plastic-hardening-modulus-related parameters (in particular, h_0 and γ), which means that it is possible to select a different value for H_0^* than that identified at first sight as the most appropriate to replicate a given set of tests and, subsequently, recalibrate the plastic-hardening-modulus-related parameters. An example of application of such strategy is, for example, provided in Taborda (2011).

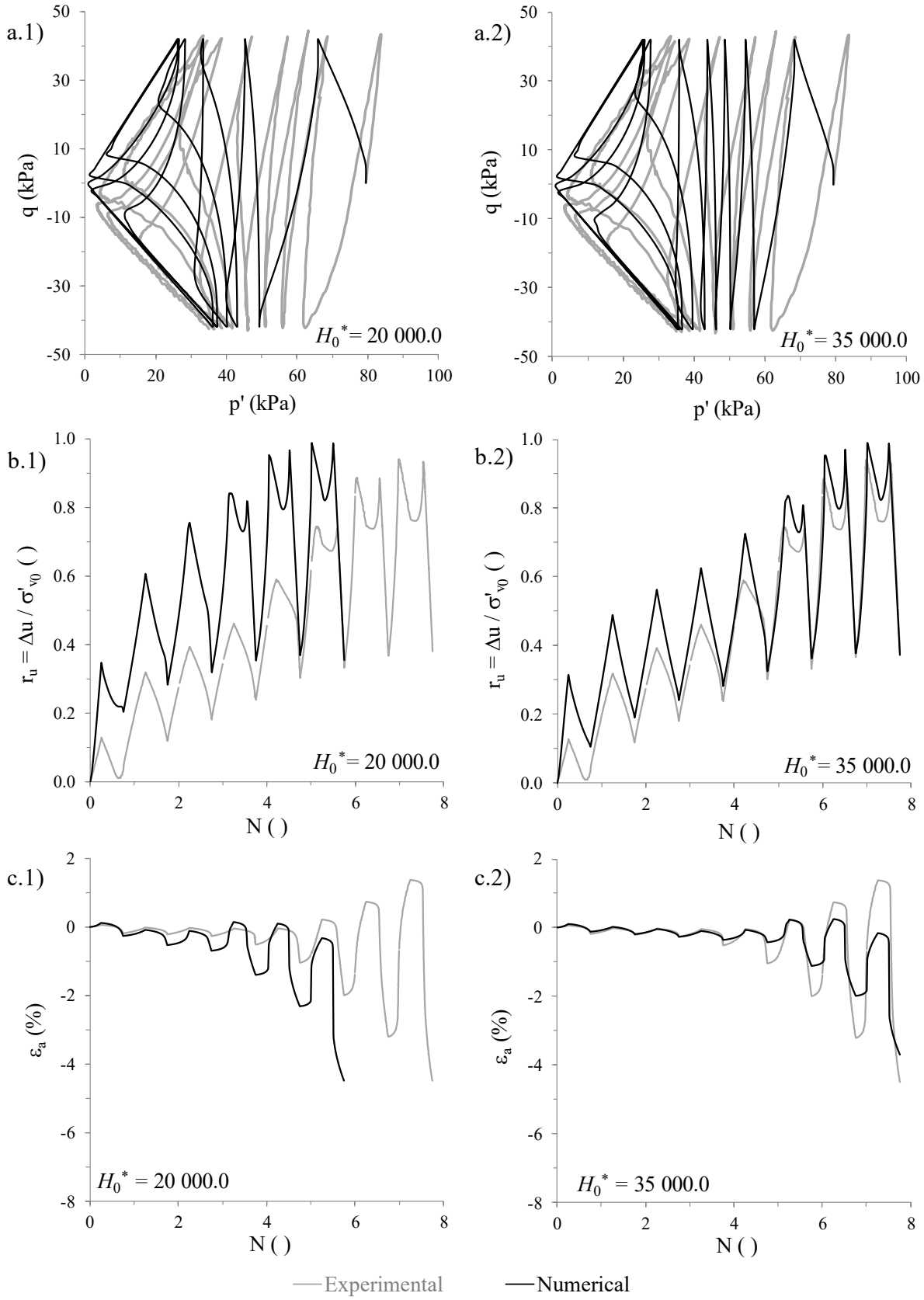

Figure 6.18 – Influence of H_0^* on the numerical simulation of test ICUCT 0.832/80/42: (a) effective stress path, (b) excess pore water pressure build-up and (c) axial strain evolution with the number of loading cycles.

From the results presented in Figure 6.16 to Figure 6.18, it can be concluded that the shearing-induced fabric anisotropy influences both monotonic and cyclic responses, with a much greater impact on the latter one. Therefore, as suggested by Taborda (2011), the calibration process of the shearing-induced fabric-related parameters should focus primarily on the cyclic response. Thus, the following strategy, proposed by Taborda (2011), was adopted in the present study:

1) Selection of two undrained cyclic triaxial (UCT) tests performed on samples consolidated under similar effective stress states. By setting the value of γ to 0.0 (to deactivate the influence of h_e on A_1) and choosing an appropriate value for h_0^* for each test, a value of H_0^* leading to a satisfactory reproduction of both UCT tests is sought. Note that, since H (Equation 6.16) depends solely on the major principal effective stress at consolidation, $\sigma'_{1,0}$, which is similar for both tests, as well as on the values assigned for the model parameters H_0 and ζ, which are considered unique for a given material, a single value for H_0^* should fit both tests. In addition, note that, since $\zeta = 0.0$ is used at this stage of the calibration process, the notation $H_0^* = H/\langle -\psi_0 \rangle$ is used to avoid confusion with the model parameter H_0. Similarly, h_0^* is used to avoid confusion with the final value of the model parameter h_0.

2) If deemed necessary, recalibration of the plastic-hardening-modulus-related parameters h_0 and γ, by using both monotonic triaxial compression and cyclic triaxial test data.

3) By setting ζ to 0.0 and using a trial-and-error procedure, inference of the value of H_0^* resulting in the best possible reproduction of each UCT test. Based on the obtained $(\sigma'_{1,0}/p'_{ref},\ H_0^*)$ data, a non-linear regression analysis is performed to calibrate H_0 and ζ.

According to the proposed methodology, tests ICUCT 0.832/80/42 and ICUTC 0.651/80/43 were selected. In these tests, samples prepared to very different initial void ratio ($e_0 = 0.832$ and $e_0 = 0.651$, respectively) were consolidated to a mean effective stress of $p'_0 = 80$ kPa and subjected to a similar deviatoric stress oscillation of $\Delta q = \pm 42$ kPa and $\Delta q = \pm 43$ kPa, respectively. A series of numerical simulations were subsequently performed for both tests, in order to find the best possible set of values for h_0^* and H_0^*. Starting with the simulation of the ICUCT 0.832/80/42 test, it was previously shown in Figure 6.18 that a good approximation of the experimental data is obtained when using that $H_0^* = 35\,000.0$ in conjunction with the current values of h_0 and γ. Nevertheless, other combinations of h_0^* and H_0^* values were tested, in an attempt to identify the best possible combination of values for these quantities.

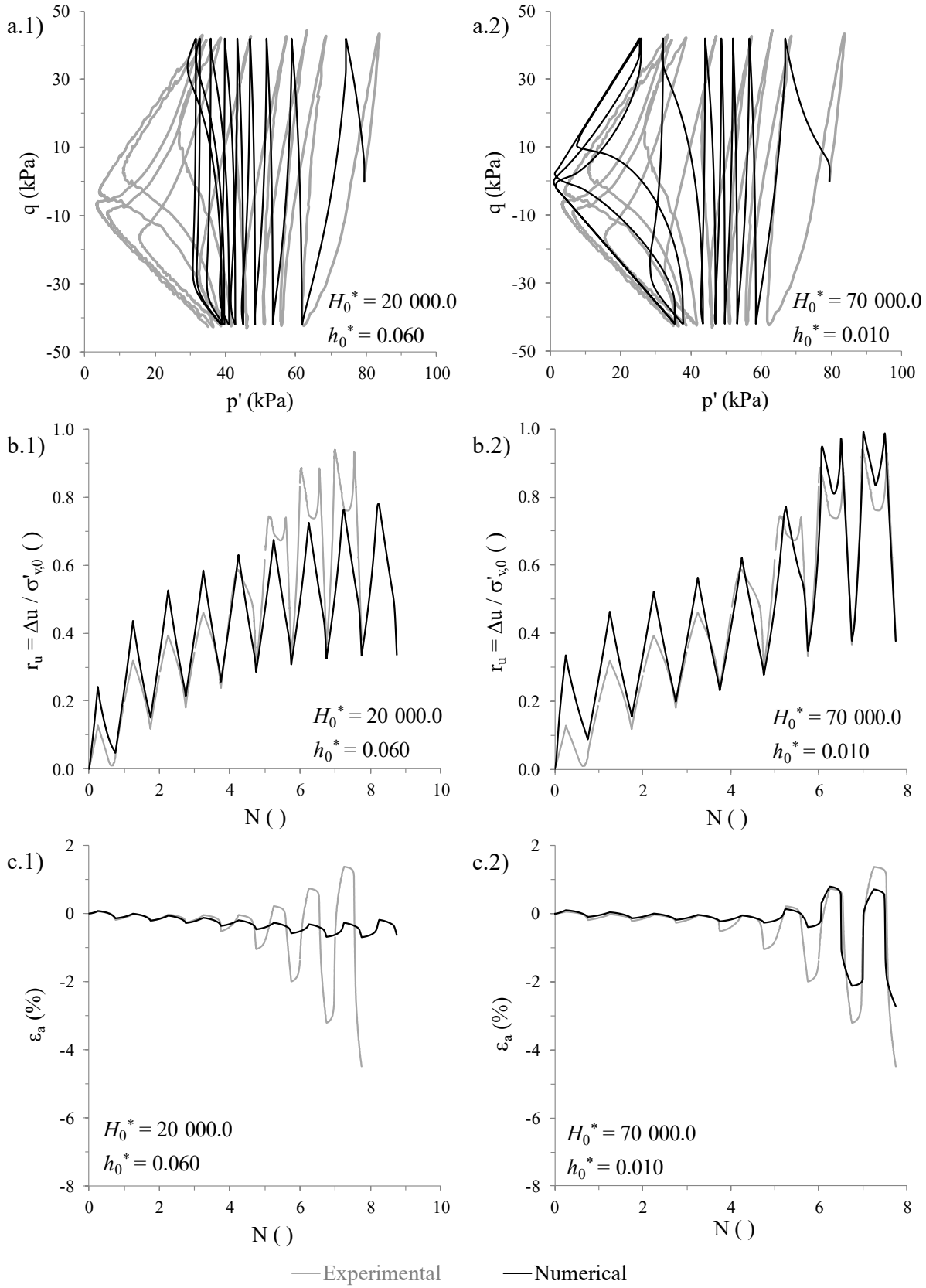

Figure 6.19 – Effect of two different sets of H_0^* and h_0^* values on the numerical simulation of test ICUCT 0.832/80/42: (a) effective stress path, (b) excess pore water pressure build-up and (c) axial strain evolution with the number of loading cycles.

For instance, Figure 6.19 compares the results of two different numerical simulations – one of them employing $H_0^* = 20\,000.0$ and $h_0^* = 0.060$, while the other one adopting $H_0^* = 70\,000.0$ and $h_0^* = 0.010$ – with the corresponding laboratory test data. It can be observed that, when using the former set of parameters ($H_0^* = 20\,000.0$ and $h_0^* = 0.060$), the rate of excess pore water pressure generation is overestimated during the first 5 loading cycles (i.e. approximately up to the first crossing of the phase transformation line). An opposite trend seems to be registered during the remaining loading cycles, with the effective stress path tending very slowly to zero mean effective stress, contrary to the experimental observations. The accumulation of axial strain is also much smaller than that measured in the experiment. Moreover, although an overall better reproduction of test ICUCT 0.832/80/42 is obtained when employing the set of parameters $H_0^* = 70\,000.0$ and $h_0^* = 0.010$ (rather than when using $H_0^* = 20\,000.0$ and $h_0^* = 0.060$), it can be seen that the increase in the excess pore water pressures during the 5th cycle (corresponding to the first crossing of the phase transformation line) obtained in the numerical analysis clearly overestimates that measured in the experiment. In effect, this aspect is mainly governed by the magnitude of the state parameter C (Equation 6.17). By comparing the results shown in Figure 6.18 and Figure 6.19, it may be concluded that, among the three different values tested until this moment, $H_0^* = 35\,000.0$ provides the best approximation for test ICUCT 0.832/80/42.

Subsequently, a series of numerical analysis were conducted to find out the set of values for h_0^* and H_0^* leading to best replication of test ICUCT 0.651/80/43. Figure 6.20 compares the results of two different numerical simulations – one of them employing $H_0^* = 35\,000.0$ in conjunction with the current values of the plastic-hardening-modulus-related parameters ($\alpha = 1.000$, $\beta = 0.300$, $h_0 = 0.132$, $\gamma = 0.999$, $e_{max} = 0.960$ and $\mu = 0.500$) and the other simulation using $H_0^* = 20\,000.0$ and $h_0^* = 0.060$ – with the experimental data. Note that these sets of values were also used in the simulations of test ICUCT 0.832/80/42. It is apparent that none of the employed set of parameters is able to reproduce adequately the complete experimental data. In particular, it can be observed that, irrespective of the model parameters used in the numerical analysis, once the phase transformation line is crossed and the stress path is reverted, a significantly faster reduction of the mean affective stress is simulated by the constitutive model, in comparison to that observed in the experiment. As a result, the accumulation of axial strain is overestimated from that moment by the constitutive model. In addition, Figure 6.20 shows that, irrespective of the values adopted for h_0^* and H_0^*, the oscillations of the excess pore water pressure during loading are overestimated by the constitutive model. Nevertheless, a satisfactory reproduction of the permanent accumulation of excess pore water pressure with loading appears to be obtained, particularly when employing $H_0^* = 35\,000.0$ in conjunction with the current values of the plastic-hardening-modulus-related parameters.

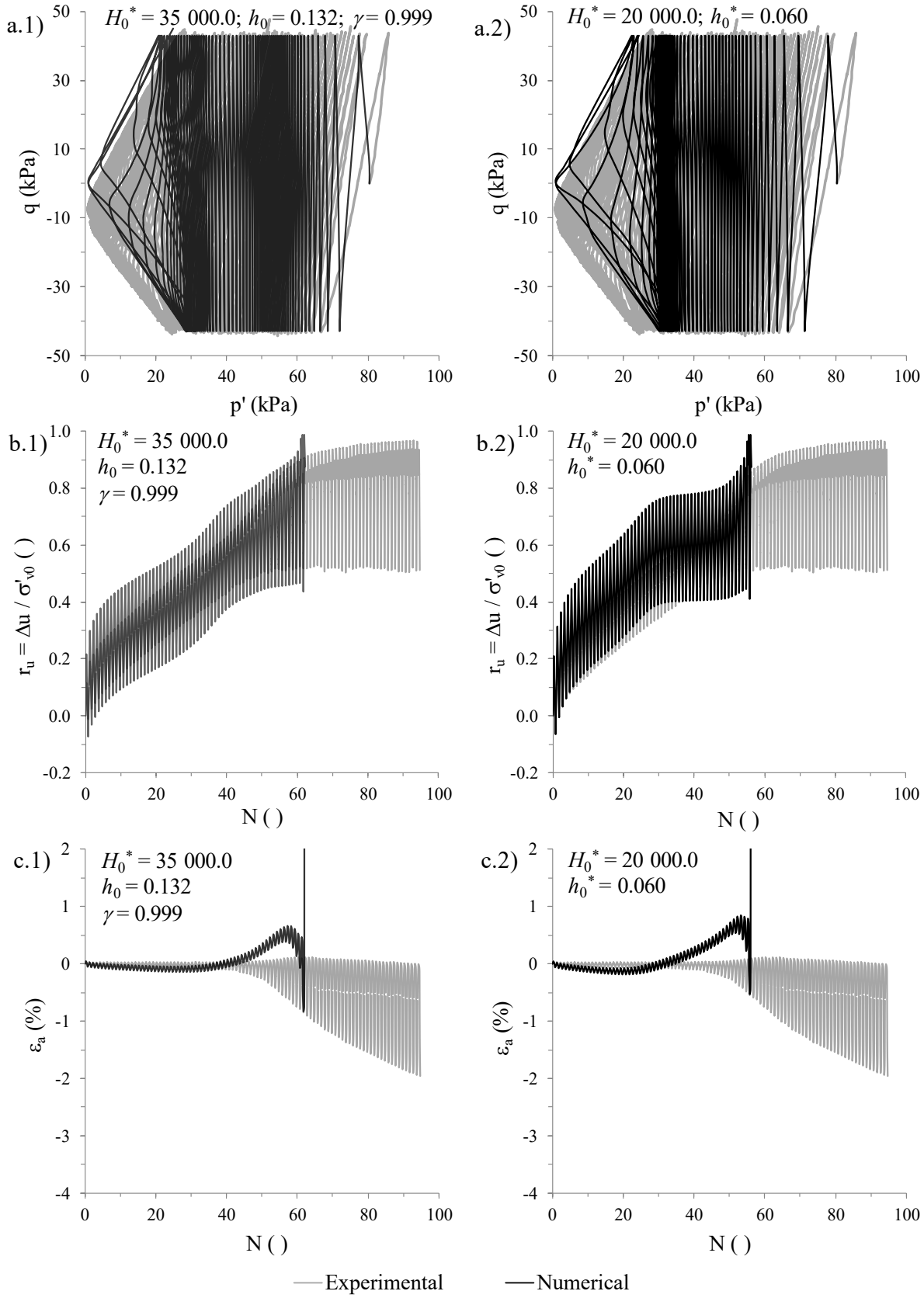

Figure 6.20 – Effect of H_0^* and h_0^* on the numerical simulation of test ICUCT 0.651/80/43: (a) effective stress path, (b) excess pore water pressure build-up and (c) axial strain evolution with the number of loading cycles.

Based on the results obtained in these initial simulations of tests ICUCT 0.832/80/42 and ICUCT 0.651/80/43, it can be concluded that $H_0^* = 35\,000.0$ provides a good initial estimation, when used in conjunction with the current values of the plastic-hardening-modulus-related parameters ($\alpha = 1.000$, $\beta = 0.300$, $h_0 = 0.132$, $\gamma = 0.999$, $e_{max} = 0.960$ and $\mu = 0.500$). Nevertheless, it was pointed out that, although introduced to address the simulation of cyclic loading, the isotropic component of the shearing-induced fabric tensor affects the early contractive stages of the modelled response of UMTC tests performed on loose and moderately loose samples. More specifically, the introduction of the shearing-induced fabric component leads to the reproduction of a stiffer stress-strain response and a less compliant effective stress path during the early stage of loading (Figure 6.16). To improve slightly this aspect, it was decided to increase the value of β from 0.30 to 0.60. Furthermore, since this alteration enforces the recalibration of the plastic-hardening-modulus-related parameters h_0, γ and e_{max}, as defined in step 2) of the calibration strategy, it was also decided to adopt $H_0^* = 45\,000.0$, rather than $H_0^* = 35\,000.0$, to obtain a slightly better match of the reduction of stiffness upon the first crossing of the dilatancy surface, particularly for moderately loose samples. Therefore, following the methodology previously described in Section 6.10.4 and having $\alpha = 1.000$, $\beta = 0.300$, $\mu = 0.500$ and $H_0^* = 45\,000.0$, the model parameters h_0, γ and e_{max} were recalibrated against results of monotonic and cyclic triaxial tests performed on samples consolidated to $p'_0 = 80$ kPa. The obtained results are presented in Figure 6.21. Note that the $h_0^* - e_0$ line corresponding to the previous set of parameters (i.e. obtained in Section 6.10.4) is also displayed in the figure for comparison purposes. Although a different value for β was used at this stage, hampering firm conclusions from being reached, it seems that a more inclined $h_0^* - e_0$ line was obtained at this stage, illustrating the strong effect of the shearing-induced fabric tensor in both monotonic and cyclic response of sand. Additionally, it is apparent that, for monotonic tests performed on loose and moderately loose sand (namely, tests ICDMTC p↑ 0.885/80, ICDMTC p↑ 0.798/80, ICUMTC p↑ 0.876/80, ICUMTC p↑ 0.868/80 and ICUMTC p↑ 0.801/80), the values of h_0^* computed by the constitutive relationship (i.e. represented by the newly obtained $h_0^* - e_0$ line) are slightly larger than those identified as the most appropriate values (i.e. data points). This suggests that, for these tests, the constitutive model (when using this new set of model parameters) will likely overestimate the stiffness of the material, at least during the earlier stages of loading. This aspect will be discussed in detail in the following chapter. Finally, Figure 6.21 also shows that a smaller value for e_{max} is now required, to limit the model parameter h_e to a positive value. At this stage, a value of $e_{max} = 0.900$ was selected, resulting in a minimum value for h_e of about 0.002. To sum up, the following plastic-hardening-modulus-related parameters were adopted at this stage: $\alpha = 1.000$, $\beta = 0.600$, $h_0 = 0.200$, $\gamma = 1.100$, $e_{max} = 0.900$ and $\mu = 0.500$.

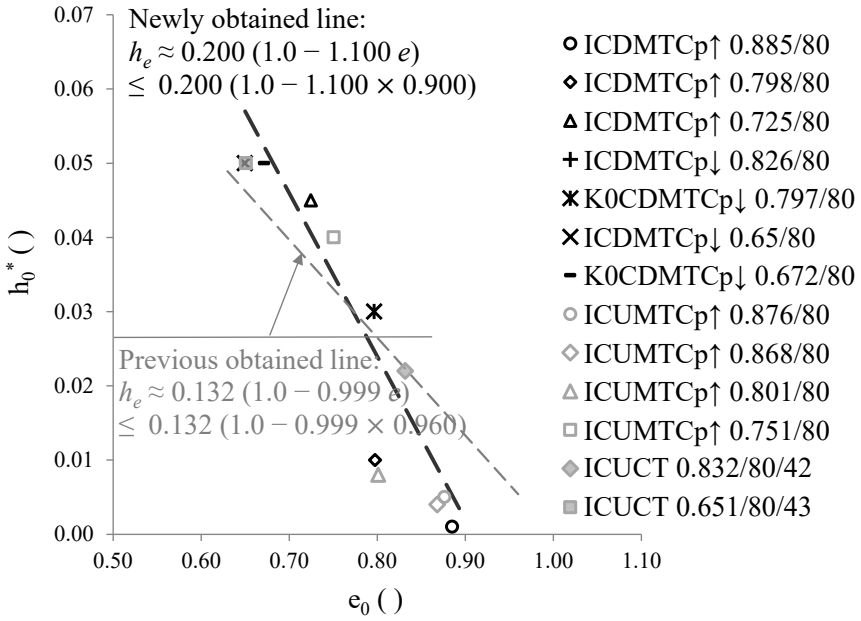

Figure 6.21 – Recalibration of the plastic-hardening-modulus-related parameters using monotonic triaxial compression and cyclic triaxial tests where samples were consolidated to a mean effective stress of 80 kPa.

The calibration proceeded to step 3), where each UCT test available was modelled by setting ζ to 0.0 and selecting an appropriate value for H_0^*. The obtained results are indicated in Table 6.3, together with the initial conditions of each laboratory test.

Table 6.3 – Values of H_0^* obtained by a trial-and-error procedure for all available undrained cyclic triaxial tests.

Test ID [1]	e_0 [2] ( )	p'_0 (kPa)	ψ_0 [2] ( )	$\lvert\Delta q\rvert$ [3] (kPa)	H_0^* ( )
ICUCT 0.821/25/13	0.821	25.0	-0.140	13.0	200 000.0
ICUCT 0.777/25/18	0.777	25.0	-0.140	18.0	170 000.0
ICUCT 0.771/80/32	0.771	80.0	-0.137	32.0	55 000.0
ICUCT 0.803/80/36	0.803	80.0	-0.137	36.0	80 000.0
ICUCT 0.832/80/42	0.832	80.0	-0.129	42.0	55 000.0
ICUCT 0.804/80/48	0.804	80.0	-0.136	48.0	5 000.0
ICUCT 0.773/80/56	0.773	80.0	-0.138	56.0	1 000.0
ICUCT 0.805/135/40	0.805	135.0	-0.120	40.0	40 000.0
ICUCT 0.830/135/54	0.830	135.0	-0.128	54.0	55 000.0
ICUCT 0.793/135/67.5	0.793	135.0	-0.128	67.5	5 000.0
ICUCT 0.651/80/43	0.651	80.0	-0.285	43.0	35 000.0
ICUCT 0.652/80/72	0.652	80.0	-0.284	72.0	30 000.0
ICUCT 0.652/80/88	0.652	80.0	-0.284	88.0	30 000.0

[1] Test identifier nomenclature is detailed in Chapter 2 Chapter 3; [2] post-consolidation values; [3] deviatoric stress oscillation.

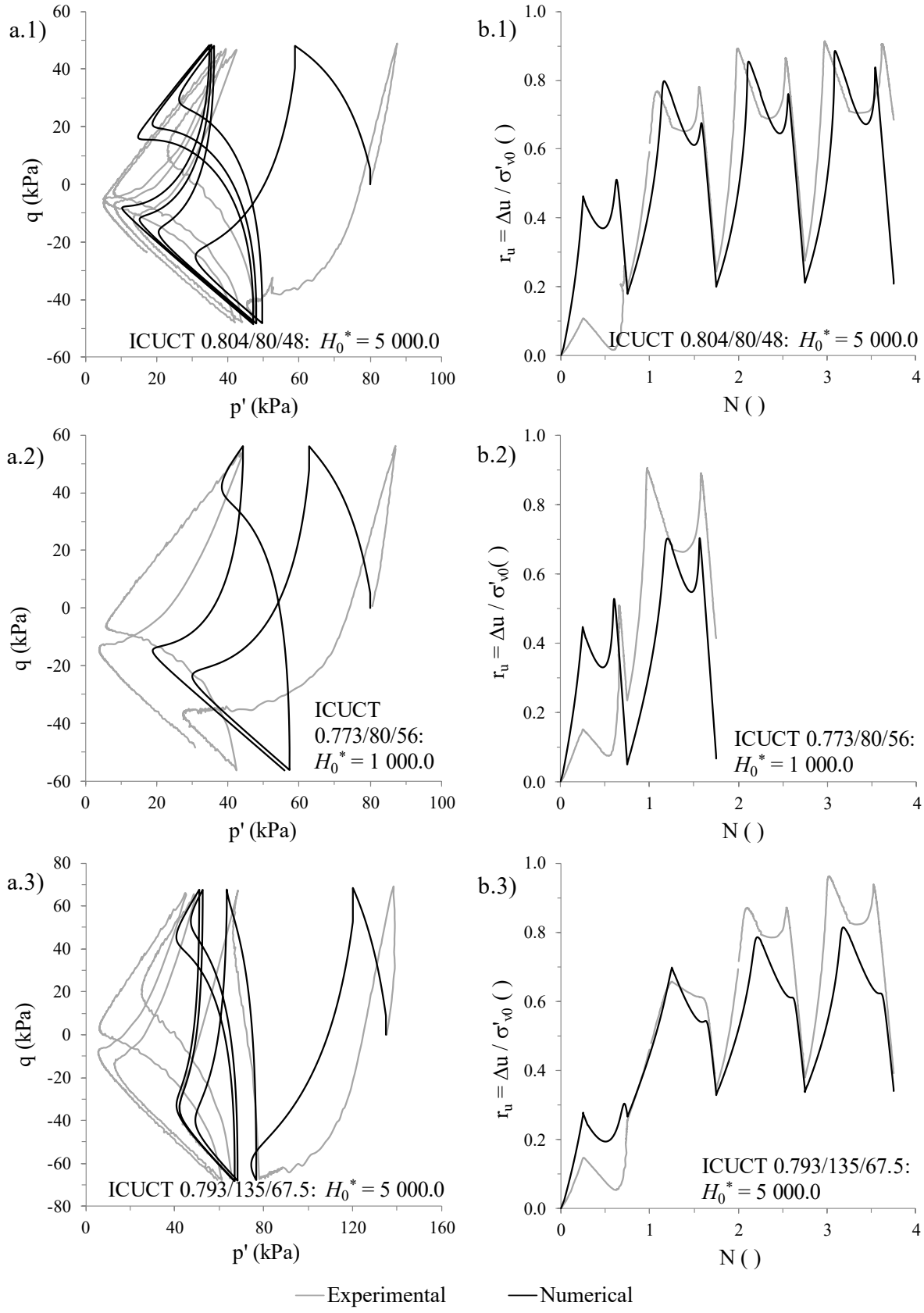

Figure 6.22 – Calibration of H_0^* for tests ICUCT 0.804/80/48, ICUCT 0.773/80/56 and ICUCT 0.793/135/67.5: (a) effective stress path and (b) excess pore water pressure build-up with the number of loading cycles.

By analysing the values presented in Table 6.3, it is apparent that satisfactory simulations of tests ICUCT 0.804/80/48, ICUCT 0.773/80/56 and ICUCT 0.793/135/67.5 (presented in grey) would require very low values for H_0^*. In these three tests, the samples were sheared under large cyclic stress ratios (CSRs), exhibiting very soft responses in triaxial extension during the first loading cycle. As a result, severe reductions of the effective stresses were observed in these tests, with the onset of cyclic mobility occurring just after two to four loading cycles, as illustrated in Figure 6.22. Although it is apparent in the figure that, for all three tests, the constitutive model would be able to replicate satisfactorily the measured response, the values of H_0^* obtained in the analysis are clearly smaller than those require to simulate adequately the remaining tests conducted on samples consolidated under similar mean effective stresses ($p'_0 = 80$ or 135 kPa), as indicated in Table 6.3. It was, therefore, decided to exclude these three tests from the calibration process. Note that similar findings were also reached by Taborda (2011) when simulating the undrained cyclic response of Leighton Buzzard Fraction-E sand. In particular, the author observed that the constitutive model was unable to capture the very soft response observed in one UCT test using a large CSR, where a dense sample was observed to reach cyclic mobility after just two loading cycles. This suggests that the problem is not related to the model parameters obtained for Hostun sand in the current calibration process, rather to the ability of the constitutive model to capture the very soft response of sand typically observed in tests where large oscillations stresses are applied to the samples, leading to the onset of cyclic mobility in just very few cycles. Note, nevertheless, that, as suggested by Taborda (2011), the introduction of the inherent fabric anisotropy component in the formulation of the constitutive model is expected to improve the ability of the model to replicate the response observed in these tests. This aspect will be explored in the following section.

Having plotted the $\left(\sigma'_{1,0}/p'_{ref},\ H_0^*\right)$ data values, as depicted in Figure 6.23, a non-linear regression analysis was subsequently performed to determine the model parameters H_0 and ζ. The following values were obtained: $H_0 = 43\,000.0$ and $\zeta = 1.00$.

Note that, apart from the numerical stability-related parameters, whose calibration is presented in Section 6.13, the determination of the shearing-induced fabric-related parameters marks the end of the calibration process for the original version of the model.

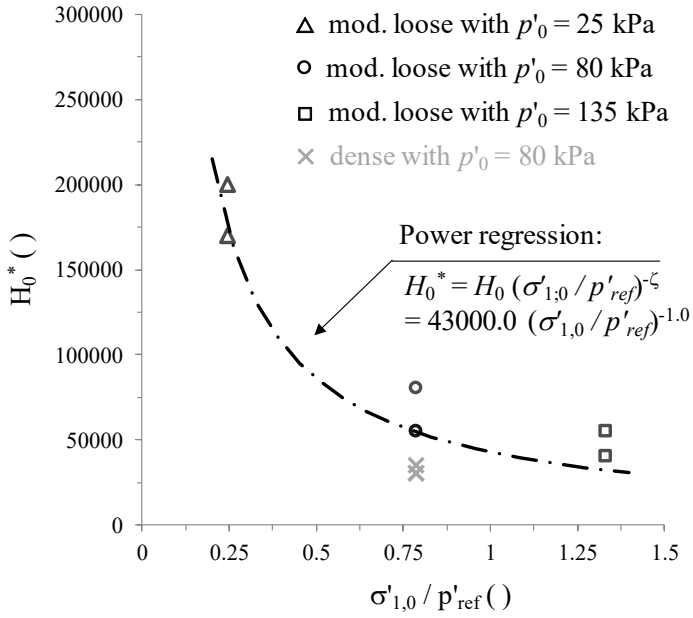

Figure 6.23 – Calibration of the shearing-induced fabric-related parameters.

6.12 Inherent fabric anisotropy

As detailed in Section 4.3.3, the inherent fabric anisotropy formulation introduces a new tensor $\boldsymbol{F_A}$ (Equation 6.19). Moreover, the interaction of this new tensor with the deviatoric loading direction tensor, $\boldsymbol{n}$, defines a new scalar-valued state parameter A_F (Equation 6.20).

$$\boldsymbol{F_A} = \begin{bmatrix} F_{xx} & F_{xy} & F_{xz} \\ F_{yx} & F_{yy} & F_{yz} \\ F_{zx} & F_{zy} & F_{zz} \end{bmatrix} = \begin{bmatrix} 1/2\ (1-a) & 0 & 0 \\ 0 & a & 0 \\ 0 & 0 & 1/2\ (1-a) \end{bmatrix} \tag{6.19}$$

$$A_F = g(\theta, c^a)\ \boldsymbol{F_A} : \boldsymbol{n} \tag{6.20}$$

where g is the interpolation function (Equation 4.36), θ is the modified Lode's angle (Equation 4.37) and c^a is the positive value of the ratio between A_F in triaxial extension, $A_{F,e}$, and its value in triaxial compression, $A_{F,c}$, i.e. $c^a = -A_{F,e}/A_{F,c}$.

The anisotropic state parameter, A_F, affects the position of the CSL in the $e - p'$ space (Equation 6.21), by relocating its intersection with the e-axis (Equation 6.22).

$$e_{cs} = (e_{cs})_A - \lambda \left(\frac{p'}{p'_{ref}}\right)^{\xi} \tag{6.21}$$

$$(e_{cs})_A = (e_{cs})_{ref} \exp\left(v_A \frac{\langle d^c \rangle}{d^c_{ref}} \left(A_{F,c} - A_F\right)\right) \tag{6.22}$$

where d^c is the distance in the normalised deviatoric plane from the current stress point to the CSL, while d^c_{ref} is a reference distance to the CSL (Equation 6.23).

$$d^c_{ref} = \sqrt{\frac{2}{3}}\ (\alpha^c_\theta + \alpha^c_{\theta+\pi}) = \sqrt{\frac{2}{3}}\ (g(\theta, c^c)\ M^c_c + g(\theta+\pi, c^c)\ M^c_c - 2m) \tag{6.23}$$

More specifically, since $d^c > 0$ for initially denser-than-critical samples (as it is the case of all samples tested in the present study) and $A_{F,c} - A_F < 0$ for loading conditions other than triaxial compression (TC), and providing that $v_A > 0$ (as reported in the literature), it follows that $\exp\left(v_A \frac{\langle d^c \rangle}{d^c_{ref}}\left(A_{F,c} - A_F\right)\right) < 1$ under such loading conditions and, therefore, $(e_{cs})_A < (e_{cs})_{ref}$ while $d^c > 0$. This relocation of the CSL affects the value of the state parameter, ψ (Equation 6.24), and, consequently, the positions of both bounding and dilatancy surfaces (Equations 6.25 and 6.26, respectively), which are linearly dependent on ψ. This means that the relocation of the CSL with A_F requires, in principle, the recalibration of the positions of the dilatancy and bounding surfaces for triaxial extension (TE) loading, as it will be detailed later.

$$\psi = e - e_{cs} = e - (e_{cs})_A + \lambda \left(p'/p'_{ref}\right)^{\xi} \tag{6.24}$$

$$M^b_{c,e} = M^c_{c,e} + k^b_{c,e} \langle -\psi \rangle \tag{6.25}$$

$$M^d_{c,e} = M^c_{c,e} + k^d_{c,e} \psi \tag{6.26}$$

Indeed, recalling that, according to the two-surface plasticity framework (Manzari and Dafalias, 1997), the gradient of the plastic potential, $\partial \boldsymbol{P}/\partial \boldsymbol{\sigma}'$, and the plastic hardening modulus, A_1, depend on the distances between the current effective stress point and its projection on the dilatancy and bounding surfaces, respectively, it can be further concluded that the relocation of the CSL with A_F affects these two aspects of the constitutive model, as pointed out in Chapter 4.

Additional influence on A_1 is introduced by the plastic multiplier h_A (Equation 6.27).

$$h_A = exp\left[\left(\frac{A_{F,c} - A_F}{A_{F,c} - A_{F,e}}\right)^{1.25} ln(k_A)\right] \tag{6.27}$$

From Equations 6.19 to 6.27, it can be observed that three additional model parameters are introduced by the inherent fabric anisotropy formulation, namely a, v_A and k_A. The first of these parameters is a measure of the orientation of the particle distribution. According to Dafalias *et al.* (2004), a is expected to have a value between 0.0 and 1.0 / 3.0 for sand. While the former value corresponds to the case where particles "lie" entirely on the horizontal plane, which is only expectable for extremely thin and long grains (such as montmorillonite grains), the latter value resembles a statistically isotropic orientation of particles, which, according to the authors, would solely be attainable by spherical grains with identical size. Further investigation on appropriate values for the model parameter a was undertaken by Papadimitriou *et al.* (2005). In particular, these authors performed a series of numerical simulations to evaluate the ability of the constitutive model developed by Dafalias *et al.* (2004), which includes an inherent fabric anisotropy formulation, to capture the effect of the method of sample preparation on the undrained monotonic response of sand. While concluding that the constitutive relationship was able to replicate the different responses obtained by several different methods of sample preparation, the authors suggested that the

value of a is more affected by the nature of the grains (mineralogy, particle shape and size distribution) than by the method of sample's preparation, with values in the range of 0.28 – 0.31 being adopted for Toyoura sand prepared by dry deposition, air pluviation, wet tamping and dry rodding. Values within this range were also adopted by Loukidis and Salgado (2009). Specifically, $a = 0.29$ was adopted by these authors to the simulation of the response of dry-deposited Toyoura sand, while a slightly larger value of $a = 0.31$ was adopted for slurry-deposited and water-pluviated Ottawa sand. Taking into account that the particle shape and size distribution of Hostun sand are, respectively, similar to those of Toyoura and Ottawa sands (Section 2.2.1), $a = 0.29$ was adopted in the present study.

Regarding the other two model parameters, v_A determines the magnitude of the effect of A_f on the CSL, as given by Equation 6.22, while k_A controls the difference in stiffness between the two extreme cases of loading direction (TC and TE), as given by Equation 6.27. Ideally, these model parameters would be calibrated by trial and error against results of torsional shearing tests. By varying the angle α of the major principal effective stress, σ'_1, to the axis of the sample and/or the coefficient $b = (\sigma'_2 - \sigma'_3)/(\sigma'_1 - \sigma'_3)$ defining the magnitude of the intermediate principal effective stress, σ'_2, in relation to the major and minor principal effective stresses, σ'_1 and σ'_3 respectively, different values for A_f would be obtained, allowing for the calibration of Equation 6.22 and Equation 6.27. Details on this procedure can be found, for example, in Loukidis and Salgado (2009). Alternatively, in the absence of torsional shearing test data, as it is the present case, results of monotonic triaxial extension (MTE) and cyclic triaxial (CT) tests can be employed in the calibration process.

Before detailing the strategy adopted for the calibration of the model parameters v_A and k_A, three aspects should be highlighted. Firstly, assuming that $c^a = c^c = 0.72$ and having $a = 0.29$, it follows that, in the present study, the value of the anisotropic state parameter, A_F, in TC, designated as $A_{F,c}$, is about -0.053 (Equation 6.28), while in TE, $A_{F,e}$ is approximately 0.038 (Equation 6.29). These values define the range of variation of A_F.

$$\begin{aligned} A_{F,c} = g(\theta, c^a)\, \boldsymbol{F} : \boldsymbol{n} &= 1 \times \frac{1}{\sqrt{6}} \left[\frac{1}{2}(1-a) \times (-1) + a \times (2) + \frac{1}{2}(1-a) \times (-1)\right] \\ &= \frac{3\,a - 1}{\sqrt{6}} = \frac{3 \times 0.29 - 1}{\sqrt{6}} \approx -0.053 \end{aligned} \tag{6.28}$$

$$\begin{aligned} A_{F,e} = g(\theta, c^a)\, \boldsymbol{F} : \boldsymbol{n} &= c^a \times \frac{1}{\sqrt{6}} \left[\frac{1}{2}(1-a) \times (1) + a \times (-2) + \frac{1}{2}(1-a) \times (1)\right] \\ &= c^a\, \frac{1 - 3\,a}{\sqrt{6}} = 0.72 \times \frac{1 - 3 \times 0.29}{\sqrt{6}} \approx 0.038 \end{aligned} \tag{6.29}$$

Secondly, as noted before, the inherent fabric anisotropy component has no impact on the modelled response under TC loading (i.e. when $A_F = A_{F,c}$), since, under such loading conditions, it follows that $(e_{cs})_A = (e_{cs})_{ref}$ (Equation 6.22) and $h_A = 1.0$ (Equation 6.27). Therefore, when solely monotonic response is of interest, there should be, in principle, no need to recalibrate the plastic-hardening-modulus-related parameters previously calibrated

against results of monotonic triaxial compression tests, with the introduction of the inherent fabric anisotropy component simply enhancing the modelled response under loading conditions other than triaxial compression (e.g. in triaxial extension).

Thirdly, as explained before, due to the relocation of the CSL for loading conditions other than triaxial compression (Equation 6.22), it might be necessary to recalibrate the model parameters k_e^d and k_e^b, defining, respectively, the positions of the dilatancy and bounding surfaces for triaxial extension (TE) loading. Difficulties arise, however, from the dependency of the relocation of the CSL on the value selected for v_A (Equation 6.22), meaning that an iterative procedure may be required to recalibrate k_e^d and k_e^b. In an attempt to avoid such complexity, a parametric study was performed to assess the impact of different values of v_A on stress ratio, η, – state parameter, ψ, data corresponding to the occurrence of phase transformation and peak stress ratio states in TE tests and, therefore, to evaluate the need for recalibrating k_e^d and k_e^b. With this purpose, the procedure described in Section 6.7 was followed once again, with the sole difference consisting of the dependence, at this stage, of ψ on $(e_{cs})_A$, as given by Equation 6.24, rather than directly on $(e_{cs})_{ref}$.

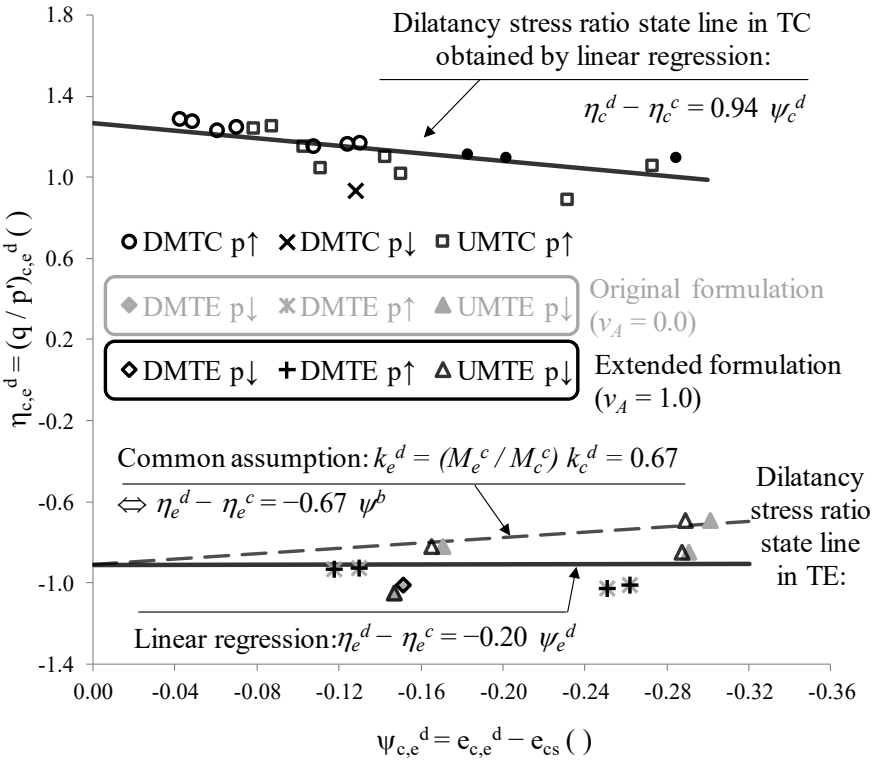

Figure 6.24 – Influence of the relocation of the CSL with v_A = 1.0 on the stress ratio at phase-transformation state as a function of the state parameter.

Figure 6.24 compares $\eta_e^d - \psi_e^d$ data obtained when using with $v_A = 1.0$ (represented in black) with that obtained before when using the original version of the constitutive model, i.e. when considering $v_A = 0.0$ (represented in grey). It is apparent that differences between the two data sets are limited to UMTE p↓ test data. Indeed, these differences do not suggest a

different trend in the obtained results, with the previously adopted dilatancy line in TE, characterised by $k_e^d = 0.67$, corresponding to the simplification $k_e^b = k_c^b\ (M_e^c/M_c^c)$ proposed by Papadimitriou and Bouckovalas (2002), still providing the overall best fit for the newly obtained data (including data obtained from DMTE p↓ and DMTE p↑ test results). Once again, it is evident that some data scatter exists, likely due to the approximations required to estimate the dilatancy coefficient and inherent unreliability of triaxial extension data, as discussed in Section 6.7.

Similarly, Figure 6.25 compares $\eta_e^d - \psi_e^d$ data obtained when using with $v_A = 10.0$ (represented in black) with that obtained when using the original version of the constitutive model (represented in grey). Once again, it is apparent that the influence of the relocation of the CSL on the position of the dilatancy line in TE is limited to data inferred from UMTE p↓ test results and, once more, does not suggest any drastic alteration to the position of the dilatancy line. It should be noted, nevertheless, that the validity of these conclusions might be restricted to the present data.

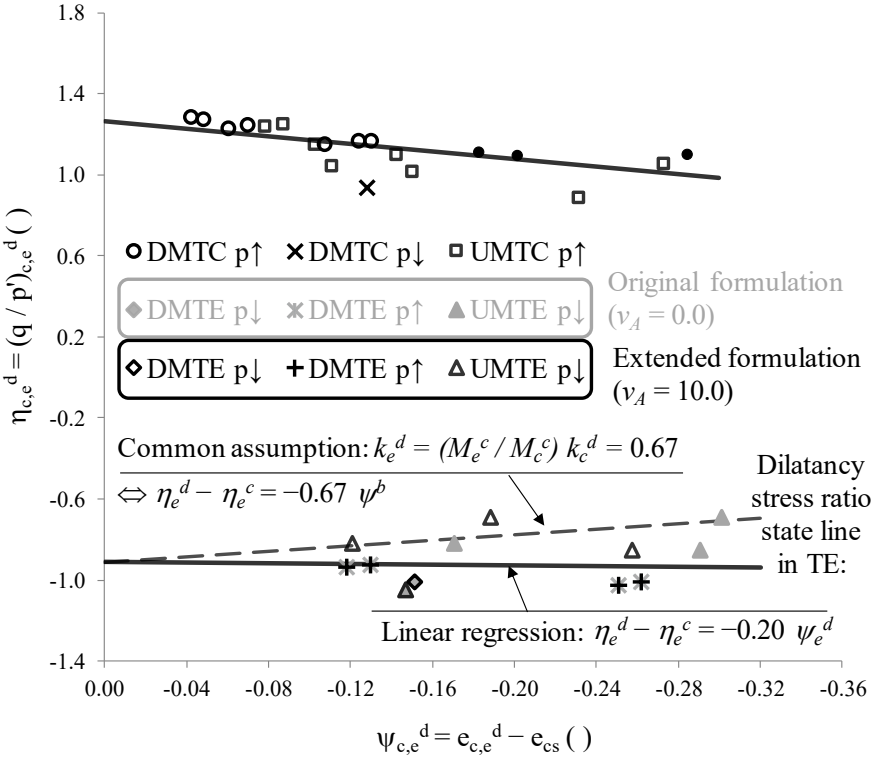

Figure 6.25 – Influence of the relocation of the CSL with v_A = 10.0 on the stress ratio at phase-transformation state as a function of the state parameter.

A similar parametric study was performed to assess the influence of the relocation of the CSL on the position of the bounding line in TE. It was concluded that, regardless of the value of v_A adopted in the analysis, the relocation of the CSL, as defined by Equation 6.22, has practically no impact on the position of the bounding line in TE. In fact, for the present study, all peak stress ratio data points obtained from triaxial extension tests, η_e^b, are greater (in absolute

value) than critical stress ratio, η_e^c, meaning that, when peak stress ratio state is reached, $\langle d^c \rangle \approx 0$ and, therefore, $(e_{cs})_A \approx (e_{cs})_{ref}$ (Equation 6.22). Given this conclusion, and for brevity of the presentation, the obtained results are not presented here. Note, nevertheless, that the results obtained in a small parametric study focusing on the impact of v_A on the simulated response, which will be presented later, will also provide evidence on this conclusion.

Considering the experimental data available, at least two completely different strategies could have been established at this stage. One possible strategy would consist of using the complete set of model parameters obtained until this point, including the shearing-induced fabric-related parameters, and, by trial and error, trying to find out the values of v_A and k_A allowing for the best possible reproduction of both monotonic triaxial extension and cyclic triaxial test data. The main drawback of this approach is that, as shown later, the shearing-induced fabric component is observed to have a very strong influence on the modelled response, not only when reproducing cyclic response, but also monotonic response. This means that it would be difficult to assess the most appropriate values for v_A and k_A. Moreover, by following this strategy, there would be no guarantee that the obtained values for v_A and k_A would be appropriate for the simulation of monotonic loading if the shearing-induced fabric component would be deactivated. Therefore, it was considered more consistent moving back in the calibration process to the end of the calibration of the plastic-hardening-modulus-related parameters (Section 6.10) and, based on the set of values established up to that point, calibrating the inherent fabric anisotropy component. Subsequently, the model parameters related to the shearing-induced fabric component were recalibrated by following a methodology similar to that employed in the previous section. As detailed later, by following this strategy, a single set of values for v_A and k_A improving the modelled monotonic triaxial extension response was identified. It can be argued that, by adopting this strategy, it would have been more logical to calibrate the inherent-anisotropy-related parameters before the calibration of the shearing-induced fabric-related parameters (i.e. to switch the present section with the previous one), since this would eliminate the need of calibrating the shearing-induced fabric-related parameters twice (i.e. before and after the introduction of the inherent fabric anisotropy component). However, as explained before, it was considered important to obtain two different sets of model parameters: one excluding the inherent fabric anisotropy component (by setting $a = 0.333$, $v_A = 0.0$ and $k_A = 1.0$) and, therefore, making use of the formulation originally proposed by Taborda *et al.* (2014), and another set of model parameters activating the inherent fabric anisotropy component.

Prior to the determination of the precise magnitude of v_A and k_A, two small parametric studies were performed to evaluate the impact of these model parameters on the simulated monotonic response. With this purpose, test ICUMTE p↓ 0.799/80 was reproduced by employing four different values for v_A: 0.0 (corresponding to the original formulation), 1.0, 5.0 and 10.0. For the remaining model parameters, the values obtained in the previous

sections (Section 6.3 to 6.10) were used. Moreover, as explained before, $a = 0.29$ was adopted in the present study, while $k_A = 1.0$ was employed to deactivate the effect of h_A (Equation 6.27) and, therefore, to focus the attention, at this stage, only on the effect of v_A. The obtained numerical results are compared to those registered in the laboratory in Figure 6.26. It can be observed that very similar numerical results are obtained when using $v_A = 0.0$ and $v_A = 1.0$. Unfortunately, it is apparent that, in both cases, the effective stress state at phase transformation – which can be associated with the occurrence of the minimum mean effective stress under undrained conditions (Ishihara *et al.*, 1975), as mentioned before – is slightly underpredicted in relation to that measured in the experiment (Figure 6.26a). Indeed, it can be seen that the prediction of this distinctive state is worse as values for v_A greater than 1.0 are employed in the numerical analysis. In fact, it is apparent that v_A has a strong effect during the early stages of the test simulation (in this particular case, for axial strains up to about 3 to 4 %), while vanishing for the later stages. This aspect is particularly evident when comparing the modelled stress-strain curves among each other for axial strains greater than 4 %, with the computed curves being observed to be practically parallel. Note that similar observations were obtained when simulating the remaining available undrained monotonic triaxial extension tests (namely, tests ICUMTE p↓ 0.790/25, ICUMTE p↓ 0.658/25 and ICUMTE p↓ 0.650/80).

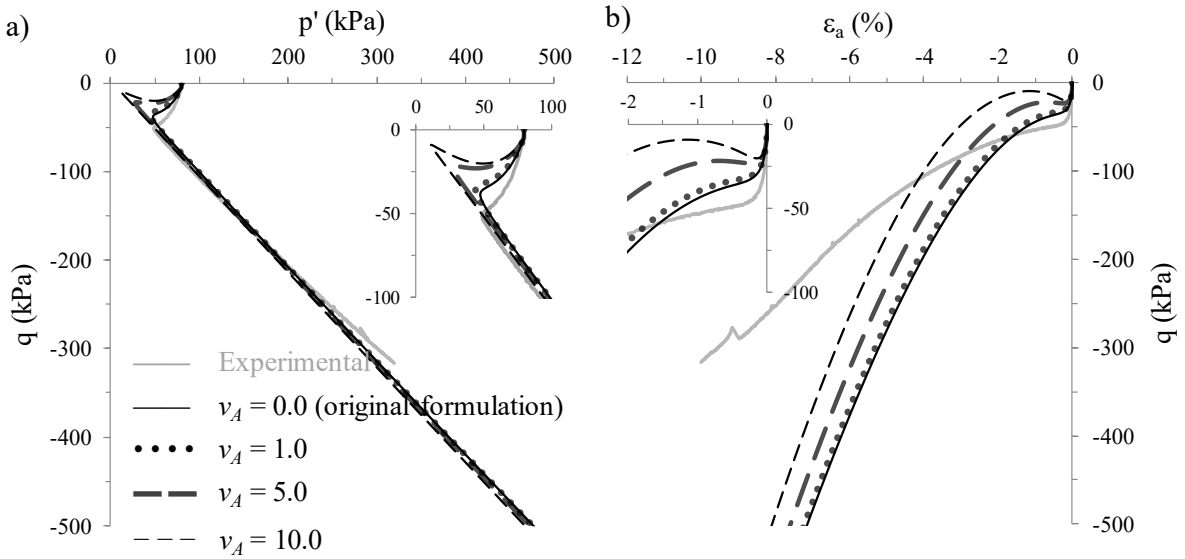

Figure 6.26 – Influence of v_A on the numerical simulation of test ICUMTE p↓ 0.799/80 in terms of: (a) effective stress path and (b) stress-strain response.

Further insight into the effect of v_A on the modelled response was obtained by simulating test ICDMTE p↑ 0.798/80. Note that, similar to the previous set of simulations, the following values were assigned to v_A: 0.0 (corresponding to the original formulation), 1.0, 5.0 and 10.0. The results obtained in each of these three different numerical simulations are compared with those measured in the laboratory in Figure 6.27. It is apparent that, in this case, the adoption of a value of v_A greater than 1.0 in the numerical analysis allows for a slightly better reproduction of the volumetric response measured in the experiment, with a value of $v_A =$

5.0 also resulting in a better prediction of the stress-strain response in relation to that computed when using $v_A = 0.0$. Conversely, the results obtained when using $v_A = 1.0$ in the numerical analysis are very similar to those obtained when employing $v_A = 0.0$. In both cases, the volumetric contraction observed during the early stages of the test is considerably underpredicted, while slightly overpredicting the stress-strain response measured during that stage of the experiment. Similar observations were obtained when simulating the remaining available ICDMTE p↑ and K0DMTE p↑ tests.

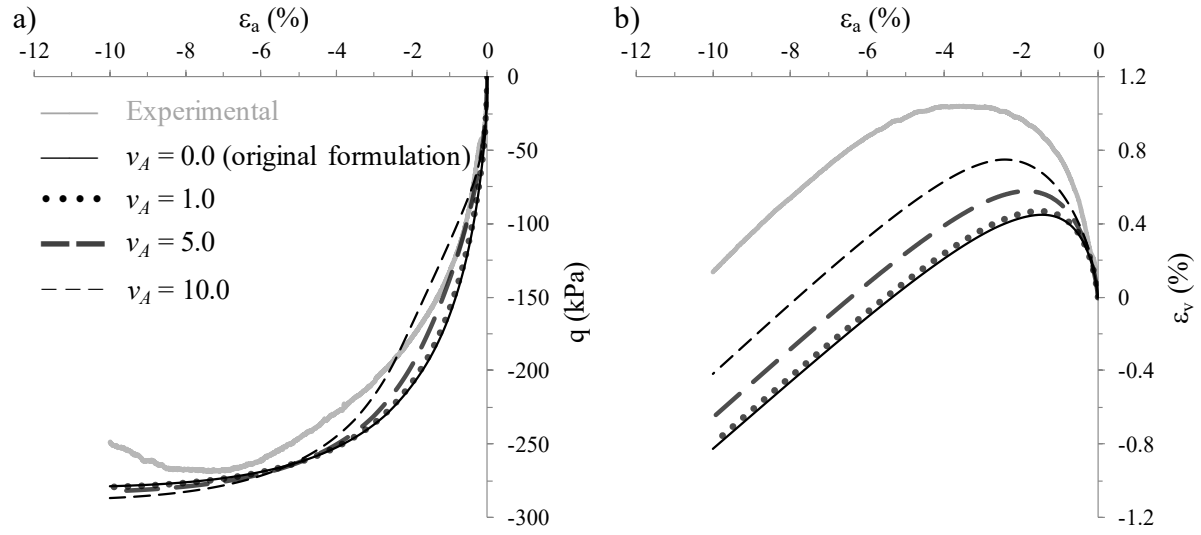

Figure 6.27 – Influence of v_A on the numerical simulation of test ICDMTE p↑ 0.798/80: (a) stress-strain response and (b) evolution of volumetric strain with axial strain.

Test ICDMTE p↓ 0.793/80 was also reproduced using the four different values of v_A (0.0, 1.0, 5.0 and 10.0). It can be seen that the adoption of a value for v_A greater than 1.0 would allow for a better reproduction of the observed volumetric response, while resulting in a worse prediction of the measured stress-strain response.

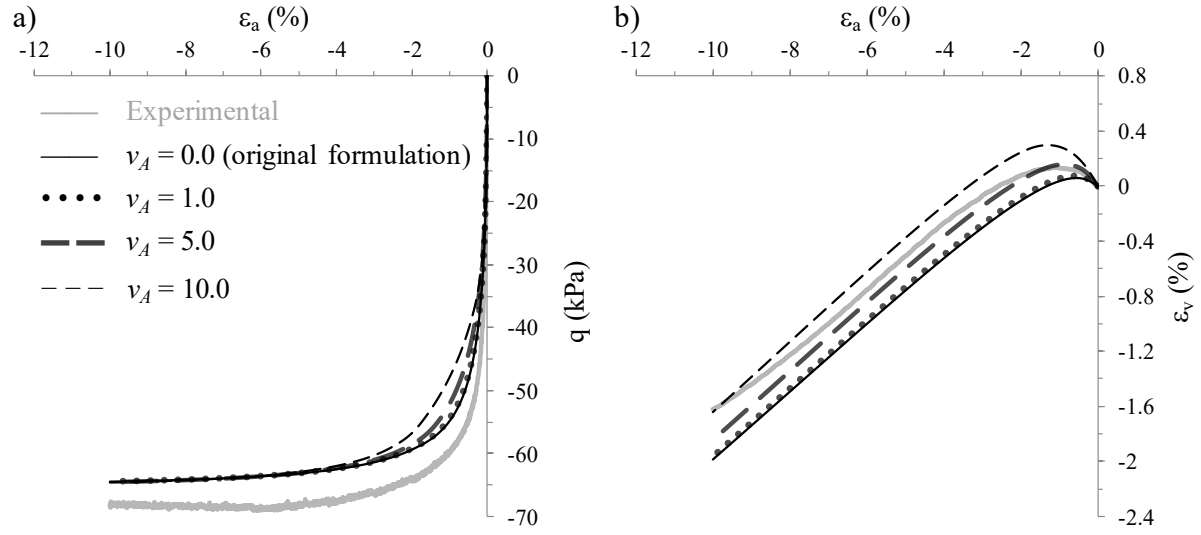

Figure 6.28 – Influence of v_A on the numerical simulation of test ICDMTE p↓ 0.793/80: (a) stress-strain response and (b) evolution of volumetric strain with axial strain.

In addition, a series of simulations were performed to evaluate the impact of the model parameter k_A on the modelled response. With that purpose, $v_A = 0.0$ was employed to deactivate the effect of v_A (Equation 6.22), while three different values of k_A were tested: $k_A = 1.0$ (i.e. no effect on the modelled response), $k_A = 0.75$ and $k_A = 0.50$. Once more, $a = 0.29$ was adopted in this study and the values obtained in the previous sections (Section 6.3 to 6.10) were adopted for the remaining model parameters. Figure 6.29 depicts the results obtained when simulating test ICUMTE p↓ 0.799/80, together with those measured in the laboratory. Similar to what was observed when employing a value for v_A greater than 1.0, it is apparent that softer stress-strain responses are obtained when values of k_A smaller than 1.0 are employed in the numerical analysis (Figure 6.29b), resulting in a more compliant effective stress path (Figure 6.29a). Note, however, that, on the contrary to v_A, the value adopted for k_A affects the modelled response throughout loading (i.e. from the beginning to the end of the simulation). Despite the underprediction of the stress-strain response measured during the early stages of this test, it seems that a value of k_A smaller than 1.0 allows for a better reproduction of the stress-strain response measured in the laboratory during the later stages of loading (i.e. for axial strains greater than about 2 %).

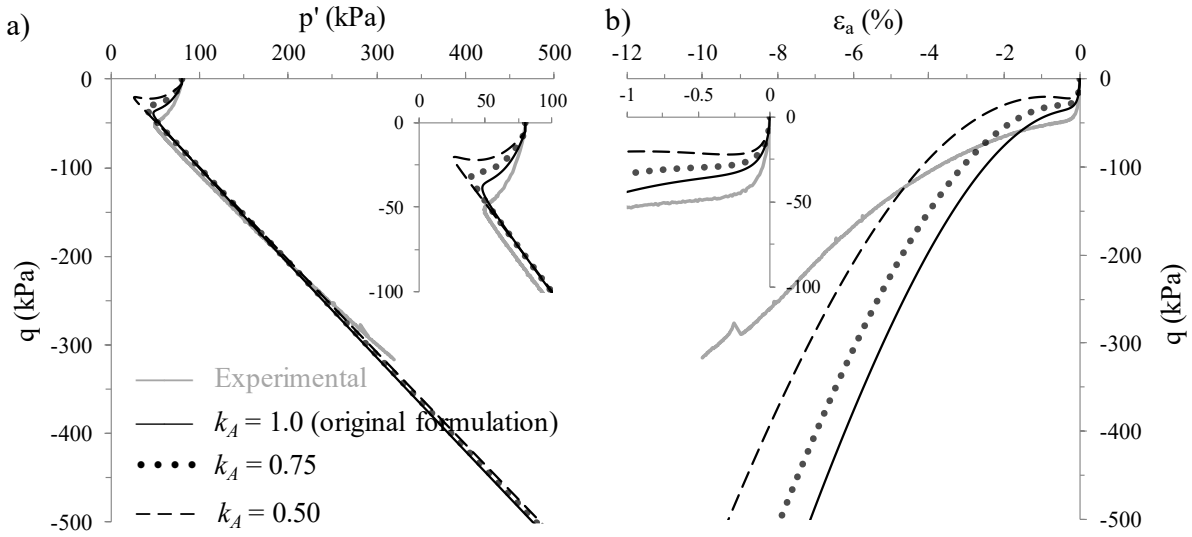

Figure 6.29 – Influence of k_A on the numerical simulation of test ICUMTE p↓ 0.799/80: (a) effective stress path and (b) stress-strain response.

Complementary, the three different values of k_A (1.0, 0.75 and 0.5) were employed to the simulation of test ICDMTE p↑ 0.798/80. Figure 6.30 compares the results obtained in these three different numerical simulations with those obtained in the laboratory. It can be observed that, by reducing the value of k_A from 1.0 to 0.5, a much softer stress-strain response is simulated, as well as a higher contractive volumetric response. In this case, a value for k_A in between 0.5 and 0.75 would likely result in the best possible reproduction of the measured stress-strain response, while also improving the reproduction of the observed volumetric response in relation to the modelled response when using the original formulation of the constitutive model (i.e. when using $k_A = 1.0$).

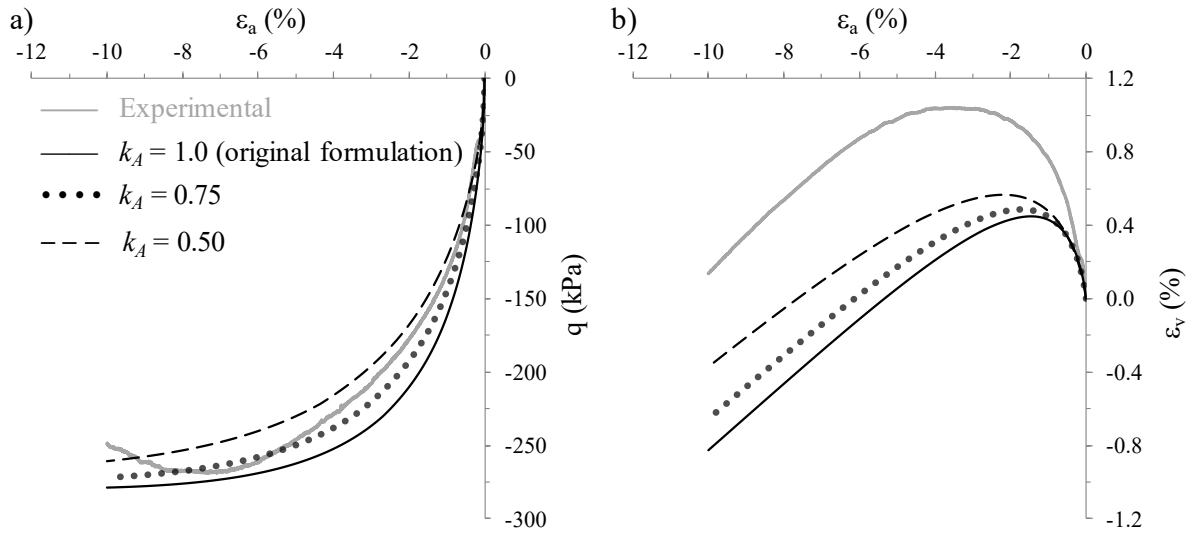

Figure 6.30 – Influence of k_A on the numerical simulation of test ICDMTE p↑ 0.798/80: (a) stress-strain response and (b) evolution of volumetric strain with axial strain.

In relation to test ICDMTE p↓ 0.793/80, it can be observed in Figure 6.31 that the best approximation of the volumetric response measured in test would likely be obtained when employing a value for k_A in between 0.5 and 0.75. Conversely, in terms of stress-strain response, it is apparent that, regardless of the value selected for k_A, the measured stress-strain is underpredicted.

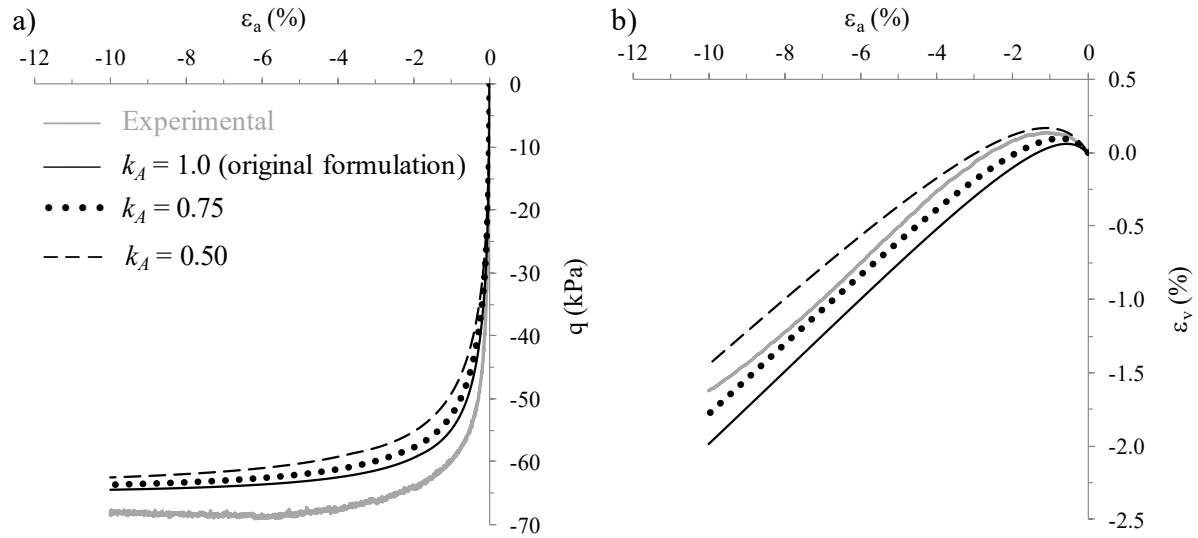

Figure 6.31 – Influence of k_A on the numerical simulation of test ICDMTE p↓ 0.793/80: (a) stress-strain response and (b) evolution of volumetric strain with axial strain.

From the set of results obtained in these two small parametric studies, it can be concluded that:

- the model parameter v_A seems to impact solely the modelled response during the early stages of loading (in the case of the simulated laboratory tests, for axial strains up to 3 to 4%); its impact seems only significant when values larger than 1.0 are used in the numerical analysis;

- the adoption of a value for v_A greater than 1.0 seems to improve the reproduction of the volumetric response observed in ICDMTE p↑, K0DMTE p↑ and ICDMTE p↓ tests; it also improves the stress-strain response measured during the early stages of loading of both ICDMTE p↑ and K0DMTE p↑ tests; however, it increases significantly the discrepancies between the modelled and measured minimum mean effective stresses in ICUMTE p↓ tests;
- the model parameter k_A affects the modelled response throughout loading;
- the adoption of a value for k_A smaller than 1.0 seems to improve the reproduction of the volumetric response observed in ICDMTE p↑, K0DMTE p↑ and ICDMTE p↓ tests; it also improves the stress-strain response registered throughout loading of both ICDMTE p↑ and K0DMTE p↑ tests; moreover, although the discrepancies between the modelled and measured minimum mean effective stresses in ICUMTE p↓ tests are increased when using a value for k_A smaller than 1.0 (as also observed when employing a value for v_A greater than 1.0), it seems to result in a better approximation of the stiffness exhibited by the samples subjected to this type of loading within the medium to large strain range.

Taking into account the conclusions reached in the aforementioned parametric studies, it was decided to adopt $v_A = 1.0$ (which seems to have little impact on the simulation of the available monotonic triaxial extension tests) and to seek, by trial and error, a value for k_A resulting in an improved prediction of the overall stress-strain responses registered in all available tests, as well as volumetric responses observed in ICDMTE p↑, K0DMTE p↑ and ICDMTE p↓ tests. Note that the lesser importance given at this point to the accurate prediction of the minimum mean effective stress in ICUMTE p↓ tests is justified by the fact that the subsequent introduction of the shearing-induced fabric component will likely affect this aspect of the response, as observed when calibrating the original formulation of the model (Section 6.11).

Having carried out simulations using different values of k_A, it was concluded that $k_A = 0.60$ allows for the best possible reproduction of the available triaxial extension test data. Figure 6.32 compares the results of the numerical simulations of the four available ICUMTE p↓ tests when using the original formulation of the model (i.e. not activating the inherent fabric anisotropy component by using $a = 0.333$, $v_A = 0.0$ and $k_A = 1.0$) with those obtained when employing the extended formulation (i.e. $a = 0.29$, $v_A = 1.0$ and $k_A = 0.60$). The experimental results are also depicted in the figure for comparison purposes. As anticipated, it is apparent that, although slightly increasing the discrepancies in terms of predicted effective stress state at phase transformation, the extended formulation slightly improves the modelled stress-strain response of all tests for axial strains greater than about 2 %.

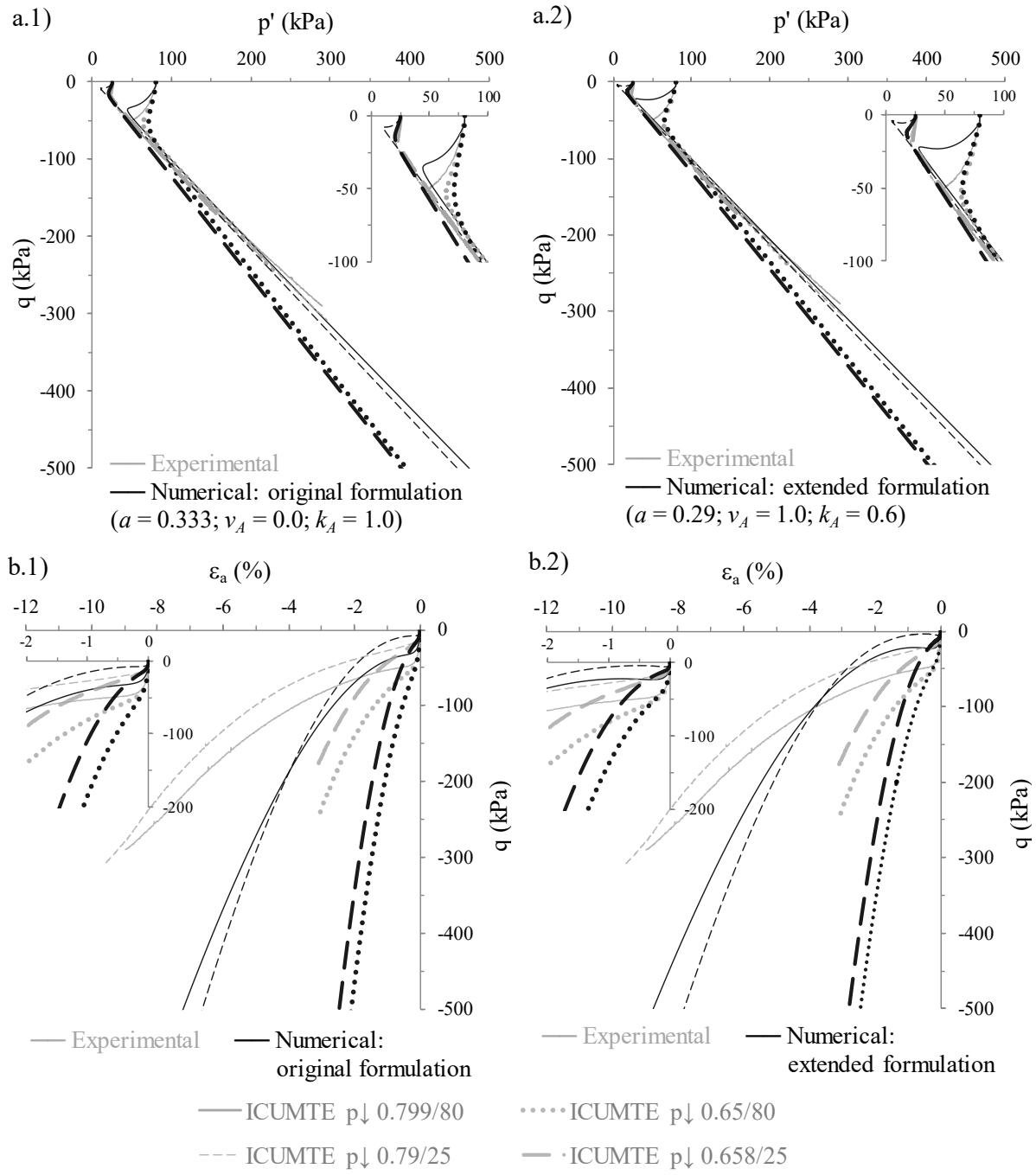

Figure 6.32 – Numerical simulation of all available ICUMTE p↓ tests using the original and extended formulations of the constitutive model: (a) effective stress path and (b) stress-strain response.

With respect to the drained monotonic triaxial extension tests, Figure 6.33 compares the results of the numerical simulations of the four available ICDMTE p↑ and K0DMTE p↑ tests, as well as the available ICDMTE p↓ tests when using the original and extended formulations of the constitutive model. The experimental results are also presented in the figure for comparison purposes. Although not drastically, it can be observed that both stress-strain and volumetric responses registered in all tests are improved when using the extended formulation.

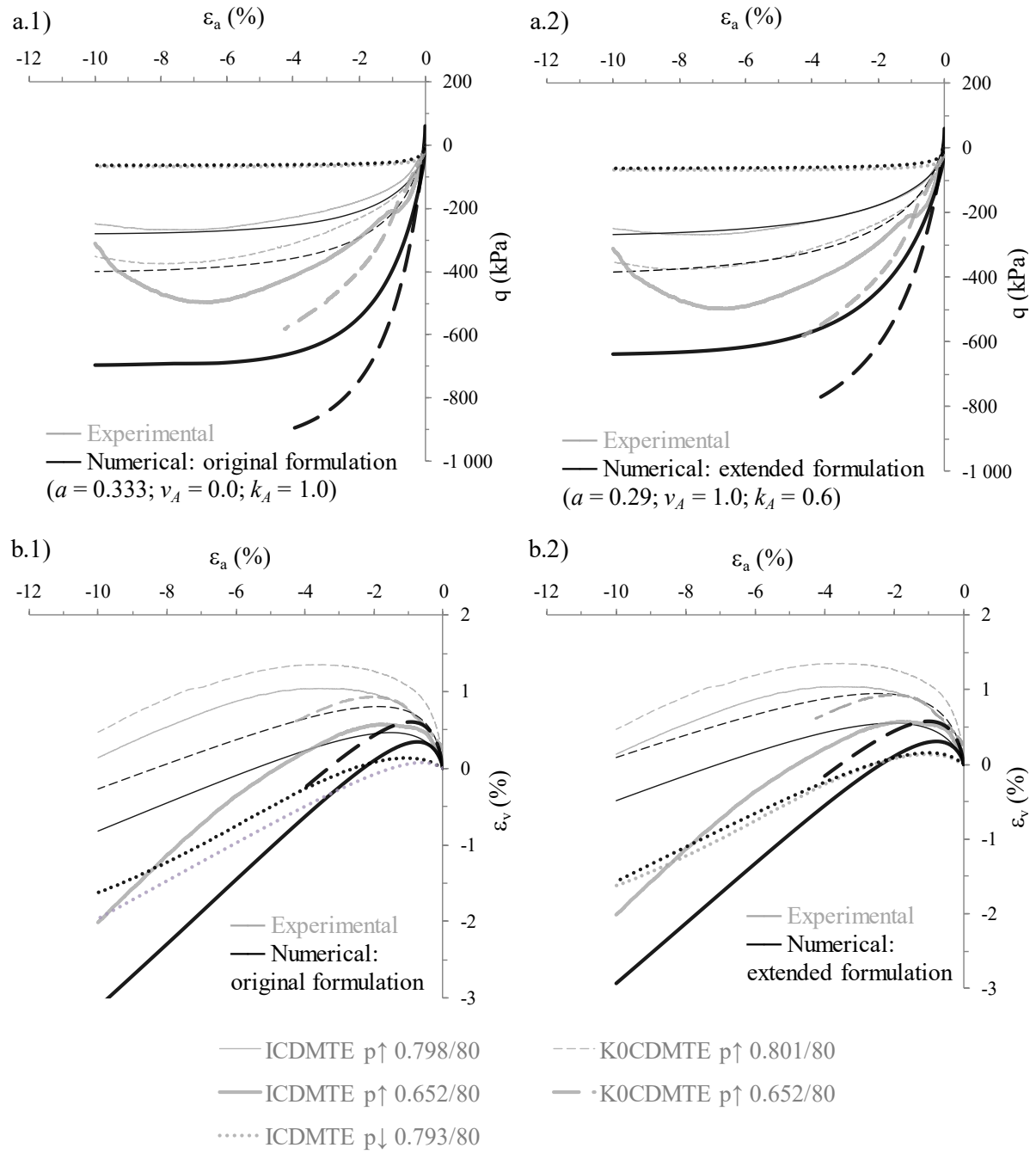

Figure 6.33 – Numerical simulation of all available ICDMTE p↑, K0DMTE p↑ and ICDMTE p↓ tests using the original and extended formulations of the constitutive model: (a) stress-strain response and (b) evolution of volumetric strain with axial strain.

The following step of the calibration process consisted of the recalibration of the model parameters related to the shearing-induced fabric component. A methodology similar to that described in Section 6.11 was adopted, involving the following steps:

a) Selection of two undrained cyclic triaxial (UCT) tests performed on samples consolidated under similar effective stress states. By setting the value of γ to 0.0 (to deactivate the influence of h_e on A_1) and choosing an appropriate value for h_0^* for each test, a value of H_0^* leading to a satisfactory reproduction of both UCT tests is sought.

b) Recalibration of the plastic-hardening-modulus-related parameters h_0 and γ against results of drained and undrained monotonic triaxial compression (DMTC and UMTC, respectively), drained and undrained monotonic triaxial extension (DMTE and UMTE, respectively) and undrained cyclic triaxial (UCT) tests.

c) By setting ζ to 0.0 and using, once more, a trial-and-error procedure, inference of the value of H_0^* leading to the best possible reproduction of each UCT test. Estimation of appropriate values of H_0 and ζ by performing a non-linear regression over $(\sigma'_{1,0}/p'_{ref},\ H_0^*)$ data.

Once more, tests ICUCT 0.832/80/42 and ICUCT 0.651/80/43 were chosen to infer an initial value for H_0^* – step a). After testing several values H_0^*, it was concluded that $H_0^* = 45\,000.0$, when used in conjunction with the current values of h_0 and γ, provides a satisfactory initial approximation of both tests, as illustrated in Figure 6.34. It is interesting to observe that, when compared to the results obtained with the original formulation of the constitutive model (Figure 6.18 and Figure 6.20), a greater tendency to accumulate strains in extension during the later stages of loading is obtained in this case.

The following step concerned the recalibration of the plastic-hardening-modulus-related parameters – step b). As explained in Section 6.11, the recalibration of these parameters was deemed necessary, since the activation of the shearing-induced fabric component was observed to have a strong impact not only on the modelled cyclic response, as intended, but also on the early stages of the modelled monotonic response of Hostun sand. Therefore, following a similar strategy to that employed in Section 6.11, it was decided to increase the value assigned to β from 0.30 to 0.60, to allow for the simulation of a more curved effective stress path under undrained shearing (Section 6.10.3). Subsequently, by setting $\gamma = 0.0$ and $\zeta = 0.0$, while keeping $\mu = 0.500$ and $H_0^* = 45\,000.0$, the value of h_0^* resulting in the best possible simulation of each available DMTC, UMTC, DMTE, UMTE and UCT tests performed on samples consolidated to $p'_0 = 80$ kPa was estimated. The obtained results are depicted in Figure 6.35. Note that, to enable a direct comparison with the previously adopted model parameters, the $h_0^* - e_0$ line obtained before the introduction of the shearing-induced fabric tensor (characterised by $h_0 = 0.132$ and $\gamma = 0.999$), as well as that corresponding to the original formulation of the constitutive relationship (characterised by $h_0 = 0.200$ and $\gamma = 1.100$) are also presented in the figure.

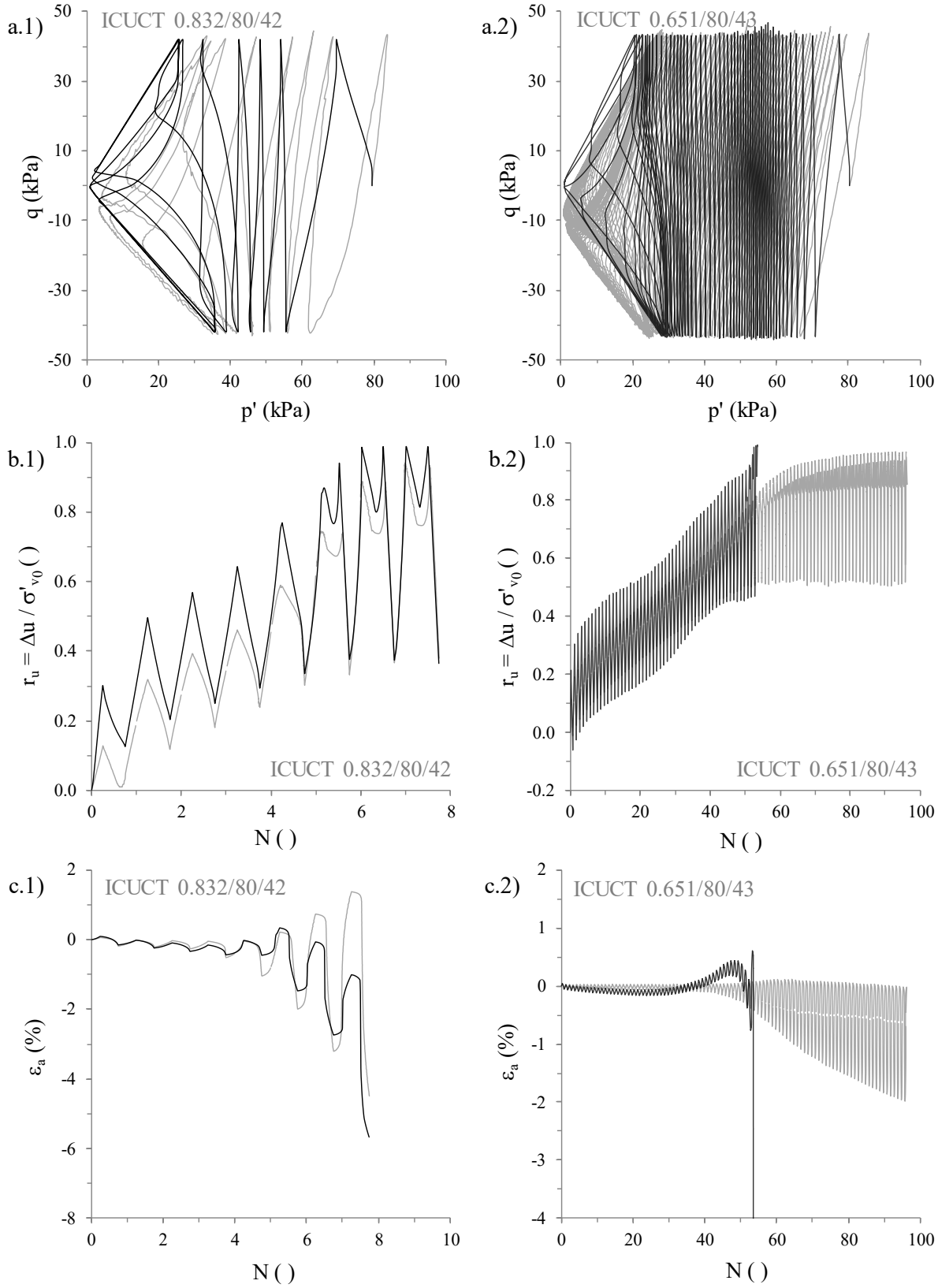

— Experimental — Numerical ($h_0 = 0.132$; $\gamma = 0.999$; $a = 0.29$; $v_A = 1.0$; $k_A = 0.7$; $H_0^* = 45\,000.0$)

Figure 6.34 – Numerical simulation of tests ICUCT 0.832/80/42 and ICUCT 0.651/80/43 using the extended formulation of the model and a value of 45 000.0 for H_0^*: (a) effective stress path, (b) excess pore water pressure build-up and (c) axial strain evolution with the number of loading cycles.

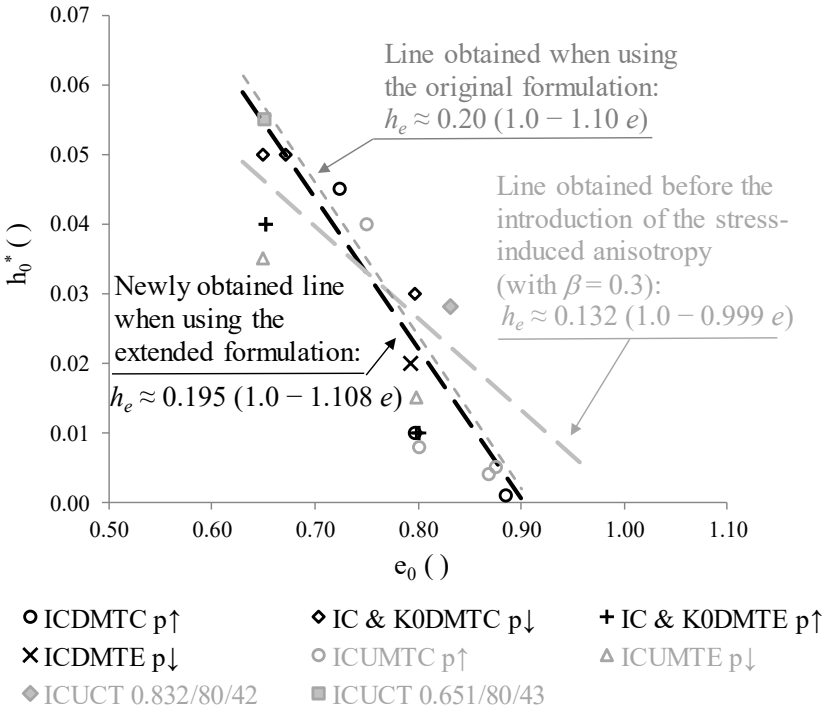

Figure 6.35 – Recalibration of the plastic-hardening-modulus-related parameters using monotonic triaxial compression and cyclic triaxial tests where samples were consolidated to a mean effective stress of 80 kPa.

Similar to what was observed when employing the original formulation of the constitutive relationship, a much more inclined $h_0^* - e_0$ line was obtained after the introduction of the shearing-induced fabric component, highlighting the strong influence of this component on the modelled response. In effect, it can be observed that the adequate replication of drained and undrained monotonic triaxial compression tests performed on loose and moderately loose samples (i.e. having larger values of e_0) require very small values of h_0^*, due to the previously discussed influence of the shearing-induced fabric component on the early stages of the modelled response. In addition, it can be observed that the newly obtained line – characterised by $h_0 = 0.195$, $\gamma = 1.108$ and $e_{max} = 0.900$ – is practically coincident with that obtained when employing the original formulation of the constitutive model. Unfortunately, it is apparent that both lines tend to overpredict the h_0^* values identified as those leading to the best possible reproduction of drained and undrained monotonic triaxial extension tests (ICDMTE p↓, IC & K0DMTE p↑ and ICUMTE p↓ tests).

The calibration proceeded to step c), where each UCT test available was modelled by setting ζ to 0.0 and selecting an appropriate value for H_0^*. The obtained results are indicated in Table 6.4, together with the initial conditions of each laboratory test. It can be observed that the H_0^* values listed in this table are slightly larger than those obtained in the previous section when using the original formulation of the constitutive model (Table 6.3). In effect, this could be expected, since a stiffer response in triaxial compression (before the first crossing of the phase transformation line) is required to counterbalance the softer response in triaxial

extension introduced by the inherent fabric anisotropy component and, therefore, to reproduce a similar undrained cyclic resistance (i.e. to obtain a similar number of loading to the onset of cyclic mobility).

Table 6.4 – Values of H_0^* obtained by a trial-and-error procedure for all available undrained cyclic triaxial tests when using the extended formulation of the constitutive model.

Test ID [1]	e_0 [2] ( )	p'_0 (kPa)	ψ_0 [2] ( )	$\lvert\Delta q\rvert$ [3] (kPa)	H_0^* ( )
ICUCT 0.821/25/13	0.821	25.0	-0.140	13.0	230 000.0
ICUCT 0.777/25/18	0.777	25.0	-0.140	18.0	180 000.0
ICUCT 0.771/80/32	0.771	80.0	-0.137	32.0	68 000.0
ICUCT 0.803/80/36	0.803	80.0	-0.137	36.0	90 000.0
ICUCT 0.832/80/42	0.832	80.0	-0.129	42.0	65 000.0
ICUCT 0.804/80/48	0.804	80.0	-0.136	48.0	15 000.0
ICUCT 0.773/80/56	0.773	80.0	-0.138	56.0	3 000.0
ICUCT 0.805/135/40	0.805	135.0	-0.120	40.0	50 000.0
ICUCT 0.830/135/54	0.830	135.0	-0.128	54.0	70 000.0
ICUCT 0.793/135/67.5	0.793	135.0	-0.128	67.5	8 000.0
ICUCT 0.651/80/43	0.651	80.0	-0.285	43.0	45 000.0
ICUCT 0.652/80/72	0.652	80.0	-0.284	72.0	40 000.0
ICUCT 0.652/80/88	0.652	80.0	-0.284	88.0	40 000.0

[1] Test identifier nomenclature is detailed in Chapter 2 Chapter 3; [2] Post-consolidation values; [3] deviatoric stress oscillation.

It is also noteworthy that, as observed before when using the original formulation of the constitutive model, the H_0^* values required to simulate properly tests ICUCT 0.804/80/48, ICUCT 0.773/80/56 and ICUCT 0.793/135/67.5 (coloured in grey) are significantly smaller than those required to simulate the remaining tests. Note that, in these three tests, where large cyclic stress ratios were used, the samples exhibited very soft responses in triaxial extension during the first loading cycle, resulting in a severe reduction of the effective stress, with cyclic mobility being triggered just after two to four loading cycles, as shown in Figure 6.36. Unfortunately, this suggests that, although bringing additional flexibility to the constitutive model and slightly improving the modelled response for triaxial extension, the incorporation of the inherent fabric anisotropy component into the constitutive relationship may still be insufficient to replicate accurately the very wide range of undrained cyclic responses of Hostun sand registered in the present laboratory testing programme, with samples requiring from two to seventy-seven loading cycles to the onset of cyclic mobility.

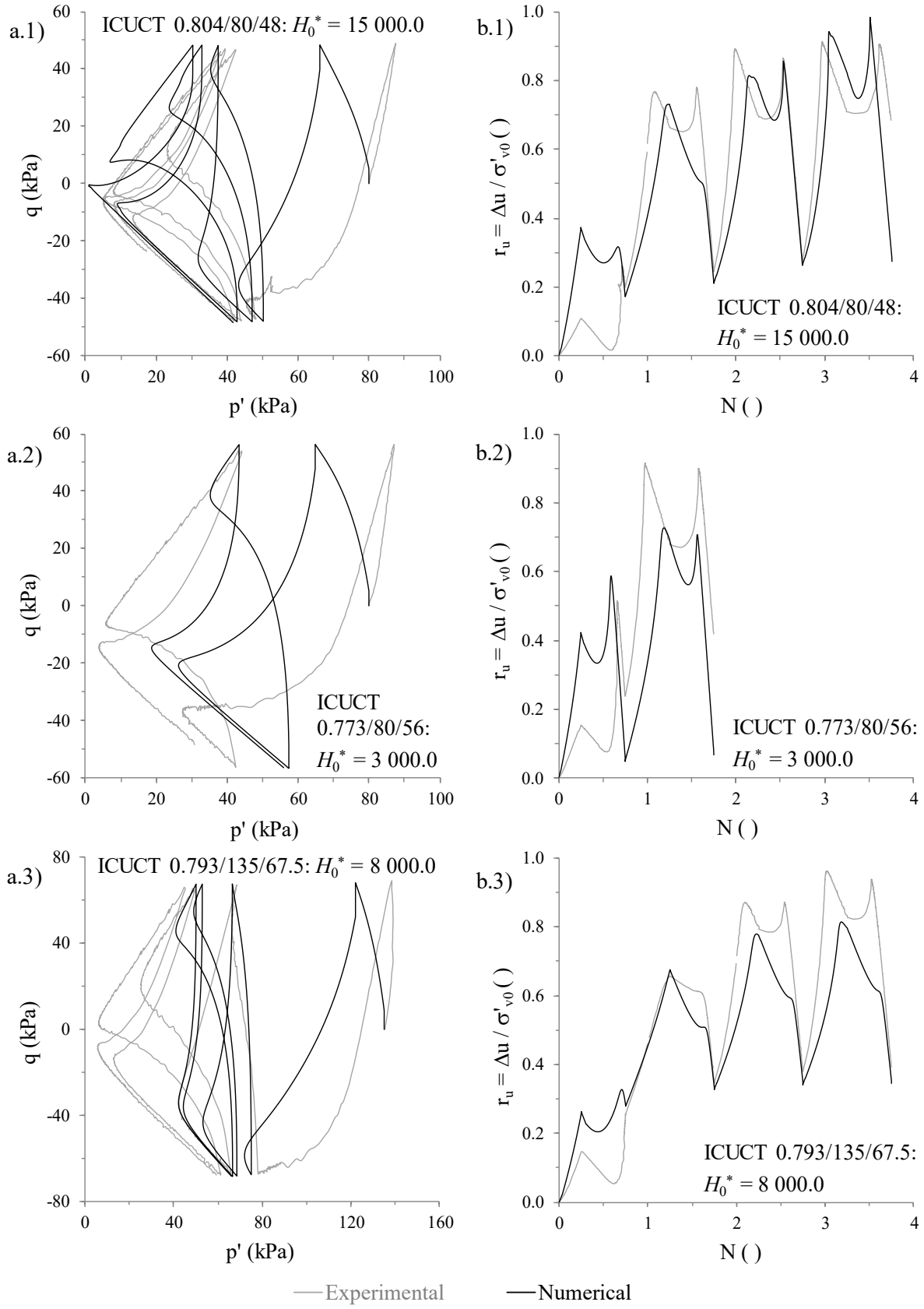

Figure 6.36 – Calibration of H_0^* when using the extended formulation to the simulation of tests ICUCT 0.804/80/48, ICUCT 0.773/80/56 and ICUCT 0.793/135/67.5: (a) effective stress path and (b) excess pore water pressure build-up with the number of loading cycles.

Having plotted the $\left(\sigma'_{1,0}/p'_{ref},\ H_0^*\right)$ data values, as depicted in Figure 6.23, a non-linear regression analysis was performed to determine the model parameters H_0 and ζ. The following values were obtained: $H_0 = 55\,000.0$ and $\zeta = 0.85$. It can be seen in the figure that the newly obtained curve plots above that obtained when using the original formulation of the constitutive model.

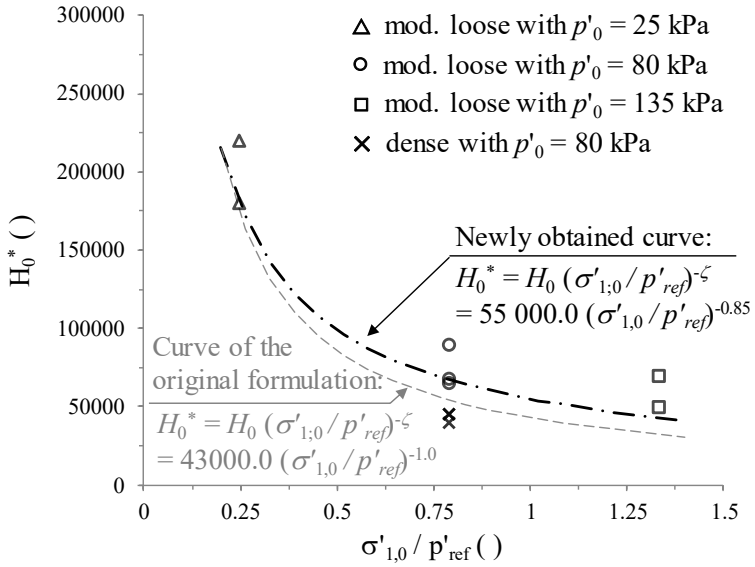

Figure 6.37 – Calibration of the shearing-induced fabric-related parameters when using the extended formulation of the constitutive model.

6.13 Numerical stability-related parameters

The final model parameters to be calibrated are:

1) m defining the opening of the primary yield surface (Equation 4.34);
2) p'_{ys} defining the position of the low-stress (also termed as secondary) yield surface (Equation 4.71);
3) p'_{min} defining a lower limit for the maximum shear modulus, G_{max} (Equation 4.25), as well as G_{min} defining a lower limit for the current value of the tangent shear modulus, G_{tan} (Equation 4.26);
4) $h_{f,min}$ and $h_{f,max}$ imposing, respectively, a lower and an upper limit to the magnitude of the plastic multiplier h_f, i.e. to the contribution of the shearing-induced fabric tensor, $\boldsymbol{F}$, to the plastic hardening modulus associated with the primary yield surface, A_1 (Equations 4.55, 4.56 and 4.57);
5) maximum value of the shearing-induced fabric index, H_{max} (Equations 4.69 and 4.70).

As discussed in more detail in Taborda (2011), these model parameters were introduced to improve the numerical stability of the constitutive relationship, particularly when simulating boundary-value problems involving liquefaction-related phenomena, where materials undergo very low effective stresses. As such, these model parameters lack any relevant

physical meaning and, therefore, their calibration typically require performing small parametric studies to decide on the values that lead to a satisfactory reproduction of the available data, while ensuring numerical stability and, possibly, reducing the computational cost of the numerical integration of the constitutive relationship. As detailed later, the results of the parametric analyses conducted in the present study enable to conclude that the values established in previous studies (Papadimitriou and Bouckovalas, 2002; Loukidis and Salgado, 2009; Taborda, 2011; Taborda *et al.*, 2014) are also suitable for the present case. This suggest that reference values may be established for these model parameters (at least for clean sand), eventually reducing the effort required to calibrate this constitutive relationship in future applications. Before describing the value adopted for each model parameter, it is important to note that, to shorten the presentation, only results obtained when using the original version of the model (i.e. not including the inherent fabric anisotropy component) are presented in this section. Note, nevertheless, that similar results were obtained when using the extended version of the constitutive model.

Starting with the model parameter m, since it defines the elastic domain, it is expected to have particular impact on the simulation of cyclic response at very small strains (e.g. simulation of vibrations due to machine foundation). Moreover, as highlighted by Loukidis and Salgado (2009), it plays an important role of ensuring numerical stability during the integration of the constitutive model. According to Manzari and Dafalias (1997), a value of 0.050 M_c^c, which is typically close to 0.065 for most of silica sands, leads to a satisfactory numerical performance of the constitutive model. This value was adopted by Papadimitriou and Bouckovalas (2002), Taborda (2011) and Taborda *et al.* (2014) and is also considered in the present study.

Regarding p'_{ys}, as pointed out by Taborda *et al.* (2014), its value should be large enough to prevent the stress point from reaching extremely low effective stresses, for which the non-linearity of the constitutive relationship is known to increase substantially, therefore keeping the computational effort within reasonable limits. On the other hand, the value assigned to p'_{ys} should be small enough to avoid meaningful alteration of the modelled response. As illustrated in Figure 6.38, while a large value as $p'_{ys} = 10.0$ kPa would restrict the ability of the constitutive model to replicate the large excess pore water pressure ratios observed in the laboratory tests (in most cases, close to 1.0), as well as the accumulation of large strains, a value of $p'_{ys} = 1.0$ kPa does not seem to have any detrimental impact on the modelled response. Since this value was also observed to ensure numerical stability during the simulation of boundary-value problems involving liquefaction by Taborda (2011), it was adopted in the present study.

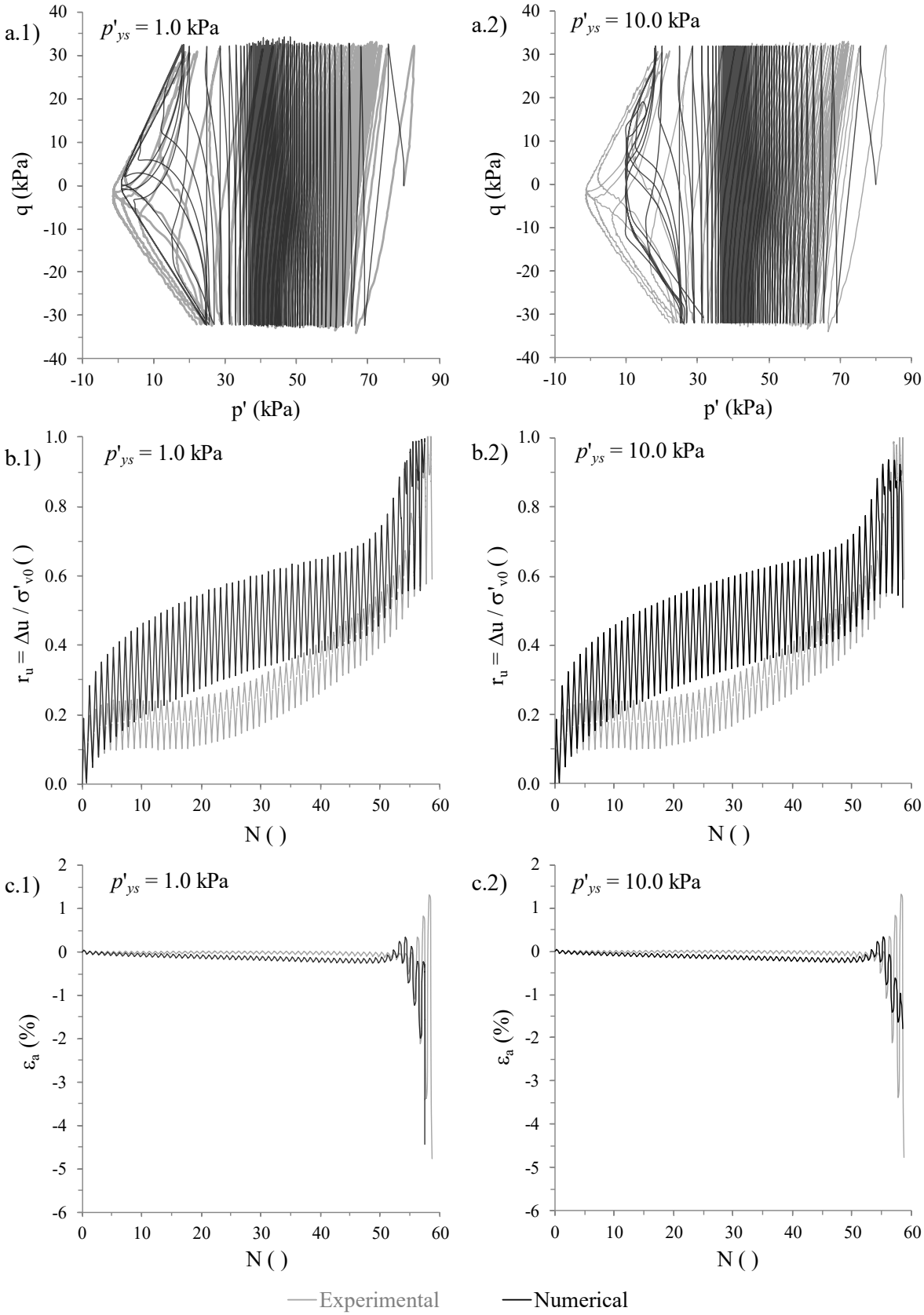

Figure 6.38 – Impact of p'_{ys} on the numerical simulation of test ICUCT 0.771/80/32: (a) effective stress path, (b) excess pore water pressure ratio build-up and (c) axial strain evolution with the number of loading cycles.

As highlighted by Taborda (2011), due to the dependence of the plastic hardening modulus associated with the primary yield surface, A_1, on the tangent shear modulus, G_{tan}, through the plastic multiplier h_g (Equation 4.62), the lower limit for the maximum shear modulus, G_{max}, implicitly limits the magnitude of the A_1. As such, this lower limit may play an important role in the limitation of the accumulation of excessively large strains under very low effective stresses. In effect, the results of a small parametric studies using all available UCT test data (not presented here for brevity of the presentation) enabled to conclude that, by adopting $p'_{min} = 10.0$ kPa, it seems possible to limit the accumulation of strains under very low effective stresses to reasonable values, particularly for dense sand, as it will be clear in the following chapter. Note that an identical value was selected by Taborda (2011) when calibrating the BSPM for Nevada sand. Note also that, alternatively, it would have been possible to impose a lower limit on G_{tan} through the model parameter G_{min}. However, as pointed out by Taborda (2011), since G_{tan} depend on several other factors besides p', such as on the density of the material and distance of the current stress point to that at last shear reversal, it seems more consistent to impose a lower limit to G_{max} through p'_{min}.

Subsequently, an upper limit to the magnitude of the fabric index, H_{max}, was established. This limit may be particularly important when simulating the response of initially denser-than-critical sand ($\psi_0 < 0.0$) subjected to very low effective stresses. Under such conditions, and when no restriction is applied, a very large magnitude of H is likely be obtained, leading to very large oscillations of the shearing-induced fabric tensor (Equation 4.66 and 4.67) and, consequently, of the plastic hardening modulus, which might compromise the stability of the numerical analysis. As suggested by Taborda (2011), to find an appropriate value for H_{max}, the initial conditions of each available UCT test, in terms of major principal effective stress, $\sigma'_{1,0}$, and state parameter, ψ_0, – see, for example, Table 6.3 – should be compared with the values given by Equation 4.69, re-written below for clarity.

$$H = H_0 \left(\frac{\sigma'_{1,0}}{p'_{ref}} \right)^{-\zeta} \langle -\psi_0 \rangle \tag{6.30}$$

where $H_0 = 43000.0$ and $\zeta = 1.00$ were obtained for the original version of the constitutive model (Section 6.11). The comparison is illustrated in Figure 6.39, where lines corresponding to $H = 1\,000.0$, $H = 5\,000.0$, $H = 10\,000.0$ and $H = 50\,000.0$ are plotted together with the experimental ($\sigma'_{1,0}$, ψ_0) values. It can be observed that the value of $H = 50\,000.0$ provides an upper limit for the initial states of all samples. This value was adopted in the present study.

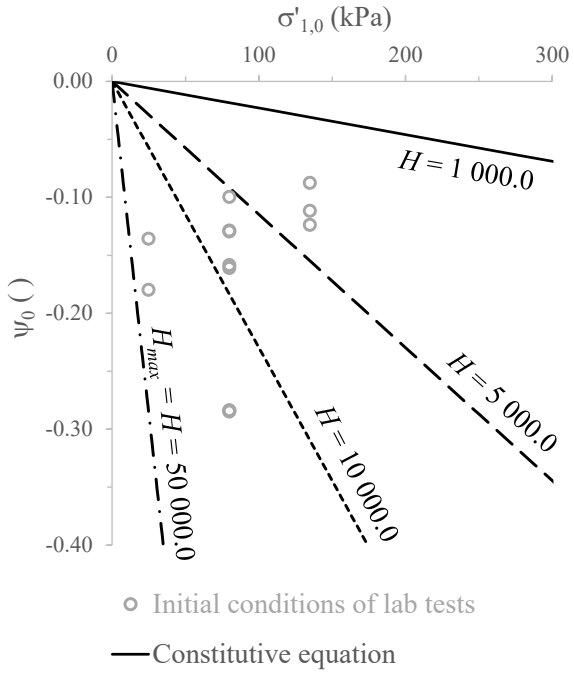

Figure 6.39 – Contours of the fabric index *H*.

Finally, small parametric studies were performed to evaluate the impact of $h_{f,min}$ and $h_{f,max}$, on the modelled response. Note that these model parameters limit the magnitude of the plastic multiplier h_f (i.e. the contribution of $\boldsymbol{F}$ to A_1). Once again, it was concluded that the values adopted by Taborda (2011) in previous studies were also adequate to the present case, consisting of setting $h_{f,min} = 0.1$ and $h_{f,max} = 100.0$.

6.14 Summary of model parameters

Table 6.5 summarises the four sets of model parameters obtained during the calibration of both original and extended formulations of the bounding surface plasticity model (BSPM) for Hostun sand. The sets of parameters belonging to the category "A) Static" were optimised to the simulation of the monotonic response of Hostun sand and, therefore, should not be employed in the simulation of its cyclic response. Conversely, the sets of parameters belonging to the category "B) Dynamic" make use of the shearing-induced fabric component of the constitutive model, which introduces the effect of the cyclic history on the modelled response. This component allows for the simulation of a more compliant effective stress path once the phase transformation line is crossed and the effective stress path is reversed – an aspect identified as crucial to the adequate simulation of liquefaction-related phenomena (Papadimitriou and Bouckovalas, 2002). For each pair of sets of parameters (A and B), there is one set that makes use of the original formulation of the model, as proposed by Taborda *et al.* (2014), and another set that makes use of the extended formulation of the model by activating the inherent fabric anisotropy component. As pointed out before, this component increases the ability of the constitutive model to replicate the response of sand for loading conditions other than triaxial compression. Note that the differences between the sets of

model parameters belonging to the categories "A) Static" and "B) Dynamic" are highlighted in bold, while the three additional model parameters required by the inherent fabric anisotropy component are presented in grey.

Table 6.5 – Model parameters for Hostun sand.

Sets of parameters	A) Static		B) Dynamic	
	A.1) Original formulation	A.2) Extended formulation	B.1) Original formulation	B.2) Extended formulation
Non-linear elasticity				
C_g	293.0	293.0	293.0	293.0
m_g	2.97	2.97	2.97	2.97
n_g	0.49	0.49	0.49	0.49
κ	2.00	2.00	2.00	2.00
a_1	0.46	0.46	0.46	0.46
γ_1	7.02×10^{-4}	7.02×10^{-4}	7.02×10^{-4}	7.02×10^{-4}
p'_{min}	1.0 kPa (1)	1.0 kPa (1)	10.0 kPa	10.0 kPa
G_{min}	1.0 kPa (1)	1.0 kPa (1)	1.0 kPa (1)	1.0 kPa (1)
ν	0.18	0.18	0.18	0.18
Model surfaces				
p'_{ref}	101.3 kPa	101.3 kPa	101.3 kPa	101.3 kPa
$(e_{CS})_{ref}$	1.000	1.000	1.000	1.000
λ	0.070	0.070	0.070	0.070
ξ	0.360	0.360	0.360	0.360
M_c^c	1.265	1.265	1.265	1.265
M_e^c	0.911	0.911	0.911	0.911
k_c^d	0.940	0.940	0.940	0.940
k_e^d	0.677	0.677	0.677	0.677
k_c^b	2.810	2.810	2.810	2.810
k_e^b	2.024	2.024	2.024	2.024
m	0.065	0.065	0.065	0.065
p'_{ys}	1.0 kPa	1.0 kPa	1.0 kPa	1.0 kPa
Stress-dilatancy relationship				
A_0	1.000	1.000	1.000	1.000
Plastic hardening modulus				
h_0	**0.132**	**0.132**	**0.200**	**0.195**
γ	**0.999**	**0.999**	**1.100**	**1.080**
e_{lim}	**0.960**	**0.960**	**0.900**	**0.900**
α	1.000	1.000	1.000	1.000
μ	0.500	0.500	0.500	0.500
β	**0.300**	**0.300**	**0.600**	**0.600**
Shearing-induced fabric component				
H_0	**0.0** (2)	**0.0** (2)	**43 000.0**	**55 000.0**
ζ	**0.0** (2)	**0.0** (2)	**1.00**	**0.85**
H_{max}	(2)	(2)	50 000.0	50 000.0
$h_{f,min}$	(2)	(2)	0.1	0.1
$h_{f,max}$	(2)	(2)	100.0	100.0

Table 6.5 – Model parameters for Hostun sand.

Sets of parameters	A) Static		B) Dynamic	
	A.1) Original formulation	A.2) Extended formulation	B.1) Original formulation	B.2) Extended formulation
Inherent fabric anisotropy component				
a	**0.333** [(2)]	**0.290**	**0.333** [(2)]	**0.290**
v_A	**0.000** [(2)]	**1.000**	**0.000** [(2)]	**1.000**
k_A	**1.000** [(2)]	**0.600**	**1.000** [(2)]	**0.600**

[(1)] Not used. [(2)] Component not activated when using this set of model parameters.

Table 6.6 compares the dynamic set of model parameters B.1 obtained in the present study for Hostun sand with other sets of parameters employed in other studies published in the literature using other sands as reference material (Taborda, 2011; Taborda *et al.*, 2014; Williams, 2014). For future reference, the range of values employed for each parameter in the studies under comparison is included in the table, highlighting in bold the values established by the present study. It is interesting to observe that the values of k_c^d and k_e^d, defining the position of the dilatancy surface in triaxial compression (TC) and in triaxial extension (TE), respectively, obtained in the present study for Hostun sand are the lowest among the values obtained in all studies. Since the critical stress ratio in TC, $M_{c,e}^c$, does not vary significantly for the sands under comparison and the equation defining the dilatancy surface is linearly dependent on the state parameter, ψ (Equation 4.5), it can be concluded that denser-than-critical samples ($\psi < 0$) of Hostun sand tends to start dilating for higher stress ratios than those required by the other sands (Leighton Buzzard, Nevada and Fraser river sands) having a similar ψ. Along the same lines, the fact that the values of k_c^b and k_e^b, characterising the position of the bounding surface in TC and TE (Equation 4.4), respectively, obtained for Hostun sand defines the upper limits of their ranges (although not being significantly higher than the values obtained for the other sands) suggests that denser-than-critical samples ($\psi < 0$) of Hostun sand tend to mobilise higher peak stress ratios than those reached by the other sands under comparison having a similar value of ψ.

Table 6.6 – Comparison of the set of parameters obtained in the present study with those employed in other studies reported in the literature.

Sets of parameters	Hostun sand (set B.1)	Leighton Buzzard sand	Nevada sand	Fraser river sand	Range of values
Reference	present study	Taborda, (2011)	Taborda *et al.* (2014)	Williams (2014)	
Non-linear elasticity					
C_g	293.0	623.0 [(1)]	518.6 [(1)]	422.0 [(1)]	[(1)]
m_g	2.97	[(1)]	[(1)]	[(1)]	[(1)]
n_g	0.49	0.50 [(1)]	0.50 [(1)]	0.50 [(1)]	[(1)]
κ	2.00	2.00	2.00	2.00	2.00
a_1	0.46	0.50	0.30	0.44	0.30 – 0.46
γ_1	7.02×10^{-4}	5.5×10^{-4}	6.5×10^{-4}	1.59×10^{-3}	$5.5 \times 10^{-4} – 1.59 \times 10^{-3}$
p'_{min} (kPa)	10.0	5.0	10.0	[(2)]	5.0 – 10.0

Table 6.6 – Comparison of the set of parameters obtained in the present study with those employed in other studies reported in the literature.

Sets of parameters	Hostun sand (set B.1)	Leighton Buzzard sand	Nevada sand	Fraser river sand	Range of values
Reference	present study	Taborda, (2011)	Taborda *et al.* (2014)	Williams (2014)	
G_{min}	(2)	(2)	(2)	(2)	(2)
ν	0.180	0.135	0.200	0.200	0.135 – 0.200
Model surfaces					
p'_{ref} (kPa)	101.3	101.3	100.0	100.0	100.0 – 101.3
$(e_{CS})_{ref}$	1.000	1.010	0.887	0.840	0.840 – 1.010
λ	0.070	0.080	0.079	0.030	0.030 – 0.080
ξ	0.360	0.350	0.250	0.660	0.250 – 0.660
M_c^c	1.265	1.180	1.290	1.376	1.180 – 1.376
M_e^c	0.911	0.850	0.900	1.000	0.850 – 1.000
$\boldsymbol{k_c^d}$	**0.940**	2.140	2.350	1.670	**0.940** – 1.670
$\boldsymbol{k_e^d}$	**0.677** (3)	1.542 (3)	1.640 (3)	1.214 (3)	**0.677** – 1.640
$\boldsymbol{k_c^b}$	**2.810**	1.920	2.180	2.670	1.920 – **2.810**
$\boldsymbol{k_e^b}$	**2.024** (3)	1.383 (3)	1.521 (3)	1.940 (3)	1.383 – **2.024**
m	0.065	0.065	0.065	0.050	0.050 – 0.065
p'_{ys} (kPa)	1.0	1.0	1.0	1.0	1.0
Stress-dilatancy relationship					
A_0	1.000	1.050	1.460	1.000	1.000 – 1.460
Plastic hardening modulus					
h_0	0.200	0.047	0.613	0.100	0.047 – 0.613
γ	1.100	0.956	1.214	0.650	0.650 – 1.214
e_{lim}	0.900	0.934	0.818	0.946	0.818 – 0.946
α	1.000	1.000	1.000	1.000	1.000
μ	0.500	0.623	1.500	0.000	0.000 – 1.500
β	0.600	0.750	0.000	-0.300	-0.300 – 0.750
Shearing-induced fabric component					
$\boldsymbol{H_0}$	**43 000.0**	8 021.2	12 239.4	12 600	8 021.2 – **43 000.0**
$\boldsymbol{\zeta}$	**1.00**	2.40	1.59	2.00	**1.00** – 2.40
H_{max}	5.0×10^4	6.0×10^4	2.0×10^6	(2)	5.0×10^4 – 2.0×10^6
$h_{f,min}$	0.1	0.1	0.1	(2)	0.1
$h_{f,max}$	100.0	100.0	100.0	(2)	100.0

(1) In the previous studies, $G_{max} = C_g\, p'_{ref}\, \frac{1}{0.3+0.7\, e^2} \left(\frac{p'}{p'_{ref}}\right)^{n_g}$, with $n_g = 0.50$ was considered; this equation was replaced by $G_{max} = C_g\, p'_{ref}\, \frac{(m_g - e)^2}{1+e} \left(\frac{p'}{p'_{ref}}\right)^{n_g}$ in the present version of the model. (2) Not used. (3) The assumptions $k_e^d = k_c^d\, (M_e^c / M_c^c)$ and $k_e^b = k_c^b\, (M_e^c / M_c^c)$, proposed by Papadimitriou and Bouckovalas (2002), were employed in all studies.

Nevertheless, the most appreciable difference between the values obtained for Hostun sand and those reported in the literature for other sands concerns those characterising the shearing-induced fabric component. In particular, it can be observed that the value assigned to the shearing-induced fabric index constant, H_0, is clearly above those employed in other studies. This suggests that, when compared with the other sands, a stronger stiffening effect

is expected to be observed for Hostun sand under effective stress paths below the dilatancy surface and, therefore, a greater number of loading cycles are likely required to reach cyclic mobility under similar conditions. To illustrate this aspect, a small parametric study was performed, comprising the simulation of tests ICUCT 0.771/80/32, ICUCT 0.803/80/36 and ICUCT 0.832/80/42 using three different values for H_0: 21 500, 43 000.0 and 86 000.0. Note that the intermediate value corresponds to that obtained during the calibration process (set B.1), while the smallest and largest values correspond, respectively, to half and double of the intermediate value. With respect to the remaining model parameters, the values indicated in Table 6.6 for the set B.1 were employed. The results obtained in these simulations are presented in Figure 6.40, in terms of cyclic resistance ratio (CRR) against the number of loading cycles required to the onset of cyclic mobility, N_{liq}. Note that, as indicated in the figure, CRR is given by the ratio of the deviatoric stress oscillation (inducing cyclic mobility in a given number of loading cycles), $|\Delta q|$, to twice the isotropic effective stress at consolidation, σ'_0 (note that all samples were isotropically consolidated). Moreover, it should be noted that, to be consistent with the criterion used before when analysing the experimental data (Chapter 3), cyclic mobility was considered triggered when a residual (i.e. corresponding to a null deviatoric stress) excess pore water pressure ratio, $r_{u,res}$, of 0.95 was obtained. The choice of the cyclic mobility criterion is, nevertheless, expected to have no influence on the conclusions reached in this small parametric study, as discussed in detail in Chapter 3. Finally, note that, for reference, experimental data is also plotted in Figure 6.40. As expected, it can be seen that the smaller the value assigned to H_0, the lesser the number of loading cycles required to the onset of cyclic mobility (in other words, the smaller the undrained cyclic resistance simulated by the constitutive model). Furthermore, it is apparent that $H_0 = 43\,000.0$ allows for a better reproduction of experimental data than the remaining two values.

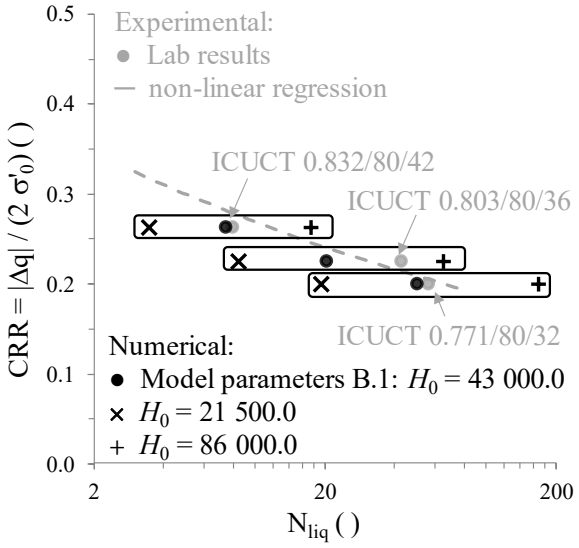

Figure 6.40 – Effect of different values of shearing-induced fabric index constant H_0 on the numerical reproduction of undrained cyclic triaxial resistance of Hostun sand.

A plausible explanation for the need of a larger value of H_0 for Hostun sand than those used for other sands in other studies is provided in Figure 6.41, which compares the undrained cyclic resistance of Hostun, Leighton Buzzard and Nevada sands, inferred, in all cases, from undrained cyclic triaxial (UCT) test data used for the calibration of the constitutive model. Note that, in the study undertaken by Williams (2014) on Fraser river sand, undrained cyclic direct simple shear test data was used for the calibration of the model, hampering a direct comparison with data presented in Figure 6.41. It is apparent that Hostun sand is significantly more resistant than the other two sands. For instance, while a moderately loose sample of Nevada sand ($D_r \approx 40 - 60$ %) consolidated to $\sigma'_0 = 80$ kPa requires a single loading cycle to the onset of cyclic mobility when subjected to a cyclic stress ratio of $CSR = 0.25$, a significantly larger number of loading cycles (of about 15) are required by a sample of Hostun sand having a similar initial density ($D_r \approx 50$ %), consolidated under an identical effective stress state and sheared under a similar CSR. The discrepancies between the undrained cyclic strengths of Hostun and Leighton Buzzard sands are even larger. Specifically, while a moderately dense sample of Leighton Buzzard sand ($D_r \approx 50$ %) consolidated to $\sigma'_0 = 120$ kPa requires a single loading cycle to the onset of cyclic mobility when subjected to $CSR = 0.20$, a much larger number of loading cycles are required to induce cyclic mobility on a similarly prepared sample of Hostun sand subjected to a similar CSR (note that $N_{liq} \approx 20$ are required by a Hostun sand sample consolidated to $\sigma'_0 = 135$ kPa and, therefore, more than twenty loading cycles would be likely required by a sample consolidated to $\sigma'_0 = 120$ kPa).

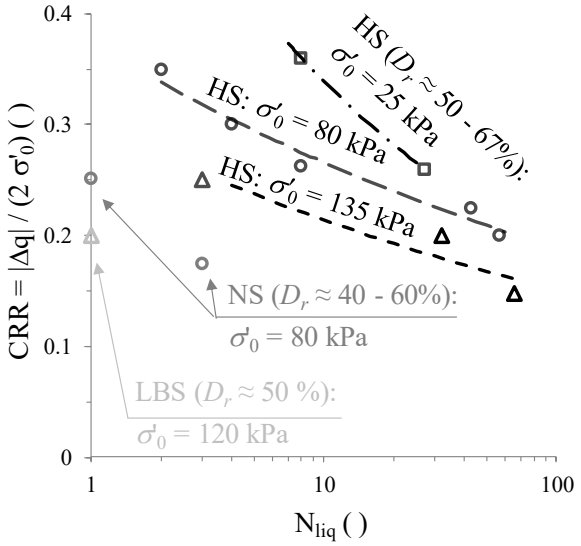

Figure 6.41 – Experimental characterisation of the undrained cyclic triaxial resistance of moderately loose samples of Hostun, Leighton Buzzard and Nevada sands.

It is perhaps important to highlight that the undrained cyclic resistance predicted by the present constitutive model is not solely dependent on the value of fabric index constant, H_0. For instance, the plastic multiplier h_0 has also a strong influence on this aspect. As such, it would have been possible to adopt a larger value of h_0, while reducing the value assigned to H_0, in which case the set of model parameters would likely be closer to that proposed for

Nevada sand (having $h_0 = 0.613$) by Taborda *et al.* (2014). Note, however, that such strategy would clearly deteriorate the ability of the constitutive model to simulate adequately cyclic response of Hostun sand (see, for example, Figure 6.19 where $H_0^* = 20\,000.0$ is used in conjunction with $h_0^* = 0.060$).

The ability of the constitutive model to capture key aspects of the response of Hostun sand observed in triaxial tests is further explored in Chapter 7, while the application of the model to the simulation of boundary-value problems involving liquefaction-related phenomena is presented in Chapter 8.

Chapter 7 APPLICATION OF THE BOUNDING SURFACE PLASTICITY MODEL TO THE SIMULATION OF ELEMENT LABORATORY TESTS

7.1 Introduction

Having established the model parameters leading to the best possible reproduction of the available experimental data in the previous chapter, the ability of the constitutive model to replicate key features of the monotonic and cyclic response of Hostun sand observed in element laboratory tests is explored in this chapter. More specifically, its ability to capture the effect of the initial void ratio, consolidation effective stress state and stress path direction on the modelled monotonic response of Hostun sand is firstly assessed. Although these aspects are indirectly considered during the calibration process (for example, by considering the effect of the state parameter on the positions of the bounding and dilatancy surfaces), it is important to evaluate the degree of accuracy obtained when simulating the available test data. In terms of cyclic response of Hostun sand, particular emphasis is given to the investigation of the ability of the constitutive relationship to replicate the evolutions of both secant stiffness and hysteretic damping with cyclic loading, the excess pore water pressure build-up and strain accumulation with cyclic loading, as well as the onset of cyclic mobility observed in the laboratory experiments.

All numerical simulations, whose results are presented in this chapter, were performed by using a single hybrid eight-noded isoparametric quadrilateral element with pore water pressure degrees of freedom at the corner nodes. To simulate triaxial test conditions, axisymmetric conditions were specified, with the displacements being restricted vertically along the base of the model and horizontally along the inner boundary corresponding to the axis of symmetry (i.e. left boundary of the model). In addition, to simulate undrained conditions, the displacements of the solid and fluid phases along the direction perpendicular to that defined by a given boundary of the model are tied. In terms of solicitation, uniform vertical displacements were prescribed to the nodes belonging to the top boundary of the model to reproduce the strain-controlled nature of the drained and undrained monotonic triaxial compression and extension tests. Conversely, when simulating drained isotropic compression tests, uniform normal stresses were prescribed to the nodes belonging to the top and outer (i.e. right) boundaries of the model, therefore simulating the stress-controlled nature of these tests. Finally, to allow for the adequate replication of the stress reversals imposed in cyclic triaxial tests in the laboratory, stress-controlled loading conditions were considered by applying uniform normal stresses to the nodes belonging to the top boundary of the model.

Regarding the model parameters employed in the numerical simulations, since the ultimate objective of this thesis is to assess the ability of the constitutive relationship to replicate liquefaction-related phenomena observed in dynamic centrifuge experiments (presented in the following chapter), it was decided to use the sets of model parameters belonging to the category "B) Dynamic" (Table 6.5) for the simulation of both monotonic and cyclic triaxial tests. Nevertheless, whenever relevant, the obtained results are compared with those obtained when employing one of the sets of parameters optimised for the simulation of the monotonic response of Hostun sand, belonging to the category "A) Static" (Table 6.5). Further comparison between the results obtained when using "dynamic" and "static" sets of parameters is provided in Appendix A.

In terms of structure of this chapter, the ability of the original formulation of the constitutive model, as proposed by Taborda *et al.* (2014), is firstly assessed in Section 7.2. With this purpose, the set of model parameters "B.1) Dynamic – original formulation" are employed to the simulation of all available monotonic and cyclic test data. Subsequently, in Section 7.3, the results obtained when using the set "B.2) Dynamic – extended formulation", which activates the inherent fabric anisotropy component and, therefore, makes use of the extended formulation of the constitutive model, are presented. Note that, since the inherent fabric anisotropy component affects only the modelled response for loading conditions other than triaxial compression, Section 7.3 focuses only on the simulation of monotonic triaxial extension tests and cyclic triaxial tests. Finally, Section 7.4 summarises the main results and conclusions obtained from these numerical simulations.

7.2 Original formulation of the constitutive model

7.2.1 Monotonic response

7.2.1.1 Available data

Table 7.1 summarises the designation and initial conditions of the two drained isotropic compression (DIC) tests, as well as thirty-two drained (D) and undrained (U) monotonic triaxial compression and extension (MTC and MTE, respectively) tests performed on Hostun sand. It can be observed that samples were prepared to a wide range of void ratios (from 0.650 to 0.885) and isotropically or anisotropically consolidated (IC and K0C, respectively) under various mean effective stresses: 25, 50, 80, 135, 200 and 500 kPa. Moreover, it can be seen that samples were sheared under five different stress paths: isotropic compression (IC), monotonic triaxial compression with increasing mean stress (MTC p↑) – which is the most conventional stress path followed in triaxial compression tests – , monotonic triaxial compression with decreasing mean stress (MTC p↓), monotonic triaxial extension with decreasing mean stress (MTE p↓) – which is the most conventional stress path followed in triaxial extension tests – , and, lastly, monotonic triaxial extension with increasing mean stress (MTE p↑).

Table 7.1 – Designation and initial conditions of the monotonic triaxial compression and triaxial extension tests on Hostun sand.

Type of test	Designation [§]	e_0 ( )	$\sigma'_{r,0}$ (kPa)	$\sigma'_{a,0}$ (kPa)	p'_0 (kPa)	q_0 (kPa)	ψ_0 ( )	Loading (p↑/p↓)
Drained isotropic compression (DIC)	ICDIC 0.794/25	0.787	25.0	25.0	25.0	0.0	-0.174	p↑&p↓
	ICDIC 0.659/25	0.653	25.0	25.0	25.0	0.0	-0.308	p↑&p↓
Undrained monotonic triaxial compression (UMTC)	ICUMTC p↑ 0.876/80	0.876	80.0	80.0	80.0	0.0	-0.059	p↑
	ICUMTC p↑ 0.868/80	0.868	80.0	80.0	80.0	0.0	-0.067	p↑
	ICUMTC p↑ 0.843/135	0.843	135.0	135.0	135.0	0.0	-0.079	p↑
	ICUMTC p↑ 0.783/25	0.783	25.0	25.0	25.0	0.0	-0.175	p↑
	ICUMTC p↑ 0.801/80	0.801	80.0	80.0	80.0	0.0	-0.135	p↑
	ICUMTC p↑ 0.815/135	0.815	135.0	135.0	135.0	0.0	-0.108	p↑
	ICUMTC p↑ 0.686/25	0.686	25.0	25.0	25.0	0.0	-0.272	p↑
	ICUMTC p↑ 0.751/80	0.751	80.0	80.0	80.0	0.0	-0.185	p↑
	ICUMTC p↑ 0.694/135	0.694	135.0	135.0	135.0	0.0	-0.229	p↑
Drained monotonic triaxial compression (DMTC)	ICDMTC p↑ 0.875/50	0.875	50.0	50.0	50.0	0.0	-0.071	p↑
	ICDMTC p↑ 0.885/80	0.885	80.0	80.0	80.0	0.0	-0.050	p↑
	ICDMTC p↑ 0.846/200	0.846	200.0	200.0	200.0	0.0	-0.064	p↑
	ICDMTC p↑ 0.835/500	0.835	500.0	500.0	500.0	0.0	-0.040	p↑
	ICDMTC p↑ 0.829/25	0.829	25.0	25.0	25.0	0.0	-0.129	p↑
	ICDMTC p↑ 0.798/80	0.798	80.0	80.0	80.0	0.0	-0.138	p↑
	ICDMTC p↑ 0.804/135	0.804	135.0	135.0	135.0	0.0	-0.118	p↑
	ICDMTC p↑ 0.667/25	0.667	25.0	25.0	25.0	0.0	-0.291	p↑
	ICDMTC p↑ 0.725/80	0.725	80.0	80.0	80.0	0.0	-0.211	p↑
	ICDMTC p↑ 0.728/135	0.728	135.0	135.0	135.0	0.0	-0.195	p↑
	ICDMTC p↓ 0.826/80	0.826	80.0	80.0	80.0	0.0	-0.109	p↓
	K0CDMTC p↓ 0.797/80	0.797	60.0	120.0	80.0	60.0	-0.139	p↓
	ICDMTC p↓ 0.650/80	0.650	80.0	80.0	80.0	0.0	-0.286	p↓
	K0CDMTC p↓ 0.672/80	0.672	60.0	120.0	80.0	60.0	-0.264	p↓
Undrained monotonic triaxial extension (UMTE)	ICUMTE p↓ 0.790/25	0.790	25.0	25.0	25.0	0.0	-0.167	p↓
	ICUMTE p↓ 0.799/80	0.799	80.0	80.0	80.0	0.0	-0.137	p↓
	ICUMTE p↓ 0.658/25	0.658	25.0	25.0	25.0	0.0	-0.299	p↓
	ICUMTE p↓ 0.650/80	0.650	80.0	80.0	80.0	0.0	-0.286	p↓
Drained monotonic triaxial extension (DMTE)	ICDMTE p↑ 0.798/80	0.798	80.0	80.0	80.0	0.0	-0.138	p↑
	K0CDMTE p↑ 0.801/80	0.801	60.0	120.0	80.0	60.0	-0.137	p↑
	ICDMTE p↑ 0.652/80	0.652	80.0	80.0	80.0	0.0	-0.284	p↑
	K0CDMTE p↑ 0.652/80	0.652	60.0	120.0	80.0	60.0	-0.284	p↑
	ICDMTE p↓ 0.793/80	0.793	80.0	80.0	80.0	0.0	-0.143	p↓

[§] The designation identifies (1) type of consolidation: IC or K0C for isotropic or anisotropic consolidation, respectively; (2) type of drainage: D or U for drained or undrained condition, respectively; (3) type of loading: IC for isotropic compression, MTC p↑ for monotonic triaxial compression with increasing mean stress, MTC p↓ for monotonic triaxial compression with decreasing mean stress, MTE p↓ for monotonic triaxial extension with decreasing mean stress, and MTE p↑ for monotonic triaxial extension with increasing mean stress; (4) void ratio immediately after consolidation, e_0; and (5) mean effective stress immediately after consolidation, p'_0.

Note that, while in this chapter the results of the simulations of several different monotonic tests are presented together to provide an overall assessment of the performance of the constitutive model, the results obtained in each simulation are individually presented in Appendix A.

7.2.1.2 Influence of the initial void ratio

7.2.1.2.1 Undrained conditions

The results of the simulations of isotropically consolidated undrained monotonic triaxial compression tests with increasing mean stress (ICUMTC p↑ tests) on samples consolidated to a mean effective stress, p'_0, of 80 kPa are presented in Figure 7.1.

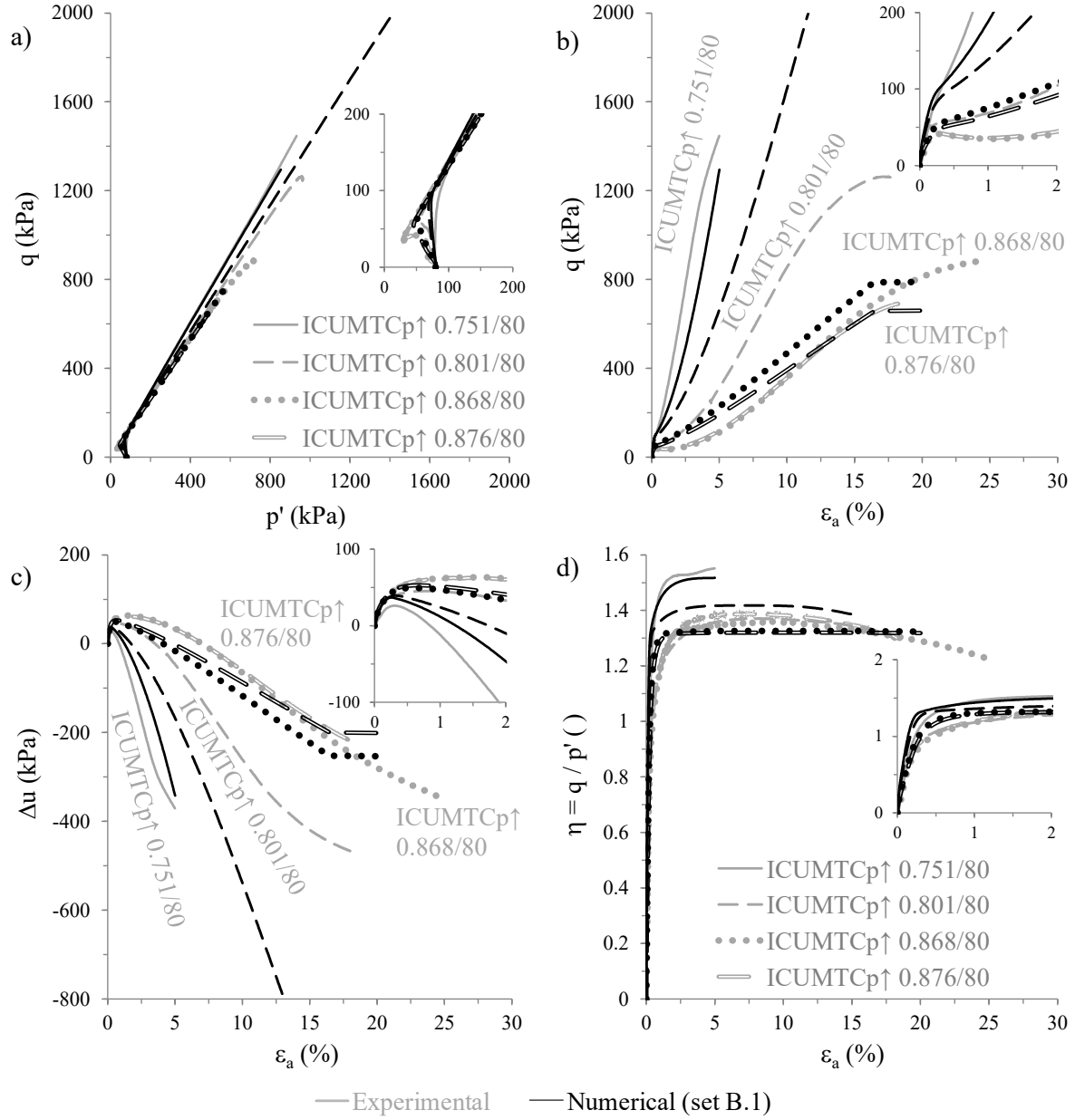

Figure 7.1 – Influence of the initial void ratio on the numerical simulation of ICUMTC p↑ tests performed on samples consolidated to p'_0 = 80 kPa: (a) effective stress path, (b) stress-strain response, (c) excess pore water pressure build-up and (d) stress ratio evolution with axial strain.

It can be seen that, apart from test ICUMTC p↑ 0.801/80, a satisfactory agreement between the numerical and experimental data was obtained. More important, the obtained results suggest that the constitutive model is able to capture the effect of the initial void ratio on the modelled response, including the stiffer stress-strain response, lesser tendency to generate positive (i.e. compression-type) excess pore water pressures during the early stages of loading and higher rate of generation of negative (i.e. suction-type) excess pore water pressures during the later stages of loading as samples are denser, as observed in the laboratory experiments.

Note, nevertheless, that, despite being able to describe the general trend observed in tests ICUMTC p↑ 0.868/80 and ICUMTC p↑ 0.876/80, discrepancies between numerical and experimental data can be observed during the earlier stages of loading. Specifically, it is apparent that, when using this set of model parameters, the constitutive model is unable to replicate the highly-curved-shape effective stress path, as well as the minimum effective stress registered in the experiment. As discussed in Section 6.11, this seems to be a detrimental consequence of the activation of the shearing-induced fabric component. In effect, although introduced to deal with cyclic loading, this component of the model affects the initial contractive phase of the modelled monotonic response, during which positive excess pore water pressures are generated. As shown in Figure 7.2, when using the set of model parameters “A.1) Static – original formulation” (which was optimised for monotonic loading and, therefore, does not activate the shearing-induced fabric component), a much better replication of the response observed during the earlier stages of experiment is obtained, with the constitutive model being inclusively able to predict with satisfactory accuracy the occurrence of the undrained instability (UI) state, corresponding to the local maximum of the deviatoric stress in the deviatoric stress – mean effective stress space (e.g. Ishihara, 1993). As mentioned before, this local maximum of deviatoric stress is often employed in the prediction of conditions leading to flow liquefaction under monotonic loading (e.g. Sladen *et al.*, 1985; Alarcon-Guzman *et al.*, 1988; Nakata *et al.*, 1998).

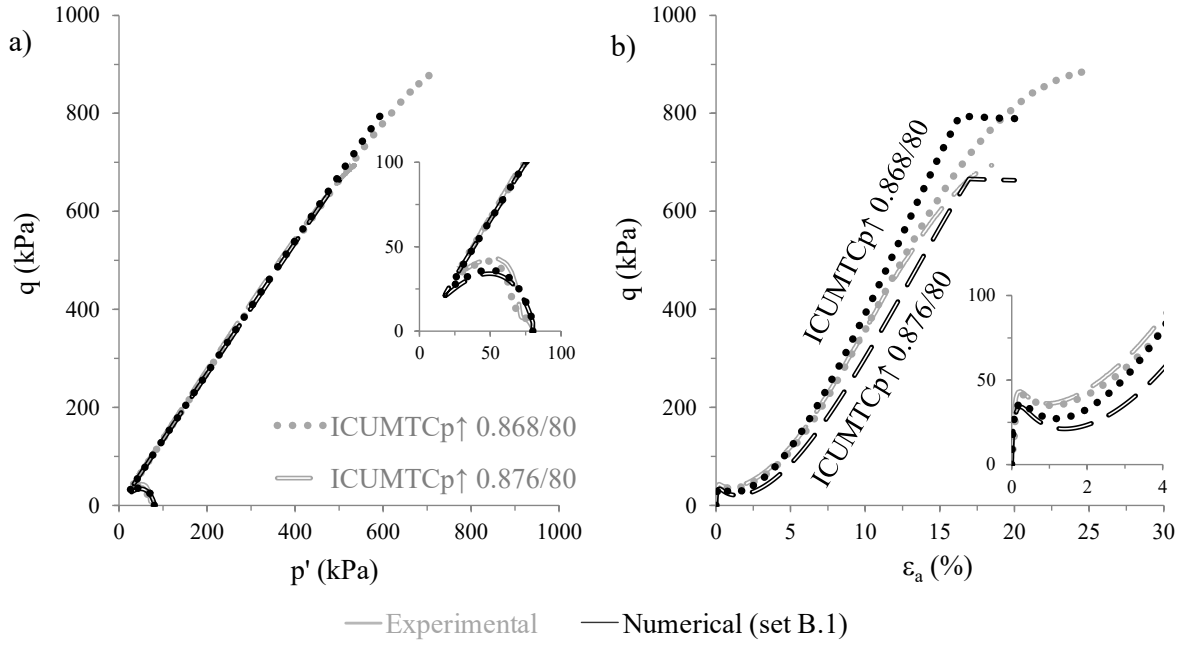

Figure 7.2 – Numerical simulation of tests ICUMTC p↑ 0.868/80 and ICUMTC p↑ 0.876/80 using the set of model parameters optimised for monotonic loading: (a) effective stress path and (b) stress-strain response.

In addition, Figure 7.3 depicts the results obtained in the numerical simulations of ICUMTC p↑ tests conducted on samples consolidated to $p'_0 = 135$ kPa, together with the results registered in the laboratory. Apart from test ICUMTC p↑ 0.843/135, it is apparent that a satisfactory agreement between the two sets of data was obtained, both in terms of stress-strain response and excess pore water pressure ratio generation with loading. Once again, a significantly better reproduction of test ICUMTC p↑ 0.843/135 is obtained when using the set of model parameters optimised for monotonic loading "A.1) Static – original formulation", as shown in Appendix A.

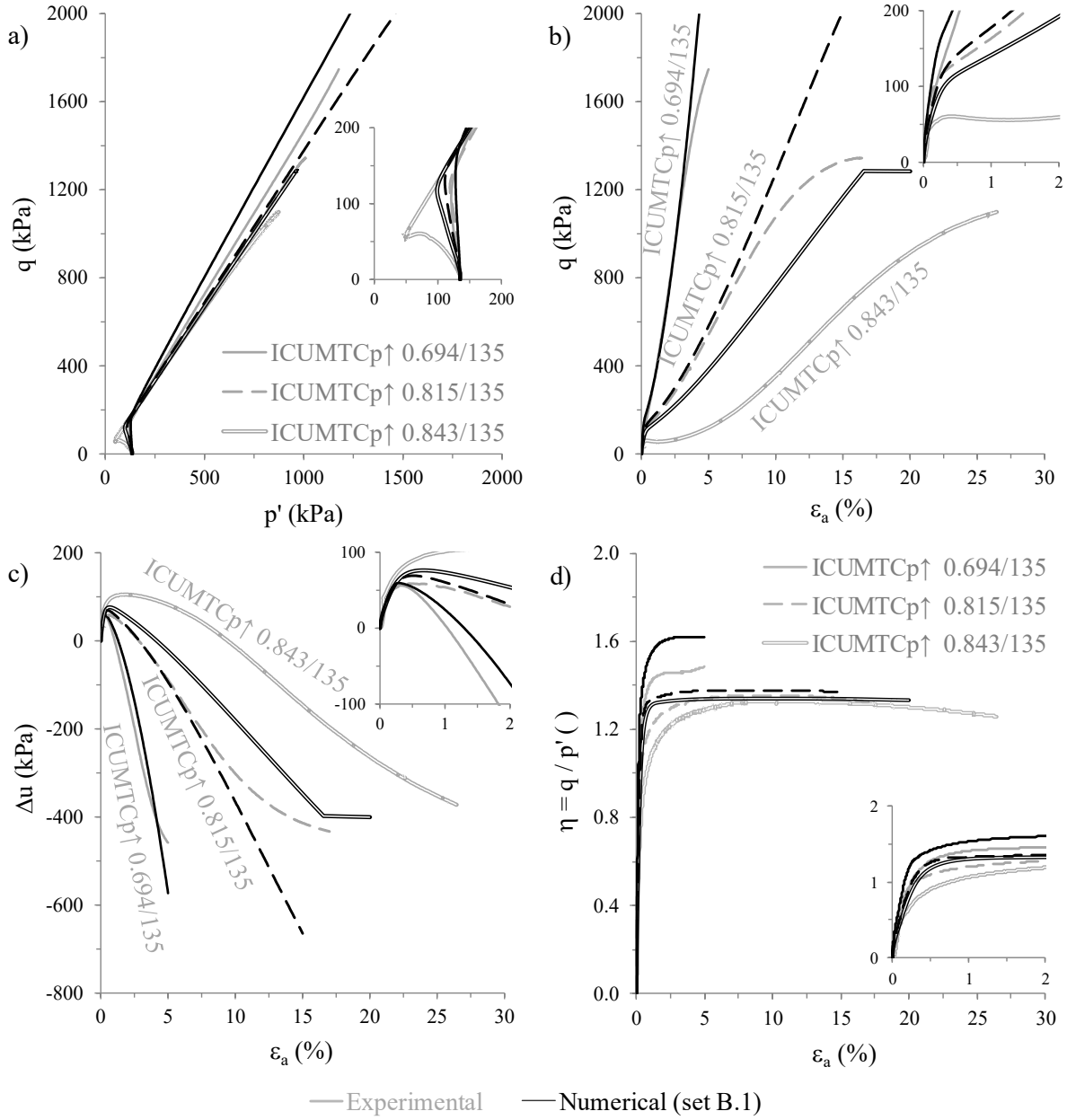

Figure 7.3 – Influence of the initial void ratio on the numerical simulation of ICUMTC p↑ tests performed on samples consolidated to p'_0 = 135 kPa: (a) effective stress path, (b) stress-strain response, (c) excess pore water pressure build-up and (d) stress ratio evolution with axial strain.

7.2.1.2.2 Drained conditions

Figure 7.4 presents the outcome of the numerical simulations of isotropically consolidated drained monotonic triaxial compression tests with increasing mean stress (ICDMTC p↑ tests) on samples consolidated to $p'_0 = 80$ kPa, together with the experimental data.

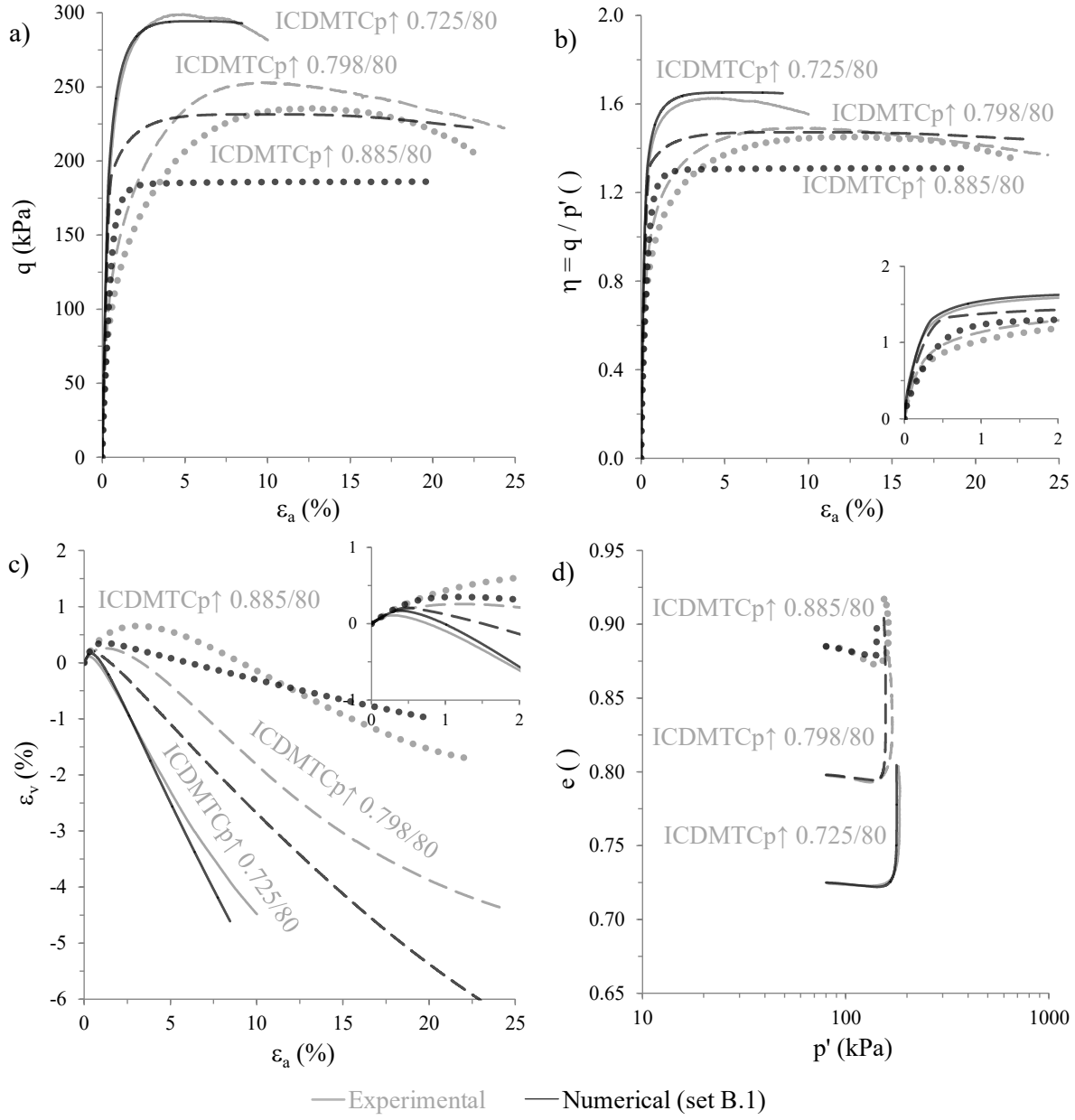

Figure 7.4 – Influence of the initial void ratio on the numerical simulation of ICDMTC p↑ tests performed on samples consolidated to p'_0 = 80 kPa: (a) stress-strain response, (b) stress ratio evolution with axial strain, (c) volumetric strain evolution with axial strain and (d) void ratio evolution with mean effective stress.

Similar to what was observed for the undrained tests, the stress-strain responses obtained for tests performed on loose and moderately loose samples (in this case, tests ICDMTC p↑ 0.885/80 and ICDMTC p↑ 0.798/80) are considerably stiffer than those registered in the experiment, particularly during the earlier stages of loading, during which samples tend to exhibit a contractive response. As pointed out before, this discrepancy seems to be mainly related to the detrimental effect of the shearing-induced fabric component of the constitutive model on the modelled monotonic response. As shown in Figure 7.5, when this component is not activated (i.e. when using the set of model parameters optimised for monotonic loading "A.1) Static – original formulation"), a considerably better reproduction of

the experimental data is obtained. Indeed, in this case, it can be seen that, as samples are initially looser, the modelled peak stress is observed to occur at a greater axial strain, as registered in the laboratory experiment.

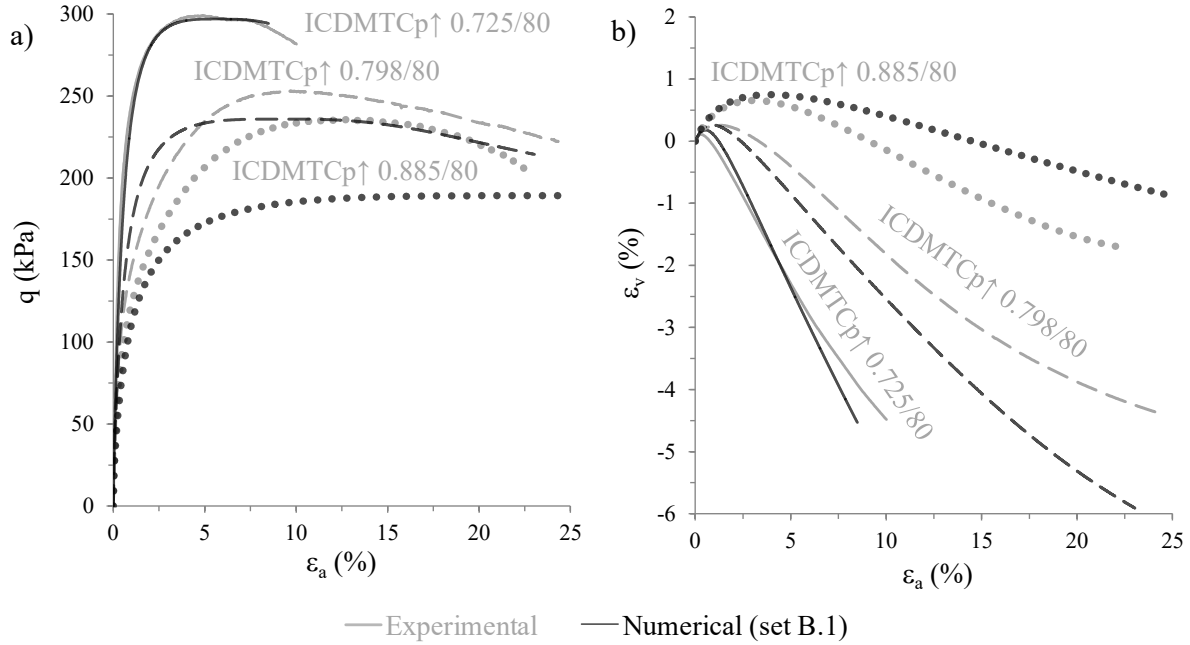

Figure 7.5 – Numerical simulation of the ICDMTC p↑ tests performed on samples consolidated to p'_0 = 80 kPa by using the set of model parameters optimised for monotonic loading: (a) stress-strain response and (b) volumetric strain evolution with axial strain.

Additionally, Figure 7.6 depicts the results obtained in the numerical simulations of ICDMTC p↑ tests performed on samples consolidated to $p'_0 = 135$ kPa, together with the results registered in the laboratory. The results obtained in the numerical simulations are, in this case, slightly better than those obtained for tests on samples consolidated to $p'_0 = 80$ kPa. Note, however, that, in this case, the available data does not include a test on a very loose sample (such as the sample subjected to test ICDMTC p↑ 0.885/80).

To sum up, it can be mentioned that, in general, regardless of the mean effective stress at consolidation, the constitutive model seems able to capture satisfactorily the effect of the void ratio on the modelled response, with a stiffer stress-strain response and more dilatant response being predicted for initially denser samples, as observed experimentally. Unfortunately, the introduction of the shearing-induced fabric component seems to have a detrimental impact on the modelled response obtained for the earlier stages of loading, particularly for loose samples – a fact anticipated during the calibration process (Section 6.11).

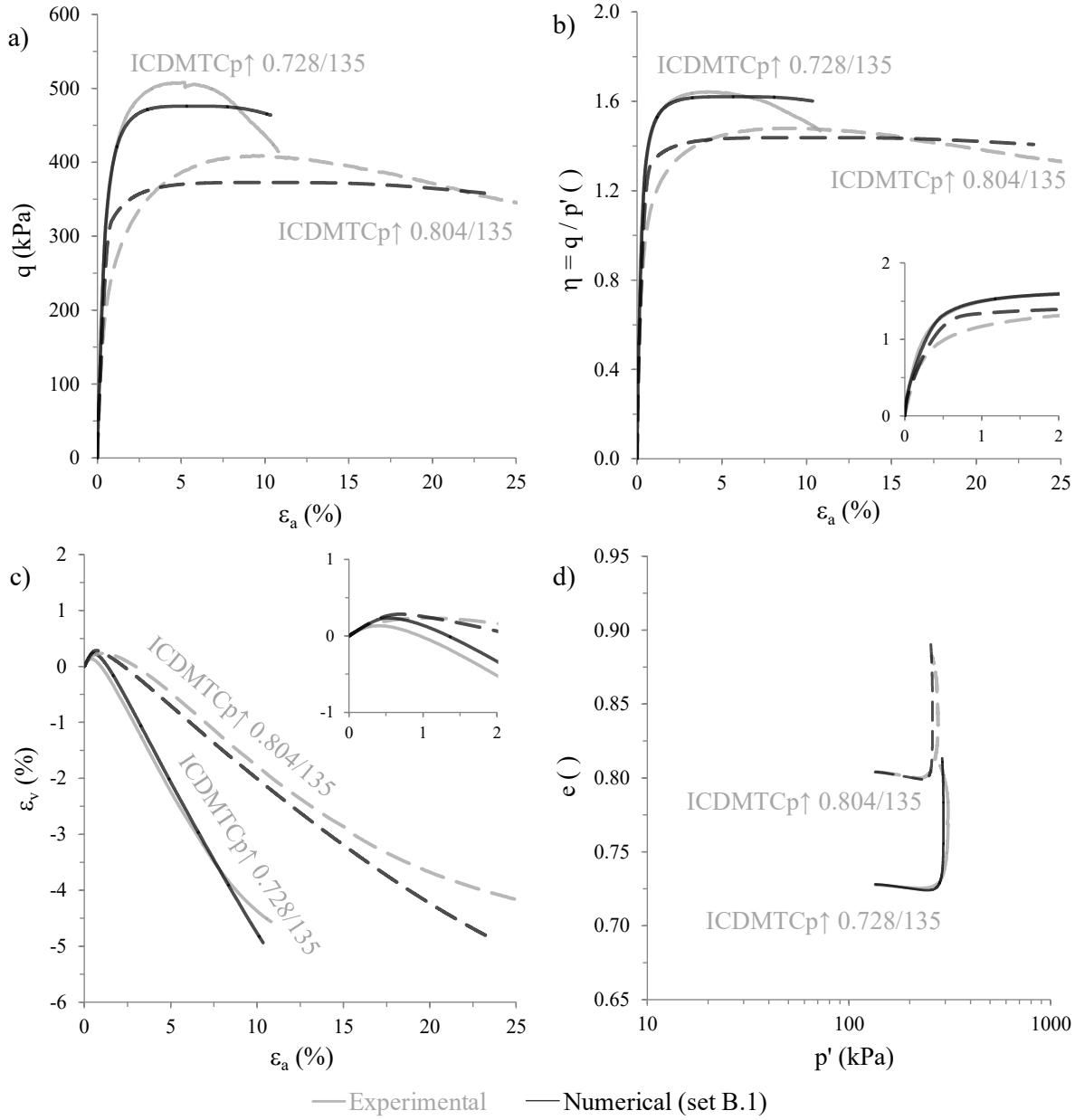

Figure 7.6 – Influence of the initial void ratio on the numerical simulation of ICDMTC p↑ tests performed on samples consolidated to p'_0 = 135 kPa: (a) stress-strain response, (b) stress ratio evolution with axial strain, (c) volumetric strain evolution with axial strain and (d) void ratio evolution with mean effective stress.

7.2.1.3 Influence of the initial confining stress

7.2.1.3.1 Undrained conditions

Figure 7.7 depicts the results of the numerical simulations of ICUMTC p↑ tests on moderately loose samples. Note that, although not identical, the initial void ratios of these tests (as indicated in the designations of the tests) are not very different from each other. It can be seen that, in general, stiffer stress-strain responses (Figure 7.7b), as well as higher rates of generation of excess pore water pressure with loading (Figure 7.7c) were obtained in the numerical simulations, when compared to those measured in the laboratory. It seems that

the small differences in terms of void ratio have a strong impact on the numerical simulation. For instance, it can be observed that, due to its smaller initial void ratio, the modelled evolution of excess pore water pressure with axial strain of test ICUMTC p↑ 0.801/80 plots below that computed for test ICUMTC p↑ 0.815/135 throughout loading – an aspect not observed in the laboratory.

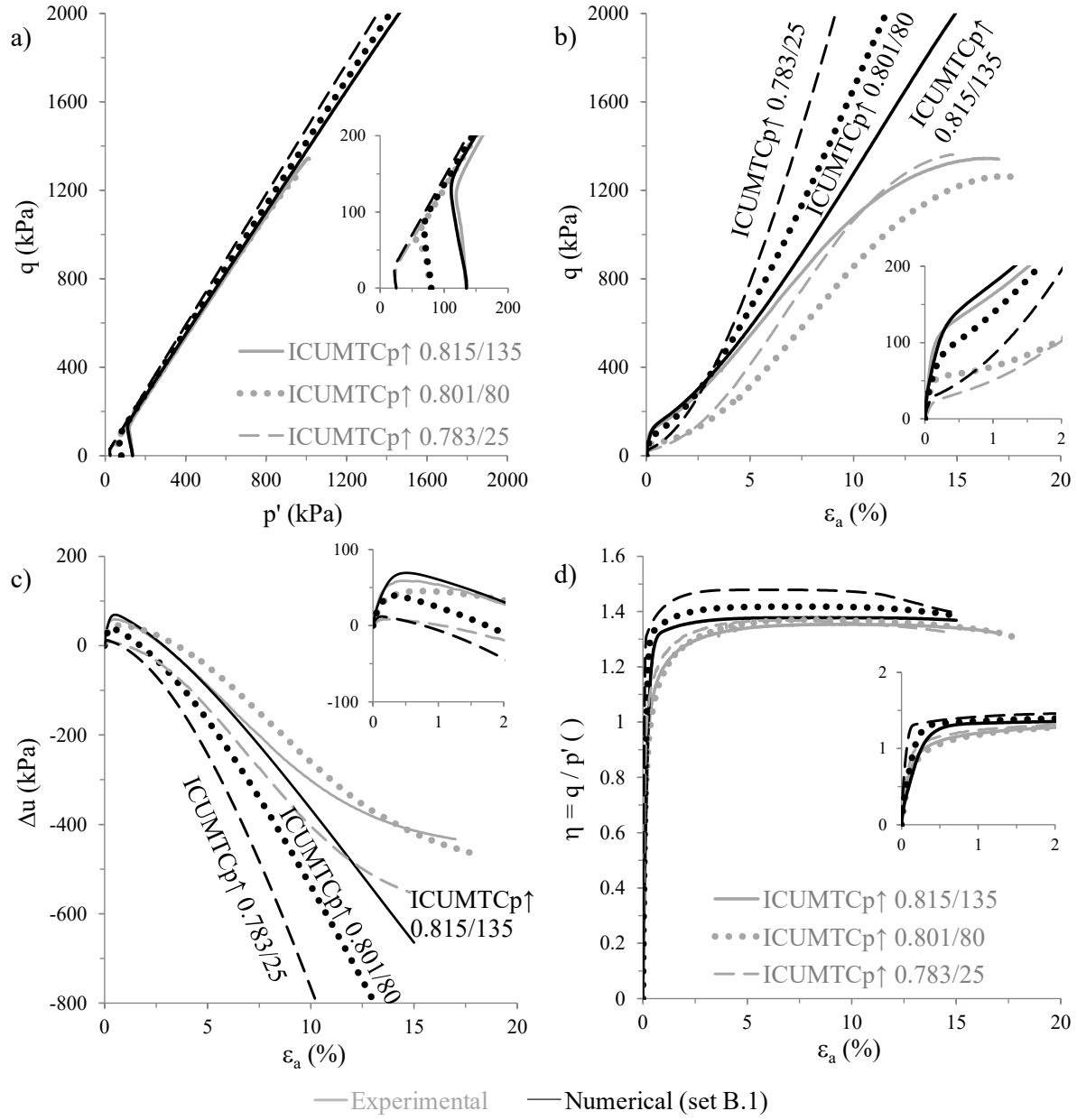

Figure 7.7 – Influence of the initial confining stress on the numerical simulation of ICUMTC p↑ tests performed on moderately loose samples: (a) effective stress path, (b) stress-strain response, (c) excess pore water pressure build-up and (d) stress ratio evolution with axial strain.

Complementary, Figure 7.8 depicts the results of the numerical simulations of two different ICUMTC p↑ tests performed on dense samples. It can be seen that, apart from the stress ratios evolution with axial strain, which are slightly overpredicted in the numerical simulation (at least during the later stages of loading), a very good agreement between numerical and experimental data was obtained. In effect, it is apparent that the constitutive model is able

to predict accurately the main trends observed in the experiment, such as the fact that samples consolidated under higher confining stresses tend to exhibit a stiffer stress-strain response, as well as to generate higher positive excess pore water pressure during the early stages of loading.

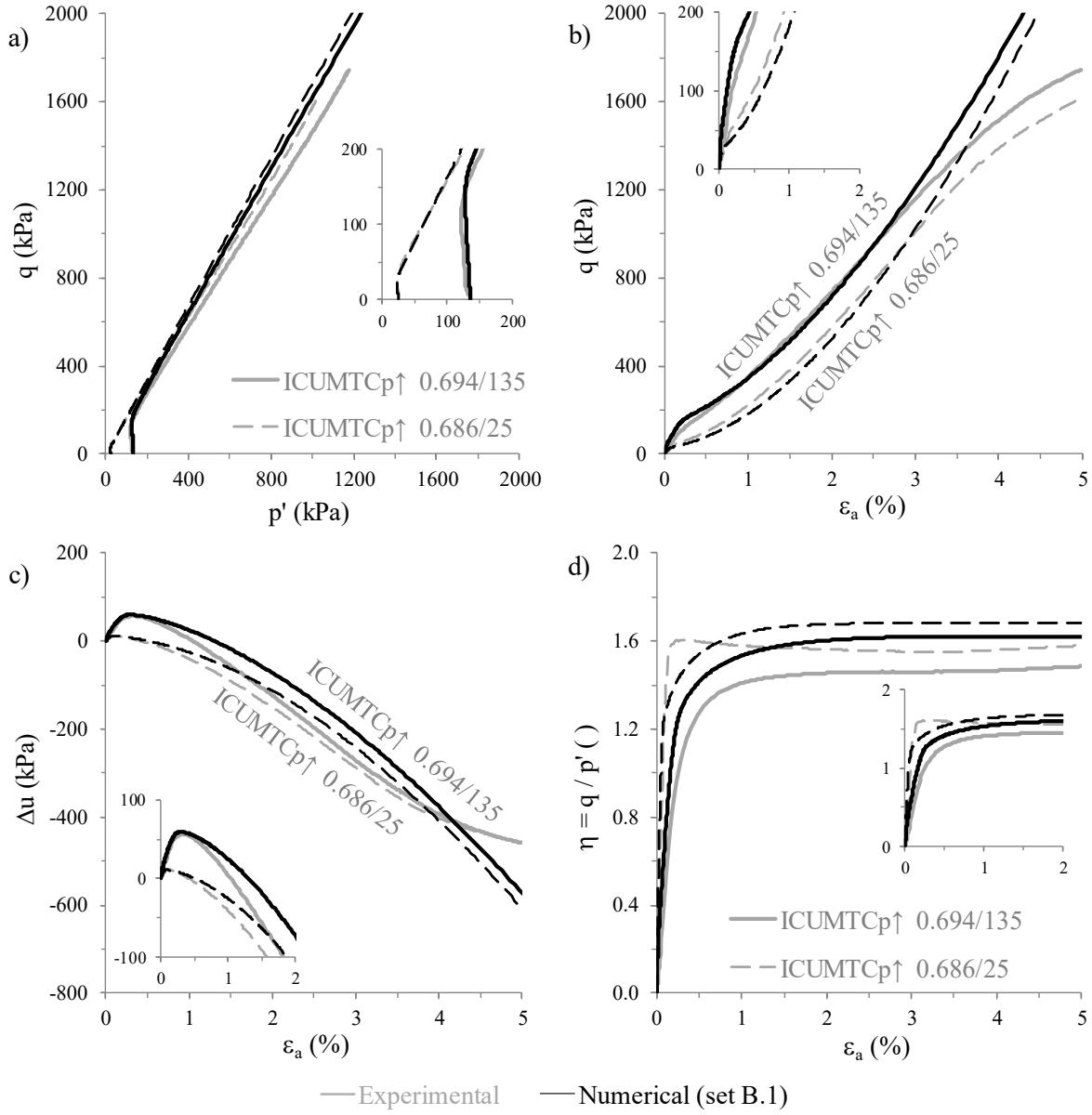

Figure 7.8 – Influence of the initial confining stress on the numerical simulation of ICUMTC p↑ tests performed on dense samples: (a) effective stress path, (b) stress-strain response, (c) excess pore water pressure build-up and (d) stress ratio evolution with axial strain.

7.2.1.3.2 Drained conditions

Figure 7.9 compares the numerical and experimental results of ICDMTC p↑ tests on loose samples. As observed before, although being able to reproduce the main trends observed in the laboratory, the agreement between numerical and experimental data is not very satisfactory, with the constitutive model overestimating the stiffness of sand during the

earlier stages of loading. Consequently, the volumetric responses obtained in the numerical simulations are underpredicted in relation to those measured in the laboratory.

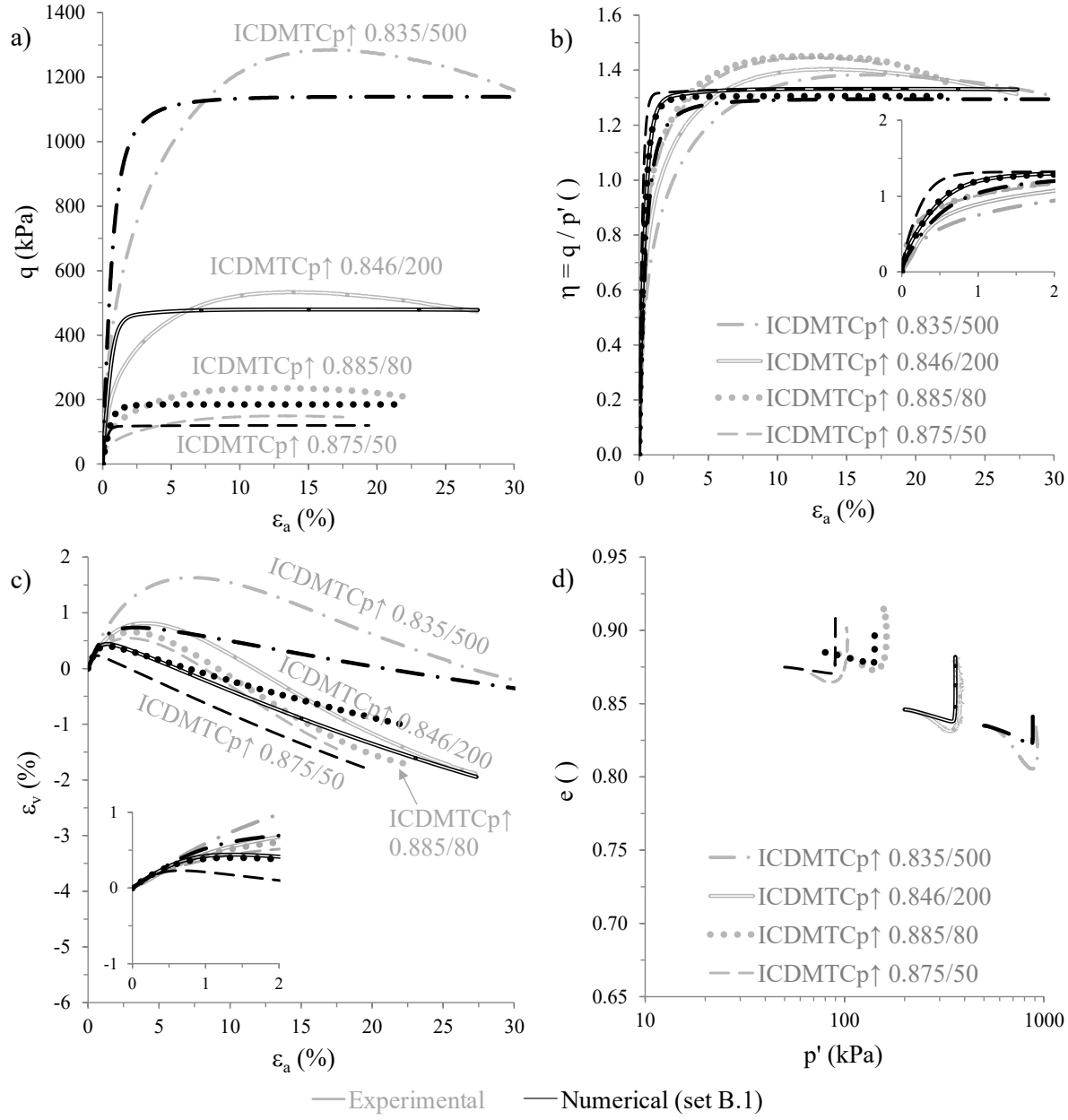

Figure 7.9 – Influence of the initial confining stress on the numerical simulation of ICDMTC p↑ tests performed on loose samples: (a) stress-strain response, (b) stress ratio evolution with axial strain, (c) volumetric strain evolution with axial strain and (d) void ratio evolution with mean effective stress.

Once more, although crucial for the accurate reproduction of the cyclic response of sand, the shearing-induced fabric component seems to have a considerably detrimental contribution to the discrepancies observed between numerical and experimental test data on loose samples. Having re-run the simulations with the set of model parameters "A.1) Static – original formulation", optimised for monotonic loading, the results are clearly more satisfactory, as shown in Figure 7.10. The fact that the modelled peak strengths are slightly underpredicted in relation to those registered in the laboratory suggests that the calibration

of the plastic hardening modulus (Section 6.10) was excessively focused on the deformation pattern (in this case, relation between volumetric and axial strains), rather than on the overall stress-strain response. A more balanced approach (i.e. giving similar importance to both aspects) could have resulted in an overall better agreement.

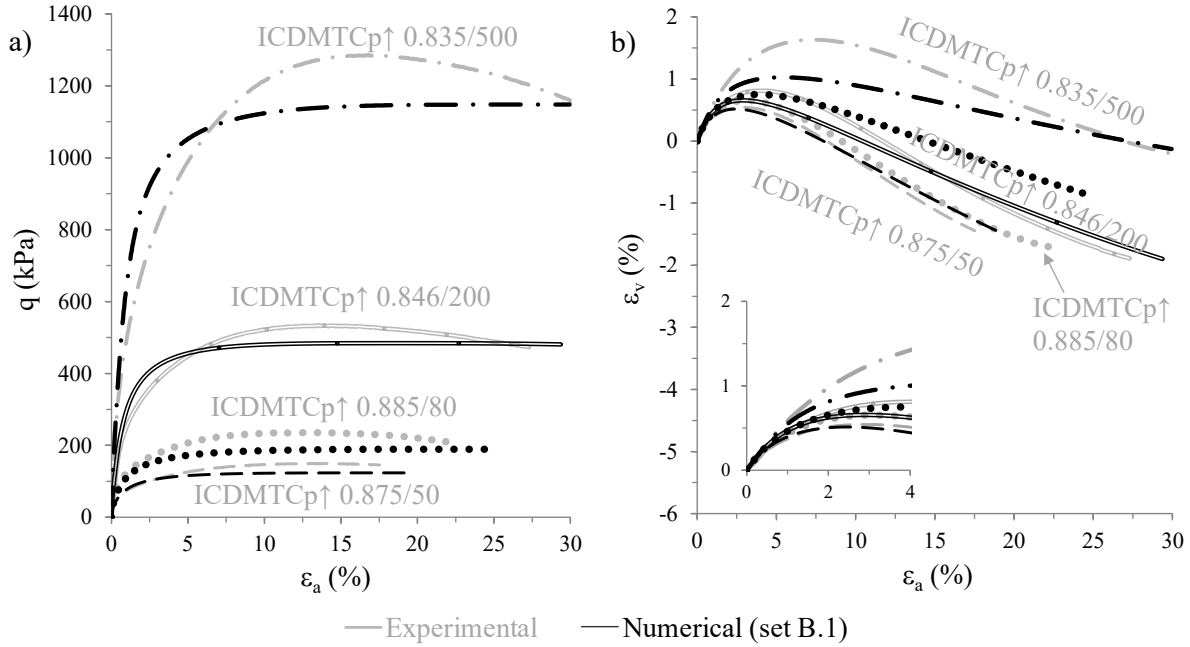

Figure 7.10 – Numerical simulation of the ICDMTC p↑ tests performed on loose samples by using the set of model parameters optimised for monotonic loading: (a) stress-strain response and (b) volumetric strain evolution with axial strain.

In addition, Figure 7.11 and Figure 7.12 compare the numerical and experimental results of ICDMTC p↑ tests on moderately loose and dense samples, respectively. It can be observed that the agreement between the numerical and experimental data is, in this case, much better than that obtained for the loosest samples (Figure 7.9), being particularly remarkable for dense samples. In general, it can be observed that the constitutive model is able to capture the main trends observed in the laboratory experiments, such as the tendency to mobilise greater shear stresses when subjected to higher confining stresses. Moreover, the numerical results suggest that the confining stress has little influence on the stress ratio and volumetric strain evolutions with strain level for the mean effective stress range under analysis (25 to 135 kPa), as observed in the laboratory.

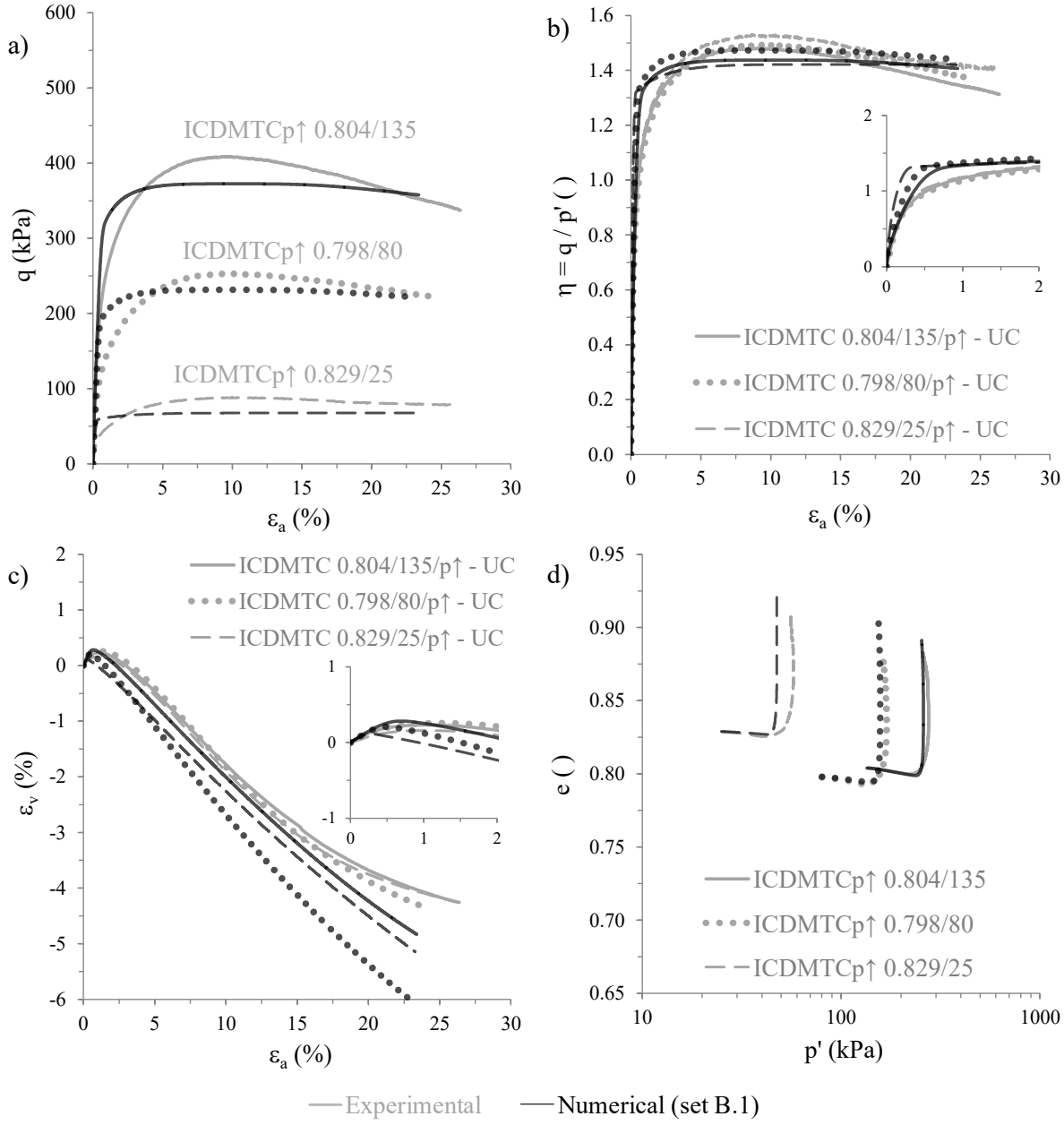

Figure 7.11 – Influence of the initial confining stress on the numerical simulation of ICDMTC p↑ tests performed on moderately loose samples: (a) stress-strain response, (b) stress ratio evolution with axial strain, (c) volumetric strain evolution with axial strain and (d) void ratio evolution with mean effective stress.

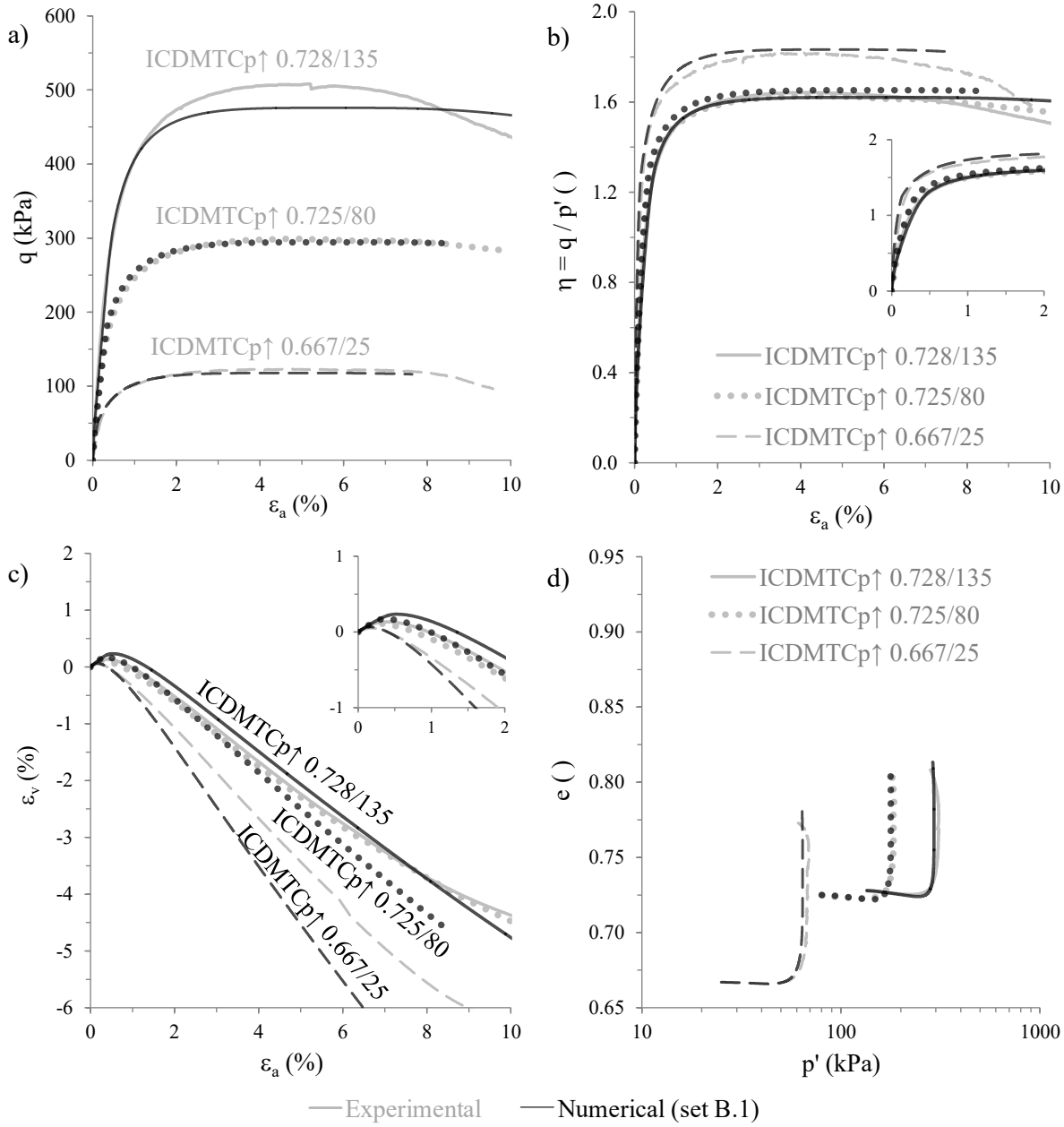

Figure 7.12 – Influence of the initial confining stress on the numerical simulation of ICDMTC p↑ tests performed on dense samples: (a) stress-strain response, (b) stress ratio evolution with axial strain, (c) volumetric strain evolution with axial strain and (d) void ratio evolution with mean effective stress.

7.2.1.4 Influence of stress path direction

7.2.1.4.1 Drained isotropic compression

Figure 7.13 depicts the results of the simulations of the two isotropically consolidated drained isotropic compression (ICDIC) tests performed on a moderately loose and on a dense sample of Hostun sand (ICDIC 0.787/20 and ICDIC 0.653/20, respectively). The experimental data is also presented in the figure for comparison. It can be observed that the constitutive model is unable to replicate adequately the response registered in the laboratory, clearly overpredicting the observed stiffer stress-strain response. This is essentially a consequence

of the open primary yield surface formulation, which implies that no plasticity is predicted under stress paths characterised by a constant stress ratio (as it is the present case). Therefore, the predicted volumetric strains (and, consequently, changes in void ratio) are solely of elastic nature. Moreover, since the stress ratio is kept constant (and equal to zero, in this type of tests), the quantity χ_{ref}^{f} (Equation 4.21) remains null throughout the calculation. Consequently, the scalar reduction factor, T (Equation 4.20) remains equal to 1.0 during the entire simulation, meaning that no reduction of the tangent shear modulus occurs (i.e. it retains its maximum value, $G_{tan} = G_{max}$). Furthermore, since a constant Poisson's ratio, ν, is assumed in the present constitutive model, no reduction of the tangent bulk modulus occurs (i.e. $K_{tan} = K_{max}$ during the entire simulation). As suggested by Taborda (2011), one of the following three different approaches might be adopted to improve this aspect: (1) replacement of the current shape of the primary yield surface by a closed shape, as, for instance, included in the BSPM proposed by Taiebat and Dafalias (2008); (2) introduction of an additional yield surface which closes the current yield surface for large values of mean effective stress, as originally proposed by Vermeer (1978) and included in the BSPM developed by Li (2002) and Gao and Zhao (2015); (3) introduction of a nonlinear reduction of the tangent bulk modulus with volumetric strain, as proposed by Jardine *et al.* (1986).

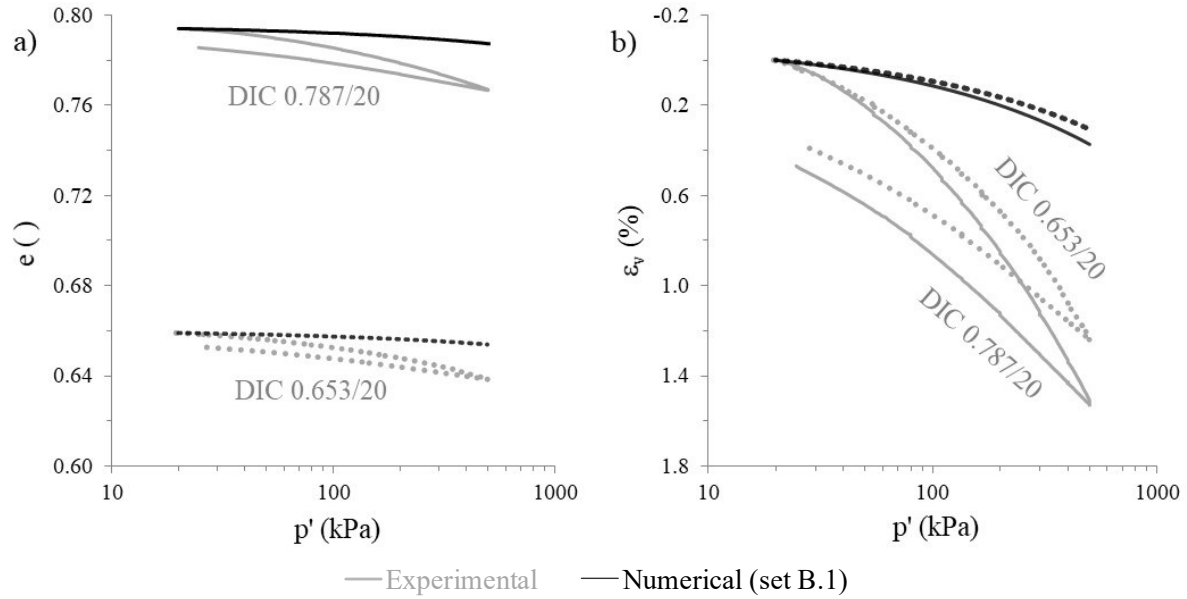

Figure 7.13 – Numerical simulation of ICDIC tests performed on a loose and on a dense sample: evolutions of (a) void ratio and of (b) volumetric strain with mean effective stress.

7.2.1.4.2 Drained monotonic triaxial compression and extension

To gain further insight into the ability of the model to capture the influence of the stress path on the monotonic response of Hostun sand, Figure 7.14 compares the results of isotropically consolidated drained monotonic triaxial compression tests with increasing and decreasing mean stress (ICDMTC p↑ and ICDMTC p↓ tests, respectively) performed on samples consolidated to $p'_0 = 80$ kPa. For reference, the experimental results are also depicted in the

figure. It can be seen that, in general, a satisfactory agreement between numerical and experimental data was obtained, especially in terms of volumetric response. As pointed out before, a plausible explanation for the slightly underestimation of the modelled peak strengths in relation to those measured in the laboratory resides on a greater importance given to the deformation pattern during calibration of the plastic hardening modulus (Section 6.10), rather than to the stress-strain response.

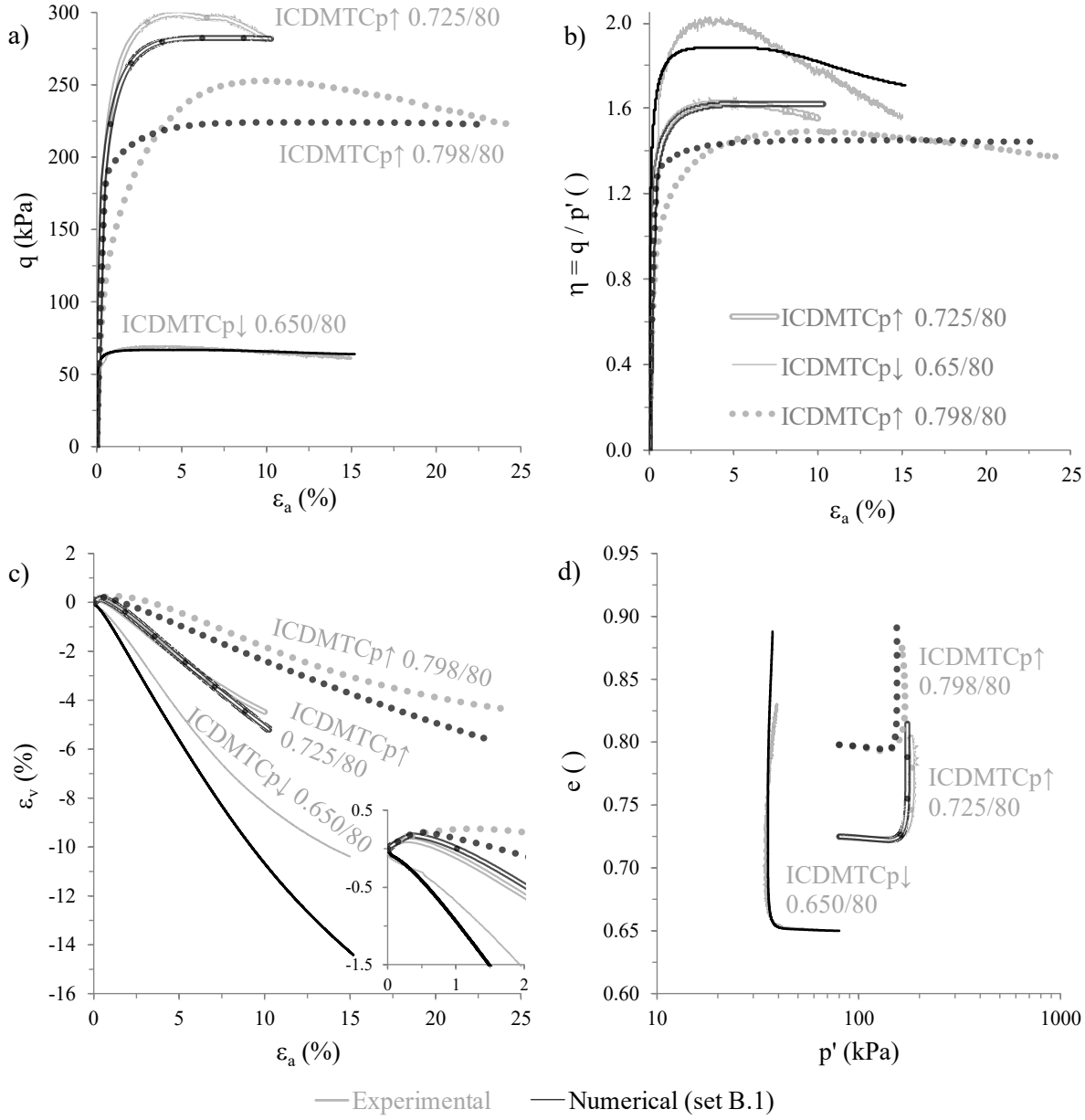

Figure 7.14 – Influence of the stress path on the numerical simulation of ICDMTC p↑ and ICDMTC p↓ tests: (a) stress-strain response, (b) stress ratio evolution with axial strain, (c) volumetric strain evolution with axial strain and (d) void ratio evolution with mean effective stress.

In addition, Figure 7.15 compares the results of isotropically consolidated drained monotonic triaxial extension tests with decreasing and increasing mean stress (ICDMTE p↓ and ICDMTE p↑ tests, respectively) performed on moderately loose samples consolidated to

$p'_0 = 80$ kPa, with those obtained in a ICDMTC p↑ test performed on a sample prepared to a similar void ratio and consolidated under the same mean effective stress. Note that, to allow for a direct comparison between the results of triaxial compression (TC) and triaxial extension (TE) tests, the deviatoric stress in TE is taken, in this case, as positive.

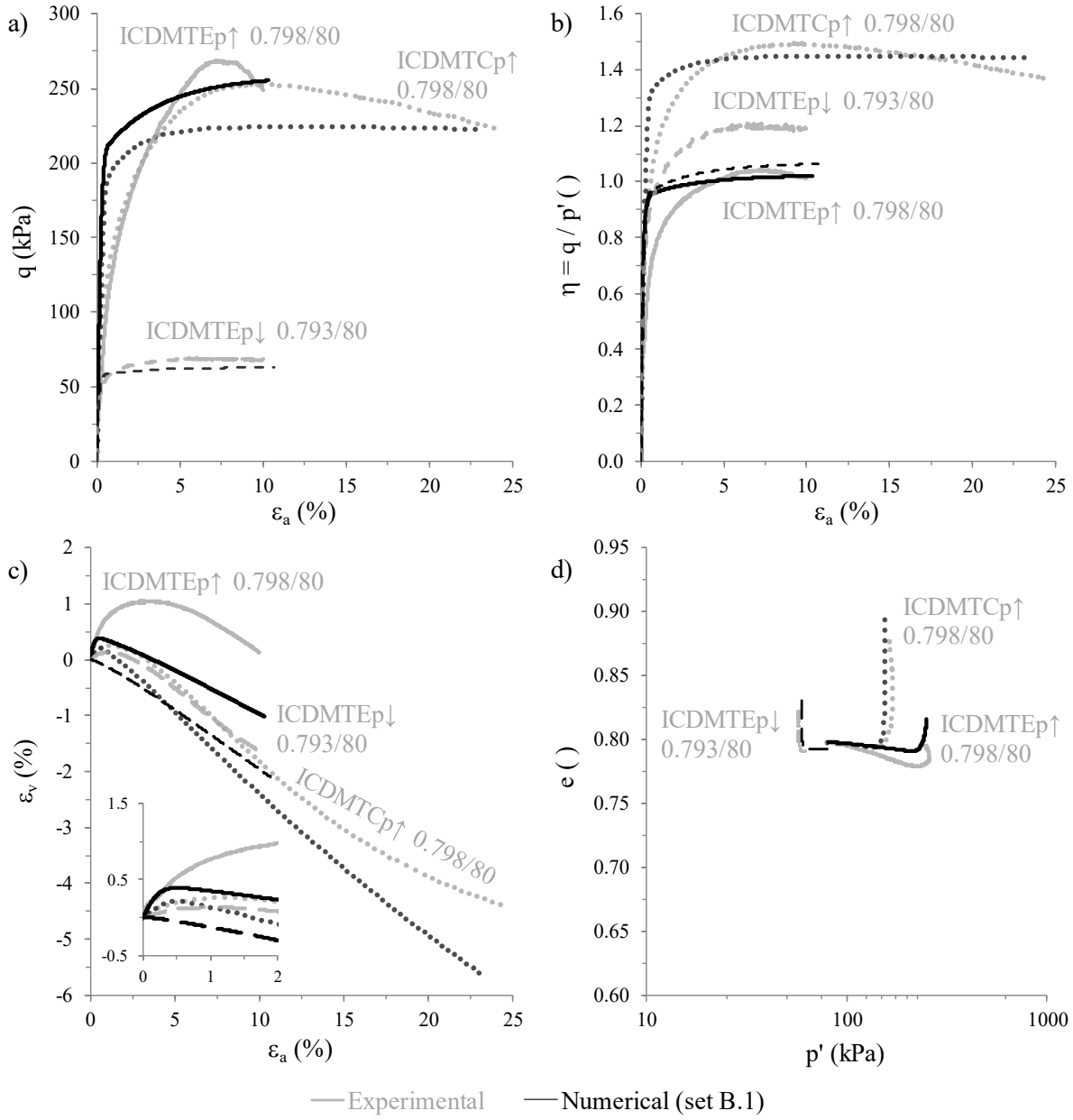

Figure 7.15 – Influence of the stress path on the numerical simulation of ICDMTC↑, ICDMTE↑ and ICDMTE↓ tests performed on moderately loose samples consolidated to p'_0 = 80 kPa: (a) stress-strain response, (b) stress ratio evolution with axial strain, (c) volumetric strain evolution with axial strain and (d) void ratio evolution with mean effective stress.

Once again, it can be seen that a considerably stiffer stress-strain response is predicted for the earlier stages of loading, mainly due to the detrimental effect of the shearing-induced fabric component on the modelled monotonic response. Nevertheless, the general trends observed in these laboratory tests, such as similar deviatoric stresses at medium to large strains in tests ICDMTC p↑ 0.798/80 and ICDMTE p↑ 0.798/80 (characterised by the

increase in mean stress during loading), appear to be captured by the constitutive model. The ability of the constitutive model to simulate triaxial extension is discussed in more detail in Section 7.3.2.

7.2.1.4.3 Undrained monotonic triaxial compression and extension

Figure 7.16 compares the results obtained in one undrained monotonic triaxial compression test with increasing mean stress (namely, test ICUMTC p↑ 0.686/25) with those obtained in one monotonic triaxial extension test with decreasing mean stress (namely, test ICUMTE p↓ 0.658/25). Note that both tests were performed on dense samples isotropically consolidated to a mean effective stress, p'_0, of 25 kPa. Note also that, to ease the comparison between the results obtained in TC and TE, the deviatoric stress in TE is taken as positive.

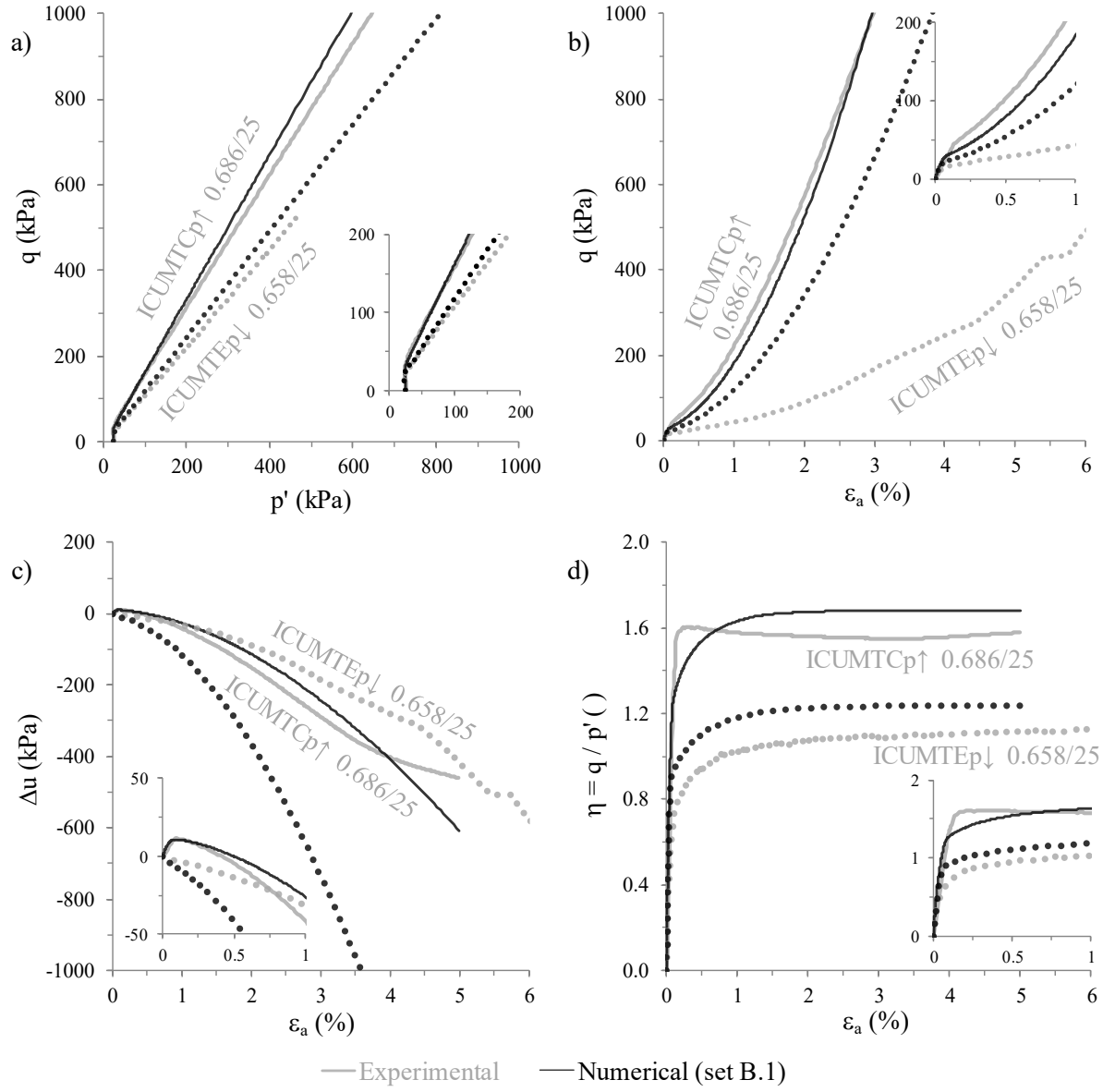

Figure 7.16 – Influence of the stress path on the numerical simulation of ICUMTC p↑ and ICUMTE p↓ tests performed on dense samples consolidated to p'_0 = 25 kPa: (a) effective stress path, (b) stress-strain response, (c) excess pore water pressure evolution with axial strain and (d) stress ratio evolution with axial strain.

It is interesting to observe that the constitutive model is able to reproduce satisfactorily important aspects of the response of sand observed in the laboratory, such as the significantly smaller stress ratio mobilised in TE (Figure 7.16d), which results in a less inclined effective stress path under such loading conditions (Figure 7.16a). The numerical results are, however, less satisfactory in terms of stress-strain response (Figure 7.16b) and evolution of excess pore water pressure with axial strain (Figure 7.16c) observed in test ICUMTE p↓ 0.658/25. In effect, although a softer stress-strain response is simulated in TE, in relation to that computed in TC, it is clearly overpredicted in relation to that measured in the laboratory. Consequently, the rate of negative excess pore water pressure accumulation with axial strain obtained in the TE test simulation is considerably higher than that observed in the experiment. Note that, by inducing a softer stress-strain response for loading conditions other than TC, the activation of the inherent fabric anisotropy component is expected to improve the response obtained for TE. This topic is explored in Section 7.3.2.

Note that similar conclusions are obtained when comparing the results of other sets of ICUMTC p↑ and ICUMTE p↓ tests (such as those performed on samples consolidated to $p'_0 = 80$ kPa). For brevity, the results obtained in these simulations are not compared here. Nevertheless, as noted before, these simulations are presented in Appendix A.

7.2.1.5 Influence of the type of consolidation

Figure 7.17 compares the experimental and numerical results of three drained monotonic triaxial compression tests with decreasing mean stress (DMTC p↓ tests). In two of these tests, a moderately loose and a dense sample were anisotropically consolidated (K0C) to an effective stress state characterised by radial and axial effective stresses of 60 kPa and 120 kPa, respectively, which correspond to a mean effective stress of 80 kPa and a deviatoric stress of 60 kPa under triaxial loading conditions (Table 7.1). In the remaining test, a dense sample was isotropically consolidated (IC) to an effective stress state characterised by a mean effective stress of 80 kPa, implying a null deviatoric stress at consolidation. It can be seen that, overall, a satisfactory agreement between both sets of data was achieved. Indeed, the constitutive model appears to be able to capture important aspects of the response, such as the similar stress ratio evolutions with axial strain, as well as similar volumetric strain responses observed for tests ICDMTC p↓ 0.650/80 and K0DMTC p↓ 0.672/80, where dense samples were subjected to different types of consolidation (isotropic and anisotropic, respectively).

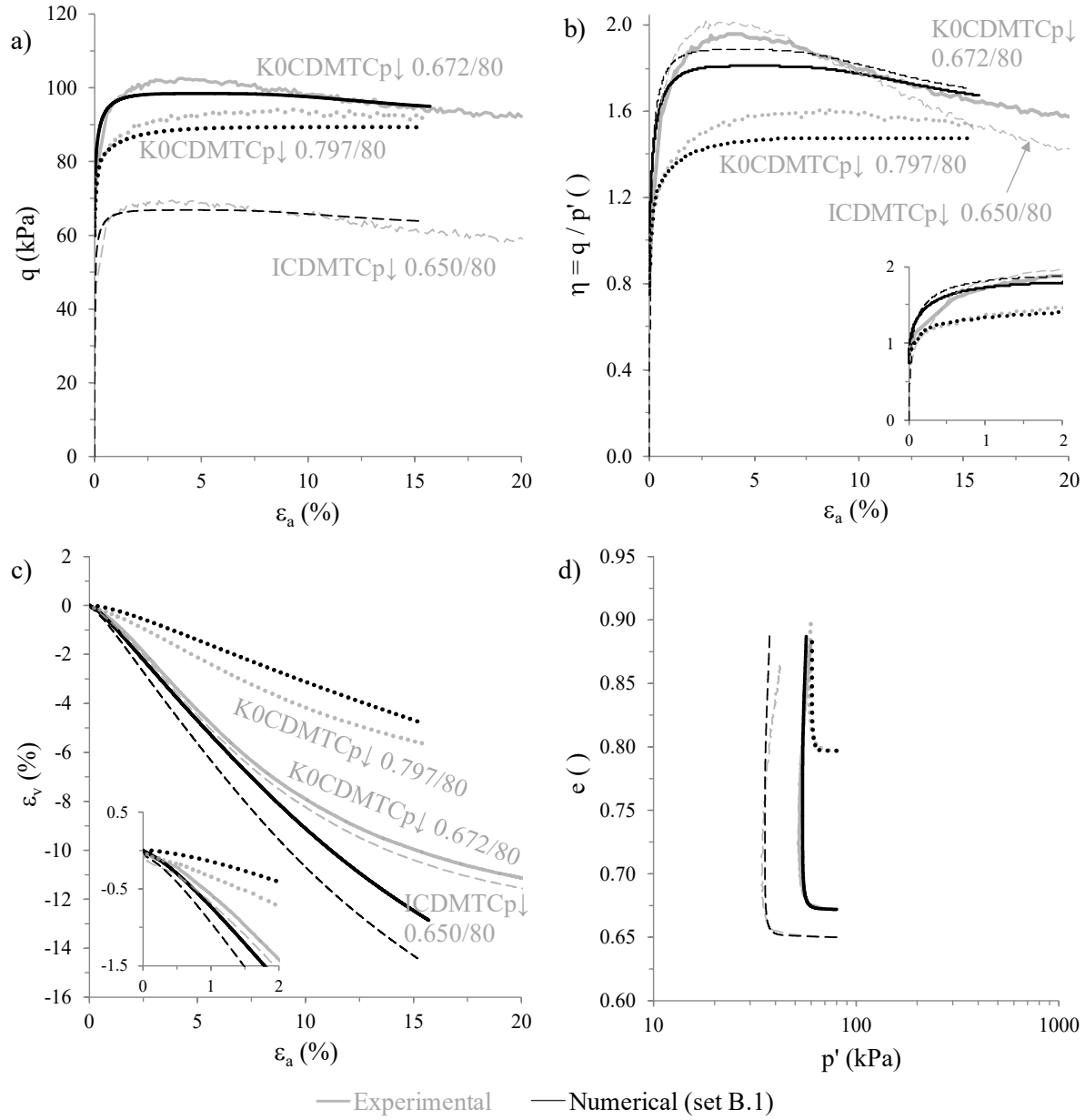

Figure 7.17 – Influence of the type of consolidation on the numerical simulation of DMTC p↓ tests: (a) stress-strain response, (b) volumetric strain evolution with axial strain, (c) volumetric strain evolution with axial strain and (d) void ratio evolution with mean effective stress.

7.2.2 Cyclic response

7.2.2.1 Aspects analysed

The ability of the BSPM to replicate important aspects of cyclic response of Hostun sand is explored in the following sections. Specifically, after performing an overall assessment of the ability of the model to replicate the effective stress path, excess pore water pressure evolution with the number of loading cycles and stress-strain response registered in the undrained cyclic triaxial (UCT) tests, the ability of the constitutive model to replicate the undrained cyclic resistance of Hostun sand, evolutions of both secant shear modulus and damping ratio with cyclic loading, as well as main trends of excess pore water pressure build-

up with the number of loading cycles observed in the laboratory is examined. Note that, since very large deformations are typically observed from the moment that cyclic mobility, as well as other liquefaction-related phenomena are triggered, capable of causing extensive damage to buildings, bridges, pipelines and other critical infrastructure built on (or buried in) a given soil deposit, the ability of the model to predict accurately the undrained cyclic resistance of the material is of upmost importance. Regarding the evolution of the secant shear modulus with cyclic loading, it influences the velocity at which shear waves propagate within a given soil deposit and, therefore, its accurate prediction is crucial to the simulation of any geotechnical problem involving shear wave propagation, such as blasting, machine vibration, pile driving and earthquake-induced loading (Kramer, 1996; Taborda *et al.*, 2016). With respect to the damping ratio, it measures the energy dissipated by the soil through hysteresis and, thus, has a strong impact on the prediction of the amplitude of deformations induced in the soil during the propagation of the shear waves. In terms of excess pore water pressure build-up with the number of loading cycles, the comparison between the response predicted by the constitutive model and that measured in the laboratory provides fundamental insight into the ability of the model to predict the severe reduction in effective stresses typically observed in very rapid phenomena (such as those involving liquefaction), which are known to impact both stiffness and strength of the material.

Lastly, the ability of the constitutive model to reproduce the volumetric strains observed in drained cyclic triaxial tests is investigated. As mentioned by Kramer (1996) and Taborda (2011), this may provide an indication about the ability of the constitutive model to predict surface settlements, which may affect structures supported by shallow foundations, as well as lifelines located at shallow depths.

7.2.2.2 Available data

Table 7.2 summarises the designation and initial conditions of the fifteen cyclic triaxial tests performed on Hostun sand, including thirteen isotropically consolidated undrained cyclic triaxial (ICUCT) tests, as well as one isotropically consolidated (IC) and one anisotropically consolidated (K0C) drained cyclic triaxial (ICDCT and K0CDCT, respectively) tests. It can be observed that the samples were prepared to very different void ratios (with e_0 ranging from 0.651 to 0.820), consolidated under three different mean effective stresses (namely, $p'_0 =$ 25, 80 and 135 kPa) and subjected to two-way symmetric deviatoric shear stress oscillations (i.e. similar deviatoric stress amplitude in triaxial compression and in triaxial extension), Δq. Under undrained conditions, the samples were tested until large strains and excess pore water pressures were measured in the test. Conversely, under drained conditions, tests were stopped when a given number of loading cycles, N, as indicated in the table, was reached.

Note that, while in this chapter the results of the numerical simulations of several different cyclic triaxial tests are presented together to provide an overall assessment of the

performance of the model, the results obtained in each simulation are individually presented in Appendix B.

Table 7.2 –Designation, initial sample's and loading conditions of the cyclic triaxial tests performed on Hostun sand.

Type of test	Designation [(§)]	e_0 ( )	p'_0 (kPa)	Δq (kPa)	ψ_0 ( )	$CSR = \lvert\Delta q\rvert/(2\,p'_0)$ ( )	N ( )
Undrained cyclic triaxial (UCT)	ICUCT 0.821/25/13	0.821	25.0	±13.0	-0.136	0.260	[(†)]
	ICUCT 0.777/25/18	0.777	25.0	±18.0	-0.181	0.360	[(†)]
	ICUCT 0.771/80/32	0.771	80.0	±32.0	-0.165	0.200	[(†)]
	ICUCT 0.803/80/36	0.803	80.0	±36.0	-0.133	0.225	[(†)]
	ICUCT 0.832/80/42	0.832	80.0	±42.0	-0.104	0.263	[(†)]
	ICUCT 0.804/80/48	0.804	80.0	±48.0	-0.132	0.300	[(†)]
	ICUCT 0.773/80/56	0.773	80.0	±56.0	-0.162	0.350	[(†)]
	ICUCT 0.805/135/40	0.805	135.0	±40.0	-0.117	0.148	[(†)]
	ICUCT 0.830/135/54	0.830	135.0	±54.0	-0.092	0.200	[(†)]
	ICUCT 0.793/135/67.5	0.793	135.0	±67.5	-0.129	0.250	[(†)]
	ICUCT 0.651/80/43	0.651	80.0	±43.0	-0.299	0.269	[(†)]
	ICUCT 0.652/80/72	0.652	80.0	±72.0	-0.285	0.450	[(†)]
	ICUCT 0.652/80/88	0.652	80.0	±88.0	-0.284	0.550	[(†)]
Drained cyclic triaxial (DCT)	K0CDCT 0.811/80/30	0.811	80.0 [(‡)]	±30.0	-0.125	–	10
	ICDCT 0.820/135/81	0.820	135.0	±81.0	-0.102	–	10

[(§)] The designation identifies: (1) type of consolidation: IC for isotropic consolidation; (2) type of drainage: D or U for drained or undrained test, respectively; (3) type of loading: CT for cyclic triaxial; (4) void ratio immediately after consolidation; and (5) mean effective stress immediately after consolidation; (6) deviatoric stress oscillation applied in the test: $|\Delta q|$.

[(†)] The undrained cyclic triaxial tests were stopped when large strains were observed (typically, for moderately loose samples, the accumulation of double amplitude axial strain of 5% was used as criterion to stop the test).

[(‡)] In this test, the sample was subjected to anisotropic consolidation, with the axial and radial effective stresses at consolidation being 120 and 60 kPa, respectively.

7.2.2.3 Overview of the undrained cyclic triaxial test results

Figure 7.18 compares the numerical and experimental results obtained for two isotropically consolidated undrained cyclic triaxial (ICUCT) tests performed on samples prepared to similar void ratios and consolidated under the same isotropic confining stress of 80 kPa, while subjected to different deviatoric stress oscillation, Δq. In particular, $\Delta q = \pm 32$ kPa was applied in test ICUCT 0.771/80/32, while a larger value of $\Delta q = \pm 42$ kPa was imposed in test ICUCT 0.832/80/42. It can be observed that both tests are very satisfactorily reproduced by the constitutive model. This can be considered remarkable, given the very different responses observed in these two tests, particularly in terms of number of loading cycles required to the onset of cyclic mobility. Perhaps unsurprisingly due to its key role in the calibration of the model parameters related to the shearing-induced fabric component, the agreement between numerical and experimental data in terms of this aspect of the response is slightly better for test ICUCT 0.830/80/42.

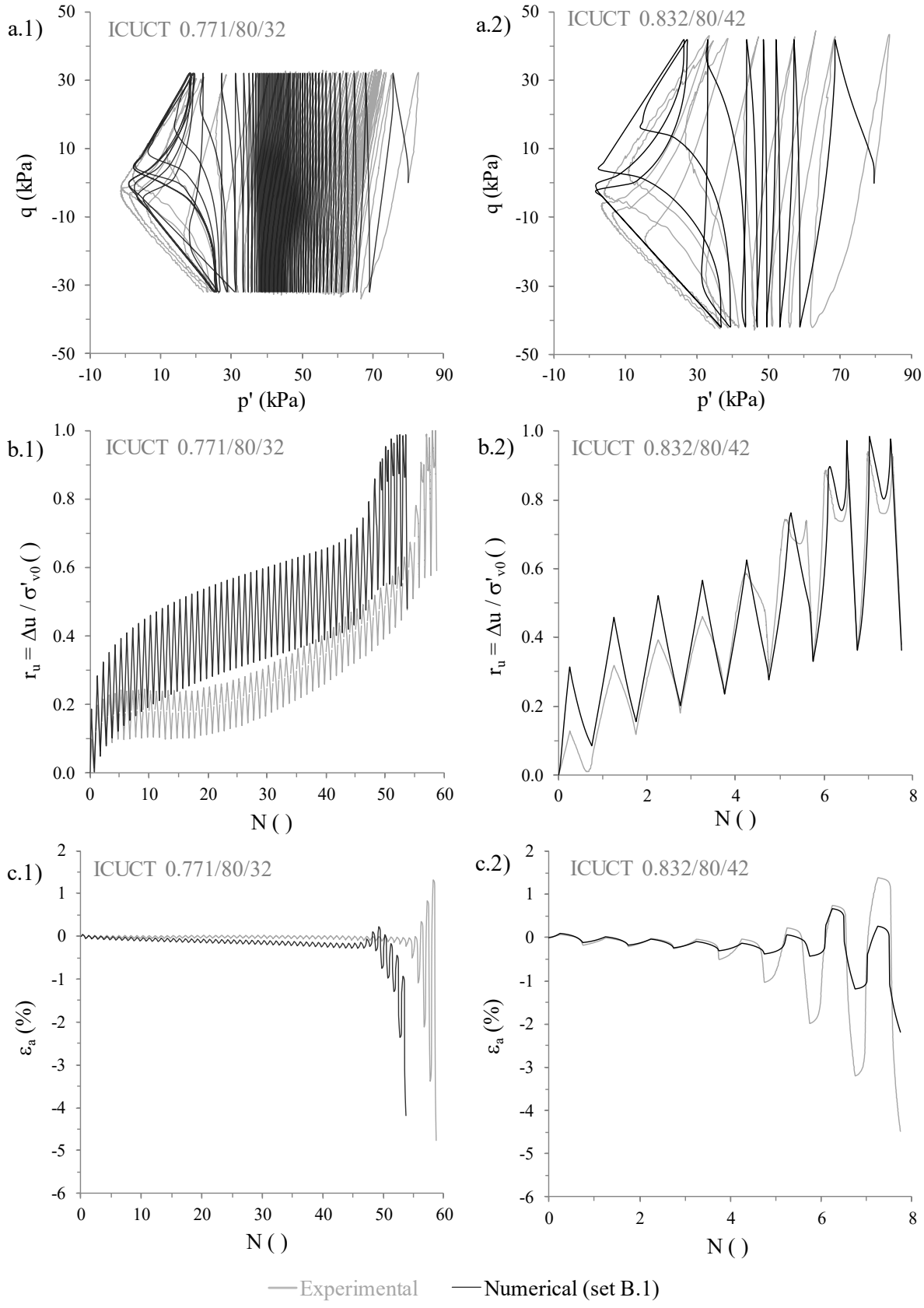

Figure 7.18 – Numerical simulation of tests ICUCT 0.771/80/32 and ICUCT 0.832/80/42: (a) effective stress path, (b) excess pore water pressure ratio build-up and (c) axial strain evolution with the number of loading cycles.

Indeed, the constitutive model seems able to capture important features of the cyclic response of sand observed in the laboratory tests, such as the stiffening of the response after the first loading cycle, as well as the significant increase in excess pore water pressure and axial strain after the first crossing of the phase transformation line and subsequent reversal of the stress path. One aspect of the cyclic response of sand that seems to be less accurately replicated by the constitutive model consists of the rate of accumulation of axial strain under very low effective stresses. This aspect is more clearly illustrated in Figure 7.19, which depicts the evolution of double amplitude axial strain, $\varepsilon_{a,da}$, with the number of loading cycles, N, for these two tests. Particularly for test ICUCT 0.832/80/42, it is apparent that the rate of accumulation of $\varepsilon_{a,da}$ with N is underpredicted in the numerical analysis (particularly evident when comparing the increase in $\varepsilon_{a,da}$ obtained during the last loading cycle). Among other possibilities, the slight increase of the value assigned to the model parameter γ, scaling the effect of the void ratio on the plastic multiplier h_e (Equation 4.60), would likely improve this aspect of the modelled response. Note, however, that this would likely result in a worse prediction of the monotonic response of loose Hostun sand observed in UMTC p↑ and DMTC p↑ tests, as discussed in Section 6.11.

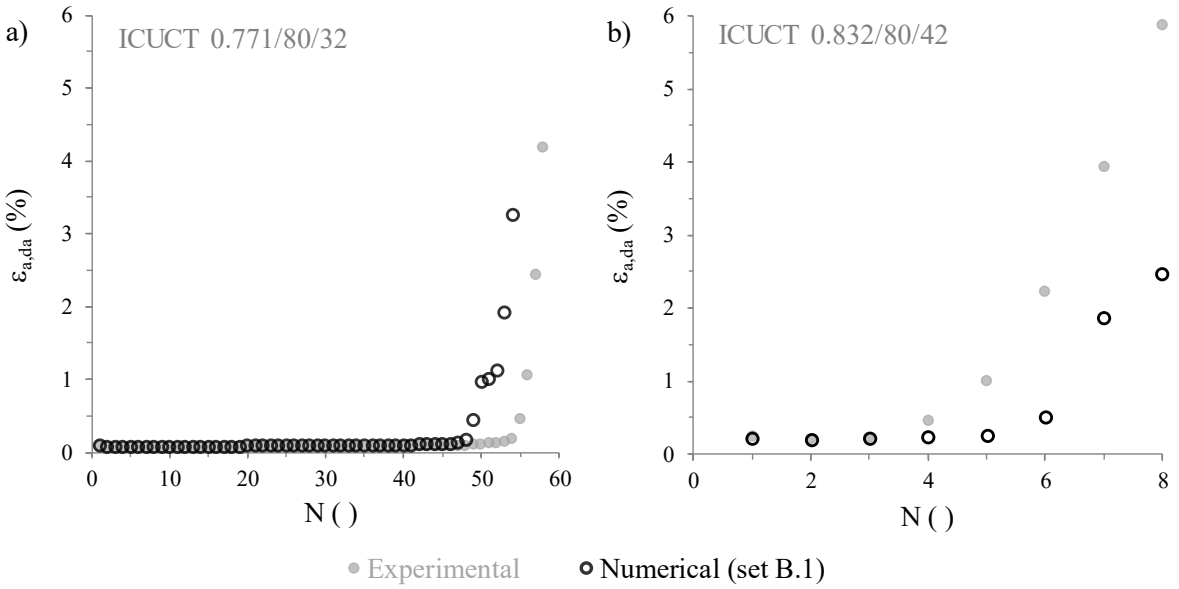

Figure 7.19 – Double amplitude axial strain evolution with the number of loading cycles registered for tests: (a) ICUCT 0.771/80/32 and (b) ICUCT 0.832/80/42.

As anticipated during the calibration process (Chapter 6), a much less satisfactory agreement between numerical and experimental data is obtained when simulating tests ICUCT 0.804/80/48 and ICUCT 0.773/80/56. In these tests, large cyclic stress ratios were applied to the samples. As a result, samples exhibited a very soft response during the first loading cycle in triaxial extension, leading to the occurrence of cyclic mobility in very few loading cycles (two to four cycles). The comparison between numerical and experimental results obtained for test ICUCT 0.804/80/48 is provided in Figure 7.20. It is apparent that the constitutive model predicts a much larger number of loading cycles to reach low effective

stresses. Similar conclusions were obtained for test ICUCT 0.773/80/56, whose results are presented in Appendix B.

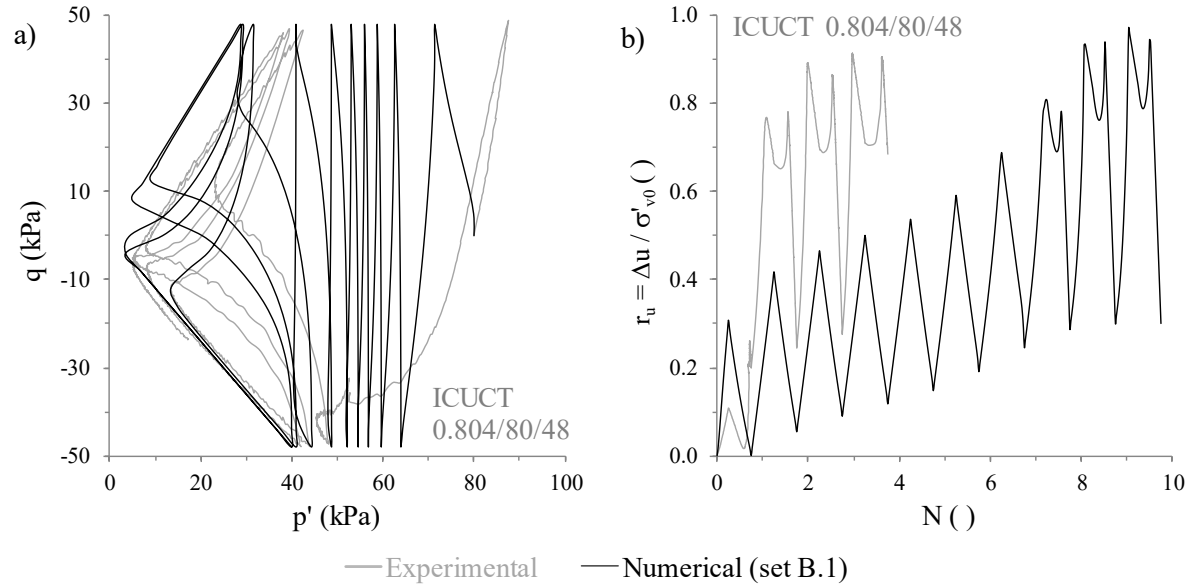

Figure 7.20 – Numerical simulation of test ICUCT 0.804/80/48: (a) effective stress path and (b) excess pore water pressure ratio build-up with the number of loading cycles.

In addition, Figure 7.21 compares the numerical and experimental results obtained for tests ICUCT 0.651/80/43 and ICUCT 0.652/80/88, both of them conducted on dense samples. It can be seen that the constitutive model underpredicts the rate of excess pore water pressure build-up with cyclic loading measured in the former test, particularly after the first twenty loading cycles. Consequently, the number of loading cycles required to reach large values of $r_u = \Delta u / \sigma'_{v,0}$ in the numerical analysis are overestimated in relation to those registered in the laboratory, with the accumulation of large axial strains also occurring later in the numerical simulation. With respect to test ICUCT 0.652/80/88, a much better agreement between numerical and experimental data was obtained, particularly in terms of excess pore water pressure generation with the number of loading cycles. In terms of axial strain accumulation with cyclic loading, it is apparent that the constitutive model tends to underpredict the measured response during the loading cycles preceding the onset of cyclic mobility (i.e. before reaching values of r_u close to unit). Nevertheless, as cyclic mobility is triggered, the magnitude of the computed axial strains seems to approach that measured in the laboratory.

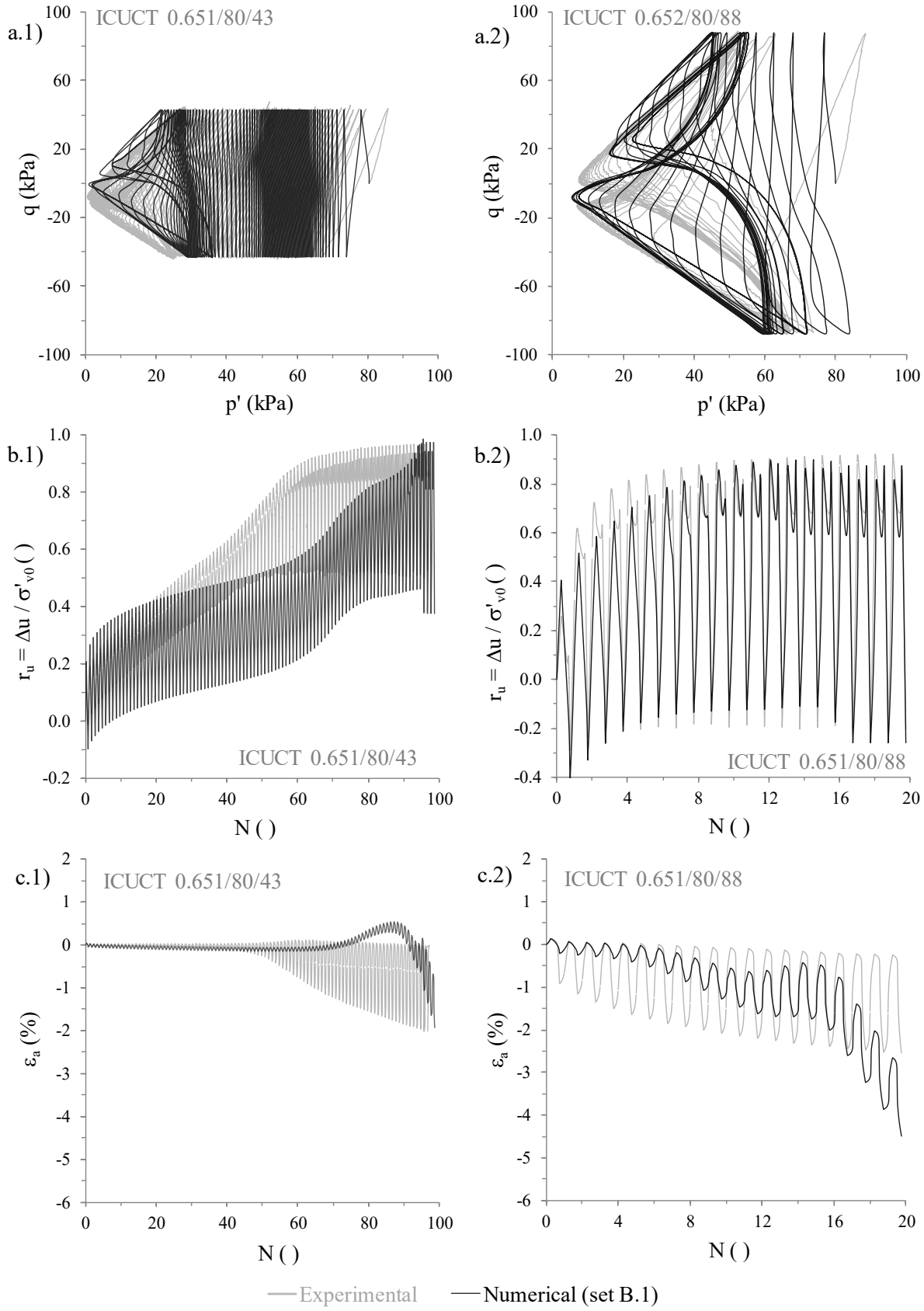

Figure 7.21 – Numerical simulation of tests ICUCT 0.651/80/43 and ICUCT 0.652/80/88: (a) effective stress path, (b) excess pore water pressure ratio build-up and (c) axial strain evolution with the number of loading cycles.

To get insight into the ability of the constitutive model to capture the cyclic response of Hostun sand when subjected to different initial confining stresses, the numerical results obtained for test ICUCT 0.777/25/18 are firstly compared with those obtained for test ICUCT 0.832/80/42 (Figure 7.22). The experimental results are also included in the figure for reference. Note that, in these laboratory tests, although the samples were consolidated under different isotropic effective stresses and subjected to different deviatoric stress amplitudes, similar responses were measured, particularly in terms of number of loading cycles required to the onset of cyclic mobility. Indeed, it is interesting to observe that the constitutive model is able to capture adequately this aspect, matching well the excess pore water pressure evolution with cyclic loading observed in both tests. As pointed out before, the aspect of the cyclic response that seems less satisfactorily reproduced in the numerical analysis consists of the smaller axial strain accumulation in relation to that measured in the laboratory, particularly when large excess pore water pressures are reached.

In addition, Figure 7.23 compares the numerical and experimental results obtained for tests ICUCT 0.771/80/32 and ICUCT 0.805/135/40. As observed for the previous pair of tests, similar responses were measured in both tests in the laboratory, despite the different consolidation stresses and deviatoric stress oscillations applied to the samples. It is apparent that, once more, an overall satisfactory agreement between experimental and numerical data was obtained, despite the slight overprediction of the rate of excess pore water pressure increase in test ICUCT 0.805/135/40, which is particularly evident for the early stages of loading.

Taking into account that a relatively wide range of void ratios and consolidation pressures were used in the laboratory tests, which resulted in very different cyclic responses, particularly in terms of number of loading cycles required to trigger cyclic mobility, it seems reasonable to conclude that the constitutive model shows an overall satisfactory performance. As mentioned before, the exception seems to consist of tests where samples exhibited a highly anisotropic response during the first loading cycle, with very few loading cycles being required to the onset of cyclic mobility (namely, tests ICUCT 0.804/80/48, ICUCT 0.773/80/56 and ICUCT 0.793/135/67.5).

In what follows, the ability of the constitutive model to simulate key aspects of the cyclic response of sand is further explored.

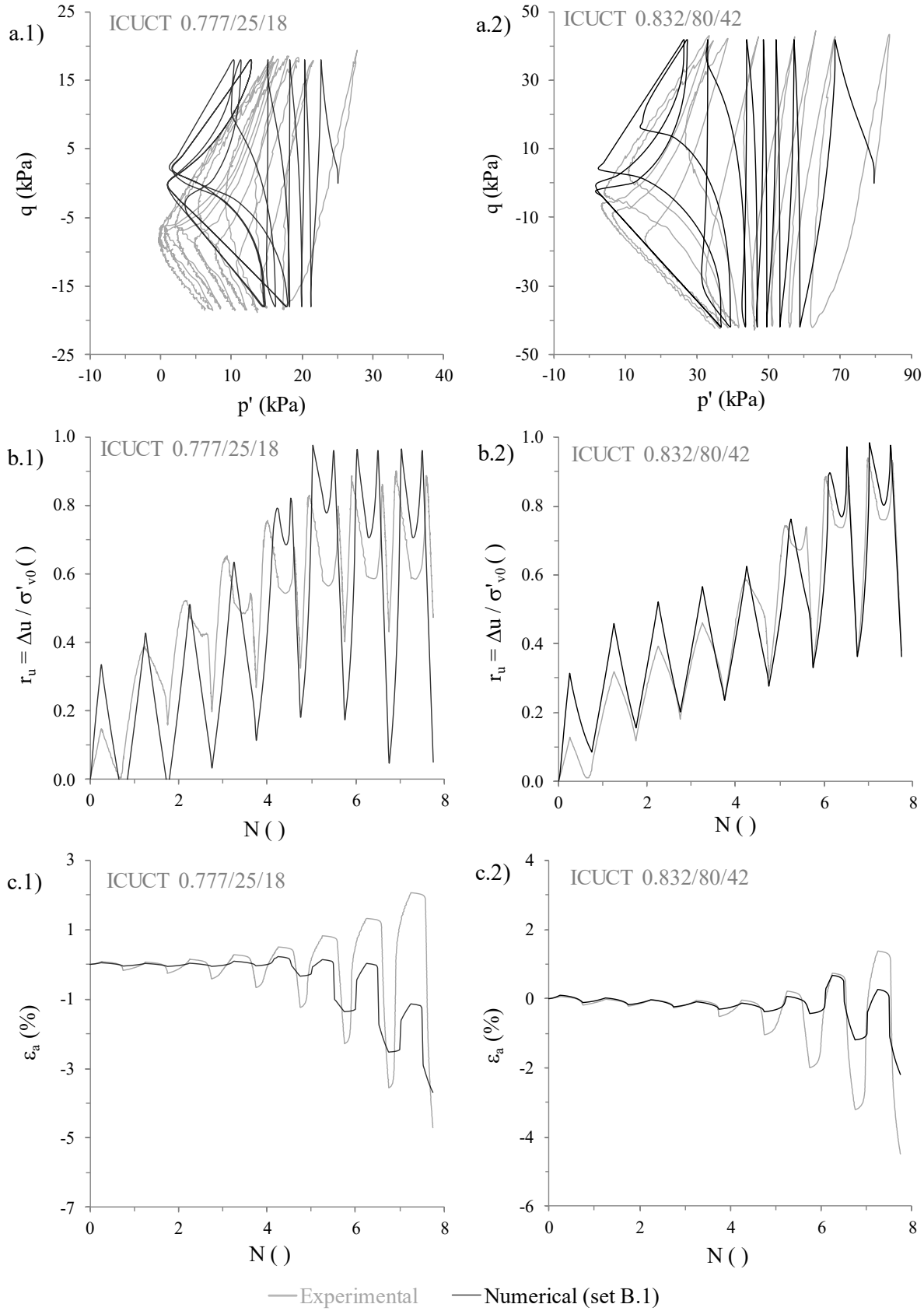

Figure 7.22 – Numerical simulation of tests ICUCT 0.777/25/18 and ICUCT 0.832/80/42: (a) effective stress path, (b) excess pore water pressure ratio build-up and (c) axial strain evolution with the number of loading cycles.

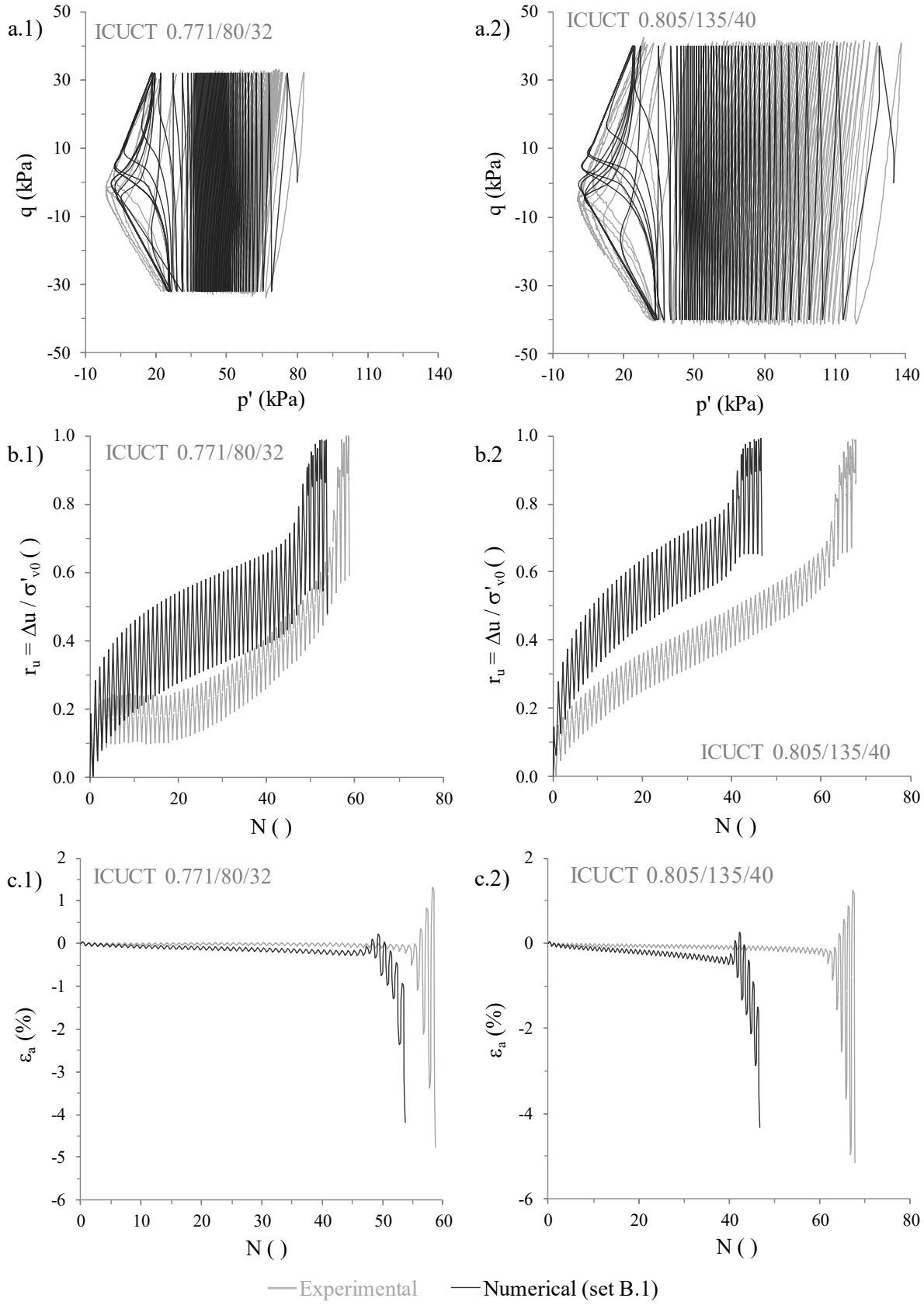

Figure 7.23 – Numerical simulation of tests ICUCT 0.771/80/32 and ICUCT 0.805/135/40: (a) effective stress path, (b) excess pore water pressure ratio build-up and (c) axial strain evolution with the number of loading cycles.

7.2.2.4 Undrained cyclic resistance

The choice to implement a Bounding Surface Plasticity Model (BSPM) was mainly justified by its greater ability to simulate liquefaction-related phenomena in comparison to simpler models available in the literature, such as cyclic non-linear models (as detailed, for example, in Taborda (2011)). Therefore, it is of upmost importance to evaluate its ability to predict the undrained cyclic resistance of sand, which has been commonly defined by the number of loading cycles of constant shear stress amplitude required to induce cyclic mobility, N_{liq}. With that purpose, a suitable criterion defining the onset of cyclic mobility is required. As discussed in Chapter 3, in the present study, the development of a residual (i.e. corresponding to a null deviatoric stress) excess pore water pressure ratio of $r_{u,res} = \Delta u_{res}/\sigma'_{v,0} = 0.95$ is adopted as the criterion to the onset of cyclic mobility. The application of this criterion is illustrated in Figure 7.24.

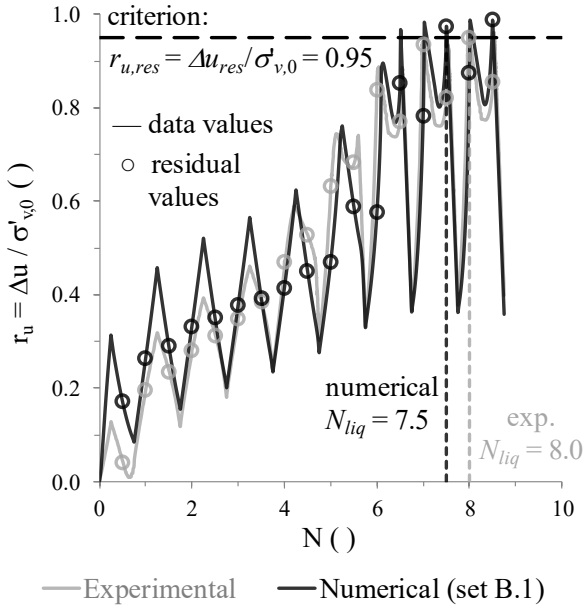

Figure 7.24 – Illustration of the application of the criterion adopted to define the onset of cyclic mobility based on the experimental and numerical results of test ICUCT 0.832/80/42.

Having clarified the cyclic mobility criterion to be used in the present study, it is also important to point out, as traditionally defined in the literature (e.g. Seed and Idriss, 1970a; Seed *et al.*, 1975; Idriss and Boulanger, 2006), the designation "cyclic resistance ratio" (CRR) is used to define the uniform cyclic stress ratio (CSR) causing liquefaction in a given number of loading cycles. Moreover, it is important to note that CSR is defined as (e.g. Ishihara, 1996):

$$CSR = \frac{|\Delta q|}{2\,p'_0} \tag{7.1}$$

where $|\Delta q|$ is the two-way symmetric deviatoric stress oscillation applied to the sample during the shearing phase and p'_0 is the mean effective stress at consolidation (see Table 7.2).

Figure 7.25 compares the undrained cyclic resistance obtained from the numerical and experimental results of all available ICUCT tests performed on both moderately loose samples (characterised by $e_0 \approx 0.771 - 0.832$, corresponding to $D_r \approx 50 - 70$ %) and dense samples (characterised by $e_0 = 0.651 - 0.652$, corresponding to $D_r \approx 102$ %) consolidated to $p'_0 = 80$ kPa. Note that both experimental and numerical results are described by power relationships of the form (e.g. Idriss and Boulanger, 2006):

$$CRR = a \ N_{liq}{}^{-b} \tag{7.2}$$

where a and b are material parameters. Note also that, as discussed in Chapter 3 and it is apparent in the figure, test ICUCT 0.652/80/72 is excluded from the analysis, since the $CRR - N_{liq}$ data point observed for this test has been found to plot far away from the trend described by the $CRR - N_{liq}$ data points observed for tests ICUCT 0.651/80/43 and ICUCT 0.652/80/72. It can be observed that, providing that the results obtained for tests ICUCT 0.804/80/48 and ICUCT 0.773/80/56 (where large CSRs were applied to the samples, inducing a very soft response in triaxial extension) are also excluded from the analysis, very similar undrained cyclic resistance curves are obtained from numerical and experimental data, with the agreement being particularly remarkable for moderately loose samples.

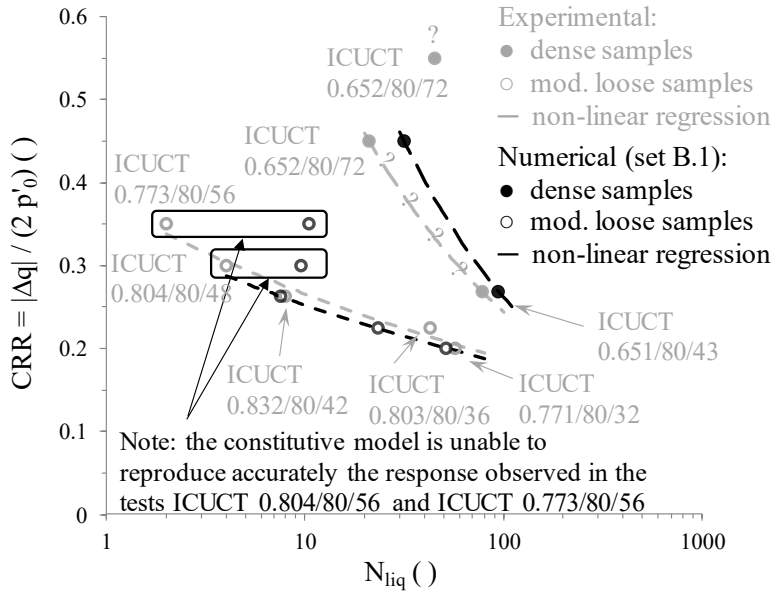

Figure 7.25 – Comparison between the undrained cyclic resistance of Hostun sand predicted by the original formulation of the constitutive model and that observed in the laboratory for ICUCT tests performed on moderately loose and dense samples consolidated under $p'_0 = 80$ kPa.

Additionally, Figure 7.26 compares the undrained cyclic resistance obtained from the experimental and numerical results of all available ICUCT tests performed on moderately loose samples (i.e. having $D_r \approx 50 - 70$ %) consolidated under three different isotropic confining stresses: 25, 80 and 135 kPa. Once again, it is apparent that the constitutive model is unable to reproduce adequately the $CRR - N_{liq}$ data observed for the test using the largest CSR from the analysis (i.e. test ICUCT 0.793/135/67.5). With respect to the remaining tests, it

can be observed that the constitutive model tends to underpredict the undrained cyclic resistance of Hostun sand, particularly for the two tests where samples were consolidated to $p'_0 = 135$ kPa (i.e. tests ICUCT 0.805/135/40 and ICUCT 0.830/135/54). Nevertheless, it is important to highlight that the constitutive model is able to capture qualitatively the effect of the mean effective stress at consolidation on the undrained cyclic resistance, with the two points corresponding to the tests performed on samples consolidated to $p'_0 = 25$ kPa (represented with triangles) and to $p'_0 = 135$ kPa (represented with squares) plotting, respectively, above and below the curve describing the predicted undrained cyclic resistance for $p'_0 = 80$ kPa, as observed in the laboratory.

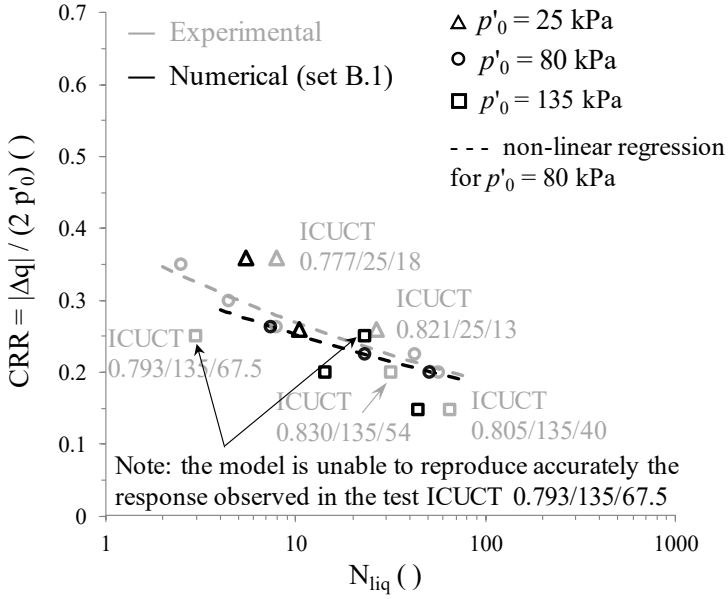

Figure 7.26 – Comparison between the undrained cyclic resistance of Hostun sand predicted by the original formulation of the constitutive model and that observed in the laboratory for ICUCT tests performed on moderately loose samples consolidated under $p'_0 =$ 25, 80 and 135 kPa.

Since the undrained cyclic resistance of Hostun sand was not explicitly considered during the calibration process, and taking into account the very wide undrained cyclic resistances observed in the laboratory (with samples requiring from two to seventy-eight loading cycles to the onset of cyclic mobility), it may be concluded that the constitutive model shows a very satisfactory ability to predict the undrained cyclic resistance of Hostun sand.

7.2.2.5 Normalised secant shear modulus and damping ratio evolutions with cyclic loading

Due to their importance to the interpretation and simulation of wave propagation phenomena, several laboratory apparatuses and techniques were developed to enable the characterisation of the evolutions of shear modulus and damping ratio with strain amplitude. In particular, within the very small to medium strain range, resonant column tests are commonly performed, while, for large strains, the evolution of both quantities are typically obtained from stress-strain curves measured in cyclic torsional shear, cyclic direct simple

shear or cyclic triaxial tests, in most cases, performed using constant cyclic strain amplitude loading conditions (i.e. imposing strain-controlled shear reversals).

Section 3.5.3.2 presents the detailed procedure adopted in the present research for determining the secant shear modulus, G_{sec}, normalised by the maximum (i.e. at very small strains) shear modulus, G_{max}, and damping ratio, ξ, based on stress-strain loops measured in undrained cyclic triaxial tests. It is important to note, however, that due to the fact that the shear reversals were controlled by a deviatoric stress condition in the conducted UCT tests, it is inappropriate to compare the evolutions of the normalised secant shear modulus, G_{sec} / G_{max}, obtained from modelled and measured stress-strain loops, in terms of strain amplitude. In effect, since peak deviatoric stresses are imposed in both laboratory experiments and corresponding numerical simulations, the evolutions of G_{sec} / G_{max} merely depict the differences in the strain amplitude associated with each cycle, meaning that a seemingly perfect match between the two datasets would arise, with points just shifted along a unique relationship. Clearly, this is not an obstacle when performing cyclic tests with strain-controlled shear reversals, since, in such case, for a given strain amplitude, the discrepancy in applied stress would be directly visible through the difference in G_{sec}. Given the above, in the present study, the number of loading cycles, N, normalised by the number of loading cycles required to the onset of cyclic mobility, N_{liq}, are used to compare the evolution of G_{sec} / G_{max} with cyclic loading obtained from experimental and numerical results. For consistency, the damping ratio, ξ, is also plotted as a function of N / N_{liq}, although, in this case, it would have been possible to compare its evolution as a function of strain amplitude (for example, as a function of single amplitude axial strain, $\varepsilon_{a,sa}$, as in Section 3.5.3.4). It should be clear, however, that the adoption of this strategy does not mean that it is believed that either G_{sec} / G_{max} or ξ are primarily a function of N / N_{liq}. In fact, it is well established that for sand both quantities are primarily a function of strain amplitude, while being only slightly affected by the number of loading cycles (Seed *et al.*, 1986; Vucetic and Dobry, 1991; Ishihara, 1996; Darendeli, 2001; Taborda, 2011). Naturally, in the present case, since UCT test data is used and, therefore, strain amplitude (among other factors) changes from cycle to cycle, both G_{sec} / G_{max} and ξ are observed to evolve indirectly with N / N_{liq}. Lastly, it is important to note that, as discussed in Chapter 3 and observed in other studies concerning the evaluation of damping ratio under undrained cyclic loading conditions (e.g. Matasović and Vucetic, 1993; Wang and Kuwano, 1999; Elgamal *et al.*, 2005), the value of ξ is observed to drop substantially during the later stages of the test. A detailed discussion on possible causes of this phenomenon is presented in Section 3.5.3.3.

Having defined the methodology employed in the present study, Figure 7.27 compares the evolutions of both G_{sec} / G_{max} and ξ with N / N_{liq} obtained from experimental and numerical results of tests ICUCT 0.771/80/32 and ICUCT 0.832/80/42. Note that, in these tests, moderately loose samples (i.e. having $D_r \approx 50 - 70$ %) were consolidated under an isotropic

confining stress of 80 kPa, though sheared under different deviatoric stress oscillations and, therefore, under different cyclic stress ratios (CSRs) – see Table 7.2.

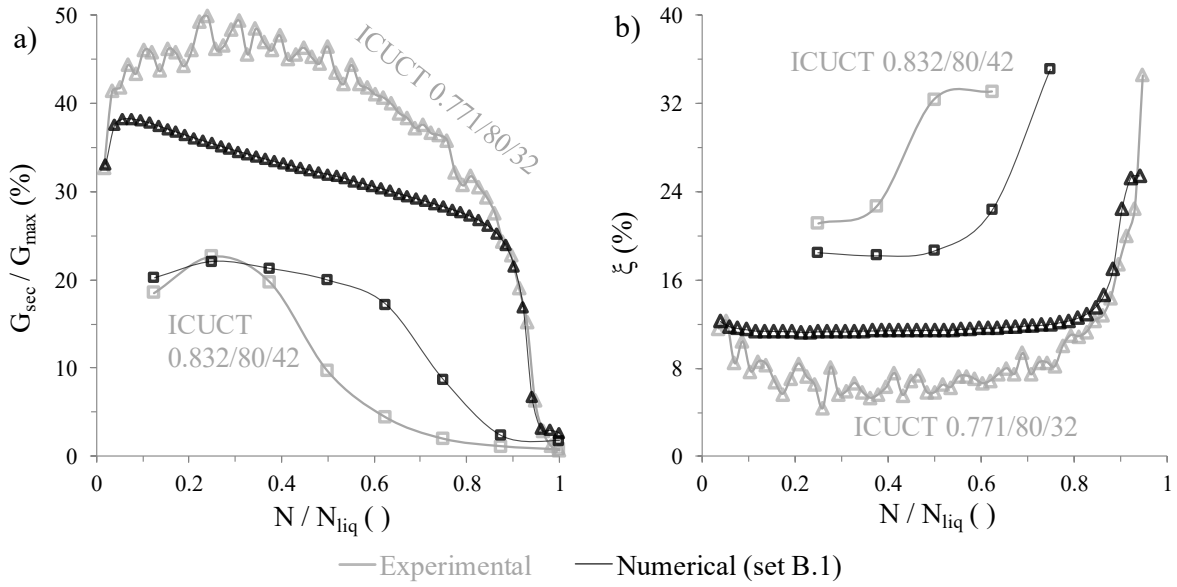

Figure 7.27 – Effect of the cyclic stress ratio on the (a) normalised secant shear modulus and (b) damping ratio evolutions with the normalised number of loading cycles obtained from experimental and numerical data.

Starting by inspecting the evolution of G_{sec} / G_{max} with N / N_{liq} (Figure 7.27a), it is apparent that the constitutive model is able to replicate qualitatively the main trends observed in the laboratory, including the slight increase in G_{sec} / G_{max} after the first loading cycle – a phenomenon typically observed when the effective stress path remains below the phase transformation line (PTL) and often termed as "stiffening unloading-reloading response" (Papadimitriou and Bouckovalas, 2002). Moreover, it can be observed that the constitutive model is able to reproduce the sharp reduction in G_{sec} / G_{max} once the PTL (which, as mentioned before, can be associated with the projection of the dilatancy surface in the $q - p'$ space) is crossed and the effective stress path is reversed. Nevertheless, it is apparent that, in the case of test ICUCT 0.832/80/42, the sharp reduction in G_{sec} / G_{max} occurs slightly later in the numerical analysis than observed in the experiment. This may suggest that the model parameter k_e^d, defining the position of the PTL in TE, may have been slightly overestimated during the calibration process (i.e. the PTL in TE should have been reached earlier in the numerical simulation). In fact, as discussed in Section 6.7.3, given the scatter in terms of stress ratio at phase transformation in TE, η_e^d, – state parameter at PT, ψ_e^d, data obtained from drained and undrained monotonic TE tests, it was necessary to adopt the simplification $k_e^d = k_c^d\ (M_e^c/M_c^c)$ proposed by Papadimitriou and Bouckovalas (2002) and often employed in the literature (e.g. Loukidis and Salgado, 2009; Taborda *et al.*, 2014). Although it would be possible to adjust slightly the value assigned to this model parameter to improve the simulation of this aspect of the response of Hostun sand, such methodology is considered

unnecessary at this point, particularly given the overall satisfactory reproductions obtained for these two tests (Figure 7.18).

In addition, it can be observed that, for test ICUCT 0.832/80/42, the reduction in G_{sec} / G_{max} with N / N_{liq} occurs faster in the numerical simulation (from $N/N_{liq} \approx 0.65$ to $N/N_{liq} \approx 0.85$) than observed in the experiment (from $N/N_{liq} \approx 0.4$ to $N/N_{liq} \approx 0.85$). As discussed in Section 6.11, it would be possible to improve the reproduction of this aspect of the response by reducing slightly the value assigned to the shearing-induced fabric index constant, H_0. Note, however, that such alteration would likely result in a less accurate replication of the evolution of G_{sec} / G_{max} during the preceding loading cycles, since H_0 affects not only the softening response after the crossing of the PTL and reversal of the effective stress path, but also the stiffening unloading-reloading response for effective stress paths below the PTL, as explained in detail in Section 4.2.4. This suggests that the shearing-induced fabric component of the constitutive model may require future improvement – a conclusion that will be reiterated during this chapter. In this case, the improvement of the formulation could consist of removing the dependency of the model parameter C (Equation 4.68) – which controls the rate of evolution of the deviatoric component of the shearing-induced fabric tensor, $\boldsymbol{f}$ (Equation 4.67) – on the maximum value ever registered by the isotropic component of the shearing-induced fabric tensor, f_p. In effect, this alteration would remove the interdependency between f_p and $\boldsymbol{f}$ and, therefore, allow for an independent control of the stiffening unloading-reloading response for effective stress paths below the PTL (which is controlled by f_p) and softening response after the crossing of the PTL and reversal of the effective stress path (which is controlled by $\boldsymbol{f}$).

In terms of ξ – N / N_{liq} curves (Figure 7.27b), the agreement between numerical and experimental results appears to be overall satisfactory, with both sets of data showing a sharp increase in ξ as the onset of cyclic mobility is approached. It is, nevertheless, apparent that the peak value of ξ is slightly overpredicted by the constitutive model for test ICUCT 0.832/80/42, while the opposite trend is observed for test ICUCT 0.771/80/32.

Further insight into the ability of the model to reproduce the evolutions of both G_{sec} / G_{max} and ξ with N / N_{liq} is provided in Figure 7.28, which compares the curves obtained from laboratory measurements and numerical analyses of tests ICUCT 0.832/80/42 and ICUCT 0.651/80/43. Note that, in these tests, samples prepared to different void ratios ($e =$ 0.832 and 0.651, respectively) were consolidated under the same effective stress state and sheared under a similar deviatoric stress oscillation (and, therefore, a similar CSR). It is apparent that the constitutive model is able to replicate the main trends observed in the laboratory, such as the occurrence of higher values of G_{sec} / G_{max} with N / N_{liq}, as well as smaller values of ξ with N / N_{liq} for the test conducted on the denser sample than for the test performed on the looser sample. As observed before, it seems that the sharp decrease of G_{sec} / G_{max} and concurrent sharp increase of ξ occur later (i.e. for higher values of N / N_{liq}) in

the numerical simulations than observed in the laboratory – an aspect that could be possibly improved by reducing slightly the value assigned to k_e^d, defining the position of the PTL in TE.

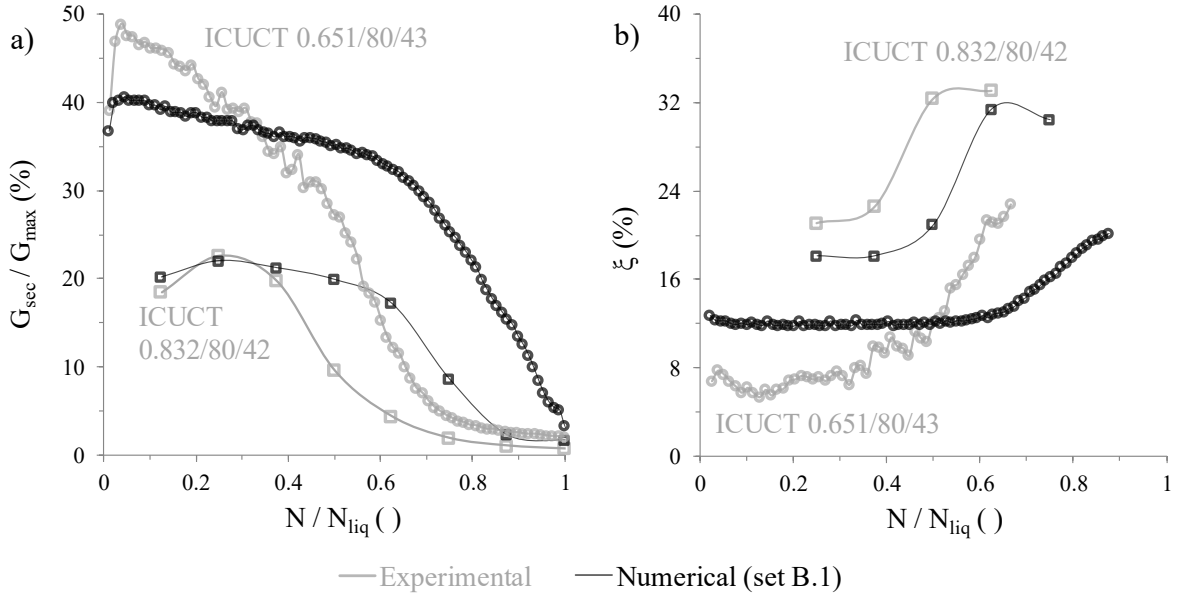

Figure 7.28 – Effect of the void ratio on the (a) normalised secant shear modulus and (b) damping ratio evolutions with the normalised number of loading cycles obtained from experimental and numerical results.

Lastly, Figure 7.29 compares the experimental and numerical results obtained for tests ICUCT 0.821/25/13 and ICUCT 0.832/80/42 conducted on samples prepared to similar void ratios, though consolidated under different mean effective stresses (25 and 80 kPa, respectively). Nevertheless, note that similar cyclic stress ratios were applied in both tests, namely: $CSR = 0.260$ for test ICUCT 0.821/25/13 and $CSR = 0.263$ for test ICUCT 0.832/80/42. It is interesting to observe that the sample consolidated under the smaller mean effective stress (i.e. subjected to test ICUCT 0.821/25/13) exhibited a consistently stiffer (in normalised terms) stress-strain response during cyclic loading than that observed in test ICUCT 0.832/80/42 (Figure 7.29a) – an aspect successfully captured by the constitutive model. This does not mean, however, that, for a given strain amplitude, larger values of G_{sec} / G_{max} would be obtained for test ICUCT 0.821/25/13 than for test ICUCT 0.832/80/42. In effect, as shown in Chapter 3, the opposite trend appears to be observed (i.e. the $G_{sec} / G_{max} - \varepsilon_{a,da}$ curve corresponding to test ICUCT 0.821/25/13 plots below that corresponding to test ICUCT 0.832/80/42). With respect to ξ (Figure 7.29b), the constitutive model seems to capture reasonably well the trends observed in the laboratory, although underpredicting slightly the peak value measured in test ICUCT 0.821/25/13.

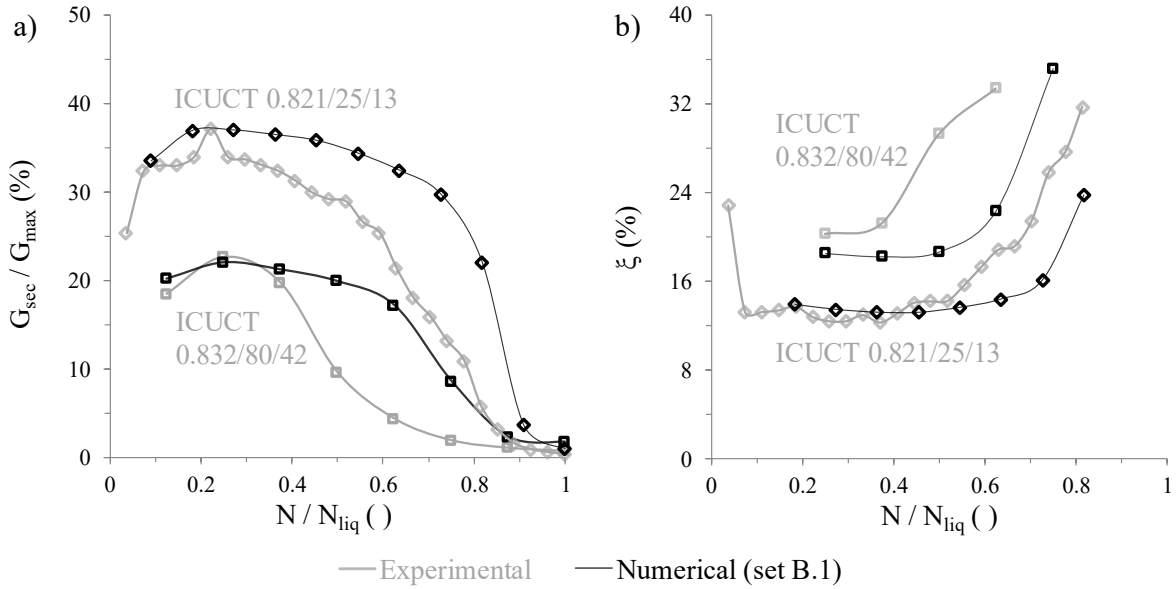

Figure 7.29 – Effect of the effective mean stress at consolidation on the (a) normalised secant shear modulus and (b) damping ratio evolutions with the normalised number of loading cycles obtained from experimental and numerical results.

7.2.2.6 Excess pore water pressure build-up with cyclic loading

The final aspect of the undrained cyclic response of Hostun sand to be investigated concerns the rate of the excess pore water pressure build-up with the number of loading cycles. This aspect is commonly studied by plotting the excess pore water pressure ratio, r_u, as a function of the ratio of the number of loading cycles to that required to the onset of cyclic mobility, N / N_{liq}, with several expressions being proposed in the literature, such as that given by Equation 7.3 (Seed *et al.*, 1975b).

$$r_u = \frac{1}{2} + \frac{1}{\pi} asin\left(2\left(\frac{N}{N_{liq}}\right)^{1/\alpha} - 1\right) \tag{7.3}$$

where α is a model parameter, for which a value of 0.70 was reported as appropriate to describe the average response measured in undrained cyclic triaxial and simple shear tests performed on Monterey sand by Seed *et al.* (1975b).

Following the strategy adopted in Chapter 3, rather than the excess pore water pressure ratio, r_u, the average values of the residual excess pore water pressure ratio, $r_{u,res,av}$, are employed in the present study. The computation of the values of this quantity is illustrated in Figure 7.30 for test ICUCT 0.832/80/42.

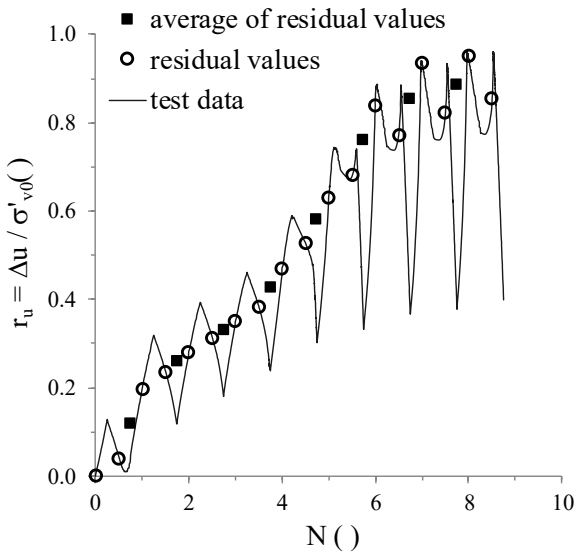

Figure 7.30 – Illustration of the computation of the average values of the residual excess pore water pressure ratio evolution with the number of loading cycles measured in test ICUCT 0.832/80/42.

Figure 7.31 compares the evolution of $r_{u,res,av}$ with N / N_{liq} obtained from numerical and experimental data of ICUCT tests performed on samples consolidated to $p'_0 = 80$ kPa. Note that, as a reference, the outcome of Seed *et al.* (1975b)'s proposal with $\alpha = 0.70$ is included in the figure. Starting with the curves obtained from experimental data, it is apparent that very different evolutions of $r_{u,res,av}$ with N / N_{liq} are obtained for the several tests, which do not seem accurately represented by Equation 7.3 (at least when employing a single value for α). As discussed in Chapter 3, among other factors, CSR seems to have a great impact: in general, and for a given relative density, the higher the CSR, the higher the rate of $r_{u,res,av}$ increase during the earlier stages of loading, with the opposite trend being observed for the later stages of loading. The influence of CSR on the curves obtained from numerical data seems more limited (i.e. numerical curves plot closer to each other). Since the reproduction of this aspect of the response of sand is largely controlled by the shearing-induced fabric component of the constitutive model, this suggests that further improvement of this component may be required in the future. As mentioned before, it may be beneficial to remove the dependency of the model parameter C (Equation 4.68) on the maximum value ever registered by the isotropic component of the shearing-induced fabric tensor, f_p, allowing for a more independent control of the modelled response before and after the crossing of the phase transformation line (and, therefore, additional flexibility).

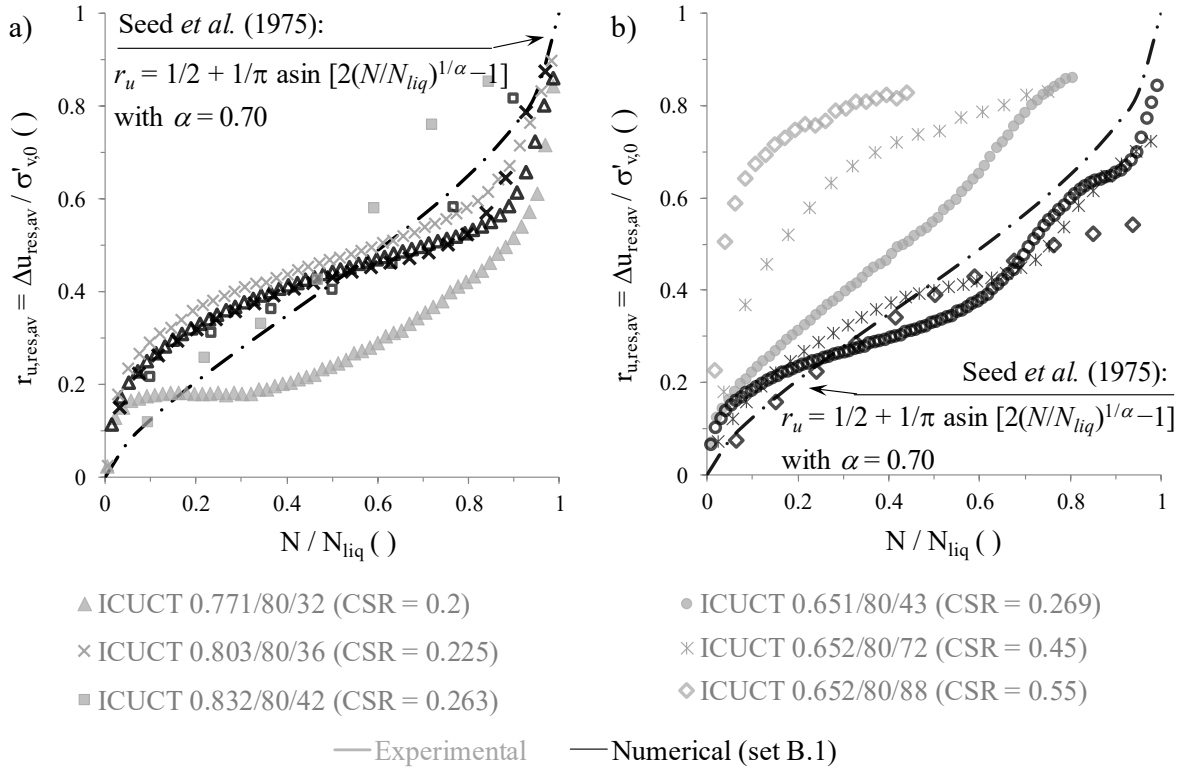

Figure 7.31 – Average residual excess pore water pressure ratio as a function of the normalised number of loading cycles obtained from experimental and numerical results of ICUCT tests performed on a) moderately loose samples and b) dense samples, in both cases consolidated to $p'_0 = 80$ kPa.

In addition, Figure 7.32 compares the results obtained from numerical and experimental data of ICUCT tests conducted on samples prepared to similar void ratios and consolidated to mean effective stresses of 25 and 135 kPa. Starting by analysing the sets of curves corresponding to $p'_0 = 25$ kPa (Figure 7.32a), it seems that, in general, the constitutive model underestimates the excess pore water pressure build-up rate for $N/N_{liq} \leq 0.80$ (which is particularly evident for test ICUCT 0.777/25/18), while the opposite trends appears to be observed for $N/N_{liq} > 0.80$. Once again, this appears to be a detrimental consequence of the interdependency of the evolutions of the isotropic and deviatoric components, f_p (Equation 4.66) and $\boldsymbol{f}$ (Equation 4.67), of the shearing-induced fabric tensor through the quantity C (Equation 4.68). More specifically, for samples consolidated under very low effective stresses, large values of H are, in general, required to simulate accurately the rate of excess pore water pressure build-up with loading observed in the laboratory tests. This means that f_p increases quickly with cyclic loading. Since C is given by the maximum absolute value ever registered by f_p (Equation 4.68), a quickly development of $\boldsymbol{f}$ is also registered once the phase transformation line is crossed, leading to a strong decrease of the plastic hardening modulus as the effective stress path is reversed and, consequently, to a very fast increase of excess pore water pressure. Probably, the introduction of a new formulation for C, independent of f_p, would improve the ability of the constitutive model to reproduce this aspect of the response of sand.

In relation to the samples consolidated to $p'_0 = 135$ kPa (Figure 7.32b), it can be observed that the constitutive model overestimates the excess pore water pressure build-up rate with the number of loading cycles for both tests. Nevertheless, it is apparent that the curves obtained from numerical and experimental data are qualitatively similar.

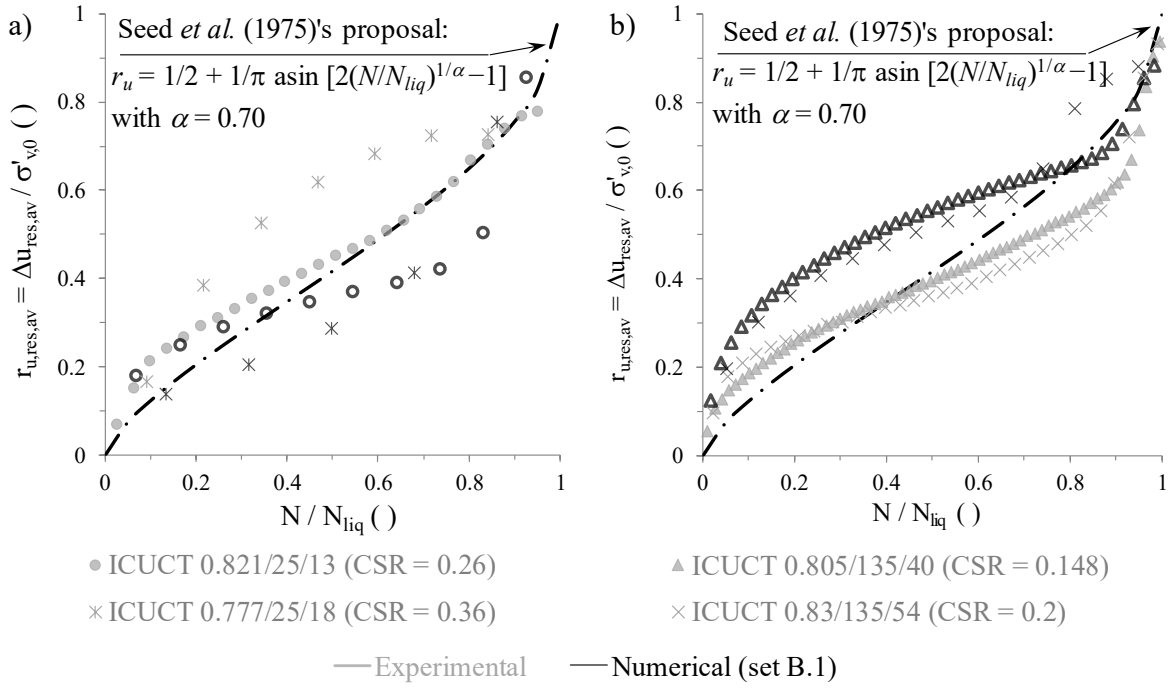

Figure 7.32 – Average residual excess pore water pressure ratio as a function of the normalised number of loading cycles obtained from experimental and numerical results of ICUCT tests performed on moderately loose samples consolidated under isotropic effective stresses of a) 25 kPa and b) 135 kPa.

7.2.2.7 Volumetric strains induced by cyclic loading

The ability of the constitutive model to predict volumetric strains induced by drained cyclic triaxial (DCT) loading was also investigated. As pointed out by Taborda (2011), this aspect is particularly important when assessing the performance of structures particularly sensitive to surface settlements, such as railways, highways, pipelines, historic buildings, among others.

Two DCT tests performed on moderately loose samples were simulated. In the first of these tests, termed as test K0DCT 0.811/80/30, the sample was anisotropically consolidated to an axial effective stress of $\sigma'_{a,0} = 120$ kPa and a radial effective stress of $\sigma'_{r,0} = 60$ kPa, corresponding to a mean effective stress of $p'_0 = 80$ kPa and to a deviatoric stress of $q_0 = 60$ kPa. The sample was subsequently subjected to 10 loading cycles having a deviatoric stress oscillation of $\Delta q = \pm 30$ kPa, by varying the axial stress from $\sigma'_a = 90$ kPa to $\sigma'_a = 150$ kPa and vice-versa. Conversely, in test ICDCT 0.820/135/81, the sample was isotropically consolidated to $\sigma'_{a,0} = \sigma'_{r,0} = \sigma'_0 = 135$ kPa and subjected to a larger deviatoric stress oscillation of $\Delta q = \pm 81$ kPa. The results obtained in the numerical simulations of these tests are compared with those registered in the laboratory in Figure 7.33.

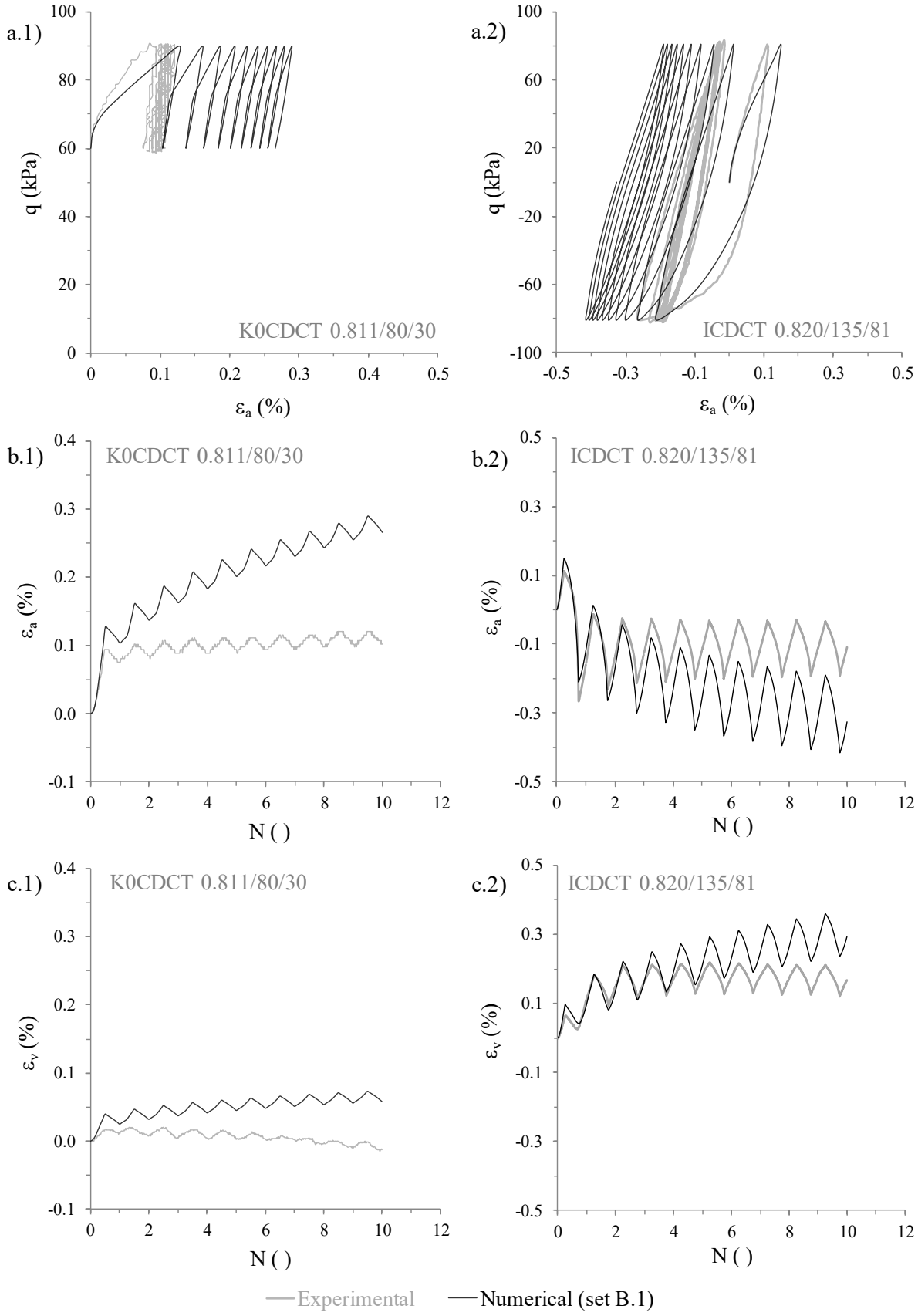

Figure 7.33 – Numerical simulation of tests K0CDCT 0.811/80/30 and ICDCT 0.820/135/81: (a) stress-strain response, (b) axial strain evolution with the number of loading cycles and (c) volumetric strain evolution with the number of loading cycles.

It can be observed that a satisfactory agreement between numerical and experimental data is obtained for the first three loading cycles of test ICDCT 0.820/135/81. However, as the number of loading cycles increase, the agreement between numerical and experimental data is less satisfactory, with the constitutive model overpredicting the axial and volumetric strain evolutions with loading. With respect to test K0DCT 0.811/80/30, it can be seen that the constitutive model tends to overpredict the measured response, both in terms of axial and volumetric strain accumulation with the number of loading cycles, particularly after the first loading cycle. Note that similar conclusions were obtained by Taborda (2011) when simulating isotropically consolidated drained simple shear tests. Nevertheless, according to this author, the ability of the constitutive model to predict volumetric strains observed in the laboratory tests seems to improve for higher strain levels – unfortunately, the available experimental data does not allow for the assessment of this aspect for Hostun sand.

7.3 Extended formulation of the constitutive model

7.3.1 General aspects

An inherent fabric anisotropy component was introduced into the constitutive relationship to improve its ability to replicate accurately the response of sand for loading conditions other than triaxial compression. In particular, as detailed in Section 4.3.3, when this component of the constitutive model is activated, the plastic hardening modulus depend on a scalar-valued anisotropic state parameter, A_F, which measures the interaction between the a second-order symmetric tensor $\boldsymbol{F_A}$, which describes the inherent fabric anisotropy of the material, with the direction of loading in the normalised deviatoric stress ratio plane $\boldsymbol{n}$. Therefore, the extended formulation of the model accounts for the effect of the inherent fabric anisotropy of the material on its response.

Since this component was added to the original formulation of the constitutive model proposed by Taborda *et al.* (2014), it was considered important to investigate whether the activation of this component allows for a better replication of the available experimental data. With that purpose, a new series of simulations of drained and undrained triaxial extension tests, as well as undrained cyclic triaxial tests were carried out using the set of model parameters “B.2) Dynamic – Extended formulation” (Table 6.5). The results obtained in these newly performed simulations are compared with those previously obtained when using the original formulation of the constitutive model (i.e. when using the set of parameters “B.1) Dynamic – Original formulation”). Once again, it is important to highlight that, since the ultimate objective of this thesis consists of assessing the ability of the constitutive relationship to replicate liquefaction-related phenomena observed in dynamic centrifuge experiments (presented in the following chapter), the responses obtained when using the sets of parameters optimised for the simulation of monotonic loading (i.e. sets of parameters belonging to the category “A) Static”) are not presented here. Note, however, that the results obtained when employing the set of parameters “A.2) Static – Extended formulation” to the

simulation of drained and undrained triaxial extension tests were already presented in the previous chapter, when calibrating the inherent fabric anisotropy component of the model (Section 6.12), leading to the conclusion that the modelled response is slightly improved when using the extended formulation (particularly in terms of stress-strain response within medium to large strain range).

The results of the simulations of the available monotonic triaxial extension tests are firstly presented (in Section 7.3.2), while the results of the simulations of the available cyclic triaxial tests are subsequently presented (in Section 7.3.3).

7.3.2 Monotonic triaxial extension test simulations

Figure 7.34 compares the outcome of the numerical simulations of the isotropically consolidated undrained monotonic triaxial extension tests with decreasing mean stress (ICUMTE p↓ tests) performed by using the original and extended constitutive relationships (i.e. by employing the sets of model parameters "B.1) Dynamic – Original formulation" and "B.2) Dynamic – Extended formulation", respectively). The experimental data is also depicted in the figure (in grey colour) for comparison purposes. It is apparent that the two sets of numerical data are very similar, suggesting that, at least when using these sets of model parameters, the inherent fabric anisotropy component has little impact on the modelled response. This is perhaps surprising, given that noticeable differences between results of simulations of these laboratory tests when employing the sets of model parameters belonging to the category "A.1) Static - Original formulation" (not considering inherent fabric anisotropy) and "A.2) Static - Extended formulation" (considering inherent fabric anisotropy) had been observed (see Section 6.12). Given that the main difference between sets of model parameters belonging to the categories "A) Static" and "B) Dynamic" consist of the activation of the shearing-induced fabric component (which introduced the effect of recent cyclic history on the modelled response), it is plausible that the shearing-induced fabric component may be supressing the effect of the inherent fabric anisotropy on the modelled response – an aspect that will be further investigated below. It is also apparent that none of the sets of model parameters is able to capture adequately the response observed in the laboratory. In particular, it is observed that, regardless of the test, the modelled response is significantly stiffer than that measured in the experiment throughout loading, leading to the generation of smaller positive excess pore water pressures during the earlier stages of loading, as well as greater negative excess pore water pressures during the later stages of loading.

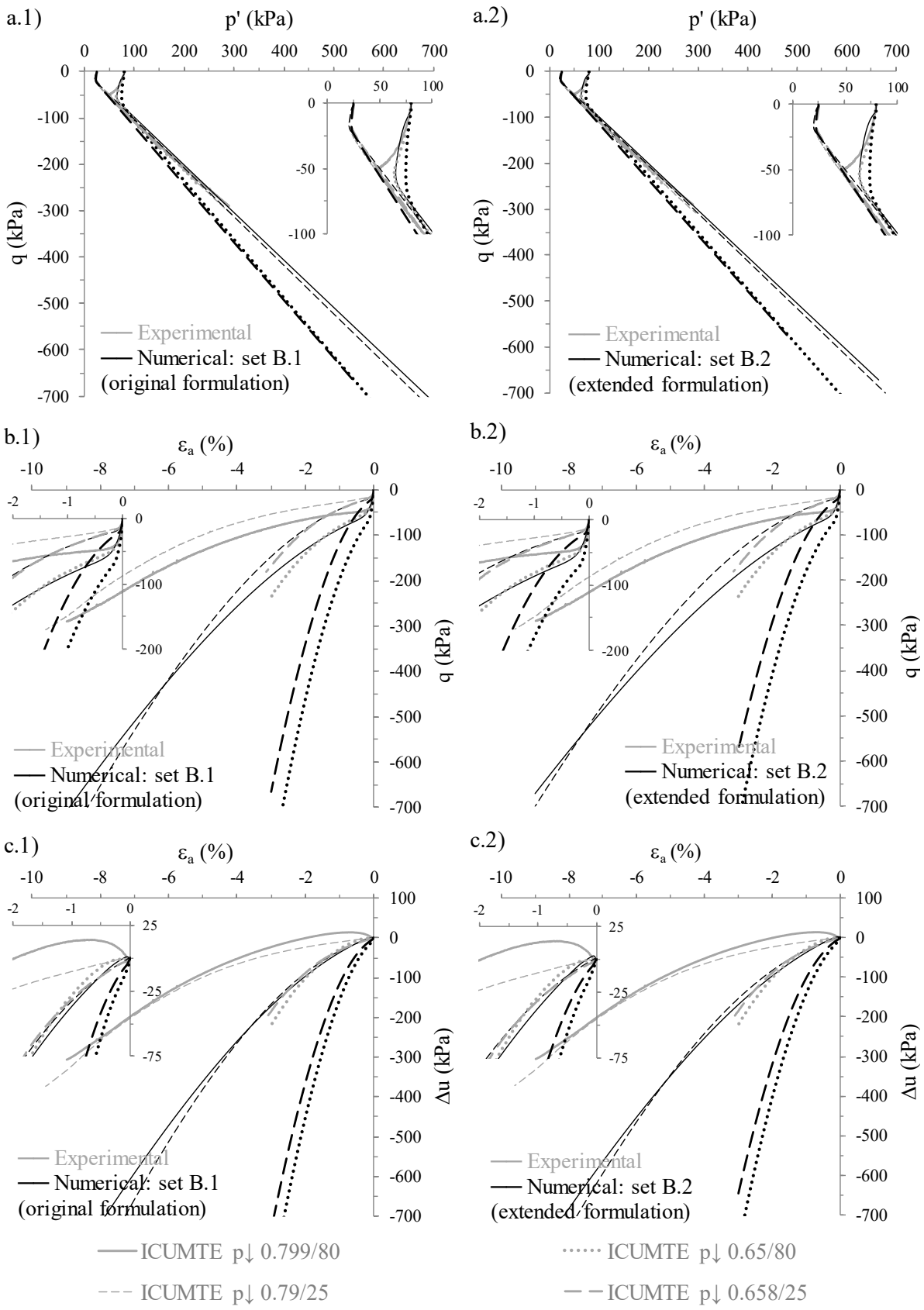

Figure 7.34 – Numerical simulation of all available ICUMTE p↓ tests using the original and extended formulations of the constitutive model: (a) effective stress path, (b) stress-strain response and (c) excess pore water pressure evolution with axial strain.

To investigate the apparent suppression of the effect of the inherent fabric anisotropy component on the modelled response due to the activation of the shearing-induced fabric component, test ICUMTE p↓ 0.650/80 was simulated once again. In this simulation, the model parameter set "B.1) Dynamic – Original formulation" was modified to include the effect of the inherent fabric anisotropy by setting $a = 0.29$, $v_A = 0.0$ and $k_A = 0.6$ (rather than considering the standard set of values which removes the impact of this component of the formulation, i.e. $a = 0.333$, $v_A = 0.0$ and $k_A = 1.0$, as in the previous simulation). The results obtained in this newly performed simulation are compared with those obtained in the previous simulation when using the set B.1 in Figure 7.35. Note that the main advantage of comparing the results of these two simulations (rather than, for example, further exploring the results obtained when using the set B.2) consists of having the same values for all model parameters (including those required by the shearing-induced fabric component), except for those required by the inherent fabric anisotropy component. It can be observed that, although identical values have been adopted for the shearing-induced fabric component of the constitutive model, higher values of the plastic multiplier h_f are obtained when the inherent fabric anisotropy component is activated (Figure 7.35d). This could, in fact, be expected, since the activation of the latter component results in a steady reduction of the plastic hardening modulus associated with the primary surface, A_1, during loading in triaxial extension (Figure 7.35e) and, consequently, in a greater accumulation of deviatoric strain, as well as volumetric strain (Figure 7.35c). Moreover, since the evolution of f_p is directly proportional to the accumulation of volumetric strain (Equation 4.66), a greater increase in f_p occurs during the earlier stages of loading (i.e. during compressive volumetric plastic straining), leading to higher values of h_f (Equation 4.56). This means that, when the inherent fabric anisotropy component is activated, and under this type of loading, A_1 is, on one hand, scaled down by the plastic multiplier h_A and, on the other hand, scaled up by the plastic multiplier h_f. In other words, during the early stages of the modelled response (in this case, less than 1% of axial strain), the effect of the inherent fabric anisotropy on the plastic hardening modulus is partly counterbalanced by the effect of the isotropic component of the shearing-induced fabric tensor. Furthermore, it can be observed that, although the plastic multiplier h_f reaches 1.0 (i.e. vanishes) as the response of sand changes from plastic volumetric contraction to dilation and holds this value until the end of loading (Figure 7.35f), the plastic hardening modulus has already reached a very small value at that moment (in this case, smaller than 200 kPa, as shown in the detail of Figure 7.35f) and, consequently, the impact of $h_A = 0.6$ (Figure 7.35e) on the computed response is limited.

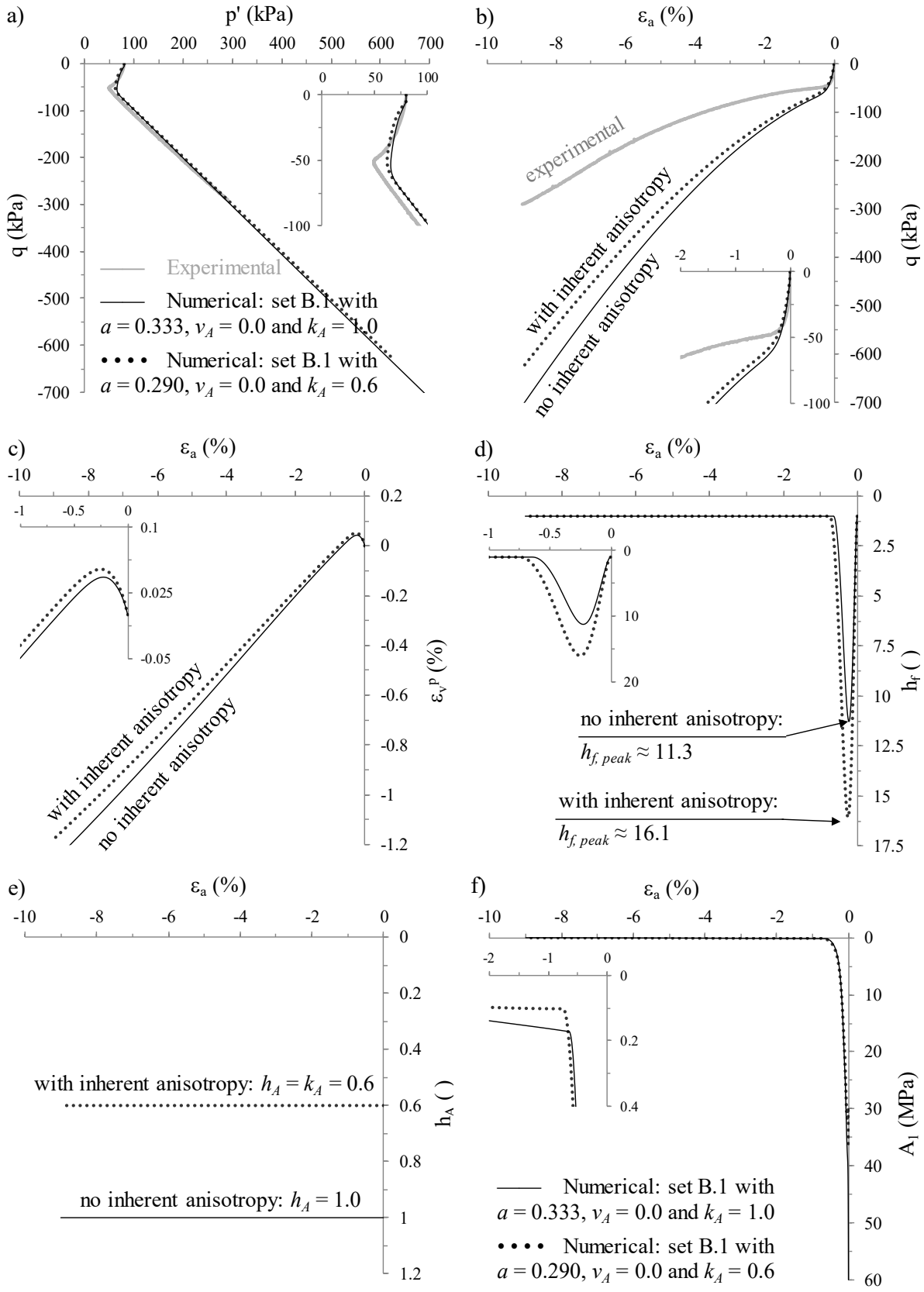

Figure 7.35 – Influence of the inherent fabric anisotropy through the use of k_A < 1.0 on the numerical simulation of test ICUMTE p↓ 0.799/80: (a) effective stress path and (b) stress-strain response; (c) plastic volumetric strain, (d) plastic multiplier h_f, (e) plastic multiplier h_A and (f) plastic hardening modulus evolutions with axial strain.

To evaluate the impact of the model parameter v_A on the modelled response, an additional simulation of test ICUMTEp↓ 0.650/80 was conducted by employing the set "B.1) Dynamic – Original formulation" in conjunction with $a = 0.29$, $v_A = 1.0$ and $k_A = 1.0$. The outcome of this simulation is compared with that of the simulation using the unaltered set B.1 in Figure 7.36. It can be seen that the effect of employing a value for v_A greater than 0.0 (i.e. the effect of relocating the critical state line (CSL) during loading) is also counterbalanced during the early stages of loading by a faster increase in the value of h_f.

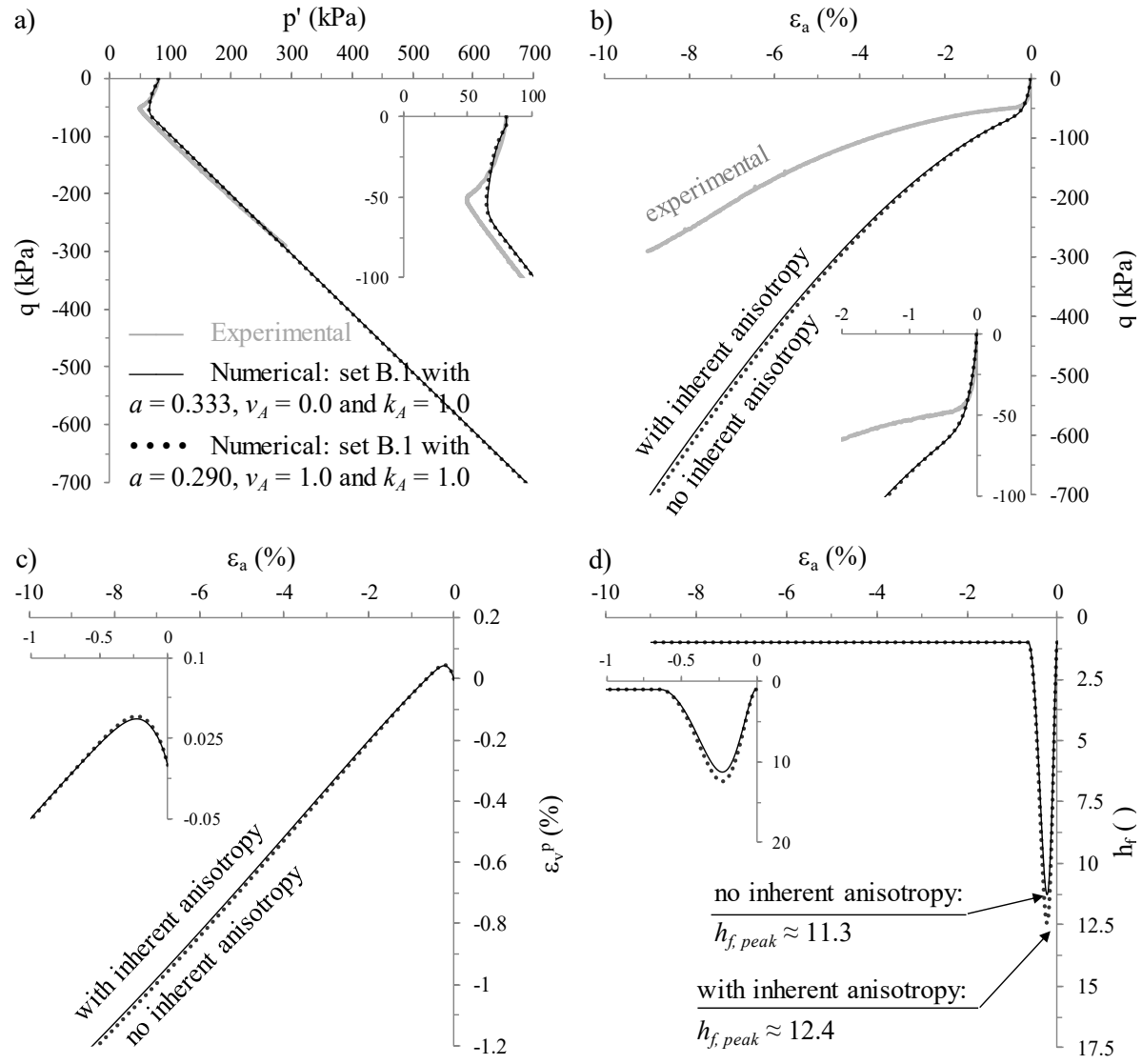

Figure 7.36 – Influence of the inherent fabric anisotropy through the use of v_A > 0.0 on the numerical simulation of test ICUMTE p↓ 0.799/80: (a) effective stress path, (b) stress-strain response, (c) plastic volumetric strain and (d) plastic multiplier h_f evolution with axial strain.

Note that, although the counterbalancing effect of the shearing-induced fabric and inherent fabric anisotropy components on the plastic hardening modulus is expected to occur regardless of the values assigned to the model parameters, it is acknowledged that the large value of H_0 required, in the present study, to model accurately the cyclic response of Hostun sand (at least when compared with values employed for other sands, as discussed in

Section 6.14) likely increased the impact of the former component on the modelled response and, consequently, reduced that of the latter component. In addition, note that the available laboratory test is limited to triaxial test data, suggesting that further investigation on this topic using other element laboratory tests would likely enrich the conclusions reached in the present study.

A possible strategy to circumvent this conflict between the shearing-induced fabric and inherent fabric anisotropy components might consist of developing a new formulation for the former component based on strain-energy-related principles (e.g. as a function of dissipated energy per unit volume). Note that, in such case, the shearing-induced fabric component would not affect the monotonic response, due to the absence of shear reversals. Note also that, based on results of undrained cyclic triaxial test performed using uniform and non-uniform loading conditions, Azeiteiro *et al.* (2017b) concluded that residual excess pore water pressure build-up during cyclic loading appears to be very satisfactorily correlated with the accumulation of dissipated energy per unit volume, irrespective of the loading pattern used in each test. Indeed, this conclusion seems to agree well with those reached in other experimental studies (e.g. Towhata and Ishihara, 1985; Figueroa *et al.*, 1994; Dief and Figueroa, 2007; Polito *et al.*, 2013; Kokusho, 2013), emphasising the suitability of energy concepts for the prediction of the occurrence of liquefaction-related phenomena. Lastly, note that a general algorithm has been proposed in the literature to assess the dissipated energy per unit volume simulated by a given constitutive model based on the registered response in three-dimensional stress-strain space (Taborda *et al.*, 2016), which might assist the development of a new formulation for the evolution of the shearing-induced fabric tensor.

Figure 7.37 depicts the results of simulations of anisotropically and isotropically consolidated drained monotonic triaxial extension tests with increasing mean stress (K0CDMTE p↑ and ICDMTE p↑, respectively) performed using the original and extended formulations of the constitutive model. The results of the experimental results are also presented in the figure (in grey colour) for comparison. Also in this case, it is apparent that the results obtained when using the set "B.2) Dynamic – Extended formulation" are very similar to those obtained when using the set "B.1) Dynamic – Original formulation", particularly for moderately loose samples (i.e. samples subjected to tests ICDMTE p↑ 0.798/80 and K0DMTE p↑ 0.801/80). Indeed, considerably worse predictions of the responses observed in these tests have been obtained in these newly performed simulations, in comparison to those obtained when using the sets of model parameters belonging to the category "A) Static" (see Section 6.12). Once more, this suggests that, although introduced to deal with cyclic loading, the shearing-induced fabric component seems to have a significant detrimental impact on the simulation of the monotonic response of Hostun sand, with a considerably stiffer response being generally predicted during the early stages of loading in comparison with that obtained in the numerical simulations not considering this component of the model, as well as observed in the laboratory. As mentioned before, the replacement of the existing formulation of the shearing-

induced fabric component by another formulated in terms of strain-energy concepts would likely overcome this issue.

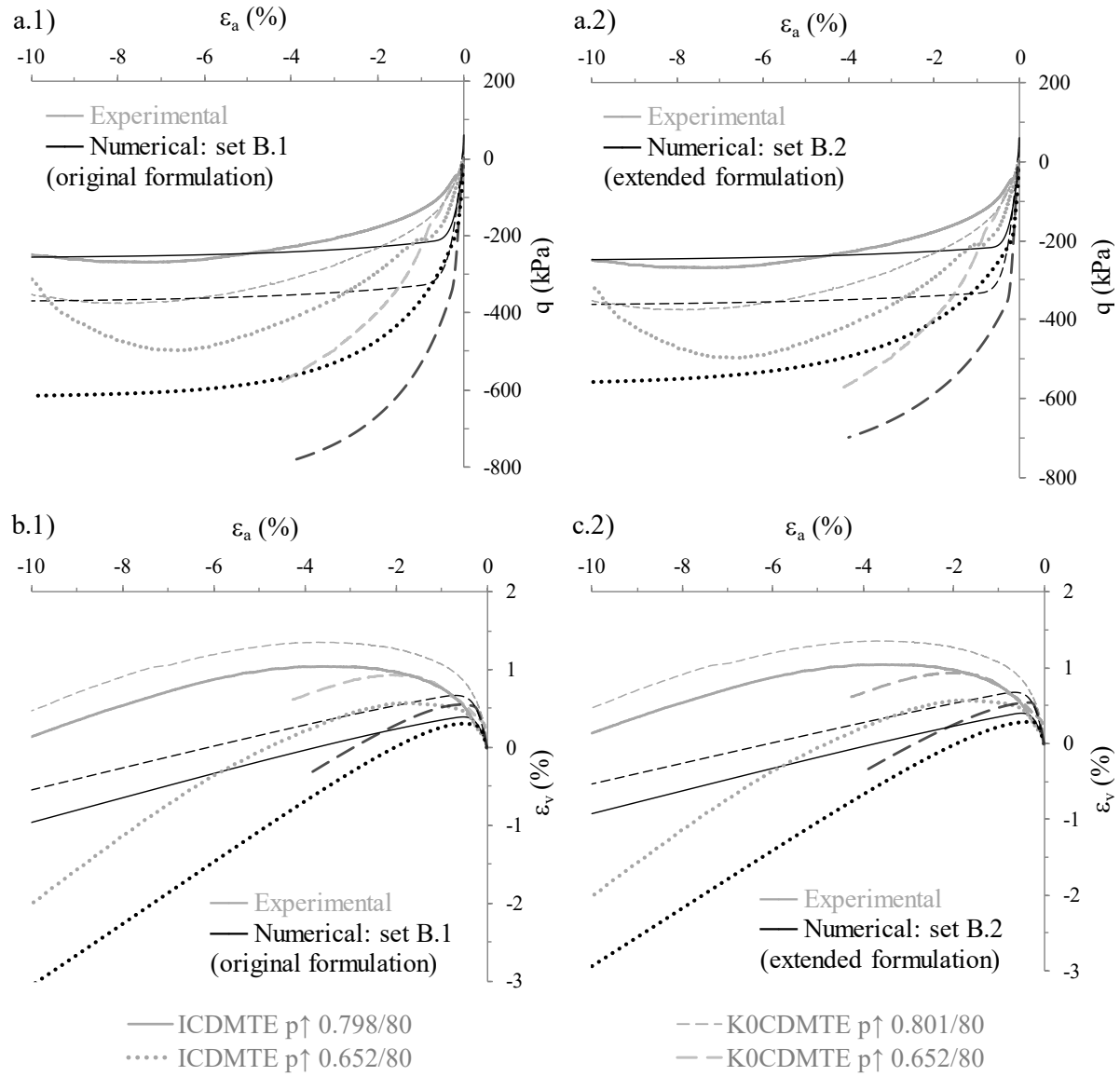

Figure 7.37 – Numerical simulation of ICDMTE p↑ tests using the original and extended formulations of the constitutive model: (a) stress-strain response and (b) volumetric strain evolution with axial strain.

7.3.3 Undrained cyclic triaxial test simulations

Figure 7.38 compares the results of the numerical simulations of test ICUCT 0.832/80/42 using the original (i.e. set B.1) and extended (i.e. set B.2) formulations of the constitutive model. The experimental data is also presented in the figure for comparison purposes.

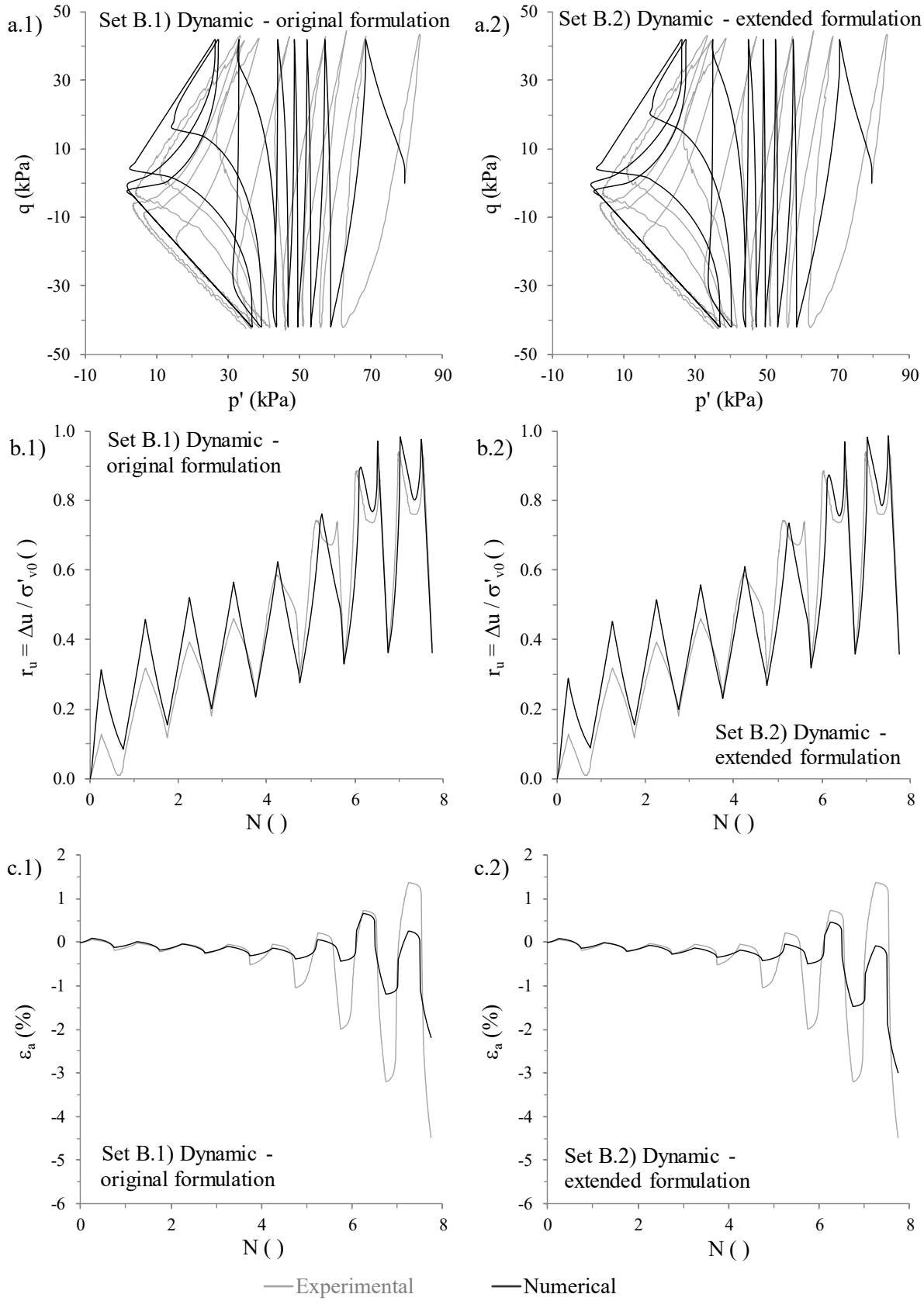

Figure 7.38 – Numerical simulation of test ICUCT 0.832/80/42 using the original and extended formulations of the constitutive model: (a) effective stress path, (b) excess pore water pressure ratio build-up and (c) axial strain evolution with the number of loading cycles.

It is apparent that very similar results were obtained in both numerical simulations. The discrepancies between both sets of numerical data seem practically restricted to the slightly larger accumulation of axial strains in triaxial extension during the last loading cycles when using the extended version of the model, due to the softer stress-strain response induced by the plastic multiplier h_A under this type of loading. This aspect can be more clearly observed in Figure 7.39. It is apparent that the rate of accumulation of double amplitude during the last loading cycles obtained when using the extended formulation is closer to that observed in the laboratory. This figure also shows that, regardless of the formulation of the constitutive model used (i.e. original or extended), the onset of accumulation of large axial strains occurs later in the numerical simulation than registered in the laboratory.

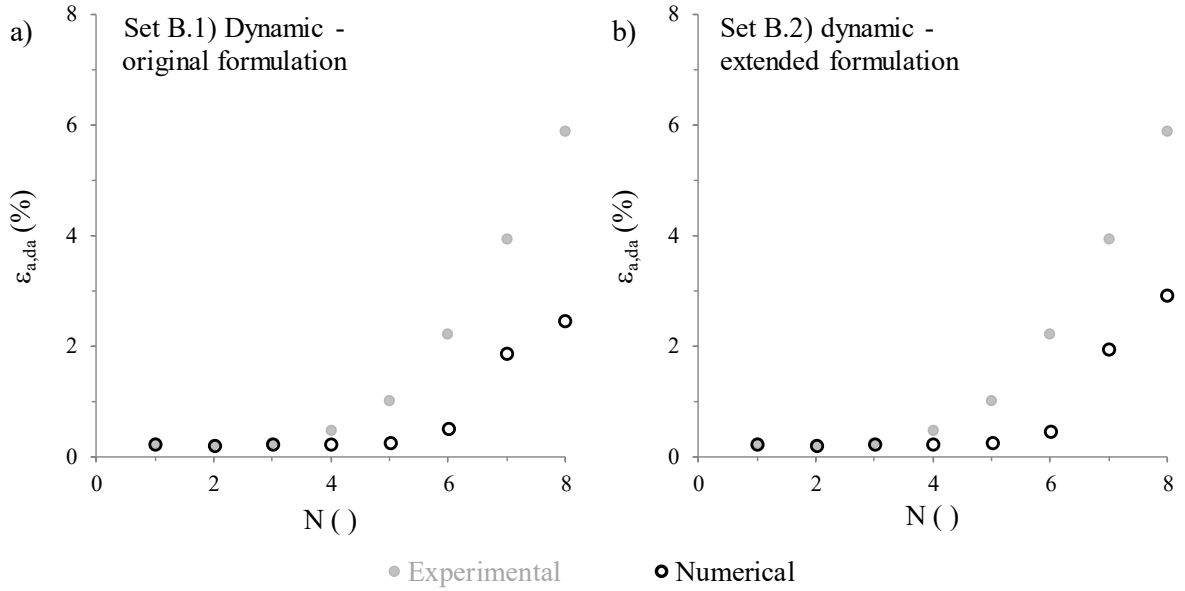

Figure 7.39 – Double amplitude axial strain evolution with the number of loading cycles obtained for test ICUCT 0.832/80/42 when using (a) the original formulation and (b) the extended formulation of the constitutive model.

To gain further insight into the impact of the inherent fabric anisotropy component on the modelled cyclic response, Figure 7.40 depicts the simulated evolutions of the plastic multiplier h_f (introducing the effect of the shearing-induced fabric component on the plastic hardening modulus) with the number of loading cycles, as well as the evolution of the product of the plastic multiplier h_A (introducing the effect of the inherent fabric anisotropy component on the plastic hardening modulus) by the plastic multiplier h_f with the number of loading cycles. Note that, when using the original formulation of the model, since $k_A = 1.0$, it follows that $h_A = 1.0$ throughout loading and, therefore, $h_A\, h_f = h_f$. It can be observed that, due to the use of a larger value for H_0 (55 000.0 rather than 43 000.0) and, particularly, to the fact that a greater increase in plastic volumetric strain is induced by the activation of the inherent fabric anisotropy component (as explained in the previous section), the magnitude of the plastic multiplier h_f during the first four loading cycles obtained when using the extended formulation is slightly greater than that obtained when employing the original formulation

(Figure 7.40a). However, when comparing the evolutions of h_A h_f (Figure 7.40b), it is apparent that the larger values of h_f obtained when using the extended version are counterbalanced by smaller values of h_A in triaxial extension and, therefore, similar values of h_A h_f are obtained when using both original and extended formulation at the end of each loading cycle (Figure 7.40b). Overall, it appears that similar average evolutions of h_A h_f (and, consequently, similar average reductions of the plastic hardening modulus) are obtained when using the original and extended formulations of the constitutive model, therefore justifying the similar responses registered in both numerical simulations.

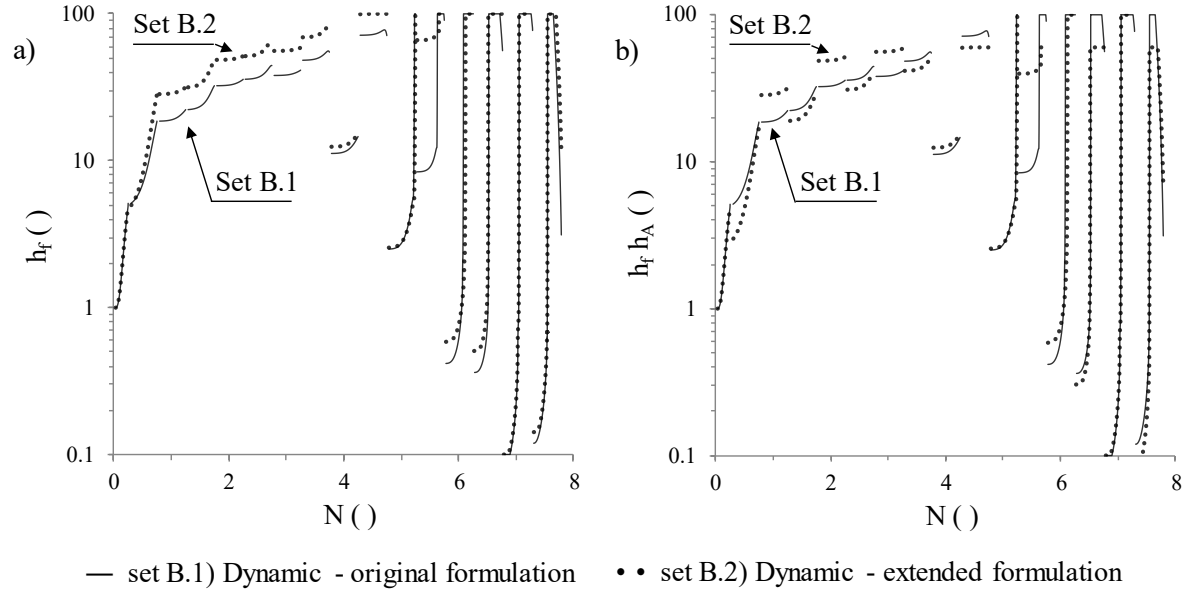

Figure 7.40 – Numerical simulation of test ICUCT 0.832/80/42 using the original and extended formulations of the constitutive model: evolution of the (a) plastic multiplier h_f and (b) product of the plastic multipliers h_f and h_A with the number of loading cycles.

In addition, Figure 7.41 compares the results of the simulation of test ICUCT 0.804/80/48 when using sets B.1 and B.2. The experimental data is also depicted in the figure, showing that, in this test, where a large cyclic stress ratio (CSR) was applied, the sample exhibited a very soft response in triaxial extension during the first loading cycle, reaching very low effective stresses just after the first two loading cycle. Unfortunately, it is apparent that the use of extended formulation of the constitutive model does not seem to improve considerably the reproduction of this laboratory test. Once more, this suggests that, at least for triaxial loading conditions, the modelled cyclic response is primarily governed by the shearing-induced fabric component of the model.

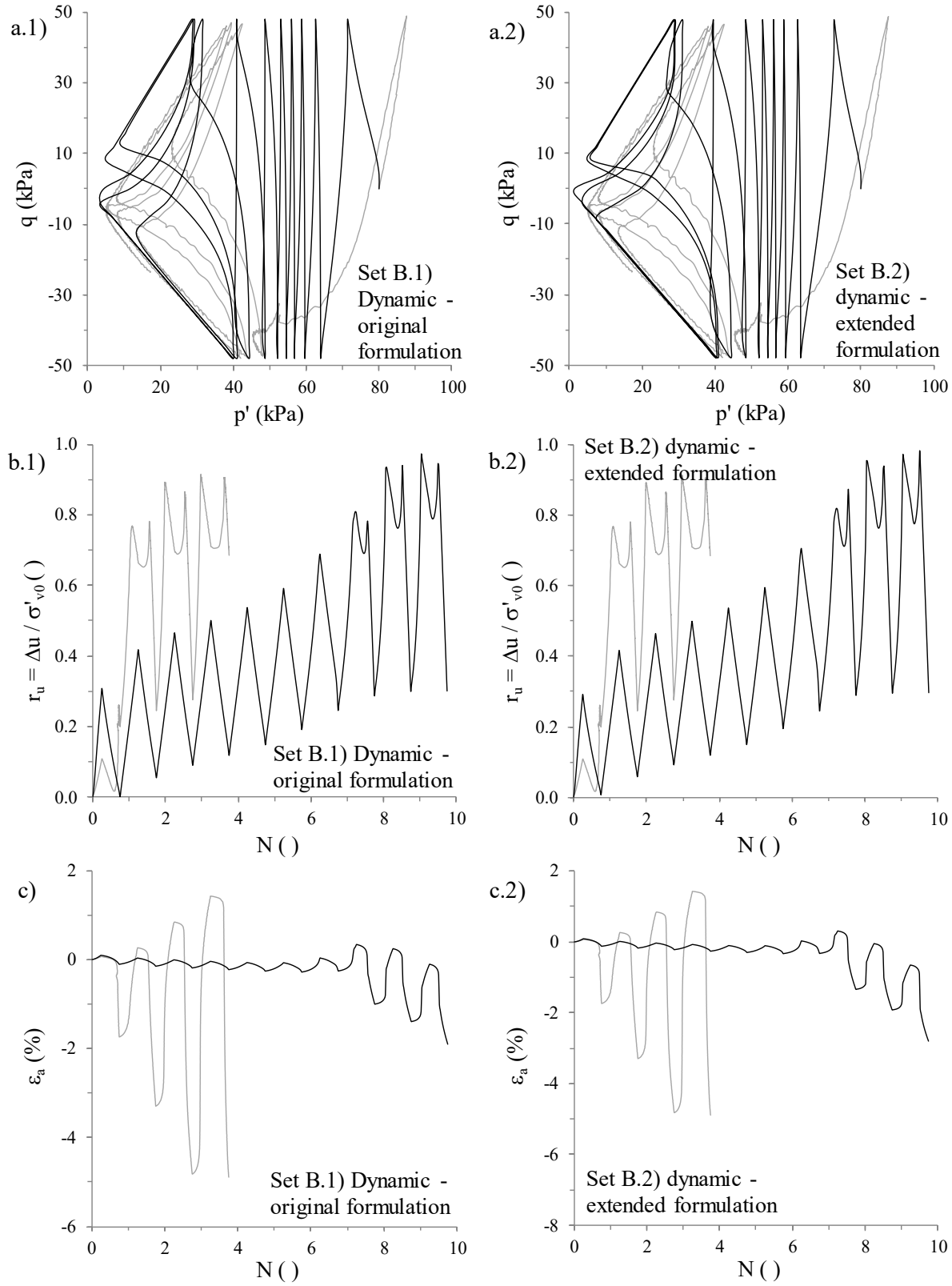

Figure 7.41 – Numerical simulation of test ICUCT 0.804/80/48 using the original and extended formulations of the constitutive model: (a) effective stress path, (b) excess pore water pressure ratio build-up and (c) axial strain evolution with the number of loading cycles.

Moreover, as also pointed out before, it seems that the effect of the inherent fabric anisotropy component on the modelled response is partly counterbalanced by the shearing-

induced fabric component, reducing the impact of the former on the modelled response. Note that similar conclusions were reached when simulating the laboratory tests ICUCT 0.773/80/56 and ICUCT 0.793/135/67.5, where large CSRs were also used. Although not presented here for brevity, the results of the simulations of these tests are presented in Appendix B.

Figure 7.42 compares the undrained cyclic resistance predicted by the extended formulation of the constitutive model with that measured in the laboratory for samples consolidated to $p'_0 = 80$ kPa. Similar to what was observed when using the original version of the model, it is apparent that, when excluding the ICUCT 0.804/80/48 and ICUCT 0.773/80/56 tests, very satisfactory reproductions of undrained cyclic resistance curves observed in the laboratory are obtained. Given the very different responses observed in these tests, including samples requiring from two to seventy-eight loading cycles to reach cyclic mobility, and the fact that a single set of model parameters was employed to the simulation of the response of both moderately loose and dense sand, the agreement can be considered very satisfactory.

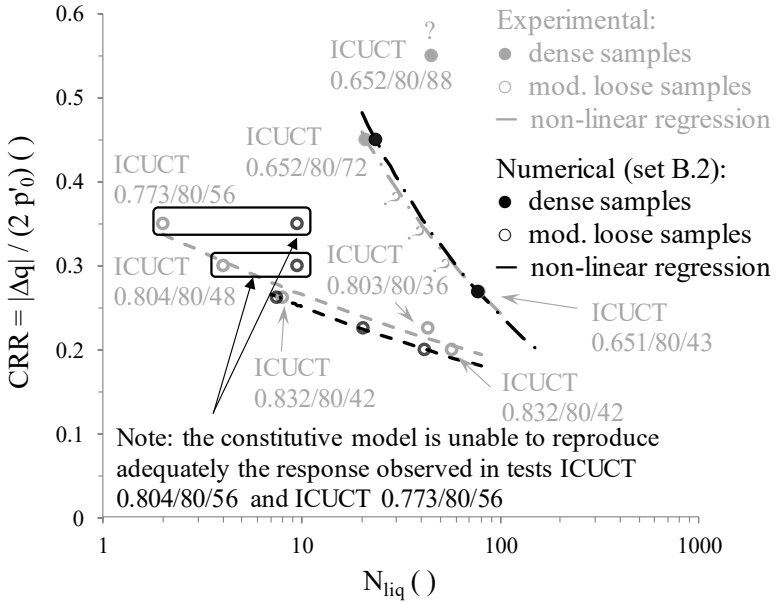

Figure 7.42 – Comparison of the undrained cyclic resistance of Hostun sand predicted by the extended formulation of the constitutive model with that observed in laboratory for ICUCT tests performed on moderately loose and dense samples consolidated under $p'_0 = 80$ kPa.

By comparing the numerical results depicted in Figure 7.42, obtained by the extended formulation of the constitutive model (i.e. the set of model parameters B.2), with those presented in Figure 7.25, obtained by using the original formulation (i.e. the set of model parameters B.1), it can be concluded that similar undrained cyclic resistance curves are predicted by both versions of the model, with a slight improvement being achieved for dense samples (note, however, that some uncertainty exists in relation to the experimentally determined curve, as discussed in Chapter 3).

At this point, it should be mentioned that, despite the several attempts, it was not possible to find a set of values for a, v_A and h_A that would improve the reproduction of the responses observed in tests ICUCT 0.804/80/48, ICUCT 0.773/80/56 and ICUCT 0.793/135/67.5, while keeping an overall satisfactory reproduction of the remaining tests. As discussed before, there seems to exist two plausible explanations:

1) the effect of the inherent fabric anisotropy component on the modelled response is partly inhibited by an opposite effect of the shearing-induced fabric component;
2) the shearing-induced fabric component appears to have a much stronger impact on the overall cyclic response than the inherent fabric anisotropy component.

These pitfalls suggest that further development of the shearing-induced fabric and/or inherent fabric anisotropy formulations may be required in the future. As pointed out before, it is believed that, due to its suitability for the prediction of excess pore water pressure build-up during cyclic loading, strain-energy-related concepts (such as the dissipated energy per unit volume) may be used to develop a new formulation for the shearing-induced fabric component. In addition, it may be necessary to redefine the contribution of these two components to the plastic hardening modulus. In fact, it is apparent that the plastic multiplier h_f has a very wide variation during loading, being even necessary to limit its range of values to prevent the occurrence of numerical instabilities. Conversely, the variation of the plastic multiplier h_A is much more restricted (namely in between the value selected for k_A and 1.0). Consequently, the impact of the inherent fabric anisotropy component seems to be significantly more limited than that of the shearing-induced fabric component. A more balanced approach might certainly benefit the concurrent use of these two components.

Lastly, similar to what was observed for the undrained cyclic resistance, the use of the extended formulation of the constitutive model (i.e. the set of model parameters B.2), instead of the original formulation (i.e. the set B.1), does not seem to produce significant alterations neither to the evolutions of the secant shear modulus and damping ratio with the number of loading cycles, nor to the evolution of residual excess pore water pressure with the number of loading cycles. Therefore, to abbreviate the presentation, those results are not presented here, with the conclusions drawn in Section 7.2.2.5 and 7.2.2.6 being applicable for the extended formulation of the constitutive model. Similarly, the activation of the inherent fabric anisotropy component does not seem to improve the volumetric response observed in DCT tests, in relation to that registered when using the original formulation, with the conclusions presented in Section 7.2.2.7 retaining their validity.

7.4 Summary and conclusions

In this chapter, the ability of the constitutive model to replicate the monotonic and cyclic response of Hostun sand registered in laboratory tests was explored. Under monotonic loading, it was shown that, in general, the constitutive model is capable of capturing the effect

of the initial void ratio, effective stress state at consolidation and stress path direction on the sand's response. While a satisfactory agreement between numerical and experimental data was obtained for tests performed on moderately loose ($D_r \approx 50 - 70\,\%$) and dense ($D_r > 70\,\%$) samples, discrepancies were observed for tests performed on loose samples ($D_r < 50\,\%$). In effect, although introduced to address the simulation of cyclic loading, the isotropic component of the shearing-induced fabric tensor was observed to affect detrimentally the initial contractive phase of the modelled monotonic response. Specifically, the constitutive model was observed to predict stiffer stress-strain responses for loose samples than those measured in the laboratory during the early stages of the experiment, therefore underpredicting the excess pore water pressure generation observed under undrained conditions or, similarly, the accumulation of compressive volumetric strains under drained conditions. It was shown, however, that when using the set of model parameters optimised for the reproduction of the monotonic response of Hostun sand (i.e. a set of model parameters not activating the shearing-induced fabric component), a good agreement between simulated and measured response of loose sand was obtained. It is also important to note that the centrifuge experiments, whose numerical simulations are presented in the following chapter, were performed only on deposits of moderately loose (i.e. having $D_r \approx 50\,\%$) and dense Hostun sand and, therefore, the overprediction of the stiffness of loose Hostun sand (i.e. having $D_r < 50\,\%$) under monotonic loading is not expected to have a relevant impact on the simulations of the centrifuge experiments.

The original formulation of the constitutive model, as proposed by Taborda (2011), was subsequently employed in the simulation of cyclic triaxial tests. Apart from the tests where samples were subjected to large cyclic stress ratios (CSRs) and required only few cycles to the onset of cyclic mobility, it was shown that, irrespective of the effective stress state at consolidation and applied deviatoric stress oscillation, the constitutive model was, in general, able to replicate satisfactorily the cyclic response of moderately loose Hostun sand observed in the laboratory, particularly in terms of excess pore water pressure generation with loading and effective stress path registered in the laboratory. In terms of accumulation of axial strain, it appeared that the constitutive model tends to underestimate this aspect of the response, particularly from the moment that very low effective stresses are reached (i.e. during the later stages of cyclic loading). In relation to the reproduction of the cyclic response of dense Hostun sand, the obtained results suggested that the constitutive model tends to underestimate slightly the rate of excess pore water pressure build-up with cyclic loading measured in the laboratory, therefore overestimating slightly the number of loading cycles required to the onset of cyclic mobility (particularly evident for the test where the sample was subjected to the smallest deviatoric stress oscillation). Furthermore, for dense samples, smaller strain accumulation than that measured in the experiment was, in general, predicted by the model during the loading cycles preceding the onset of cyclic mobility, with a better agreement being obtained afterwards. Considering the very different responses observed in the present

laboratory testing programme and the fact that a single set of model parameters was used to simulate all tests, the agreement between numerical and experimental data was considered satisfactory.

In addition, the ability of the constitutive model to capture key aspects of cyclic sand response was investigated. Starting with the undrained cyclic resistance (i.e. number of loading cycles require to the onset of cyclic mobility under constant deviatoric stress loading conditions), it was shown that, when excluding tests where samples were subjected to very large CSRs inducing cyclic mobility in very few cycles, a good match between numerical and experimental data was obtained for both moderately loose ($D_r \approx 50 - 70\,\%$) and dense ($D_r \approx 102\,\%$) samples. Subsequently, the evolutions of both secant shear modulus (normalised by the shear modulus at small-strains) and damping ratio with the number of loading cycles (normalised by that required to the onset of cyclic mobility) simulated by the constitutive model were compared to those observed in the laboratory. It was shown that the constitutive model is able to replicate qualitatively the main trends observed in the laboratory, including the stiffening unloading-reloading response for effective stress paths remaining below the phase transformation line (PTL), particularly evident during the first loading cycles, and sharp reduction in stiffness once the phase transformation line is crossed and the effective stress path is reversed. Indeed, it was suggested that, to allow for an independent control of both aspects of the cyclic response (i.e. stiffening before the crossing of the phase transformation line and softening after its crossing and reversal of stress path), it would be beneficial to remove the interdependency between the isotropic and deviatoric components of the shearing-induced fabric tensor, f_p and $\boldsymbol{f}$, respectively. In terms of damping ratio evolution, it appeared that, under this type of loading, the model tends to underestimate slightly the values observed in the laboratory. Attention was afterwards given to the ability of the model to replicate the rate of excess pore water pressure generation with the normalised number of loading cycles measured in the laboratory. It was apparent that the effect of cyclic stress ratio (CSR) on the curves obtained from numerical data was more limited than that observed from the experimental data, suggesting, once more, that the shearing-induced fabric component may require future improvement. Finally, the performance of the model when simulating the volumetric strains of saturated sands observed under drained cyclic loading was evaluated. While a good agreement between numerical and experimental data was obtained for the first two to three loading cycles, it was shown that the model tended to overpredict the axial and volumetric strains measured in the laboratory experiments with further loading.

The potential benefits of using the extended formulation of the model, which includes an inherent fabric anisotropy component, were subsequently investigated by using the set of model parameters “B.2) Dynamic -extended formulation”. Starting by simulating drained and undrained monotonic triaxial extension tests, it was observed that the reduction in the plastic hardening modulus associated with the primary yield surface, A_1, imposed by the inherent

fabric anisotropy component through the plastic multiplier h_A is counterbalanced during the early stages of loading by an opposite effect of the shearing-induced fabric component through the plastic multiplier h_f. Consequently, the modelled responses obtained by using the set of model parameters B.2 were observed to be similar to those predicted by the set of model parameters "B.1) Dynamic -original formulation" (which makes uses of the original formulation of the model). It was noted that, as a future improvement, a possible strategy to overcome this incompatibility would consist of developing a new formulation for the shearing-induced fabric component based on strain-energy-related principles (e.g. dissipated energy per unit volume), since, in such case, the shearing-induced fabric formulation would not impact the monotonic response, while being used for cyclic loading, as intended.

Subsequently, results of simulations of undrained cyclic triaxial tests obtained when using the set of model parameters B.2 (i.e. the extended formulation of the model) were compared to those previously obtained when using the set of model parameters B.1 (i.e. the original formulation of the model). Unfortunately, it was, once more, observed that similar results were obtained when employing the two different sets of model parameters. Two plausible causes for the observed results were discussed: (1) the effect of the inherent fabric anisotropy component on the modelled response is partly inhibited by an opposite effect of the shearing-induced fabric component, as also observed for the monotonic triaxial extension test data; (2) overall, the shearing-induced fabric component has a much stronger influence on the modelled cyclic response than the inherent fabric anisotropy component. It was suggested that the contributions of these two components to the plastic hardening modulus should be redefined in the future.

As a final note, it should be highlight that the present study involved the simulation of a very large number of laboratory tests (thirty-two monotonic triaxial compression and extension tests, as well as fifteen cyclic triaxial tests) performed on samples prepared to a wide range of void ratios and consolidated under several different confining stresses. As such, the expectations were not to reach a perfect match with all available experimental data, but to get insight into the ability of the constitutive model to capture the most relevant aspects of both monotonic and cyclic response of Hostun sand. Although it has been acknowledged that the shearing-induced fabric formulation and its coupling with the inherent fabric anisotropy formulation may require future improvement, it also seems fair to mention that the constitutive model seems able to reproduce satisfactorily key aspects of the response of Hostun sand, including its resistance to cyclic mobility.

Chapter 8 APPLICATION OF THE BOUNDING SURFACE PLASTICITY MODEL TO THE SIMULATION OF THE DYNAMIC RESPONSE OF SHALLOW FOUNDATIONS BUILT ON LIQUEFIABLE SAND DEPOSITS

8.1 Introduction

Having investigated the ability of the implemented Bounding Surface Plasticity model (BSPM) to reproduce element laboratory tests, the present chapter focuses on the characterisation of its performance when simulating the response of sand under general loading conditions, such as those encountered in boundary-value problems. It is of particular interest to characterise the ability of the constitutive model to predict the occurrence of liquefaction-related phenomena and their effects. With that purpose, and considering the scarcity of field monitoring data on these phenomena, as well as the difficulties inherent to the characterisation of natural/intact sandy soils, the results of two dynamic centrifuge experiments are employed as benchmark for the Finite Element analyses. It should be noted that both centrifuge experiments were performed at the Schofield Centre, University of Cambridge, U.K., as part of a collaborative research project between the University of Cambridge and the University of Coimbra (Marques *et al.*, 2012a, 2012b, 2012c, 2014a, 2014b, 2014c, 2015). Moreover, note that, in both centrifuge experiments, Hostun sand was employed as model material and, therefore, the results of the calibration of the BSPM against results of element laboratory tests presented in Chapter 6 are employed in the numerical simulations of the centrifuge experiments.

Before presenting the results of the numerical simulations, a brief overview of the experimental research programme is provided, including its background, main objectives and main characteristics. Subsequently, the particular aspects of each centrifuge experiment are described and the obtained experimental results are briefly presented and discussed. Finally, the numerical procedure is described in detail and the computed numerical results are compared with those obtained in the experiment. In the first centrifuge experiment, particular emphasis is given to the characterisation of the ability of the numerical tool to simulate basic aspects of sand-structure interaction under dynamic loading, as well as to predict accurately the influence of different bearing pressures (induced by a lighter and a heavier adjacent shallow foundations) on the overall performance of the system under dynamic loading. Conversely, in the second experiment, the focus is given to the characterisation of the ability of the numerical tool to replicate the impact of narrow densification zones and high-permeability zones on the mitigation of liquefaction effects.

8.2 Overview of the experimental programme

8.2.1 Background

As part of his PhD research programme, Coelho (2007) carried out a total of fourteen centrifuge experiments in the Schofield Centre's 10 m-beam centrifuge facility, including:

- three centrifuge tests concerning the dynamic response of saturated level deposits of loose ($D_r = 50\,\%$), moderately loose ($D_r = 60\,\%$) and dense ($D_r = 80\,\%$) sand, intended to characterise the fundamental mechanisms governing the response of sand deposits located far from the influence of structures (i.e. under "free-field" conditions);
- two centrifuge tests concerning the behaviour of two different small deck-bridges supported on shallow foundations and built on a loose ($D_r = 50\,\%$) deposit of saturated sand to investigate the fundamental mechanisms governing the sand-structure interaction;
- five centrifuge tests on models representing identical small deck-bridges supported on shallow foundations and resting on densified zones with different widths, aimed at identifying the benefits of densification, as well as its optimal width;
- four centrifuge tests intended to investigate the benefits from using both narrow densification zones and impermeable barriers to the mitigation of liquefaction effects and, consequently, to the improvement of the performance of shallow foundations built on liquefiable sand deposits.

Based on the obtained experimental results, Coelho (2007) concluded that:

- during dynamic loading, dilative sand response is typically observed in the zone of the deposit under the influence of the shallow foundation, due to the occurrence of further stress concentration in that zone of the model; despite this fact, significant co-seismic displacements are registered during this phase, mostly due to the reduction of stiffness and strength of the sand deposit caused by excess pore pressure generation and/or migration from other zones of the model; indeed, the most effective liquefaction resistance measure for this phase seems to consist of the densification of the zone of the deposit under the influence of the foundation, since it increases dilation (and, consequently, the stability of the foundation) and reduces settlements; the optimal densification width seems to correspond to that of the shallow foundation (i.e. there seems to be no additional benefits in extending the densification width beyond the limits of the shallow foundation);
- after the end of dynamic loading, an excess pore pressure migration from the zones of the deposit farther away from the structure (often termed as "free-field", although such designation is not entirely correct due to the relatively small size of the model) to the zones of the deposit located underneath the foundation seems to occur,

resulting in a further reduction of the stiffness and strength of sand at those locations and, therefore, in a further reduction of the bearing capacity; this excess pore pressure migration seems also to justify the larger magnitude of settlements measured during this phase in the zone of the deposit underneath the foundation in relation to that registered in the free-field; indeed, the most effective liquefaction resistance measure for this phase appears to consist of high-capacity drains or impermeable barriers, reducing/preventing excess pore pressure migration from occurring.

Although significant advancement in the understanding of the fundamental mechanisms governing the response of shallow foundations under dynamic loading causing liquefaction had been achieved, Coelho (2007) highlighted the need for further investigation on the following aspects:

- the influence of the characteristics of the structure on its performance; specifically, the impact of the bearing pressure transmitted by the shallow foundation to the underlying sand deposit on the overall performance of the sand-structure system, both in terms of settlements and seismic energy transmitted to the structure;
- the most cost-effective combination of liquefaction resistance measures, particularly in terms of the depth of the densification and length of the impermeable barriers or high capacity drains;
- the influence of the characteristics of the dynamic motion used in the experiment on excess pore pressure generated in the sand deposit, as well as on the settlements and rotation of the structure.

8.2.2 Main objectives and characteristics of the research programme

As part of a Seismic Engineering Research Infrastructures for European Synergies (SERIES) Transnational Access Use Agreement, a dynamic centrifuge testing programme using the 10 m-diameter Turner Beam Centrifuge at the Schofield Centre, University of Cambridge, U.K. – whose details of construction and operation are provided in Schofield (1980) – was undertaken by the PhD candidate Andreia Silva Marques. The centrifuge testing programme was designed to investigate the following aspects (Marques *et al.*, 2014a):

- the influence of the bearing pressure induced by different shallow foundations on their performance under dynamic loading causing liquefaction;
- the potential interaction effects between neighbouring shallow foundations, particularly in terms of potential differential settlements occurring in the foundations;
- the use of densification and high-capacity vertical drains for the mitigation of liquefaction effects.

As detailed in Marques *et al.* (2014a), to accomplish the aforementioned objectives, the following two centrifuge models, which are schematically illustrated in Figure 8.1, were tested (note that all indicated dimensions and input motions are in prototype scale):

- *Centrifuge model A (CM-A): Adjacent shallow foundations resting on a uniform moderately loose sand deposit subjected to dynamic loading causing liquefaction* – study on the dynamic response of two rigid structures (henceforth designated as "shallow foundations"), consisting of solid steel bocks and having an identical base area of 3.0 x 3.0 m^2, while different heights of 0.750 and 1.225 m, spaced 13.5 m apart (between axes) and resting on a 18.0 m-thick saturated deposit of moderately loose Hostun sand (reported as $D_r \approx 50\%$); the fluid table was located at the sand deposit surface; the vertical stresses applied by the lighter and heavier shallow foundations to the underlying sand deposit were about 58 kPa and 95 kPa, respectively.
- *Centrifuge model B (CM-B): Use of narrow densified zones and high-capacity vertical drains to improve the performance of adjacent shallow foundations resting on a sand deposit subjected to dynamic loading causing liquefaction* – study on the dynamic response of two similar solid steel structures (henceforth also designated as "shallow foundations"), with an identical height of 1.225 m and a base area of 3.0 x 3.0 m^2, spaced 13.5 m apart (between axes) and resting on saturated and densified columns of Hostun sand (reported as $D_r \approx 80\%$) with dimensions of 5.0 x 5.0 m^2 in plan (i.e. 1.0 m wider than the base dimension of the built-on shallow foundation for each of its side) and length of 18.0 m (i.e. extending to the bottom of the model); one of the densified sand columns was encased along its full length by a drainage geocomposite simulating closely spaced high-capacity vertical drains; the remaining deposit consisted of moderately loose Hostun sand (reported as $D_r \approx 50\%$) and was also saturated, with the fluid table being located at the ground surface; both shallow foundations applied a vertical stress of 95 kPa (corresponding to that applied by the heavier foundation of the CM-A) to the underlying sand deposit.

As pointed out by Marques *et al.* (2014a), a similar input motion was intended to be applied to all centrifuge models, consisting of 25 loading cycles with a frequency of 1 Hz (i.e. 25 s of duration) and a maximum acceleration of 0.3 g. Moreover, a centrifugal acceleration of 50 *g* was used in all tests.

All three models were prepared and tested in an Equivalent Shear Beam (ESB) container, consisting of a stack of aluminium alloy rectangular frames, separated by rubber layers (Marques *et al.*, 2014a). As discussed by Zeng and Schofield (1996), this container is designed in such way that the laterals walls tend to achieve a similar stiffness to the adjacent soil, consequently minimising the interaction effects between the soil and its boundaries. As pointed out by Coelho (2007), this match is likely less effective when simulating liquefaction-related phenomena. During such experiments, the stiffness of soil is observed to reduce significantly, while the stiffness of the walls remains unchanged, likely increasing the boundary effects. As suggested by the author, it is important to assess the boundary effects, particularly from the moment liquefaction is observed to initiate.

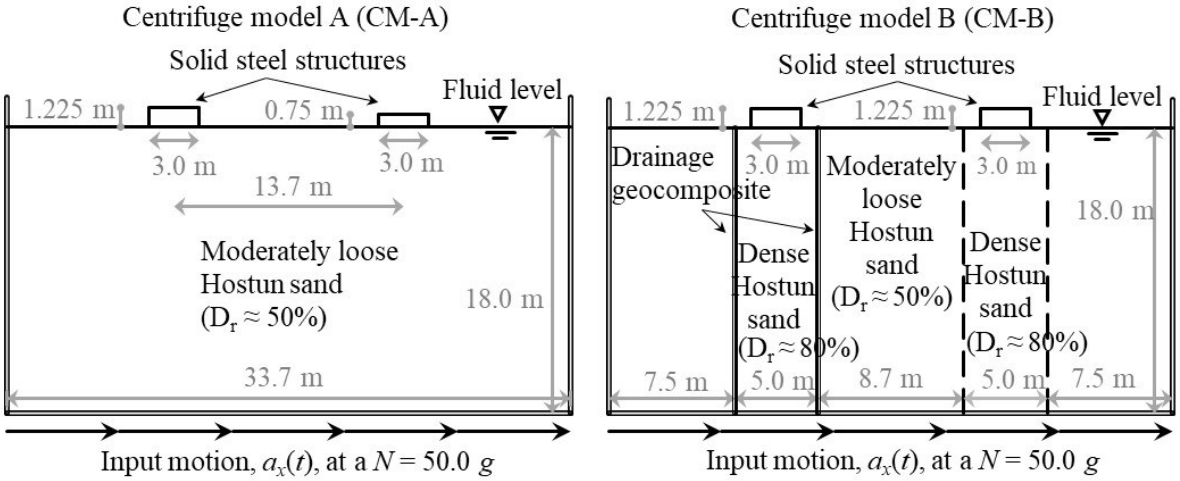

Notes:

A laminar box was used in all centrifuge experiments;

A solution of methylcellulose in water was used as pore fluid to circumvent the conflict between the scaling laws for dynamic time and diffusion time;

All dimensions are in prototype scale.

Figure 8.1 – Schematic illustration of the centrifuge models (adapted from Marques et al., 2014a).

Similar to the element laboratory test programme (Chapter 2), air pluviation technique was employed to prepare all centrifuge models. Moreover, to allow for the creation of the densified zones in CM-B, thin-wall metallic boxes were temporarily employed to support sand, being removed as the pluviation process was completed (Marques *et al.*, 2014a). This procedure was not required when the densified sand column was fully encased by a drainage geocomposite (i.e. for the densified zone on the left side of CM-B, as illustrated in Figure 8.1). After pluviation of sand was completed, the models were saturated with a viscous fluid. More specifically, as reported by Marques *et al.* (2014a), a solution of hydroxypropyl methylcellulose in water was used as pore fluid. This fluid has a viscosity about 50 times greater than that of water, therefore, circumventing the conflict of scaling laws between dynamic time and diffusion/consolidation time (as previously discussed in Section 5.3.2.2) and allowing for the direct interpretation of the obtained results in prototype scale (e.g. Adamidis and Madabhushi, 2015). Note that the adoption of this strategy is typically termed as "viscosity scaling" (Coelho, 2007). In terms of saturation process, the pore fluid was allowed to slowly flow through the model by creating a small differential pressure between the top and base of the model – a procedure similar to that adopted in triaxial testing (Section 2.3.1.2). The saturation process was considered concluded when a given volume of fluid, determined beforehand, had been inserted in the model (Marques *et al.*, 2014a). Further details on this procedure and required equipment can be found in Stringer *et al.* (2009) and Stringer and Madabhushi (2009).

To minimise undesirable disturbances to the model, it was only loaded after the swing and the Stored Angular Momentum (SAM) actuator were attached to the centrifuge beam. As described by Madabhushi *et al.* (1998), this type of actuator uses the energy stored in a pair

of spinning flywheels connected to a rod to apply approximately sinusoidal input motions of selected amplitude, frequency and duration to the model. As the model was finally transported and placed into the swinging platform, the shallow foundations were appropriately positioned in the model. The centrifugal acceleration was subsequently slowly increased until the desired value of 50 *g* was observed (Marques *et al.*, 2014a). Before applying the intended dynamic loading, the model was left spinning for some minutes at 50 *g* until the pore pressures within the model were observed to stabilise.

Besides the evaluation of the performance of innovative hybrid techniques to mitigate liquefaction effects, this centrifuge test programme intended to assist the development of numerical tools to be used in performance-based design practice (Coelho *et al.*, 2010b).

8.3 Centrifuge model A – Adjacent shallow foundations resting on a uniform moderately loose sand deposit subjected to dynamic loading causing liquefaction

8.3.1 Brief description of the experiment and obtained results

8.3.1.1 Configuration and instrumentation of the experiment

The centrifuge model A (CM-A) intended to investigate the dynamic response of two adjacent shallow foundations resting on a uniform and saturated moderately loose deposit of Hostun sand (reported as $D_r \approx 50\%$). Figure 8.2 and Figure 8.3 illustrate the final configuration of the centrifuge experiment, including the location of the monitoring instruments, whose coordinates, both in model and prototype scale, are indicated in Table 8.1. Note that the 1.225 m-high (in prototype scale) solid steel shallow foundation located on the left side of the model is termed as “heavier”, while the 0.750 m-high (in prototype scale) solid steel shallow foundation located on the right side of the model is termed as “lighter”.

In relation to the instrumentation used in the centrifuge experiment, it can be observed in Figure 8.3 and Table 8.1 that three different vertical alignments were selected for measuring the horizontal accelerations and excess pore pressures developed in the sand deposit: $x = 10.0$ m (corresponding to the axis of the heavier shallow foundation), $x = 16.75$ m (corresponding to half distance from the axes of the shallow foundations) and $x = 23.7$ m (corresponding to the axis of the lighter shallow foundation). While data acquired at these monitoring positions might be sufficient to adequately characterise the dynamic response of the deposit, it might not provide sufficient information about potential boundary effects, which have been shown to affect the measured acceleration time-histories and transient excess pore pressures at positions close to the centrifuge walls in previous centrifuge test programmes (Coelho *et al.*, 2003; Teymur and Madabhushi, 2003).

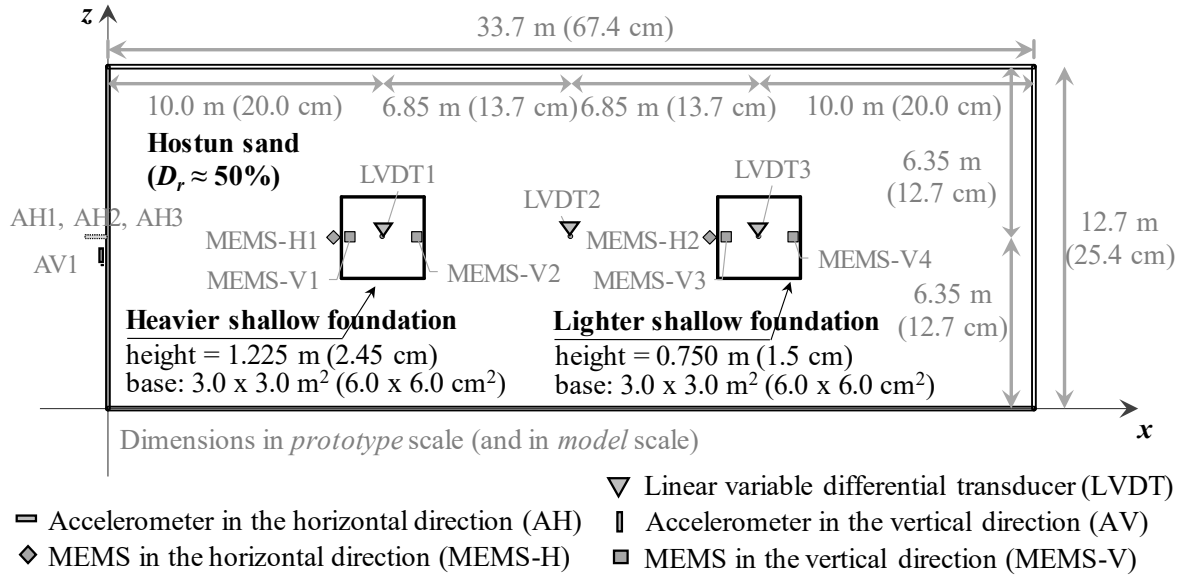

Figure 8.2 – Plan view of CM-A and location of some monitoring instruments (adapted from Marques *et al.*, 2014a).

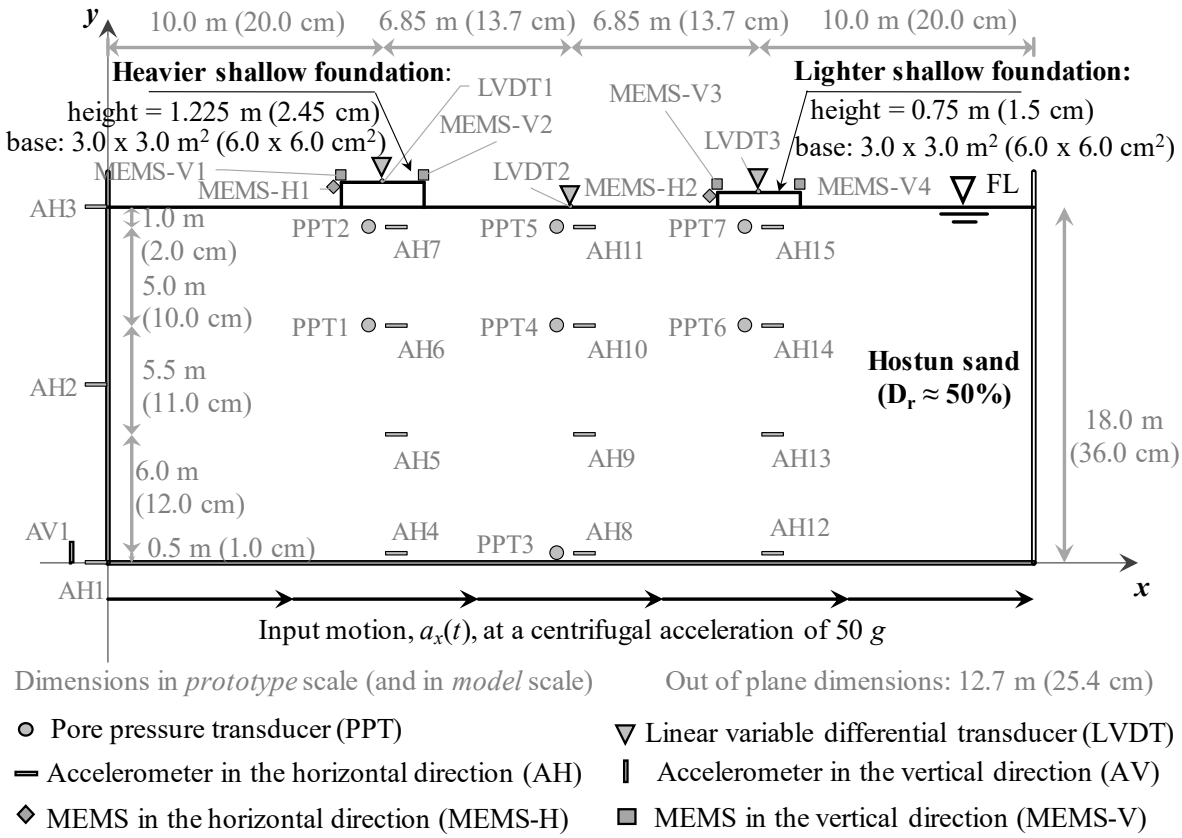

Figure 8.3 – Side view of CM-A and location of the monitoring instruments (adapted from Marques *et al.*, 2014a).

Table 8.1 – Type and positioning of the monitoring instruments used in CM-A (adapted from Marques *et al.*, 2014a).

Instrument type	ID	Model scale			Prototype scale		
		x (cm)	*y* (cm)	*z* (cm)	*x* (m)	*y* (m)	*z* (m)
Accelerometer measuring in the vertical direction	AV1	0.0	0.0	12.7	0.00	0.00	6.35
Accelerometer measuring in the horizontal direction	AH1	0.0	0.0	12.7	0.00	0.00	6.35
	AH2	0.0	18.0	12.7	0.00	9.00	6.35
	AH3	0.0	36.0	12.7	0.00	18.00	6.35
	AH4	20.0	1.0	12.7	10.00	0.50	6.35
	AH5	20.0	13.0	12.7	10.00	6.50	6.35
	AH6	20.0	24.0	12.7	10.00	12.00	6.35
	AH7	20.0	34.0	12.7	10.00	17.00	6.35
	AH8	33.7	1.0	12.7	16.85	0.50	6.35
	AH9	33.7	13.0	12.7	16.85	6.50	6.35
	AH10	33.7	24.0	12.7	16.85	12.00	6.35
	AH11	33.7	34.0	12.7	16.85	17.00	6.35
	AH12	47.4	1.0	12.7	23.70	0.50	6.35
	AH13	47.4	13.0	12.7	23.70	6.50	6.35
	AH14	47.4	24.0	12.7	23.70	12.00	6.35
	AH15	47.4	34.0	12.7	23.70	17.00	6.35
Linear variable differential transformer (LVDT)	LVDT1	20.0	38.45	12.7	10.00	19.225	6.35
	LVDT2	33.7	36.0	12.7	16.85	18.00	6.35
	LVDT3	47.4	37.5	12.7	23.70	18.75	6.35
Pore pressure transducer (PPT)	PPT1	20.0	24.0	12.7	10.00	12.00	6.35
	PPT2	20.0	34.0	12.7	10.00	17.00	6.35
	PPT3	33.7	1.0	12.7	16.85	0.50	6.35
	PPT4	33.7	24.0	12.7	16.85	12.00	6.35
	PPT5	33.7	34.0	12.7	16.85	17.00	6.35
	PPT6	47.4	24.0	12.7	23.70	12.00	6.35
	PPT7	47.4	34.0	12.7	23.70	17.00	6.35
Microelectromechanical system (MEMS) measuring in the vertical direction	MEMS-V1	17.0	38.45	12.7	8.50	19.225	6.35
	MEMS-V2	23.0	38.45	12.7	11.50	19.225	6.35
	MEMS-V3	44.4	37.5	12.7	22.20	18.75	6.35
	MEMS-V4	50.4	37.5	12.7	25.20	18.75	6.35
MEMS measuring in the horizontal direction	MEMS-H1	17.0	38.45	12.7	8.50	19.225	6.35
	MEMS-H3	44.4	37.5	12.7	22.20	18.75	6.35

In what follows, all dimensions, input motions and results are presented only in prototype scale. As mentioned before, since a viscous solution of hydroxypropyl methylcellulose in water was used as the pore fluid in the centrifuge experiments, the centrifuge test results obtained in model scale can be extrapolated to prototype scale.

8.3.1.2 Horizontal acceleration time-histories

Starting with the horizontal acceleration-time histories, Figure 8.4 depicts the results obtained for the three accelerometers positioned along the left wall of the centrifuge container (i.e. AH1, AH2 and AH3). It can be observed that, unfortunately, the accelerometer AH1, positioned at the base of the centrifuge model, malfunctioned during the test and,

consequently, the horizontal acceleration-time history effectively applied to the model was not recorded.

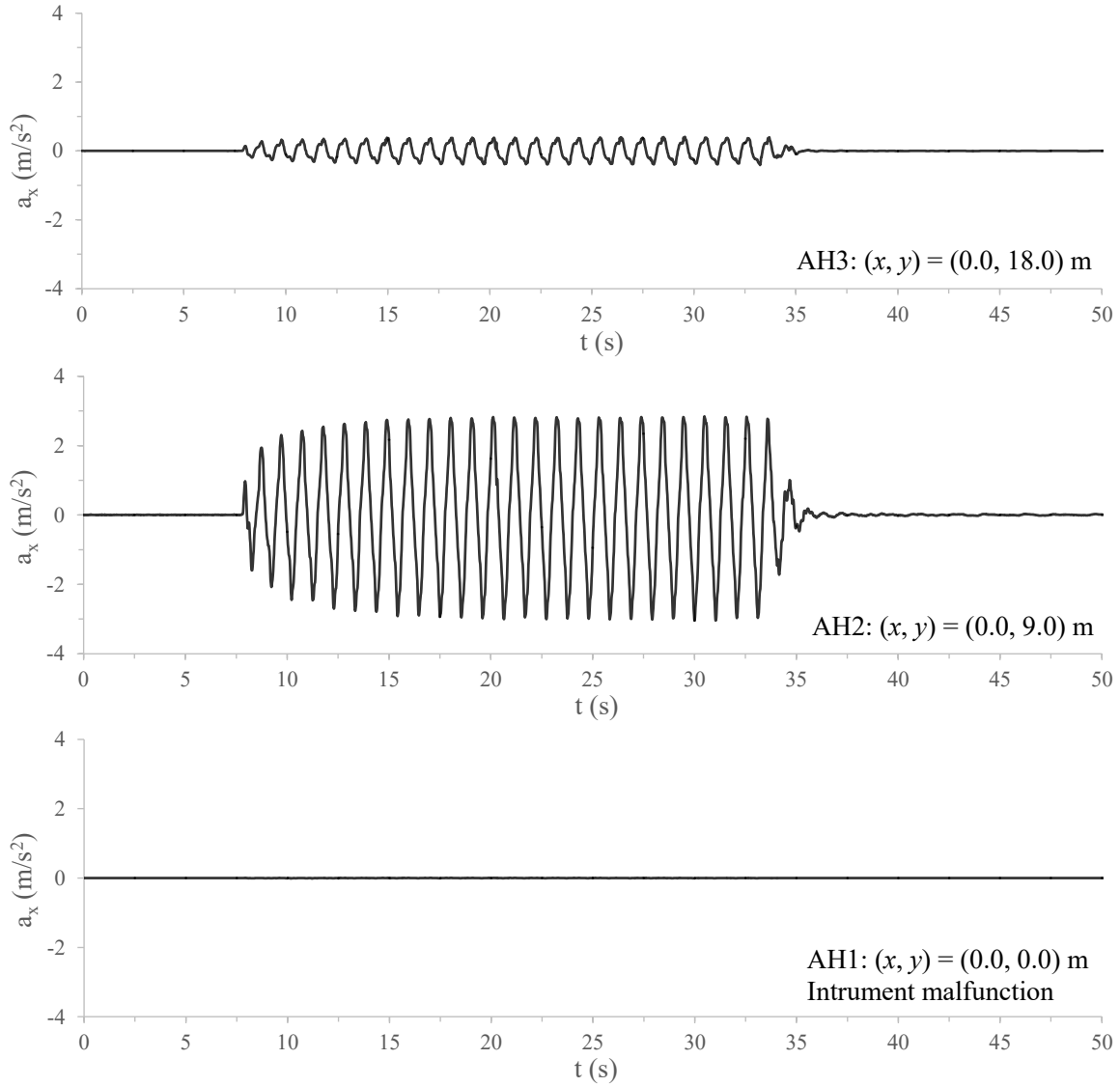

Figure 8.4 – Measured horizontal acceleration time-histories at three different monitoring positions along the left wall of CM-A.

Nevertheless, as highlighted by Marques *et al.* (2014a), since an identical input motion was intended to be applied to all performed centrifuge tests (Section 8.2.2), there is no reason to believe that the input motion applied to CM-A differed significantly from that applied to CM-B. Having that in mind, Figure 8.5 depicts the horizontal acceleration-time history recorded at the base of CM-B (i.e. at $(x, y) = (0.0, 0.0)$ m) and compares the horizontal acceleration time-histories measured in both CM-A and CM-B at the middle position of the centrifuge wall (i.e. at $(x, y) = (0.0, 9.0)$ m). Note that, as discussed in Coelho (2007), the responses measured at the walls of the centrifuge container are expected to be nearly independent of the response of the materials inside the container. In effect, providing that a time delay of about 1.05 s between the starting of the shaking in CM-B and in CM-A is amended, it can be observed in

Figure 8.5 that similar acceleration time-history trends seem to have been recorded in both experiments at $(x, y) = (0.0, 9.0)$ m.

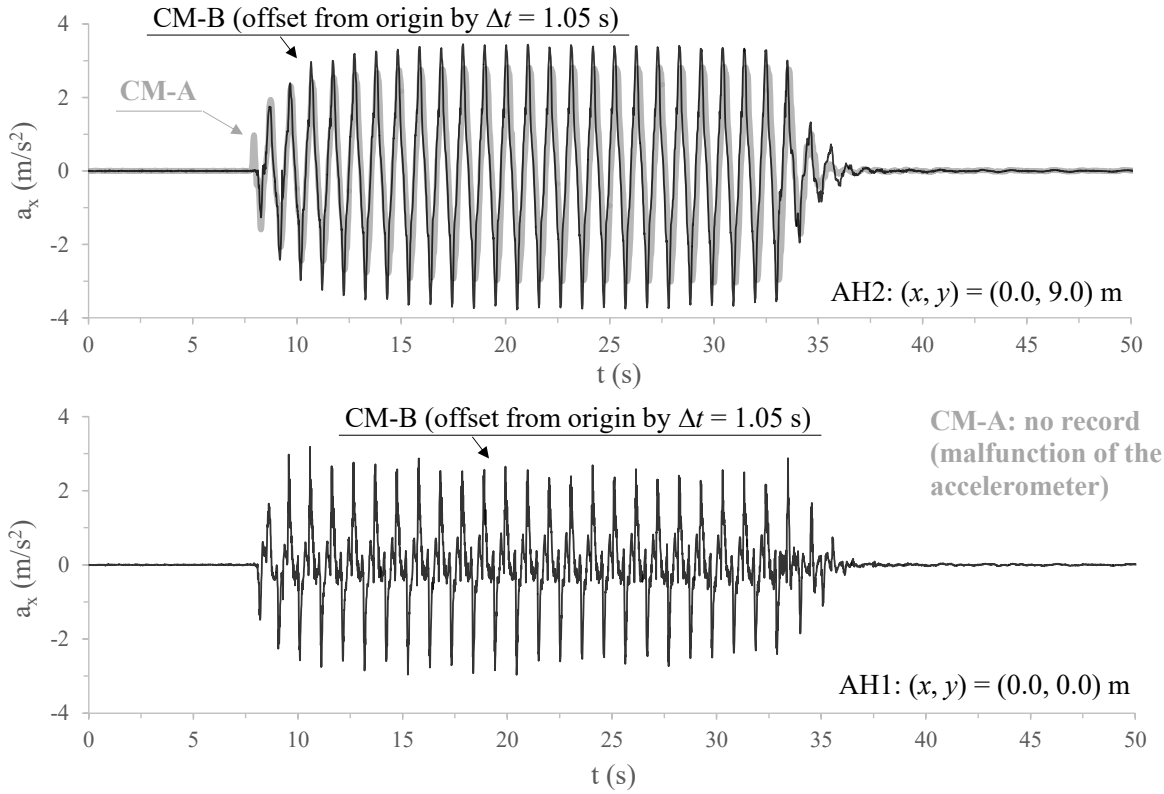

Note: Correction applied to the acceleration time-history measured in CM-B: $t_{cor} = t - 1.05$, where t is the time recorded in the experiment and t_{cor} is the time after correction.

Figure 8.5 – Recorded horizontal acceleration time-histories at two different positions along the left wall of CM-A and CM-B.

Furthermore, as shown in Figure 8.6, a closer match between the horizontal acceleration time-histories recorded in both CM-A and CM-B at $(x, y) = (0.0, 9.0)$ m can be obtained by scaling down the amplitude of the accelerations registered in CM-B by a factor of 0.806, corresponding to the ratio of the maximum amplitude registered in CM-B to that measured in CM-A at that position. Indeed, by applying a similar amplitude correction to the motion registered at $(x, y) = (0.0, 0.0)$ m in CM-B, the horizontal acceleration-time history depicted in Figure 8.6 is obtained. Since a better methodology to the estimation of the input motion of CM-A was not found, the acceleration time-history corresponding to $(x, y) = (0.0, 0.0)$ m depicted in Figure 8.6 was used for the numerical simulation of the CM-A. Therefore, in what follows, this acceleration time-history is referred to as "estimated input motion" for CM-A.

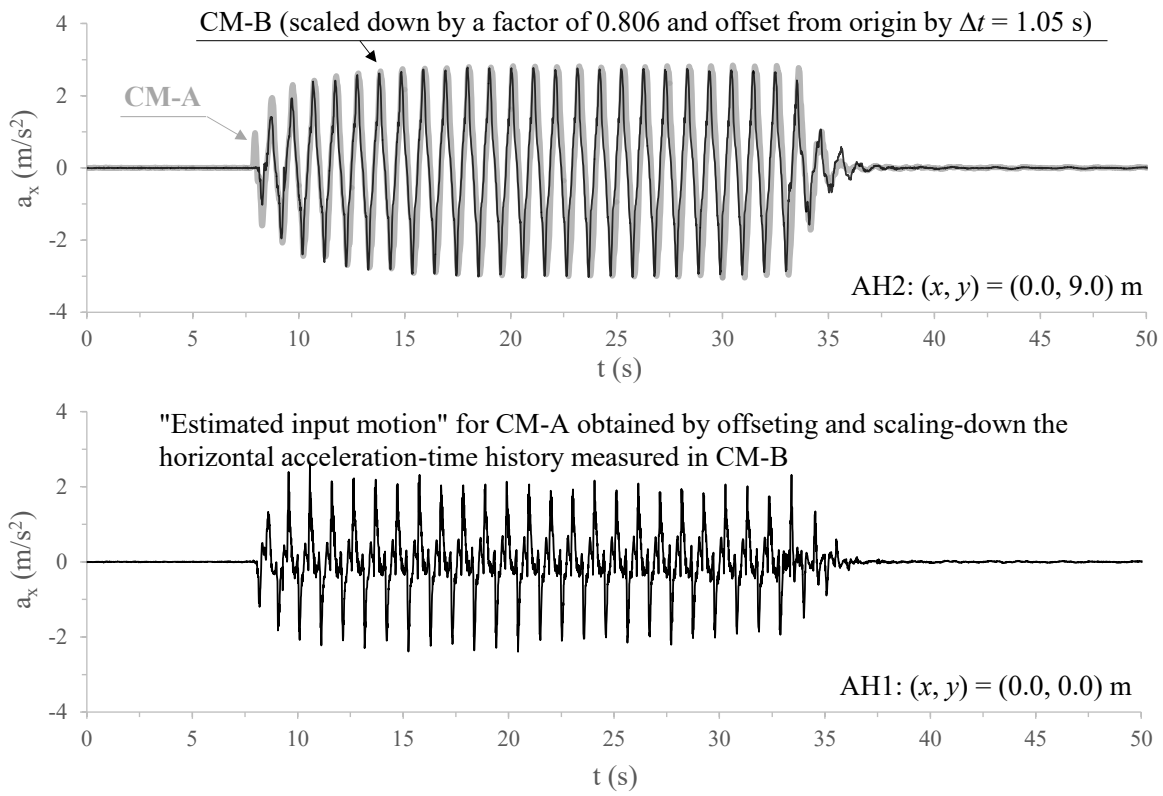

Note: Corrections applied to the acceleration time-history measured in CM-B: (1) $t_{cor} = t - 1.05$, where t is the time recorded in the experiment and t_{cor} is the time after correction; (2) $a_{cor} = 0.806\ a$, where a is the acceleration measured in the experiment and a_{cor} is the acceleration after correction.

Figure 8.6 – Estimation of the input motion for CM-A by scaling-down the amplitude of the horizontal acceleration time-histories measured in CM-B.

By observing Figure 8.6, it is apparent that the horizontal peak accelerations applied to the model were presumably smaller than the intended value of ±3.0 m/s^2. Although it can be argued that the inaccuracies inherent to the estimation of the input motion might be responsible for these lower than intended values, it should be noted that much smaller peak accelerations than intended (of about ±2.0 m/s^2, rather than ±3.0 m/s^2) were also measured in another centrifuge experiment included in the experimental programme reported by Marques *et al.* (2014a). Moreover, although a sinusoidal-type loading was specified as input, Figure 8.6 shows that local peaks were recorded in between the maximum acceleration peaks during the majority of the duration of the solicitation. In effect, by observing the corresponding Fourier Spectrum depicted in Figure 8.7, which was computed using the computer software SeismoSignal 2018 (Seismosoft, 2018), it can be concluded that the solicitation was not single-frequency as intended. Nevertheless, it can be seen that the predominant frequency matches that intended (about 1.0 Hz).

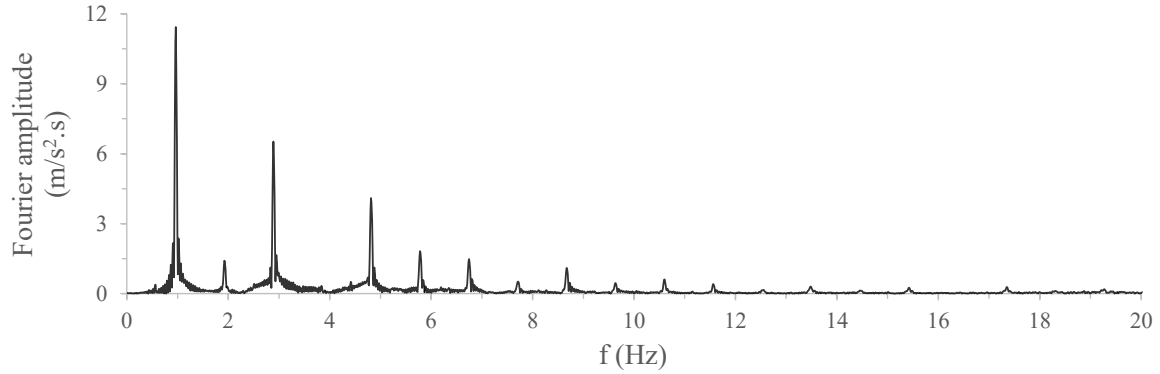

Figure 8.7 – Fourier spectrum of the estimated input motion for CM-A.

In addition, Figure 8.8 depicts the horizontal acceleration-time histories registered at several different monitoring positions within the sand deposit located along a vertical alignment coincident with the axis of the heavier shallow foundation ($x = 10.0$ m). It is interesting to observe that, during the first two cycles of loading, similar acceleration values were measured at every level, probably due to the low excess pore pressures generated within the model at this early stage (as discussed in more detailed later). Conversely, after these two initial loading cycles, the peak acceleration values appear to be attenuated, particularly at the shallower monitoring positions. This observation is consistent with the larger excess pore pressures observed at this stage of the experiment and, consequently, with the lower effective stresses, lower stiffness of the material and greater material damping.

The horizontal accelerations measured at the top of the heavier shallow foundation, $(x, y) = (8.5, 19.225)$ m, are compared with those measured at the top monitoring position within the underlying sand deposit, $(x, y) = (10.0, 17.0)$ m, in Figure 8.9. As expected, due to the large stiffness of the solid shallow foundation, it can be seen that the acceleration time-histories recorded at these two locations have similar patterns. As also expected, it is apparent that the horizontal peak accelerations recorded at the top of the shallow foundation are larger than those recorded within the sand deposit. In fact, as established by the theory of wave propagation (e.g. Kramer, 1996), when a body wave propagating through a homogeneous, isotropic and elastic medium reaches a free boundary, where stresses cannot be transmitted, the amplitude of the acceleration registered at that location tends to be double of that registered within the medium. Naturally, since, in the present case, the responses of materials (particularly of sand) are likely neither isotropic nor elastic, with both hysteretic and viscous damping likely contributing to the dissipation of energy, the horizontal peak accelerations recorded at the top of the shallow foundation are not exactly double amplitude of those registered within the sand deposit. Moreover, as discussed later, interaction effects between the two shallow foundations included in the model might have also influenced the accelerations transmitted from the sand deposit to the shallow foundations.

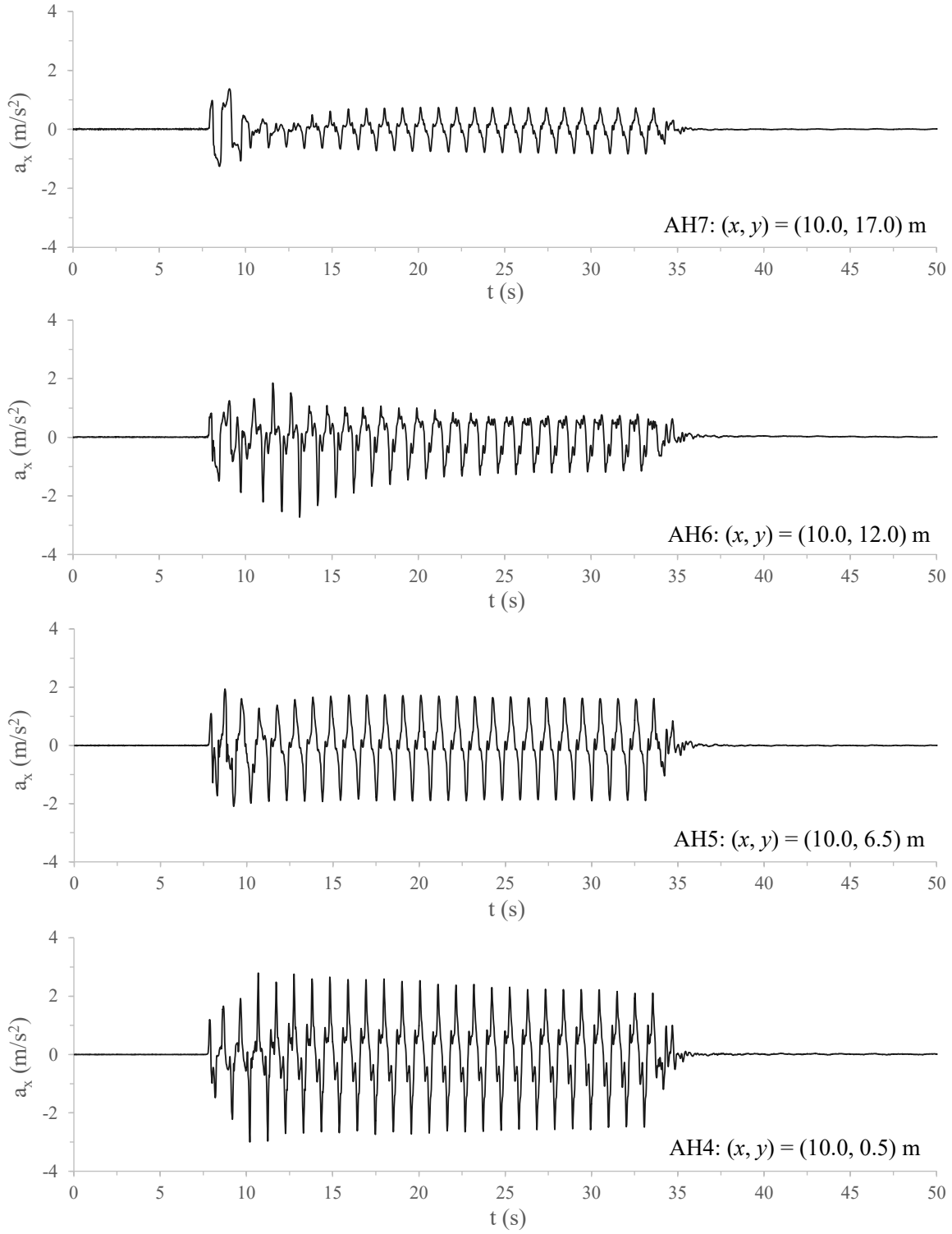

Figure 8.8 – Measured horizontal acceleration time-histories along a vertical alignment coincident with the axis of the heavier shallow foundation for CM-A.

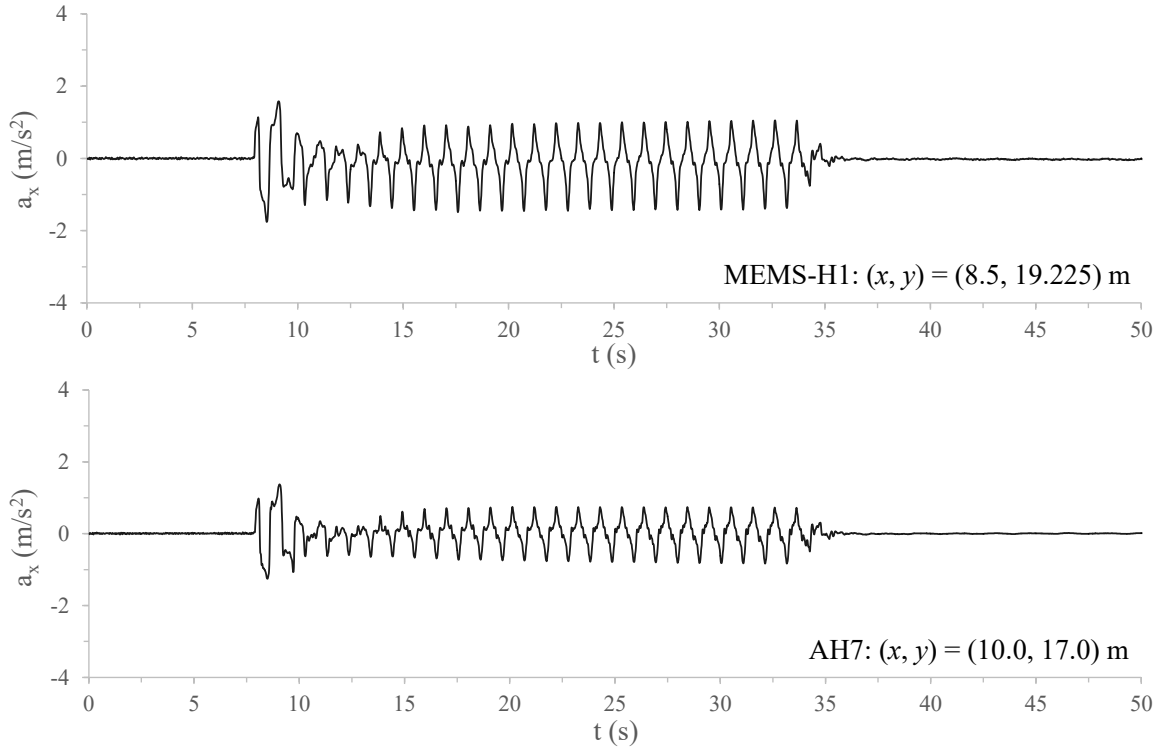

Figure 8.9 – Measured horizontal acceleration time-histories at the top of the heavier shallow foundation and underneath it for CM-A.

The Fourier spectra corresponding to the acceleration time-histories measured at the shallowest monitoring position within the sand deposit (i.e. at $(x, y) = (10.0, 17.0)$ m) and at the top of the heavier shallow foundation (i.e. at $(x, y) = (8.5, 19.225)$ m) are compared with the Fourier spectrum of the estimated input motion in Figure 8.10. Note that these Fourier spectra were, once more, computed using the software SeismoSignal 2018 (Seismosoft, 2018). As typically observed in this type of problems involving liquefaction, it is apparent that the motions recorded at the top monitoring positions (i.e. at $(x, y) = (10.0, 17.0)$ m and $(x, y) = (8.5, 19.225)$ m) are characterised by smaller peak Fourier amplitudes than those characterising the input motion. Nevertheless, the two predominant frequencies (of about 1 and 3 Hz) seem to be, in general, very similar for all three motions, suggesting that the predominant frequency content of the input motion remained practically unchanged during the centrifuge experiment. Conversely, the high frequency content of the input motion (above 10 Hz) seems practically filtered by the sand deposit during the experiment, as expected. Note that similar conclusions are obtained when comparing the motions recorded at the top monitoring positions with that recorded at the deepest position within the sand deposit (i.e. at $(x, y) = (10.0, 0.5)$ m), suggesting that the aforementioned conclusions are valid despite the approximate nature of the input motion obtained for CM-A.

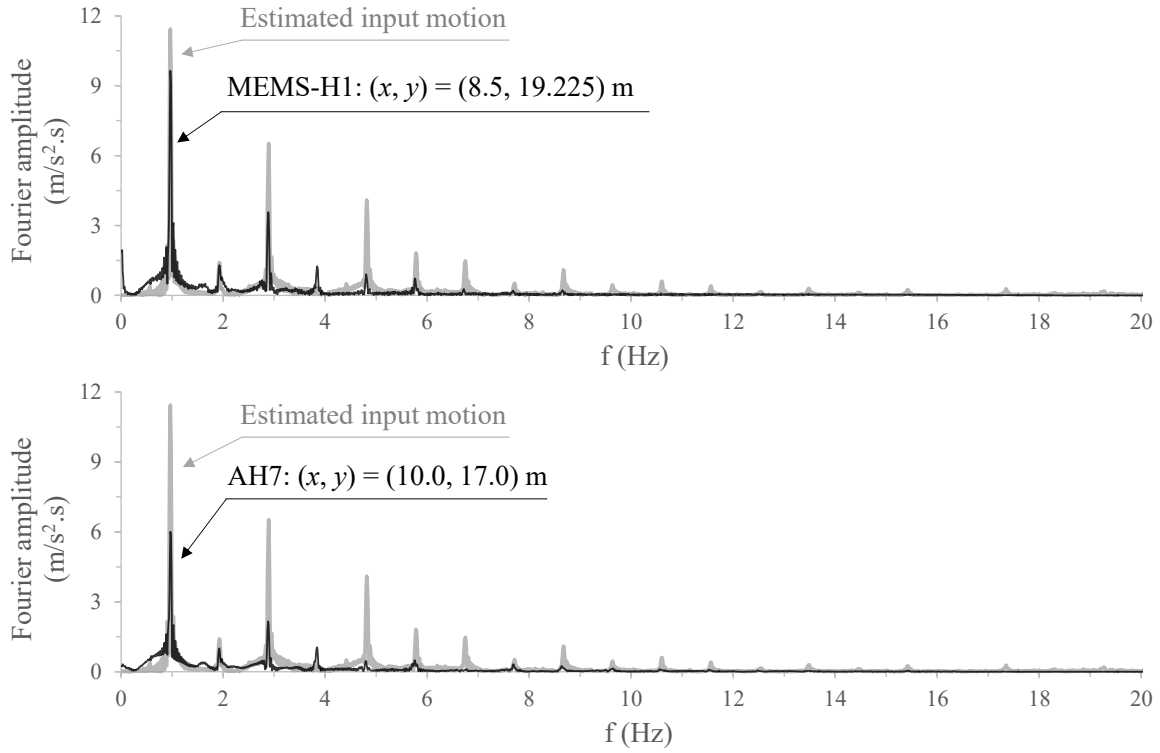

Figure 8.10 – Comparison of the Fourier spectra of the horizontal acceleration time-histories recorded at the top of the heavier shallow foundation and underneath it with that corresponding to the estimated input motion for CM-A.

Figure 8.11 depicts the horizontal acceleration-time at several different monitoring positions located along a vertical alignment coincident with the axis of the lighter shallow foundation ($x = 23.7$ m). Similar to what was observed for the heavier shallow foundation, Figure 8.11 suggests that, after the first two loading cycles, a significant attenuation of the peak accelerations occurred at shallow levels, likely due to the large excess pore pressure ratios measured during that period in the model.

In addition, Figure 8.12 compares the horizontal accelerations recorded at the top of the lighter shallow foundation (i.e. at $(x, y) = (22.2, 18.75)$ m) with those measured at the top monitoring position within the underlying sand deposit (i.e. at $(x, y) = (23.7, 17.0)$ m). Similar to what was observed for the heavier shallow foundation, it can be seen that the amplitude of the accelerations at the top of the shallow foundation are larger than those registered within the sand deposit. Note, however, that, in this case, the horizontal accelerations reached amplitudes significantly larger than double of those recorded in the underlying sand deposit. As suggested by Marques *et al.* (2012a) and explained in more detail later, interaction effects between the two shallow foundations included in the model might have strongly influenced the motions transmitted from the sand deposit to each shallow foundation.

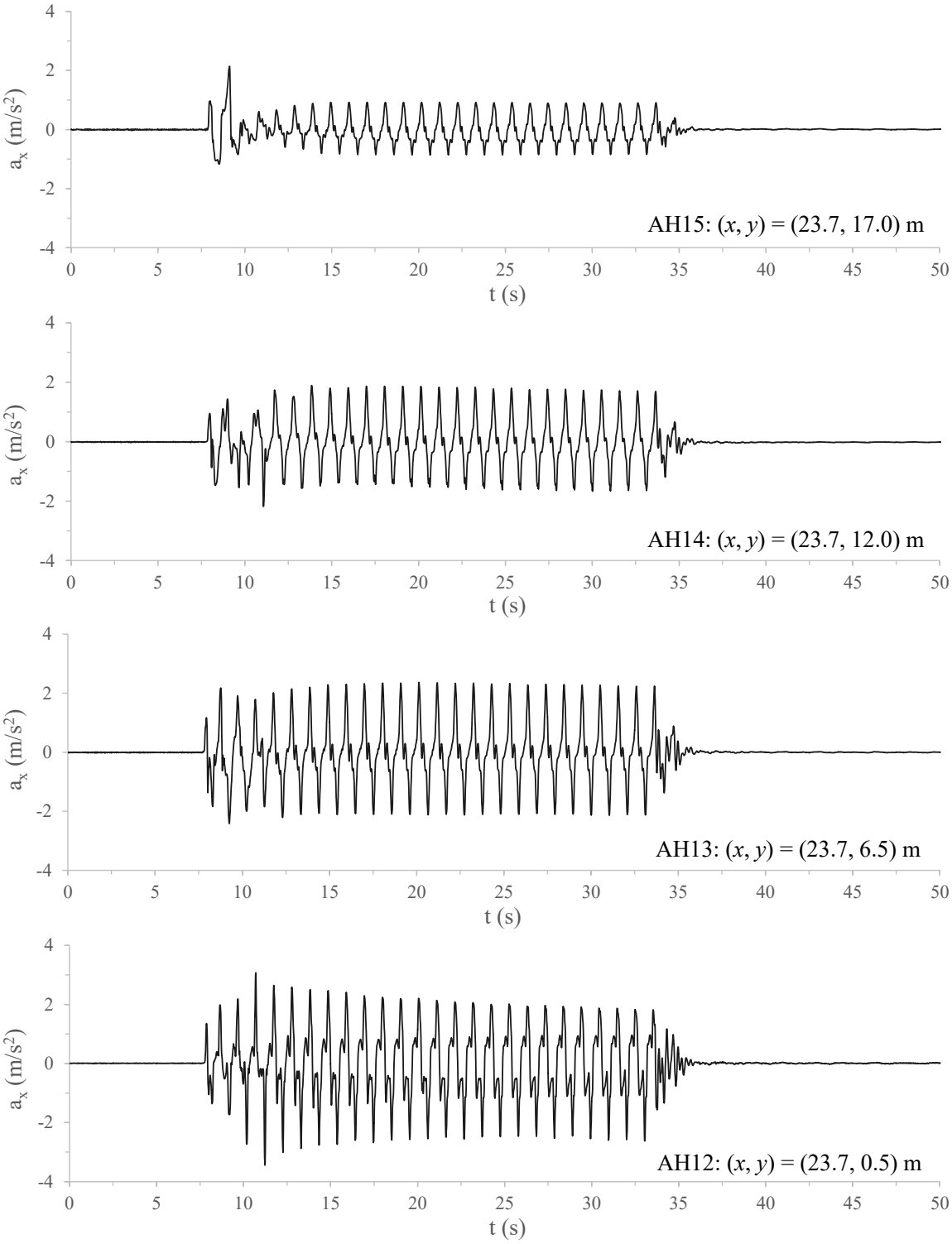

Figure 8.11 – Measured horizontal acceleration time-histories along a vertical alignment coincident with the axis of the lighter shallow foundation for CM-A.

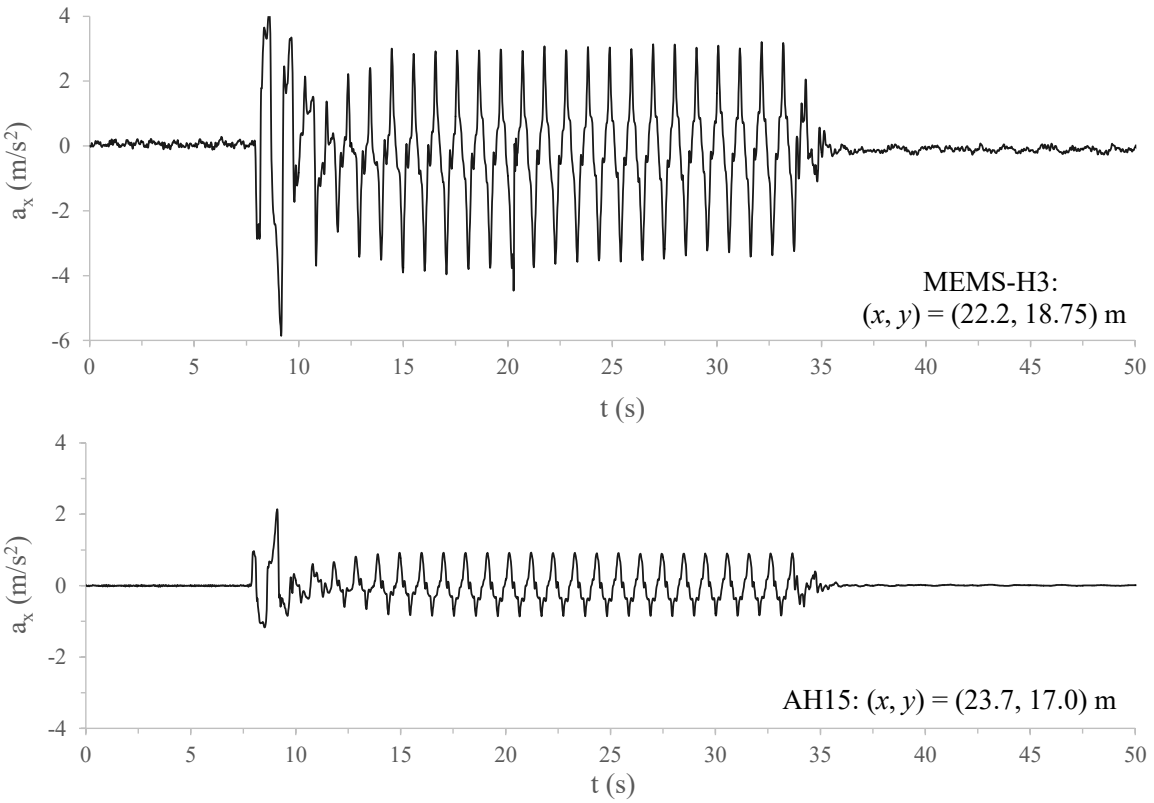

Figure 8.12 – Measured horizontal acceleration time-histories at the top of the lighter shallow foundation and underneath it for CM-A.

To gain further insight into the differences between the horizontal motions transmitted and propagated through the shallow foundations, Figure 8.13 compares the horizontal acceleration time-histories recorded at the top of the heavier and lighter shallow foundations (i.e. at $(x, y) = (8.5, 19.225)$ m and $(x, y) = (22.2, 18.75)$ m, respectively), as well as at the top monitoring positions within the sand deposit underneath the shallow foundations (i.e. at $(x, y) = (10.0, 17.0)$ m and $(x, y) = (23.7, 17.0)$ m, respectively). Their respective Fourier spectra are presented in Figure 8.14. By inspecting both Figure 8.13 and Figure 8.14, it is clear that much larger peak accelerations (with more than double of the amplitude) were measured at the top of the lighter shallow foundation in relation to those measured at the top of the heavier shallow foundation. According to Marques *et al.* (2012a), these discrepancies can be explained by the Newton's second law of motion, which establishes that the vector sum of the forces acting on an object is equal to the mass of that object multiplied by the acceleration of the object. Based on this law and assuming that similar forces were transmitted to the base of both shallow foundations, the authors concluded that the amplitude of the accelerations recorded at the top of the lighter shallow foundation had to be necessarily larger than those registered at the top of the heavier shallow foundation.

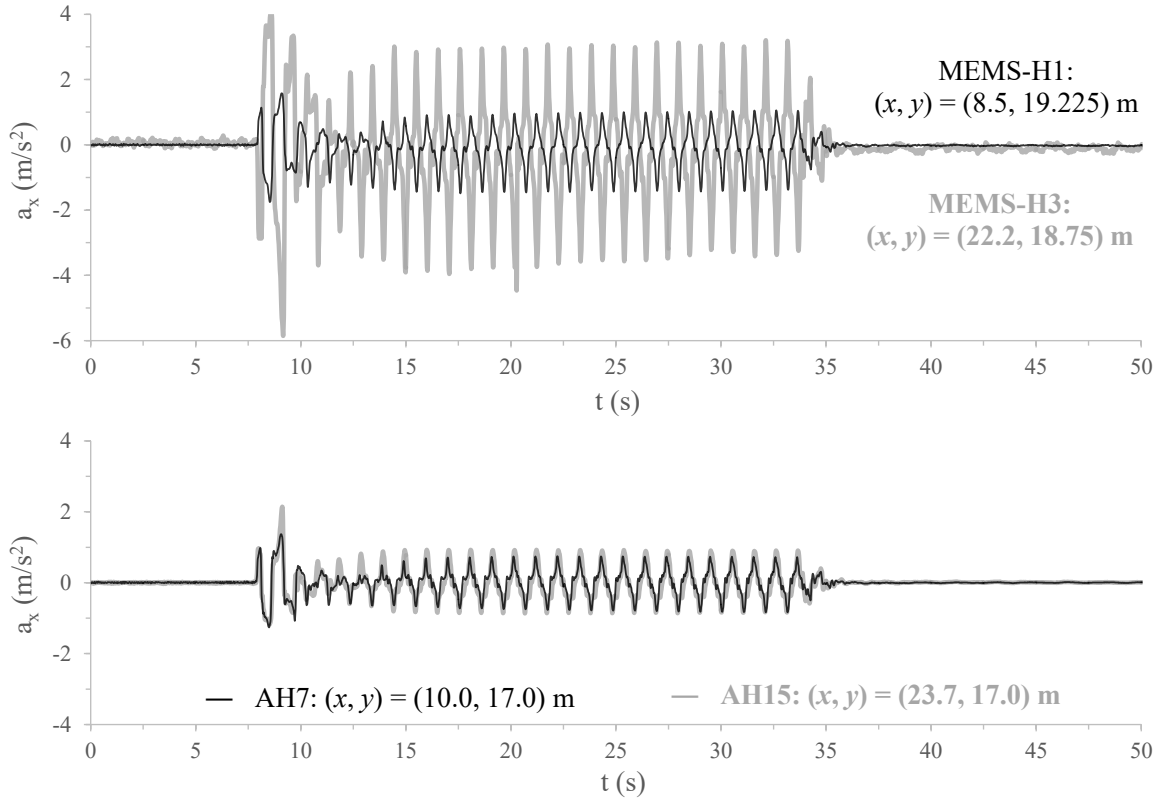

Figure 8.13 – Comparison of the horizontal acceleration time-histories measured at the top of the heavier and lighter shallow foundations and underneath them for CM-A.

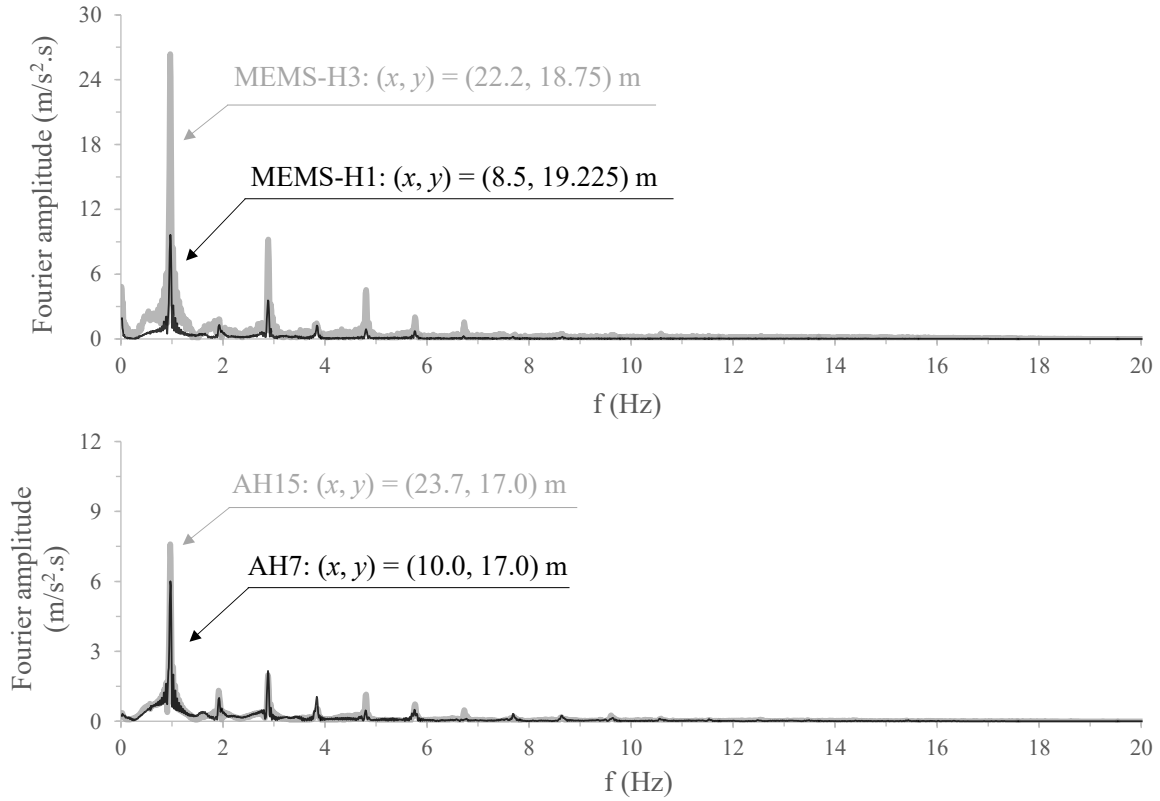

Figure 8.14 – Comparison of the Fourier spectra of the horizontal acceleration time-histories measured at the top of the heavier and lighter shallow foundations and underneath them for CM-A.

Still regarding the results presented in Figure 8.13 and Figure 8.14, three additional aspects are noteworthy. Firstly, it can be seen that very similar horizontal acceleration time-histories were registered within the sand deposit underneath both shallow foundations, suggesting that the different vertical stresses induced by the lighter and heavier foundations in the underlying sand deposit had little impact on this aspect of the measured response (Marques *et al.*, 2012b). Secondly, it is apparent in Figure 8.13 that the horizontal acceleration-time histories recorded at the top of the shallow foundations differ from each other not only in terms of amplitude, as mentioned before, but also in terms of instants of time at which the maximum peaks occurred, indicating that the shallow foundations oscillated (in this direction) out of phase. Finally, it appears that, although having very different amplitudes, the frequency contents of the horizontal motions registered at the top of the shallow foundations are qualitatively similar.

The horizontal acceleration time-histories measured at several monitoring positions located along a vertical alignment coincident with the middle of the model ($x = 16.85$ m) are depicted in Figure 8.15. Once again, the ground motion seems to be attenuated at the two shallower monitoring positions (i.e. at $(x, y) = (16.85, 12.0)$ m and $(x, y) = (16.85, 17.0)$ m) after the first two loading cycles. Despite this fact, as observed for monitoring positions located along the axes of the shallow foundations, the two predominant frequencies of the input motions (of about 1 and 3 Hz) were, in general, preserved, as shown in Figure 8.16, which compares the Fourier spectrum of the acceleration time-history measured at the shallowest monitoring position within the sand deposit (i.e. at $(x, y) = (16.85, 17.0)$ m) with that of the estimated input motion.

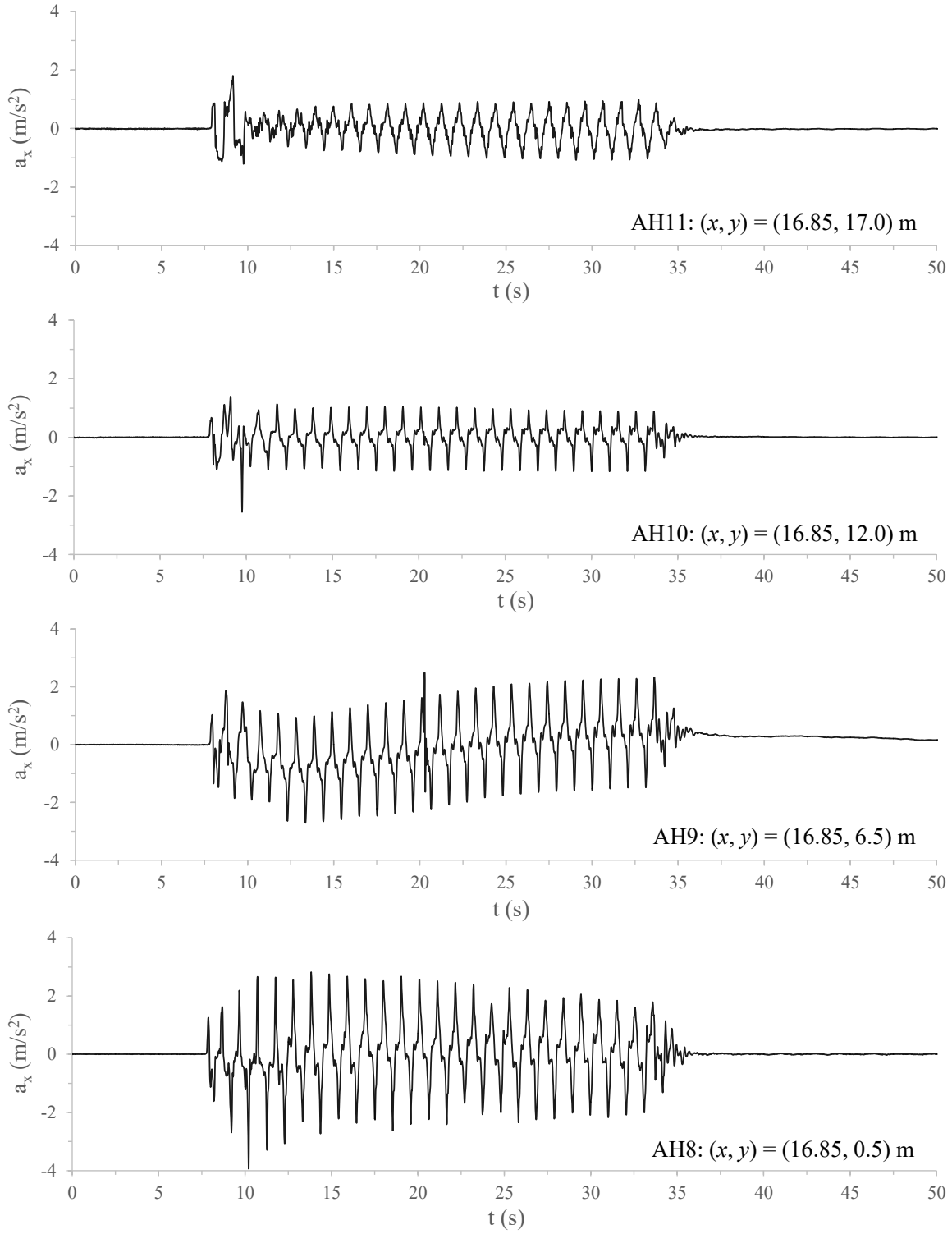

Figure 8.15 – Measured horizontal acceleration time-histories for a vertical alignment coincident with the middle of the model for CM-A.

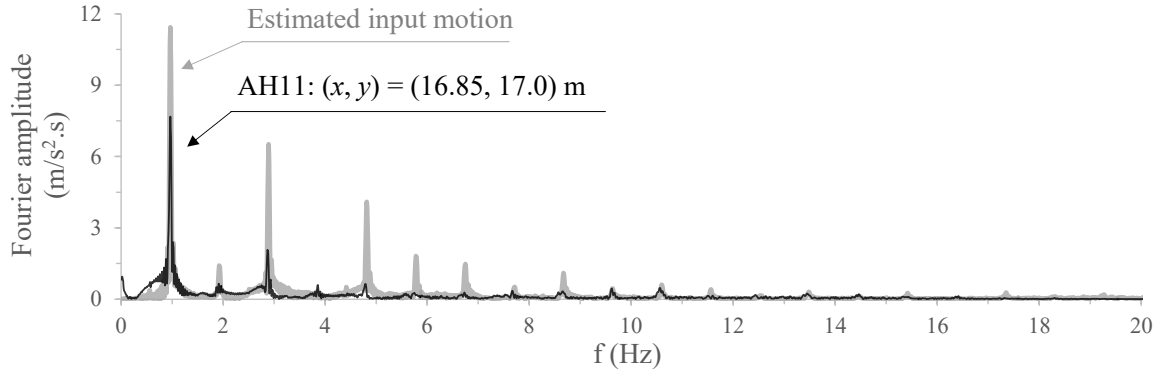

Figure 8.16 – Comparison of the Fourier spectrum of the horizontal acceleration time-history recorded at shallowest monitoring positions located along a vertical alignment coincident with the middle of the model with that of the estimated input motion for CM-A.

8.3.1.3 Vertical acceleration time-histories

The vertical acceleration time-histories recorded at the left and right top edges of the heavier shallow foundation (i.e. at $(x, y) = (8.5, 19.225)$ m and at $(x, y) = (11.5, 19.225)$ m, respectively) are compared with that recorded at the base of the centrifuge model (i.e. at $(x, y) = (0.0, 0.0)$ m) in Figure 8.17. It can be seen that the vertical input excitation is characterised by considerably smaller amplitudes (of about one third) than those characterising the estimated input horizontal motion. Despite this fact, it can be seen that large vertical peak accelerations were recorded at both top edges of the heavier shallow foundation, with amplitudes even larger than those characterising the horizontal peak accelerations measured at the left edge of the shallow foundation (Figure 8.9). Moreover, it is apparent that the vertical acceleration time-histories measured at the left and right top edges of the heavier shallow foundation appear to be in phase. Note, nevertheless, that the amplitudes of the peak accelerations are slightly different, which suggests that the shallow foundation oscillated during the experiment. This aspect can be more clearly observed in Figure 8.18, which depicts the semi-sum (i.e. average value) and semi-difference of the vertical accelerations measured at the edges of the heavier shallow foundation. Note that, while the former quantity reflects the vertical motion of the shallow foundation during cyclic loading, the latter quantity provides an indication of the rotational motion of the shallow foundation (Coelho, 2007). The obtained results suggest that the shallow foundation oscillated with a relatively constant frequency and amplitude during dynamic loading. As discussed later, this oscillation might, however, have been induced by a non-intentional rocking motion involving the entire centrifuge model (rather than an individual rocking motion of the shallow foundation).

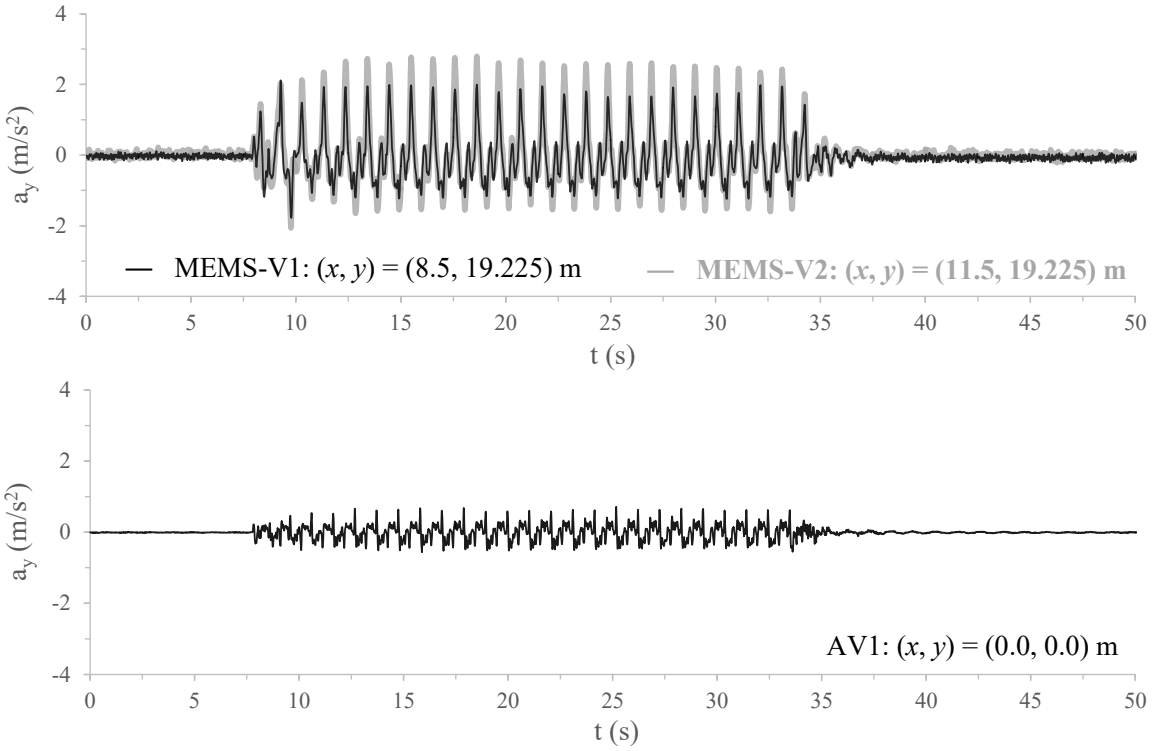

Figure 8.17 – Measured vertical acceleration time-histories at the base of the model and at the left and right top edges of the heavier shallow foundation for CM-A.

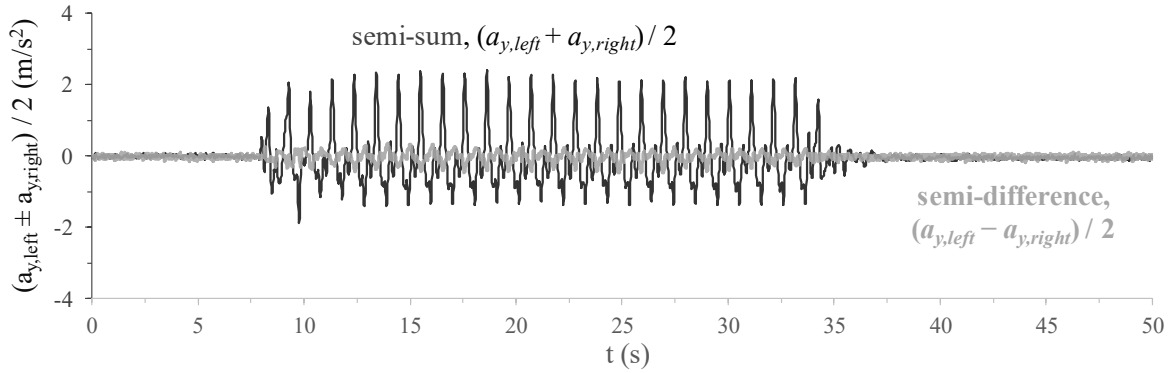

Figure 8.18 – Semi-sum and semi-difference of the vertical accelerations measured at the left and right top edges of the heavier shallow foundation for CM-A.

In addition, Figure 8.19 presents the Fourier spectra of the vertical acceleration time-histories measured at the left and right edges of the shallow foundation. It can be observed that the vertical excitation recorded at the right corner of the shallow foundation (i.e. at $(x, y) = (11.5, 19.225)$ m) is characterised by slightly larger Fourier amplitudes than those characterising the vertical excitation measured at the other edge of the shallow foundation (i.e. at $(x, y) = (8.5, 19.225)$ m), as it could also be concluded from the acceleration time-history. In terms of frequency content, practically no differences can be observed between the two Fourier spectra.

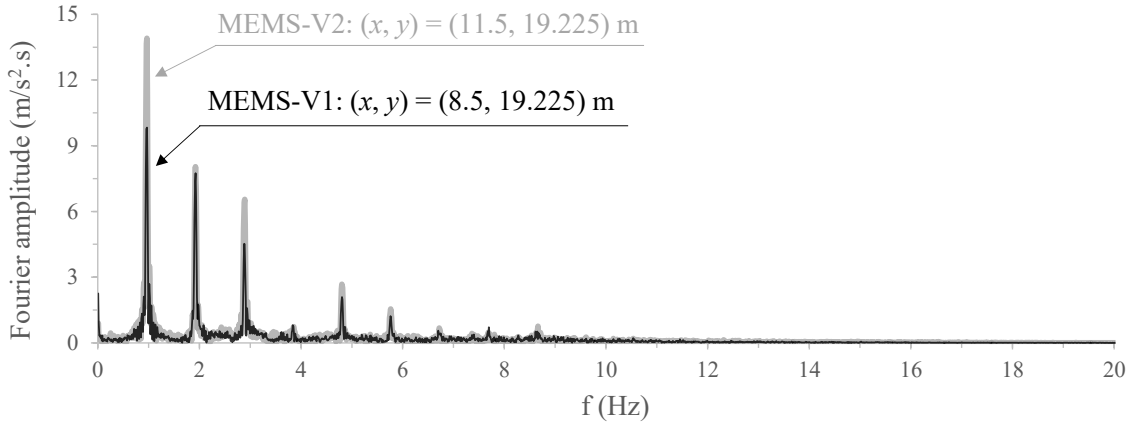

Figure 8.19 – Fourier spectra of the vertical acceleration time-histories recorded at the left and right top edges of the heavier shallow foundation for CM-A.

Similarly, Figure 8.20 compares the vertical acceleration time-histories recorded at the left and right top edges of the lighter shallow foundation (i.e. at $(x, y) = (22.2, 18.75)$ m and $(x, y) = (25.2, 18.75)$ m, respectively) with that recorded at the base of the model (i.e. at $(x, y) = (0.0, 0.0)$ m). Also in this case, much larger vertical accelerations were measured at the top of the shallow foundation than those applied to the bottom of the model.

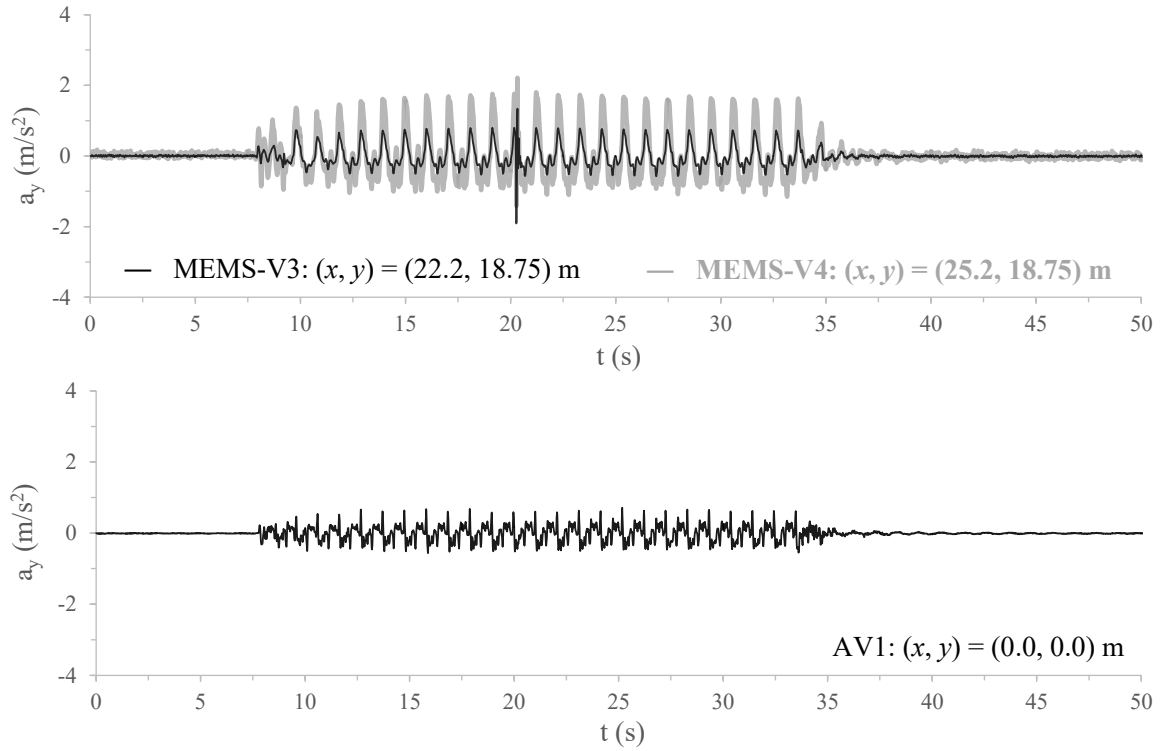

Figure 8.20 – Measured vertical acceleration time-histories at the base of the model and at the left and right top edges of the lighter shallow foundation for CM-A.

Moreover, as also observed for the heavier shallow foundation, although the vertical motions reaching the left and right top edges of the lighter shallow foundation appear to be in phase, they are characterised by different peak amplitudes, suggesting that the shallow foundation oscillated during cyclic loading. This aspect can be more clearly observed in Figure 8.21, which depicts the semi-sum and semi-difference and semi-difference of the vertical accelerations

measured at the edges of the lighter shallow foundation. As observed for the heavier shallow foundation, it seems that the lighter shallow foundation oscillated with a relatively constant frequency and amplitude during cyclic loading.

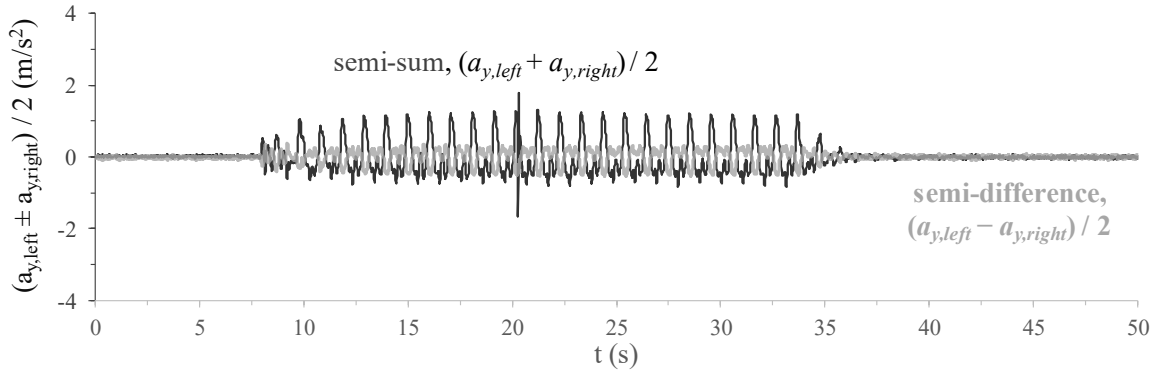

Figure 8.21 – Semi-sum and semi-difference of the vertical accelerations measured at the left and right top edges of the lighter shallow foundation for CM-A.

The Fourier spectra of the vertical motions registered at both top edges of the lighter shallow foundation are presented in Figure 8.22. Similar to what was observed for the heavier shallow foundation, the vertical excitation recorded at the right edge of the lighter shallow foundation (i.e. $(x, y) = (25.2, 18.75)$ m) is characterised by larger Fourier amplitudes than that recorded at the left edge of the shallow foundation (i.e. at $(x, y) = (22.2, 18.75)$ m), while having similar frequency content.

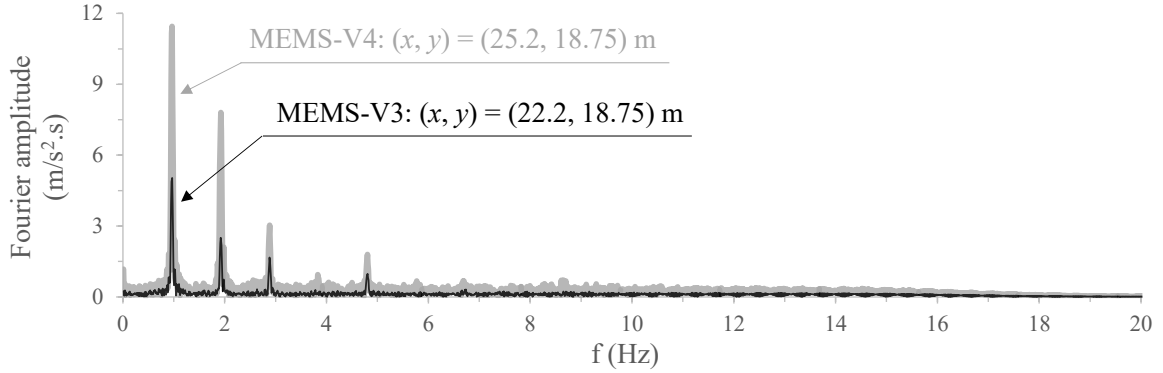

Figure 8.22 – Fourier spectra of the vertical acceleration time-histories recorded at the left and right top edges of the lighter shallow foundation for CM-A.

To gain further insight into the measured response, the vertical acceleration time-histories measured at the left top edges of the heavier and lighter shallow foundations are depicted together in Figure 8.23. Similarly, the vertical acceleration time-histories measured at the right top edges of both shallow foundations are shown together in Figure 8.24. Regardless of comparing the values registered at the left edges of the two shallow foundations or right edges, it is apparent that, although the acceleration time-histories are out of phase and have different amplitudes, they seem to be characterised by similar frequencies of oscillation, suggesting that a non-intentional rocking-type mechanism involving the entire centrifuge

model may have occurred during the experiment (Marques *et al.*, 2012c, 2014c). This global rocking mechanism might explain the oscillations observed for each shallow foundation.

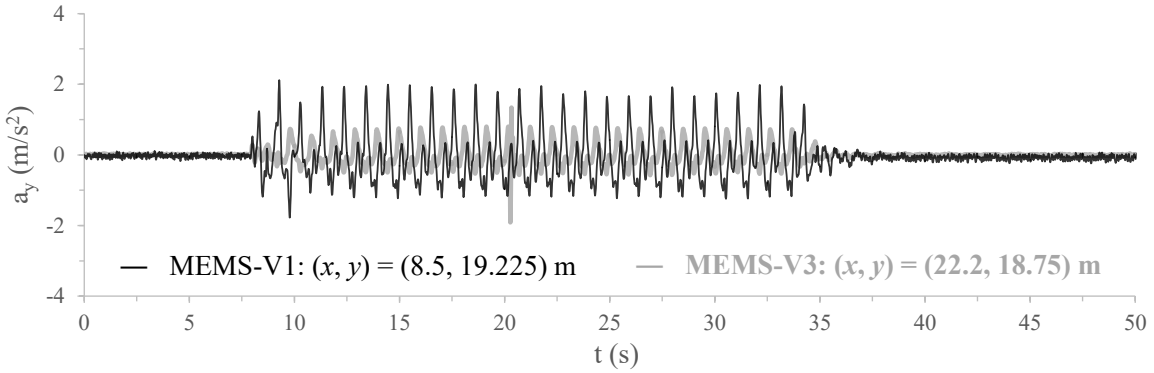

Figure 8.23 – Measured vertical acceleration time-histories at the left edges of the heavier and lighter shallow foundations for CM-A.

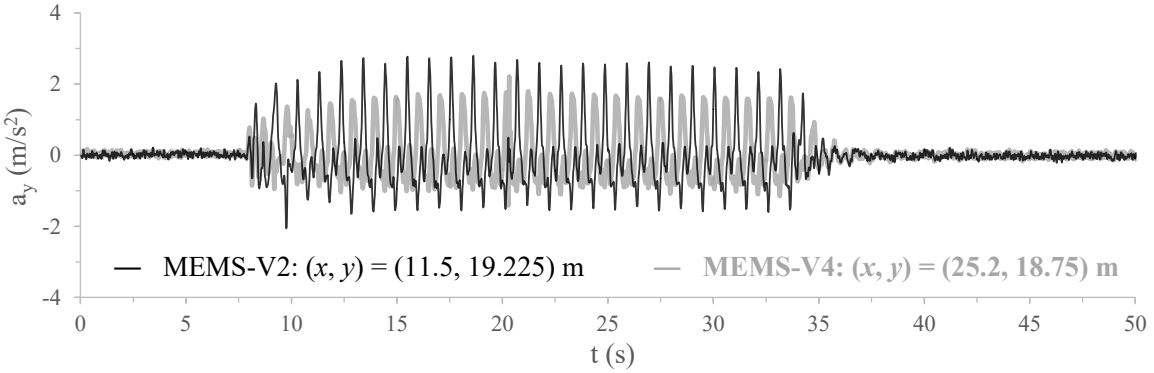

Figure 8.24 – Measured vertical acceleration time-histories at the right edges of the heavier and lighter shallow foundations for CM-A.

8.3.1.4 Excess pore pressures

Figure 8.25 compares the evolutions of excess pore pressure with time measured during dynamic loading and shortly after its end at two different monitoring levels ($y = 12.0$ m and $y = 17.0$ m) located along alignments coincident with the axes of the heavier and lighter shallow foundations ($x = 10.0$ m and $x = 23.7$ m, respectively). Complementary, Figure 8.26 depicts the long-term dissipations of the excess pore pressure at those monitoring positions. Starting by analysing the response registered at the deepest level ($y = 12.0$ m), both under the heavier and the lighter shallow foundations (i.e. at $(x, y) = (10.0, 12.0)$ m and $(x, y) = (23.7, 12.0)$ m, respectively), excess pore pressure built-up rapidly as shaking started, reaching significantly large values just after the first few loading cycles. From that moment and until the end of shaking, although considerably large oscillations of excess pore pressures were measured, the residual values (i.e. those corresponding to temporarily null shear stresses) were kept practically constant (with values close to 60 kPa). As shaking ended, the dissipation of the excess pore pressures occurred at a very slow rate until $t \approx 200$ s, probably due to the constant supply of water resulting from the upward flow of water typically observed in this type of problem when drainage is only allowed through the ground surface

(e.g. Coelho, 2007). From $t \approx 200$ s, the dissipation rate was considerably greater, with the consolidation process lasting until $t \approx 700 - 800$ s. Indeed, both during excitation and consolidation, very slight discrepancies can be observed between data recorded at these two monitoring positions (i.e. at $(x, y) = (10.0, 12.0)$ m and at $(x, y) = (23.7, 12.0)$ m), suggesting that, at this depth (of about 6 m), the influence of the different vertical stresses induced by the shallow foundations on the observed excess pore pressures was already very limited.

With respect to the excess pore pressure registered at the shallowest level ($y = 17.0$ m), a different trend from that registered at the deeper monitoring position (i.e. at $y = 12.0$ m) can be observed in Figure 8.25 and Figure 8.26, with residual excess pore pressures gradually increasing during shaking. As often observed in this type of problems (e.g. Coelho, 2007), it can be seen that excess pore pressures further increased after the end of shaking until $t \approx 250$ s, likely due to excess pore pressure migration from the zones of the sand deposit located farther from the shallow foundations to the zones under their influence. Indeed, the excess pore pressure measured at about $t \approx 250$ s is about 2.5 times greater than that measured during shaking, which might have a catastrophic impact on the bearing capacity of the sand deposit (Coelho, 2007). Moreover, it can be seen that, at this level, the dissipation of the excess pore pressures only started at $t \approx 300$ s, with stabilisation of the excess pore pressure being only observed at $t \approx 700 - 800$ s. As pointed out by Marques *et al.* (2012a), the fact that excess pore pressures were observed to stabilise with a value of about 10 kPa (rather than 0 kPa) is likely a detrimental consequence of the large settlement experienced by the transducer.

Still regarding the results registered at the shallowest level ($y = 17.0$ m), it is apparent that, although the stresses induced by the shallow foundations in the underlying sand deposit are different, the discrepancies between the responses measured underneath the heavier and lighter shallow foundations (i.e. at $(x, y) = (10.0, 17.0)$ m and at $(x, y) = (23.7, 17.0)$ m, respectively) are practically restricted to the magnitude of the oscillation of the excess pore pressures during shaking. As expected, larger oscillations were measured in the sand under the influence of the heavier shallow foundation, due to the higher effective stresses induced by this foundation.

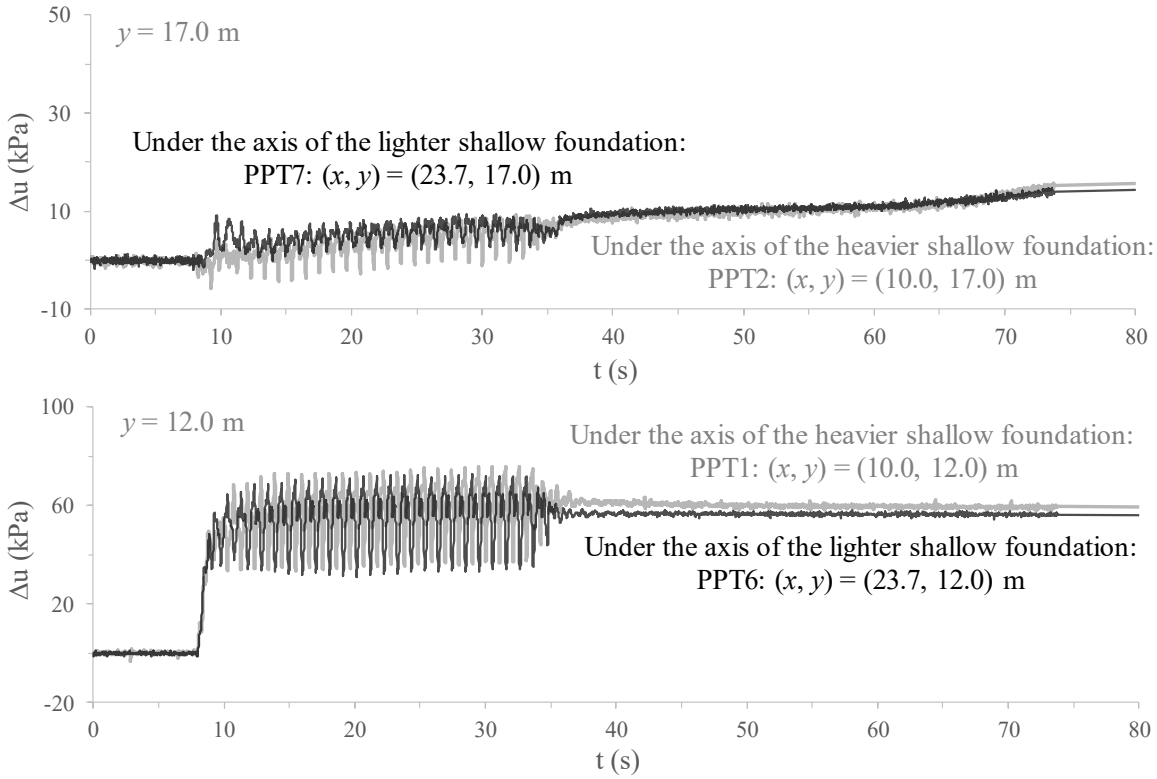

Figure 8.25 – Excess pore pressure evolution with time during dynamic loading and shortly after its end measured at two different monitoring positions located along vertical alignments coincident with the axes of the heavier and lighter shallow foundations for CM-A.

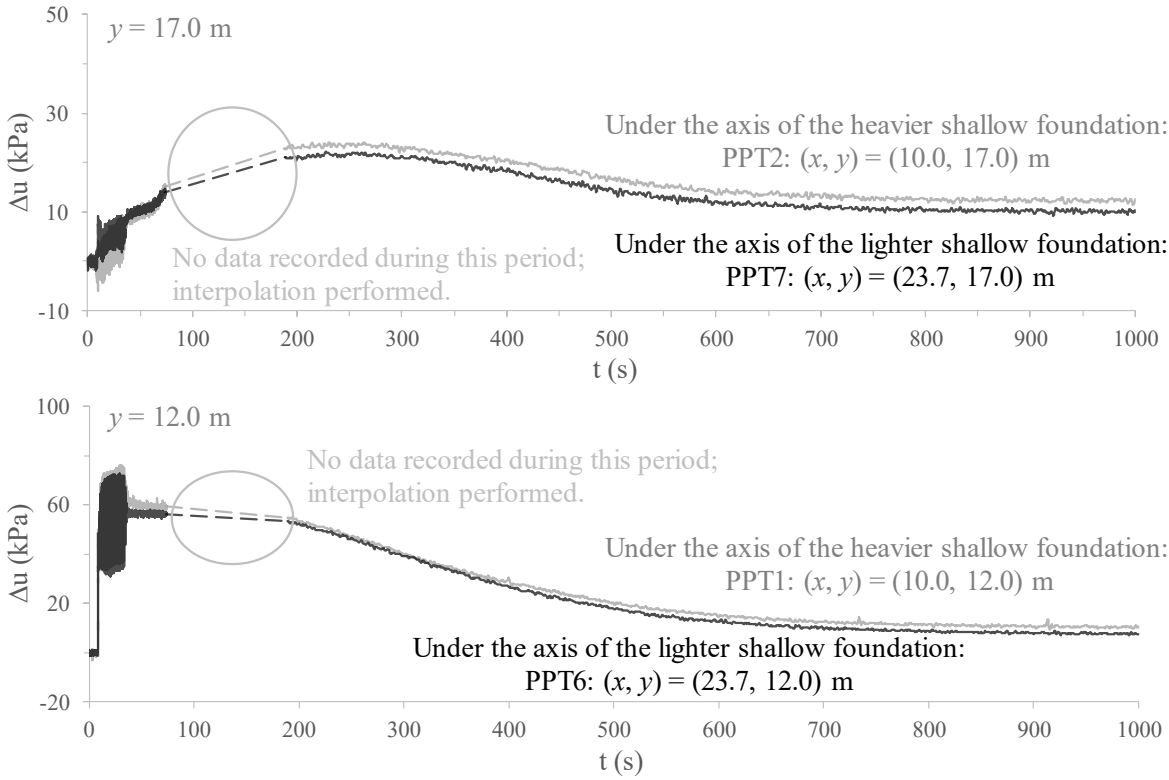

Figure 8.26 – Long-term dissipation of excess pore pressures at two different monitoring positions located along vertical alignments coincident with the axes of the heavier and lighter shallow foundations for CM-A.

In addition, Figure 8.27 compares the evolutions of excess pore pressure with time measured at three different monitoring positions located along a vertical alignment coincident with the middle of the model with those measured along a vertical alignment coincident with the axis of the heavier shallow foundation during shaking and shortly after its end. The long-term dissipations of the excess pore pressure at those monitoring positions are depicted in Figure 8.28. Perhaps surprisingly, it can be seen that co-seismic excess pore pressures registered at the shallowest monitoring position in the middle of the model (i.e. at $(x, y) = (16.85, 17.0)$ m) are similar to those measured immediately underneath the heavier shallow foundation (i.e. at $(x, y) = (10.0, 17.0)$ m). Note, however, that these results might have been detrimentally affected by the different settlements of the pore pressure transducers, as suggested by the different values of excess pore pressure registered at those locations at the end of consolidation phase (i.e. at $t \approx 700 - 800$ s). Significantly different trends are, nevertheless, observed as shaking ended (i.e. from $t \approx 40$ s), with the excess pore pressures being observed to rise significantly underneath the shallow foundation (as discussed before), while remaining practically constant in the middle of the model until the start of their dissipation (i.e. until $t \approx 300$ s). At the intermediate level ($y = 12.0$ m), excess pore pressures were observed to rapidly increase with loading both under the heavier shallow foundation (i.e. at $(x, y) = (10.0, 17.0)$ m) and in the middle of the model (i.e. at $(x, y) = (16.85, 17.0)$ m). With further loading, greater oscillations of excess pore pressure were recorded at the monitoring position located along a vertical alignment coincident with the axis of the heavier shallow foundation (i.e. at $(x, y) = (10.0, 12.0)$ m), probably due to the slightly higher initial effective stresses installed in that zone of the deposit. Moreover, it is apparent that larger residual excess pore pressures were registered at the end of shaking at $(x, y) = (10.0, 12.0)$ m than at $(x, y) = (16.85, 12.0)$ m. With respect to the deepest position ($y = 0.5$ m), pore pressure measurements were only undertaken at the monitoring position $(x, y) = (16.85, 0.5)$ m. Similar to what was observed for the intermediate level, excess pore pressures rose quickly as shaking started, reaching large values close to the initial vertical effective stress after the first few loading cycles.

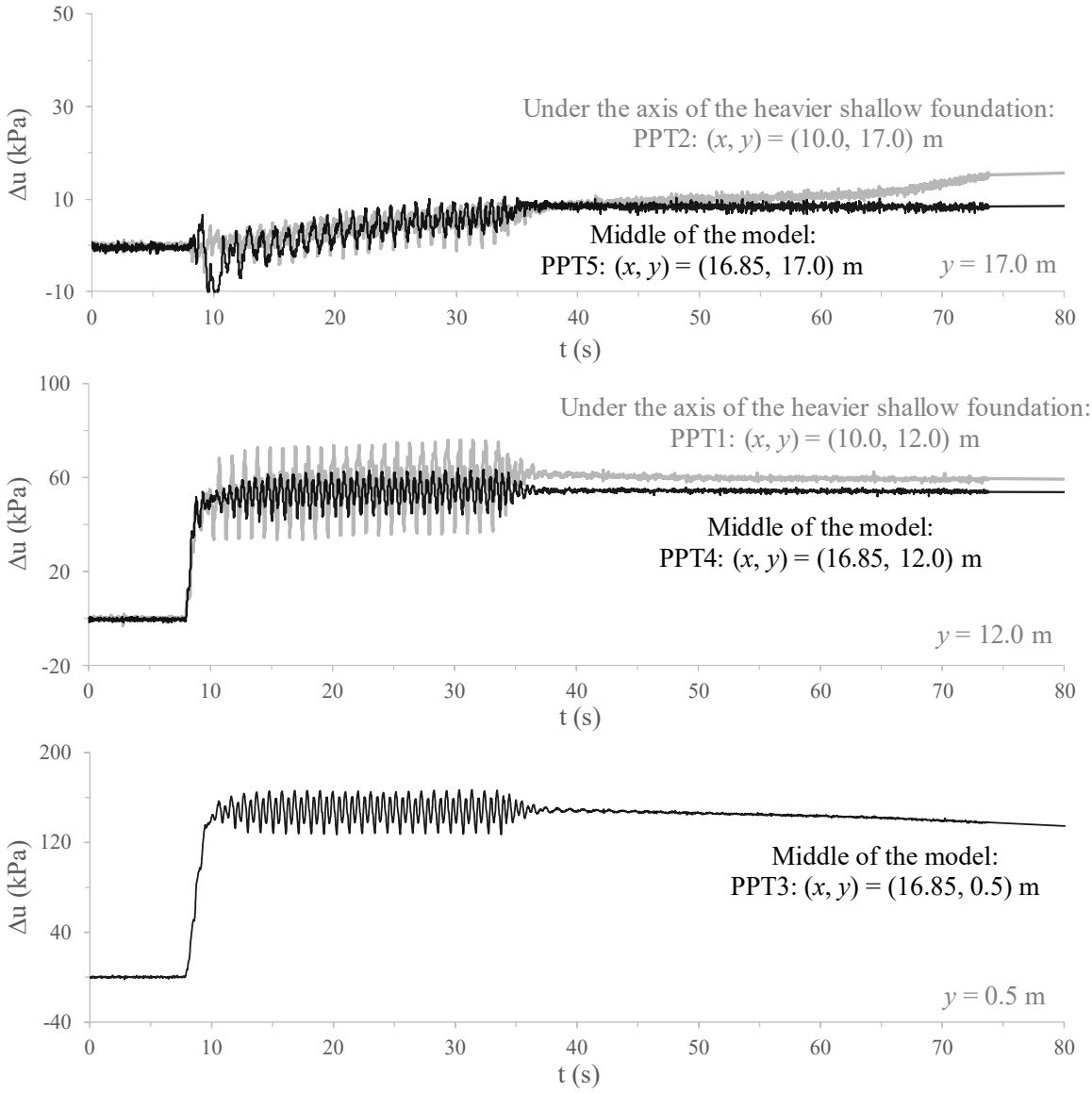

Figure 8.27 – Excess pore pressure evolution with time during dynamic loading and shortly after its end measured at three different monitoring positions located along vertical alignments coincident with the axis of the heavier shallow foundation and middle of the model for CM-A.

In terms of long-term dissipation of excess pore pressures (Figure 8.28), it can be seen that, at the deepest level ($y = 0.5$ m), where pore pressures were only measured in the middle of the model (i.e. at $(x, y) = (16.85, 0.5)$ m), dissipation of excess pore pressures started practically from the moment that shaking was over (i.e. from $t \approx 40$ s), occurring progressively until $t \approx 700 - 800$ s. Due to the upwards migration of excess pore pressure, dissipations at the shallower levels were only initiated (at least, at a significant rate) later. In particular, at the intermediate level ($y = 12.0$ m), excess pore pressures were only observed to start decreasing at a significant rate from $t \approx 200$ s, both at $(x, y) = (10.0, 12.0)$ m and at $(x, y) = (16.85, 12.0)$ m. Conversely, at the shallowest level ($y = 17.0$ m), the measured responses in sand under the shallow foundation (i.e. at $(x, y) = (10.0, 17.0)$ m) and farther from its influence (i.e. at $(x, y) = (16.85, 17.0)$ m) exhibit different trends. Specifically, while excess pore pressures continued to increase significantly after the end of shaking at the

monitoring position underneath the shallow foundation, excess pore pressures at the middle of the model remained practically constant until $t \approx 300$ s. A plausible explanation for these differences may consist of the longest drainage path associated with the position underneath the shallow foundation. Additionally, as noted before, measured excess pore pressures might have been affected by the different settlements of the transducers, with larger settlements being observed for sand underneath the shallow foundations, as detailed in the following section.

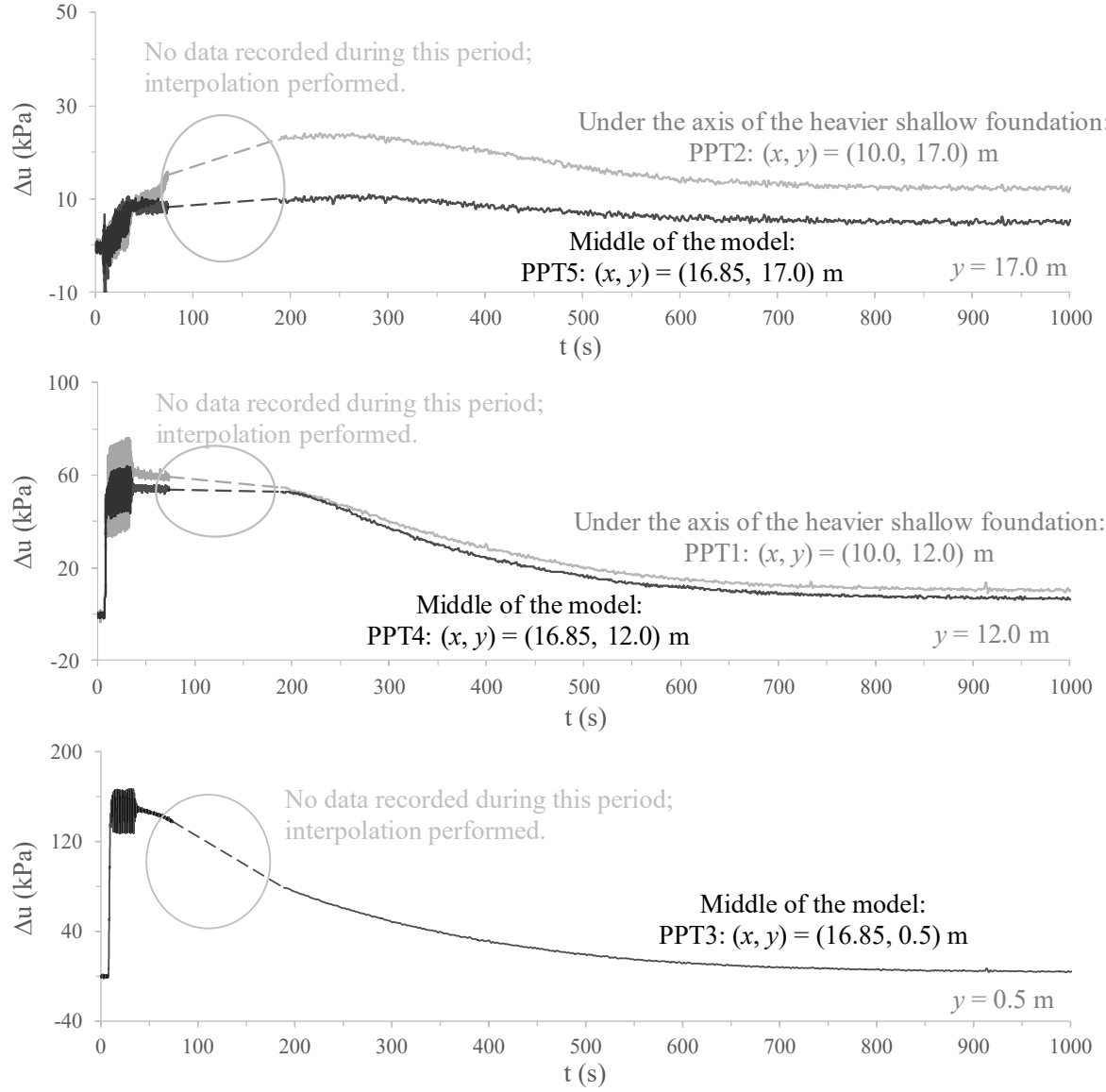

Figure 8.28 – Long-term dissipation of excess pore pressures at three different monitoring positions located along vertical alignments coincident with the axis of the heavier shallow foundation and middle of the model for CM-A.

8.3.1.5 Settlements

The final aspect to be analysed concerns the settlements measured at the top of heavier and lighter shallow foundations, respectively at $(x, y) = (10.0, 19.225)$ m and $(x, y) = (23.7, 18.75)$ m, as well as those registered at the ground surface in between both shallow

foundations (i.e. at $(x, y) = (16.85, 18.0)$ m). Figure 8.29 compares the settlements measured at these three different monitoring positions during the dynamic excitation and shortly after its end, while Figure 8.30 depicts the long-term settlements (i.e. until pore pressures were observed to stabilise).

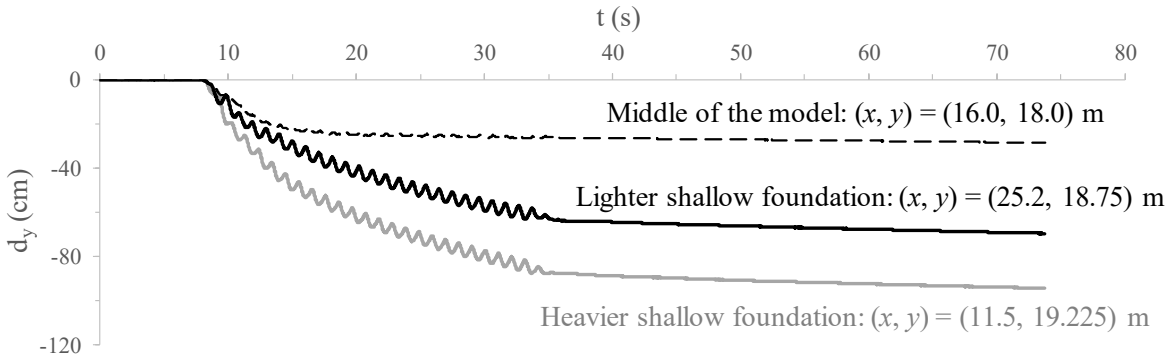

Figure 8.29 – Measured settlements at the top of the shallow foundations and at the ground surface in between them during shaking and shortly after its end for CM-A.

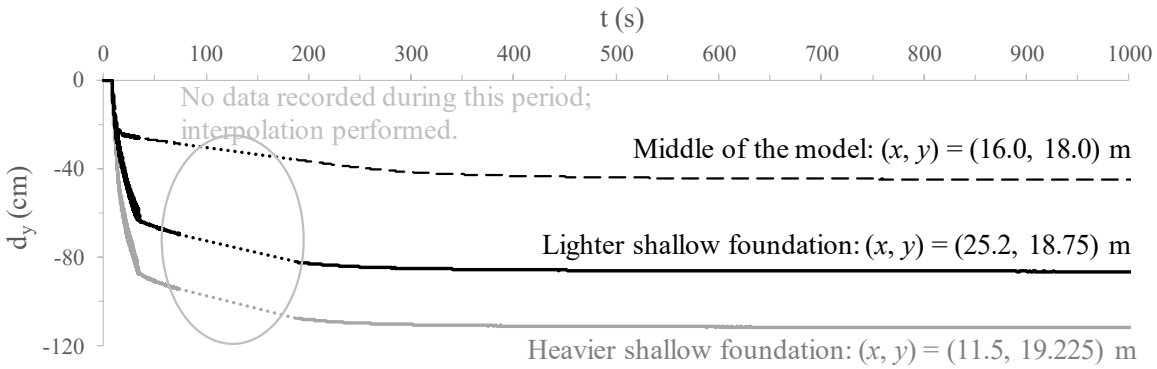

Figure 8.30 – Measured settlements at the top of the shallow foundations and at the ground surface in between them until the complete dissipation of excess pore pressures for CM-A.

As expected, due to the greater vertical stresses induced by the heavier shallow foundation in the underlying sand deposit (of about 95 kPa), in comparison to those applied by the lighter shallow foundation (of about 68 kPa), larger settlements were measured at the top of the heavier shallow foundation. Specifically, shortly after the end of shaking (at $t \approx 40$ s), a settlement of about 88 cm was measured for the heavier shallow foundation, while a smaller value of approximately 64 cm was registered for the lighter shallow foundation, meaning that, during that period, the settlement of the lighter shallow foundation is about 73 % of that registered for the heavier shallow foundation. Regarding the monitoring position situated at the ground surface in between the shallow foundations, the settlements observed throughout the experiment were much smaller than those registered for the shallow foundations, as expected. In particular, a total settlement of about 27 cm was measured shortly after the end of dynamic loading (i.e. at $t \approx 40$ s).

Moreover, it is interesting to observe in Figure 8.30 that the largest portion of the settlements occurred during the excitation. For instance, a final value of about 112 cm was measured at

the top of the heavier shallow foundation at the end of the experiment, which compares with a settlement of approximately 88 cm registered during shaking (i.e. until $t \approx 40$ s). This means that approximately 78 % of the total settlement of that shallow foundation occurred concurrently with the application of the dynamic loading, only the remaining portion of 22 % occurring after the end of shaking. Furthermore, a closer inspection of the settlements occurring solely after the end of the solicitation enables to conclude that its greatest portion effectively occurred until $t \approx 300$ s. In fact, during such period (i.e. 40 s $< t <$ 300 s), despite the cessation of dynamic loading, excess pore pressures were observed to increase in the zones of the deposit under the influence of the shallow foundations (Figure 8.28). Similar observations are valid for the lighter shallow foundation, with approximately 74 % of the settlements occurring concurrently with the application of dynamic loading.

Although settlements have been only measured at three different positions during the centrifuge experiment, post-test visual inspections were carried out after draining the model (Marques *et al.*, 2012a). The measured displacements of the ground surface and shallow foundations are depicted in Figure 8.31. Note that, since the model had to be unloaded from the centrifuge beam and drained before undertaking the post-visual measurements, the displacements shown in this figure are, in general, slightly different from those obtained immediately after the end of the experiment (and presented in the previous figures). Nevertheless, assuming that similar displacements were induced at every position of the ground surface by the drainage of the model, these post-test visual inspections may enable to roughly define a settlement profile of the ground surface. In Figure 8.31, it is interesting to observe that the shallow foundations "punched through" the sand deposit (i.e. the shallow foundations settled more than surrounding sand). It is also noteworthy that, while the heavier shallow foundation seems to have practically retained its horizontal position during the experiment, the lighter shallow foundation appears to have rotated slightly to the direction of the heavier shallow foundation. This may indicate that the presence of the heavier shallow foundation influenced the deformation mechanism of the lighter one.

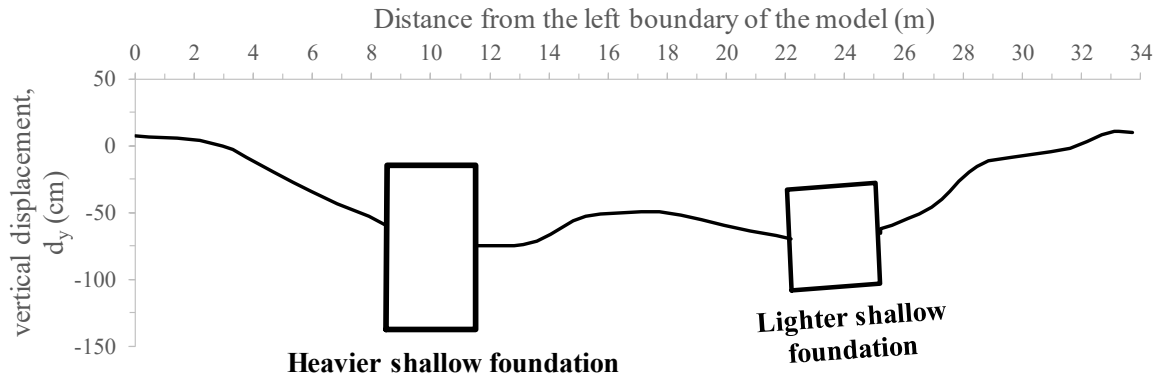

Figure 8.31 – Measured settlement profile of the ground surface and shallow foundations after the complete drainage of the model for CM-A.

8.3.2 Numerical analysis

8.3.2.1 General aspects

Given the relevance of the interaction between the pore fluid and solid phases of porous material when simulating liquefaction-related phenomena, a fully coupled non-linear dynamic finite element analysis was performed using FEMEPDYN. As described before, the complete formulation "$d^s - d^f - u$" (where d^s and d^f designate, respectively, the solid and pore fluid displacement degrees of freedom, while u designates the pore pressure degree of freedom) of the equation of the motion is implemented into FEMEPDYN, making it suitable for the simulation of a wide range of problems, from those involving quasi-static loading to very rapid loading (Zienkiewicz *et al.*, 1980; Grazina, 2009). Note that this formulation is often referred to as "$u - w - p$" (Zienkiewicz *et al.*, 1980). Eight-noded isoparametric quadrilateral elements with pore pressure degrees of freedom assigned to the four corner nodes (i.e. hybrid elements) were used to model the response of the sand deposit. Conversely, both heavier and lighter shallow foundations were considered non-porous, with eight-noded isoparametric finite elements with no pore pressure degrees of freedom (i.e. ordinary single-phase elements) being used to model their responses.

Moreover, since the use of a viscous solution of hydroxypropyl methylcellulose in water as pore fluid in the centrifuge experiments allowed for the direct interpretation of the centrifuge test results in prototype scale, the numerical simulation was performed in prototype scale.

Regarding the model geometry, although a generalised 3D formulation of the BSPM has been implemented into FEMEPDYN, the current version of the code is only able to perform 2D dynamic simulations. Therefore, a 2D plane strain simplification was adopted in the present numerical analysis, requiring a correction of the contribution of the shallow foundation to the initial stress state, with the adopted methodology being comprehensively described in the following section, together with the presentation of the obtained results. Note that, even if the code would allow for a 3D dynamic simulation, this type of calculation typically requires powerful computational resources, which, in most cases, are not available (Taborda, 2011). As a result, despite the evident 3D nature of this type of the problem, it has been usual to adopt a 2D plane strain simplification to replicate it, as exemplified by several numerical simulations of the VELACS experiments performed by different authors (e.g. Popescu and Prevost, 1993; Taiebat *et al.*, 2007; Andrianopoulos *et al.*, 2010a; Taborda, 2011). Moreover, it is important to note that the centrifuge container was solely shaken in the direction coincident with the larger horizontal dimension of the container (i.e. in-plane horizontal direction of Figure 8.3).

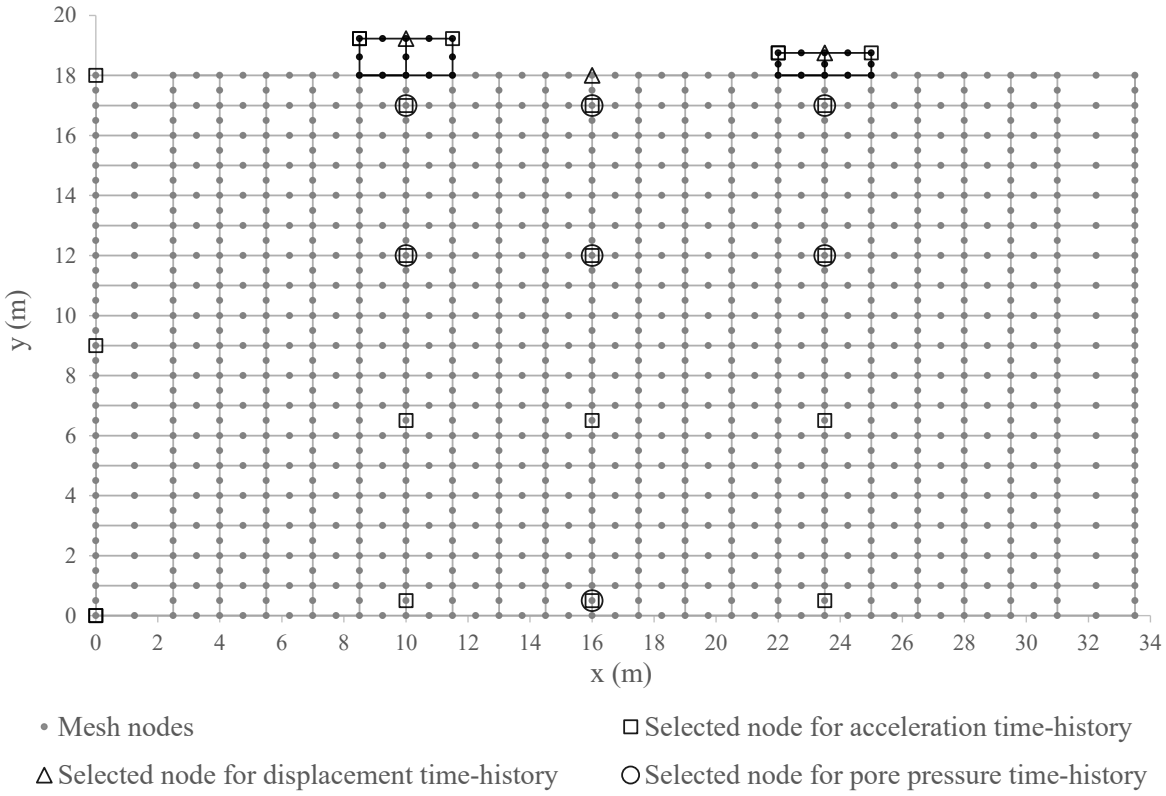

Figure 8.32 – Employed finite element mesh for the simulation of CM-A.

When performing dynamic finite element analysis, particular attention should be given to the proper choice of the size of the elements and time discretisation to prevent the filtering of relevant frequencies of the input motion (e.g. Bathe, 1996; Grazina, 2009; Taborda, 2011). Although empirical guidelines concerning the influence of these aspects have been proposed in the literature (e.g. Kuhlemeyer and Lysmer, 1973; Bathe, 1996; Haigh *et al.*, 2005), its applicability for numerical simulations of liquefaction-related phenomena seems to be limited (Taborda, 2011). In effect, the adequate selection of spatial and time discretisation likely depends on the constitutive model employed, as well as on the numerical algorithms implemented into a given FE code (Bathe, 1996; Grazina, 2009; Taborda, 2011). Therefore, prior to the simulation of CM-A and CM-B, a parametric study on the influence of these aspects was conducted. The methodology, tested cases and obtained results are detailed in Appendix D. Briefly, it was concluded that a satisfactory compromise between accuracy and computational effort may be obtained when employing elements with a size of 1.0 m and a time step of 0.0125 s. Taking that into account, the FE mesh illustrated in Figure 8.32 was adopted for the current numerical analysis. Apart from the elements located along the lateral boundaries of the model (which had a slightly larger dimension), the FE mesh adopted to model the sand deposit consisted of elements with $L \times H = 1.5 \times 1.0$ m^2 (where L is the width and H is the height). Note that, due to the likely predominant vertical propagation of shear waves, the horizontal dimension of the elements is expected to have much smaller influence on the analysis than the vertical dimension of the elements, thus justifying the adoption of a larger dimension to the elements in the horizontal direction. Complementary, elements with

$L \times H = 1.5 \times 1.225$ m^2 and $L \times H = 1.5 \times 0.750$ m^2 were used to model the heavier and lighter shallow foundations, respectively. In terms of time step, a constant value of $\Delta t =$ 0.0125 s was adopted. Since a total duration of 250 s was required to simulate the application of the dynamic excitation and subsequent dissipation of excess pore pressures, the adoption of $\Delta t = 0.0125$ s resulted in a total of 20 000 increments.

In relation to the time-integration algorithm used to solve the equation of motion, the generalised-α (or CH-α) method, proposed by Chung and Hulbert (1993) and implemented into FEMEPDYN by Grazina (2009), was selected. As detailed in Grazina (2009), by adopting $\alpha_f = 4/9$, $\alpha_m = 3\alpha_f - 1 = 1/3$, $\alpha = \left(1 - \alpha_f\right)^2 \approx 0.3086$ and $\beta = 3/2 - 2\alpha_f \approx 0.6111$ for the parameters controlling the algorithm, which result in a spectral radius at infinity of $\rho_\infty \approx$ 0.800 for a single degree of freedom (SDOF) oscillator, the method verifies the conditions of unconditional stability and second order accuracy, also achieving the optimal high frequency dissipation with minimal low frequency impact. As demonstrated, for example, by Kontoe (2006), Grazina (2009) and Tsaparli *et al.* (2017), this latter attribute is particularly important to mitigate the detrimental impact of spurious high frequencies of the excitation on the FE results, particularly when no Rayleigh damping is employed in the numerical analysis, which is the present case. Further details on the time-integration algorithm and its implementation into FEMEPDYN can be found in Grazina (2009).

In terms of boundary conditions, the estimated horizontal acceleration time-history shown in Figure 8.6 was prescribed at the nodes located along the bottom boundary of the mesh. Moreover, since the vertical motion was disregarded in this numerical analysis, the vertical displacements of the nodes at the bottom boundary were restricted. With respect to the lateral boundaries of the model, in order to model the flexible walls of the centrifuge container, the horizontal and vertical displacements were tied along nodes of the same height. Note that, although the model was not perfectly symmetric about a vertical axis coincident with its middle (due to the presence of shallow foundations with different heights and, therefore, different self-weights), the lateral boundaries were considered to be sufficiently far away from the zone of influence of the shallow foundations to allow for the application of this boundary condition. Note also that other dynamic boundary conditions, such as absorbent or free-field boundary conditions (refer, for example, to Kontoe (2006) for further information), are not yet available in FEMEPDYN. This means that the choice was limited to the use of tied degrees of freedom or to the application of the accelerations measured at the base of the centrifuge model, with this latter approach being, in general, more suitable for the simulation of effects of containers with rigid walls (as in VELACS model 1 and 12 – Section 5.3.2.2).

The hydraulic regime of the centrifuge test was characterised by the possibility of drainage solely through the ground surface. To simulate this aspect, conditions of no flow were applied to the bottom and lateral boundaries of the mesh, by tying the displacements in the solid and

fluid phases in the direction perpendicular to that defined by the boundary. In addition, a pore pressure boundary condition of $u = 0.0$ kPa was imposed at the corner nodes defining the top of the sand deposit (except those defining the sand-structure contact).

8.3.2.2 Material properties

The bounding surface plasticity model (BSPM) was used to model the mechanical response of the deposit of Hostun sand. Since substantial improvements of the modelled response were unfortunately not observed when using the inherent fabric component of the model to the simulation of cyclic triaxial tests, this component was not used in the present finite element analysis. This means that the set of model parameters "B.1) Original formulation", listed in Table 6.5, was adopted for this numerical simulation. Note, nevertheless, that a comparative FE analysis was performed by employing the set of model parameters "B.2) Extended formulation" (see also Table 6.5), with the obtained results being presented in Appendix E. Moreover, it should be noted that, although possible, Rayleigh damping was not introduced in the analysis, since the constitutive model already predicts the occurrence of material damping both at small strains, due to its cyclic non-linear elastic component, and at medium to large strains, mainly due to the occurrence of plasticity. For further details on this topic, please refer to Taborda (2011).

According to Marques *et al.* (2014a), the initial density of the Hostun sand deposit in CM-A was $D_r \approx 50\%$. By using the maximum and minimum void ratios experimentally determined in the present study, respectively of $e_{max} = 1.000$ and $e_{min} = 0.660$, the following initial void ratio would be obtained:

$$e = e_{max} - D_r\,(e_{max} - e_{min}) \approx 1.000 - 0.50 \times (1.000 - 0.66) \approx 0.830 \tag{8.1}$$

Different values of e_{min} and e_{max} were, however, reported by Marques *et al.* (2014a). Specifically, based on the outcome of a laboratory study on Hostun sand carried out by Mitrani (2006) at the University of Cambridge, $e_{max} = 1.067$ and $e_{min} = 0.555$ were reported, leading to the following void ratio:

$$e = e_{max} - D_r\,(e_{max} - e_{min}) \approx 1.067 - 0.50 \times (1.067 - 0.555) \approx 0.811 \tag{8.2}$$

While it is unclear which value of void ratio was effectively achieved in the model preparation, it seems more reasonable to assume that a target value of the void ratio (and not of the relative density) was used to control the air pluviation of the sand deposit. Therefore, in the present study, it was assumed that the void ratio of the sand deposit at the beginning of the centrifuge test was $e \approx 0.811$ (corresponding to $D_r \approx 56\%$, according to e_{min} and e_{max} determined in the present study).

Having defined the initial void ratio, and given the density of the solid particles of $G_s = 2.64$, the saturated unit weight, γ_{sat}, was estimated as 18.7 kN/m^3 (Equation 8.3), corresponding to a mass density, ρ, of about 1.906 g/cm^3 (Equation 8.4).

$$\gamma_{sat} = \gamma_w \frac{G_s + e}{1.0 + e} \approx 9.81 \times \frac{2.64 + 0.811}{1.0 + 0.811} \approx 18.7 \text{ kN/m}^3 \quad (8.3)$$

$$\rho = \frac{\gamma_{sat}}{g} \approx \frac{18.7}{9.81} \approx 1.906 \text{ g/cm}^3 \quad (8.4)$$

In terms of the hydraulic conductivity of the sand deposit, Equation 8.5, proposed by Lauer and Engel (2005) for Hostun sand, was employed. It is perhaps important to note that the main physical characteristics of Hostun sand used in the laboratory testing programme reported in Lauer and Engel (2005), such as particle size distribution, grain shape and density of solid particles, are very similar to those characterising Hostun sand used in the present study (Section 2.2). Furthermore, the values of the minimum and maximum void ratios reported in Lauer and Engel (2005), respectively $e_{min} = 0.65$ and $e_{max} = 1.03$, are also very close to those experimentally determined in the present study ($e_{min} = 0.66$ and $e_{max} = 1.00$, respectively). Since the physical properties have a great influence on the hydraulic conductivity of sandy materials – as suggested, for instance, by the Hazen and Kozeny-Carman's empirical formulas (e.g. Carrier III, 2003) – , the results presented in Lauer and Engel (2005) were considered more representative of the characteristics of Hostun sand used in the present study (including in the centrifuge experiments) than those obtained in other experimental studies (e.g. Mokni and Desrues, 2013). In addition, it should be noted that, since no information was available on the hydraulic conductivity anisotropy of the material, a single value was used to define the hydraulic conductivity in both horizontal and vertical directions (i.e. $k_x = k_y$ was considered in the present study).

$$k_x = k_y = (6.1\, e - 1.3) \times 10^{-4} = (6.1 \times 0.811 - 1.3) \times 10^{-4} \approx 3.65 \times 10^{-4} \text{ m/s} \quad (8.5)$$

In relation to the solid steel shallow foundations, a simple isotropic linear elastic model was used to model their responses. This model requires only two parameters, with a shear modulus of $G = 76.9$ GPa and a Poisson's ratio of $\nu = 0.30$ (i.e. typical stiffness characteristics of steel) being, in this case, specified. For consistency, the mass density of this material, ρ, was estimated based on the weight of the shallow foundations required to apply to the underlying sand deposit the corrected value of the vertical stress, $\Delta\sigma_v^*$, during the generation of the initial stress state (as described in detail in the following section):

$$\rho = \frac{\Delta\sigma_v^*}{g\, h} \quad (8.6)$$

where g is the acceleration of gravity ($g \approx 9.81$ m/s^2) and h is the height of the solid shallow foundation.

Finally, the only input parameter required for the pore fluid consists of its bulk modulus, with $K_f \approx 2.2$ GPa being adopted in the present study. Note that this value was also adopted by Taborda (2011) when simulating VELACS experiments, as described in Chapter 5.

8.3.2.3 Generation of the initial stress state

Although it would have been possible to simulate a similar procedure to that employed in the centrifuge test (i.e. deposition of sand, followed by the placement of the shallow foundations and finally by the increase in centrifugal acceleration), such detail would not necessarily result in a more accurate initial stress state, while bringing excessive complexity to this phase of the calculation (Taborda, 2011). Therefore, a methodology similar to that followed by this author during the generation of the initial stress state of VELACS model 12 (Section 5.3.2.2.4) was employed in the present study, consisting of the use of a gravity loading procedure, in which body (or gravity) forces are applied to the elements of the mesh, which are considered weightless at the start of the analysis – for further details on this procedure, refer, for example, to Potts and Zdravkovic (1999). Naturally, the body forces are computed by multiplying the mass density of each material by the acceleration of gravity (in this analysis, $g \approx 9.81$ m/s^2 since the model was reproduced in prototype scale). Concurrently, a hydrostatic pore pressure profile, characterised by a linear variation between a value of $u = 0.0$ kPa at the surface of the sand deposit and $u = \gamma_{pf} H = 9.81 \times 18.0 \approx 176.6$ kPa at its bottom, was introduced in the analysis. Note that, according to experimental studies on methylcellulose conducted by Stewart *et al.* (1998), the mass density of this fluid is very similar to that of water, thus justifying the use of $\gamma_{pf} \approx \gamma_w \approx 9.81$ kN/m^3 in the definition of the pore pressures. Having defined the total stresses and pore pressures, the effective stresses were computed by using Terzaghi's principle of effective stress.

Similar, once more, to the methodology used by Taborda (2011) to the generation of the initial stress state of VELACS model 12 (Chapter 5), a linear isotropic elastic model was employed during this phase of the analysis to model the responses of both sand deposit and shallow foundations, with uniform stiffness parameters being adopted to limit the occurrence of significant shear stress localisations at the sand-structure contact (which would likely have a detrimental impact on the subsequent dynamic phase). More specifically, a shear modulus of $G = 76.9$ GPa (corresponding to that assigned for the shallow foundation during the dynamic calculation) and a Poisson's ratio of $\nu = 0.333$ were selected. It is perhaps important to note that the particular value selected for the shear modulus during this initial phase is not important, since obtained displacements were reset to zero before the start of the following dynamic phase. With respect to the value of Poisson's ratio, it was particularly chosen to obtain a coefficient of earth pressure at rest (i.e. ratio of horizontal to vertical effective stresses at rest), K_0, close to 0.50 in the zones of the deposit far from the influence of the shallow foundations. In fact, by assuming zero lateral strain, these quantities are related by the theory of isotropic elasticity through Equation 8.7 (e.g. Bowles, 1996):

$$K_0 = \frac{\nu}{1.0 - \nu} = \frac{0.333}{1.0 - 0.333} \approx 0.50 \tag{8.7}$$

Moreover, to limit the occurrence of large shear stresses in the sand deposit, the Mohr-Coulomb failure criterion was used together with the linear elastic model for this material, with a friction angle of $\phi' = \text{asin}\{3.0\,M_c^c/(6.0 + M_c^c)\} = \text{asin}\{3.0 \times 1.265/(6.0 + 1.265)\} \approx 31.5°$, an apparent cohesion of $c' = 0.0$ kPa and a dilatancy angle of $\psi = 0.0°$ being adopted.

In terms of boundary conditions, standard displacement boundary conditions for static analyses were applied during this phase, consisting of restricting the horizontal displacements along the lateral boundaries of the model, as well as horizontal and vertical displacements of the nodes belonging to the bottom boundary of the model. No restrictions needed to be applied to the pore fluid, since, during this phase, the sand deposit was considered to respond in fully drained conditions (i.e. no excess pore pressures were generated in the deposit during this phase).

Clearly, the aforementioned methodology implies that the mass densities of all materials are known beforehand, allowing for the determination of the body forces of each element according to the mesh geometry. As explained before, due to impossibility of reproducing the 3D nature of the problem in a 2D plane strain analysis, a procedure is required to estimate the value of the mass density of the strip shallow foundations resulting in a stress state similar to that computed in a 3D analysis. Although other strategies could have been followed (such as using another FE code to perform comparative 2D plane strain and 3D analyses), in the present study, the solutions of the theory of elasticity were employed to obtain a comparison between the vertical stress change in the interior of a homogeneous, isotropic and elastic semi-infinite space induced by a vertical load uniformly distributed over a square 3.0×3.0 m^2 area (corresponding to the base of both heavier and lighter shallow foundations) and that imposed by a vertical load uniformly distributed over a 3.0 m-wide strip area (corresponding to the 2D plane strain assumption). In particular, while the solutions derived by Carothers (1920) were directly used to determine the vertical stress increment induced by the strip loading in any point of a domain, a more elaborate procedure was required to determine the vertical stress increment induced by the square loading. Specifically, after applying the solutions derived by Giroud (1970) to determine the vertical stress change under the corner of the square 3.0×3.0 m^2 loaded area, the method of superposition (which is valid for a homogeneous, isotropic and elastic semi-infinite space) was employed to determine the vertical stress change in other points of the domain. For brevity, and taking into account that the analytical solutions derived by Carothers (1920) and Giroud (1970) are widely published in the literature (e.g. Poulos and Davis, 1974), the mathematical expressions are not presented here.

Figure 8.33 depicts the elastic vertical stress increment normalised by the magnitude of the surface load obtained for three different vertical alignments coincident with the centre, middle right point and right extremity of the loaded area (which, for the heavier shallow foundation, coincide with $x = 10.0$, 10.75 and 11.5 m, respectively, while, for lighter shallow

foundation, coincide with $x = 23.5$, 24.25 and 25.0 m, respectively). It can be seen that, apart from the elevation at which the load is applied (i.e. at $y = 18.0$ m), for which identical values are obtained for both square and strip loading, the vertical stress increment induced by the strip loading is consistently larger than that induced by the square loading, as expected. Furthermore, it is apparent that the largest discrepancies in terms of normalised stresses between both sets of data is observed for levels in the range of $15.0\text{ m} \geq y \geq 10.0\text{ m}$ (i.e. approximately from 3.0 m to 8.0 m below the loaded area).

Naturally, the different stress changes imposed by the square and strip loadings are likely to induce different settlements in the sand deposit. By using, once more, the solutions of the theory of elasticity (e.g. Timoshenko and Goodier, 1951; Bowles, 1996), it is possible to obtain a comparison of the immediate settlements to be expected when vertical uniform square and strip loadings are applied at the surface of an homogeneous, isotropic and elastic semi-infinite space. Note that, according to those analytical solutions (please refer to the aforementioned references for further details), the settlement is a function of the value of the loading, the dimensions of the loaded area, the base embedment depth (which, in this case, is null), the thickness of the deposit and its elastic stiffness properties (e.g. shear modulus and Poisson's ratio). Nevertheless, since the intention is solely to compare the ratio of the settlements produced by different loading types, it should be noted that the exact values of the elastic stiffness parameters adopted in the analysis are not relevant, providing that identical values are employed in both calculations (i.e. for the two different loading types). Similarly, the precise value of the load is not important, providing that a unique value is used in both computations. In relation to the thickness of the deposit, as suggested by Bowles (1996), rather than using its entire thickness ($H = 18.0$ m), it was assumed, in both computations, that the influence of the thickness of the deposit is limited to a depth of about $H_{infl} = 5\,B$, where B is the width of the foundation. Since $B = 3.0$ m, it follows that $H_{infl} = 15.0$ m was considered in the present study.

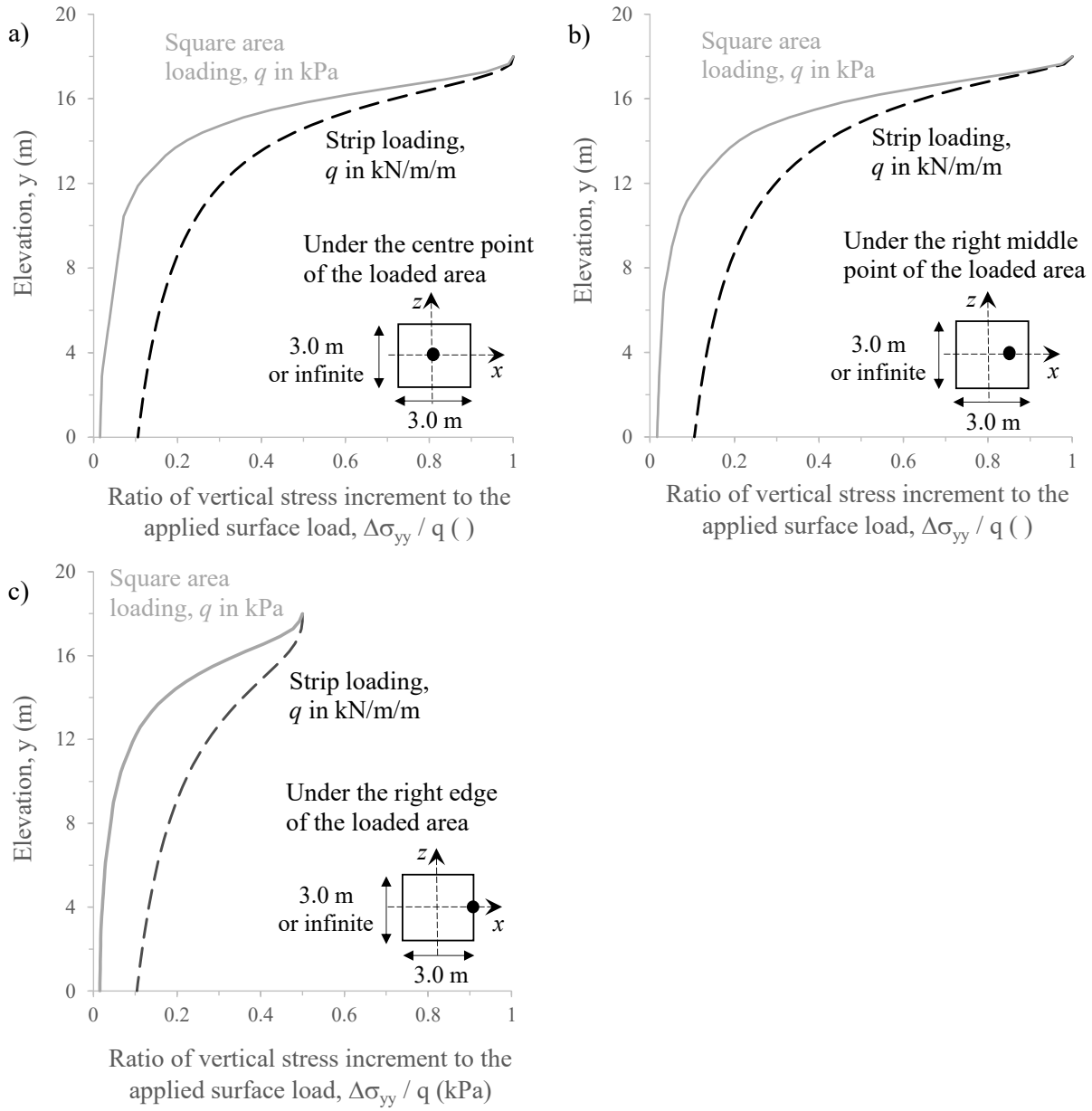

Figure 8.33 – Normalised vertical stress increment induced in an elastic domain by a uniform square loading and by a uniform strip loading with identical magnitude for three different vertical alignments coincident with: (a) centre, (b) right middle point and (c) right edge of the loaded area.

Having applied the aforementioned methodology, Figure 8.34 depicts the ratio of the immediate settlement caused by a uniform vertical strip loading to that resulting from a uniform vertical square loading, particularly at the following three points of the deposit surface: centre of the loaded area; middle right point of the loaded area and extremity of the loaded area. As expected, it can be observed that the settlements obtained for the strip loading largely exceed those corresponding to the square loading. Specifically, it can be seen that the ratio of settlement for the centre point of the loaded area is about 1.682 greater when a strip loading is applied. This ratio is further increased to the side of the loaded area, with a ratio of 1.929 being obtained at the extremity of the loaded area.

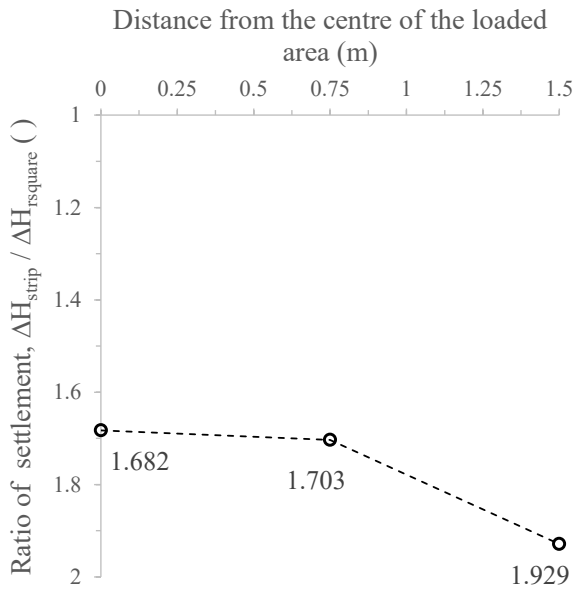

Figure 8.34 – Ratio of the immediate surface settlement induced by a uniform strip loading to that caused by a uniform square loading computed using elastic solutions.

By employing a methodology similar to that followed by Popescu and Prevost (1993) for the estimation of the load reduction to be considered in numerical simulation of the VELACS model 12 (Section 5.3.2.2.4), a load reduction factor of $\xi = (1.0 - 1.0/1.682) \times 100 \approx 40.6\%$ is required to obtain a similar immediate settlement at the centre point for both types of loading. Interestingly, even though Popescu and Prevost (1993) estimated the reduction load factor by comparing the settlements registered in a 2D plane strain FE analysis with those obtained in a 3D FE analysis, rather than by employing analytical elastic solutions, the reduction factor reported by the authors for VELACS model 12 ($\xi = 36.7\%$) is very close to that obtained in this case ($\xi = 40.6\%$). Indeed, the reduction load factor suggested by Popescu and Prevost (1993) for VELACS model 12 was adopted by Taborda (2011) and Andrianopoulos *et al.* (2010a) for the numerical simulation of VELACS model 12, allowing for a very good numerical prediction of the surface settlements registered during dynamic loading in the centrifuge experiment. Therefore, although a more refined procedure could have been employed, a load reduction factor of $\xi \approx 40.6\%$ was considered appropriate. This reduction leads to a maximum vertical stress increment applied by the heavier shallow foundation (with a height of $h = 1.225$ m) and by the lighter shallow foundation (with a height of $h = 0.75$ m) to the underlying sand deposit of, respectively, $\Delta\sigma_v^* \approx (1.0 - 0.406) \times 95.0 \approx 56.4$ kPa and $\Delta\sigma_v^* \approx (1.0 - 0.406) \times 58.0 \approx 34.5$ kPa. Given Equation 8.6, this means that a mass density of $\rho \approx 4.7$ g/cm^3 was considered for both heavier and lighter shallow foundations in the numerical analysis.

To gain insight into the impact of the obtained load reduction, Figure 8.35 compares the vertical stress increment induced by a uniform square loading of magnitude q with that resulting from the application of a uniform strip loading with reduced magnitude of $q_{red} = (1.0 - \xi)\, q = (1.0 - 0.406)\, q = 0.594\, q$. Once again, the comparison is performed for three

different vertical alignments coincident with the centre, middle right point and right extremity of the loaded area.

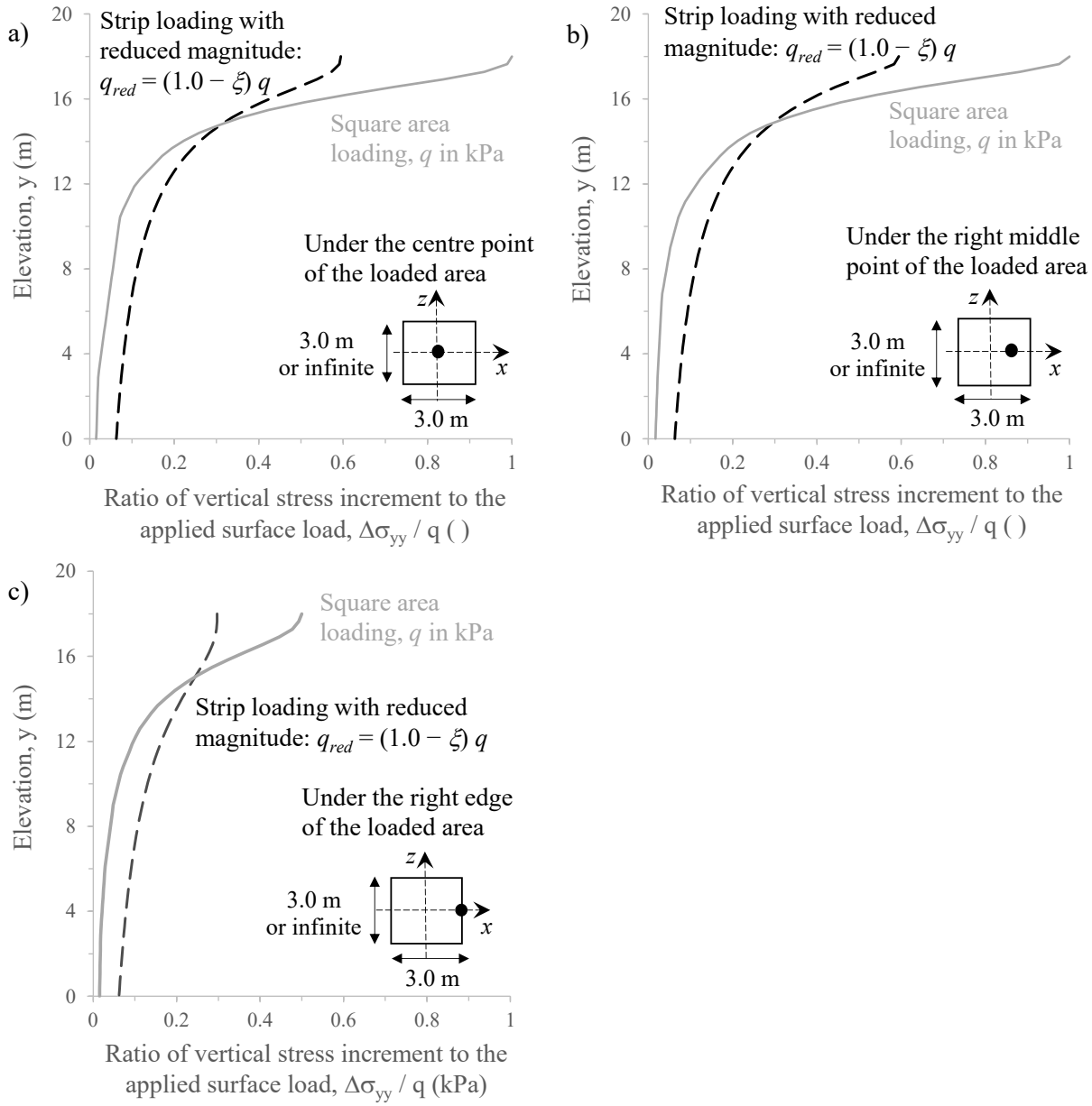

Figure 8.35 – Normalised vertical stress increment induced in an elastic domain by a uniform square loading and by a uniform strip loading with reduced magnitude for three different vertical alignments coincident with: (a) centre, (b) right middle point and (c) right edge of the loaded area.

As expected, even though similar immediate settlements are likely obtained from these two different types of loading, the vertical stress change induced in the underlying material do not match at every depth. In particular, it can be seen that, regardless of the alignment, the vertical stress change resulting from the application of the reduced strip loading is smaller than that induced by the square loading at shallow depths (approximately for the first 3.0 m of depth), with the opposite trend being observed for deeper depths.

Having defined the mass density of the shallow foundations ($\rho = 4.7$ g/cm^3, as indicated before), the previously described gravity loading procedure was employed to generate the initial effective stress state in the FE model. Figure 8.36 depicts the effective stresses obtained for four different vertical alignments located on the left side of the model: $x = 1.25$ m (i.e. close to the left boundary of the model), $x = 4.75$ m (i.e. at approximately half distance from the centre of the heavier shallow foundation to the left boundary of the model), $x = 9.25$ m (i.e. at the left middle point of the heavier shallow foundation) and $x = 10.75$ m (i.e. at right middle point of the heavier shallow foundation). For comparison, the vertical effective stresses computed by using the solutions of the theory of elasticity for a strip loading (Carothers, 1920; Poulos and Davis, 1974) are also depicted in the figure. It is apparent that the vertical effective stress distribution computed by FEMEPDYN match well that obtained by using elastic solutions. It is also interesting to note in Figure 8.36 that, as expected, the shallow foundation has a much stronger influence on the computed vertical effective stresses than on the horizontal effective stresses (note that the scale of vertical effective stress is double of those corresponding to the horizontal effective stresses).

Regarding the right side of the model, the computed effective stresses are presented in Figure 8.37 for four different vertical alignments: $x = 22.75$ m and $x = 24.25$ m (i.e. at the left and right middle points of the lighter shallow foundation, respectively), $x = 28.75$ m (i.e. at half distance from the centre of the lighter shallow foundation to the right boundary of the model) and $x = 32.25$ m (i.e. close to the right boundary of the model). Note that these vertical alignments are symmetric to those used to inspect the effective stresses under the left shallow foundation of the model about the axis corresponding to the middle of the model. Once again, the vertical effective stresses computed by FEMEPDYN agree very well with those obtained from the solutions of the theory of elasticity. By comparing the results presented in this figure with those shown in Figure 8.36, it is apparent that the effective stresses induced by the lighter shallow foundation are significantly smaller than those induced by the heavier one, as expected.

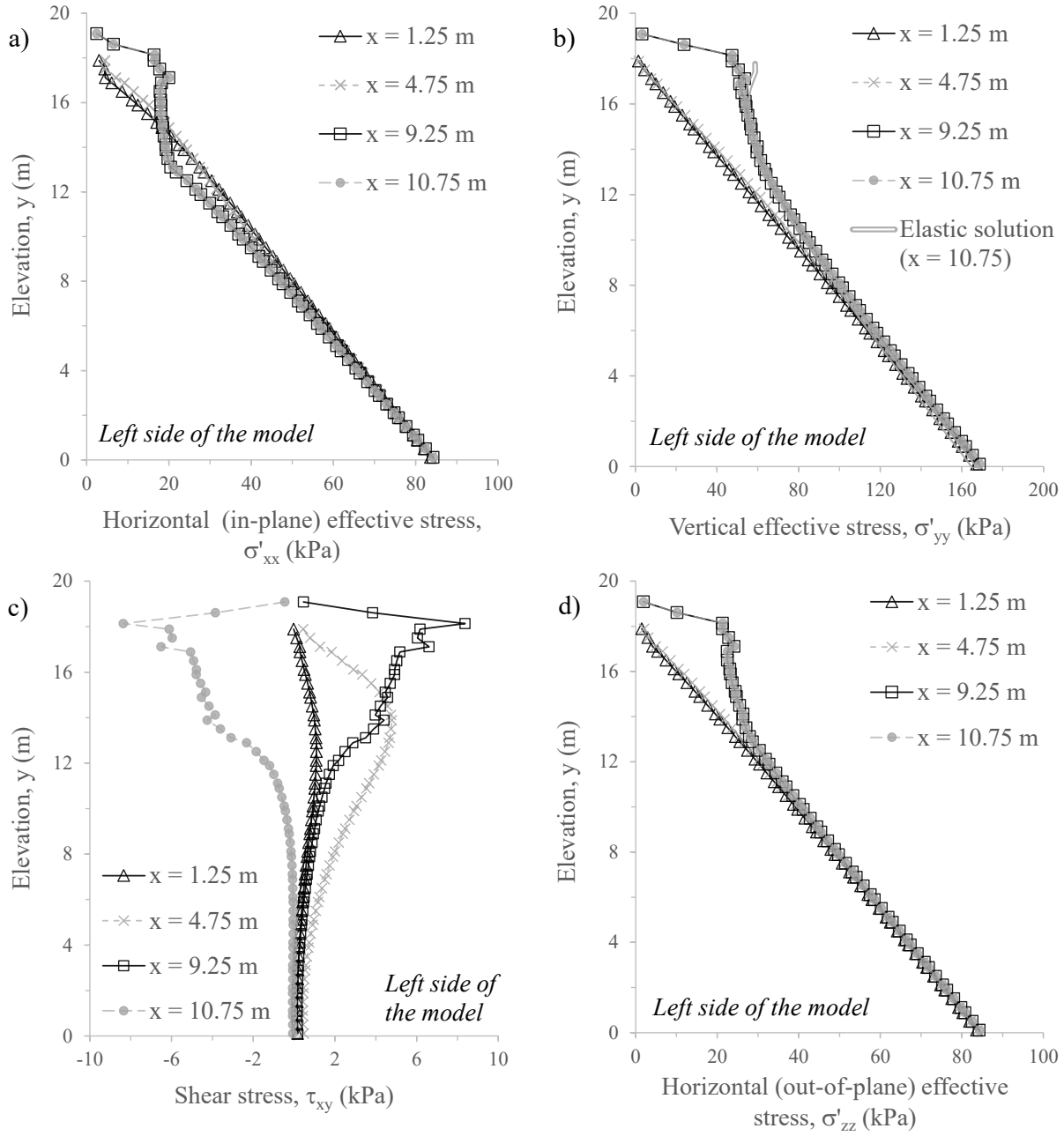

Figure 8.36 – Computed initial effective stresses for four different vertical alignments located on the left side of CM-A: (a) horizontal (in-plane) effective stress; (b) vertical effective stress; (c) shear stress; (d) horizontal (out-of-plane) effective stress.

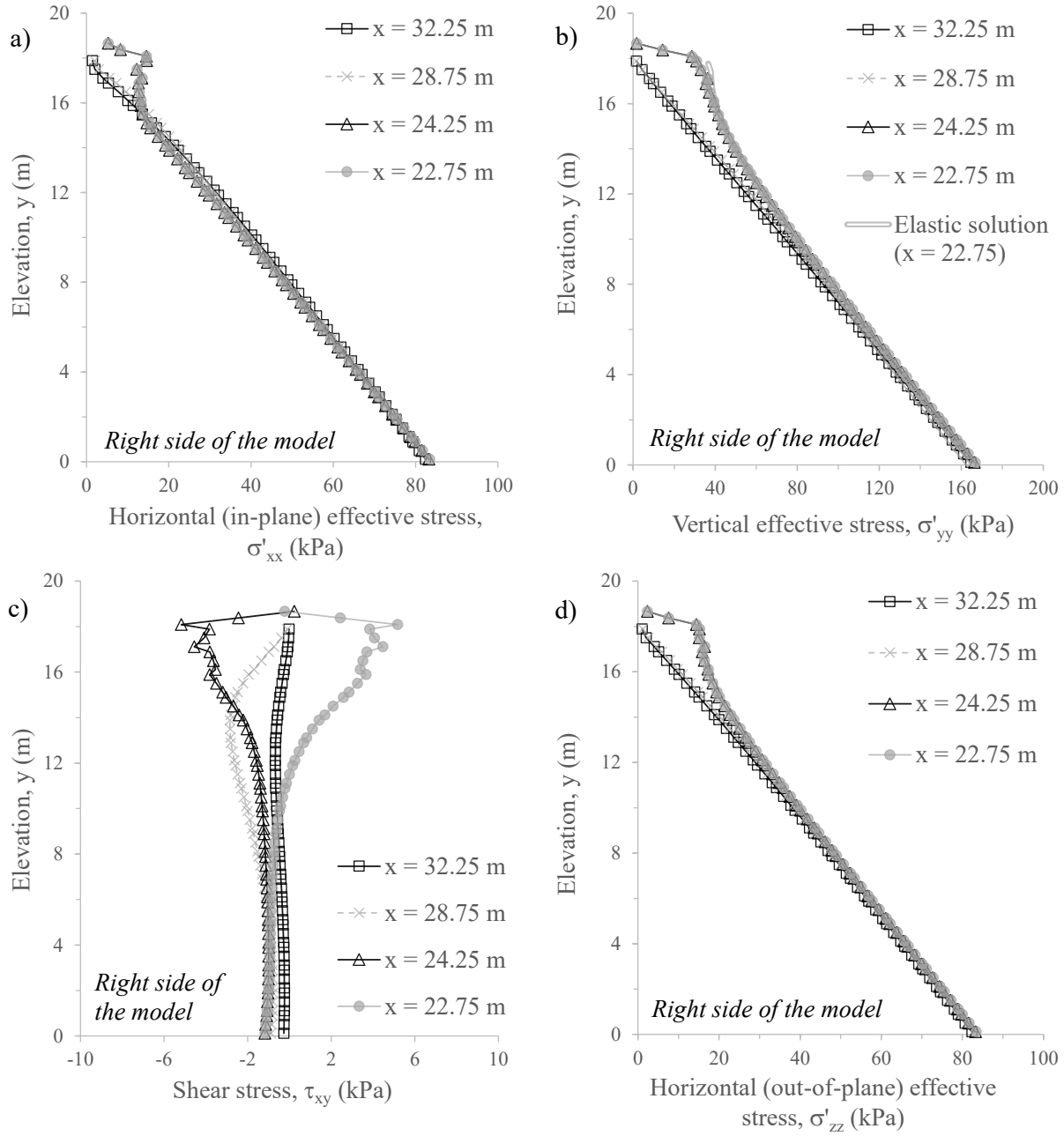

Figure 8.37 – Computed initial effective stresses for four different vertical alignments located on the right side of CM-A: (a) horizontal (in-plane) effective stress; (b) vertical effective stress; (c) shear stress; (d) horizontal (out-of-plane) effective stress.

In both Figure 8.36 and Figure 8.37, it is interesting to observe that very similar horizontal and vertical effective stresses were computed for $x = 1.25$ m and $x = 4.75$ m, as well as for $x = 28.75$ m and for $x = 32.25$ m. This suggests that, for these alignments, the influence of the shallow foundations on the initial stress state of the sand deposit is already practically negligible. This aspect can be more clearly observed in Figure 8.38, which depicts the initial effective stress state for four different horizontal alignments: $y = 0.50$ m (i.e. close to the bottom boundary of the model), $y = 9.50$ m (i.e. at approximately middle depth of the sand deposit), $y = 14.50$ m (i.e. at approximately one third of the depth of the sand deposit) and $y = 17.50$ m (i.e. close to the surface of the sand deposit).

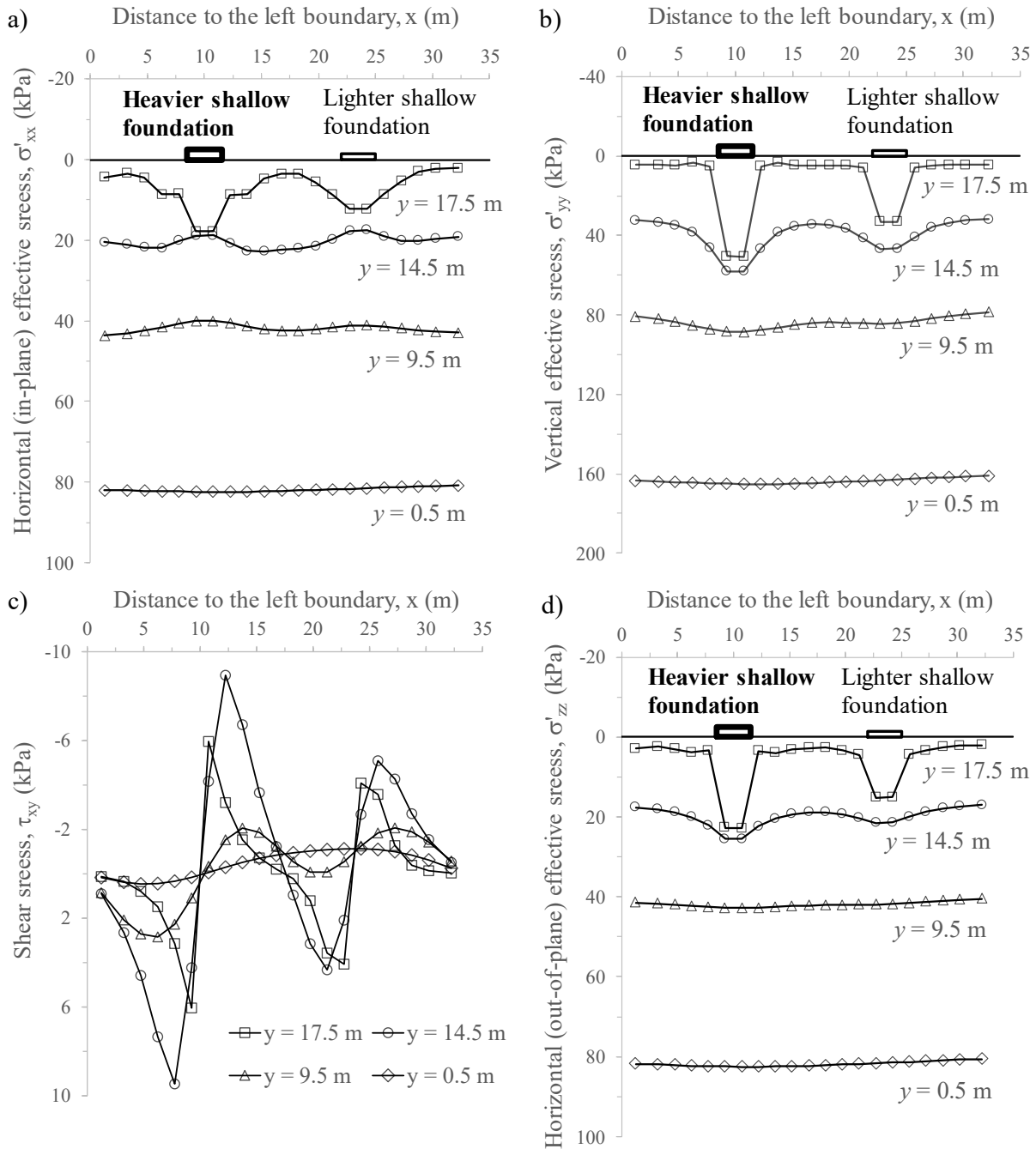

Figure 8.38 – Computed initial effective stresses for four different horizontal alignments of CM-A: (a) horizontal (in-plane) effective stress; (b) vertical effective stress; (c) shear stress; (d) horizontal (out-of-plane) effective stress.

It can be seen that the shallow foundations have little effect on the effective stresses generated in the zones of the sand deposit located close to the lateral boundaries of the model (i.e. zones approximately delimited by $0.0\text{ m} \leq x < 5.0\text{ m}$ and by $28.5\text{ m} < x \leq 33.5\text{ m}$). Similarly, the impact of the shallow foundations on the effective stresses obtained in the zone of the deposit located in between them (i.e. approximately $15.25\text{ m} < x < 18.25\text{ m}$) is very limited. As also expected, the influence of the shallow foundations on the initial effective stress state reduces significantly with depth. It can be observed that, for instance, at the middle depth of the model (i.e. $y = 9.5\text{ m}$), the effective stresses generated in the

zones under the shallow foundations (i.e. zones approximately delimited by 8.5 m $\leq x \leq$ 11.5 m and by 22.0 m $\leq x \leq$ 25.0 m.) are only about 10 % higher than those obtained in the remaining deposit of sand (i.e. to the sides and middle of the model). Furthermore, at the bottom depth (i.e. $y = 0.5$ m), the influence of the shallow foundations on the initial effective stresses seem practically negligible, as also expected. Indeed, this seems to support the assumption made when estimation the load reduction, ξ, that only part of the sand deposit is contributing to the occurrence of immediate settlements, as suggested by Bowles (1996).

As pointed out by Taborda (2011), since the modelled response of sand is greatly influenced by its stress ratio ($\eta = q/p'$, in the triaxial stress space), it is also important to analyse the initial stress state in terms of deviatoric stress, *q,* – mean effective stress, *p'*. Note that the invariants *q* and *p'* are given by Equation 8.8 and Equation 8.9, respectively.

$$p' = \frac{\sigma'_{xx} + \sigma'_{yy} + \sigma'_{zz}}{3} \tag{8.8}$$

$$q = \frac{1}{\sqrt{2}}\sqrt{\left(\sigma'_{xx} - \sigma'_{yy}\right)^2 + \left(\sigma'_{yy} - \sigma'_{zz}\right)^2 + (\sigma'_{zz} - \sigma'_{xx})^2 + 6\left({\tau_{xy}}^2 + {\tau_{xz}}^2 + {\tau_{yz}}^2\right)} \tag{8.9}$$

Moreover, the stress ratio, η, can be related to the coefficient of earth pressure at rest, K_0, through Equation 8.10 (which assumes, as a simplification, triaxial loading conditions).

$$\eta = \frac{q}{p'} = \frac{\sigma'_{yy} - \sigma'_{xx}}{\frac{\sigma'_{yy} + 2\,\sigma'_{xx}}{3}} = \frac{3\,(1 - K_0)}{1 + 2\,K_0} \tag{8.10}$$

Figure 8.39 depicts the *q* – *p'* profiles for Gauss points located along the previously analysed four vertical alignments located on the left side of the model (i.e. $x = 1.25$ m, $x = 4.75$ m, $x = 9.25$ m and $x = 10.75$ m) and four vertical alignments located on the right side of the model (i.e. $x = 22.75$ m, $x = 24.25$ m, $x = 28.75$ m and $x = 32.25$ m). A line corresponding to the critical state (CS) strength in triaxial compression (TC), i.e. $\eta = M_c^c = 1.265 \Leftrightarrow K_0 \approx 0.26$ (Equation 8.10), one corresponding to the coefficient of earth pressure at rest of $K_0 = 0.50 \Leftrightarrow \eta \approx 0.75$ and another one corresponding to the stress ratio of $\eta = 0.55 \Leftrightarrow K_0 \approx 0.60$ are also plotted in the figure. It can be observed that the effective stress states at the majority of the Gauss points located along the vertical alignments farther away from the influence of the shallow foundations (i.e. along $x = 1.25$ m, $x = 4.75$ m, $x = 28.75$ m and $x = 32.25$ m) are characterised by stress ratios close to $\eta = 0.75 \Leftrightarrow K_0 = 0.50$, as intended by adopting a linear elastic isotropic model coupled with the Mohr-Coulomb failure criterion and a Poisson's ratio of $\nu = 0.333$ during this phase of the analysis. Conversely, larger stress ratios were, in general, obtained for Gauss points located underneath the shallow foundations (i.e. along $x = 9.25$ m, $x = 10.75$ m, $x = 22.75$ m and $x = 24.25$ m).

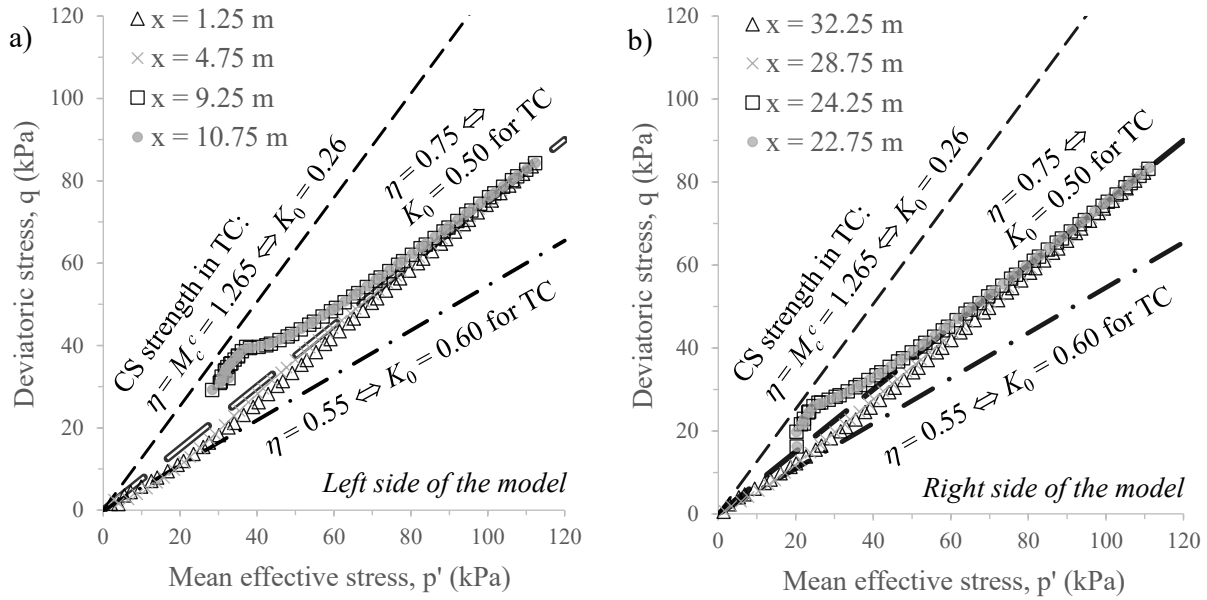

Figure 8.39 – Computed initial stress state in terms of deviatoric stress as a function of the mean effective stress at Gauss points located along four different vertical alignments located on: (a) the left side of CM-A and (b) right side of CM-A.

Further insight into the initial stress state is provided in Figure 8.40, which depicts the stress ratio, η, – state parameter, $\psi = e - e_{cs}$, profiles obtained for Gauss points located along $x = 9.25$ m and $x = 24.25$ m (i.e. underneath the heavier and lighter shallow foundations, respectively), together with dilatancy stress ratio, $\eta = M_\theta^d$ (Equation 8.12), and critical state (CS) stress ratio, $\eta = M_\theta^c$ (Equation 8.11), – state parameter, ψ, profiles predicted by the constitutive model at those points.

$$M_\theta^c = g(\theta, c^c)\, M_c^c \tag{8.11}$$

$$M_\theta^d = M_\theta^c + g(\theta, c^d)\, k_c^d\, \psi = g(\theta, c^c)\, M_c^c + g(\theta, c^d)\, k_c^d\, \psi = M_\theta^c + g(\theta, c^d)\, k_c^d\, \psi \tag{8.12}$$

where:

$$M_{c,e}^d = M_{c,e}^c + k_{c,e}^d\, \psi = M_{c,e}^c + k_{c,e}^d \left(e - (e_{cs})_{ref} + \lambda \left(\frac{p'}{p'_{ref}} \right)^{\xi} \right) \tag{8.13}$$

$$g(\theta, c^{c,d}) = \frac{2\, c^{c,d}}{\frac{1 + c^{d,c,b}}{2} - \frac{1 - c^{c,b}}{2} \cos(3\theta)} - \left[\frac{1 + c^{c,d}}{2} + \frac{1 - c^{c,b}}{2} \cos(3\theta) \right] \tag{8.14}$$

$$\cos(3\theta) = \left(\frac{3\sqrt{3}}{2} \frac{\overline{J_3}}{\left(\overline{J_2}\right)^{3/2}} \right) \tag{8.15}$$

$$c^{c,d} = \frac{M_e^{c,d}}{M_c^{c,d}} \tag{8.16}$$

and $\overline{J_2}$ and $\overline{J_3}$ are, respectively, the modified second and third invariants of the effective stress, given by:

$$\overline{J_2} = 1/2\,\bar{\boldsymbol{r}} : \bar{\boldsymbol{r}} = \frac{1}{6}\left[\left(\bar{r}_{xx} - \bar{r}_{yy}\right)^2 + \left(\bar{r}_{yy} - \bar{r}_{zz}\right)^2 + \left(\bar{r}_{zz} - \bar{r}_{xx}\right)^2\right] + \bar{r}_{xy}{}^2 + \bar{r}_{xz}{}^2 + \bar{r}_{yz}{}^2 \tag{8.17}$$

$$\overline{J_3} = det\,\bar{\boldsymbol{r}} = \bar{r}_{xx}\,\bar{r}_{yy}\,\bar{r}_{zz} - \bar{r}_{xx}\,\bar{r}_{yz}{}^2 - \bar{r}_{yy}\,\bar{r}_{xz}{}^2 - \bar{r}_{zz}\,\bar{r}_{xy}{}^2 + 2\,\bar{r}_{xy}\,\bar{r}_{yz}\,\bar{r}_{yz} \tag{8.18}$$

with the radial tensor, $\bar{\boldsymbol{r}}$, being given by the difference between the stress ratio tensor, $\boldsymbol{r}$, and the back-stress tensor, $\boldsymbol{\alpha}$:

$$\bar{\boldsymbol{r}} = \boldsymbol{r} - \boldsymbol{\alpha} \tag{8.19}$$

$$\boldsymbol{r} = \frac{\boldsymbol{s}}{p'} = \begin{bmatrix} \dfrac{\sigma'_{xx} - p'}{p'} & \dfrac{\tau_{xy}}{p'} & \dfrac{\tau_{xz}}{p'} \\ \dfrac{\tau_{yx}}{p'} & \dfrac{\sigma'_{yy} - p'}{p'} & \dfrac{\tau_{yz}}{p'} \\ \dfrac{\tau_{zx}}{p'} & \dfrac{\tau_{zy}}{p'} & \dfrac{\sigma'_{zz} - p'}{p'} \end{bmatrix} \tag{8.20}$$

$$\boldsymbol{\alpha} = \begin{bmatrix} \alpha_{xx} & \alpha_{xy} & \alpha_{xz} \\ \alpha_{yx} & \alpha_{yy} & \alpha_{yz} \\ \alpha_{zx} & \alpha_{zy} & \alpha_{zz} \end{bmatrix} \tag{8.21}$$

It is apparent that, although located inside both dilatancy and critical surfaces, the initial stress states obtained for Gauss points located at shallower depths (characterised by larger negative values of $\psi = e - e_{cs}$, as a result of the smaller mean effective stresses and, consequently, larger values of e_{cs}) are closer to the dilatancy surface than the initial stress points corresponding to deeper zones of the deposit of sand. These Gauss points will likely exhibit a smaller tendency to contract (and, therefore, to generate positive excess pore pressures under undrained conditions) when subjected to dynamic loading.

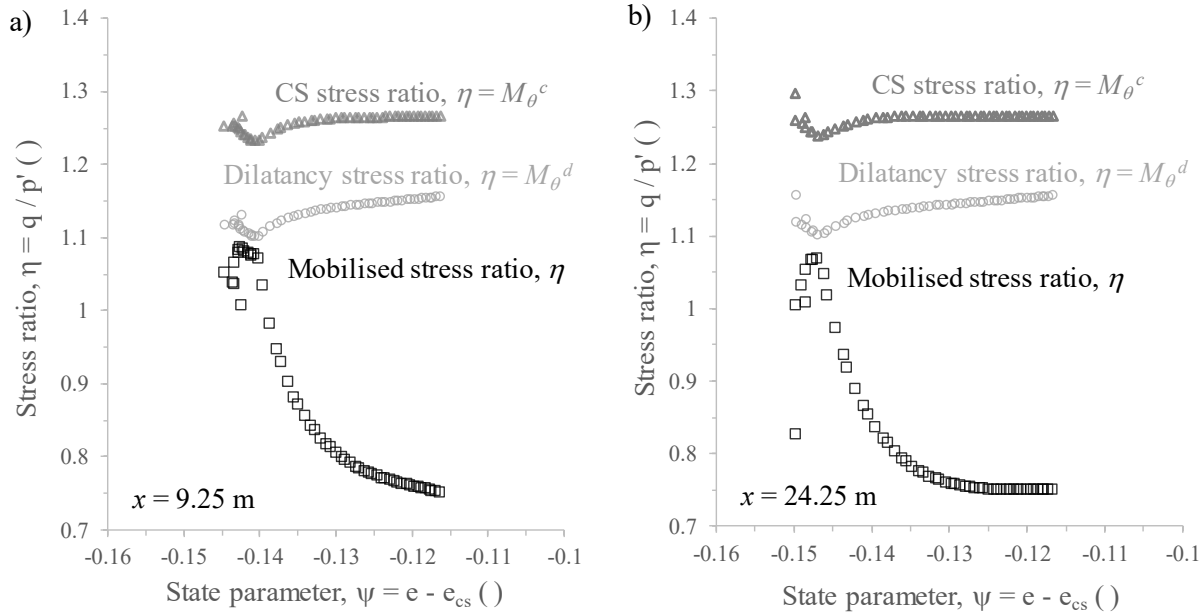

Figure 8.40 – Mobilised, dilatancy and critical state stress ratios as a function of the state parameter at Gauss points located along: (a) a vertical alignment crossing the heavier shallow foundation of CM-A and (b) a vertical alignment crossing the lighter shallow foundation of CM-A.

The state parameter profiles for Gauss points located along the four different horizontal alignments that have been recurrently used to analyse the results of this initial phase (i.e. $y =$ 0.50 m, $y =$ 9.50 m, $y =$ 14.50 m and $y =$ 17.50 m) are depicted in Figure 8.41. Note that the position of the ground surface, in terms of the value of the state parameter, is merely indicative, corresponding to a mean effective stress of 1.0 kPa (which is the lower limit imposed by the low-stress yield surface). It can be observed that the values of the state parameter vary within the range of -0.17 to -0.11. By comparing these values with those characterising the initial state of moderately loose samples subjected to undrained cyclic triaxial testing (Section 3.4), it can be concluded that the laboratory test programme was able to cover the initial states of different zones of the sand deposit of CM-A, as intended.

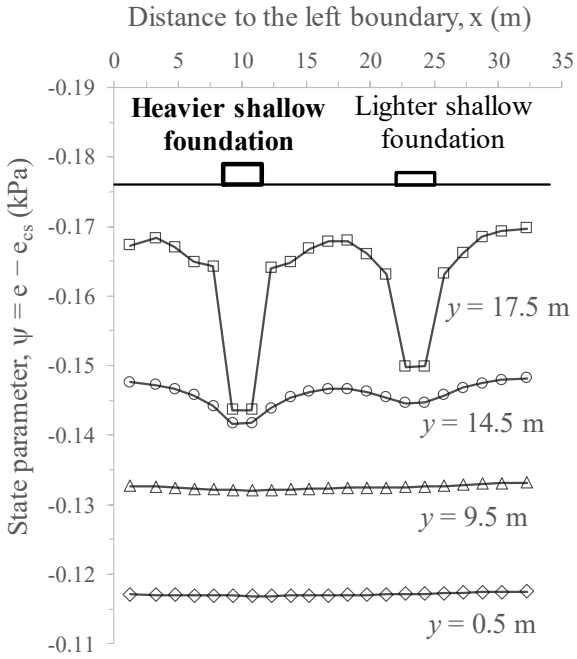

Figure 8.41 – Computed initial state parameter for Gauss points located along four different horizontal alignments of CM-A.

Finally, to assess the impact of the procedure adopted for the generation of the initial stress state in the FE model, a comparative analysis was performed by using a different procedure, termed as "staged construction" and consisting of the following two stages: 1) computation of the effective stresses within the sand deposit in the absence of the shallow foundations (i.e. by assuming "greenfield conditions" and using a K_0 procedure) and 2) simulation of the construction of the shallow foundations on the sand deposit (i.e. activation of the elements simulating the shallow foundations). Naturally, since the intention was solely to evaluate the impact of the two different methods, a linear elastic model coupled with the Mohr-Coulomb failure criterion having the same parameters indicated before was also adopted in this analysis. The obtained results are compared with those previously computed when using a gravity loading procedure in Figure 8.42. Interestingly, very similar effective stresses were computed by using both procedures, with slight discrepancies between both sets of data being only observed for the shallowest depth immediately underneath the shallow

foundations. This suggests that any of described procedures would be acceptable to generate the initial stress state. In the present case, the results obtained when employing the gravity loading procedure were adopted for the subsequent dynamic phase.

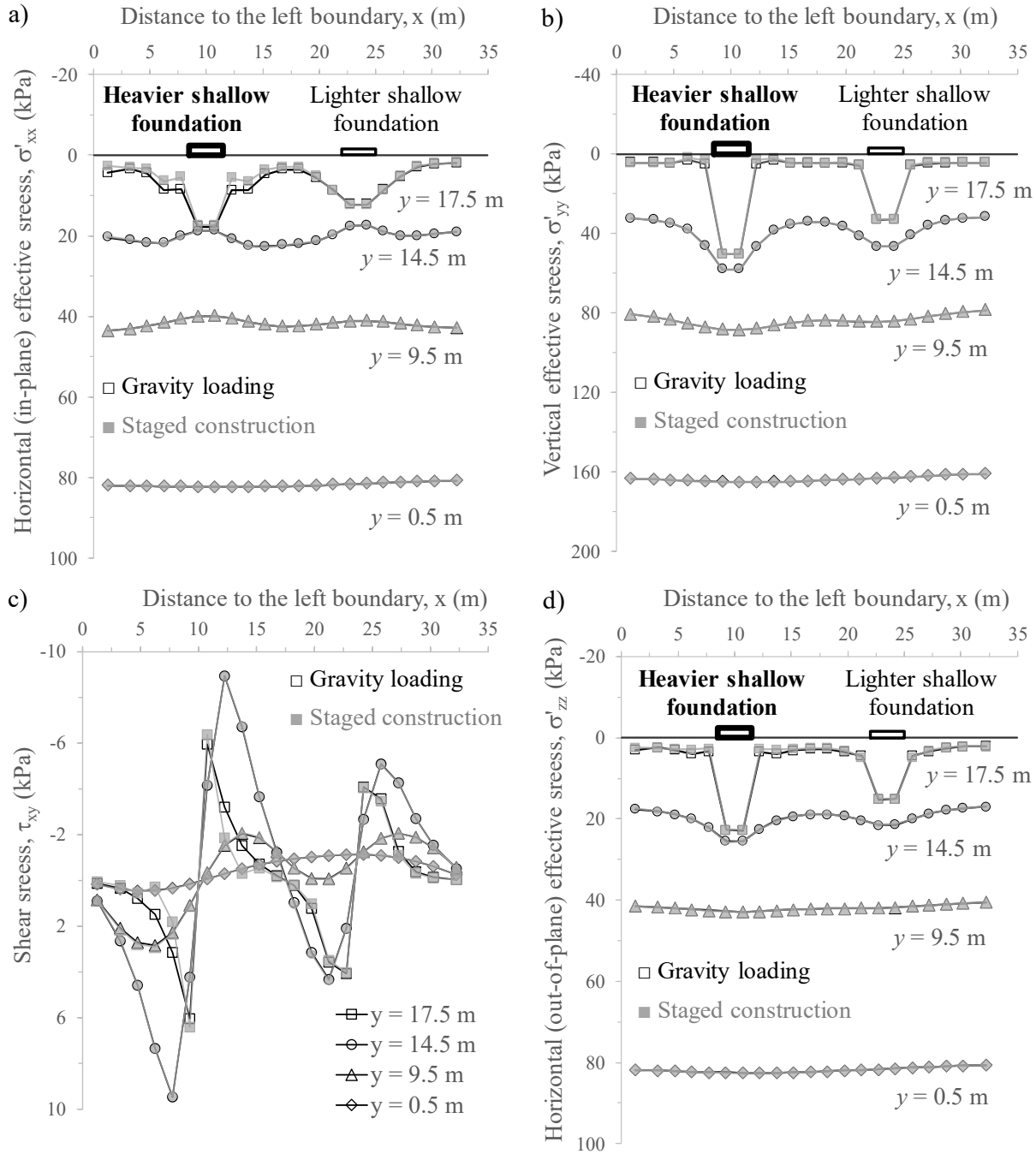

Figure 8.42 – Comparison of the initial effective stresses computed by using a gravity loading procedure with those obtained when using a staged construction procedure for CM-A: (a) horizontal (in-plane) effective stress; (b) vertical effective stress; (c) shear stress; (d) horizontal (out-of-plane) effective stress.

8.3.2.4 Dynamic analysis

8.3.2.4.1 Horizontal acceleration time-histories

The horizontal acceleration time-histories computed at several different positions located along a vertical alignment coincident with the axis of the heavier shallow foundation ($x = 10.0$ m) are compared with those recorded in the centrifuge experiment in Figure 8.43. Note that, to ease their visualisation and comparison, all experimental and numerical signals presented in this section were filtered using SeismoSignal version 2018 (Seismosoft, 2018), specifically by employing a fourth-order Butterworth-type filter with limit frequencies of 0.1 and 25 Hz. At the bottom of the sand deposit (i.e. at $(x, y) = (10.0, 0.5)$ m), small discrepancies between the experimental and numerical sets of results can be observed, in terms of both amplitude and time of occurrence of the peak accelerations. These small discrepancies are likely a detrimental consequence of the approximations required to compute the input motion (Section 8.3.1.2). These inaccuracies seem also to affect the computed response at $(x, y) = (10.0, 6.5)$ m, where the computed peak accelerations appear to be slightly smaller than those registered in the experiment. For the upper levels of the deposit (i.e. at $(x, y) = (10.0, 12.0)$ m and $(x, y) = (10.0, 17.0)$ m), the agreement between numerical and experiment sets of data appears to be overall satisfactory. Indeed, at these shallow depths, it is particularly interesting to note that the numerical model was able to predict the reduction of the amplitudes of the accelerations after the first coupled of significant loading cycles, with the agreement being particularly remarkable at $(x, y) = (10.0, 12.0)$ m. As mentioned before, this significant alteration of the motion is probably the result of the severe reduction of the stiffness of the sand deposit and increase in material damping, occurring concurrently with the generation of large excess pore pressures and, consequently, significant reduction of the effective stresses.

In addition, Figure 8.44 compares the computed and measured horizontal acceleration time-histories at the top left edge of the heavier shallow foundation (i.e. at $(x, y) = (8.5, 19.225)$ m), as well as at the top position within the underlying sand deposit (i.e. at $(x, y) = (10.0, 17.0)$ m). It can be seen that a reasonable agreement between numerical and experimental data was obtained in terms of the amplitude of the accelerations, perhaps with the exception of the period ranging from 11.0 s to 14.0 s (i.e. from the third to the fifth significant loading cycles) during which the accelerations obtained in the numerical analysis are higher than those measured in the experiment. This might be a detrimental consequence of the approximations required to simulate the 3D nature of the problem in a 2D plane strain analysis, with the discrepancies between the effective stress state obtained in a 3D analysis and those obtained in a 2D plane strain analysis being particularly evident at shallow depths, as described in Section 8.3.2.3. In addition, there appears to exist a small time delay between the modelled and measured response at both monitoring positions. Since this small time delay is also observed for the motion registered at $(x, y) = (10.0, 12.0)$ m (Figure 8.43), it

might be related to the small underestimation of the rate of excess pore pressure build-up during the earlier stages of loading at that monitoring position, as discussed in more detail later.

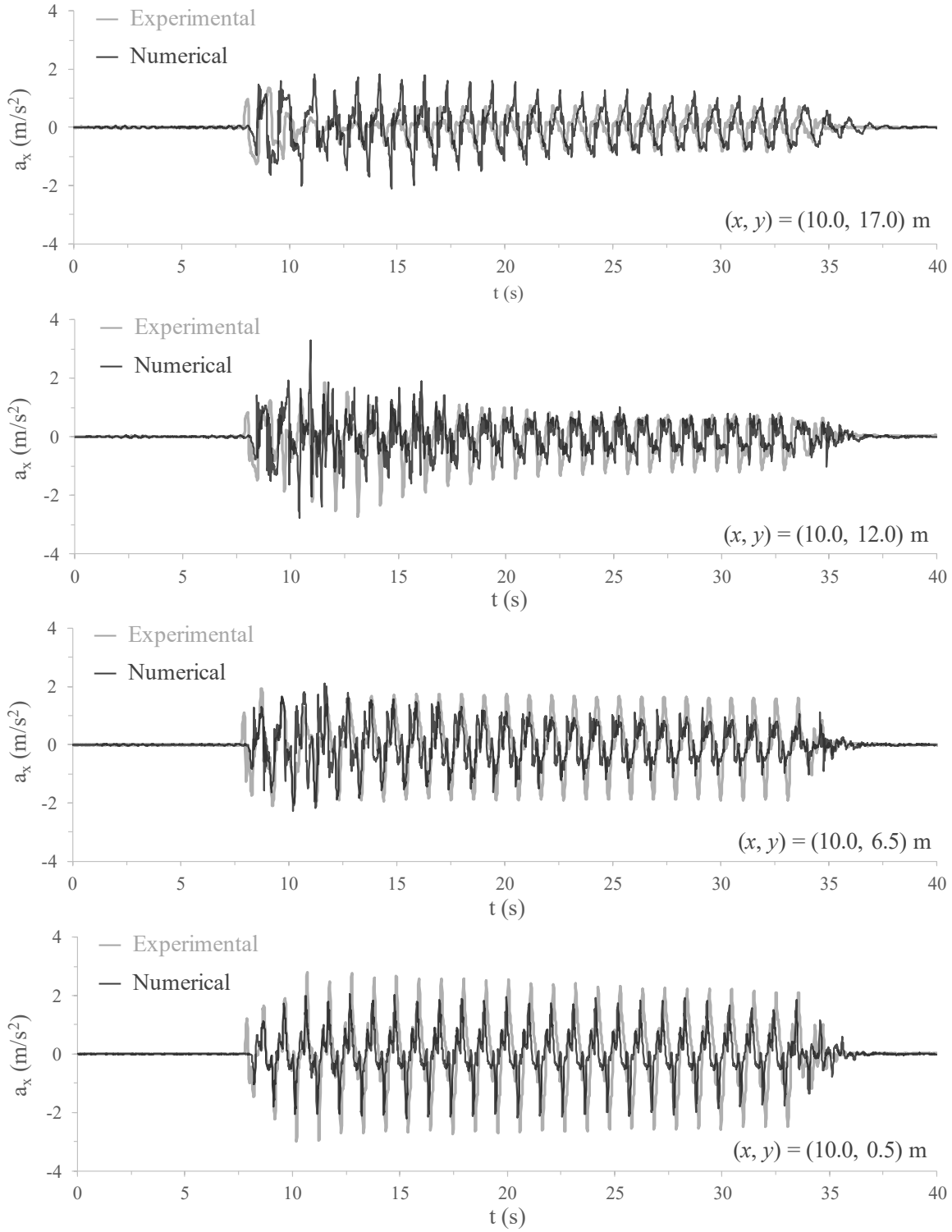

Figure 8.43 – Measured and computed horizontal acceleration time-histories at several positions located along a vertical alignment coincident with the axis of the heavier shallow foundation for CM-A.

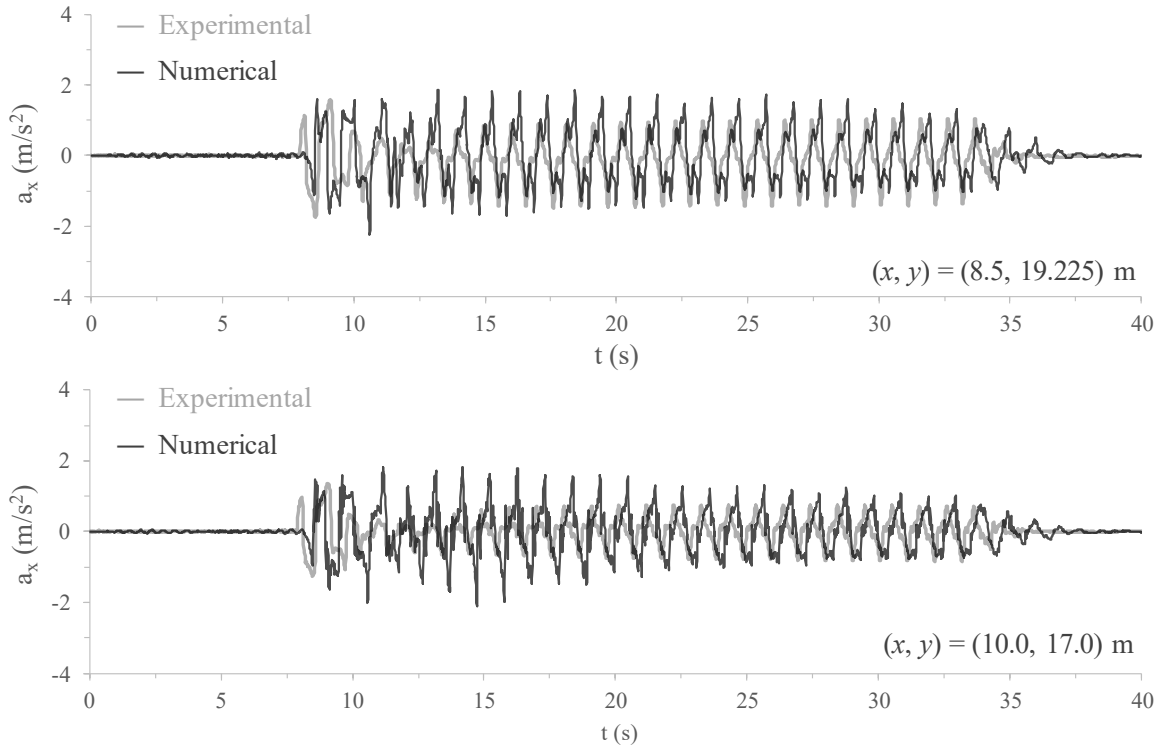

Figure 8.44 – Measured and computed horizontal acceleration time-histories at the top of the heavier shallow foundation and underneath it for CM-A.

Regarding the horizontal acceleration time-histories registered under the lighter shallow foundation (i.e. at several monitoring positions located along an alignment coincident with the axis of the shallow foundation, defined by $x = 23.7$ m in the experiment and $x = 23.5$ m in the numerical analysis, with the latter value being used as reference henceforth), Figure 8.45 compares the results obtained in the numerical analysis with those measured in the centrifuge experiment. Overall, it can be observed that a satisfactory agreement between numerical and experimental data was obtained, although the acceleration time-histories (particularly the positive peak values) computed at $(x, y) = (23.5, 6.5)$ m and $(x, y) = (23.5, 12.0)$ m appear to be considerably underestimated from $t \approx 14$ s in relation to those recorded during the experiment. In addition, the negative peak values of accelerations are overestimated at the shallowest level (i.e. at $(x, y) = (23.5, 17.0)$ m). Nevertheless, it is particularly noteworthy the fact that the numerical tool is able to reproduce adequately the attenuation of the motion at that level after the first two significant loading cycles, as observed in the experiment.

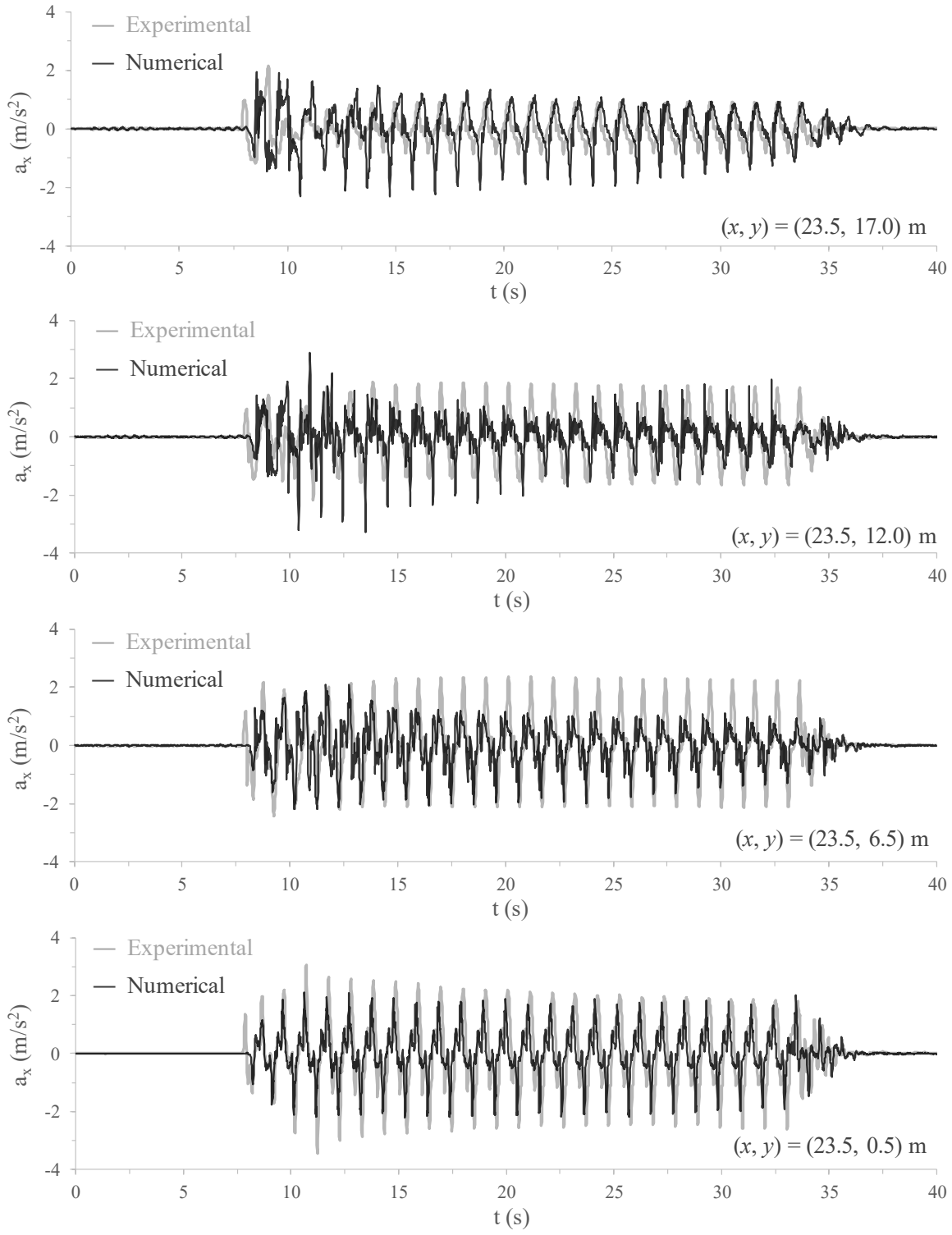

Figure 8.45 – Measured and computed horizontal acceleration time-histories at several positions located along a vertical alignment coincident with the axis of the lighter shallow foundation for CM-A.

Additionally, Figure 8.46 compares the computed and measured horizontal acceleration time-histories at the top left edge of the lighter shallow foundation (i.e. at $(x, y) = (22.0, 18.75)$ m in the numerical model), as well as at the top position within the underlying sand deposit (i.e. at $(x, y) = (23.5, 17.0)$ m in the numerical model). It can be seen that the agreement

between numerical and experimental data registered at the top of the shallow foundation is much less satisfactory than that reached for motions registered within the sand deposit, with the accelerations computed at the top of the shallow foundation being underestimated in relation to those measured in the experiment. This suggests that the numerical tool was not able to capture adequately the strong effect of the different masses of the shallow foundations on the horizontal accelerations propagated through them, as reported by Marques *et al.* (2012a). In effect, by comparing the results presented in Figure 8.46 and Figure 8.44, it can be concluded that peak horizontal accelerations with similar amplitude were obtained at the top of both heavier and lighter shallow foundations in the numerical analysis, while in the experiment much larger peak accelerations were measured at the top of the lighter shallow foundation than those recorded at the top of the heavier one. This aspect might require further investigation in the future.

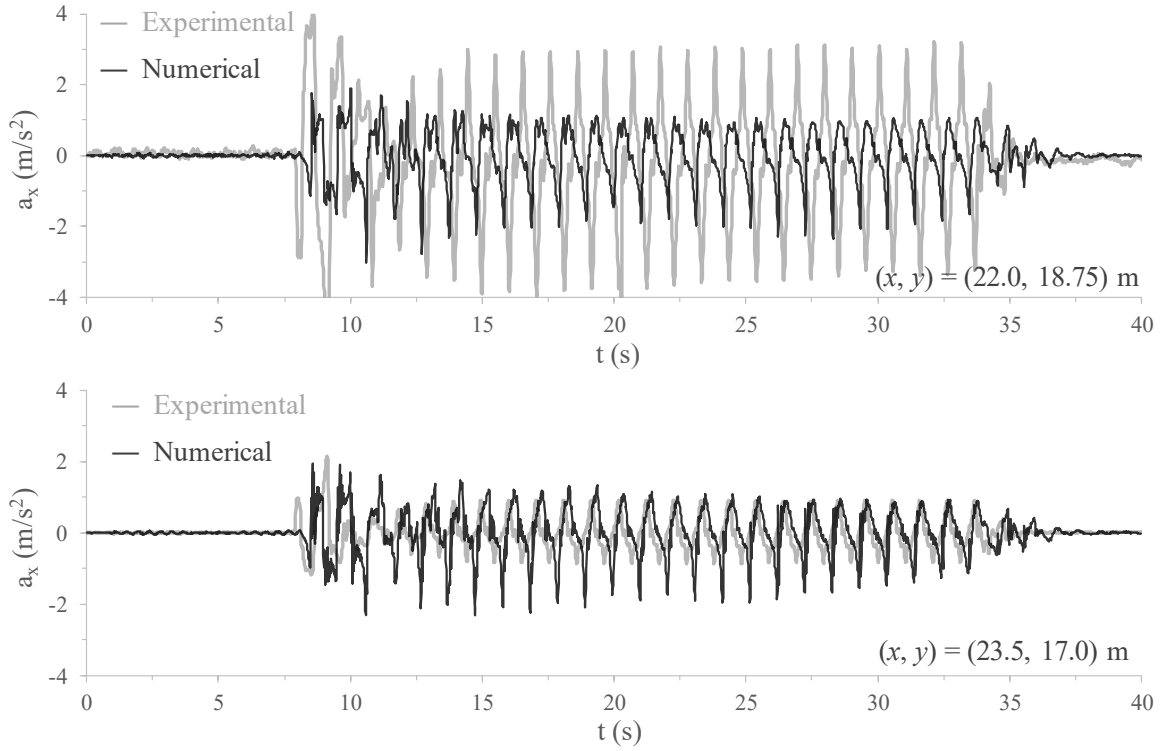

Figure 8.46 – Measured horizontal acceleration time-histories at the top of the lighter shallow foundation and underneath it for CM-A.

The computed horizontal acceleration time-histories at several positions located along a vertical alignment corresponding to half distance from the axes of both shallow foundations are depicted in Figure 8.47, together with those registered in the experiment. It can be observed that, in general, a very good agreement between numerical and experimental sets of data was obtained, with the constitutive model being able to reproduce the main trends observed in the experiment, such as the attenuation of peak accelerations for the shallower monitoring positions after the first two significant loading cycles. Similar to what observed for the other two vertical alignments, the acceleration time-history computed at $(x, y) = (16.0, 6.0)$ m appear to be underestimated (particularly the positive peak accelerations) from

$t \approx 14$ s in relation to that recorded during the experiment, suggesting that the constitutive model might have overestimated the increase in damping of the sand deposit at that location.

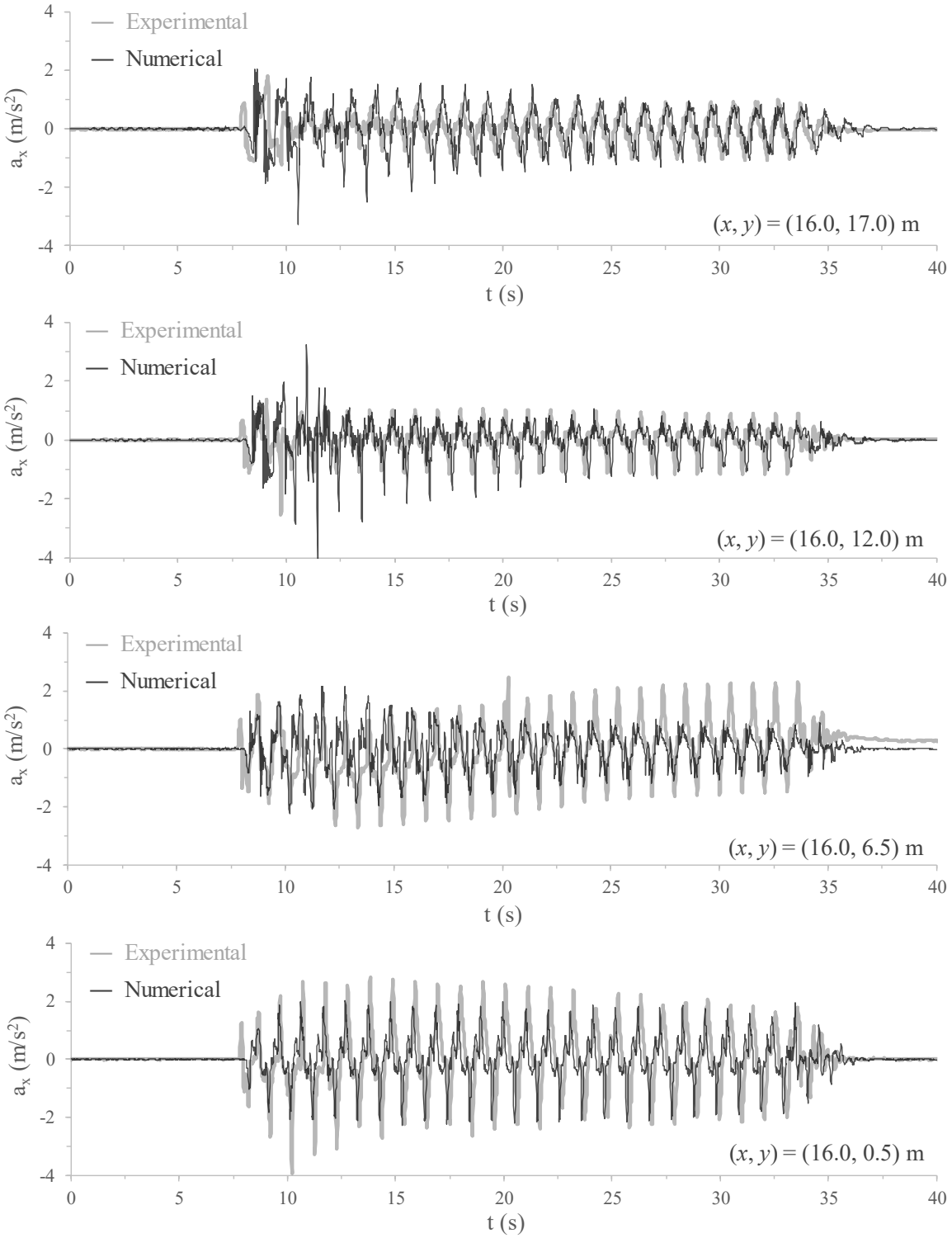

Figure 8.47 – Measured and computed horizontal acceleration time-histories at several positions located along a vertical alignment coincident with the middle of the model for CM-A.

8.3.2.4.2 Vertical acceleration time-histories

Figure 8.48 depicts the vertical acceleration time-histories computed at the base of the model (i.e. at $(x, y) = (0.0, 0.0)$ m) and at the left and right top edges of the heavier shallow

foundation (i.e. at $(x, y) = (8.5, 19.225)$ m and $(x, y) = (11.5, 19.225)$ m, respectively), together with those measured in the centrifuge experiment.

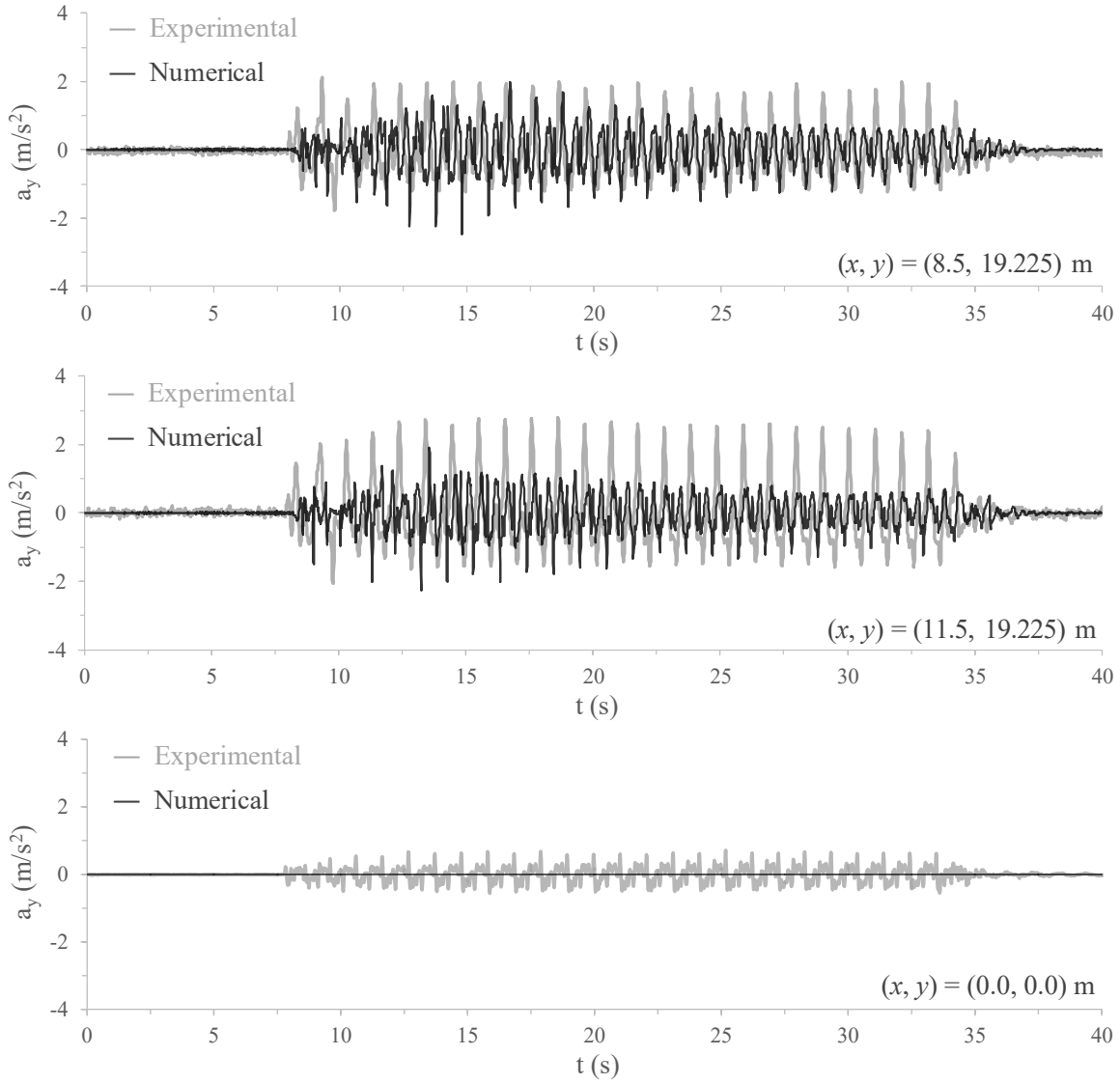

Figure 8.48 – Measured and computed vertical acceleration time-histories at the base of the model and at the left and right top edges of the heavier shallow foundation for CM-A.

It can be observed that, although null vertical accelerations were prescribed at the nodes belonging to the bottom boundary of the numerical model, significantly large vertical accelerations were computed at the top of the shallow foundations (with amplitudes similar to those characterising the horizontal motion), as also observed in the experiment. Note, however, that the vertical peak accelerations obtained in the numerical analysis, particularly at the right top edge (i.e. at $(x, y) = (11.5, 19.225)$ m), have smaller amplitudes than those recorded in the experiment. A plausible explanation might reside on the fact that a non-intended rocking motion seemed to have been applied to the entire centrifuge model during the experiment, as discussed in Section 8.3.1.3.

In addition, Figure 8.49 compares directly the computed acceleration time-histories at $(x, y) = (8.5, 19.225)$ m and $(x, y) = (11.5, 19.225)$ m. Note that, for clarity of the

presentation, only the results obtained for the period ranging from 15 s to 20 s are presented in the figure. Nevertheless, a similar pattern is observed for the remaining period of cyclic loading. It is apparent that, although having similar amplitudes, some local peaks occur out of phase, suggesting that rocking motion was simulated in the numerical analysis. This aspect can be more clearly observed in Figure 8.50, which compares the semi-sum (i.e. average values) and semi-difference of the vertical accelerations computed at $(x, y) = (8.5, 19.225)$ m and $(x, y) = (11.5, 19.225)$ m during the same period. It can be seen that, due to the out-of-phase occurrence of local peaks, the semi-difference of vertical acceleration time-history presents some peaks, indicating the occurrence of oscillations. It should be noted, however, that the magnitude of these oscillations can be considered small (at least, when compared to the very large settlements), with a permanent rotation of the shallow foundation of about 0.5° being obtained at the end of dynamic loading, as shown later.

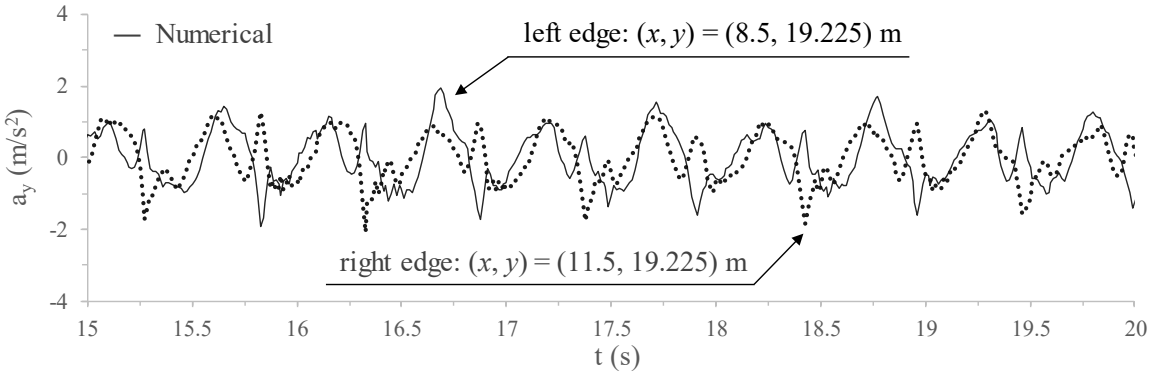

Figure 8.49 – Computed vertical acceleration time-histories at the left and right top edges of the heavier shallow foundation during the period ranging from 15 s to 20 s for CM-A.

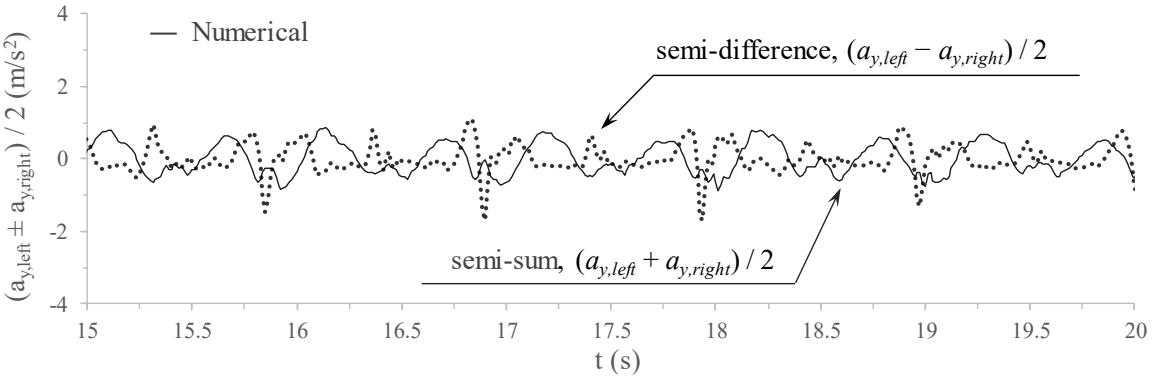

Figure 8.50 – Semi-sum and semi-difference of the vertical accelerations computed at the left and right top edges of the heavier shallow foundation during the period ranging from 15 s to 20 s for CM-A.

With respect to the vertical acceleration time-histories registered for the lighter shallow foundation, Figure 8.51 compares the numerical and experimental sets of data. As obtained for the heavier shallow foundation, the vertical peak accelerations computed by FEMEPDYN appear to be smaller than those measured in the experiment, particularly at the right top edge of the lighter shallow foundation (i.e. at $(x, y) = (25.0, 18.75)$ m). Moreover, the comparison of the vertical accelerations obtained in the numerical analysis at the left and

right top edges of the shallow foundation (i.e. $(x, y) = (22.0, 18.75)$ m at and $(x, y) = (25.0, 18.75)$ m, respectively), reveals that, although having similar amplitudes, some local peaks occur out-of-phase (Figure 8.52). This suggests the occurrence of oscillations during dynamic loading. Nevertheless, as noted for the heavier shallow foundation, the amplitude of these oscillations can be considered small, with a permanent rotation of about 0.7° being obtained at the end of dynamic loading for the lighter shallow foundation, as shown later.

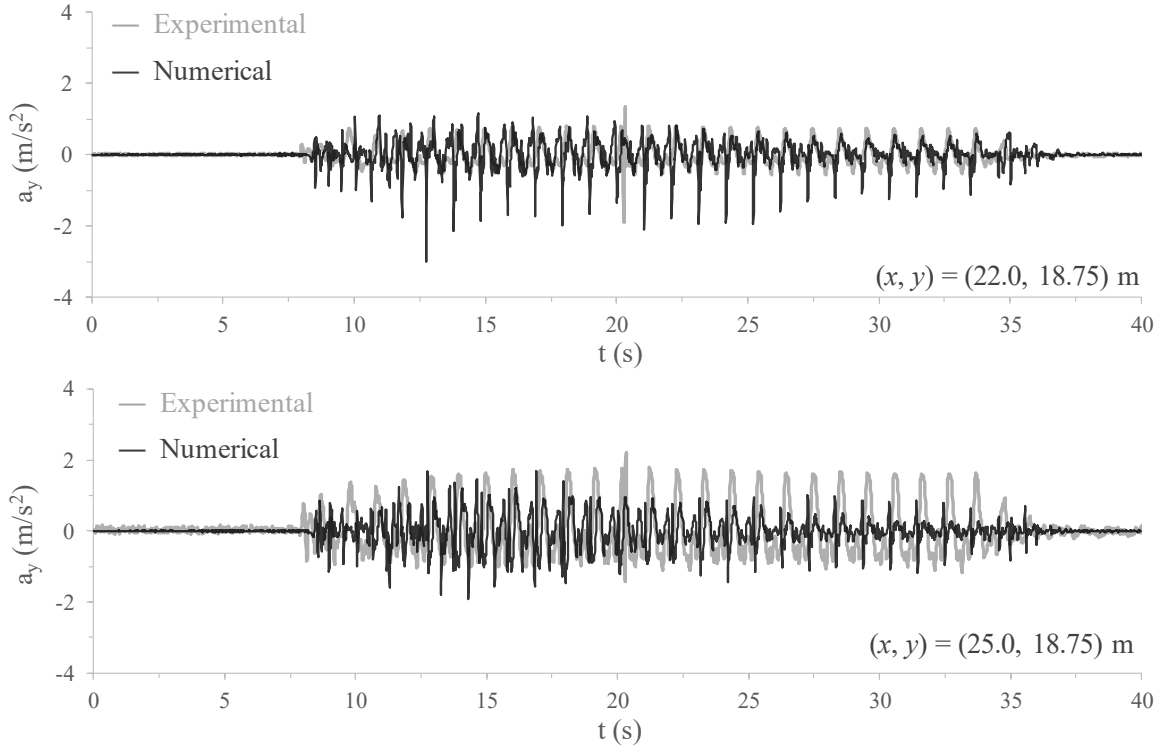

Figure 8.51 – Measured and computed vertical acceleration time-histories at the left and right top edges of the lighter shallow foundation for CM-A.

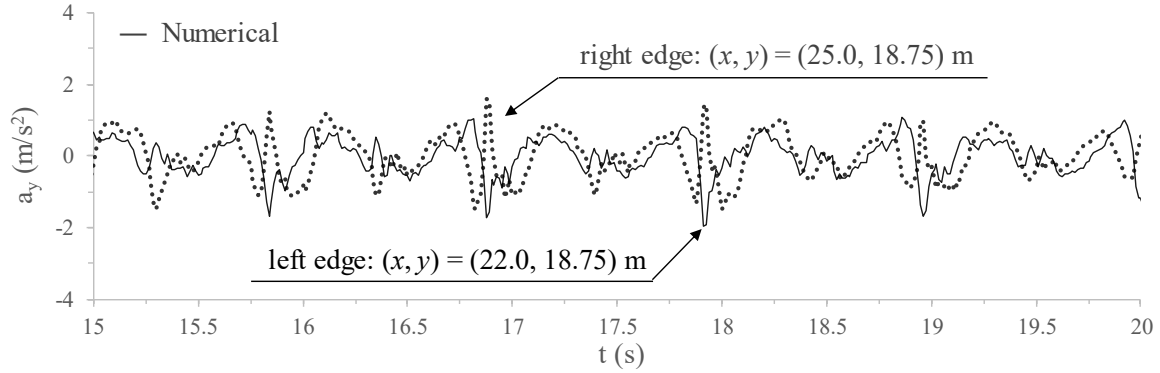

Figure 8.52 – Computed vertical acceleration time-histories at the left and right top edges of the lighter shallow foundation during the period ranging from 15 s to 20 s for CM-A.

Further insight into the obtained results is provided in Figure 8.53, which compares the vertical acceleration time-histories computed at the left edges of both shallow foundations during the period [15, 20] s. Complementary, Figure 8.54 compares the computed vertical acceleration time-histories at the right edges of the both shallow foundations during an identical period. Although having slightly different amplitudes, it is apparent that the peak

vertical accelerations computed at the edges of the shallow foundations occur at similar instants of time, suggesting that the shallow foundations oscillated in phase. As highlighted before, although an out-of-phase oscillation of the shallow foundations was observed in the centrifuge experiment, this was probably the result of a non-intentional rocking motion imposed to the entire centrifuge model during the experiment and, therefore, not a physical mechanism introduced by the sand-structure system during the experiment.

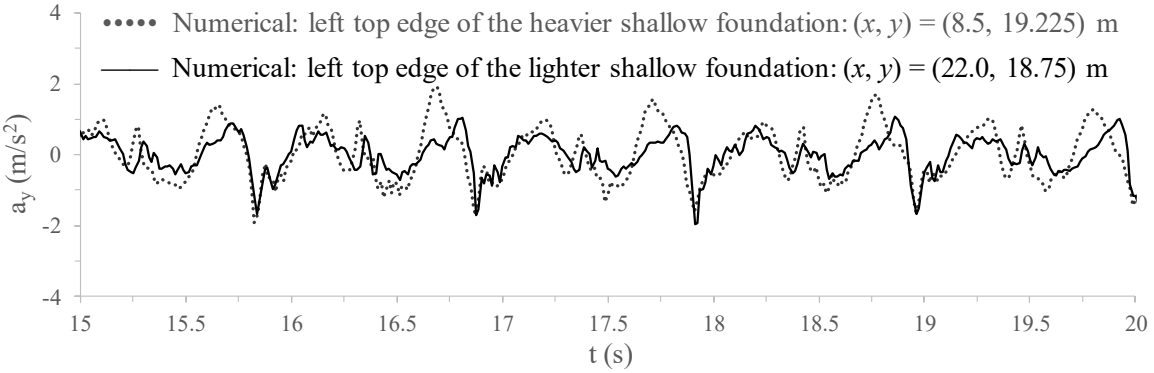

Figure 8.53 – Computed vertical acceleration time-histories at the left edges of the heavier and lighter shallow foundations during the period ranging from 15 s to 20 s for CM-A.

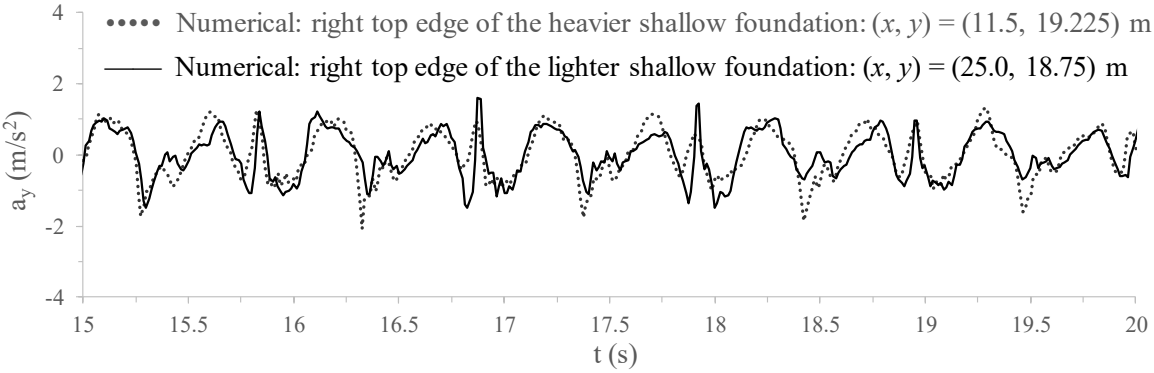

Figure 8.54 – Computed vertical acceleration time-histories at the right edges of the heavier and lighter shallow foundations during the period ranging from 15 s to 20 s for CM-A.

8.3.2.4.3 Excess pore pressures

The computed evolutions of the excess pore pressures with time for vertical alignments coincident with the axis of the heavier shallow foundation ($x = 10.0$ m) and with the axis of the lighter one ($x = 23.5$ m) are shown in Figure 8.55 and Figure 8.56, respectively, together with the experimental results.

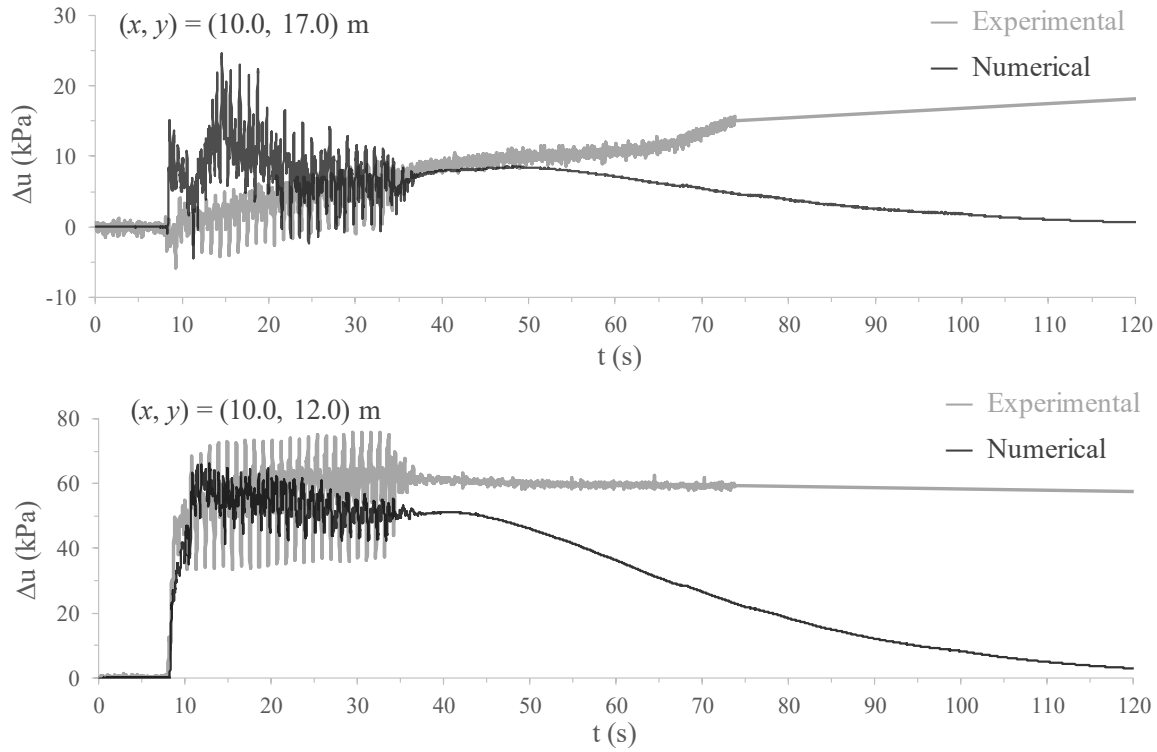

Figure 8.55 – Computed and measured excess pore pressure build-up at two different positions located along a vertical alignment coincident with the axis of the heavier shallow foundation for CM-A.

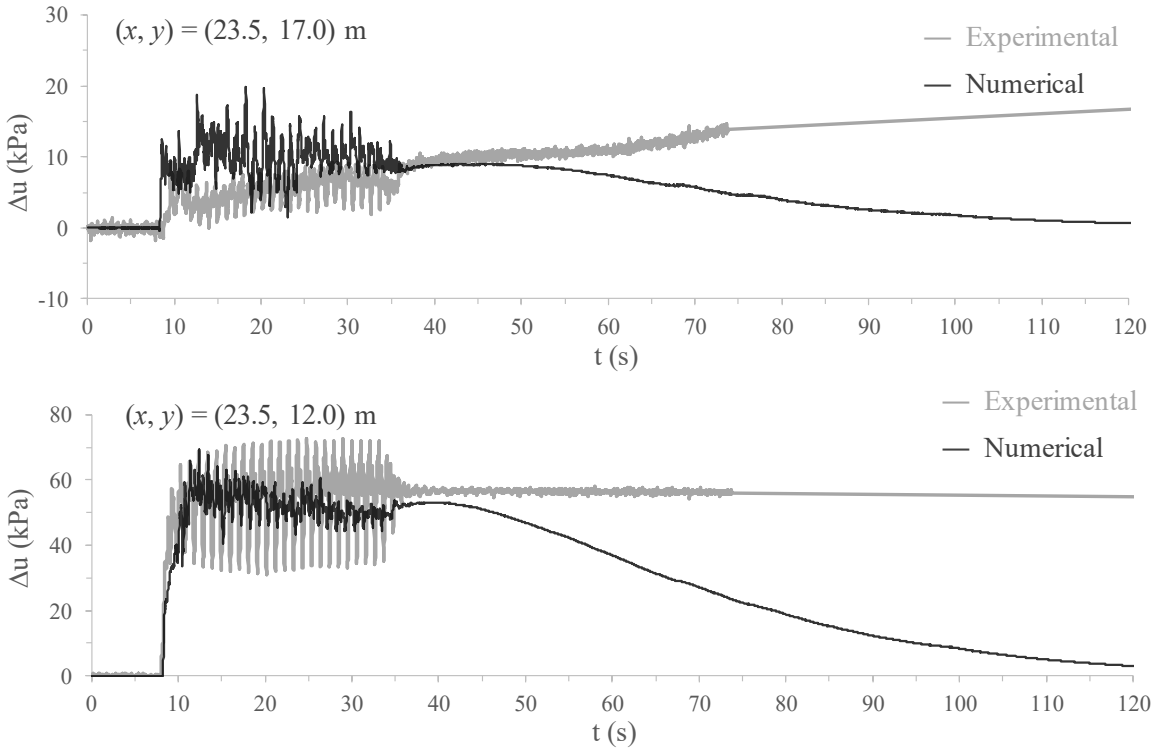

Figure 8.56 – Computed and measured excess pore pressure build-up at two different positions located along a vertical alignment coincident with the axis of the lighter shallow foundation for CM-A.

It can be observed that, at the deepest level of both alignments (i.e. at $(x, y) = (10.0, 12.0)$ m and $(x, y) = (23.5, 12.0)$ m), the numerical tool was able to reproduce satisfactorily the

excess pore pressure build-up during the first half of the shaking period (until $t \approx 20.0$ s). The agreement between numerical and experimental results is slightly less satisfactory for the subsequent shaking period, with the numerical model slightly underpredicting excess pore pressures. Conversely, at the shallowest level of both vertical alignments (i.e. at $(x, y) = (10.0, 17.0)$ m and $(x, y) = (23.7, 17.0)$ m), the opposite trend appears to be observed, with the constitutive model generally overestimating the excess pore pressures with dynamic loading, particularly during the first half of the shaking period. This overestimation might be a detrimental consequence of the simplification of the 3D nature of the problem by assuming 2D plane strain conditions. In effect, as discussed in Section 8.3.2.3, the 2D plane strain simplification appears to result in a slight underestimation of the effective stresses induced in the zones of the deposit immediately underneath the shallow foundations. It is, therefore, possible that, at those locations, the effective stress points are slightly farther away from the dilatancy surface than they would likely be in a full 3D model, implying that a higher tendency to contract and, therefore, to generate greater positive excess pore pressures under practically undrained conditions might have been simulated.

Greater discrepancies between numerical and experimental data are observed during the consolidation phase (i.e. phase during which excess pore pressure dissipation occurs), with the constitutive model significantly overpredicting the rate at which dissipation occurs. This undesirable aspect was also observed by Taborda (2011) when simulating the centrifuge experiments VELACS model 1 and VELACS model 12. As highlighted by the author, due to its open yield surface formulation, the constitutive model tends to largely overestimate the stiffness under stress paths characterised by approximately constant stress ratios – which are likely to occur after the end of shaking (i.e. during the consolidation phase) – and, therefore, to overpredict the rate of excess pore pressure dissipation during that stage. Consequently, the numerical tool is unable to reproduce the increase of excess pore pressure observed after the end of shaking in the centrifuge experiment, eventually overestimating the bearing capacity of the sand deposit during this phase of the experiment. Note that this pitfall of the constitutive model has been also identified when simulating drained isotropic compression tests, which are characterised by constant stress ratio loading (Section 7.2.1.4.1).

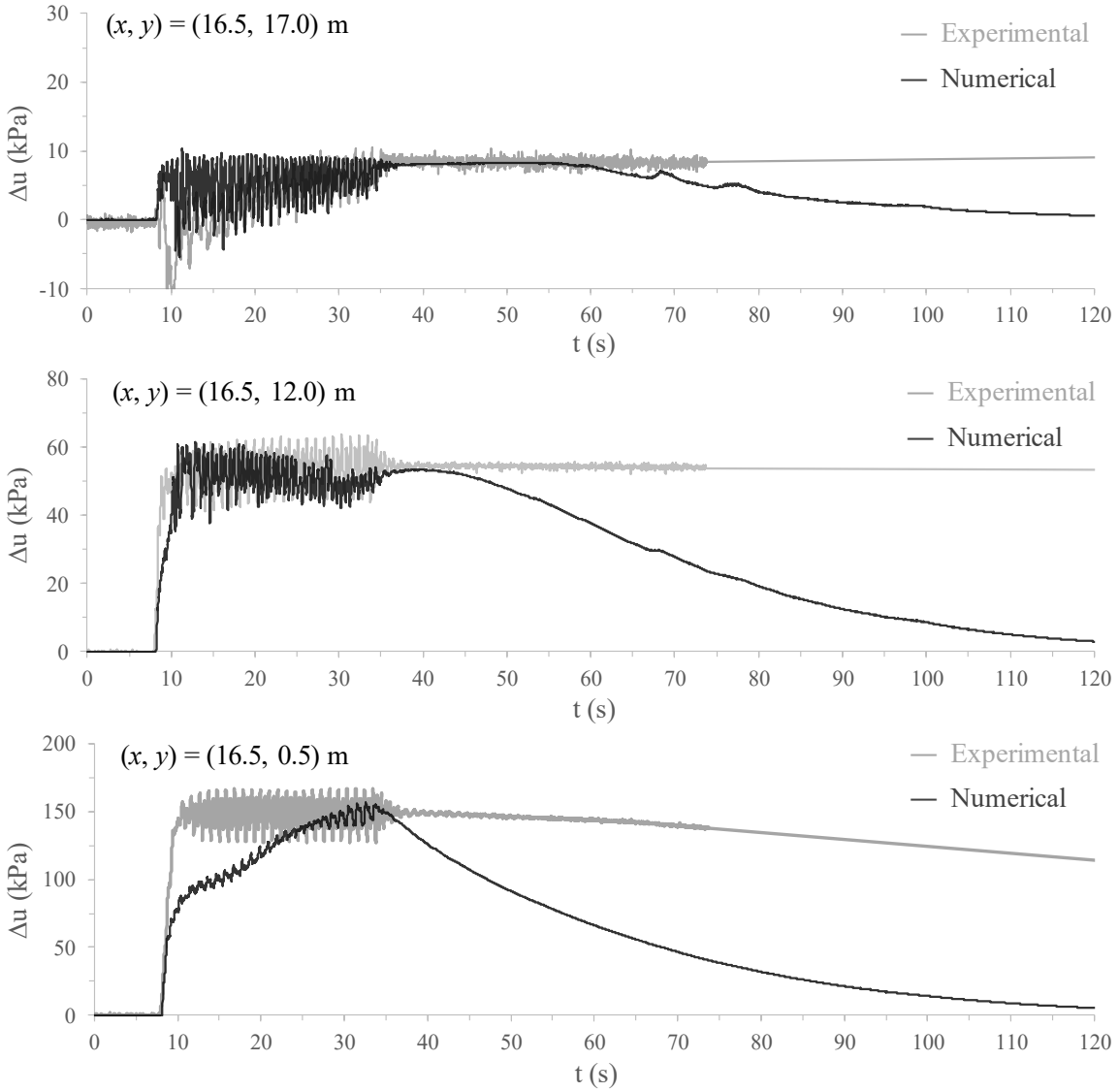

Figure 8.57 – Computed and measured excess pore pressure build-up at three different positions located along a vertical alignment coincident with the middle of the model for CM-A.

The computed evolutions of the excess pore pressures with time at three different levels located along a vertical alignment coincident with the middle of the model ($x = 16.0$ m in the numerical model) are shown in Figure 8.57, together with those registered in the experiment. Similar to what was observed for the vertical alignments coincident with the axes of the shallow foundations, the numerical model appears to overpredict slightly excess pore pressure generation at the shallowest position (i.e. at $(x, y) = (16.0, 17.0)$ m) during the first half of shaking, while slightly underestimating this aspect at the deeper levels, particularly at $(x, y) = (16.0, 0.5)$ m. In addition, it is apparent that the excess pore pressure dissipation in the numerical model is much faster than that measured in the experiment, as also observed for the positions under the shallow foundations. Nevertheless, as observed experimentally, the dissipation of excess pore pressures is observed to start earlier at the deepest levels of the sand deposit, suggesting that the numerical tool was able to reproduce the upward flow of water typically observed during the consolidation phase in this type of problems.

The computed excess pore pressures at $t = 37.5$ s (approximately corresponding to the end of shaking) are illustrated in Figure 8.58. Note that this contour plot was obtained by using the post-processing module of the software GiD version 7.2 (GiD, 2002). Details about the integration of FEMEPDYN with GiD can be found in Grazina (2009). As expected, the largest excess pore pressures, with values close to 140 kPa, are obtained at the bottom of the model, due to the highest effective stresses existing at that location at the start of the analysis, as well as largest distance to the ground surface, which consists of a seepage hydraulic boundary condition of the model (i.e. a boundary where water can flow in or out freely). Interestingly, apart from the very deep zones of the deposit, the lines of identical excess pore pressures are relatively horizontal, meaning that similar excess pore pressures are generated below the two shallow foundations, despite the different stress levels induced by the shallow foundations in the sand deposit. This aspect seems to agree with the experimental observations, since very similar excess pore pressures at the end of dynamic loading were measured at the following three monitoring positions: $(x, y) = (10.0, 12.0)$ m (i.e. under the heavier shallow foundation), at $(x, y) = (16.85, 12.0)$ m (i.e. in between both shallow foundations) and at $(x, y) = (23.7, 12.0)$ m (i.e. under the lighter shallow foundation).

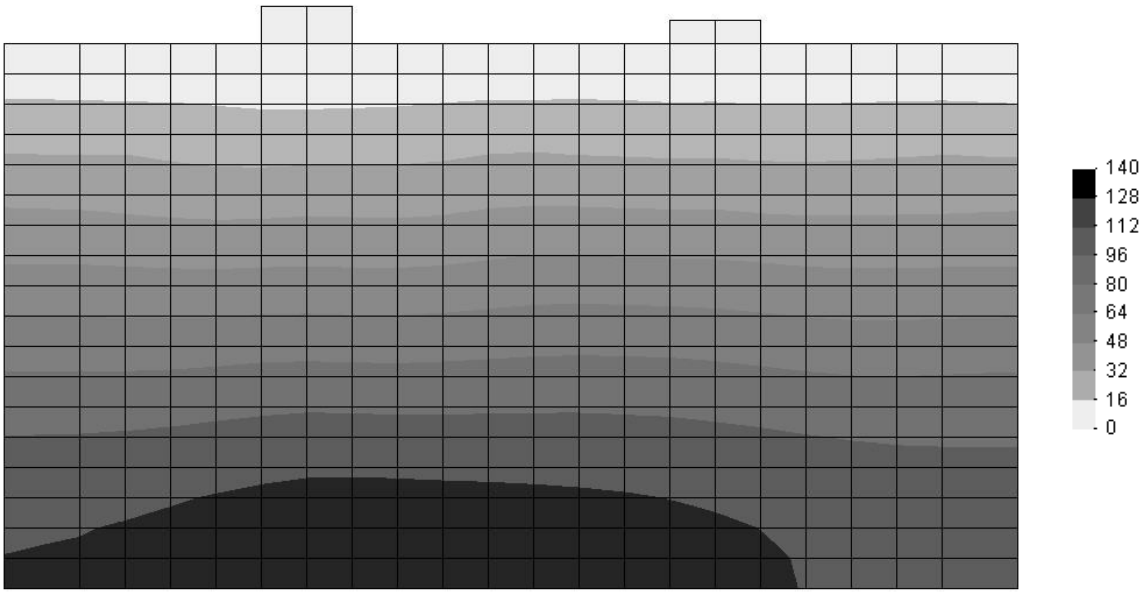

Figure 8.58 – Excess pore pressures (in kPa) at the end of dynamic loading ($t = 37.5$ s) for CM-A.

In addition, Figure 8.59 illustrates the excess pore pressure ratio, r_u, obtained in the numerical analysis at $t = 37.5$ s (i.e. approximately at the end of shaking). Although other possibilities would exist, for consistency with the definition used in laboratory testing, r_u is defined as the ratio of the excess pore pressure, Δu, to the initial vertical effective stress, $\sigma'_{v,0}$. It can be observed that, apart from the zone below the shallow foundations (having higher initial effective stresses), large values of r_u (in general, above 0.7) are obtained at the end of shaking in the model. This seems to agree well with the experimental results, where large excess pore pressures, with magnitudes similar to those of the initial vertical effective stress, were

measured at every monitoring position located along the alignment coincident with the middle of the model ($x = 16.0$ m in the numerical model), even at the bottom of the sand deposit (i.e. at $(x, y) = (16.0, 0.5)$ m), while not reaching the values of the initial vertical effective stresses below the shallow foundations.

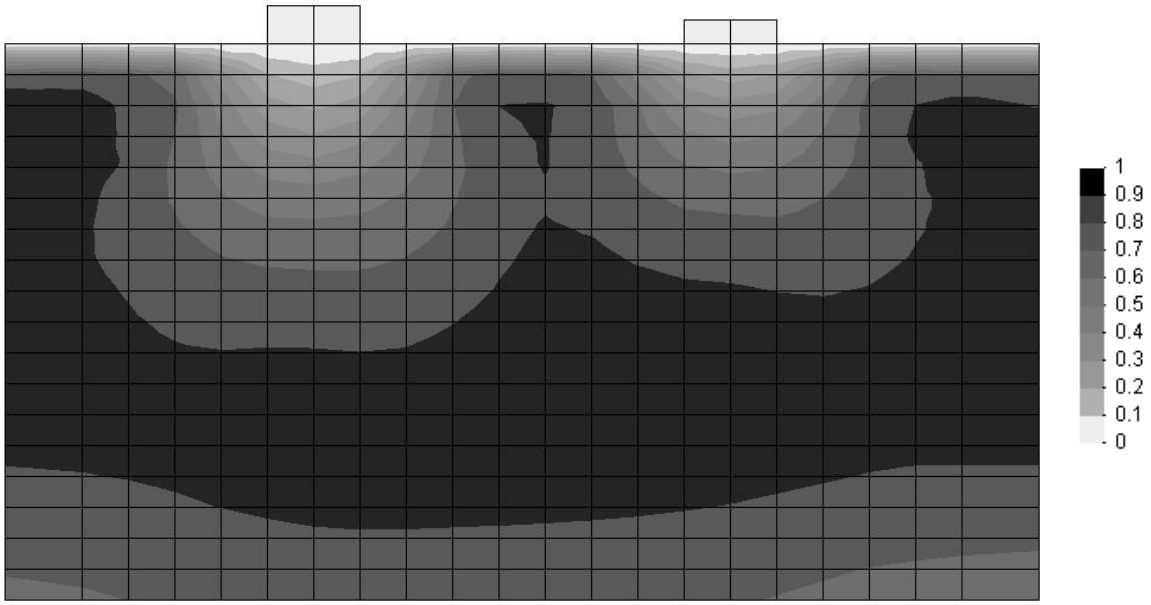

Figure 8.59 – Excess pore pressure ratio at the end of dynamic loading ($t = 37.5$ s) for CM-A.

8.3.2.4.4 Settlements

The computed evolutions of settlements during shaking and shortly after its end at the top of the heavier and lighter shallow foundations (i.e. at $(x, y) = (10.0, 19.225)$ m and $(x, y) = (23.7, 18.75)$ m, respectively) are compared with those measured in the experiment in Figure 8.60. It can be observed that the onset of deformation occurs slightly later in the numerical model than in the centrifuge experiment, probably due to the approximations required to estimate the input signal used in the numerical analysis, as well as due to the small underprediction of the excess pore pressure build-up during the earlier stages of loading (particularly observed at $(x, y) = (10.0, 12.0)$ m and $(x, y) = (23.5, 12.0)$ m), likely resulting in a small overprediction of the stiffness of the sand deposit during that early stage. Moreover, it can be observed that the rate of settlement obtained in the numerical analysis during shaking is slightly higher than that measured in the experiment, leading to a slight overestimation of the magnitude of settlement occurring during that phase of the experiment (of about 23 and 9 % for the heavier and lighter shallow foundations). Nevertheless, considering the complexity of the phenomena involved in this type of problems and the simplifications required to simulate this problem, it seems fair to mention that a good agreement between numerical and experimental data was reached during the application of dynamic loading.

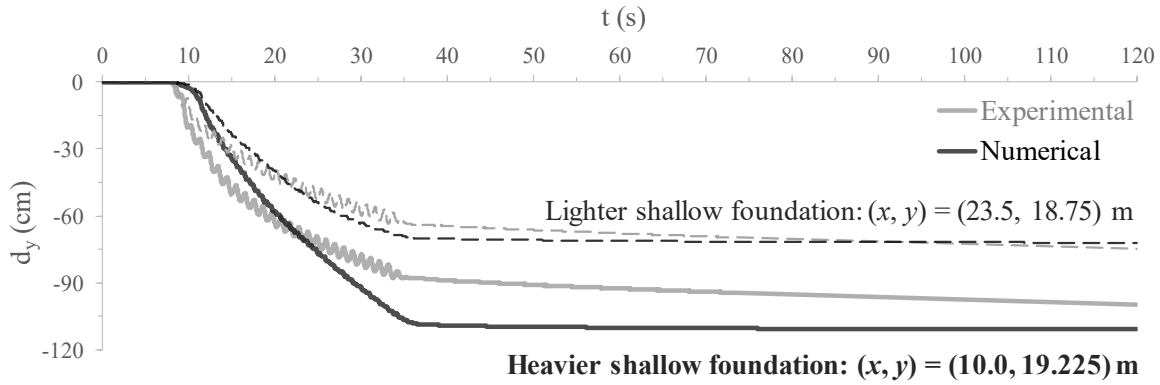

Figure 8.60 – Computed and measured settlements at the top of the heavier and lighter shallow foundations during shaking and shortly after its end for CM-A.

Perhaps unsurprisingly at this point, the agreement between computed and measured structural settlements occurring during the consolidation stage is much less satisfactory, with the numerical model underpredicting these settlements. As shown in Figure 8.61, this is particularly evident for the period ranging from $t \approx 36.0$ s (corresponding to the end of shaking) to $t \approx 300.0$ s, during which excess pore pressures were observed to increase significantly in the zones of the sand deposit immediately under the shallow foundations in the centrifuge experiment (Figure 8.55 and Figure 8.56). As mentioned before, this aspect is not properly simulated by the numerical model, with a significantly less excess pore pressure build-up in the zones of the deposit below the shallow foundations being registered after the end of shaking, probably justifying the underprediction of the settlements occurring during this stage of the analysis. As also pointed out before, this seems to be mainly a detrimental consequence of the open primary yield surface formulation adopted by the constitutive model, leading to the prediction of solely elastic response for stress paths characterised by approximately constant stress ratios.

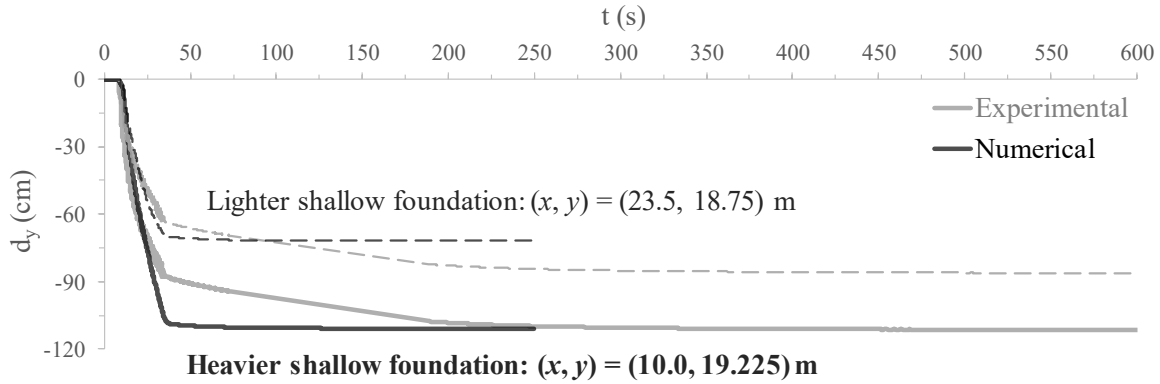

Figure 8.61 – Computed and measured settlements at the top of the heavier and lighter shallow foundations until the complete dissipation of the excess pore pressures for CM-A.

Regarding the settlements registered at the surface of the sand deposit in between shallow foundations, it is apparent in Figure 8.62 that the deformation pattern obtained in the numerical analysis differs from that measured in the experiment. Specifically, while the numerical model predicts significant heave, the opposite trend (i.e. settlement / subsidence)

is observed in the experiment. These discrepancies seem to arise from the fact that a practically undrained response was obtained for sand during shaking, while the results measured in the experiment seem to indicate the occurrence of a partially drained response. In effect, as investigated in Section 8.3.2.5, this mismatch appears to be mainly explained by the inability of the numerical tool to predict the occurrence of a temporary increase in the hydraulic conductivity of the liquefied sand deposit during dynamic loading in relation to the value of this property measured in conventional laboratory tests (e.g. permeameter tests) – a phenomenon reported in similar centrifuge studies (e.g. Scott, 1986a; Coelho, 2007; Su *et al.*, 2009) and numerically investigated by several authors when simulating VELACS model 1 (Manzari and Arulanandan, 1993; Taiebat *et al.*, 2007; Andrianopoulos *et al.*, 2010a; Taborda, 2011). In effect, although evidence on the mechanism responsible for this co-seismic increase of hydraulic conductivity is not available, Coelho (2007) suggested that the occurrence of transient cracks in the sand deposit under very low effective stresses and large vertical hydraulic gradients might be a plausible explanation. Indeed, this author suggested that the hydraulic conductivity of a homogeneous deposit of Leighton Buzzard sand might have increased by about twenty times of its original value during similar dynamic centrifuge tests, also intending to study liquefaction-related phenomena. This aspect was also studied by Taborda (2011), when reproducing VELACS model 1 (which was described in Section 5.3.2.2.3). This author demonstrated that the co-seismic settlements registered in the free-field in this type of problems are largely controlled by the value of the hydraulic conductivity adopted for the material in the numerical analysis, with the numerical tool largely underestimating the settlements observed in the free-field when the value measured in conventional element laboratory tests (in the case, permeameter test) is used in the simulation. Furthermore, based on a computational study, Taborda (2011) concluded that the hydraulic conductivity of Nevada sand might have reached a value of about six to seven times greater than its original value (i.e. measured in permeameter test) under dynamic excitation. Indeed, having proposed a simple non-linear hydraulic model describing the increase of the hydraulic conductivity of the sand deposit when large excess pore pressure ratios are obtained in the analysis, the author was able to match satisfactorily the settlements observed in the free-field.

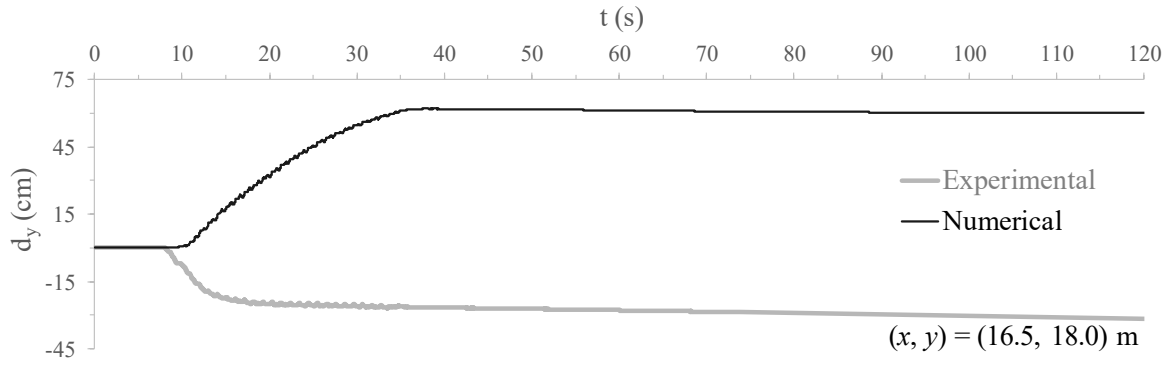

Figure 8.62 – Computed and measured settlements at the ground surface in between the two shallow foundations during shaking and shortly after its end for CM-A.

In addition, Figure 8.63 compares the ground settlement profile obtained at the end of the numerical analysis with that obtained from post-test measurements undertaken in the centrifuge facility after the complete dissipation of the excess pore pressures (Marques *et al.*, 2012a). Note that the post-test measurements shown in this figure are uniformly scaled to match the settlement of the heavier shallow foundation measured by the linear variable differential transducer (LVDT) located at $(x, y) = (10.0, 19.225)$ m during the experiment (i.e. $d_y \approx 112.0$ cm at $t \approx 600.0$ s). It is apparent that the numerical model predicts a movement of sand from the zones of the deposit under the influence of the shallow foundations to the zones farther from their influence (sides and middle of the model). Conversely, in the centrifuge experiment, the shallow foundations appear to have "punched through" the sand deposit, eventually getting partially buried in the sand deposit. Indeed, it is apparent that the change in volume of the sand deposit estimated from the ground settlement profile obtained in the numerical simulation is significantly smaller than that observed in the experiment. This aspect can be more clearly observed in Figure 8.64, which illustrates the numerical ground settlement profile at $t = 37.5$ s (i.e. approximately at the end of dynamic loading) and the corresponding change in volume of the sand deposit. It can be observed that the change in volume is only about 0.69 m^2.m. Since the initial volume of the sand deposit is approximately 603.0 m^2.m, the co-seismic volumetric strain change of the whole sand deposit can be estimated as 0.11 %, suggesting that, during this phase, practically fully undrained response was modelled. Note that, although experimental information about the ground settlement profile at $t = 37.5$ s is not available, it seems reasonable to assume that it might have a similar shape to that illustrated in Figure 8.63, since the majority of the settlement were observed to occur concurrently with the application of loading and similar trends (including the occurrence of subsidence in between shallow foundations) were registered by the instrumentation used in the centrifuge test. In such case, the experimental co-seismic change in volume of the whole sand deposit could be estimated as 15.5 m^2.m, which gives a co-seismic volumetric strain change of 2.57 % (note that, to ease the visualisation, and since it would be simply obtained by scaling that presented in Figure 8.63, the experimental ground settlement profile and its corresponding change in volume are omitted from Figure 8.64). This

strongly suggests that, on the contrary to what was obtained in the numerical analysis, the sand deposit responded in partially drained conditions during the experiment. Indeed, as suggested before, a plausible explanation for the inability of the numerical tool to predict this type of response may reside on the fact that a constant value for the hydraulic conductivity of the sand deposit was considered in the numerical analysis, while the hydraulic conductivity of the sand deposit might have increased concurrently with the application of loading in the experiment. This aspect is further investigated in Section 8.3.2.5.

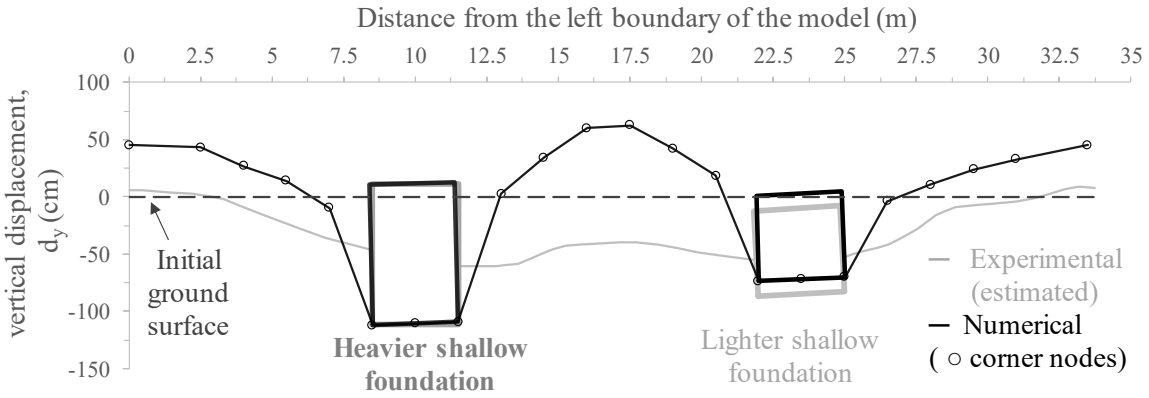

Figure 8.63 – Numerical and experimental ground settlement profile after the complete dissipation of excess pore pressures for CM-A.

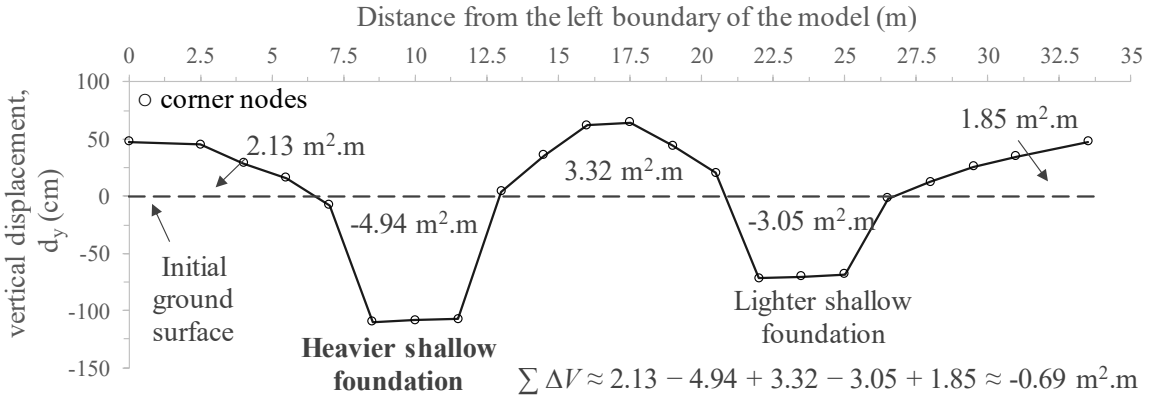

Figure 8.64 – Numerical ground settlement profile at the end of dynamic loading (t = 37.5 s) and corresponding change in volume of the sand deposit for CM-A.

Still regarding Figure 8.63, it can be seen that an excellent prediction of the rotation of the shallow foundations was obtained in the numerical analysis, being particularly relevant the ability of the numerical tool to capture the influence of the heavier shallow foundation on the deformation mechanism of the lighter one, as observed in the centrifuge experiment.

Further insight into the deformation mechanism predicted in the numerical analysis is provided in Figure 8.65, which compares the deformed mesh at three different instants of time (t = 25, 37.5 and 50 s) with the undeformed mesh (i.e. model at t = 0 s). Note that the scale of the deformations is equal to that of the model geometry (i.e. a scale of 1.0 was used to plot the deformed meshes). Moreover, note that accumulated total displacement vectors (scaled by a factor of 3.0 to aid the presentation) are also displayed in the figure to highlight

the deformation mechanism. It is apparent that the shallow foundations progressively settle by pushing sand to the sides, as mentioned before. Moreover, it is interesting to observe that the deformation mechanism of the heavier shallow foundation (positioned on the left side) affects that of the lighter shallow foundation, with this latter one tending to move to the right, while slightly rotating.

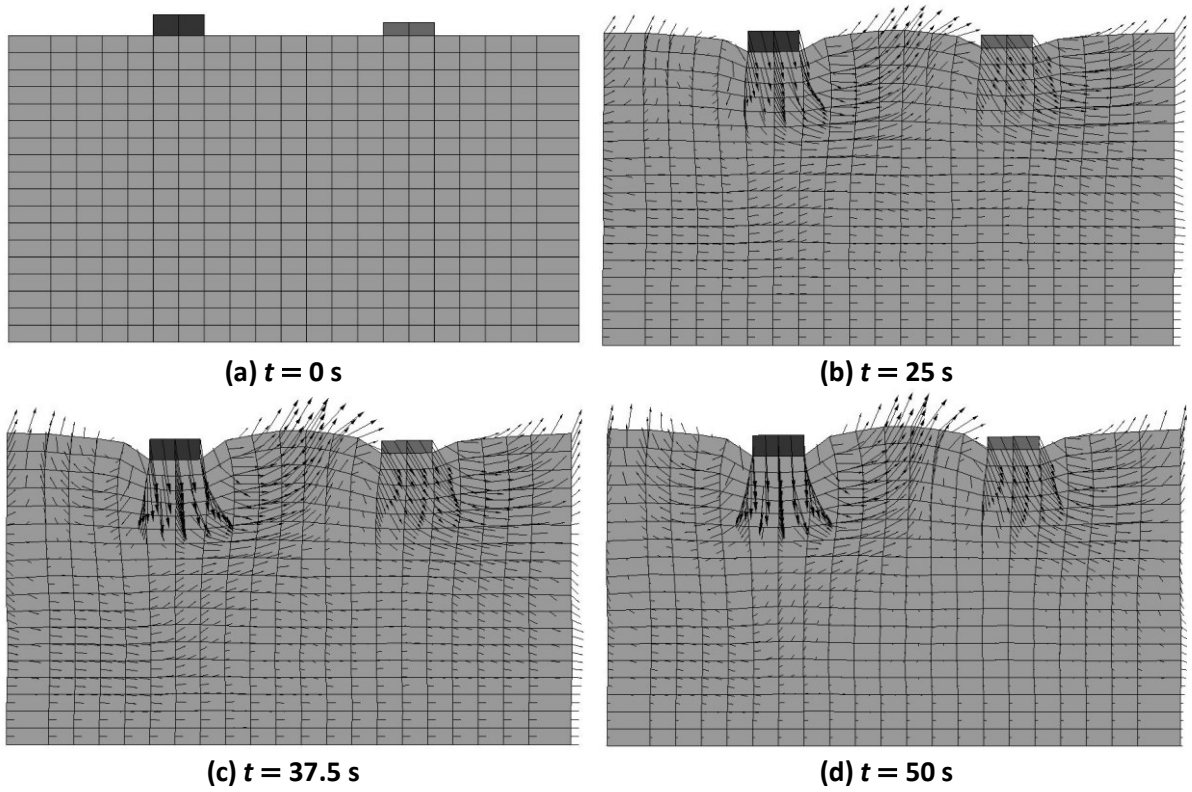

(a) $t = 0$ s **(b) $t = 25$ s**

(c) $t = 37.5$ s **(d) $t = 50$ s**

Figure 8.65 – Deformed mesh and displacement vectors at different instants of time for CM-A.

8.3.2.4.5 Vertical effective stresses

Due to the large excess pore pressure generated during dynamic loading, as well as pore fluid migration observed in this type of problems, which might compromise the bearing capacity of the foundations, it is of particular interest to inspect the evolution of the vertical effective stresses with time. With this purpose, Figure 8.66 illustrates the vertical effective stresses computed at six different instants of time: $t = 0$ s (corresponding to the start of the analysis), $t = 25$ s (corresponding to approximately half of the duration of dynamic loading), $t = 37.5$ s (at the end of dynamic loading) and $t = 50$, 75 and 125 s (three different instants of time of the consolidation phase). As expected, it can be observed that the effective vertical stresses decrease rapidly as dynamic loading starts, particularly in the zones of the model farther away from the shallow foundations (i.e. sides of the model and middle of the model). The fact that the effective stresses are not symmetric about an axis corresponding to the middle of the model at $t = 25$ s seems consistent with the direction of the displacement of the shallow foundations, which appear to be slightly inclined to the right, as previously illustrated in Figure 8.65. Moreover, it can be seen that, slightly after the end of dynamic (i.e. at $t = 37.5$ s), very

low effective stresses exist practically in the whole model, apart from the zones immediately underneath the shallow foundations. This is, indeed, consistent with the excess pore pressure ratios obtained in the numerical analysis at that instant of time (Figure 8.59). As dynamic loading ceases and dissipation of excess pore pressures occurs, the effective vertical stresses progressively increase from bottom to the top of the model, as also expected. Note that similar trends are observed for the horizontal effective stresses.

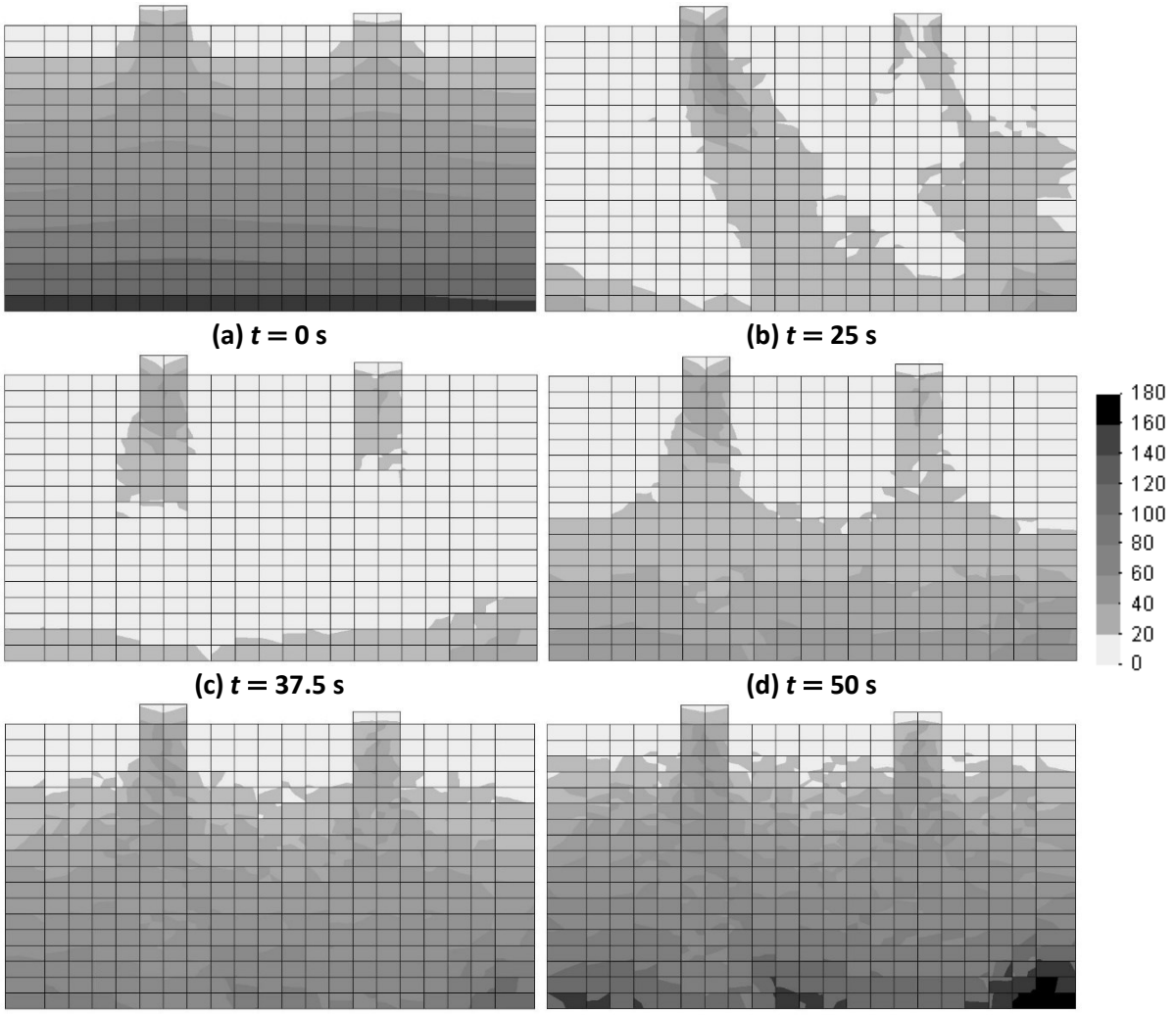

Figure 8.66 – Vertical effective stresses (in kPa) at different instants of time for CM-A.

8.3.2.5 Dynamic analysis with variable hydraulic conductivity

8.3.2.5.1 Non-linear hydraulic model proposed by Taborda (2011)

A comprehensive study on the influence of the hydraulic conductivity on the response of a level ground deposit of sand subjected to dynamic loading inducing cyclic mobility – VELACS model 1 (briefly described in Section 5.3.2.2.3) – was performed by Taborda (2011). Specifically, having observed that the numerical predictions largely underestimated both rate and magnitude of ground settlements observed in the centrifuge experiment, the author performed a series of finite element analyses adopting different hydraulic conductivities for

the sand deposit. The author verified that the increase in hydraulic conductivity of the sand deposit led to an increase in the rate and magnitude of settlements registered at the surface of the deposit. Furthermore, the author suggested that, although the increase in hydraulic conductivity may be insufficient by itself to describe accurately all aspects of the response of sand measured in the experiment (particularly in terms of observed excess pore pressures, as discussed later), it allows for a significantly better numerical reproduction of the settlements occurring in the free-field during dynamic loading. Indeed, the author proposed a simple non-linear hydraulic model describing the variation of the hydraulic conductivity, k, with the excess pore pressure ratio, r_u, as given by Equation 8.22 (note that, for simplicity of the presentation, the hydraulic conductivity is described in this equation as a one-dimensional property).

$$\frac{k}{k_0} = 1.0 + \left(\frac{k_{max}}{k_0} - 1.0\right)\left(\frac{r_u}{r_u^*}\right)^{n_k} \leq \frac{k_{max}}{k_0} \tag{8.22}$$

where k_0 is the initial hydraulic conductivity (i.e. the value measured in conventional laboratory tests, such as in permeameter tests), k_{max} / k_0 is the ratio of the maximum hydraulic conductivity reached in the experiment to its initial value, while, r_u^* and n_k are two additional model parameters with no physical meaning defining, respectively, the value of r_u above which the hydraulic conductivity remains at its maximum value and the sharpness of its increase.

As illustrated in Figure 8.67a, to obtain a steep variation of the hydraulic conductivity with the excess pore pressure ratio, a relatively large value for n_k is required. Note, however, that the selected value should not be too large, otherwise numerical instabilities might arise during the numerical analysis. A value of $n_k = 10.0$ was used by Taborda (2011) in the numerical simulation of VELACS model 1. In terms of r_u^* (whose value is naturaly limited by the range of values admissible for the excess pore pressure ratio, i.e. between 0.0 and 1.0), Figure 8.67b shows that, the larger the value of r_u^*, the greater the value of r_u required to increase the hydraulic conductivity. Note that $r_u^* = 0.9$ was employed by Taborda (2011) in the numerical simulation of VELACS model 1, implying that the hydraulic conductivity remaining practically unaltered until $r_u < 0.7$, while reaching its maximum for $r_u \geq 0.9$, as highlighted by the author.

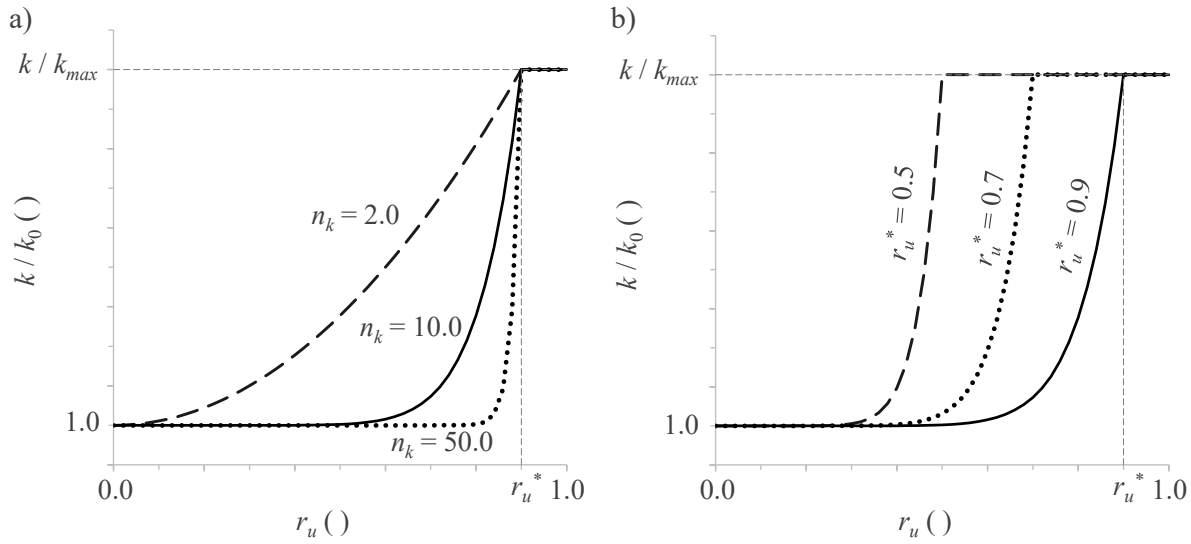

Figure 8.67 – Effect of (a) n_k and (b) r_u^* on the variation of hydraulic conductivity with the excess pore pressure ratio (adapted from Taborda, 2011).

With the main objective of studying the influence of this aspect on the numerical simulation of CM-A, particularly on the settlements obtained for the zone of the deposit located in between shallow foundations, the hydraulic model proposed by Taborda (2011) was implemented into FEMEPDYN. As such, rather than constant throughout dynamic loading, the hydraulic conductivity of each element of the sand deposit was varied according to Equation 8.22 during this phase of the analysis. Note that details about the mathematical formulation of the equation of motion, as implemented into FEMEPDYN, are omitted here, since a detailed description of this aspect can be found in Grazina (2009). Moreover, it should be highlight that, although it would have been possible to vary both cartesian components of the hydraulic conductivity during the numerical analysis (as performed, for example, by Taborda (2011) when simulating VELACS model 1), in the present study, only the vertical component, k_y, was varied during the analysis. In effect, as suggested by Coelho (2007), although evidence of the physical mechanism governing the increase in hydraulic conductivity in a liquefied sand deposit during dynamic loading is not available, it seems reasonable to assume that transient cracks may occur in the sand deposit under very low effective stresses and large hydraulic gradients observed during this phase of the experiment. Indeed, since drainage is only possible through the surface of the sand deposit and, consequently, the upwards flow of water is mainly oriented along the vertical direction, it may be further assumed that the orientation of the cracks is mainly vertical, therefore, affecting mainly the vertical hydraulic conductivity of the sand deposit.

In terms of model parameters, Equation 8.22 requires the selection of values for k_{max} / k_0 (which, as explained before, corresponds, in this case, to $k_{y,max} / k_{y,0}$), r_u^* and n_k. Starting by the last two model parameters, given the lack of experimental data which could be used to calibrate the proposed equation, the values employed by Taborda (2011) in the numerical simulation of VELACS model 1 were adopted in the present study: $r_u^* = 0.9$ and $n_k = 10.0$.

Regarding the first of these parameters, $k_{y,max}/k_{y,0} = 100.0$ was assumed. Although it can be argued that this value is large, it should be noted that the main purpose of this study is solely to assess whether the inability of the numerical tool to reproduce accurately the response observed in between shallow foundations in CM-A (particularly in terms of measured surface settlements) may be justified by an increase in hydraulic conductivity of the sand deposit during dynamic loading, as suggested in the literature (Coelho, 2007; Taborda, 2011). Naturally, for all remaining model parameters, the values adopted in the previous simulation were also employed in this analysis (Section 8.3.2.1), to allow for a direct comparison of the obtained results. Along the same lines, the mesh, boundary conditions, numerical control parameters and initial conditions (including initial stress state) considered in this simulation were identical to those adopted in the previous analysis.

In the following sections, the results obtained in this numerical analysis with variable hydraulic conductivity are compared with those obtained in the previously performed analysis with constant hydraulic conductivity, as well as with those measured in the experiment. Focus is given to the excess pore pressures and surface settlements. Note, nevertheless, that the complete set of results (including horizontal and vertical accelerations) obtained in the analysis with variable hydraulic conductivity can be found in Appendix F.

8.3.2.5.2 Excess pore pressures

Figure 8.68 compares the evolutions of the excess pore pressures with time obtained in the newly performed numerical analysis with variable hydraulic conductivity with those obtained in the previous numerical analysis with constant hydraulic conductivity at two different positions located along a vertical alignment coincident with the axis of the heavier shallow foundation ($x = 10.0$ m). Similarly, Figure 8.69 compares the excess pore pressures obtained in the two numerical analyses at two different positions located along a vertical alignment coincident with the axis of the lighter shallow foundation ($x = 23.5$ m). In both figures, the experimental results are also presented for comparison. It can be observed that similar co-seismic excess pore pressures were obtained in the two different numerical analyses at the deeper level of both alignments (i.e. at $(x, y) = (10.0, 12.0)$ m and $(x, y) = (23.5, 12.0)$ m), agreeing satisfactorily with the response measured in the experiment. Conversely, as shaking was over, different numerical responses were obtained in the two analyses. Specifically, it is apparent that the rate of dissipation of excess pore pressures obtained in the numerical analysis with variable hydraulic conductivity is much higher than that computed in the numerical analysis with constant hydraulic conductivity. Since the hydraulic conductivity considered for the sand deposit during this phase was identical in both analysis (and equal to the initial hydraulic conductivity, k_0), this suggests that the post-seismic migration of excess pore pressures from other zones of the model to this location obtained in the analysis with variable hydraulic conductivity is significantly smaller than that computed in the analysis with constant hydraulic conductivity. As detailed later, this is likely a consequence of the smaller

excess pore pressures generated in the analysis with variable hydraulic conductivity in zones of the sand deposit where the influence of the shallow foundations is either small or negligible (basically, all zones where very large values of r_u were computed in the analysis with constant hydraulic conductivity – Figure 8.59).

Regarding the excess pore pressures computed at the shallower level of both alignments (i.e. at $(x, y) = (10.0, 17.0)$ m and $(x, y) = (23.7, 17.0)$ m), it can be seen that a clearly worse prediction of this aspect of the response was obtained in the newly performed analysis with variable hydraulic conductivity, with much higher excess pore pressures being computed at this location during dynamic loading. In effect, by increasing only the vertical hydraulic conductivity of the sand deposit, it is possible that high excess pore pressures, mainly migrating from deeper zones of the sand deposit, accumulate at this location, where drainage is not allowed, due to the presence of the impervious shallow foundation. A better reproduction of this aspect of the response would be likely obtained by increasing both horizontal and vertical components of the hydraulic conductivity of the sand deposit.

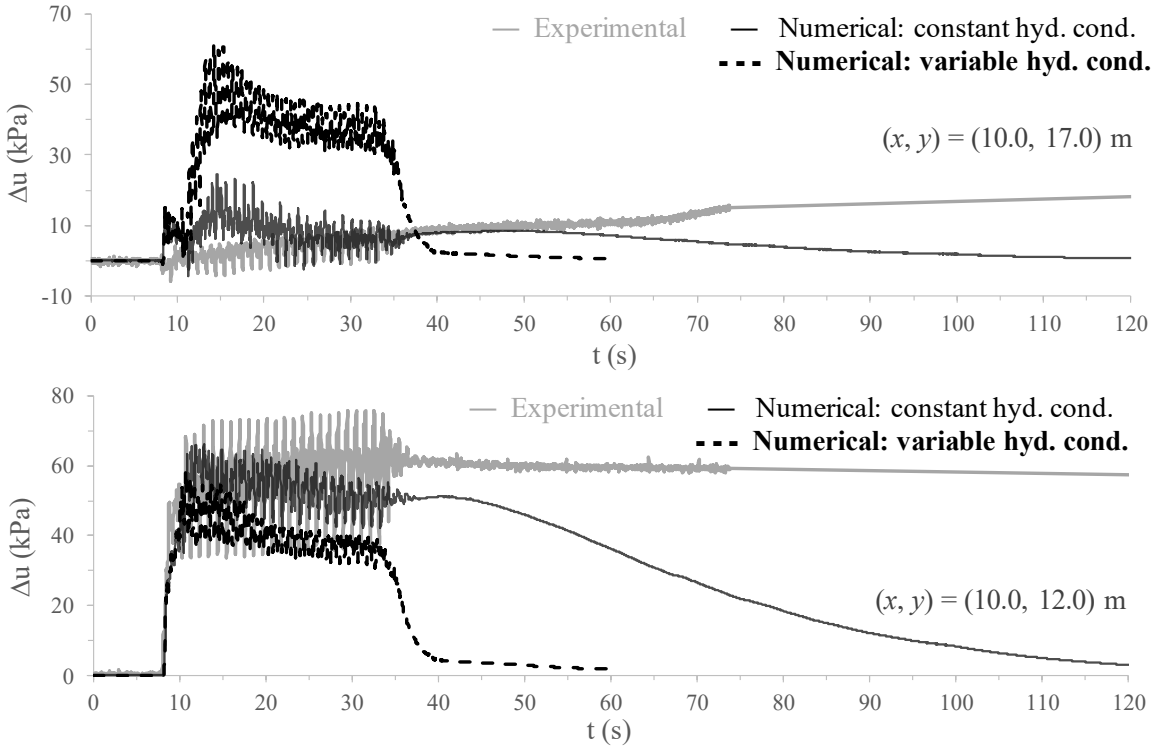

Figure 8.68 – Comparison of the excess pore pressures evolutions with time obtained in numerical analyses with constant and variable hydraulic conductivity with those measured in the experiment for a vertical alignment coincident with the axis of the heavier shallow foundation of CM-A.

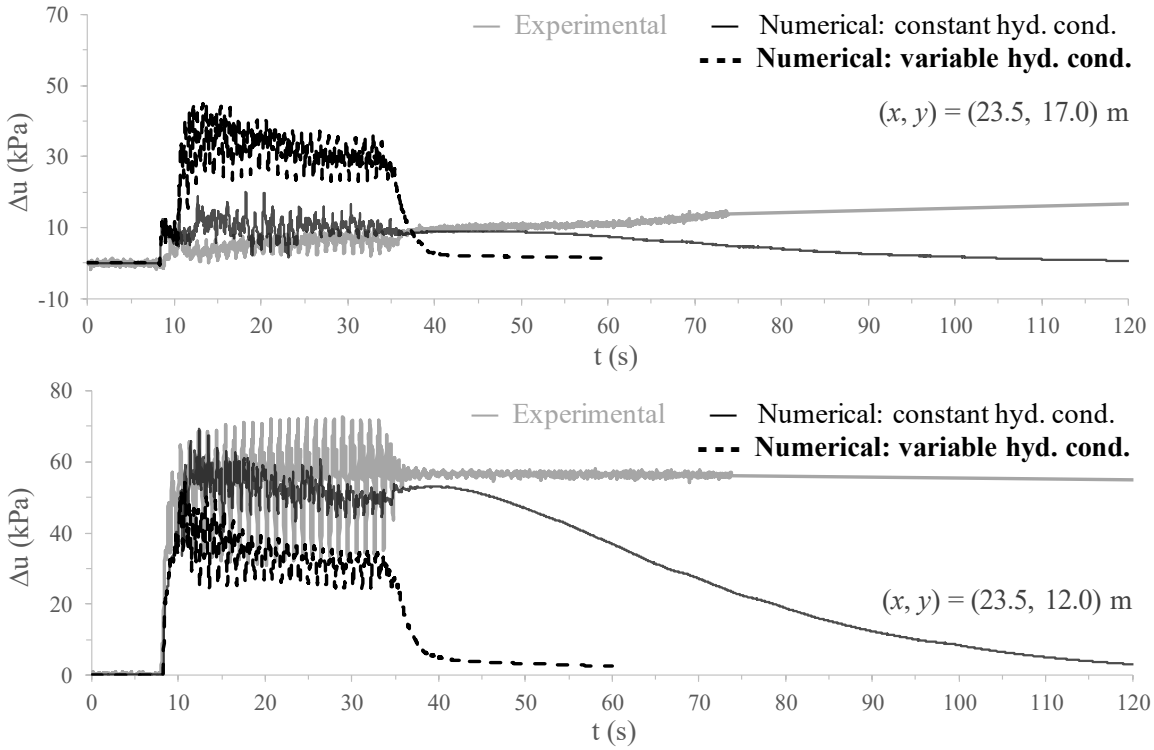

Figure 8.69 – Comparison of the excess pore pressures evolutions with time obtained in numerical analyses with constant and variable hydraulic conductivity with those measured in the experiment for a vertical alignment coincident with the axis of the lighter shallow foundation for CM-A.

The evolutions of the excess pore pressures with time computed in both numerical analyses at three different levels located along a vertical alignment coincident with the middle of the model ($x = 16.5$ m in the numerical model) are shown in Figure 8.57, together with those registered in the experiment. It can be observed that, after an initial increase, a sudden decrease of the excess pore pressures at the two shallower positions (i.e. at $(x, y) = (16.5, 17.0)$ m and $(x, y) = (16.5, 12.0)$ m) was obtained in the newly performed analysis, due to the increase in vertical hydraulic conductivity of the deposit. Similarly, the excess pore pressures at the deepest position (i.e. at $(x, y) = (16.5, 0.5)$ m) were also underestimated in the newly performed analysis, although remaining relatively constant after the initial increase. It is apparent that a much better reproduction of the response observed in the experiment at these three positions was obtained in the previous numerical simulation assuming constant hydraulic conductivity.

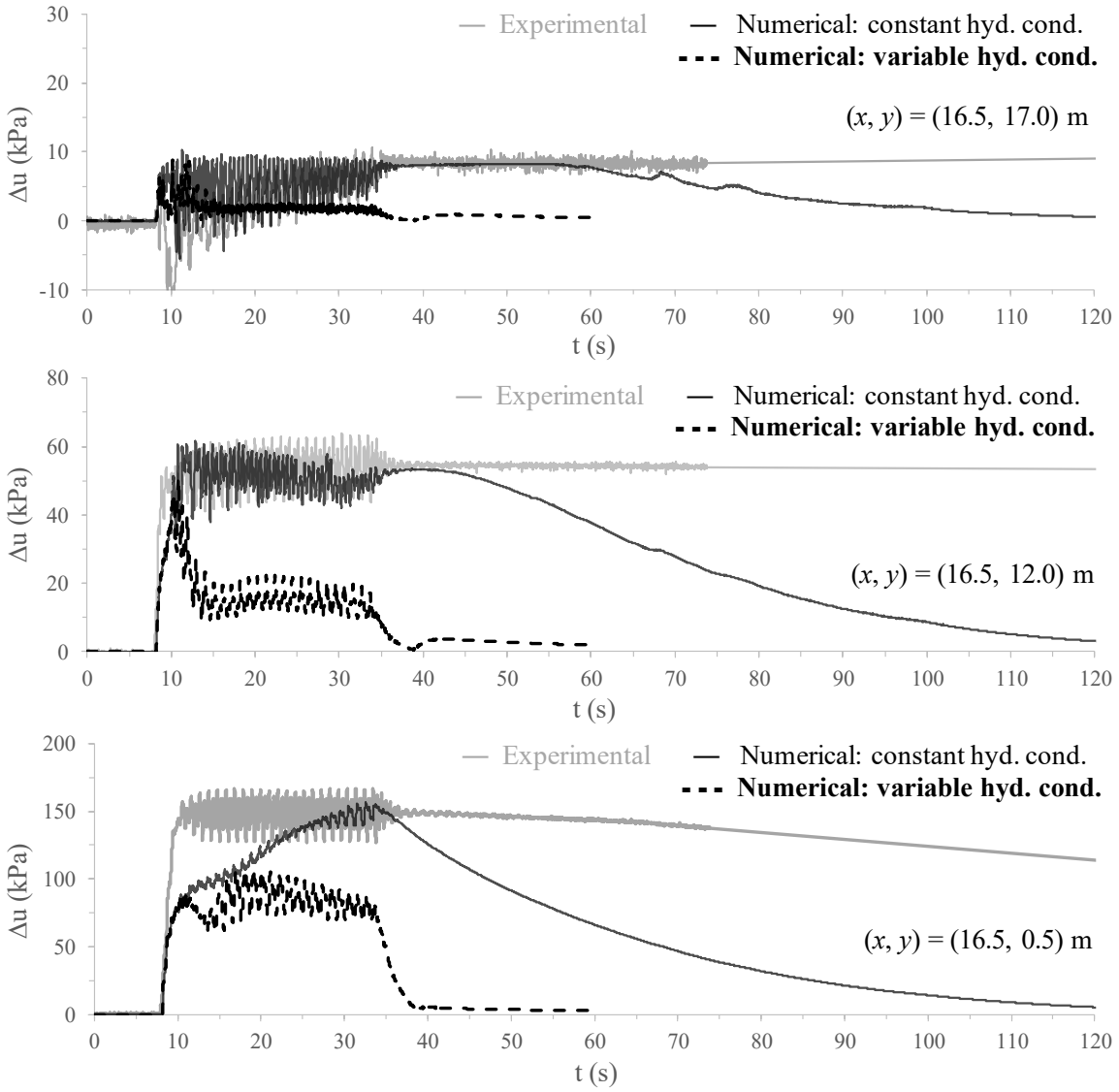

Figure 8.70 – Comparison of the excess pore pressures evolutions with time obtained in numerical analyses with constant and variable hydraulic conductivity with those measured in the experiment for a vertical alignment coincident with the middle of the model for CM-A.

Figure 8.71 illustrates the excess pore pressure ratio, r_u, obtained in the newly performed numerical analysis with variable hydraulic conductivity approximately at the end of shaking (i.e. at $t = 37.5$ s). Contrary to what was obtained in the previous numerical analysis with constant hydraulic conductivity (Figure 8.59), it is apparent that relatively low values of r_u (in general, below 0.4) were obtained at the end of shaking in this newly performed analysis. Furthermore, it is clear that the larger values are obtained underneath the shallow foundations, suggesting, once more, that the increase in the hydraulic conductivity did not lead to an improved reproduction of this aspect of the response of sand. This aspect, however, might deserve further investigation in the future, by employing more reasonable values for the increase in hydraulic conductivity of sand during dynamic loading.

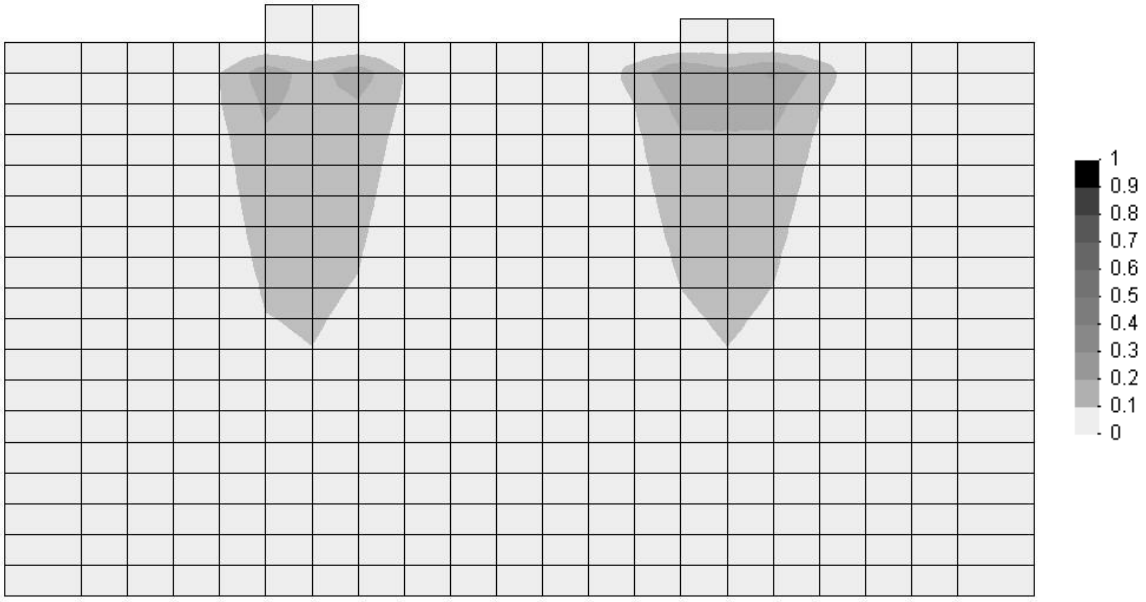

Figure 8.71 – Excess pore pressure ratio obtained in the analysis with variable hydraulic conductivity at the end of dynamic loading ($t = 37.5$ s) for CM-A.

8.3.2.5.3 Settlements

The evolutions of settlements at the top of the heavier and lighter shallow foundations (i.e. at $(x, y) = (10.0, 19.225)$ m and $(x, y) = (23.7, 18.75)$ m, respectively) obtained in both numerical analyses are compared with those measured in the experiment in Figure 8.72. It can be observed that a smaller rate of structural settlement accumulation is obtained when considering variable hydraulic conductivity, which is likely the detrimental consequence of the overall underestimation of the excess pore pressures generated during dynamic loading and, therefore, overestimation of the stiffness of the sand deposit.

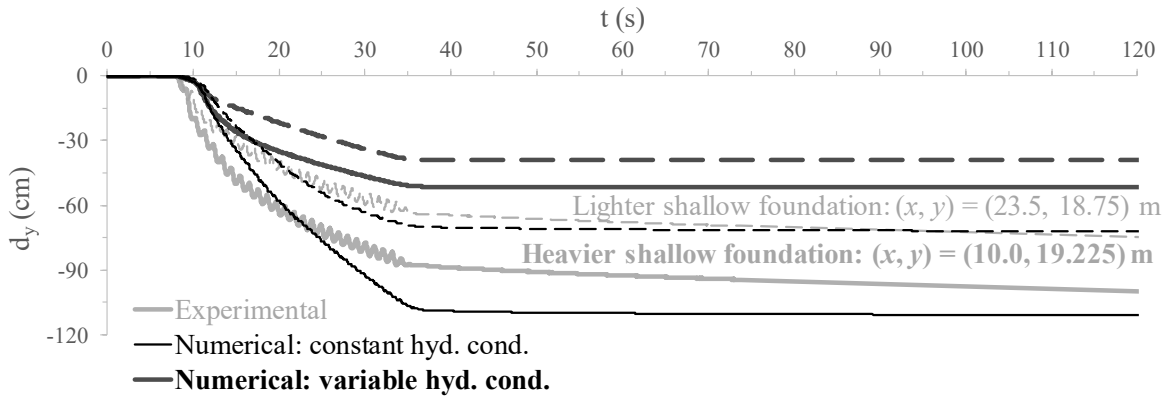

Figure 8.72 – Comparison of the structural settlements obtained in numerical analyses with constant and variable hydraulic conductivity with those measured in the experiment for CM-A.

In addition, Figure 8.73 compares the settlements obtained in the two numerical analyses at the surface of the sand deposit in between shallow foundations. The experimental measurements are also presented for comparison. It can be observed that, contrary to what was obtained in the simulation with constant hydraulic conductivity, downwards vertical displacement (i.e. settlement/subsidence) is obtained in the simulation with variable

hydraulic conductivity, as observed in the experiment. This suggests that the hydraulic conductivity plays a fundamental role in the modelled response. Moreover, as suggested in previous experimental studies (e.g. Scott, 1986a; Coelho, 2007; Su *et al.*, 2009), as well as numerically investigated by several authors (Manzari and Arulanandan, 1993; Taiebat *et al.*, 2007; Andrianopoulos *et al.*, 2010a; Taborda, 2011), the increase of the hydraulic conductivity of the liquefied sand deposit during dynamic loading may explain the large co-seismic settlements observed in the zones of the model farther from the shallow foundations in the centrifuge experiment.

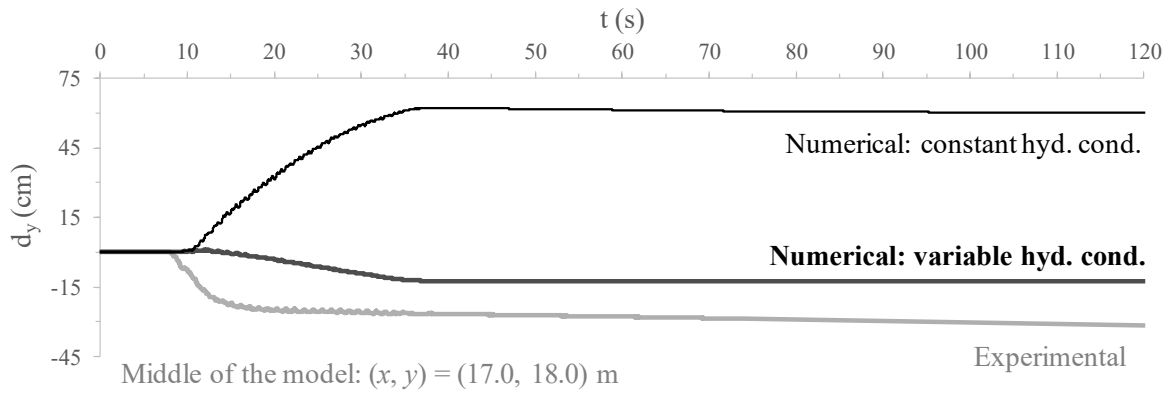

Figure 8.73 – Comparison of the settlements obtained in numerical analyses with constant and variable hydraulic conductivity at the surface of the sand deposit in between the two shallow foundations with those measured in the experiment for CM-A.

Figure 8.74 compares the ground settlement profile obtained at the end of both numerical analyses with that inferred from post-test measurements undertaken in the centrifuge facility after the complete dissipation of the excess pore pressures (Marques *et al.*, 2012a). As noted before, the post-test measurements shown in this figure are uniformly scaled to match the settlement of the heavier shallow foundation measured by the linear variable differential transducer (LVDT) located at $(x, y) = (10.0, 19.225)$ m during the experiment (i.e. $d_y \approx$ 112.0 cm at $t \approx 600.0$ s). Although still underestimating the total change in volume observed in the experiment (in this case, a total volume change of 5.8 m^2.m was obtained), it is clear that an improved replication of this aspect of the response was obtained in the newly performed numerical analysis considering the variation of the hydraulic conductivity of the liquefied sand deposit under dynamic excitation than in the previous analysis considering constant hydraulic conductivity.

Furthermore, by comparing the deformation mechanism obtained in the previous numerical analysis with constant hydraulic conductivity (Figure 8.65) with that obtained in the newly performed numerical analysis with variable hydraulic conductivity (Figure 8.75), it appears that the latter resembles more the one observed in the centrifuge experiment, as significantly lesser lateral movement of sand from the zone under the influence of the shallow foundations to the zone in between them can now be observed.

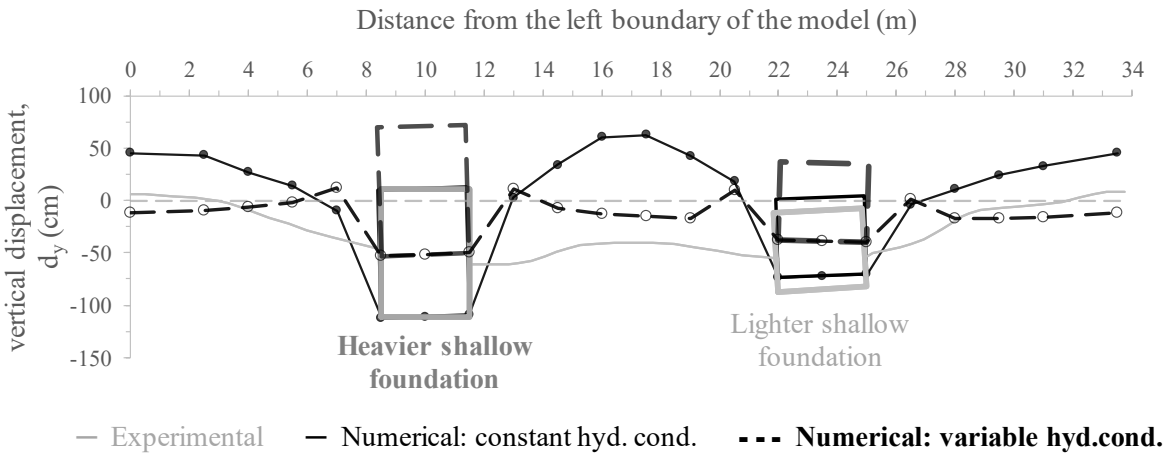

Figure 8.74 – Comparison of the settlement profiles of the ground surface and shallow foundations after the complete dissipation of excess pore pressures obtained in numerical analyses with constant and variable hydraulic conductivity and inferred from post-test measurements for CM-A.

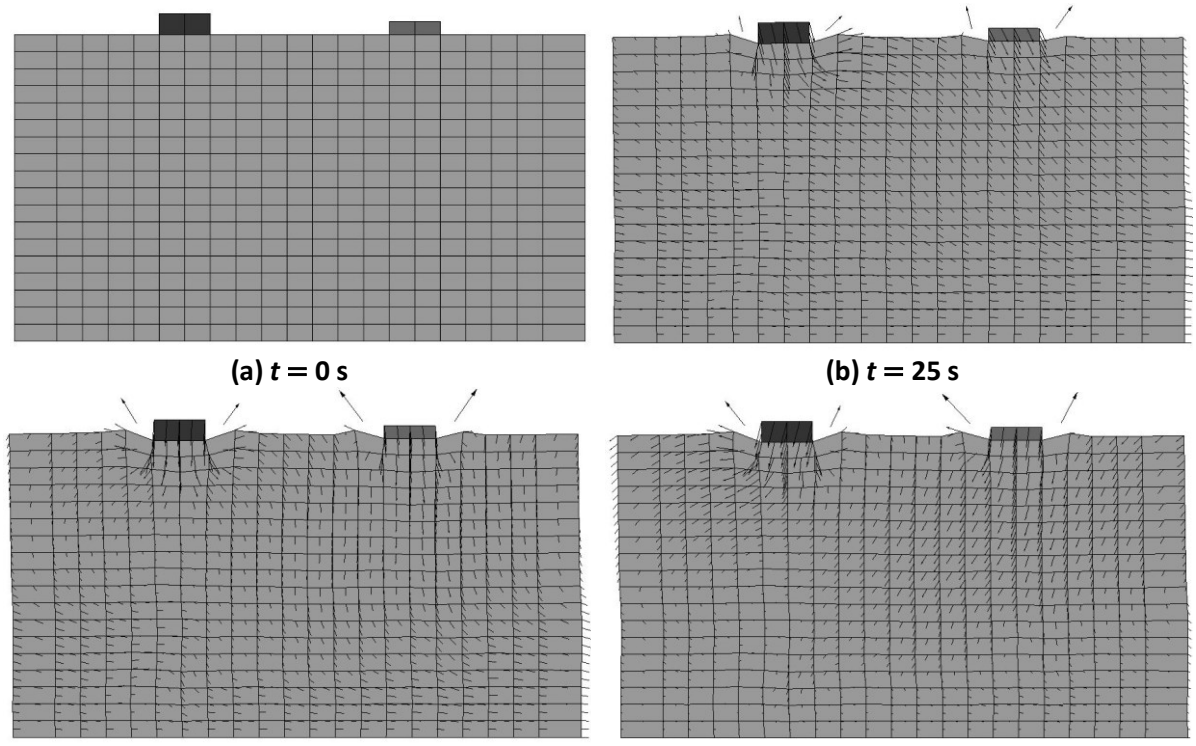

(a) $t = 0$ s **(b) $t = 25$ s**

(c) $t = 37.5$ s **(d) $t = 50$ s**

Figure 8.75 – Deformed mesh and displacement vectors at different instants of time obtained in the numerical analysis with variable hydraulic conductivity for CM-A.

8.4 Centrifuge model B – Use of narrow densified zones and high-capacity vertical drains to improve the performance of adjacent shallow foundations resting on a sand deposit subjected to dynamic loading causing liquefaction

8.4.1 Brief description of the experiment and obtained results

8.4.1.1 Configuration and instrumentation of the experiment

The centrifuge model B (CM-B) intended to investigate the performance of two different techniques in the mitigation of liquefaction effects: narrow densified columns and the combined use of narrow densified columns and high-capacity vertical drains. Similar to CM-A, two adjacent shallow foundations were used in CM-B. However, in this case, both shallow foundations consisted of prismatic $B \times L \times H = 3.0 \times 3.0 \times 1.225$ m^3 (in prototype scale) solid-steel blocks inducing a vertical stress in the underlying sand deposit of 95 kPa (i.e. both shallow foundations were similar to the "heavier shallow foundation" used in CM-A).

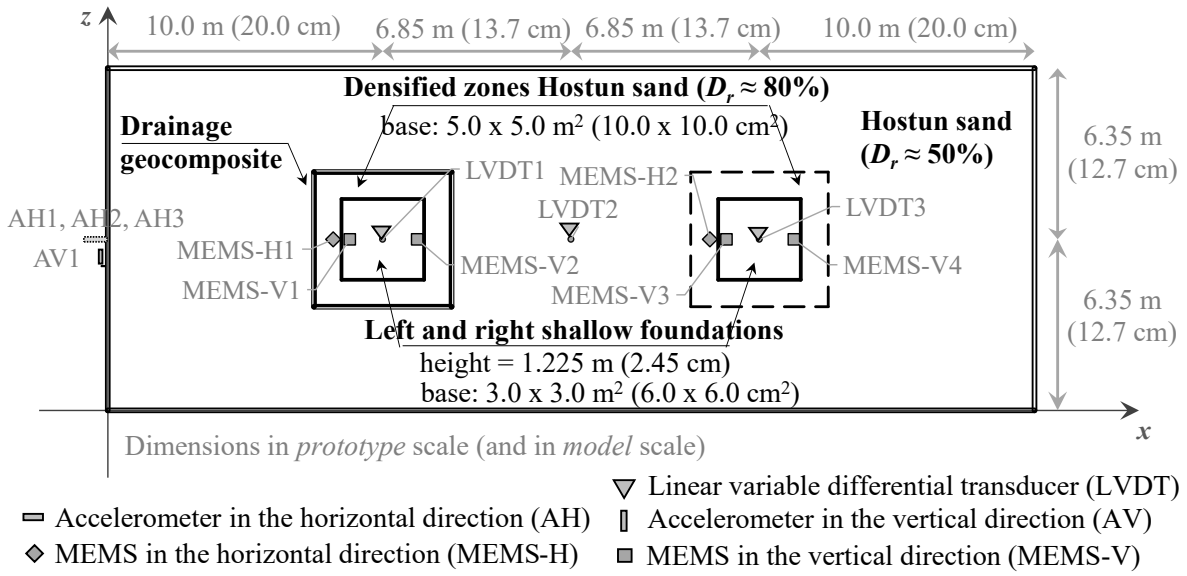

Figure 8.76 – Plan view of CM-B and location of some monitoring instruments (adapted from Marques *et al.*, 2015).

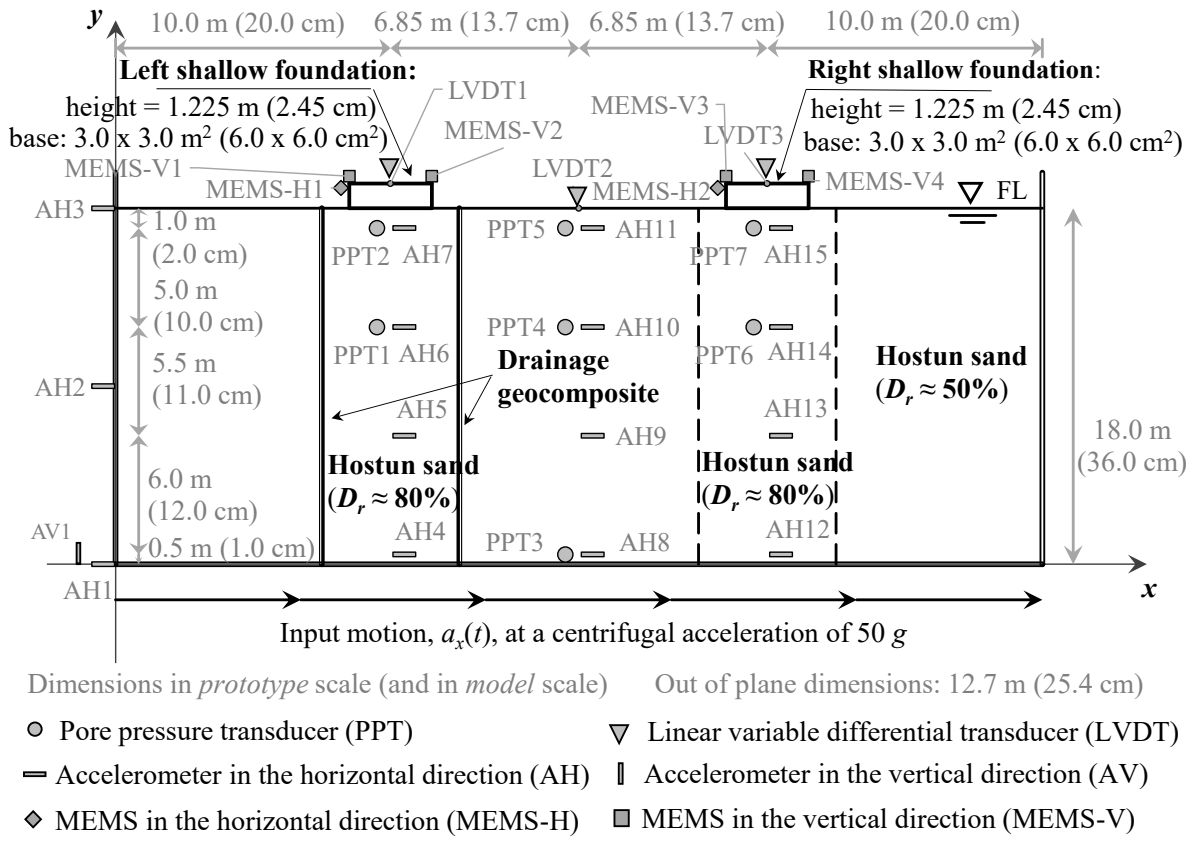

Figure 8.77 – Side view of CM-B and location of the monitoring instruments (adapted from Marques *et al.*, 2015).

The final configuration of the centrifuge experiment is illustrated in Figure 8.77. It can be observed that the shallow foundation on the left side of the model was placed on a 5.0 m-width densified column of Hostun sand (reported as $D_r \approx 80\%$), which, in turn, was fully embedded by a drainage geocomposite TERRAM 1B1, consisting of an extruded high density polyethylene (HDPE) net drainage core with a non-woven polypropylene (PP) geotextile filter bonded to both sides (TERRAM Geosynthetics, 2018), which intended to simulate closely spaced high-capacity vertical drains (Marques *et al.*, 2014a, 2015). Conversely, the shallow foundation on the right side of the model was solely placed on a 5.0 m-width densified column of Hostun sand (reported as $D_r \approx 80\%$), with no drainage geocomposite being used. Similar to CM-A, the remaining sand deposit consisted of moderately loose Hostun sand ($D_r \approx 50\%$), with both loose and dense sand deposits being fully saturated with a viscous solution of Hydroxypropyl Methylcellulose in water. Note that, in what follows, the shallow foundation on the left side of the model, resting on a densified sand column embedded by a drainage geocomposite, is termed as “left shallow foundation”, while the shallow foundation on the right side of the model, resting on a densified sand column, is designated as “right shallow foundation”.

The location of the monitoring instruments is also depicted in the figure, with their coordinates, both in model and prototype scale, being indicated in Table 8.2. Similar to CM-A, it can be observed in Figure 8.77 and Table 8.2 that three different vertical alignments were

selected for measuring the horizontal accelerations and excess pore pressures developed in the model, namely: $x = 10.0$ m (corresponding to the axis of the left shallow foundation), $x = 16.75$ m (corresponding to half distance from axes of the shallow foundations) and $x = 23.7$ m (corresponding to the axis of the right shallow foundation). As mentioned before, while data acquired at these monitoring positions might be sufficient to adequately characterise the dynamic response of the deposit, it might not provide sufficient information about potential boundary effects, which have been shown to affect the measured acceleration time-histories and transient excess pore pressures at positions close to the centrifuge walls in previous centrifuge test programmes (Coelho *et al.*, 2003; Teymur and Madabhushi, 2003).

Table 8.2 – Type and positioning of the monitoring instruments used in CM-B.

Instrument type	ID	Model scale			Prototype scale		
		x (cm)	*y* (cm)	*z* (cm)	*x* (m)	*y* (m)	*z* (m)
Accelerometer measuring in the vertical direction	AV1	0.0	0.0	12.7	0.00	0.00	6.35
Accelerometer measuring in the horizontal direction	AH1	0.0	0.0	12.7	0.00	0.00	6.35
	AH2	0.0	18.0	12.7	0.00	9.00	6.35
	AH3	0.0	36.0	12.7	0.00	18.00	6.35
	AH4	20.0	1.0	12.7	10.00	0.50	6.35
	AH5	20.0	13.0	12.7	10.00	6.50	6.35
	AH6	20.0	24.0	12.7	10.00	12.00	6.35
	AH7	20.0	34.0	12.7	10.00	17.00	6.35
	AH8	33.7	1.0	12.7	16.85	0.50	6.35
	AH9	33.7	13.0	12.7	16.85	6.50	6.35
	AH10	33.7	24.0	12.7	16.85	12.00	6.35
	AH11	33.7	34.0	12.7	16.85	17.00	6.35
	AH12	47.4	1.0	12.7	23.70	0.50	6.35
	AH13	47.4	13.0	12.7	23.70	6.50	6.35
	AH14	47.4	24.0	12.7	23.70	12.00	6.35
	AH15	47.4	34.0	12.7	23.70	17.00	6.35
Linear variable differential transformer (LVDT).	LVDT1	23.0	38.45	12.7	10.00	19.225	6.35
	LVDT2	26.85	36.0	12.7	16.85	18.00	6.35
	LVDT3	43.8	37.5	12.7	23.70	18.75	6.35
Pore pressure transducer (PPT)	PPT1	20.0	24.0	12.7	10.00	12.00	6.35
	PPT2	20.0	34.0	12.7	10.00	17.00	6.35
	PPT3	33.7	1.0	12.7	16.85	0.50	6.35
	PPT4	33.7	24.0	12.7	16.85	12.00	6.35
	PPT5	33.7	34.0	12.7	16.85	17.00	6.35
	PPT6	47.4	24.0	12.7	23.70	12.00	6.35
	PPT7	47.4	34.0	12.7	23.70	17.00	6.35
Microelectromechanical system (MEMS) measuring in the vertical direction	MEMS-V1	17.0	38.45	12.7	8.50	19.225	6.35
	MEMS-V2	23.0	38.45	12.7	11.50	19.225	6.35
	MEMS-V3	44.4	37.5	12.7	22.20	18.75	6.35
	MEMS-V4	50.4	37.5	12.7	25.20	18.75	6.35
MEMS measuring in the horizontal direction	MEMS-H1	17.0	38.45	12.7	8.50	19.225	6.35
	MEMS-H3	44.4	37.5	12.7	22.20	18.75	6.35

In what follows, all dimensions, input motions and results are presented only in prototype scale.

8.4.1.2 Horizontal acceleration time-histories

Figure 8.78 depicts the horizontal acceleration time-histories recorded at three different monitoring positions on the centrifuge model wall.

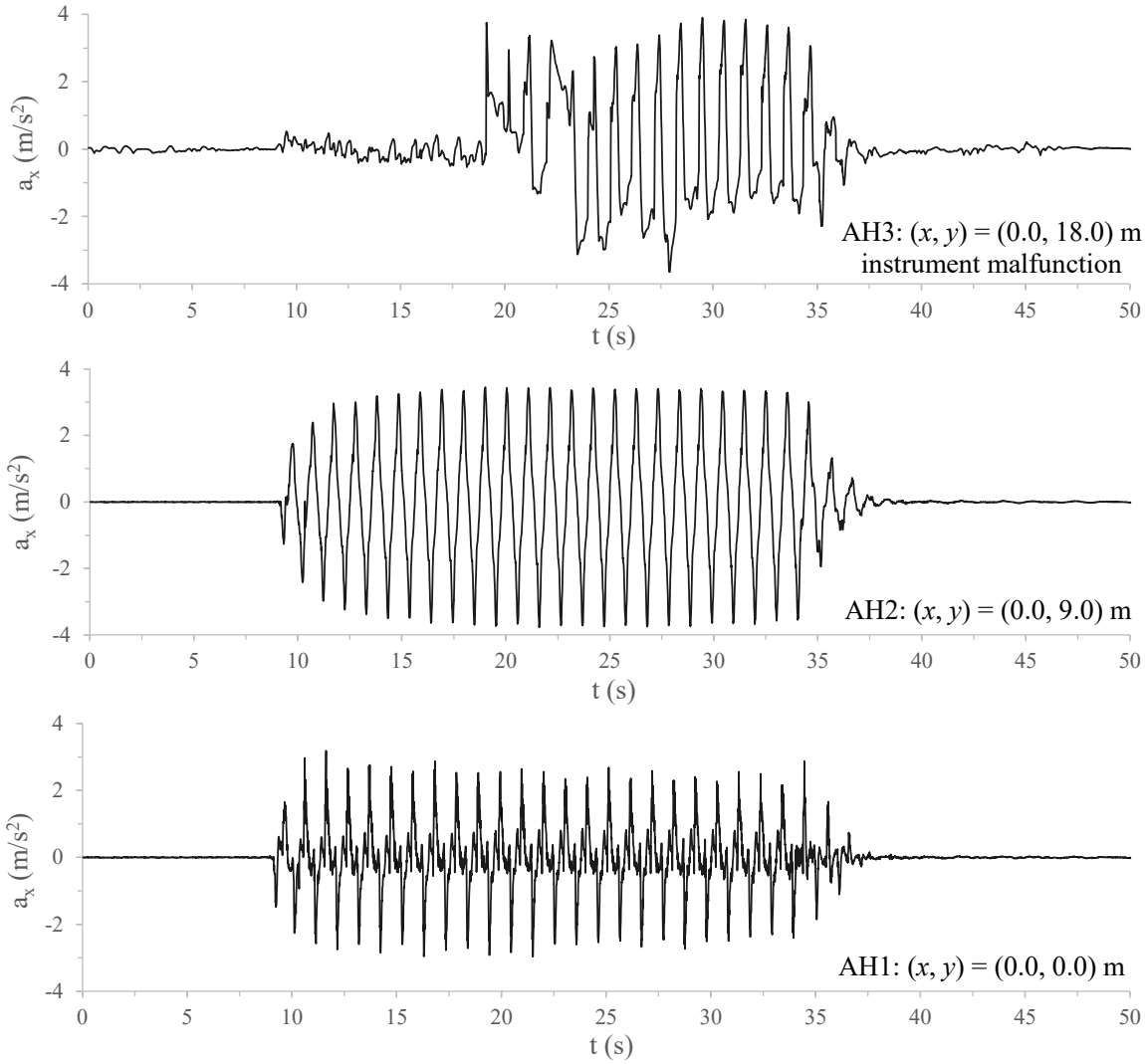

Figure 8.78 – Measured horizontal acceleration time-histories at three different monitoring positions along the left wall of CM-B.

It is apparent that the accelerometer located at the top position malfunctioned during the test and, therefore, the results obtained at that position are useless. Nevertheless, in this centrifuge test, the horizontal motion applied to the base of the centrifuge model, henceforth referred to as "input horizontal motion", was properly recorded by the accelerometer AH1 located at $(x, y) = (0.0, 0.0)$ m. It can be seen that, in general, the input motion is characterised by peak accelerations slightly smaller than the intended value of ±3.0 m/s^2. Moreover, although a single-frequency sinusoidal loading was intended to be applied to the model, Figure 8.78 shows that local peaks were recorded in between the maximum

acceleration peaks during the majority of the duration of the input horizontal motion, suggesting the presence of other frequencies in the input motion. Interestingly, these non-intended local peaks seem to be strongly attenuated from the base of the centrifuge container (i.e. from the monitoring position $(x, y) = (0.0, 0.0)$ m) to the middle position on its lateral wall (i.e. to the monitoring position $(x, y) = (0.0, 9.0)$ m). Conversely, the maximum (global) peaks are amplified from the base to the middle of the centrifuge wall, reaching values close to ±4.0 m/s^2. In effect, the inspection of the Fourier Spectra of these horizontal motions, computed using the software SeismoSignal version 2018 (Seismosoft, 2018) and depicted in Figure 8.79, enables to confirm that the Fourier amplitude of the predominant frequency (of about 1 Hz) is amplified from $(x, y) = (0.0, 0.0)$ m to $(x, y) = (0.0, 9.0)$ m, while the Fourier amplitudes of the remaining frequencies of the motion are attenuated.

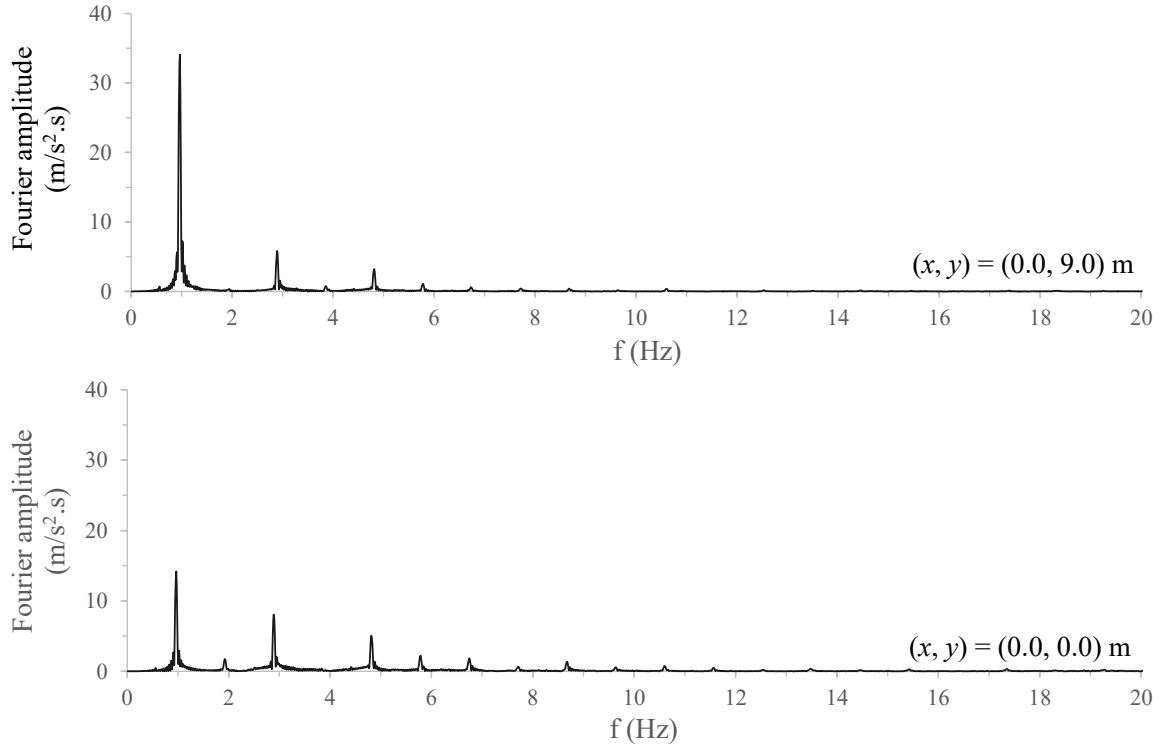

Figure 8.79 – Fourier spectra of the acceleration time-histories measured at two different monitoring positions along the left wall of CM-B.

Figure 8.80 compares the horizontal acceleration time-histories registered at four different monitoring positions located along a vertical alignment coincident with the axis of the left shallow foundation ($x = 10.0$ m) with that recorded at the base of the model (i.e. at $(x, y) = (0.0, 0.0)$ m). Complementary, Figure 8.81 compares the horizontal acceleration time-histories recorded at the left top edge of the left shallow foundation (i.e. at $(x, y) = (8.5, 19.225)$ m) with that registered at $(x, y) = (0.0, 0.0)$ m.

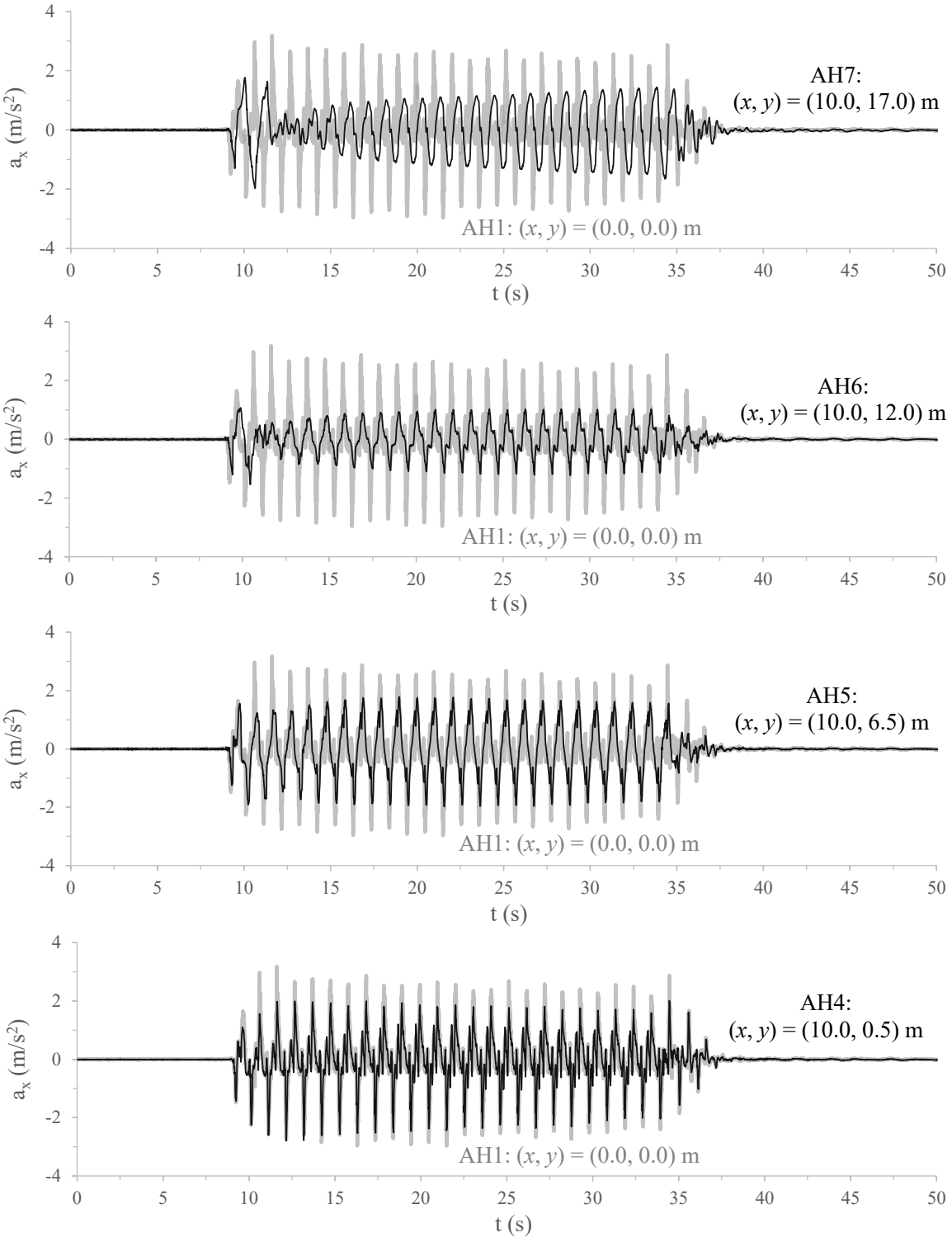

Figure 8.80 – Comparison of the horizontal acceleration time-histories recorded at several monitoring positions located along a vertical alignment coincident with the axis of the left shallow foundation with that recorded at the base of the model for CM-B.

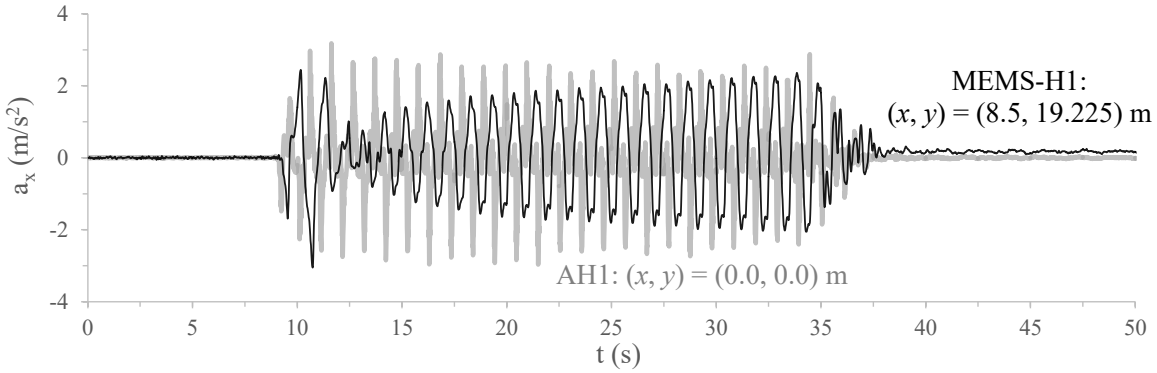

Figure 8.81 – Comparison of the horizontal acceleration time-histories recorded at the top of the left shallow foundation and underneath it with that recorded at the base of the model for CM-B.

Similar to CM-A, a significant attenuation of the horizontal peak accelerations is observed after the first two significant loading cycles (i.e. at $t \approx 12$ s) at the two shallower monitoring positions within the sand deposit (i.e. at $(x, y) = (10.0, 12.0)$ m and $(x, y) = (10.0, 17.0)$ m) and, consequently, at the top of the shallow foundation (i.e. at $(x, y) = (8.5, 19.225)$ m). This is likely a consequence of the large excess pore pressures generated in the model at this stage of the experiment, reducing significantly the effective stresses and stiffness of the sand deposit, while leading to the increase in material damping. Interestingly, after a couple of loading cycles succeeding this sudden attenuation of the horizontal accelerations, their peak values are observed to gradually increase until the end of shaking, although never reaching again the amplitudes registered during the first two significant loading cycles. This seems also consistent with the gradual decrease of the excess pore pressures measured at $(x, y) = (10.0, 12.0)$ m during this period of the experiment, likely induced by the drainage capacity provided by the drainage geocomposite, as detailed later.

Note that, as expected, due to the upwards propagation of the shear waves, there is a small time delay between the motion recorded at the base of the model and those recorded within the sand deposit. Naturally, this delay increases as the monitoring position locates farther away from the base of the model.

In terms of frequency content, Figure 8.82 compares the Fourier spectra corresponding to the horizontal acceleration time-histories measured at the three top monitoring positions – $(x, y) = (10.0, 12.0)$ m, $(x, y) = (10.0, 17.0)$ m and $(x, y) = (8.5, 19.225)$ m – with that corresponding to the input motion (i.e. recorded at $(x, y) = (0.0, 0.0)$ m). It is apparent that the Fourier amplitude corresponding to the predominant frequency of the input motion (about 1 Hz) is slightly amplified at the shallowest depths of the sand deposit (i.e. at $(x, y) = (10.0, 17.0)$ m) – and, as expected, further amplified at the top of the shallow foundation (i.e. at $(x, y) = (8.5, 19.225)$ m), which is a free surface. Moreover, the signals recorded at shallow depths and at the top of the shallow foundation seem richer in terms of frequencies lower than 1.0 Hz, with the opposite trend being observed for frequencies greater than 1.0 Hz.

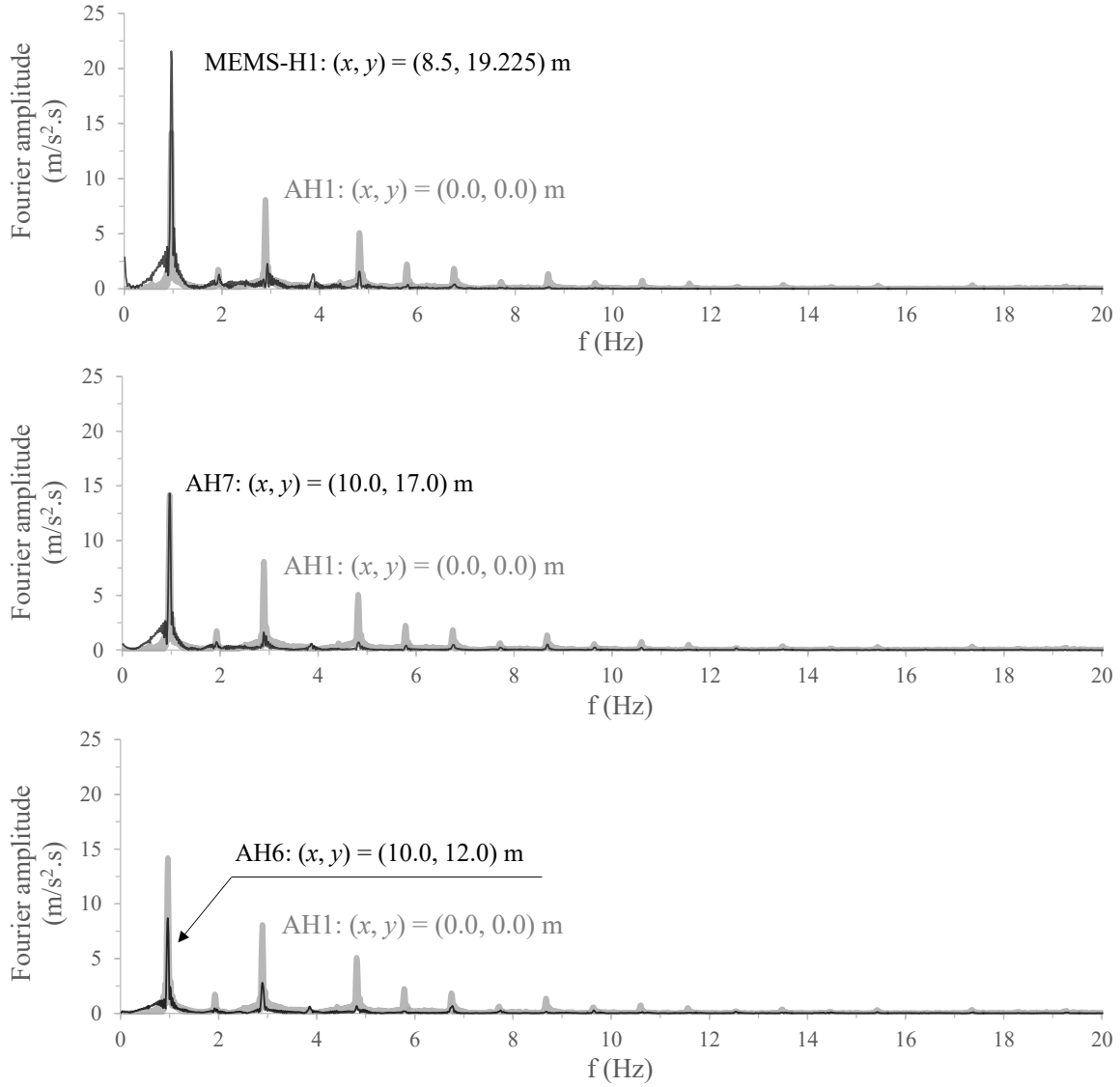

Figure 8.82 – Comparison of the Fourier spectra of the horizontal acceleration time-histories recorded at the top of the left shallow foundation and underneath it with that corresponding to the horizontal acceleration time-history recorded at the base of the model for CM-B.

The horizontal acceleration time-histories recorded at several monitoring positions located along a vertical alignment coincident with the axis of the right shallow foundation ($x = 23.7$ m) are compared with that recorded at the base of the model (i.e. at $(x, y) = (0.0, 0.0)$ m) in Figure 8.83.

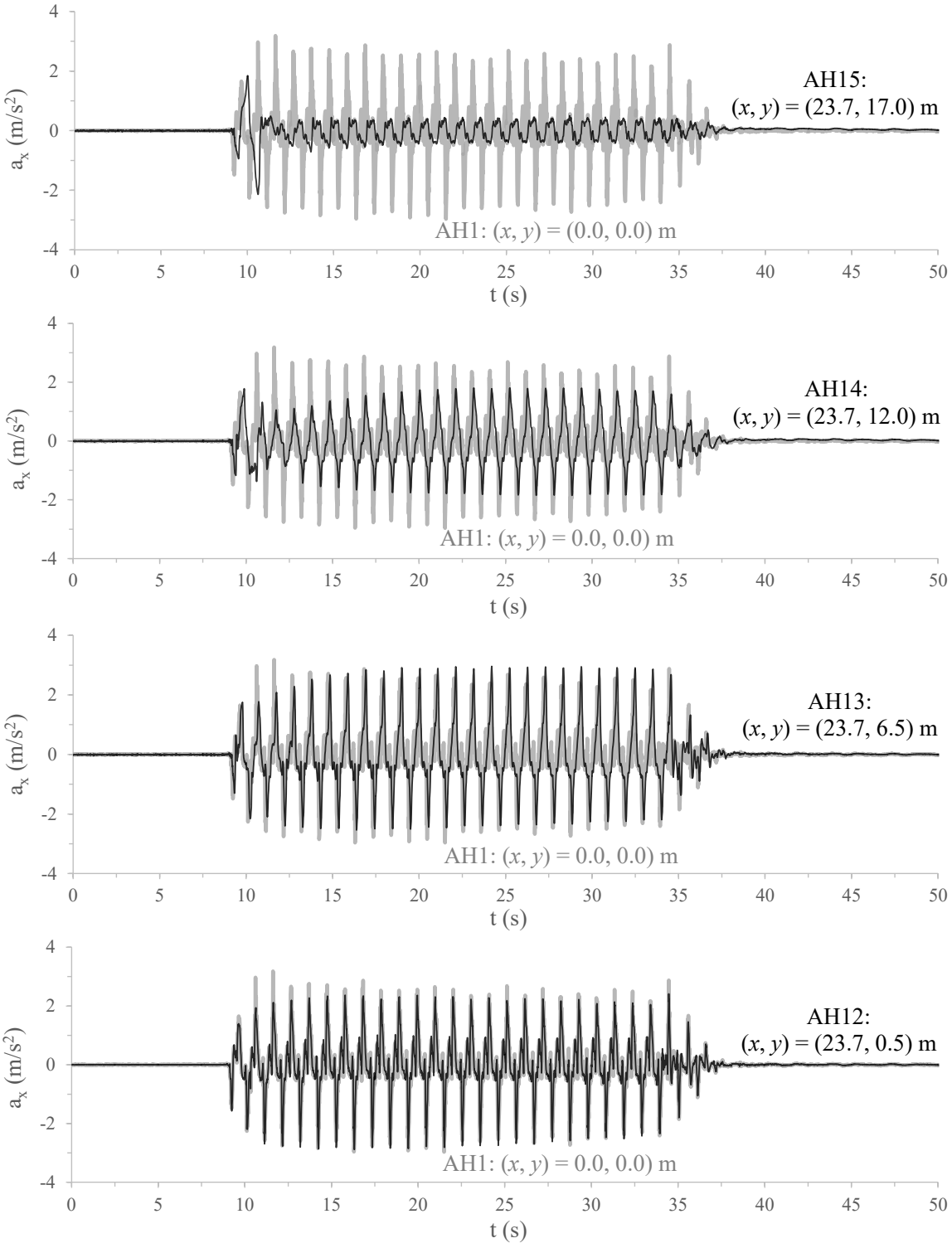

Figure 8.83 – Comparison of the horizontal acceleration time-histories recorded at several monitoring positions located along a vertical alignment coincident with the axis of the right shallow foundation with that recorded at the base of the model for CM-B.

Similar to what was observed for the vertical alignment coincident with the axis of left shallow foundation, as well as for CM-A, accelerations with similar amplitudes were measured at every monitoring position during the first and part of the second significant loading cycles, with a strong attenuation of the motion being observed afterwards, particularly at the

shallowest monitoring position: $(x, y) = (23.7, 17.0)$ m. As pointed out before, this attenuation seems consistent with the large excess pore pressures generated in the model at this stage of the centrifuge experiment. Note, however, that, contrary to what was observed at the monitoring position underneath the left shallow foundation (i.e. at $(x, y) = (10.0, 17.0)$ m), rather than gradually increasing, the peak accelerations recorded at $(x, y) = (23.7, 17.0)$ m seem to remain practically constant (with values smaller than ±0.5 m/s^2) during the remaining loading cycles. This seems consistent with the different trends observed for the excess pore pressures registered under the two shallow foundations. Specifically, while the excess pore pressures are observed to gradually decrease after its sudden initial increase in the zone of the sand deposit under the influence of the left shallow foundation of the model, the excess pore pressures continue to slightly build-up in the zones of the sand deposit under the influence of the right shallow foundation of the model. This suggests that the drainage geocomposite plays a key role in the mitigation and dissipation of excess pore pressures developed on the left side of the model, as discussed in more detail later. Moreover, as expected and also observed for the left side of the model, there seems to exist a small time delay between the peak horizontal accelerations recorded at the top monitoring position (i.e. at $(x, y) = (23.7, 17.0)$ m) and those registered at deeper levels of the sand deposit.

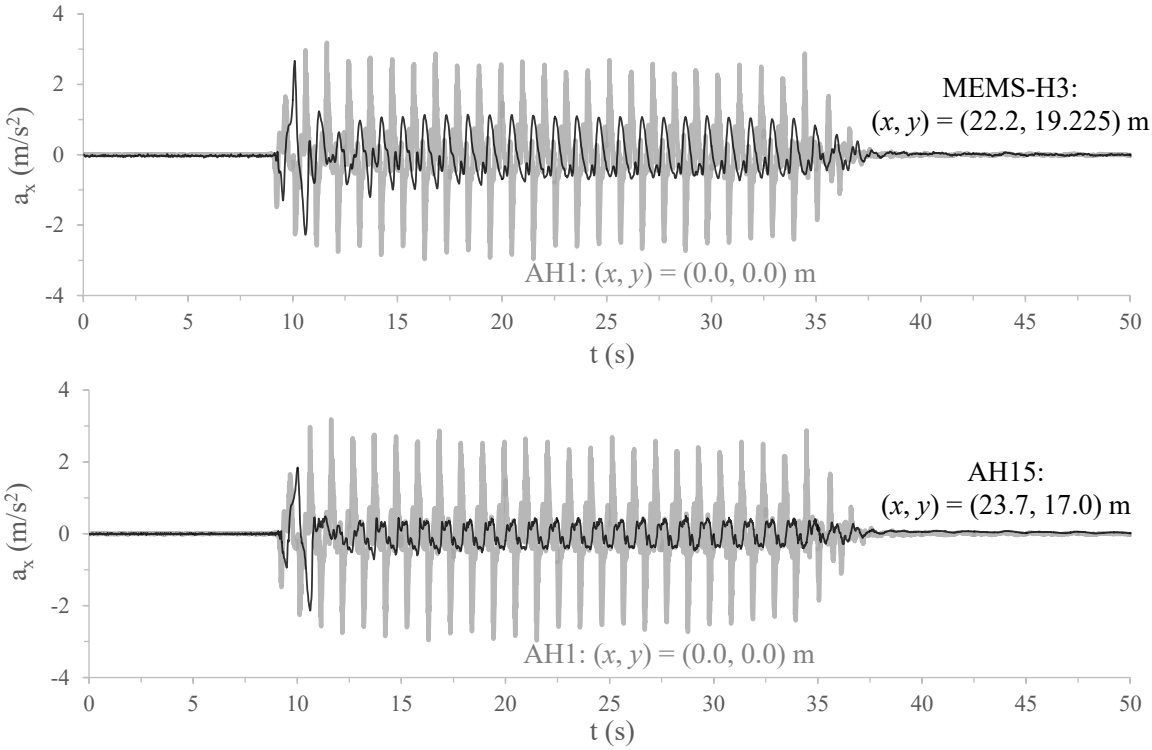

Figure 8.84 – Comparison of the horizontal acceleration time-histories recorded at the top of the right shallow foundation and underneath it with that recorded at the base of the model for CM-B.

In addition, Figure 8.84 compares the horizontal acceleration time history recorded at the top left edge of the right shallow foundation (i.e. at $(x, y) = (22.2, 19.225)$ m), as well as at the shallowest position within the sand deposit underneath that shallow foundation (i.e. at

$(x, y) = (23.7, 17.0)$ m) with that registered at the base of the model (i.e. at $(x, y) = (0.0, 0.0)$ m). As explained before based on the theory of wave propagation, the peak accelerations registered at the top of the shallow foundation (which defines a free surface) are considerably larger than those registered within the sand deposit.

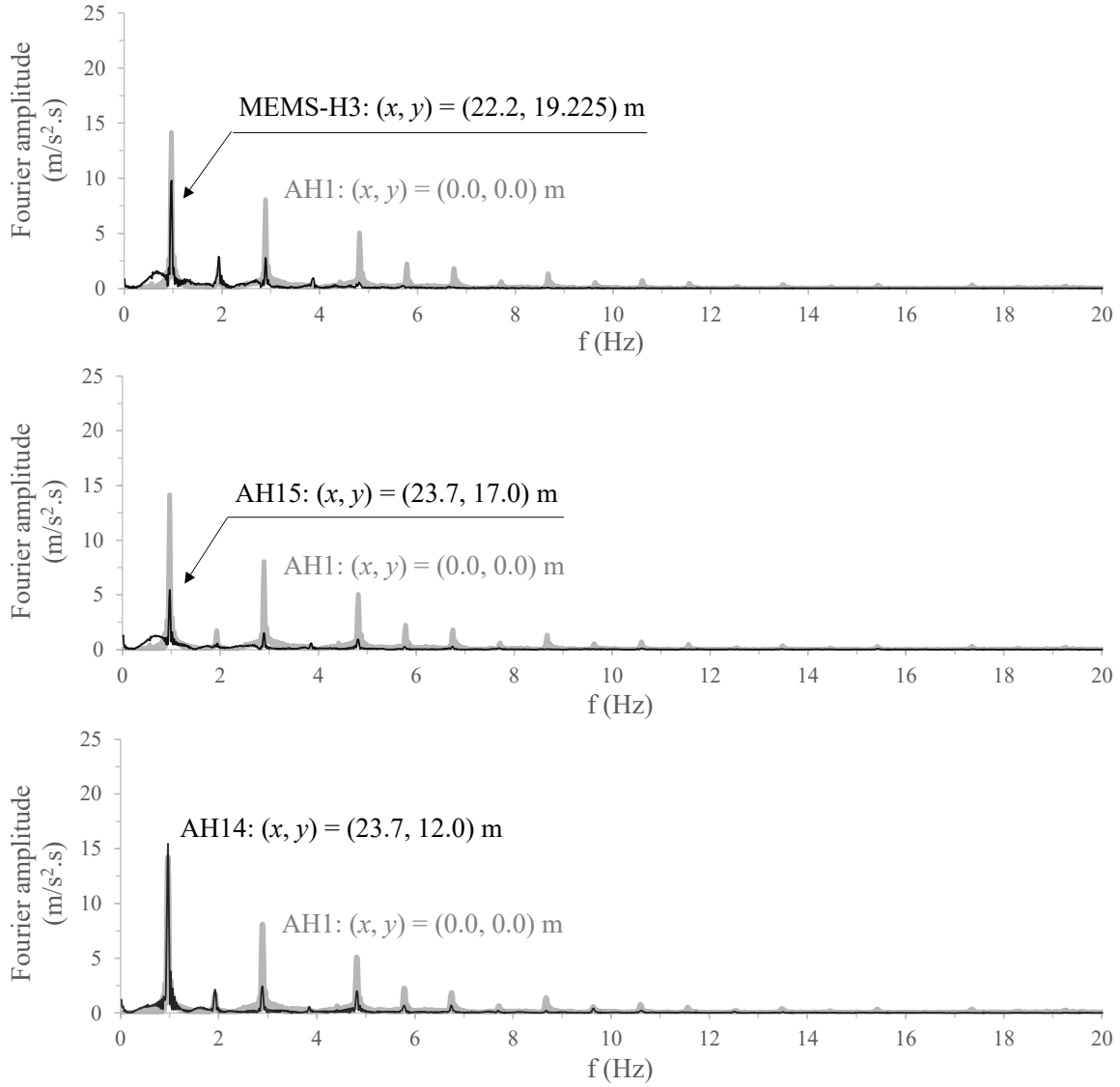

Figure 8.85 – Comparison of the Fourier spectra of the horizontal acceleration time-histories recorded at the top of the right shallow foundation and underneath it with that that corresponding to the horizontal acceleration time-history recorded at the base of the model for CM-B.

The frequency content of the motions recorded at the three shallower monitoring positions along vertical alignment corresponding to the axis of the right shallow foundation – $(x, y) = (22.2, 19.225)$ m, $(x, y) = (23.7, 17.0)$ m and $(x, y) = (23.7, 12.0)$ m – are compared with that of the input motion (i.e. recorded at $(x, y) = (0.0, 0.0)$ m) in Figure 8.85. Contrary to what was observed for the signals recorded on the left side of the model, in this case, the signals registered at the top monitoring position within the sand deposit (i.e. at $(x, y) = (23.7, 17.0)$ m) and at the top of the shallow foundation (i.e. at $(x, y) = (22.2, 19.225)$ m) are

characterised by maximum Fourier amplitudes smaller than that characterising the input motion. This is, in fact, consistent with the strong attenuation of the response observed on this side of the model. Regarding the remaining content of the signals, as observed for the other side of the model, it is apparent that the signals recorded at the top monitoring positions are richer in terms of low-frequency content (in particular, below the predominant frequency of the input motion, of about 1 Hz), while being poorer in terms of frequencies above 2 Hz.

The acceleration time-histories measured at several different monitoring positions located along a vertical alignment coincident with the middle of the model are compared with that recorded at the base of the model in Figure 8.86. Once again, it is apparent that a strong attenuation of the ground motion occurred after the first two significant loading cycles, likely due to the large excess pore pressures observed in the model during this stage of the analysis, as shown later. This attenuation is particularly intense at the shallowest monitoring position (i.e. at $(x, y) = (16.85, 17.0)$ m), with peak accelerations of about ±0.5 m/s^2 being recorded from the moment that attenuation occurs until the end of dynamic loading, as also observed for the right side of the model (having no drainage geocomposite).

This strong attenuation is also perceptible in Figure 8.87, which compares the Fourier spectra of the acceleration time-histories measured at the shallowest monitoring with that of the input signal. It is apparent that the amplitudes of all predominant frequencies of the signal measured at $(x, y) = (16.85, 17.0)$ m are significantly attenuated in relation to those corresponding to the signal measured at the base of the model.

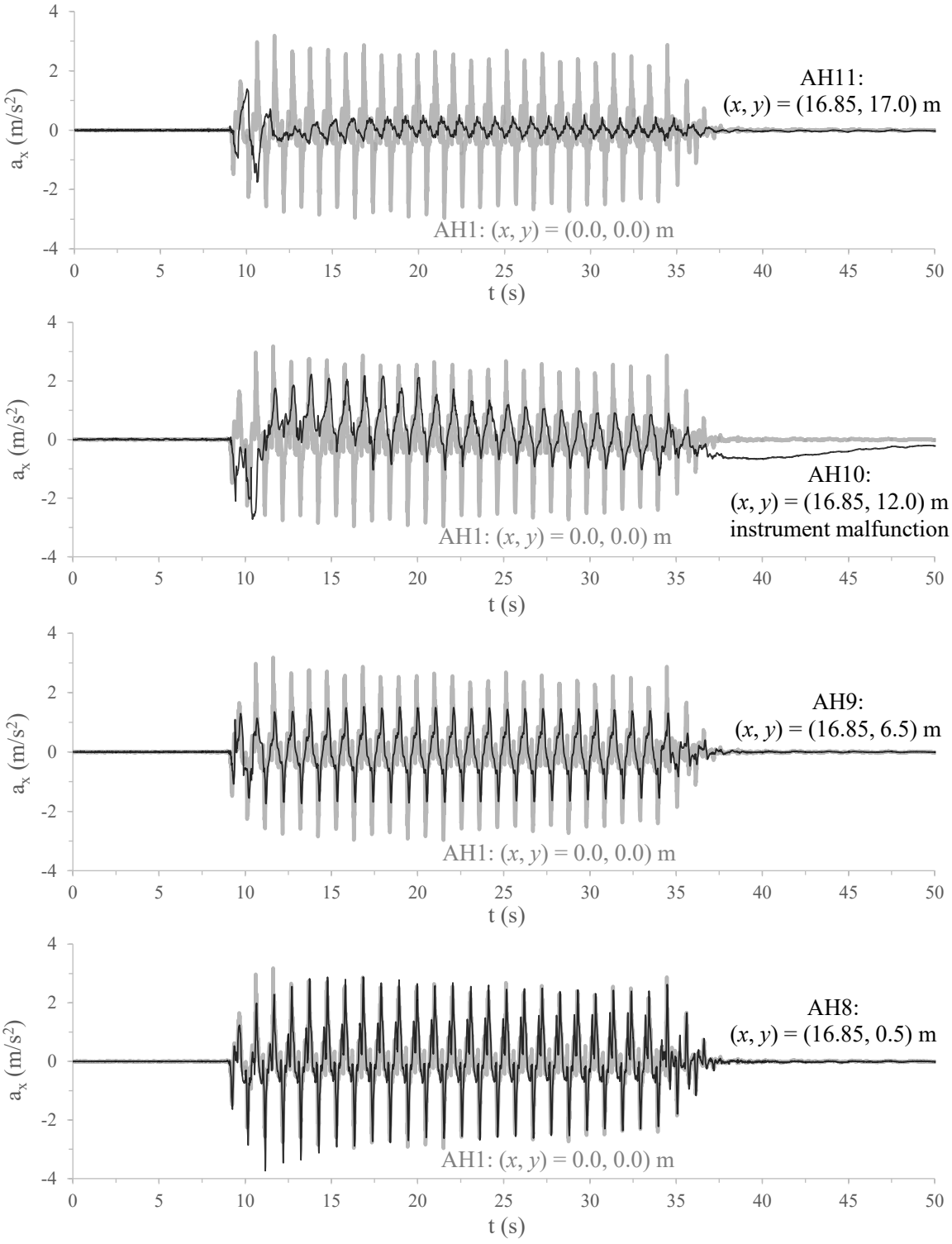

Figure 8.86 – Comparison of the horizontal acceleration time-histories recorded at several monitoring positions located along a vertical alignment coincident with the middle of the model with that corresponding to the horizontal acceleration time-history recorded at the base of the model for CM-B.

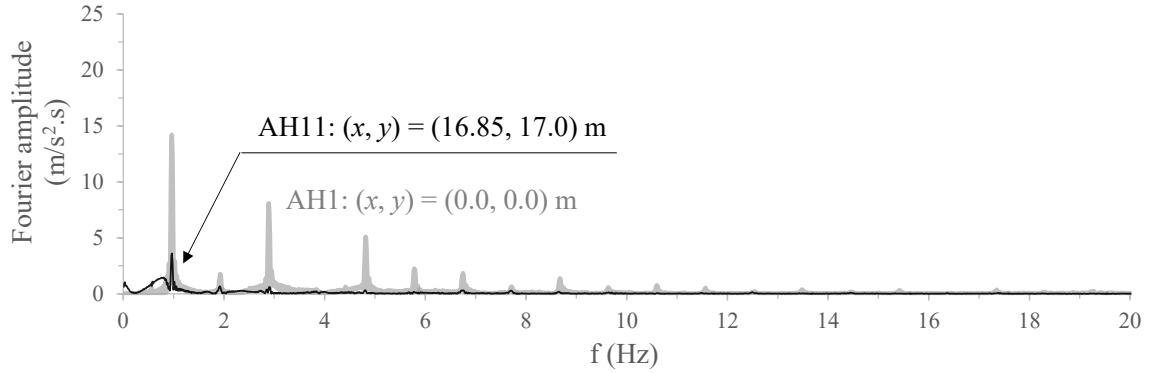

Figure 8.87 – Comparison of the Fourier spectrum of the horizontal acceleration time-history recorded at the shallowest monitoring position in between the two shallow foundations with that of the horizontal acceleration time-history recorded at the base of the model for CM-B.

8.4.1.3 Vertical acceleration time-histories

The vertical acceleration time-histories recorded at the top left and top right edges of the left shallow foundation (i.e. at $(x, y) = (8.5, 19.225)$ m and $(x, y) = (11.5, 19.225)$ m, respectively) are compared with that registered at the base of the model (i.e. at $(x, y) = (0.0, 0.0)$ m) in Figure 8.17.

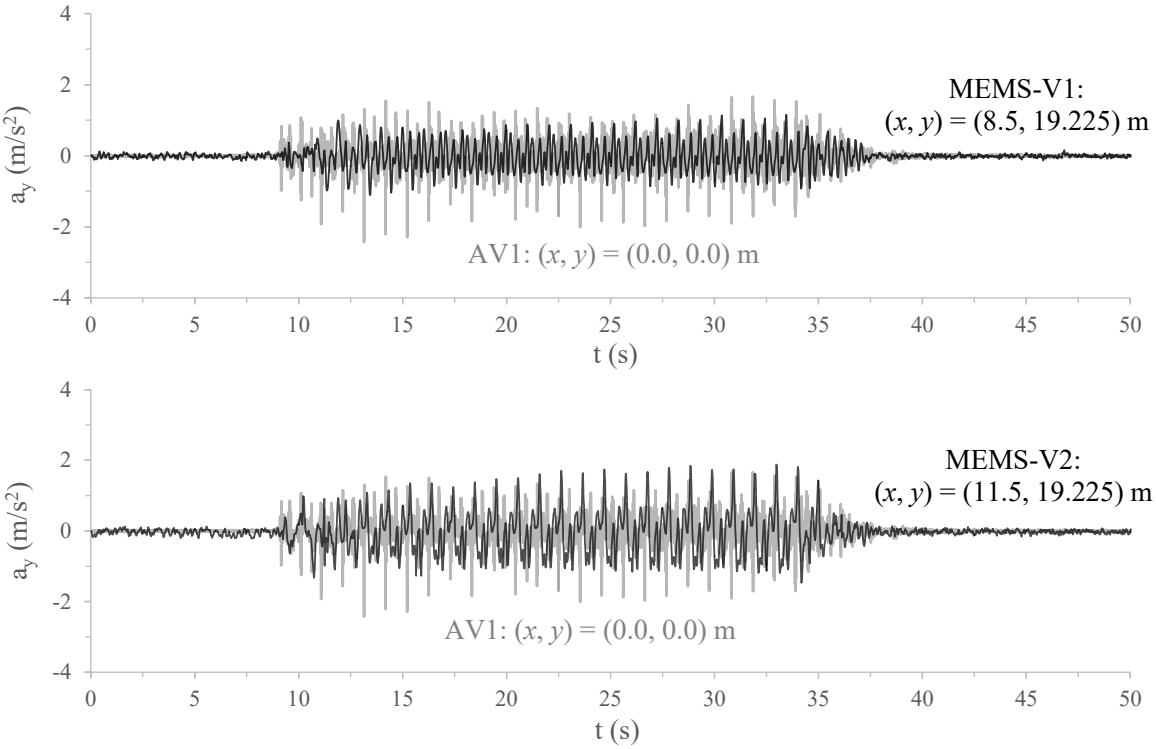

Figure 8.88 – Measured vertical acceleration time-histories at the base of the model and at the left and right top edges of the left shallow foundation for CM-B.

Although the intention was to apply null vertical accelerations at the base of the centrifuge model (Marques *et al.*, 2014a, 2015), it can be seen that considerable vertical accelerations were, in fact, measured at $(x, y) = (0.0, 0.0)$ m, with amplitudes of roughly half of those characterising the horizontal input motion. Similarly, significant vertical accelerations were

measured at the top edges of the shallow foundation, with the peak values registered at the right edge exceeding those measured at the left edge.

As shown in Figure 8.89 (which, for clarity of the presentation, includes only results for the period ranging from 15 s to 25 s), although the maximum peak accelerations measured at the left and right top edges of the shallow foundation seem to occur practically in phase, the amplitudes of the peak accelerations are slightly different, suggesting that this shallow foundation oscillated during dynamic loading. This seems to be confirmed in Figure 8.90, which depicts the semi-sum (i.e. average value) and semi-difference of the vertical accelerations measured at the edges of the left shallow foundation. As mentioned before, the latter quantity provides an indication of the rotational motion of the shallow foundation. Note, nevertheless, that, as it was apparent for CM-A, this rotational movement might have been induced, at least partly, by a non-intentional rocking motion of the entire centrifuge model (rather than just by a rocking motion of the shallow foundation itself).

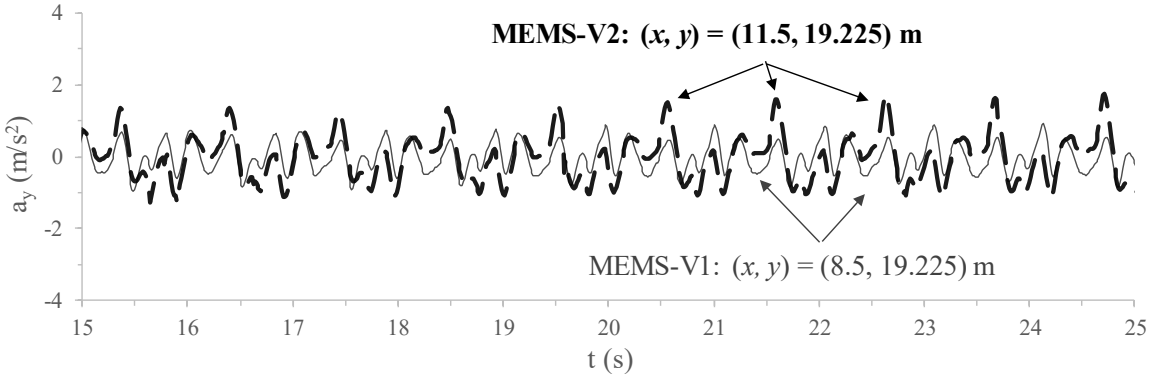

Figure 8.89 – Measured vertical acceleration time-histories at the left and right top edge of the left shallow foundation during the period ranging from 15 to 25 s for CM-B.

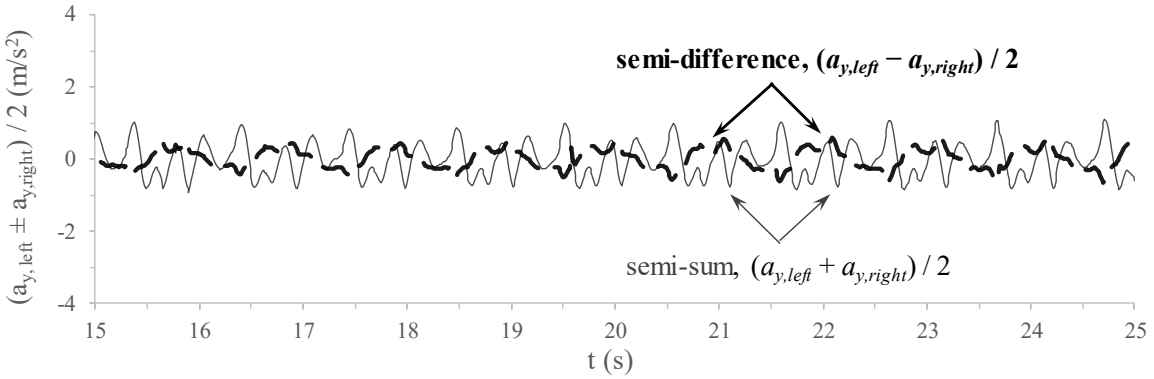

Figure 8.90 – Semi-sum and semi-difference of the vertical accelerations measured at the left and right top edge of the left shallow foundation during the period ranging from 15 to 25 s for CM-B.

The Fourier spectra of the vertical acceleration time-histories measured at the edges of the left shallow foundation are compared with that of the vertical input motion in Figure 8.91. It can be observed that the vertical motions recorded at the edges of the shallow foundation are, in general, characterised by larger Fourier amplitudes than those characterising the input motion, at least for the first five predominant frequencies (1, 2, 3, 4 and 5 Hz).

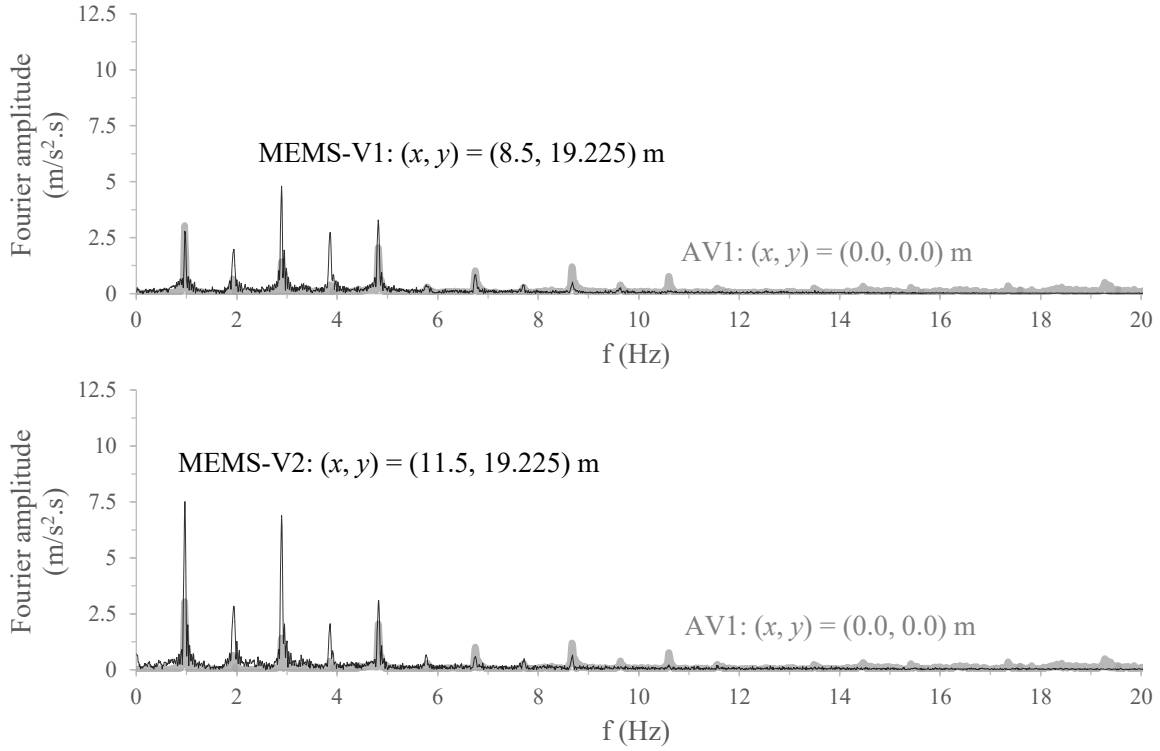

Figure 8.91 – Fourier spectra of the vertical acceleration time-histories measured at the base of the model and at the top edges of the left shallow foundation for CM-B.

With respect to the vertical accelerations at the top left and top right edges of the right shallow foundation (i.e. at $(x, y) = (22.2, 19.225)$ m and $(x, y) = (25.2, 19.225)$ m, respectively), the recorded vertical signals are compared to that registered at the base of the model (i.e. at $(x, y) = (0.0, 0.0)$ m) in Figure 8.92. It can be seen that the acceleration time-histories recorded at the left and right edges of this shallow foundation are characterised by similar amplitudes (particularly after $t \approx 12$ s).

Further comparison between the two vertical signals recorded at the top of the right shallow foundation is provided in Figure 8.93, for the period ranging from 15 s to 25 s. It is apparent that, in this case, while being characterised by similar amplitudes, the signals occur slightly out of phase, indicating that this shallow foundation also oscillated during dynamic loading.

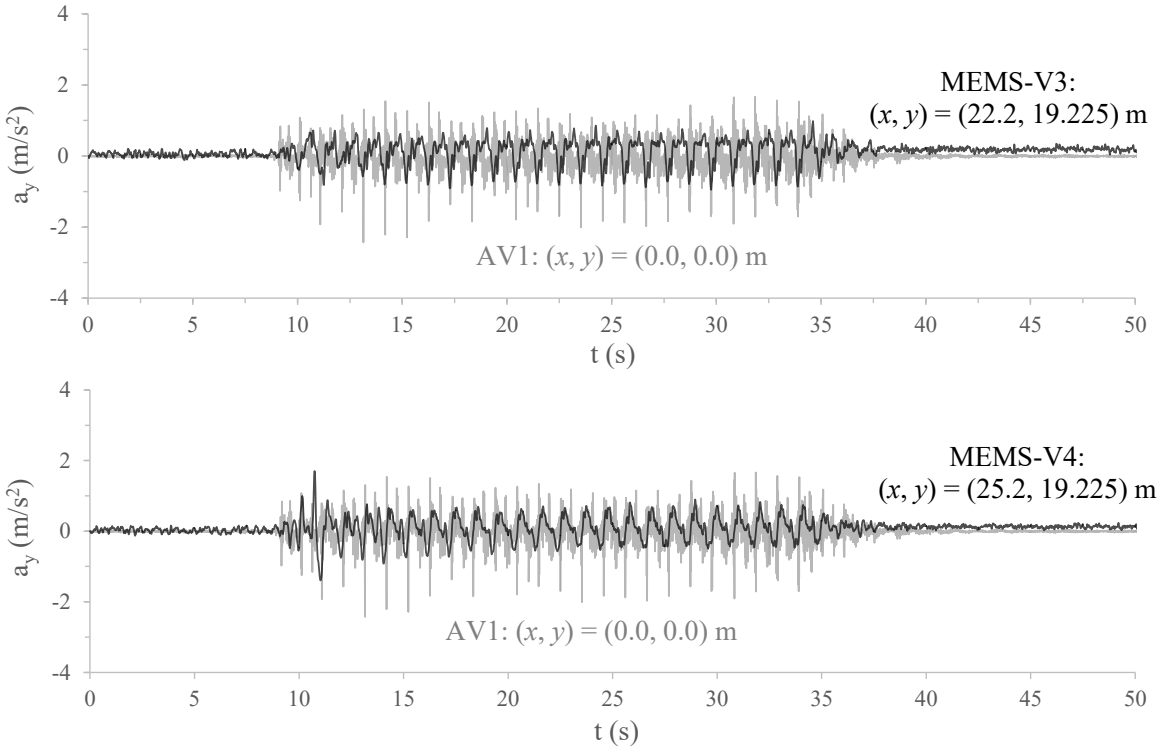

Figure 8.92 – Measured vertical acceleration time-histories at the base of the model and at the top edges of the right shallow foundation for CM-B.

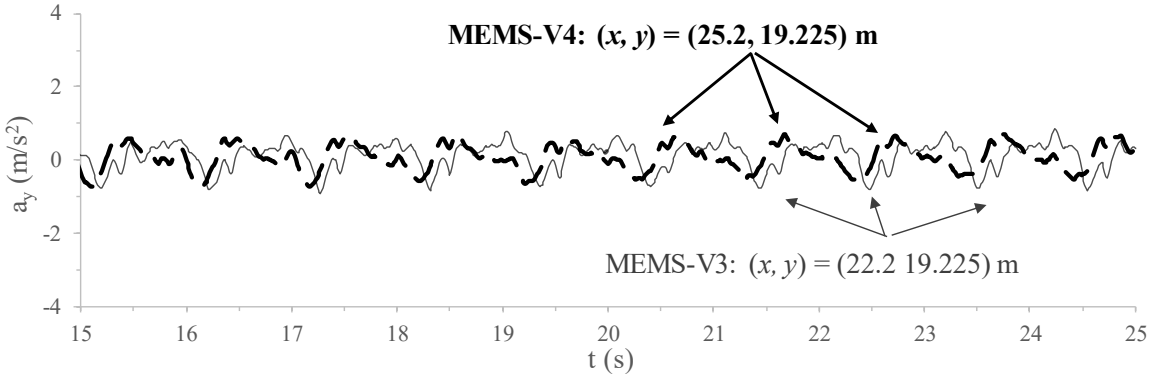

Figure 8.93 – Measured vertical acceleration time-histories at the left and right top edges of the right shallow foundation during the period ranging from 15 to 25 s for CM-B.

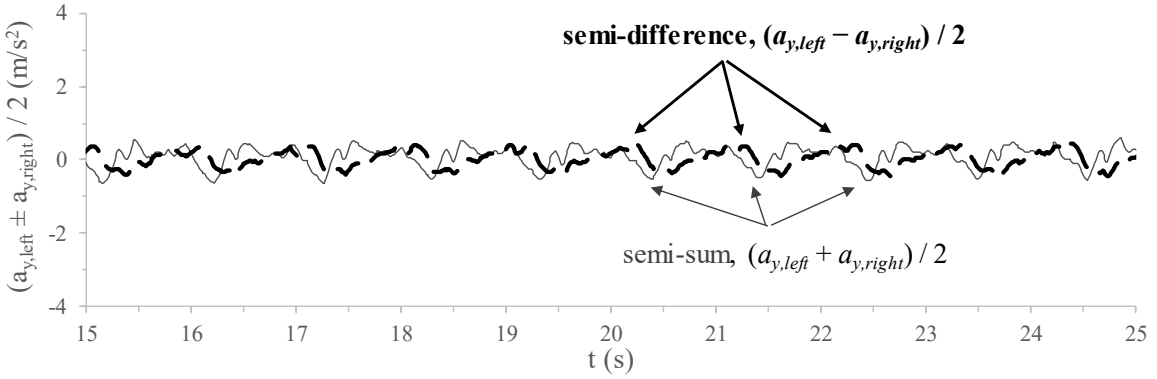

Figure 8.94 – Semi-sum and semi-difference of the vertical accelerations measured at the left and right top edges of the right shallow foundation during the period ranging from 15 to 25 s for CM-B.

The Fourier spectra corresponding to the motions recorded at the top of the right shallow foundation are shown in Figure 8.95. It can be observed that similar spectra were obtained for the vertical motions measured at the left and right edges of the shallow foundation (i.e. at $(x, y) = (22.2, 19.225)$ m and $(x, y) = (25.2, 19.225)$ m, respectively), corroborating the conclusions drawn when inspecting the acceleration time-histories.

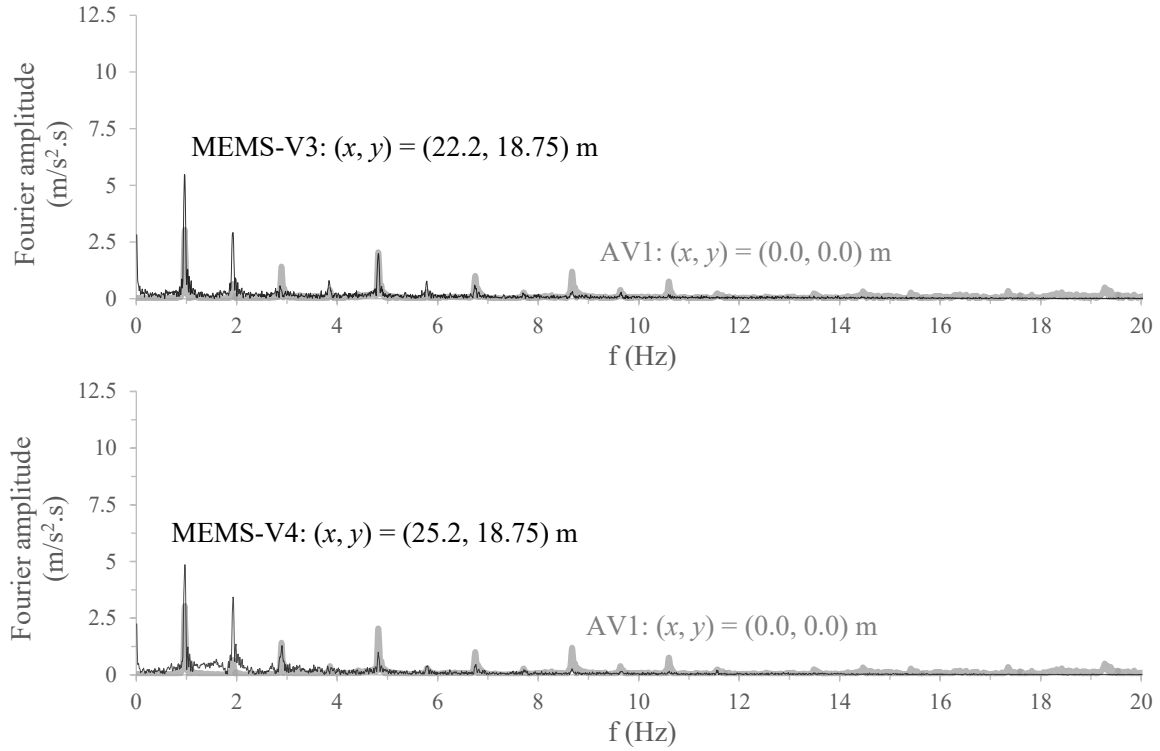

Figure 8.95 – Fourier spectra of the vertical acceleration time-histories measured the base of the model and at the top edges of the right shallow foundation for CM-B.

To gain further insight into the measured response, the vertical acceleration time-histories measured at the left top edges of the two shallow foundations are depicted together in Figure 8.96. Similarly, the vertical acceleration time-histories measured at the right top edges of the two shallow foundations are shown together in Figure 8.97. It is apparent the acceleration time-histories measured at the top of the left shallow foundation and at the top of the lighter one are characterised by different amplitudes and different frequencies of oscillation. This suggests that, even though a non-intentional rocking-type mechanism involving the entire centrifuge model might have occurred during this experiment (as observed for CM-A), individual rocking of at least one of the shallow foundations likely occurred during the experiment.

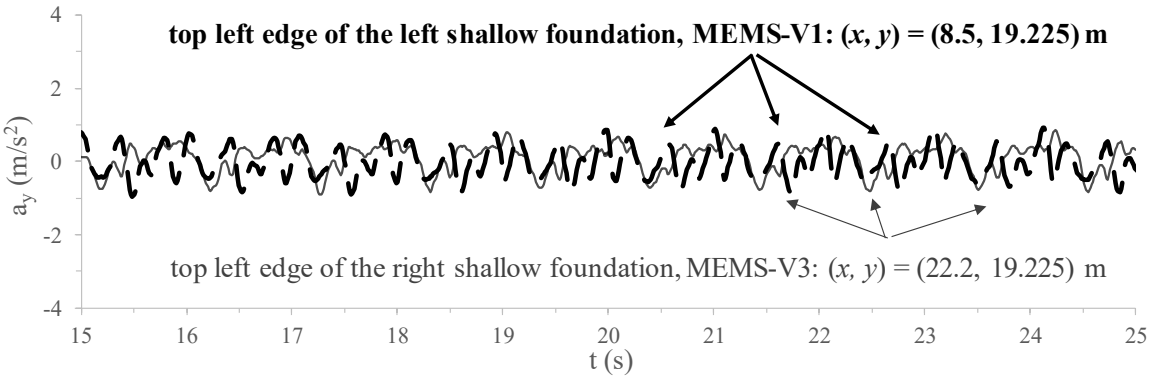

Figure 8.96 – Measured vertical acceleration time-histories at the top left edges of the two shallow foundations during the period ranging from 15 to 25 s for CM-B.

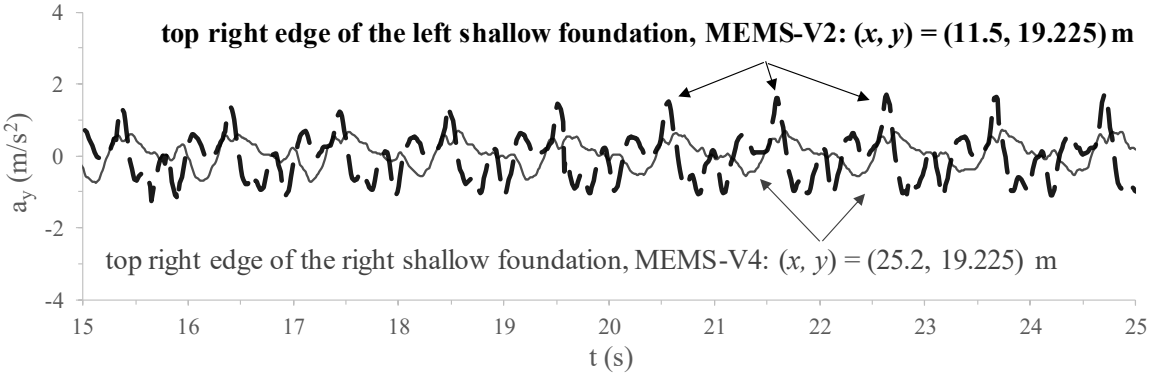

Figure 8.97 – Measured vertical acceleration time-histories at the top right edges of the two shallow foundations during the period ranging from 15 to 25 s for CM-B.

8.4.1.4 Excess pore pressures

Figure 8.98 compares the evolutions of excess pore pressure with time measured during dynamic loading and shortly after its end at two different monitoring levels ($y = 12.0$ m and $y = 17.0$ m) located along alignments coincident with the axes of the left and right shallow foundations ($x = 10.0$ m and $x = 23.7$ m, respectively). Complementary, Figure 8.99 depicts the long-term dissipations of the excess pore pressure at those monitoring positions. It is apparent that the responses measured at the monitoring positions located on the left side of the model (i.e. at $(x, y) = (10.0, 12.0)$ m and $(x, y) = (10.0, 17.0)$ m) are considerably different from those registered at the monitoring positions located on the right side of the model (i.e. at $(x, y) = (23.7, 12.0)$ m and $(x, y) = (23.7, 17.0)$ m), which suggests that the drainage geocomposite enclosing the left densified sand column had a great impact on this aspect of the response, as intended. Specifically, it can be seen that, after an initial steep rise, the excess pore pressures are observed to gradually decrease with dynamic loading at $(x, y) = (10.0, 12.0)$ m, while the opposite trend is observed at $(x, y) = (23.7, 12.0)$ m. Indeed, when shaking is over ($t \approx 38$ s), the excess pore pressure at $(x, y) = (10.0, 12.0)$ m is already smaller than 20 kPa, being less than half of the value observed at $(x, y) = (23.7, 12.0)$ m.

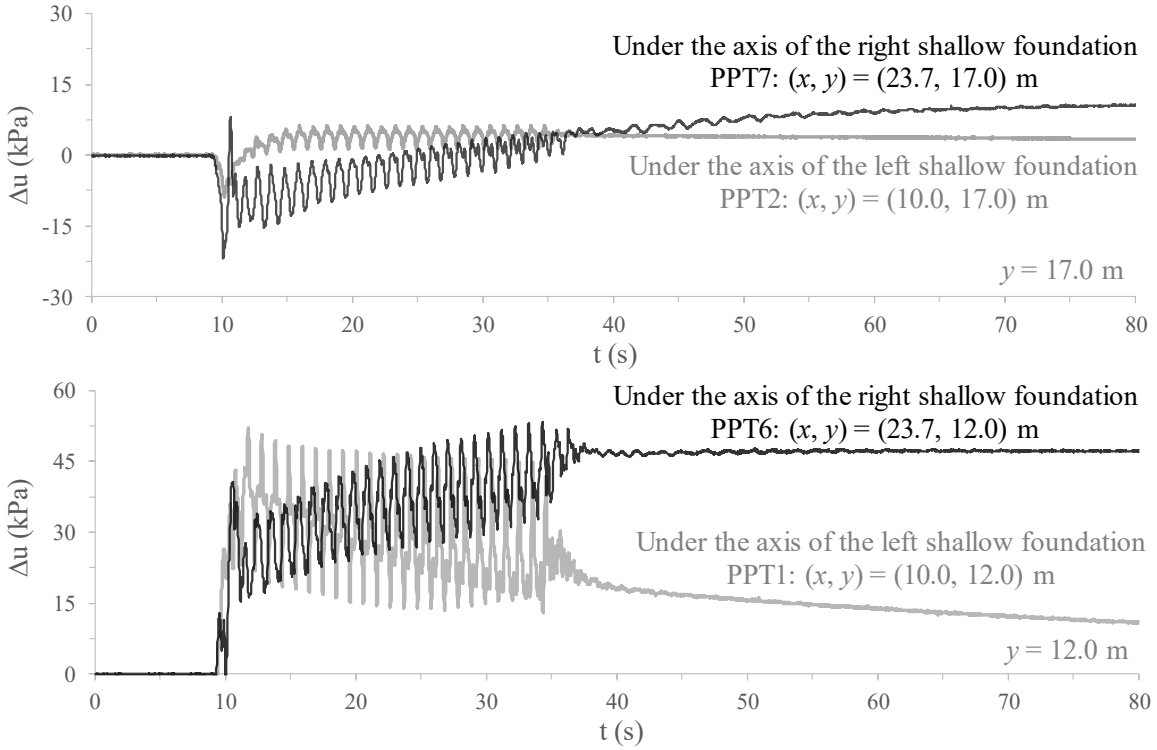

Figure 8.98 – Excess pore pressure evolution with time during dynamic loading and shortly after its end measured at two different monitoring positions located along vertical alignments coincident with the axes of the left and right shallow foundations for CM-B.

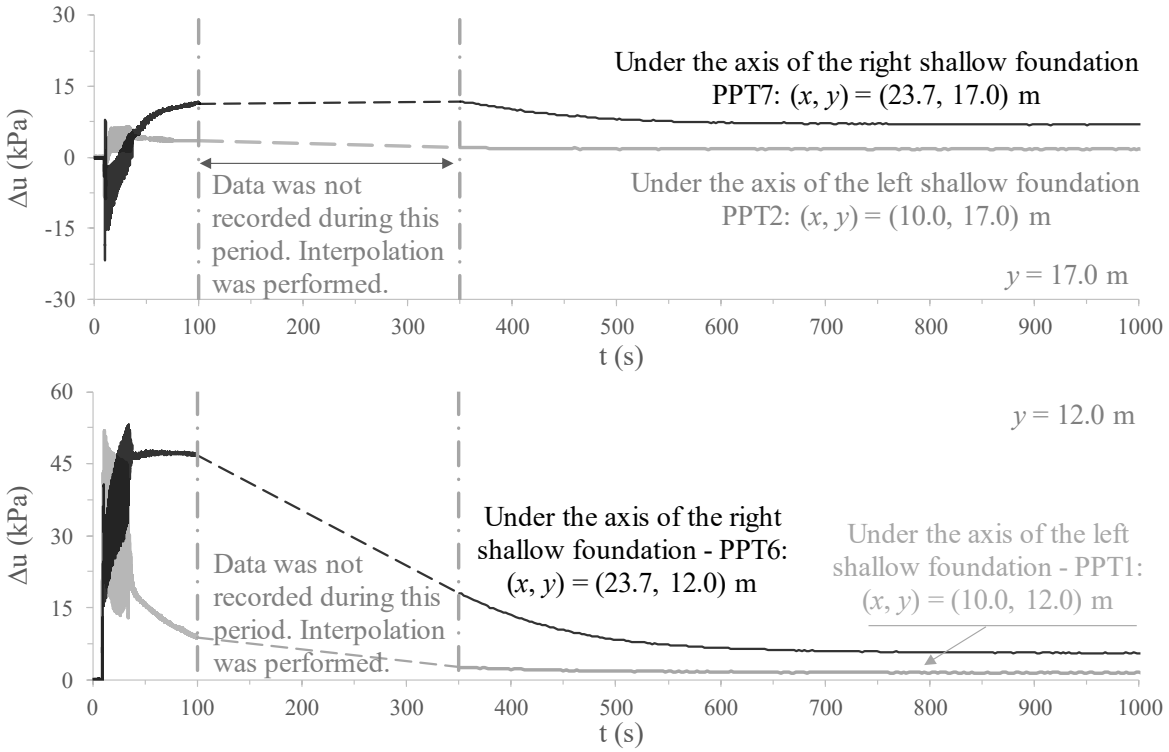

Figure 8.99 – Long-term dissipation of excess pore pressures at two different monitoring positions located along vertical alignments coincident with the axes of the left and right shallow foundations for CM-B.

Moreover, although complete stabilisation of excess pore pressures at $(x, y) = (10.0, 12.0)$ m seems only to occur when $t \approx 400$ s, it is noteworthy that, at $t \approx 80$ s, the

excess pore pressure is already as low as 10 kPa, which is roughly one fifth of the maximum excess pore pressure generated during dynamic loading. At that instant of time, the dissipation of excess pore pressures is still to be initiated at $(x, y) = (23.7, 12.0)$ m, being only completed when $t \approx 700$ s.

With respect to the responses measured at the shallower monitoring positions (i.e. at $(x, y) = (10.0, 17.0)$ m and $(x, y) = (23.7, 17.0)$ m), it can be seen that negative (i.e. suction, tensile) excess pore pressures are generated under both shallow foundations as dynamic loading starts. As suggested by Coelho (2007), this type of response is likely induced by stress redistribution from the zones of the deposit farther from the shallow foundations to the zones under their influence. Note that, due to the presence of the shallow foundations, the zones of the deposit under their influence are initially subjected to higher effective stresses and, therefore, have greater stiffnesses than the surrounding zones. Moreover, note that, as observed in triaxial testing, dense sand tend to dilate under monotonic loading and, therefore, under practically undrained conditions, negative excess pore pressures are likely generated. The fact that smaller negative excess pore pressures are generated in the zone of the deposit under the influence of the left shallow foundation (i.e. at $(x, y) = (10.0, 17.0)$ m) than in the zone under the influence of the right shallow foundation (i.e. at $(x, y) = (23.7, 17.0)$ m) is probably a consequence of the higher drainage capacity induced in the former zone by the drainage geocomposite. In effect, not only smaller negative excess pore pressures are generated during the first loading cycles, but also smaller positive excess pore pressures build-up during the remaining loading period at $(x, y) = (10.0, 17.0)$ m. Furthermore, as shaking is over, the excess pore pressures appear to dissipate continuously at $(x, y) = (10.0, 17.0)$ m, while the opposite trend seems to be observed at $(x, y) = (23.7, 17.0)$ m. As pointed out by Coelho (2007) and Marques *et al.* (2014a), this post-seismic excess pore pressure increase observed at $(x, y) = (23.7, 17.0)$ m is likely the result of excess pore pressure migration from the bottom to the top of the deposit, as well as from the zones of the deposit farther from this shallow foundation to the zones under its influence. Remarkably, this phenomenon appears to be strongly mitigated on the left side of the model by the existence of the drainage geocomposite. It is perhaps important to note that the small (although not null) excess pore pressures observed at the final of the dissipation period (from $t \approx 700$ s), particularly at the monitoring positions located on the right side of the model (i.e. at $(x, y) = (23.7, 12.0)$ m and $(x, y) = (23.7, 17.0)$ m), are likely the detrimental consequence of the settlement undergone by the pore pressure transducers. Full dissipation of excess pore pressures is expected to have occurred.

Additionally, Figure 8.100 depicts the excess pore pressures generated during dynamic loading and shortly after its end at several positions located along a vertical alignment coincident with the middle of the model (represented in black), together with those obtained for vertical alignments coincident with the axes of the shallow foundations (represented in

grey). The corresponding long-term excess pore pressure dissipations are shown in Figure 8.101.

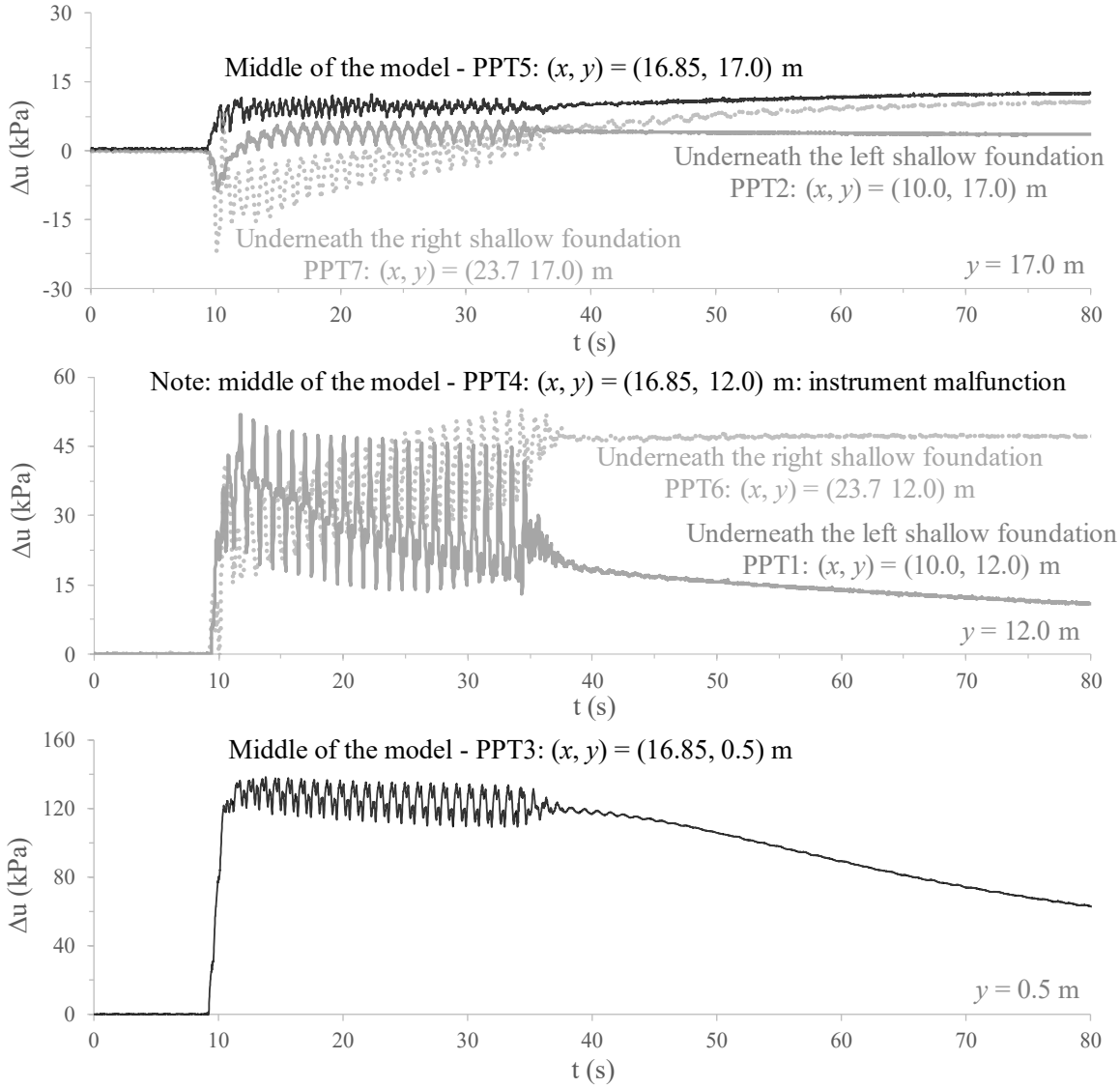

Figure 8.100 – Excess pore pressure evolution with time during dynamic loading and shortly after its end measured at three different monitoring positions located along vertical alignments coincident with the axes of the shallow foundations and middle of the model for CM-B.

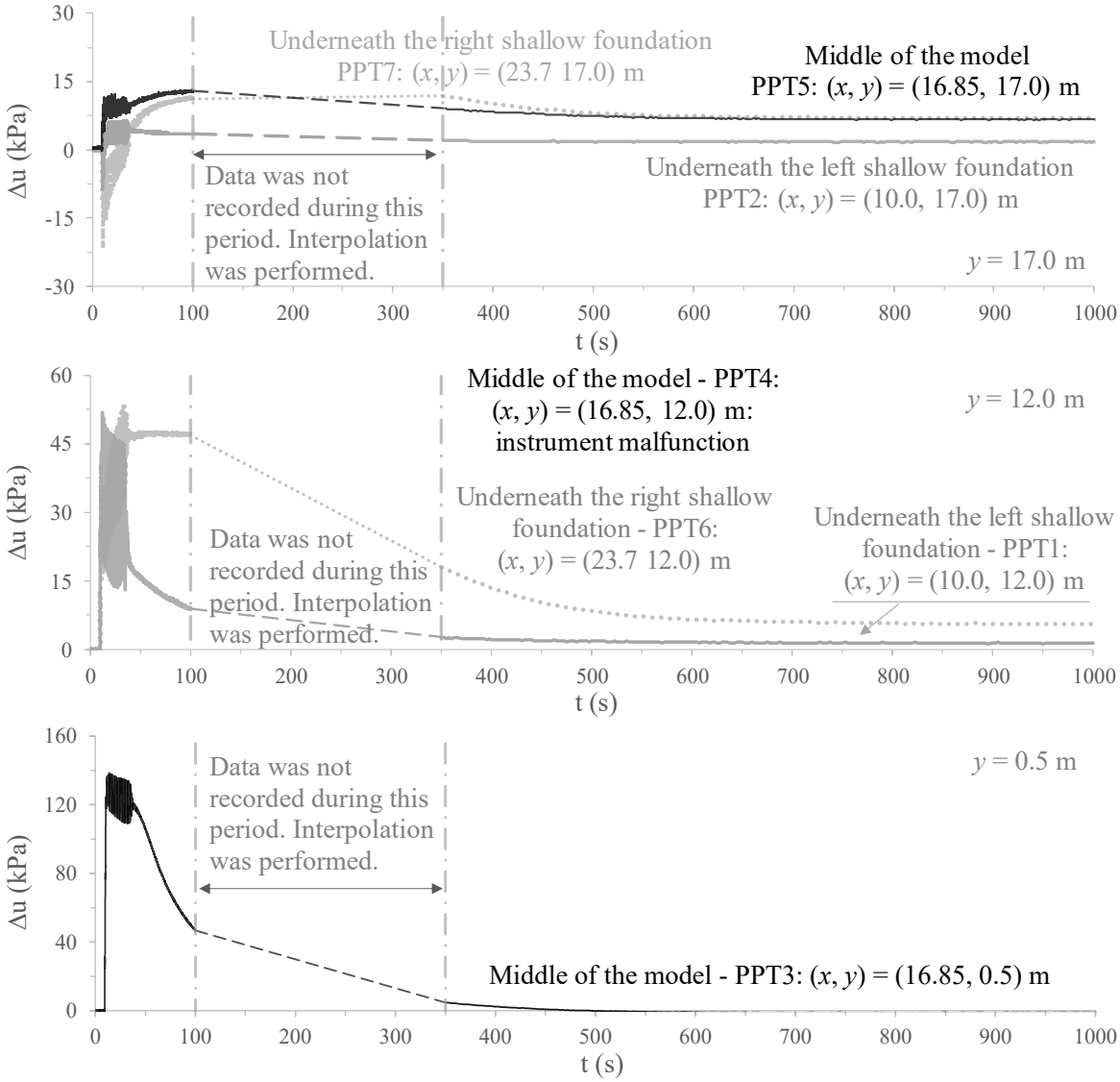

Figure 8.101 – Long-term dissipation of excess pore pressures at three different monitoring positions located along vertical alignments coincident with the axes of the shallow foundations and middle of the model for CM-B.

Unfortunately, it was reported that the pore pressure transducer PPT4, located in the middle of the model, more specifically at $(x, y) = (16.85, 12.0)$ m, malfunctioned during the test and, therefore, comparisons between the excess pore pressures generated in the middle of the model and those generated under the shallow foundations are solely possible for the shallowest level ($y = 17.0$ m). At that level, it can be seen that, contrary to the response observed in the densified zones of the deposit under the influence of the shallow foundations (i.e. at the monitoring positions $(x, y) = (10.0, 17.0)$ m and $(x, y) = (23.7, 17.0)$ m), positive excess pore pressures are generated from the beginning of dynamic loading in the middle of the model (i.e. at the monitoring position $(x, y) = (16.85, 17.0)$ m), with a value of 10 kPa being reached just after the first couple of loading cycles. Moreover, it is apparent that, as dynamic loading progresses, the excess pore pressures measured at $(x, y) = (16.85, 17.0)$ m remain approximately constant, contrasting with the increase observed at $(x, y) =$

$(23.7, 17.0)$ m. As dynamic loading ceases, the excess pore pressures at $(x, y) = (16.85, 17.0)$ m are observed to continuously increase during a significant period (at least, until $t \approx 100$ s), probably due to the excess pore pressure migration from the bottom to the top of the deposit. Note that, unfortunately, due to the lack of experimental data in the period ranging from 100 to 350 s, it is not possible to know the exact moment at which excess pore pressures stop increasing and start dissipating. Interestingly, although a similar trend (i.e. excess pore pressure build-up after the end of dynamic loading) is observed in the zone of the deposit under the influence of the right shallow foundation (i.e. at $(x, y) = (23.7, 17.0)$ m), the rate at which it occurs is significantly higher at this location. This may indicate that excess pore pressures migrate not only vertically (i.e. from the bottom to the top of the deposit), but also laterally (i.e. from the zones of the deposit farther from this shallow foundation to the zones under its influence), as suggested by Coelho (2007) and Marques *et al.* (2014a).

Still regarding the shallowest monitoring positions, two additional aspects are noteworthy. Firstly, while the excess pore pressures in the middle of the model and underneath the right shallow foundation are only observed to stabilise when $t \approx 600 - 700$ s is reached, the dissipation of the excess pore pressures underneath the left shallow foundation, where the densified sand column was embedded by a drainage geocomposite, occurs faster, as discussed before, and seems already completed when $t \approx 400$ s is reached. Secondly, the residual excess pore pressures observed at the end of the experiment at $(x, y) = (16.85, 17.0)$ m and $(x, y) = (23.7, 17.0)$ m are probably the detrimental consequence of the settlement undergone by the pore pressure transducers at those locations. As highlighted before, full dissipation of excess pore pressures is expected to have occurred.

In relation to the deepest level ($y = 0.5$ m), excess pore pressures were only monitored in the middle of the model, particularly at $(x, y) = (16.85, 0.5)$ m. It can be seen that large excess pore pressures are generate as soon as dynamic loading is applied. After the first couple of loading cycles, however, these larger excess pore pressures are observed to reduce with dynamic loading, although at a very small rate. The rate of excess pore pressure dissipation is significantly increased as dynamic loading ceases, with the dissipation appearing completed when $t \approx 500$ s.

In addition, it is interesting to compare the excess pore pressure evolutions with time measured in this centrifuge model (CM-B) – where the shallow foundations were built on densified sand columns, one of them encased by a drainage geocomposite – with those registered in the previous centrifuge model (CM-A). Note that the lighter shallow foundation of CM-A, located on the right side of that model, is excluded from this comparison, since the stresses applied by this shallow foundation to the underlying sand deposit are smaller than those applied by the heavier shallow foundation of CM-A, as well as both shallow foundations of CM-B (which have a similar weight to that of CM-A, although the term “heavier” has been used to distinguish the shallow foundation of CM-A).

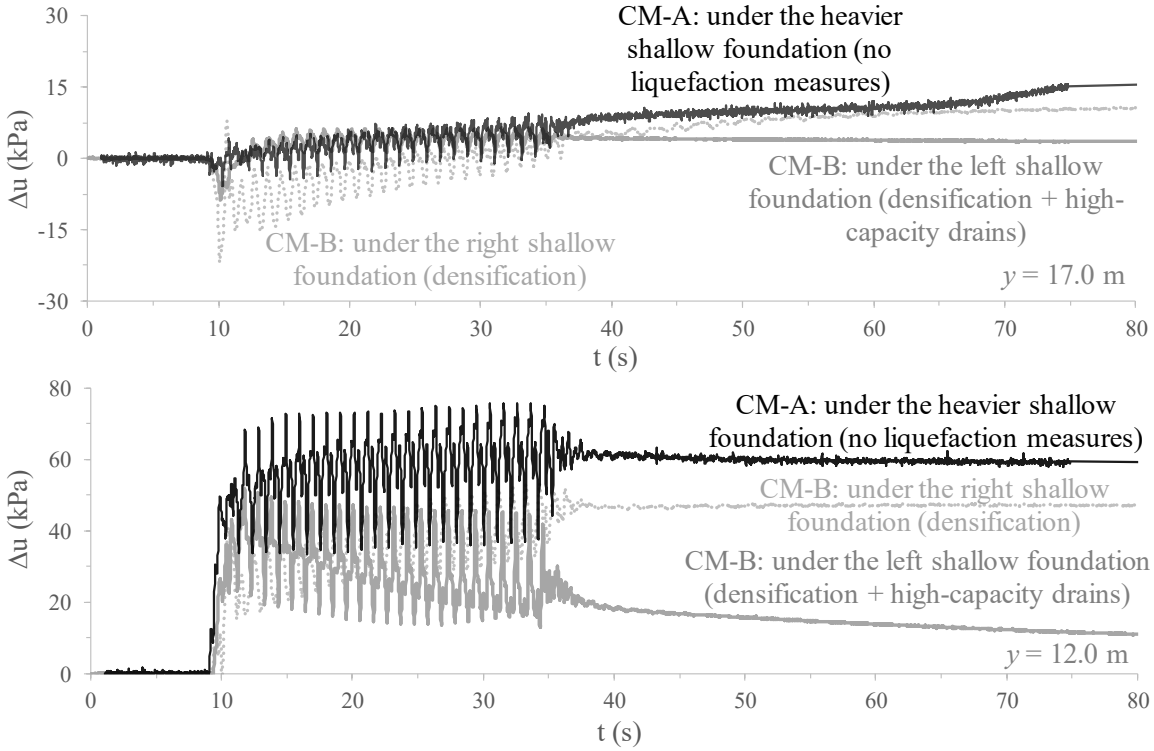

Figure 8.102 – Comparison of the excess pore pressure generated during shaking and shortly after its end in CM-A and CM-B at monitoring positions underneath the shallow foundations.

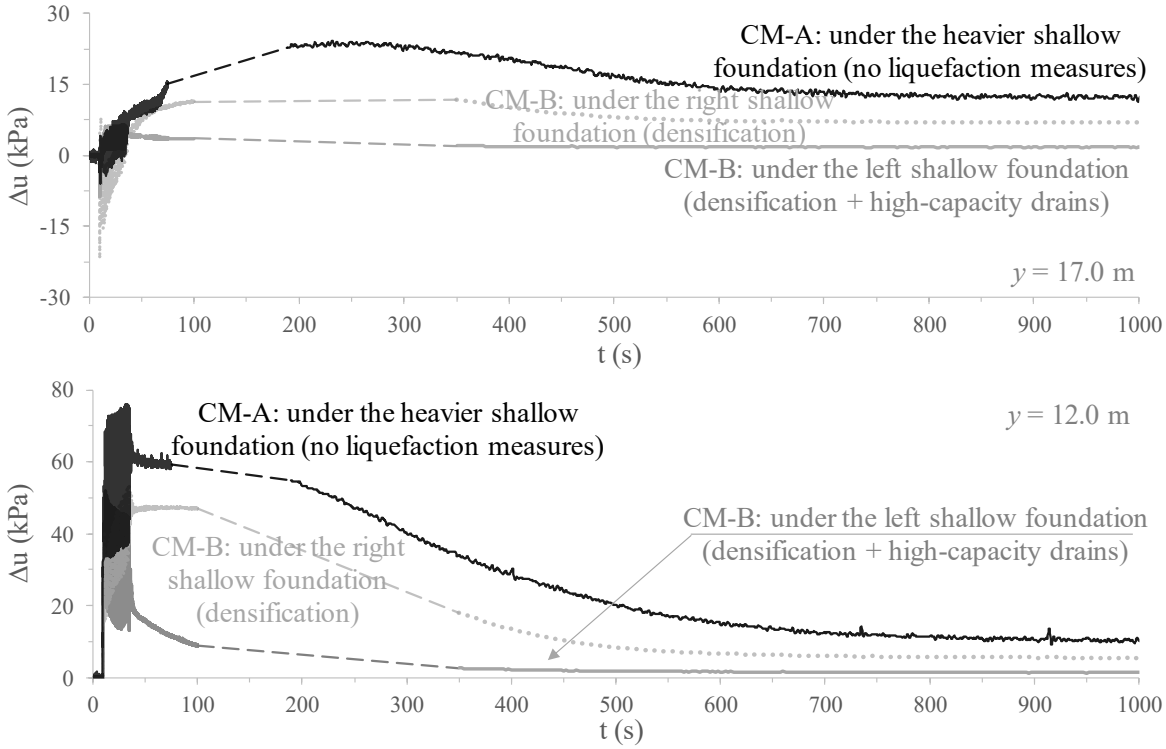

Figure 8.103 – Comparison of the long-term dissipation of excess pore pressures measured in CM-A and CM-B at monitoring positions underneath the shallow foundations.

Figure 8.102 depicts the excess pore pressure developed during dynamic loading and shortly after its end for CM-A (in black) and CM-B (in grey), underneath the shallow foundations. Complementary, Figure 8.103 presents the long-term dissipation of the excess pore pressures

at those monitoring positions. Note that the time delay between the measured responses in these two different centrifuge experiments was corrected in order to ease the comparison. It is apparent that densification improves the performance of the sand deposit, with significant negative (i.e. suction, tensile) excess pore pressures being generated during dynamic loading at the shallowest level ($y = 17.0$ m) underneath the right shallow foundation of CM-B (built-on a densified sand column), in relation to those generated for the (heavier) shallow foundation of CM-A. Densification seems also to contribute to a better post-seismic performance of the shallow foundation. In particular, Figure 8.103 shows that smaller positive excess pore pressures develop underneath the right shallow foundation of CM-B when compared to those generated underneath the heavier shallow foundation of CM-A. It is unclear, however, whether this enhanced response is solely the result of densification or the presence of the drainage geocomposite in the model (even if about 10 m far away) might have also slightly contributed to the registered improvement. In fact, as discussed later, the drainage geocomposite might have contributed to mitigate the excess pore pressures generated in the middle of the model in CM-B, which, in turn, might have resulted in smaller post-seismic excess pore pressure migration from the middle of the model to the zone under the influence of the right shallow foundation. Nevertheless, it is clear from Figure 8.102 and Figure 8.103 that the combination of densification with the drainage geocomposite simulating high-capacity vertical drains result in much smaller excess pore pressure generation during dynamic loading, as well as higher rate of excess pore pressure dissipation after the end of dynamic loading at both levels ($y = 12.0$ m and $y = 17.0$ m).

Finally, Figure 8.104 compares the excess pore pressure evolutions during dynamic loading and shortly after its end registered at the bottom (i.e. at $(x, y) = (16.85, 0.5)$ m) and top (i.e. $(x, y) = (16.85, 17.0)$ m) monitoring positions within the sand deposit for a vertical alignment coincident with the middle of the model in CM-A (in black) and CM-B (in grey). Their corresponding long-term dissipation curves are plotted in Figure 8.105. Starting by inspecting the responses measured at $(x, y) = (16.85, 0.5)$ m, it is apparent that slightly smaller excess pore pressures are developed in CM-B than in CM-A. Furthermore, it can be seen that the excess pore pressures tend to decrease slightly during dynamic loading in CM-B, while remaining practically constant during that stage of the experiment in CM-A. Indeed, as dynamic loading ceases, a much faster dissipation of excess pore pressure occurs in CM-B than in CM-A. This suggests that the drainage geocomposite encasing the left densified sand column in CM-B may have also contributed to a better performance of the deposit of loose sand (i.e. zone of the deposit in between the densified sand columns). Conversely, the influence of the drainage geocomposite on the evolution of excess pore pressures at the top monitoring position (i.e. $(x, y) = (16.85, 17.0)$ m) seems much more limited (or even inexistent), with slightly larger excess pore pressures being measured in CM-B than in CM-A both during shaking and shortly after its end.

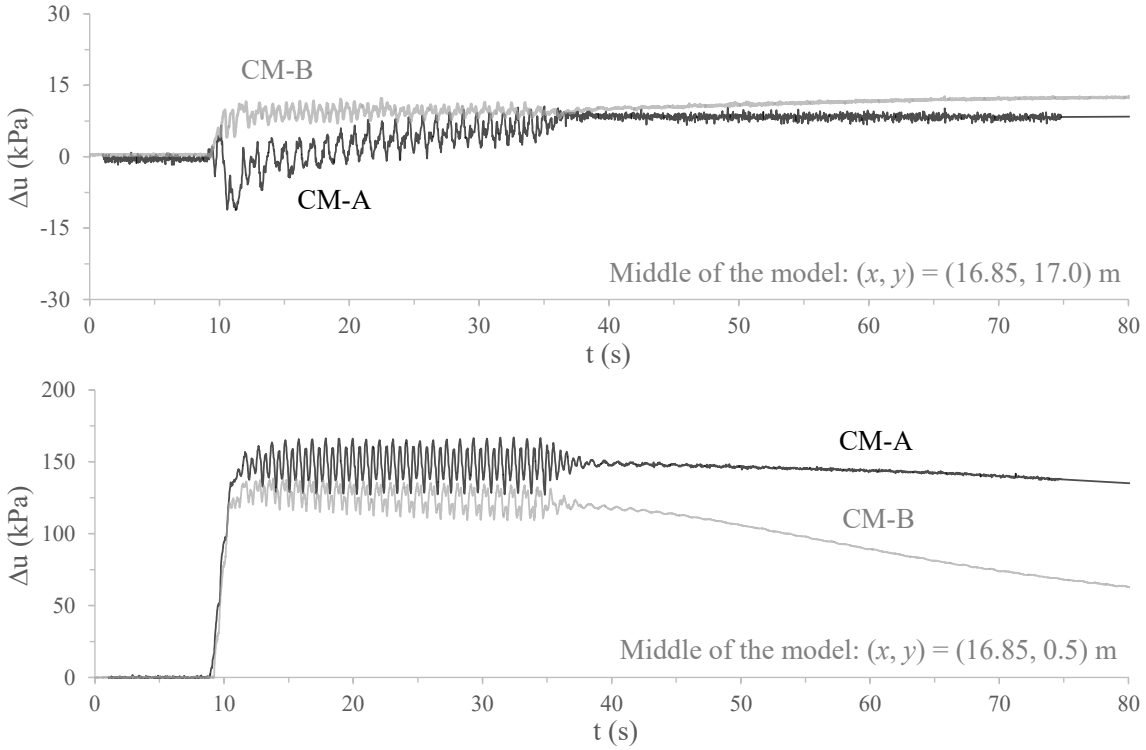

Figure 8.104 – Comparison of the excess pore pressure generated during shaking and shortly after its end in CM-A and CM-B for a vertical alignment coincident with the middle of the model.

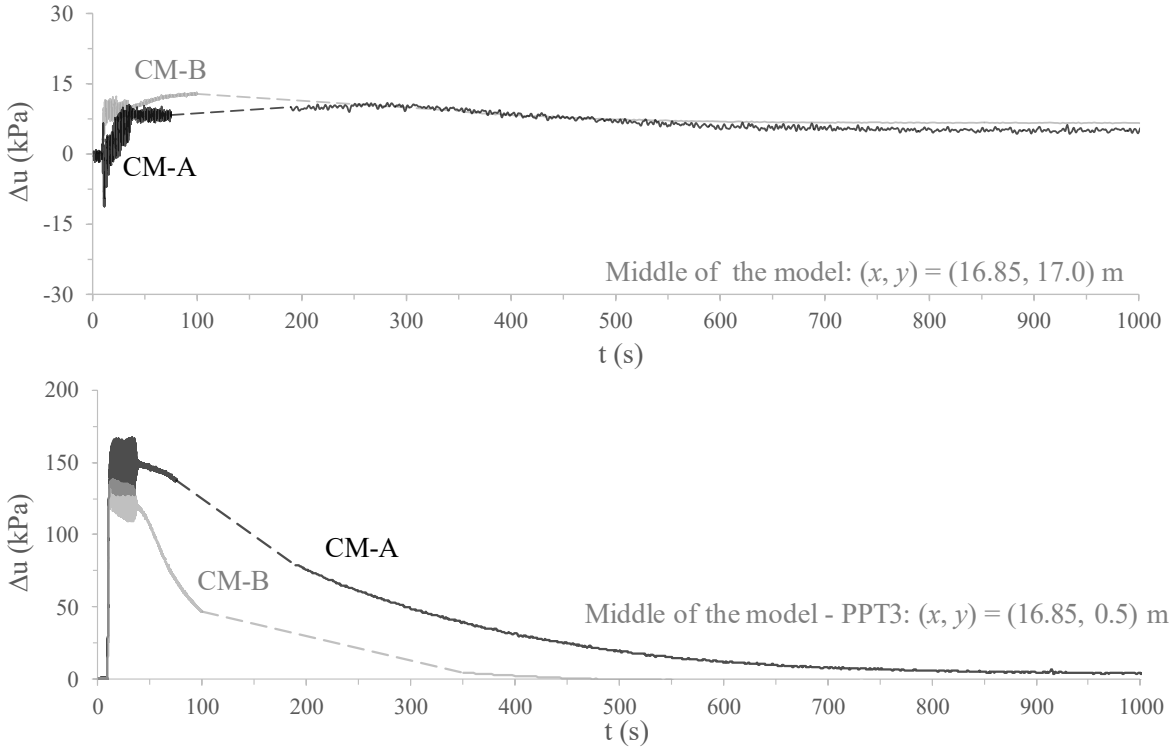

Figure 8.105 – Comparison of the long-term dissipation of excess pore pressures measured in CM-A and CM-B for a vertical alignment coincident with the middle of the model.

8.4.1.5 Settlements

Figure 8.106 depicts the settlements measured at the top of the shallow foundations and at the ground surface in between the shallow foundations occurring concurrently with the

application of the dynamic loading and until shortly after its end. Complementary, Figure 8.107 depicts the evolution of the settlements at those monitoring positions until the complete dissipation of excess pore pressures in the model. It can be observed that the settlement registered for the left shallow foundation, built on a densified sand column embedded by a drainage geocomposite, is significantly smaller than that measured for the right shallow foundation, built-on a densified sand column either during shaking or after its end. Specifically, a total settlement of about 10 cm was measured at the top of the left shallow foundation (i.e. at $(x, y) = (10.0, 19.225)$ m), while a value of approximately 52 cm (i.e. more than five times greater) was registered at the top of the right shallow foundation (i.e. at $(x, y) = (23.7, 19.225)$ m) during the application of dynamic loading (i.e. until $t \approx 36.0$ s). Similarly, during the period between the end of loading and the complete stabilisation of the pore pressures in the model (i.e. consolidation phase), the settlement registered for the left shallow foundation of the model (of only about 3 cm) is much smaller than that obtained for the right one (of about 21 cm). Indeed, the settlement registered for the left shallow foundation is even smaller than that registered at ground surface in between the shallow foundations (of approximately of 37 cm during the dynamic phase and 17 cm during the consolidation stage). This clearly indicates that the drainage geocomposite strongly enhanced the performance of the sand-structure system both during shaking and after its end.

Indeed, the fact that drainage geocomposite simulating closely spaced high-capacity vertical drains improves the response of the sand deposit during shaking by reducing the excess pore pressure generated in the zones of the deposit under the influence of the shallow foundation and, consequently, reducing the observed settlements suggests that the use of high-capacity vertical drains as a measure to mitigate liquefaction effects has a great potential, being probably more attractive than other mitigation techniques, such as cut-off walls (either slurry walls or sheet pile walls). In effect, the centrifuge test results obtained by Coelho (2007) on the use of densified sand columns encased by a membrane simulating a flexible impermeable barrier to mitigate liquefaction effects revealed that the impermeable barrier solely enhanced the performance of the sand deposit during the consolidation stage (i.e. after the end of dynamic loading), by preventing the lateral excess pore pressure migration from the zones of the deposit farther from the shallow foundation to the zones under its influence.

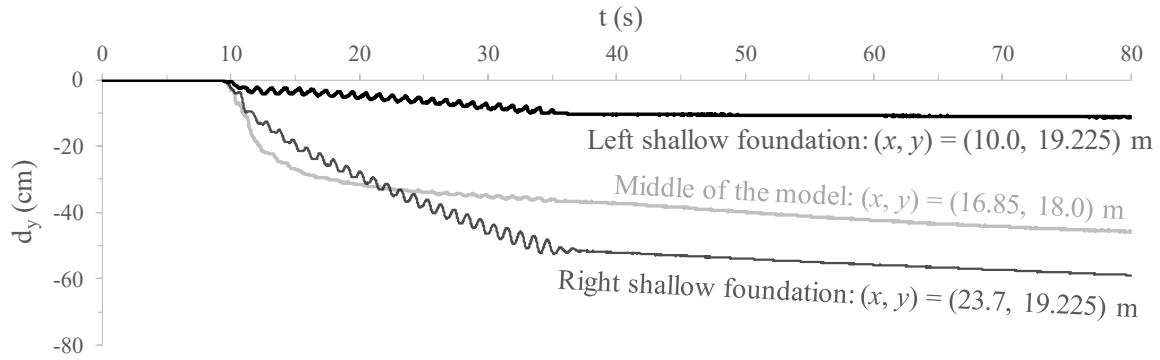

Figure 8.106 – Measured settlements at the top of the shallow foundations and at the ground surface in between them during shaking and shortly after its end for CM-B.

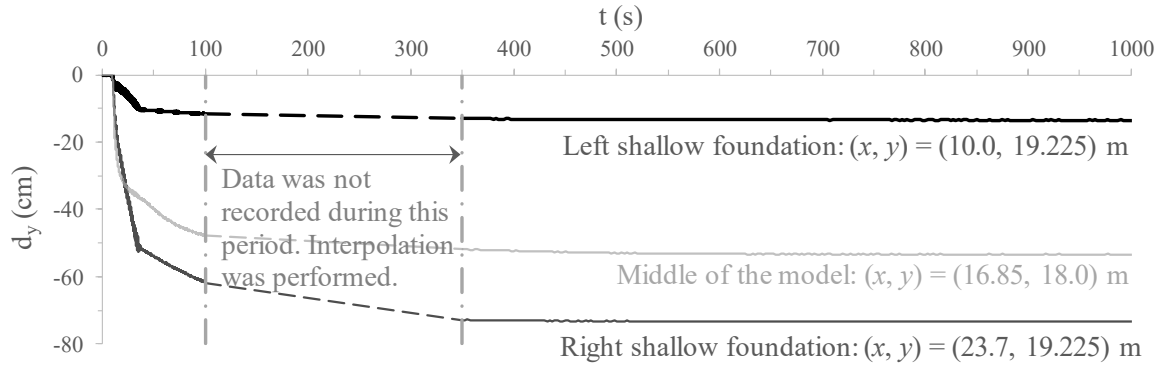

Figure 8.107 – Measured settlements at the top of the shallow foundations and at the ground surface in between them until the complete dissipation of excess pore pressures for CM-B.

The ground surface settlement and the final positions of the shallow foundations obtained from post-test visual inspections are shown in Figure 8.108. Note that the values indicated in this figure are different from those measured immediately after the end of the centrifuge experiment, since complete drainage of the model was performed before undertaking the post-test visual inspections (Marques *et al.*, 2014a, 2015). Nevertheless, the values indicated in this figure allow for a comparison of the settlements at different locations of the model. Several aspects are worth mentioning. Firstly, it is apparent that large relative displacements parallel to the drainage geocomposite (i.e. slipping) occurred during the experiment, with the deposit of loose sand undergoing much larger settlements than the left densified sand column embedded by the drainage geocomposite. Secondly, it appears that the right shallow foundation of the model slipped to the right of the model during the experiment, eventually resting partially on loose sand, rather than on the densified sand column. Note that, before the start of the centrifuge test, the right shallow foundation was centred on the densified sand column. Naturally, this might have influence both settlement and rotation of this shallow foundation. In effect, it appears that this shallow foundation was partially buried in sand only on its right side. Finally, it is interesting to observe that the left shallow foundation practically retained its horizontal position during the experiment, with no “punching trough” sand apparently occurring.

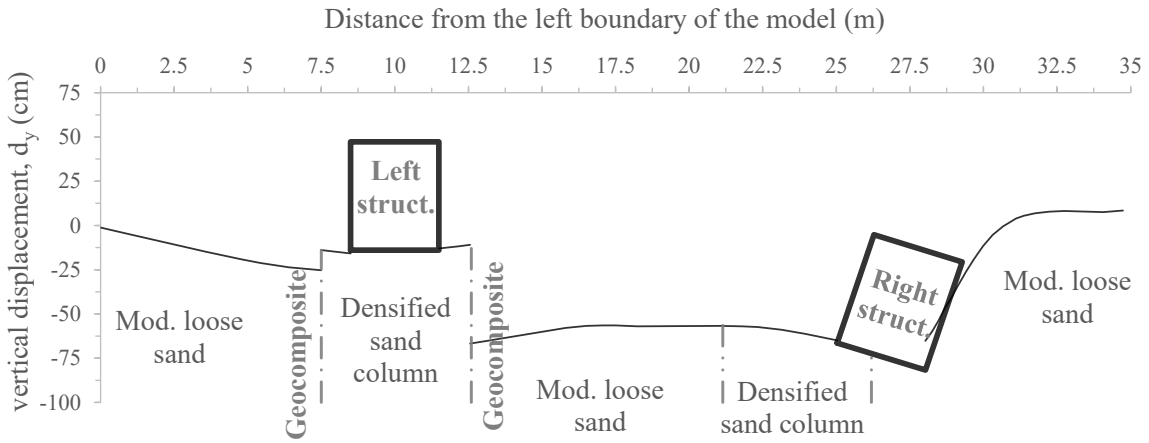

Figure 8.108 – Measured settlement profile of the ground surface and shallow foundations after the complete drainage of the model for CM-B.

In addition, Figure 8.109 compares the settlements measured at the top of the shallow foundations employed in CM-A (represented in black) and CM-B (represented in grey) during dynamic loading and shortly after its end, with Figure 8.110 extending the presentation for the entire periods of the experiments. While the use of a densified sand column enabled the reduction of the final settlement in about 34 % (from about 112 cm to 73 cm) in relation to that obtained for the case in which no measures to mitigate liquefaction effects were applied (i.e. heavier shallow foundation in CM-A), the combined use of densification and drainage geocomposite simulating closely spaced high-capacity vertical drains resulted in a settlement reduction of about 88% (from approximately 112 cm to 14 cm) in relation to the case in which no measures were applied.

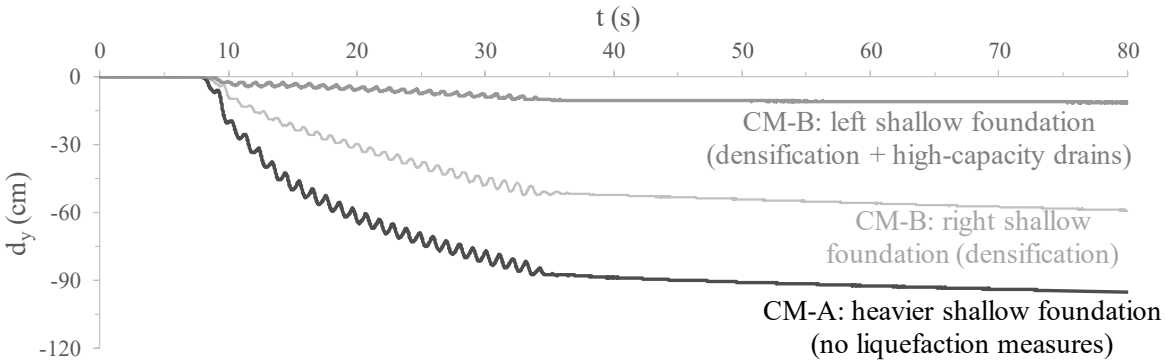

Figure 8.109 – Comparison of the settlements measured at the top of the shallow foundations during shaking and shortly after its end for CM-A and CM-B.

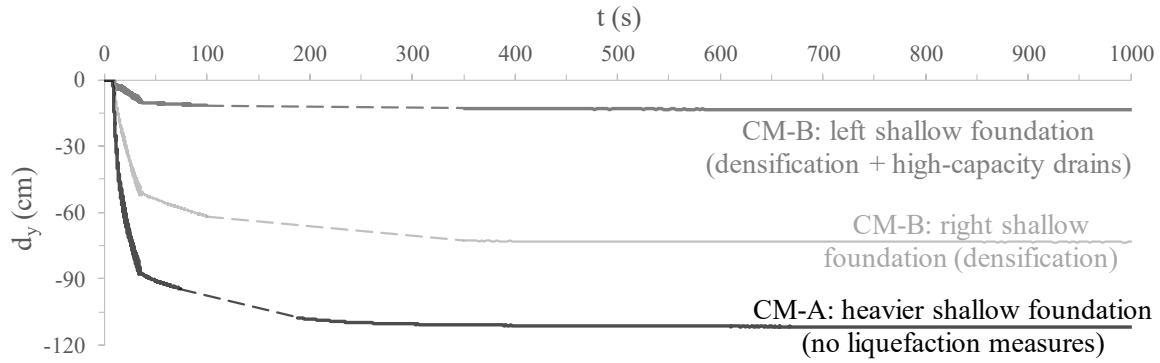

Figure 8.110 – Comparison of the settlements measured at the top of the shallow foundations until the complete dissipation of the excess pore pressures for CM-A and CM-B.

8.4.2 Numerical analysis

8.4.2.1 General aspects

Given the relevance of the interaction between the pore fluid and solid phases of porous material when simulating liquefaction-related phenomena, a fully coupled non-linear dynamic finite element analysis was performed using FEMEPDYN. Eight-noded isoparametric quadrilateral elements with pore pressure degrees of freedom assigned to the four corner nodes (i.e. hybrid elements) were used to model the response of both moderately loose and dense deposits of sand. Similarly, two columns of hybrid eight-noded isoparametric quadrilateral elements were used to model the drainage geocomposite. This strategy was deemed necessary to introduce the hydraulic conductivity estimated for the drainage geocomposite in the analysis. Other types of elements available in FEMEPDYN (such as interface elements) would only allow for fully permeable or fully impermeable response. Note, nevertheless, that interface elements were eventually introduced in the analysis with the objective of simulating the interaction between the drainage geocomposite (more specifically, its non-woven geotextile filter) and surrounding loose sand, allowing for slipping to occur at that location, as observed in the centrifuge experiment. Although a similar strategy could have been employed to model the interaction between drainage geocomposite and dense sand, it was considered unnecessary, since practically no slipping was observed at that location in the centrifuge experiment (Figure 8.108). Regarding the shallow foundations, due to their very low hydraulic conductivity nature, eight-noded isoparametric finite elements with no pore pressure degrees of freedom (i.e. ordinary single-phase elements) were employed.

Similar to the numerical modelling of CM-A, a 2D plane strain simplification was assumed in this numerical analysis, implying a correction of the contribution of the shallow foundations to the initial stress state. As detailed in the following section, the correction factor established for the simulation of CM-A was also considered appropriate for this case. Furthermore, the conclusions of the parametric study on the influence of the spatial discretisation presented in Appendix D were taken, once more, into account, with elements with $L \times H = 1.0 \times 1.0$ m^2

(where *L* is the width and *H* is the height) being preferentially used to model the deposits of both loose and dense sands.

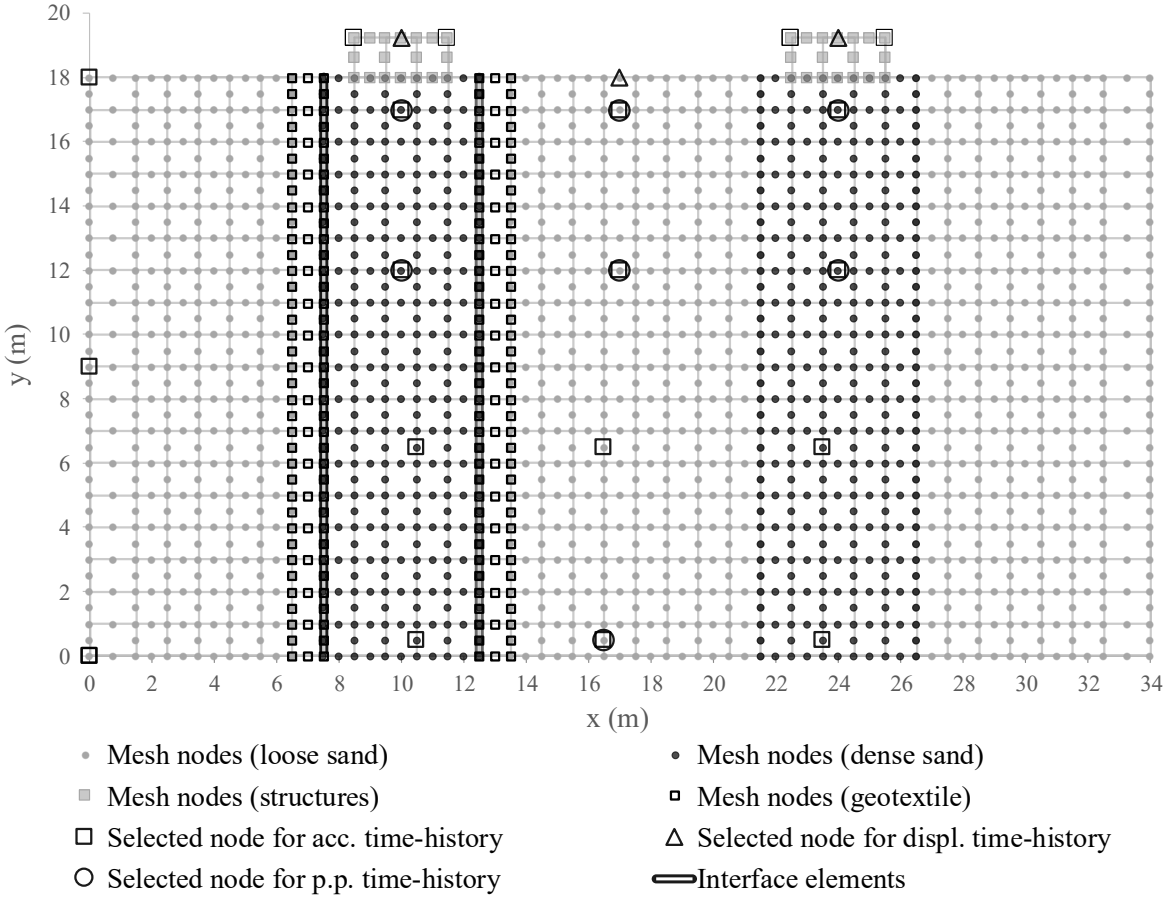

Figure 8.111 – Employed finite element mesh for the simulation of CM-B.

As illustrated in Figure 8.111, the adopted FE mesh includes a total of 636 elements: 6 of them consisting of ordinary single-phase eight-noded elements with a size of $L \times H = 1.0 \times 1.225$ m^2 representing the shallow foundations; 558 hybrid eight-noded elements modelling the deposits of sand, 36 of them having a size of $L \times H = 1.5 \times 1.0$ m^2 and being located along the lateral boundaries of the model, while the remaining having a size of $L \times H = 1.0 \times 1.0$ m^2; 36 hybrid eight-noded elements with a size of $L \times H = 1.0 \times 1.0$ m^2 modelling the drainage geocomposite; and, finally, 36 hybrid six-noded interface elements with $H = 1.0$ m modelling the sand-geotextile interaction. Note that, as originally formulated by Goodman *et al.* (1968) and detailed in Almeida e Sousa (1999) and Grazina (2009), the interface elements available in FEMEPDYN have zero thickness. In addition, it should be noted that some degrees of freedom of the interface elements were restricted. In particular, to guarantee the continuity of pore pressures, their associated degrees of freedom (at the corner nodes of the elements) were tied at each level. Moreover, to prevent gapping or overlapping (i.e. relative displacement perpendicular to the interface element) from triggering numerical instabilities during the numerical analysis (as observed by Grazina (2009)), the horizontal displacement degrees of freedom of each pair of nodes (i.e. nodes

having identical coordinates) were also tied, meaning that only slipping (i.e. relative displacement parallel to the interface element) was allowed to occur. Regarding the size of the elements simulating the geotextile, it is perhaps important to note that a small parametric study was performed to assess the influence of the width of these elements on the obtained results (particularly on the excess pore pressures developed in the model). Since similar results (not presented here for brevity) were obtained when using either 0.25 m- or 1.0 m-width elements, it was decided to select the latter size, which results in a more homogeneous mesh.

In terms of time step, and, once more, similar to what was considered for CM-A, a constant value of $\Delta t = 0.0125$ s was adopted in the analysis. Since a total duration of 250 s was required to simulate the application of the dynamic excitation and subsequent dissipation of excess pore pressures, the adoption of $\Delta t = 0.0125$ s resulted in a total of 20 000 increments.

With respect to the time-integration algorithm used to solve the equation of motion, the generalised-α method (Chung and Hulbert, 1993) was selected once more. As detailed in Grazina (2009), by adopting $\alpha_f = 4/9$ and $\alpha_m = 3/2 - 2\alpha_f = 11/18$ for the parameters controlling the algorithm, which result in a spectral radius at infinity of $\rho_\infty \approx 0.800$ for a single degree of freedom oscillator, the method verifies the conditions of unconditional stability and second order accuracy, also achieving the optimal high frequency dissipation with minimal low frequency impact. Moreover, this algorithm verifies the conditions of unconditional stability and second order accuracy. As demonstrated, for example, by Kontoe (2006), Grazina (2009) and Tsaparli *et al.* (2017), this latter attribute is particularly important to mitigate the detrimental impact of spurious high frequencies of the excitation on the FE results, particularly when no Rayleigh damping is employed in the numerical analysis, which is the present case. Further details on the time-integration algorithm and its implementation into FEMEPDYN can be found in Grazina (2009).

Similar boundary conditions to those specified in CM-A were considered in this numerical analysis. Specifically, the horizontal acceleration time-history shown in Figure 8.78 was prescribed at the nodes located along the bottom boundary of the mesh, while restricting the vertical displacements of those nodes (i.e. the vertical input motion was disregarded). With respect to the lateral boundaries of the model, in order to model the flexible walls of the centrifuge container, the horizontal and vertical displacements were tied along nodes of the same height. Note that, although the model was not symmetric about a vertical axis coincident with its middle (due to the presence of geotextile), the lateral boundaries were considered to be sufficiently far away from the zone of influence of the shallow foundations to allow for the application of this boundary condition.

In terms of hydraulic regime, conditions of no flow were imposed at the bottom and lateral boundaries of the mesh, by tying the displacements in the solid and fluid phases in the direction perpendicular to that defined by the boundary. In addition, a pore pressure

boundary condition of $u = 0.0$ kPa was imposed at the corner nodes of the elements defining the top of the sand deposit (except those defining the sand-structure contact), allowing drainage to occur at the ground surface.

8.4.2.2 Material properties

The mechanical response of Hostun sand deposit was, once more, modelled using the BSPM, with the set of model parameters "B.1) Original formulation" indicated in Table 6.5. Although possible, Rayleigh damping was not introduced in the analysis, since the constitutive model already predicts the occurrence of material damping both at small strains, due to its cyclic non-linear elastic component, and at medium to large strains, mainly due to the occurrence of plasticity. For further details on this topic, please refer to Taborda (2011).

As mentioned by Marques *et al.* (2014a), the densified sand columns were prepared to $D_r \approx 80\%$, while the remaining sand deposit was prepared to $D_r \approx 50\%$. By using the maximum ($e_{max} = 1.067$) and minimum ($e_{min} = 0.555$) void ratios reported in Marques *et al.* (2014a) – which are different from those experimentally determined in the present study, as explained before – the initial void ratio of the loose and dense sand deposits were estimated as $e \approx 0.811$ (Equation 8.23) and $e \approx 0.657$ (Equation 8.24), respectively.

$$e = e_{max} - D_r\,(e_{max} - e_{min}) \approx 1.067 - 0.50 \times (1.067 - 0.555) \approx 0.811 \tag{8.23}$$

$$e = e_{max} - D_r\,(e_{max} - e_{min}) \approx 1.067 - 0.80 \times (1.067 - 0.555) \approx 0.657 \tag{8.24}$$

Having defined the initial void ratio, and given the density of the solid particles of $G_s = 2.64$, the saturated unit weight of loose Hostun sand was estimated as $\gamma_{sat} = 18.7$ kN/m^3, which corresponds to a mass density of $\rho \approx 1.906$ g/cm^3 (Equation 8.25). For dense Hostun sand, $\gamma_{sat} \approx 19.5$ kN/m^3 and $\rho \approx 1.990$ g/cm^3 were obtained (Equation 8.26).

$$\begin{aligned} &\gamma_{sat} = \gamma_w\,\frac{G_s + e}{1.0 + e} \approx 9.81 \times \frac{2.64 + 0.811}{1.0 + 0.811} \approx 18.7 \text{ kN/m}^3 \Leftrightarrow \\ &\rho = \frac{\gamma_{sat}}{g} \approx \frac{18.7}{9.81} \approx 1.906 \text{ g/cm}^3 \end{aligned} \tag{8.25}$$

$$\begin{aligned} &\gamma_{sat} = \gamma_w\,\frac{G_s + e}{1.0 + e} \approx 9.81 \times \frac{2.64 + 0.657}{1.0 + 0.657} \approx 19.5 \text{ kN/m}^3 \Leftrightarrow \\ &\rho = \frac{\gamma_{sat}}{g} \approx \frac{19.5}{9.81} \approx 1.990 \text{ g/cm}^3 \end{aligned} \tag{8.26}$$

In terms of the hydraulic conductivity of the sand deposit, as justified before, the outcome of the experimental study on Hostun sand carried out by Lauer and Engel (2005) was considered in the present study, with the hydraulic conductivity coefficients of $k_x = k_y \approx 3.65 \times 10^{-4}$ m/s (Equation 8.27) and $k_x = k_y \approx 2.71 \times 10^{-4}$ m/s (Equation 8.28) being adopted for loose and dense sand, respectively.

$$k_x = k_y = (6.1\,e - 1.3) \times 10^{-4} = (6.1 \times 0.811 - 1.3) \times 10^{-4} \approx 3.65 \times 10^{-4} \text{ m/s} \tag{8.27}$$

$$k_x = k_y = (6.1\,e - 1.3) \times 10^{-4} = (6.1 \times 0.657 - 1.3) \times 10^{-4} \approx 2.71 \times 10^{-4} \text{ m/s} \tag{8.28}$$

In relation to the solid elements simulating the drainage geocomposite, although other strategies would have been possible, identical mechanical characteristics to those adopted for moderately loose Hostun sand were considered. Naturally, a different hydraulic conductivity was assigned to this material. Assuming that clogging did not occur during the centrifuge test, the horizontal hydraulic conductivity, k_x, was assumed to be identical to the cross hydraulic conductivity specified by the geotextile's manufacturer (TERRAM Geosynthetics, 2018): $k_x \approx 5.0 \times 10^{-2}$ m/s (which is about one hundred times greater than that of sand). Regarding the vertical hydraulic conductivity, k_y, assuming that neither clogging, bending or kinking occurred during the test and that the flow capacity of the geotextile is constant with depth (i.e. not significantly affected by the higher lateral pressures expected to occur at deeper levels), its value was estimated based on the discharge capacity of $Q = 6.5 \times 10^{-4}$ m^3/s/m specified by the geotextile's manufacturer (TERRAM Geosynthetics, 2018). More specifically, by applying the Darcy's law (which assumes the occurrence of a laminar flow), as shown by Equation 8.29, a vertical hydraulic conductivity of $k_y \approx 1.3 \times 10^{-1}$ m/s was obtained (which is about one thousand times greater than that of sand).

$$k_y = \frac{Q}{i\,A} \approx \frac{6.5 \times 10^{-4}}{1.0 \times (0.005 \times 1.0)} \approx 1.3 \times 10^{-1} \text{ m/s} \tag{8.29}$$

where i is the vertical hydraulic gradient (which is roughly 1.0 for a vertical drain) and A is cross-section area where the laminar flow occurs (which is given by the width of the elements simulating the drainage core of the geocomposite times its length on the plane perpendicular to that of the FE analysis).

It is perhaps important to note that similar results would likely be obtained if the mechanical properties of dense (rather than loose) Hostun sand would have been assigned to the geotextile – which, naturally, would imply locating the elements simulating the geocomposite within the left densified sand column, rather than surrounding it (Figure 8.111). In effect, the most important aspect to be modelled is the preferential drainage path provided by the geotextile, meaning that the most influential property consists of its hydraulic conductivity.

Regarding the interface elements, their mechanical response in FEMEPDYN is defined by a linear elastic model coupled with the associated Mohr-Coulomb failure criterion (Almeida e Sousa, 1999; Grazina, 2009). As such, elastic gapping or overlapping (i.e. relative displacement perpendicular to the direction of the interface) is directly proportional to the elastic normal stiffness, K_n (in units of Force/Length^3), while elastic slipping (i.e. relative displacement parallel to the direction of the interface) is directly proportional to the elastic shear stiffness, K_s (also in units of Force/Length^3). Regarding the strength parameters, values for apparent cohesion, c'_i, and friction angle, ϕ'_i, need to be defined. Unfortunately, due to the lack of experimental data, only a very rough estimation of the value of these parameters is possible. Although other strategies could have been devised (e.g. parametric study to evaluate the parameters that best reproduce the centrifuge test data), to keep consistent with the

approach followed in this study that all material parameters are calibrated *à priori* based on available element laboratory test data (or field test data, if it would have been the case), it was decided to use results published in the literature to calibrate the model parameters. Moreover, it should be noted that particular emphasis was given to the calibration of the strength parameters, due to the relevance of the plastic response of materials in this type of problems involving liquefaction-related phenomena. In most of experimental studies of interface strength properties, the friction of the interface is defined in relation to that of sand, by using the concept of coefficient of interaction (often termed by some authors as "interface efficiency"). As detailed, for example, in Vieira *et al.* (2013), this quantity is defined as the ratio of the maximum shear stress developed in a soil–geosynthetic interface (typically measured in direct shear tests) to the maximum shear stress developed in soil (measured in the same type of test). Having performed a large laboratory testing programme consisting of more than 450 direct shear tests on sand-polymer interfaces at low confining stresses (of about 20.7 kPa), O'Rourke *et al.* (1990) concluded that the coefficient of interaction of medium- and high-density polyethylene linings contacting with different sands at various densities is relatively constant, within the range of 0.55 to 0.65, with the highest values being obtained for a fluvial sub-angular sand. Higher values have been, nevertheless, suggested from other laboratory studies. In particular, based on results of large-scale direct shear tests on interfaces between moderately loose and dense silica sand and a high-strength composite geotextile, Vieira *et al.* (2013) obtained coefficients of interaction, in general, slightly above 0.80. Similarly, Abu-Farsakh *et al.* (2007) reported a coefficient of interaction of 0.74 for a dense sand–woven geotextile interface tested in a large-scale direct shear test device. A comprehensive experimental study on sand-geotextile interface was also performed Markou (2018), involving not only small- and large-scale direct shear tests on several different sands and non-woven polypropylene geotextile interfaces, but also triaxial compression tests on reinforced sand samples. This author reported coefficients of interaction within 0.67 and 0.73 for a sub-angular dense sand contacting with a non-woven polypropylene geotextile. Considering the outcome of these experimental studies, it was decided to adopt a value of 0.67 for the coefficient of interaction. Assuming zero apparent cohesion and a friction angle for loose Hostun sand of 31.5° (corresponding to its critical-state value in triaxial compression loading conditions – Section 6.4), the friction angle of the interface, ϕ'_i, was set to 21.1°.

With respect to the stiffness parameters, due to the scarcity of published data, which could be used as reference, the approach followed consisted of estimating firstly the lower limit tangent elastic shear modulus predicted by the constitutive model for loose Hostun sand (having an initial void ratio, *e*, of 0.811 and model parameters indicated in Table 6.5):

$$(G_{tan})_{lim} = \frac{C_g\, p'_{ref} \dfrac{(m_g - e)^{2.0}}{1+e} \left(\dfrac{p'_{min}}{p'_{ref}}\right)^{n_g}}{1.0 + \kappa \left(\dfrac{1.0}{a_1} - 1.0\right)} = \frac{293.0 \times 101.3 \dfrac{(2.97 - 0.811)^{2.0}}{1 + 0.811} \left(\dfrac{10.0}{101.3}\right)^{0.49}}{1.0 + 2.0 \left(\dfrac{1.0}{0.46} - 1.0\right)} \approx 7337.6 \text{ kPa} \tag{8.30}$$

Assuming an interface thickness, t_i, of 0.1 m (which corresponds to about three times the mean grain size of Hostun sand in prototype scale) and considering that the elastic shear stiffness of the interface is smaller than that of the surrounding material, with the reduction being proportional to the square of the coefficient of interaction, f_g, as proposed in Brinkgreve *et al.* (2019), the elastic shear stiffness of the interface, K_s, was estimated as:

$$K_s = \frac{f_g^{\,2.0}\,(G_{tan})_{lim}}{t_i} = \frac{0.67^{2.0} \times 7337.6}{0.1} \approx 3.30 \times 10^4 \text{ kN/m}^3 \tag{8.31}$$

Note that it was not necessary to estimate a value for the elastic normal stiffness of the interface, K_n, since the horizontal displacements of the interface nodes were tied at each level, as mentioned before.

Still regarding the interface stiffness properties, it is perhaps noteworthy that, although it would have been possible to consider several different materials in depth and relate, for example, the elastic stiffness properties of the interface to those of the surrounding sand at the start of the analysis, it is believed that such detail would result in unnecessary complexity, most probably without greatly increasing the accuracy of the analysis. Furthermore, note that such approach would not anyway account for the strong reduction of stiffness of sand typically observed in this type of problems.

With respect to the solid steel shallow foundations, a simple isotropic linear elastic model with a shear modulus of $G = 76.9$ GPa and a Poisson's ratio of $\nu = 0.30$ was used to model their mechanical responses. Similar to CM-A, their mass density, ρ, was estimated based on the weight required to apply to the underlying sand deposit the corrected value of the vertical stress, $\Delta\sigma_v^*$, during the generation of the initial stress state. Specifically, as detailed in the following section, a mass density of $\rho = 4.75$ g/cm^3, corresponding to a vertical stress of $\Delta\sigma_v^* \approx$ 57.1 kPa (Equation 8.32), was employed.

$$\rho = \frac{\Delta\sigma_v^*}{g\,h} \approx \frac{57.1}{9.81 \times 1.225} \approx 4.75 \text{ g/cm}^3 \tag{8.32}$$

Finally, the only input parameter required for the pore fluid consisted of its bulk modulus, with $K_f \approx 2.2$ GPa being adopted in the numerical analysis (as also considered in the simulation of CM-A).

8.4.2.3 Generation of the initial stress state

Similar to CM-A, a gravity loading procedure was employed to generate the initial stress state in the model, consisting of the application of body forces to the elements of the mesh, which are considered weightless at the start of the analysis, as a boundary condition – for further details on this procedure, refer, for example, to Potts and Zdravkovic (1999). Concurrently, a hydrostatic pore pressure profile, characterised by a linear variation between a pore pressure of $u = 0.0$ kPa at the surface of the sand deposit and $u = \gamma_{pf} H = 9.81 \times 18.0 \approx 176.6$ kPa at its bottom, was introduced in the analysis. By combining these two actions, the initial effective stress state was computed by using Terzaghi's principle of effective stress. As also described for CM-A, during this calculation phase, a linear elastic isotropic model and uniform stiffness parameters ($G = 76.9$ GPa and $\nu = 0.333$) were specified for all materials, to prevent the occurrence of large shear stresses at the sand-structure interfaces. As mentioned before, by adopting $\nu = 0.333$, a value of $K_0 \approx 0.50$ was obtained in the zones of the deposit far from the shallow foundations (Equation 8.7). In addition, the Mohr-Coulomb criterion with $\phi' = 31.5°$, $c' = 0.0$ kPa and $\psi = 0.0°$ was adopted for the sand deposits, to prevent the occurrence of large stress ratios in these materials. Fully drained conditions were assumed during this stage and standard displacement boundary conditions for static analyses were applied, consisting of restricting the horizontal displacements along the lateral boundaries of the model, as well as horizontal and vertical displacements of the nodes belonging to the bottom boundary of the model.

In relation to the mass density of each shallow foundation, as explained before, it can be directly related to the vertical stress induced by the shallow foundation in the underlying sand deposit (Equation 8.32). Furthermore, as described in detail for CM-A (Section 8.3.2.3), due to the impossibility of simulating a square shallow foundation in a 2D plane strain analysis, a correction for the vertical stress induced by that shallow foundation in the underlying sand deposit is required. For CM-A, a reduction factor of $\xi = 40.0\%$ was found by comparing the immediate settlement induced by a square and strip loading in an elastic, homogeneous and isotropic half space (Carothers, 1920; Giroud, 1970; Poulos and Davis, 1974; Bowles, 1996). Taking into account that the geometry of CM-B is very similar to that of CM-A (in particular, the aspects which have great influence on the analysis, such as the contact area between the shallow foundation and the sand deposit, the null embedment depth, the thickness of the deposit and its characteristics), the reduction factor of $\xi = 40.6$ % was also adopted for the present numerical analysis. This means that a maximum vertical stress change of $\Delta\sigma_v^* \approx (1.0 - 0.406) \times 95.0 \approx 56.4$ kPa was considered in the analysis, rather than the value of $\Delta\sigma_v = 95.0$ kPa reported in the experiment (Marques *et al.*, 2014a). This means that a mass density of $\rho \approx 4.7$ g/cm^3 was considered for both left and right shallow foundations in the numerical analysis (Equation 8.32).

Figure 8.112 depicts the effective stresses obtained for three different vertical alignments on the left side of the model: $x = 0.75$ m (i.e. close to the left boundary of the model), $x = 4.0$ m (i.e. at approximately half distance from the centre of the left shallow foundation to the left boundary of the model) and $x = 10.0$ m (i.e. axis of the left shallow foundation). It can be seen that the intended vertical stress increment of $\Delta\sigma_v^* \approx 57.1$ kPa was adequately applied to the zone of the deposit immediately underneath the shallow foundation. Furthermore, as expected, a much more limited horizontal stress increment (less than half of the vertical stress increment) was applied to that zone of the deposit. Moreover, it is apparent that the influence of the shallow foundation is practically restricted to the zones of the deposit underneath it, with similar horizontal and vertical effective stresses being obtained for $x = 0.75$ m and $x = 4.0$ m. In addition, it is apparent that, at levels deeper than 8 – 10 m, the influence of the shallow foundation on the effective stress state of the sand deposit is practically negligible, with the vertical stress distribution computed for $x = 10.0$ m being similar to that obtained for $x = 0.75$ m and $x = 4.0$ m. Note that a similar effective stress state is obtained for the right side of the model.

Complementary, Figure 8.113 presents the effective stresses generated in the model for four horizontal different horizontal alignments: $y = 0.50$ m (i.e. close to the bottom boundary of the model), $y = 9.50$ m (i.e. at approximately middle depth of the sand deposit), $y = 14.50$ m (i.e. at approximately one third of the depth of the sand deposit) and $y = 17.50$ m (i.e. close to the surface of the sand deposit). It can be observed that, as expected, in this case, the initial effective stresses are practically symmetric in relation to a vertical alignment located at half distance from the left to the right boundaries ($x = 17.0$ m). Moreover, as observed for CM-A, the impact of the shallow foundations on the effective stresses generated in the zones of the sand deposit located close to the lateral boundaries of the model (i.e. zones approximately delimited by $0.0\text{ m} \leq x < 5.0\text{ m}$ and by $29.0\text{ m} < x \leq 34.0$ m), as well in between shallow foundations (i.e. approximately $15.0\text{ m} < x < 18.0$ m) is small. Similarly, it is apparent that the influence of the shallow foundations on the initial effective stress state reduces significantly with depth. For instance, at the middle depth of the model (i.e. $y = 9.5$ m), the effective stresses generated in the zones under the shallow foundations (i.e. zones approximately delimited by $8.5\text{ m} \leq x < 11.5$ m and by $22.5\text{ m} \leq x \leq 25.5$ m.) are only about 10 % higher than those obtained in the remaining deposit of sand (i.e. to the sides and middle of the model).

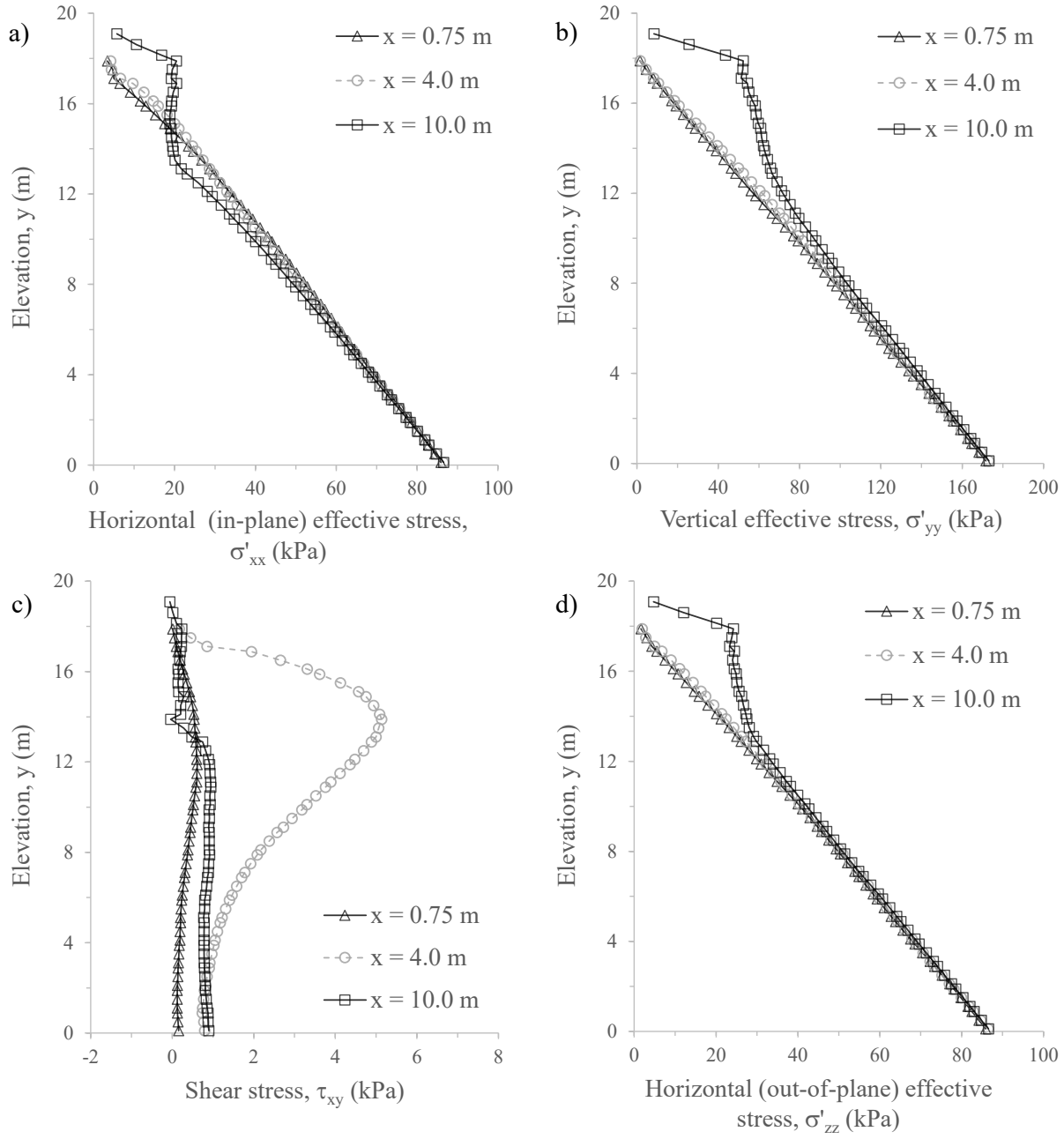

Figure 8.112 – Computed initial effective stresses for three different vertical alignments located on the left side of CM-B: (a) horizontal (in-plane) effective stress; (b) vertical effective stress; (c) shear stress; (d) horizontal (out-of-plane) effective stress..

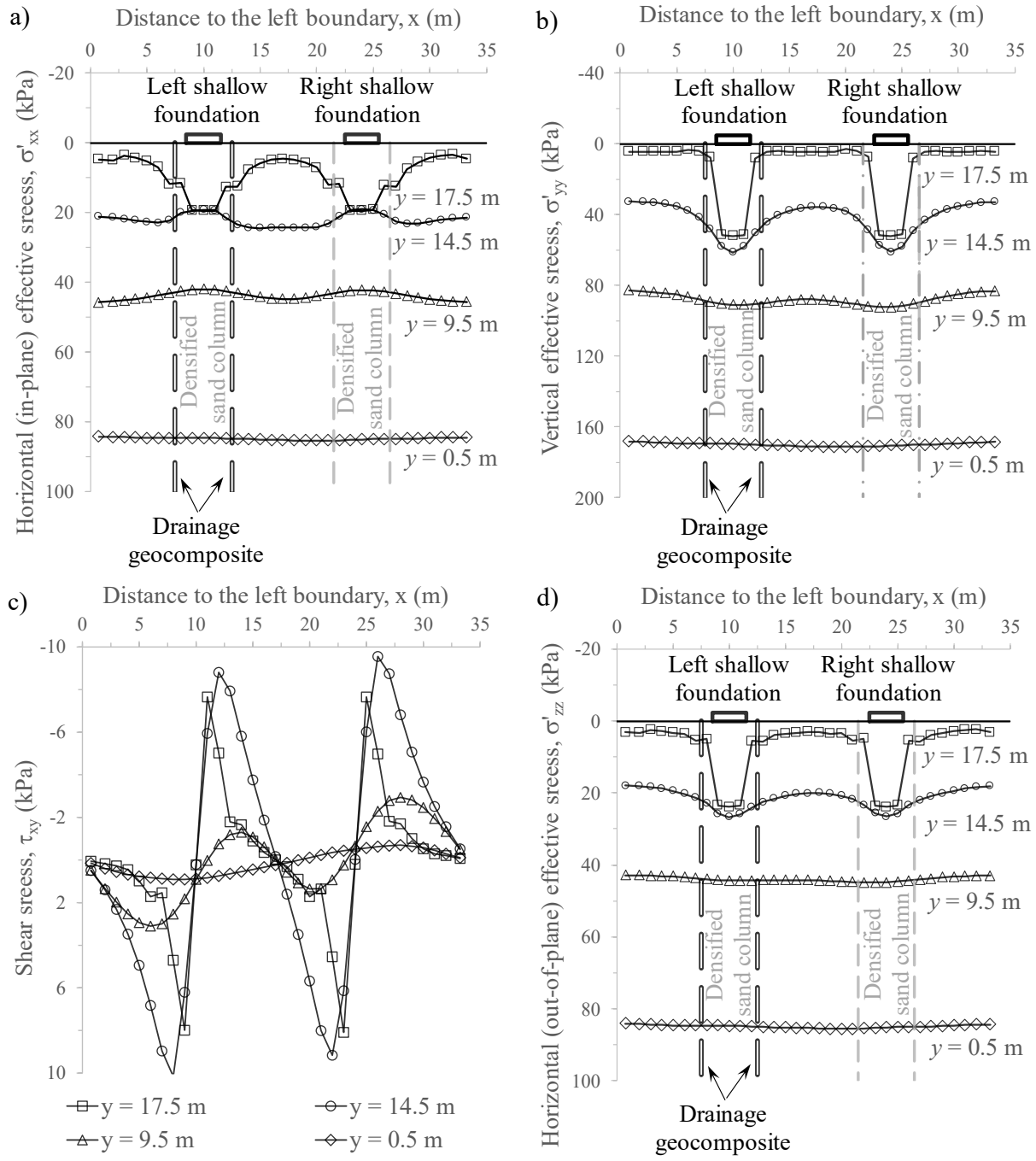

Figure 8.113 – Computed initial effective stresses for four different horizontal alignments of CM-B: (a) horizontal (in-plane) effective stress; (b) vertical effective stress; (c) shear stress; (d) horizontal (out-of-plane) effective stress.

Further insight into the initial effective stress state is provided in Figure 8.114, which presents the deviatoric stress, q (Equation 8.8), – mean effective stress, p' (Equation 8.9), profiles for Gauss points located along the three different vertical alignments analysed before: $x = 0.75$ m, $x = 4.0$ m and $x = 10.0$ m. A line corresponding to the critical state (CS) strength in triaxial compression (TC) – i.e. $\eta = M_c^c = 1.265 \Leftrightarrow K_0 \approx 0.26$ (Equation 8.10) – , one corresponding to the coefficient of earth pressure at rest of $K_0 = 0.50 \Leftrightarrow \eta \approx 0.75$ and another one corresponding to the stress ratio of $\eta = 0.55 \Leftrightarrow K_0 \approx 0.60$ are also plotted in

the figure. It can be observed that most Gauss points located along vertical alignments farther from the influence of the shallow foundations (i.e. $x = 0.75$ m and $x = 4.0$ m) have stress ratios close to $\eta = 0.75 \Leftrightarrow K_0 = 0.50$, as intended. Conversely, larger stress ratios are obtained for Gauss points located under the influence of the shallow foundations ($x =$ 10.0 m).

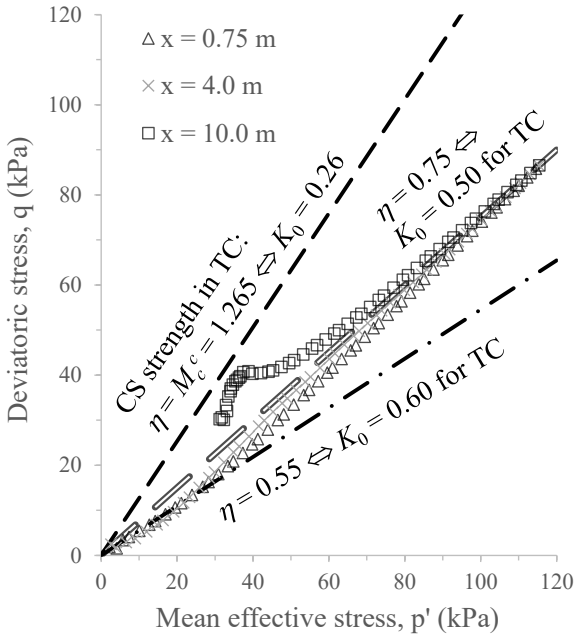

Figure 8.114 – Computed initial stress state in terms of deviatoric stress as a function of the mean effective stress at Gauss points located along three different vertical alignments located on the left side of CM-B.

Indeed, as shown in Figure 8.115, and contrary to what was observed for CM-A, some of the Gauss points located underneath the left shallow foundation (particularly, those located at shallow depths, which are characterised by smaller mean effective stresses and, therefore, smaller values of the state parameter, $\psi = e - e_{cs}$) are characterised by $\eta - \psi$ states plotting above the dilatancy surface, implying that dilative response (and, therefore, generation of negative excess pore pressures under undrained conditions) will likely occur during dynamic loading. Note that this is also valid for the zone of the deposit under the influence of the right shallow foundation of the model, as it is apparent in Figure 8.116, which depicts the state parameter profiles for the three different horizontal alignments that have been used to analyse the results of this initial phase (i.e. $y = 0.50$ m, $y = 9.50$ m, $y = 14.50$ m and $y =$ 17.50 m). Note that, in this figure, the position of the ground surface, in terms of the value of the state parameter, is merely indicative, corresponding to a mean effective stress of 1.0 kPa (which is the lower limit imposed by the low-stress yield surface).

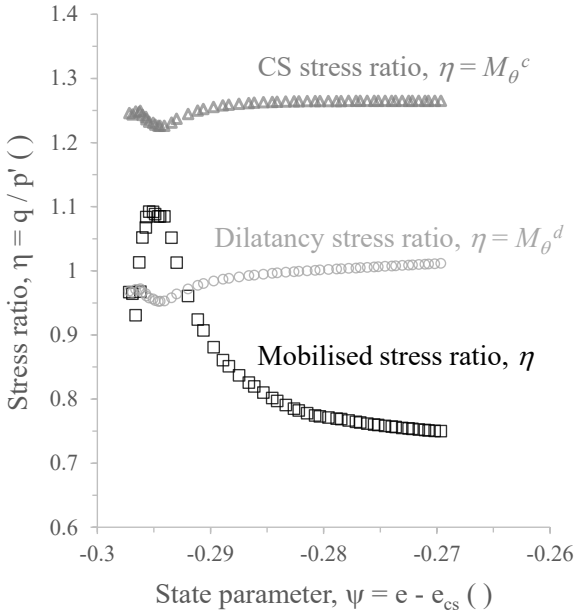

Figure 8.115 – Mobilised, dilatancy and critical state stress ratios as a function of the state parameter at Gauss points located along a vertical alignment coincident with the axis of the left shallow foundation of CM-B.

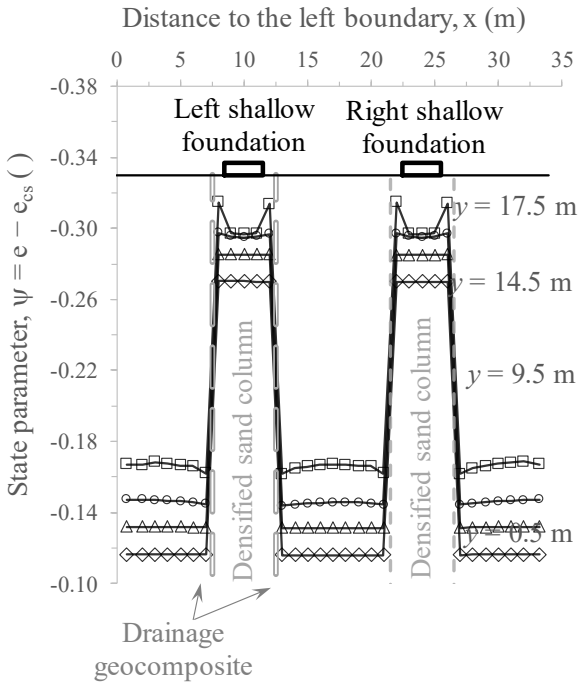

Figure 8.116 – Computed initial state parameter for Gauss points located along four different horizontal alignments of CM-B.

It can be observed that the values of the state parameter vary within the very wide range of −0.33 to −0.11. By comparing these values with those characterising the initial state of the samples subjected to undrained cyclic triaxial testing (Section 3.4), it can be concluded that this lowest limit ($\psi_0 = -0.33$) is slightly below the lowest initial state parameter of samples subjected to cyclic triaxial test ($\psi_0 = -0.29$). This is perhaps unsurprising, given the very small mean effective stresses characterising the shallow levels of the sand deposit, which are

difficult to reproduce in laboratory testing. Moreover, note that most of Gauss points of CM-B are, in fact, characterised by values of the state parameter greater than -0.29.

8.4.2.4 Dynamic analysis

8.4.2.4.1 Horizontal acceleration time-histories

The horizontal acceleration time-histories computed at several different positions located along a vertical alignment coincident with the axis of the left shallow foundation ($x = 10.0$ m) are compared with those recorded in the centrifuge experiment in Figure 8.117. Note that the two deepest positions (i.e. at $(x, y) = (10.0, 0.5)$ m and $(x, y) = (10.0, 6.0)$ m) are not precisely located along $x = 10.0$ m, rather along $x = 10.5$ m, to be compatible with the selected mesh (Figure 8.111). Nevertheless, at these deep locations, very similar results were obtained either along $x = 9.5$ m or $x = 10.5$ m, meaning that similar results would be also expected at $x = 10.0$ m. Moreover, note that, to ease their simultaneous visualisation and comparison, all experimental and numerical acceleration time-histories presented in this section were filtered using a fourth-order Butterworth-type filter with limit frequencies of 0.1 Hz and 25 Hz, available in the software SeismoSignal version 2018 (Seismosoft, 2018). It can be seen that a good match between numerical and experimental data was obtained at the two deepest positions. A less satisfactory agreement was registered at the two shallowest positions (i.e. at $(x, y) = (10.0, 12.0)$ m and $(x, y) = (10.0, 17.0)$ m), with the numerical tool overpredicting the peak horizontal accelerations, particularly from the moment that the attenuation of the horizontal motion was observed in the experiment (approximately after the second significant loading cycle). As detailed later, this overprediction seems to be a detrimental consequence of the underprediction of the excess pore pressures generated at these locations (and, consequently, underprediction of material damping) during this stage of the analysis. Given this overestimation of the peak horizontal accelerations at the shallow depths of the sand deposit, the motion registered at the left top of the shallow foundation (i.e. at $(x, y) = (8.5, 19.225)$ m) is also overestimated in relation to that recorded in the experiment, as shown in Figure 8.118.

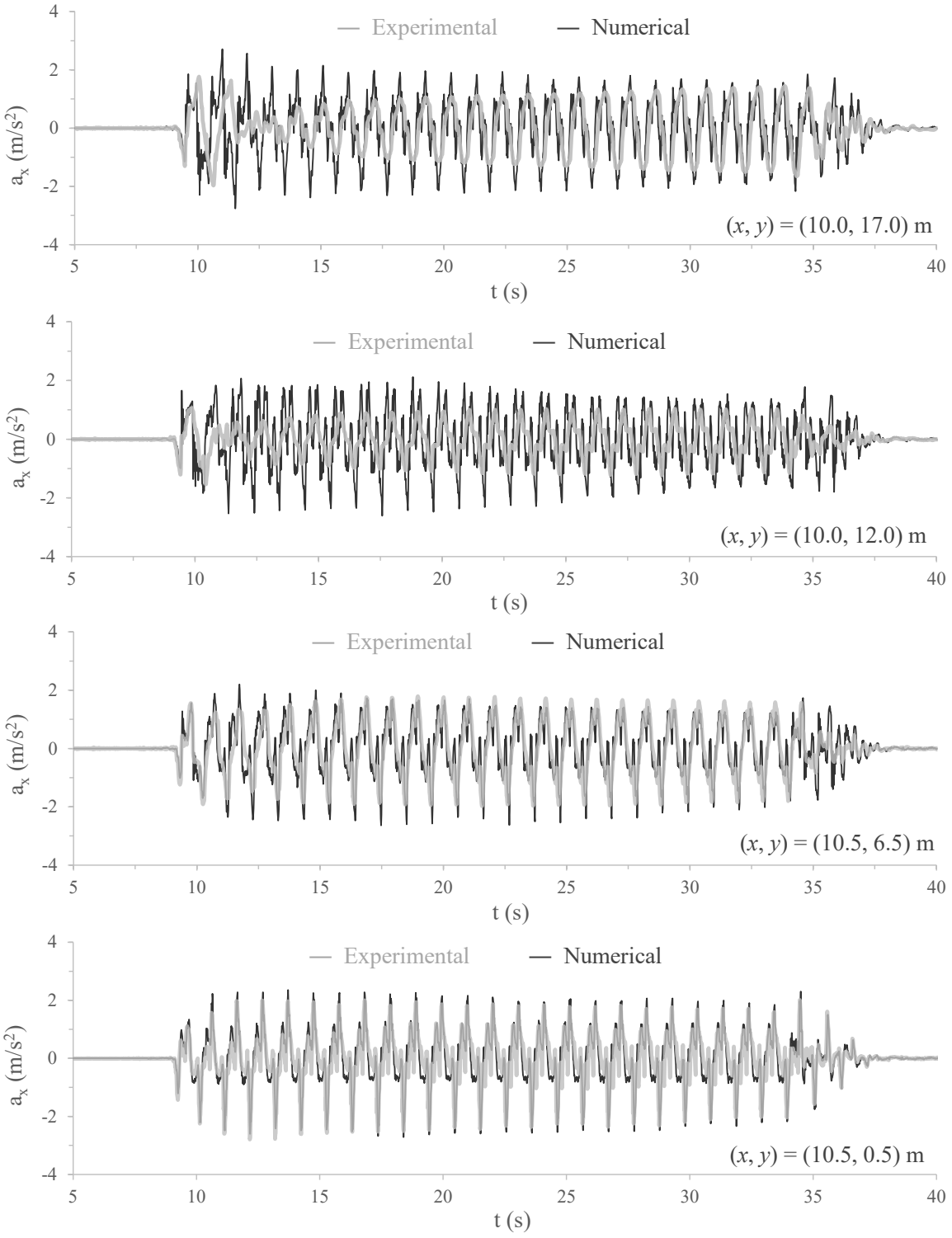

Figure 8.117 – Measured and computed horizontal acceleration time-histories at several positions located along a vertical alignment coincident with the axis of the left shallow foundation for CM-B.

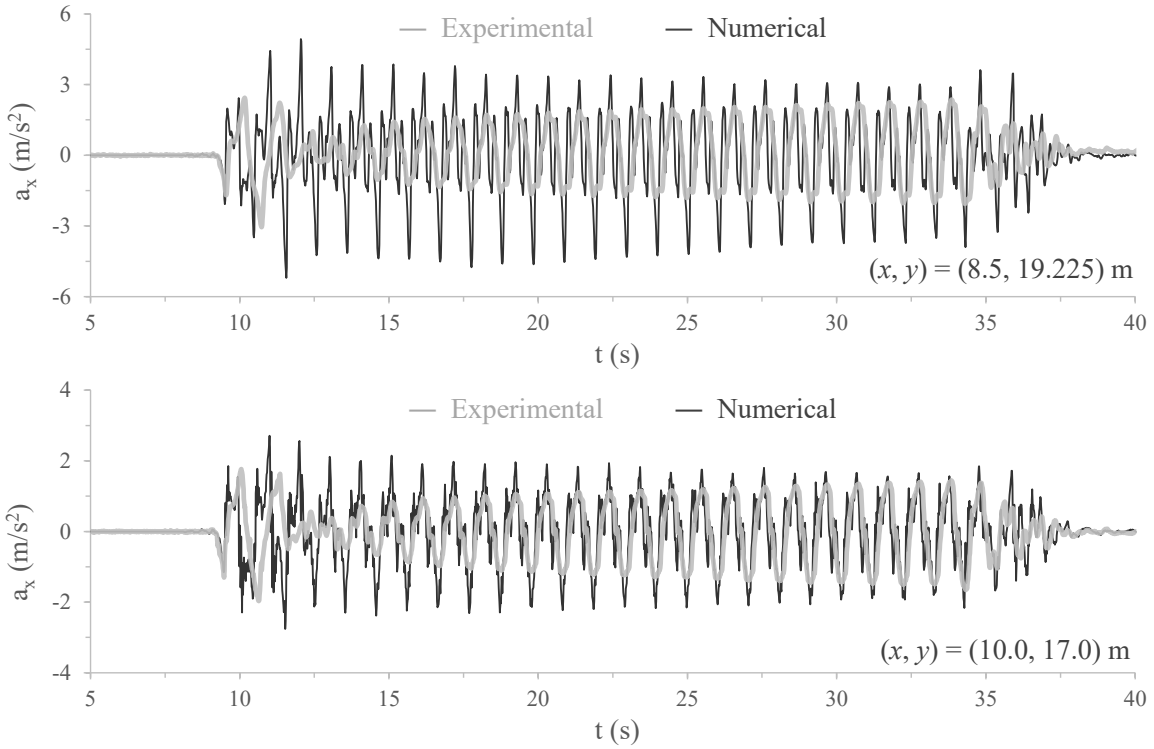

Figure 8.118 – Measured and computed horizontal acceleration time-histories at the top of the left shallow foundation and underneath it for CM-B.

In relation to the right side of the model, Figure 8.119 compares the computed and measured horizontal acceleration-time histories at several positions located along a vertical alignment coincident with the axis of the right shallow foundation ($x = 24.0$ m in the numerical model). Note that, due to mesh compatibility, the two deepest positions are not precisely located along $x = 24.0$ m, rather along $x = 23.5$ m. As observed for the left side of the model, at those elevations, very similar results were obtained either along $x = 23.5$ m or $x = 24.5$ m, meaning that similar results would be also expected at $x = 24.0$ m. Complementary, Figure 8.120 compares the horizontal acceleration-time histories registered at the left top edge of the right shallow foundation (i.e. at $(x, y) = (22.5, 19.225)$ m in the numerical model) and at the shallowest monitoring position within the sand deposit underneath that shallow foundation (i.e. at $(x, y) = (24.0, 17.0)$ m). A satisfactory match between numerical and experimental sets of data can be observed for the three deepest positions: $(x, y) = (23.5, 0.5)$ m, $(x, y) = (23.5, 6.5)$ m and $(x, y) = (24.0, 12.0)$ m (particularly, for the deepest and shallowest of these three positions). Conversely, it can be seen that the horizontal acceleration-time history at the shallowest position within the sand deposit (i.e. at $(x, y) = (24.0, 17.0)$ m) is overpredicted in the numerical analysis, with the numerical tool being unable to predict accurately the attenuation of the horizontal peak accelerations after the second significant loading cycle. Since larger accelerations are transmitted to the shallow foundation, the horizontal acceleration-time history obtained at $(x, y) = (22.5, 19.225)$ m is also overestimated in relation to that recorded in the experiment.

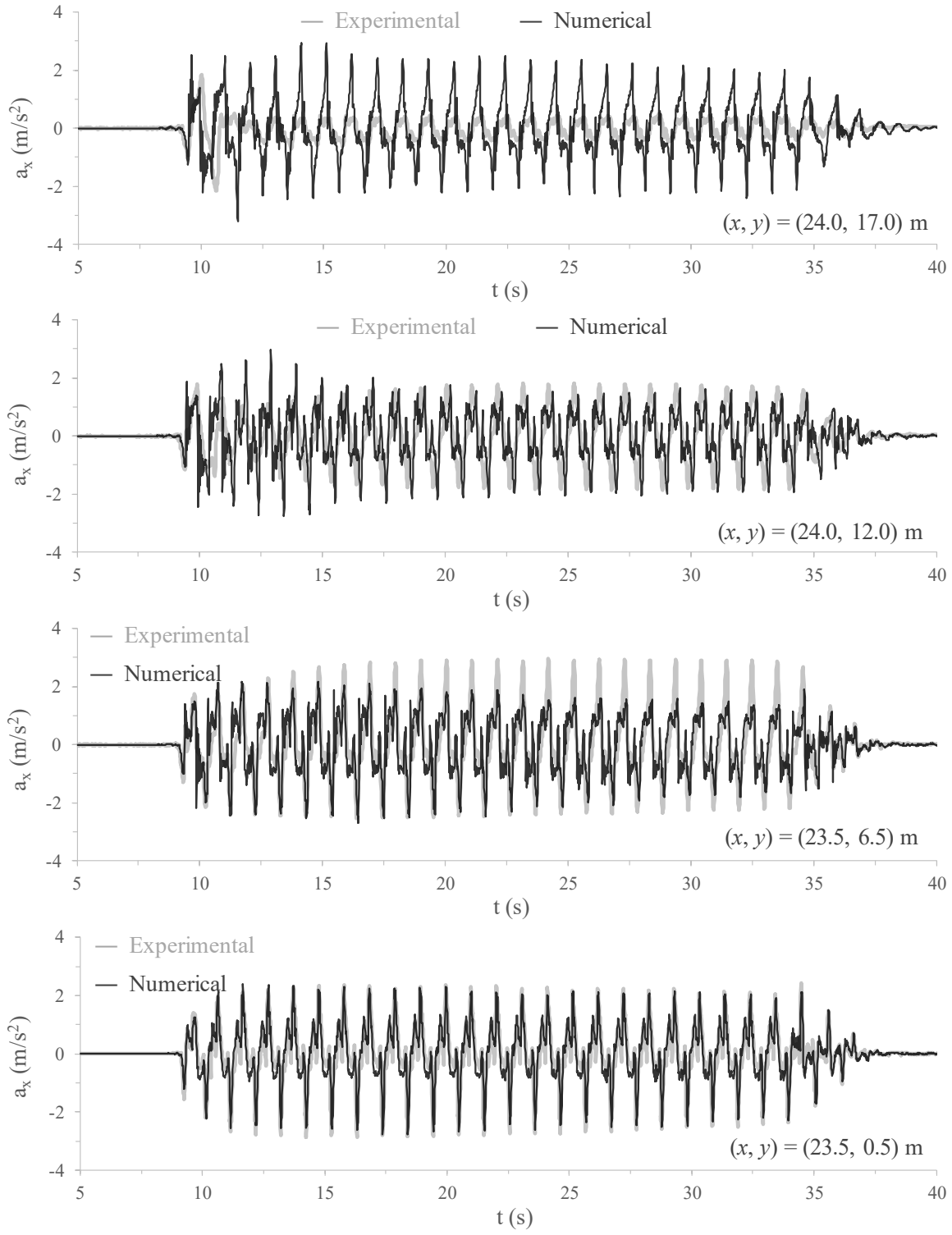

Figure 8.119 – Measured and computed horizontal acceleration time-histories at several positions located along a vertical alignment coincident with the axis of the right shallow foundation for CM-B.

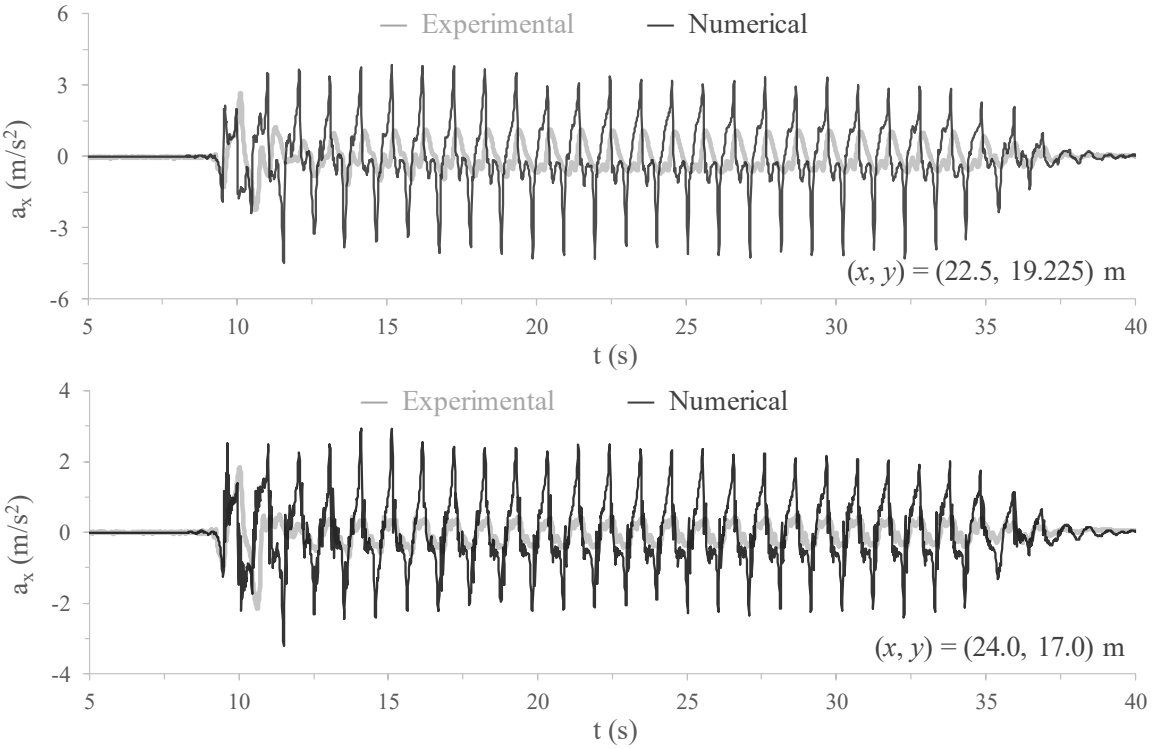

Figure 8.120 – Measured and computed horizontal acceleration time-histories at the top of the right shallow foundation and underneath it for CM-B.

The horizontal acceleration time-histories computed at four different positions located along a vertical alignment corresponding to half distance from the axes of the shallow foundations ($x = 17.0$ m in the numerical model) are compared with those recorded in the experiment in Figure 8.121 (note that, once more, the two deepest positions are located slightly to the left of the alignment defined by $x = 17.0$ m). Similar to what was observed for the other two vertical alignments inspected before, it can be seen that a good agreement between numerical and experimental data was overall obtained for the three deepest positions: $(x, y) = (17.0, 0.5)$ m, $(x, y) = (17.0, 6.0)$ m and $(x, y) = (17.0, 12.0)$ m. The numerical tool seems, however, unable to replicate the strong attenuation of the horizontal peak accelerations at the shallowest position within the sand deposit (i.e. at $(x, y) = (17.0, 17.0)$ m) observed in the experiment after the second significant loading cycle. As discussed in detail later, this seems to be a detrimental consequence of the overestimation of the additional drainage capacity provided by the geocomposite during the analysis, leading to the underprediction of the excess pore pressure generated in this zone of the model during dynamic loading. In fact, a better agreement between numerical and experimental data in terms of accelerations computed at shallow depths of the sand deposit was reached when simulating the previous centrifuge experiment (Figure 8.45) – which did not include any drainage geocomposite – , with the numerical tool being able to capture accurately the attenuation of the horizontal peak accelerations at shallow depths of the sand deposit.

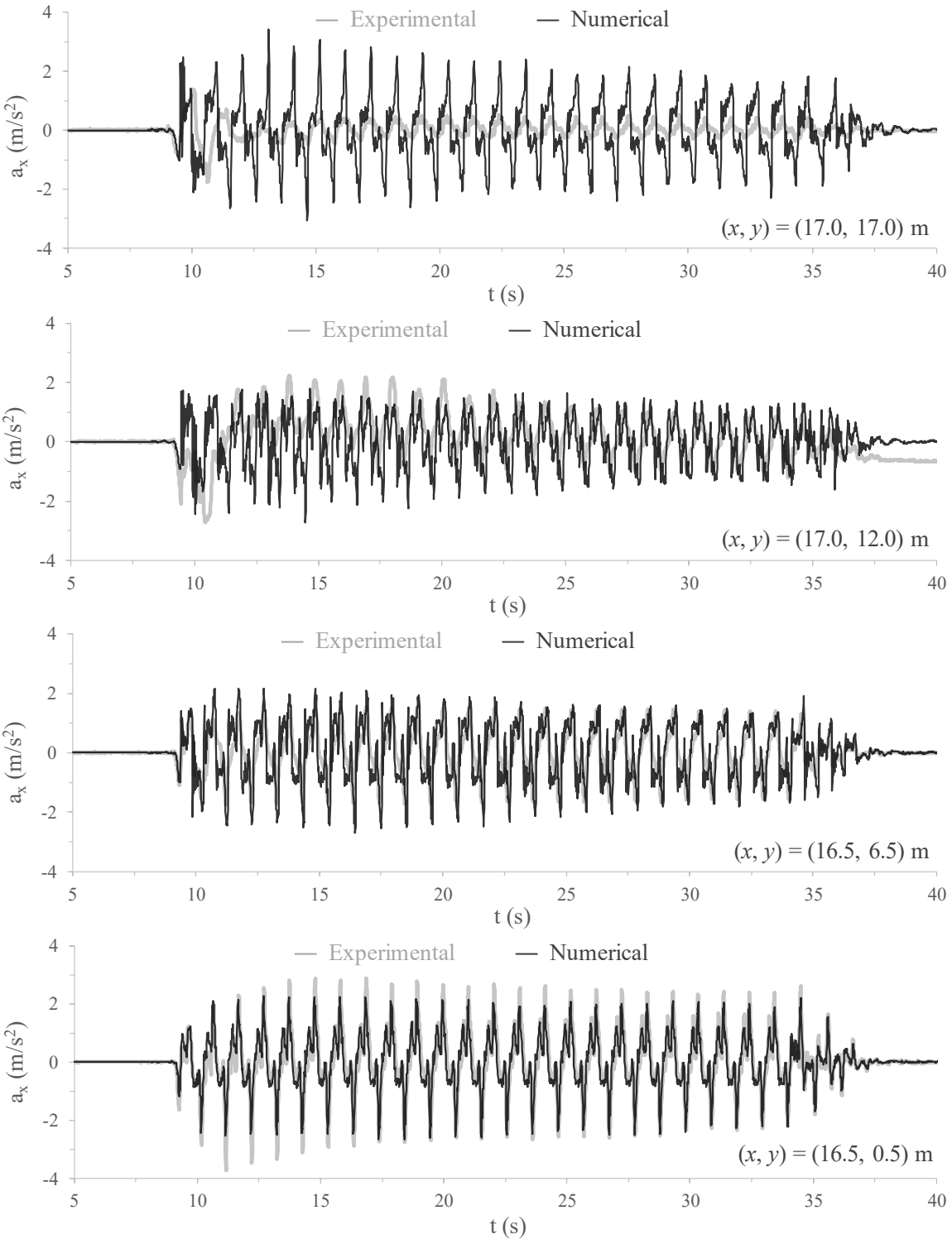

Figure 8.121 – Measured and computed horizontal acceleration time-histories at several positions located along a vertical alignment coincident with the middle of the CM-B.

8.4.2.4.2 Vertical acceleration time-histories

Figure 8.122 depicts the vertical acceleration time-histories computed at the base of the model (i.e. at $(x, y) = (0.0, 0.0)$ m) and at the left and right top edges of left shallow foundation (i.e. at $(x, y) = (8.5, 19.225)$ m and $(x, y) = (11.5, 19.225)$ m, respectively), together with those measured in the centrifuge experiment. It can be observed that, although

zero vertical accelerations were prescribed at the nodes belonging to the bottom boundary of the numerical model, large vertical peak accelerations were computed at the top of the shallow foundations, with amplitudes not very different from the horizontal ones, as observed in the experiment (although, in the experiment, vertical accelerations have been imposed at the base of the centrifuge model). Similar to what was observed for the horizontal accelerations, it seems that the numerical tool overpredict the vertical peak accelerations at the top of this shallow foundation, which is likely a consequence of the underprediction of the excess pore pressures generated in the densified sand deposit underlying this shallow foundation.

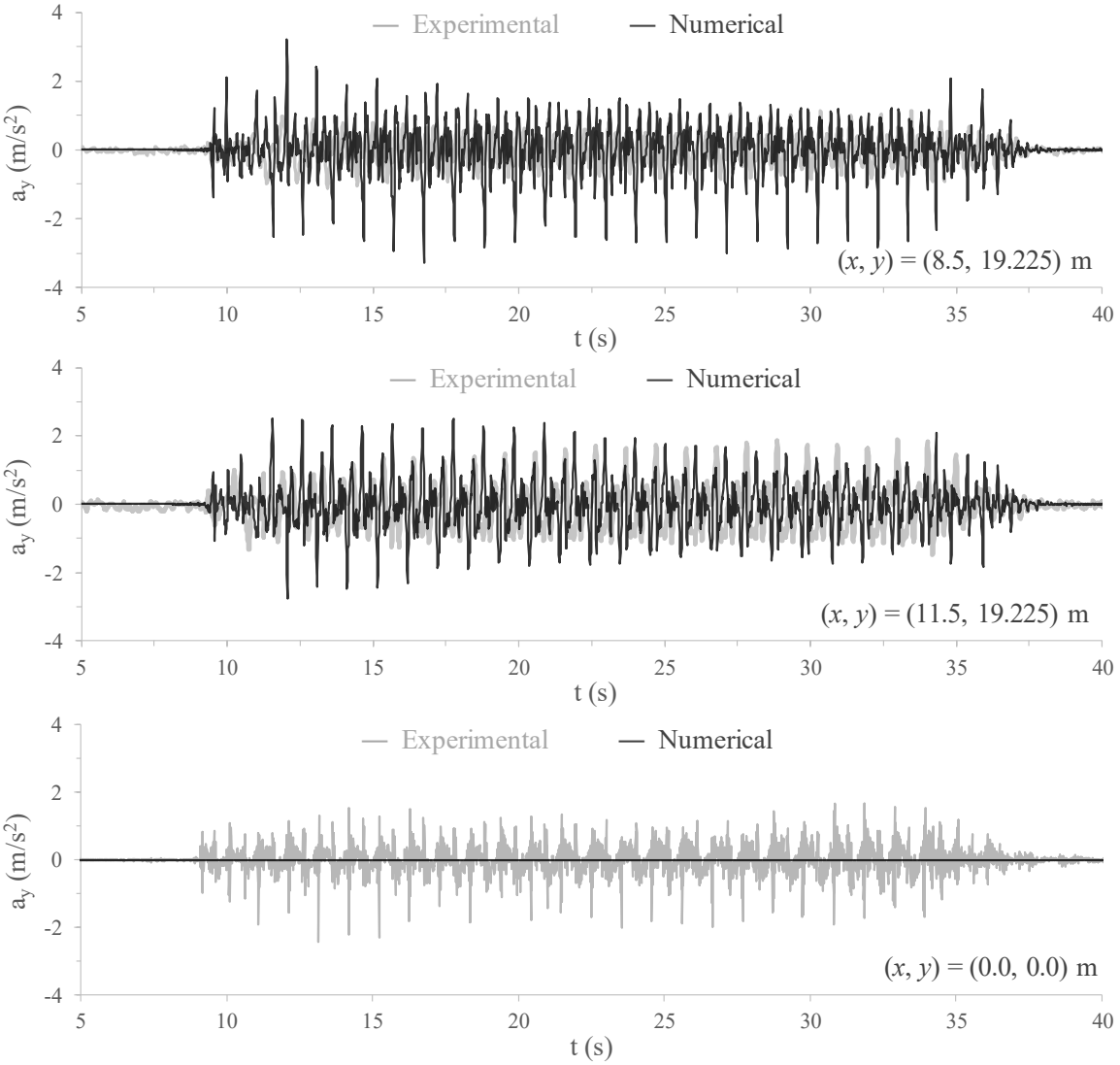

Figure 8.122 – Measured and computed vertical acceleration time-histories at the base of the model and at the left and right top edges of the left shallow foundation for CM-B.

In addition, Figure 8.123 compares directly the computed acceleration time-histories at the edges of the left shallow foundation. Note that, to ease the visualisation, only the results obtained for the period ranging from 15 s to 25 s are depicted in the figure. It is apparent that local peaks occur out of phase, suggesting that the left shallow foundation oscillated during cyclic loading. This seems to be confirmed in Figure 8.124, which depicts the semi-sum (i.e.

average value) and semi-difference of the vertical accelerations computed at the left and right top edges of this shallow foundation. The fact that the semi-difference varies with time suggests that rocking motion was simulated. Note that, although similar results were observed in the experiment, the measured rotational movement might have been induced, at least partly, by a non-intentional rocking motion of the entire centrifuge model (rather than just by a rocking motion of the shallow foundation itself), as discussed in Section 8.4.1.3.

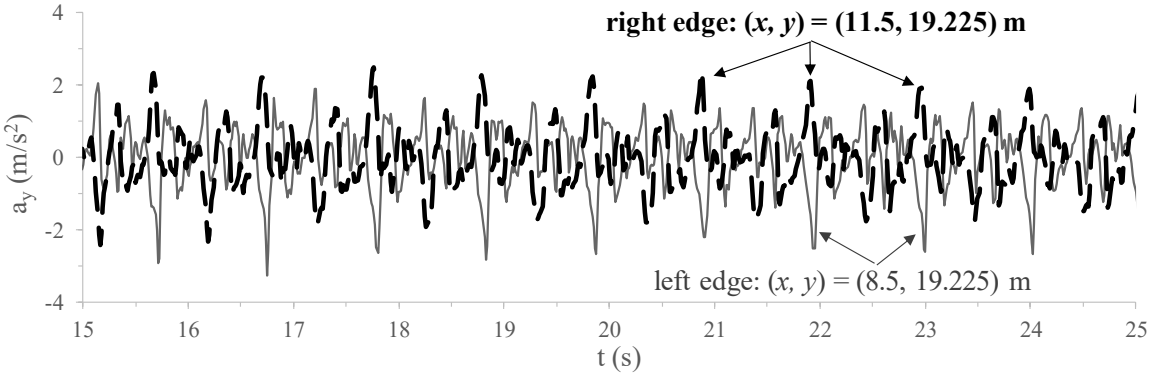

Figure 8.123 – Computed vertical acceleration time-histories at the left and right top edge of the left shallow foundation during the period ranging from 15 to 25 s for CM-B.

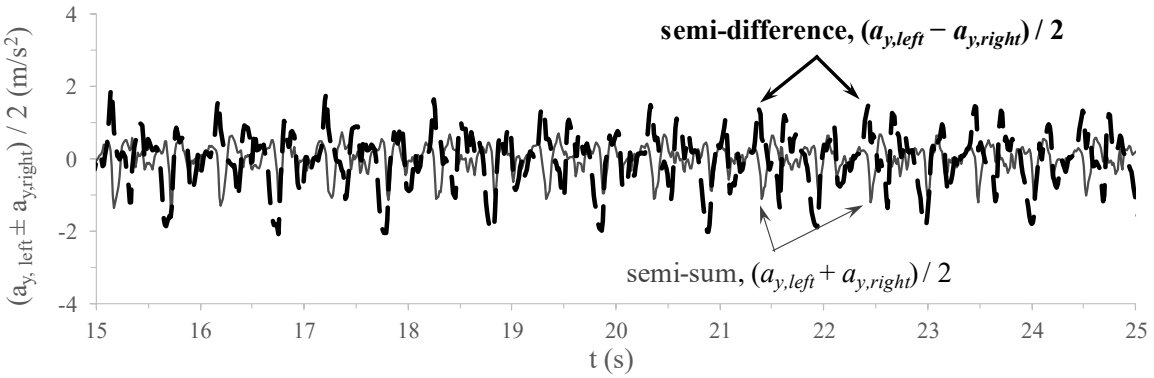

Figure 8.124 – Semi-sum and semi-difference of the vertical accelerations computed at the left and right top edges of the left shallow foundation during the period ranging from 15 to 20 s for CM-B.

In terms of the vertical acceleration time-histories obtained for the right shallow foundation, Figure 8.125 depicts the computed values at its left and right top edges (i.e. at $(x, y) = (22.5, 19.225)$ m and $(x, y) = (25.5, 19.225)$ m, respectively, in the numerical model), together with those recorded in the experiment. It can be observed that the computed local maximum peaks are larger than those registered in the experiment, suggesting that the constitutive model overpredicted the occurrence of dilation in the zone of the model underneath this shallow foundation.

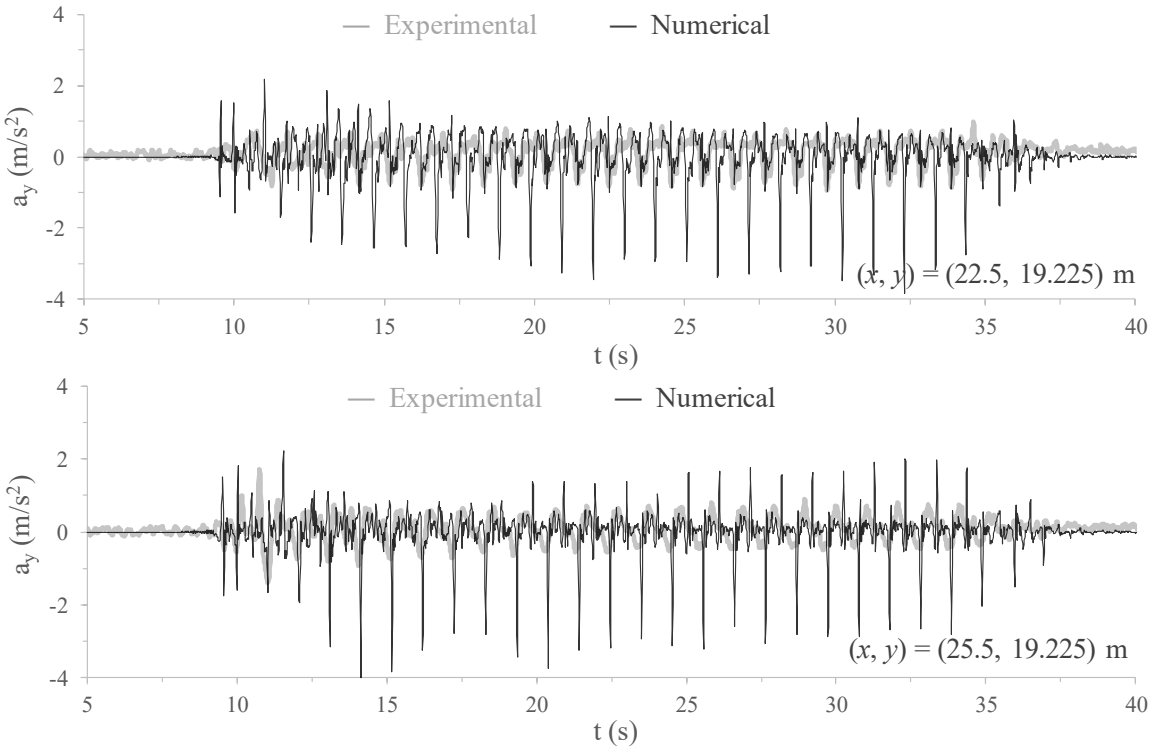

Figure 8.125 – Measured and computed vertical acceleration time-histories at the base of the model and at the left and right top edges of the right shallow foundation for CM-B.

Moreover, as obtained for the left shallow foundation of the model, the peak vertical accelerations computed at the left and right top corners of the right shallow foundation seem to occur out of phase (Figure 8.126). In effect, as more clearly observed in Figure 8.127, the shallow foundation was observed to oscillate during the numerical analysis, suggesting that a rocking motion was simulated. As noted for the left shallow foundation of the model, although similar results were measured in the experiment, it is unclear whether the oscillation was induced by a non-intentional rocking motion of the entire centrifuge model, by individual rocking motion of the shallow foundation or both concurrently (Section 8.4.1.3).

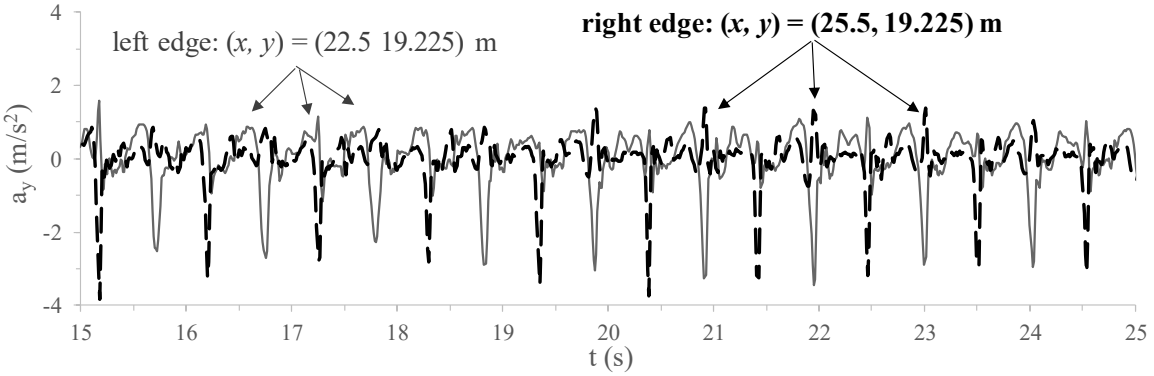

Figure 8.126 – Computed vertical acceleration time-histories at the left and right top edge of the right shallow foundation during the period ranging from 15 to 25 s for CM-B.

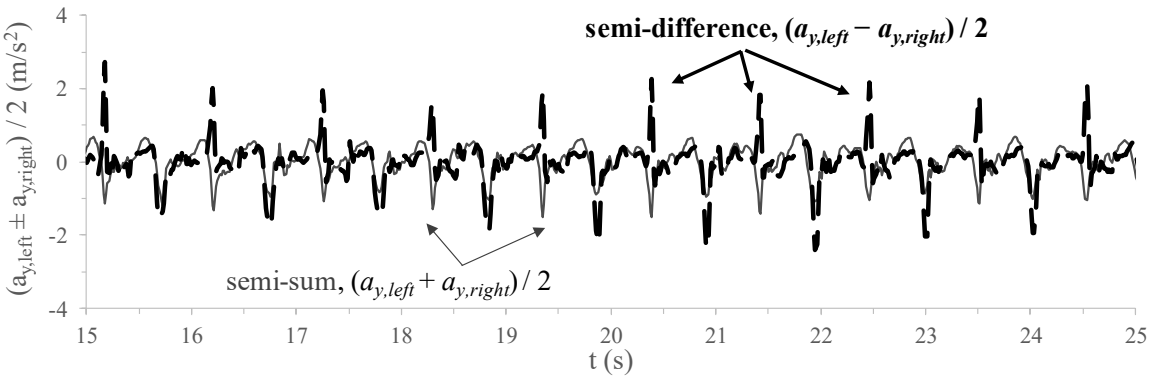

Figure 8.127 – Semi-sum and semi-difference of the vertical accelerations computed at the left and right top edges of the right shallow foundation during the period ranging from 15 to 20 s for CM-B.

8.4.2.4.3 Excess pore pressures

The evolutions of the excess pore pressures with time computed for vertical alignments coincident with the axis of the left shallow foundation ($x = 10.0$ m) and right one ($x = 24.0$ m in the numerical model) are, respectively, shown in Figure 8.128 and Figure 8.129, together with the experimental data. Overall, it is apparent that a much better agreement between numerical and experimental sets of data was obtained for the zones of the model located under the right shallow foundation (Figure 8.129) than under the left one (Figure 8.128), with the numerical tool underpredicting the excess pore pressures observed at the two positions located along a vertical alignment coincident with the axis of the left shallow foundation: $(x, y) = (10.0, 17.0)$ m and $(x, y) = (10.0, 12.0)$ m. Since the main difference between the left and right side of the model consisted of the presence of the drainage geocomposite (which, as described before, was numerically simulated by two columns of elements having larger hydraulic conductivity than the surrounding elements simulating the sand deposit), it can be concluded that the numerical model overestimated the drainage capacity provided by the geocomposite, although specifications from the manufacturer have been used to estimate the hydraulic conductivity of the geocomposite, as described in Section 8.4.2.2. A plausible explanation resides in the 2D plane strain simplification adopted in the numerical analysis, with the geocomposite being simulated as a continuous element in the out-of-plane direction (Figure 8.111), while, in fact, it consisted of an open prism in the experiment, with a width of about 5.0 m in the out-of-plane direction in the centrifuge experiment (Figure 8.76 and Figure 8.77). In addition, and perhaps seeming less probable, it can be argued that clogging, kinking or other physical mechanisms might have occurred during the centrifuge experiment, which are not considered in the numerical analysis.

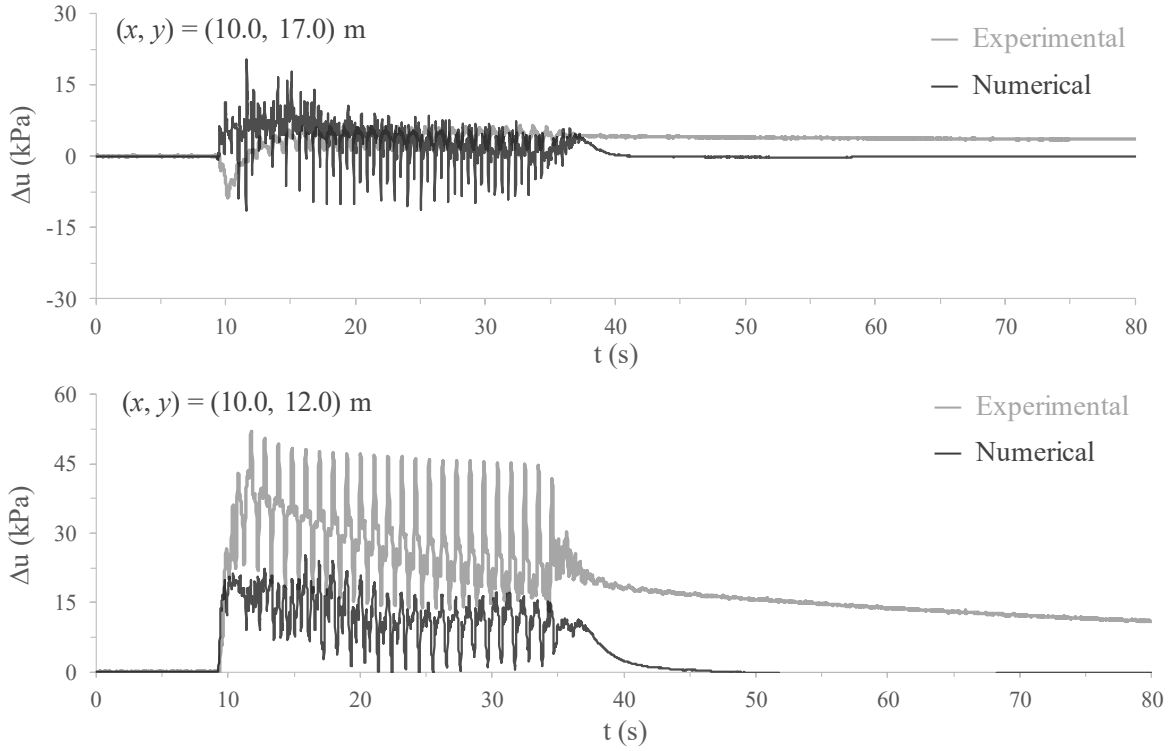

Figure 8.128 – Computed and measured excess pore pressure build-up at two different positions located along a vertical alignment coincident with the axis of the left shallow foundation for CM-B.

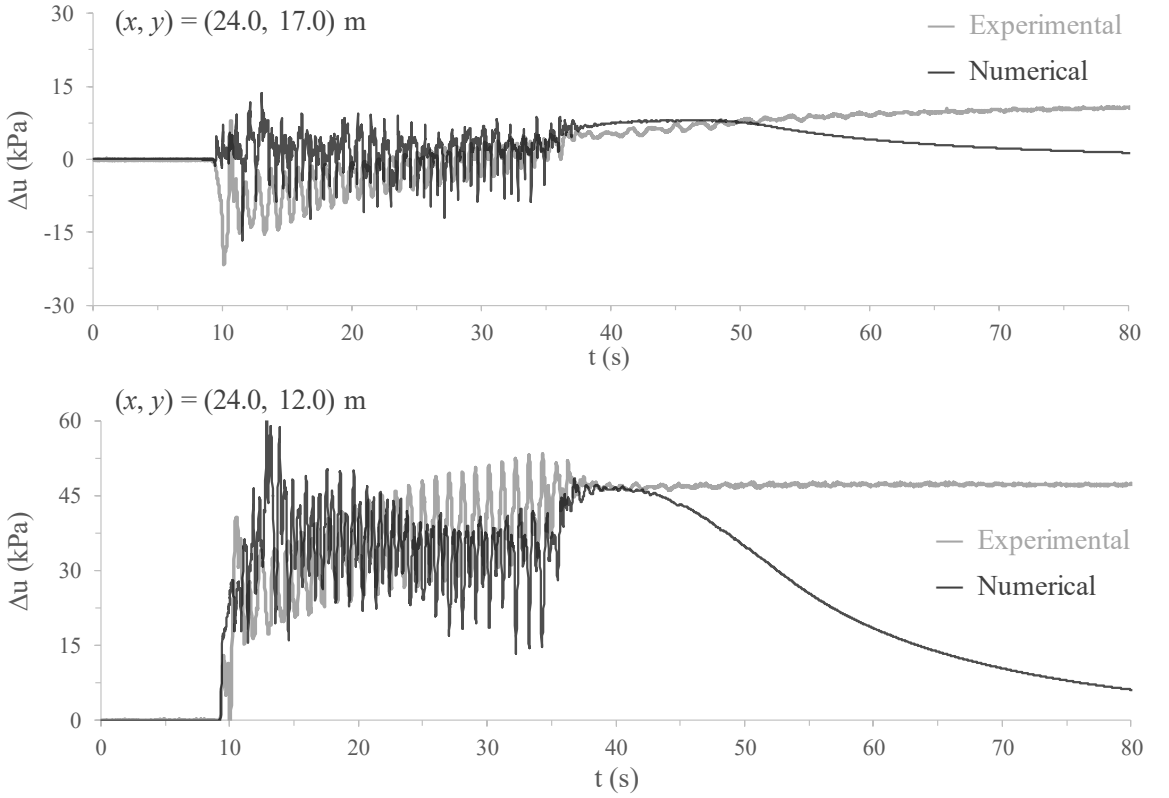

Figure 8.129 – Computed and measured excess pore pressure build-up at two different positions located along a vertical alignment coincident with the axis of the right shallow foundation for CM-B.

Moreover, it can be observed in both figures that, during the early stages of loading (i.e. during the first two significant loading cycles), the numerical tool predicted the generation of positive (i.e. compression-type) excess pore pressures in the zones of the deposit immediately underneath both shallow foundations (i.e. at $(x, y) = (10.0, 17.0)$ m and $(x, y) = (24.0, 17.0)$ m), while the opposite trend (i.e. suction-type excess pore pressure) was observed in the experiment. Once again, this might be a detrimental consequence of the 2D plane strain simplification, with the contribution of the shallow foundations to the initial effective stresses generated at shallow depths of the sand deposit being likely underestimated, as discussed before. In effect, providing that larger effective stresses would have been computed in the zone of the sand deposit located immediately underneath the shallow foundations, dilatant response would have likely been triggered, which, under mostly undrained conditions, would have likely resulted in generation of negative excess pore pressure generation, as observed in the experiment.

In relation to the consolidation phase, similar to the CM-A, the rate of excess pore pressure dissipation computed by the numerical tool is much higher than that registered in the centrifuge experiment. As explained before, this seems to be a detrimental consequence of the open yield surface formulation of the constitutive model, which results in a significant overprediction of the stiffness of sand under stress paths characterised by approximately constant stress ratios – which are likely imposed after the end of shaking (i.e. during the consolidation phase). Similar conclusions were reported by Taborda (2011) when inspecting the results obtained in the numerical simulation of VELACS models 1 and 12.

The computed evolutions of the excess pore pressures with time at three different positions located along a vertical alignment coincident with the middle of the model ($x = 17.00$ m in the numerical model) are shown in Figure 8.130, together with those measured in the experiment. It is apparent that the excess pore pressures are slightly underpredicted in the numerical analysis. This suggests that the drainage capacity of the geocomposite was overestimated in the numerical analysis, as discussed before, and may have affected also the computed excess pore pressure build-up in the middle of the model.

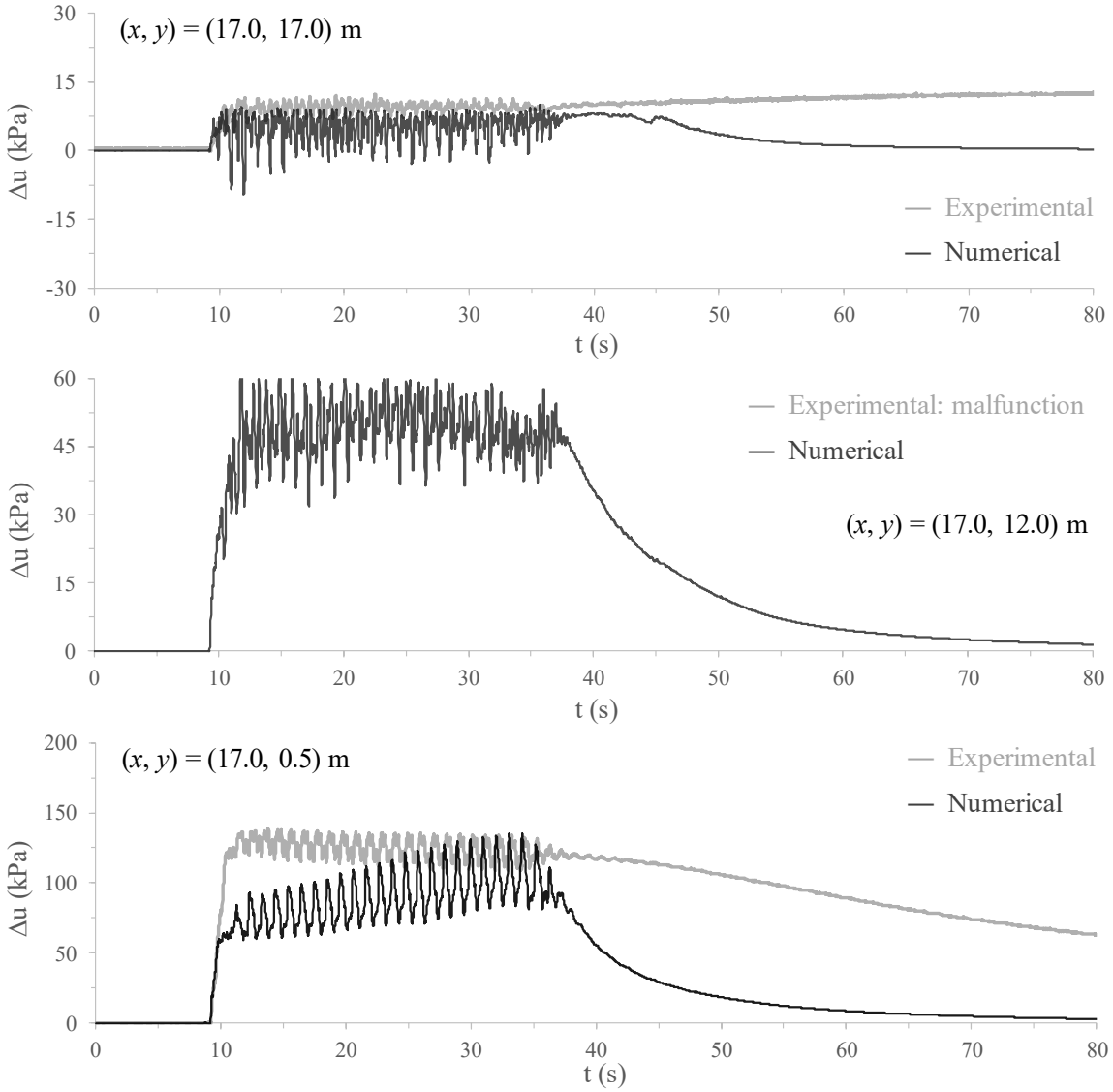

Figure 8.130 – Computed and measured excess pore pressure build-up at two different positions located along a vertical alignment coincident with the middle of the model for CM-B.

The computed excess pore pressures at $t = 38$ s (approximately corresponding to the end of shaking) are illustrated in Figure 8.131. Note that this contour plot was obtained by using the post-processing software GiD version 7.2 (GiD, 2002). As noted before, details about the integration between FEMEPDYN and GiD can be found in Grazina (2009). As expected, it is apparent that smaller excess pore pressures were generated at shallow depths, due to the small initial effective stresses, as well as in the zones of the model close to the columns of elements having higher hydraulic conductivity (i.e. the columns of elements simulating the geocomposite). Moreover, it can be seen that the additional capacity of drainage provided by geocomposite has a significant impact on the mitigation of excess pore pressures generated in the left densified sand column and, in a less degree, in between densified sand columns.

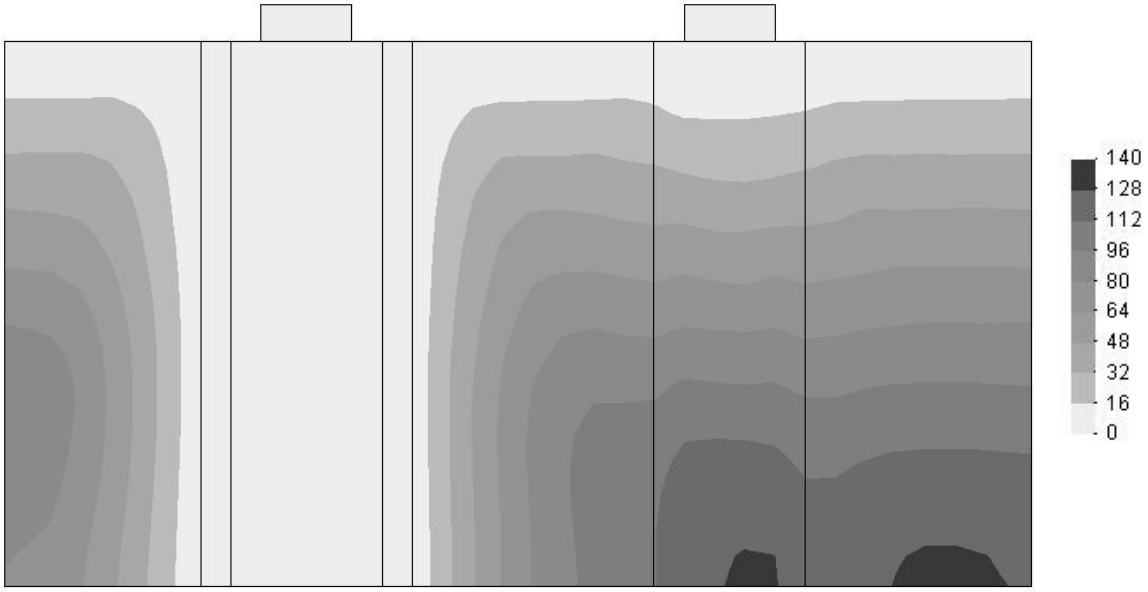

Figure 8.131 – Excess pore pressures (in kPa) at the end of dynamic loading ($t = 38$ s) for CM-B.

In addition, Figure 8.132 illustrates the excess pore pressure ratio, r_u, obtained in the numerical analysis also at $t = 38$ s. Note that, as considered for CM-A, r_u is defined as the ratio of the excess pore pressure, Δu, to the initial vertical effective stress, $\sigma'_{v,0}$. Perhaps unsurprisingly at this point, it can be seen that large values of r_u were only obtained in zones of the deposit close to the lateral boundaries, as well as close to the ground surface in between shallow foundations and under the right shallow foundation of the model at deep levels (where the influence of the shallow foundation on the effective stress state appears to be small). Once again, it is apparent the strong effect of the additional drainage capacity provided by the geocomposite on the limitation of the excess pore pressures generated on the left densified sand column, as well as middle of the model (particularly at deep levels).

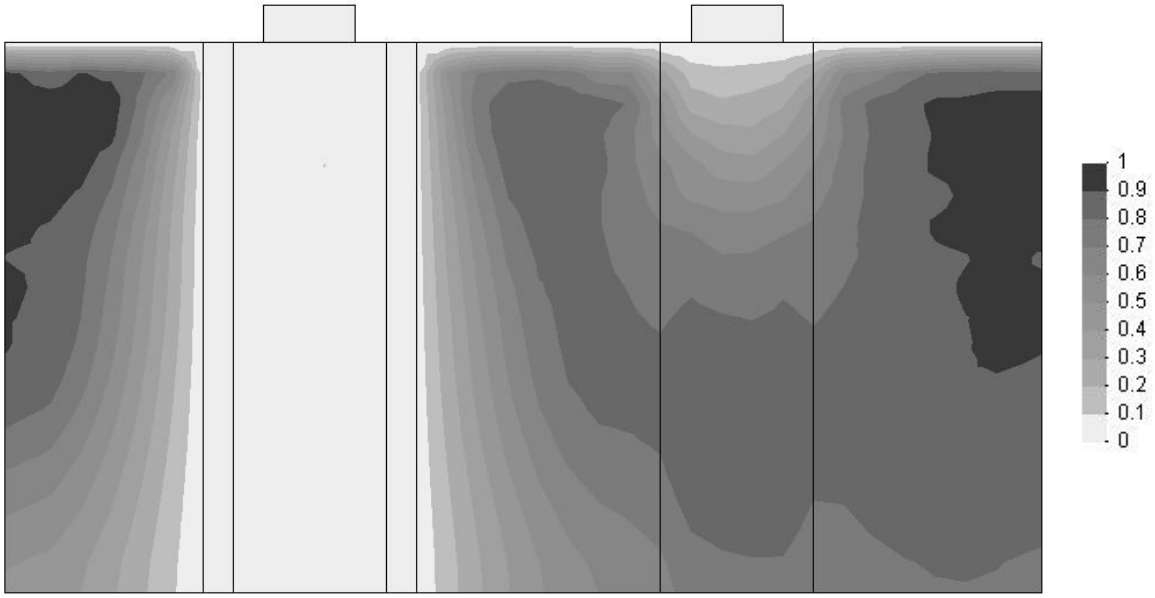

Figure 8.132 – Excess pore pressure ratio at the end of dynamic loading ($t = 38$ s) for CM-B.

8.4.2.4.4 Settlements

The computed evolutions of the settlements during shaking and shortly after its end for the left and right shallow foundations of the model are depicted in Figure 8.133, together with the experimental results. Starting with the left shallow foundation, it can be observed that the numerical tool slightly underpredicts the rate and final magnitude of settlement, which is, in fact, consistent with the underprediction of the excess pore pressures generated in the densified sand deposit under the influence of this shallow foundation, likely overpredicting the stiffness of sand. Nevertheless, considering the 2D plane strain simplification adopted in the numerical analysis, which likely affect the effective stresses and drainage capacity of the geocomposite, the agreement between numerical and experimental data may be considered very satisfactory. In effect, at the end of shaking (i.e. at $t \approx 38$ s), the computed settlement for the left shallow foundation reached a value of about 8.8 cm, while a settlement of about 10.4 cm was measured at that instant of time in the experiment.

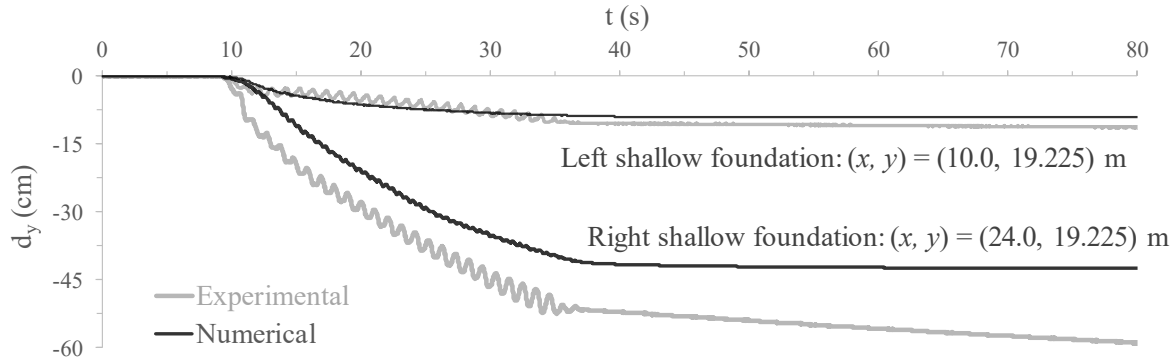

Figure 8.133 – Computed and measured settlements at the top of the left and right shallow foundations for CM-B.

With respect to the settlements obtained for the right shallow foundation, it is apparent that the rate at which it occurs in the numerical analysis is very similar to that measured in the experiment up to about 25 s (disregarding the slightly later onset of settlement observed for the numerical analysis). From that moment, the rate of settlement computed in the numerical analysis is slightly smaller than that registered in the experiment, resulting in a smaller final magnitude of settlement (of about 20%) at the end of dynamic loading. This underprediction appears, however, to be justified by the fact that, during the centrifuge experiment, the right shallow foundation was observed to move significantly to the right of the model. In fact, post-test measurements of the final settlement profile revealed that part of the right shallow foundation was eventually resting on the loose sand deposit, rather than on the densified sand deposit, as intended (Marques *et al.*, 2014a, 2015). This aspect is illustrated in Figure 8.134, which compares the computed and measured (i.e. inferred from post-test measurements) ground settlement profile at the end of the experiment. Note that the post-test measurements shown in this figure are uniformly scaled to match the final settlements of the shallow foundations measured by the linear variable differential transducer (LVDT) placed at the top of the shallow foundations. It can be observed that, although the computed

settlement for the right shallow foundation is effectively smaller than that measured in the experiment for the shallow foundation, as well as smaller than that measured at the centre of the densified sand column, where the shallow foundation was initially placed, the discrepancy to this latter position can be considered small, particularly considering the fact that the settlements occurring during the consolidation phase (which consist of about 30 % of the total settlement measured in the experiment) are largely underpredicted by the constitutive model, due to its open primary yield surface formulation.

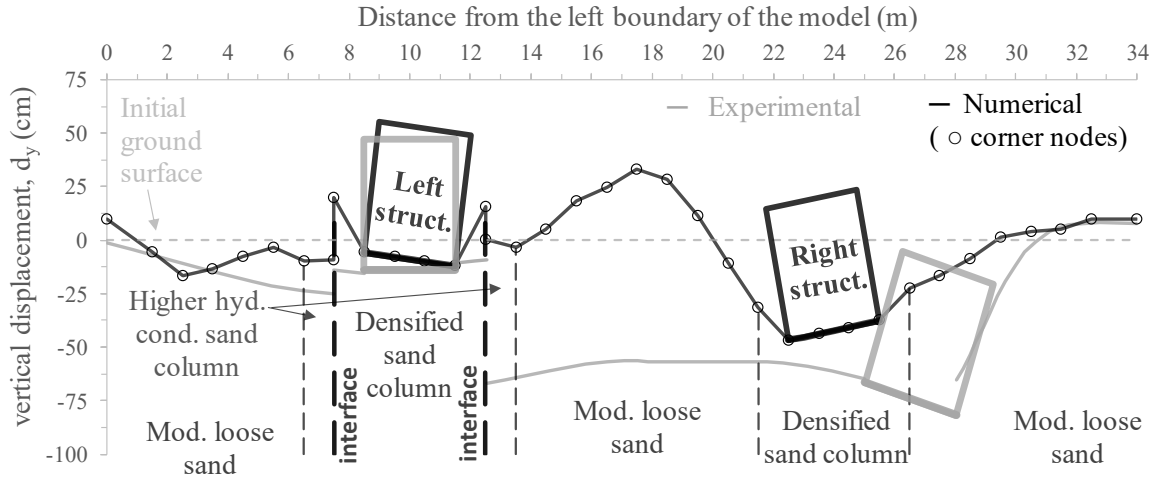

Figure 8.134 – Computed and measured settlement profile of the ground surface and shallow foundations after the complete dissipation of excess pore pressures for CM-B.

Contrary to what was observed for CM-A, Figure 8.134 suggests that the numerical tool overpredicted the rotation of the shallow foundations. In effect, it is apparent that the shallow foundations are rotated towards each other at the end of the numerical analysis. Note that, in the experiment, the left shallow foundation was observed to remain practically level, while the right shallow foundation was observed to rotate towards the right, probably due to the unexpected sliding to the outside of the densified sand column (Marques *et al.*, 2014a, 2015). This overprediction of the rotation of the shallow foundations might be related to the numerical simulation of a rocking mechanism, which might have been more limited in the experiment, as discussed before.

Although the introduction of the interface elements allowed for the occurrence of relative shear displacements at their location, the computed relative displacements are significantly smaller than those registered in the experiment, particularly on the right side of the left shallow foundation, where a relative displacement of about 50 cm was registered in the experiment. As clearly illustrated in Figure 8.135, this seems to be related to the inability of the numerical tool to capture the significant subsidence occurring at the ground surface in between shallow foundations. As suggested in previous studies (e.g. Scott, 1986a; Coelho, 2007; Taborda, 2011) and numerically investigated for CM-A, this inability might be, at least partially, explained by a temporary increase of the hydraulic conductivity of the sand deposit during dynamic loading in relation to the value of this property measured in conventional

laboratory tests, which is not captured in the numerical analysis. Indeed, the introduction of hydraulic models establishing a variation of the hydraulic permeability with excess pore pressure ratio appears to lead to a better replication of the measured response, as discussed in Section 8.3.2.5, although the observed discrepancies (particularly in terms of excess pore pressures generated in the model) indicated that further investigation is required.

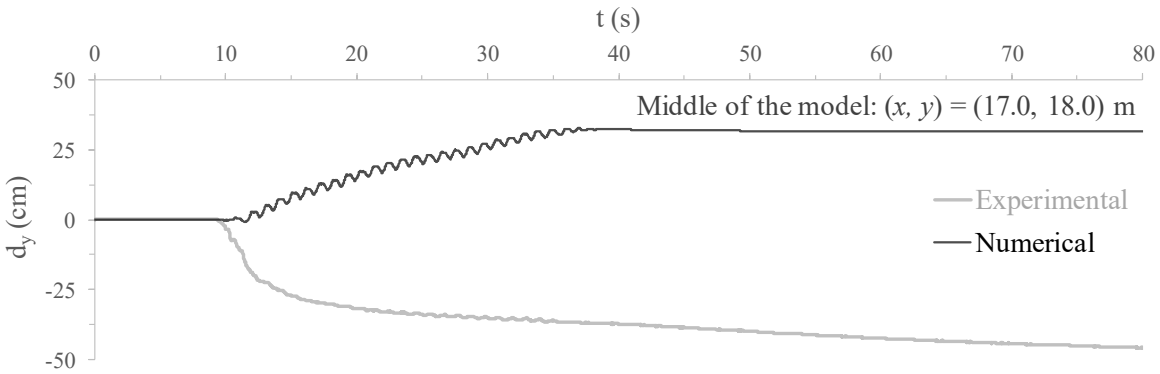

Figure 8.135 – Computed and measured settlements at the ground surface in between shallow foundations for CM-B.

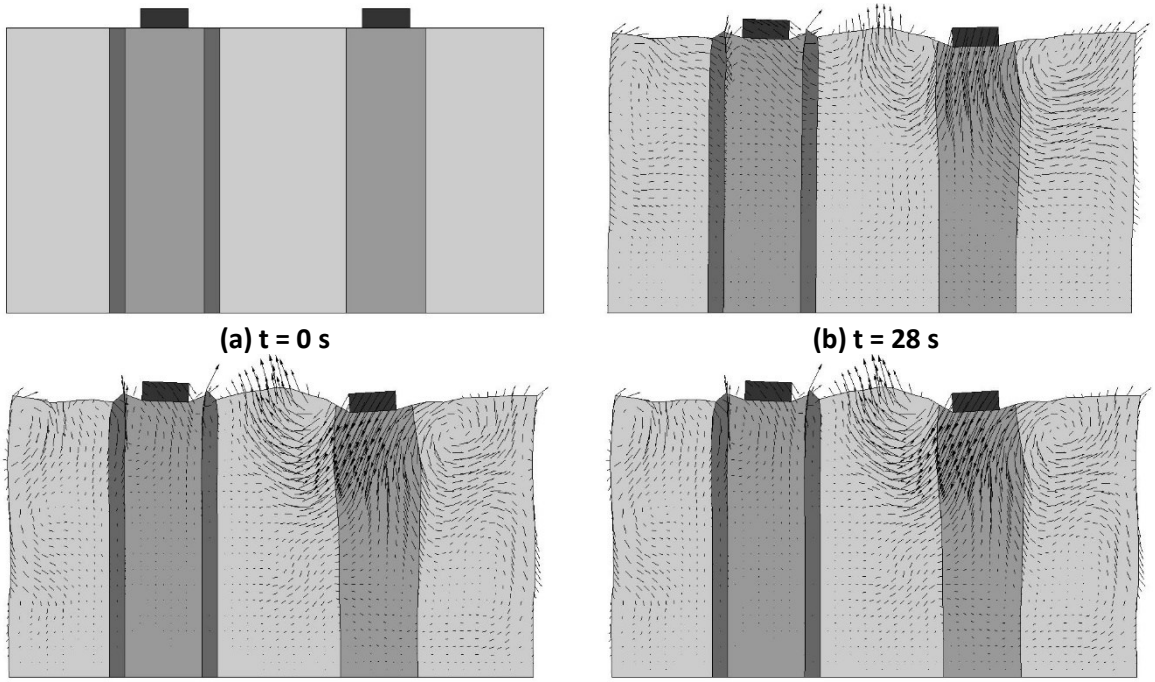

(a) t = 0 s **(b) t = 28 s**

(c) t = 38 s **(d) t = 48 s**

Figure 8.136 – Deformed mesh and displacement vectors at different instants of time for CM-B.

Further insight into the deformation mechanism predicted in the numerical analysis is provided in Figure 8.136, which compares the deformed mesh at three different instants of time (t = 28, 38 and 48 s) with the undeformed mesh (i.e. model at t = 0 s). To ease the visualisation, the scale of the deformations is twice that of the model geometry. Moreover, the accumulated total displacement vectors (scaled by a factor of 6.0 to aid the presentation) are also displayed in the figure to highlight the deformation mechanism. It is interesting to observe the different deformation mechanisms of the two shallow foundations. While the

right shallow foundation appears to push sand to the sides, particularly to the middle of the model, the left shallow foundation seems to punch through sand, clearly illustrating the strong effect of drainage on the deformation mechanism, as well as the beneficial contribution of the interface elements to the more accurate simulation of the interaction between sand and the geotextile interfaces. Moreover, it is noteworthy that, contrary to what was observed for CM-A, in this case, the deformation mechanisms of the two shallow foundations do not seem to interact with each other.

Finally, Figure 8.137 compares the computed and measured settlements of the shallow foundations having similar weight (i.e. heavier shallow foundation for CM-A and both shallow foundations for CM-B). While a slightly greater settlement rate was predicted for CM-A, a very good agreement in terms of numerical and experimental settlement rate was obtained for CM-B. Perhaps more important, it is apparent that the numerical tool was able to predict the main trends observed in the experiments, with particular emphasis for the great enhancement of the combined use of densification and drainage geocomposite simulating closely spaced high-capacity vertical drains on the overall response of the system.

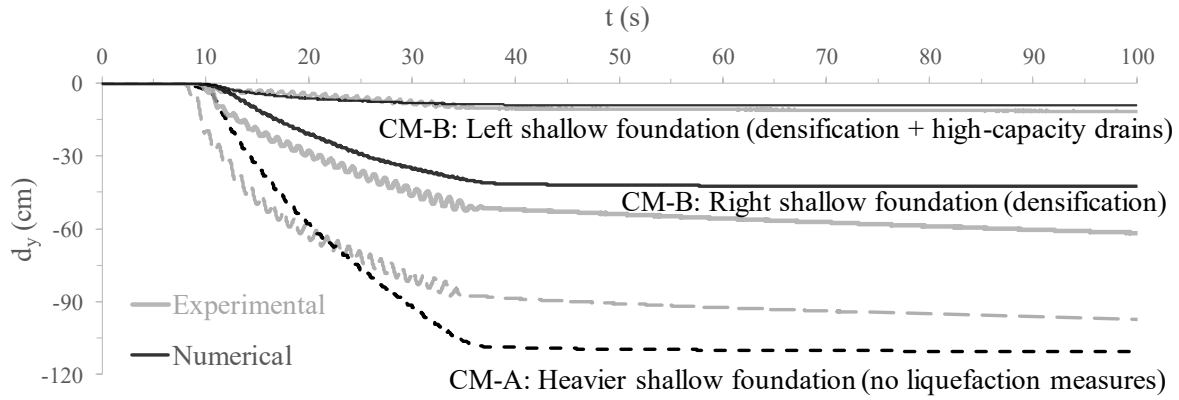

Figure 8.137 – Comparison of the computed and measured settlements at the top of the shallow foundations for CM-A and CM-B.

8.4.2.4.5 Vertical effective stresses

Figure 8.138 illustrates the vertical effective stresses computed at four different instants of time: $t = 0$ s (i.e. at the start of the analysis), $t = 18$ s (i.e. during dynamic loading), $t = 38$ s (i.e. at the end of dynamic loading) and $t = 78$ s (i.e. practically at the end of the consolidation phase). As expected, very different vertical effective evolutions with dynamic loading are observed for the left and right sides of the model. Specifically, while the effective vertical stresses are substantially reduced in the zones of the model under the influence of the right shallow foundation, particularly at middle depth of the right densified sand column and zones around it, the effective stresses appear to be only slightly reduced in the left densified sand column. As dynamic loading ceases and dissipation of excess pore pressures occurs, the effective vertical stresses progressively increase from bottom to the top of the model, as also expected. Note that similar trends are observed for the horizontal effective stresses.

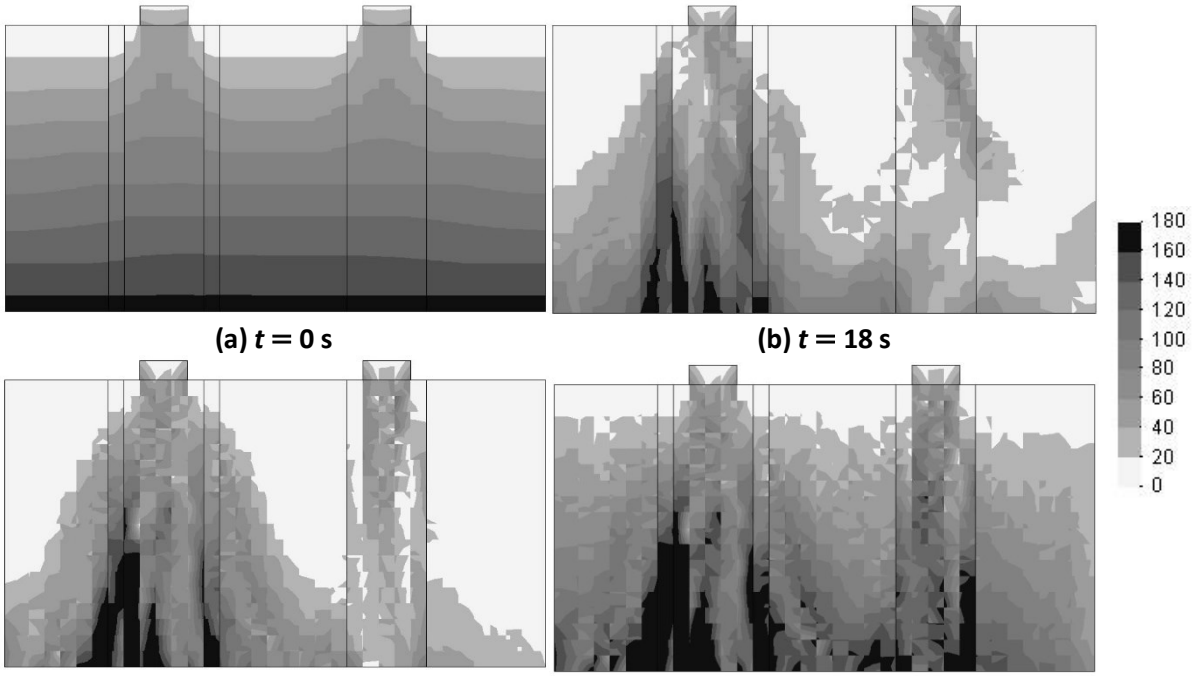

(a) $t = 0$ s **(b) $t = 18$ s**

(c) $t = 38$ s **(d) $t = 78$ s**

Figure 8.138 – Vertical effective stresses (in kPa) at different instants of time for CM-B.

8.5 Summary and conclusions

In this chapter, the performance of the bounding surface plasticity model (BSPM) implemented into FEMEPDYN was evaluated in the context of boundary-value problems. Specifically, the results of two centrifuge experiments concerning the response of adjacent shallow foundations built on liquefiable sand deposits subjected to dynamic loading were used as benchmark for the dynamic finite element analyses. In the first centrifuge experiment, the adjacent shallow foundations, consisting of solid steel structures, were built on a uniform deposit of saturated loose sand and, therefore, the focus was given to the ability of the constitutive relationship to reproduce the basic aspects of sand-structure interaction under dynamic loading. Complementary, techniques to mitigate liquefaction effects were used in the second centrifuge experiment, including narrow densified columns and a drainage geocomposite simulating closely spaced high-capacity drains, increasing the complexity of the numerical analysis. Particular emphasis was given, in this second analysis, to the evaluation of the ability of the constitutive model to simulate the response of deposits with different initial densities using a single set of model parameters, as well as to replicate the impact of the additional drainage capacity provided by the geocomposite on the response of sand.

Prior to the presentation and discussion of the finite element analyses and obtained results, an overview of the dynamic centrifuge testing programme undertaken by the PhD candidate Andreia Silva Marques was given, followed by a brief description of the obtained experimental results. The general aspects of the dynamic finite element analysis were subsequently described, including the time-integration algorithm employed, spatial and time discretisation and boundary conditions adopted, as well as characteristics adopted for the different

materials (such as initial density, stiffness and strength properties and hydraulic conductivity). Due to the simplification of the 3D configuration of the problem by assuming a plane strain condition, the methodology used to estimate the contributions of the shallow foundations to the initial stress state was thoroughly characterised and discussed, to ascertain potential detrimental impacts on the modelled response. Finally, the results obtained in each dynamic finite element analysis were compared with those obtained in the corresponding centrifuge experiment and conclusions were drawn about the ability of the constitutive model to capture the main phenomena observed in the experiments.

In relation to the first centrifuge model (CM-A), concerning the response of two adjacent shallow foundations resting on a uniform deposit of saturated loose sand subjected to dynamic loading causing liquefaction, it was concluded that the constitutive model was able to replicate key aspects of the dynamic response of sand, such as:

- attenuation of the input motion due to the strong degradation of sand stiffness and concurrent increase in material damping;
- accurate prediction of the excess pore pressure evolution with dynamic loading at different locations of the sand deposit;
- satisfactory prediction of the settlements registered for both heavier and lighter shallow foundations during dynamic loading.

Conversely, the constitutive model was not able to reproduce satisfactorily the following aspects:

- excess pore pressures build-up during the first half of dynamic loading in the zones of the deposit immediately underneath the foundation, with the constitutive model overpredicting this aspect of the sand response;
- rate at which the excess pore pressure dissipates after the end of shaking (i.e. during the consolidation phase), with the constitutive model overpredicting this aspect;
- rate and magnitude of the structural settlements occurring during the consolidation stage, with the constitutive model underpredicting the observed settlements.

While the first aspect may be attributed to the simplifications required to simulate the 3D nature of the problem by assuming 2D plane strain conditions, the inability of the constitutive model to reproduce accurately the response of sand during consolidation seems related to the open primary yield surface formulation of the model, which leads to the prediction of solely elastic response under stress paths characterised by approximately constant stress ratios. Note that this aspect was also reported by Taborda (2011) when reproducing other centrifuge experiments.

Still regarding CM-A , it was further observed that the following aspects were not satisfactorily captured in the numerical analysis:

- magnitude of the inertia effects introduced by the different masses of the shallow foundations, with the horizontal accelerations registered for the lighter shallow foundation being underestimated in relation to those measured in the experiment;
- inability to predict the deformation mechanism observed in the centrifuge experiment, characterised by a progressive punching of the shallow foundations through the sand deposit during the experiment; conversely, in the numerical analysis, a movement of sand from the zones of the deposit under the influence of the shallow foundations to the zones farther from their influence (sides and middle of the model) was predicted; as a consequence, the displacements registered in the numerical analysis at the ground surface in between the two shallow foundations, as well as on the sides of the shallow foundations differ significantly from those measured in the experiment.

Note that these aspects cannot be directly considered as pitfalls of the constitutive model, since other aspects of the numerical analysis seem to have influenced the computed response. In relation to the former aspect, it may be argued that the 2D plane strain simplification might have considerably influenced the response measured immediately underneath the shallow foundations, as pointed out before when addressing the discrepancies in terms of excess pore pressures generated at those locations. Regarding the deformation mechanism, it was attributed to the inability of the numerical tool to predict the occurrence of partially drained response of sand during dynamic loading. In fact, it has been extensively suggested in the literature (e.g. Scott, 1986a; Manzari and Arulanandan, 1993; Coelho, 2007; Taiebat *et al.*, 2007; Su *et al.*, 2009; Andrianopoulos *et al.*, 2010a; Taborda, 2011) that a temporary increase in hydraulic conductivity of the liquefied sand deposit in relation to the value of this property measured in conventional laboratory tests (e.g. permeameter tests) might occur during dynamic loading, likely due to the formation of transient cracks in the sand deposit under very low effective stresses and large vertical hydraulic gradients. To investigate this aspect, the numerical simulation of CM-A was re-run considering a simple variable hydraulic conductivity model proposed by Taborda (2011) linking the value of this property to the excess pore pressure ratio. Although significant discrepancies were obtained in this subsequent analysis in terms of excess pore pressures generated in the model and computed structural settlements, suggesting that further investigation is required, it was shown that a considerable improvement of the reproduction of the deformation mechanism observed in the experiment and, consequently, of the settlements registered in between the two shallow foundations was obtained.

With respect to the results obtained for the second centrifuge model (CM-B), which assessed the use of narrow densified zones and high-capacity vertical drains to improve the performance of adjacent shallow foundations when subjected to dynamic loading, it was concluded that:

- apart from the zones of the deposit located immediately underneath the shallow foundations, the constitutive model was able to predict satisfactorily the modification of the input motion due to the degradation of sand stiffness and concurrent increase in material damping;
- satisfactory prediction of the excess pore pressure evolution with dynamic loading under the right shallow foundation of the model; note that, on this side of the model, only densification was used as technique to mitigate liquefaction effects;
- overestimation of the drainage capacity of the geocomposite, with smaller excess pore pressure accumulation under the left shallow foundation of the model and in the middle of the model being obtained in the numerical than those measured in the experiment;
- very satisfactory prediction of the rate and magnitude of settlements registered for both shallow foundations during the dynamic phase; presumably, the agreement in terms of the magnitude of settlement of the right shallow foundation could have been even better if the shallow foundation had been observed to remain on the densified sand column during the centrifuge experiment, as intended (Marques *et al.*, 2014a, 2015);
- similar to CM-A, overprediction of the rate of dissipation of excess pore pressures after the end of shaking, as well as underestimation of the settlements occurring during this stage of the experiment; as mentioned before, this is likely a consequence of the open shape of the primary yield surface, which results in an overestimation of the stiffness of sand under stress paths characterised by approximately constant stress ratios.

Overall, in terms of the performance of the bounding surface plasticity model, it can be concluded that the constitutive model was able to predict accurately the generation of excess pore pressure during dynamic loading in both loose and dense deposits of Hostun sand. As a result, the constitutive model captured satisfactorily the reduction of stiffness and concurrent increase in material damping with dynamic loading and, therefore, the modification of the input motion. A satisfactory prediction of the co-seismic structural settlements was also obtained in the numerical analysis. Taking into account that both centrifuge experiments were simulated using model parameters calibrated solely against results of element laboratory tests, it suggests that the constitutive model has an extensive ability to simulate the occurrence and development of liquefaction-related phenomena, as well as the performance of shallow foundations under such circumstances.

In order to expand the modelling capabilities of the constitutive model, it seems particularly important to improve the simulated response under stress paths characterised by approximately constant stress ratios. Under such loading conditions, the stiffness of sand appears to be greatly overpredicted by the constitutive model, resulting in the overprediction of the rate of excess pore pressure dissipation, as well as underprediction of settlements. As suggested by Taborda (2011), possible solutions may include: (1) replacement of the current

shape of the primary yield surface by a closed shape (e.g. Taiebat and Dafalias, 2008); (2) introduction of an additional yield surface which closes the current yield surface for large values of mean effective stress (Li, 2002); or (3) introduction of a nonlinear degradation of the secant bulk modulus with volumetric strain to complement the degradation of secant shear stiffness with shear strain (Jardine *et al.*, 1986).

Chapter 9 SUMMARY, CONCLUSIONS AND RECOMMENDATIONS

9.1 Introduction

The great development of the capabilities of finite element codes in recent years and their growing use in current engineering practice have revealed the need for the implementation of constitutive models capable of modelling accurately the response of soil under general loading conditions. Indeed, the adequate simulation of complex dynamic phenomena, such as those involving liquefaction, requires the use of advanced constitutive models able to capture important features of cyclic soil response, including the reduction of shear stiffness and concurrent increase in damping ratio with strain amplitude, the modification of the response of soil once the phase transformation line is crossed and stress path is reversed, the occurrence of flow liquefaction or cyclic mobility and the accumulation of very large strains. Furthermore, the constitutive model should be able to predict accurately the effect of stress state and density on the response of soil using a single set of model constants. Among the vast number of constitutive models available in the literature, bounding surface plasticity models (BSPM) have been a subject of great interest in recent years, not only due to their ability to reproduce adequately the aforementioned key aspects of cyclic soil response, but also due to their modularity and flexibility, which simplify their further expansion to enhance their modelling capabilities. Indeed, a successful application of such strategy was undertaken by Taborda (2011) and Taborda *et al.* (2014) by performing a detailed computational study on the expansion of a bounding surface plasticity model for sand originally proposed by Manzari and Dafalias (1997) and further developed by Papadimitriou and Bouckovalas (2002). While retaining the main constitutive ingredients from the original version (such as the dependence of the plastic hardening modulus and flow rule on the distances from the current stress point to its projection on the bounding and dilatancy surfaces, respectively), the more recent versions of Papadimitriou and Bouckovalas (2002) and Taborda *et al.* (2014) have been shown greater ability to simulate accurately cyclic sand response under a wide range of strain amplitudes. Furthermore, when compared to the precedent versions, the alterations introduced by Taborda *et al.* (2014) have increased the overall flexibility and accuracy of the constitutive model, while being numerically stable at very low effective stresses, which is a crucial requirement when simulating boundary-value problems involving liquefaction-related phenomena. Having selected the formulation proposed by Taborda *et al.* (2014) as a starting point, the following objectives were established for the present PhD research:

- expansion of the constitutive relationship proposed by Taborda *et al.* (2014) by replacing the expression for the small-strain elastic stiffness modulus with a more general one, as well as by introducing an inherent fabric anisotropy component proposed in the literature, enhancing the ability of the constitutive relationship to

capture the effect of the direction of the major principal effective stress in relation to the axis of the deposition of the particles on the modelled response;
- implementation of the proposed constitutive relationship into the finite element code FEMEPDYN, developed at the University of Coimbra;
- extensive investigation of the ability of the constitutive model to replicate the response of sand observed in element laboratory tests and centrifuge tests involving liquefaction-related phenomena.

It is important to note that the third objective was solely possible due to a collaboration established with another PhD research programme, which included centrifuge testing at the Turner Beam Centrifuge facility of the University of Cambridge, United Kingdom. Specifically, as part of a Seismic Engineering Research Infrastructures for European Synergies (SERIES) Transnational Access Use Agreement, a centrifuge-based study on the performance of shallow foundations built on liquefiable sand deposits when subjected to dynamic loading was undertaken by a PhD candidate, Andreia Silva Marques. Given the lack of field monitoring data concerning this type of phenomena, the results of these centrifuge experiments represented an excellent opportunity to evaluate the performance of the newly implemented constitutive model in the context of boundary-value problems involving liquefaction. To bridge the gap between centrifuge and numerical modelling, it was considered fundamental to perform an extensive laboratory characterisation of the material used in the dynamic centrifuge experiments – namely, air-pluviated Hostun sand. With that purpose, an extensive element laboratory testing programme, including bender element tests, as well as large number of monotonic and cyclic triaxial tests, was undertaken, allowing for the characterisation of the response of air-pluviated Hostun sand under a wide range of strains. Indeed, besides providing fundamental insight into important aspects of the monotonic and cyclic response of Hostun sand and, therefore, assisting the interpretation of the response measured in the centrifuge experiments, the results obtained in the element laboratory tests provided reliable data for the calibration of the BSPM.

The following sections summarise the performed research and main conclusions drawn from the obtained results. The final section of this chapter presents recommendations for future investigation.

9.2 Laboratory characterisation of the monotonic and cyclic response of Hostun sand

In the first part of the thesis, consisting of Chapter 2 and Chapter 3, the element laboratory testing programme carried out on air-pluviated Hostun sand was thoroughly described. The obtained experimental results were presented and interpreted using a state parameter concept (Been and Jefferies, 1985) in conjunction with concepts of critical state soil mechanics (CSSM) framework (Roscoe *et al.*, 1958; Schofield and Wroth, 1968) and bounding surface plasticity (BSP) framework (Dafalias and Popov, 1975; Dafalias, 1986; Manzari and Dafalias,

1997; Li and Dafalias, 2000) to assess the distinctive features of Hostun sand response. In addition, key aspects of the cyclic response of Hostun sand were examined, including the reduction of the normalised secant shear stiffness and concurrent increase of damping ratio with strain amplitude, the generation of excess pore water pressure with cyclic loading, the occurrence of phase transformation and subsequent modification of the response of sand upon stress reversal and the onset of cyclic mobility under undrained conditions.

To characterise the response of Hostun sand at very small strains, a series of bender element tests were performed both on a moderately loose and on a dense sample subjected to drained isotropic compression (DIC) loading. More specifically, after saturation, the samples were gradually consolidated to higher isotropic effective stress levels and, at each stress level, single sine pulses with varying frequencies were transmitted to the top end of the samples, with the vertically propagated signal being subsequently recorded at the bottom end of the sample. A first unloading, reloading and second unloading phases were performed, with bender element measurements being taken at each stress level, to assess the influence of the previous stress history (or, in other words, overconsolidation) on the estimated G_{max}. Two different methods of interpretation, one in the time domain (TD) and the other in the frequency domain (FD), were employed in the estimation of the arrival time of the shear wave. Having compared the arrival times estimated by both methods, it was apparent that the results obtained when using the TD method were more consistent with the recorded signal and, therefore, only this set of results was used for estimating the shear modulus at very small strains, G_{max}. It was concluded that, for this type of loading (i.e. DIC loading), the previous stress history has little influence on G_{max} and, therefore, G_{max} can be solely related to the current void ratio, e, and mean effective stress, p', as suggested in previous studies (e.g. Hardin, 1965; Hardin and Black, 1966; Hardin and Drnevich, 1972a; Lo Presti *et al.*, 1997; Zhou and Chen, 2005). Furthermore, having used the obtained results for the calibration of a well-known equation proposed in the literature (Hardin, 1965; Hardin and Black, 1966a), it was found that a dependence of G_{max} on approximately the square root of p' (i.e. $n_g = 0.49$) fitted well the experimental data, as also proposed in the literature for other sands (e.g. Hardin and Black, 1966b; Kokusho, 1980; Benz, 2007). Indeed, it was shown that the bender element test results obtained in the present study are similar to those obtained by Hoque and Tatsuoka (2000) when using small-amplitude cyclic triaxial loading on dry samples of Hostun sand locally instrumented by strain gauges.

With the objective of characterising the monotonic response of air-pluviated Hostun sand within the medium to large strain range, a series of drained and undrained monotonic triaxial compression and extension tests were subsequently conducted on samples prepared to a wide range of void ratios and consolidated under several different isotropic and anisotropic stress states. Moreover, samples were sheared along four different stress paths possible to be applied in a stress path cell of Bishop and Wesley (1975)'s type to assess the stress path effects on the measured response. As expected, the obtained results suggest that the

response of Hostun sand is highly dependent on its void ratio and effective stress state at consolidation. More specifically, it was shown that denser sands tend to exhibit stiffer stress-strain responses and greater tendency to dilate (i.e. to start dilating at smaller strain levels and at a higher rate) when compared to looser sands. Naturally, under undrained conditions, since the total volumetric strain remains constant throughout loading, the greater tendency to dilate of denser sands manifests itself through a smaller tendency to generate positive (i.e. compressive) excess pore water pressures during the early stages of loading and a greater tendency to generate negative (i.e. suction, tensile) excess pore water pressures during the later stages of loading. As a consequence of their stiffer and more dilatant responses, denser sands typically mobilise higher deviatoric stresses, as well as higher stress ratios (or, equivalently, shearing resistances) during loading than those mobilised by looser sands. Moreover, at very large strains, similar stress ratios tended to be mobilised by either (initially) denser or (initially) looser sands, as postulated by the CSSM framework (Roscoe *et al.*, 1958; Schofield and Wroth, 1968). Regarding the effect of the mean effective stress at consolidation, the experimental results showed that, as expected, samples prepared to similar void ratios and consolidated under higher mean effective stresses tend to exhibit stiffer stress-strain responses and mobilise larger deviatoric stresses than samples consolidated to lower mean effective stresses. Moreover, the higher the effective stress at consolidation, the greater the tendency to generate larger positive (i.e. compressive) volumetric strains, which, under undrained conditions, is manifested by the generation of larger positive excess pore water pressures. In relation to the stress ratios mobilised during shearing, they were observed to be less dependent on the mean effective stress at consolidation than on the initial void ratio of the samples for the range of effective stress states at consolidation considered in the present laboratory testing programme. Indeed, as also postulated by the CSSM framework, at very large strains, samples tended to exhibit similar stress ratios, irrespectively of the effective stress at consolidation. With respect to the influence of the type of consolidation (i.e. either isotropic or anisotropic), the experimental results showed that anisotropically consolidated samples tend to reach slightly larger peak deviatoric stresses than isotropically consolidated samples, while having little impact on other aspects of the response of sand.

To extend further the interpretation of the experimental results, a state-parameter approach, originally proposed by Been and Jefferies (1985), was used in conjunction with CSSM and BSP concepts to characterise the distinctive states of the monotonic response of Hostun sand, namely the critical state (CS), peak-stress-ratio state (PSRS), phase-transformation state (PTS) and undrained instability state (UIS). Starting with the CS – i.e. the state at which "soil continues to deform at constant stress and constant void ratio", as defined by Roscoe *et al.* (1958) – , results of both drained and undrained monotonic triaxial compression tests conducted on loose samples (i.e. having relative densities below 50%) were used for the prediction of the CS strength of Hostun sand, as well as the critical state line (CSL) in the void

ratio, *e*, – mean effective stress, *p*', space. Additional data found in the literature (Konrad, 1993; Benahmed, 2001; Desrues, 2013) were used to corroborate the proposed CSL, which appears to be independent of the sample preparation method and drainage conditions. Subsequently, the PTS (i.e. the state at which the response of sand changes from plastic contraction to plastic dilation, meaning that dilatancy is temporarily null) and the PSRS (i.e. the state at which the maximum angle of shearing resistance is mobilised) were characterised. Irrespective of the stress state and void ratio at consolidation, drainage conditions and stress-path direction, these two distinctive states appeared to be adequately described by simple linear state-dependent relationships. The very good agreement between PTS data inferred from drained and undrained tests was particularly remarkable, given the assumptions required to determine the occurrence of this state under drained conditions, involving the estimation of the dilatancy coefficient and, therefore, of plastic strains developed in each test. Conversely, under undrained conditions, the PTS can be simply identified by a local minimum in *p*' (Ishihara *et al.*, 1975). In addition, the UIS (i.e. the state corresponding to a temporary maximum value of undrained shear strength at relatively small-strains) was characterised. As suggested by other authors (e.g. Ishihara, 1993), the available data suggested that the mean effective stress state at UIS is strongly correlated with the mean effective stress at consolidation. When compared with other results presented in the literature, it appeared that, contrary to what was observed for the CS, the method of sample preparation influences the occurrence of the UIS. Finally, the results of drained triaxial compression tests performed on both loose and dense samples were used to calibrate (and, therefore, to examine) a stress-dilatancy relationship proposed by Manzari and Dafalias (1997) and employed by the BSPM used in the present study. This stress-dilatancy relationship defines the dilatancy coefficient as a function of the difference between the current stress ratio and the stress ratio at PTS (termed as "dilatancy stress ratio" in the context of BSPM). It was found that the experimental data was adequately described by the proposed relationship.

In addition, a series of drained and undrained cyclic triaxial tests were carried out to investigate the cyclic response of air-pluviated Hostun sand. Due to the fact that liquefaction-related phenomena involve the generation of large excess pore water pressures, a much larger number of tests were performed under undrained conditions than under drained conditions. Once more, samples were prepared to different void ratios and consolidated under various isotropic effective stress states, allowing for the evaluation of the effect of these aspects on the cyclic response of sand. Two-way symmetric deviatoric stress oscillations (i.e. similar deviatoric stress amplitude in triaxial compression and in triaxial extension) with different amplitudes were applied to the samples. As expected, the results of undrained cyclic triaxial (UCT) tests confirmed that air-pluviated Hostun sand is susceptible to cyclic mobility. Irrespective of the initial conditions of the test (i.e. initial void ratio and effective stress state at consolidation), as well as amplitude of cyclic loading, the excess pore water pressure was observed to build-up in each cycle, resulting in a progressive reduction of the mean effective

stress and shear stiffness. Eventually, effective stresses close to zero were reached in all tests, with large strains being accumulated. Furthermore, as suggested in previous studies (Ishihara *et al.*, 1975; Nemat-Nasser and Tobita, 1982; Papadimitriou *et al.*, 2001), the cyclic response of Hostun sand appeared to be strongly affected by the crossing of the phase transformation line (PTL). Specifically, as a stress reversal occurs after the crossing of the PTL, a much more compliant response (i.e. a stronger reduction of the mean effective stress than that measured in the previous loading cycles) was observed, which may suggest that the arrangement of the particle contacts (i.e. the structure of sand) may be altered by the occurrence of dilation, as suggested in the literature (e.g. Nemat-Nasser and Tobita, 1982). In relation to the effect of the void ratio and isotropic confining stress at consolidation, the results of the conducted UCT tests enabled to conclude that looser samples subjected to higher initial effective stresses tend to generate larger excess pore water pressures in each loading cycle and, therefore, to reach cyclic mobility in a smaller number of loading cycles when compared to samples subjected to similar cyclic stress ratios (CSR). Moreover, the higher the CSR applied to the sample, the smaller the number of loading cycles required to reach cyclic mobility. These experimental observations agree well with those reported in the literature for other sands (e.g. Seed and Lee, 1966; Seed and Idriss, 1970a; Dobry *et al.*, 1982; Tatsuoka *et al.*, 1986a, 1986b; Youd *et al.*, 2001).

To extend further the characterisation of the cyclic response of Hostun sand, the obtained UCT test results were used to assess the reduction of the normalised secant shear stiffness, G_{sec} / G_{max}, and concurrent increase in damping ratio, ξ, with strain level (in particular, single amplitude axial strain, $\varepsilon_{a,sa}$, was considered in the present study). Note that, while the shear modulus can be related to the velocity of propagation of shear waves, the damping ratio provides a measure of the energy dissipated by the material during cyclic loading. As reported in the literature for other materials (e.g. Darendeli, 2001), it was concluded that the void ratio has a minor influence on the evolution of G_{sec} / G_{max} with $\varepsilon_{a,sa}$, seeming also to have little impact on the evolution of ξ with $\varepsilon_{a,sa}$. In terms of mean effective stress at consolidation, this quantity appears to affect both aspects: the higher the mean effective stress at consolidation, the larger G_{sec} / G_{max} for a given $\varepsilon_{a,sa}$, while the opposite tend to occur in terms of $\xi - \varepsilon_{a,sa}$ curves. These findings seem to agree well with those reported in the literature for other sands (Seed and Idriss, 1970b; Vucetic and Dobry, 1991; Ishibashi and Zhang, 1993; Darendeli, 2001).

The following aspect to be characterised was the undrained cyclic resistance of Hostun sand (i.e. resistance to the onset of cyclic mobility). Specifically, by adopting a criterion based on the accumulation of a residual excess pore water pressure ratio, $r_{u,res}$ (i.e. corresponding to null deviatoric stress) close to unit, undrained cyclic resistance curves for moderately loose and dense samples were established. As widely reported in the literature (e.g. Seed and Idriss, 1970a; Tatsuoka *et al.*, 1986b; Ishihara, 1996; Jefferies and Been, 2006; Idriss and Boulanger, 2006), the obtained curves showed that a smaller number of loading cycles are required to

trigger cyclic mobility for looser samples than for denser samples. Similarly, a smaller number of loading cycles are required to reach cyclic mobility for samples consolidated under higher mean effective stresses or subjected to larger CSR. When comparing the response of Hostun sand with two other well-known sands (specifically, Ottawa and Toyoura sands), it was concluded that the undrained cyclic resistance of Hostun sand is higher than those exhibited by the other two sands.

Subsequently, the evolution of $r_{u,res}$ with cyclic loading was studied. When plotted as a function of the normalised number of loading cycles, N / N_{liq} (where N_{liq} is the number of cycles required to the onset of liquefaction), it was concluded that similar evolutions of $r_{u,res}$ are obtained for samples sheared under similar CSR, regardless of the void ratio, e, and isotropic effective stress at consolidation, σ'_0 (note that all samples subjected to UCT tests were consolidated under isotropic effective stresses). Conversely, when different values of CSR are used in the tests, different evolutions of $r_{u,res}$ are registered. Specifically, the higher the CSR applied to the sample, the higher the rate of $r_{u,res}$ increase during the earlier stages of loading, with the opposite trend being observed during the later stages of loading. Further insight into the evolution of $r_{u,res}$ with undrained cyclic loading was obtained by plotting $r_{u,res}$ as a function of the normalised energy dissipated per unit volume, either by using the quantity $\Delta W / \sigma'_0$ or $\Delta W / \Delta W_{liq}$ (where ΔW is the dissipated energy per unit volume and ΔW_{liq} is the value of this quantity when liquefaction is triggered – known as capacity energy). The obtained curves suggest that the relationship between $r_{u,res}$ and $\Delta W / \sigma'_0$ is practically independent of e and σ'_0, though dependent on the CSR applied to the sample. Conversely, the relationship between $r_{u,res}$ and $\Delta W / \Delta W_{liq}$ seems to be practically independent of the values of σ'_0 and CSR, though dependent on e. This suggests that, although recent efforts have been made to find out a relationship that would be simultaneously independent of e, σ'_0 and CSR, either by using element laboratory testing (e.g. Figueroa *et al.*, 1994; Liang *et al.*, 1995; Kokusho, 2013; Azeiteiro *et al.*, 2017b), centrifuge testing (e.g. Dief and Figueroa, 2007) or numerical modelling (e.g. Tsaparli *et al.*, 2017a), further investigation on this topic is still required.

The final aspect to be investigated was the volumetric strain response of moderately loose samples of Hostun sand under drained cyclic loading. As expected, samples exhibited a tendency to contract (i.e. to develop contractive volumetric strains) when sheared under drained conditions. Moreover, as also reported in the literature for other sand (e.g. López-Querol and Coop, 2012), it was observed that progressively smaller volumetric strains were accumulated during loading, eventually stabilising with further loading. Moreover, as also observed under undrained conditions, a softer response of Hostun sand was registered in triaxial extension than in triaxial compression.

9.3 Implementation of a bounding surface plasticity model into a finite element code

The second part of this thesis, consisting of Chapter 4 and Chapter 5, comprised a comprehensive description of the constitutive model adopted in the present study, the modifications introduced to its original formulation and the numerical algorithms used to implement it into a finite element code. This part concluded with validation exercises, whose results suggested that the implementation of the constitutive relationship was successful.

Among the vast number of constitutive models available in the literature, a bounding surface plasticity model (BSPM), originally formulated by Manzari and Dafalias (1997) and further developed by Papadimitriou and Bouckovalas (2002), Taborda (2011) and Taborda *et al.* (2014) was chosen to be implemented into FEMEPDYN. Besides its extensive ability to replicate both monotonic and cyclic response of sand, proven by the successful simulation of element laboratory tests and centrifuge experiments by the aforementioned authors, the following aspects were considered essential for its selection:

- reliable key constitutive ingredients, such as: (a) the incorporation of critical state soil mechanics (CSSM) concepts (Roscoe *et al.*, 1958; Schofield and Wroth, 1968), which provide a reference state for the response of sand; (b) the dependence of the shearing response on the state parameter, ψ (Been and Jefferies, 1985), which enables the accurate prediction of the occurrence of distinctive states of the response of sand, such as the phase transformation state and the peak stress ratio state, using a single set of parameters, as discussed in Chapter 2 and Chapter 6; (c) the incorporation of a state-dependent stress-dilatancy relationship, which appears to characterise adequately the response of sand, as shown in Chapter 2 and Chapter 6; (d) the incorporation of bounding surface plasticity concepts (Dafalias and Popov, 1975; Mróz *et al.*, 1979; Dafalias, 1986), relating the plastic hardening modulus to the distance from the current stress point to its projection on the bounding surface, enabling the adequate reproduction of the highly non-linear response of sand before failure (Loukidis and Salgado, 2009); indeed, when used in conjunction with a small kinematically-hardening yield surface, the bounding surface plasticity concepts can successfully address the simulation of cyclic loading (Manzari and Dafalias, 1997).
- flexibility and modularity, allowing for its expansion with a relatively low effort (Taborda *et al.*, 2014).

Furthermore, it was highlighted that, although many other versions of the model – i.e. originating from the initial proposal of Manzari and Dafalias (1997) – have been proposed in the literature (e.g. Dafalias and Manzari, 2004; Dafalias *et al.*, 2004; Taiebat and Dafalias, 2008; Loukidis and Salgado, 2009; Andrianopoulos *et al.*, 2010; Woo and Salgado, 2015), the formulation proposed by Papadimitriou and Bouckovalas (2002) and further extended by Taborda (2011) and Taborda *et al.* (2014) present the following advantages:

- ability to describe adequately the cyclic response of sand under a wide range of strain amplitudes; in particular, by incorporating a cyclic non-linear elastic formulation of Ramberg and Osgood (1943)'s type, Papadimitriou and Bouckovalas (2002) showed that the constitutive model is able to reproduce the stress-strain response of sand at small strains, both in terms of secant shear stiffness and hysteretic damping evolutions with strain level; moreover, Papadimitriou and Bouckovalas (2002) showed that the ability of the constitutive model to replicate cyclic response within the medium to large strain range was greatly enhanced in relation to its original version by affecting the plastic hardening modulus by a scalar quantity reflecting the effect of fabric evolution with shearing; this modification allowed the simulation of continuously stiffer unloading-reloading response observed both under drained and undrained stress paths beneath the dilatancy surface (which can be associated with the phase transformation line described by Ishihara *et al*, (1975)) – a response often termed as "densification" – , as well as a more compliant response once dilatancy surface is crossed and stress path is reversed, eventually leading to cyclic mobility, as observed in the laboratory (e.g. Ishihara *et al.*, 1975);
- ability to describe flow liquefaction, as well as flow with limited deformation, with a greater control being achieved after the introduction of a new parameter defining the nonlinearity of the relationship between the hardening modulus and the proximity to the bounding surface by Taborda (2011) and Taborda *et al.* (2014);
- enhanced prediction of the response of dense sand after the adoption of a power law equation to describe the critical state line (CSL) in the void ratio, e, – mean effective stress, p', space (Taborda, 2011; Taborda *et al.*, 2014);
- increased computational efficiency achieved through the introduction of a secondary low-stress yield surface to the model formulation, which is particularly relevant when simulating boundary-value problems involving liquefaction-related phenomena (Taborda, 2011; Taborda *et al.*, 2014).

In addition, the choice for the version proposed by Taborda (2011) and Taborda *et al.* (2014) was also justified by the availability of a large amount of numerical data concerning the simulation of both element laboratory and centrifuge tests, which were used as benchmark for the validation of the implementation of the constitutive model into FEMEPDYN.

As suggested by several authors (e.g. Papadimitriou and Bouckovalas, 2002; Dafalias and Manzari, 2004; Dafalias *et al.*, 2004; Taborda *et al.*, 2014), the modular structure of the constitutive model allows, in principle, for the modification of any component of its formulation or to the addition of new components without affecting the remaining components. Having this aspect in mind, two alterations were introduced to improve the overall flexibility, as well as to increase the accuracy of the constitutive model. Firstly, the equation defining the influence of the void ratio, $f(e)$, on the maximum shear modulus, G_{max}, was replaced by a more general equation, which has been largely employed in experimental

studies, including the one undertaken in the first part of this PhD research. Secondly, a literature review on other versions of the constitutive model proposed in the literature (Dafalias and Manzari, 2004; Loukidis and Salgado, 2009; Li and Dafalias, 2012; Williams, 2014; Woo and Salgado, 2015) suggested that the ability of the constitutive relationship to replicate the response of sand for loading conditions other than triaxial compression was considerably improved when including an inherent fabric anisotropy component. Indeed, Williams (2014) showed that this component allows the replication of the effect on the response of sand of changes in the angle α of the major principal effective stress, σ'_1, to the axis of the sample – a feature widely observed in hollow cylinder torsional shear tests, which is not captured by the constitutive relationship proposed by Taborda *et al.* (2014). A further motivation for the introduction of the inherent fabric anisotropy component consisted of the apparent inability of the original formulation to predict accurately highly anisotropic soil response observed in some undrained cyclic triaxial tests (Taborda, 2011). Among the several formulations available in the literature, the one proposed by Williams (2014) was chosen to be incorporated in the present constitutive model, due to its compliance with the CSSM framework and the fact that it did not imply profound alterations to the formulation proposed by Taborda *et al.* (2014). It is important to note that, should there be a lack of experimental evidence supporting its use, this newly introduced component may be deactivated by selecting specific values for its model parameters, therefore guaranteeing compatibility with the version proposed by Taborda (2011) and Taborda *et al.* (2014). Indeed, this philosophy also underlaid the alterations introduced by Taborda (2011) and Taborda *et al.* (2014) to the version developed by Papadimitriou and Bouckovalas (2002).

Attention was subsequently given to the implementation of the constitutive model into FEMEPDYN, which plays a key role in two distinct operations of FE method (Potts and Zdravkovic, 1999; Taborda, 2011): the computation of the element tangent stiffness matrix, which is subsequently assembled into the global tangent stiffness matrix, and the computation of the effective stress change corresponding to a given strain increment. While the first operation consisted solely of writing the constitutive equations, the second operation required the use of a stress point algorithm. Based on an extensive literature review of available algorithms, their merits and drawbacks, it was concluded that explicit integration schemes with automatic sub-stepping and error control have been typically preferred over semi-explicit and implicit schemes, particularly for the implementation of BSPMs (e.g. Zhao *et al.*, 2005; Andrianopoulos *et al.*, 2010a; Taborda, 2011; E-Kan and Taiebat, 2014; Xu and Zhang, 2015; Vilhar *et al.*, 2018). It was, therefore, decided to adopt the modified forward Euler scheme with automatic sub-stepping and error control introduced by Sloan (1987) and Sloan *et al.* (2001) to integrate the present BSPM into FEMEPDYN. The operations required in each step of the scheme were comprehensively described, giving particular attention to the additional operations required by the co-existence of two yield surfaces, which can be simultaneously active.

Having implemented the stress integration algorithm and constitutive equations into FEMEPDYN, focus was given to its validation. Due to the lack of theoretical or analytical solutions, the strategy consisted of comparing the results obtained using FEMEPDYN with those obtained by a validated finite element code. More specifically, results of simulations of element laboratory tests and centrifuge tests obtained by Taborda (2011) when using the Imperial College Finite Element Program (ICFEP) were employed as a benchmark for the validation of the implementation procedures. Starting with the element laboratory tests, it was shown that, when using similar numerical precisions, an excellent agreement between the results obtained by FEMEPDYN and ICFEP (Taborda, 2011; Taborda, personal communication, April 2015) was reached, irrespective of the type of analysis (axisymmetric or plane strain), as well as boundary and loading conditions applied in each simulated test. Subsequently, two different dynamic centrifuge experiments performed as part of the large collaborative research project VErification of Liquefaction Analysis by Centrifuge Studies (VELACS) were numerically reproduced. The first of these centrifuge experiments – VELACS model 1 – comprised a 10 m-thick (in prototype scale), level deposit of saturated loose ($D_r \approx$ 40%) Nevada sand subjected to a horizontal sinusoidal-type motion applied at its base. It was shown that, overall, a very good agreement between the results computed by FEMEPDYN and those presented in the literature (Taborda, 2011) was obtained in terms of horizontal acceleration time-histories, as well as excess pore water pressure and settlement evolutions with time. The second centrifuge experiment – VELACS model 12 – comprised a 4.0 m-tall (in prototype scale) solid structure partially embedded into a 6.0 m-thick (in prototype scale) deposit of fully-saturated moderately dense ($D_r \approx$ 60%) Nevada sand and a 1.0 m-thick (in prototype scale) low-permeability deposit of Bonnie silt. Although a different constitutive model had to be employed to model the response of Bonnie silt in relation to that used by Taborda (2011), very similar results were obtained in terms of horizontal and vertical acceleration time-histories, as well as excess pore water pressure and settlement evolutions with time, suggesting that the original version, as proposed by Taborda (2011) and Taborda *et al.* (2014), was successfully implemented into FEMEPDYN and could be applied to the simulation of the performance of shallow foundations when subjected to dynamic loading causing liquefaction. The final part of the validation routine involved the simulation of an undrained cyclic direct simple shear (UCDSS) test by using the extended version of the model (i.e. activating the inherent fabric anisotropy component). The obtained results were compared with those presented in the literature (Williams, 2014). Once again, a remarkable agreement between both sets of numerical data was obtained, suggesting that this additional component of the model was also successfully implemented.

9.4 Application of a bounding surface plasticity model to the simulation of monotonic and cyclic element laboratory tests

The third and final part of this thesis included Chapter 6, Chapter 7 and Chapter 8 and explored the ability of the constitutive model to simulate accurately liquefaction-related phenomena observed in both element laboratory tests and centrifuge experiments, after its calibration solely against the results of the element laboratory tests obtained in the first stage of this PhD research (Chapter 2 and Chapter 3). This aspect intended to replicate the methodology typically followed during the design stage of geotechnical engineering projects, where the response of materials is solely characterised based on element laboratory or field tests. It is important to reinforce that a single set of model constants were employed in all performed simulations, irrespective of the density and initial effective stress state of sand.

In Chapter 6, the methodology adopted for the calibration of the bounding surface plasticity model (BSPM) constants against element laboratory test data was firstly described. Following the guidelines suggested in the literature for this type of models (Loukidis and Salgado, 2009; Taborda, 2011), a hierarchical approach was used, establishing the sequential calibration of the model parameters according to their physical relevance and independence from the remaining parameters. In particular, the calibration focused firstly on the material parameters defining clear features of sand response, including: the critical state line (CSL) in the void ratio, e, – mean effective stress, p', space; the critical state (CS) strength; and the isotropic elastic stiffness at very small strains (defined by the shear modulus at small strains, G_{max}, and Poisson's ratio, ν). While the small-strain parameters were calibrated against results of bender elements, the critical-state parameters were calibrated against results of drained and undrained monotonic triaxial compression tests. Subsequently, the calibration process focused on the quantities that, despite having a numerical nature, control physical features of the modelled response. This included the model parameters defining the positions of the bounding and dilatancy surfaces (which, as mentioned before, are identified by the occurrence of the peak stress ratio and phase transformation ratio, respectively), the model parameter defining the state-dependent stress-dilatancy relationship, as well as the model parameters defining the reduction of the elastic shear stiffness modulus with deviatoric stress ratio (in relation to its value at last shear reversal). These model parameters were also obtained by interpreting and analysing data obtained from drained and undrained monotonic triaxial compression and extension tests. It was particularly highlighted that the cyclic non-linear elastic formulation plays an important role in making compatible the stress-dilatancy response obtained from drained and undrained test data, as required by the fundamental principles of soil mechanics (Loukidis and Salgado, 2009), while allowing for the use of realistic values of G_{max} and ν estimated from bender element measurements.

The calibration process moved subsequently to a more complex stage, which involved the estimation of the model parameters having no physical meaning and related to the plastic

hardening modulus, shearing-induced fabric and inherent fabric anisotropy components. At this point, a series of computational analyses were required to assess the impact of each parameter on the modelled response and, based on the obtained results, decide on the best value to be assigned to the parameter. Starting with the plastic hardening modulus-related parameters, it was observed that the model constant β, which defines the non-linearity of equation introducing the effect of the distance from the current stress point to its projection on the bounding surface on the plastic hardening modulus, has a strong influence on the shape of the effective stress path obtained for undrained shearing and, therefore, in the ability of the constitutive model to accurately predict the occurrence of the undrained instability state, as, indeed, reported in the literature (Loukidis and Salgado, 2009; Taborda, 2011). Moreover, it was noted that the dependency of the plastic hardening modulus on the mean effective stress and void ratio, as proposed by the constitutive relationship, appears to increase the accuracy of the modelled response. The calibration focused subsequently on the parameters required by the shearing-induced fabric component. Based on a preliminary parametric study, it was shown that, as expected, this component has a tremendous impact on the number of loading cycles required to the onset of cyclic mobility and, therefore, its calibration should primarily focus on this aspect of the response of sand. Nevertheless, it was shown that, although introduced to address the simulation of cyclic response, this component also affects the early stages of the modelled monotonic response (particularly of loose and moderately loose sand samples, which exhibit a greater tendency to contract during the early stages of loading). Due to this, a readjustment of the model parameters affecting the plastic hardening modulus was necessary, leading to a very complex trial-and-error process. Unfortunately, at the end of this process, it was concluded that, although allowing for a satisfactory reproduction of the majority of the available undrained cyclic triaxial tests, the selected values for the shearing-induced fabric-related parameters would not result in an adequate reproduction of three particular undrained cyclic triaxial tests, where samples exhibited a very soft response in triaxial extension during the first loading cycle and cyclic mobility was initiated in very few cycles – indeed, similar difficulties were previously reported by Taborda (2011), motivating the introduction of the inherent fabric anisotropy component in the present study.

Attention was subsequently given to the calibration of the parameters required by the inherent fabric anisotropy component. This was a very challenging task, due to the absence of hollow cylinder torsional shear test data, which, contrary to triaxial test data, would allow for the independent evaluation of the effect of anisotropy and magnitude of the intermediate principal effective stress on the response of sand. To obtain a set of model parameters appropriate for the simulation of both monotonic and cyclic response, the adopted strategy comprised the following two steps: firstly, moving back in the calibration process to the end of the calibration of the plastic hardening modulus-related parameters and, based on the set of values established up to that point, calibrating the inherent fabric anisotropy component

against results of monotonic triaxial extension tests; secondly, recalibrating the shearing-induced fabric-related parameters. It was shown that the inherent fabric anisotropy component brings additional flexibility to the constitutive relationship, enabling the simulation of a softer response of sand under triaxial extension loading than that predicted by the formulation proposed by Taborda *et al.* (2014). Having subsequently recalibrated the shearing-induced fabric-related constants, it was found that, contrary to the expectations, only a very slight improvement was obtained in terms of the reproduction of the three undrained cyclic triaxial tests where samples exhibited a very soft response in triaxial extension during the first loading cycle and cyclic mobility was initiated in very few cycles.

In total, four different sets of model parameters were proposed for Hostun sand, two of them – belonging to the category "Static" (i.e. not activating the shearing-induced fabric component) – optimised for the simulation of its monotonic response and the remaining two sets – belonging to the category "Dynamic" (i.e. activating the shearing-induced fabric component) – suitable for the simulation of its cyclic response. Among each pair of sets, one of them made use of the original formulation of the constitutive model proposed by Taborda *et al.* (2014) – "Original formulation" – , while the other set made use of the extended formulation of the constitutive model through the activation of the inherent fabric anisotropy component – "Extended formulation". The proposed values for Hostun sand were subsequently compared with those published in the literature for other sands (Taborda, 2011; Taborda *et al.*, 2014; Williams, 2014). It was concluded that, while the great majority of the values proposed for Hostun sand were within the range of values reported in the literature, the value obtained for the shearing-induced fabric index constant, H_0, was considerably higher than the values reported in the literature for other sands (namely, Leighton Buzzard, Nevada and Fraser river sands). Indeed, having compared the undrained cyclic resistance of Hostun sand with those exhibited by the other sands, it was clear that Hostun sand shows greater resistance to the onset of cyclic mobility and, therefore, requires a greater value for H_0.

In Chapter 7, the ability of the original and extended formulations of the model to replicate key aspects of the monotonic and cyclic responses of Hostun sand registered in laboratory tests was further explored. Starting with the application of the original formulation of the constitutive model to the simulation of drained and undrained monotonic triaxial compression and extension tests, it was observed that, in general, the constitutive relationship was able to capture adequately the effect of the initial void ratio, consolidation stresses and stress path direction on the response of sand. It was, however, noted that, while a satisfactory agreement between numerical and experimental data was achieved for tests performed on moderately loose and dense samples (i.e. having relative densities before shearing, $D_{r,0}$, in the range of 50 – 70 % and above 70 %, respectively), some discrepancies were observed for tests performed on loose samples (i.e. having $D_{r,0} < 50\%$). This was attributed to the large value of the shearing-induced fabric index constant, H_0, required to

simulate cyclic loading, which, as anticipated during the calibration process, was observed to practically eliminate the initial contractive phase of the modelled monotonic response, which is a significant feature of the response of loose samples. The original formulation of the constitutive model was subsequently employed to the simulation of cyclic triaxial tests. Apart from the tests where samples were subjected to large cyclic stress ratios and required only few cycles to the onset of cyclic mobility, it was shown that, irrespective of the consolidation stress and applied cyclic stress ratio, the constitutive model was, in general, able to satisfactorily replicate the undrained cyclic response of moderately loose Hostun sand ($D_r \approx 50 - 70\%$) observed in the laboratory, particularly in terms of excess pore water pressure generation with loading and effective stress path registered in the laboratory. A slightly less satisfactory agreement with experimental data was obtained for dense samples ($D_r \approx 102$ %), with the constitutive model tending to underestimate the material's undrained cyclic resistance (particularly evident for the test using a small cyclic stress ratio). Furthermore, for dense samples, a smaller strain accumulation than that measured in the experiment was, in general, predicted by the constitutive model during the loading cycles preceding the onset of cyclic mobility, while a better agreement being obtained afterwards.

To gain more insight into the performance of the original formulation of the constitutive model, the undrained cyclic resistance predicted by the constitutive model was compared with that measured in the laboratory. It was shown that, when excluding tests where samples were subjected to very large CSRs inducing cyclic mobility in very few cycles, very similar trends were obtained for moderately loose sand ($D_r \approx 50 - 70\%$). The agreement between numerical and experimental data was slightly less satisfactory for dense sand ($D_r \approx 102$ %). Subsequently, the evolutions of the secant shear modulus (normalised by the shear modulus at very small strains), as well as of the damping ratio with the number of loading cycles (normalised by those required to the onset of cyclic mobility) were inferred from the simulated stress-strain loops and compared with those previously inferred from experimental data (Chapter 3). It was shown that the constitutive model is able to replicate qualitatively the main trends observed in the laboratory, including the stiffening unloading-reloading response for effective stress paths remaining below the phase transformation line (PTL), particularly evident during the first loading cycles, and sharp reduction in stiffness once the phase transformation line is crossed and the effective stress path is reversed. In terms of damping ratio evolution, it appeared that, under this type of loading, the model tends to underestimate slightly the values observed in the laboratory. Nevertheless, a good qualitative agreement between the shape of the damping ratio curves inferred from numerical and experimental data was obtained. Focus was subsequently given to the ability of the constitutive model to replicate the excess pore water pressure generation with the normalised number of loading cycles observed in the laboratory tests. Once more, it was apparent that a better agreement between numerical and experimental data was obtained for moderately loose sand than for dense sand. Moreover, it was observed that the effect of

cyclic stress ratio on the curves obtained from numerical data was more limited than that inferred from experimental data, suggesting that the shearing-induced fabric component may require future improvement. Lastly, the original formulation of the constitutive model was applied to the simulation of drained cyclic triaxial tests, with the purpose of evaluating the ability of the constitutive model to simulate the volumetric strain accumulation with cyclic loading. While a good agreement between numerical and experimental data was obtained during the initial stages of loading (first few loading cycles), it was apparent that the model tended to overpredict slightly the axial and volumetric strains measured in the laboratory experiments during the remaining loading cycles.

To complement the investigation of the ability of the constitutive model to replicate the response of sand observed in element laboratory tests, the available drained and undrained monotonic triaxial extension tests were simulated using the extended formulation, with the obtained results being compared with those previously obtained when using the original formulation of the constitutive model proposed by Taborda *et al.* (2014). In these simulations, only the set of model parameters belonging to the category "Dynamic" were used. Perhaps surprisingly, the obtained results suggested that the use of the extended formulation resulted in only a slight improvement of the modelled response. In effect, a detailed investigation of the response obtained when using the extended formulation revealed that, during the early stages of loading, the reduction in the plastic hardening modulus imposed by the inherent fabric anisotropy tensor was greatly inhibited by an opposite effect of the isotropic part of the shearing-induced fabric tensor. Similarly, it was apparent that very limited improvement was obtained when simulating undrained cyclic triaxial tests using the extended formulation of the constitutive model. Besides the aforementioned opposite effects of the two components on the plastic hardening modulus, it was observed that the slightly softer response in triaxial extension induced by the inherent fabric anisotropy component was counterbalanced by a slightly stiffer response in triaxial compression, suggesting that the impact of the shearing-induced fabric component on the modelled cyclic response is much greater than that of the inherent fabric anisotropy component.

9.5 Application of a bounding surface plasticity model to the simulation of dynamic centrifuge experiments

The final part of the present research (Chapter 8) involved the application of the constitutive model to the simulation of two dynamic centrifuge experiments concerning the performance of shallow foundations built on liquefiable sands deposits subjected to cyclic loading. Note that these centrifuge experiments were performed by the PhD candidate Andreia Silva Marques at the Schofield Centre, University of Cambridge, United Kingdom. Note also that all dimensions and results mentioned in the present text refer to prototype scale. In fact, as reported by Marques *et al.* (2012b, 2012c, 2014a, 2014b, 2015), since a solution of hydroxypropyl methylcellulose in water with a viscosity of about 50 times greater than that

of water was used as pore fluid in centrifuge experiments carried out under a centrifugal acceleration of 50 g, the well-known conflict of scaling laws between dynamic time and diffusion/consolidation time was circumvented, allowing for the direct interpretation of the results in prototype scale. As a result, the numerical simulations were performed in prototype scale, with the obtained results being directly compared with those extrapolated from the experiment. Regarding the configuration of the first centrifuge model – abbreviately designated as CM-A –, two solid steel structures, representing adjacent shallow foundations, were placed on a level, uniform, 18.0 m-thick, saturated deposit of moderately loose Hostun sand (i.e. characterised by $e \approx 0.811$, which corresponds to $D_r \approx 56$ %). Although the contact area between each structure and the underlying sand deposit was similar, the height of the structures was different and, therefore, different vertical stresses were applied by each structure to the underlying sand deposit. In terms of dynamic loading, a sinusoidal-type motion comprising 25 loading cycles with a frequency of 1 Hz (therefore, comprising a total duration of 25 s) and peak accelerations of about ±2.0 – 3.0 m/s^2 was applied at the base of the model. Due to the absence of any technique to mitigate the occurrence of liquefaction, this dynamic centrifuge experiment represented an excellent opportunity for the evaluation of the ability of the newly developed numerical tool to reproduce basic aspects of sand-structure interaction under dynamic loading, as well as the triggering and development of liquefaction. While also focussing on the response of two shallow foundations resting on a level saturated deposit of sand when subjected to a similar motion applied at its base, the second centrifuge model – designated as CM-B – aimed at investigating the use of different techniques to mitigate liquefaction effects. In particular, rather than consisting of a uniform sand deposit, narrow (i.e. having a width only slightly larger than that of the overlying structures) densified zones (characterised by $e \approx 0.657$, which corresponds to $D_r \approx 101$ %) were created in the model. In addition, a drainage geocomposite was used to simulate closely spaced high-capacity vertical drains surrounding the narrow densified sand column created on the left side of the model. It represented, therefore, a great opportunity to evaluate the ability of the numerical tool to reproduce the impact of different liquefaction techniques on the performance of shallow foundations under dynamic loading.

Starting with the first centrifuge model (CM-A), the measured response was firstly described, giving particular attention to the horizontal and vertical acceleration time-histories, as well as excess pore pressure evolution with time registered at several different positions located along three different vertical alignments: two of them coincident with the axes of the shallow foundations and the other one corresponding to the middle of the model (i.e. at half distance from the axes of the two shallow foundations). In addition, the settlements registered in the experiment at the top of the shallow foundations and at the ground surface in between them were presented, followed by the presentation of the ground surface settlement profile at the end of the experiment, inferred from post-test measurements. It was noted that, unfortunately, due to the malfunction of the accelerometer placed at the base of the

centrifuge model, the horizontal acceleration time-history applied to the model during the experiment was not recorded. Nevertheless, since similar motions were reportedly intended to be applied to both centrifuge models (Marques *et al.*, 2014a), the input horizontal motion was estimated based on that recorded in the other centrifuge experiment, as well as on the comparison of the motions recorded at similar positions of the centrifuge container's wall in both experiments. The main aspects of the numerical analysis were subsequently described, including the type of analysis, mesh, time-integration algorithm and time step, boundary conditions, as well as characteristics adopted for the different materials. It was noted that, due to uncertainties concerning the influence of the mesh and time step employed in the dynamic analysis, particularly when simulating liquefaction-related phenomena, a preliminary parametric study on the influence of these aspects was carried out (Appendix D), allowing for the selection of appropriate values for these aspects of the analysis. Particular attention was also given to the generation of the initial stress state, since the 3D configuration of the problem was simplified by performing a 2D plane strain analysis, requiring a correction of the contribution of the shallow foundations to the initial stress state of the sand deposit. The implications arising from this simplification were carefully assessed, assisting the interpretation of the results obtained in the subsequent dynamic analysis. The results obtained in the numerical analysis of CM-A were subsequently compared to those registered in the experiment. It was concluded that the constitutive model was able to capture accurately important aspects of the response, such as the generation of large excess pore pressures with dynamic loading and concurrent alteration of the input motion due to the reduction in stiffness and increase in damping of sand, as well as the progressive accumulation of structural settlement with dynamic loading. Indeed, the agreement between computed and measured settlements during this phase of the analysis was considered very satisfactory, particularly given the complexity of the phenomena involved, the large settlements observed (of about 1.0 m for the heavier shallow foundation), simplifications required in the numerical analysis and the fact that model parameters were solely calibrated against results of element laboratory tests. It was noted, however, that the constitutive model tended to overestimate the increase in excess pore pressures in the zones of the deposit immediately underneath the shallow foundations, probably due to the simplifications required to simulate the 3D configuration of the problem by assuming 2D plane strain geometry. Moreover, it was observed that the constitutive model largely overestimated the rate at which excess pore water pressure dissipates during the consolidation phase, while underpredicting the rate and magnitude of settlements occurring during this phase. As previously suggested by Taborda (2011), this inability was attributed to the open primary yield surface formulation of the constitutive model, which leads to the prediction of solely elastic response under stress paths characterised by approximately constant stress ratios. In addition, it was noted that the type of deformation mechanism observed in the experiment, characterised by a progressive "punch through" and concurrent accumulation of settlement

of the surface of the sand deposit, was not properly captured in the analysis. In effect, the results obtained in the numerical simulation suggested a movement of sand from the zones of the deposit under the influence of the shallow foundations to the zones farther from their influence (sides and middle of the model) during dynamic loading, showing little volumetric change, contrary to the response measured in the experiment. Given these observations, it was argued that this mismatch could be explained by the inability of the numerical tool to predict the occurrence of partly drained response (rather than practically undrained). Indeed, as previously suggested by several authors when inspecting results of similar centrifuge experiments (e.g. Scott, 1986; Coelho, 2007; Taiebat *et al.*, 2007; Andrianopoulos *et al.*, 2010b; Taborda, 2011), it was hypothesised that a temporary increase in the vertical hydraulic conductivity of the liquefied sand deposit in relation to the value of this property measured in conventional laboratory tests (e.g. permeameter tests) during dynamic loading might have occurred in the experiment, at least in the zones of the model farther away from the influence of the shallow foundations, decisively contributing to the occurrence of partly drained response. As an attempt to replicate this aspect, the numerical simulation of CM-A was re-run considering a simple variable hydraulic conductivity model proposed by Taborda (2011), which stipulate a steep increase in this property as large values of the excess pore pressure ratio are reached in the analysis. A considerable improvement of the predicted deformation mechanism was obtained in this analysis, even though the excess pore pressures and structural settlements were substantially less accurate than those obtained in the previous numerical analysis.

Focus was subsequently given to the second centrifuge model, which, as mentioned before, concerned the use of narrow densified zones and high-capacity vertical drains to improve the performance of adjacent shallow foundations subjected to dynamic loading. As for CM-A, the main characteristics of the experiment were firstly described, followed by an interpretation of the experimental results. The main aspects of the numerical analysis of CM-B were described afterwards, giving, in this case, particular emphasis to the methodology used to simulate the drainage geocomposite, which was not employed in CM-A. The methodology and results of the initial stress generation were, also in this case, presented in detail, since a 2D plane strain simplification was, once again, adopted in the numerical analysis. The obtained results were subsequently analysed, leading to the conclusion that, apart from an overprediction of the drainage capacity of the geocomposite, which led to an underprediction of the excess pore pressures generated on the side of the geocomposite, a satisfactory agreement between numerical and experimental data was obtained. Indeed, it was apparent that, once more, the main aspects of the sand-structure interaction observed in the centrifuge experiment were adequately captured by the numerical tool, such as the co-seismic increase in excess pore pressures in both moderately loose and dense sand deposits, resulting in the reduction in stiffness and increase in damping of sand and, consequently, modification of the motion, as well as the accumulation of structural settlements. Moreover, the agreement

between computed and measured rate and magnitude of structural settlements occurring during dynamic loading was considered very satisfactory, particularly given the fact that a single set of model constants solely calibrated against results of element laboratory tests was used to model the response of both moderately loose and dense sand. This suggests that the constitutive model may be successfully employed during the design of geotechnical structures under dynamic loading.

9.6 Recommendations for future research

Although constitutive models based on bounding surface plasticity framework are nowadays implemented into several academic and commercial finite element and finite difference codes, the characterisation of their performance to the simulation of different boundary-value problems is still insufficient or, at least, not widely available in the literature. For instance, it would be important to evaluate the ability of the constitutive relationship to replicate the response of retaining structures, such as sheet pile walls and earth dams, where the horizontal displacements play a key role in the overall performance of the geotechnical structure. Similarly, it would be interesting to apply the constitutive model to other types of dynamic problems, such as those involving traffic- and train-induced vibrations, which are of upmost importance in modern societies, or explosions. This would possibly contribute to the further evaluation of the ability of the constitutive model, while also allowing for the establishment of typical range of values for its model parameters.

Moreover, even though the constitutive model has been particularly developed to address the simulation of cyclic response of sand, it would be interesting to assess its ability to simulate adequately static boundary-value problems. A satisfactory performance under such conditions would certainly contribute to its recurrent use in design practice, which may involve the evaluation of the performance of the structure for both serviceability and ultimate limit states under both static and dynamic loading conditions. For instance, during the design phase of an earth-filled dam, it may be necessary to evaluate its performance for the following two extreme scenarios: (1) occurrence of a rapid drawdown during the operational phase of the dam; and (2) occurrence of an earthquake. Naturally, it would be desirable to use a single constitutive model (preferably with a single set of model parameters), to replicate the construction of the dam, its impoundment, operation phase and, finally, the occurrence of each of the aforementioned extreme situations. Unfortunately, although several constitutive models developed from the original proposal of Manzari and Dafalias (1997) have been shown to be able to capture key aspects of monotonic response of sand and sandy-silt mixtures observed in element laboratory tests (e.g. Dafalias and Manzari, 2004; Dafalias *et al.*, 2004; Loukidis and Salgado, 2009; Taborda, 2011), with a satisfactory performance being also observed in the present study for Hostun sand (Chapter 7), few applications have been reported on its use to the simulation of static boundary-value problems (i.e. problems where change of loading with time is not a primary concern). Indeed, the fact that the constitutive

model was calibrated for Hostun sand in the present study might eventually instigate its more recurrent use, at least for research purposes, since Hostun sand has been often used as model material in centrifuge experiments performed at the University of Cambridge involving not only dynamic loading conditions (e.g. Marques *et al.*, 2014a; Chian *et al.*, 2014; Adamidis and Madabhushi, 2018), but also static loading conditions (e.g. Li and Bolton, 2014).

A significant obstacle to using this constitutive model in current practice resides in the significant complexity and time cost of its calibration process, apart from the need for a significant amount of experimental data. In effect, although the hierarchical approach adopted in the present study allows for an efficient calibration of the material parameters characterising physical features of the modelled response (such as critical state, boundary and dilatancy surfaces, as well as stress-dilatancy relationship), the complexity of the process increases significantly when calibrating the significantly large number of model parameters required by the plastic hardening modulus, as well as by the shearing-induced fabric and inherent fabric anisotropy components, which have no physical meaning. The application of optimisation techniques, such as genetic algorithms (Simpson and Priest, 1993; Taborda *et al.*, 2008; Azeiteiro, 2008; Azeiteiro *et al.*, 2009; Taborda, 2011; Pedro, 2013), at least to the calibration of the plastic-hardening-modulus-related parameters, might reduce the required effort and subjectivity of this stage of the calibration process, therefore contributing to its use in design practice. It should be noted, nevertheless, that, even when employing optimisation techniques, it is of great advantage having well established range of values for each model parameter, since it ensures that physically acceptable values (or, at least, reasonable values) are obtained for the model parameters. Once more, this highlights the need for further calibration of this constitutive model for more materials.

It would be also interesting to evaluate the ability of the extended formulation of the constitutive model to the simulation of hollow cylinder torsional shear tests. Naturally, since a large amount of monotonic and cyclic triaxial test data was obtained in the present study, complemented with bender element test data, the ideal situation would consist of having hollow cylinder test data on Hostun sand available and re-assessing the calibration of the inherent fabric anisotropy component. In such case, it would be interesting to re-run the numerical analysis of the centrifuge experiments to evaluate further the impact of this component on the modelled response. Alternatively, experimental data on Coimbra sand may be used. In fact, as part of a collaborative research programme involving the University of Coimbra, University of Porto and Instituto Superior Técnico of Lisbon, a large amount of experimental data on Coimbra sand was obtained, including bender element, resonant column, oedometer, triaxial and hollow cylinder torsional shear test data (e.g. Santos *et al.*, 2012; Araújo Santos, 2015). Therefore, a step forward in the research previously developed in Portugal may consist of calibrating this constitutive model for Coimbra sand and use it for the evaluation of the performance of geotechnical structures located in Portugal (at least, along Mondego riverbanks) under dynamic loading. Note, however, that, due to the loading

conditions applied in this type of test, the numerical simulation of hollow cylinder torsional shear tests requires the use of a 3D finite element method (or other methods allowing for the simulation of 3D boundary conditions, such as Fourier series aided finite element code – please refer to Potts and Zdravkovic (1999)) and, therefore, further development of FEMEPDYN is still required. It is important, however, to note that a full-3D implementation of the bounding surface plasticity model was performed in the present research, making it suitable to be used by either a 2D or a 3D finite element code.

In addition, the present study highlighted the need for further improvement of the formulation of the constitutive model, to enhance its modelling capabilities. In particular, it seems of upmost importance to improve the modelled response under stress paths characterised by approximately constant stress ratios. As clearly observed when simulating drained isotropic compression tests (Chapter 7), the stiffness of the material is largely overpredicted by the constitutive model under such type of stress path, leading to the underprediction of the observed displacements. Indeed, as observed when simulating centrifuge experiments (Chapter 8), the rate of dissipation of excess pore pressures during the consolidation phase seems to be largely overpredicted, while significantly underpredicting the settlements occurring during this phase. As previously suggested by Taborda (2011), one of the following three different approaches may be adopted: (1) replacement of the current shape of the primary yield surface by a closed shape, as, for instance, included in the BSPM proposed by Taiebat and Dafalias (2008); (2) introduction of an additional yield surface which closes the current yield surface for large values of mean effective stress, as originally proposed by Vermeer (1978) and included in the BSPM developed by Li (2002) and Gao and Zhao (2015); (3) introduction of a nonlinear degradation of the secant bulk modulus with volumetric strain to complement the degradation of secant shear stiffness with shear strain, as proposed, for example, by Jardine *et al.* (1986).

Moreover, it was shown in Chapter 6 and Chapter 7 that, although introduced to address the simulation of cyclic loading, the shearing-induced fabric component of the constitutive model may detrimentally affect the ability of the constitutive model to replicate the early stages of the monotonic response of loose and moderately loose sand (typically exhibiting a tendency to contract during the early stages of shearing). Furthermore, it was shown in Chapter 7 that this component, as it is currently formulated, partly inhibits the effect of the inherent fabric anisotropy component on the modelled response by imposing an increase in the plastic hardening modulus during contractive phases of the modelled response, counterbalancing the reduction in this model quantity imposed by the inherent fabric anisotropy component. A possible strategy to solve this apparent incompatibility may consist of developing a new formulation for the shearing-induced fabric component based on strain-energy-related principles (e.g. dissipated energy per unit volume), since, in such case, the shearing-induced fabric tensor should have little or no impact on the modelled monotonic response, while playing a key role in cyclic response, as intended. Note that this component of the formulation

is crucial to the accurate simulation of cyclic response, as demonstrated by fact that the great majority of the BSPM develop to address the simulation of cyclic loading include a shearing-induced fabric component in its formulation, either affecting the plastic hardening modulus (e.g. Papadimitriou and Bouckovalas, 2002; Andrianopoulos *et al.*, 2010b; Taborda, 2011) or the dilatancy coefficient (e.g. Dafalias and Manzari, 2004; Gao and Zhao, 2015). On the other hand, the inherent fabric component extends the ability of the constitutive model, enabling, for instance, to capture the effect of direction of the major principal effective stress to the vertical axis of the sample on the modelled response of sand, as observed in hollow cylinder torsional shear tests (e.g. Dafalias and Manzari, 2004; Loukidis and Salgado, 2009; Li and Dafalias, 2012; Williams, 2014; Woo and Salgado, 2015; Gao and Zhao, 2015).

Still regarding the coupling between the shearing-induced fabric and inherent fabric anisotropy components of the model, it was shown in Chapter 6 and Chapter 7 that, contrary to the initial expectations, the introduction of the latter component into the formulation of the constitutive model was not sufficient to improve significantly the ability of the constitutive relationship to simulate undrained cyclic triaxial tests where samples exhibited a very soft response in triaxial extension during the first loading cycle, leading to the occurrence of cyclic mobility in just a very few (1 to 4) loading cycles. In effect, besides the aforementioned counterbalancing effects of the shearing-induced fabric and inherent fabric anisotropy components during the contractive phases of the modelled response, it was clear that the influence of the latter component on the simulation of cyclic response is significantly smaller than that exerted by the former component. This suggests that the contribution of the two components to the plastic hardening modulus need to be reformulated in the future. Alternatively, since both aspects are related to the effect of the orientation of the particles (or of the voids) and their evolution during loading on the modelled response, as postulated in Li and Dafalias (2012), it may be preferable to replace these two components by a single one, which can concurrently capture the aspects currently simulated by both components. Indeed, this may require significant research effort, particularly due to the experimental difficulties in measuring sand fabric and its evolution with cyclic loading, with numerical methods (such as discrete element methods) being generally used to provide a micromechanical description of the phenomena (e.g. Yimsiri and Soga, 2001, 2010).

REFERENCES

Abu-Farsakh, M., Coronel, J. and Tao, M. (2007). Effect of soil moisture content and dry density on cohesive soil-geosynthetic interactions using large direct shear tests. *Journal of Materials in Civil Engineering, ASCE*, **19** (7), 540–549.

Adamidis, O. and Madabhushi, S.P.G. (2015). Use of viscous pore fluids in dynamic centrifuge modelling. *International Journal of Physical Modelling in Geotechnics*, **15** (3), 141–149.

Adamidis, O. and Madabhushi, S.P.G. (2018). Deformation mechanisms under shallow foundations on liquefiable layers of varying thickness. *Géotechnique*, **68** (7), 602–613.

Alarcon-Guzman, A., Leonards, G.A. and Chameau, J.L. (1988). Undrained monotonic and cyclic strength of sands. *Journal of Geotechnical Engineering, ASCE*, **114** (10), 1089–1109.

Almeida e Sousa, J.N.V. (1999). *Tunnels in soil: behaviour and numerical modelling*. PhD thesis. University of Coimbra, Coimbra (in Portuguese).

Alshibli, K., Godbold, D. and Hoffman, K. (2004). The Louisiana plane strain apparatus for soil testing. *Geotechnical Testing Journal*, **27** (4), 337–346.

Alvarado, G. (2007). *Influence of late cementation on the behaviour of reservoir sands*. PhD thesis. Imperial College London, London.

Alvarado, G. and Coop, M.R. (2007). Influence of stress level in bender element performance for triaxial tests. *Proceedings of 4th International Conference on Earthquake Geotechnical Engineering*, Thessaloniki, Greece, 25-28 June 2007, paper no. 1419.

Alvarado, G. and Coop, M.R. (2012). On the performance of bender elements in triaxial tests. *Géotechnique*, **62** (1), 1–17.

Andrianopoulos, K.I., Papadimitriou, A.G. and Bouckovalas, G.D. (2010a). Bounding surface plasticity model for the seismic liquefaction analysis of geostructures. *Soil Dynamics and Earthquake Engineering*, **30** (10), 895–911.

Andrianopoulos, K.I., Papadimitriou, A.G. and Bouckovalas, G.D. (2010b). Explicit integration of bounding surface model for the analysis of earthquake soil liquefaction. *International Journal for Numerical and Analytical Methods in Geomechanics*, **34** (15), 1586–1614.

Araújo Santos, L.M. (2015). *Characterisation of the mechanical behaviour of Coimbra sand under generalised load conditions*. PhD thesis. University of Coimbra, Coimbra (in Portuguese).

Argyris, J.H., Faust, G., Szimmat, J., Warnke, E.P., *et al.* (1974). Recent developments in the finite element analysis of prestressed concrete reactor vessels. *Nuclear Engineering and Design*, **28** (1), 42–75.

Arroyo, M., Muir Wood, D. and Greening, P.D. (2003). Source near-field effects and pulse tests in soil samples. *Géotechnique*, **53** (3), 337–345.

Arroyo, M., Muir Wood, D., Greening, P.D., Medina, L., et al. (2006). Effects of sample size on bender-based axial G_0 measurements. *Géotechnique*, **56** (1), 39–52.

Arulanandan, K. and Scott, R.F. (eds.) (1993). *Verification of numerical procedures for the*

analysis of soil liquefaction problems. Proceedings of the International Conference, Davis, California, U.S., 17-20 October 1993. Rotterdam, the Netherlands, CRC Press/Balkema.

Arulmoli, K., Muraleetharan, K.K., Hossain, M.M. and Fruth, L.S. (1992). *VELACS: Verifications of Liquefaction Analyses by Centrifuge Studies. Laboratory Testing Program. Soil Data Report*. The Earth Technology Corporation. Earth Technology Project No. 90-0562.

ASTM International (2002). *ASTM D854-02: Standard test methods for specific gravity of soil solids by water pycnometer*. West Conshohocken, PA.

ASTM International (2006a). *ASTM D4253-00: Standard test methods for maximum index density and unit weight of soils using a vibratory table*. West Conshohocken, PA.

ASTM International (2006b). *ASTM D4254-00: Standard test methods for minimum index density and unit weight of soils and calculation of relative density*. West Conshohocken, PA.

Azeiteiro, R.J.N. (2008). *Application of Genetic Algorithms to the calibration of constitutive models for soils*. MSc thesis. University of Coimbra, Coimbra (in Portuguese).

Azeiteiro, R.J.N., Coelho, P.A.L.F., Taborda, D.M.G. and Grazina, J.C. (2015) Dissipated energy in undrained cyclic triaxial tests. *Proceedings of the 6th International Conference on Earthquake Geotechnical Engineering*, Christchurch, New Zealand, 1-4 November 2015, paper no. 220.

Azeiteiro, R.J.N., Coelho, P.A.L.F., Taborda, D.M.G. and Grazina, J.C.D. (2017a). *Critical state-based interpretation of the monotonic behavior of Hostun sand*. **20** (20), 1–14.

Azeiteiro, R.J.N., Coelho, P.A.L.F., Taborda, D.M.G. and Grazina, J.C.D. (2017b). Energy-based evaluation of liquefaction potential under non-uniform cyclic loading. *Soil Dynamics and Earthquake Engineering*, **92** (1), 650–665.

Azeiteiro, R.N., Coelho, P.A.L.F., Taborda, D.M.G., Pedro, A., *et al.* (2009). Computational study of the performance of a Genetic Algorithms-based-software. *Proceedings of the 1st International Symposium on Computational Geomechanics,* Juan-les-Pins, Cote d'Azur, France, 29 April – 1 May 2009.

Azeiteiro, R.J.N., Marques, V.D. and Coelho, P.A.L.F. (2012) Effect of singular peaks in uniform cyclic loading on the liquefaction resistance of a sand. *Proceedings of the 2nd International Conference on Performance-Based Design in Earthquake Geotechnical Engineering,* Taormina, Italy, 28–30 May 2012, paper no. 6.13.

Baldi, G. and Nova, R. (1984). Membrane Penetration Effects in Triaxial Testing. *Journal of Geotechnical Engineering, ASCE*, **110** (3), 403–420.

Baziar, M.H. and Sharafi, H. (2011). Assessment of silty sand liquefaction potential using hollow torsional tests - an energy approach. *Soil Dynamics and Earthquake Engineering*, **31** (7), 857–865.

Bathe, K.-J. (1996). *Finite element procedures*. New Jersey, U.S., Prentice-Hall.

Been, K., Crooks, J.H.A., Becker, D.E. and Jefferies, M.G. (1986). The cone penetration test in sands: part I, state parameter interpretation. *Géotechnique*, **36** (2), 239–249.

Been, K. and Jefferies, M.G. (1985). A state parameter for sands. *Géotechnique*, **35** (2), 99–112.

Been, K. and Jefferies, M.G. (2004). Stress-dilatancy in very loose sand. *Canadian geotechnical journal*, **41** (5), 972–989.

Been, K., Jefferies, M.G. and Hachey, J. (1991). The critical state of sands. *Géotechnique*, **41** (3), 365–381.

Been, K., Lingnau, B.E., Crooks, J.H.A. and Leach, B. (1987). Cone penetration test calibration for Erksak (Beaufort Sea) sand. *Canadian Geotechnical Journal*, **24**601–610.

Benahmed, N. (2001). *Comportement mécanique d'un sable sous cisaillement monotone et cyclique : application aux phénomènes de liquéfaction et de mobilité cyclique*. PhD thesis. École Nationale des Ponts et Chaussées (ENPC), Paris (in French).

Benahmed, N., Canou, J. and Dupla, J.-C. (2004). Initial structure and static liquefaction properties of sand. *Comptes Rendus Mécanique*, **332** (11), 887–894.

Benz, T. (2007). *Small-Strain Stiffness of Soils and its Numerical Consequences Small-Strain Stiffness of Soils and its Numerical Consequences*. PhD thesis. Institut für Geotechnik, Universität Stuttgart, Stuttgart.

Berrill, J.B. and Davis, R.O. (1985). Energy dissipation and seismic liquefaction of sands: revised model. *Soils and Foundations*, **25** (2), 106–118.

Bianchini, G., Puccini, P. and Saada, A.S. (1989) Information package. In: A.S. Saada and G. Bianchini (eds.). *Constitutive equations for granular non-cohesive soils. Proceedings of the International Workshop on Constitutive Equations for Granular Non-cohesive Soils, Cleveland, U.S., 22-24 July 1987.* Rotterdam, the Netherlands, CRC Press/Balkema.

Bianchini, G., Saada, A., Puccini, P., Lanier, J., et al. (1991). Complex stress paths and validation of constitutive models. *Geotechnical Testing Journal*, **14** (1), 13–25.

Bishop, A.W. and Wesley, L.D. (1975). A hydraulic triaxial apparatus for controlled stress path testing. *Géotechnique*, **25** (4), 657–670.

Bishop, A.W.A. and Henkel, D.J.D. (1962) *The measurement of soil properties in the triaxial test*. Second Edi. Edward Arnold.

Blewett, J., Blewett, I.J. and Woodward, P.K. (2000). Phase and amplitude responses associated with the measurement of shear-wave velocity in sand by bender elements. *Canadian Geotechnical Journal*, **37**1348–1357.

Booker, J.R., Rahman, M.S. and Seed, H.B. (1976). *GADFLEA – A computer program for the analysis of pore pressure generation and dissipation during cyclic or earthquake loading.* Earthquake Engineering Research Center, University of California, Berkeley, California. Report EERC 76-24.

Borja, R.I. (1991). Cam-Clay plasticity, Part II: Implicit integration of constitutive equation based on a nonlinear elastic stress predictor. *Computer Methods in Applied Mechanics and Engineering*, **88** (2), 225–240.

Borja, R.I. and Lee, S.R. (1990). Cam-Clay plasticity, Part I: Implicit integration of elasto-plastic constitutive relations. *Computer Methods in Applied Mechanics and Engineering*, **78** (1), 49–72.

Borja, R.I., Lin, C.H. and Montáns, F.J. (2001). Cam-clay plasticity, Part IV: Implicit integration of anisotropic bounding surface model with nonlinear hyperelasticity and ellipsoidal

loading function. *Computer Methods in Applied Mechanics and Engineering*, **190** (26–27), 3293–3323.

Borja, R.I., Sama, K.M. and Sanz, P.F. (2003). On the numerical integration of three- invariant elastoplastic constitutive models. *Computer Methods in Applied Mechanics and Engineering*, **192** (9–10), 1227–1258.

Boulanger, R.W. and Idriss, I.M. (2014). *CPT and SPT based liquefaction triggering procedures.* University of California, Davis, California. Report UCD/CGM-14/01.

Bowles, J.E. (1996) *Foundation Analysis and Design*. 5th Edition. New York, McGraw-Hill.

Brinkgreve, R.B.J., Zampich, L.M. and Ragi Manoj, N. (2019). *PLAXIS 2D Reference manual – CONNECT Edition V20*. Delft, the Netherlands, Plaxis bv.

Byrne, P.M., Puebla, H., Chan, D.H., Soroush, A., et al. (2000). CANLEX full-scale experiment and modelling. *Canadian Geotechnical Journal*, **37** (3), 543–562.

Büttner, J. and Simeon, B. (2002). Runge-Kutta methods in elastoplasticity. *Applied Numerical Mathematics*, **41** (4), 443–458.

Camacho-Tauta, J.F., Cascante, G., Viana da Fonseca, A. and Santos, J.A. (2015). Time and frequency domain evaluation of bender element systems. *Géotechnique*, **65** (7), 548–562.

Carothers, S.D. (1920). Plane strain: the direct determination of stress. *Proceedings of the Royal Society A: Mathematical, Physical and Engineering Sciences*, **97** (4), 110–123.

Carraro, J.A.H., Bandini, P. and Salgado, R. (2003). Liquefaction Resistance of Clean and Nonplastic Silty Sands Based on Cone Penetration Resistance. *Journal of Geotechnical and Geoenvironmental Engineering, ASCE*, **129** (11), 965–976.

Carrier III, W.D. (2003). Goodbye, Hazen; Hello, Kozeny-Carman. *Journal of Geotechnical and Geoenvironmental Engineering, ASCE*, **129** (11), 1054–1056.

Carriglio, F., Ghionna, V.N., Jamiolkowski, M. and Lancellotta, R. (1990). Stiffness and penetration resistance of sands versus state parameter. *Journal of Geotechnical Engineering, ASCE*, **116** (6), 1015–1020.

Casagrande, A. (1975). Liquefaction and cyclic deformations of sands: a critical review. *Proceedings of the 5th Panamerican Conference on Soil Mechanics and Foundation Engineering*, Buenos Aires, Argentina, 17-22 November 1975, pp. 80-133.

Castro, G. (1969). *Liquefaction of sands*. PhD thesis. Harvard University, Cambridge.

Chaudhary, S.K., Kuwano, J. and Hayano, Y. (2004). Measurement of quasi-elastic stiffness parameters of dense Toyoura sand in hollow cylinder apparatus and triaxial apparatus with bender elements. *Geotechnical Testing Journal*, **27** (1), 23–35.

Chian, S.C., Tokimatsu, K. and Madabhushi, S.P.G. (2014). Soil liquefaction–induced uplift of underground structures: physical and numerical modeling. *Journal of Geotechnical and Geoenvironmental Engineering, ASCE*, **140** (10), 1-18.

Cho, G.-C., Dodds, J. and Santamarina, J.C. (2006). Particle shape effects on packing density, stiffness and strength: natural and crushed sands. *Journal of Geotechnical and Geoenvironmental Engineering, ASCE*, **132** (5), 591–602.

Chung, J. and Hulbert, G.M. (1993). A time integration algorithm for structural dynamics with improved numerical dissipation: the generalized-α method. *Journal of Applied Mechanics*, **60** (2), 371.

Clayton, C.R.I. (2011). Stiffness at small strain: research and practice. *Géotechnique*, **61** (1), 5–37.

Clayton, C.R.I. and Heymann, G. (2001). Stiffness of geomaterials at very small strains. *Géotechnique*, **51** (3), 245–255.

Clayton, C.R.I., Theron, M. and Best, A.I. (2004). The measurement of vertical shear-wave velocity using side-mounted bender elements in the triaxial apparatus. *Géotechnique*, **54** (7), 495–498.

Coelho, P.A.L.F. (2007). *In situ densification as a liquefaction resistance measure for bridge foundations*. PhD thesis. University of Cambridge, Cambridge.

Coelho, P.A.L.F., Azeiteiro, R.J.N., Costa, A.L.D., Marques, A.S.P.S., *et al.* (2017). Effects of earthquake-induced liquefaction: Integrated research tools towards optimum reduction of society vulnerability. *Proceedings of the 19th International Conference on Soil Mechanics and Geotechnical Engineering*, Seoul, 17-21 September 2017, pp. 1501-1504.

Coelho, P.A.L.F., Azeiteiro, R.J.N., Marques, V.D., Santos, L.M.A., *et al.* (2013). Challenges to the laboratory evaluation of field liquefaction resistance. *Proceedings of the 18th International Conference on Soil Mechanics and Geotechnical Engineering*, Paris, 2-6 September 2013, pp. 1459-1462.

Coelho, P.A.L.F., Haigh, S.K. and Madabhushi, S.P.G. (2003). Boundary Effects in Dynamic Centrifuge Modelling of liquefaction in sand deposits. *Proceedings of the 16th ASCE Engineering Mechanics Conference*, University of Washington, Seattle, U.S., 16-18 July 2002.

Coelho, P.A.L.F., Viggiani, G., Pastor, M. and Lenart, S. (2010). *TA project: Shallow foundations exposed to seismic liquefaction: a centrifuge-based study on the level and mitigation of the effects*. Seismic Engineering Research Infrastructures for European Synergies. European Commission. Framework programme 7. Report.

Crisfield, M.A. (1991) *Non-linear finite element analysis of solids and structures*. 1st Edition. Chichester, West Sussex, U.K., Wiley.

Dafalias, Y.F. (1986). Bounding surface plasticity. I: Mathematical foundation and hypoplasticity. *Journal of Engineering Mechanics, ASCE*, **112** (9), 966–987.

Dafalias, Y.F. and Manzari, M.T. (2004). Simple plasticity sand model accounting for fabric change effects. *Journal of Engineering Mechanics, ASCE*, **130** (6), 622–634.

Dafalias, Y.F., Papadimitriou, A.G. and Li, X.S. (2004). Sand plasticity model accounting for inherent fabric anisotropy. *Journal of Engineering Mechanics, ASCE*, **130** (11), 1319–1333.

Dafalias, Y.F., Papadimitriou, A.G., Li, X.S. and Manzari, M.T. (2006). Generic Constitutive Ingredients in CSSM Models for Sands. In: Wu W., Yu HS. (eds). *Modern Trends in Geomechanics. Springer Proceedings in Physics*, vol 106, Berlin, Springer.

Dafalias, Y.F. and Popov, E.P. (1975). A model of nonlinearly hardening materials for complex

loading. *Acta Mechanica*, **21** (3), 173–192.

Darendeli, M.B. (2001). *Development of a new family of normalized modulus reduction and material damping curves*. PhD Thesis. University of Texas, Austin.

Davis, R.O. and Berrill, J.B. (1982). Energy dissipation and seismic liquefaction in sands. *Earthquake Engineering and Structural Dynamics*, **10**59–68.

Davis, R.O. and Berrill, J.B. (2001). Pore Pressure and Dissipated Energy in Earthquakes - Field Verification. *Journal of Geotechnical and Geoenvironmental Engineering, ASCE*, **127**269–274.

De Alba, P., Chan, C.K. and Seed, H.B. (1975). *Determination of soil liquefaction characteristics by large laboratory tests.* Earthquake Engineering Research Center, University of California, Berkeley, California. Report EERC 75-14.

De Gennaro, V., Canou, J., Dupla, J.C. and Benahmed, N. (2004). Influence of loading path on the undrained behaviour of a medium loose sand. *Canadian Geotechnical Journal*, **41** (1), 166–180.

Desrues, J. (1998). Localisation Patterns in Ductile and Brittle Geomaterials. In: de Borst, R. and van der Giessen, E. (eds.). *Material instabilities in solids*. New York, U.S., Wiley.

Desrues, J. (2013). *ALERT 2007 database on strain localisation in tests on Hostun sand : full experimental data sets of biaxial and triaxial tests.* Access to the database (personal communication, 5th June 2013).

Desrues, J., Chambon, R., Mokni, M. and Mazerolle, F. (1996). Void ratio evolution inside shear bands in triaxial sand specimens studied by computed tomography. *Géotechnique*, **46** (3), 529–546.

Desrues, J. and Georgopoulos, I.-O. (2006). An investigation of diffuse failure modes in undrained triaxial tests on loose sand. *Soils and Foundations*, **46** (5), 585–594.

Desrues, J., Lanier, J. and Stutz, P. (1985). Localization of the deformation in tests on sand sample. *Engineering fracture mechanics*, **21** (4), 909–921.

Desrues, J. and Viggiani, G. (2004). Strain localization in sand: an overview of the experimental results obtained in Grenoble using stereophotogrammetry. *International Journal for Numerical and Analytical Methods in Geomechanics*, **28** (4), 279–321.

Dief, H.M. and Figueroa, J.L. (2007). Liquefaction assessment by the unit energy concept through centrifuge and torsional shear tests. *Canadian Geotechnical Journal*, **44** (11), 1286–1297.

Doanh, T., Dubujet, P. and Protière, X. (2012). On the undrained strain-induced anisotropy of loose sand. *Acta Geotechnica*, **8** (3), 293–309.

Doanh, T. and Ibraim, E. (2000). Minimum undrained strength of Hostun RF sand. *Géotechnique*, **50** (4), 377–392.

Doanh, T., Ibraim, E. and Matiotti, R. (1997). Undrained instability of very loose Hostun sand in triaxial compression and extension. Part 1: experimental observations. *Mechanics of cohesive-frictional materials*, **2** (1), 47–70.

Dobry, R., Ladd, R.S., Yokel, F.Y., Chung, R.M., *et al.* (1982). *Prediction of pore water pressure buildup and liquefaction of sands during earthquakes by the cyclic strain method*.

Commerce Department, National Institute of Standards and Technology (NIST), Series 138.

Dowell, M. and Jarratt, P. (1972). The 'Pegasus' method for computing the root of an equation. *BIT Numerical Mathematics*, **12** (4), 503–508.

Dubujet, P. and Doanh, T. (1997). Undrained instability of very loose Hostun sand in triaxial compression and extension. Part 2: theoretical analysis using an elastoplasticity model. *Mechanics of cohesive-frictional materials*, **2** (1), 71–92.

Dyvik, R. and Madshus, C. (1985). Lab measurements of Gmax using bender elements. *Proceedings of the ASCE Annual Convention, Advances in the Art of Testing Soils under Cyclic Conditions*, Detroit, Michigan, U.S., 24 October 1985.

E-Kan, M. and Taiebat, H.A. (2014). On implementation of bounding surface plasticity models with no overshooting effect in solving boundary value problems. *Computers and Geotechnics*, **55**, 103–116.

Elgamal, A., Yang, Z., Lai, T., Kutter, B.L., et al. (2005). Dynamic Response of Saturated Dense Sand in Laminated Centrifuge Container. *Journal of Geotechnical and Geoenvironmental Engineering, ASCE*, **131** (5), 598–609.

Escribano, D.E. and Nash, D.F.T. (2015). Changing anisotropy of G0 in Hostun sand during drained monotonic and cyclic loading. *Soils and Foundations*, **55** (5), 974–984.

Ezaoui, A., Benedetto, H. Di and Bang, D. Van (2007). Anisotropic Behaviour of Sand in the Small Strain Domain. Experimental Measurements and Modelling. In: Ling H.I., Callisto L., Leshchinsky D., Koseki J. (eds). *Soil stress-strain behavior: measurement, modeling and analysis. Solid mechanics and its applications*, vol 146. Dordrecht, the Netherlands, Springer.

Figueroa, J.L., Saada, A.S., Liang, L. and Dahisaria, N.M. (1994). Evaluation of soil liquefaction by energy principles. *Journal of Geotechnical Engineering, ASCE*, **120** (9), 1554–1569.

Finge, Z., Doanh, T. and Dubujet, P. (2006). Undrained anisotropy of Hostun RF loose sand: new experimental investigations. *Canadian Geotechnical journal*, **43** (11), 1195–1212.

Finn, W.D.L., Pickering, D.J. and Bransby, P.L. (1971). Sand liquefaction in triaxial and simple shear tests. *Journal of the Soil Mechanics and Foundations Division, ASCE*, **97** (4), 639–659.

Fioravante, V. (2000). Anisotropy of small strain stiffness of Ticino and Kenya sands from seismic wave propagation measured in triaxial testing. *Soils and Foundations*, **40** (4), 129–142.

Flavigny, E., Desrues, J. and Palayer, B. (1990). Le sable d'Hostun «RF». *Revue française de géotechnique*, **53**, 67-70.

Gajo, A. and Wood, M.D. (1999). Severn–Trent sand: a kinematic-hardening constitutive model: the *q* – *p* formulation. *Géotechnique*, **49** (5), 595–614.

Gao, Z. and Zhao, J. (2015). Constitutive modeling of anisotropic sand behavior in monotonic and cyclic loading. *Journal of Engineering Mechanics, ASCE*, **141** (8), 04015017.

GiD (2002). *GiD 7.2 – The universal, adaptive and user-friendly pre- and post- processing system for computer analysis in science and engineering*. Available from:

http://www.gidhome.com/.

Giroud, J.-P. (1970). Stresses under linearly loaded rectangular area. *Journal of the Soil Mechanics and Foundations Division, ASCE*, **96** (1), 263–268.

Goodman, R.E., Taylor, R.L. and Brekke, T.L. (1968). A model for the mechanics of jointed rock. *Journal of the Soil Mechanics and Foundations Division, ASCE*, **94** (3), 637–659.

Grazina, J.C. (2009). *Dynamic modelling of elastoplastic soil deposits with viscous-coupled behaviour. Application to flexible retaining walls under seismic loading*. PhD thesis. University of Coimbra, Coimbra (in Portuguese).

Haigh, S.K., Ghosh, B. and Madabhushi, S.P.G. (2005). Importance of time step discretisation for nonlinear dynamic finite element analysis. *Canadian Geotechnical Journal*, **42** (3), 957–963.

Han, B., Zdravkovic, L., Kontoe, S. and Taborda, D.M.G. (2016). Numerical investigation of the response of the Yele rock fill dam during the 2008 Wenchuan earthquake. *Soil Dynamics and Earthquake Engineering*, **88** (9), 124–142.

Hardin, B.O. (1965). Dynamic versus static shear modulus for dry sand. *Materials Research and Standards*, **5** (5), 232–235.

Hardin, B.O. (1978). The nature of stress-strain behavior for soils. *Proceedings of Earthquake Engineering and Soil Dynamics, ASCE*, Pasadena, 19-21 June 1978, pp. 3-89.

Hardin, B.O. and Black, W.L. (1966). Sand stiffness under various triaxial stresses. *Journal of the Soil Mechanics and Foundations Division, ASCE*, **92** (2), 27–42.

Hardin, B.O. and Black, W.L. (1968). Vibration modulus of normally consolidated clay. *Journal of the Soil Mechanics and Foundations Division, ASCE*, **94** (SM 2), 353–369.

Hardin, B.O. and Drnevich, V.P. (1972a). Shear modulus and damping in soils: design equations and curves. *Journal of the Soil Mechanics and Foundations Division, ASCE*, **98** (SM7), 667–692.

Hardin, B.O. and Drnevich, V.P. (1972b). Shear modulus and damping in soils: measurement and parameter effects. *Journal of the Soil Mechanics and Foundations Division, ASCE*, **98** (SM6), 603–624.

Hardin, B.O. and Richart, F.E. (1963). Elastic wave velocities in granular soils. *Journal of the Soil Mechanics and Foundations Division, ASCE*, **89** (1), 33–65.

Hardy, S. (2003). *The implementation and application of dynamic finite element analysis to geotechnical problems*. PhD thesis. Imperial College London, London.

Head, K.H. (1994). *Manual of soil laboratory testing. Volume 2: permeability, shear strength and compressibility tests*. Second edition. New York, U.S., Wiley.

Head, K.H. (1998). *Manual of soil laboratory testing. Volume 3: effective stress tests*. Second edition. Chichester, West Sussex, U.K., Wiley.

Hiley, R.A. and Rouainia, M. (2008). Explicit Runge-Kutta methods for the integration of rate-type constitutive equations. *Computational Mechanics*, **42** (1), 53–66.

Hong, P.Y., Pereira, J.M., Cui, Y.J. and Tang, A.M. (2012). Explicit integration of a thermo-mechanical model for clays. *Computers and Geotechnics*, **46**, 13–25.

Hoque, E. (2005). Elasto-plastic deformation of hostun sand during cyclic loading in triaxial test. *Journal - The Institution of Engineers, Malaysia*, **66** (1), 13–18.

Hoque, E. and Tatsuoka, F. (2000). Kinematic elasticity of a granular material. *Proceedings of ISRM International Symposium*, Melbourne, Australia, 19-24 November 2000.

Hosono, Y. and Yoshimine, M. (2004). Liquefaction of sand in simple shear condition. In: Triantafyllidis, T. (ed.). *Cyclic behaviour of soils and liquefaction phenomena*. *Proceedings of the International Conference,* Bochum, Germany, 31 March - 2 April 2004. CRC Press.

Houlsby, G.T., Amorosi, A. and Rojas, E. (2005). Elastic moduli of soils dependent on pressure: a hyperelastic formulation. *Géotechnique*, **55** (5), 383–392.

Hueckel, T. and Nova, R. (1979). Some hysteresis effects of the behaviour of geologic media. *International Journal of Solids and Structures*, **15** (8), 625–642.

Ibraim, E., Christiaens, P. and Pope, M. (2011). Development of A hollow cylinder torsional apparatus for pre-failure deformation and large strains behaviour of sand. *Geotechnical Engineering Journal of the SEAGS & AGSSEA, Special Issue on Soil Behaviour*, **42**, 58-68.

Idriss, I.M. and Boulanger, R.W. (2006). Semi-empirical procedures for evaluating liquefaction potential during earthquakes. *Soil Dynamics and Earthquake Engineering*, **26** (2–4), 115–130.

Ishibashi, I. and Zhang, X. (1993). Unified dynamic shear moduli and damping ratios of sand and clay. *Soils and Foundations*, **33** (1), 182–191.

Ishihara, K. (1993). Liquefaction and flow failure during earthquakes. *Géotechnique*, **43** (3), 351–451.

Ishihara, K. (1996) *Soil behaviour in earthquake geotechnics*. Oxford, Oxford University Press.

Ishihara, K. and Li, S.-I. (1972). Liquefaction of saturated sand in triaxial torsional shear test. *Soils and Foundations*, **12** (2), 19-39.

Ishihara, K. and Takatsu, H. (1979). Effects of overconsolidation and K0 conditions on the liquefaction characteristics of sands. *Soils and Foundations*, **19** (4), 59–68.

Ishihara, K., Tatsuoka, F. and Yasuda, S. (1975). Undrained deformation and liquefaction of sand under cyclic stresses. *Soils and Foundations*, **15** (1), 29–44.

Ishihara, K. and Yasuda, S. (1972). Sand liquefaction due to irregular excitation. *Soils and foundations*, **12** (4), 65-77.

Ishihara, K. and Yasuda, S. (1975). Sand liquefaction in hollow cylinder torsion under irregular excitation. *Soils and Foundations*, **15** (1), 45-59.

Iwasaki, T., Tatsuoka, F. and Takagi, Y. (1978). Shear moduli of sand under cyclic torsional shear loading. *Soils and Foundations*, **18** (1), 39–56.

Jafarzadeh, F., Javaheri, H., Sadek, T. and Muir Wood, D. (2008). Simulation of anisotropic deviatoric response of Hostun sand in true triaxial tests. *Computers and Geotechnics*, **35** (5), 703–718.

Jardine, R.J., Potts, D.M., Fourie, A.B. and Burland, J.B. (1986). Studies of the influence of non-linear stress–strain characteristics in soil–structure interaction. *Géotechnique*, **36** (3), 377–396.

Jefferies, M.G. (1993). Nor-Sand: a simple critical state model for sand. *Géotechnique*, **43** (1), 91–103.

Jefferies, M.G. and Been, K. (2006). *Soil liquefaction. A critical state approach*. 1st edition, London, CRC Press.

Jeremic, B., Cheng, Z., Taiebat, M. and Dafalias, Y.F. (2008). Numerical simulation of fully saturated porous media. *International Journal for Numerical and Analytical Methods in Geomechanics*, **32** (13), 1635–1660.

Jovičić, V., Coop, M.R. and Simić, M. (1996). Objective criteria for determining Gmax from bender element tests. *Géotechnique*, **46** (2), 357–362.

Klotz, E.U. and Coop, M.R. (2001). An investigation of the effect of soil state on the capacity of driven piles in sands. *Géotechnique*, **51** (9), 733–751.

Klotz, E.U. and Coop, M.R. (2002). On the identification of critical state lines for sands. *Geotechnical Testing Journal*, **25** (3), 1-14.

Kokusho, T. (1980). Cyclic triaxial test of dynamic soil properties for wide strain range. *Soils and Foundations*, **20** (2), 56–60.

Kokusho, T. (2013). Liquefaction potential evaluations: energy-based method versus stress-based method. *Canadian Geotechnical Journal*, **50** (9), 1088–1099.

Konrad, J.-M. (1993). Undrained response of loosely compacted and cyclic compression sands during monotonic tests. *Géotechnique*, **43** (1), 69–89.

Konrad, J.-M. (1998). Sand state from cone penetrometer tests: a framework considering grain crushing stress. *Géotechnique*, **48** (2), 201–215.

Konrad, J.-M., Flavigny, E. and Meghachou, M. (1991). Comportement non drainê du sable d'Hostun lâche. *Revue française de géotechnique*, **54**, 53–64.

Kontoe, S. (2006). *Development of time integration schemes and advanced boundary conditions for dynamic geotechnical analysis*. PhD thesis. Imperial College London, London.

Kontoe, S., Zdravković, L., Potts, D.M. and Menkiti, C.O. (2011). On the relative merits of simple and advanced constitutive models in dynamic analysis of tunnels. *Geotechnique*, **61** (10), 815–829.

Kramer, S.L. (1996) *Geotechnical earthquake engineering*. New Jersey, Prentice-Hall.

Krieg, R.D. (1975). A practical two surface plasticity theory. *Journal of Applied Mechanics*, **42** (3), 641-646.

Kuhlemeyer, R.L. and Lysmer, J. (1973). Finite element method accuracy for wave propagation problems. *Journal of the Soil Mechanics and Foundations Division, ASCE*, **99** (5), 421–427.

Kuwano, R. and Jardine, R.J. (2002). On the applicability of cross-anisotropic elasticity to granular materials at very small strains. *Géotechnique*, **52** (10), 727–749.

La Rochelle, P., Leroueil, S., Trak, B., Blais-Leroux, L., *et al*. (1988). Observational approach to membrane and area corrections in triaxial tests. In: Donaghe, R., Chaney, R., and Silver, M. (eds.). *Advanced Triaxial Testing of Soil and Rock*, West Conshohocken, PA, ASTM International, pp. 715–731.

Lade, P.V. (2006). Assessment of test data for selection of 3-D failure criterion for sand. *International Journal for Numerical and Analytical Methods in Geomechanics*, **30** (4), 307–333.

Lade, P.V. and Hernandez, S.B. (1977). Membrane penetration effects in undrained test. *Journal of Geotechnical Engineering, ASCE*, **103** (GT2), 109–125.

Lam, W.-K. and Tatsuoka, F. (1988). Effects of initial anisotropic fabric and intermediate principal stress on strength and deformation characteristics of sand. *Soils and Foundations*, **28** (1), 89–106.

Lanier, J., Zitouni, Z., Saada, A., Puccini, P., *et al.* (1989). Comparison of three dirnensional tests performed with a true triaxial apparatus and a hollow cylinder device. *Revue Française de Géotechnique*, **49** (10), 67–76.

Lauer, C. and Engel, J. (2005). A triaxial device for unsaturated sand — New Developments. In: Schanz T. (eds). *Unsaturated Soils: Experimental Studies*. *Springer Proceedings in Physics*, vol. 93, Berlin, Springer.

Law, K.T., Cao, Y.L. and He, G.N. (1990). An energy approach for assessing seismic liquefaction potential. *Canadian Geotechnical Journal*, **27** (3), 320–329.

Lee, J.-S. and Santamarina, J.C. (2005). Bender elements: performance and signal interpretation. *Journal of Geotechnical and Geoenvironmental Engineering, ASCE*, **131** (9), 1063–1070.

Lee, K.L. and Albaisa, A. (1974). Earthquake induced settlements in saturated sands. *Journal of the Soil Mechanics and Foundations Division, ASCE*, **100** (GT4), 387–406.

Li, X.S. (2002). A sand model with state-dependent dilatancy. *Geotechnique*, **52** (3), 173–186.

Li, X.S., Dafalias, Y.F. and Wang, Z.-L. (1999). State-dependent dilatancy in critical-state constitutive modelling of sand. *Canadian Geotechnical Journal*, **36** (4), 599–611.

Li, X.S. and Dafalias, Y.F. (2000). Dilatancy for cohesionless soils. *Géotechnique*, **50** (4), 449–460.

Li, X.S. and Dafalias, Y.F. (2004). A constitutive framework for anisotropic sand including non-proportional loading. *Geotechnique*, **54** (1), 41–55.

Li, X.S. and Dafalias, Y.F. (2012). Anisotropic critical state theory: role of fabric. *Journal of Engineering Mechanics, ASCE*, **138** (3), 263–275.

Li, X.S. and Wang, Y. (1998). Linear representation of steady-state line for sand. *Journal of Geotechnical and Geoenvironmental Engineering, ASCE*, **124** (12), 1215–1217.

Li, Y. and Bolton, M. (2014). Energy conservation validates deformation mechanisms around model cantilever wall excavations in sand. *Géotechnique*, **64** (6), 419–429.

Liang, L., Figueroa, J.L. and Saada, A.S. (1995). Liquefaction under random loading: unit energy approach. *Journal of Geotechnical Engineering, ASCE*, **121** (11), 776–781.

Ling, H.I. and Yang, S. (2006). Unified sand model based on the critical state and generalized plasticity. *Journal of Engineering Mechanics, ASCE*, **132** (12), 1380–1391.

Lins, Y. and Schanz, T. (2005). Determination of hydro-mechanical properties of sand. Schanz T. (eds). *Unsaturated Soils: Experimental Studies*. *Springer Proceedings in Physics*, vol. 93,

Berlin, Springer.

Lins, Y., Zou, Y. and Schanz, T. (2007). Physical modeling of SWCC for granular materials. In: Schanz T. (eds). *Theoretical and Numerical Unsaturated Soil Mechanics. Springer Proceedings in Physics*, vol 113, Berlin, Springer.

Lo Presti, D.C.F., Jamiolkowski, M., Pallara, O., Cavallaro, A., *et al.* (1997). Shear modulus and damping of soils. *Géotechnique*, **47** (3), 603–617.

Lo Presti, D.C.F., Pallara, O., Lancellotta, R., Armandi, M., *et al.* (1993). Monotonic and cyclic loading behavior of two sands at small strains. *Geotechnical Testing Journal*, **16** (4), 409–424.

López-Querol, S. and Coop, M.R. (2012). Drained cyclic behaviour of loose Dogs Bay sand. *Géotechnique*, **62** (4), 281–289.

Loukidis, D. and Salgado, R. (2009). Modeling sand response using two-surface plasticity. *Computers and Geotechnics*, **36** (1–2), 166–186.

Luccioni, L.X., Pestana, J.M. and Taylor, R.L. (2001). Finite element implementation of non-linear elastoplastic constitutive laws using local and global explicit algorithms with error control. *International Journal for Numerical Methods in Engineering*, **50** (5), 1191–1212.

Madabhushi, S.P.G. (1994). Effect of pore fluid in dynamic centrifuge modelling. In: Leung, C.F., Lee, F.H. and Tan, T.S. (eds.). *Centrifuge 94: Proceedings of the International Conference, Singapore, 31 August-2 September 1994*. Rotterdam, the Netherlands, CRC Press/Balkema.

Madabhushi, S.P.G. (2004). Modelling of earthquake damage using geotechnical centrifuges. *Current Science*, **87** (10), 1405–1416.

Madabhushi, S.P.G., Schofield, A.N. and Lesley, S. (1998) A new stored angular momentum (SAM) based earthquake actuator. In: T. Kimura, O. Kusakabe, and J. Takemura (eds.). *Centrifuge 98: Proceedings of the International Conference, Tokyo, Japan, 23-25 September 1998*. Rotterdam, the Netherlands, CRC Press/Balkema.

Mancuso, C., Simonelli, A.L. and Vinale, F. (1989) Numerical analysis of in situ s-wave measurements. *Proceedings of the 12th International Conference on Soil Mechanics*, Rio De Janeiro, Brazil, 13-18 August 1989.

Manzanal, D., Pastor, M., Antonio, J. and Merodo, F. (2011). *Generalized plasticity state parameter-based model for saturated and unsaturated soils . Part II : Unsaturated soil modeling*. **35** (18), 1899–1917.

Manzari, M.T. and Arulanandan, K. (1993) Numerical predictions for model no 1. In: Arulanandan, K. and Scott, R.F. (eds.). *Verification of numerical procedures for the analysis of soil liquefaction problems. Proceedings of the International Conference, Davis, California, U.S., 17-20 October 1993*. Rotterdam, the Netherlands, CRC Press/Balkema.

Manzari, M.T. and Dafalias, Y.F. (1997). A critical state two-surface plasticity model for sands. *Géotechnique*, **47** (2), 255–272.

Manzari, M.T. and Nour, M.A. (1997). On implicit integration plasticity of Bounding Surface Plasticity Models. *Computers & Structures*, **63** (3), 385–395.

Markou, I.N. (2018). A Study on Geotextile—Sand Interface Behavior Based on Direct Shear

and Triaxial Compression Tests. *International Journal of Geosynthetics and Ground Engineering*, **4** (1), 1–15.

Marques, A.S.P.S., Coelho, P.A.L.F., Cilingir, U., Haigh, S.K., *et al.* (2012a). Centrifuge modelling of liquefaction-induced effects on a shallow foundation. *Proceedings of the 13th National Conference in Geotechnics*, Lisbon, Portugal, 17-20 April 2012.

Marques, A.S.P.S., Coelho, P.A.L.F., Cilingir, U., Haigh, S.K., *et al.* (2012b). Centrifuge modelling of liquefaction-induced effects on shallow foundations with different bearing pressures. *Proceedings of the 2nd European conference on Physical Modelling in Geotechnics,* Delft, Netherlands, 23-24 April 2012.

Marques, A.S.P.S., Coelho, P.A.L.F., Cilingir, U., Haigh, S.K., *et al.* (2012c). Earthquake-Induced Liquefaction Effects on a Shallow Foundation. *Proceedings of the 15th World Conference on Earthquake Engineering*, Lisbon, Portugal, 24-28 September 2012.

Marques, A.S.P.S., Coelho, P.A.L.F., Haigh, S.K. and Madabhushi, S.P.G. (2014a). Centrifuge modeling of liquefaction effects on shallow foundations. In: Ilki A., Fardis M. (eds) *Seismic Evaluation and Rehabilitation of Structures. Geotechnical, Geological and Earthquake Engineering*, vol 26. Springer, Cham.

Marques, A.S.P.S., Coelho, P.A.L.F., Haigh, S.K. and Madabhushi, S.P.G. (2014b). Centrifuge modeling of liquefaction effects on shallow foundations. *Proceedings of the 8th International Conference on Physical Modelling in Geotechnics*, Perth, Australia, 14–17 January 2014, pp. 1039-1044.

Marques, A.S.P.S., Coelho, P.A.L.F., Haigh, S.K. and Madabhushi, S.P.G. (2014c) Centrifuge modeling of seismic liquefaction effects on adjacent shallow foundations. In: Gaudin, C. and White, D. (eds.). *Proceedings of the 8th International Conference on Physical Modelling in Geotechnics, Perth, Australia, 14-17 January 2014*. Rotterdam, the Netherlands, CRC Press/Balkema.

Marques, A.S.P.S., Coelho, P.A.L.F., Haigh, S.K. and Madabhushi, S.P.G. (2015). Centrifuge modelling of the behaviour of shallow foundations in liquefiable ground. *Proceedings of the 6th International Conference on Earthquake Geotechnical Engineering*, Christchurch, New Zealand, 1-4 November 2015.

Masing, V.G. (1926). Eigenspannungen und verfestigung beim messing. *Proceedings of the 2nd International Congress for Applied Mechanics*. Zurich, Switzerland, 12–17 September 1926.

Matasović, N. and Vucetic, M. (1993). Cyclic characterization of liquefiable sands. *Journal of Geotechnical Engineering, ASCE*, **119** (11), 1805–1822.

Mitrani, H. (2006). *Liquefaction remediation techniques for existing buildings*. PhD thesis. University of Cambridge, Cambridge.

Miura, S. and Toki, S. (1982). A sample preparation method and its effect on static and cyclic deformation-strength properties of sand. *Soils and Foundations*, **22** (1), 62–77.

Mokni, M. and Desrues, J. (1999). Strain localization measurements in undrained plane-strain biaxial tests on Hostun RF sand. *Mechanics of Cohesive-Frictional Materials*, **4**, 419–441.

Mooney, M., Finno, R.J. and Viggiani, M.G. (1998). Unique critical state for sand? *Journal of Geotechnical and Geoenvironmental Engineering, ASCE*, **124** (11), 1100–1108.

Morgenstern, N.R., Vick, S.G., Viotti, C.B. and Watts, B.D. (2016). *Fundão Tailings Dam Review Panel. Report on the immediate causes of the failure of the Fundao Dam*.

Mróz, Z., Norris, V.A. and Zienkiewicz, O.C. (1979). Application of an anisotropic hardening model in the analysis of elasto–plastic deformation of soils. *Géotechnique*, **29** (1), 1–34.

Mulilis, J.P., Arulanandan, K., Mitchell, J.K., Chan, C.K., et al. (1977). Effects of sample preparation on sand liquefaction. *Journal of the Geotechnical Engineering Division, ASCE*, **103** (2), 91–108.

Murthy, T.G., Loukidis, D., Carraro, J.A.H., Prezzi, M., et al. (2007). Undrained monotonic response of clean and silty sands. *Géotechnique*, **57** (3), 273–288.

Nagase, H. and Ishihara, K. (1988). Liquefaction-induced compaction and settlement of sand during earthquakes. *Soils and Foundations*, **28** (1), 65–76.

Nakata, Y., Hyodo, M., Murata, H. and Yasufuku, N. (1998). Flow deformation of sands subjected to principal stress rotation. *Soils and foundations*, **38** (2), 115–128.

Nemat-Nasser, S. and Shokooh, A. (1979). A unified approach to densification and liquefaction of cohesionless sand in cyclic shearing. *Canadian Geotechnical Journal*, **16** (4), 659–678.

Nemat-Nasser, S. and Tobita, Y. (1982). Influence of fabric on liquefaction and densification potential of cohesionless sand. *Mechanics of Materials*, **1** (1), 43–62.

Nova, R. (1982) A constitutive model for soil under monotonic and cyclic loading. In: Pande, G. N. and Zienkiewicz, C. (eds.). *Soil mechanics - transient and cyclic loading*. Chichester, U.K., Wiley.

Nova, R. and Wood, D.M. (1979). A constitutive model for sand in triaxial compression. *International Journal for Numerical and Analytical Methods in Geomechanics*, **3** (3), 255–278.

O'Kelly, B.C. and Naughton, P.J. (2009). Study of the yielding of sand under generalized stress conditions using a versatile hollow cylinder torsional apparatus. *Mechanics of Materials*, **41** (3), 187–198.

O'Rourke, T.D., Druschel, S.J. and Netravali, A.N. (1990). Shear strength characteristics of sand-polymer interfaces. *Journal of Geotechnical Engineering, ASCE*, **116** (3), 451–469.

Oda, M. (1972). Initial fabrics and their relations to mechanical properties of granular material. *Soils and Foundations*, **12** (1), 17–36.

Okada, N. and Nemat-Nasser, S. (1994). Energy dissipation in inelastic flow of saturated cohesionless granular media. *Géotechnique*, **44** (1), 1–19.

Okamura, M., Abdoun, T.H., Dobry, R., Sharp, M.K., et al. (2001). Effects of sand permeability and weak aftershocks on earthquake-induced lateral spreading. *Soils and Foundation*, **41** (6), 63–77.

Ortiz, M. and Simo, J.C. (1985). A unified approach to finite deformation elastoplastic analysis based on the use of hyperelastic constitutive equations. *Computer Methods in Applied Mechanics and Engineering*, **49** (2), 221–245.

Ortiz, M. and Simo, J.C. (1986). An analysis of a new class of integration algorithms for elastoplastic constitutive relations. *International Journal for Numerical Methods in Engineering*, **23** (3), 353–366.

Oztoprak, S. and Bolton, M.D. (2012). Stiffness of sands through a laboratory test database. *Géotechnique*, **63** (1), 1–17.

Pal, S., Wathugala, G.W. and Kundu, S. (1996). Calibration of a constitutive model using genetic algorithms. *Computers and Geotechnics*, **19** (4), 325–348.

Pan, K. and Yang, Z.X. (2017). Effects of initial static shear on cyclic resistance and pore pressure generation of saturated sand. *Acta Geotechnica*, **13** (2), 473–487.

Papadimitriou, A.G. and Bouckovalas, G.D. (2002). Plasticity model for sand under small and large cyclic strains: a multiaxial formulation. *Soil Dynamics and Earthquake Engineering*, **22** (3), 191–204.

Papadimitriou, A.G., Bouckovalas, G.D. and Dafalias, Y.F. (2001). Plasticity model for sand under small and large cyclic strains. *Journal of Geotechnical and Geoenvironmental Engineering, ASCE*, **127** (11), 973–983.

Papadimitriou, A.G., Dafalias, Y.F. and Li, X.S. (2014). Anisotropic sand model and fabric evolution until the critical state. *Numerical Methods in Geotechnical Engineering –*, **2**85–89.

Papadimitriou, A.G., Dafalias, Y.F. and Yoshimine, M. (2005). Plasticity modeling of the effect of sample preparation method on sand response. *Soils and foundations*, **45** (2), 109–124.

Papadopoulos, P. and Taylor, R.L. (1995). On the loading/unloading conditions of infinitesimal discrete elastoplasticity. *Engineering Computations*, **12** (4), 373–383.

Pastor, M., Zienkiewicz, O.C. and Chan, A.H.O. (1990). Generalized plasticity and the modelling of soil behaviour. *International Journal for Numerical and Analytical Methods in Geomechanics*, **14** (3), 151–190.

Peacock, W.H. and Seed, H.B. (1968). Sand liquefaction under cyclic loading simple shear conditions. *Journal of the Soil Mechanics and Foundations Division, ASCE*, **94** (3), 689–708.

Pedro, M.G. (2013). *Geotechnical investigation of ivens shaft in Lisbon*. PhD thesis. Imperial College London, London.

Pennington, D.S., Nash, D.F.T. and Lings, M.L. (1997). Anisotropy of G0 shear stiffness in Gault clay. *Géotechnique,* **47** (3), 391–398.

Polito, C., Green, R.A., Dillon, E. and Sohn, C. (2013). Effect of load shape on relationship between dissipated energy and residual excess pore pressure generation in cyclic triaxial tests. *Canadian Geotechnical Journal*, **50** (10), 1118–1128.

Polito, C.P., Green, R.A. and Lee, J. (2008). Pore pressure generation models for sands and silty soils subjected to cyclic loading. *Journal of Geotechnical and Geoenvironmental Engineering, ASCE*, **134** (10), 1490–1500.

Popescu, R. and Prevost, J.H. (1993) Numerical class 'a' predictions for models Nos 1, 2, 3, 4a, 4b, 6, 7, 11 & 12. In: Arulanandan, K. and Scott, R.F. (eds.). *Verification of numerical procedures for the analysis of soil liquefaction problems. Proceedings of the International Conference, Davis, California, U.S., 17-20 October 1993*. Rotterdam, the Netherlands, CRC Press/Balkema.

Potts, D.M. and Ganendra, D. (1994). An evaluation of substepping and implicit stress point

algorithms. *Computer Methods in Applied Mechanics and Engineering*, **119** (3–4), 341–354.

Potts, D.M. and Gens, A. (1985). A critical assessment of methods of correcting for drift from the yield surface in elasto-plastic finite element analysis. *International Journal for Numerical and Analytical Methods in Geomechanics*, **9** (2), 149–159.

Potts, D.M. and Zdravkovic, L. (1999). *Finite element analysis in geotechnical engineering. Theory*. London, U.K., Thomas Telford Publishing.

Poulos, S.J. (1981). The Steady State of Deformation. *Journal of the Geotechnical Engineering Division, ASCE*, **107** (5), 553–562.

Poulos, H.G. and Davis, E.H. (1974). *Elastic solutions for soil and rock mechanics*. London, U.K., Wiley.

Pradhan, T.B.S., Tatsuoka, F. and Horii, N. (1988). Strength and deformation characteristics of sand in torsional simple shear. *Soils and Foundations*, **28** (3), 131–148.

Prévost, J.-H. (1977). Mathematical modelling of monotonic and cyclic undrained clay behaviour. *International Journal for Numerical and Analytical Methods in Geomechanics*, **1** (2), 195–216.

Ramberg, W. and Osgood, W.R. (1943). *Description of stress-strain curves by three parameters*. National Advisory Committee for Aeronautics. Technical Note No. 902.

Richart, F.E, Hall, J.R. and Woods, R.D. (1970). *Vibration of soils and foundations*. New Jersey, U.S., Prentice-Hall.

Riemer, M.F., Seed, R.B., Nicholson, P.G. and Jong, H.-L. (1990). Steady state testing of loose sands: limiting minimum density. *Journal of Geotechnical Engineering, ASCE,* **116** (2), 332–337.

Riemer, M.F.M. and Seed, R.B.R. (1997). Factors affecting apparent position of steady-state line. *Journal of Geotechnical and Geoenvironmental Engineering, ASCE*, **123** (3), 281–288.

Robertson, P.K., Wride, C.E., List, B.R., Atukorala, U., *et al.* (2000). The CANLEX project: summary and conclusions. *Canadian Geotechnical Journal*, **37** (3), 563–591.

Robertson, P.K., de Melo, L., Williams, D.J. and Wilson, G.W. (2019). *Report of the expert panel on the technical causes of the failure of Feijão dam I*.

Rollins, K.M. and Seed, H.B. (1990). Influence of buildings on potential liquefaction damage. *Journal of Geotechnical Engineering, ASCE*, **116** (2), 165–185.

Roscoe, K.H., Schofield, A.N. and Thurairajah, A. (1964) An evaluation of test data for selecting a yield criterion for soils. In: *Laboratory Shear Testing of Soils*, West Conshohocken, PA, ASTM International, pp. 111–128.

Roscoe, K.H., Schofield, A.N. and Wroth, C.P. (1958). On the yielding of soils. *Géotechnique*, **8** (1), 22–53.

Rouainia, M. and Wood, D.M. (2001). Implicit numerical integration for a kinematic hardening soil plasticity model. *International Journal for Numerical and Analytical Methods in Geomechanics*, **25** (13), 1305–1325.

Rowe, P.W. (1962). The stress-dilatancy relation for static equilibrium of an assembly of

particles in contact. *Proceedings of the Royal Society A: Mathematical, Physical and Engineering Sciences*, vol. 269, 500–527.

Russell, A. R. and Muir Wood, D. (2010). A comparison of critical state models for sand under conditions of axial symmetry. *Géotechnique*, **60** (2), 133–140.

Sadek, T. and Lings, M. (2007). Wave transmission in Hostun sand: multiaxial experiments. *Rivista Italiana di Geotecnica*, **41** (2), 69–84.

Sadrekarimi, A. and Olson, S.M. (2012). Effect of sample-preparation method on critical-state behavior of sands. *Geotechnical Testing Journal*, **35** (4), 1–15.

Sanchez-Salinero, I., Roesset, J.M., Stokoe, K.H. and Kenneth, H. (1986). *Analytical studies of body wave propagation and attenuation*. University of Texas, Austin, California. Report GR86-15.

Santamarina, J.C. and Fam, M.A. (1997). Discussion: Interpretation of bender element tests. *Géotechnique*, **47** (4), 873–877.

Schanz, T. and Vermeer, P. (1996). Angles of friction and dilatancy of sand. *Géotechnique*, **46** (1), 145–151.

Schanz, T., Vermeer, P.A. and Bonnier, P.G. (1999). The hardening soil model: formulation and verification. In: Brinkgreve, R. (ed.). *Beyond 2000 in Computational Geotechnics*. Rotterdam, the Netherlands, CRC Press, pp. 281–296.

Schofield, A.N. (1980). Cambridge Geotechnical Centrifuge Operations. *Géotechnique*, **30** (3), 227–268.

Schofield, A. and Wroth, P. (1968). *Critical state soil mechanics*. McGraw Hill, London.

Scott, R.F. (1986a). Soil properties from centrifuge liquefaction tests. *Mechanics of Materials*, **5** (2), 199–206.

Scott, R.F. (1986b). Solidification and consolidation of a liquefied sand column. *Soils and Foundations*, **26** (4), 23–31.

Seed, H.B. (1981). Earthquake-resistant design of earth dams. *Proceedings of the 1st International Conferences on Recent Advances in Geotechnical Earthquake Engineering and Soil Dynamics*, St. Louis, MO, USA, 26 April – 2 May 1981, pp. 1157–1173.

Seed, H.B. and Idriss, I.M. (1970a). *A simplified procedure for evaluating soil liquefaction potential.* Earthquake Engineering Research Center, University of California, Berkeley, California. Report EERC 70-9.

Seed, H.B. and Idriss, I.M. (1970b). *Soil moduli and damping factors for dynamic response analyses.* Earthquake Engineering Research Center, University of California, Berkeley, California. Report EERC 70-10.

Seed, H.B. and Idriss, I.M. (1971). Simplified procedure for evaluating soil liquefaction potential. *Journal of the Soil Mechanics and Foundations Division, ASCE*, **97** (9), 1249–1273.

Seed, H.B., Idriss, I.M., Makdidi, F. and Nanerjee, N. (1975a). *Representation of irregular stress time histories by equivalent uniform stress series in liquefaction analyses.* Earthquake Engineering Research Center, University of California, Berkeley, California. Report EERC 75-29.

Seed, H.B. and Lee, K.L. (1966). Liquefaction of saturated sands during cyclic loading. *Journal of the Soil Mechanics and Foundations Division, ASCE*, **92** (6), 105–134.

Seed, H.B., Martin, P.P. and Lysmer, J. (1975b) *The generation and dissipation of pore water pressures during soil liquefaction*. Earthquake Engineering Research Center, University of California, Berkeley, California. Report EERC 75-26.

Seismosoft (2018). A computer program for signal processing of strong-motion data. Available from: http://www.seismosoft.com.

Shen, C.K., Harder, L.F., Vrymoed, J.L. and Bennett, W. (1978) Dynamic response of a sand under random loading. *Proceedings of Earthquake Engineering and Soil Dynamics, ASCE*, Pasadena, 19-21 June 1978, pp. 852–863.

Shirley, D.J. (1978). An improved shear wave transducer. *The Journal of the Acoustical Society of America*, **63** (5), 1643–1645.

Shirley, D.J. and Hampton, L.D. (1978). Shear-wave measurements in laboratory sediments. *The Journal of the Acoustical Society of America*, **63** (2), 607–613.

Simcock, K.J., Davis, R.O., Berrill, J.B. and Mullenger, G. (1983). Cyclic triaxial tests with continuous measurement of dissipated energy. *Geotechnical Testing Journal,* **6** (1), 35–39.

Simpson, A.R. and Priest, S.D. (1993). The application of genetic algorithms to optimisation problems in geotechnics. *Computers and Geotechnics*, **15** (1), 1–19.

Sladen, J.A., D'Hollander, R.D. and Krahn, J. (1985). The liquefaction of sands, a collapse surface approach. *Canadian Geotechnical Journal*, **22** (4), 564–578.

Sloan, S.W. (1987). Substepping schemes for numerical integration of elasto-plastic stress-strain relations. *International Journal for Numerical Methods in Engineering*, **24** (5), 893–911.

Sloan, S.W., Abbo, A.J. and Sheng, D. (2001). Refined explicit integration of elastoplastic models with automatic error control. *Engineering Computations*, **18** (1), 121–194.

Stamatopoulos, C.A. (2010). An experimental study of the liquefaction strength of silty sands in terms of the state parameter. *Soil Dynamics and Earthquake Engineering*, **30** (8), 662–678.

Stewart, D.P., Chen, Y.-R. and Kutter, B.L. (1998). Experience with the use of methylcellulose as a viscous pore fluid in centrifuge models. *Geotechnical Testing Journal*, **21** (4), 365–369.

Stringer, M.E. and Madabhushi, S.P.G. (2009). Novel computer-controlled saturation of dynamic centrifuge models using high viscosity fluids. *Geotechnical Testing Journal*, **32** (6), 559–564.

Stringer, M.E. and Madabhushi, S.P.G. (2013). Axial load transfer in liquefiable soils for free-standing piles. *Géotechnique*, **63** (5), 400–409.

Stringer, M.E. and Madabhushi, S.P.G. (2013). Re-mobilization of pile shaft friction after an earthquake. *Canadian Geotechnical Journal*, **50** (9), 979–988.

Stringer, M.E., McMahon, B.T. and Madabhushi, S.P.G. (2009). *CAM-Sat : Computer controlled saturation for geotechnical centrifuge modelling*.University of Cambridge, Cambridge,

Technical report CUED/D-SOILS/TR348.

Su, D., Li, X.-S. and Xing, F. (2009). Estimation of the apparent permeability in the dynamic centrifuge tests. *Geotechnical Testing Journal*, **23** (1), 1–9.

Taborda, D.M.G. (2011). *Development of constitutive models for application in soils dynamics*. PhD thesis. Imperial College London, London.

Taborda, D.M.G. (2015). Numerical simulation of undrained monotonic and cyclic triaxial tests on Leighton Buzzard sand (personal communication, 19th April 2015).

Taborda, D.M.G., Coelho, P.A.L.F., Antunes, D. and Pedro, A. (2008) Genetic Algorithms as a calibration method for constitutive models. *Proceedings of the 11th National Conference in Geotechnics, Coimbra, Portugal,* 7–11 April 2008 (in Portuguese).

Taborda, D.M.G., Potts, D.M. and Zdravković, L. (2016). On the assessment of energy dissipated through hysteresis in finite element analysis. *Computers and Geotechnics*, **71**, 180–194.

Taborda, D.M.G., Zdravković, L., Kontoe, S. and Potts, D.M. (2014). Computational study on the modification of a bounding surface plasticity model for sands. *Computers and Geotechnics*, **59**, 145–160.

Taiebat, M. and Dafalias, Y.F. (2008). SANISAND: Simple anisotropic sand plasticity model. *International Journal for Numerical and Analytical Methods in Geomechanics*, **32** (8), 915–948.

Taiebat, M., Shahir, H. and Pak, A. (2007). Study of pore pressure variation during liquefaction using two constitutive models for sand. *Soil Dynamics and Earthquake Engineering*, **27** (1), 60–72.

Tatsuoka, F., Iwasaki, T., Yoshida, S., Fukushima, S., *et al.* (1979). Shear modulus and damping by drained tests on clean sand specimens reconstituted by various methods. *Soils and Foundations*, **19** (1), 39–54.

Tatsuoka, F., Ochi, K., Fujii, S. and Okamoto, M. (1986a). Cyclic undrained triaxial and torsional shear strength of sands for different sample preparation methods. *Soils and Foundations*, **26** (3), 23–41.

Tatsuoka, F., Sakamoto, M., Kawamura, T. and Fukushima, S. (1986b). Strength and deformation characteristics of sand in plane strain compression at extremely low pressures. *Soils and Foundations*, **26** (1), 65–84.

Tatsuoka, F., Tokio, S., Miura, S., Kato, H., et al. (1986c). Some factors affecting cyclic undrained triaxial strength of sand. *Soils and Foundations*, **26** (3), 99–116.

Tatsuoka, F. and Hoque, E. (2004). Effects of stress ratio on small-strain stiffness during triaxial shearing. *Géotechnique*, **54** (7), 429–439.

Tektronix (1998) *WSTRO: WaveStar software for oscilloscopes*. Available from: http://uk.tek.com/datasheet/wstro.

Terram Geosynthetics (2018). *Declaration of performance no. 0338-CPR-0040-2018: Terram 1B1*. Available from: http://www.terram.com/.

Teymur, B. and Madabhushi, S.P.G. (2003). Experimental study of boundary effects in dynamic centrifuge modelling. *Géotechnique*, **53** (7), 655–663.

Thusyanthan, N.I. and Madabhushi, S.P.G. (2003). *Scaling of seepage flow velocity in centrifuge models.* University of Cambridge, Cambridge, U.K. Technical report CUED/DSOILS/TR326.

Tika, T., Kallioglou, P., Papadopoulou, A. and Pitilakis, K. (2003). Shear modulus and damping of natural sands. In: DiBenedetto, H., Doanh, T., Geoffroy, H. and Sauzeat, C. (eds.). *Deformation Characteristics of Geomaterials: Proceedings of the 3rd International Symposium, Lyon, France, 22 - 24 September 2003*. Leiden, the Netherlands, CRC Press/Balkema.

Timoshenko, S. and Goodier, J.N. (1951). *Theory of Elasticity*. 2nd edition. London, U.K., McGraw-Hill.

Toki, S., Tatsuoka, F., Miura, S., Yoshimi, Y., et al. (1986). Cyclic undrained triaxial strength of sand by a cooperative test program. *Soils and Foundations*, **26** (3), 117–128.

Toll, D.G. (1993). A computer control system for stress path triaxial testing. In: B.H.V. Topping (ed.). *Developments in Civil and Construction Engineering Computing*. Edinburgh, UK, Civil-Comp Press.

Towhata, I. (2008). History of geotechnical earthquake engineering in Japan. *Proceedings of the 14th World Conference on Earthquake Engineering*, Beijing, China, 12 - 17 October 2008.

Towhata, I. and Ishihara, K. (1985). Shear work and pore water pressure in undrained shear. *Soils and Foundations*, **25** (3), 73–85.

Tsaparli, V., Kontoe, S., Taborda, D.M.G. and Potts, D.M. (2016). Vertical ground motion and its effects on liquefaction resistance of fully saturated sand deposits. *Proceedings of the Royal Society A: Mathematical, Physical and Engineering Sciences*, **472**, 2016.0434.

Tsaparli, V., Kontoe, S., Taborda, D.M.G. and Potts, D.M. (2017). The importance of accurate time-integration in the numerical modelling of P-wave propagation. *Computers and Geotechnics*, **86**, 203–208.

Tsinidis, G., Pitilakis, K., Madabhushi, G. and Heron, C. (2015). Dynamic response of flexible square tunnels: centrifuge testing and validation of existing design methodologies. *Géotechnique*, **65** (5), 401–417.

Uthayakumar, M. and Vaid, Y.P. (1998). Static liquefaction of sands under multiaxial loading. *Canadian Geotechnical Journal*, **35** (2), 273–283.

Vaid, Y.P. and Chern, J.C. (1983). Effect of static shear on resistance to liquefaction. *Soils and Foundations*, **23** (1), 47–60.

Vaid, Y.P., Chung, E.K.F. and Kuerbis, R.H. (1990). Stress path and steady state. *Canadian Geotechnical Journal*, **27** (1), 1–7.

Vaid, Y.P. and Negussey, D. (1988). Preparation of reconstituted sand specimens. In: Ronald C. Chaney and Marshall L. Silver Robert T. Donaghe (eds.). *Advanced Triaxial Testing of Soil and Rock*, West Conshohocken, PA, ASTM International, pp. 405–417.

Vaid, Y.P. and Negussey, D. (1984). Relative density of pluviated sand samples. *Soils and Foundations*, **24** (2), 101–105.

Vaid, Y.P. and Sasitharan, S. (1992). The strength and dilatancy of sand. *Canadian*

Geotechnical Journal, **29** (3), 522–526.

Vaid, Y.P. and Sivathayalan, S. (2000). Fundamental factors affecting liquefaction susceptibility of sands. *Canadian Geotechnical Journal*, **37** (3), 592–606.

Vaid, Y.P. and Sivathayalan, S. (1996). Static and cyclic liquefaction potential of Fraser Delta sand in simple shear and triaxial tests. *Canadian Geotechnical Journal*, **33**284–289.

Vaid, Y.P. and Thomas, J. (1995). Liquefaction and postliquefaction behaviour of sand. *Journal of Geotechnical Engineering, ASCE*, **121** (2), 163–173.

Venda Oliveira, P. (2000). *Embankments on soft soils: numerical modelling*. PhD thesis. University of Coimbra, Coimbra (in Portuguese).

Verdugo, R. and Ishihara, K. (1996). The steady state of sandy soils. *Soils and foundations*, **36** (2), 81–91.

Vermeer, P.A. (1978). A double hardening model for sand. *Géotechnique*, **28** (4), 413–433.

Viana da Fonseca, A., Ferreira, C. and Fahey, M. (2009). A framework interpreting bender element tests, combining time-domain and frequency-domain methods. *Geotechnical Testing Journal*, **32** (2), 1–17.

Vieira, C.S., Lopes, M.L. and Caldeira, L.M. (2013). Sand-geotextile interface characterisation through monotonic and cyclic direct shear tests. *Geosynthetics International*, **20** (1), 26–38.

Viggiani, G. and Atkinson, J.H. (1995). Interpretation of bender element tests. *Géotechnique*, **45** (1), 149–154.

Vilhar, G., Laera, A., Foria, F., Gupta, A., et al. (2018). Implementation , validation and application of PM4Sand model in PLAXIS. *Geotechnical Special Publication*, **292**, 200–211.

Vucetic, M. (1994). Cyclic threshold shear strains in soils. *Journal of Geotechnical Engineering, ASCE*, **120** (12), 2208–2228.

Vucetic, M. and Dobry, R. (1991). Effect of soil plasticity on cyclic response. *Journal of Geotechnical Engineering, ASCE,* **117** (1), 89–107.

Wang, G.X. and Kuwano, J. (1999). Shear modulus and damping of clayey sands. *Journal of Earthquake Engineering*, **3** (2), 271–285.

Wichtmann, T. and Triantafyllidis, T. (2004). Influence of a cyclic and dynamic loading history on dynamic properties of dry sand, part II: Cyclic axial preloading. *Soil Dynamics and Earthquake Engineering*, **24** (11), 789–803.

Williams, J.D. (2014). *Modelling of anisotropic sand behaviour under generalised loading conditions*. MSc thesis. Imperial College London, London.

Woo, S.I. and Salgado, R. (2014). Determination of an image point on a surface based on a π-plane-based algorithm. *Computational Mechanics*, **53** (5), 1033–1046.

Woo, S.I. and Salgado, R. (2015). Bounding surface modeling of sand with consideration of fabric and its evolution during monotonic shearing. *International Journal of Solids and Structures*, **63** (6), 277–288.

Wood, D.M., Belkheir, K. and Liu, D. (1994). Strain softening and state parameter for sand

modelling. *Géotechnique*, **44** (2), 335–339.

Wood, D.M., Sadek, T., Dihoru, L. and Lings, M.L. (2007). Deviatoric stress response envelopes from multiaxial tests on sand. In: *Soil stress-strain behavior: measurement, modeling and analysis. Solid Mechanics and Its Applications*, vol 146, Dordrecht, Springer, pp. 253–262.

Xu, T.H. and Zhang, L.M. (2015). Numerical implementation of a bounding surface plasticity model for sand under high strain-rate loadings in LS-DYNA. *Computers and Geotechnics*, **66**, 203–218.

Yamamoto, Y., Hyodo, M. and Orense, R.P. (2010). Liquefaction resistance of sandy soils under partially drained condition. *Journal of Geotechnical and Geoenvironmental Engineering, ASCE*, **135** (8), 1032–1044.

Yamamuro, J. and Lade, P. (1995). Strain localization in extension tests on granular materials. *Journal of Engineering Mechanics, ASCE*, **121** (7), 828–836.

Yamamuro, J.A. and Lade, P. V (1997). Static liquefaction of very loose sands. *Canadian Geotechnical Journal*, **34** (6), 905–917.

Yamashita, S., Kawaguchi, T., Nakata, Y., Fujiwara, T., *et al.* (2009). Interpretation of international parallel test on the measurement of Gmax using bender elements. *Soils and Foundations*, **49** (4), 631–650.

Yamazaki, F., Towhata, I. and Ishihara, K. (1985) Numerical model for liquefaction problem under multi-directional shearing on horizontal plane. *Proceedings of the 15th International Conference on Numerical Methods in Geomechanics*, Nagoya, Japan, 1-5 April 1985.

Yang, Z. and Elgamal, A. (2007). Multi-surface cyclic plasticity sand model with Lode angle effect. *Geotechnical and Geological Engineering*, **26** (3), 335–348.

Yang, J. and Li, X.S. (2004). State-dependent strength of sands from the perspective of unified modeling. *Journal of Geotechnical and Geoenvironmental Engineering, ASCE*, **130** (2), 186–198.

Yoshimine, M., Ishihara, K. and Vargas, W. (1998). Effects of principal stress direction and intermediate principal stress on undrained shear behavior of sand. *Soils and Foundations*, **38** (3), 179–188.

Yoshimine, M. and Kataoka, M. (2007) Steady state of sand in triaxial extension test. Proceedings of the *International Workshop on Earthquake Hazards and Mitigation*. Guwahati, India, 7-8 December 2007.

Youd, T.L., Idriss, I.M., Andrus, R.D., Arango, I., *et al.* (2001). Liquefaction resistance of soils: summary report from the 1996 NCEER and 1998 NCEER/NSF workshops on evaluation of liquefaction resistance of soils. *Jounral of Geotechnical and Geoenvironmental Engineering, ASCE*, **127** (April), 297–313.

Youd, T.L., Steidl, J.H. and Nigbor, R.L. (2004). Lessons learned and need for instrumented liquefaction sites. *Soil Dynamics and Earthquake Engineering*, **24** (9–10), 639–646.

Yu, H.S. (1994). State parameter from self-boring pressuremeter tests in sand. *Journal of Geotechnical Engineering, ASCE*, **120** (12), 2118–2135.

Zeng, X. and Schofield, A.N. (1996). Design and performance of an equivalent-shear-beam

container for earthquake centrifuge modelling. *Géotechnique*, **46** (1), 83–102.

Zhang, Z.L. (1995). Explicit consistent tangent moduli with a return mapping algorithm for pressure-dependent elastoplasticity models. *Computer Methods in Applied Mechanics and Engineering*, **121** (1–4), 29–44.

Zhao, J., Sheng, D., Rouainia, M. and Sloan, S.W. (2005). Explicit stress integration of complex soil models. *International Journal for Numerical and Analytical Methods in Geomechanics*, **29** (12), 1209–1229.

Zhou, Y.G. and Chen, Y.M. (2005). Influence of seismic cyclic loading history on small strain shear modulus of saturated sands. *Soil Dynamics and Earthquake Engineering*, **25** (5), 341–353.

Zienkiewicz, O.C., Bicanic, N. and Shen, F.Q. (1989). Earthquake Input Definition and the Trasmitting Boundary Conditions. *Advances in Computational Nonlinear Mechanics*, 109–138.

Zienkiewicz, O.C., Chan, A.H.C., Pastor, M., Schrefler, B.A., *et al.* (1999). *Computational Geomechanics: with special reference to earthquake engineering*. Wiley.

Zienkiewicz, O.C., Chang, C.T. and Bettess, P. (1980). Drained, undrained, consolidating and dynamic behaviour assumptions in soils. *Géotechnique*, **30** (4), 385–395.

Zienkiewicz, O.C., Leung, K.H. and Pastor, M. (1985). Simple model for transient soil loading in earthquake analysis. I. Basic model and its application. *International Journal for Numerical and Analytical Methods in Geomechanics*, **9** (5), 453–476.

Zlatović, S. and Ishihara, K. (1997). Normalised behaviour of very loose non-plastic soils: effects of fabric. *Soils and Foundations*, **37** (4), 47–56.

Appendix A MEASURED AND SIMULATED MONOTONIC RESPONSE OF HOSTUN SAND

A.1 Introduction

This appendix compares the experimental results of each monotonic triaxial test performed on Hostun sand (Chapter 2) with the results of its numerical simulation (Chapter 7).

A.2 Monotonic triaxial compression tests

A.2.1.1 Model parameters used in the simulations

Two different sets of model parameters were employed in the numerical simulations of monotonic triaxial compression tests: "A) Static", which was optimised for the simulation of the monotonic response of Hostun sand, and "B) Dynamic", which makes use of the stress-induced anisotropy component of the constitutive model introducing the effect of the cyclic history on the modelled response. The values of the two sets of model parameters are indicated in Table A.1. Note that the differences between the two sets of parameters are highlighted in bold. Moreover, note that the calibration of these parameters can be found in Chapter 6.

Table A.1 – Model parameters used in the monotonic triaxial compression test simulations.

Sets of parameters	A) Static	B) Dynamic
C_g	293.0	293.0
m_g	2.97	2.97
n_g	0.49	0.49
κ	2.00	2.00
a_1	0.46	0.46
γ_1	7.02 x 10^{-4}	7.02 x 10^{-4}
p'_{min}	1.0 kPa (1)	10.0 kPa
G_{min}	1.0 kPa (1)	1.0 kPa (1)
ν	0.18	0.18
Model surfaces		
p'_{ref}	101.3 kPa	101.3 kPa
$(e_{CS})_{ref}$	1.000	1.000
λ	0.070	0.070
ξ	0.360	0.360
M_c^c	1.265	1.265
M_e^c	(2)	(2)
k_c^d	0.940	0.940
k_e^d	(2)	(2)
k_c^b	2.810	2.810
k_e^b	(2)	(2)

Table A.1 – Model parameters used in the monotonic triaxial compression test simulations.

Sets of parameters	A) Static	B) Dynamic
m	0.065	0.065
p'_{ys}	1.0 kPa	1.0 kPa
Stress-dilatancy		
A_0	1.00	1.00
Plastic hardening modulus		
$\boldsymbol{h_0}$	**0.132**	**0.200**
$\boldsymbol{\gamma}$	**0.999**	**1.100**
$\boldsymbol{e_{lim}}$	**0.960**	**0.900**
α	1.000	1.000
μ	0.500	0.500
$\boldsymbol{\beta}$	**0.300**	**0.600**
Stress-induced anisotropy		
$\boldsymbol{H_0}$	**0.0** (1)	**43 000.0**
$\boldsymbol{\zeta}$	**0.0** (1)	**1.00**
H_{max}	(1)	5.0×10^4
$h_{f,min}$	(1)	0.1
$h_{f,max}$	(1)	100.0
Inherent anisotropy		
a	(2)	(2)
v_A	(2)	(2)
k_A	(2)	(2)

(1) Not used. (2) Not relevant, since this component has no impact on the modelled response under monotonic triaxial compression loading conditions.

A.2.1.2 Undrained monotonic triaxial compression tests

Table A.2 – Designation and initial conditions of the isotropically consolidated undrained monotonic triaxial compression with increasing mean stress (ICUMTC p↑) tests.

Designation (§)	e_0 ( )	$\sigma'_{r,0}$ (kPa)	$\sigma'_{a,0}$ (kPa)	p'_0 (kPa)	q_0 (kPa)	Loading (p↑ or p↓)
ICUMTC p↑ 0.876/80	0.876	80.0	80.0	80.0	0.0	p↑
ICUMTC p↑ 0.868/80	0.868	80.0	80.0	80.0	0.0	p↑
ICUMTC p↑ 0.843/135	0.843	135.0	135.0	135.0	0.0	p↑
ICUMTC p↑ 0.783/25	0.783	25.0	25.0	25.0	0.0	p↑
ICUMTC p↑ 0.801/80	0.801	80.0	80.0	80.0	0.0	p↑
ICUMTC p↑ 0.815/135	0.815	135.0	135.0	135.0	0.0	p↑
ICUMTC p↑ 0.686/25	0.686	25.0	25.0	25.0	0.0	p↑
ICUMTC p↑ 0.751/80	0.751	80.0	80.0	80.0	0.0	p↑
ICUMTC p↑ 0.694/135	0.694	135.0	135.0	135.0	0.0	p↑

(§) The designation identifies (1) type of consolidation: IC for isotropic consolidation; (2) type of drainage: U for undrained condition; (3) type of loading: MTC p↑ for monotonic triaxial compression with increasing mean stress; (4) void ratio immediately after consolidation; and (5) mean effective stress immediately after consolidation.

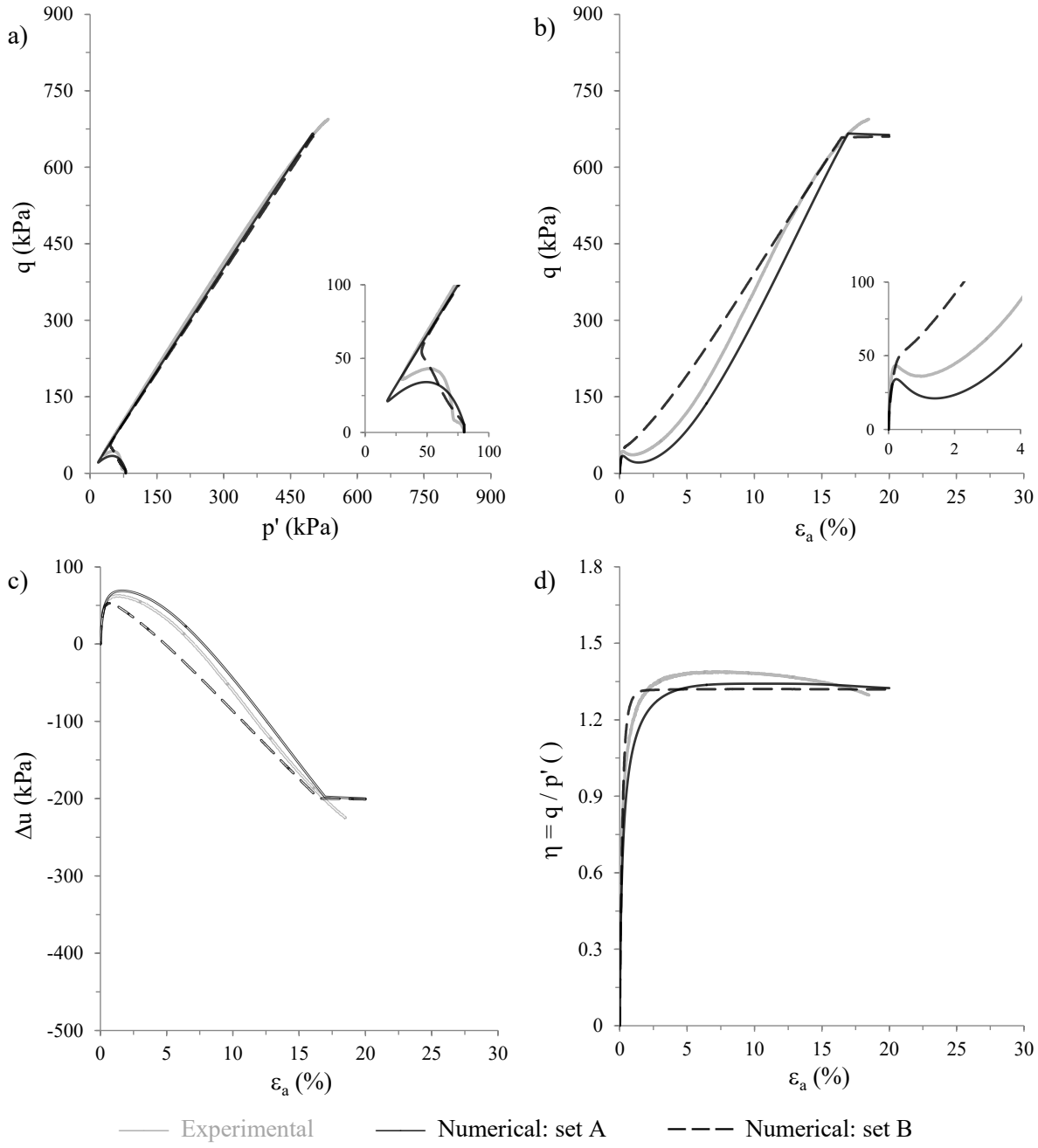

Figure A.1 – Experimental and numerical results of test ICUMTC p↑ 0.876/80: (a) effective stress path; (b) stress-strain response; (c) excess pore water pressure build-up; and (d) stress ratio evolution with axial strain.

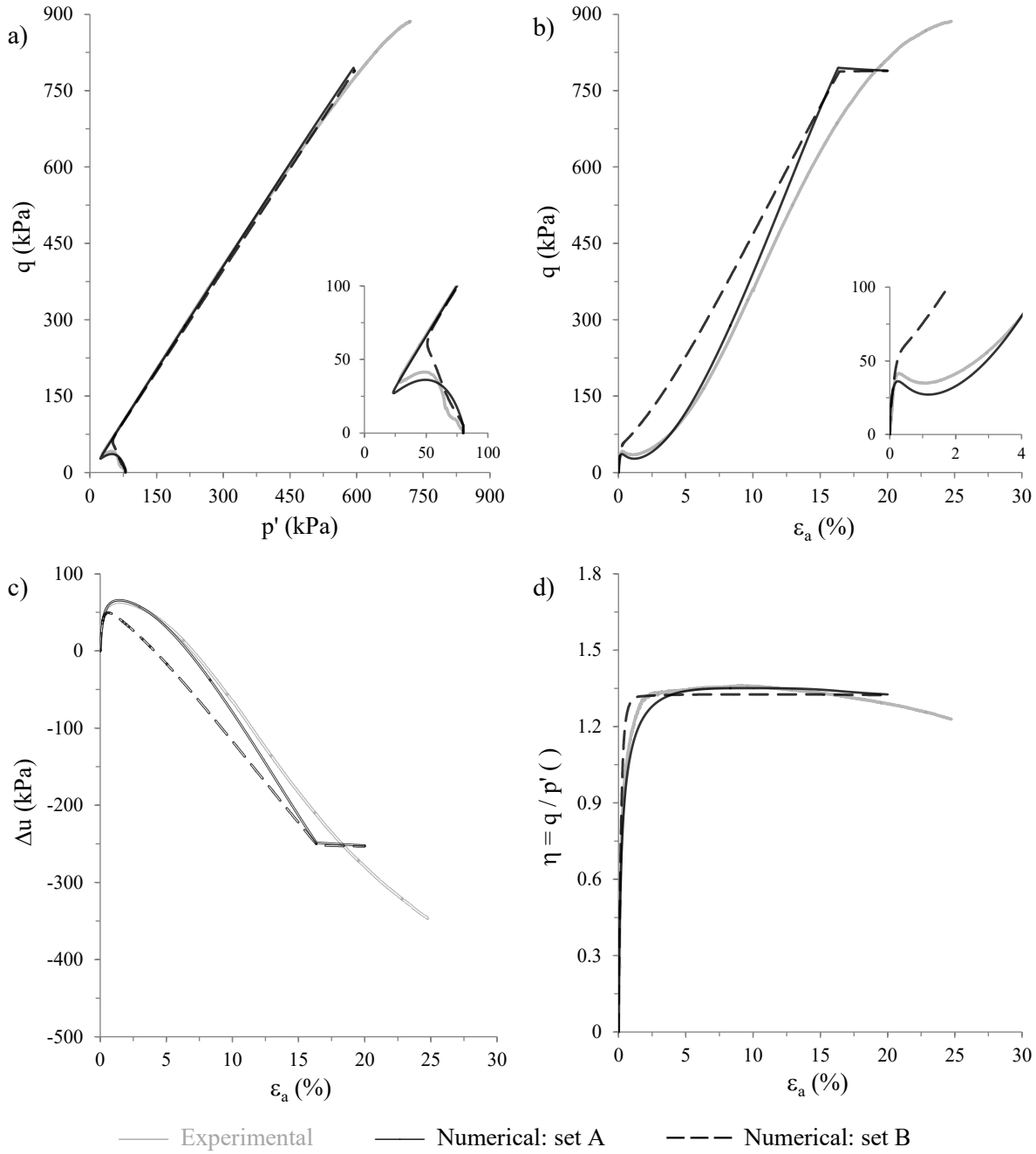

Figure A.2 – Experimental and numerical results of test ICUMTC p↑ 0.868/80: (a) effective stress path; (b) stress-strain response; (c) excess pore water pressure build-up; and (d) stress ratio evolution with axial strain.

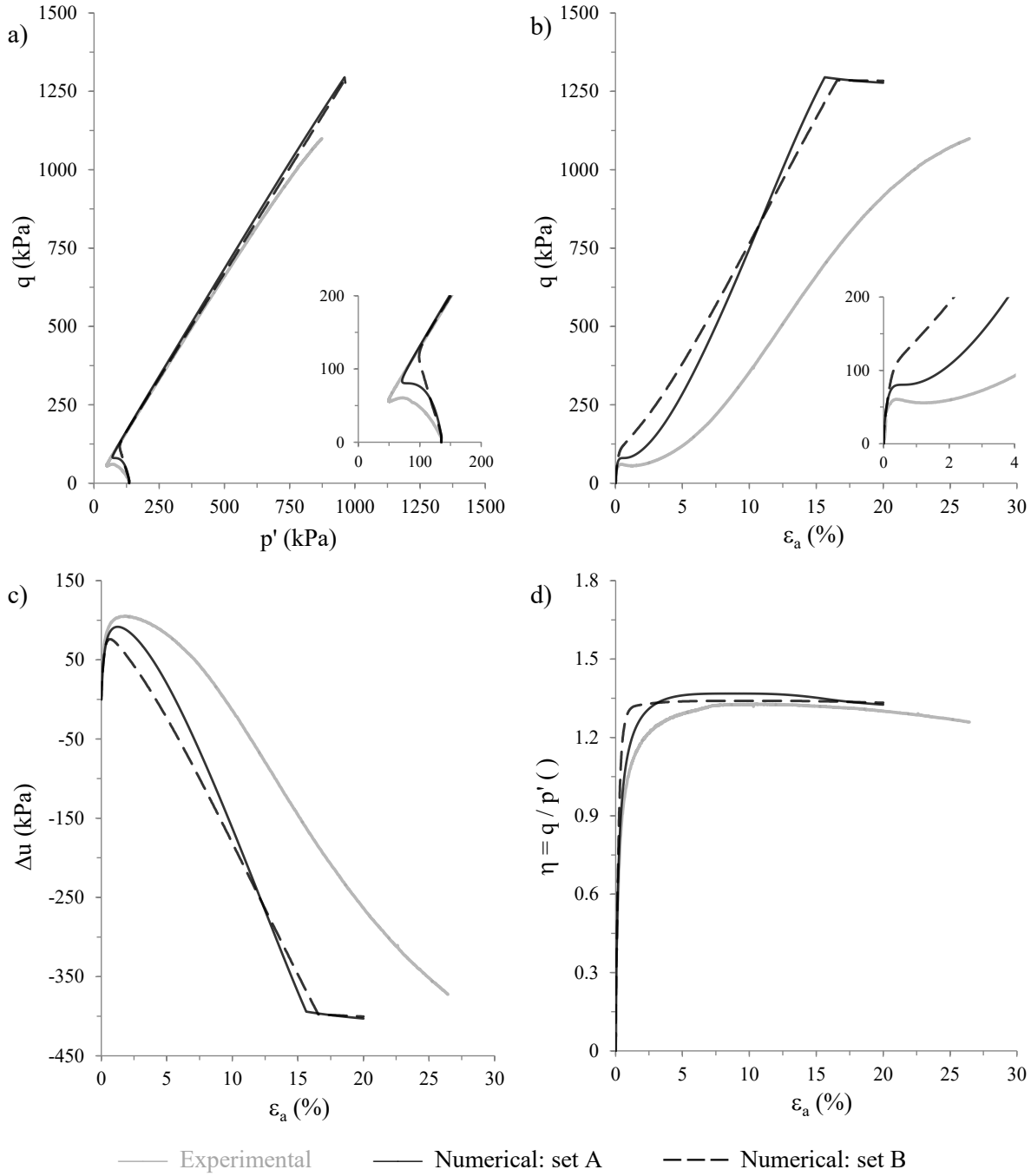

Figure A.3 – Experimental and numerical results of test ICUMTC p↑ 0.843/135: (a) effective stress path; (b) stress-strain response; (c) excess pore water pressure build-up; and (d) stress ratio evolution with axial strain.

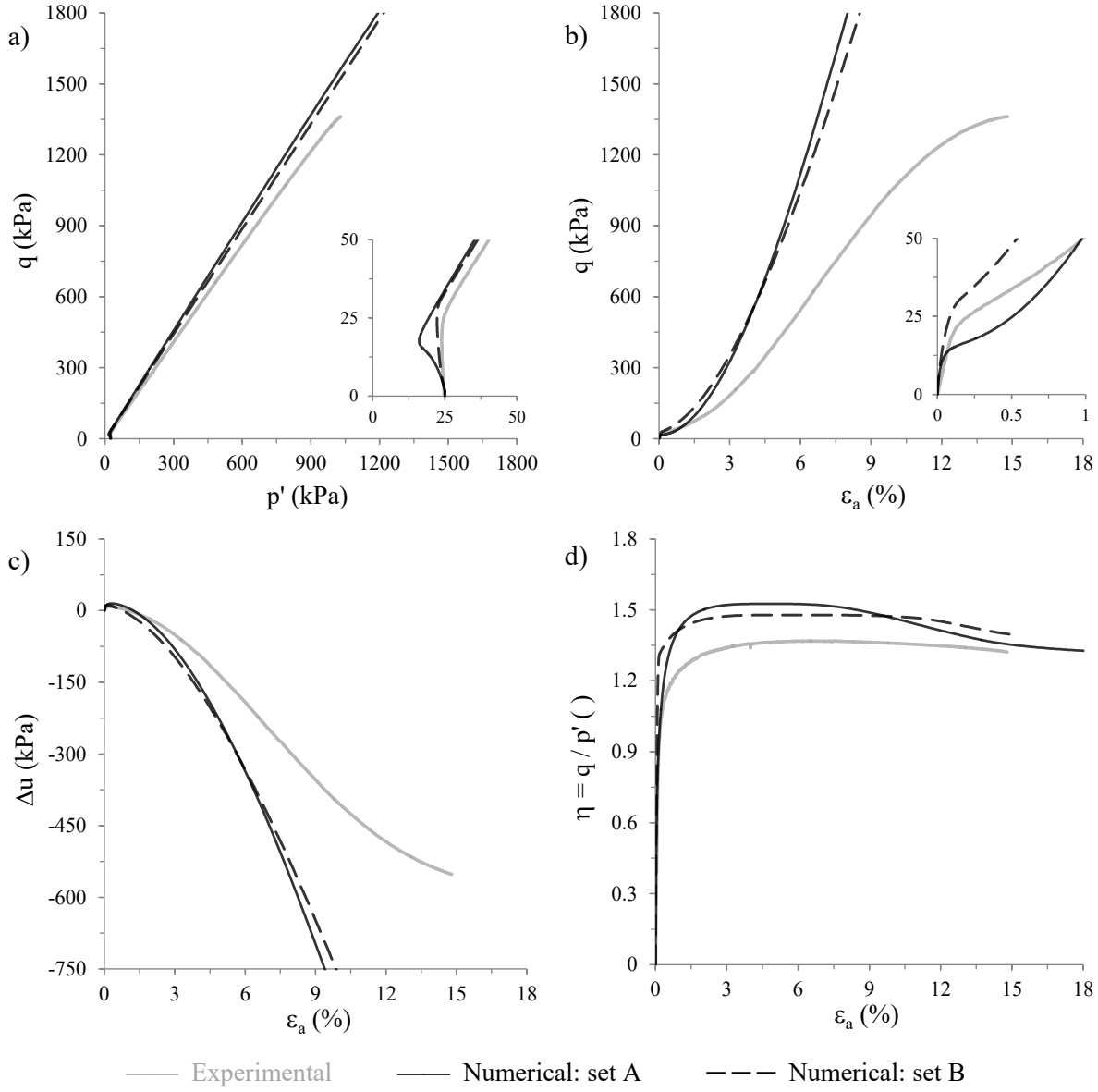

Figure A.4 – Experimental and numerical results of test ICUMTC p↑ 0.783/25: (a) effective stress path; (b) stress-strain response; (c) excess pore water pressure build-up; and (d) stress ratio evolution with axial strain.

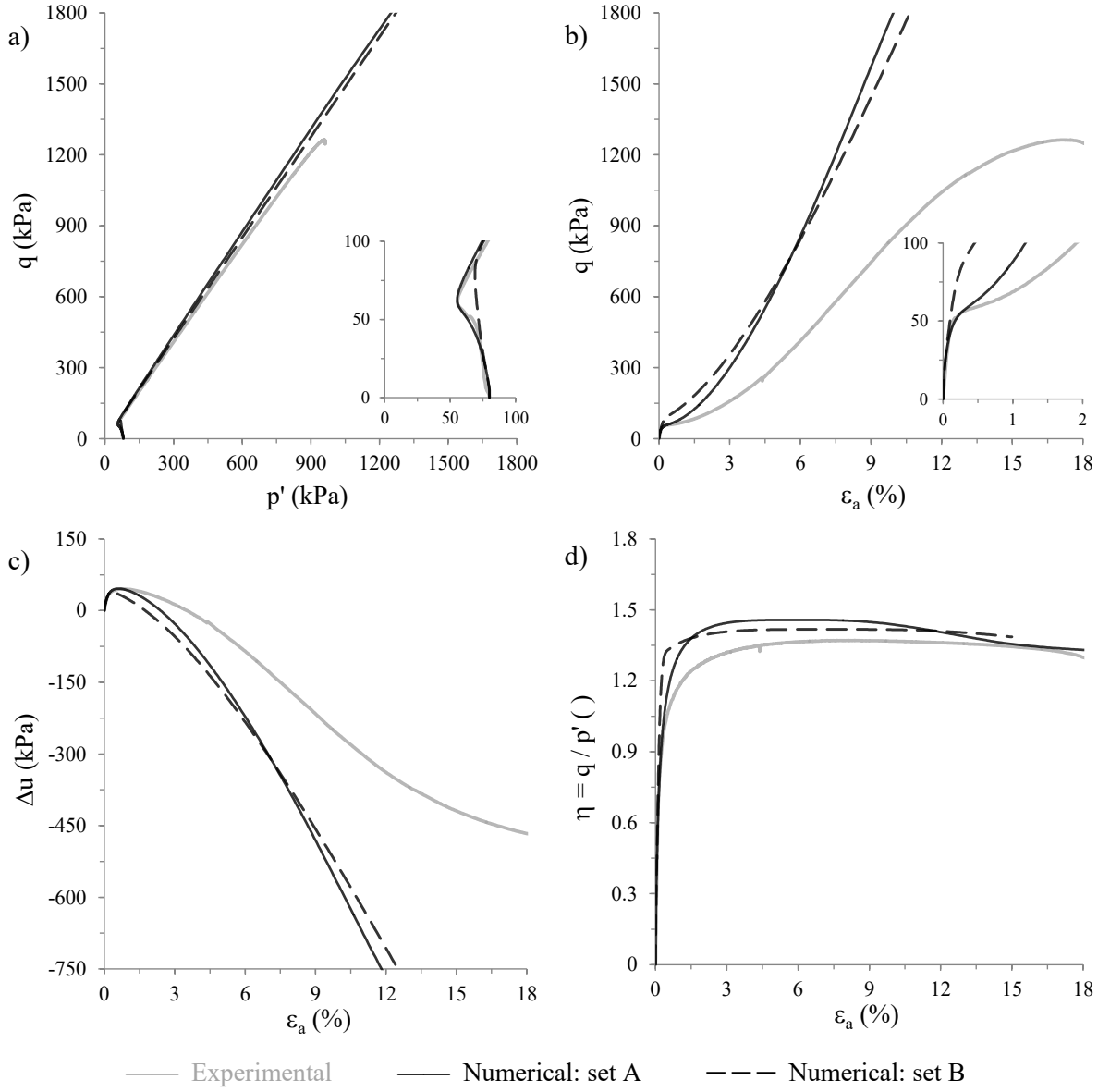

Figure A.5 – Experimental and numerical results of test ICUMTC p↑ 0.801/80: (a) effective stress path; (b) stress-strain response; (c) excess pore water pressure build-up; and (d) stress ratio evolution with axial strain.

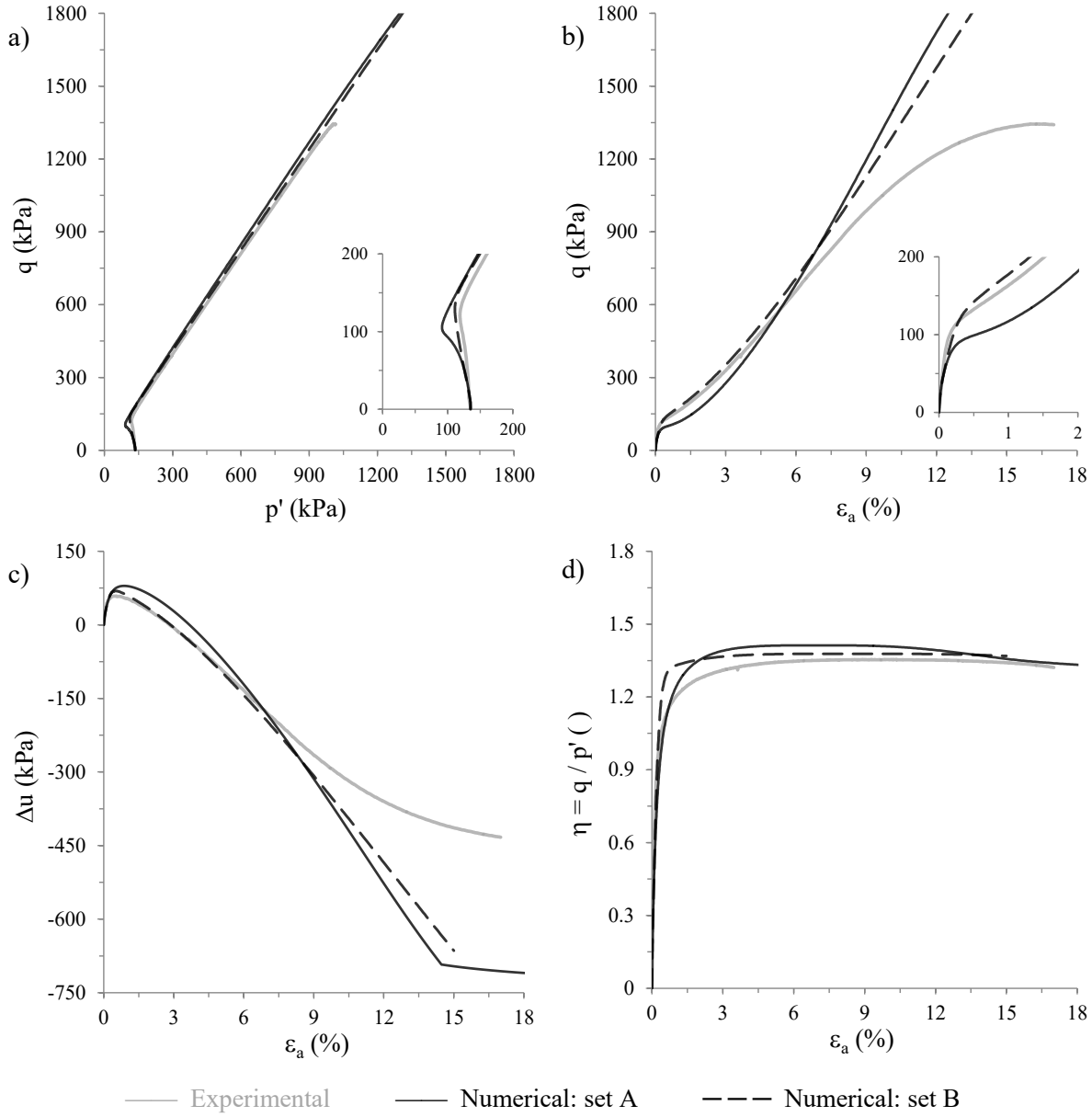

Figure A.6 – Experimental and numerical results of test ICUMTC p↑ 0.815/135: (a) effective stress path; (b) stress-strain response; (c) excess pore water pressure build-up; and (d) stress ratio evolution with axial strain.

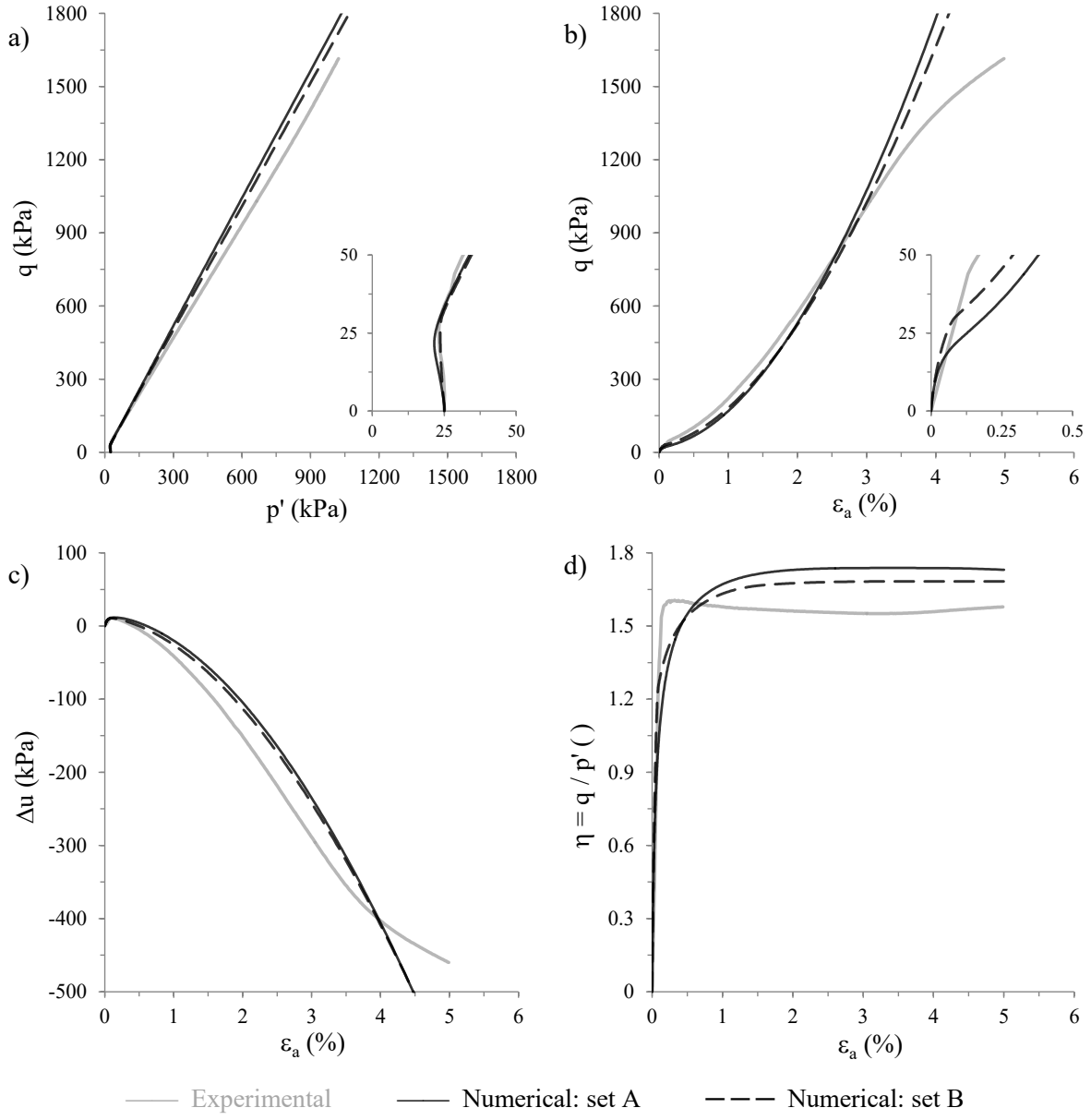

Figure A.7 – Experimental and numerical results of test ICUMTC p↑ 0.686/25: (a) effective stress path; (b) stress-strain response; (c) excess pore water pressure build-up; and (d) stress ratio evolution with axial strain.

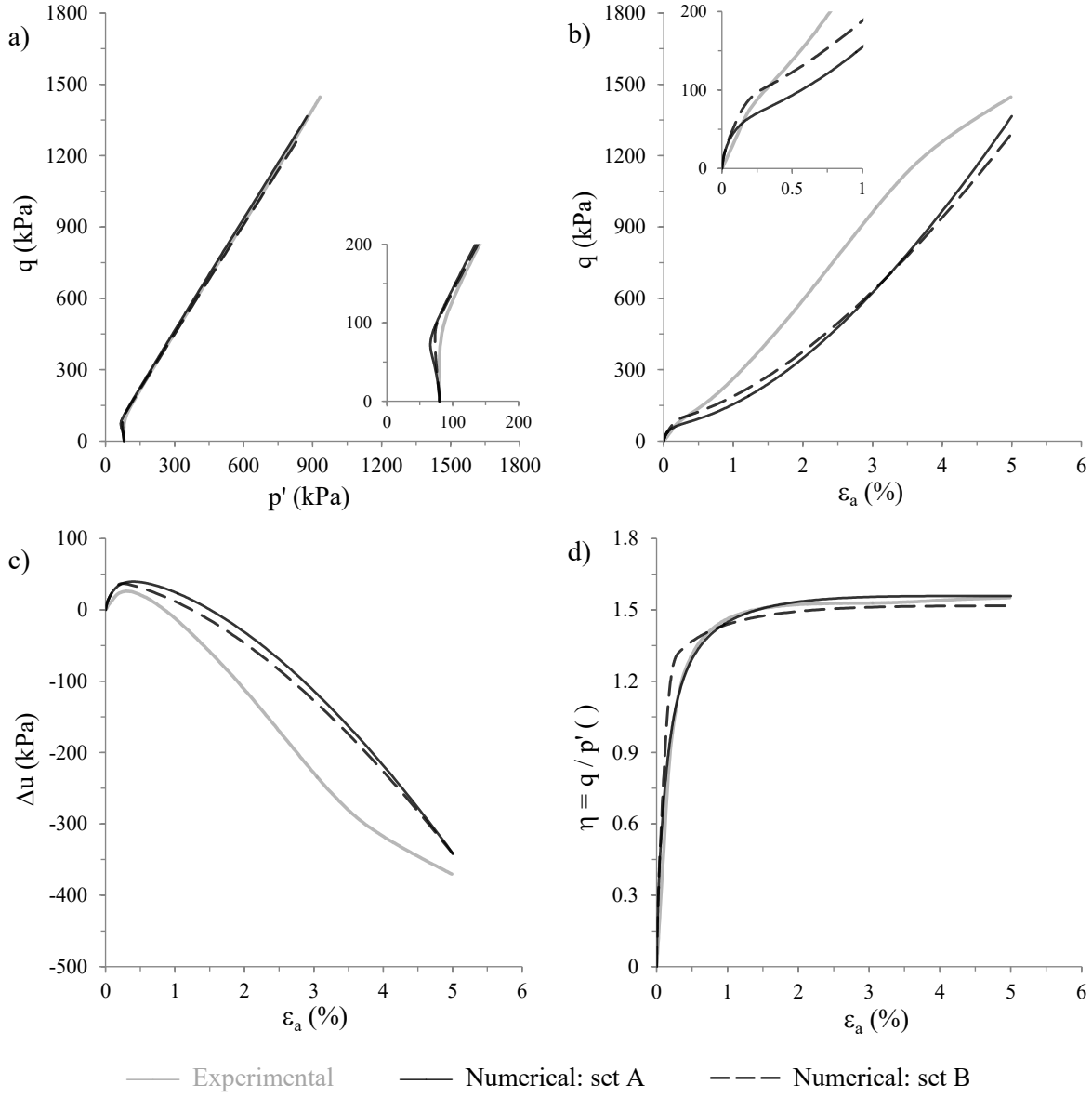

Figure A.8 – Experimental and numerical results of test ICUMTC p↑ 0.751/80: (a) effective stress path; (b) stress-strain response; (c) excess pore water pressure build-up; and (d) stress ratio evolution with axial strain.

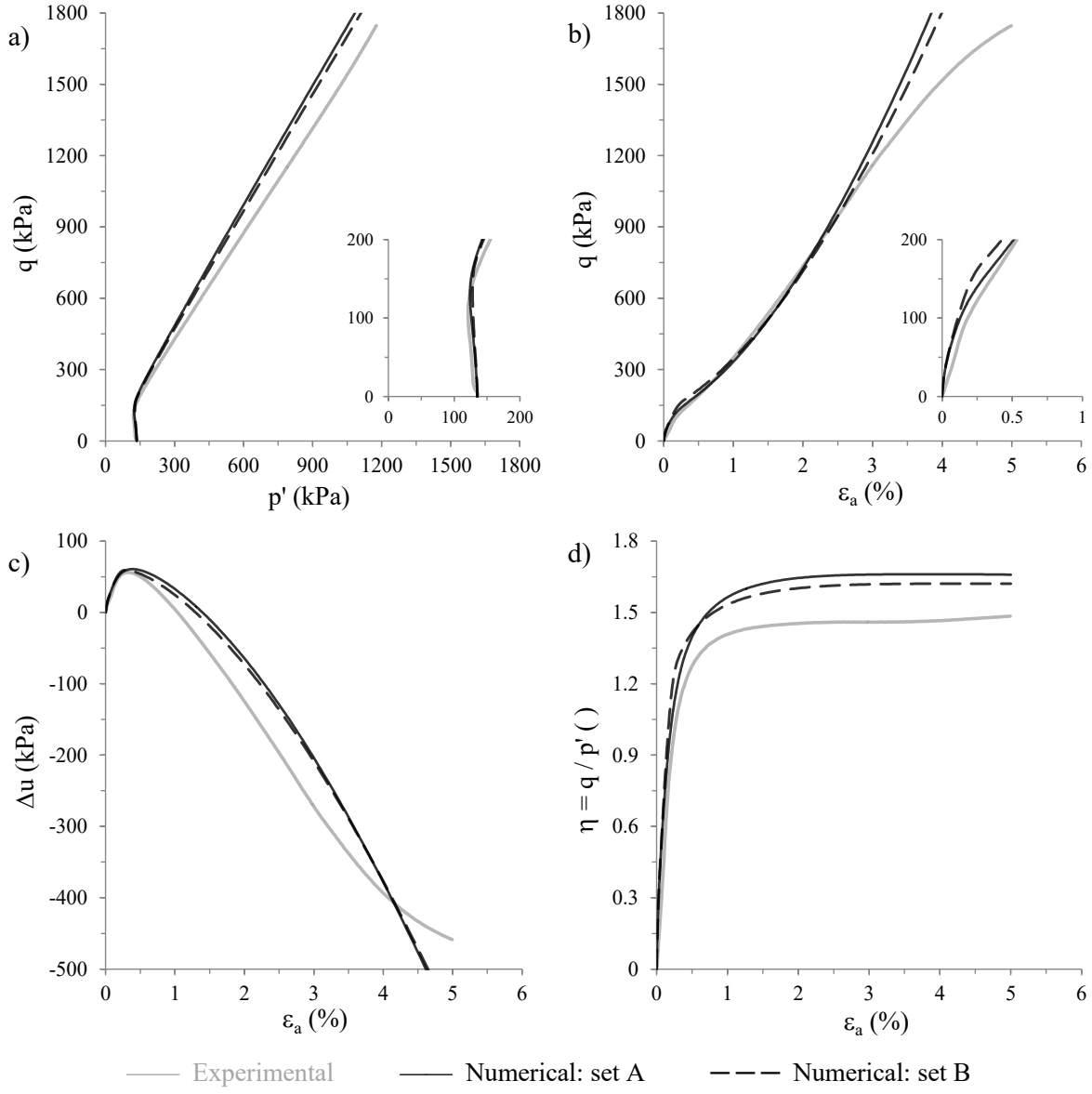

Figure A.9 – Experimental and numerical results of test ICUMTC p↑ 0.694/135: (a) effective stress path; (b) stress-strain response; (c) excess pore water pressure build-up; and (d) stress ratio evolution with axial strain.

A.2.1.3 Drained monotonic triaxial compression tests

Table A.3 – Designation and initial conditions of the drained monotonic triaxial compression tests.

Type of test	Designation [(§)]	e_0 ( )	$\sigma'_{r,0}$ (kPa)	$\sigma'_{a,0}$ (kPa)	p'_0 (kPa)	q_0 (kPa)	Loading (p↑ or p↓)
Drained isotropic compression (DIC)	ICDIC 0.794/25	0.794	25.0	25.0	25.0	0.0	p↑&p↓
	ICDIC 0.659/25	0.659	25.0	25.0	25.0	0.0	p↑&p↓
Drained monotonic triaxial compression (DMTC)	ICDMTC p↑ 0.875/50	0.875	50.0	50.0	50.0	0.0	p↑
	ICDMTC p↑ 0.885/80	0.885	80.0	80.0	80.0	0.0	p↑
	ICDMTC p↑ 0.846/200	0.846	200.0	200.0	200.0	0.0	p↑
	ICDMTC p↑ 0.835/500	0.835	500.0	500.0	500.0	0.0	p↑
	ICDMTC p↑ 0.829/25	0.829	25.0	25.0	25.0	0.0	p↑
	ICDMTC p↑ 0.798/80	0.798	80.0	80.0	80.0	0.0	p↑
	ICDMTC p↑ 0.804/135	0.804	135.0	135.0	135.0	0.0	p↑
	ICDMTC p↑ 0.667/25	0.667	25.0	25.0	25.0	0.0	p↑
	ICDMTC p↑ 0.725/80	0.725	80.0	80.0	80.0	0.0	p↑
	ICDMTC p↑ 0.728/135	0.728	135.0	135.0	135.0	0.0	p↑
	K0CDMTC p↓ 0.797/80	0.797	60.0	120.0	80.0	60.0	p↓
	ICDMTC p↓ 0.650/80	0.650	80.0	80.0	80.0	0.0	p↓
	K0CDMTC p↓ 0.672/80	0.672	60.0	120.0	80.0	60.0	p↓

[(§)] The designation identifies (1) type of consolidation: IC or K0C for isotropic or anisotropic consolidation, respectively; (2) type of drainage: D for drained condition; (3) type of loading: IC for isotropic compression, MTC p↑ for monotonic triaxial compression with increasing mean stress, MTC p↓ for monotonic triaxial compression with decreasing mean stress; (4) void ratio immediately after consolidation; and (5) mean effective stress immediately after consolidation.

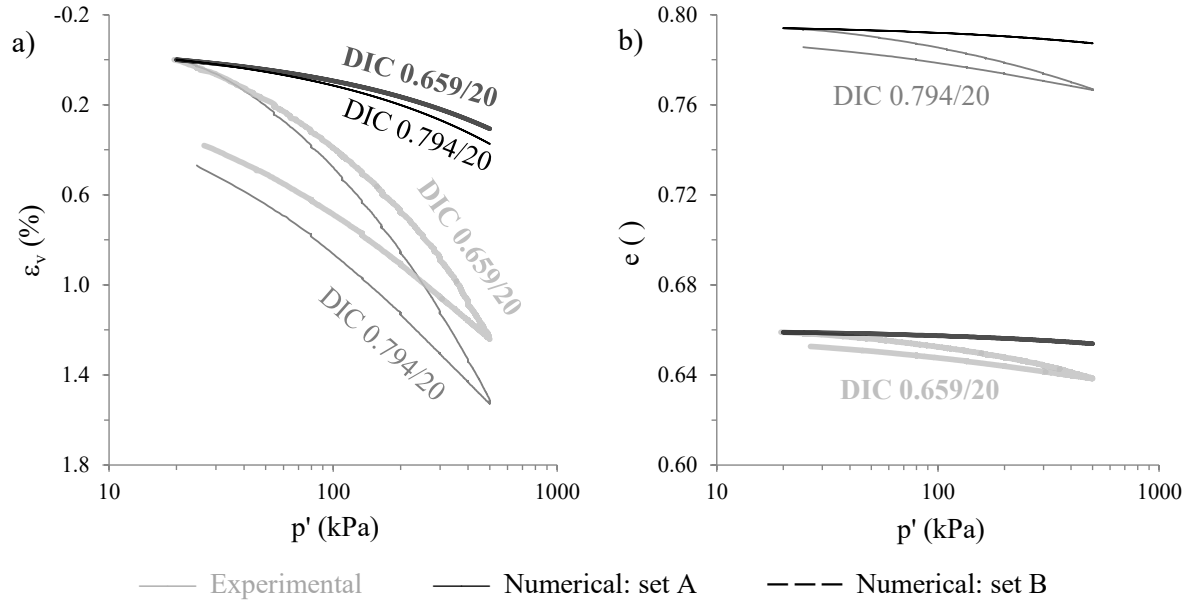

Figure A.10 – Experimental and numerical results of tests ICDIC 0.794/25 and ICDIC 0.794/25: (a) volumetric strain and (b) void ratio evolutions with mean effective stress (note that, for these two tests, the numerical curves corresponding to the set A and set B are coincident).

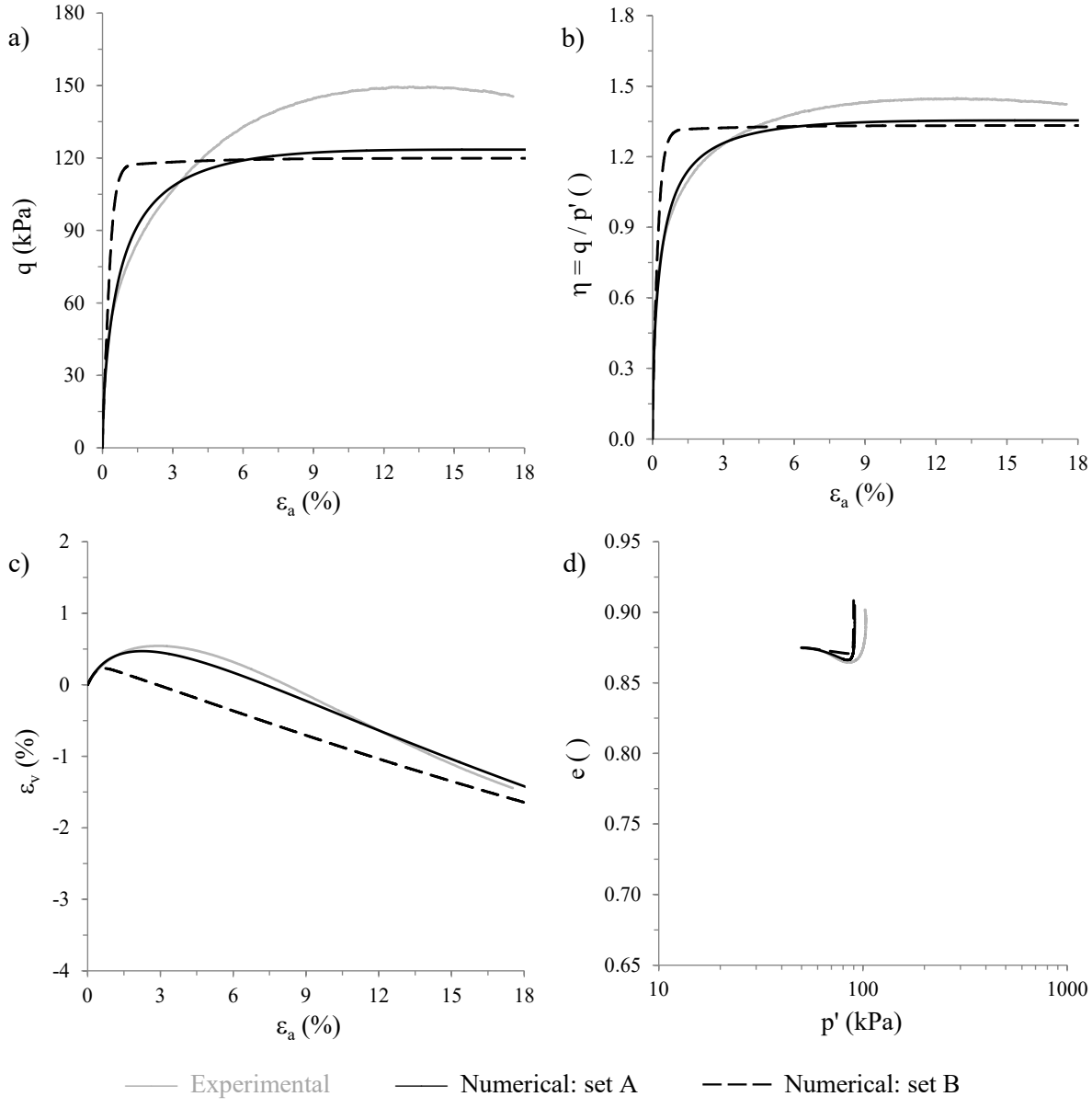

Figure A.11 – Experimental and numerical results of test ICDMTC p↑ 0.875/50: (a) deviatoric stress evolution with axial strain; (b) stress ratio evolution with axial strain; (c) volumetric strain evolution with axial strain; and (d) void ratio evolution with mean effective stress.

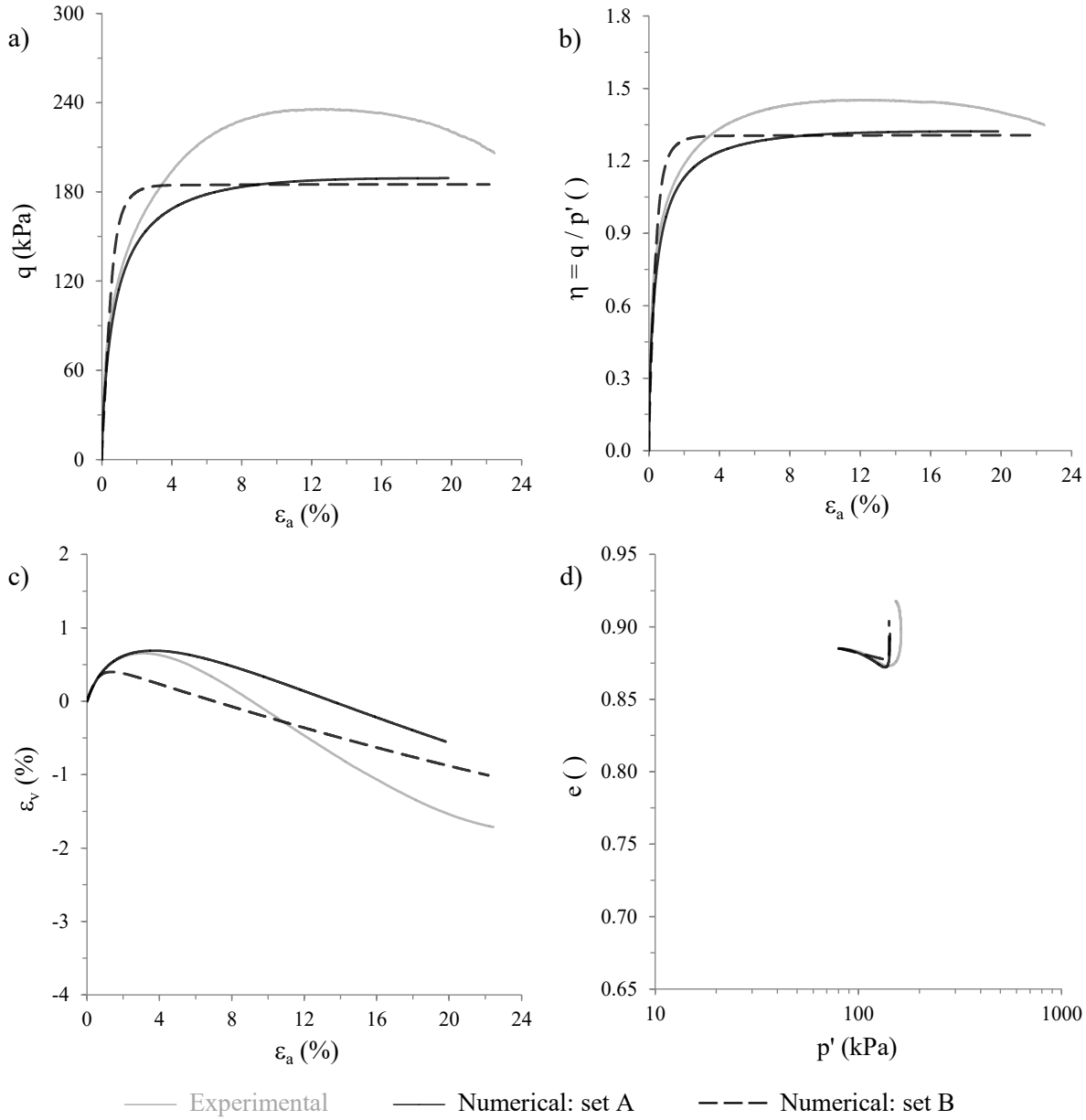

Figure A.12 – Experimental and numerical results of test ICDMTC p↑ 0.885/80: (a) deviatoric stress evolution with axial strain; (b) stress ratio evolution with axial strain; (c) volumetric strain evolution with axial strain; and (d) void ratio evolution with mean effective stress.

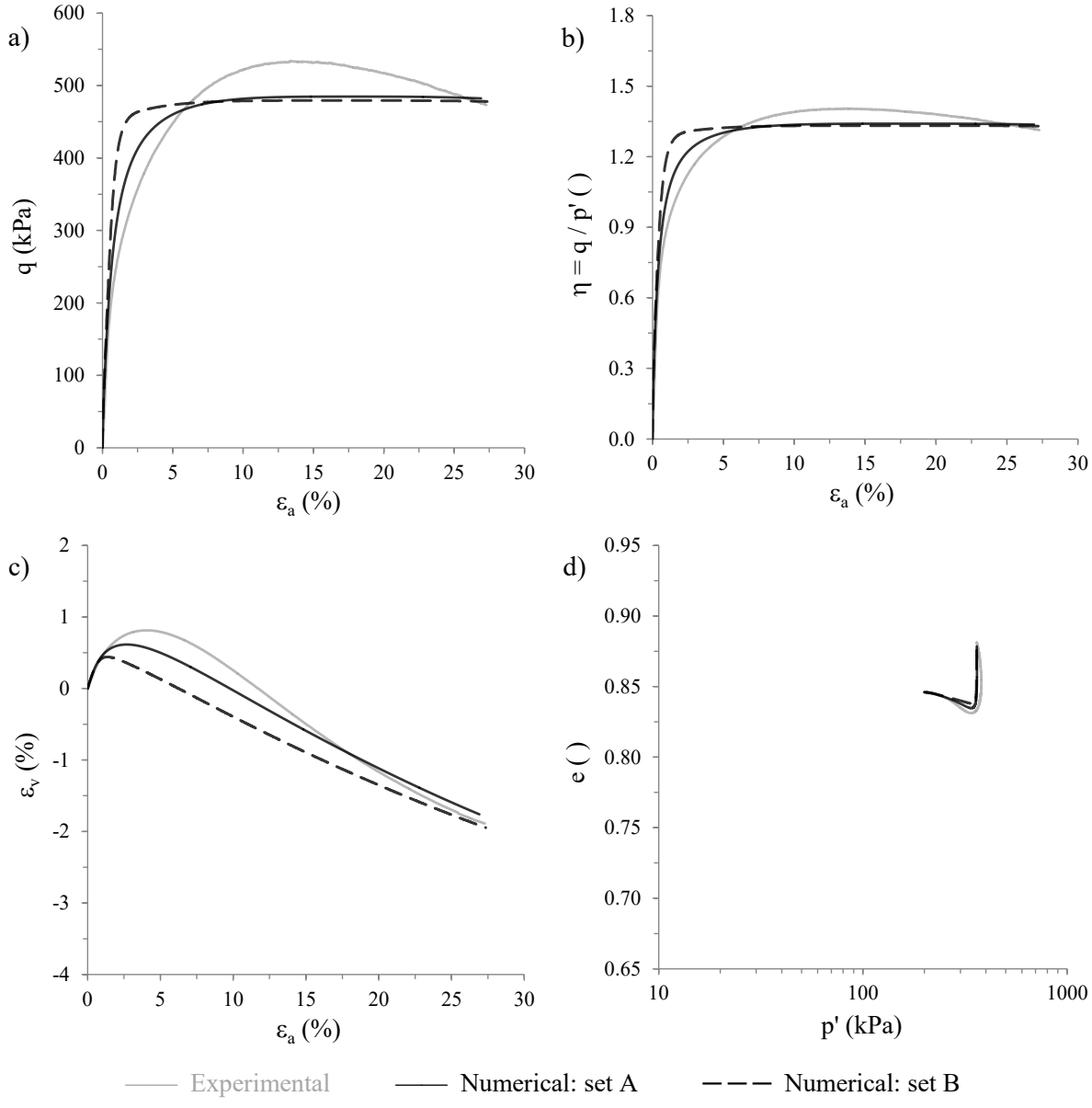

Figure A.13 – Experimental and numerical results of test ICDMTC p↑ 0.846/200: (a) deviatoric stress evolution with axial strain; (b) stress ratio evolution with axial strain; (c) volumetric strain evolution with axial strain; and (d) void ratio evolution with mean effective stress.

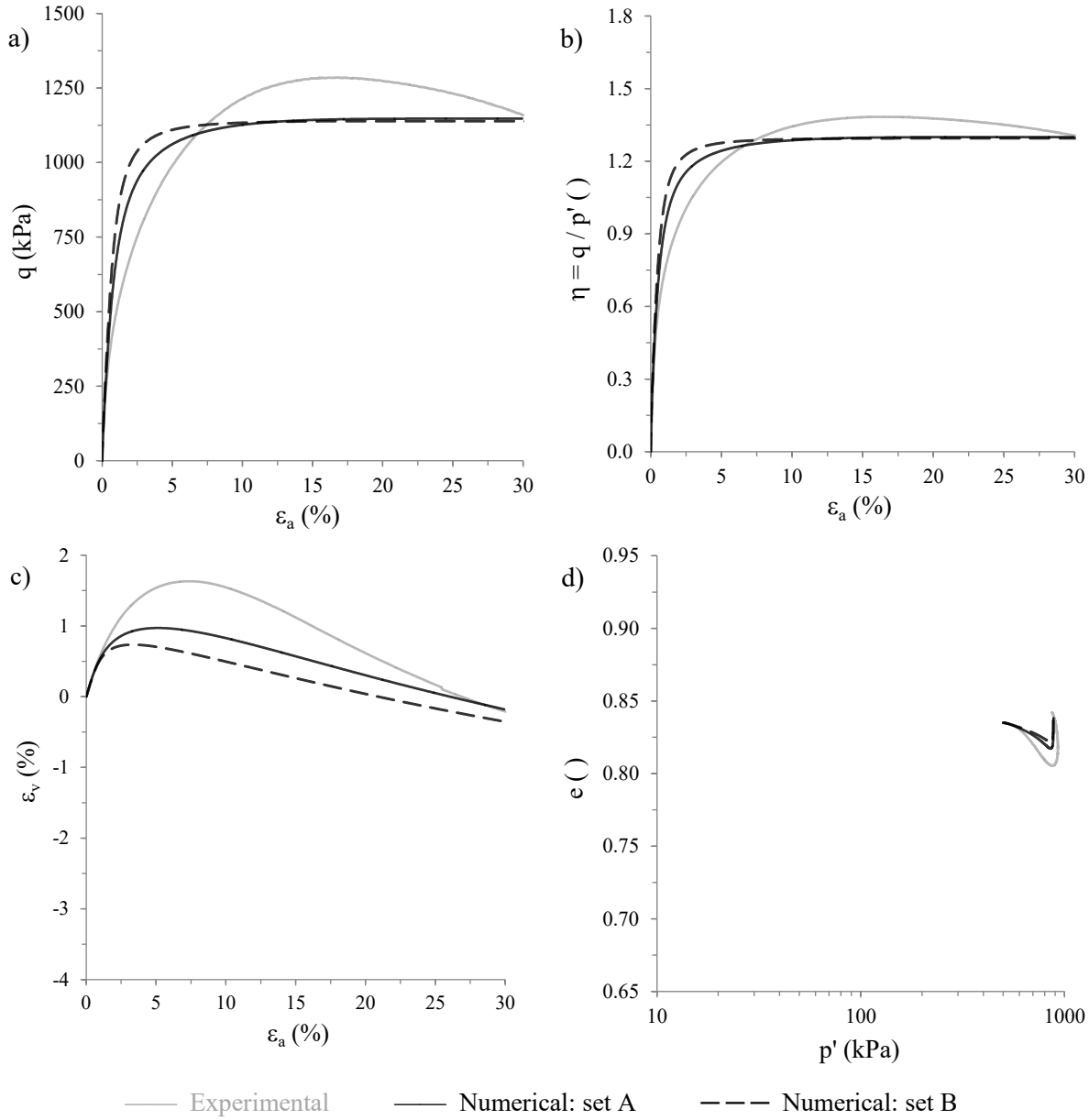

Figure A.14 – Experimental and numerical results of test ICDMTC p↑ 0.835/500: (a) deviatoric stress evolution with axial strain; (b) stress ratio evolution with axial strain; (c) volumetric strain evolution with axial strain; and (d) void ratio evolution with mean effective stress.

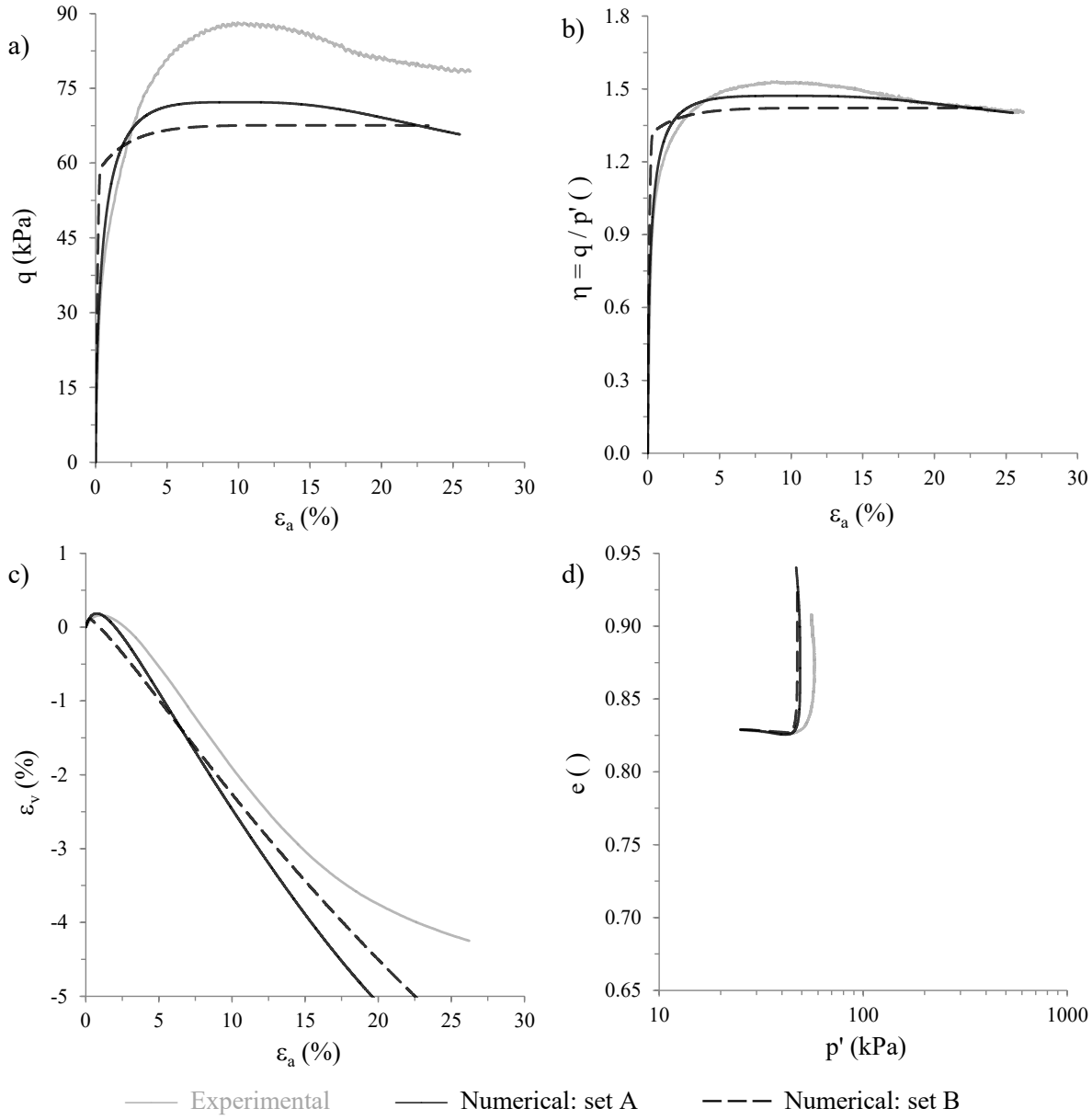

Figure A.15 – Experimental and numerical results of test ICDMTC p↑ 0.829/25: (a) deviatoric stress evolution with axial strain; (b) stress ratio evolution with axial strain; (c) volumetric strain evolution with axial strain; and (d) void ratio evolution with mean effective stress.

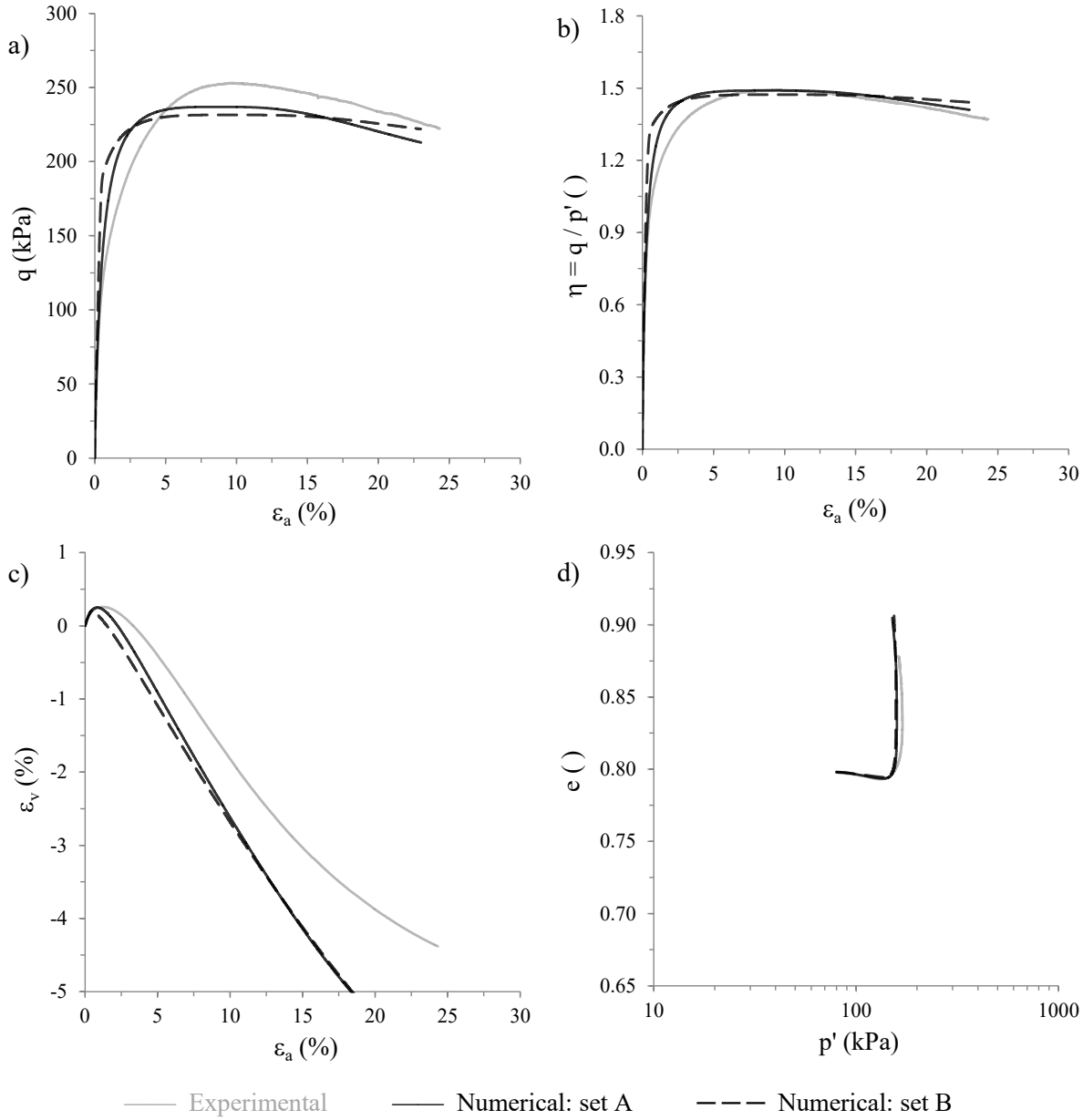

Figure A.16 – Experimental and numerical results of test ICDMTC p↑ 0.798/80: (a) deviatoric stress evolution with axial strain; (b) stress ratio evolution with axial strain; (c) volumetric strain evolution with axial strain; and (d) void ratio evolution with mean effective stress.

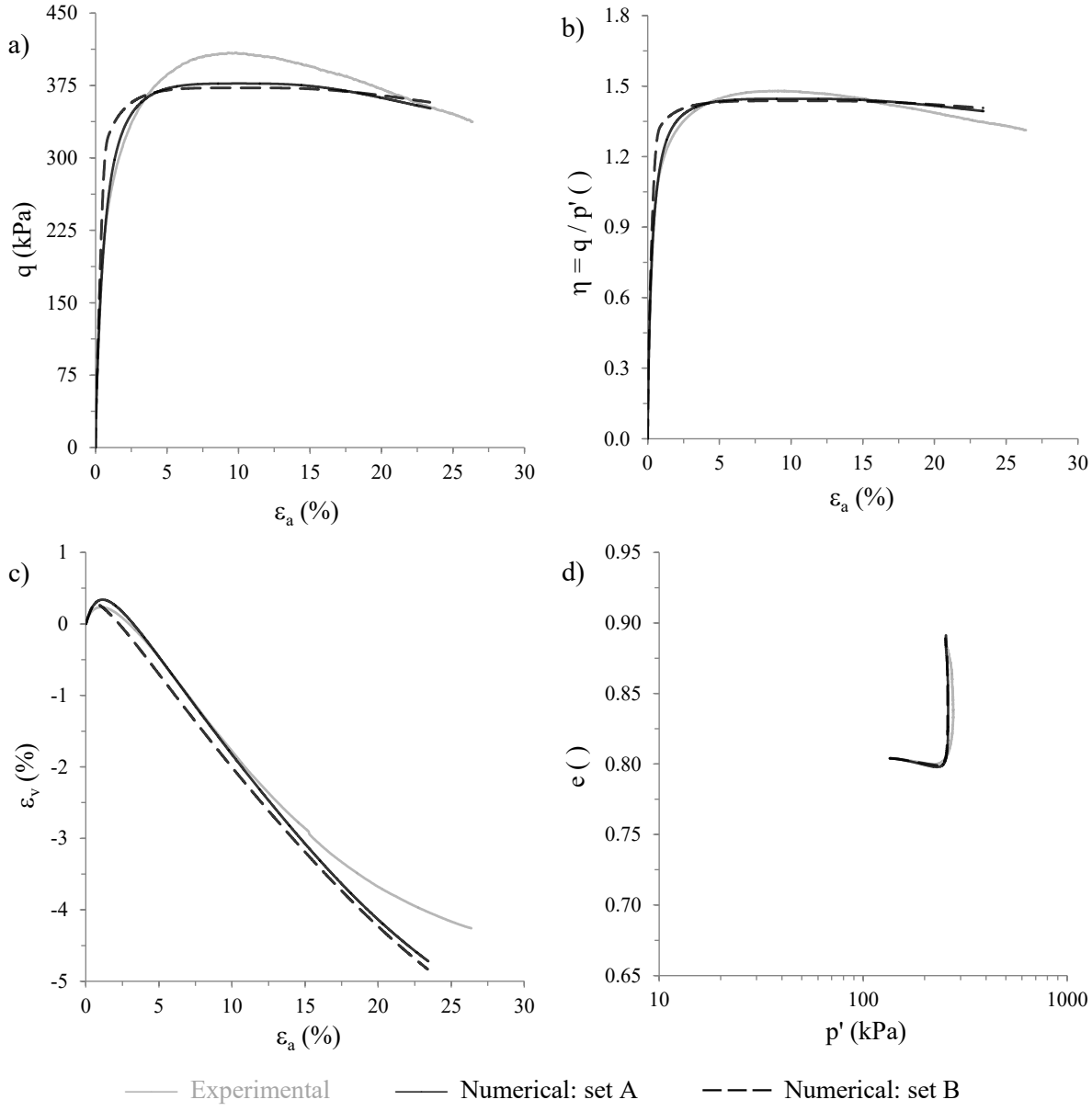

Figure A.17 – Experimental and numerical results of test ICDMTC p↑ 0.804/135: (a) deviatoric stress evolution with axial strain; (b) stress ratio evolution with axial strain; (c) volumetric strain evolution with axial strain; and (d) void ratio evolution with mean effective stress.

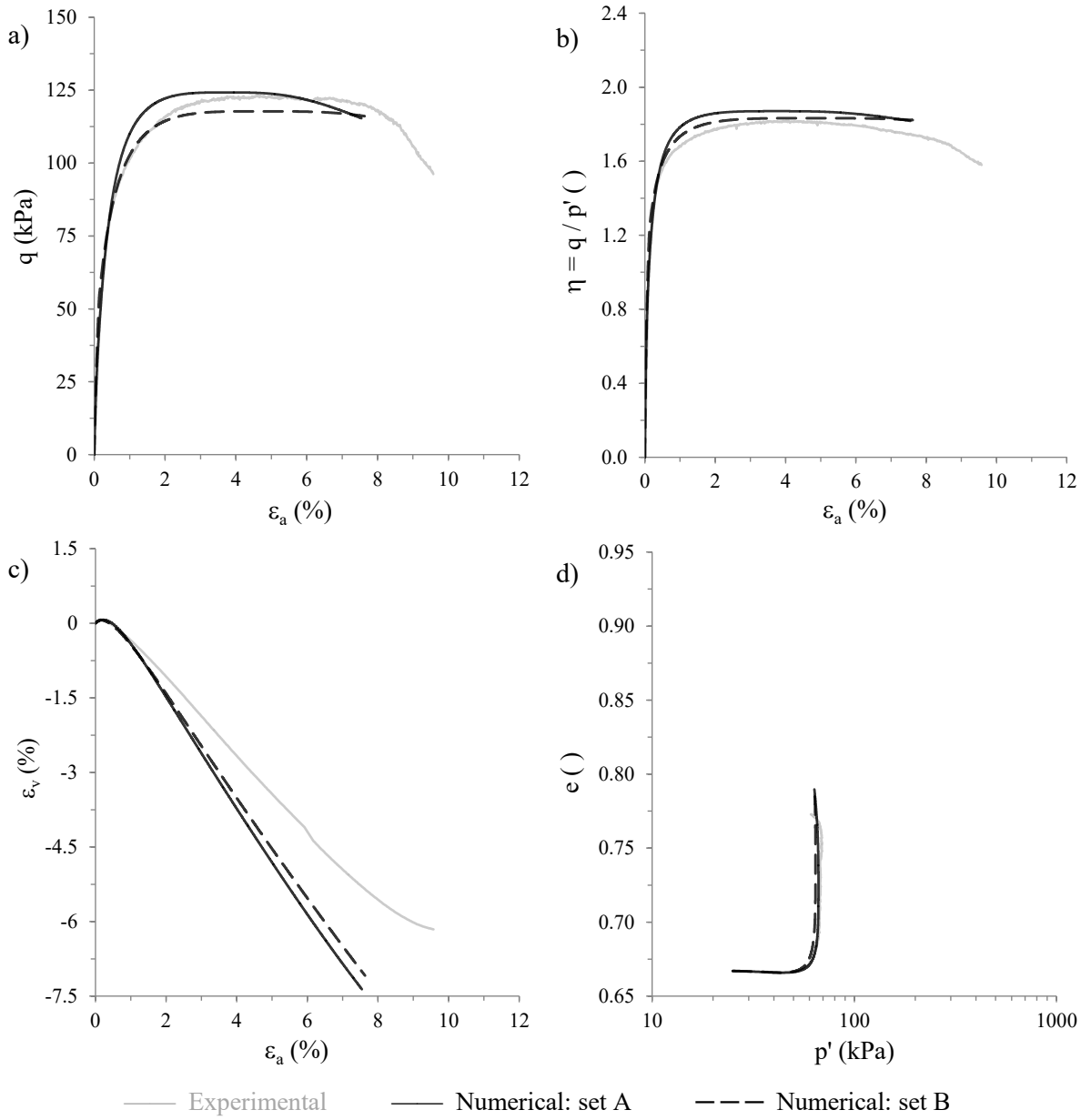

Figure A.18 – Experimental and numerical results of test ICDMTC p↑ 0.667/25: (a) deviatoric stress evolution with axial strain; (b) stress ratio evolution with axial strain; (c) volumetric strain evolution with axial strain; and (d) void ratio evolution with mean effective stress.

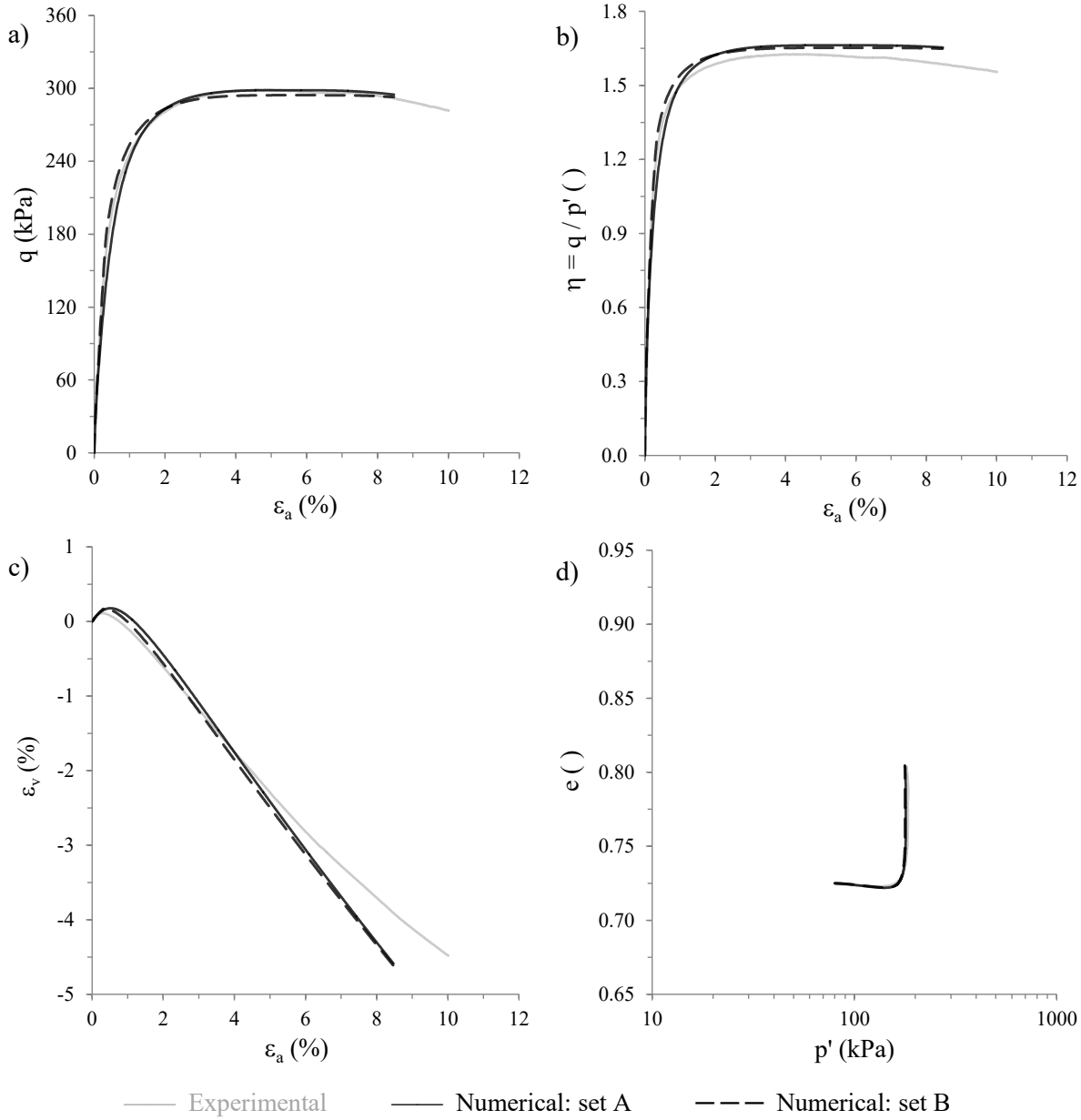

Figure A.19 – Experimental and numerical results of test ICDMTC p↑ 0.725/80: (a) deviatoric stress evolution with axial strain; (b) stress ratio evolution with axial strain; (c) volumetric strain evolution with axial strain; and (d) void ratio evolution with mean effective stress.

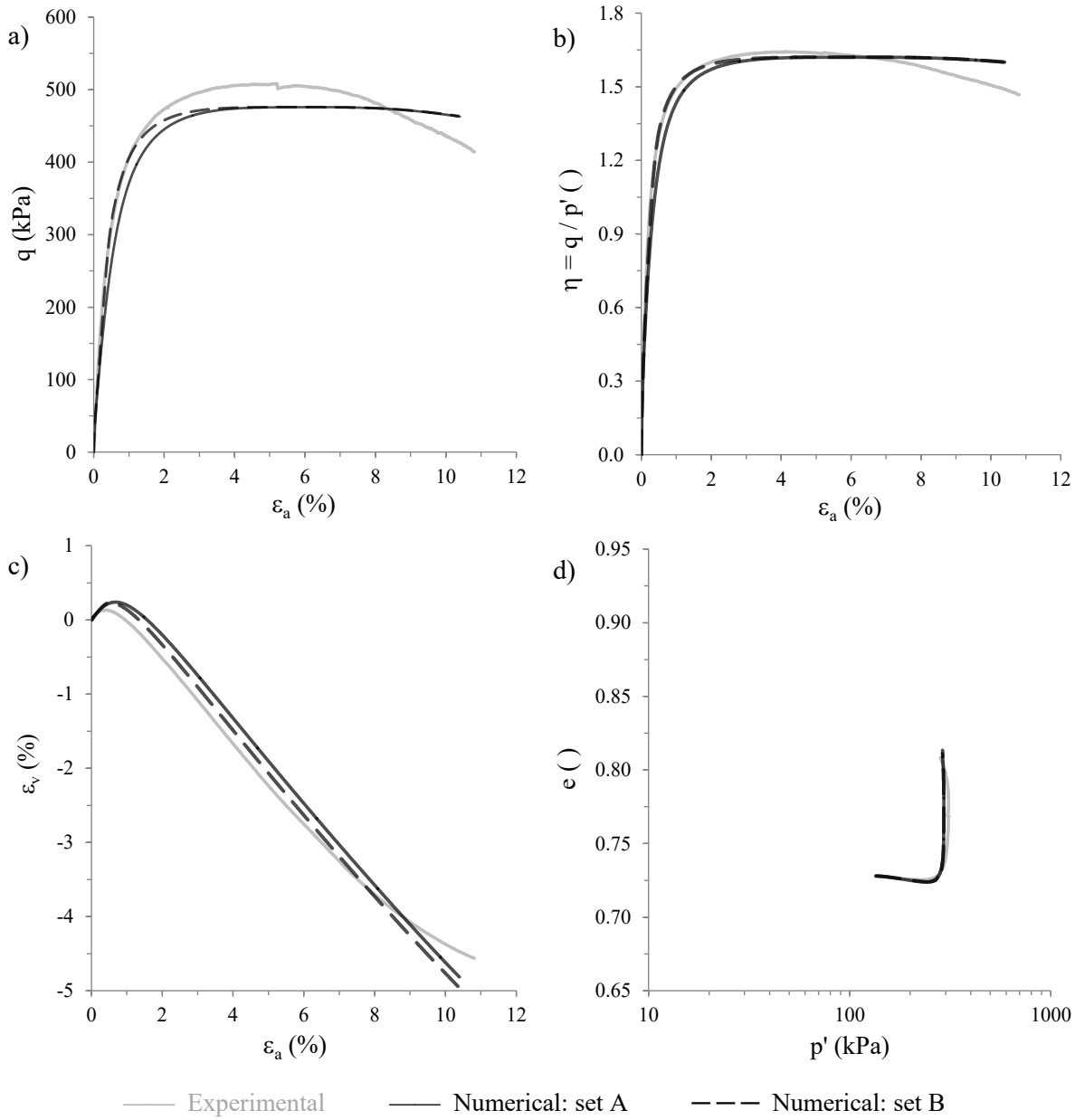

Figure A.20 – Experimental and numerical results of test ICDMTC p↑ 0.728/135: (a) deviatoric stress evolution with axial strain; (b) stress ratio evolution with axial strain; (c) volumetric strain evolution with axial strain; and (d) void ratio evolution with mean effective stress.

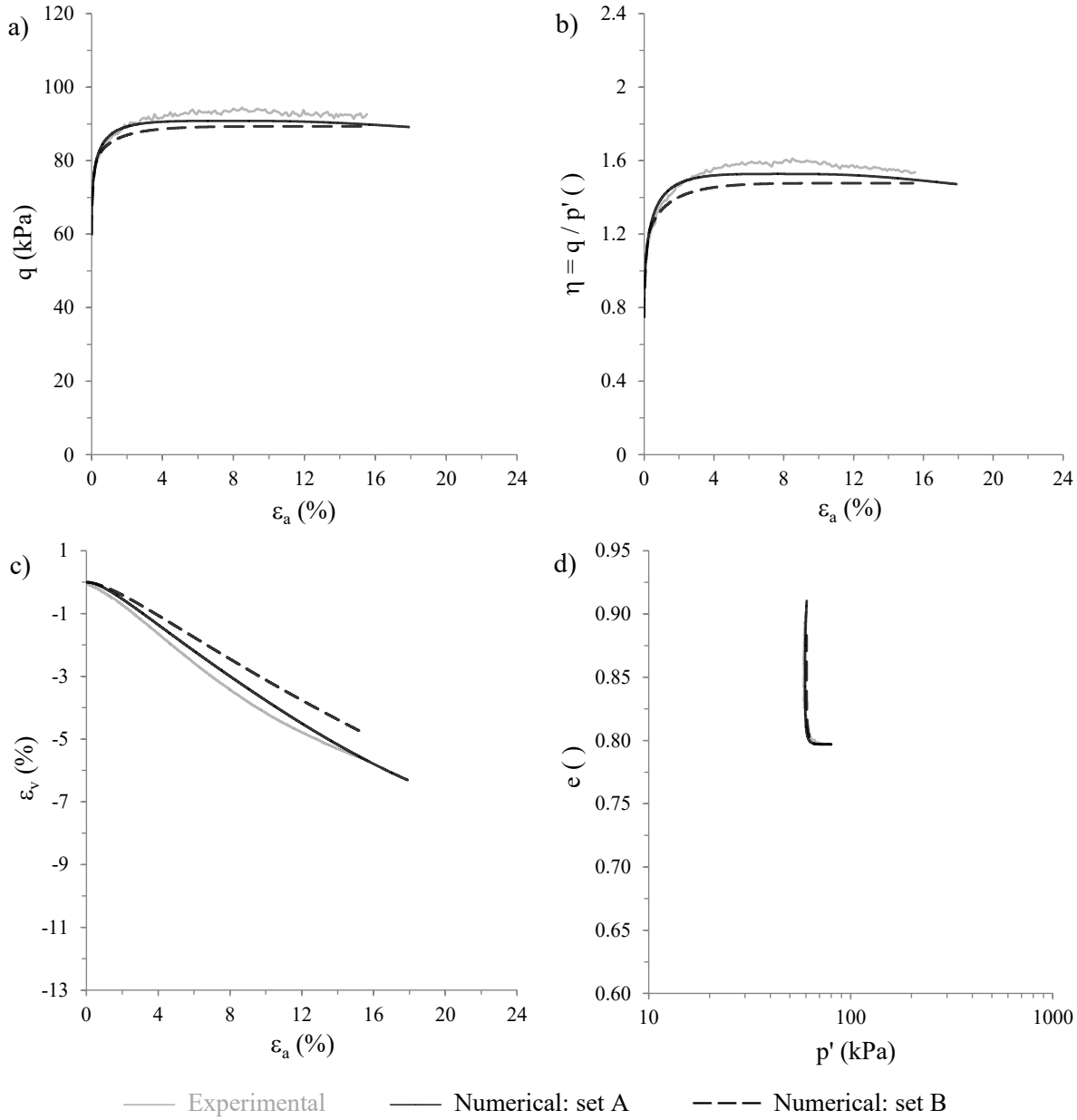

Figure A.21 – Experimental and numerical results of test K0CDMTC p↓ 0.797/80: (a) deviatoric stress evolution with axial strain; (b) stress ratio evolution with axial strain; (c) volumetric strain evolution with axial strain; and (d) void ratio evolution with mean effective stress.

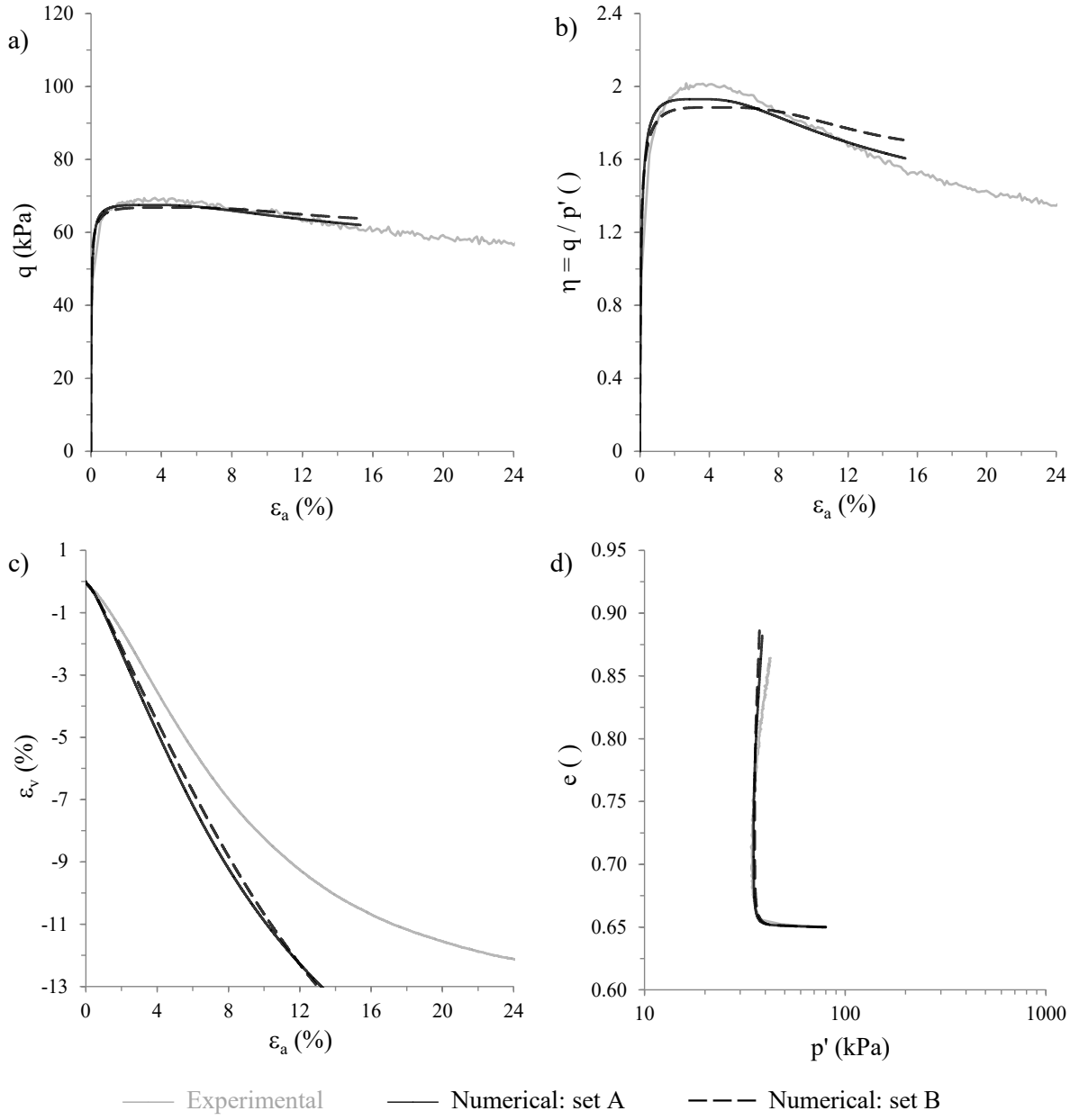

Figure A.22 – Experimental and numerical results of test ICDMTC p↓ 0.650/80: (a) deviatoric stress evolution with axial strain; (b) stress ratio evolution with axial strain; (c) volumetric strain evolution with axial strain; and (d) void ratio evolution with mean effective stress.

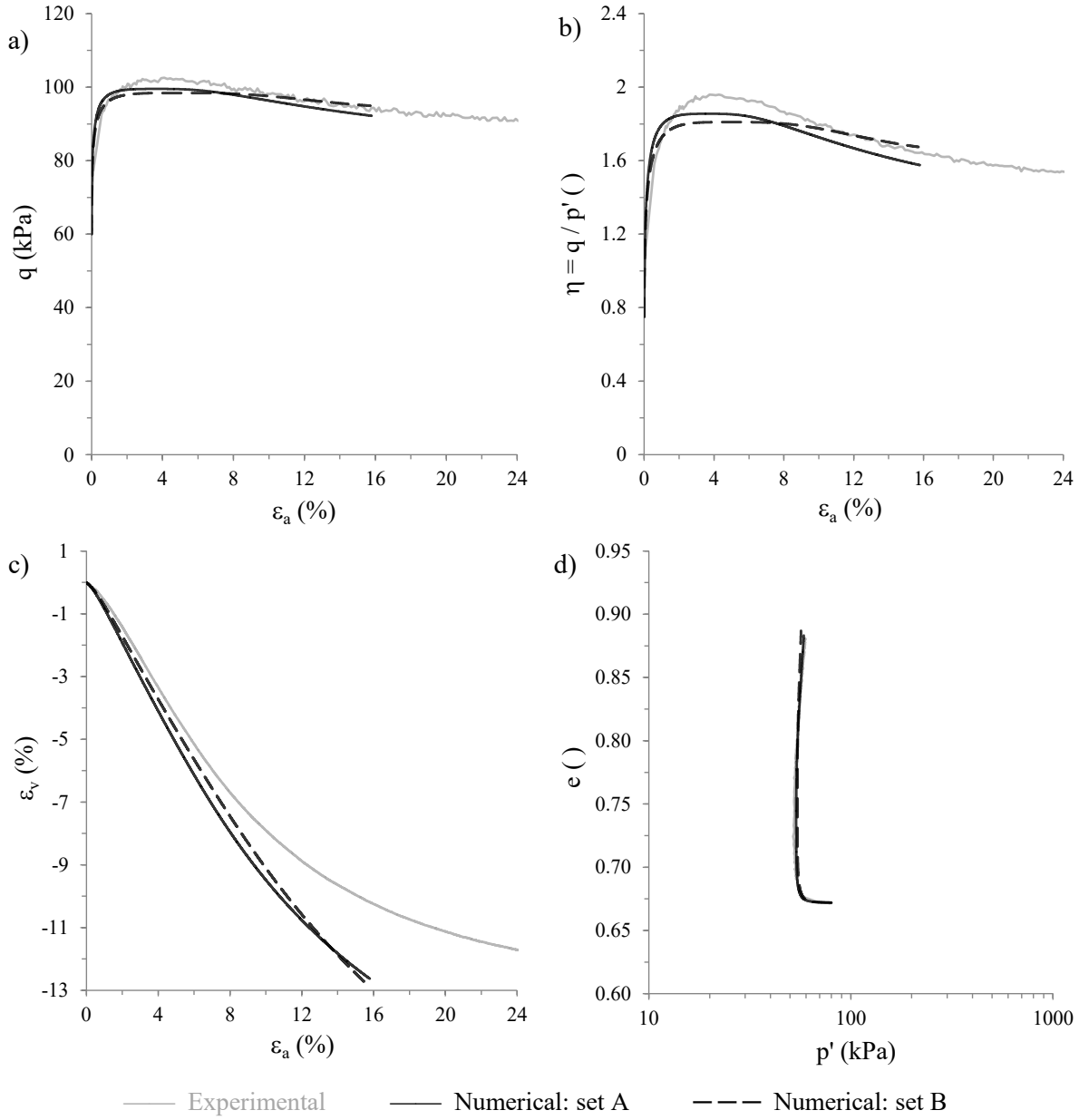

Figure A.23 – Experimental and numerical results of test K0CDMTC p↓ 0.672/80: (a) deviatoric stress evolution with axial strain; (b) stress ratio evolution with axial strain; (c) volumetric strain evolution with axial strain; and (d) void ratio evolution with mean effective stress.

A.3 Monotonic triaxial extension tests

A.3.1.1 Model parameters used in the simulations

As indicated in Table A.4, four different sets of model parameters were employed in the numerical simulations of monotonic triaxial extension tests. Two of the sets belong to the category "A) Static", which was optimised for the simulation of the monotonic response of Hostun sand, while the remaining two sets belong to the category "B) Dynamic", which makes use of the stress-induced anisotropy component of the constitutive model introducing the effect of the cyclic history on the modelled response. Among each pair of sets (A or B), one makes use of the original formulation of the model, as proposed by Taborda *et al.* (2014), while the other makes use of the extended formulation of the model by activating the inherent (i.e. fabric-related) anisotropy component. This component increases the ability of the constitutive model to capture soil response for loading conditions other than triaxial compression. Note that the differences between the sets of model parameters belonging to the categories "A) Static" and "B) Dynamic" are highlighted in bold, while the three additional model parameters required by the extended formulation of the constitutive model are presented in grey. The calibration of these parameters can be found in Chapter 6.

Table A.4 – Model parameters used in the monotonic triaxial extension test simulations.

	A) Static		B) Dynamic	
Sets of parameters	A.1) Original formulation	A.2) Extended formulation	B.1) Original formulation	B.2) Extended formulation
Non-linear elasticity				
C_g	293.0	293.0	293.0	293.0
m_g	2.97	2.97	2.97	2.97
n_g	0.49	0.49	0.49	0.49
κ	2.00	2.00	2.00	2.00
a_1	0.46	0.46	0.46	0.46
γ_1	7.02×10^{-4}	7.02×10^{-4}	7.02×10^{-4}	7.02×10^{-4}
p'_{min}	1.0 kPa (1)	1.0 kPa (1)	10.0 kPa	10.0 kPa
G_{min}	1.0 kPa (1)	1.0 kPa (1)	1.0 kPa (1)	1.0 kPa (1)
ν	0.18	0.18	0.18	0.18
Model surfaces				
p'_{ref}	101.3 kPa	101.3 kPa	101.3 kPa	101.3 kPa
$(e_{CS})_{ref}$	1.000	1.000	1.000	1.000
λ	0.070	0.070	0.070	0.070
ξ	0.360	0.360	0.360	0.360
M_c^c	1.265	1.265	1.265	1.265
M_e^c	0.911	0.911	0.911	0.911
k_c^d	0.940	0.940	0.940	0.940
k_e^d	0.677	0.677	0.677	0.677
k_c^b	2.810	2.810	2.810	2.810
k_e^b	2.024	2.024	2.024	2.024
m	0.065	0.065	0.065	0.065
p'_{ys}	1.0 kPa	1.0 kPa	1.0 kPa	1.0 kPa

Table A.4 – Model parameters used in the monotonic triaxial extension test simulations.

Sets of parameters	A) Static		B) Dynamic	
	A.1) Original formulation	A.2) Extended formulation	B.1) Original formulation	B.2) Extended formulation
Stress-dilatancy				
A_0	1.00	1.00	1.00	1.00
Plastic hardening modulus				
h_0	**0.132**	**0.132**	**0.200**	**0.195**
γ	**0.999**	**0.999**	**1.100**	**1.080**
e_{lim}	**0.960**	**0.960**	**0.900**	**0.900**
α	1.000	1.000	1.000	1.000
μ	0.500	0.500	0.500	0.500
β	**0.300**	**0.300**	**0.600**	**0.600**
Stress-induced anisotropy				
H_0	**0.0** (2)	**0.0** (2)	**43 000.0**	**55 000.0**
ζ	**0.0** (2)	**0.0** (2)	**1.00**	**0.85**
H_{max}	(2)	(2)	5.0×10^4	5.0×10^4
$h_{f,min}$	(2)	(2)	0.1	0.1
$h_{f,max}$	(2)	(2)	1 000.0	1 000.0
Inherent anisotropy				
a	**0.333** (2)	**0.290**	**0.333** (2)	**0.290**
v_A	**0.000** (2)	**1.000**	**0.000** (2)	**1.000**
k_A	**1.000** (2)	**0.600**	**1.000** (2)	**0.600**

(1) Not used. (2) Component not activated when using this set of parameters.

A.3.1.2 Undrained monotonic triaxial extension tests

Table A.5 – Designation and initial conditions of the isotropically consolidated undrained monotonic triaxial extension with decreasing mean stress (ICUMTE p↓) tests.

Designation (§)	e_0 ( )	$\sigma'_{r,0}$ (kPa)	$\sigma'_{a,0}$ (kPa)	p'_0 (kPa)	q_0 (kPa)	Loading (p↑ or p↓)
ICUMTE p↓ 0.790/25	0.790	25.0	25.0	25.0	0.0	p↓
ICUMTE p↓ 0.799/80	0.799	80.0	80.0	80.0	0.0	p↓
ICUMTE p↓ 0.658/25	0.658	25.0	25.0	25.0	0.0	p↓
ICUMTE p↓ 0.650/80	0.650	80.0	80.0	80.0	0.0	p↓

(§) The designation identifies (1) type of consolidation: IC for isotropic consolidation; (2) type of drainage: U for undrained condition; (3) type of loading: MTE p↓ for monotonic triaxial extension with decreasing mean stress; (4) void ratio immediately after consolidation; and (5) mean effective stress immediately after consolidation.

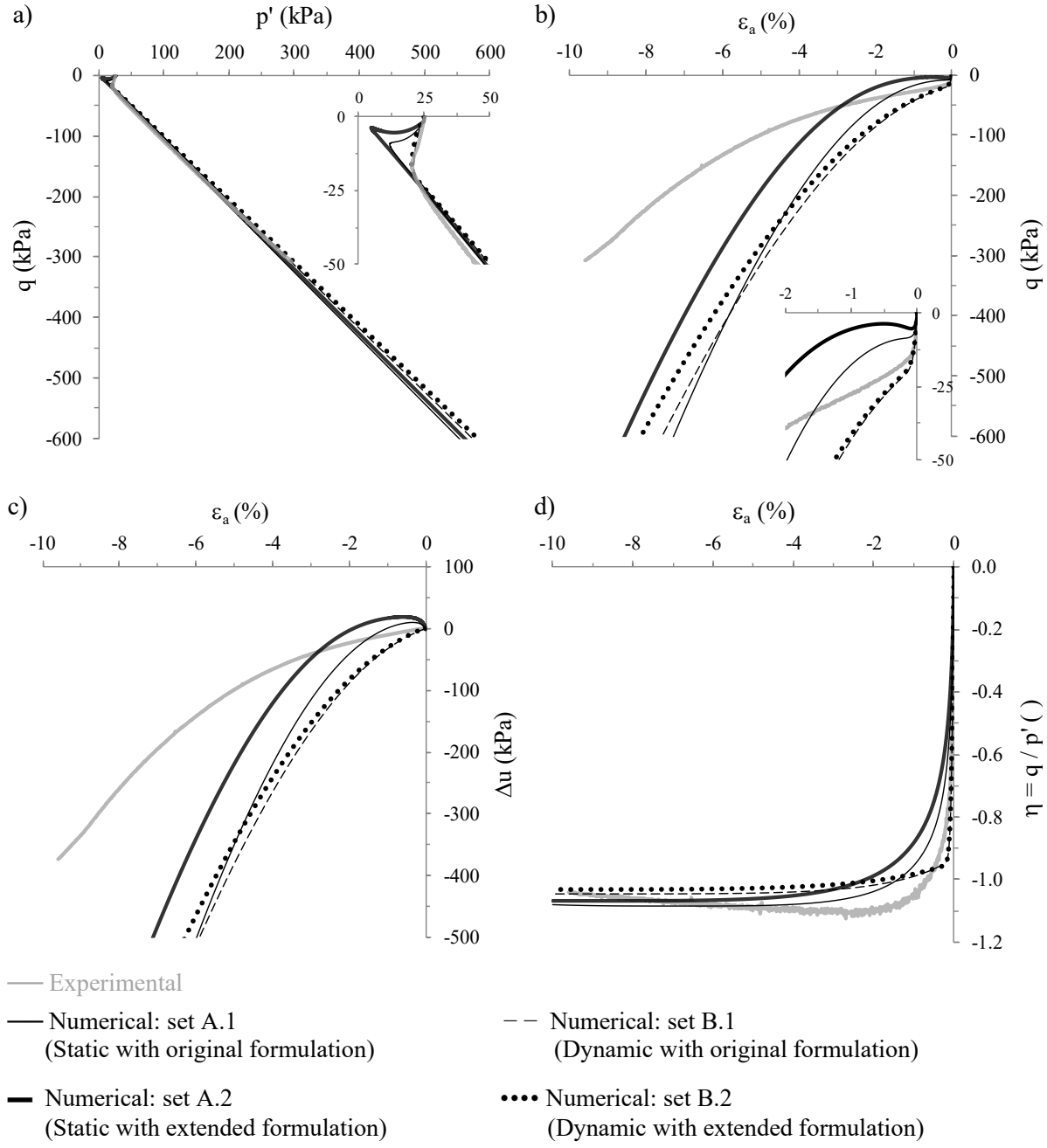

Figure A.24 – Experimental and numerical results of test ICUMTE p↓ 0.790/25: (a) effective stress path; (b) stress-strain response; (c) excess pore water pressure build-up; and (d) stress ratio evolution with axial strain.

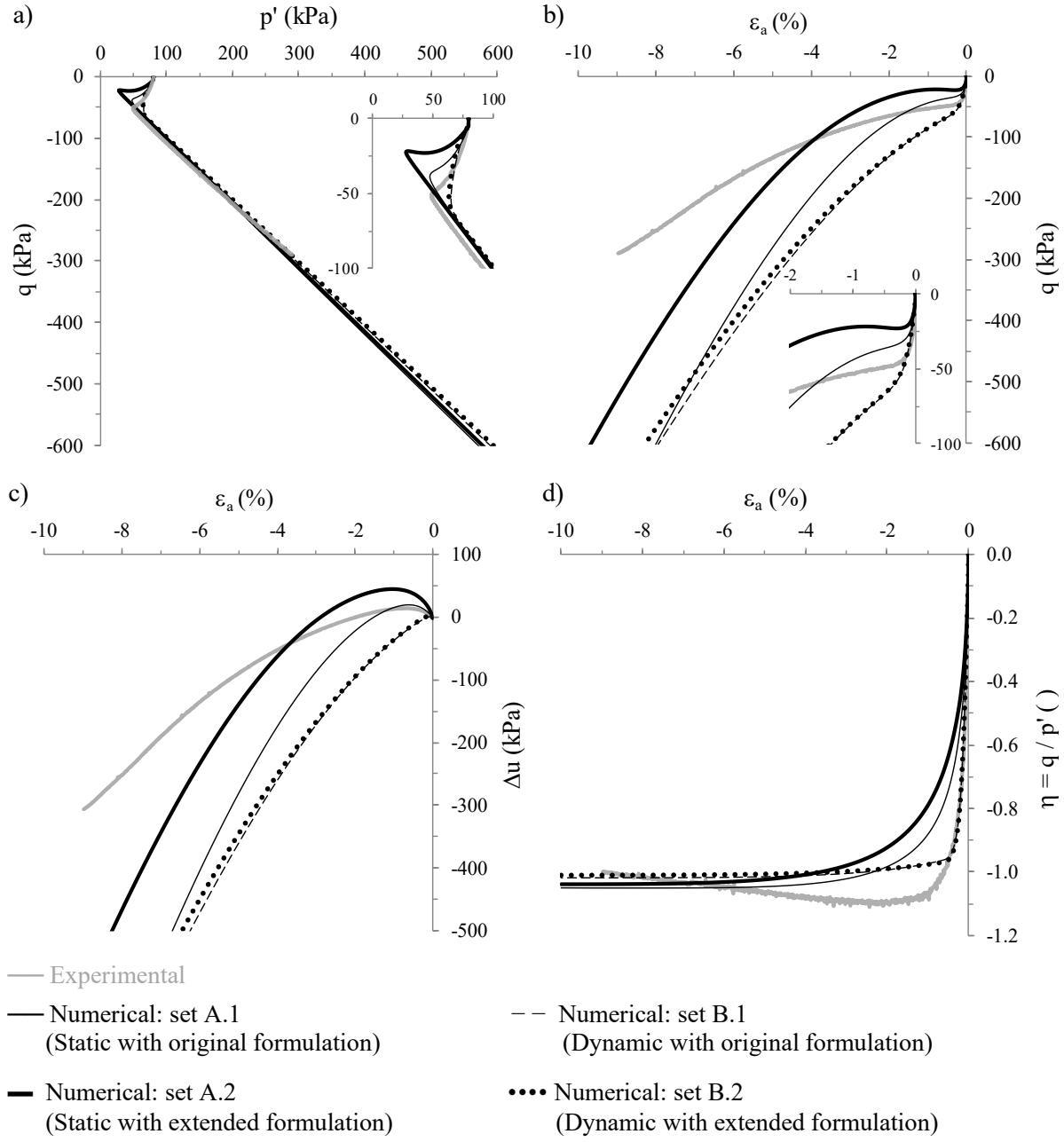

Figure A.25 – Experimental and numerical results of test ICUMTE p↓ 0.799/80: (a) effective stress path; (b) stress-strain response; (c) excess pore water pressure build-up; and (d) stress ratio evolution with axial strain.

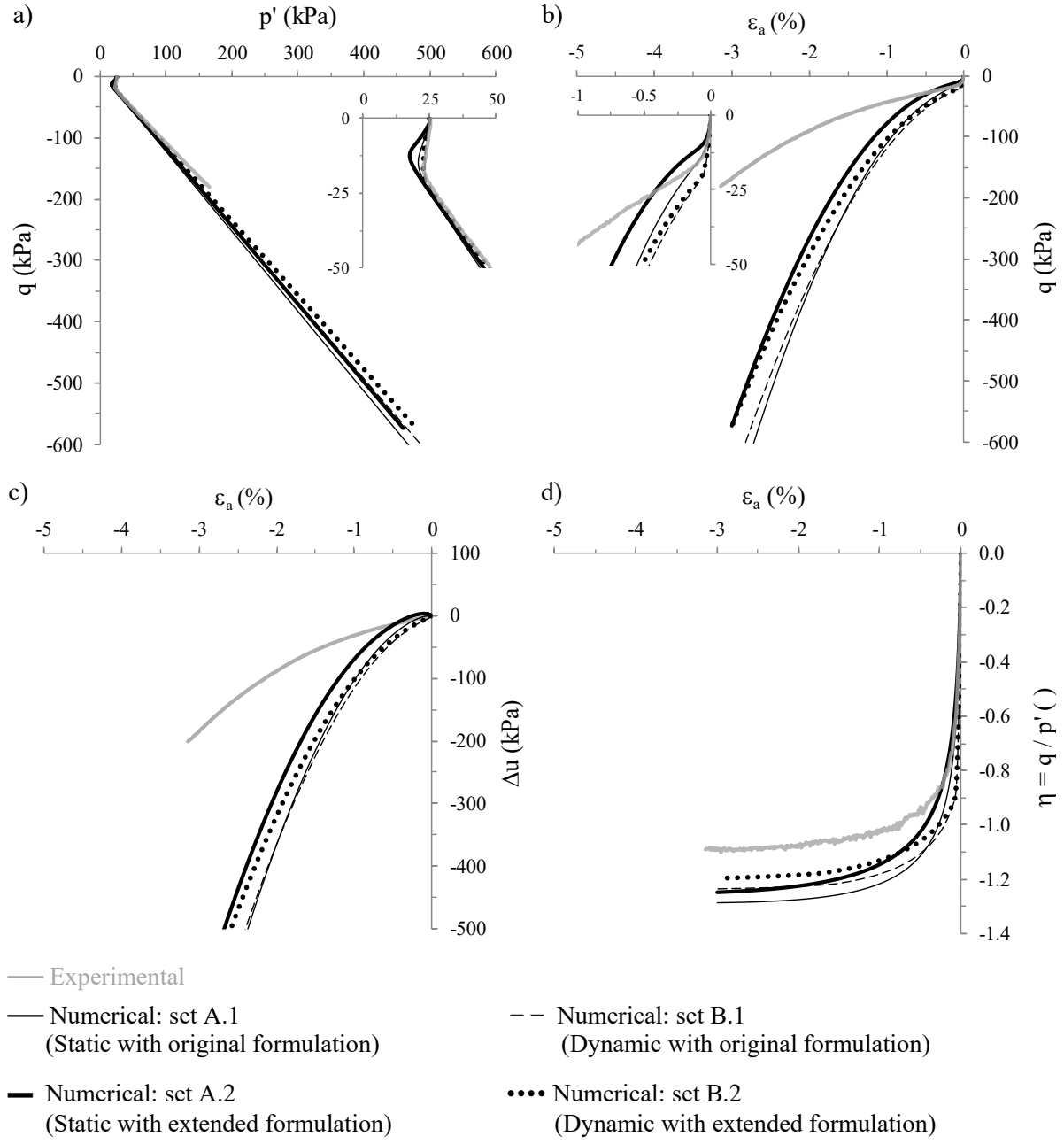

Figure A.26 – Experimental and numerical results of test ICUMTE p↓ 0.658/25: (a) effective stress path; (b) stress-strain response; (c) excess pore water pressure build-up; and (d) stress ratio evolution with axial strain.

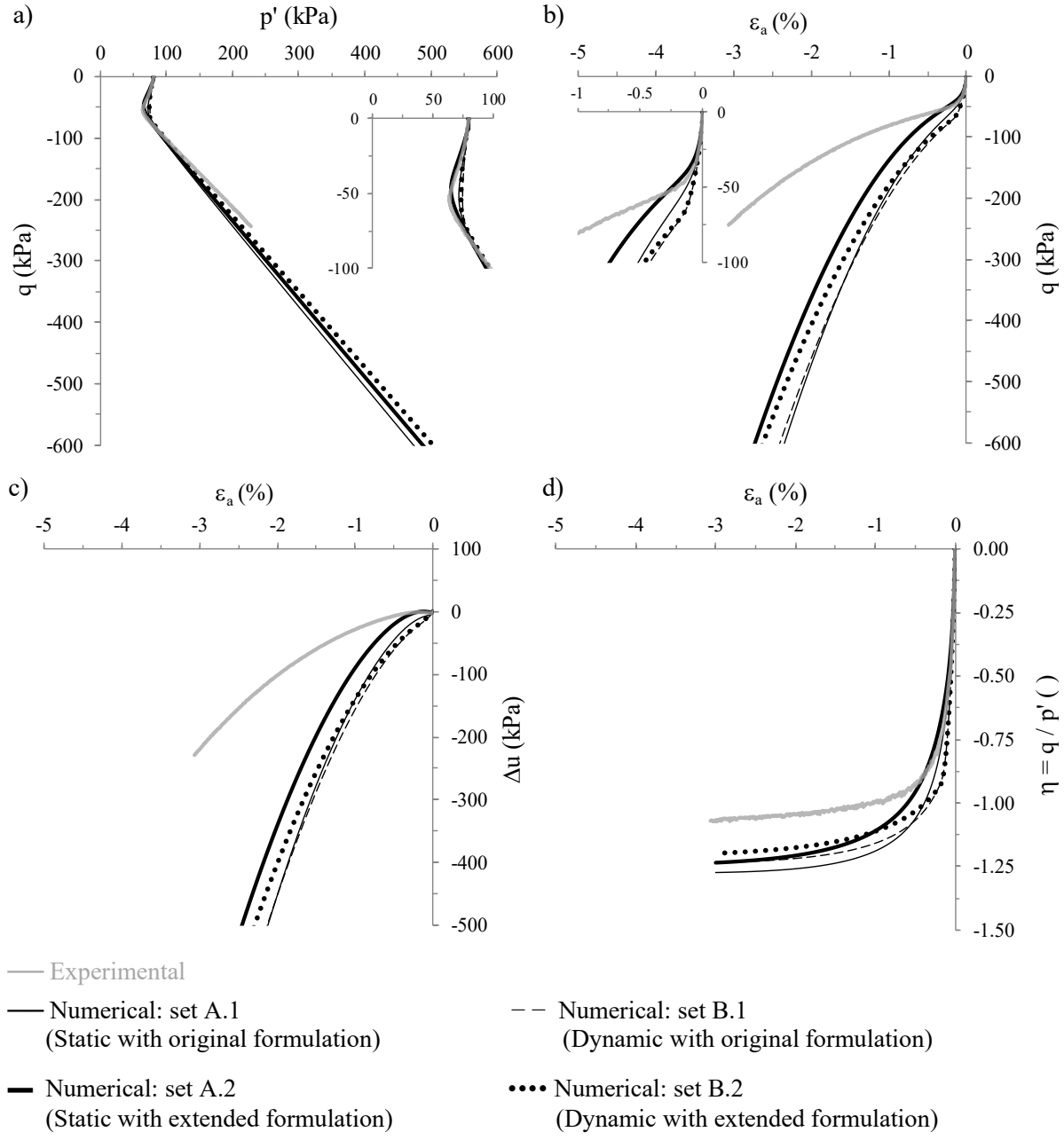

Figure A.27 – Experimental and numerical results of test ICUMTE p↓ 0.650/80: (a) effective stress path; (b) stress-strain response; (c) excess pore water pressure build-up; and (d) stress ratio evolution with axial strain.

A.3.1.3 Drained monotonic triaxial extension tests

Table A.6 – Designation and initial conditions of the drained monotonic triaxial extension tests.

Designation [(§)]	e_0 ( )	$\sigma'_{r,0}$ (kPa)	$\sigma'_{a,0}$ (kPa)	p'_0 (kPa)	q_0 (kPa)	Loading (p↑ or p↓)
ICDMTE p↑ 0.798/80	0.798	80.0	80.0	80.0	0.0	p↑
K0CDMTE p↑ 0.801/80	0.801	60.0	120.0	80.0	60.0	p↑
ICDMTE p↑ 0.652/80	0.652	80.0	80.0	80.0	0.0	p↑
K0CDMTE p↑ 0.652/80	0.652	60.0	120.0	80.0	60.0	p↑
ICDMTE p↓ 0.793/80	0.793	80.0	80.0	80.0	0.0	p↓

[(§)] The designation identifies (1) type of consolidation: IC or K0C for isotropic or anisotropic consolidation, respectively; (2) type of drainage: D for drained condition; (3) type of loading: MTE p↓ for monotonic triaxial extension with decreasing mean stress and MTE p↑ for monotonic triaxial extension with increasing mean stress; (4) void ratio immediately after consolidation; and (5) mean effective stress immediately after consolidation.

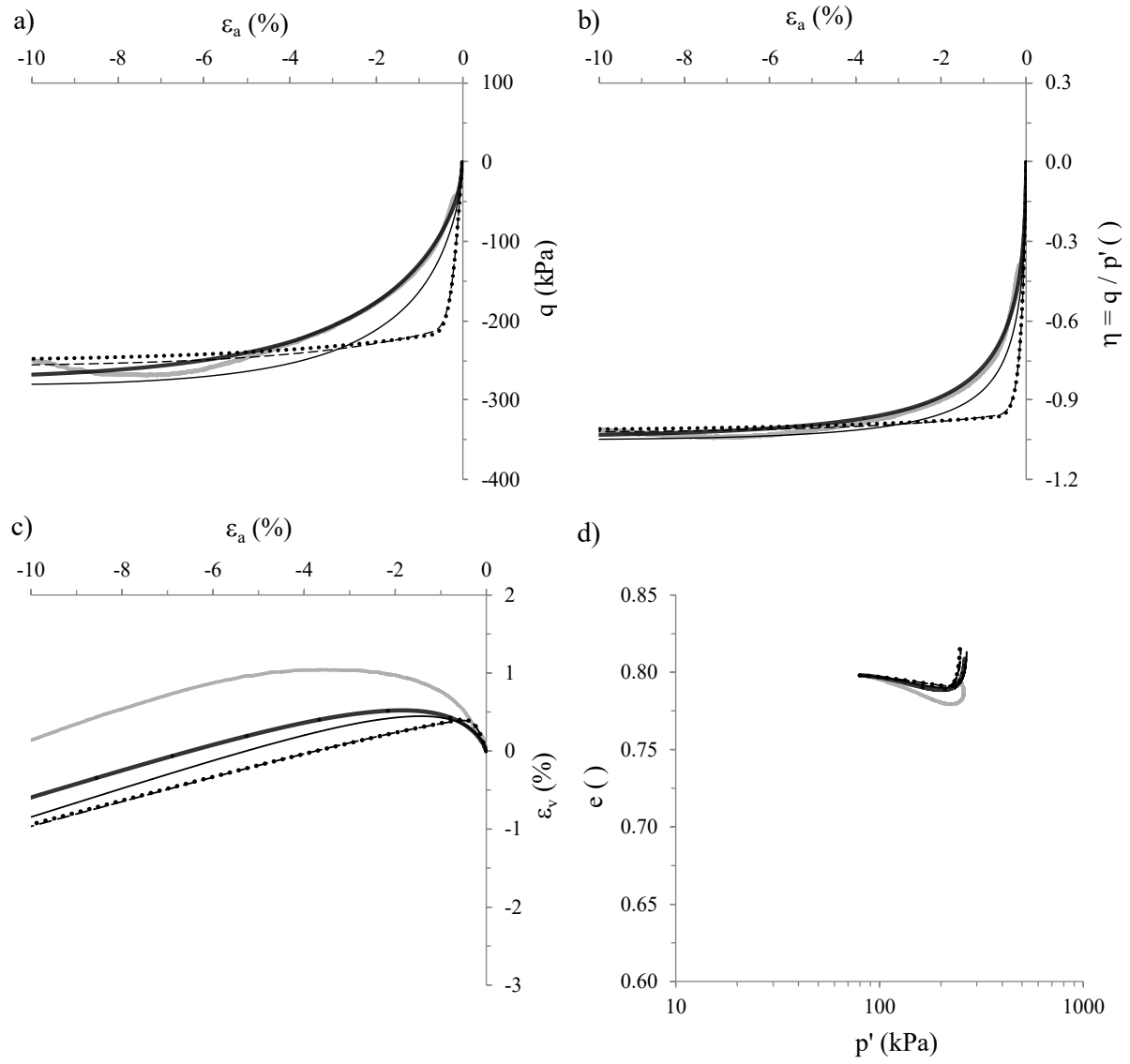

Figure A.28 – Experimental and numerical results of test ICDMTE p↑ 0.798/80: (a) deviatoric stress evolution with axial strain; (b) stress ratio evolution with axial strain; (c) volumetric strain evolution with axial strain; and (d) void ratio evolution with mean effective stress.

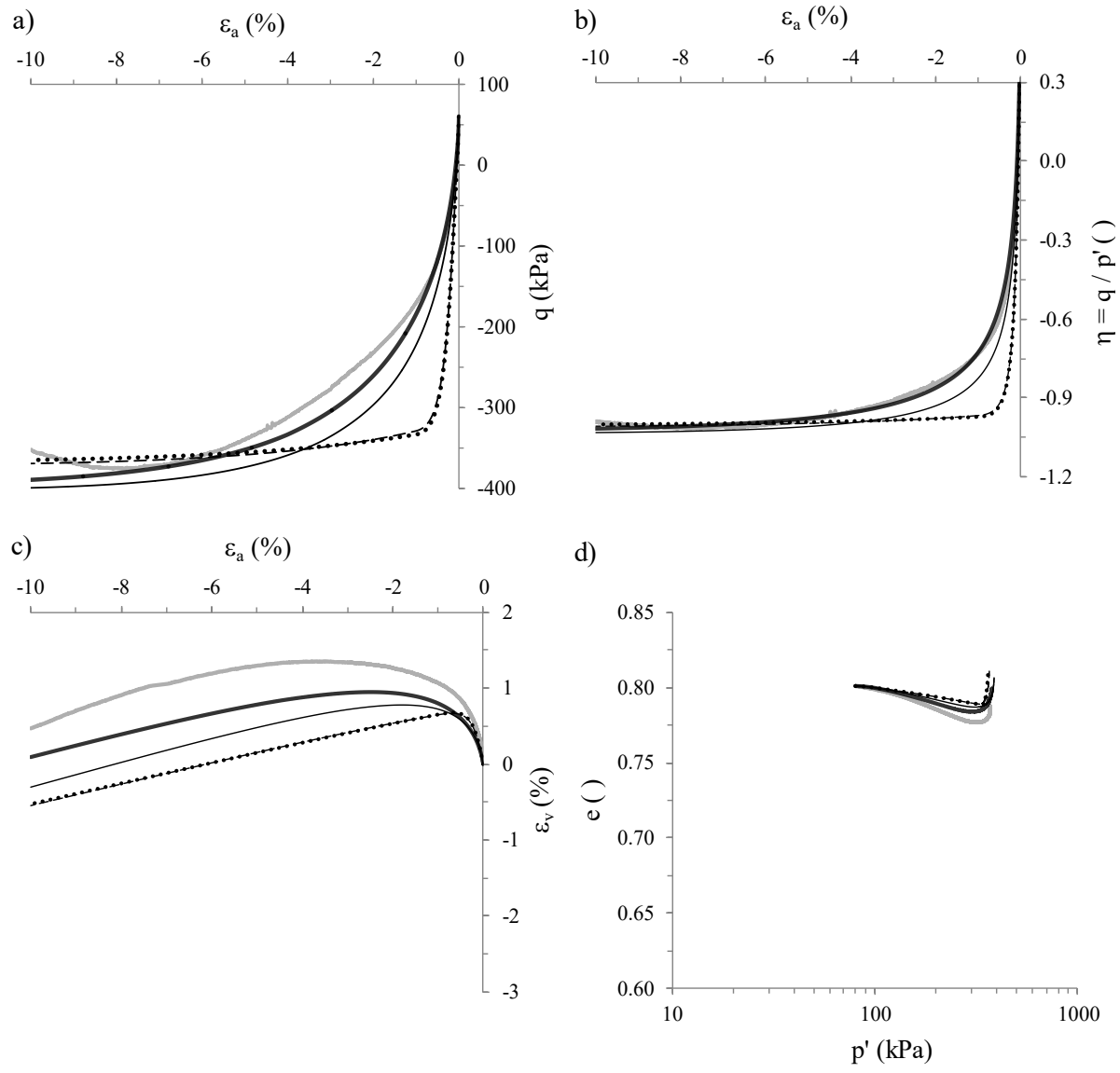

Figure A.29 – Experimental and numerical results of test K0CDMTE p↑ 0.801/80: (a) deviatoric stress evolution with axial strain; (b) stress ratio evolution with axial strain; (c) volumetric strain evolution with axial strain; and (d) void ratio evolution with mean effective stress.

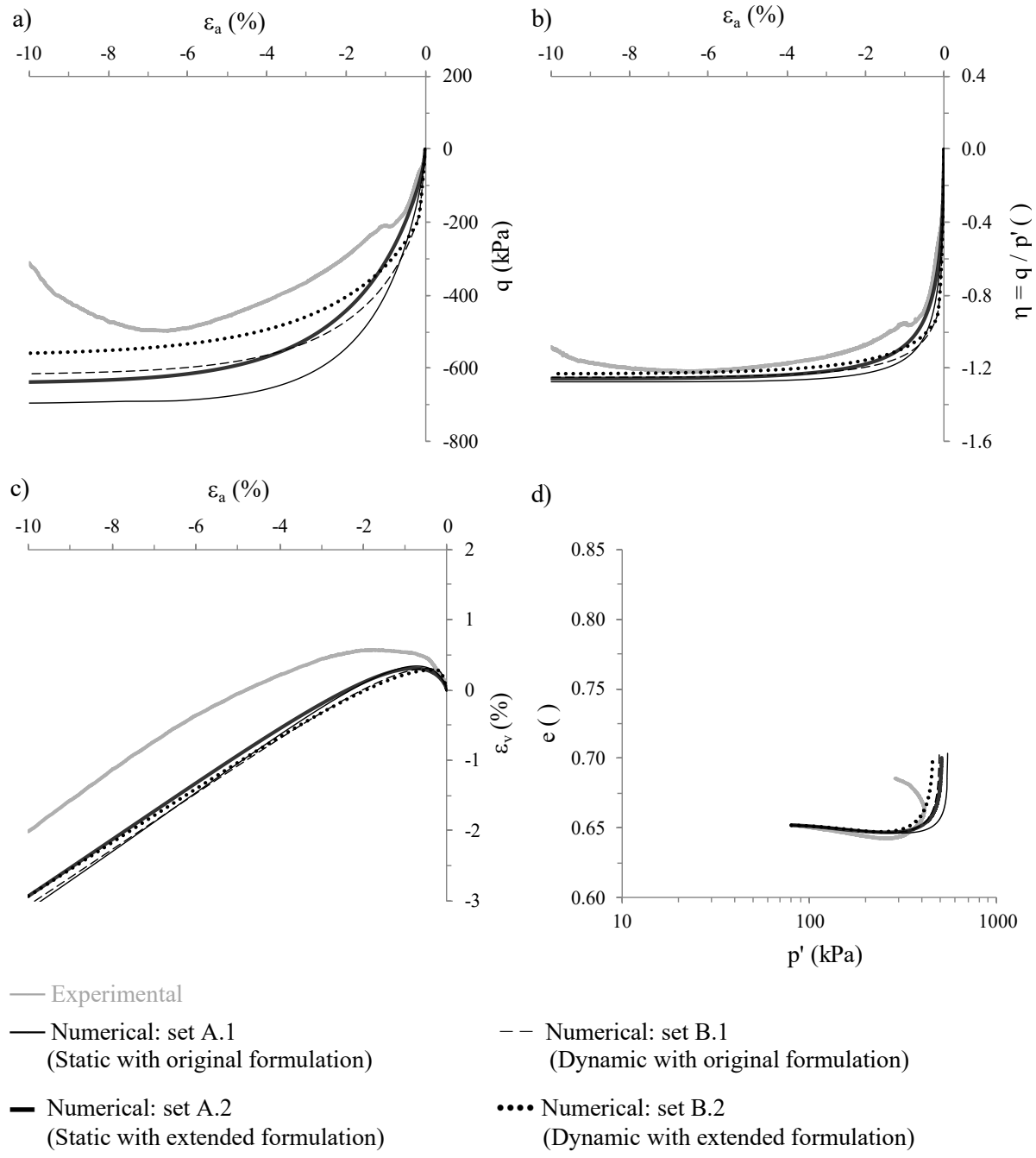

Figure A.30 – Experimental and numerical results of test ICDMTE p↑ 0.652/80: (a) deviatoric stress evolution with axial strain; (b) stress ratio evolution with axial strain; (c) volumetric strain evolution with axial strain; and (d) void ratio evolution with mean effective stress.

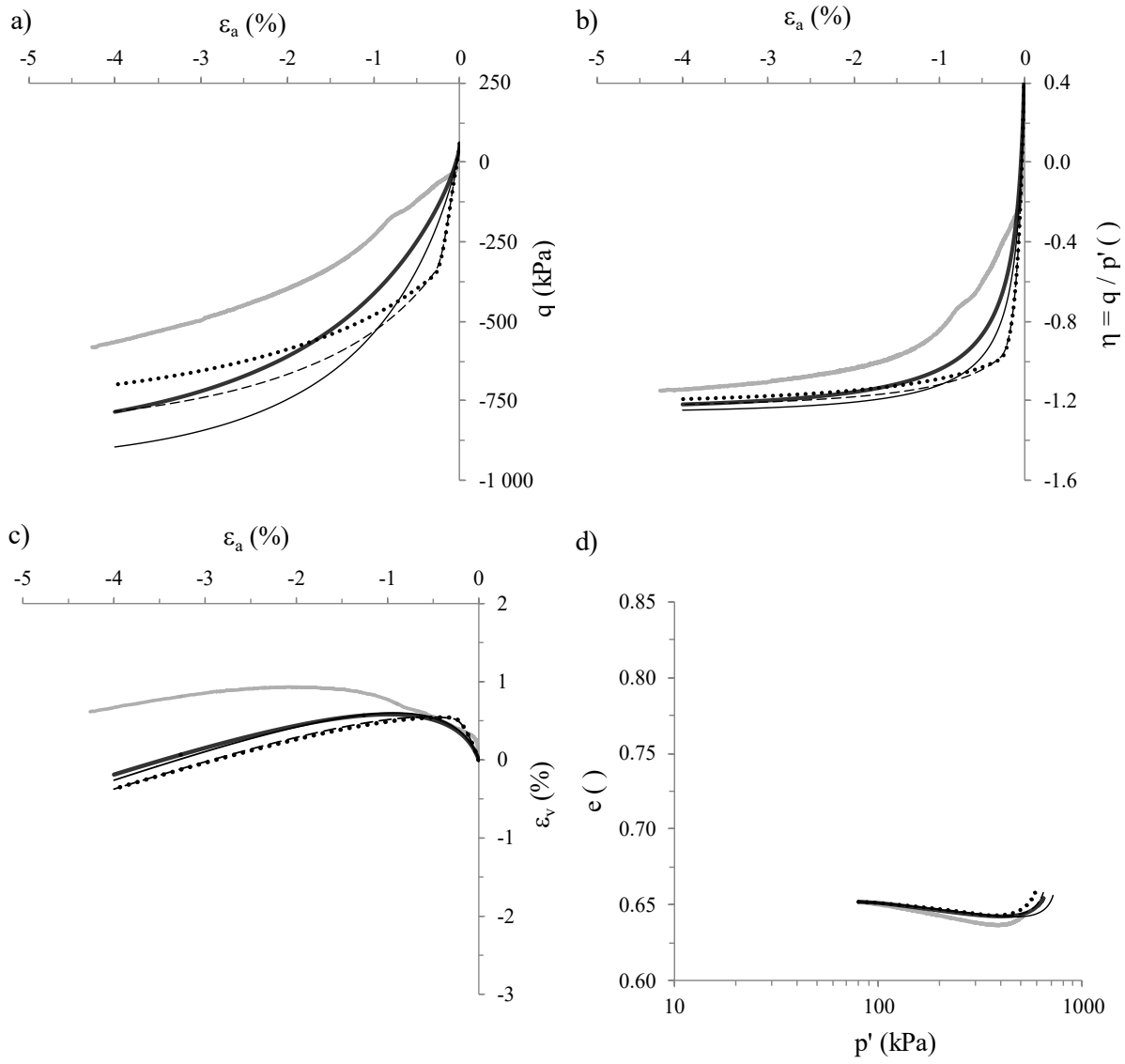

Figure A.31 – Experimental and numerical results of test K0CDMTE p↑ 0.652/80: (a) deviatoric stress evolution with axial strain; (b) stress ratio evolution with axial strain; (c) volumetric strain evolution with axial strain; and (d) void ratio evolution with mean effective stress.

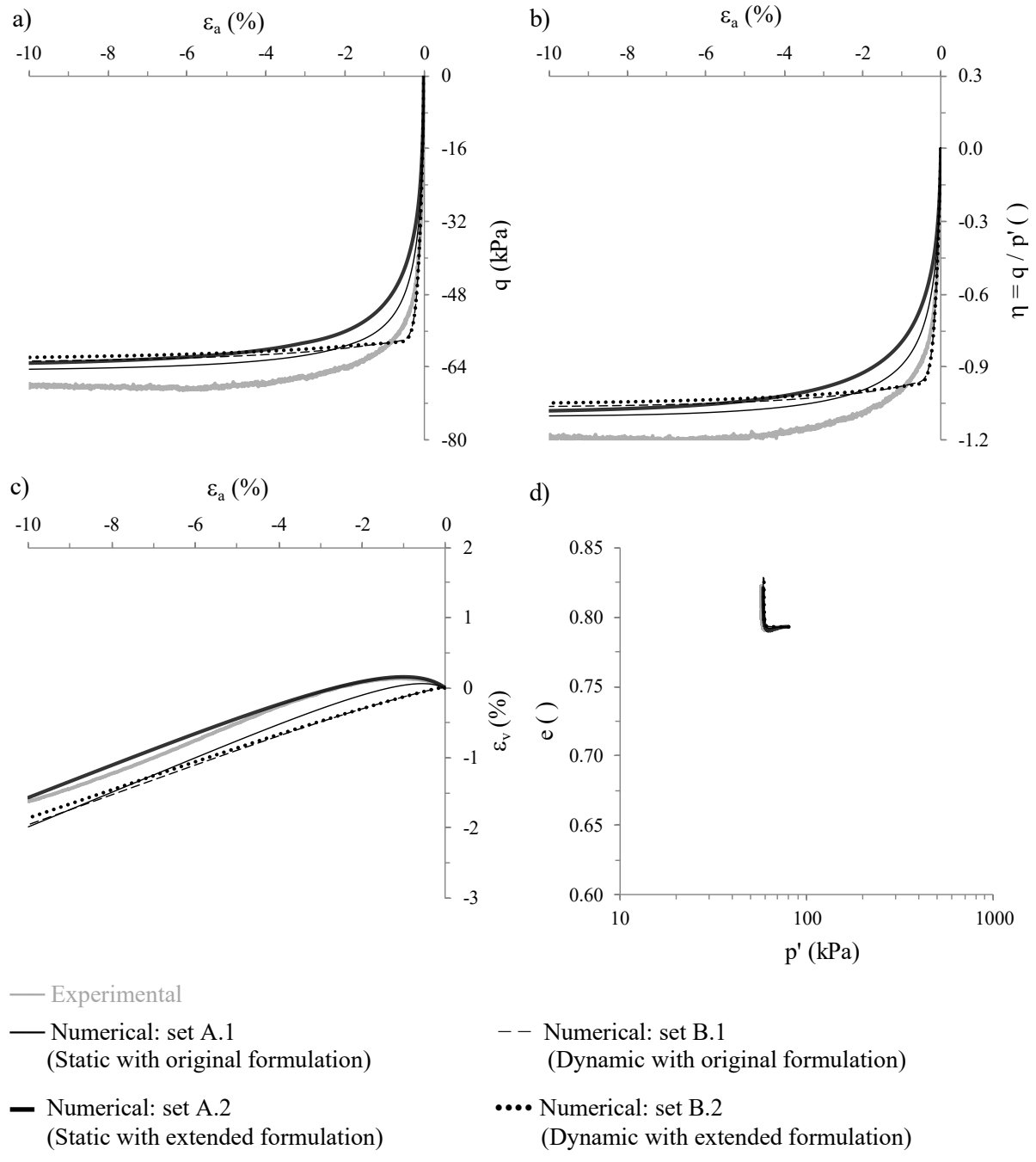

Figure A.32 – Experimental and numerical results of test ICDMTE p↓ 0.793/80: (a) deviatoric stress evolution with axial strain; (b) stress ratio evolution with axial strain; (c) volumetric strain evolution with axial strain; and (d) void ratio evolution with mean effective stress.

Appendix B MEASURED AND SIMULATED CYCLIC RESPONSE OF HOSTUN SAND

B.1 Introduction

This appendix compares the experimental results of each cyclic triaxial test performed on Hostun sand (Chapter 3) with the results of its numerical simulation (Chapter 7).

B.2 Designation and initial conditions of each cyclic triaxial test

Table B.1 summarises the designation and initial conditions of the fifteen cyclic triaxial tests performed on Hostun sand, including thirteen isotropically consolidated undrained cyclic triaxial (ICUCT) tests, as well as one isotropically consolidated (IC) and one anisotropically consolidated (K0C) drained cyclic triaxial (ICDCT and K0CDCT, respectively) tests. It can be observed that the samples were prepared to very different void ratios (with e_0 ranging from 0.651 to 0.820), consolidated under three different mean effective stresses (namely, $p'_0 =$ 25, 80 and 135 kPa) and subjected to two-way symmetric deviatoric shear stress oscillations (i.e. similar deviatoric stress amplitude in triaxial compression and in triaxial extension), Δq.

Table B.1 – Designation and initial conditions of the cyclic triaxial tests performed on Hostun sand.

Type of test	Designation [§]	e_0 ( )	p'_0 (kPa)	Δq (kPa)	ψ_0 [ו] ( )	N ( )
Undrained cyclic triaxial (UCT)	ICUCT 0.821/25/13	0.821	25.0	±13.0	-0.136	[†]
	ICUCT 0.777/25/18	0.777	25.0	±18.0	-0.181	[†]
	ICUCT 0.771/80/32	0.771	80.0	±32.0	-0.165	[†]
	ICUCT 0.803/80/36	0.803	80.0	±36.0	-0.133	[†]
	ICUCT 0.832/80/42	0.832	80.0	±42.0	-0.104	[†])
	ICUCT 0.804/80/48	0.804	80.0	±48.0	-0.132	[†]
	ICUCT 0.773/80/56	0.773	80.0	±56.0	-0.162	[†]
	ICUCT 0.805/135/40	0.805	135.0	±40.0	-0.117	[†]
	ICUCT 0.830/135/54	0.830	135.0	±54.0	-0.092	[†]
	ICUCT 0.793/135/67.5	0.793	135.0	±67.5	-0.129	[†]
	ICUCT 0.651/80/43	0.651	80.0	±43.0	-0.299	[†]
	ICUCT 0.652/80/72	0.652	80.0	±72.0	-0.285	[†]
	ICUCT 0.652/80/88	0.652	80.0	±88.0	-0.284	[†]
Drained cyclic triaxial (DCT)	K0CDCT 0.811/80/30	0.811	80.0 [‡]	±30.0	-0.125	10
	ICDCT 0.820/135/81	0.820	135.0	±81.0	-0.102	10

[§] The designation identifies: (1) type of consolidation: IC for isotropic consolidation; (2) type of drainage: D or U for drained or undrained test, respectively; (3) type of loading: CT for cyclic triaxial; (4) void ratio immediately after consolidation; and (5) mean effective stress immediately after consolidation; (6) deviatoric stress oscillation applied in the test: $|\Delta q|$.

[†] The undrained cyclic triaxial tests were stopped when large strains were observed (typically, for moderately loose samples, the accumulation of double amplitude axial strain of 5% was used as criterion to stop the test).

[ו] See Chapter 3.

[‡] In this test, the sample was subjected to anisotropic consolidation, with the axial and radial effective stresses at consolidation being 120 and 60 kPa, respectively.

B.3 Model parameters used in the simulations

As indicated in Table B.2, two different sets of model parameters were employed in the numerical simulations of cyclic triaxial tests: one of them (termed as "set B.1) Dynamic – original formulation") makes use of the original formulation of the model, as proposed by Taborda *et al.* (2014), while the other one (termed as "set B.2) Dynamic – extended formulation") makes use of the extended formulation of the model by activating the inherent (i.e. fabric-related) anisotropy component. This component increases the ability of the constitutive model to capture soil response for loading conditions other than triaxial compression. Note that the differences between the values of the plastic-hardening-modulus-related parameters are highlighted in bold, while the values assigned to the three additional model parameters required by the extended formulation of the constitutive model are presented in grey. The calibration of these parameters can be found in Chapter 6.

Table B.2 – Model parameters used in the cyclic triaxial test simulations.

Sets of parameters	B) Dynamic	
	B.1) Original formulation	B.2) Extended formulation
Non-linear elasticity		
C_g	293.0	293.0
m_g	2.97	2.97
n_g	0.49	0.49
κ	2.00	2.00
a_1	0.46	0.46
γ_1	7.02×10^{-4}	7.02×10^{-4}
p'_{min}	10.0 kPa	10.0 kPa
G_{min}	1.0 kPa (1)	1.0 kPa (1)
ν	0.18	0.18
Model surfaces		
p'_{ref}	101.3 kPa	101.3 kPa
$(e_{CS})_{ref}$	1.000	1.000
λ	0.070	0.070
ξ	0.360	0.360
M_c^c	1.265	1.265
M_e^c	0.911	0.911
k_c^d	0.940	0.940
k_e^d	0.677	0.677
k_c^b	2.810	2.810
k_e^b	2.024	2.024
m	0.065	0.065
p'_{ys}	1.0 kPa	1.0 kPa
Stress-dilatancy		
A_0	1.00	1.00
$\boldsymbol{h_0}$	**0.200**	**0.195**
$\boldsymbol{\gamma}$	**1.100**	**1.080**
$\boldsymbol{e_{lim}}$	**0.900**	**0.900**

Table B.2 – Model parameters used in the cyclic triaxial test simulations.

Sets of parameters	B) Dynamic	
	B.1) Original formulation	B.2) Extended formulation
α	1.000	1.000
μ	0.500	0.500
β	**0.600**	**0.600**
H_0	**43 000.0**	**55 000.0**
ζ	**1.00**	**0.85**
H_{max}	5.0×10^4	5.0×10^4
$h_{f,min}$	0.1	0.1
$h_{f,max}$	1 000.0	1 000.0
Inherent anisotropy		
a	**0.333** [(2)]	**0.290**
v_A	**0.000** [(2)]	**1.000**
k_A	**1.000** [(2)]	**0.600**

[(1)] Not used. [(2)] Component not activated when using this set of parameters.

B.4 Simulations using the original formulation of the constitutive model

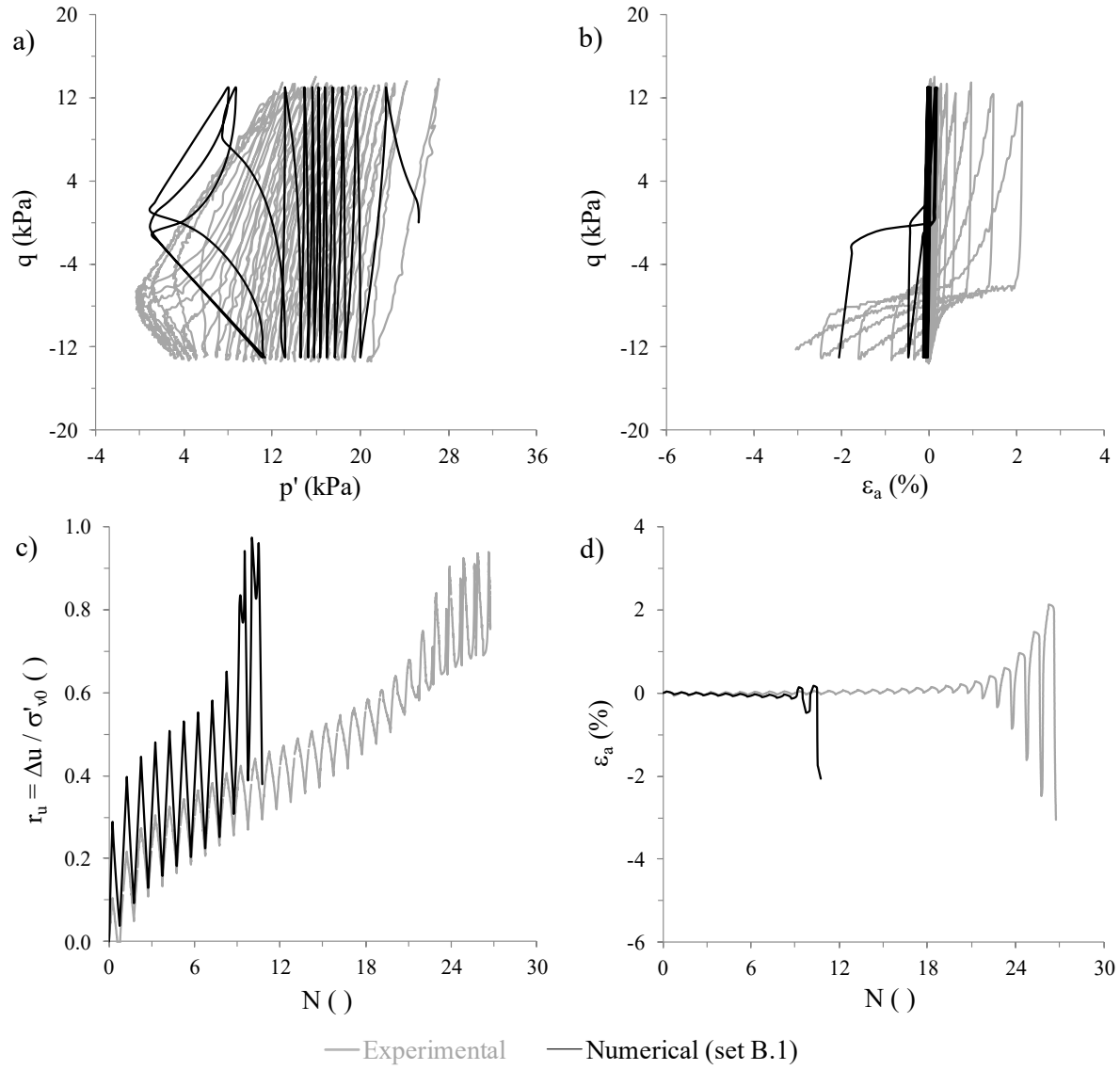

Figure B.1 – Experimental and numerical results of test ICUCT 0.821/25/13: (a) effective stress path, (b) stress-strain response; (c) excess pore water pressure ratio build-up with the number of loading cycles; and (d) axial strain evolution with the number of loading cycles.

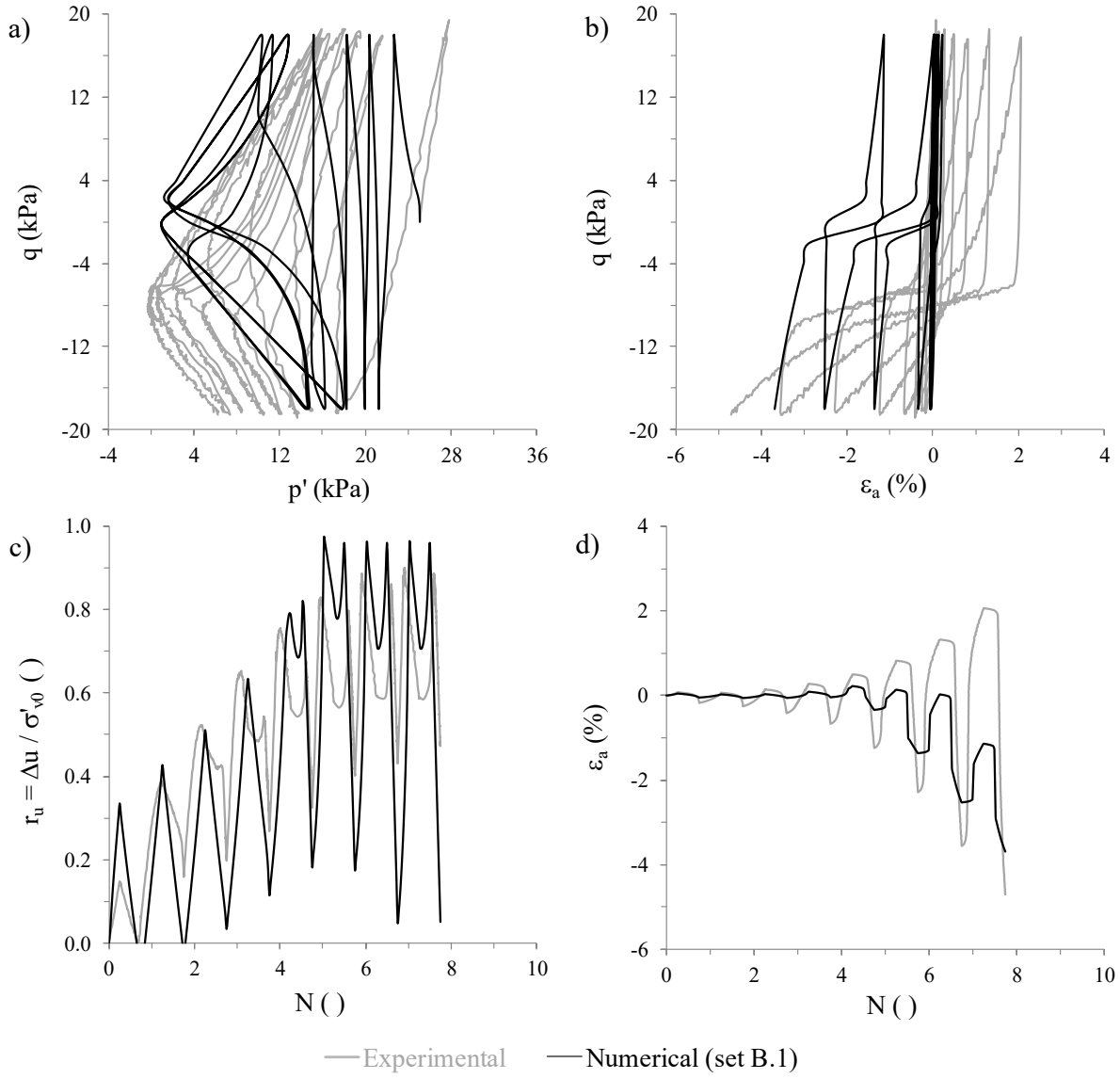

Figure B.2 – Experimental and numerical results of test ICUCT 0.777/25/18: (a) effective stress path, (b) stress-strain response; (c) excess pore water pressure ratio build-up with the number of loading cycles; and (d) axial strain evolution with the number of loading cycles.

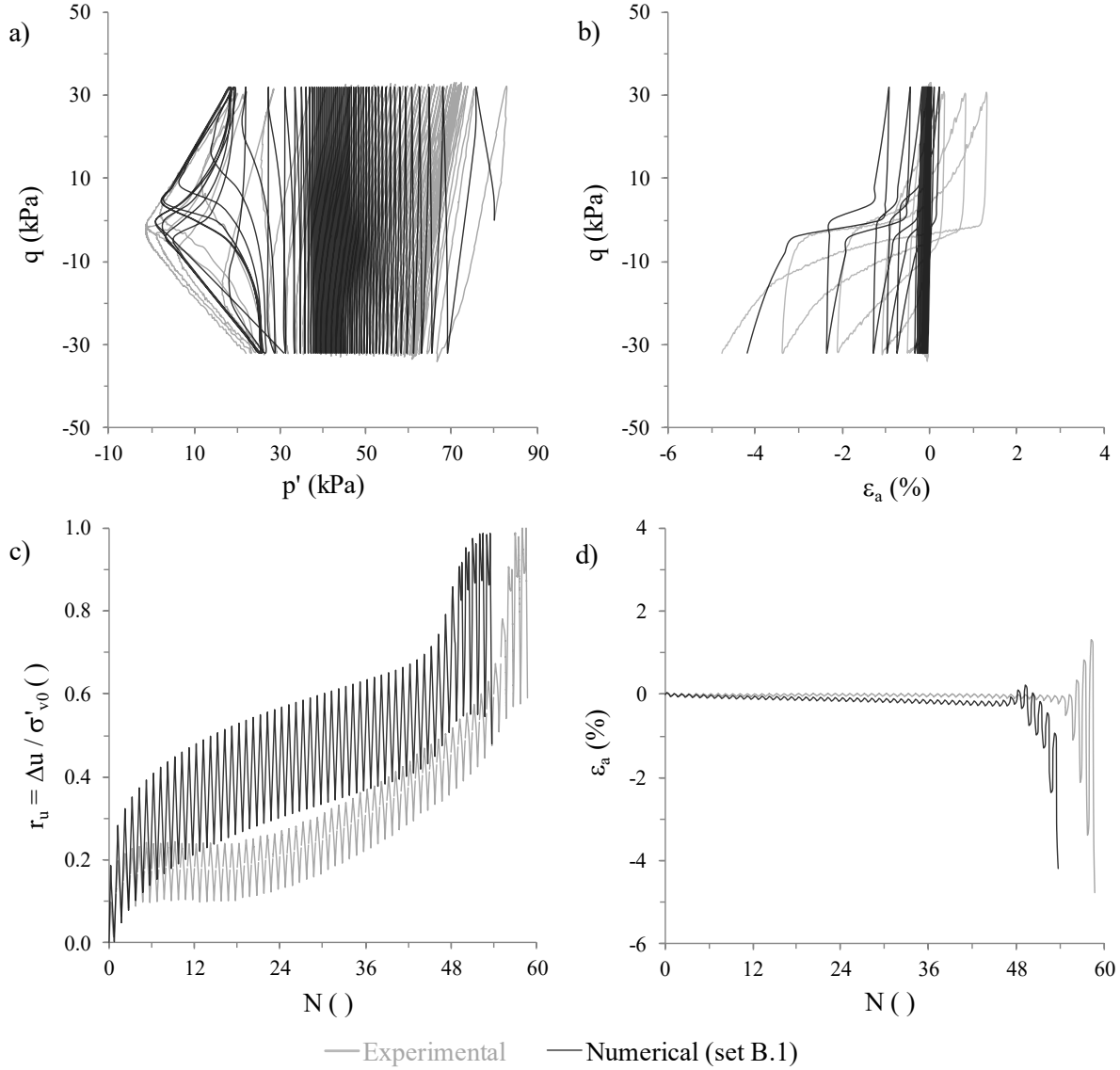

Figure B.3 – Experimental and numerical results of test ICUCT 0.771/80/32: (a) effective stress path, (b) stress-strain response; (c) excess pore water pressure ratio build-up with the number of loading cycles; and (d) axial strain evolution with the number of loading cycles.

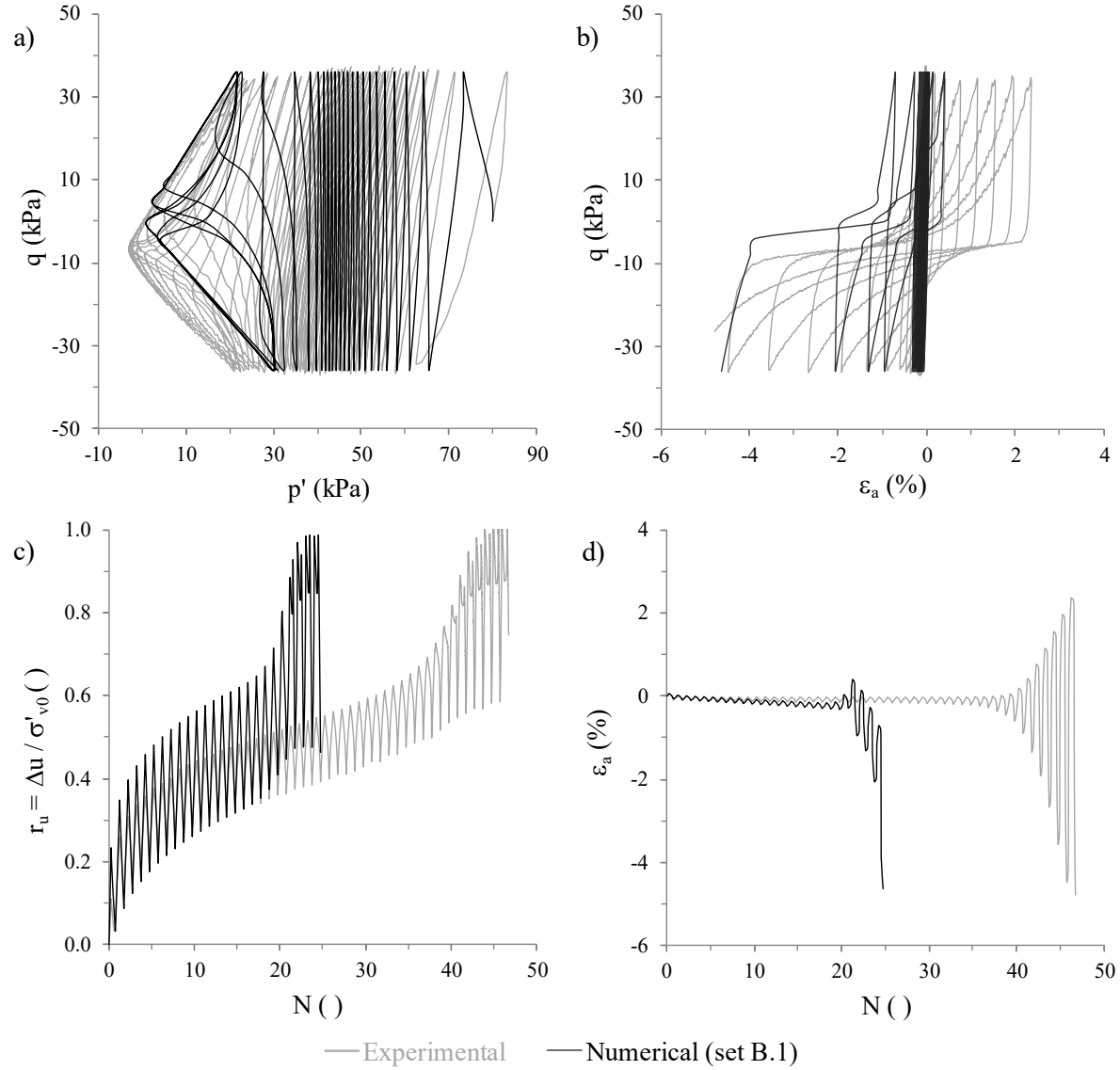

Figure B.4 – Experimental and numerical results of test ICUCT 0.803/80/36: (a) effective stress path, (b) stress-strain response; (c) excess pore water pressure ratio build-up with the number of loading cycles; and (d) axial strain evolution with the number of loading cycles.

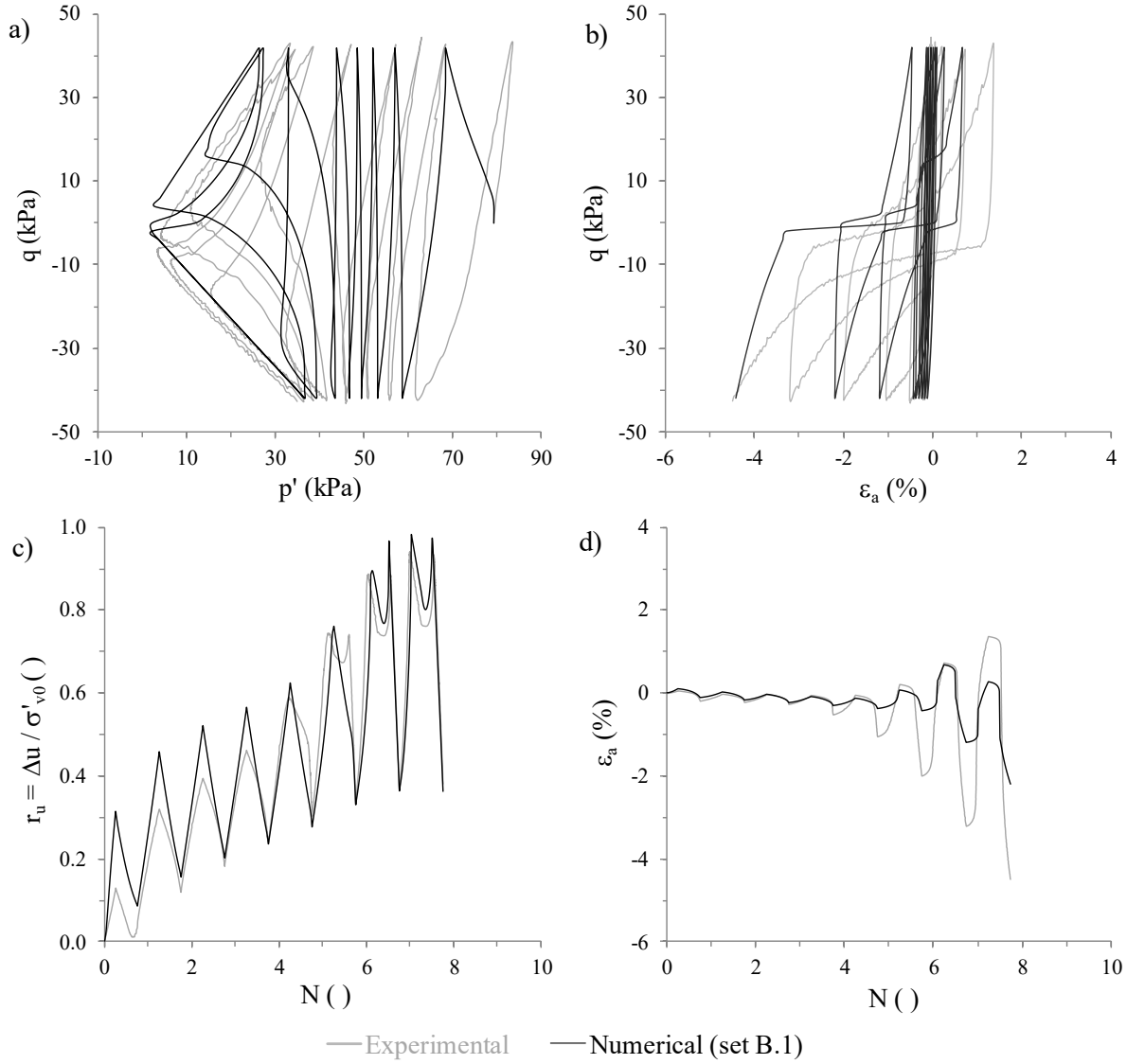

Figure B.5 – Experimental and numerical results of test ICUCT 0.832/80/42: (a) effective stress path, (b) stress-strain response; (c) excess pore water pressure ratio build-up with the number of loading cycles; and (d) axial strain evolution with the number of loading cycles.

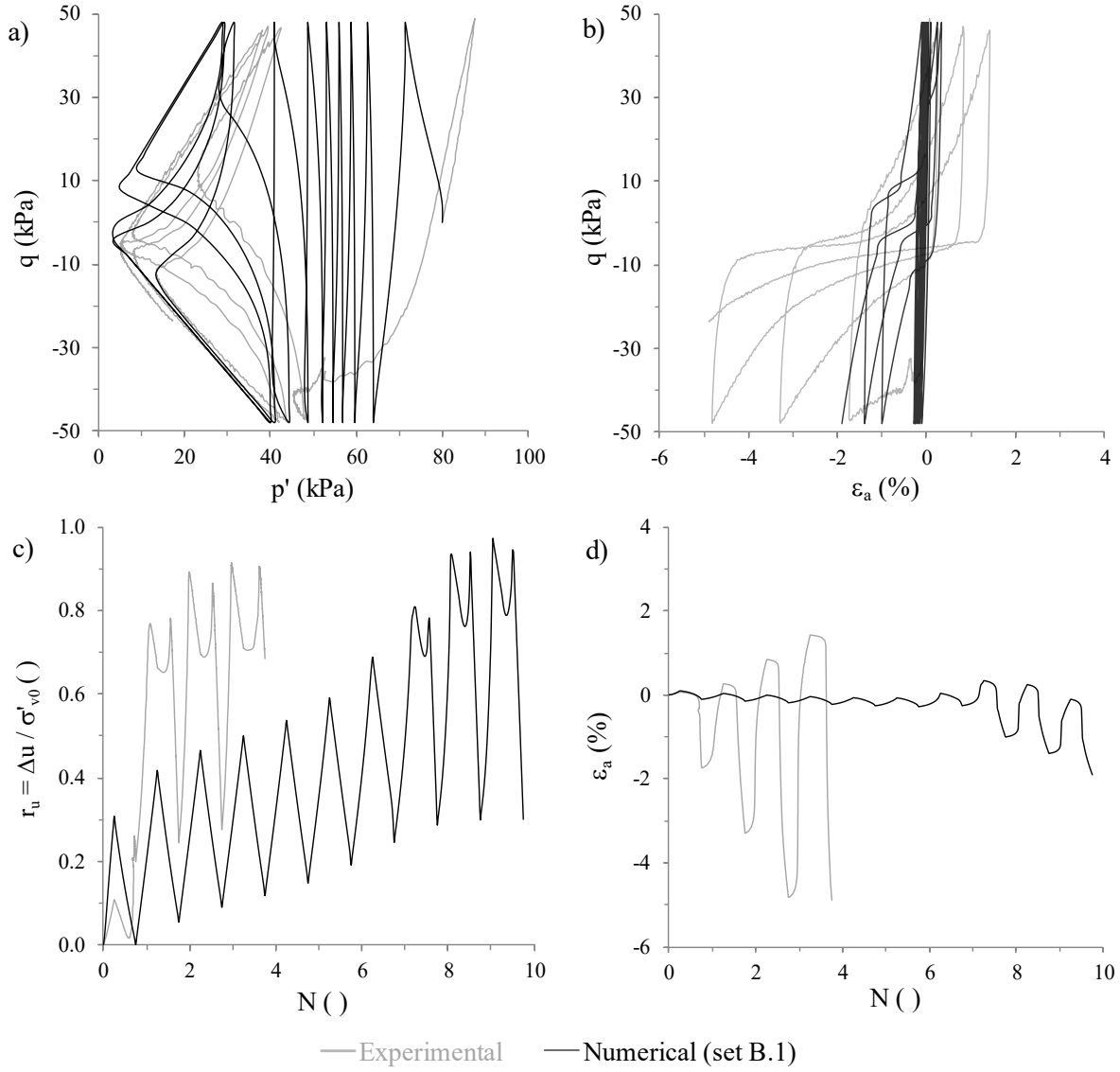

Figure B.6 – Experimental and numerical results of test ICUCT 0.804/80/48: (a) effective stress path, (b) stress-strain response; (c) excess pore water pressure ratio build-up with the number of loading cycles; and (d) axial strain evolution with the number of loading cycles.

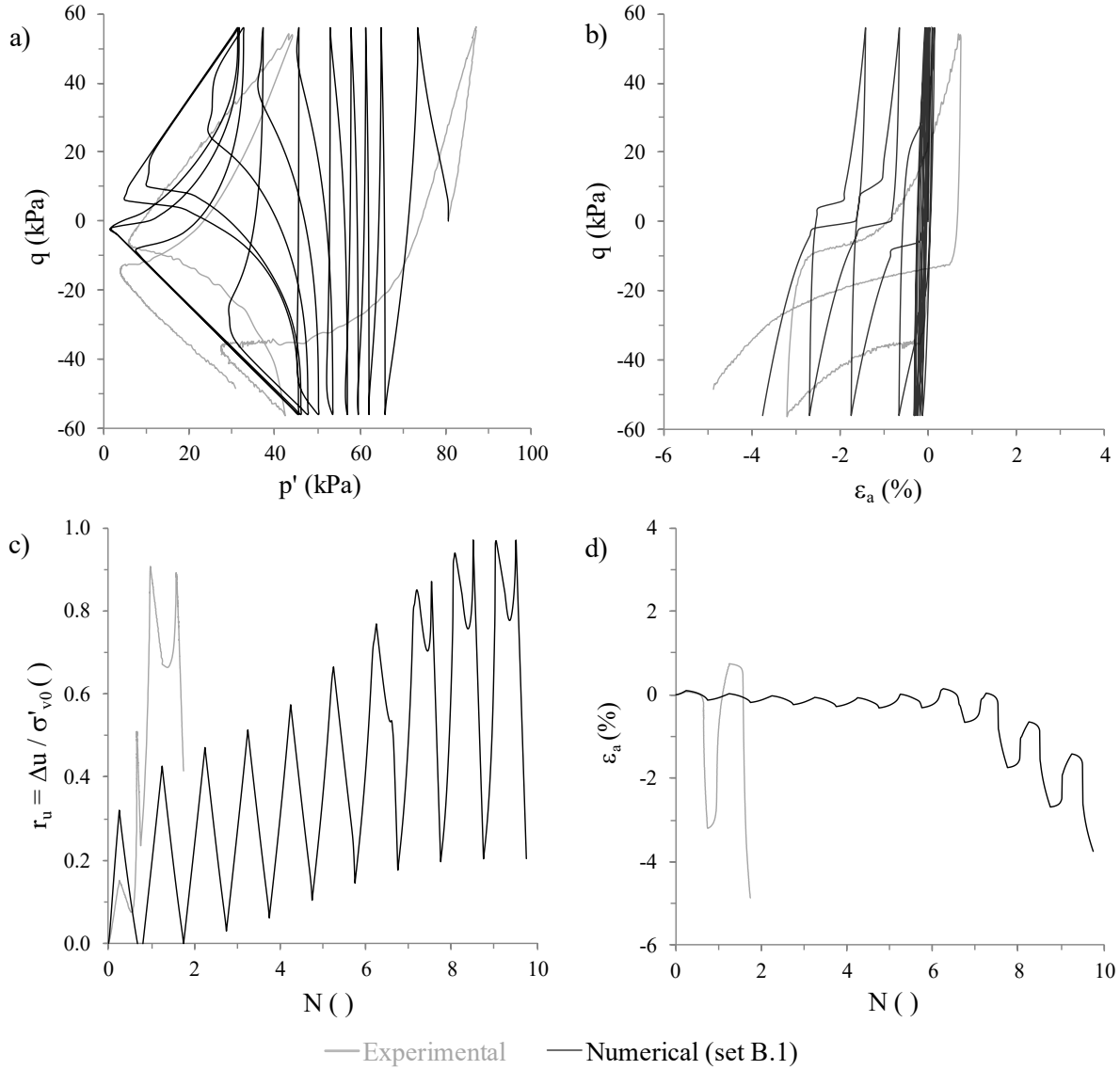

Figure B.7 – Experimental and numerical results of test ICUCT 0.773/80/56: (a) effective stress path, (b) stress-strain response; (c) excess pore water pressure ratio build-up with the number of loading cycles; and (d) axial strain evolution with the number of loading cycles.

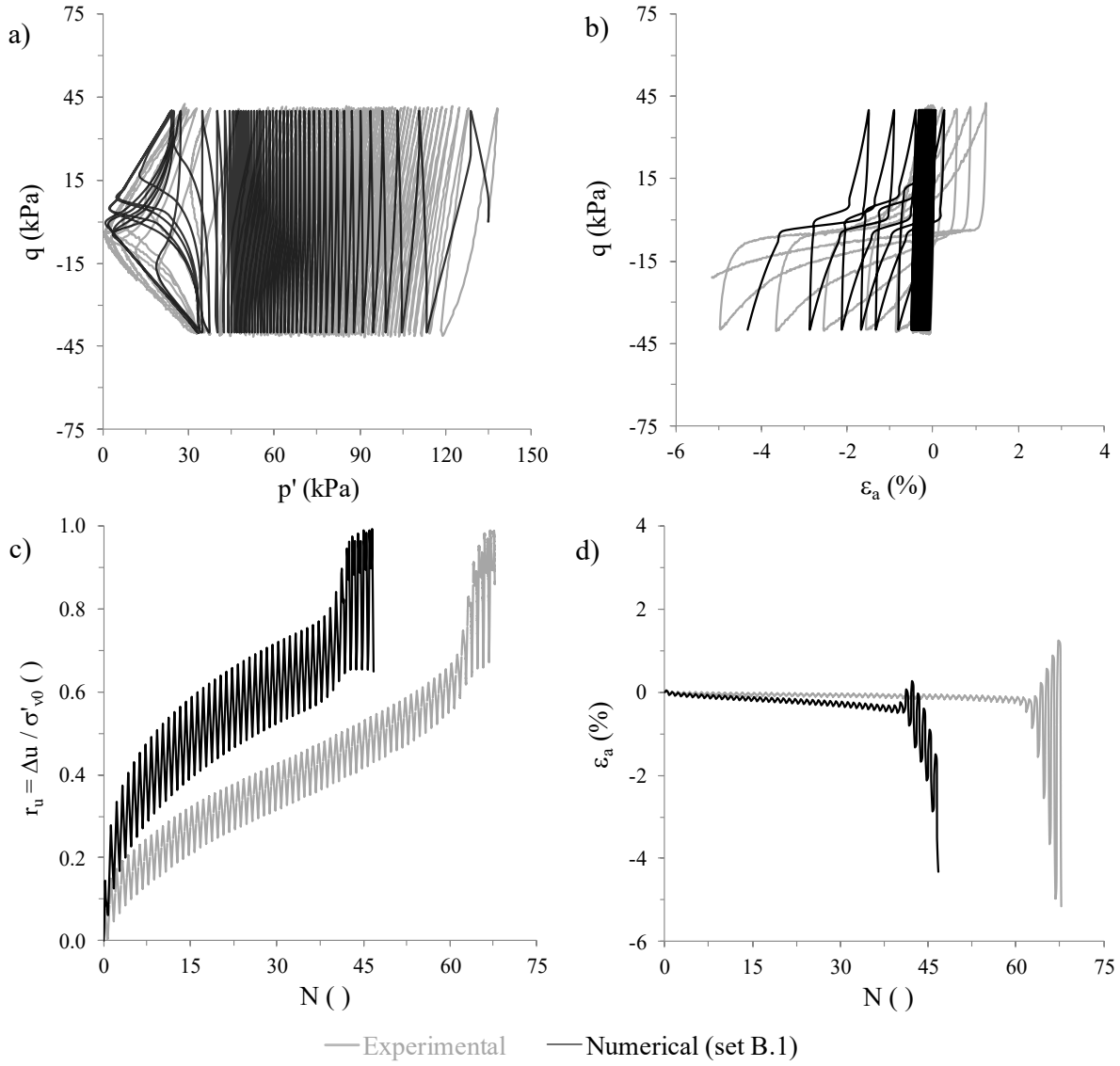

Figure B.8 – Experimental and numerical results of test ICUCT 0.805/135/40: (a) effective stress path, (b) stress-strain response; (c) excess pore water pressure ratio build-up with the number of loading cycles; and (d) axial strain evolution with the number of loading cycles.

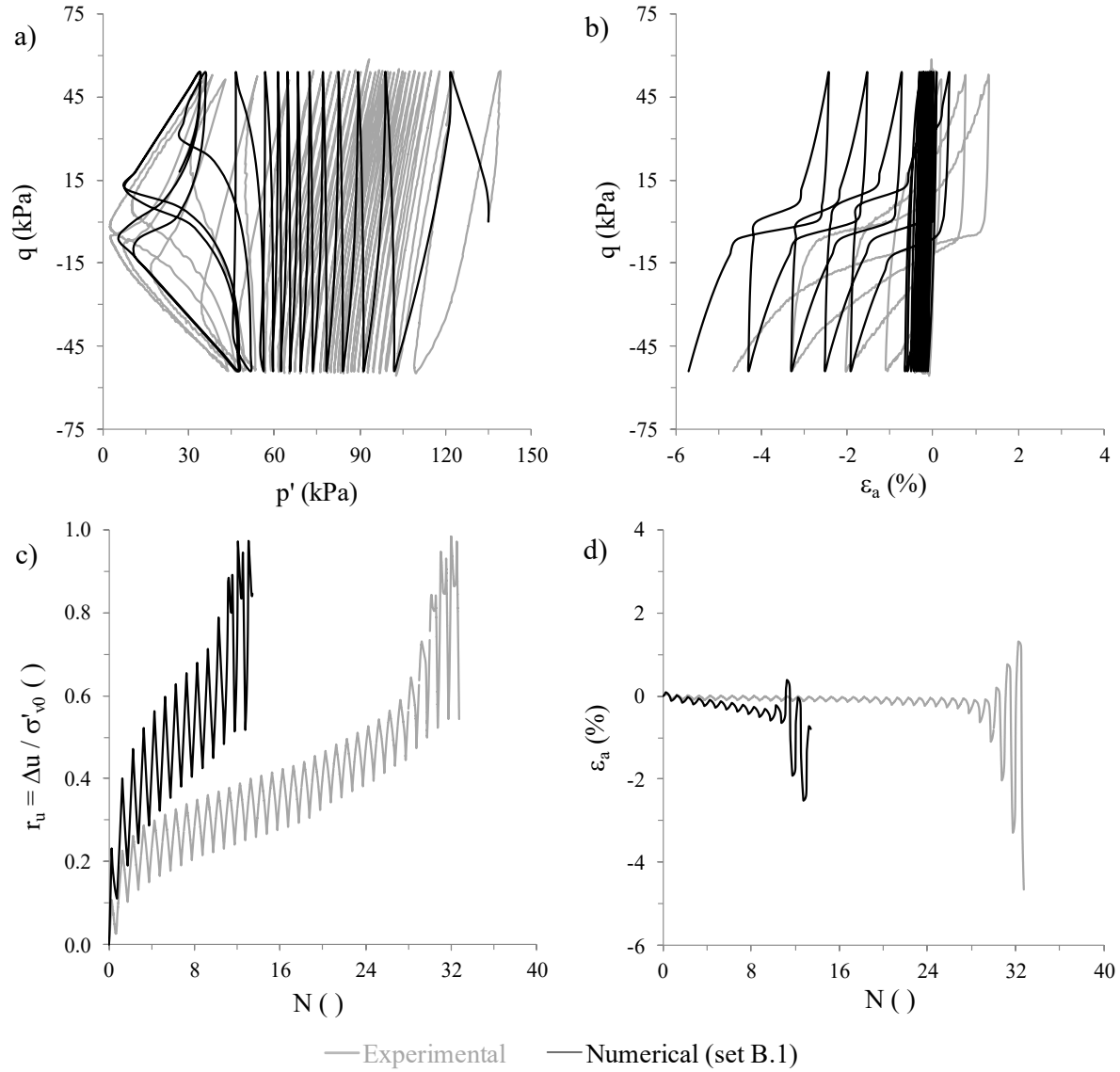

Figure B.9 – Experimental and numerical results of test ICUCT 0.830/135/54: (a) effective stress path, (b) stress-strain response; (c) excess pore water pressure ratio build-up with the number of loading cycles; and (d) axial strain evolution with the number of loading cycles.

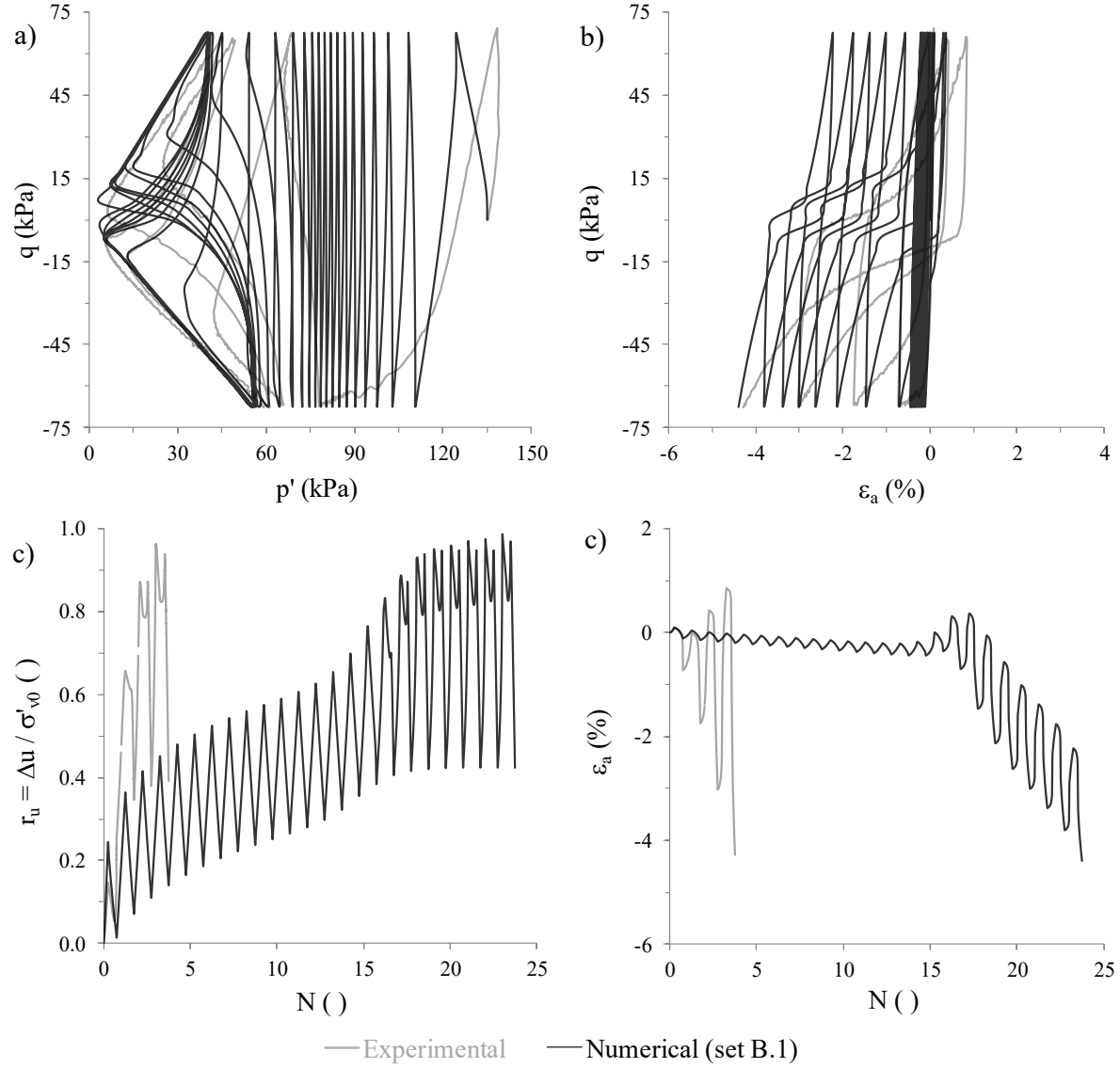

Figure B.10 – Experimental and numerical results of test ICUCT 0.793/135/67.5: (a) effective stress path, (b) stress-strain response; (c) excess pore water pressure ratio build-up with the number of loading cycles; and (d) axial strain evolution with the number of loading cycles.

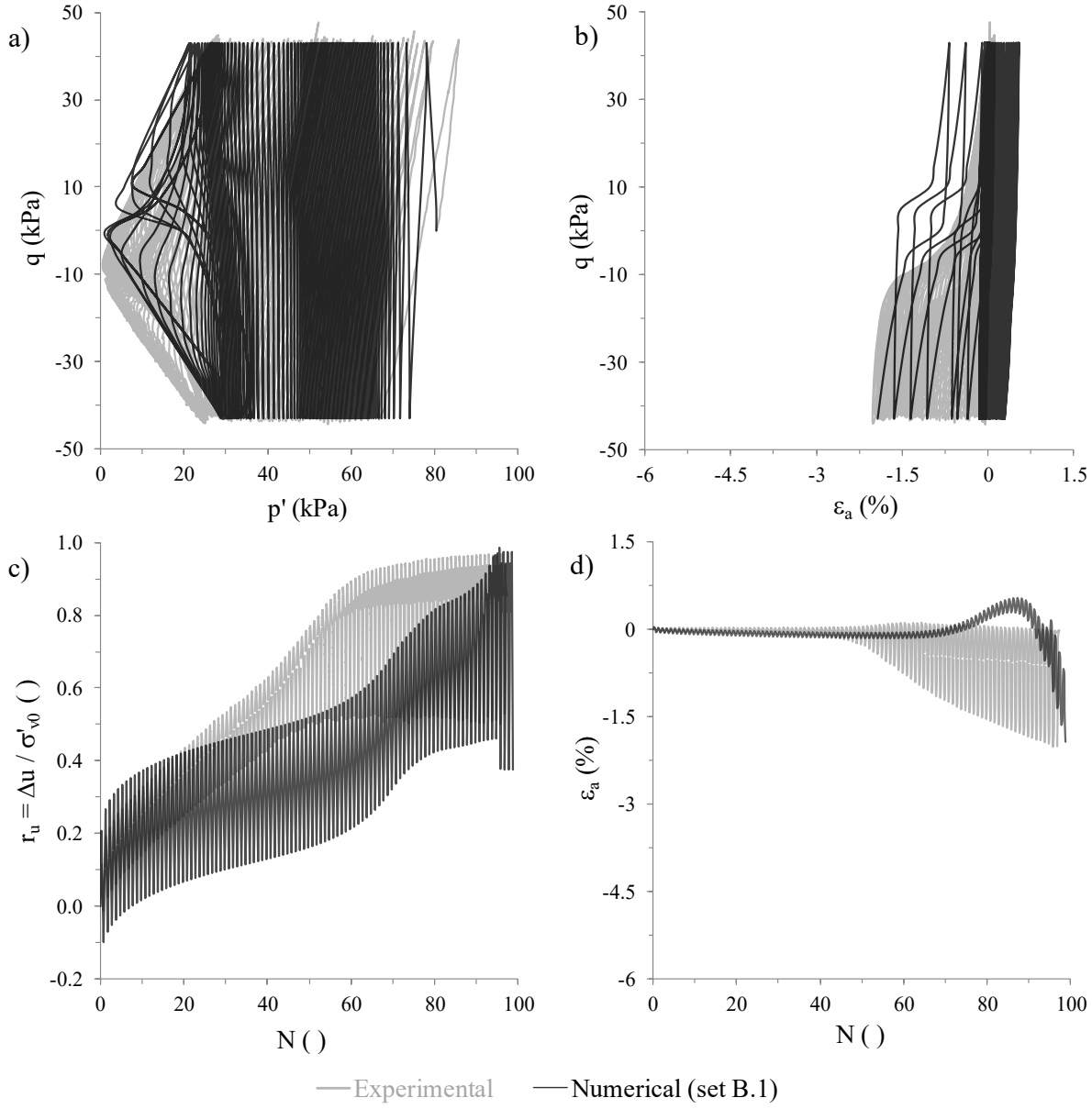

Figure B.11 – Experimental and numerical results of test ICUCT 0.651/80/43: (a) effective stress path, (b) stress-strain response; (c) excess pore water pressure ratio build-up with the number of loading cycles; and (d) axial strain evolution with the number of loading cycles.

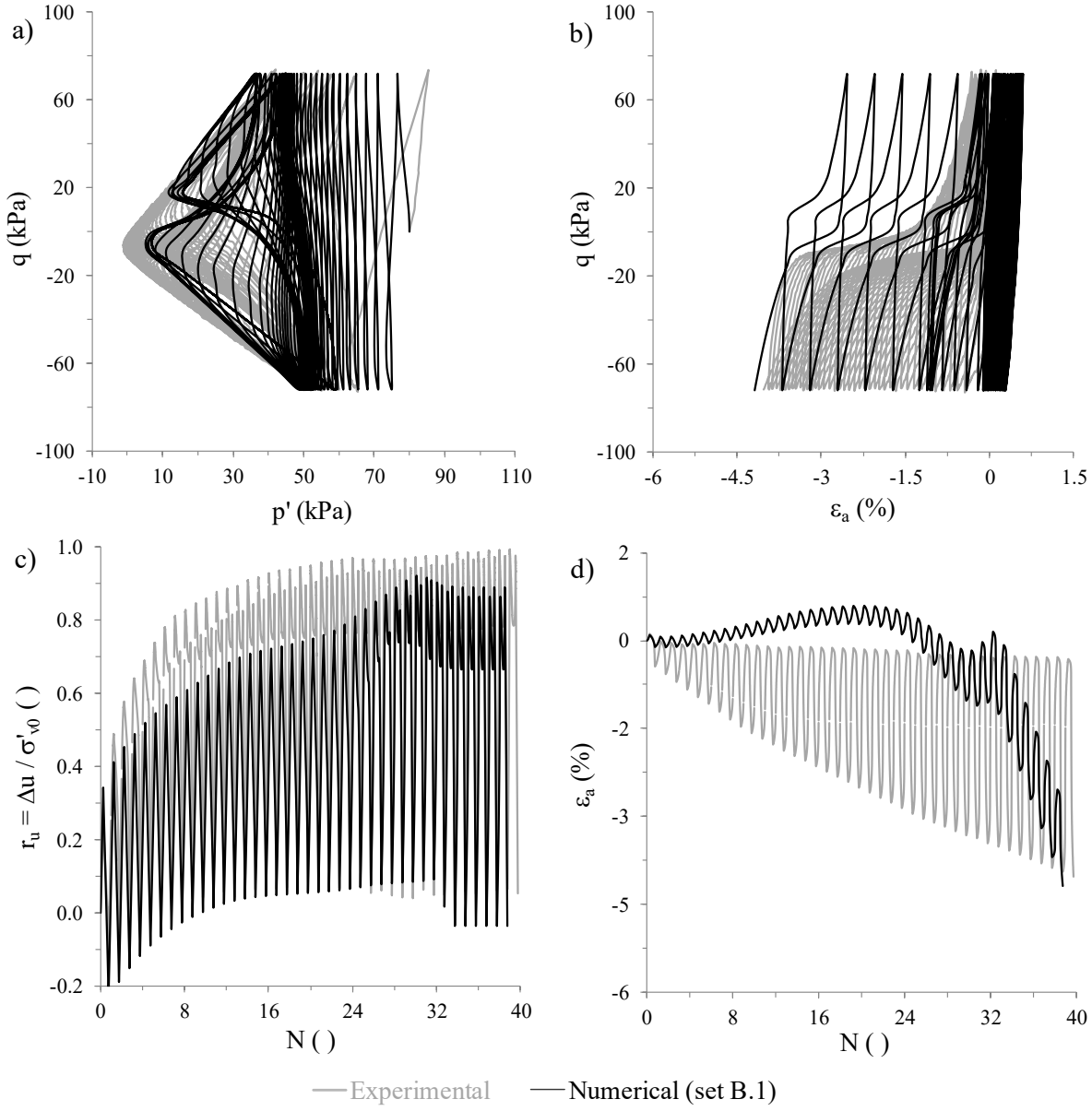

Figure B.12 – Experimental and numerical results of test ICUCT 0.652/80/77: (a) effective stress path, (b) stress-strain response; (c) excess pore water pressure ratio build-up with the number of loading cycles; and (d) axial strain evolution with the number of loading cycles.

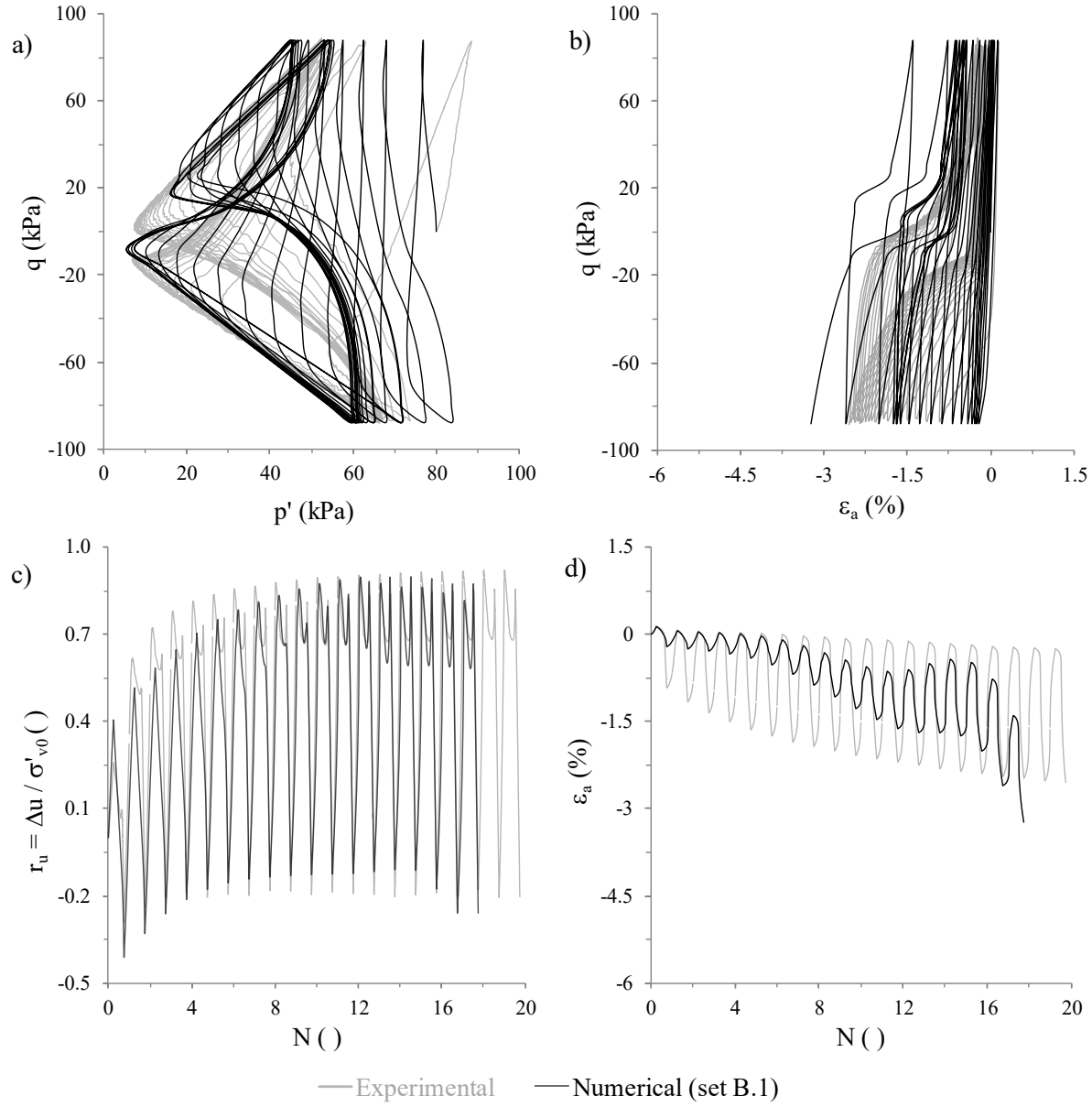

Figure B.13 – Experimental and numerical results of test ICUCT 0.652/80/88: (a) effective stress path, (b) stress-strain response; (c) excess pore water pressure ratio build-up with the number of loading cycles; and (d) axial strain evolution with the number of loading cycles.

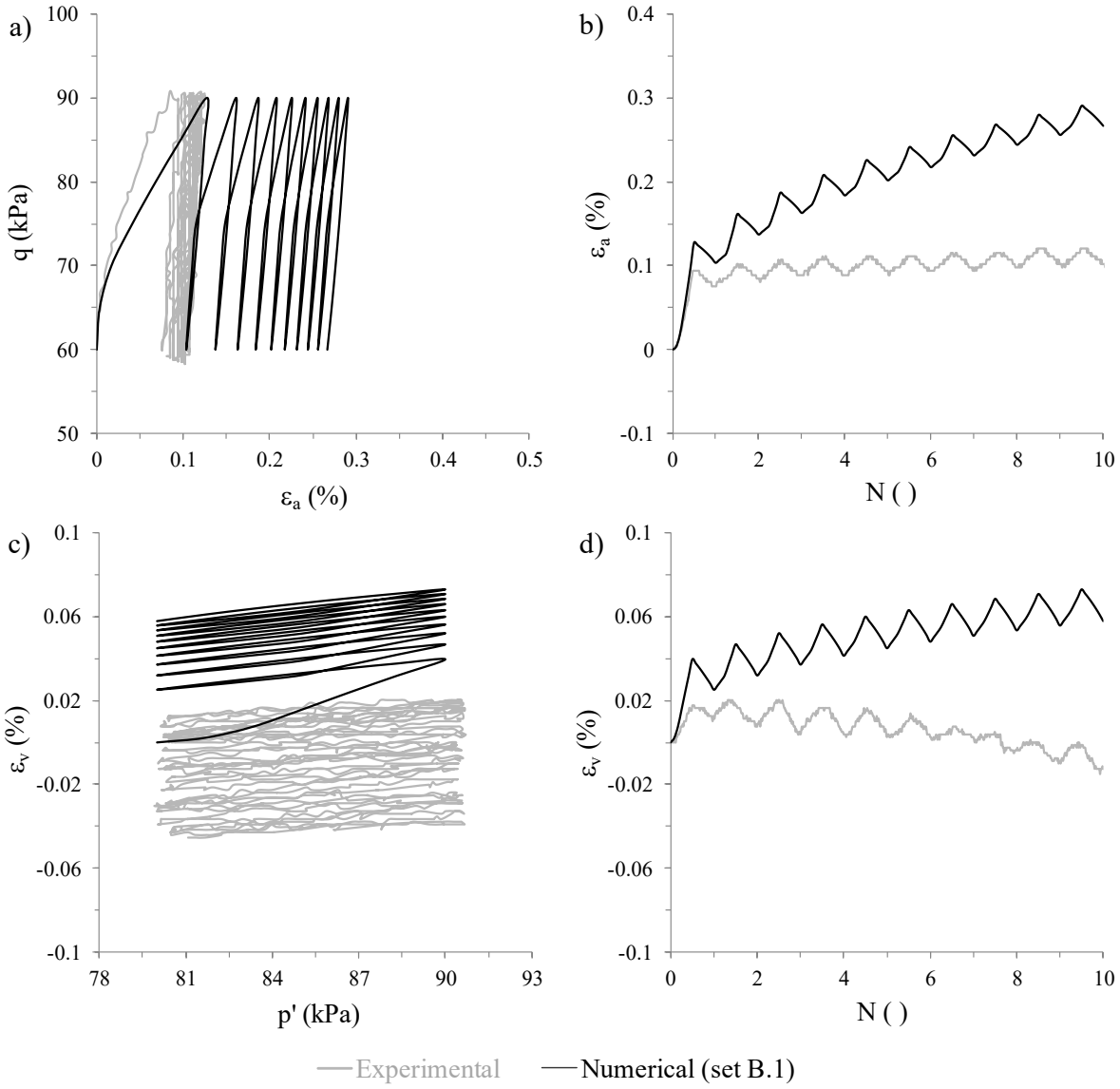

Figure B.14 – Experimental and numerical results of test K0CDCT 0.811/80/30: (a) stress-strain response; (b) axial strain evolution with the number of loading cycles; (c) volumetric strain evolution with mean effective stress; and (d) volumetric strain evolution with the number of loading cycles.

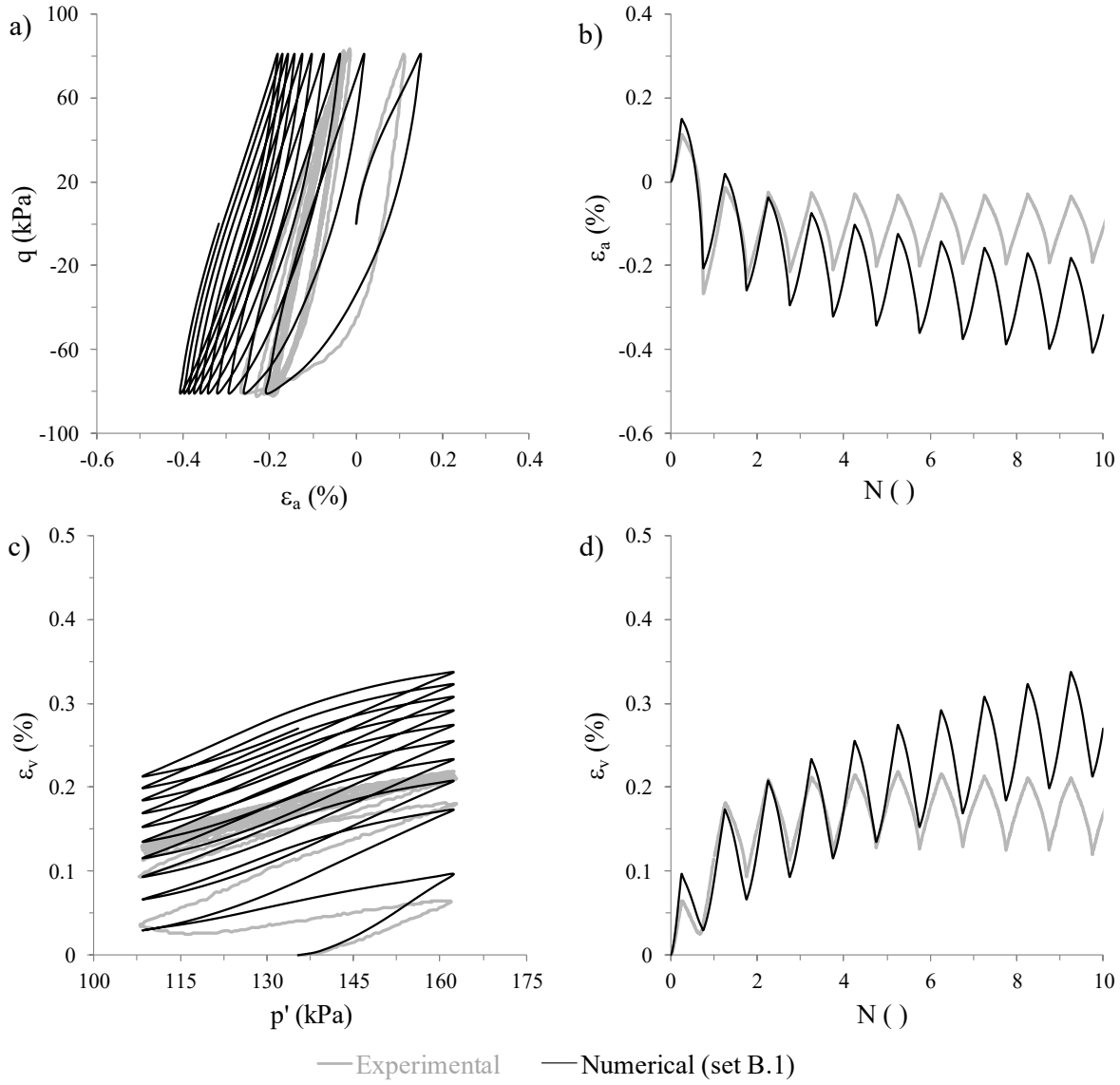

Figure B.15 – Experimental and numerical results of test ICDCT 0.820/135/81: (a) stress-strain response; (b) axial strain evolution with the number of loading cycles; (c) volumetric strain evolution with mean effective stress; and (d) volumetric strain evolution with the number of loading cycles.

B.5 Simulations using the extended formulation of the constitutive model

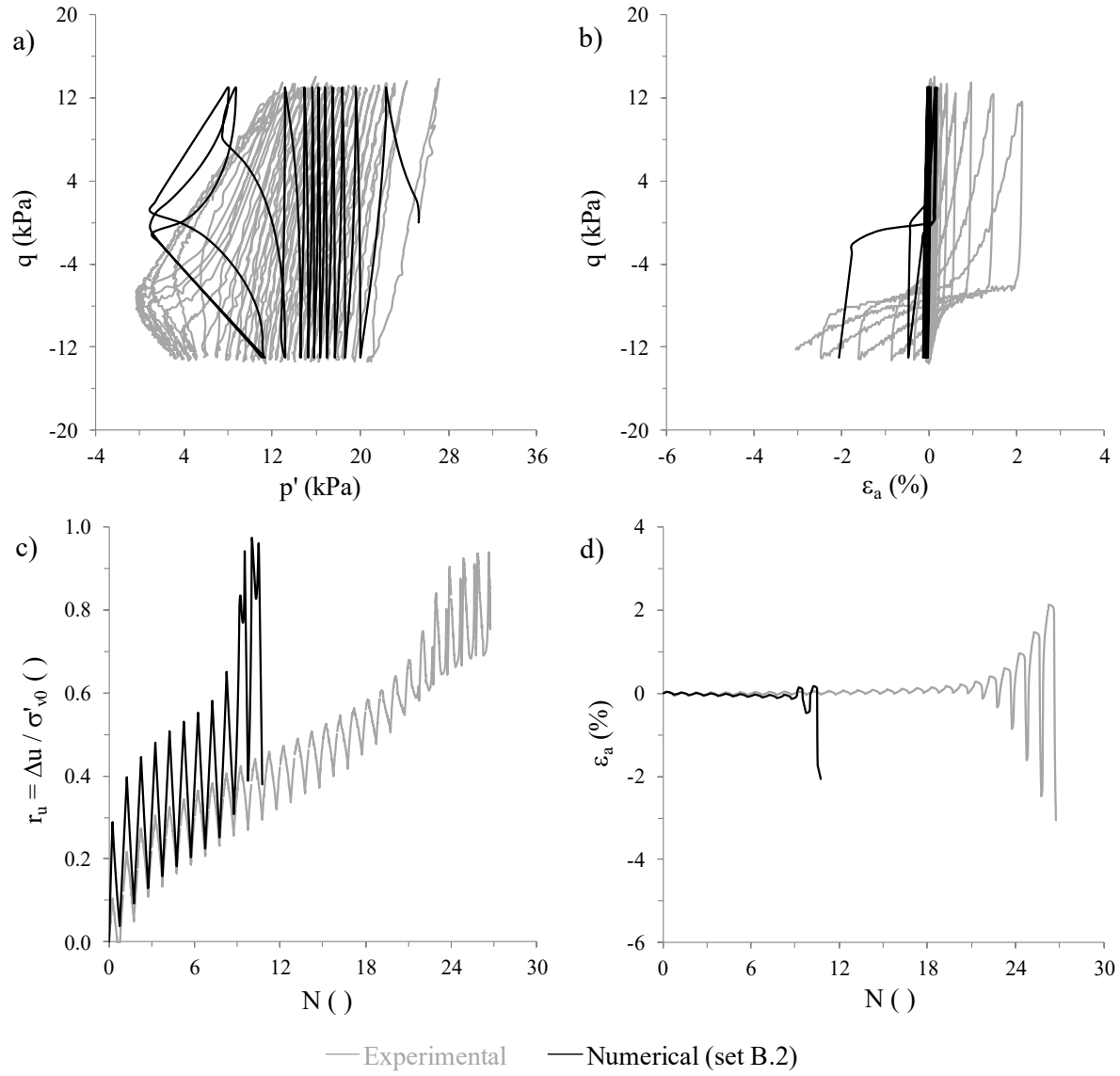

Figure B.16 – Experimental and numerical results of test ICUCT 0.821/25/13: (a) effective stress path, (b) stress-strain response; (c) excess pore water pressure ratio build-up with the number of loading cycles; and (d) axial strain evolution with the number of loading cycles.

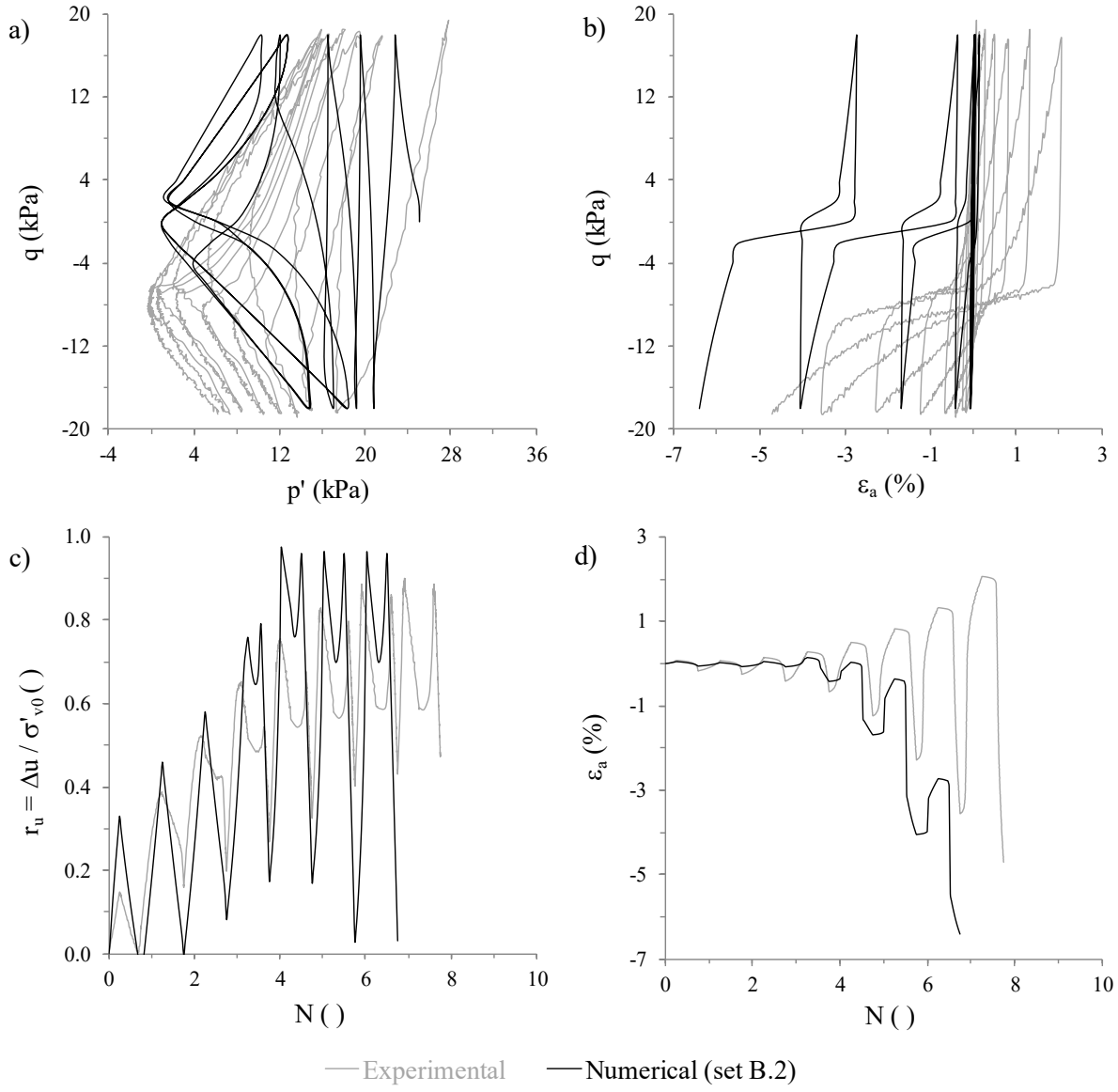

Figure B.17 – Experimental and numerical results of test ICUCT 0.777/25/18: (a) effective stress path, (b) stress-strain response; (c) excess pore water pressure ratio build-up with the number of loading cycles; and (d) axial strain evolution with the number of loading cycles.

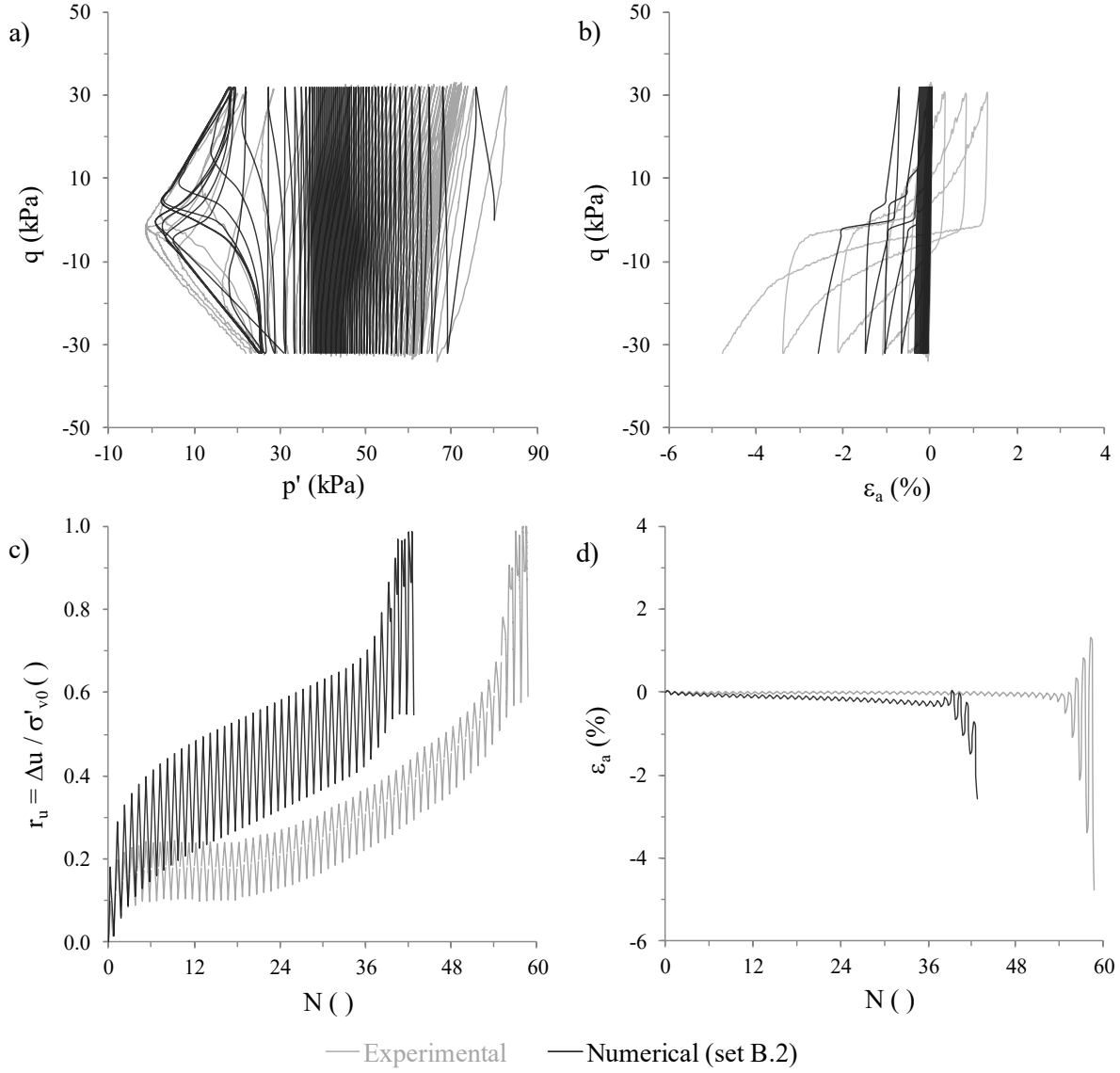

Figure B.18 – Experimental and numerical results of test ICUCT 0.771/80/32: (a) effective stress path, (b) stress-strain response; (c) excess pore water pressure ratio build-up with the number of loading cycles; and (d) axial strain evolution with the number of loading cycles.

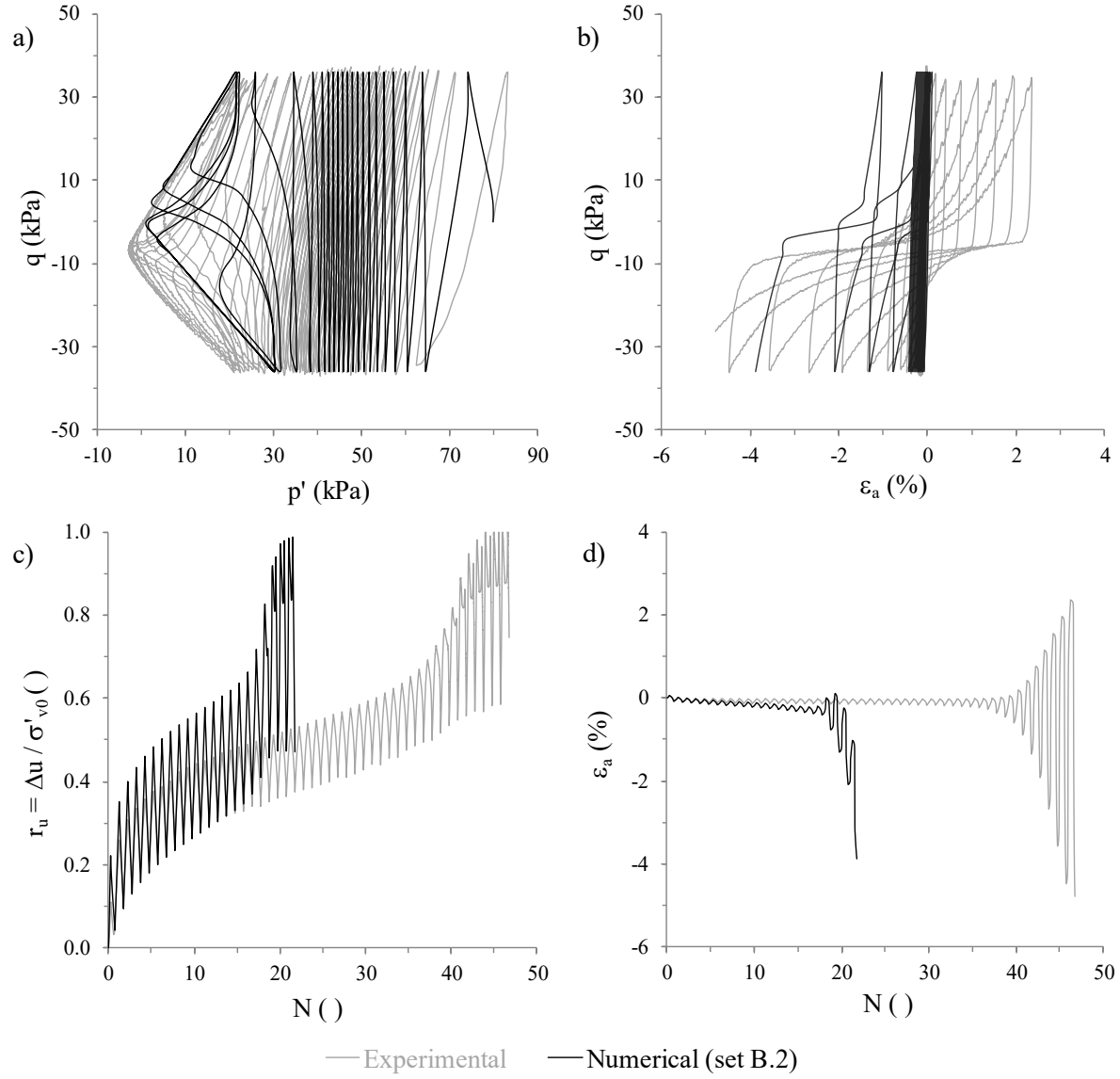

Figure B.19 – Experimental and numerical results of test ICUCT 0.803/80/36: (a) effective stress path, (b) stress-strain response; (c) excess pore water pressure ratio build-up with the number of loading cycles; and (d) axial strain evolution with the number of loading cycles.

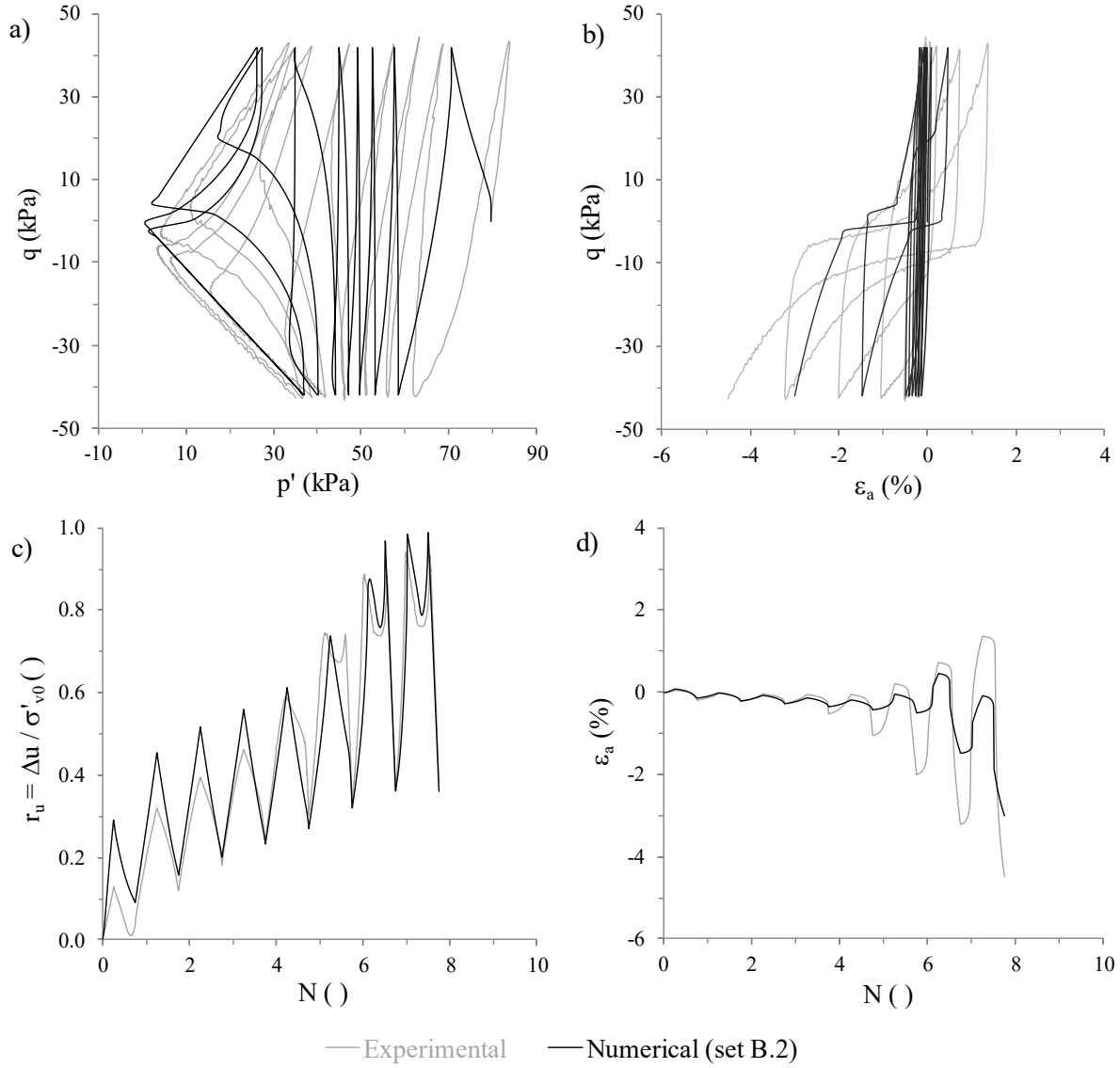

Figure B.20 – Experimental and numerical results of test ICUCT 0.832/80/42: (a) effective stress path, (b) stress-strain response; (c) excess pore water pressure ratio build-up with the number of loading cycles; and (d) axial strain evolution with the number of loading cycles.

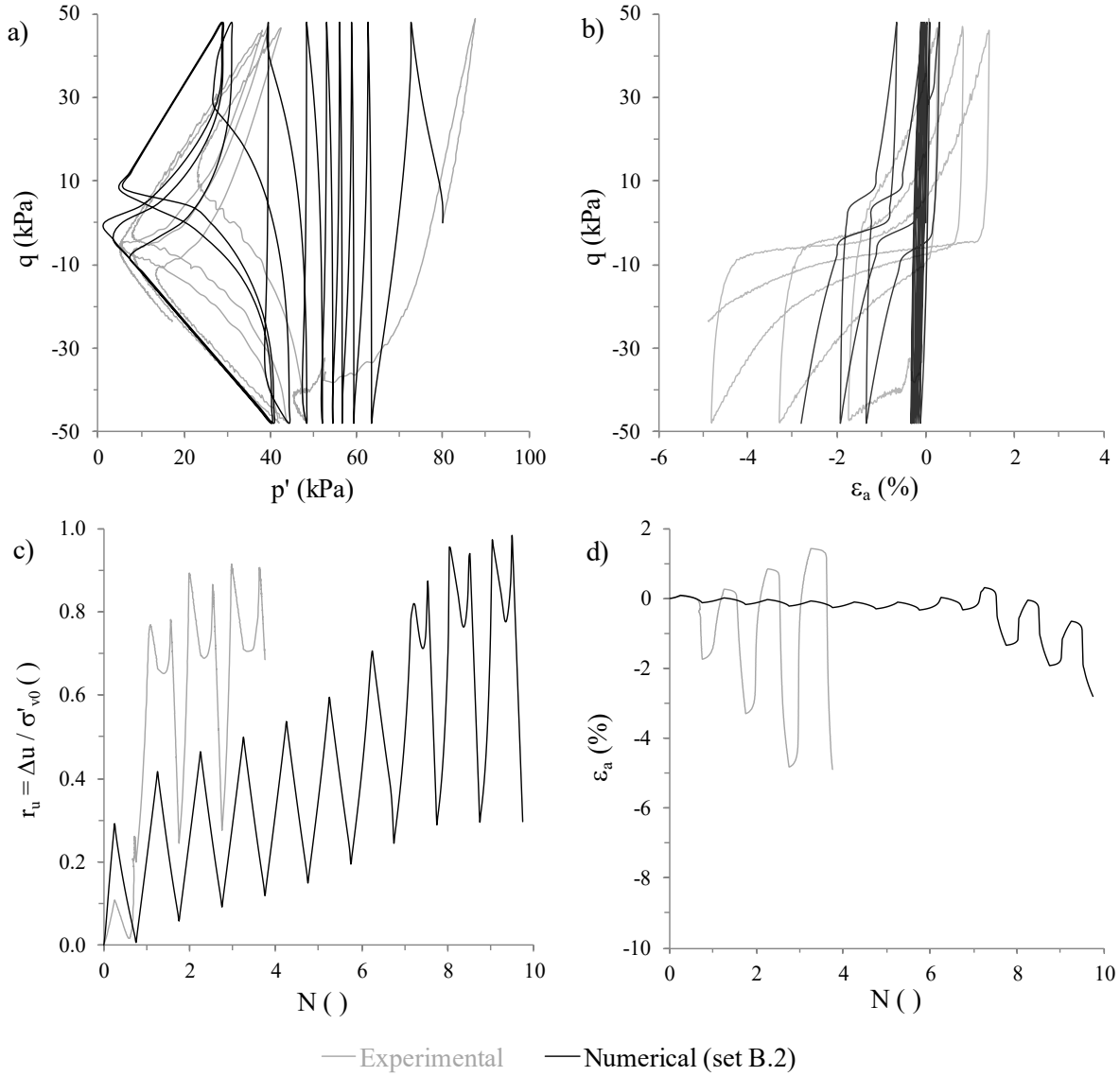

Figure B.21 – Experimental and numerical results of test ICUCT 0.804/80/48: (a) effective stress path, (b) stress-strain response; (c) excess pore water pressure ratio build-up with the number of loading cycles; and (d) axial strain evolution with the number of loading cycles.

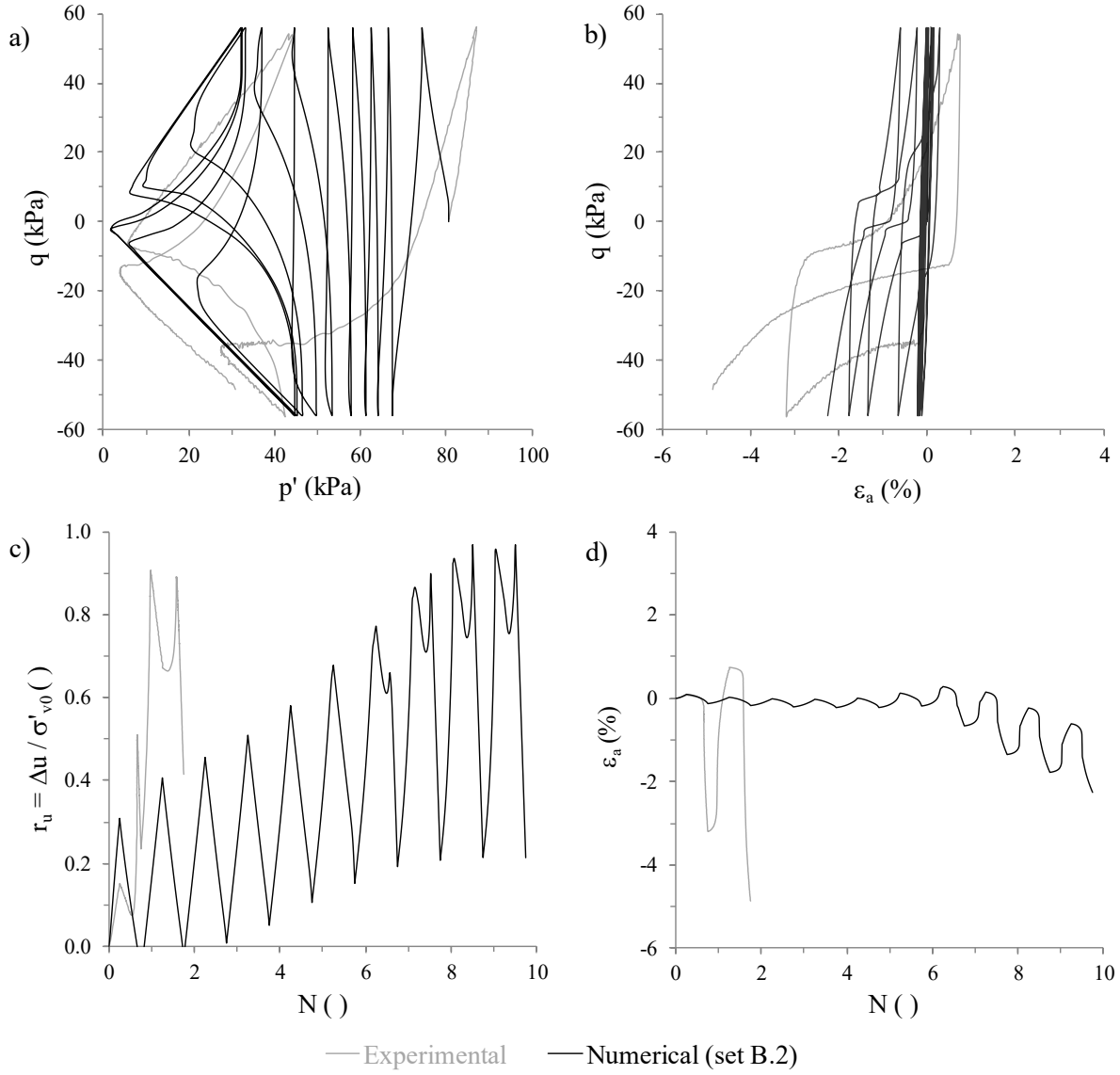

Figure B.22 – Experimental and numerical results of test ICUCT 0.773/80/56: (a) effective stress path, (b) stress-strain response; (c) excess pore water pressure ratio build-up with the number of loading cycles; and (d) axial strain evolution with the number of loading cycles.

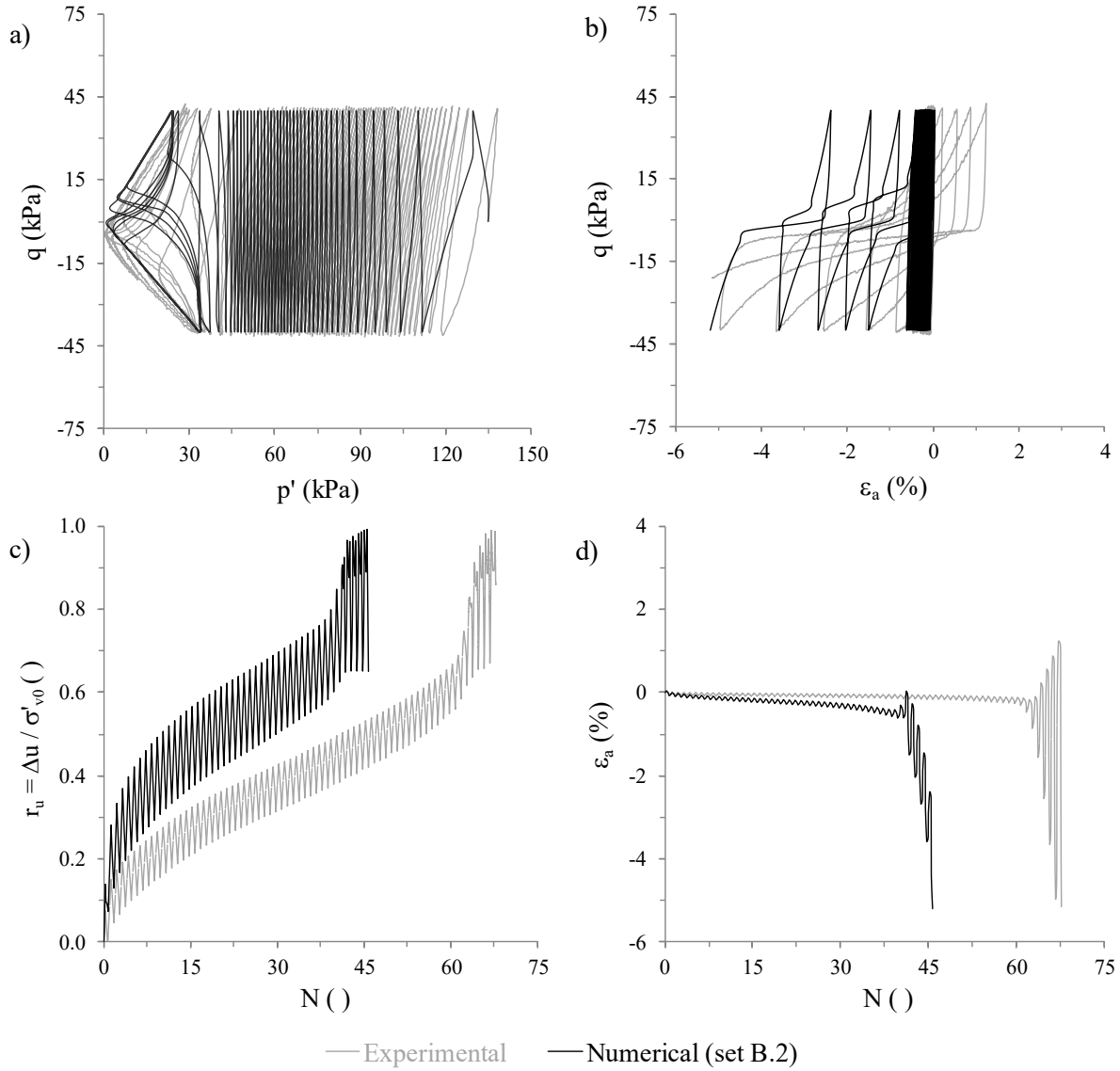

Figure B.23 – Experimental and numerical results of test ICUCT 0.805/135/40: (a) effective stress path, (b) stress-strain response; (c) excess pore water pressure ratio build-up with the number of loading cycles; and (d) axial strain evolution with the number of loading cycles.

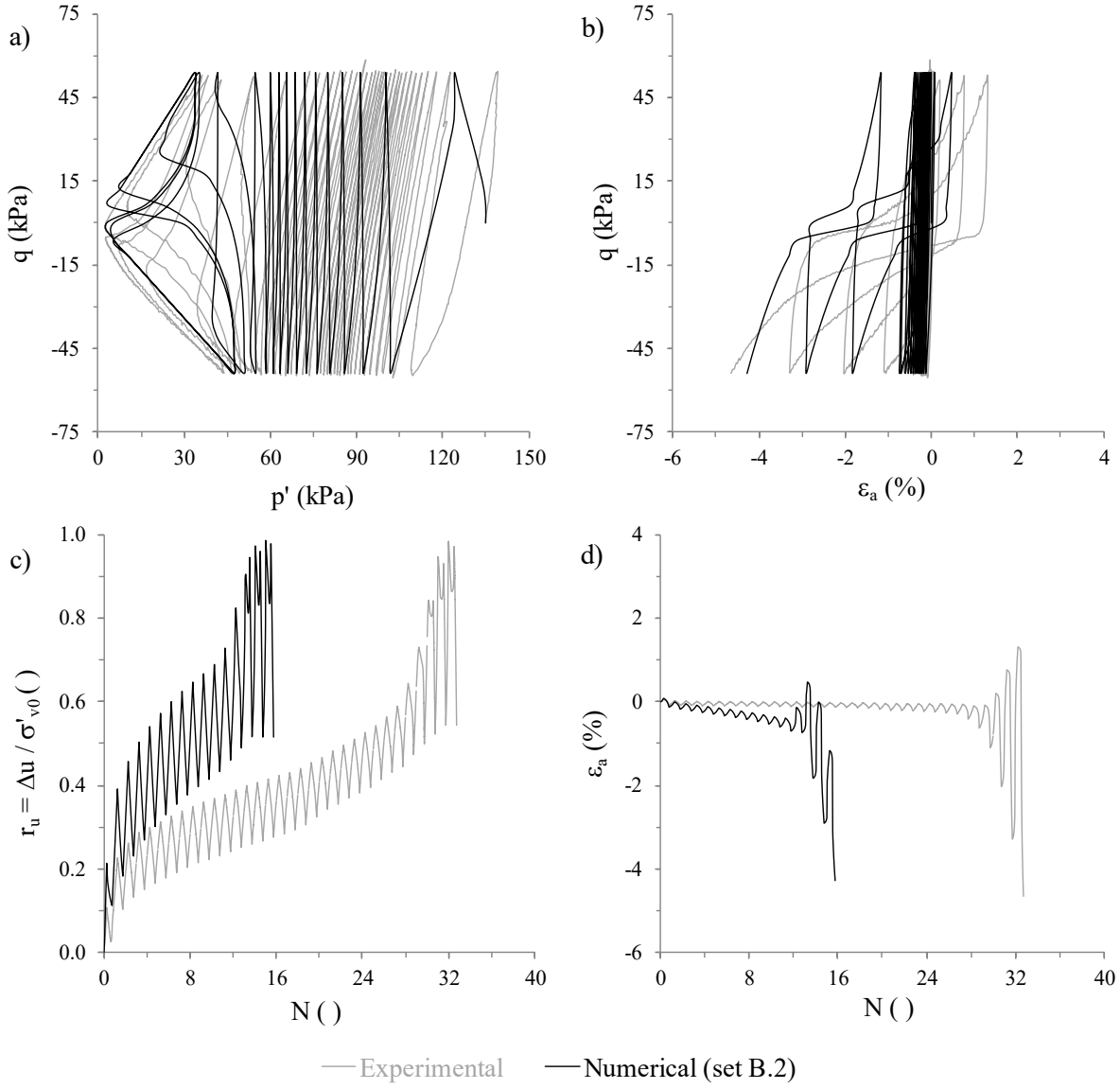

Figure B.24 – Experimental and numerical results of test ICUCT 0.830/135/54: (a) effective stress path, (b) stress-strain response; (c) excess pore water pressure ratio build-up with the number of loading cycles; and (d) axial strain evolution with the number of loading cycles.

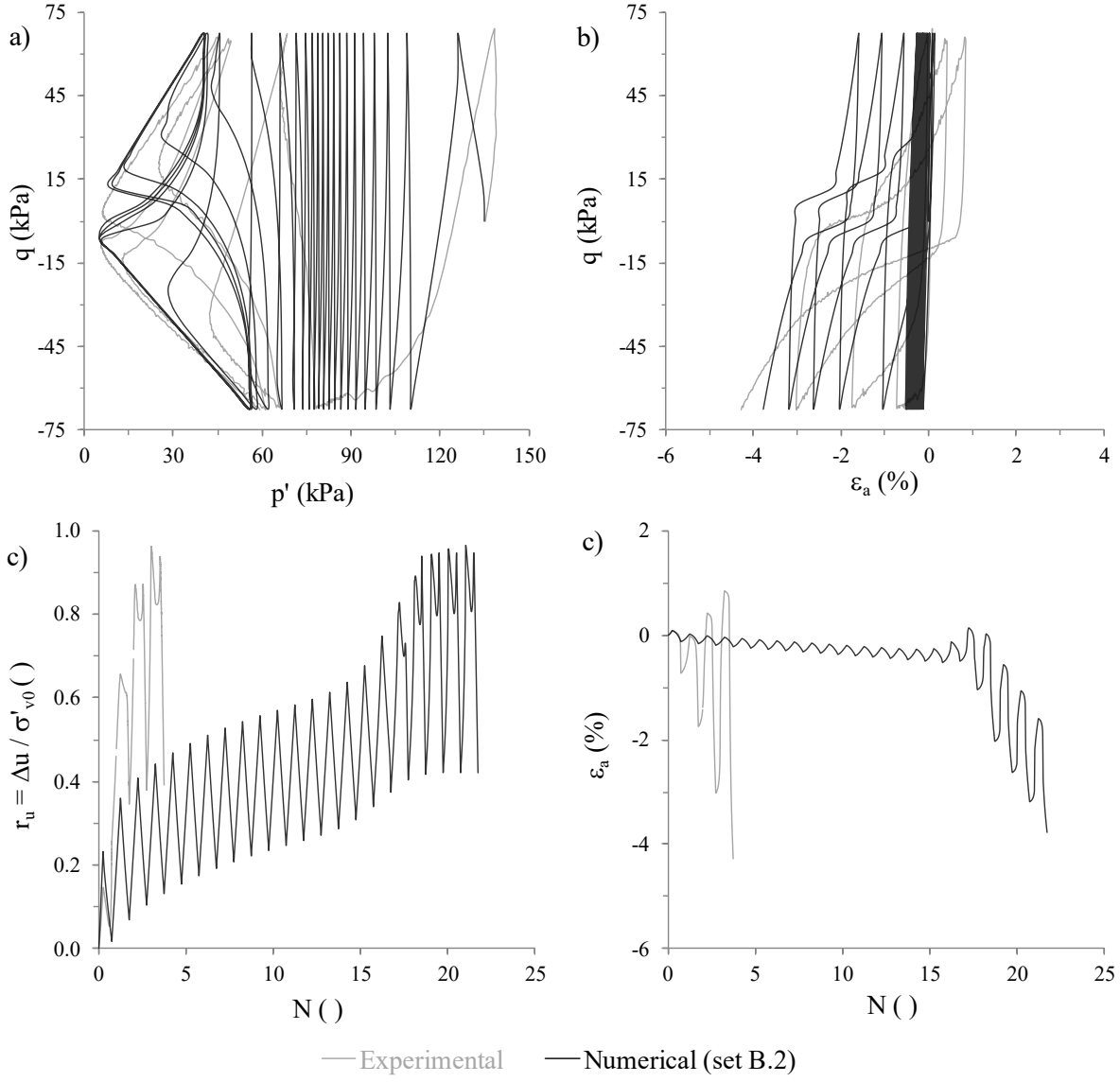

Figure B.25 – Experimental and numerical results of test ICUCT 0.793/135/67.5: (a) effective stress path, (b) stress-strain response; (c) excess pore water pressure ratio build-up with the number of loading cycles; and (d) axial strain evolution with the number of loading cycles.

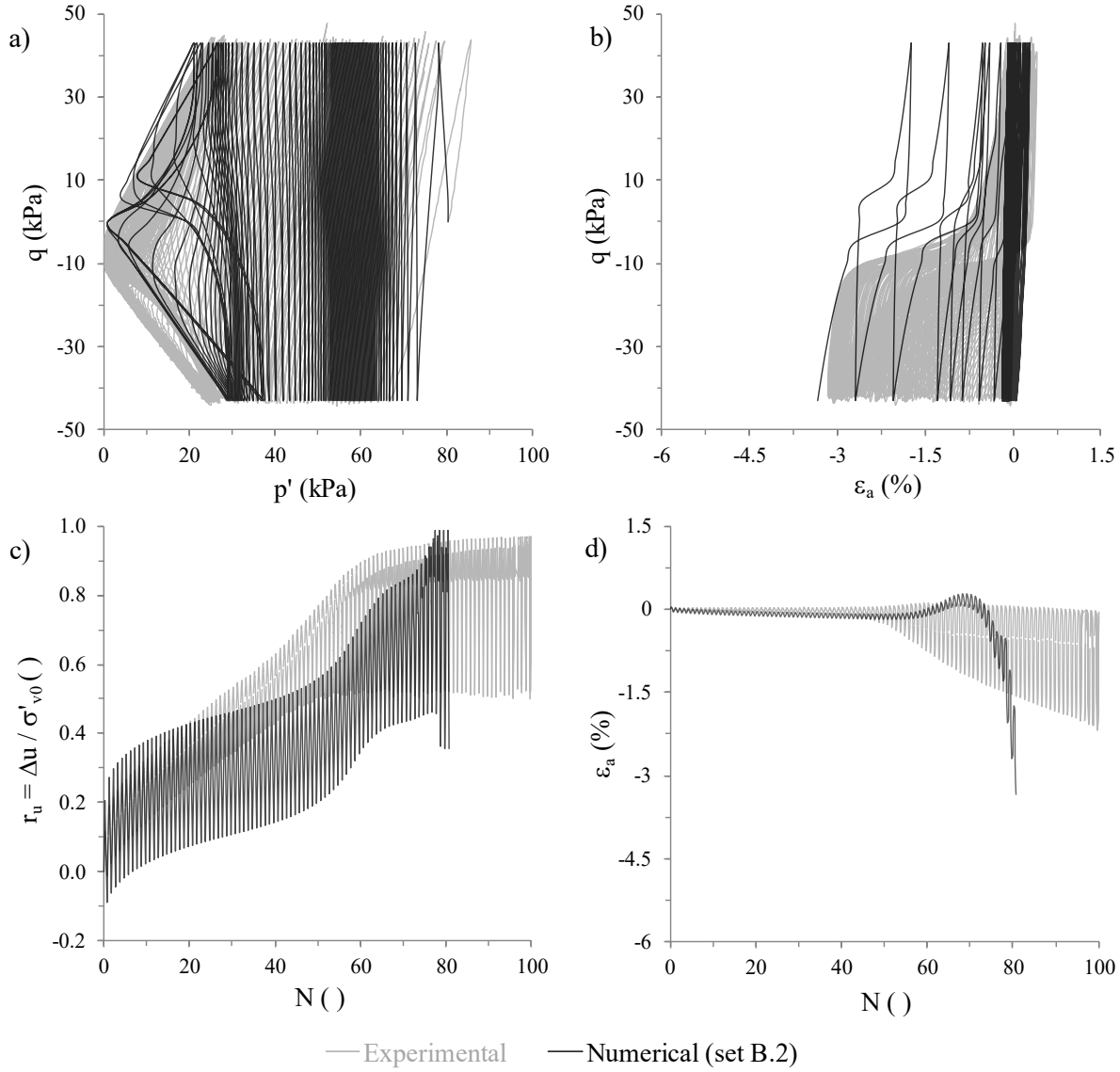

Figure B.26 – Experimental and numerical results of test ICUCT 0.651/80/43: (a) effective stress path, (b) stress-strain response; (c) excess pore water pressure ratio build-up with the number of loading cycles; and (d) axial strain evolution with the number of loading cycles.

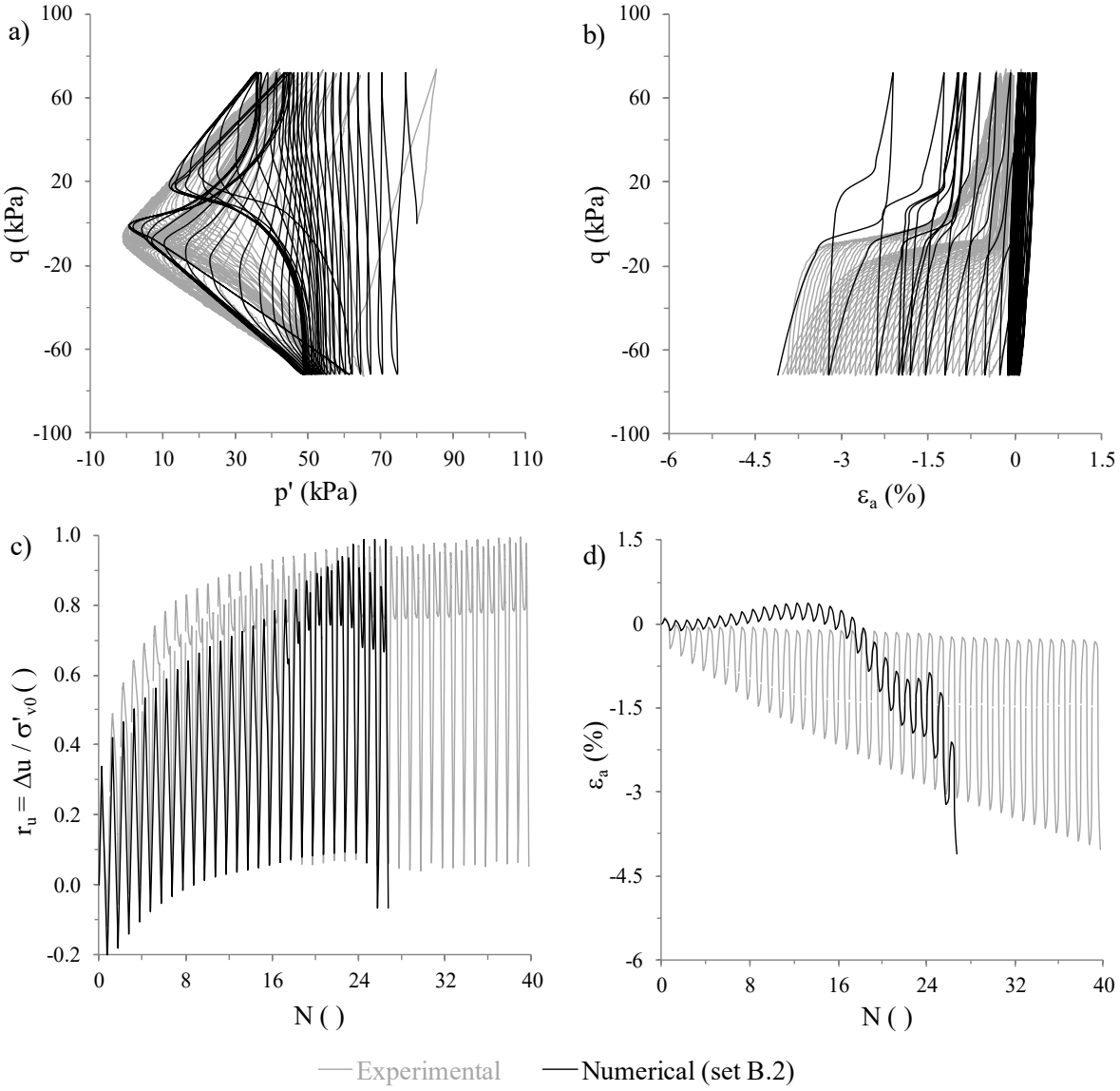

Figure B.27 – Experimental and numerical results of test ICUCT 0.652/80/77: (a) effective stress path, (b) stress-strain response; (c) excess pore water pressure ratio build-up with the number of loading cycles; and (d) axial strain evolution with the number of loading cycles.

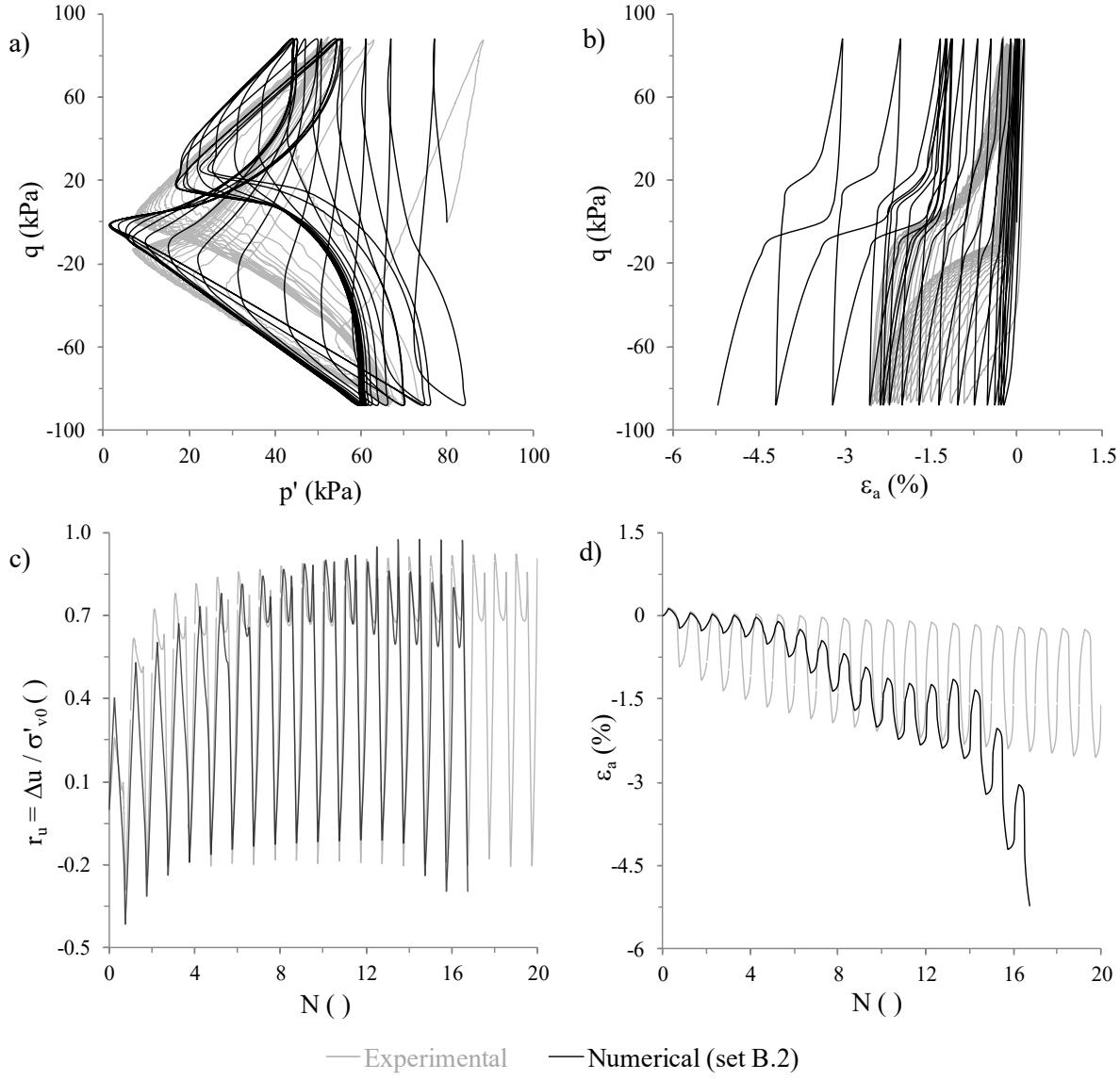

Figure B.28 – Experimental and numerical results of test ICUCT 0.652/80/88: (a) effective stress path, (b) stress-strain response; (c) excess pore water pressure ratio build-up with the number of loading cycles; and (d) axial strain evolution with the number of loading cycles.

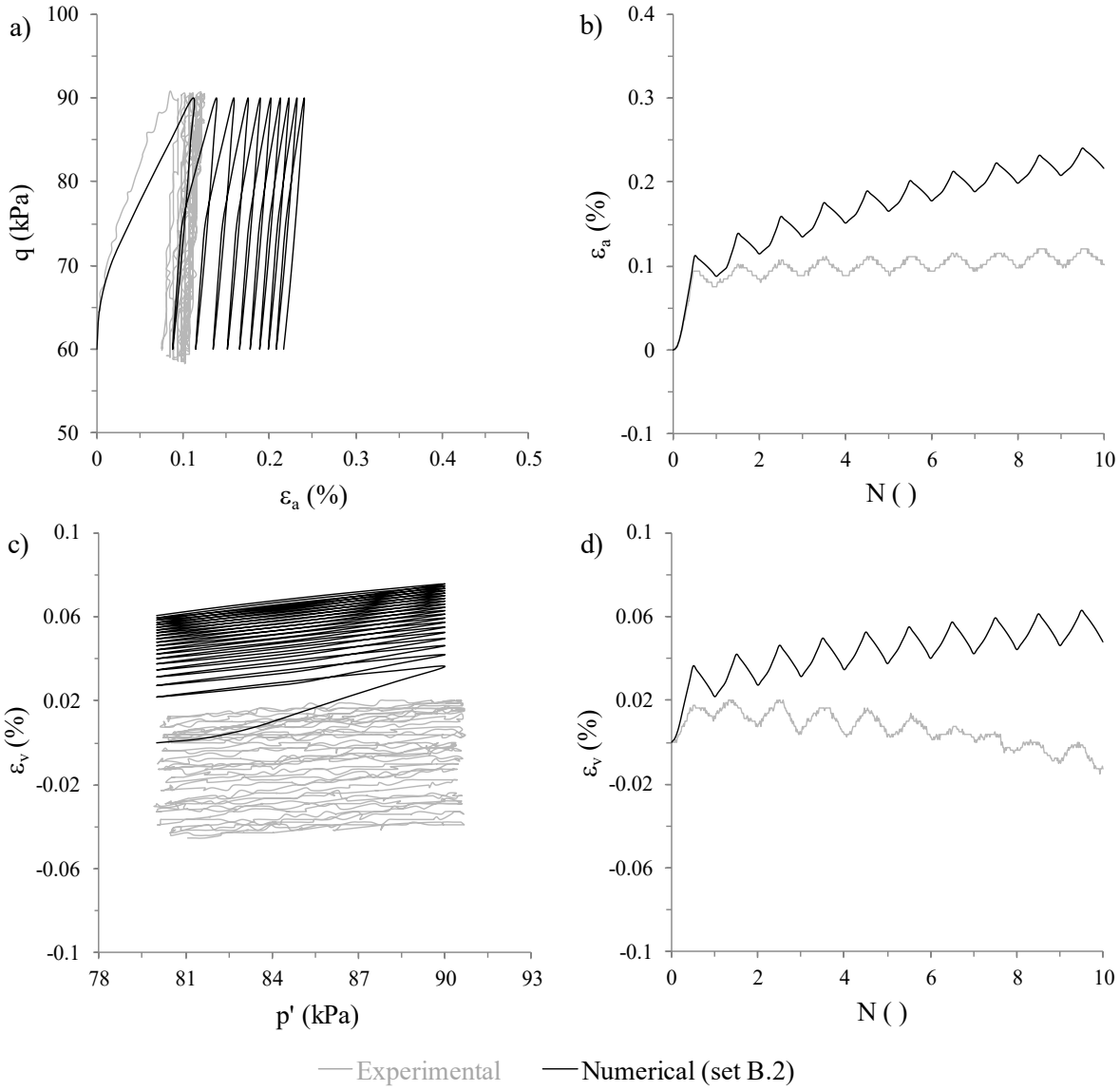

Figure B.29 – Experimental and numerical results of test K0CDCT 0.811/80/30: (a) stress-strain response; (b) axial strain evolution with the number of loading cycles; (c) volumetric strain evolution with mean effective stress; and (d) volumetric strain evolution with the number of loading cycles.

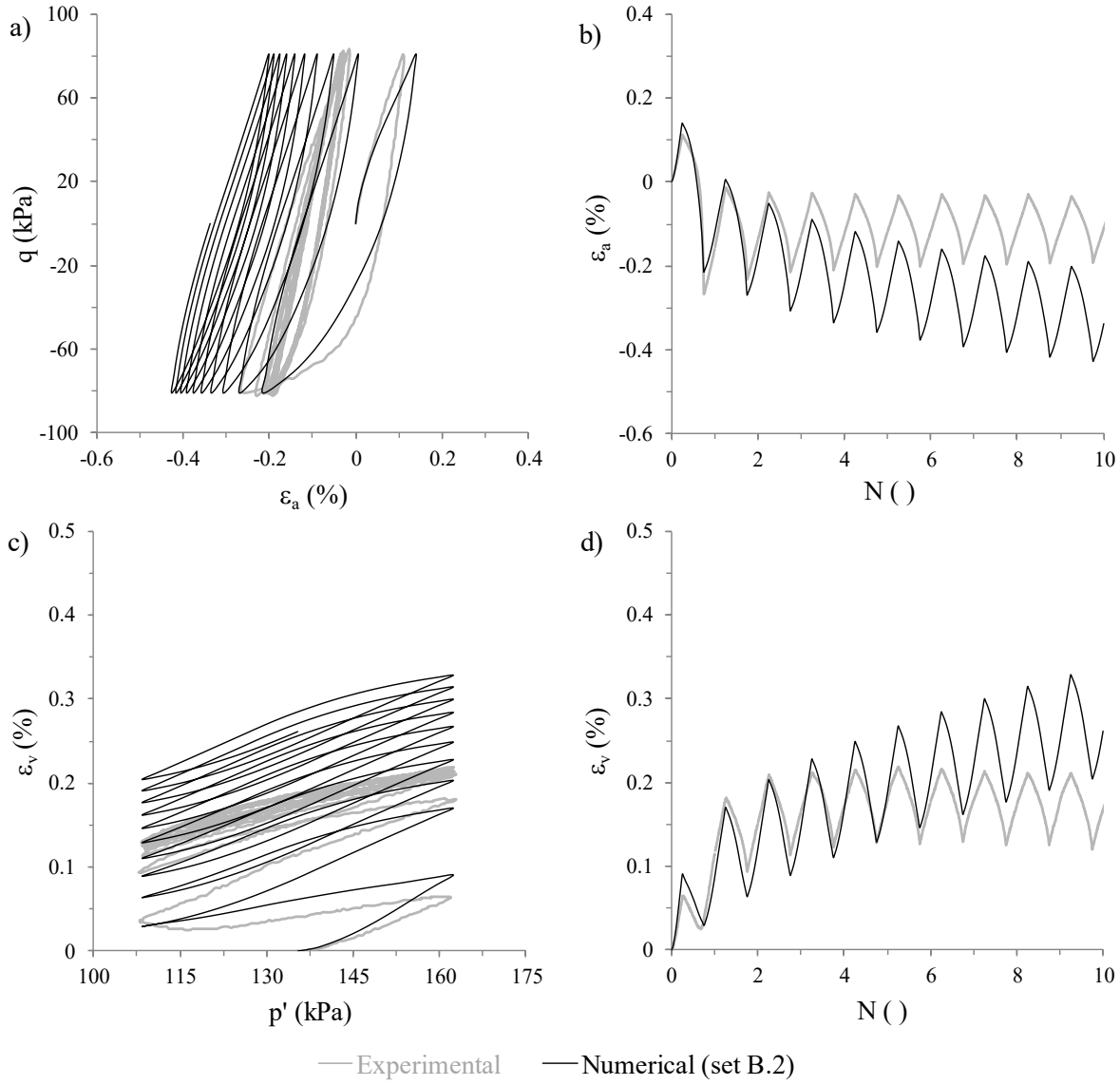

Figure B.30 – Experimental and numerical results of test ICDCT 0.820/135/81: (a) stress-strain response; (b) axial strain evolution with the number of loading cycles; (c) volumetric strain evolution with mean effective stress; and (d) volumetric strain evolution with the number of loading cycles.

Appendix C APPLICATION OF A MODIFIED FORWARD EULER SCHEME WITH AUTOMATIC SUB-STEPPING AND ERROR CONTROL TO THE STRESS INTEGRATION OF A BOUNDING SURFACE PLASTICITY MODEL

C.1 Explicit stress point integration

Table C.1 presents the operations required to integrate the present bounding surface plasticity model by using a modified forward Euler scheme with automatic sub-stepping and error control, as originally introduced by Sloan (1987) and further developed by Sloan *et al.* (2001). It is important to note that, due to their symmetrical form, second-order tensors are represented by an array, while fourth-order tensors are represented by a matrix. Moreover, the implementation of the constitutive model into FEMEPDYN makes use of a standard vector representation (i.e. a contravariant representation) for the symmetric stress tensor (where $\tau_{ij} = \sigma_{ij}$ with $i \neq j$ are the shear stress components) and the use of an engineering representation (i.e. a covariant representation) for the symmetric strain tensor (where $\gamma_{ij} = 2.0\ \varepsilon_{ij}$ $i \neq j$ are the shear strain components). For consistency, a contravariant representation is adopted for fourth-order tensors (e.g., elastic constitutive matrix, [$\boldsymbol{D}$]). For further details on the compressed matrix representations of symmetric second- and fourth-order tensors, refer, for example, to Bathe (1996) or to Helnwein (2001).

Table C.1 – Explicit stress integration scheme for the present bounding surface plasticity model.

Step	Description
1	**Initialisation of model variables**
	Given the total strain increment, $\{\Delta\boldsymbol{\varepsilon}\} = \{\Delta\varepsilon_{xx} \quad \Delta\varepsilon_{yy} \quad 2.0\Delta\varepsilon_{xy} \quad \Delta\varepsilon_{zz} \quad 2.0\Delta\varepsilon_{xz} \quad 2.0\Delta\varepsilon_{yz}\}^{\mathrm{T}} = \{\Delta\varepsilon_{xx} \quad \Delta\varepsilon_{yy} \quad \Delta\gamma_{xy} \quad \Delta\varepsilon_{zz} \quad \Delta\gamma_{xz} \quad \Delta\gamma_{yz}\}^{\mathrm{T}}$, enter with the initial values of: - effective stresses: $\{\boldsymbol{\sigma'}\} = \{\sigma'_{xx} \quad \sigma'_{yy} \quad \tau_{xy} \quad \sigma'_{zz} \quad \tau_{xz} \quad \tau_{yz}\}^{\mathrm{T}}$; - elastic strains: $\{\boldsymbol{\varepsilon^e}\} = \{\varepsilon^e_{xx} \quad \varepsilon^e_{yy} \quad \gamma^e_{xy} \quad \varepsilon^e_{zz} \quad \gamma^e_{xz} \quad \gamma^e_{yz}\}^{\mathrm{T}}$; - plastic strains associated with the primary and secondary yield surfaces, respectively: $\{\boldsymbol{\varepsilon^p_1}\} = \{\varepsilon^p_{xx,1} \quad \varepsilon^p_{yy,1} \quad \gamma^p_{xy,1} \quad \varepsilon^p_{zz,1} \quad \gamma^p_{xz,1} \quad \gamma^p_{yz,1}\}^{\mathrm{T}}$ and $\{\boldsymbol{\varepsilon^p_2}\} = \{\varepsilon^p_{xx,2} \quad \varepsilon^p_{yy,2} \quad \gamma^p_{xy,2} \quad \varepsilon^p_{zz,2} \quad \gamma^p_{xz,2} \quad \gamma^p_{yz,2}\}^{\mathrm{T}}$; - total strains: $\{\boldsymbol{\varepsilon}\} = \{\boldsymbol{\varepsilon^e}\} + \{\boldsymbol{\varepsilon^p_1}\} + \{\boldsymbol{\varepsilon^p_2}\} = \{\varepsilon_{xx} \quad \varepsilon_{yy} \quad \gamma_{xy} \quad \varepsilon_{zz} \quad \gamma_{xz} \quad \gamma_{yz}\}$; - void ratio, $e = e_0$; - elastic state parameters: effective stresses and strains at last shear reversal, $\{\boldsymbol{\sigma'^{SR}}\} = \{\sigma'^{SR}_{xx} \quad \sigma'^{SR}_{yy} \quad \tau^{SR}_{xy} \quad \sigma'^{SR}_{zz} \quad \tau^{SR}_{xz} \quad \tau^{SR}_{yz}\}^{\mathrm{T}}$ and $\{\boldsymbol{\varepsilon^{SR}}\} = \{\varepsilon^e_{xx} \quad \varepsilon^e_{yy} \quad \gamma^e_{xy} \quad \varepsilon^e_{zz} \quad \gamma^e_{xz} \quad \gamma^e_{yz}\}^{\mathrm{T}}$, respectively; void ratio at last shear reversal, e^{SR}, and the scaling factor, N; - plastic state parameters: back-stress tensor, $\{\boldsymbol{\alpha}\} = \{\alpha_{xx} \quad \alpha_{yy} \quad \alpha_{xy} \quad \alpha_{zz} \quad \alpha_{xz} \quad \alpha_{yz}\}^{\mathrm{T}}$; isotropic and deviatoric components of the stress-induced anisotropy tensor, respectively, f_p and $\{\boldsymbol{f}\} =$

Table C.1 – Explicit stress integration scheme for the present bounding surface plasticity model.

Step	Description
	$\{f_{xx} \quad f_{yy} \quad f_{xy} \quad f_{zz} \quad f_{xz} \quad f_{yz}\}^{\mathrm{T}}$, their rate of evolution, H, as well as stress-induced anisotropy constant C; - inherent anisotropy tensor, $\{\boldsymbol{F}\} = \{F_{xx} \quad F_{yy} \quad F_{xy} \quad F_{zz} \quad F_{xz} \quad F_{yz}\}^{\mathrm{T}} = \left\{\frac{1.0}{2.0}(1.0-a) \quad a \quad 0.0 \quad \frac{1.0}{2.0}(1.0-a) \quad 0.0 \quad 0.0\right\}^{\mathrm{T}}$. Determine the small-strain shear modulus at last shear reversal: $G_{max}^{SR} = C_g\, p'_{ref} \frac{(m_g - e)^{2.0}}{1.0+e}\left(\frac{p'^{SR}}{p'_{ref}}\right)^{n_g} \geq C_g\, p'_{ref} \frac{(m_g - e)^{2.0}}{1.0+e}\left(\frac{p'_{min}}{p'_{ref}}\right)^{n_g}$ Determine the initial positions of the primary and secondary yield surfaces: $F_1 = \sqrt{(\{\boldsymbol{s}\} - p'\{\boldsymbol{\alpha}\}):(\{\boldsymbol{s}\} - p'\{\boldsymbol{\alpha}\})} - \sqrt{2.0/3.0}\; m\, p'$ where [1]: $(\{\boldsymbol{s}\} - p'\{\boldsymbol{\alpha}\}):(\{\boldsymbol{s}\} - p'\{\boldsymbol{\alpha}\}) = \left(\sigma'_{xx} - p'(1.0+\alpha_{xx})\right)^2 + \left(\sigma'_{yy} - p'\left(1.0+\alpha_{yy}\right)\right)^2 + \left(\sigma'_{zz} - p'(1.0+\alpha_{zz})\right)^2 + 2.0\left(\tau_{xy} - p'\,\alpha_{xy}\right)^2 + 2.0\,(\tau_{xz} - p'\,\alpha_{xz})^2 + 2.0\left(\tau_{yz} - p'\,\alpha_{yz}\right)^2$ $F_2 = p'_{YS} - p'$ where: $p' = \frac{\sigma'_{xx} + \sigma'_{yy} + \sigma'_{zz}}{3.0}$
2	**Elastic trial**
2.1	Initialise variables of the modified forward Euler scheme required to the integration of the purely elastic response (i.e. elastic trial): $\Delta T_n = 1.0$ and $T_n = 0.0$. Initialise variable informing which yield surface is active: $IYIELD = 0$.
2.2	If $T_n < 1.0$ then: Determine the sub-step strain increment: $\{\Delta\boldsymbol{\varepsilon_{ss}}\} = \Delta T_n\, \{\Delta\boldsymbol{\varepsilon}\}$. Save the pseudo time at the beginning of the sub-step increment, $T_{n-1} = T_n$. Save temporarily the effective stresses and void ratio at the beginning of the sub-step increment, $\{\boldsymbol{\sigma'_{mem}}\} = \{\boldsymbol{\sigma'}\}$ and $e_{mem} = e$, respectively, as well as the positions of the yield surfaces at the beginning of the sub-step increment, $F_{1,mem} = F_1$ and $F_{2,mem} = F_2$. Save temporarily the values of the elastic state parameters corresponding to the beginning of the sub-step increment: $\{\boldsymbol{\sigma'^{SR}_{mem}}\} = \{\boldsymbol{\sigma'^{SR}}\}$, $\{\boldsymbol{\varepsilon^{SR}_{mem}}\} = \{\boldsymbol{\varepsilon^{SR}}\}$, $e^{SR}_{mem} = e^{SR}$, and $N_{mem} = N$. Continue to step 2.3. Else: Move to step 4. End if.
2.3	Check whether a shear strain reversal occurs, according to the methodology described in Section C.2. Enter with the current strain state, $\{\boldsymbol{\varepsilon}\}$, and the sub-step strain increment, $\{\Delta\boldsymbol{\varepsilon_{ss}}\}$. If a shear reversal occurs, then: Update the elastic state parameters: $\{\boldsymbol{\sigma'^{SR}}\} = \{\boldsymbol{\sigma'}\}$, $\{\boldsymbol{\varepsilon^{SR}}\} = \{\boldsymbol{\varepsilon}\}$, $e^{SR} = e$, $N = 2.0$. Update the small-strain shear modulus at last shear reversal: $G_{max}^{SR} = C_g\, p'_{ref} \frac{(m_g - e)^{2.0}}{1.0+e}\left(\frac{p'^{SR}}{p'_{ref}}\right)^{n_g} \geq C_g\, p'_{ref} \frac{(m_g - e)^{2.0}}{1.0+e}\left(\frac{p'_{min}}{p'_{ref}}\right)^{n_g}$

Table C.1 – Explicit stress integration scheme for the present bounding surface plasticity model.

Step	Description

End if.

Determine the small-strain shear modulus corresponding to the current stress state and material's state:

$$G_{max} = C_g\, p'_{ref} \frac{\left(m_g - e\right)^{2.0}}{1.0 + e} \left(\frac{p'}{p'_{ref}}\right)^{n_g} \geq C_g\, p'_{ref} \frac{\left(m_g - e\right)^{2.0}}{1.0 + e} \left(\frac{p'_{min}}{p'_{ref}}\right)^{n_g}$$

Determine the tangent shear modulus:

$$G_{tan} = \frac{G_{max}}{T} \geq G_{min}$$

where:

$$T = 1.0 + \kappa \left(\frac{1.0}{a_1} - 1.0\right) \left(\frac{\chi^r_{ref}}{N\, \eta_1}\right)^{\kappa - 1.0} \geq 1.0 + \kappa \left(\frac{1.0}{a_1} - 1.0\right)$$

with [1]:

$$\chi^r_{ref} = \sqrt{\frac{1.0}{2.0}}\, \|\{\boldsymbol{r}\} - \{\boldsymbol{r^{SR}}\}\|_2 = \sqrt{\frac{1.0}{2.0}} \sqrt{(\{\boldsymbol{r}\} - \{\boldsymbol{r^{SR}}\}) : (\{\boldsymbol{r}\} - \{\boldsymbol{r^{SR}}\})}$$

$$= \sqrt{\frac{1.0}{2.0}} \sqrt{\begin{array}{c} \left(\frac{\sigma'_{xx} - p'}{p'} - \frac{\sigma'^{SR}_{xx} - p'^{SR}}{p'^{SR}}\right)^{2.0} + \left(\frac{\sigma'_{yy} - p'}{p'} - \frac{\sigma'^{SR}_{yy} - p'^{SR}}{p'^{SR}}\right)^{2.0} + \\ \left(\frac{\sigma'_{zz} - p'}{p'} - \frac{\sigma'^{SR}_{zz} - p'^{SR}}{p'^{SR}}\right)^{2.0} + 2.0 \left(\frac{\tau_{xy}}{p'} - \frac{\tau^{SR}_{xy}}{p'^{SR}}\right)^{2} + \\ 2.0 \left(\frac{\tau_{xz}}{p'} - \frac{\tau^{SR}_{xz}}{p'^{SR}}\right)^{2.0} + 2.0 \left(\frac{\tau_{yz}}{p'} - \frac{\tau^{SR}_{yz}}{p'^{SR}}\right)^{2.0} \end{array}}$$

and

$$\eta_1 = a_1 \left(\frac{G^{SR}_{max}}{p'^{SR}}\right) \gamma_1$$

Determine the tangent bulk modulus:

$$K_{tan} = \frac{2.0\,(1.0 + \nu)}{3.0\,(1.0 - 2.0\,\nu)} G_{tan}$$

Compute the elastic constitutive matrix:

$$[\boldsymbol{D}(\{\boldsymbol{\sigma'}\})] = \begin{bmatrix} K_{tan} + \frac{4.0}{3.0}G_{tan} & K_{tan} - \frac{2.0}{3.0}G_{tan} & 0.0 & K_{tan} - \frac{2.0}{3.0}G_{tan} & 0.0 & 0.0 \\ K_{tan} - \frac{2.0}{3.0}G_{tan} & K_{tan} + \frac{4.0}{3.0}G_{tan} & 0.0 & K_{tan} - \frac{2.0}{3.0}G_{tan} & 0.0 & 0.0 \\ 0.0 & 0.0 & G_{tan} & 0.0 & 0.0 & 0.0 \\ K_{tan} - \frac{2.0}{3.0}G_{tan} & K_{tan} - \frac{2.0}{3.0}G_{tan} & 0.0 & K_{tan} + \frac{4.0}{3.0}G_{tan} & 0.0 & 0.0 \\ 0.0 & 0.0 & 0.0 & 0.0 & G_{tan} & 0.0 \\ 0.0 & 0.0 & 0.0 & 0.0 & 0.0 & G_{tan} \end{bmatrix}$$

2.4 Compute the first-order approximation of changes in effective stresses [2]:
$\left\{\Delta\boldsymbol{\sigma'^{(1)}}\right\} = [\boldsymbol{D}(\{\boldsymbol{\sigma'}\})]\, \{\Delta\boldsymbol{\varepsilon_{ss}}\}$

2.5 Update temporarily the effective stress state: $\left\{\boldsymbol{\sigma'^{(1)}}\right\} = \{\boldsymbol{\sigma'_{mem}}\} + \left\{\Delta\boldsymbol{\sigma'^{(1)}}\right\}$

Update temporarily the void ratio using a small-strain formulation: $e = e_{mem} - (1.0 + e_{init})\, \Delta\varepsilon_{ss,v}$, where e_{init} is the void ratio of the material at the beginning of the FE analysis and

Table C.1 – Explicit stress integration scheme for the present bounding surface plasticity model.

Step	Description
	$\Delta\varepsilon_{ss,v} = \Delta\varepsilon_{ss,xx} + \Delta\varepsilon_{ss,yy} + \Delta\varepsilon_{ss,zz}$ is the volumetric component of the sub-step strain increment. Update the small-strain shear modulus, G_{max}, the tangent shear modulus, G_{tan}, the tangent bulk modulus, K_{tan}, and the elastic constitutive matrix, [$\boldsymbol{D}$], using the updated effective stress state, $\{\boldsymbol{\sigma'^{(1)}}\}$, and void ratio, e, and the equations previously presented in step 2.3.
2.6	Compute the second-order approximation of changes in effective stresses [2]: $\{\Delta\boldsymbol{\sigma'^{(2)}}\} = [\boldsymbol{D}(\{\boldsymbol{\sigma'^{(1)}}\})]\,\{\Delta\boldsymbol{\varepsilon_{ss}}\}$
2.7	Compute the modified forward Euler approximation of changes in effective stresses: $\{\Delta\boldsymbol{\sigma'}\} = \dfrac{\{\Delta\boldsymbol{\sigma'^{(1)}}\} + \{\Delta\boldsymbol{\sigma'^{(2)}}\}}{2.0}$ Determine the relative error in the modified forward Euler approximation of the effective stresses [1]: $R_\sigma \approx \dfrac{1.0}{2.0}\dfrac{\left\|\left(\{\Delta\boldsymbol{\sigma'^{(2)}}\} - \{\Delta\boldsymbol{\sigma'^{(1)}}\}\right)\right\|_2}{\|\{\boldsymbol{\sigma'_{mem}}\} + \{\Delta\boldsymbol{\sigma'}\}\|_2} = \dfrac{1.0}{2.0}\sqrt{\dfrac{\left(\{\Delta\boldsymbol{\sigma'^{(2)}}\} - \{\Delta\boldsymbol{\sigma'^{(1)}}\}\right):\left(\{\Delta\boldsymbol{\sigma'^{(2)}}\} - \{\Delta\boldsymbol{\sigma'^{(1)}}\}\right)}{(\{\boldsymbol{\sigma'_{mem}}\} + \{\Delta\boldsymbol{\sigma'}\}):(\{\boldsymbol{\sigma'_{mem}}\} + \{\Delta\boldsymbol{\sigma'}\})}}$
2.8	Compare the obtained relative error R_σ with the tolerance $SSTOL$[4]. If $R_\sigma > SSTOL$ and $\Delta T_n > \Delta T_{n,min}$ then: The sub-step is not successful and, consequently, a smaller pseudo-time step needs to be used in the integration process. Restore the effective stress state, void ratio and elastic state parameters corresponding to the beginning of the sub-step increment: $\{\boldsymbol{\sigma'}\} = \{\boldsymbol{\sigma'_{mem}}\}$, $e = e_{mem}$, $\{\boldsymbol{\sigma'^{SR}}\} = \{\boldsymbol{\sigma'^{SR}_{mem}}\}$, $\{\boldsymbol{\varepsilon^{SR}}\} = \{\boldsymbol{\varepsilon^{SR}_{mem}}\}$, $e^{SR} = e^{SR}_{mem}$, and $N = N_{mem}$. Compute: $\zeta = \max\{0.9\sqrt{SSTOL/R_\sigma}, 0.1\}$ and $\Delta T_n = max\,\{\zeta\Delta T_n,\ \Delta T_{n,min}\}$. Return to step 2.3. Else: The sub-step is considered successful. Update the effective stress state: $\{\boldsymbol{\sigma'}\} = \{\boldsymbol{\sigma'_{mem}}\} + \{\Delta\boldsymbol{\sigma'}\}$. Compute a new pseudo-time step multiplier, according to the following condition: if the previous sub-step or the one before failed: $\zeta = \min\{0.9\sqrt{SSTOL/R_\sigma}, 1.0\}$, otherwise: $\zeta = \min\{0.9\sqrt{SSTOL/R_\sigma}, 1.1\}$. Continue to step 2.9. End if
2.9	Update the positions of the primary and secondary yield surfaces: $F_1 = \sqrt{(\{\boldsymbol{s}\} - p'\{\boldsymbol{\alpha}\}):(\{\boldsymbol{s}\} - p'\{\boldsymbol{\alpha}\})} - \sqrt{2.0/3.0}\ m\,p'$ $F_2 = p'_{YS} - p'$ Determine the portion β of the sub-step increment, $\{\Delta\boldsymbol{\varepsilon_{ss}}\} = \Delta T_n\,\{\Delta\boldsymbol{\varepsilon}\}$, which is purely elastic[4]: If $F_1 \le YTOL$ and $F_2 \le YTOL$ then: The response is purely elastic over the entire sub-step increment. Set $\beta = 1.0$. Update the elastic strain increment: $\{\Delta\boldsymbol{\varepsilon^e}\} = \beta\{\Delta\boldsymbol{\varepsilon_{ss}}\}$. Update the elastic strains: $\{\boldsymbol{\varepsilon^e}\} = \{\boldsymbol{\varepsilon^e}\} + \{\Delta\boldsymbol{\varepsilon^e}\}$. Set the new pseudo-time step: $\Delta T_n = \max\{\zeta\Delta T_n,\ \Delta T_{n,min}\}$. Check that $T_n + \Delta T_n$ does not exceed 1.0, i.e.: $\Delta T_n = \min\{\zeta\Delta T_n,\ 1.0 - T_n\}$. Update the pseudo-time: $T_n = T_{n-1} + \Delta T_n$. Return to step 2.2.

Table C.1 – Explicit stress integration scheme for the present bounding surface plasticity model.

Step	Description

Else:

If ($F_{1,mem} < -YTOL$ and $F_1 > YTOL$ and $F_2 \leq YTOL$) or
($F_1 \leq YTOL$ and $F_{2,\,mem} < -YTOL$ and $F_2 > YTOL$) or
($F_{1,mem} < -YTOL$ and $F_1 > YTOL$ and $F_{2,\,mem} < -YTOL$ and $F_2 > YTOL$) then:

A transition from purely elastic to elasto-plastic response occurs.

Compute the value of β and the stress state, $\{\boldsymbol{\sigma}'\} = \{\boldsymbol{\sigma}'_{\boldsymbol{mem}}\} + \{\Delta\boldsymbol{\sigma}'\}$, lying on the primary yield surfaces ($IYIELD = 1$), on the secondary yield surface ($IYIELD = 2$) or at the intersection between both yield surfaces ($IYIELD = 3$), by applying the Pegasus method, as described in Section C.3.

Update the elastic strain increment: $\{\Delta\boldsymbol{\varepsilon}^{\boldsymbol{e}}\} = \beta\{\Delta\boldsymbol{\varepsilon}_{\boldsymbol{ss}}\}$.

Update the elastic strains: $\{\boldsymbol{\varepsilon}^{\boldsymbol{e}}\} = \{\boldsymbol{\varepsilon}^{\boldsymbol{e}}\} + \{\Delta\boldsymbol{\varepsilon}^{\boldsymbol{e}}\}$.

Update the void ratio: $e = e_{mem} - (1.0 + e_{init})\,\beta\,\Delta\varepsilon_{ss,v}$.

Update the positions of the primary and secondary yield surfaces:

$F_1 = \sqrt{(\{\boldsymbol{s}\} - p'\{\boldsymbol{\alpha}\}) : (\{\boldsymbol{s}\} - p'\{\boldsymbol{\alpha}\})} - \sqrt{2.0/3.0}\; m\, p'$

$F_2 = p'_{YS} - p'$

Move to step 3.1.

Else:

One or both yield surfaces were active from the beginning of the sub-step increment.

Check whether an elasto-plastic unloading has occurred during the current sub-step increment [4].

If $F_1 > YTOL$ then:

Compute [1]:

$$\cos\varpi_1 = \frac{\left\{\frac{\partial F_1}{\partial \boldsymbol{\sigma}'}\right\} : \{\Delta\boldsymbol{\sigma}'\}}{\left\|\left\{\frac{\partial F_1}{\partial \boldsymbol{\sigma}'}\right\}\right\|_2 \|\{\Delta\boldsymbol{\sigma}'\}\|_2} = \frac{\left\{\frac{\partial F_1}{\partial \boldsymbol{\sigma}'}\right\} : \{\Delta\boldsymbol{\sigma}'\}}{\sqrt{\left\{\frac{\partial F_1}{\partial \boldsymbol{\sigma}'}\right\} : \left\{\frac{\partial F_1}{\partial \boldsymbol{\sigma}'}\right\}}\;\sqrt{\{\Delta\boldsymbol{\sigma}'\} : \{\Delta\boldsymbol{\sigma}'\}}}$$

where the gradient of the primary yield surface is given by:

$$\left\{\frac{\partial F_1}{\partial \boldsymbol{\sigma}'}\right\} = \left\{\frac{\partial F_1}{\partial \sigma'_{xx}} \;\; \frac{\partial F_1}{\partial \sigma'_{yy}} \;\; \frac{\partial F_1}{\partial \tau_{xy}} \;\; \frac{\partial F_1}{\partial \sigma'_{zz}} \;\; \frac{\partial F_1}{\partial \tau_{xz}} \;\; \frac{\partial F_1}{\partial \tau_{yz}}\right\}^{\mathrm{T}} = -\frac{1.0}{3.0}\, V\{\boldsymbol{I}\} + \{\boldsymbol{n}\}$$

$$= -\frac{1.0}{3.0}\left[\{\boldsymbol{\alpha}\}\{\boldsymbol{n}\} + \sqrt{\frac{2.0}{3.0}}\, m\right]\{\boldsymbol{I}\} + \{\boldsymbol{n}\}$$

with:

$$\left\{\frac{\partial F_1}{\partial \sigma'_{xx}}\right\} = -\frac{1.0}{3.0}\left[\alpha_{xx}n_{xx} + \alpha_{yy}n_{yy} + \alpha_{zz}n_{zz} + 2.0\;\alpha_{xy}n_{xy} + 2.0\;\alpha_{xz}n_{xz} + 2.0\;\alpha_{yz}n_{yz} + \sqrt{\frac{2.0}{3.0}}m\right] + n_{xx}$$

$$\left\{\frac{\partial F_1}{\partial \sigma'_{yy}}\right\} = -\frac{1.0}{3.0}\left[\alpha_{xx}n_{xx} + \alpha_{yy}n_{yy} + \alpha_{zz}n_{zz} + 2.0\;\alpha_{xy}n_{xy} + 2.0\;\alpha_{xz}n_{xz} + 2.0\;\alpha_{yz}n_{yz} + \sqrt{\frac{2.0}{3.0}}m\right] + n_{yy}$$

Table C.1 – Explicit stress integration scheme for the present bounding surface plasticity model.

Step	Description

$$\left\{\frac{\partial F_1}{\partial \tau_{xy}}\right\} = n_{xy}$$

$$\left\{\frac{\partial F_1}{\partial \sigma'_{zz}}\right\} = -\frac{1.0}{3.0}\left[\alpha_{xx}n_{xx} + \alpha_{yy}n_{yy} + \alpha_{zz}n_{zz} + 2.0\,\alpha_{xy}n_{xy} + 2.0\,\alpha_{xz}n_{xz} + 2.0\,\alpha_{yz}n_{yz} + \sqrt{\frac{2.0}{3.0}}m\right] + n_{zz}$$

$$\left\{\frac{\partial F_1}{\partial \tau_{xz}}\right\} = n_{xz}$$

$$\left\{\frac{\partial F_1}{\partial \tau_{yz}}\right\} = n_{yz}$$

Set $\cos\varpi = \cos\varpi_1$.

End if

If $F_2 > YTOL$ then:

Compute [(1)]:

$$\cos\varpi_2 = \frac{\left\{\frac{\partial F_2}{\partial \boldsymbol{\sigma}'}\right\}:\{\Delta\boldsymbol{\sigma}'\}}{\left\|\left\{\frac{\partial F_2}{\partial \boldsymbol{\sigma}'}\right\}\right\|_2 \|\{\Delta\boldsymbol{\sigma}'\}\|_2} = \frac{\left\{\frac{\partial F_2}{\partial \boldsymbol{\sigma}'}\right\}:\{\Delta\boldsymbol{\sigma}'\}}{\sqrt{\left\{\frac{\partial F_2}{\partial \boldsymbol{\sigma}'}\right\}:\left\{\frac{\partial F_2}{\partial \boldsymbol{\sigma}'}\right\}}\sqrt{\{\Delta\boldsymbol{\sigma}'\}:\{\Delta\boldsymbol{\sigma}'\}}}$$

where the gradient of the primary yield surface is given by:

$$\left\{\frac{\partial F_2}{\partial \boldsymbol{\sigma}'}\right\} = \left\{\frac{\partial F_2}{\partial \sigma'_{xx}} \;\; \frac{\partial F_2}{\partial \sigma'_{yy}} \;\; \frac{\partial F_2}{\partial \tau_{xy}} \;\; \frac{\partial F_2}{\partial \sigma'_{zz}} \;\; \frac{\partial F_2}{\partial \tau_{xz}} \;\; \frac{\partial F_2}{\partial \tau_{yz}}\right\}^{\mathrm{T}} = -\frac{1.0}{3.0}\{\boldsymbol{I}\}$$

with:

$$\left\{\frac{\partial F_2}{\partial \sigma'_{xx}}\right\} = \left\{\frac{\partial F_2}{\partial \sigma'_{yy}}\right\} = \left\{\frac{\partial F_2}{\partial \sigma'_{zz}}\right\} = -\frac{1.0}{3.0}$$

$$\left\{\frac{\partial F_2}{\partial \tau_{xy}}\right\} = \left\{\frac{\partial F_2}{\partial \tau_{xz}}\right\} = \left\{\frac{\partial F_2}{\partial \tau_{yz}}\right\} = 0.0$$

Set $\cos\varpi = \cos\varpi_2$.

End if

If $F_1 > YTOL$ and $F_2 > YTOL$ then:

$\cos\varpi = \min\{\cos\varpi_1, \cos\varpi_2\}$

End if

If $\cos\varpi < -LTOL$ then:

An elasto-plastic unloading has occurred. Compute the value of β and the stress state, $\{\boldsymbol{\sigma}'\} = \{\boldsymbol{\sigma}'_{mem}\} + \{\Delta\boldsymbol{\sigma}'\}$, lying on the primary yield surfaces ($IYIELD = 1$), on the secondary yield surface ($IYIELD = 2$) or at the intersection between both yield surfaces ($IYIELD = 3$), by applying the Pegasus method, as described in Section C.3.

Update the elastic strain increment: $\{\Delta\boldsymbol{\varepsilon}^{\boldsymbol{e}}\} = \beta\{\Delta\boldsymbol{\varepsilon}_{\boldsymbol{ss}}\}$.

Update the elastic strains: $\{\boldsymbol{\varepsilon}^{\boldsymbol{e}}\} = \{\boldsymbol{\varepsilon}^{\boldsymbol{e}}\} + \{\Delta\boldsymbol{\varepsilon}^{\boldsymbol{e}}\}$.

Update the void ratio: $e = e_{mem} - (1.0 + e_{init})\,\beta\,\Delta\varepsilon_{ss,v}$.

Update the positions of the primary and secondary yield surfaces:

$F_1 = \sqrt{(\{\boldsymbol{s}\} - p'\{\boldsymbol{\alpha}\}):(\{\boldsymbol{s}\} - p'\{\boldsymbol{\alpha}\})} - \sqrt{2.0/3.0}\; m\, p'$

$F_2 = p'_{YS} - p'$

Table C.1 – Explicit stress integration scheme for the present bounding surface plasticity model.

Step	Description
	Move to step 3.1.
	Else:
	The response is elasto-plastic over the entire sub-step increment.
	Set $\beta = 0.0$.
	Restore the effective stress state, void ratio and positions of the yield surfaces corresponding to the beginning of the sub-step increment: $\{\boldsymbol{\sigma'}\} = \{\boldsymbol{\sigma'_{mem}}\}$, $e = e_{mem}$, $F_1 = F_{1,mem}$ and $F_2 = F_{2,mem}$.
	Restore the values of the elastic state parameters corresponding to the beginning of the sub-step increment: $\{\boldsymbol{\sigma'^{SR}}\} = \{\boldsymbol{\sigma'^{SR}_{mem}}\}$, $\{\boldsymbol{\varepsilon^{SR}}\} = \{\boldsymbol{\varepsilon^{SR}_{mem}}\}$, $e^{SR} = e^{SR}_{mem}$, and $N = N_{mem}$.
	Move to step 3.1.
	End if.
	End if.
	End if
3	**Elasto-plasticity**
3.1	Determine the part of the strain increment that has not yet been integrated: $\{\Delta\boldsymbol{\varepsilon^{ep}}\} = [(1.0 - T_{n-1}) + (1.0 - \beta)\,\Delta T_n]\{\Delta\boldsymbol{\varepsilon}\}$.
	Initialise variables of the modified forward Euler scheme required to the integration of the elasto-plastic response: $\Delta T_n^{ep} = 1.0$ and $T_n^{ep} = 0.0$.
3.2	If $T_n^{ep} < 1.0$ then:
	Determine the sub-step strain increment: $\{\Delta\boldsymbol{\varepsilon^{ep}_{ss}}\} = \Delta T_n^{ep}\,\{\Delta\boldsymbol{\varepsilon^{ep}}\}$.
	Save temporarily:
	- the current effective stresses and plastic strains: $\{\boldsymbol{\sigma'_{mem}}\} = \{\boldsymbol{\sigma'}\}$ and $\{\boldsymbol{\varepsilon^{p}_{mem}}\} = \{\boldsymbol{\varepsilon^{p}}\}$, respectively.
	- the current void ratio: $e_{mem} = e$.
	- the current values of the elastic state parameters: $\{\boldsymbol{\sigma'^{SR}_{mem}}\} = \{\boldsymbol{\sigma'^{SR}}\}$, $\{\boldsymbol{\varepsilon^{SR}_{mem}}\} = \{\boldsymbol{\varepsilon^{SR}}\}$, $e^{SR}_{mem} = e^{SR}$, and $N_{mem} = N$.
	- the current back-stress tensor: $\{\boldsymbol{\alpha_{mem}}\} = \{\boldsymbol{\alpha}\}$.
	- the isotropic and deviatoric components of the stress-induced anisotropy tensor: $f_{p_{mem}} = f_p$ and $\{\boldsymbol{f_{mem}}\} = \{\boldsymbol{f}\}$, respectively; as well as the current value of the model parameter defining the evolution of $\{\boldsymbol{f}\}$: $C_{mem} = C$.
	- the current positions of the yield surfaces: $F_{1,mem} = F_1$ and $F_{2,mem} = F_2$.
	Continue to step 3.3.
	Else:
	Stress integration is completed. Move to step 4.
	End if.
3.3	Check whether a shear strain reversal occurs, according to the methodology described in Section C.2. Enter with the current strain state, $\{\boldsymbol{\varepsilon}\}$, and the sub-step strain increment, $\{\Delta\boldsymbol{\varepsilon^{ep}_{ss}}\}$. If a shear reversal occurs, then:
	Update the elastic state parameters: $\{\boldsymbol{\sigma'^{SR}}\} = \{\boldsymbol{\sigma'}\}$, $\{\boldsymbol{\varepsilon^{SR}}\} = \{\boldsymbol{\varepsilon}\}$, $e^{SR} = e$, $N = 2.0$. Update the small-strain shear modulus at last shear reversal: $G^{SR}_{max} = C_g\,p'_{ref}\dfrac{(m_g - e)^{2.0}}{1.0 + e}\left(\dfrac{p'^{SR}}{p'_{ref}}\right)^{n_g} \geq C_g\,p'_{ref}\dfrac{(m_g - e)^{2.0}}{1.0 + e}\left(\dfrac{p'_{min}}{p'_{ref}}\right)^{n_g}$
	End if.

Table C.1 – Explicit stress integration scheme for the present bounding surface plasticity model.

Step	Description

Update the small-strain shear modulus, G_{max}, the tangent shear modulus, G_{tan}, the tangent bulk modulus, K_{tan}, and the elastic constitutive matrix, [$\boldsymbol{D}$], using the current effective stress state, $\{\boldsymbol{\sigma'}\}$, current void ratio, e, and the current values of the elastic state parameters, according to the equations previously presented in step 2.3.

Based on the current effective stress state, $\{\boldsymbol{\sigma'}\}$, and back-stress-ratio tensor, $\{\boldsymbol{\alpha}\}$, determine the radial tensor:

$$\{\bar{\boldsymbol{r}}\} = \left\{\bar{r}_{xx} \;\; \bar{r}_{yy} \;\; \bar{r}_{xy} \;\; \bar{r}_{zz} \;\; \bar{r}_{xz} \;\; \bar{r}_{yz}\right\}^T = \{\boldsymbol{r}\} - \{\boldsymbol{\alpha}\}$$
$$= \left\{\frac{\sigma'_{xx} - p'}{p'} - \alpha_{xx} \;\; \frac{\sigma'_{yy} - p'}{p'} - \alpha_{yy} \;\; \frac{\tau_{xy}}{p'} - \alpha_{xy} \;\; \frac{\sigma'_{zz} - p'}{p'} - \alpha_{zz} \;\; \frac{\tau_{xz}}{p'} - \alpha_{xz} \;\; \frac{\tau_{yz}}{p'} - \alpha_{yz}\right\}^T$$

Determine the corresponding deviatoric loading direction, $\{\boldsymbol{n}\}$:

$$\{\boldsymbol{n}\} = \left\{n_{xx} \;\; n_{yy} \;\; n_{xy} \;\; n_{zz} \;\; n_{xz} \;\; n_{yz}\right\}^T = \frac{\{\bar{\boldsymbol{r}}\}}{\sqrt{2.0/3.0}\; m}$$
$$= \left\{\frac{\bar{r}_{xx}}{\sqrt{2.0/3.0}\; m} \;\; \frac{\bar{r}_{yy}}{\sqrt{2.0/3.0}\; m} \;\; \frac{\bar{r}_{xy}}{\sqrt{2.0/3.0}\; m} \;\; \frac{\bar{r}_{zz}}{\sqrt{2.0/3.0}\; m} \;\; \frac{\bar{r}_{xz}}{\sqrt{2.0/3.0}\; m} \;\; \frac{\bar{r}_{yz}}{\sqrt{2.0/3.0}\; m}\right\}^T$$

Determine the modified Lode's angle, θ:

$$\overline{J_2} = \frac{1.0}{2.0}\{\boldsymbol{n}\}:\{\boldsymbol{n}\} = \frac{1.0}{6.0}\left[\left(n_{xx} - n_{yy}\right)^{2.0} + \left(n_{yy} - n_{zz}\right)^{2.0} + \left(n_{zz} - n_{xx}\right)^{2.0}\right] + {n_{xy}}^{2.0} + {n_{xz}}^{2.0} + {n_{yz}}^{2.0}$$

$$\overline{J_3} = det\{\boldsymbol{n}\} = n_{xx}\, n_{yy}\, n_{zz} - n_{xx}\, {n_{yz}}^{2.0} - n_{yy}\, {n_{xz}}^{2.0} - n_{zz}\, {n_{xy}}^{2.0} + 2.0\, n_{xy}\, n_{yz}\, n_{yz}$$

$$\cos(3.0\,\theta) = \left(\frac{3.0\sqrt{3.0}}{2.0}\,\frac{\overline{J_3}}{\left(\overline{J_2}\right)^{3.0/2.0}}\right) \Leftrightarrow \theta = \left[\cos^{-1}\left(\frac{3.0\sqrt{3.0}}{2.0}\,\frac{\overline{J_3}}{\left(\overline{J_2}\right)^{3.0/2.0}}\right)\right] \Big/ 3.0$$

Calculate the current value of the inherent anisotropic state variable, A_F, based on the inherent anisotropy tensor, $\{\boldsymbol{F}\}$, and on the current values of the deviatoric loading direction, $\{\boldsymbol{n}\}$, and modified Lode's angle, θ:

$$A_F = g(\theta, c^a)\{\boldsymbol{F}\}:\{\boldsymbol{n}\}$$
$$= g(\theta, c^a)\left(F_{xx}n_{xx} + F_{yy}n_{yy} + F_{zz}n_{zz} + 2.0\,F_{xy}n_{xy} + 2.0\,F_{xz}n_{xz} + 2.0\,F_{yz}n_{yz}\right)$$
$$= g(\theta, c^a)\left[\frac{1.0}{2.0}(1.0 - a)\,n_{xx} + a\,n_{yy} + \frac{1.0}{2.0}(1.0 - a)\,n_{zz}\right]$$

where

$$g(\theta, c^a) = \frac{2.0\,c^a}{\frac{1.0 + c^a}{2.0} - \frac{1.0 - c^a}{2.0}\cos(3.0\,\theta)} - \left[\frac{1.0 + c^a}{2.0} + \frac{1.0 - c^a}{2.0}\cos(3.0\,\theta)\right]$$

and it is assumed that $c^a = c^c = M_e^c / M_c^c$, as proposed by Dafalias *et al.* (2004).

Similarly, determine the inherent anisotropic state variable in triaxial compression and in triaxial extension, respectively:

$$A_{F,c} = g(0.0, c^a)\,\{\boldsymbol{F}\}:\{\boldsymbol{n_c}\} = \;(-1.0 + 3.0\,a)/\sqrt{6.0}$$

$$A_{F,e} = g(\pi/3.0, c^a)\,\{\boldsymbol{F}\}:\{\boldsymbol{n_e}\} = c^a\;(1.0 - 3.0\,a)/\sqrt{6.0} = -c^a\,A_{F,c}$$

where:

$$\{\boldsymbol{n_c}\} = 1.0/\sqrt{6.0}\;\{-1.0 \quad 2.0 \quad 0.0 \quad -1.0 \quad 0.0 \quad 0.0\}^{\mathrm{T}}$$

$$\{\boldsymbol{n_e}\} = 1.0/\sqrt{6.0}\;\{1.0 \quad -2.0 \quad 0.0 \quad 1.0 \quad 0.0 \quad 0.0\}^{\mathrm{T}}$$

Determine the distance from the current stress point to the critical surface:

$$d^c = (\{\boldsymbol{\alpha}^c\} - \{\boldsymbol{\alpha}\}):\{\boldsymbol{n}\} = \sqrt{2.0/3.0}\ (g(\theta, c^c)\ M_c^c - m)\ - \{\boldsymbol{\alpha}\}:\{\boldsymbol{n}\}$$
$$= \sqrt{2.0/3.0}\ (g(\theta, c^c)\ M_c^c - m)$$
$$- \left(\alpha_{xx}n_{xx} + \alpha_{yy}n_{yy} + \alpha_{zz}n_{zz} + 2.0\ \alpha_{xy}n_{xy} + 2.0\ \alpha_{xz}n_{xz} + 2.0\ \alpha_{yz}n_{yz}\right)$$

and the reference distance to the critical surface:

$$d_{ref}^c = \sqrt{2.0/3.0}\ [\ g(\theta, c^c)\ M_c^c + g(\theta + \pi, c^c)\ M_c^c - 2.0\ m]$$

where:

$$g(\theta, c^c) = \frac{2.0\ c^c}{\frac{1.0 + c^c}{2.0} - \frac{1.0 - c^c}{2.0}\cos(3.0\ \theta)} - \left[\frac{1.0 + c^c}{2.0} + \frac{1.0 - c^c}{2.0}\cos(3.0\ \theta)\right]$$

with $c^c = M_e^c / M_c^c$.

Determine the void ratio at CSL for the current mean effective stress, p':

$$e_{CS} = (e_{CS})_A - \lambda\left(\frac{p'}{p'_{ref}}\right)^{\xi} = (e_{CS})_{ref}\ exp\left[v_A\ \frac{\langle d^c \rangle}{d_{ref}^c}\ (A_{F,c} - A_F)\right] - \lambda\left(\frac{p'}{p'_{ref}}\right)^{\xi}$$

and the current state parameter:

$$\psi = e - e_{CS}$$

Determine the distance from the current stress point to the dilatancy surface:

$$d^d = \left(\{\boldsymbol{\alpha}^d\} - \{\boldsymbol{\alpha}\}\right):\{\boldsymbol{n}\} = \sqrt{2.0/3.0}\ \left[g(\theta, c^d)\ \left(M_c^c + k_c^d\ \psi\right) - m\right]\ - \{\boldsymbol{\alpha}\}:\{\boldsymbol{n}\}$$
$$= \sqrt{2.0/3.0}\ \left[g(\theta, c^d)\ \left(M_c^c + k_c^d\ \psi\right) - m\right]$$
$$- \left(\alpha_{xx}n_{xx} + \alpha_{yy}n_{yy} + \alpha_{zz}n_{zz} + 2.0\ \alpha_{xy}n_{xy} + 2.0\ \alpha_{xz}n_{xz} + 2.0\ \alpha_{yz}n_{yz}\right)$$

where:

$$g(\theta, c^b) = \frac{2.0\ c^b}{\frac{1.0 + c^b}{2.0} - \frac{1.0 - c^b}{2.0}\ cos(3.0\ \theta)} - \left[\frac{1.0 + c^b}{2.0} + \frac{1.0 - c^b}{2.0}\cos(3.0\ \theta)\right]$$

with:

$$c^d = \frac{M_e^d}{M_c^d} = \frac{M_e^c + k_e^d\ \psi}{M_c^c + k_c^d\ \psi}$$

Determine the distance from the current stress point to the bounding surface:

$$d^b = \left(\{\boldsymbol{\alpha}^b\} - \{\boldsymbol{\alpha}\}\right):\{\boldsymbol{n}\} = \sqrt{2.0/3.0}\ \left[g(\theta, c^b)\ \left(M_c^c + k_c^b\ \langle -\psi \rangle\right) - m\right]\ - \{\boldsymbol{\alpha}\}:\{\boldsymbol{n}\}$$
$$= \sqrt{2.0/3.0}\ \left[g(\theta, c^b)\ \left(M_c^c + k_c^b\ \langle -\psi \rangle\right) - m\right]$$
$$- \left(\alpha_{xx}n_{xx} + \alpha_{yy}n_{yy} + \alpha_{zz}n_{zz} + 2.0\ \alpha_{xy}n_{xy} + 2.0\ \alpha_{xz}n_{xz} + 2.0\ \alpha_{yz}n_{yz}\right)$$

and the reference distance to the bounding surface:

$$d_{ref}^b = \sqrt{2.0/3.0}\ \left[\ g(\theta, c^b)\ \left(M_c^c + k_c^b\ \langle -\psi \rangle\right) + g(\theta + \pi, c^b)\ \left(M_c^c + k_c^b\ \langle -\psi \rangle\right) - 2.0\ m\right]$$

where:

$$g(\theta, c^b) = \frac{2.0\ c^b}{\frac{1.0 + c^b}{2.0} - \frac{1.0 - c^b}{2.0}\ cos(3.0\ \theta)} - \left[\frac{1.0 + c^b}{2.0} + \frac{1.0 - c^b}{2.0}\ cos(3.0\ \theta)\right]$$

with:

$$c^b = \frac{M_e^b}{M_c^b} = \frac{M_e^c + k_e^b\ \langle -\psi \rangle}{M_c^c + k_c^b\ \langle -\psi \rangle}$$

Evaluate the positions of the yield surfaces:

$$F_1 = \sqrt{(\{\boldsymbol{s}\} - p'\{\boldsymbol{\alpha}\}):(\{\boldsymbol{s}\} - p'\{\boldsymbol{\alpha}\})} - \sqrt{2.0/3.0}\ m\ p'$$
$$F_2 = p'_{YS} - p'$$

Compute the gradients of the yield surfaces:

Table C.1 – Explicit stress integration scheme for the present bounding surface plasticity model.

Step	Description

$$\left\{\frac{\partial F_1}{\partial \boldsymbol{\sigma}'}\right\} = \left\{\frac{\partial F_1}{\partial \sigma'_{xx}} \quad \frac{\partial F_1}{\partial \sigma'_{yy}} \quad \frac{\partial F_1}{\partial \tau_{xy}} \quad \frac{\partial F_1}{\partial \sigma'_{zz}} \quad \frac{\partial F_1}{\partial \tau_{xz}} \quad \frac{\partial F_1}{\partial \tau_{yz}}\right\}^{\mathrm{T}} = -\frac{1.0}{3.0}\, V\{\boldsymbol{I}\} + \{\boldsymbol{n}\}$$

$$= -\frac{1.0}{3.0}\left[\{\boldsymbol{\alpha}\}:\{\boldsymbol{n}\} + \sqrt{\frac{2.0}{3.0}}\, m\right]\{\boldsymbol{I}\} + \{\boldsymbol{n}\}$$

where:

$$\left\{\frac{\partial F_1}{\partial \sigma'_{xx}}\right\} = -\frac{1.0}{3.0}\left[\alpha_{xx}n_{xx} + \alpha_{yy}n_{yy} + \alpha_{zz}n_{zz} + 2.0\,\alpha_{xy}n_{xy} + 2.0\,\alpha_{xz}n_{xz} + 2.0\,\alpha_{yz}n_{yz} + \sqrt{\frac{2.0}{3.0}}m\right] + n_{xx}$$

$$\left\{\frac{\partial F_1}{\partial \sigma'_{yy}}\right\} = -\frac{1.0}{3.0}\left[\alpha_{xx}n_{xx} + \alpha_{yy}n_{yy} + \alpha_{zz}n_{zz} + 2.0\,\alpha_{xy}n_{xy} + 2.0\,\alpha_{xz}n_{xz} + 2.0\,\alpha_{yz}n_{yz} + \sqrt{\frac{2.0}{3.0}}m\right] + n_{yy}$$

$$\left\{\frac{\partial F_1}{\partial \tau_{xy}}\right\} = n_{xy}$$

$$\left\{\frac{\partial F_1}{\partial \sigma'_{zz}}\right\} = -\frac{1.0}{3.0}\left[\alpha_{xx}n_{xx} + \alpha_{yy}n_{yy} + \alpha_{zz}n_{zz} + 2.0\,\alpha_{xy}n_{xy} + 2.0\,\alpha_{xz}n_{xz} + 2.0\,\alpha_{yz}n_{yz} + \sqrt{\frac{2.0}{3.0}}m\right] + n_{zz}$$

$$\left\{\frac{\partial F_1}{\partial \tau_{xz}}\right\} = n_{xz}$$

$$\left\{\frac{\partial F_1}{\partial \tau_{yz}}\right\} = n_{yz}$$

and:

$$\left\{\frac{\partial F_2}{\partial \boldsymbol{\sigma}'}\right\} = \left\{\frac{\partial F_2}{\partial \sigma'_{xx}} \quad \frac{\partial F_2}{\partial \sigma'_{yy}} \quad \frac{\partial F_2}{\partial \tau_{xy}} \quad \frac{\partial F_2}{\partial \sigma'_{zz}} \quad \frac{\partial F_2}{\partial \tau_{xz}} \quad \frac{\partial F_2}{\partial \tau_{yz}}\right\}^{\mathrm{T}} = -\frac{1.0}{3.0}\{\boldsymbol{I}\}$$

where:

$$\left\{\frac{\partial F_2}{\partial \sigma'_{xx}}\right\} = \left\{\frac{\partial F_2}{\partial \sigma'_{yy}}\right\} = \left\{\frac{\partial F_2}{\partial \sigma'_{zz}}\right\} = -\frac{1.0}{3.0}$$

$$\left\{\frac{\partial F_2}{\partial \tau_{xy}}\right\} = \left\{\frac{\partial F_2}{\partial \tau_{xz}}\right\} = \left\{\frac{\partial F_2}{\partial \tau_{yz}}\right\} = 0.0$$

Compute the gradients of the plastic potentials:

$$\left\{\frac{\partial \boldsymbol{P_1}}{\partial \boldsymbol{\sigma}'}\right\} = \left\{\frac{\partial P_1}{\partial \sigma'_{xx}} \quad \frac{\partial P_1}{\partial \sigma'_{yy}} \quad \frac{\partial P_1}{\partial \tau_{xy}} \quad \frac{\partial P_1}{\partial \sigma'_{zz}} \quad \frac{\partial P_1}{\partial \tau_{xz}} \quad \frac{\partial P_1}{\partial \tau_{yz}}\right\}^{\mathrm{T}} = \frac{1.0}{3.0}\, D\{\boldsymbol{I}\} + \{\boldsymbol{n}\} = \frac{1.0}{3.0}\left(A_0\, d^d\right)\{\boldsymbol{I}\} + \{\boldsymbol{n}\}$$

where:

$$\left\{\frac{\partial P_1}{\partial \sigma'_{xx}}\right\} = \frac{1.0}{3.0}\left(A_0\, d^d\right) + n_{xx}$$

$$\left\{\frac{\partial P_1}{\partial \sigma'_{yy}}\right\} = \frac{1.0}{3.0}\left(A_0\, d^d\right) + n_{yy}$$

$$\left\{\frac{\partial P_1}{\partial \tau_{xy}}\right\} = n_{xy}$$

$$\left\{\frac{\partial P_1}{\partial \sigma'_{zz}}\right\} = \frac{1.0}{3.0}\left(A_0\, d^d\right) + n_{zz}$$

Table C.1 – Explicit stress integration scheme for the present bounding surface plasticity model.

Step	Description

$$\left\{\frac{\partial P_1}{\partial \tau_{xz}}\right\} = n_{xz}$$

$$\left\{\frac{\partial P_1}{\partial \tau_{yz}}\right\} = n_{yz}$$

and:

$$\left\{\frac{\partial \boldsymbol{P_2}}{\partial \boldsymbol{\sigma'}}\right\} = \left\{\frac{\partial P_2}{\partial \sigma'_{xx}} \;\; \frac{\partial P_2}{\partial \sigma'_{yy}} \;\; \frac{\partial P_2}{\partial \tau_{xy}} \;\; \frac{\partial P_2}{\partial \sigma'_{zz}} \;\; \frac{\partial P_2}{\partial \tau_{xz}} \;\; \frac{\partial P_2}{\partial \tau_{yz}}\right\}^{\mathrm{T}} = -\frac{1.0}{3.0}\{\boldsymbol{I}\}$$

where:

$$\left\{\frac{\partial P_2}{\partial \sigma'_{xx}}\right\} = \left\{\frac{\partial P_2}{\partial \sigma'_{yy}}\right\} = \left\{\frac{\partial P_2}{\partial \sigma'_{zz}}\right\} = -\frac{1.0}{3.0}$$

$$\left\{\frac{\partial P_2}{\partial \tau_{xy}}\right\} = \left\{\frac{\partial P_2}{\partial \tau_{xz}}\right\} = \left\{\frac{\partial P_2}{\partial \tau_{yz}}\right\} = 0.0$$

Determine the plastic hardening modulus associated with the primary yield surface:

$$A_1 = p'\, h_A\, h_b\, h_e\, h_f\, h_g\, d^b$$

where:

$$h_A = exp\left[\left(\frac{A_{F,c} - A_F}{A_{F,c} - A_{F,e}}\right)^{1.25} ln(k_A)\right]$$

$$h_b = \left(\frac{p'}{p'_{ref}}\right)^{\mu-1.0} \left(\frac{\left| d^b \right|}{\left| d^b_{ref} - \left|d^b\right| \right|}\right)^{\beta+1.0}$$

$$h_e = h_0\,(1.0 - \gamma e) \;\geq h_0(1.0 - \gamma e_{lim})$$

$$h_{f,min} \leq h_f = \frac{1.0 + \left\langle f_p \right\rangle^{2.0}}{1.0 + \langle\{\boldsymbol{f}\}:\{\boldsymbol{n}\}\rangle} \leq h_{f,max}$$

$$h_g = G^{\alpha}_{tan}$$

with:

$$\{\boldsymbol{f}\}:\{\boldsymbol{n}\} = f_{xx}n_{xx} + f_{yy}n_{yy} + f_{zz}n_{zz} + 2.0\,f_{xy}n_{xy} + 2.0\,f_{xz}n_{xz} + 2.0\,f_{yz}n_{yz}$$

And the plastic hardening modulus associated with the secondary yield surface:

$$A_2 = 0.0$$

3.4 Compute the plastic multipliers:

If $|F_1| \leq YTOL$ and $F_2 < -YTOL$ then:

Only the primary yield surface is active: $IYIELD = 1$.

Using the current values of the elastic constitutive matrix, $[\boldsymbol{D}]$, gradient of the primary yield surface, $\{\partial F_1/\partial \boldsymbol{\sigma'}\}$, gradient of the plastic potential associated with the primary yield surface, $\{\partial \boldsymbol{P_1}/\partial \boldsymbol{\sigma'}\}$, and the current sub-step strain increment, $\{\Delta \boldsymbol{\varepsilon^{ep}_{ss}}\}$, determine the plastic multiplier associated with the primary yield surface [2), 3)]:

$$\lambda_1 = \frac{\left\{\frac{\partial F_1}{\partial \boldsymbol{\sigma'}}\right\}^{\mathrm{T}} [\boldsymbol{D}]\,\{\Delta \boldsymbol{\varepsilon^{ep}_{ss}}\}}{\left\{\frac{\partial F_1}{\partial \boldsymbol{\sigma'}}\right\}^{\mathrm{T}} [\boldsymbol{D}] \left\{\frac{\partial \boldsymbol{P_1}}{\partial \boldsymbol{\sigma'}}\right\} + A_1}$$

Set the plastic multiplier associated with the secondary yield surface to $\lambda_2 = 0.0$.

Else if $F_1 < -YTOL$ and $|F_2| \leq YTOL$ then:

Only the secondary yield surface is active: $IYIELD = 2$.

Table C.1 – Explicit stress integration scheme for the present bounding surface plasticity model.

Step	Description
	Using the current values of the elastic constitutive matrix, $[\boldsymbol{D}]$, gradient of the secondary yield surface, $\{\partial F_2/\partial \boldsymbol{\sigma}'\}$, gradient of the plastic potential associated with the secondary yield surface, $\{\partial \boldsymbol{P_2}/\partial \boldsymbol{\sigma}'\}$, and the current sub-step strain increment, $\{\Delta \boldsymbol{\varepsilon_{ss}^{ep}}\}$, determine the plastic multiplier associated with the secondary yield surface [2, 3]: $$\lambda_2 = \frac{\left\{\frac{\partial F_2}{\partial \boldsymbol{\sigma}'}\right\}^{\mathrm{T}} [\boldsymbol{D}] \{\Delta \boldsymbol{\varepsilon_{ss}^{ep}}\}}{\left\{\frac{\partial F_2}{\partial \boldsymbol{\sigma}'}\right\}^{\mathrm{T}} [\boldsymbol{D}] \left\{\frac{\partial \boldsymbol{P_2}}{\partial \boldsymbol{\sigma}'}\right\} + A_2}$$ Set the plastic multiplier associated with the primary yield surface to $\lambda_1 = 0.0$.
Else if $\lvert F_1\rvert \leq YTOL$ and $\lvert F_2\rvert \leq YTOL$ then:	
	The stress point is at the intersection of both yield surfaces and the actual active yield surface(s) should be determined. Using the current values of the elastic constitutive matrix, $[\boldsymbol{D}]$, gradients of the primary and secondary yield surfaces, $\{\partial F_1/\partial \boldsymbol{\sigma}'\}$ and $\{\partial F_2/\partial \boldsymbol{\sigma}'\}$, respectively, gradients of the plastic potentials associated with the primary and secondary yield surfaces, $\{\partial \boldsymbol{P_1}/\partial \boldsymbol{\sigma}'\}$ and $\{\partial \boldsymbol{P_2}/\partial \boldsymbol{\sigma}'\}$, respectively, and the current sub-step strain increment, $\{\Delta \boldsymbol{\varepsilon_{ss}^{ep}}\}$, determine the plastic multipliers associated with the primary and secondary yield surfaces, assuming that both are simultaneously active [2, 3]: $$\lambda_1 = \frac{L_{22}\, T_1 - L_{12}\, T_2}{L_{11}\, L_{22} - L_{12}\, L_{21}}$$ $$\lambda_2 = \frac{L_{11}\, T_2 - L_{21}\, T_1}{L_{11}\, L_{22} - L_{12}\, L_{21}}$$ where: $$L_{11} = \left\{\frac{\partial F_1}{\partial \boldsymbol{\sigma}'}\right\}^{\mathrm{T}} [\boldsymbol{D}] \left\{\frac{\partial \boldsymbol{P_1}}{\partial \boldsymbol{\sigma}'}\right\} + A_1$$ $$L_{12} = \left\{\frac{\partial F_1}{\partial \boldsymbol{\sigma}'}\right\}^{\mathrm{T}} [\boldsymbol{D}] \left\{\frac{\partial \boldsymbol{P_2}}{\partial \boldsymbol{\sigma}'}\right\}$$ $$L_{21} = \left\{\frac{\partial F_2}{\partial \boldsymbol{\sigma}'}\right\}^{\mathrm{T}} [\boldsymbol{D}] \left\{\frac{\partial \boldsymbol{P_1}}{\partial \boldsymbol{\sigma}'}\right\}$$ $$L_{22} = \left\{\frac{\partial F_2}{\partial \boldsymbol{\sigma}'}\right\}^{\mathrm{T}} [\boldsymbol{D}] \left\{\frac{\partial \boldsymbol{P_2}}{\partial \boldsymbol{\sigma}'}\right\} + A_2$$ $$T_1 = \left\{\frac{\partial F_1}{\partial \boldsymbol{\sigma}'}\right\}^{\mathrm{T}} [\boldsymbol{D}] \{\Delta \boldsymbol{\varepsilon_{ss}^{ep}}\}$$ $$T_2 = \left\{\frac{\partial F_2}{\partial \boldsymbol{\sigma}'}\right\}^{\mathrm{T}} [\boldsymbol{D}] \{\Delta \boldsymbol{\varepsilon_{ss}^{ep}}\}$$
	If $\lambda_1 > 0.0$ and $\lambda_2 > 0.0$, then:
	Both plastic mechanisms are simultaneously active: $IYIELD = 3$. The values obtained for λ_1 and λ_2 are correct.
	Else if $\lambda_1 > 0.0$ and $\lambda_2 \leq 0.0$, then:
	Only the plastic mechanism associated with the primary yield surface is active: $IYIELD = 1$. Therefore, $\lambda_2 = 0.0$ and λ_1 should be recalculated [2, 3]: $$\lambda_1 = \frac{\left\{\frac{\partial F_1}{\partial \boldsymbol{\sigma}'}\right\}^{\mathrm{T}} [\boldsymbol{D}] \{\Delta \boldsymbol{\varepsilon_{ss}^{ep}}\}}{\left\{\frac{\partial F_1}{\partial \boldsymbol{\sigma}'}\right\}^{\mathrm{T}} [\boldsymbol{D}] \left\{\frac{\partial \boldsymbol{P_1}}{\partial \boldsymbol{\sigma}'}\right\} + A_1}$$
	Else if $\lambda_1 \leq 0.0$ and $\lambda_2 > 0.0$, then:

Table C.1 – Explicit stress integration scheme for the present bounding surface plasticity model.

Step	Description

Only the plastic mechanism associated with the secondary yield surface is active: $IYIELD = 2$. Therefore, $\lambda_1 = 0.0$ and λ_2 should be recalculated [2), (3)]:

$$\lambda_2 = \frac{\left\{\frac{\partial F_2}{\partial \boldsymbol{\sigma'}}\right\}^{\mathrm{T}} [\boldsymbol{D}] \{\Delta \boldsymbol{\varepsilon_{ss}^{ep}}\}}{\left\{\frac{\partial F_2}{\partial \boldsymbol{\sigma'}}\right\}^{\mathrm{T}} [\boldsymbol{D}] \left\{\frac{\partial \boldsymbol{P_2}}{\partial \boldsymbol{\sigma'}}\right\} + A_2}$$

End if.

End if.

3.5 Compute the first-order approximation of changes in effective stresses [2), (3)]:

$$\left\{\Delta \boldsymbol{\sigma'^{(1)}}\right\} = [\boldsymbol{D}] \{\Delta \boldsymbol{\varepsilon_{ss}^{ep}}\} - \lambda_1 [\boldsymbol{D}] \left\{\frac{\partial \boldsymbol{P_1}}{\partial \boldsymbol{\sigma'}}\right\} - \lambda_2 [\boldsymbol{D}] \left\{\frac{\partial \boldsymbol{P_2}}{\partial \boldsymbol{\sigma'}}\right\}$$

Compute the first-order approximation of changes in plastic strains [3)]:

$$\left\{\Delta \boldsymbol{\varepsilon_1^{p(1)}}\right\} = \lambda_1 \left\{\frac{\partial \boldsymbol{P_1}}{\partial \boldsymbol{\sigma'}}\right\}$$

$$\left\{\Delta \boldsymbol{\varepsilon_2^{p(1)}}\right\} = \lambda_2 \left\{\frac{\partial \boldsymbol{P_2}}{\partial \boldsymbol{\sigma'}}\right\}$$

$$\left\{\Delta \boldsymbol{\varepsilon^{p(1)}}\right\} = \left\{\Delta \boldsymbol{\varepsilon_1^{p(1)}}\right\} + \left\{\Delta \boldsymbol{\varepsilon_2^{p(1)}}\right\}$$

Compute the first-order approximation of the evolution of the back-stress tensor:

$$\left\{\Delta \boldsymbol{\alpha^{(1)}}\right\} = \lambda_1 h_A h_b h_e h_f h_g \left(\{\boldsymbol{\alpha^b}\} - \{\boldsymbol{\alpha}\}\right) =$$

$$= \lambda_1 h_A h_b h_e h_f h_g \left(\sqrt{2.0/3.0}\ \left[g(\theta, c^b)\left(M_c^c + k_c^b \langle -\psi \rangle\right) - m\right] \{\boldsymbol{n}\} - \{\boldsymbol{\alpha}\}\right)$$

Compute the first-order approximation of the evolution of the isotropic and deviatoric components of the stress-induced anisotropy tensor, respectively:

$$\Delta f_p^{(1)} = H \Delta \varepsilon_v^{p(1)}$$

$$\left\{\Delta \boldsymbol{f^{(1)}}\right\} = -H \left\langle -\Delta \varepsilon_v^{p(1)} \right\rangle [C \{\boldsymbol{n}\} + \{\boldsymbol{f}\}]$$

where:

$$\Delta \varepsilon_v^{p(1)} = \Delta \varepsilon_{v,1}^{p\ (1)} + \Delta \varepsilon_{v,2}^{p\ (1)} = \Delta \varepsilon_{xx,1}^{p\ (1)} + \Delta \varepsilon_{yy,1}^{p\ (1)} + \Delta \varepsilon_{zz,1}^{p\ (1)} + \Delta \varepsilon_{xx,2}^{p\ (1)} + \Delta \varepsilon_{yy,2}^{p\ (1)} + \Delta \varepsilon_{zz,2}^{p\ (1)}$$

3.6 Update the effective stresses and back-stress tensor, respectively:

$$\{\boldsymbol{\sigma'}\} = \{\boldsymbol{\sigma'_{mem}}\} + \left\{\Delta \boldsymbol{\sigma'^{(1)}}\right\}$$

$$\{\boldsymbol{\alpha}\} = \{\boldsymbol{\alpha_{mem}}\} + \left\{\Delta \boldsymbol{\alpha^{(1)}}\right\}$$

Update the isotropic and deviatoric components of the stress-induced anisotropy tensor, respectively:

$$f_p = f_{p,\,mem} + \Delta f_p^{(1)}$$

$$\{\boldsymbol{f}\} = \left\{\boldsymbol{f_{mem}}\right\} + \left\{\Delta \boldsymbol{f^{(1)}}\right\}$$

Update the value of C, which depends on the maximum ever registered value of f_p:

If $\left|f_p\right|^{2.0} > C_{mem}$ then:

$$C = \left|f_p\right|^{2.0}$$

End if

Update the void ratio: $e = e_{mem} - (1.0 + e_{init})\, \Delta \varepsilon_{ss,v}^{ep}$, where $\Delta \varepsilon_{ss,v}^{ep} = \Delta \varepsilon_{ss,xx}^{ep} + \Delta \varepsilon_{ss,yy}^{ep} + \Delta \varepsilon_{ss,zz}^{ep}$.

Using the recently updated values of $\{\boldsymbol{\sigma'}\}$, e, $\{\boldsymbol{\alpha}\}$, f_p and $\{\boldsymbol{f}\}$ and the equations previously presented in step 3.2, update the following quantities:

Table C.1 – Explicit stress integration scheme for the present bounding surface plasticity model.

Step	Description
	- the small-strain shear modulus, G_{max}, the tangent shear modulus, G_{tan}, the tangent bulk modulus, K_{tan}, and finally the elastic constitutive matrix, $[\boldsymbol{D}]$; - the radial tensor, $\{\bar{\boldsymbol{r}}\}$, the deviatoric loading direction, $\{\boldsymbol{n}\}$, and the modified Lode's angle, θ; - the inherent anisotropic state variable, A_F, the distance from the current stress point to the critical surface, d^c, the reference distance to the critical surface, d^c_{ref}, the void ratio at CSL, e_{CS}, and the state parameter, ψ; - the distance from the current stress point to the dilatancy and bounding surfaces, d^d and d^b, respectively, as well as the reference distance to the bounding surface, d^b_{ref}; - the positions of the primary and secondary yield surfaces, F_1 and F_2, respectively, and the corresponding gradients, $\{\partial F_1/\partial \boldsymbol{\sigma}'\}$ and $\{\partial F_2/\partial \boldsymbol{\sigma}'\}$, respectively; - the gradients of the plastic potentials associated with the primary and secondary yield surfaces, $\{\partial \boldsymbol{P_1}/\partial \boldsymbol{\sigma}'\}$ and $\{\partial \boldsymbol{P_2}/\partial \boldsymbol{\sigma}'\}$, respectively; - the hardening moduli associated with the primary and secondary yield surfaces, A_1 and A_2, respectively.
	Update the plastic multipliers associated with the primary and secondary yield surfaces, λ_1 and λ_2: If $IYIELD = 1$ then [2), 3)]: $\lambda_1 = \dfrac{\left\{\dfrac{\partial F_1}{\partial \boldsymbol{\sigma}'}\right\}^{\mathrm{T}} [\boldsymbol{D}] \{\Delta \boldsymbol{\varepsilon}^{\boldsymbol{ep}}_{\boldsymbol{ss}}\}}{\left\{\dfrac{\partial F_1}{\partial \boldsymbol{\sigma}'}\right\}^{\mathrm{T}} [\boldsymbol{D}] \left\{\dfrac{\partial \boldsymbol{P_1}}{\partial \boldsymbol{\sigma}'}\right\} + A_1}$ $\lambda_2 = 0.0$ Else if $IYIELD = 2$ then [2), 3)]: $\lambda_1 = 0.0$ $\lambda_2 = \dfrac{\left\{\dfrac{\partial F_2}{\partial \boldsymbol{\sigma}'}\right\}^{\mathrm{T}} [\boldsymbol{D}] \{\Delta \boldsymbol{\varepsilon}^{\boldsymbol{ep}}_{\boldsymbol{ss}}\}}{\left\{\dfrac{\partial F_2}{\partial \boldsymbol{\sigma}'}\right\}^{\mathrm{T}} [\boldsymbol{D}] \left\{\dfrac{\partial \boldsymbol{P_2}}{\partial \boldsymbol{\sigma}'}\right\} + A_2}$ Else if $IYIELD = 3$ then [2), 3)]: $\lambda_1 = \dfrac{L_{22}\, T_1 - L_{12}\, T_2}{L_{11}\, L_{22} - L_{12}\, L_{21}}$ $\lambda_2 = \dfrac{L_{11}\, T_2 - L_{21}\, T_1}{L_{11}\, L_{22} - L_{12}\, L_{21}}$ where [2), 3)]: $L_{11} = \left\{\dfrac{\partial F_1}{\partial \boldsymbol{\sigma}'}\right\}^{\mathrm{T}} [\boldsymbol{D}] \left\{\dfrac{\partial \boldsymbol{P_1}}{\partial \boldsymbol{\sigma}'}\right\} + A_1$ $L_{12} = \left\{\dfrac{\partial F_1}{\partial \boldsymbol{\sigma}'}\right\}^{\mathrm{T}} [\boldsymbol{D}] \left\{\dfrac{\partial \boldsymbol{P_2}}{\partial \boldsymbol{\sigma}'}\right\}$ $L_{21} = \left\{\dfrac{\partial F_2}{\partial \boldsymbol{\sigma}'}\right\}^{\mathrm{T}} [\boldsymbol{D}] \left\{\dfrac{\partial \boldsymbol{P_1}}{\partial \boldsymbol{\sigma}'}\right\}$ $L_{22} = \left\{\dfrac{\partial F_2}{\partial \boldsymbol{\sigma}'}\right\}^{\mathrm{T}} [\boldsymbol{D}] \left\{\dfrac{\partial \boldsymbol{P_2}}{\partial \boldsymbol{\sigma}'}\right\} + A_2$ $T_1 = \left\{\dfrac{\partial F_1}{\partial \boldsymbol{\sigma}'}\right\}^{\mathrm{T}} [\boldsymbol{D}] \{\Delta \boldsymbol{\varepsilon}^{\boldsymbol{ep}}_{\boldsymbol{ss}}\}$

Table C.1 – Explicit stress integration scheme for the present bounding surface plasticity model.

Step	Description

$$T_2 = \left\{\frac{\partial F_2}{\partial \boldsymbol{\sigma'}}\right\}^{\mathrm{T}} [\boldsymbol{D}] \{\Delta \boldsymbol{\varepsilon_{ss}^{ep}}\}$$

End if.

3.7 Compute the second-order approximation of changes in effective stresses [2), 3)]:

$$\left\{\Delta \boldsymbol{\sigma'^{(2)}}\right\} = [\boldsymbol{D}] \{\Delta \boldsymbol{\varepsilon_{ss}^{ep}}\} - \lambda_1 [\boldsymbol{D}] \left\{\frac{\partial \boldsymbol{P_1}}{\partial \boldsymbol{\sigma'}}\right\} - \lambda_2 [\boldsymbol{D}] \left\{\frac{\partial \boldsymbol{P_2}}{\partial \boldsymbol{\sigma'}}\right\}$$

Compute the second-order approximation of changes in plastic strains [3)]:

$$\left\{\Delta \boldsymbol{\varepsilon_1^{p(2)}}\right\} = \lambda_1 \left\{\frac{\partial \boldsymbol{P_1}}{\partial \boldsymbol{\sigma'}}\right\}$$

$$\left\{\Delta \boldsymbol{\varepsilon_2^{p(2)}}\right\} = \lambda_2 \left\{\frac{\partial \boldsymbol{P_2}}{\partial \boldsymbol{\sigma'}}\right\}$$

$$\left\{\Delta \boldsymbol{\varepsilon^{p(2)}}\right\} = \left\{\Delta \boldsymbol{\varepsilon_1^{p(2)}}\right\} + \left\{\Delta \boldsymbol{\varepsilon_2^{p(2)}}\right\}$$

Compute the second-order approximation of the evolution of the back-stress tensor:

$$\left\{\Delta \boldsymbol{\alpha^{(2)}}\right\} = \lambda_1 h_A h_b h_e h_f h_g \left(\left\{\boldsymbol{\alpha^b}\right\} - \{\boldsymbol{\alpha}\}\right) =$$

$$= \lambda_1 h_A h_b h_e h_f h_g \left(\sqrt{2.0/3.0}\left[g(\theta, c^b)\left(M_c^c + k_c^b \langle -\psi \rangle\right) - m\right]\{\boldsymbol{n}\} - \{\boldsymbol{\alpha}\}\right)$$

Compute the second-order approximation of the evolution of the isotropic and deviatoric components of the stress-induced anisotropy tensor, respectively:

$$\Delta f_p^{(2)} = H \Delta \varepsilon_v^{p(2)}$$

$$\left\{\Delta \boldsymbol{f^{(2)}}\right\} = -H \left\langle -\Delta \varepsilon_v^{p(2)} \right\rangle [C\{\boldsymbol{n}\} + \{\boldsymbol{f}\}]$$

where:

$$\Delta \varepsilon_v^{p(2)} = \Delta \varepsilon_{v,1}^{p\ (2)} + \Delta \varepsilon_{v,2}^{p\ (2)} = \Delta \varepsilon_{xx,1}^{p\ (2)} + \Delta \varepsilon_{yy,1}^{p\ (2)} + \Delta \varepsilon_{zz,1}^{p\ (2)} + \Delta \varepsilon_{xx,2}^{p\ (2)} + \Delta \varepsilon_{yy,2}^{p\ (2)} + \Delta \varepsilon_{zz,2}^{p\ (2)}$$

3.8 Compute the modified forward Euler approximation of changes in effective stresses, changes in plastic strains and changes in the back-stress tensor, respectively:

$$\{\Delta \boldsymbol{\sigma'}\} = \frac{\left\{\Delta \boldsymbol{\sigma'^{(1)}}\right\} + \left\{\Delta \boldsymbol{\sigma'^{(2)}}\right\}}{2.0}$$

$$\{\Delta \boldsymbol{\varepsilon_1^p}\} = \frac{\left\{\Delta \boldsymbol{\varepsilon_1^{p(1)}}\right\} + \left\{\Delta \boldsymbol{\varepsilon_1^{p(2)}}\right\}}{2.0}$$

$$\{\Delta \boldsymbol{\varepsilon_2^p}\} = \frac{\left\{\Delta \boldsymbol{\varepsilon_2^{p(1)}}\right\} + \left\{\Delta \boldsymbol{\varepsilon_2^{p(2)}}\right\}}{2.0}$$

$$\{\Delta \boldsymbol{\varepsilon^p}\} = \{\Delta \boldsymbol{\varepsilon_1^p}\} + \{\Delta \boldsymbol{\varepsilon_2^p}\}$$

$$\{\Delta \boldsymbol{\alpha}\} = \frac{\left\{\Delta \boldsymbol{\alpha^{(1)}}\right\} + \left\{\Delta \boldsymbol{\alpha^{(2)}}\right\}}{2.0}$$

Compute the modified forward Euler approximation of the evolution of the isotropic and deviatoric components of the stress-induced anisotropy tensor, respectively:

$$\Delta f_p = \frac{\Delta f_p^{(1)} + \Delta f_p^{(2)}}{2.0}$$

$$\{\Delta \boldsymbol{f}\} = \frac{\left\{\Delta \boldsymbol{f^{(1)}}\right\} + \left\{\Delta \boldsymbol{f^{(2)}}\right\}}{2.0}$$

Determine the relative error in the modified forward Euler approximation of the effective stresses and of the back-stress tensor, respectively [1)]:

Table C.1 – Explicit stress integration scheme for the present bounding surface plasticity model.

Step	Description

$$R_\sigma = \frac{1.0}{2.0}\frac{\left\|\left\{\Delta\boldsymbol{\sigma}'^{(2)}\right\}-\left\{\Delta\boldsymbol{\sigma}'^{(1)}\right\}\right\|}{\left\|\{\boldsymbol{\sigma}'_{mem}\}+\{\Delta\boldsymbol{\sigma}'\}\right\|} = \frac{1.0}{2.0}\sqrt{\frac{\left(\left\{\Delta\boldsymbol{\sigma}'^{(2)}\right\}-\left\{\Delta\boldsymbol{\sigma}'^{(1)}\right\}\right)\left(\left\{\Delta\boldsymbol{\sigma}'^{(2)}\right\}-\left\{\Delta\boldsymbol{\sigma}'^{(1)}\right\}\right)}{\left(\{\boldsymbol{\sigma}'_{mem}\}+\{\Delta\boldsymbol{\sigma}'\}\right)\left(\{\boldsymbol{\sigma}'_{mem}\}+\{\Delta\boldsymbol{\sigma}'\}\right)}}$$

$$R_\alpha = \frac{1.0}{2.0}\frac{\left\|\left\{\Delta\boldsymbol{\alpha}^{(2)}\right\}-\left\{\Delta\boldsymbol{\alpha}^{(1)}\right\}\right\|}{\left\|\{\boldsymbol{\alpha}_{mem}\}+\{\Delta\boldsymbol{\alpha}\}\right\|} = \frac{1.0}{2.0}\sqrt{\frac{\left(\left\{\Delta\boldsymbol{\alpha}^{(2)}\right\}-\left\{\Delta\boldsymbol{\alpha}^{(1)}\right\}\right)\left(\left\{\Delta\boldsymbol{\alpha}^{(2)}\right\}-\left\{\Delta\boldsymbol{\alpha}^{(1)}\right\}\right)}{\left(\{\boldsymbol{\alpha}_{mem}\}+\{\Delta\boldsymbol{\alpha}\}\right)\left(\{\boldsymbol{\alpha}_{mem}\}+\{\Delta\boldsymbol{\alpha}\}\right)}}$$

Determine the relative error in the modified forward Euler approximation of the isotropic and deviatoric components of the stress-induced anisotropy tensor, respectively [(1)]:

$$R_{f_p} = \frac{1.0}{2.0}\sqrt{\frac{\left(\Delta f_p^{(2)}-\Delta f_p^{(1)}\right)^{2.0}}{\left(f_{p,\,mem}+\Delta f_p\right)^{2.0}}}$$

$$R_f = \frac{1.0}{2.0}\frac{\left\|\left\{\Delta\boldsymbol{f}^{(2)}\right\}-\left\{\Delta\boldsymbol{f}^{(1)}\right\}\right\|}{\left\|\left\{\boldsymbol{f}_{mem}\right\}+\{\Delta\boldsymbol{f}\}\right\|} = \frac{1.0}{2.0}\sqrt{\frac{\left(\left\{\Delta\boldsymbol{f}^{(2)}\right\}-\left\{\Delta\boldsymbol{f}^{(1)}\right\}\right)\left(\left\{\Delta\boldsymbol{f}^{(2)}\right\}-\left\{\Delta\boldsymbol{f}^{(1)}\right\}\right)}{\left(\left\{\boldsymbol{f}_{mem}\right\}+\{\Delta\boldsymbol{f}\}\right)\left(\left\{\boldsymbol{f}_{mem}\right\}+\{\Delta\boldsymbol{f}\}\right)}}$$

Determine the minimum relative error:

$$R = \max\left\{R_\sigma, R_\alpha, R_f, R_{f_p}\right\}$$

3.8 Compare the minimum relative error R with the tolerance $SSTOL$[(4)].

If $R > SSTOL$ and $\Delta T_n^{\,ep} > \Delta T_{n,min}^{\,ep}$ then:

The sub-step is not successful and, consequently, a smaller pseudo-time step needs to be used in the integration process.

Restore the effective stresses and back-stress tensor corresponding to the beginning of the sub-step increment, respectively: $\{\boldsymbol{\sigma}'\} = \{\boldsymbol{\sigma}'_{mem}\}$ and $\{\boldsymbol{\alpha}\} = \{\boldsymbol{\alpha}_{mem}\}$.

Restore the value of the void ratio corresponding to the beginning of the sub-step increment: $e = e_{mem}$.

Restore the values of the elastic state parameters corresponding to the beginning of the sub-step increment: $\{\boldsymbol{\sigma}'^{SR}\} = \{\boldsymbol{\sigma}'^{SR}_{mem}\}$, $\{\boldsymbol{\varepsilon}^{SR}\} = \{\boldsymbol{\varepsilon}^{SR}_{mem}\}$, $e^{SR} = e^{SR}_{mem}$, and $N = N_{mem}$.

Restore the isotropic and deviatoric components of the stress-induced anisotropy tensor corresponding to the beginning of the sub-step increment: $f_p = f_{p,\,mem}$ and $\{\boldsymbol{f}\} = \left\{\boldsymbol{f}_{mem}\right\}$, respectively; as well as $C = C_{mem}$.

Restore the positions of the yield surfaces corresponding to the beginning of the sub-step increment: $F_1 = F_{1,mem}$ and $F_2 = F_{2,\,mem}$.

Compute: $\zeta = max\left\{0.9\sqrt{SSTOL/R}, 0.1\right\}$ and $\Delta T_n^{\,ep} = max\left\{\zeta\,\Delta T_n^{\,ep},\ \Delta T_{n,min}^{\,ep}\right\}$.

Return to step 3.2.

Else:

The sub-step is considered successful.

Update the effective stress state and back-stress tensor, respectively:

$\{\boldsymbol{\sigma}'\} = \{\boldsymbol{\sigma}'_{mem}\} + \{\Delta\boldsymbol{\sigma}'\}$

$\{\boldsymbol{\alpha}\} = \{\boldsymbol{\alpha}_{mem}\} + \{\Delta\boldsymbol{\alpha}\}$

Update the isotropic and deviatoric components of the stress-induced anisotropy tensor, respectively:

$f_p = f_{p,\,mem} + \Delta f_p$

$\{\boldsymbol{f}\} = \left\{\boldsymbol{f}_{mem}\right\} + \{\Delta\boldsymbol{f}\}$

Update the value of C, which depends on the maximum ever registered value of f_p:

If $\left|f_p\right|^{2.0} > C_{mem}$, then:

$$C = \left|f_p\right|^{2.0}$$

Table C.1 – Explicit stress integration scheme for the present bounding surface plasticity model.

Step	Description
	End if Compute a new pseudo-time step multiplier, according to the following condition: If the previous sub-step or the one before failed: $\zeta = \min\left\{0.9\sqrt{SSTOL/R_\sigma},\ 1.0\right\}$ Else: $\zeta = \min\left\{0.9\sqrt{SSTOL/R_\sigma},\ 1.1\right\}$ End if. Continue to step 3.10. End if

3.10	Given the recently updated values of $\{\boldsymbol{\sigma}'\}$ and $\{\boldsymbol{\alpha}\}$, update the positions of the primary and secondary yield surfaces:
	$F_1 = \sqrt{(\{\boldsymbol{s}\} - p'\{\boldsymbol{\alpha}\}):(\{\boldsymbol{s}\} - p'\{\boldsymbol{\alpha}\})} - \sqrt{2.0/3.0}\ m\, p'$
	$F_2 = p'_{YS} - p'$
	When a single yield surface is active, check whether the recently updated effective stress point lies outside of the non-active yield surface(1), specifically:
	If ($IYIELD = 1$ and $F_2 > YTOL$) or ($IYIELD = 2$ and $F_1 > YTOL$), then:
	The effective stress point lies outside of the non-active yield surface. Estimate the reduction, ξ, to be apply to the pseudo-time step to bring the effective stress point to the intersection between both yield surfaces by a methodology similar to that described in Section C.3, with the main difference that the elasto-plastic response needs to be computed, rather than purely elastic response (i.e. the computations described in steps 3.2 and 3.3 replace step 2.3).
	Having obtained a value for ξ in the range]0.0, 1.0[, as well as new values for the stress increment, $\{\Delta\boldsymbol{\sigma}'\}$, evolution of the back-stress tensor, $\{\Delta\boldsymbol{\alpha}\}$, evolutions of the isotropic and deviatoric components of the state parameters, Δf_p and $\{\Delta\boldsymbol{f}\}$, respectively, update, once again, the values of the following quantities:
	$\{\boldsymbol{\sigma}'\} = \{\boldsymbol{\sigma}'_{\boldsymbol{mem}}\} + \{\Delta\boldsymbol{\sigma}'\}$
	$e = e_{mem} - (1.0 + e_{init})\ \xi\ \Delta\varepsilon^{ep}_{ss,v}$.
	$\{\boldsymbol{\alpha}\} = \{\boldsymbol{\alpha}_{\boldsymbol{mem}}\} + \{\Delta\boldsymbol{\alpha}\}$
	$f_p = f_{p,\,mem} + \Delta f_p$
	$\{\boldsymbol{f}\} = \{\boldsymbol{f}_{\boldsymbol{mem}}\} + \{\Delta\boldsymbol{f}\}$
	If $\left\lvert f_p\right\rvert^{2.0} > C_{mem}$, then:
	$C = \left\lvert f_p\right\rvert^{2.0}$
	End if
	Given the recently updated values of $\{\boldsymbol{\sigma}'\}$ and $\{\boldsymbol{\alpha}\}$, update the positions of the primary and secondary yield surfaces:
	$F_1 = \sqrt{(\{\boldsymbol{s}\} - p'\{\boldsymbol{\alpha}\}):(\{\boldsymbol{s}\} - p'\{\boldsymbol{\alpha}\})} - \sqrt{2.0/3.0}\ m\, p'$
	$F_2 = p'_{YS} - p'$
	Else:
	$\xi = 1.0$
	End if.
	Proceed to step 3.10.

3.11	Check whether *yield surface drift* occurred (4): If ($IYIELD = 1$ and $\lvert F_1\rvert > YTOL$) or

Table C.1 – Explicit stress integration scheme for the present bounding surface plasticity model.

Step	Description
	(*IYIELD* $= 2$ and $\lvert F_2 \rvert > YTOL$) or [*IYIELD* $= 3$ and ($\lvert F_1 \rvert > YTOL$ or $\lvert F_2 \rvert > YTOL$)], then: Yield surface(s) drift has occurred. Given the updated values of $\{\boldsymbol{\sigma'}\}$, e, $\{\boldsymbol{\alpha}\}$, f_p and $\{\boldsymbol{f}\}$ and the equations previously presented in Step 3.2, update the following quantities: - the small-strain shear modulus, G_{max}, the tangent shear modulus, G_{tan}, the tangent bulk modulus, K_{tan}, and finally the elastic constitutive matrix, $[\boldsymbol{D}]$; - the radial tensor, $\{\bar{\boldsymbol{r}}\}$, the deviatoric loading direction, $\{\boldsymbol{n}\}$, and the modified Lode's angle, θ; - the inherent anisotropic state variable, A_F, the distance from the current stress point to the critical surface, d^c, the reference distance to the critical surface, d^c_{ref}, the void ratio at CSL, e_{CS}, and the state parameter, ψ; - the distance from the current stress point to the dilatancy and bounding surfaces, d^d and d^b, respectively, as well as the reference distance to the bounding surface, d^b_{ref}; - the positions of the primary and secondary yield surfaces, F_1 and F_2, respectively, and the corresponding gradients, $\{\partial F_1/\partial \boldsymbol{\sigma'}\}$ and $\{\partial F_2/\partial \boldsymbol{\sigma'}\}$, respectively; - the gradients of the plastic potentials associated with the primary and secondary yield surfaces, $\{\partial \boldsymbol{P_1}/\partial \boldsymbol{\sigma'}\}$ and $\{\partial \boldsymbol{P_2}/\partial \boldsymbol{\sigma'}\}$, respectively; - the hardening moduli associated with the primary and secondary yield surfaces, A_1 and A_2, respectively. Find a new combination of effective stresses, $\{\boldsymbol{\sigma'}\}$, and state parameters, $\{\boldsymbol{\alpha}\}$, f_p and $\{\boldsymbol{f}\}$, that satisfies the yield conditions by applying the methodology described in Section C.4. A new plastic strain increment, $\{\Delta\boldsymbol{\varepsilon^p}\}$, is also obtained. Proceed to step 3.11. End if.
3.11	Update the elastic, plastic and total strains, respectively: $\{\boldsymbol{\varepsilon^e}\} = \{\boldsymbol{\varepsilon^e}\} + \{\Delta\boldsymbol{\varepsilon}^{ep}_{ss}\} - \{\Delta\boldsymbol{\varepsilon^p}\}$ $\{\boldsymbol{\varepsilon^p_1}\} = \{\boldsymbol{\varepsilon^p_{1,mem}}\} + \{\Delta\boldsymbol{\varepsilon^p_1}\}$ $\{\boldsymbol{\varepsilon^p_2}\} = \{\boldsymbol{\varepsilon^p_{2,mem}}\} + \{\Delta\boldsymbol{\varepsilon^p_2}\}$ $\{\boldsymbol{\varepsilon^p}\} = \{\boldsymbol{\varepsilon^p_1}\} + \{\boldsymbol{\varepsilon^p_2}\}$ $\{\boldsymbol{\varepsilon}\} = \{\boldsymbol{\varepsilon^e}\} + \{\boldsymbol{\varepsilon^p}\}$ Update the pseudo-time: $T_n{}^{ep} = T_{n-1}{}^{ep} + \xi\,\Delta T_n{}^{ep}$. Compute the new pseudo-time step [(2)]: $\Delta T_n{}^{ep} = \max\left\{\zeta\,\Delta T_n{}^{ep},\ \Delta T_{n,min}{}^{ep}\right\}$. Make sure that $T_n{}^{ep} + \Delta T_n{}^{ep}$ does not exceed 1.0: $\Delta T_n{}^{ep} = \min\{\zeta\,\Delta T_n{}^{ep}, 1.0 - T_n{}^{ep}\}$ Return to step 3.2.
4	**Store the final values of the state variables and state parameters** Store the final values of the stress, strain and material's state variables: - effective stresses, $\{\boldsymbol{\sigma'}\}$, - elastic strains, $\{\boldsymbol{\varepsilon^e}\}$, plastic strains associated with the primary and secondary yield surfaces, $\{\boldsymbol{\varepsilon^p_1}\}$ and $\{\boldsymbol{\varepsilon^p_2}\}$, respectively, and total strains, $\{\boldsymbol{\varepsilon}\}$. - void ratio, e. Store the final values of the elastic and plastic state parameters:

Table C.1 – Explicit stress integration scheme for the present bounding surface plasticity model.

Step	Description
	- elastic state parameters: effective stresses, strains and void ratio at last shear reversal, $\{\boldsymbol{\sigma'^{SR}}\}$, $\{\boldsymbol{\varepsilon^{SR}}\}$ and e^{SR}, respectively, and scaling factor, N; - plastic state parameters: back-stress tensor, $\{\boldsymbol{\alpha}\}$; isotropic and deviatoric components of the stress-induced anisotropy tensor, f_p and $\{\boldsymbol{f}\}$, respectively, as well as the value of the constant C.
	Exit.

(1) The trace (or inner) product of two tensors, $\boldsymbol{a}$ and $\boldsymbol{b}$, represented, for convenience, as (6 x 1) vectors $\{\boldsymbol{a}\} = \{a_{xx} \quad a_{yy} \quad a_{xy} \quad a_{zz} \quad a_{xz} \quad a_{yz}\}^{\mathrm{T}}$ and $\{\boldsymbol{b}\} = \{a_{xx} \quad a_{yy} \quad a_{xy} \quad a_{zz} \quad a_{xz} \quad a_{yz}\}^{\mathrm{T}}$ defines the operation: $\{\boldsymbol{a}\}:\{\boldsymbol{b}\} = a_{xx}\,b_{xx} + a_{yy}\,b_{yy} + a_{zz}\,b_{zz} + 2.0\,a_{xy}\,b_{xy} + 2.0\,a_{xz}\,b_{xz} + 2.0\,a_{yz}\,b_{yz}$.

The Euclidian norm of a second-order tensor $\{\boldsymbol{a}\} = \{a_{xx} \quad a_{yy} \quad a_{xy} \quad a_{zz} \quad a_{xz} \quad a_{yz}\}^{\mathrm{T}}$ is given by $\|\{\boldsymbol{a}\}\|_2 = \sqrt{\{\boldsymbol{a}\}:\{\boldsymbol{a}\}} = \sqrt{{a_{xx}}^{2.0} + {a_{yy}}^{2.0} + {a_{zz}}^{2.0} + 2.0\,{a_{xy}}^{2.0} + 2.0\,{a_{xz}}^{2.0} + 2.0\,{a_{yz}}^{2.0}}$.

(2) Matrix multiplication.

(3) To compute the plastic multipliers, as well as the elasto-plastic constitutive matrix using matrix operations (rather than tensorial operations), the derivatives of the yield surfaces, as well as the gradients of the plastic potential need to be represented in covariant coordinates. In such case, the deviatoric components of these tensors, stored in a vector, need to be scaled by 2.0. For the present constitutive model, it means that: $\{\partial F_1/\partial\,\tau_{xy}\} = 2.0\,n_{xy}$; $\{\partial F_1/\partial\,\tau_{xz}\} = 2.0\,n_{xz}$; $\{\partial F_1/\partial\,\tau_{yz}\} = 2.0\,n_{yz}$; $\{\partial P_1/\partial\,\tau_{xy}\} = 2.0\,n_{xy}$; $\{\partial P_1/\partial\,\tau_{xz}\} = 2.0\,n_{xz}$; $\{\partial P_1/\partial\,\tau_{yz}\} = 2.0\,n_{yz}$. Similarly, to compute the plastic strain change, covariant representation of the gradients of the plastic potential are required.

(4) Based on conclusions obtained in small parametric studies, as well as on literature review (Sloan, 1987; Sloan *et al.*, 2001; Potts and Zdravkovic, 1999; Zhao *et al.*, 2005; Hong *et al.*, 2012), the following values of the tolerance parameters were deemed appropriate for all numerical simulations performed in the present study: yield surface tolerance, $YTOL = 1.0\times10^{-9}$, elasto-plastic unloading tolerance, $LTOL = 1.0\times10^{-7}$, sub-stepping scheme tolerance for both elastic trial and elasto-plastic response: $SSTOL = 1.0\times10^{-5}$ and minimum pseudo time step, $\Delta T_{n,min} = \Delta T_{n,min}{}^{ep} = 1.0\times10^{-4}$.

C.2 Shear strain reversal detection

Table C.2 presents the operations performed to evaluate the occurrence of a shear strain reversal, which follows the strategy proposed by Papadimitriou and Bouckovalas (2002) and Taborda (2011).

Table C.2 – Shear strain reversal detection.

Step	Description
1	Enter with: - current strain state (1): $\{\boldsymbol{\varepsilon}\} = \{\varepsilon_{xx} \quad \varepsilon_{yy} \quad \gamma_{xy} \quad \varepsilon_{zz} \quad \gamma_{xz} \quad \gamma_{yz}\}^{\mathrm{T}} = \{\varepsilon_{xx} \quad \varepsilon_{yy} \quad 2.0\,\varepsilon_{xy} \quad \varepsilon_{zz} \quad 2.0\,\varepsilon_{xz} \quad 2.0\,\varepsilon_{yz}\}^{\mathrm{T}}$; - sub-step strain increment(1),(2): $\{\Delta\boldsymbol{\varepsilon}\} = \{\Delta\varepsilon_{xx} \quad \Delta\varepsilon_{yy} \quad \Delta\gamma_{xy} \quad \Delta\varepsilon_{zz} \quad \Delta\gamma_{xz} \quad \Delta\gamma_{yz}\}^{\mathrm{T}} = \{\Delta\varepsilon_{xx} \quad \Delta\varepsilon_{yy} \quad 2.0\,\Delta\varepsilon_{xy} \quad \Delta\varepsilon_{zz} \quad 2.0\,\Delta\varepsilon_{xz} \quad 2.0\,\Delta\varepsilon_{yz}\}^{\mathrm{T}}$; - strain state at last shear reversal(1), $\{\boldsymbol{\varepsilon^{SR}}\} = \{\varepsilon^{e}_{xx} \quad \varepsilon^{e}_{yy} \quad \gamma^{e}_{xy} \quad \varepsilon^{e}_{zz} \quad \gamma^{e}_{xz} \quad \gamma^{e}_{yz}\}^{\mathrm{T}}$.
	Initialise the variable informing about the occurrence of a shear reversal: $FLAG\_SR = 0$.

Table C.2 – Shear strain reversal detection.

Step	Description
2	Check whether the norm of the deviatoric strain increment, $\{\Delta \boldsymbol{e}\}$, is greater than a user-defined tolerance, $RTOL^{(3)}$, below which the shear strain reversal condition is ignored. Determine the norm of the deviatoric part of the sub-step strain increment: $\chi^{\Delta e} = \sqrt{\frac{1.0}{2.0}}\,\|\{\Delta \boldsymbol{e}\}\|_2 = \sqrt{\frac{1.0}{2.0}}\sqrt{\{\Delta \boldsymbol{e}\}:\{\Delta \boldsymbol{e}\}}$ $= \sqrt{\frac{1.0}{2.0}}\sqrt{\left(\Delta\varepsilon_{xx} - \frac{1.0}{3.0}\Delta\varepsilon_v\right)^{2.0} + \left(\Delta\varepsilon_{yy} - \frac{1.0}{3.0}\Delta\varepsilon_v\right)^{2.0} + \left(\Delta\varepsilon_{zz} - \frac{1.0}{3.0}\Delta\varepsilon_v\right)^{2.0} + 2.0\,\Delta\varepsilon_{xy}{}^{2.0} + 2.0\,\Delta\varepsilon_{xz}{}^{2.0} + 2.0\,\Delta\varepsilon_{yz}{}^{2.0}}$ $= \sqrt{\frac{1.0}{2.0}}\sqrt{\left(\Delta\varepsilon_{xx} - \frac{1.0}{3.0}\Delta\varepsilon_v\right)^{2.0} + \left(\Delta\varepsilon_{yy} - \frac{1.0}{3.0}\Delta\varepsilon_v\right)^{2.0} + \left(\Delta\varepsilon_{zz} - \frac{1.0}{3.0}\Delta\varepsilon_v\right)^{2.0} + \frac{1.0}{2.0}\,\Delta\gamma_{xy}{}^{2.0} + \frac{1.0}{2.0}\,\Delta\gamma_{xz}{}^{2.0} + \frac{1.0}{2.0}\,\Delta\gamma_{yz}{}^{2.0}}$ where: $\Delta\varepsilon_v = \Delta\varepsilon_{xx} + \Delta\varepsilon_{yy} + \Delta\varepsilon_{zz}$ Compare the magnitude of the sub-step strain increment with the user-defined tolerance: If $\chi^{\Delta e} \leq RTOL$ then: The deviatoric strain increment is considered too small. Exit. Else Continue to step 3. End if.
3	Compute the distance between the current deviatoric strain (i.e. value at the beginning of the sub-step increment), $\{\boldsymbol{e}\}$, and the deviatoric strain at last shear reversal point, $\{\boldsymbol{e}^{SR}\}$: $\chi^{e}_{ref} = \sqrt{\frac{1.0}{2.0}}\,\|\{\boldsymbol{e}\} - \{\boldsymbol{e}^{SR}\}\|_2 = \sqrt{\frac{1.0}{2.0}}\sqrt{(\{\boldsymbol{e}\} - \{\boldsymbol{e}^{SR}\}):(\{\boldsymbol{e}\} - \{\boldsymbol{e}^{SR}\})}$ $= \sqrt{\frac{1.0}{2.0}}\sqrt{\left[\left(\varepsilon_{xx} - \frac{1.0}{3.0}\varepsilon_v\right) - \left(\varepsilon_{xx}{}^{SR} - \frac{1.0}{3.0}\varepsilon_v{}^{SR}\right)\right]^{2.0} + \left[\left(\varepsilon_{yy} - \frac{1.0}{3.0}\varepsilon_v\right) - \left(\varepsilon_{yy}{}^{SR} - \frac{1.0}{3.0}\varepsilon_v{}^{SR}\right)\right]^{2.0} + \left[\left(\varepsilon_{zz} - \frac{1.0}{3.0}\varepsilon_v\right) - \left(\varepsilon_{zz}{}^{SR} - \frac{1.0}{3.0}\varepsilon_v{}^{SR}\right)\right]^{2.0} + 2.0\left[\varepsilon_{xy} - \varepsilon_{xy}{}^{SR}\right]^{2.0} + 2.0\left[\varepsilon_{xz} - \varepsilon_{xz}{}^{SR}\right]^{2.0} + 2.0\left[\varepsilon_{yz} - \varepsilon_{yz}{}^{SR}\right]^{2.0}}$ $= \sqrt{\frac{1.0}{2.0}}\sqrt{\left[\left(\varepsilon_{xx} - \frac{1.0}{3.0}\varepsilon_v\right) - \left(\varepsilon_{xx}{}^{SR} - \frac{1.0}{3.0}\varepsilon_v{}^{SR}\right)\right]^{2.0} + \left[\left(\varepsilon_{yy} - \frac{1.0}{3.0}\varepsilon_v\right) - \left(\varepsilon_{yy}{}^{SR} - \frac{1.0}{3.0}\varepsilon_v{}^{SR}\right)\right]^{2.0} + \left[\left(\varepsilon_{zz} - \frac{1.0}{3.0}\varepsilon_v\right) - \left(\varepsilon_{zz}{}^{SR} - \frac{1.0}{3.0}\varepsilon_v{}^{SR}\right)\right]^{2.0} + \frac{1.0}{2.0}\left[\gamma_{xy} - \gamma_{xy}{}^{SR}\right]^{2.0} + \frac{1.0}{2.0}\left[\gamma_{xz} - \gamma_{xz}{}^{SR}\right]^{2.0} + \frac{1.0}{2.0}\left[\gamma_{yz} - \gamma_{yz}{}^{SR}\right]^{2.0}}$ Compute the distance between the deviatoric strain at the end of the sub-step increment, $\{\boldsymbol{e}\} + \{\Delta \boldsymbol{e}\}$, and the deviatoric strain at last shear reversal point, $\{\boldsymbol{e}^{SR}\}$:

Table C.2 – Shear strain reversal detection.

Step	Description

$$\chi_{ref}^{e+\Delta e} = \|\{\boldsymbol{e}\} + \{\Delta\boldsymbol{e}\} - \{\boldsymbol{e}^{SR}\}\| = \sqrt{\frac{1.0}{2.0}}\sqrt{(\{\boldsymbol{e}\} - \{\boldsymbol{e}^{SR}\}):(\{\boldsymbol{e}\} - \{\boldsymbol{e}^{SR}\})}$$

$$= \sqrt{\frac{1.0}{2.0}} \sqrt{\begin{array}{c} \left[\left(\varepsilon_{xx} - \frac{1.0}{3.0}\varepsilon_v + \Delta\varepsilon_{xx} - \frac{1.0}{3.0}\Delta\varepsilon_v\right) - \left({\varepsilon_{xx}}^{SR} - \frac{1.0}{3.0}{\varepsilon_v}^{SR}\right)\right]^{2.0} + \\ \left[\left(\varepsilon_{yy} - \frac{1.0}{3.0}\varepsilon_v + \Delta\varepsilon_{yy} - \frac{1.0}{3.0}\Delta\varepsilon_v\right) - \left({\varepsilon_{yy}}^{SR} - \frac{1.0}{3.0}{\varepsilon_v}^{SR}\right)\right]^{2.0} + \\ \left[\left(\varepsilon_{zz} - \frac{1.0}{3.0}\varepsilon_v + \Delta\varepsilon_{zz} - \frac{1.0}{3.0}\Delta\varepsilon_v\right) - \left({\varepsilon_{zz}}^{SR} - \frac{1.0}{3.0}{\varepsilon_v}^{SR}\right)\right]^{2.0} + \\ 2.0\left[\varepsilon_{xy} + \Delta\varepsilon_{xy} - {\varepsilon_{xy}}^{SR}\right]^{2.0} + 2.0\left[\varepsilon_{xz} + \Delta\varepsilon_{xz} - {\varepsilon_{xz}}^{SR}\right]^{2.0} + 2.0\left[\varepsilon_{yz} + \Delta\varepsilon_{yz} - {\varepsilon_{yz}}^{SR}\right]^{2.0} \end{array}}$$

$$= \sqrt{\frac{1.0}{2.0}} \sqrt{\begin{array}{c} \left[\left(\varepsilon_{xx} + \Delta\varepsilon_{xx} - \frac{1.0}{3.0}(\varepsilon_v + \Delta\varepsilon_v)\right) - \left({\varepsilon_{xx}}^{SR} - \frac{1.0}{3.0}{\varepsilon_v}^{SR}\right)\right]^{2.0} + \\ \left[\left(\varepsilon_{yy} + \Delta\varepsilon_{yy} - \frac{1.0}{3.0}(\varepsilon_v + \Delta\varepsilon_v)\right) - \left({\varepsilon_{yy}}^{SR} - \frac{1.0}{3.0}{\varepsilon_v}^{SR}\right)\right]^{2.0} + \\ \left[\left(\varepsilon_{zz} + \Delta\varepsilon_{zz} - \frac{1.0}{3.0}(\varepsilon_v + \Delta\varepsilon_v)\right) - \left({\varepsilon_{zz}}^{SR} - \frac{1.0}{3.0}{\varepsilon_v}^{SR}\right)\right]^{2.0} + \\ \frac{1.0}{2.0}\left[\gamma_{xz} + \Delta\gamma_{xz} - {\gamma_{xz}}^{SR}\right]^{2.0} + \frac{1.0}{2.0}\left[\gamma_{xz} + \Delta\gamma_{xz} - {\gamma_{xz}}^{SR}\right]^{2.0} + \frac{1.0}{2.0}\left[\gamma_{yz} + \Delta\gamma_{yz} - {\gamma_{yz}}^{SR}\right]^{2.0} \end{array}}$$

If $\chi_{ref}^{e} > \chi_{ref}^{e+\Delta e}$, then:

Signalise that a shear strain reversal has occurred: *FLAG_SR* $= 1$ and exit.

Else:

Continue to step 4.

End if.

4 Perform an additional verification when the norm of the deviatoric strain increment is greater than the

If $\chi_{ref}^{e} \leq \chi^{\Delta e}$, then:

No shear reversal occurred. Exit.

Else:

Initialise $R = 1.0$.

Do while $R\,\chi^{\Delta e} \geq \chi_{ref}^{e}$:

$R = 0.1\ R$

End do

Table C.2 – Shear strain reversal detection.

Step	Description
	Compute the distance between the deviatoric strain at the end of the sub-step increment, reduced by a factor *R*, and the deviatoric strain at last shear reversal point:

$$\chi_{ref}^{e+R\Delta e} = \|\{\boldsymbol{e}\} + \{\Delta\boldsymbol{e}\} - \{\boldsymbol{e^{SR}}\}\| = \sqrt{\frac{1.0}{2.0}}\sqrt{(\{\boldsymbol{e}\} - \{\boldsymbol{e^{SR}}\}):(\{\boldsymbol{e}\} - \{\boldsymbol{e^{SR}}\})}$$

$$= \sqrt{\frac{1.0}{2.0}}\sqrt{\begin{aligned}&\left[\left(\varepsilon_{xx} + R\Delta\varepsilon_{xx} - \frac{1.0}{3.0}(\varepsilon_v + R\Delta\varepsilon_v)\right) - \left({\varepsilon_{xx}}^{SR} - \frac{1.0}{3.0}{\varepsilon_v}^{SR}\right)\right]^{2.0} + \\ &\left[\left(\varepsilon_{yy} + R\Delta\varepsilon_{yy} - \frac{1.0}{3.0}(\varepsilon_v + R\Delta\varepsilon_v)\right) - \left({\varepsilon_{yy}}^{SR} - \frac{1.0}{3.0}{\varepsilon_v}^{SR}\right)\right]^{2.0} + \\ &\left[\left(\varepsilon_{zz} + R\Delta\varepsilon_{zz} - \frac{1.0}{3.0}(\varepsilon_v + R\Delta\varepsilon_v)\right) - \left({\varepsilon_{zz}}^{SR} - \frac{1.0}{3.0}{\varepsilon_v}^{SR}\right)\right]^{2.0} + \\ &\frac{1.0}{2.0}\left[\gamma_{xz} + R\Delta\gamma_{xz} - {\gamma_{xz}}^{SR}\right]^{2.0} + \frac{1.0}{2.0}\left[\gamma_{xz} + R\Delta\gamma_{xz} - {\gamma_{xz}}^{SR}\right]^{2.0} + \\ &\frac{1.0}{2.0}\left[\gamma_{yz} + R\Delta\gamma_{yz} - {\gamma_{yz}}^{SR}\right]^{2.0}\end{aligned}}$$

	If $\chi_{ref}^{e} > \chi_{ref}^{e+R\Delta e}$, then:
	Signalise that a shear strain reversal has occurred: *FLAG_SR* $= 1$ and exit.
	Else:
	No shear reversal occurred. Exit.
	End if.
End if.	

(1) An engineering representation (i.e. a covariant representation) is used for the strain and incremental strain tensors (i.e. their shear components are, respectively, given by $\gamma_{ij} = 2.0\ \varepsilon_{ij}$, and $\Delta\gamma_{ij} = 2.0\ \Delta\varepsilon_{ij}$, with $i \neq j$).

(2) Since this routine is performed either during elastic trial or during elasto-plastic stress integration, the sub-strain strain increment may be given either by $\{\Delta\boldsymbol{\varepsilon_{ss}}\} = \Delta T_n\ \{\Delta\boldsymbol{\varepsilon}\}$ or by $\{\Delta\boldsymbol{\varepsilon_{ss}^{ep}}\} = \Delta T_n^{\ ep}\ (1.0 - \beta)\ \{\Delta\boldsymbol{\varepsilon_{ss}}\}$, as presented in Table C.1. To keep the presentation more general, the notation $\{\Delta\boldsymbol{\varepsilon}\}$ is used in this table.

(3) In all numerical simulations performed in the present study, *RTOL* $\leq 1.0 \times 10^{-7.0}$ was used. This value was deemed appropriate to prevent very small strain steps from triggering the shear strain reversal conditions.

C.3 Yield surface intersection

Following the strategy proposed by Hong *et al.* (2012), Table C.3 presents the operations performed to find an appropriate search interval for the Pegasus method, originally proposed by Dowell and Jarratt (1972).

Table C.3 – Defining the input range for the Pegasus method.

Step	Description
1	Enter with:
	- sub-step strain increment, (1): $\{\Delta\boldsymbol{\varepsilon}\} = \{\Delta\varepsilon_{xx} \quad \Delta\varepsilon_{yy} \quad \Delta\gamma_{xy} \quad \Delta\varepsilon_{zz} \quad \Delta\gamma_{xz} \quad \Delta\gamma_{yz}\}^{\mathrm{T}} = \{\Delta\varepsilon_{xx} \quad \Delta\varepsilon_{yy} \quad 2.0\ \Delta\varepsilon_{xy} \quad \Delta\varepsilon_{zz} \quad 2.0\ \Delta\varepsilon_{xz} \quad 2.0\ \Delta\varepsilon_{yz}\}^{\mathrm{T}}$;
	- effective stresses at the beginning of the increment, $\{\boldsymbol{\sigma'_{mem}}\} = \{\sigma'_{xx,\,mem} \quad \sigma'_{yy,\,mem} \quad \tau_{xy,\,mem} \quad \sigma'_{zz,\,mem} \quad \tau_{xz,\,mem} \quad \tau_{yz,\,mem}\}^{\mathrm{T}}$;
	- current effective stresses, $\{\boldsymbol{\sigma'}\} = \{\sigma'_{xx} \quad \sigma'_{yy} \quad \tau_{xy} \quad \sigma'_{zz} \quad \tau_{xz} \quad \tau_{yz}\}^{\mathrm{T}}$;

Table C.3 – Defining the input range for the Pegasus method.

Step	Description
	- void ratio at the beginning of the increment: e_{mem}; - current void ratio, e; - current back-stress tensor, $\{\boldsymbol{\alpha}\} = \{\alpha_{xx} \quad \alpha_{yy} \quad \alpha_{xy} \quad \alpha_{zz} \quad \alpha_{xz} \quad \alpha_{yz}\}^{\mathrm{T}}$, which does not evolve during elastic trial, as well as the mean effective stress at secondary yield, p'_{YS}; - positions of the yield surfaces at the beginning of the sub-step increment, $F_{1,mem}$ and $F_{2,\,mem}$. - current positions of the yield surfaces, F_1 and F_2. Determine which yield surface condition is violated during elastic trial: If $F_{1,mem} < -YTOL$ and $F_1 > YTOL$ and $F_2 \leq YTOL$ then: Primary yield surface condition is violated: $IYIELD = 1$. Else if $F_1 \leq YTOL$ and $F_{2,\,mem} < -YTOL$ and $F_2 > YTOL$: Secondary yield surface condition is violated: $IYIELD = 2$. Else: Both yield surface conditions are violated: $IYIELD = 3$. End if Initialise the lower and upper limits for the Pegasus method: $\beta^{(inf)} = 0.0$ and $\beta^{(sup)} = 0.9$. Initialise the auxiliary variable: $\beta_{save} = 1.0$.
2	Apply the modified forward Euler scheme to estimate the effective stress change, $\{\Delta\boldsymbol{\sigma}'\}$, corresponding to the sub-step strain increment: $\{\Delta\boldsymbol{\varepsilon_{ss}}^{(sup)}\} = \beta^{(sup)}\{\Delta\boldsymbol{\varepsilon_{ss}}\}$ [2]: - determine the elastic constitutive matrix corresponding to the beginning of the sub-step increment, $[\boldsymbol{D}(\{\boldsymbol{\sigma'_{mem}}\})]$, by following the procedure described in Step 2.3 of Table C.1; - compute a first-order approximation of effective stress change for the current sub-step increment: $\{\Delta\boldsymbol{\sigma'^{(1)}}\} = [\boldsymbol{D}(\{\boldsymbol{\sigma'_{mem}}\})]\,\{\Delta\boldsymbol{\varepsilon_{ss}}^{(sup)}\}$; - update temporarily the effective stress state: $\{\boldsymbol{\sigma'}\} = \{\boldsymbol{\sigma'_{mem}}\} + \{\Delta\boldsymbol{\sigma'^{(1)}}\}$; - update void ratio: $e = e_{mem} - (1.0 + e_{init})\,\Delta\varepsilon_{ss,v}^{(sup)}$; - update the elastic constitutive matrix using the recently updated effective stress state and void ratio, $[\boldsymbol{D}(\{\boldsymbol{\sigma'}\})]$, by following the procedure described in Step 2.3 of Table C.1; - compute a second-order approximation of effective stress changes for the current sub-step increment: $\{\Delta\boldsymbol{\sigma'^{(2)}}\} = [\boldsymbol{D}(\{\boldsymbol{\sigma'}\})]\,\{\Delta\boldsymbol{\varepsilon_{ss}}^{(sup)}\}$; - compute a modified forward Euler approximation of effective stress change for the current sub-step increment: $\{\Delta\boldsymbol{\sigma'}\} = \left(\{\Delta\boldsymbol{\sigma'^{(1)}}\} + \{\Delta\boldsymbol{\sigma'^{(2)}}\}\right)/2.0$; - update the effective stress state: $\{\boldsymbol{\sigma'}\} = \{\boldsymbol{\sigma'_{mem}}\} + \{\Delta\boldsymbol{\sigma'}\}$. Determine the corresponding values of the yield conditions: $F_1 = \sqrt{(\{\boldsymbol{s}\} - p'\{\boldsymbol{\alpha}\}):(\{\boldsymbol{s}\} - p'\{\boldsymbol{\alpha}\})} - \sqrt{2.0/3.0}\; m\, p'$ where: $(\{\boldsymbol{s}\} - p'\{\boldsymbol{\alpha}\}):(\{\boldsymbol{s}\} - p'\{\boldsymbol{\alpha}\}) = \left(\sigma'_{xx} - p'(1.0 + \alpha_{xx})\right)^{2.0} + \left(\sigma'_{yy} - p'\left(1.0 + \alpha_{yy}\right)\right)^{2.0} + \left(\sigma'_{zz} - p'(1.0 + \alpha_{zz})\right)^{2.0} + 2.0\left(\tau_{xy} - p'\,\alpha_{xy}\right)^{2.0} + 2.0\,(\tau_{xz} - p'\,\alpha_{xz})^{2.0} + 2.0\left(\tau_{yz} - p'\,\alpha_{yz}\right)^{2.0}$ $F_2 = p'_{YS} - p'$ where: $p' = \dfrac{\sigma'_{xx} + \sigma'_{yy} + \sigma'_{zz}}{3.0}$

Table C.3 – Defining the input range for the Pegasus method.

Step	Description
3	If (*IYIELD* $= 1$ and $F_1 > YTOL$) or (*IYIELD* $= 2$ and $F_2 > YTOL$) or [*IYIELD* $= 3$ and ($F_1 > YTOL$ or $F_2 > YTOL$)] then: The effective stress point is located outside the yield surface(s) and, therefore, the search interval can be reduced. Update $\beta_{save} = \beta^{(sup)}$. Reduce the upper limit of the search range: $\beta^{(sup)} = 0.9\ \beta^{(sup)}$. Return to step 2. Else if (*IYIELD* $= 1$ and $F_1 < -YTOL$) or (*IYIELD* $= 2$ and $F_2 < -YTOL$) or [*IYIELD* $= 3$ and ($F_1 < -YTOL$ and $F_2 < -YTOL$)] then: The effective stress point is located inside both yield surfaces and, therefore, the actual value of $\beta^{(sup)}$ can be used as a lower limit for the search range of the Pegasus method. Update $\beta^{(inf)} = \beta^{(sup)}$. The value of β corresponding to the previous iteration defines the upper limit of the input range for the Pegasus method: $\beta^{(sup)} = \beta_{save}$. Go to step 4. Else if (*IYIELD* $= 1$ and $\lvert F_1 \rvert \leq -YTOL$) or (*IYIELD* $= 2$ and $\lvert F_2 \rvert \leq -YTOL$) or [*IYIELD* $= 3$ and ($\lvert F_1 \rvert \leq -YTOL$ and $F_2 < -YTOL$)] or [*IYIELD* $= 3$ and ($F_1 \leq -YTOL$ and $\lvert F_2 \rvert \leq -YTOL$)] or [*IYIELD* $= 3$ and ($\lvert F_1 \rvert \leq -YTOL$ and $\lvert F_2 \rvert \leq -YTOL$)] then: The intersection with one or both yield surface was found, meaning that $\beta^{(inf)} = \beta^{(sup)}$. Go to step 4. End if.
4	Exit with: - input range for the Pegasus method, $[\beta^{(inf)},\ \beta^{(sup)}]$; - the variable informing which yield condition is violated during elastic trial, *YIELD*.

(1) To reduce the computational cost of the constitutive model integration, an engineering representation (i.e. a covariant representation) is used for the strain and incremental strain tensors (i.e. their shear components are, respectively, given by $\gamma_{ij} = 2.0\ \varepsilon_{ij}$, and $\Delta\gamma_{ij} = 2.0\ \Delta\varepsilon_{ij}$, with $i \neq j$).

(2) Before proceeding to the yield surface intersection, the modified forward Euler scheme is used to estimate the effective stress change due to a purely elastic sub-step strain increment, $\{\Delta\boldsymbol{\varepsilon}_{ss}\}$, as described in Section C.1. During that previous calculation stage, the error resulting from stress integration is controlled to remain below a user-defined tolerance, *SSTOL*. Since the size of the sub-step strain increment used in the present routine, $\{\Delta\boldsymbol{\varepsilon}_{ss}{}^{(sup)}\} = \beta^{(sup)}\{\Delta\boldsymbol{\varepsilon}_{ss}\}$, where $\beta^{(sup)} \leq 1.0$, is smaller than that used in the main routine, $\{\Delta\boldsymbol{\varepsilon}_{ss}\}$, the error introduced in the present routine is expected to be smaller than that obtained in the previous calculation stage and, therefore, smaller than the user-defined tolerance, *SSTOL*. Therefore, in this routine, there is no error control.

Having defined the input range, the Pegasus method (Dowell and Jarratt, 1972) is applied to the estimation of the yield surface intersection, as suggested by Sloan *et al.* (2001). The required operations are comprehensively described in Table C.4.

Table C.4 – Application of the Pegasus method to the estimation of the yield surface intersection.

Step	Description
1	Enter with: - sub-step strain increment[(1)]: $\{\Delta\boldsymbol{\varepsilon}\} = \{\Delta\varepsilon_{xx} \quad \Delta\varepsilon_{yy} \quad \Delta\gamma_{xy} \quad \Delta\varepsilon_{zz} \quad \Delta\gamma_{xz} \quad \Delta\gamma_{yz}\}^{\mathrm{T}} = \{\Delta\varepsilon_{xx} \quad \Delta\varepsilon_{yy} \quad 2.0\,\Delta\varepsilon_{xy} \quad \Delta\varepsilon_{zz} \quad 2.0\,\Delta\varepsilon_{xz} \quad 2.0\,\Delta\varepsilon_{yz}\}^{\mathrm{T}}$; - effective stresses at the beginning of the increment, $\{\boldsymbol{\sigma'_{mem}}\} = \{\sigma'_{xx,\,mem} \quad \sigma'_{yy,\,mem} \quad \tau_{xy,\,mem} \quad \sigma'_{zz,\,mem} \quad \tau_{xz,\,mem} \quad \tau_{yz,\,mem}\}^{\mathrm{T}}$; - current effective stresses, $\{\boldsymbol{\sigma'}\} = \{\sigma'_{xx} \quad \sigma'_{yy} \quad \tau_{xy} \quad \sigma'_{zz} \quad \tau_{xz} \quad \tau_{yz}\}^{\mathrm{T}}$; - void ratio at the beginning of the increment: e_{mem}; - current void ratio, e; - current back-stress tensor, $\{\boldsymbol{\alpha}\} = \{\alpha_{xx} \quad \alpha_{yy} \quad \alpha_{xy} \quad \alpha_{zz} \quad \alpha_{xz} \quad \alpha_{yz}\}^{\mathrm{T}}$, which does not evolve during elastic trial, as well as the mean effective stress at secondary yield, p'_{YS}; - positions of the yield surfaces at the beginning of the sub-step increment, $F_{1,mem}$ and $F_{2,\,mem}$. - current positions of the yield surfaces, F_1 and F_2. - input range for the Pegasus method: $[\beta^{(inf)},\ \beta^{(sup)}]$; - variable informing which yield condition is violated during elastic trial, *YIELD*; - maximum number of iterations of this scheme, $N_{iter,max}$[(2)]. Initialise: - the sub-step strain increment reduction: $\beta = \beta_1 = \beta_2 = 1.0$; - the variable counting the number of iterations: $N_{iter} = 0$; - the variable counting how many times this routine needs to be performed: $NTIMES = 1$.
2	Update the variable counting the number of iterations: $N_{iter} = N_{iter} + 1$. Compute the values of the yield function corresponding to the lower and upper limits of β, by performing the following sub-steps:
2.1	Apply the modified forward Euler scheme[(1)] to estimate the effective stress change, $\{\Delta\boldsymbol{\sigma'}\}$, corresponding to the sub-step strain increment $\{\Delta\boldsymbol{\varepsilon_{ss}}^{(PM)}\} = \beta^{(inf)}\{\Delta\boldsymbol{\varepsilon_{ss}}\}$: - determine the elastic constitutive matrix corresponding to the beginning of the sub-step increment, $[\boldsymbol{D}(\{\boldsymbol{\sigma'_{mem}}\})]$, by following the procedure described in Step 2.3 of Table C.1; - compute a first-order approximation of effective stress change for the current sub-step increment: $\{\Delta\boldsymbol{\sigma'^{(1)}}\} = [\boldsymbol{D}(\{\boldsymbol{\sigma'_{mem}}\})]\,\{\Delta\boldsymbol{\varepsilon_{ss}}^{(PM)}\}$; - update temporarily the effective stress state: $\{\boldsymbol{\sigma'}\} = \{\boldsymbol{\sigma'_{mem}}\} + \{\Delta\boldsymbol{\sigma'^{(1)}}\}$; - update void ratio: $e = e_{mem} - (1.0 + e_{init})\,\Delta\varepsilon_{ss,v}^{(PM)}$; - update the elastic constitutive matrix using the recently updated effective stress state and void ratio, $[\boldsymbol{D}(\{\boldsymbol{\sigma'}\})]$, by following the procedure described in Step 2.3 of Table C.1; - compute a second-order approximation of effective stress changes for the current sub-step increment: $\{\Delta\boldsymbol{\sigma'^{(2)}}\} = [\boldsymbol{D}(\{\boldsymbol{\sigma'}\})]\,\{\Delta\boldsymbol{\varepsilon_{ss}}^{(PM)}\}$; - compute a modified forward Euler approximation of effective stress change for the current sub-step increment: $\{\Delta\boldsymbol{\sigma'}\} = (\{\Delta\boldsymbol{\sigma'^{(1)}}\} + \{\Delta\boldsymbol{\sigma'^{(2)}}\})/2.0$; - update the effective stress state: $\{\boldsymbol{\sigma'}\} = \{\boldsymbol{\sigma'_{mem}}\} + \{\Delta\boldsymbol{\sigma'}\}$. Determine the corresponding values of the yield conditions: $F_1 = \sqrt{(\{\boldsymbol{s}\} - p'\{\boldsymbol{\alpha}\}):(\{\boldsymbol{s}\} - p'\{\boldsymbol{\alpha}\})} - \sqrt{2.0/3.0}\ m\,p'$ where:

Table C.4 – Application of the Pegasus method to the estimation of the yield surface intersection.

Step	Description
	$(\{\boldsymbol{s}\} - p'\{\boldsymbol{\alpha}\}):(\{\boldsymbol{s}\} - p'\{\boldsymbol{\alpha}\})$ $= \left(\sigma'_{xx} - p'(1.0 + \alpha_{xx})\right)^{2.0} + \left(\sigma'_{yy} - p'\left(1.0 + \alpha_{yy}\right)\right)^{2.0}$ $+ \left(\sigma'_{zz} - p'(1.0 + \alpha_{zz})\right)^{2.0} + 2.0\left(\tau_{xy} - p'\,\alpha_{xy}\right)^{2.0} + 2.0\,(\tau_{xz} - p'\,\alpha_{xz})^{2.0}$ $+ 2.0\left(\tau_{yz} - p'\,\alpha_{yz}\right)^{2.0}$ $F_2 = p'_{YS} - p'$ where: $p' = \dfrac{\sigma'_{xx} + \sigma'_{yy} + \sigma'_{zz}}{3.0}$
2.2	If *IYIELD* $= 1$ or (*IYIELD* $= 3$ and *NTIMES* $= 1$) then: Save $F^{(inf)} = F_1$. Repeat the operations described in step 2.1 for the sub-step strain increment $\{\Delta\boldsymbol{\varepsilon_{ss}}^{(PM)}\} = \beta^{(sup)}\{\Delta\boldsymbol{\varepsilon_{ss}}\}$. Save $F^{(sup)} = F_1$. Else if *IYIELD* $= 2$ or (*IYIELD* $= 3$ and *NTIMES* $= 2$) then: Save $F^{(inf)} = F_2$. Repeat the operations described in step 2.1 for the sub-step strain increment $\{\Delta\boldsymbol{\varepsilon_{ss}}^{(PM)}\} = \beta^{(sup)}\{\Delta\boldsymbol{\varepsilon_{ss}}\}$. Save $F^{(sup)} = F_2$. End if.
3	If $N_{iter} \leq N_{iter,max}$ then: Compute a new value for β by linear interpolation: $\beta = \beta^{(sup)} - F^{(sup)}\dfrac{\beta^{(sup)} - \beta^{(inf)}}{F^{(sup)} - F^{(inf)}}$ Apply the modified forward Euler scheme[1] to estimate the effective stress change, $\{\Delta\boldsymbol{\sigma'}\}$, corresponding to the sub-step strain increment $\{\Delta\boldsymbol{\varepsilon_{ss}}^{(PM)}\} = \beta\{\Delta\boldsymbol{\varepsilon_{ss}}\}$:, by following a similar procedure to that described in step 2.1. Determine the corresponding values of the yield conditions: $F_1 = \sqrt{(\{\boldsymbol{s}\} - p'\{\boldsymbol{\alpha}\}):(\{\boldsymbol{s}\} - p'\{\boldsymbol{\alpha}\})} - \sqrt{2.0/3.0}\ m\,p'$ $F_2 = p'_{YS} - p'$ End if.
4	If *IYIELD* $= 1$ and $\lvert F_1\rvert \leq$ *YTOL* then: The intersection with the yield surface was found. Set $\beta_1 = \beta_2 = \beta$. Go to step 5. Else if *IYIELD* $= 2$ and $\lvert F_2\rvert \leq$ *YTOL* then: The intersection with the yield surface was found. Set $\beta_1 = \beta_2 = \beta$. Go to step 5. Else if *IYIELD* $= 3$ and *NTIMES* $= 1$ and $\lvert F_1\rvert \leq$ *YTOL* then: The intersection with the yield surface was found. Set $\beta_1 = \beta$. Set $N_{iter} = 0$ and *NTIMES* $=$ *NTIMES* $+ 1$. Return to step 2. Else if *IYIELD* $= 3$ and *NTIMES* $= 2$ and $\lvert F_2\rvert \leq$ *YTOL* then: The intersection with the yield surface was found. Set $\beta_2 = \beta$.

Table C.4 – Application of the Pegasus method to the estimation of the yield surface intersection.

Step	Description
	Determine $\beta = min\{\beta_1,\ \beta_2\}$.
	Apply the modified forward Euler scheme(1) to estimate the effective stress change, $\{\Delta\boldsymbol{\sigma}'\}$, corresponding to the sub-step strain increment $\{\Delta\boldsymbol{\varepsilon_{ss}}^{(PM)}\} = \beta\{\Delta\boldsymbol{\varepsilon_{ss}}\}$, by following a similar procedure to that described in step 2.1.
	Determine the corresponding values of the yield conditions:
	$F_1 = \sqrt{(\{\boldsymbol{s}\} - p'\{\boldsymbol{\alpha}\}):(\{\boldsymbol{s}\} - p'\{\boldsymbol{\alpha}\})} - \sqrt{2.0/3.0}\ m\,p'$
	$F_2 = p'_{YS} - p'$
	Go to step 5.
	End if.
	If $N_{iter} \leq N_{iter,max}$ then:
	Set new values and proceed to a new iteration:
	If $IYIELD = 1$ then:
	Set $F^{(int)} = F_1$.
	Else if $IYIELD = 2$ then:
	Set $F^{(int)} = F_2$.
	Else if $IYIELD = 3$ and $NTIMES = 1$ then:
	Set $F^{(int)} = F_1$.
	Else if $IYIELD = 3$ and $NTIMES = 2$ then:
	Set $F^{(int)} = F_2$.
	End if.
	If $F^{(int)}\ F^{(sup)} < 0.0$, then:
	Set $\beta^{(inf)} = \beta$ and $F^{(inf)} = F^{(int)}$
	Else
	And scale down the value of $F^{(inf)}$ to prevent the retention of an end-point (Dowell and Jarratt, 1972):
	$F^{(inf)} = F^{(inf)}\ \dfrac{F^{(sup)}}{F^{(int)} + F^{(sup)}}$
	Set $\beta^{(sup)} = \beta$ and $F^{(sup)} = F^{(int)}$
	End if.
	Return to step 2.
	Else if $N_{iter} = N_{iter,max}$ then:
	The maximum number of iterations were reached. Print an error message and stop.
	End if.
5	Exit with:
	- the portion of the sub-step strain increment, which is purely elastic, $\beta = min\{\beta_1,\ \beta_2\}$;
	- the effective stress state, $\{\boldsymbol{\sigma}'\}$, lying on the yield surface and the corresponding sub-step effective stress increment, $\{\Delta\boldsymbol{\sigma}'\}$;
	- current elastic constitutive matrix, $[\boldsymbol{D}(\{\boldsymbol{\sigma}'\})]$;
	- current positions of the yield surfaces, F_1 and F_2.

(1) See notes of Table C.3.

(2) In all numerical simulations performed in the present study, $N_{iter} = 100$ was adopted. It should be noted, however, that, in general, a very fast convergence involving less than 5 iterations was achieved.

C.4 Correction of yield surface drift by projecting back

Table C.5 describes the algorithm used to correct the yield surface drift, proposed by Potts and Gens (1985), Potts and Zdravkovic (1999) and (Sloan *et al.*, 2001).

Table C.5 – Yield surface drift correction scheme.

Step	Description
1	Enter with: - sub-step strain increment [1]: $\{\Delta\boldsymbol{\varepsilon}\} = \{\Delta\varepsilon_{xx} \quad \Delta\varepsilon_{yy} \quad \Delta\gamma_{xy} \quad \Delta\varepsilon_{zz} \quad \Delta\gamma_{xz} \quad \Delta\gamma_{yz}\}^{\mathrm{T}} = \{\Delta\varepsilon_{xx} \quad \Delta\varepsilon_{yy} \quad 2.0\,\Delta\varepsilon_{xy} \quad \Delta\varepsilon_{zz} \quad 2.0\,\Delta\varepsilon_{xz} \quad 2.0\,\Delta\varepsilon_{yz}\}^{\mathrm{T}}$; - current effective stresses, $\{\boldsymbol{\sigma'}\} = \{\sigma'_{xx} \quad \sigma'_{yy} \quad \tau_{xy} \quad \sigma'_{zz} \quad \tau_{xz} \quad \tau_{yz}\}^{\mathrm{T}}$; - current void ratio, e; - current elastic strains: $\{\boldsymbol{\varepsilon^e}\} = \{\varepsilon^e_{xx} \quad \varepsilon^e_{yy} \quad \gamma^e_{xy} \quad \varepsilon^e_{zz} \quad \gamma^e_{xz} \quad \gamma^e_{yz}\}^{\mathrm{T}}$; - plastic strains associated with the primary and secondary yield surfaces, respectively: $\{\boldsymbol{\varepsilon^p_1}\} = \{\varepsilon^p_{xx,1} \quad \varepsilon^p_{yy,1} \quad \gamma^p_{xy,1} \quad \varepsilon^p_{zz,1} \quad \gamma^p_{xz,1} \quad \gamma^p_{yz,1}\}^{\mathrm{T}}$ and $\{\boldsymbol{\varepsilon^p_2}\} = \{\varepsilon^p_{xx,2} \quad \varepsilon^p_{yy,2} \quad \gamma^p_{xy,2} \quad \varepsilon^p_{zz,2} \quad \gamma^p_{xz,2} \quad \gamma^p_{yz,2}\}^{\mathrm{T}}$; - elastic state parameters: effective stresses and strains at last shear reversal, $\{\boldsymbol{\sigma'^{SR}}\} = \{\sigma'^{SR}_{xx} \quad \sigma'^{SR}_{yy} \quad \tau^{SR}_{xy} \quad \sigma'^{SR}_{zz} \quad \tau^{SR}_{xz} \quad \tau^{SR}_{yz}\}^{\mathrm{T}}$ and $\{\boldsymbol{\varepsilon^{SR}}\} = \{\varepsilon^e_{xx} \quad \varepsilon^e_{yy} \quad \gamma^e_{xy} \quad \varepsilon^e_{zz} \quad \gamma^e_{xz} \quad \gamma^e_{yz}\}^{\mathrm{T}}$, respectively; void ratio at last shear reversal, e^{SR}, and the scaling factor, N; - plastic state parameters: back-stress tensor, $\{\boldsymbol{\alpha}\} = \{\alpha_{xx} \quad \alpha_{yy} \quad \alpha_{xy} \quad \alpha_{zz} \quad \alpha_{xz} \quad \alpha_{yz}\}^{\mathrm{T}}$; isotropic and deviatoric components of the stress-induced anisotropy tensor, respectively, f_p and $\{\boldsymbol{f}\} = \{f_{xx} \quad f_{yy} \quad f_{xy} \quad f_{zz} \quad f_{xz} \quad f_{yz}\}^{\mathrm{T}}$, as well as the rate of evolution, H, and constant C; - current elastic constitutive matrix, $[\boldsymbol{D}]$; - current deviatoric loading direction, $\{\boldsymbol{n}\}$, and the modified Lode's angle, θ; - current distance from the current stress point to the bounding surface, $\{\boldsymbol{\alpha^b}\}$; - current positions of the primary and secondary yield surfaces, F_1 and F_2, respectively, as well as corresponding gradients, $\{\partial F_1/\partial\boldsymbol{\sigma'}\}$ and $\{\partial F_2/\partial\boldsymbol{\sigma'}\}$; - current gradients of the plastic potentials associated with the primary and secondary yield surfaces, $\{\partial\boldsymbol{P_1}/\partial\boldsymbol{\sigma'}\}$ and $\{\partial\boldsymbol{P_2}/\partial\boldsymbol{\sigma'}\}$, respectively; - current values of h_A, h_b, h_e, h_f and h_g, as well as current hardening moduli associated with the primary and secondary yield surfaces, A_1 and A_2, respectively; - variable informing which yield condition is active: $IYIELD = 1$ when only the primary yield surface is active; $IYIELD = 2$ when only the secondary yield surface is active; $IYIELD = 3$ when both yield surfaces are active; - maximum number of iterations of this scheme, $N_{iter,max}$ [2]. Store temporarily: $\{\boldsymbol{\sigma'_{temp}}\} = \{\boldsymbol{\sigma'}\}$; $\{\boldsymbol{\varepsilon^e_{temp}}\} = \{\boldsymbol{\varepsilon^e}\}$; $\{\boldsymbol{\varepsilon^p_{1,temp}}\} = \{\boldsymbol{\varepsilon^p_1}\}$; $\{\boldsymbol{\varepsilon^p_{2,temp}}\} = \{\boldsymbol{\varepsilon^p_2}\}$; $\{\boldsymbol{\alpha_{temp}}\} = \{\boldsymbol{\alpha}\}$; $f_{p,temp} = f_p$ and $\{\boldsymbol{f_{temp}}\} = \{\boldsymbol{f}\}$; $C_{temp} = C$; $F_{1,temp} = F_1$ and $F_{2,temp} = F_2$. Initialise the variable counting the number of iterations: $N_{iter} = 0$.
2	Update the variable counting the number of iterations: $N_{iter} = N_{iter} + 1$. Obtain an estimation for the correction to be applied to the plastic multipliers [3]: If $IYIELD = 1$ then: $\lambda_{1,cor} = \dfrac{F_1}{\left\{\dfrac{\partial F_1}{\partial\boldsymbol{\sigma'}}\right\}^{\mathrm{T}} [\boldsymbol{D}] \left\{\dfrac{\partial\boldsymbol{P_1}}{\partial\boldsymbol{\sigma'}}\right\} + A_1}$

Table C.5 – Yield surface drift correction scheme.

Step	Description

$\lambda_{2,cor} = 0.0$

Else if *IYIELD* $= 2$ then:

$\lambda_{1,cor} = 0.0$

$$\lambda_{2,cor} = \frac{F_2}{\left\{\frac{\partial F_2}{\partial \boldsymbol{\sigma'}}\right\}^{\mathrm{T}} [\boldsymbol{D}] \left\{\frac{\partial \boldsymbol{P_2}}{\partial \boldsymbol{\sigma'}}\right\} + A_2}$$

Else if *IYIELD* $= 3$ then:

$$\lambda_{1,cor} = \frac{L_{22}\, F_1 - L_{12}\, F_2}{L_{11}\, L_{22} - L_{12}\, L_{21}}$$

$$\lambda_{2,cor} = \frac{L_{11}\, F_2 - L_{21}\, F_1}{L_{11}\, L_{22} - L_{12}\, L_{21}}$$

where:

$$L_{11} = \left\{\frac{\partial F_1}{\partial \boldsymbol{\sigma'}}\right\}^{\mathrm{T}} [\boldsymbol{D}] \left\{\frac{\partial \boldsymbol{P_1}}{\partial \boldsymbol{\sigma'}}\right\} + A_1$$

$$L_{12} = \left\{\frac{\partial F_1}{\partial \boldsymbol{\sigma'}}\right\}^{\mathrm{T}} [\boldsymbol{D}] \left\{\frac{\partial \boldsymbol{P_2}}{\partial \boldsymbol{\sigma'}}\right\}$$

$$L_{21} = \left\{\frac{\partial F_2}{\partial \boldsymbol{\sigma'}}\right\}^{\mathrm{T}} [\boldsymbol{D}] \left\{\frac{\partial \boldsymbol{P_1}}{\partial \boldsymbol{\sigma'}}\right\}$$

$$L_{22} = \left\{\frac{\partial F_2}{\partial \boldsymbol{\sigma'}}\right\}^{\mathrm{T}} [\boldsymbol{D}] \left\{\frac{\partial \boldsymbol{P_2}}{\partial \boldsymbol{\sigma'}}\right\} + A_2$$

End if.

Correct the effective stresses [3]:

$$\{\Delta\boldsymbol{\sigma'}\} = -\lambda_{1,cor} [\boldsymbol{D}] \left\{\frac{\partial \boldsymbol{P_1}}{\partial \boldsymbol{\sigma'}}\right\} - \lambda_{2,cor} [\boldsymbol{D}] \left\{\frac{\partial \boldsymbol{P_2}}{\partial \boldsymbol{\sigma'}}\right\}$$

$$\{\boldsymbol{\sigma'}\} = \{\boldsymbol{\sigma'}\} + \{\Delta\boldsymbol{\sigma'}\}$$

Correct the plastic strains associated with the primary and secondary yield surfaces [3]:

$$\{\Delta\boldsymbol{\varepsilon_1^p}\} = \lambda_{1,cor} \left\{\frac{\partial \boldsymbol{P_1}}{\partial \boldsymbol{\sigma'}}\right\}$$

$$\left\{\boldsymbol{\varepsilon_1^p}\right\} = \left\{\boldsymbol{\varepsilon_1^p}\right\} + \{\Delta\boldsymbol{\varepsilon_1^p}\}$$

$$\{\Delta\boldsymbol{\varepsilon_2^p}\} = \lambda_{2,cor} \left\{\frac{\partial \boldsymbol{P_2}}{\partial \boldsymbol{\sigma'}}\right\}$$

$$\left\{\boldsymbol{\varepsilon_2^p}\right\} = \left\{\boldsymbol{\varepsilon_2^p}\right\} + \{\Delta\boldsymbol{\varepsilon_2^p}\}$$

Assuming that the total strains remain constant, correct the elastic strains [3]:

$$\{\Delta\boldsymbol{\varepsilon^e}\} = -\{\Delta\boldsymbol{\varepsilon_1^p}\} - \{\Delta\boldsymbol{\varepsilon_2^p}\} = -\lambda_{1,cor} \left\{\frac{\partial \boldsymbol{P_1}}{\partial \boldsymbol{\sigma'}}\right\} - \lambda_{2,cor} \left\{\frac{\partial \boldsymbol{P_2}}{\partial \boldsymbol{\sigma'}}\right\}$$

$$\{\boldsymbol{\varepsilon^e}\} = \{\boldsymbol{\varepsilon^e}\} + \{\Delta\boldsymbol{\varepsilon^e}\}$$

Correct the back-stress tensor:

$$\{\Delta\boldsymbol{\alpha}\} = \lambda_{1,cor}\, h_A\, h_b\, h_e\, h_f\, h_g \left(\left\{\boldsymbol{\alpha^b}\right\} - \{\boldsymbol{\alpha}\}\right)$$

$$\{\boldsymbol{\alpha}\} = \{\boldsymbol{\alpha}\} + \{\Delta\boldsymbol{\alpha}\}$$

Correct the isotropic and deviatoric components of the stress-induced anisotropy tensor:

$$\Delta f_p = H\, \Delta\varepsilon_v^p$$

$$f_p = f_{p,temp} + \Delta f_p$$

$$\{\Delta\boldsymbol{f}\} = -H \langle -\Delta\varepsilon_v^p \rangle [C \{\boldsymbol{n}\} + \{\boldsymbol{f}\}]$$

$$\{\boldsymbol{f}\} = \{\boldsymbol{f}\} + \{\Delta\boldsymbol{f}\}$$

Table C.5 – Yield surface drift correction scheme.

Step	Description
	where: $\Delta\varepsilon_v^p = \Delta\varepsilon_{v,1}^p + \Delta\varepsilon_{v,2}^p = \Delta\varepsilon_{xx,1}^p + \Delta\varepsilon_{yy,1}^p + \Delta\varepsilon_{zz,1}^p + \Delta\varepsilon_{xx,2}^p + \Delta\varepsilon_{yy,2}^p + \Delta\varepsilon_{zz,2}^p$ If $\left\|f_p\right\|^{2.0} > C$ then: $C = \left\|f_p\right\|^{2.0}$ End if
3	Update the positions of the primary and secondary yield surfaces, respectively: $F_1 = \sqrt{(\{\boldsymbol{s}\} - p'\{\boldsymbol{\alpha}\}):(\{\boldsymbol{s}\} - p'\{\boldsymbol{\alpha}\})} - \sqrt{2.0/3.0}\ m\,p'$ where: $(\{\boldsymbol{s}\} - p'\{\boldsymbol{\alpha}\}):(\{\boldsymbol{s}\} - p'\{\boldsymbol{\alpha}\})$ $= \left(\sigma'_{xx} - p'(1.0 + \alpha_{xx})\right)^{2.0} + \left(\sigma'_{yy} - p'\left(1.0 + \alpha_{yy}\right)\right)^{2.0}$ $+ \left(\sigma'_{zz} - p'(1.0 + \alpha_{zz})\right)^{2.0} + 2.0\left(\tau_{xy} - p'\,\alpha_{xy}\right)^{2.0} + 2.0\,(\tau_{xz} - p'\,\alpha_{xz})^{2.0}$ $+ 2.0\left(\tau_{yz} - p'\,\alpha_{yz}\right)^{2.0}$ $F_2 = p'_{YS} - p'$ where: $p' = \dfrac{\sigma'_{xx} + \sigma'_{yy} + \sigma'_{zz}}{3.0}$ Check whether the corrected effective stress state, $\{\boldsymbol{\sigma}'\}$, lies on the active yield surface(s): If ($IYIELD = 1$ and $\|F_1\| \le YTOL$) or ($IYIELD = 2$ and $\|F_2\| \le YTOL$) or ($IYIELD = 3$ and $\|F_1\| \le YTOL$ and $\|F_2\| \le YTOL$) then: A solution has been found. Move to step 4. Else if ($IYIELD = 1$ and $\|F_1\| < \left\|F_{1,temp}\right\|$) or ($IYIELD = 2$ and $\|F_2\| < \left\|F_{2,temp}\right\|$) or ($IYIELD = 3$ and $\sqrt{{F_1}^{2.0} + {F_2}^{2.0}} < \sqrt{{F_{1,temp}}^{2.0} + {F_{2,temp}}^{2.0}}$) then: A solution has not been found yet. Nevertheless, the effective stress state is now closer to the active yield surface(s) than before correction. If $N_{iter} < N_{iter,max}$ then: Using the updated values of $\{\boldsymbol{\sigma}'\}$, $\{\boldsymbol{\alpha}\}$, f_p and $\{\boldsymbol{f}\}$ and the equations previously presented in Step 3.2 of Table C.1, update the following quantities: - the small-strain shear modulus, G_{max}, the tangent shear modulus, G_{tan}, the tangent bulk modulus, K_{tan}, and finally the elastic constitutive matrix, $[\boldsymbol{D}]$; - the radial tensor, $\{\bar{\boldsymbol{r}}\}$, the deviatoric loading direction, $\{\boldsymbol{n}\}$, and the modified Lode's angle, θ; - the inherent anisotropic state variable, A_F, the distance from the current stress point to the critical surface, d^c, the reference distance to the critical surface, d^c_{ref}, the void ratio at CSL, e_{CS}, and the state parameter, ψ; - the distance from the current stress point to the dilatancy and bounding surfaces, d^d and d^b, respectively, as well as the reference distance to the bounding surface, d^b_{ref}; - the positions of the primary and secondary yield surfaces, F_1 and F_2, respectively, and the corresponding gradients, $\{\partial F_1/\partial\boldsymbol{\sigma}'\}$ and $\{\partial F_2/\partial\boldsymbol{\sigma}'\}$, respectively;

Table C.5 – Yield surface drift correction scheme.

Step	Description
	- the gradients of the plastic potentials associated with the primary and secondary yield surfaces, $\{\partial \boldsymbol{P_1}/\partial \boldsymbol{\sigma'}\}$ and $\{\partial \boldsymbol{P_2}/\partial \boldsymbol{\sigma'}\}$, respectively; - the hardening moduli associated with the primary and secondary yield surfaces, A_1 and A_2, respectively. Return to step 2. Else: Maximum number of iterations was reached. Print a warning message and move to step 4. End if.
	Else: Divergence occurred. Abandon the previous correction by setting: $\{\boldsymbol{\sigma'}\} = \{\boldsymbol{\sigma'_{temp}}\}$; $\{\boldsymbol{\varepsilon^e}\} = \{\boldsymbol{\varepsilon^e_{temp}}\}$; $\{\boldsymbol{\varepsilon^p_1}\} = \{\boldsymbol{\varepsilon^p_{1,temp}}\}$; $\{\boldsymbol{\varepsilon^p_2}\} = \{\boldsymbol{\varepsilon^p_{2,temp}}\}$; $\{\boldsymbol{\alpha}\} = \{\boldsymbol{\alpha_{temp}}\}$; $f_p = f_{p,temp}$ and $\{\boldsymbol{f}\} = \{\boldsymbol{f_{temp}}\}$; $C = C_{temp}$; $F_{1,temp} = F_1$ and $F_{2,temp} = F_2$. Print an error message and move to step 4. End if.
4	Exit with: - corrected effective stresses, elastic and plastic strains: $\{\boldsymbol{\sigma'}\}$, $\{\boldsymbol{\varepsilon^e}\}$, $\{\boldsymbol{\varepsilon^p_1}\}$ and $\{\boldsymbol{\varepsilon^p_2}\}$, respectively. - current elastic strains: $\{\boldsymbol{\varepsilon^e}\} = \{\varepsilon^e_{xx} \quad \varepsilon^e_{yy} \quad \gamma^e_{xy} \quad \varepsilon^e_{zz} \quad \gamma^e_{xz} \quad \gamma^e_{yz}\}^{\mathrm{T}}$; - corrected plastic state parameters: corrected back-stress tensor, $\{\boldsymbol{\alpha}\}$, corrected isotropic and deviatoric components of the stress-induced anisotropy tensor, f_p and $\{\boldsymbol{f}\}$, respectively, as well corrected constant C; - updated positions of the yield surfaces, F_1 and F_2.

(1) See notes of Table C.3.

(2) In all numerical simulations performed in the present study, $N_{iter} = 100$ was adopted. It should be noted, however, that, in general, a very fast convergence involving less than 10 iterations was achieved.

(3) To compute the plastic multipliers, as well as the elasto-plastic constitutive matrix using matrix operations (rather than tensorial operations), the derivatives of the yield surfaces, as well as the gradients of the plastic potential need to be represented in covariant coordinates. In such case, the deviatoric components of these tensors, stored in a vector, need to be scaled by 2.0. For the present constitutive model, it means that: $\{\partial F_1/\partial \tau_{xy}\} = 2.0\, n_{xy}$; $\{\partial F_1/\partial \tau_{xz}\} = 2.0\, n_{xz}$; $\{\partial F_1/\partial \tau_{yz}\} = 2.0\, n_{yz}$; $\{\partial P_1/\partial \tau_{xy}\} = 2.0\, n_{xy}$; $\{\partial P_1/\partial \tau_{xz}\} = 2.0\, n_{xz}$; $\{\partial P_1/\partial \tau_{yz}\} = 2.0\, n_{yz}$. Similarly, to compute the plastic strain change, covariant representation of the gradients of the plastic potential are required.

Appendix D INFLUENCE OF TIME STEP AND ELEMENT SIZE ON SITE RESPONSE ANALYSIS INVOLVING CYCLIC MOBILITY OF HOSTUN SAND

D.1 Introduction

When performing a dynamic analysis, it is important to ensure that the adopted spatial and time discretisation's are adequate to the simulation of the range of frequencies relevant to the boundary-value problem under analysis. Starting with the spatial discretisation, based on the outcome of a series of 2D plane strain finite element (FE) analyses using four-noded quadrangular elements with a single Gauss point (i.e. using linear interpolation) and concerning the propagation of compressional waves through a homogeneous elastic medium, Kuhlemeyer and Lysmer (1973) suggested that the accurate replication of deformations induced by the propagation of the waves required the use of elements with size, ΔL, smaller than $\lambda/10$ to $\lambda/8$, where λ is wavelength of the simulated wave (given by the ratio of its velocity of propagation to its frequency). As pointed by Bathe (1996), when using eight-noded quadrangular elements with nine Gauss points (such as those employed in all FE analyses performed in the present research), since the distance between nodes of the element is reduced to half, the empirical guideline established by Kuhlemeyer and Lysmer (1973) may be adapted to $\Delta L \leq \lambda/5$ to $\lambda/4$. Moreover, given that the velocity of the body wave, v, may vary during the analysis (which is typically the case, due to the non-linear response of soil), and the body wave may be characterised by more than a single frequency, the minimum reproducible velocity, v_{min}, of a body wave can be written as a function of the adopted ΔL, as given by Equation D.1.

$$\Delta L \leq \frac{\lambda}{4-5} \Longrightarrow \lambda_{min} \approx 4-5\,\Delta L \Leftrightarrow v_{min} \approx 4-5\,f_{max}\,\Delta L \tag{D.1}$$

where λ_{min} is the shortest wavelength and f_{max} is the highest frequency relevant to the problem under analysis.

In relation to the time step used in the analysis, it should be small enough to describe properly the propagation of the wave through soil. According to Bathe (1996) and Grazina (2009), accurate results are, in general, obtained when the Courant–Friedrichs–Lewy (CFL) condition is satisfied. This condition establishes that the time step, Δt, used in a FE analysis should be smaller than that required by a body wave to travel from a given node to an adjacent one (in other words, for a given step, a body wave should not be allowed to travel a distance greater than two adjacent nodes of the mesh). For eight-noded quadrangular elements, such as those used in the present research, this condition can be written as:

$$\Delta t \leq \frac{\Delta L}{2\,v} \Leftrightarrow v \leq \frac{\Delta L}{2\,\Delta t} \Longrightarrow v_{max} \approx \frac{\Delta L}{2\,\Delta t} \tag{D.2}$$

where v_{max} is the maximum reproducible body wave velocity.

Regarding Equation D.2, two aspects are particularly worth mentioning: (1) the adequate time step depends on the selected element size and, therefore, the evaluation of the impact of these aspects on the modelled response should be assessed concurrently; (2) a linear relationship between both quantities (i.e. time step and element size) is established by the CFL condition, suggesting that a very fine mesh requires, in principle, a very small time step, which might lead to prohibitive computational resources. This suggests that the selection of an appropriate element size is a crucial aspect of a dynamic FE analysis.

It should be noted that, for a time integration scheme providing only conditional stability (e.g. Newmark method with $\alpha \geq 1/2$ and $\beta < \alpha/2$, which, to be clear, was never used in the present research), a time step smaller than that required by the scheme to provide a stable solution should be employed, as detailed in Grazina (2009). In the present parametric study, as well as in the numerical simulations whose results are presented in Chapter 8, the generalised-α method, proposed by Chung and Hulbert (1993) and implemented into FEMEPDYN by Grazina (2009), was employed with the following set of parameters: $\alpha_f = 4/9$, $\alpha_m = 3\alpha_f - 1 = 1/3$, $\alpha = \left(1 - \alpha_f\right)^2 \approx 0.3086$ and $\beta = 3/2 - 2\alpha_f \approx 0.6111$, which results in a spectral radius at infinity $\rho_\infty = 0.80$ for a single degree of freedom (SDOF) oscillator (Grazina, 2009). As detailed by this author, when using this set of parameters, the method ensures unconditional stability and second order accuracy, also achieving the optimal high frequency dissipation with minimal low frequency impact.

Although the empirical guidelines defined by Equation D.1 and D.2 are often employed to define the element size and time step to be used in the simulation of dynamic problems, it should be highlighted that these guidelines were, in general, developed based on simplified loading and geometry conditions, as well as considering a limited degree of non-linearity for soil response. As such, there is little guarantee that these guidelines are applicable for boundary-value problems involving liquefaction-related phenomena (Taborda, 2011). Furthermore, the adequate choice of element size and time step to be used in a given dynamic analysis may depend on the numerical algorithms implemented into a given FE code (Bathe, 1996; Grazina, 2009; Taborda, 2011). It was, therefore, decided to perform a parametric study to evaluate the influence of these two aspects on the modelled cyclic response of Hostun sand. Note that, although it would have been possible to use the geometry of centrifuge model A (CM-A) – see Chapter 8 –, excessive computational resources would have likely been required to perform several computations, some of them employing very small element sizes and time steps. Therefore, it was decided to perform 1D site response analyses (i.e. considering a level ground deposit of moderately loose Hostun sand having no structure on top of it, subjected to a dynamic motion at its base) employing three different element sizes (and, consequently, three different meshes), as well as three different time steps, resulting in a total of nine different computations. As detailed in Section 5.3.2.2.3, this type of problem

can be simulated using a single column of elements with both solid and fluid displacement degrees of freedom, as well as pore pressure degree of freedom tied at each level of the mesh (Figure D.1), therefore greatly reducing the computational effort required in the analysis.

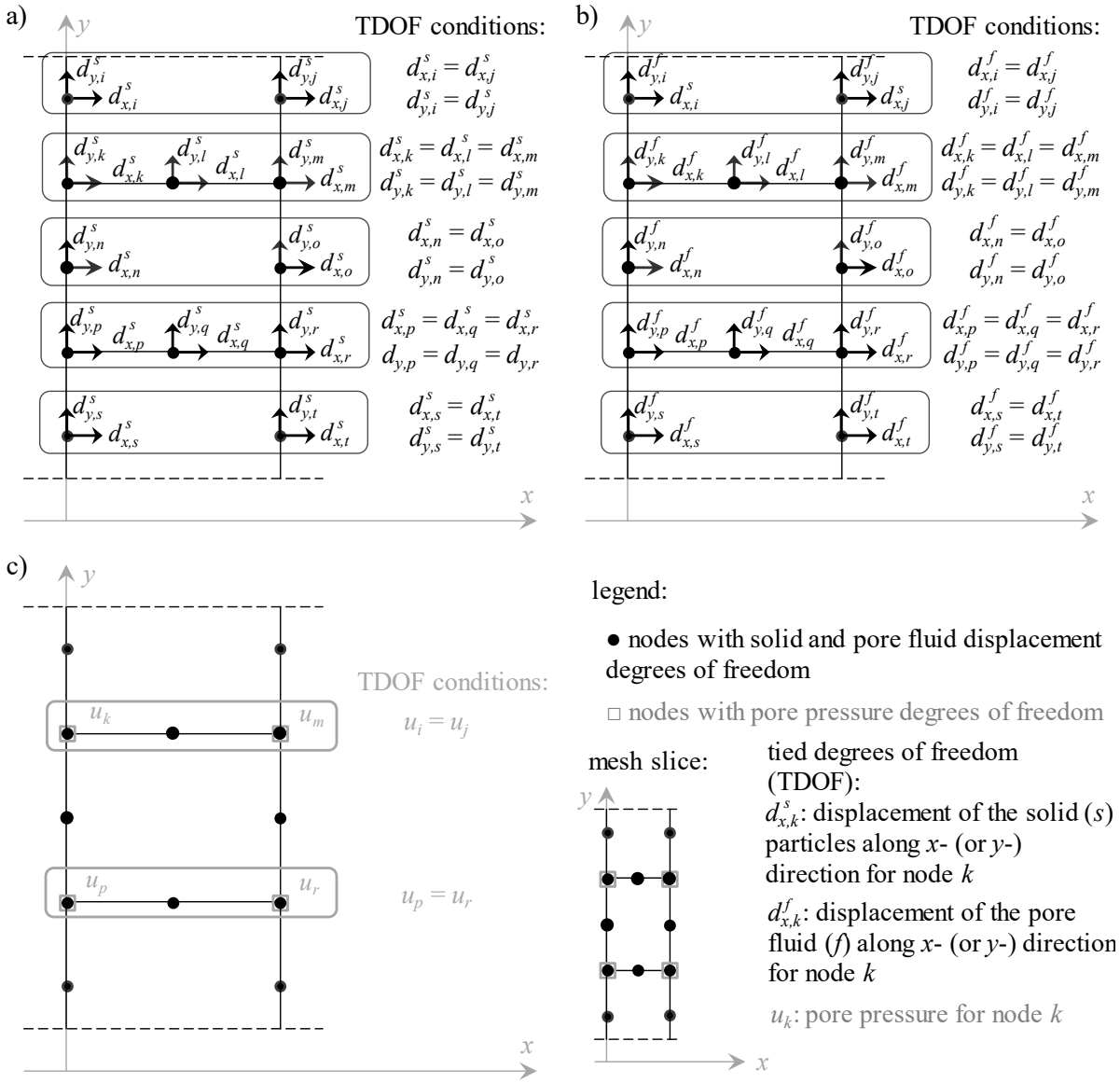

Figure D.1 – Schematic illustration of tied degrees of freedom for: a) solid displacement degrees of freedom and b) pore fluid displacement degrees of freedom and c) pore pressure degrees of freedom.

In the following section, the main characteristics of the conducted numerical analyses are described. Subsequently, the results of the conducted numerical analyses are compared in terms of evolution of excess pore pressure with time at several positions of the deposit, horizontal acceleration time-histories and corresponding Fourier spectra at ground surface, surface settlement evolution with time and computational cost. Lastly, a summary of the obtained results and reached conclusions is provided.

D.2 Characteristics of the performed finite element analyses

Table D.1 summarises the main characteristics of the mesh (in terms of element size, ΔL, and number of elements, n_{elem}, required to model the total thickness, H, of the deposit of Hostun sand), as well as the time step, Δt, and corresponding number of steps, n_{steps}, required to compute the total duration, T, of the analysis. The minimum and maximum reproducible shear wave velocities, $v_{s,min}$ and $v_{s,max}$, respectively, determined according to the guidelines provided in the literature (Equations D.1 and D.2, respectively), are also indicated in the table.

Table D.1 – Spatial and time discretisation used in the parametric study and its relation to the empirical guidelines proposed in the literature.

Computation ID	1 m0.5 / dt0.0025	2 m0.5 / dt0.00625	3 m0.5 / dt0.0125	4 m1.0 / dt0.0025	5 m1.0 / dt0.0125	6 m1.0 / dt0.0625	7 m1.5 / dt0.0025	8 m1.5 / dt0.0125	9 m1.5 / dt0.01875
Mesh	m0.5	m0.5	m0.5	m1.0	m1.0	m1.0	m1.5	m1.5	m1.5
ΔL (m)	0.5	0.5	0.5	1.0	1.0	1.0	1.5	1.5	1.5
H (m)	18.0	18.0	18.0	18.0	18.0	18.0	18.0	18.0	18.0
n_{elem} ( )	36	36	36	18	18	18	12	12	12
$f_{1,input}$ (Hz) (1)	1.0	1.0	1.0	1.0	1.0	1.0	1.0	1.0	1.0
$v_{s,min}$ (m/s) (2)	1.9	1.9	1.9	3.9	3.9	3.9	5.8	5.8	5.8
Δt (s)	0.0025	0.00625	0.0125	0.0025	0.0125	0.0625	0.0025	0.0125	0.01875
T (s) (3)	250.0	250.0	250.0	250.0	250.0	250.0	250.0	250.0	250.0
n_{steps} ( )	100000	20000	20000	100000	20000	4000	100000	20000	1333
$v_{s,max}$ (m/s) (4)	100.0	40.0	20.0	200.0	40.0	8.0	300.0	60.0	40.0

(1) The predominant frequency of the input motion applied in the dynamic centrifuge experiments presented in Chapter 8 was considered; (2) computed from Equation D.1; (3) duration of the input motion applied in the dynamic centrifuge experiments presented in Chapter 8; (4) computed from Equation D.2.

Given the predominant frequency of the input acceleration time-history intended to be applied to both CM-A and CM-B of $f_{1,input} \approx 1$ Hz (see Chapter 8), it can be observed that, for the selected mesh sizes, the values for $v_{s,min}$ provided by Equation D.1 vary between 1.9 to 5.8 m/s. Note, however, that, as discussed in more detail in Chapter 8, the horizontal motions applied to the centrifuge models were not single-frequency, as intended. This aspect is illustrated in Figure D.2, which depicts the horizontal acceleration time-history (in prototype scale) estimated for CM-A (note that, as explained in Chapter 8, the input motion of CM-A had to be estimated based on that recorded in CM-B) and the corresponding Fourier spectrum, with the frequencies corresponding to the ten highest Fourier amplitudes being highlighted. It is apparent that these frequencies are located within the range of 1 to 11 Hz. If the upper limit of this range (11 Hz) would be used for the estimation of $v_{s,min}$ (rather than $f_{1,input} \approx 1$ Hz, as shown in Table D.1), then values significantly greater than those indicated in Table D.1 would be obtained, namely varying in between 22.0 and 66.0 m/s. Note, however, that, since the natural frequency of the sand deposit is likely much smaller (in the range of 1 to 3 Hz, as discussed later), the contribution of the high-frequency content of the

input motion to the modelled response is probably limited. Nevertheless, this example illustrates the difficulties that would arise from the application of Equation D.1 to the definition of the element size.

In relation to $v_{s,max}$, Table D.1 shows that Equation D.2 provides values in the range of 8.0 to 300.0 m/s for the selected element sizes and time steps. These values can be compared with those expected at each level of the mesh when using the maximum shear modulus, G_{max}, computed by the present constitutive model (Equations D.3 and D.4). Note that the formulation of the constitutive model is comprehensively described in Chapter 4.

$$v_{s,max} = \sqrt{\frac{G_{max}}{\rho}} \tag{D.3}$$

where:

$$G_{max} = C_g \, p'_{ref} \, \frac{\left(m_g - e\right)^2}{1.0 + e} \left(\frac{p'}{p'_{ref}}\right)^{n_g} \tag{D.4}$$

with the model parameters $C_g = 293.0$, $m_g = 2.97$ and $n_g = 0.49$ being adopted for Hostun sand (Chapter 6) and a mass density of $\rho \approx 1.906$ g/cm^3 and a void ratio of $e \approx 0.811$ being estimated for the moderately loose deposit of Hostun sand used in CM-A and CM-B (Chapter 8). Moreover, for a 18 m-thick deposit of saturated Hostun sand characterised by a saturated unit weight of $\gamma_{sat} \approx 18.7$ kN/m^3 and a coefficient of earth pressure at rest of $K_0 \approx 0.50$, the initial effective mean stress, p'_0, at its bottom ($H = 18.0$ m) can be estimated as:

$$p'_0 = \left(\gamma_{sat} - \gamma_w\right) H \left(\frac{1 + 2\,K_0}{3}\right) \approx 106.7 \text{ kPa} \tag{D.5}$$

which results in a value for $v_{s,max}$ at the bottom of the sand deposit of:

$$G_{max} \approx 78.3 \text{ MPa} \Longrightarrow v_{s,max} \approx 202.7 \text{ m/s} \tag{D.6}$$

By comparing the estimated value with those provided by Equation D.2 (Table D.1), it can be concluded that computation no. 7 (termed as "m1.5 dt0.0025" and using $\Delta L = 1.5$ m and $\Delta t = 0.0025$ s) is the only one satisfying the CFL condition at the bottom of the sand deposit, while a value close to that required by the CFL condition is obtained for computation no. 4 (termed as "m1.0dt0.0025" and using $\Delta L = 1.0$ m and $\Delta t = 0.0025$ s). In both cases, however, a very small time step of $\Delta t = 0.0025$ s is employed, which might lead to very demanding computational costs, as discussed later in more detail. Two aspects should, nevertheless, be considered: (1) as shown by Equation D.4, G_{max}, and, therefore, $v_{s,max}$ depend on the mean effective stress, p', and, therefore, the values of $v_{s,max}$ computed at shallower levels are likely smaller than 202.7 m/s; (2) due to the tendency of Hostun sand to generate positive excess pore pressures when subjected to cyclic loading and, consequently, to reduce the mean effective stress during loading (as discussed in Chapter 3), $v_{s,max} \approx 202.7$ m/s might be only observed at the start of the numerical analysis, reducing with cyclic loading and,

therefore, the use of such small time step of 0.0025 s might not be necessary, as discussed in more detail later.

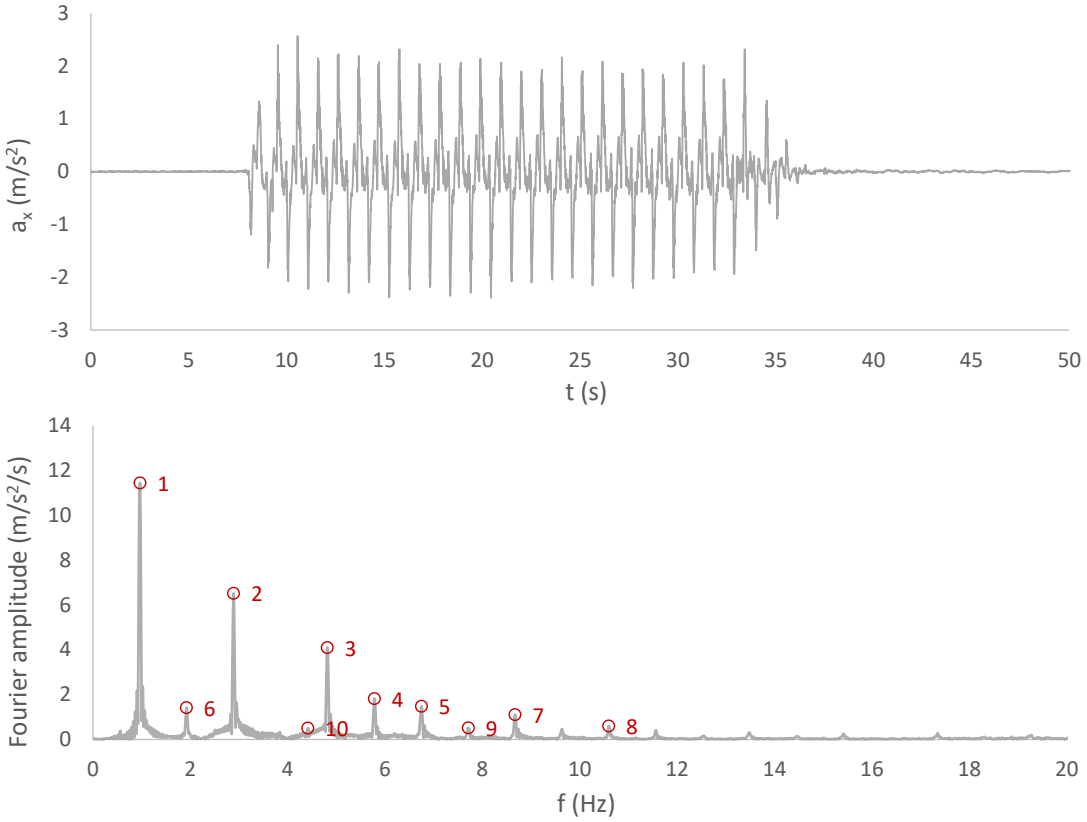

Figure D.2 – Input horizontal acceleration time-history estimated for CM- A and its corresponding Fourier spectrum.

Other aspects of the conducted numerical analyses worth mentioning include:

- Given the relevance of the interaction between the pore fluid and solid phases of porous material, fully coupled flow-deformation analyses were performed using eight-noded isoparametric quadrilateral elements with pore pressure degrees of freedom assigned to the four corner nodes (i.e. hybrid elements).
- As mentioned before, a single column of elements with tied degrees of freedom at a given level of the mesh was employed in each analysis (Figure D.1); moreover, the horizontal acceleration time-history depicted in Figure D.2 was prescribed at the nodes located along the bottom side of the mesh, with the vertical displacements of these nodes being restricted.
- In terms of groundwater flow boundary conditions, conditions of no flow were applied to the bottom and lateral boundaries of the mesh, by tying the displacements in the solid and fluid phases along the direction perpendicular to the boundary; in addition, pore pressure boundary condition of $u = 0.0$ kPa was imposed at the top boundary of the mesh, allowing drainage to occur solely through the ground surface.
- The mechanical response of the Hostun sand deposit was modelled using the BSPM together with the set of model parameters “B.1) Original formulation”, defined in

Chapter 6; although possible, Rayleigh damping was not introduced in the analysis, since the constitutive model predicts the occurrence of material damping within the full strain range and the numerical damping introduced by the time integration scheme allows for the mitigation of spurious, irregular, high-frequency oscillations.

- As mentioned before, an initial void ratio of $e \approx 0.811$, corresponding to moderately loose Hostun sand, was considered in the analysis; given the density of the solid particles of Hostun sand ($G_s = 2.64$), the saturated unit weight was estimated as $\gamma_{sat} = 18.7$ kN/m^3, which leads to a mass density of $\rho = 1.906$ g/cm^3; in terms of hydraulic properties, $k_x = k_y \approx 3.65\times10^{-4}$ m/s was assumed, based on the results presented by Lauer and Engel (2005).
- A bulk modulus of $K_f \approx 2.2$ GPa was considered for the pore fluid.
- All dimensions and results are presented in prototype scale.

D.3 Obtained numerical results

D.3.1 Influence of the time step

Figure D.3 depicts the evolutions of excess pore pressure with time obtained in three computations employing an identical mesh, consisting of elements with a size, ΔL, of 1.0 m, though different time steps: computation no. 4, termed as m1.0/dt0.0025 and employing a time step, Δt, of 0.0025 s, computation no. 5, termed as m1.0/dt0.0125 and employing $\Delta t = 0.0125$ s, and computation no. 6, m1.0/dt0.0625 and employing $\Delta t = 0.0625$ s (Table D.1). It can be observed that very similar excess pore pressure evolutions with time are obtained in computations m1.0/dt0.0025 and m1.0/dt0.0125. The very small discrepancies between the results obtained in these two computations seem practically restricted to the slightly higher oscillations of excess pore pressures obtained in the former computation, likely due to the inevitable slightly different frequency content of the acceleration time-history registered at each position (including that imposed to the base of the model, since interpolation was required to discretise the input motion in a smaller time step than that used in the centrifuge experiment of $\Delta t = 0.0125$ s). Conversely, considerable discrepancies can be observed between the results obtained in computation m1.0/dt0.0625 (employing the largest time step) and in the remaining two computations. Specifically, it can be seen that a considerably higher rate of excess pore pressure generation is predicted at the two deepest positions ($y = 0.0$ m and $y = 5.0$ m). Moreover, it is apparent that the initiation of excess pore pressure dissipation (i.e. of the consolidation phase) at each level occurs later in computation m1.0/dt0.0625 than in the remaining two computations. The dissipation rate is, nevertheless, similar in all three computations. This aspect is more clearly illustrated in Figure D.4, which depicts the evolutions of the excess pore pressure, normalised by its maximum ever reached value, as a function of time occurring after the initiation of the consolidation phase, t_{cons}, at the shallowest and deepest positions of the Hostun sand deposit ($y = 17.0$ m and $y = 0.0$ m, respectively).

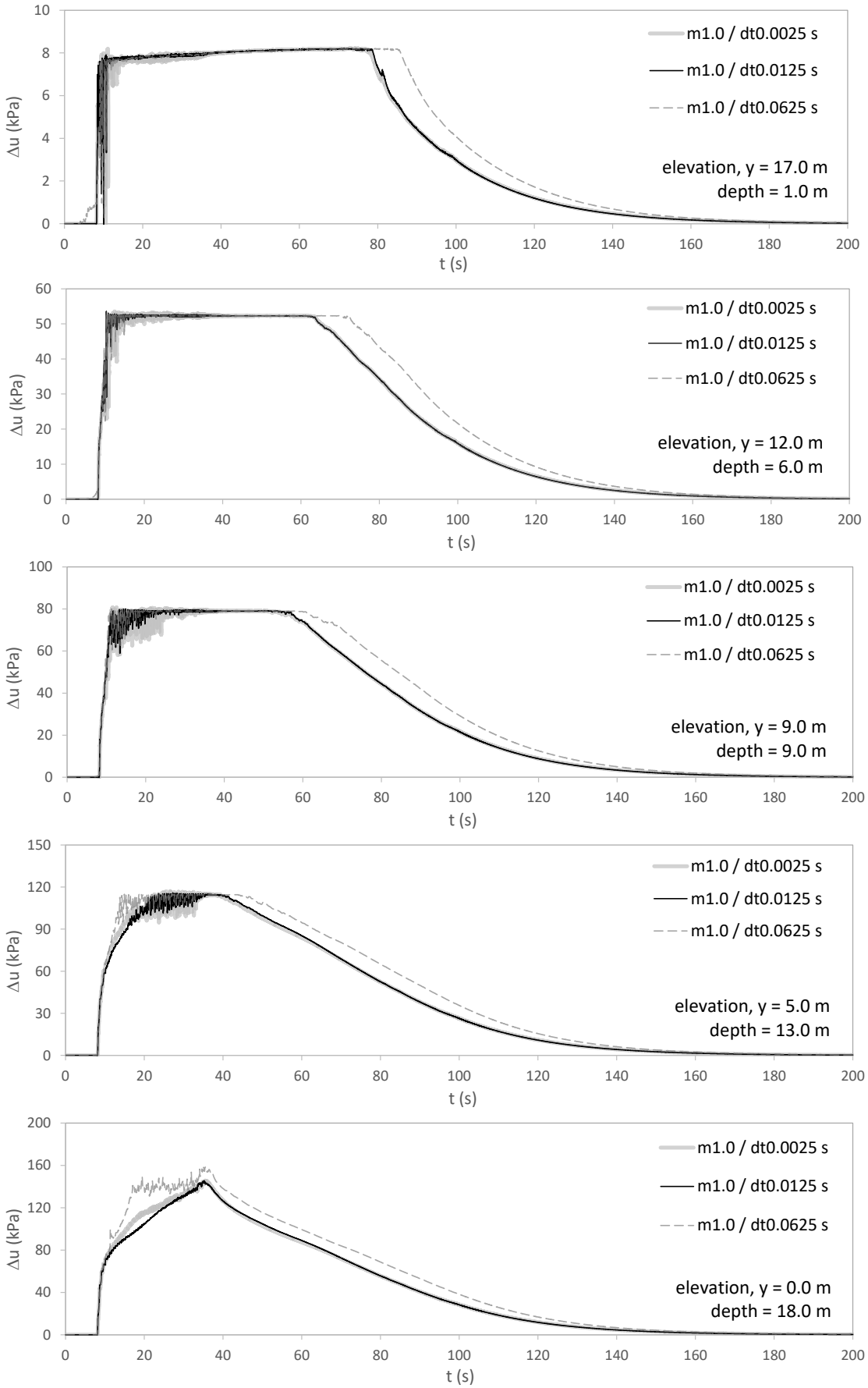

Figure D.3 – Excess pore pressure evolution with time at five different positions of the deposit of Hostun sand obtained in three computations using different time steps.

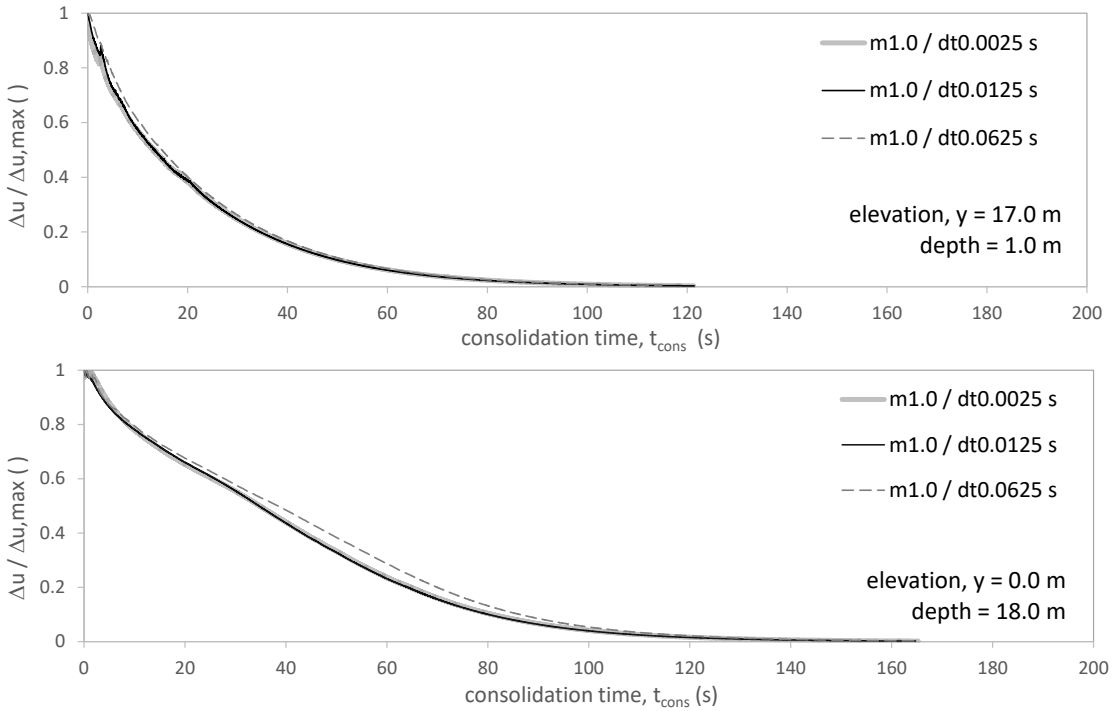

Figure D.4 – Normalised excess pore water pressure dissipation with time at two different positions of the deposit of Hostun sand obtained in three computations using different time steps.

Based on the results presented above, it can be concluded that:

- the time step used in the analysis may mainly affect: (1) the rate of excess pore pressure build-up with cyclic loading, (2) the maximum excess pore pressure reached at a given level and (3) the moment at which the dissipation of excess pore pressures starts; conversely, the rate of excess pore pressure dissipation seems fairly independent of the time step adopted in the numerical analysis;
- similar excess pore pressure evolutions with time are obtained when using $\Delta t =$ 0.0025 s and $\Delta t =$ 0.0125 s (i.e. in computations m1.0/dt0.0025 and m1.0/dt0.0125, respectively), while a higher rate of excess pore pressure build-up and a delayed onset of dissipation of excess pore pressure is observed when using the largest time step of $\Delta t =$ 0.0625 s (i.e. in computation m1.0/dt0.0625).

Similarly, it can be observed in Figure D.5 that very similar surface settlement evolutions with time are obtained in computations m1.0/dt0.0025 and m1.0/dt0.0125. Indeed, by employing Equation D.7, a maximum relative error, ΔR_{max}, of about 1.2 % is obtained between the results registered in these two computations. Conversely, larger surface settlements are obtained in computation m1.0/dt0.0625, probably due to the higher excess pore pressures obtained at the deepest position of the deposit and, more importantly, due to the fact that the onset of dissipation of excess pore pressures occurs later in this computation (meaning that the deposit of sand remained under very low effective stresses for a greater period) than in the remaining two computations. By using, once again, Equation D.7 the maximum relative error of this computation is estimated as 6.0 %.

$$\Delta R_{max} = \frac{\left|\Delta d_{y,max,\,\Delta t=0.0025\ m} - \Delta d_{y,max,\,\Delta t}\right|}{\left|\Delta d_{y,max,\,\Delta t=0.0025\ m}\right|} \times 100\ (\%) \qquad (D.7)$$

where $\Delta d_{y,max,\,\Delta t=0.0025\ m}$ is the maximum surface settlement registered in the computation using a time step of $\Delta t = 0.0025$ s (used as reference), while $\Delta d_{y,max,\,\Delta t}$ refers to the maximum surface settlement obtained in the computation under comparison (i.e. using a time step different from 0.0025 s).

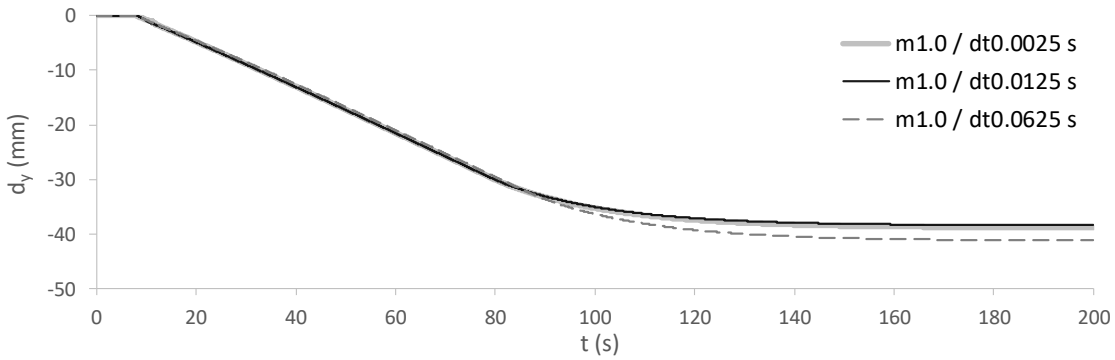

Figure D.5 – Surface settlement evolution with time for three computations using different time steps.

Further insight into the impact of the time step on the modelled response is obtained by analysing the horizontal acceleration time-histories registered at the surface of the sand deposit in these three different computations – Figure D.6. Note that, for clarity of the presentation, a bandpass filter with limit frequencies of 0.1 Hz and 25 Hz was applied to the obtained horizontal acceleration time-histories by using the computer software SeismoSignal version 2018 (Seismosoft, 2018). It appears that there is a small delay in the obtained response as a larger time step is employed in the analysis – a conclusion that agrees well with that reached by Grazina (2009) in a similar parametric study. Conversely, the amplitude of the peak accelerations seems little affected by the adopted time step. Note, however, that this conclusion may not retain its validity for other studies, particularly when only limited cyclic mobility is observed (contrary to the widespread occurrence of cyclic mobility observed in the present case).

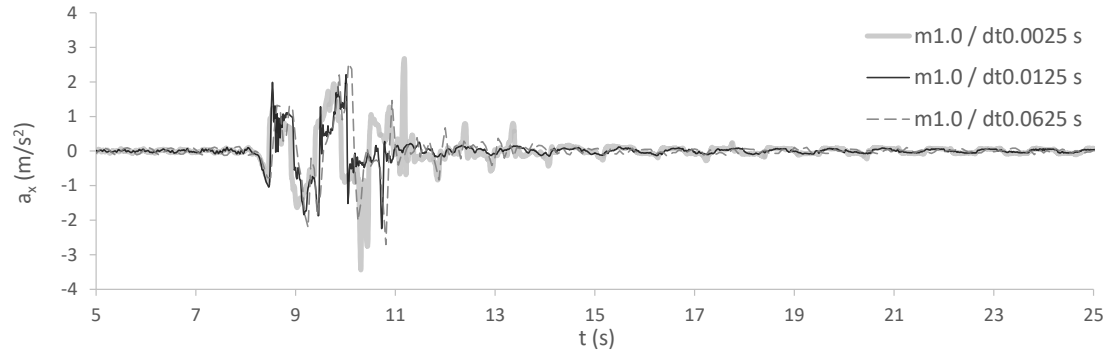

Figure D.6 – Surface horizontal acceleration time-history for three computations using different time steps.

In addition, the Fourier spectra corresponding to the horizontal acceleration time-histories registered at the surface in these three different computations are compared in Figure D.7. It is apparent that the time step slightly influences the Fourier amplitude corresponding to the predominant frequency. Moreover, when comparing the Fourier spectra obtained for computation m1.0/dt0.0625, employing the largest time step, with that obtained for computation m1.0/dt0.0025, employing the smallest time step, it seems that the frequency contents of the registered acceleration time-histories are considerably different, particularly in terms of the location of the Fourier peak amplitudes (with the exception of the predominant frequency, as pointed out before). The discrepancies between the Fourier spectra obtained for computations m1.0/dt0.0025 and m1.0/dt0.0125 are more limited, with similar patterns being observed.

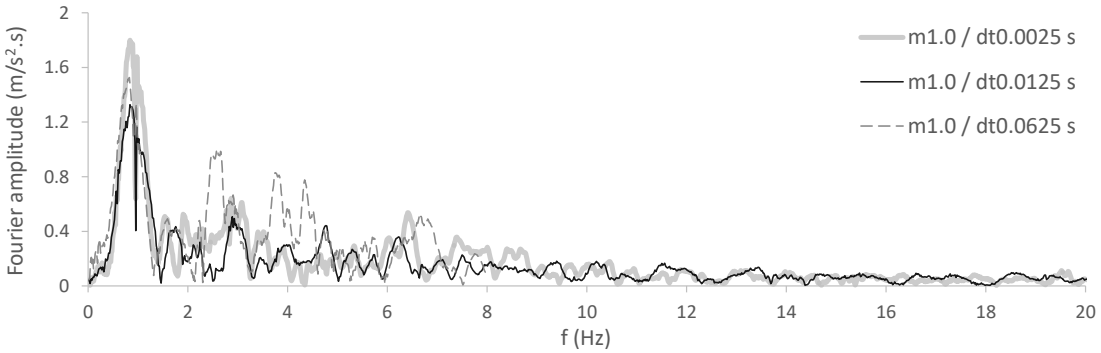

Figure D.7 – Fourier spectra of the surface horizontal acceleration time-histories registered in three computations using different time steps.

Finally, Table D.2 compares the computational cost of the three different computations, in terms of total run time, its value normalised by that obtained for computation m1.0/dt0.0025, employing the smallest time step, and per increment. It is interesting to observe that the run time of computation m1.0/dt0.0125 is about 20 % of that required by the computation m1.0/dt0.0025, with this reduction being proportional to the reduction in the number of increments used in these two analyses. Despite being smaller than that of computations m1.0/dt0.0025 and m1.0/dt0.0125, it is interesting to observe that the reduction of the run time for computation m1.0/dt0.0625 in relation to that of computation m1.0/dt0.0025 is not proportional to the reduction in the number of increments of the computation. Specifically, it can be seen that the total run time of computation m1.0/dt0.0625 is only about 8.3 % of that required by the computation m1.0/dt0.0025, despite the total number of increments of the former computation being 4.0 % of those required in the latter computation. This suggests that the computational effort spent to compute each increment of computation m1.0/dt0.0625 is about double of that required in the computations m1.0/dt0.0025 and m1.0/dt0.0125.

Table D.2 – Run times for three computations using different time steps.

Computation ID	4 m1.0/dt0.0025	5 m1.0/dt0.0125	6 m1.0/dt0.0625
Time step, Δt (s)	0.0025	0.0125	0.0625
Total number of increments, n_{inc}	100000	20000	4000
Total run time, t (min)	1096	223	91
Normalised no. of increments, n_{inc} / $\Delta t_{calc\ 4}$ (%)	–	20.0	4.0
Normalised total run time, t / $t_{calc\ 4}$ (%)	–	20.3	8.3
Normalised run time per increment, (t / n_{inc}) / ($t_{calc\ 4}$ / $n_{inc,\ calc\ 4}$) (%)	–	101.7	207.6

D.3.2 Influence of the element size

D.3.2.1 Initial considerations

To evaluate the influence of the element size, the results obtained in two different sets of computations are compared, specifically:

1) Computations no. 3 (termed as m0.5/dt0.0125), no. 5 (termed as m1.0/dt0.0125) and no. 8 (termed as m1.5/dt0.0125), employing different meshes, with element sizes of 0.5, 1.0 and 1.5 m, respectively, while using an identical time step of 0.0125 s;
2) Computations no. 2 (termed as m0.5/dt0.00625), no. 5 (termed as m1.0/dt0.0125) and no. 9 (termed as m1.5/dt0.01875), which, despite employing different element sizes and time steps, are able to reproduce an identical maximum velocity of about 40 m/s, according to the Courant–Friedrichs–Lewy (CFL) condition (Equation D.2).

D.3.2.2 Analyses using identical time steps

Starting with the first series of computations, employing 0.0125 s as time step, Figure D.8 depicts the evolutions of excess pore pressure with time at five different positions of the Hostun sand deposit.

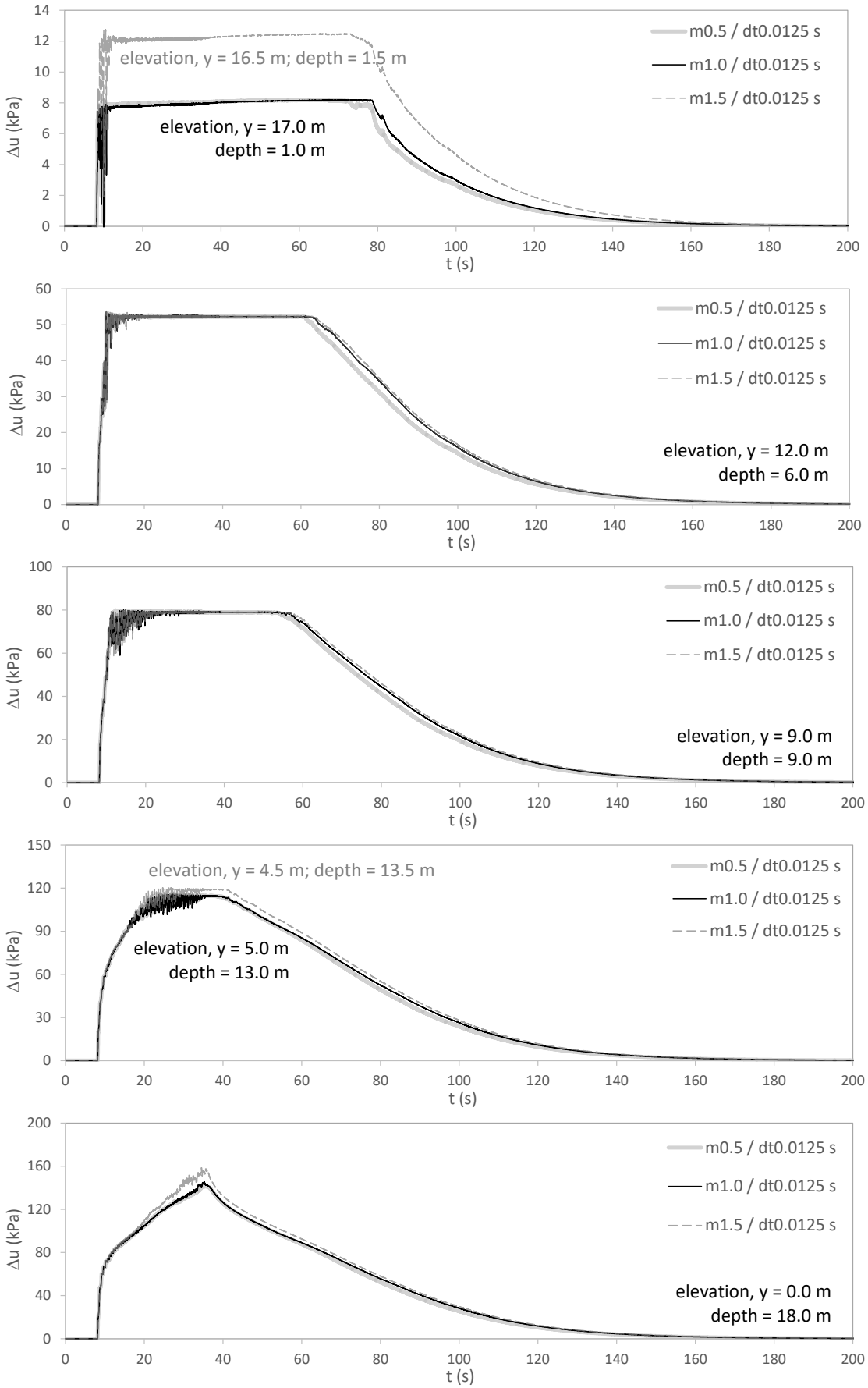

Figure D.8 – Excess pore pressure evolution with time at five different positions obtained for three computations using different element sizes and identical time steps.

It can be observed that very similar rates of excess pore pressure generation with dynamic loading, as well as maximum excess pore pressures are obtained at each level of the deposit, regardless of the element size used in the computation. The only exception seems to consist of the higher excess pore pressure reached at the bottom of the deposit in the computation employing the largest element size (m1.5/dt0.0125), in relation to registered in the remaining two computations (m0.5/dt0.0125 and m1.0/dt0.0125). At the remaining shallower positions, the discrepancies between the maximum excess pore pressures reached in computation m1.5/dt0.0125 and those obtained in the two remaining computations seem to be solely related to the differences in the geometric coordinates of the nodes used to plot the results, as noted in the figure. In terms of dissipation of excess pore pressures (i.e. consolidation phase), it seems that, as the size of the element is increased, the initiation of the dissipation is slightly delayed, with the discrepancies between the sets of results increasing at shallower depths, as a consequence of the upward flow of water occurring during this phase.

Nevertheless, similar to what was observed when using different time steps, the mesh discretisation seems to have little impact on the rate of excess pore pressure dissipation. This aspect is more clearly illustrated in Figure D.9, which compares the normalised dissipation branches obtained in the three different computations at two different positions ($y = 12.0$ m and $y = 0.0$ m). By imposing a similar starting point, similar evolutions of dissipation of normalised excess pore pressures with time are obtained.

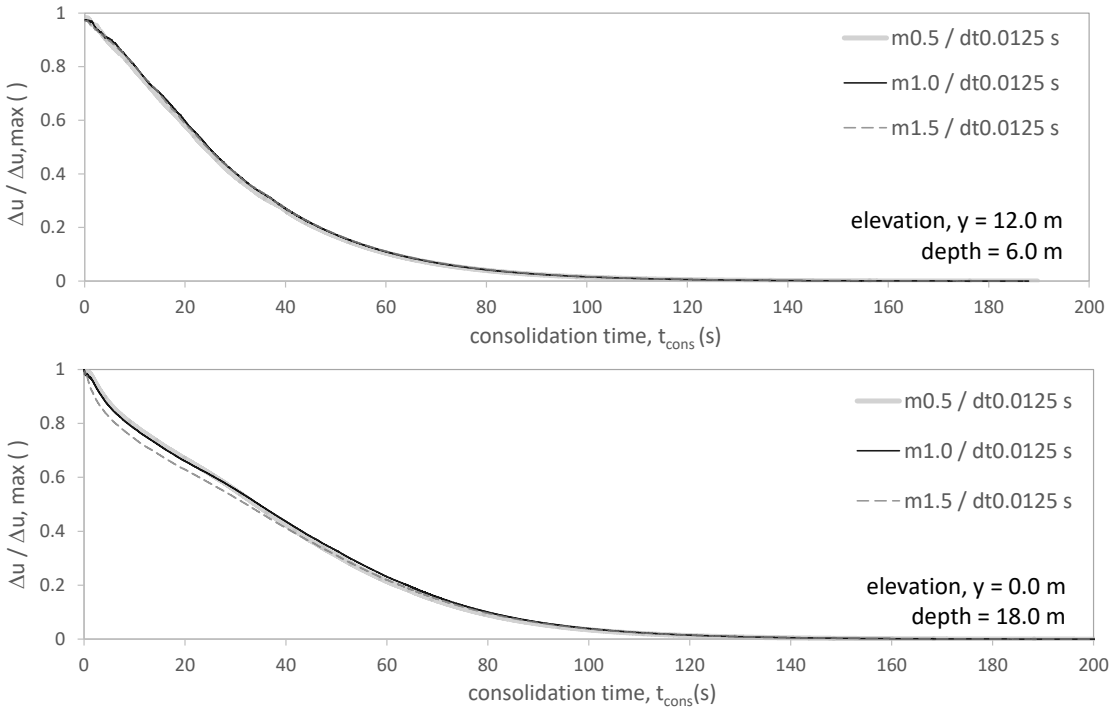

Figure D.9 – Normalised excess pore water pressure dissipation with time at two different depths obtained for three computations using different element sizes and identical time steps.

Further insight into the impact of the mesh discretisation on the numerical simulation is obtained by analysing the computed evolution of surface settlements with time (Figure D.10).

It is apparent that the surface settlements obtained in computations m0.5/dt0.0125 and m1.0/dt0.0125 are very similar. Specifically, by employing Equation D.8, a maximum relative error, ΔR_{max}, between these two computations of about 2.0 % is obtained. Conversely, larger surface settlements are obtained when adopting the larger element size of 1.5 m (i.e. in computation m1.5/dt0.0125) in relation to those registered in the computation employing the smallest element size of 0.5 m, with a maximum relative error of about 7.2 % being determined using Equation D.8.

$$\Delta R_{max} = \frac{\left|\Delta d_{y,max,\ \Delta L=0.5\ m} - \Delta d_{y,max,\ \Delta L}\right|}{\left|\Delta d_{y,max,\ \Delta L=0.5\ m}\right|} \times 100\ (\%) \tag{D.8}$$

where $\Delta d_{y,max,\ \Delta L=0.5\ m}$ is the maximum surface settlement registered in the computation using an element size of $\Delta L = 0.5$ m (used as reference), while $\Delta d_{y,max,\ \Delta L}$ refers to the maximum settlement obtained in computation under comparison (i.e. using an element size different from 0.5 m).

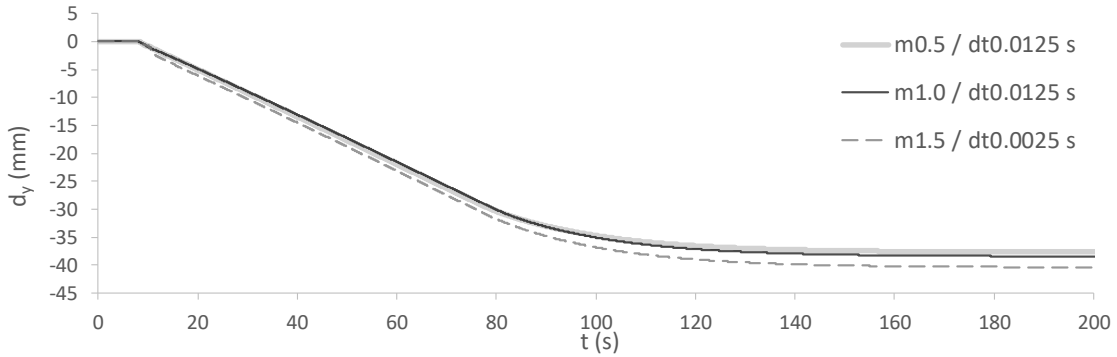

Figure D.10 – Surface settlement evolution with time obtained for three computations using different element sizes and identical time steps.

In terms of horizontal accelerations at surface, it is apparent in Figure D.11 that very similar time histories were obtained in the three computations, with the large attenuation of the accelerations after about 10 to 11 s being a consequence of the significant reduction in effective stresses and stiffness induced by the occurrence of cyclic mobility. It should be noted that a bandpass filter with limit frequencies of 0.1 and 25 Hz was applied by using the computer software SeismoSignal version 2018 (Seismosoft, 2018) to ease the comparison of the numerical results. The aforementioned software was also used to compute the Fourier spectra of the simulated horizontal motions, with the obtained results being depicted in Figure D.12. It is apparent that slight discrepancies between the Fourier spectra are solely observed for frequencies higher than 3.0 Hz (which does not include the predominant frequency of the motion, of about 1.0 Hz). Indeed, it appears that the importance of the higher frequencies (particularly, in the range of 12 Hz to 20 Hz), typically considered numerical noise, is greater when employing the largest element size of 1.5 m (i.e. for the computation m1.5/dt0.0125). This conclusion agrees well with that obtained by Taborda (2011) in a similar parametric study on Nevada sand.

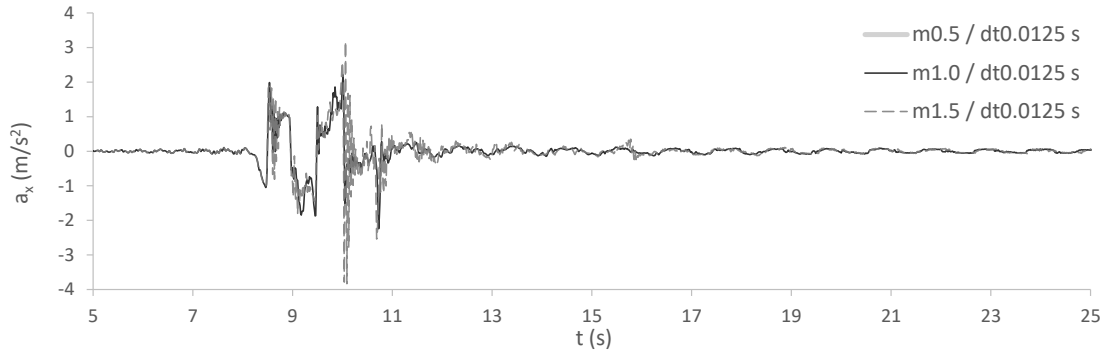

Figure D.11 – Surface horizontal acceleration time-history for three computations using different element sizes and identical time steps.

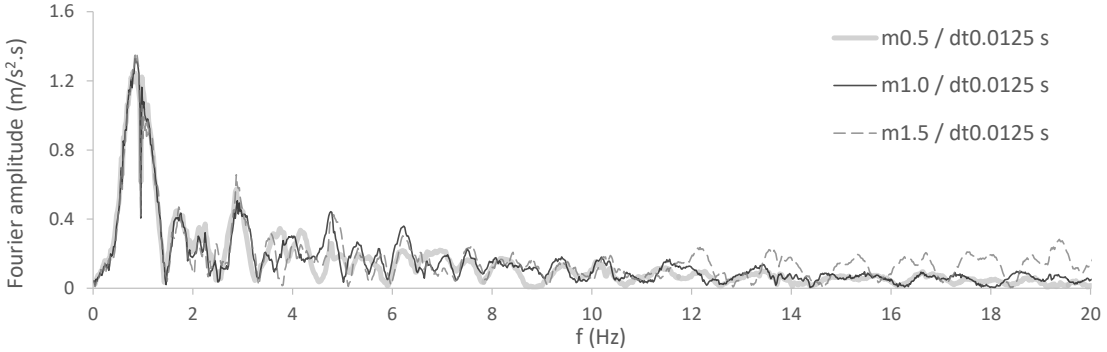

Figure D.12 – Fourier spectra of the surface horizontal acceleration time-history for three computations using different element sizes and identical time steps.

The final aspect to be analysed consists of the computational cost of these three different computations (m0.5/dt0.0125, m1.0/dt0.0125 and m1.5/dt0.0125), as indicated in Table D.3. Note that, in this case, the total run time, t, and run time per element, t / n_{elem}, are normalised in relation to those registered in the computation m0.5/dt0.0125, where the smallest element size of 0.5 m was used. It can be observed that the required time is practically proportional to the total number of elements of the mesh (which is related to the total degrees of freedom of the problem).

Table D.3 – Computational times for three computations using different element sizes and identical time steps.

Computation ID	3 m0.5/dt0.0125	5 m1.0/dt0.0125	8 m1.5/dt0.0125
Element size, ΔL (m)	0.5	1.0	1.5
Total number of elements, n_{elem}	36	18	12
Degrees of freedom (DOF), n_{DOF}	252	126	84
Total run time, t (min)	456	223	143
Normalised no. of elements, n_{elem} / $n_{elem,calc\,3}$ (%)	–	50.0	33.3
Normalised DOF, n_{DOF} / $n_{DOF,calc\,3}$ (%)	–	50.0	33.3
Normalised total run time, t / $t_{calc\,3}$ (%)	–	48.9	31.4
Normalised run time per element, (t / n_{elem}) / ($t_{calc\,3}$ / $n_{elem,\,calc\,3}$) (%)	–	97.8	94.1

It is important to note that similar conclusions were reached when analysing results obtained in three additional computations using a smaller time step of 0.0025 s, not only in terms of

horizontal acceleration time-histories and respective Fourier spectra, but also in terms of evolutions of excess pore pressures and settlements with time. For brevity, only the excess pore pressures at the shallowest position ($y = 17.0$ m), surface settlement and acceleration time-histories are presented here, respectively in Figure D.13, Figure D.14 and Figure D.15.

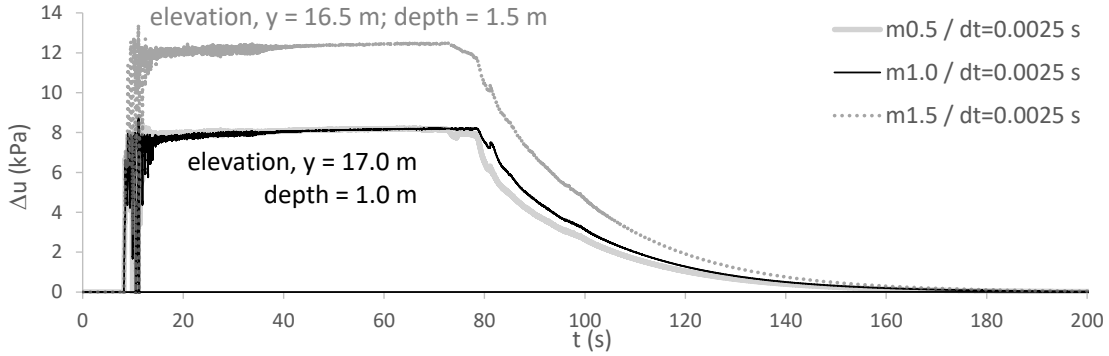

Figure D.13 – Excess pore pressure evolution with time at *y* = 17.0 m obtained for three computations using different element sizes and an identical time step of 0.0025 s.

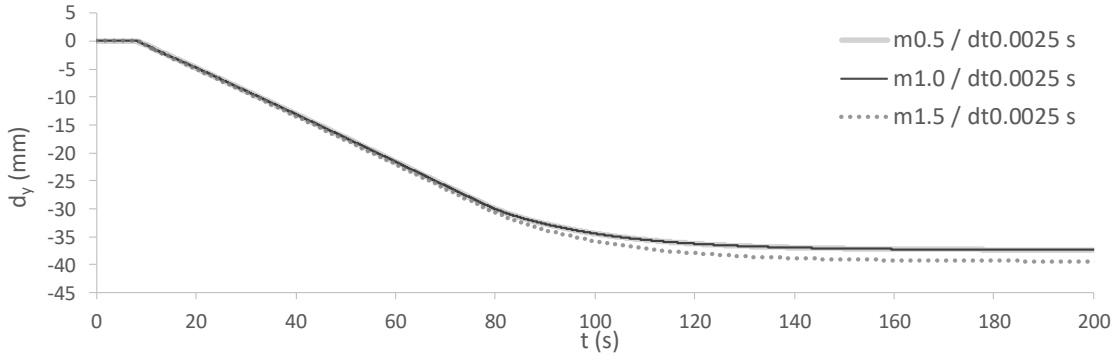

Figure D.14 – Surface settlement evolution with time for three computations using different element sizes and an identical time step of 0.0025 s.

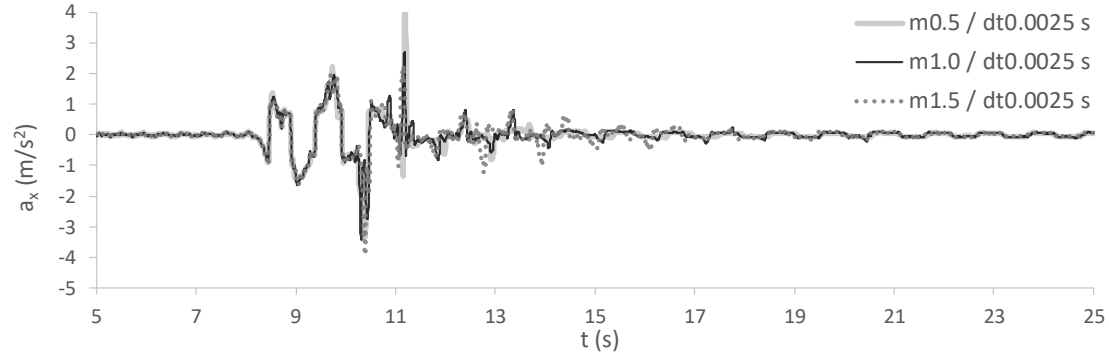

Figure D.15 – Surface horizontal acceleration time-history for three computations using different element sizes and an identical time step of 0.0025 s.

D.3.2.3 Analyses able to simulate an identical maximum velocity according to the Courant–Friedrichs–Lewy condition

Figure D.16 depicts the evolutions of excess pore pressure with time at five different positions of the Hostun sand deposit obtained in computations m0.5/dt0.00625, m1.0/dt0.0125 and m1.5/dt0.01875.

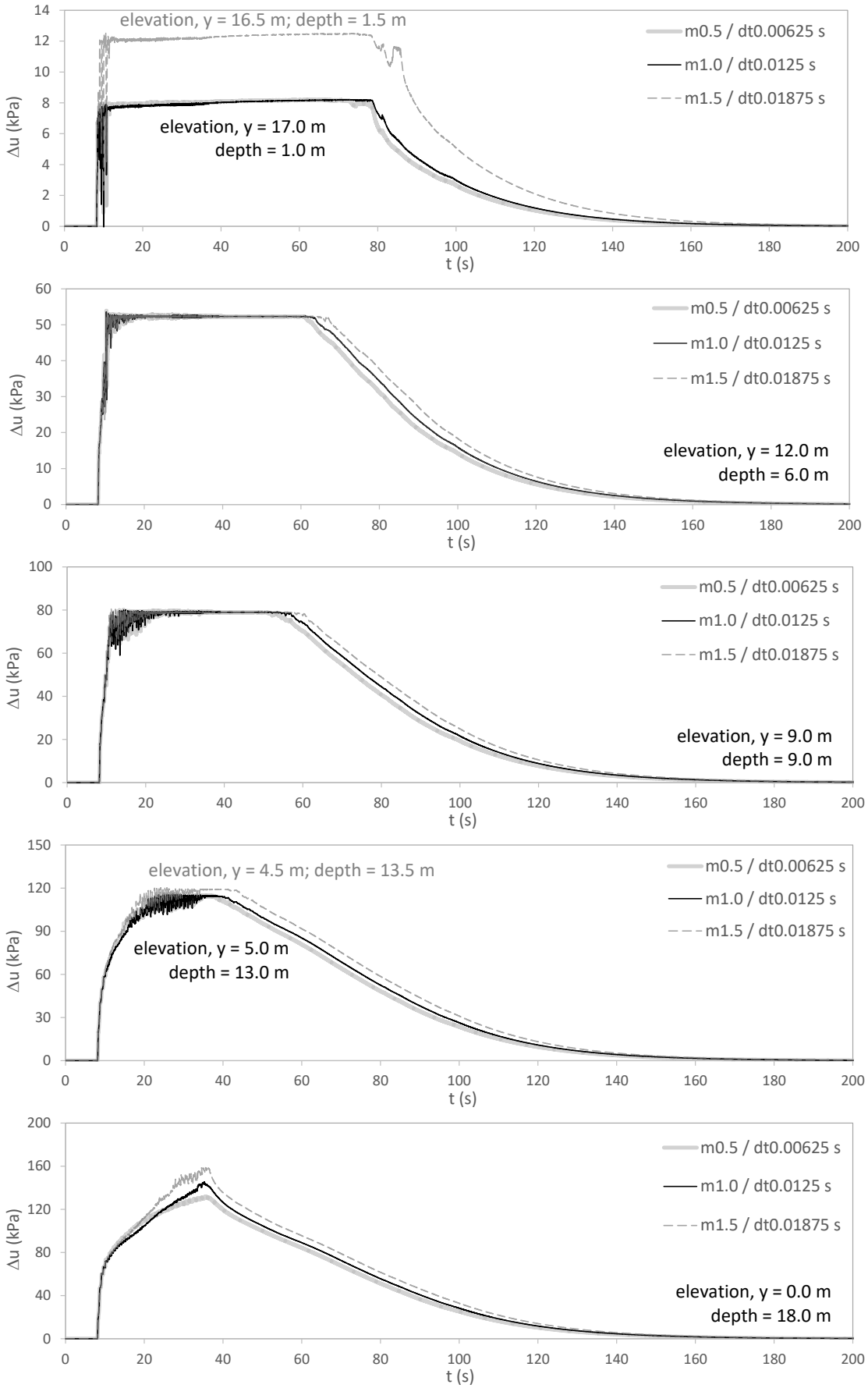

Figure D.16 – Excess pore pressure evolution with time at five different depths obtained for three different computations able to reproduce similar maximum velocities.

It can be observed that similar rates of excess pore pressure build-up with dynamic loading are obtained in these three different computations. Conversely, the maximum excess pore pressure reached at the bottom of the deposit ($y = 0.0$ m) differs slightly in these computations, with larger values appearing to be registered for coarser meshes. In addition, it can be observed that the moment at which the excess pore pressures start to dissipate (i.e. the onset of the consolidation phase) occurs later as a coarser mesh is employed in the analysis. This is likely a result of the differences in terms of excess pore pressures reached at the bottom level of the model, which affect the upward flow of water occurring during the consolidation phase.

Nevertheless, as observed for the previous analyses, when a common starting point is imposed to the dissipation curves, very similar rate of dissipations of excess pore pressures are obtained for the three different analysis, as illustrated in Figure D.9, suggesting that this aspect of sand response is practically insensitive to the element size and time step adopted in the analysis.

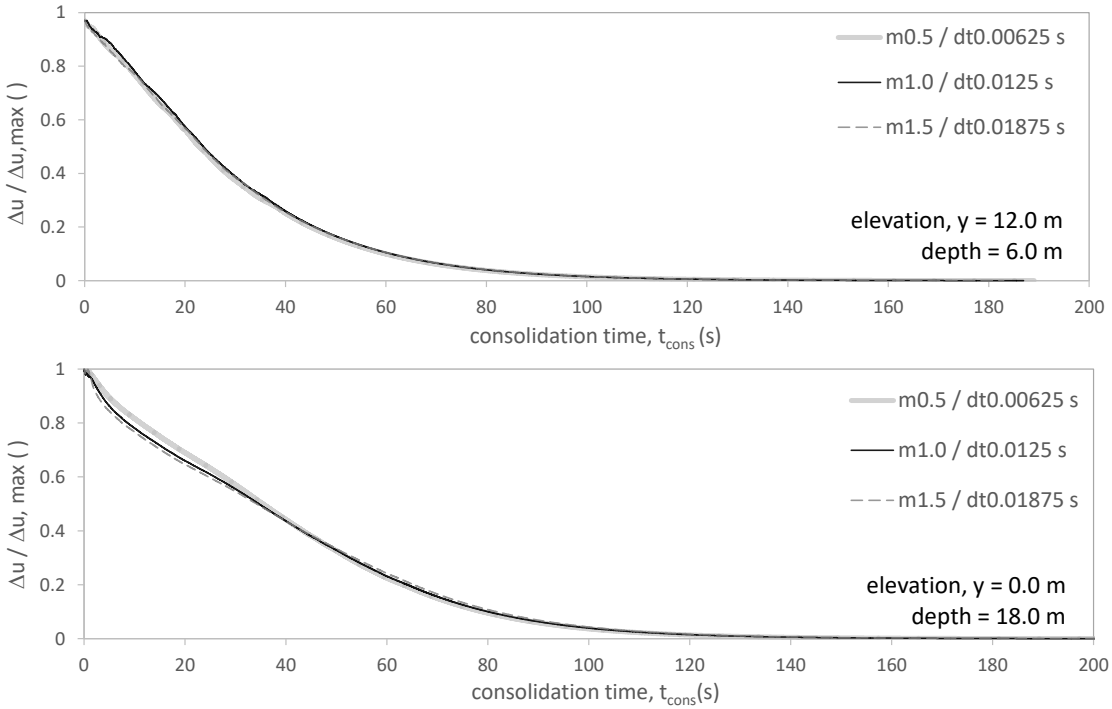

Figure D.17 – Normalised excess pore water pressure dissipation with time at two different depths obtained for three different computations able to reproduce similar maximum velocities.

The evolution of surface settlements with time obtained in the three different computations are compared in Figure D.10. It can be observed that similar surface settlements were registered in computations m0.5/dt0.00625 and m1.0/dt0.0125, employing the smallest and intermediate element sizes. In effect, the maximum settlement obtained in the latter computation is only about 2.5 % larger than that registered in computation m0.5/dt0.00625, according to Equation D.8. Conversely, considerably larger discrepancies are observed between the results obtained in the computation m1.5/dt0.01875 and those obtained in the

computation m0.5/dt0.00625, with a maximum relative error of about 10.1 % being obtained from Equation D.8.

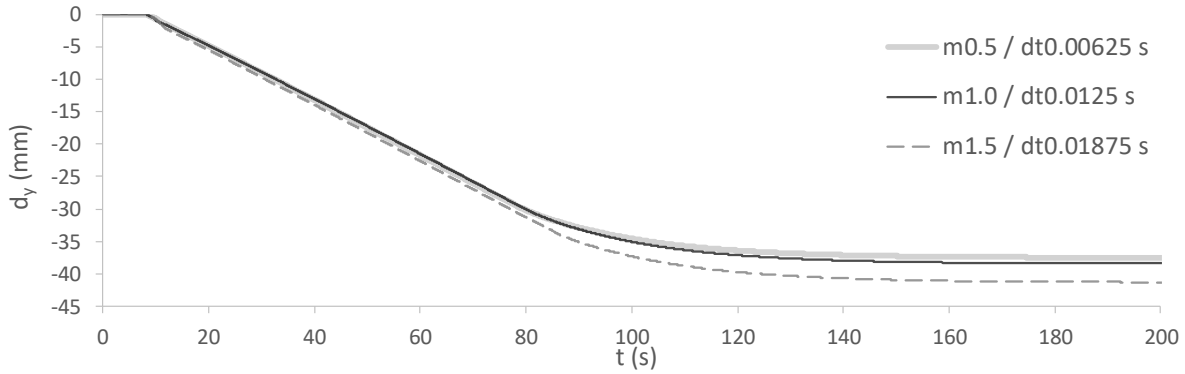

Figure D.18 – Surface settlement evolution with time for three different computations able to reproduce similar maximum velocities.

The acceleration time-histories registered at the ground surface in the three different computations are compared in Figure D.19. Note that, once more, for clarity of the presentation, a bandpass filter with limit frequencies of 0.1 and 25 Hz was applied by using the computer software SeismoSignal version 2018 (Seismosoft, 2018). It is apparent that very similar acceleration time-histories were obtained in computations m0.5/dt0.00625 and m1.0/dt0.0125. Conversely, small discrepancies can be observed between these two sets of data and that obtained in computation m1.5/dt0.01875, particularly between 10.5 and 12.0 s, where slightly larger accelerations were registered in computation m1.5/dt0.01875. This is likely a detrimental consequence of the richer high-frequency content of the surface motion registered in computation m1.5/dt0.01875, as illustrated by the Fourier spectra shown in Figure D.20. This conclusion agrees well with that drawn when analysing the previous series of computations concerning the use of an identical time step and different element sizes, as well as with the conclusions reached by Taborda (2011) in a similar parametric study.

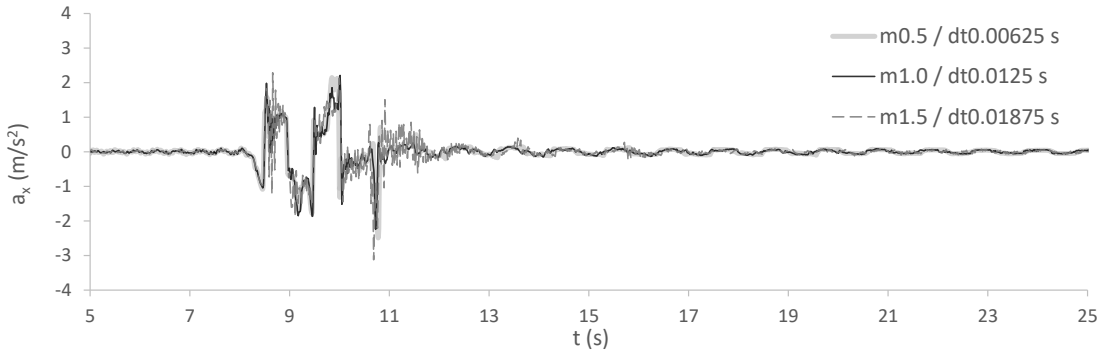

Figure D.19 – Surface horizontal acceleration time-history for three different computations able to reproduce similar maximum velocities.

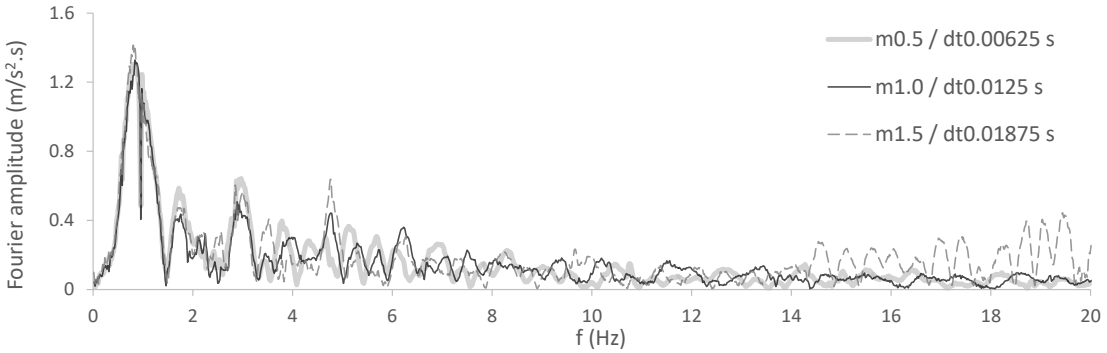

Figure D.20 – Fourier spectra of the surface horizontal acceleration time-history for three different computations able to reproduce similar maximum velocities.

Finally, the computational costs of these three different computations are compared in terms of total run time (Table D.4). It can be observed that the run time of computation m1.0/dt0.0125 and m1.5/dt0.01875 are, respectively, about 25 % and 14.2 % of that required by computation m0.5/dt0.00625.

Table D.4 – Computational times three different computations able to reproduce similar maximum velocities.

Computation ID	2 m0.5/dt0.00625	5 m1.0/dt0.0125	9 m1.5/dt0.01875
Element size, ΔL (m)	0.5	1.0	1.5
Total number of elements, n_{elem}	36	18	12
Time step, Δt (s)	0.00625	0.0125	0.01875
Total number of increments, n_{inc}	40000	20000	13333
Total run time, t (min)	894	223	127
Normalised total run time, t / $t_{calc\,2}$ (%)	–	24.9	14.2

D.4 Summary and conclusions

Given the lack of comprehensive guidelines on the spatial and time discretisation's to be adopted in the simulation of highly non-linear dynamic problems involving liquefaction-related phenomena, a parametric study on the impact of these aspects on the modelled cyclic response of Hostun sand was performed. For simplicity, the selected problem consisted of an 18 m-thick level ground deposit of moderately loose saturated Hostun sand subjected to dynamic loading. Due to the inexistence of sand-structure interaction, as well as due to the simple geometry of the problem, a single column of elements with displacement and pore pressure degrees of freedom tied at each level was used to simulate this problem, as suggested in the literature (e.g. Zienkiewicz *et al.*, 1989), reducing substantially the computational cost of the simulation and, therefore, allowing for a series of analyses to be performed in a reasonable time frame. Specifically, a total of nine different computations were performed, consisting of three different element size (0.5, 1.0 and 1.5 m) and five different time steps (0.0025, 0.00625, 0.0125, 0.01875 and 0.0625 s).

The results obtained for three calculations using an identical element size of 1.0 m, yet adopting distinct time steps (namely, 0.0025 s, 0.0125 s and 0.0625 s), were firstly compared. It was concluded that the use of a time step of 0.0625 s seemed to have a detrimental impact on the computed excess pore pressure build-up and initiation of the dissipation of the excess pore pressures (i.e. onset of the consolidation phase), as well as on the surface settlements registered in the analysis. Additionally, the use of such time step appeared to affect considerably the frequency content of the horizontal accelerations registered at the surface. Conversely, the impact of using a time step of 0.0125 s, rather than 0.0025 s, seemed significantly more limited, particularly in terms of excess pore pressures and surface settlements. When using a time step of 0.0125 s, the computational cost of the numerical analysis was reduced in about 80 %, when compared to that required to perform a similar analysis with a time step of 0.0025 s.

A subsequent parametric study focused on the impact of the element size on the simulated response. In particular, the results obtained in three computations using different meshes, consisting of elements with 0.5, 1.0 and 1.5 m of size, in conjunction with a time step of 0.0125 s, were firstly compared. Additionally, results obtained in three computations employing different element sizes and time steps, though being able to reproduce an identical maximum velocity according to the Courant–Friedrichs–Lewy (CFL) condition, were compared. Interestingly, similar conclusions were reached when analysing the results obtained in both series of analyses. Specifically, it was concluded that the mesh discretisation may slightly affect the maximum excess pore water pressures obtained in the analysis at the deepest positions of the sand deposit, with larger values tending to be registered when a coarser mesh discretisation is adopted, resulting in delays in the onset of dissipation of excess pore pressures as dynamic loading ceases. While the discrepancies between the results obtained when using an element size of 1.0 m and those obtained when employing an element size of 0.5 m seemed very reasonable, with a relative error of about 2 % being estimated, the discrepancies were observed to be considerably larger when using a larger element size of 1.5 m, with a relative error ranging from 7 to 10 %. By comparing the frequency content of the signals registered at the surface of the sand deposit in the several different computations, it was concluded that the use of a coarser mesh discretisation may lead to the increase in the relevance of the high-frequency content of the motion, typically regarded as numerical noise. This was particularly observed when comparing the results obtained in the computation using an element size of 1.5 m to those obtained in the reference computation, using an element size of 0.5 m. A minor impact was, nevertheless, observed when using a mesh consisting of elements with 1.0 m of size, suggesting that the use of this mesh discretisation allows for sufficiently accurate predictions of the cyclic response of Hostun sand, while allowing for the significant reduction of the computational cost of the analysis. In effect, the run time of the analysis employing a mesh consisting of elements with

1.0 m of size was about half of that required by the computation using an element size of 0.5 m.

Based on the results obtained in this parametric study, it can be concluded that a very satisfactory balance between accuracy and computational effort may be obtained when employing elements with a size of 1.0 m and a time step of 0.0125 s.

Appendix E DYNAMIC FINITE ELEMENT ANALYSIS OF CENTRIFUGE MODEL A USING THE EXTENDED FORMULATION OF THE BOUNDING SURFACE PLASTICITY MODEL

E.1 Introduction

This appendix contains the complete set of results of a finite element analysis of the Centrifuge model A (CM-A), entitled as "Adjacent shallow foundations resting on a uniform loose sand deposit subjected to dynamic loading causing liquefaction", using the set of model parameters "B.2) Extended formulation". While the values assigned to the model parameters are listed in Chapter 6, the employed mesh, time step, time integration algorithm, boundary conditions and initial stresses are presented in Chapter 8. To aid the presentation, the adopted mesh and nodes selected for the inspection of acceleration, displacement and excess pore pressure time-histories are illustrated in Figure F.1.

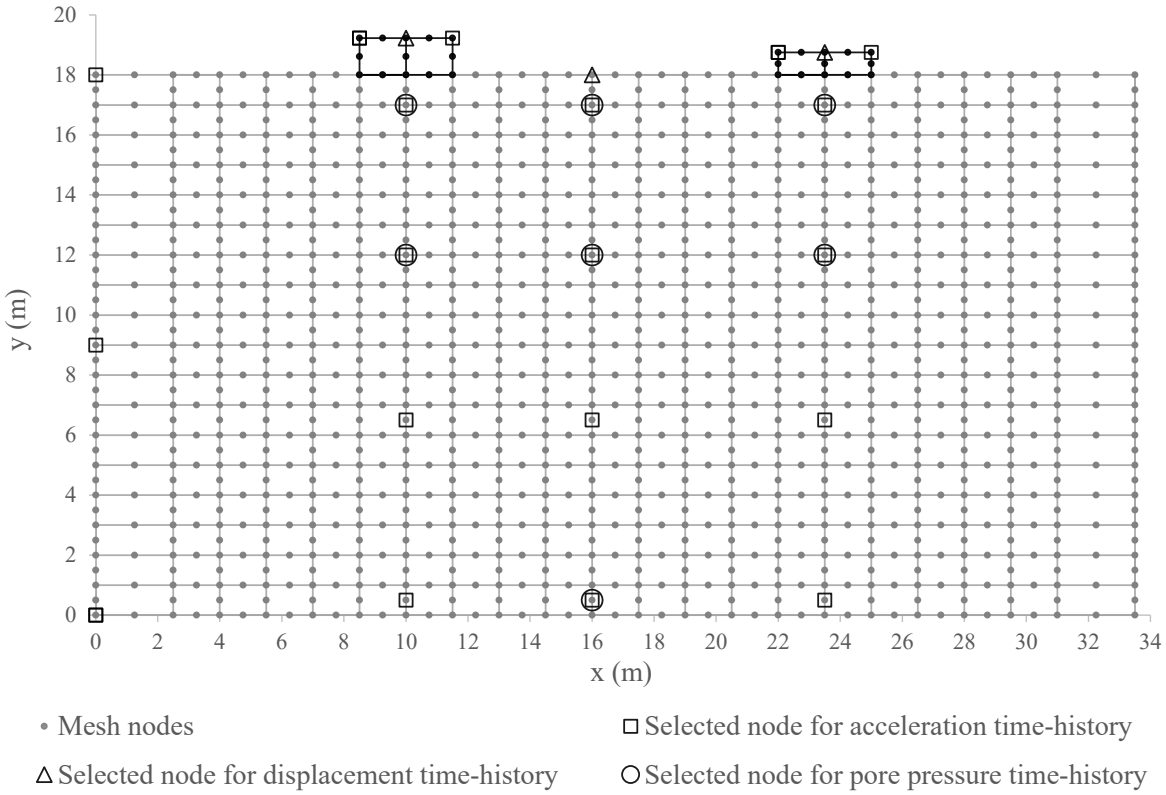

Figure E.1 – Employed finite element mesh for the simulation of CM-A.

E.2 Obtained numerical results

E.2.1 Horizontal acceleration time-histories

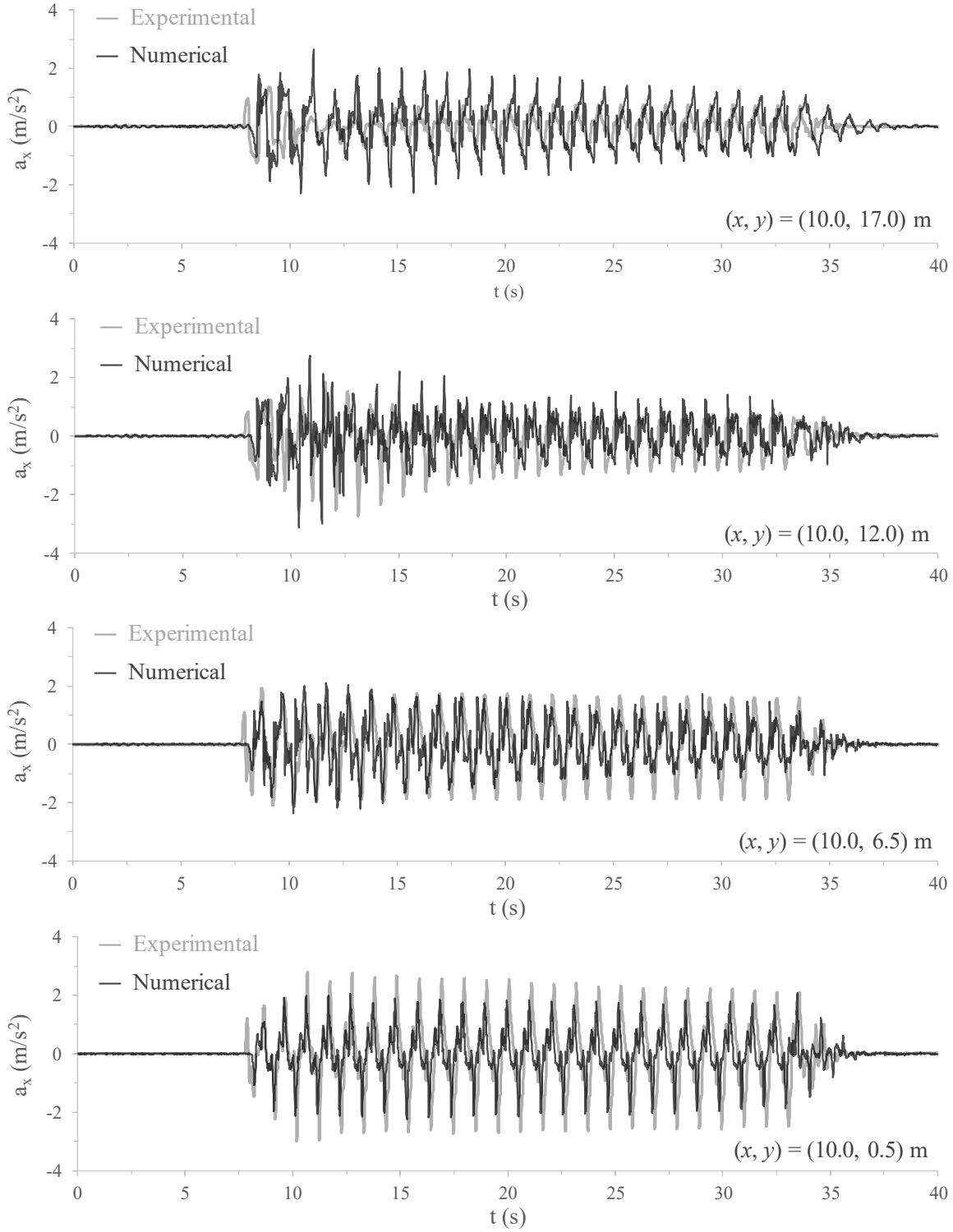

Figure E.2 – Measured and computed horizontal acceleration time-histories at several positions located along a vertical alignment coincident with the axis of the heavier shallow foundation for CM-A.

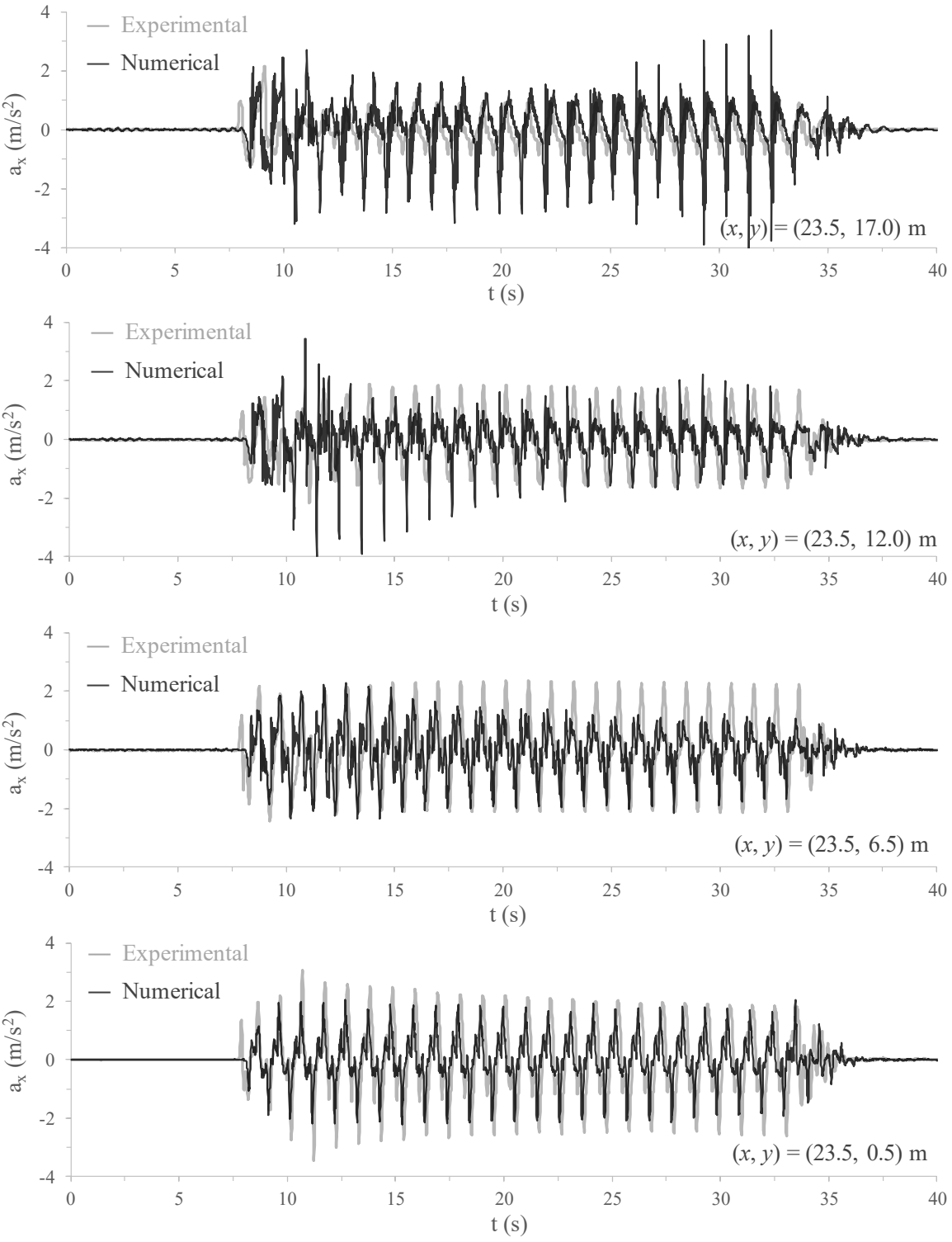

Figure E.3 – Measured and computed horizontal acceleration time-histories at several positions located along a vertical alignment coincident with the axis of the lighter shallow foundation for CM-A.

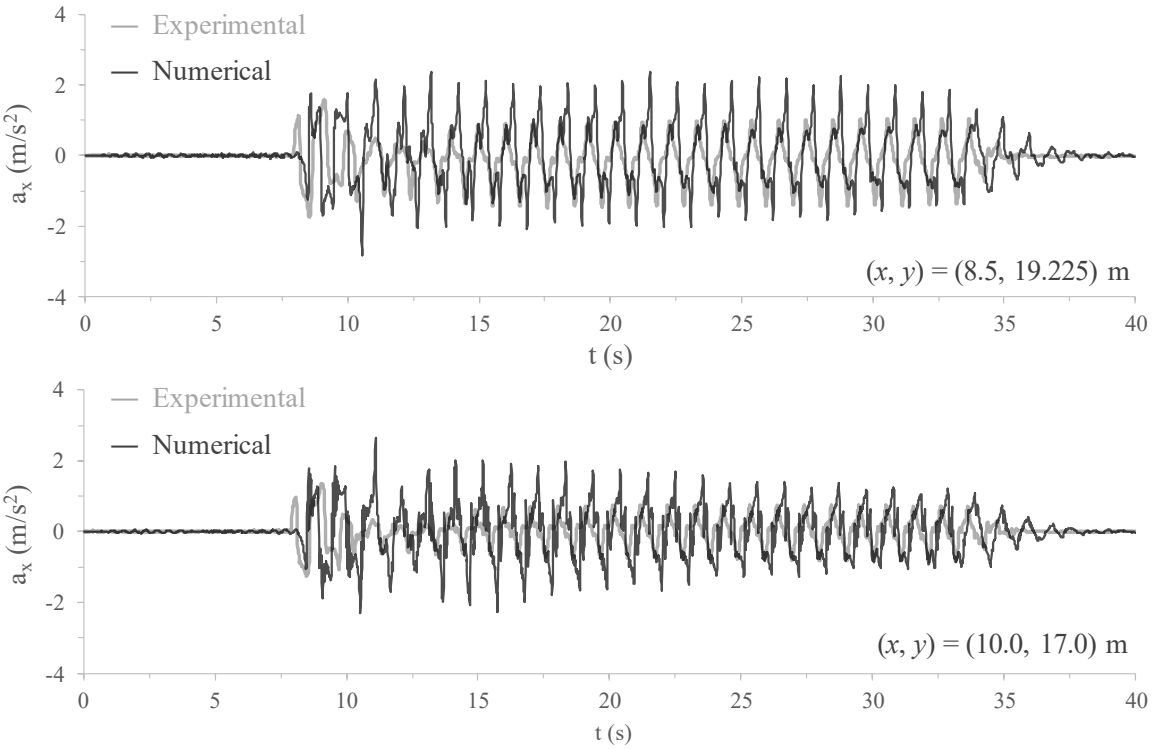

Figure E.4 – Measured and computed horizontal acceleration time-histories at the top of the heavier shallow foundation and underneath it for CM-A.

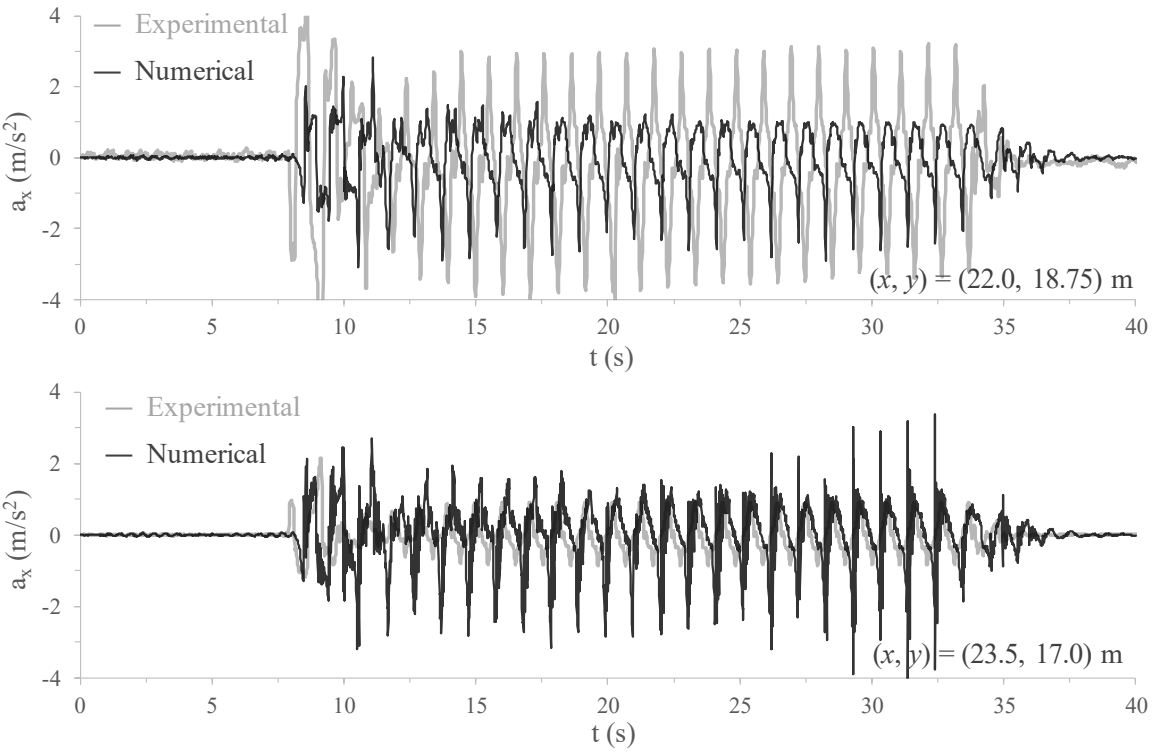

Figure E.5 – Measured horizontal acceleration time-histories at the top of the lighter shallow foundation and underneath it for CM-A.

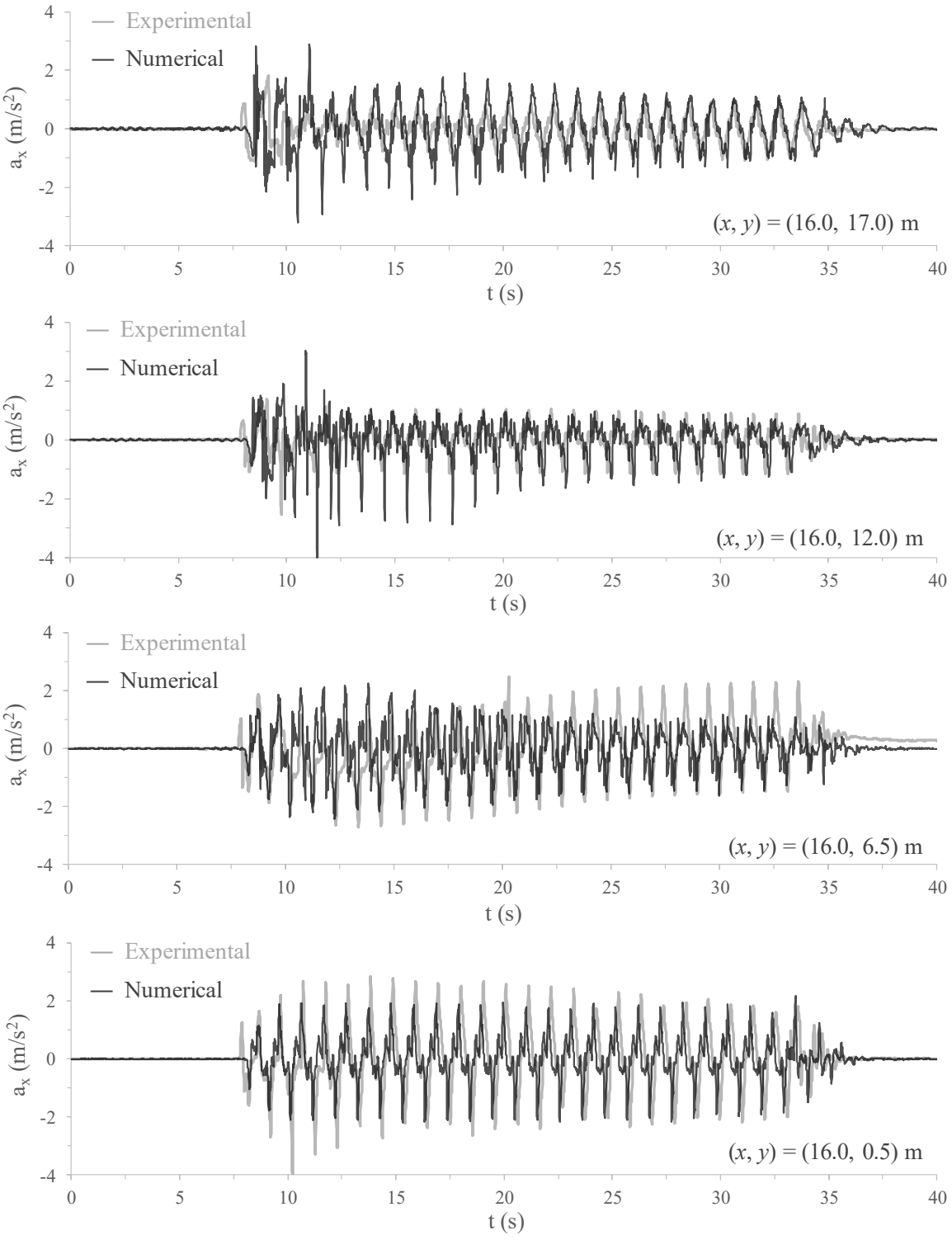

Figure E.6 – Measured and computed horizontal acceleration time-histories at several positions located along a vertical alignment coincident with the middle of the model for CM-A.

E.2.2 Vertical acceleration time-histories

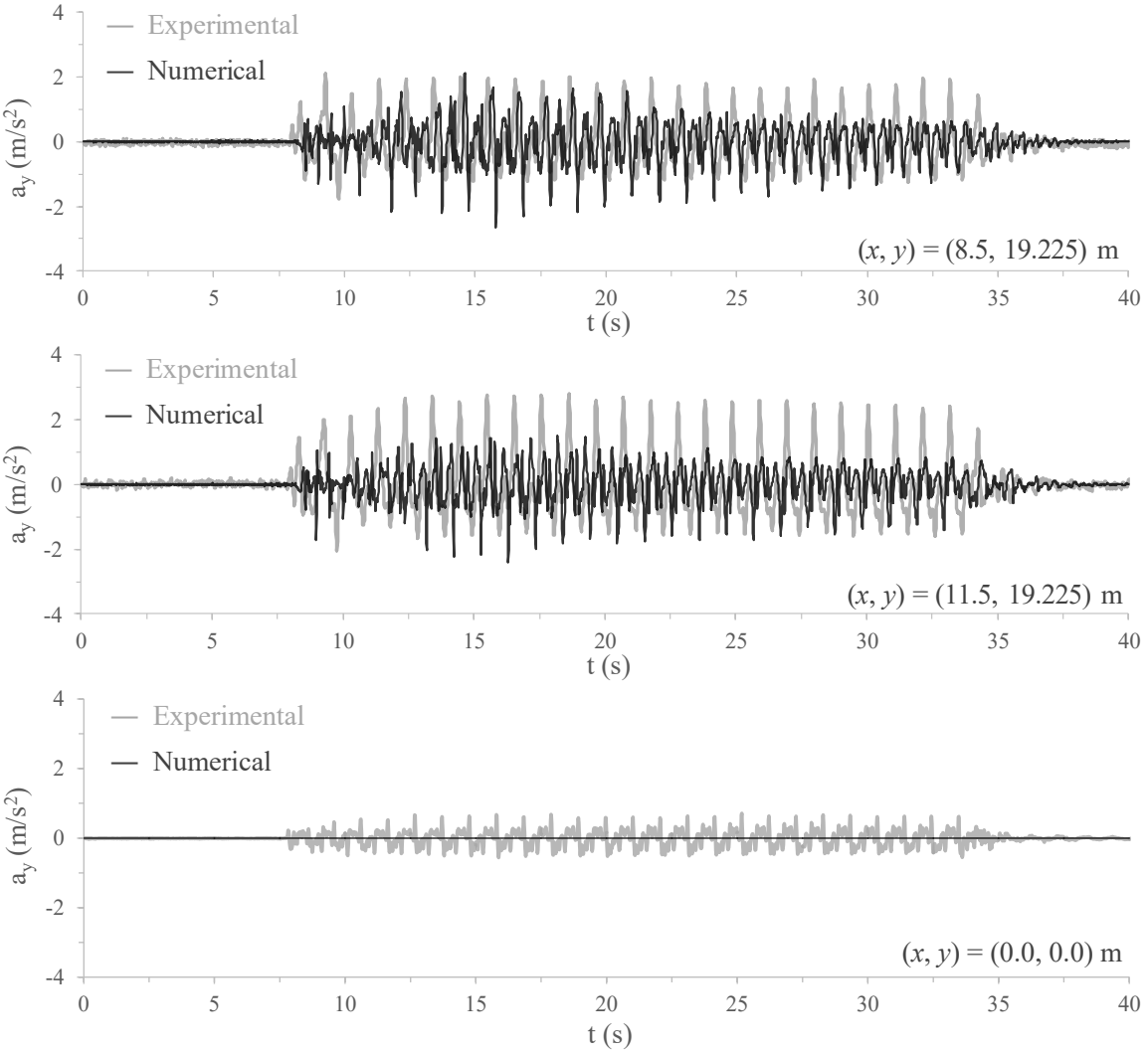

Figure E.7 – Measured and computed vertical acceleration time-histories at the base of the model and at the left and right top edges of the heavier shallow foundation for CM-A.

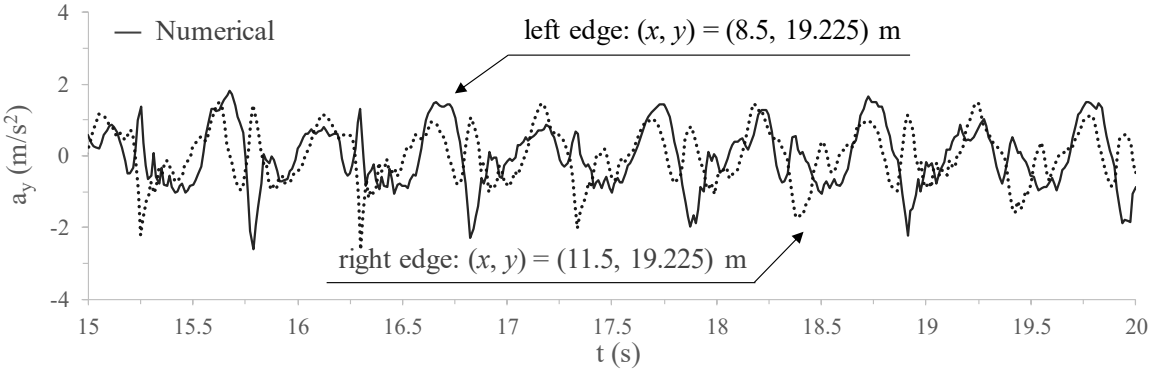

Figure E.8 – Computed vertical acceleration time-histories at the left and right top edges of the heavier shallow foundation during the period ranging from 15 s to 20 s for CM-A.

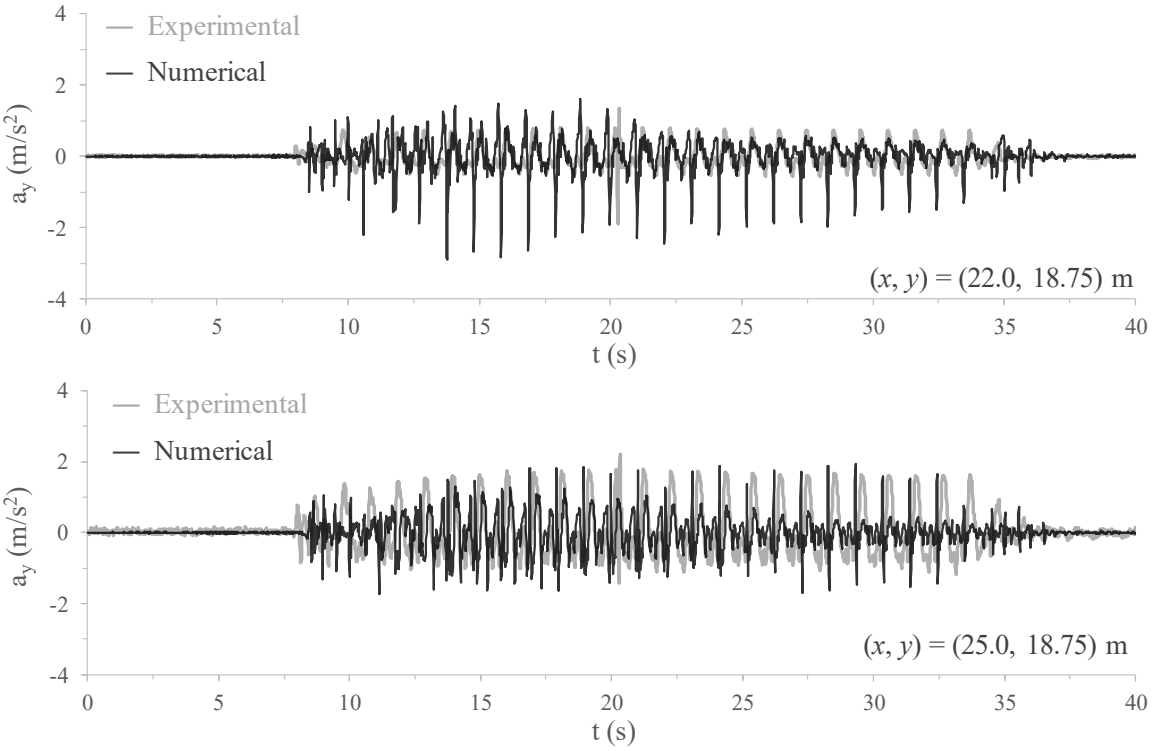

Figure E.9 – Measured and computed vertical acceleration time-histories at the left and right top edges of the lighter shallow foundation for CM-A.

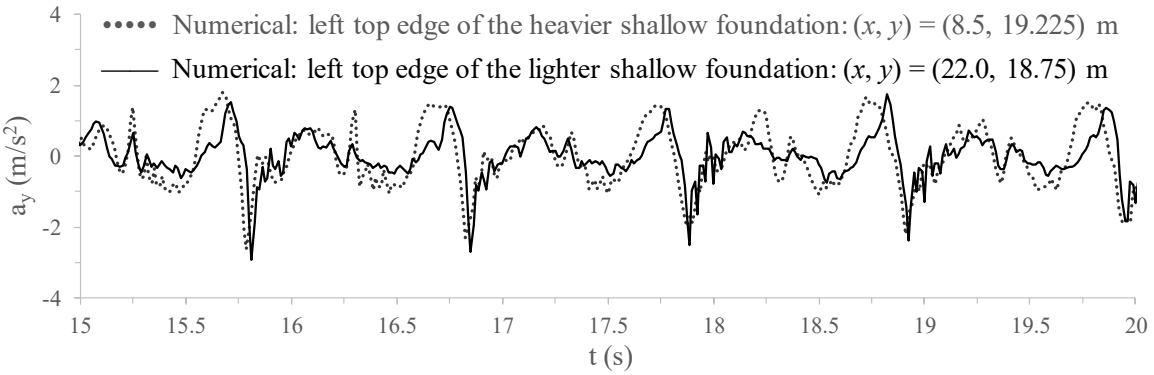

Figure E.10 – Computed vertical acceleration time-histories at the left edges of the heavier and lighter shallow foundations during the period ranging from 15 s to 20 s for CM-A.

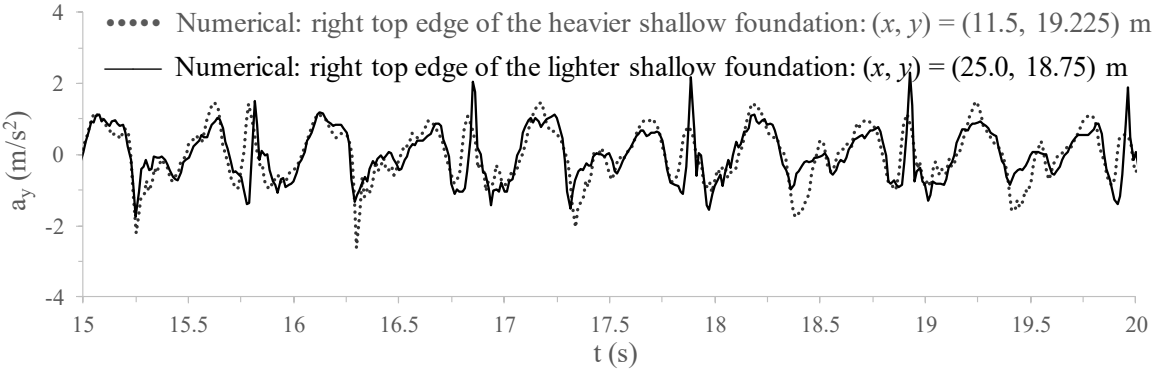

Figure E.11 – Computed vertical acceleration time-histories at the right edges of the heavier and lighter shallow foundations during the period ranging from 15 s to 20 s for CM-A.

E.2.3 Excess pore pressures

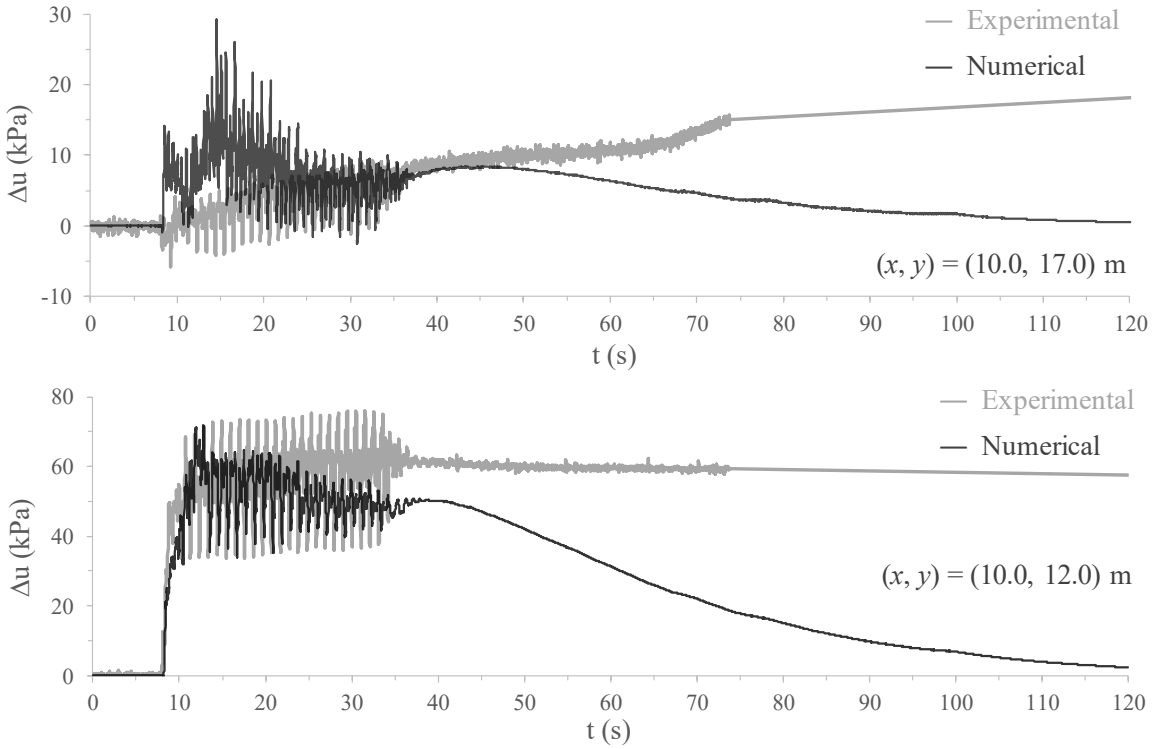

Figure E.12 – Computed and measured excess pore pressure build-up at two different positions located along a vertical alignment coincident with the axis of the heavier shallow foundation for CM-A.

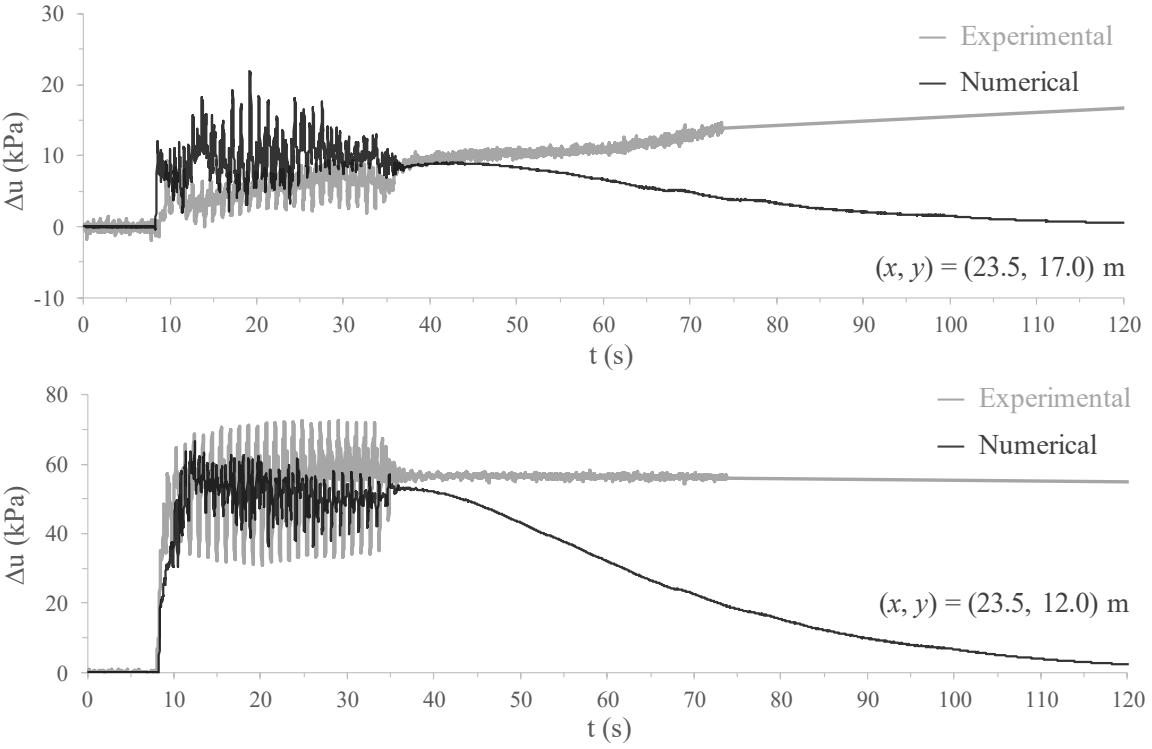

Figure E.13 – Computed and measured excess pore pressure build-up at two different positions located along a vertical alignment coincident with the axis of the lighter shallow foundation for CM-A.

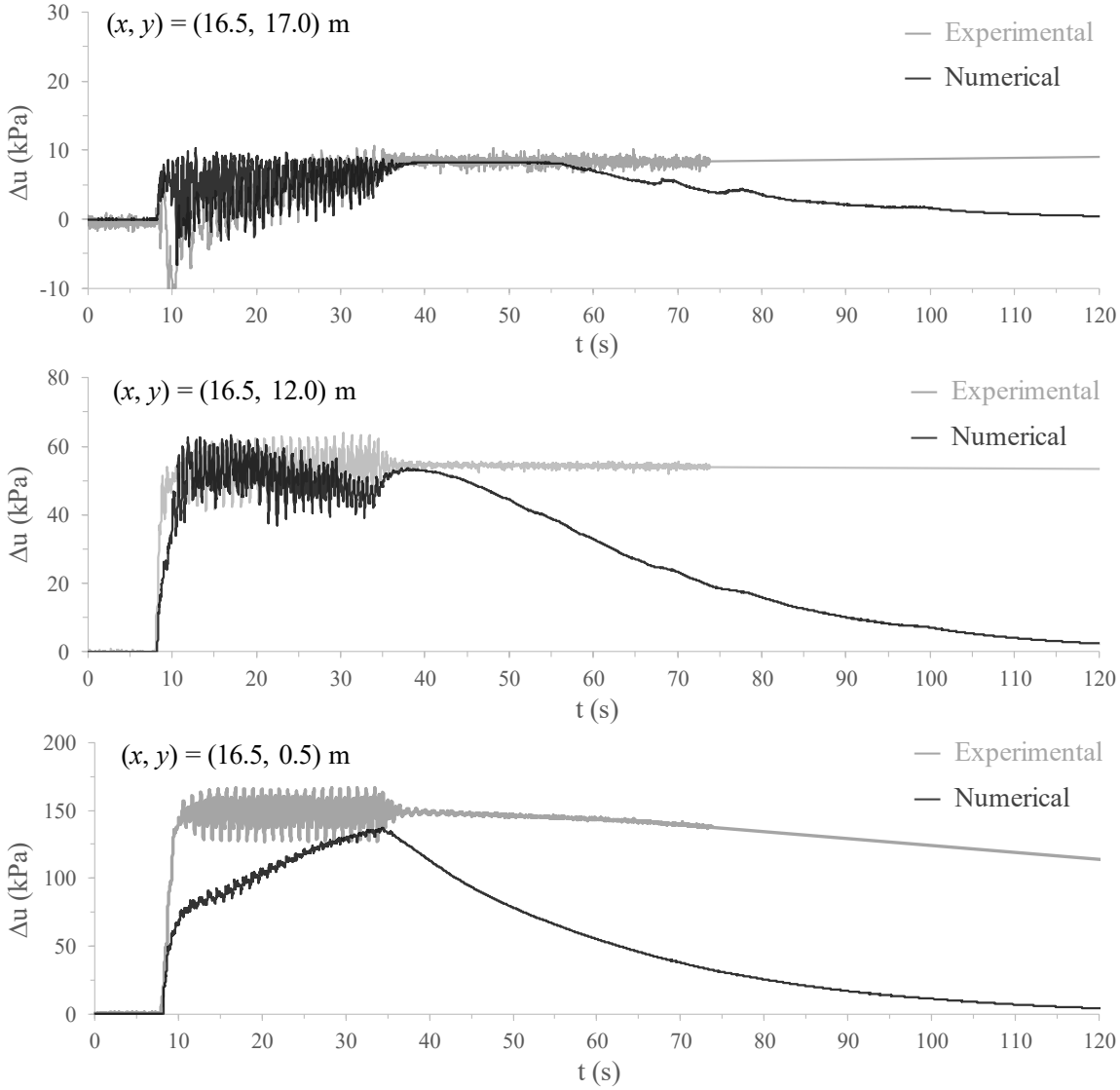

Figure E.14 – Computed and measured excess pore pressure build-up at three different positions located along a vertical alignment coincident with the middle of the model for CM-A.

E.2.4 Settlements

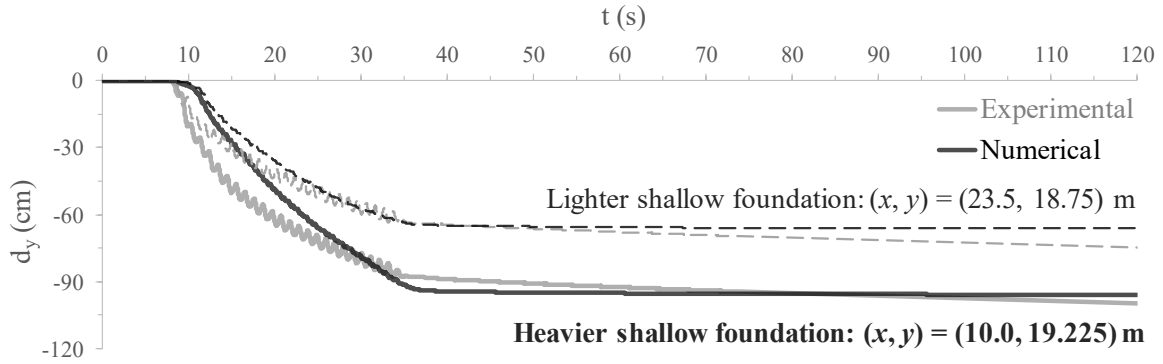

Figure E.15 – Computed and measured settlements at the top of the heavier and lighter shallow foundations during shaking and shortly after its end for CM-A.

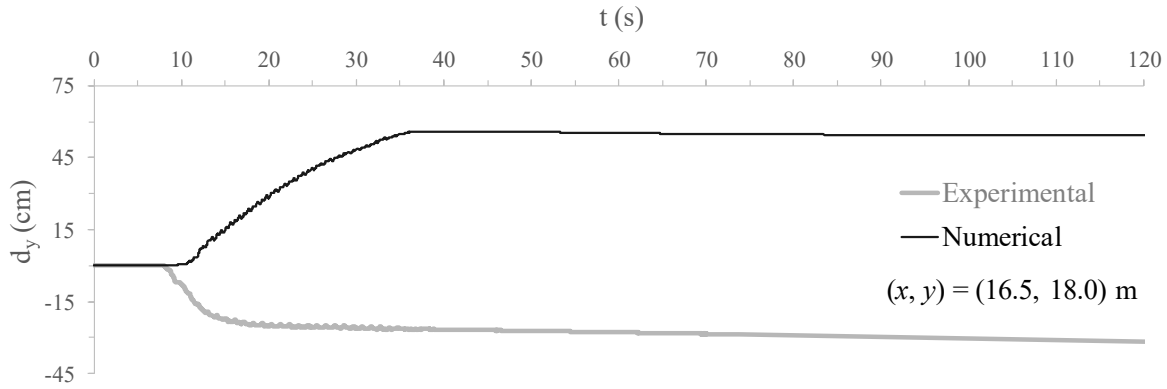

Figure E.16 – Computed and measured settlements at the ground surface in between the two shallow foundations during shaking and shortly after its end for CM-A.

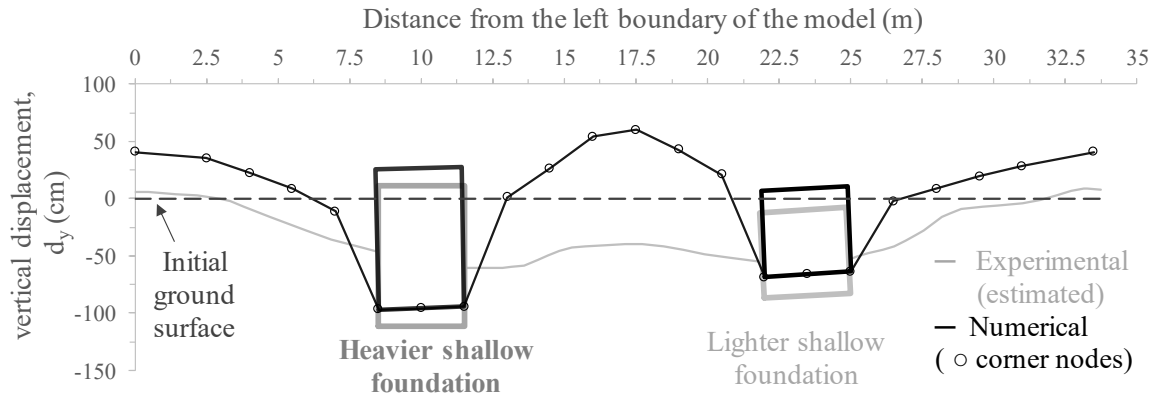

Figure E.17 – Computed and measured ground settlement profile after the complete dissipation of excess pore pressures for CM-A.

Appendix F DYNAMIC FINITE ELEMENT ANALYSIS OF CENTRIFUGE MODEL A WITH VARIABLE HYDRAULIC CONDUCTIVITY

F.1 Introduction

This appendix contains the complete set of results of a finite element analysis of the Centrifuge model A (CM-A), entitled as "Adjacent shallow foundations resting on a uniform moderately loose sand deposit subjected to dynamic loading causing liquefaction", considering a simple hydraulic model establishing the variation of the vertical hydraulic conductivity of the sand deposit with the excess pore pressure ratio. Note that this hydraulic model was proposed by Taborda (2011) and described in Chapter 8. Similarly, the employed material parameters, mesh, time step, time integration algorithm, boundary conditions and initial stresses are presented in Chapter 8. To aid the presentation, the adopted mesh and nodes selected for the inspection of acceleration, displacement and excess pore pressure time-histories are illustrated in Figure F.1.

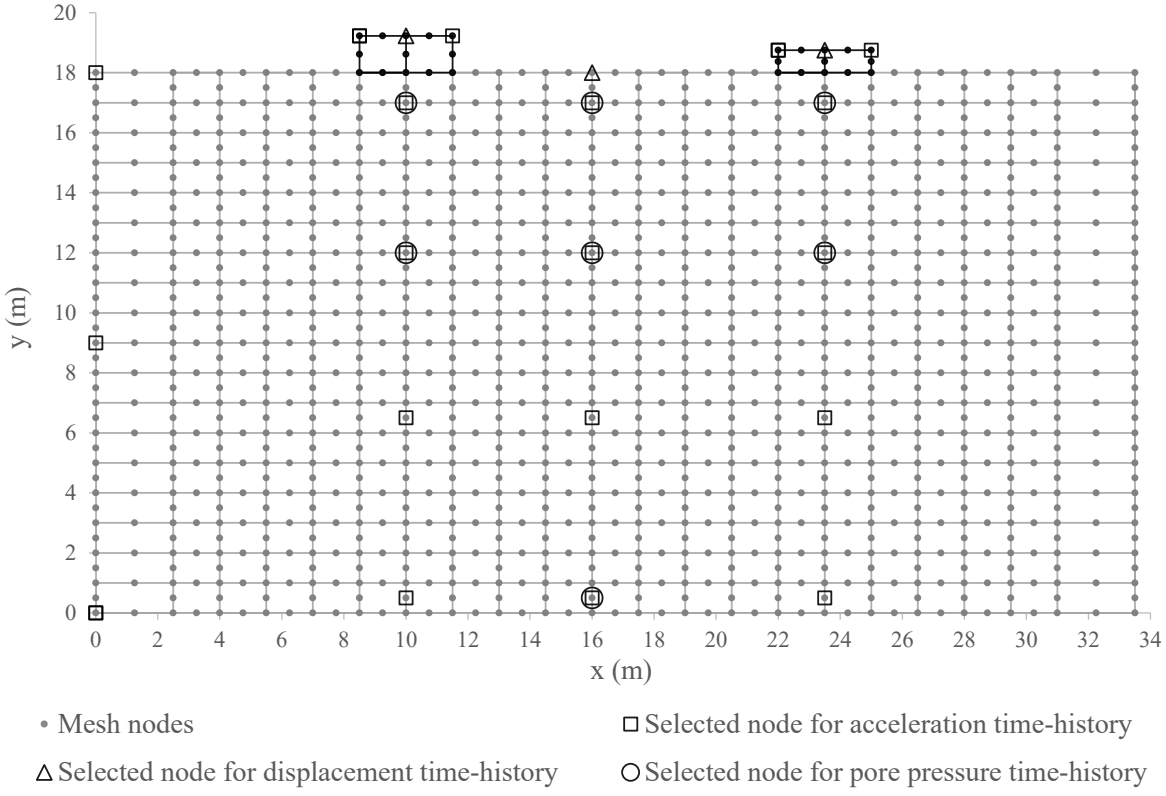

Figure F.1 – Employed finite element mesh for the simulation of CM-A.

F.2 Obtained numerical results

F.2.1 Horizontal acceleration time-histories

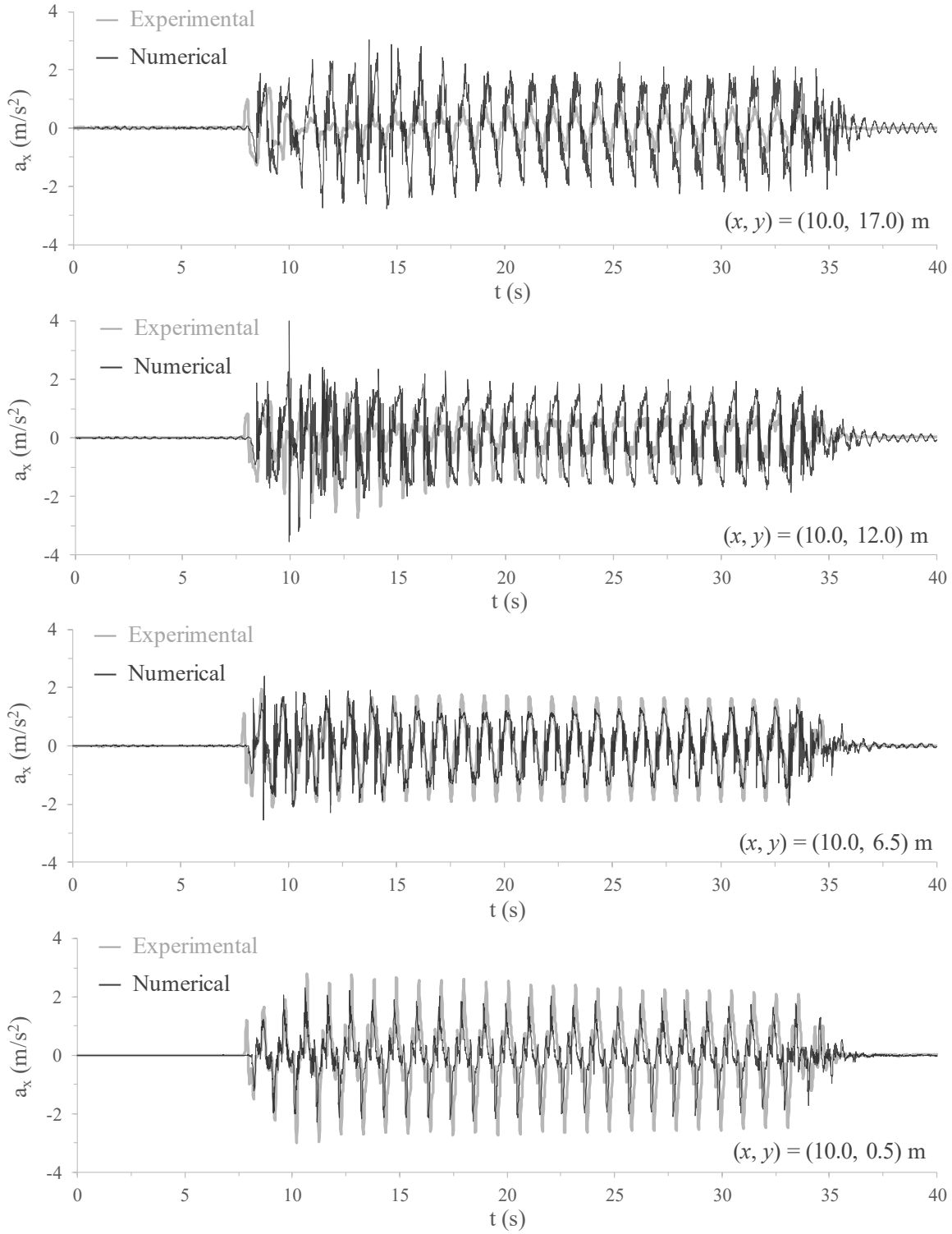

Figure F.2 – Measured and computed horizontal acceleration time-histories at several positions located along a vertical alignment coincident with the axis of the heavier shallow foundation for CM-A.

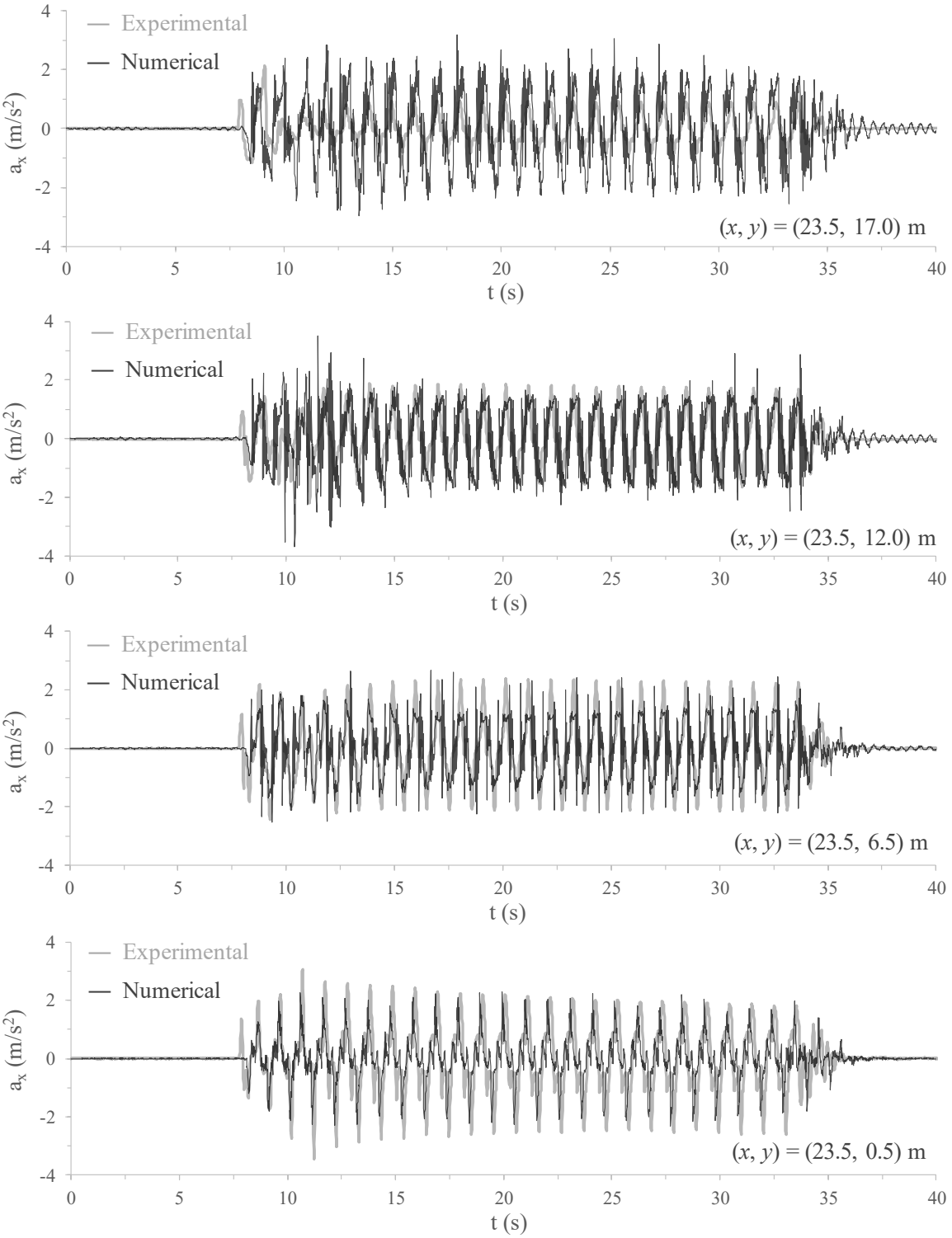

Figure F.3 – Measured and computed horizontal acceleration time-histories at several positions located along a vertical alignment coincident with the axis of the lighter shallow foundation for CM-A.

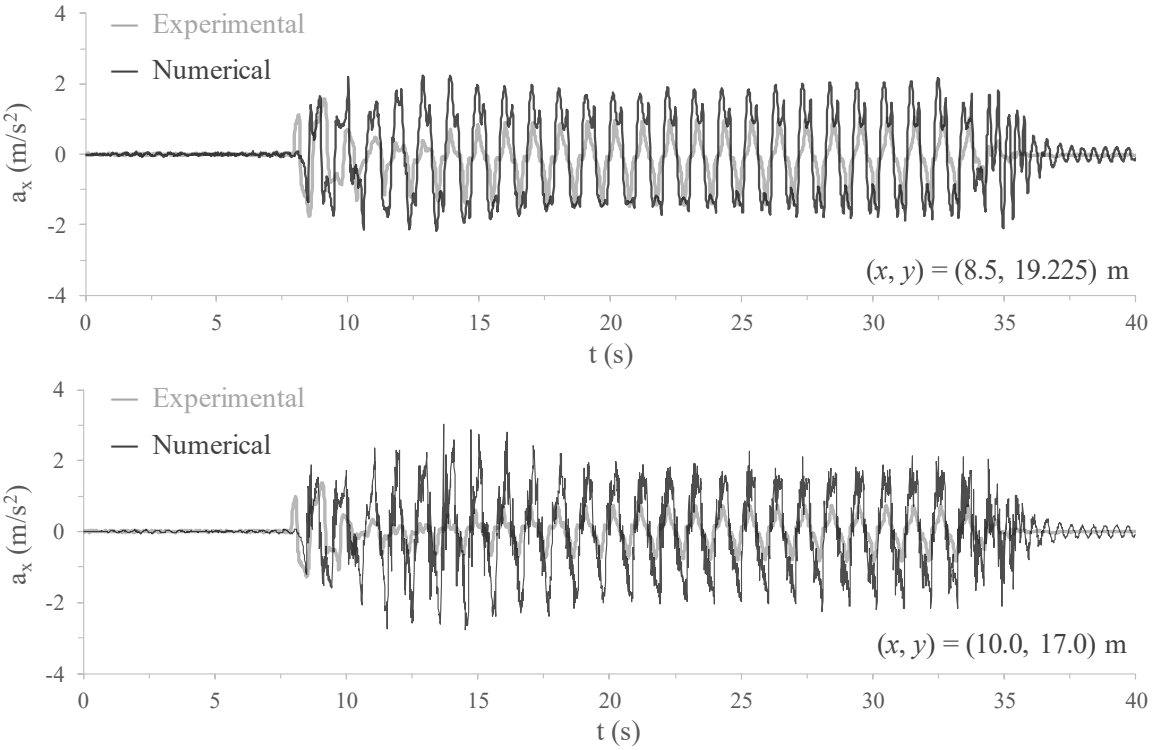

Figure F.4 – Measured and computed horizontal acceleration time-histories at the top of the heavier shallow foundation and underneath it for CM-A.

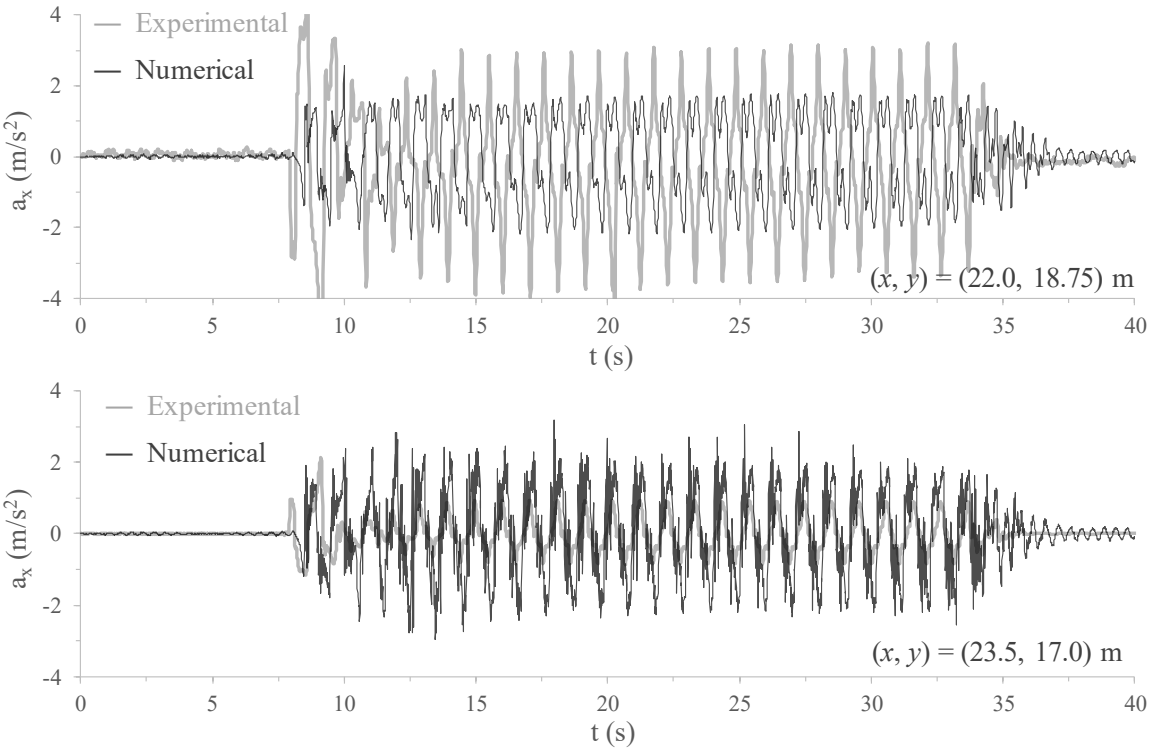

Figure F.5 – Measured horizontal acceleration time-histories at the top of the lighter shallow foundation and underneath it for CM-A.

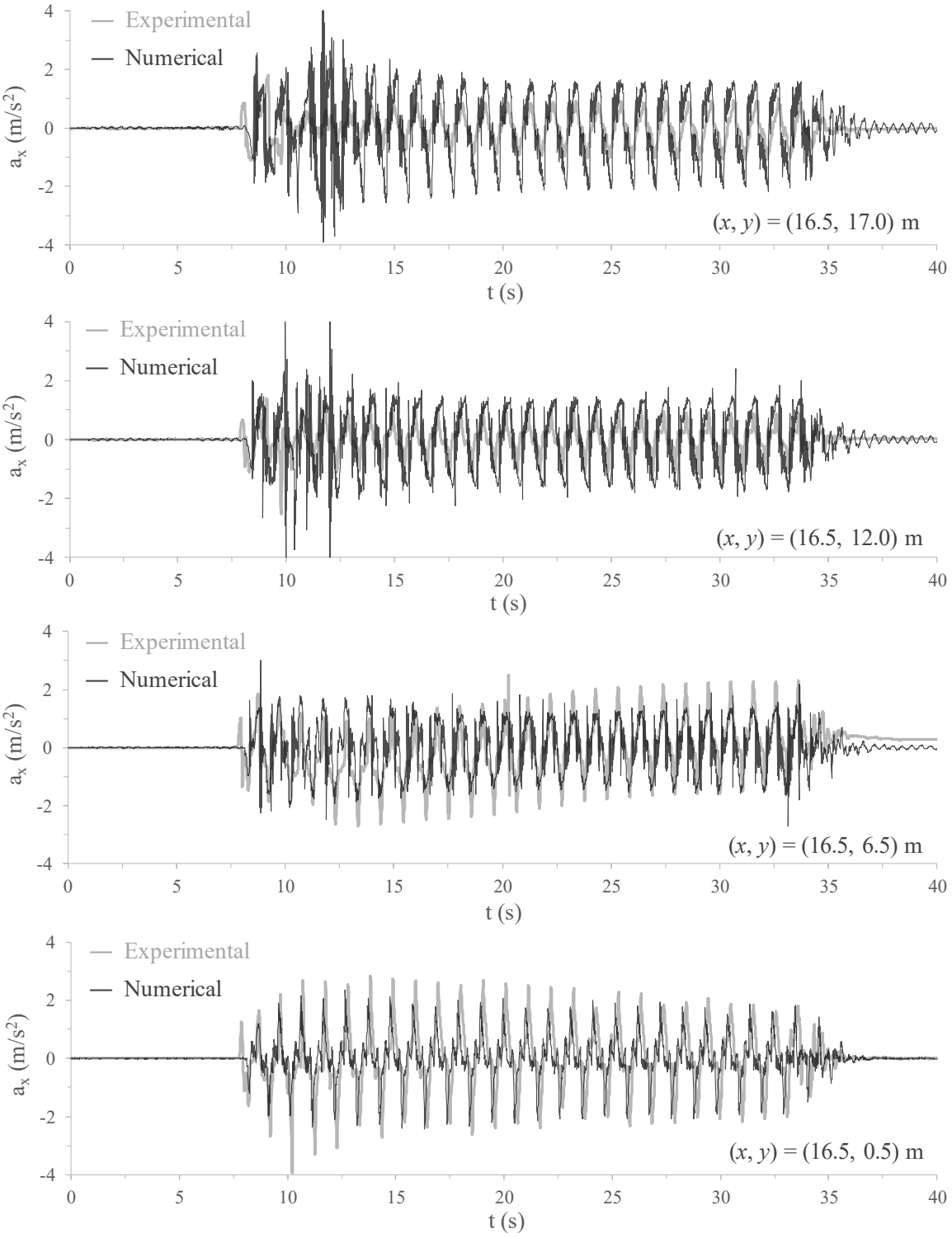

Figure F.6 – Measured and computed horizontal acceleration time-histories at several positions located along a vertical alignment coincident with the middle of the model for CM-A.

F.2.2 Vertical acceleration time-histories

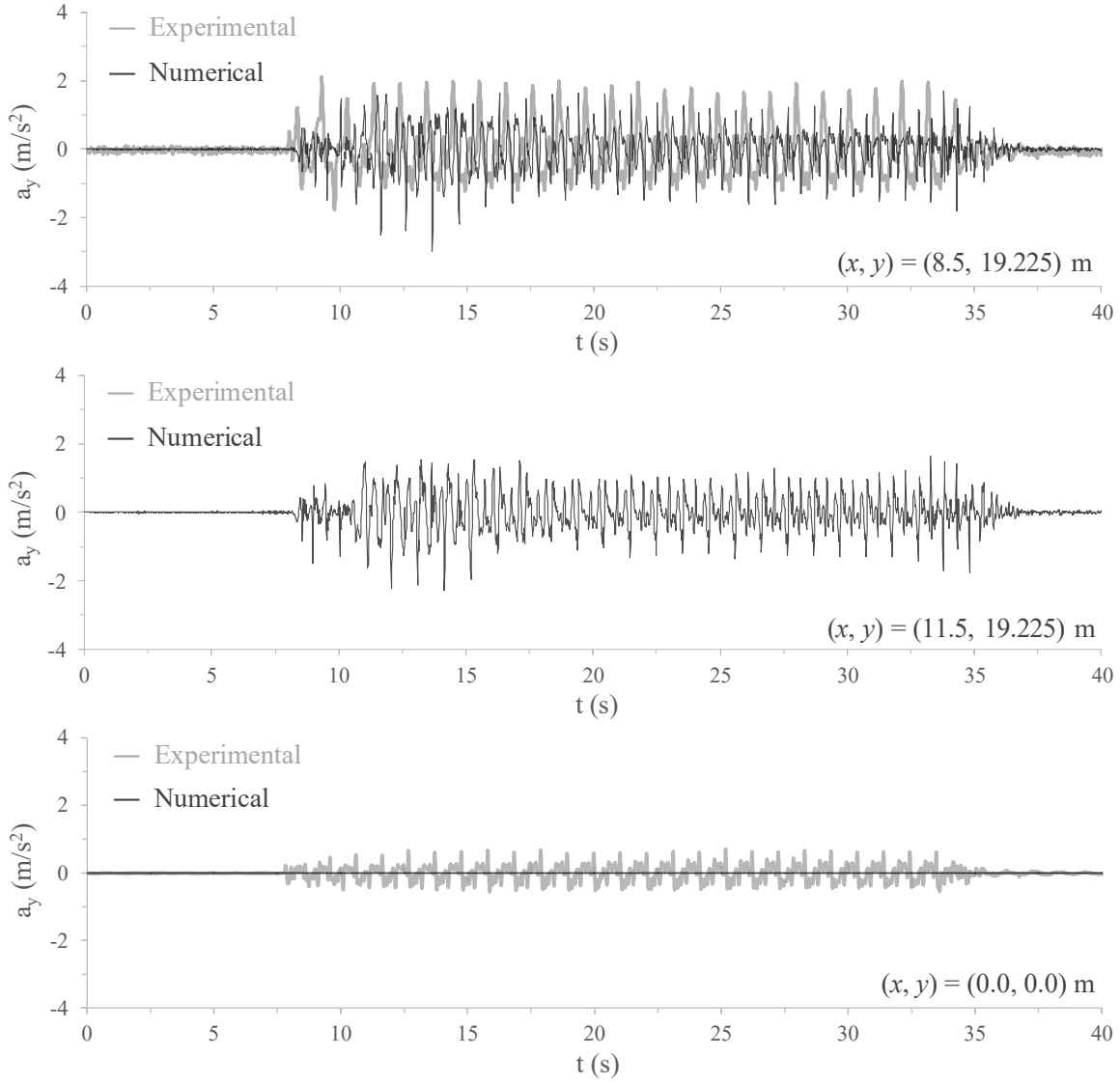

Figure F.7 – Measured and computed vertical acceleration time-histories at the base of the model and at the left and right top edges of the heavier shallow foundation for CM-A.

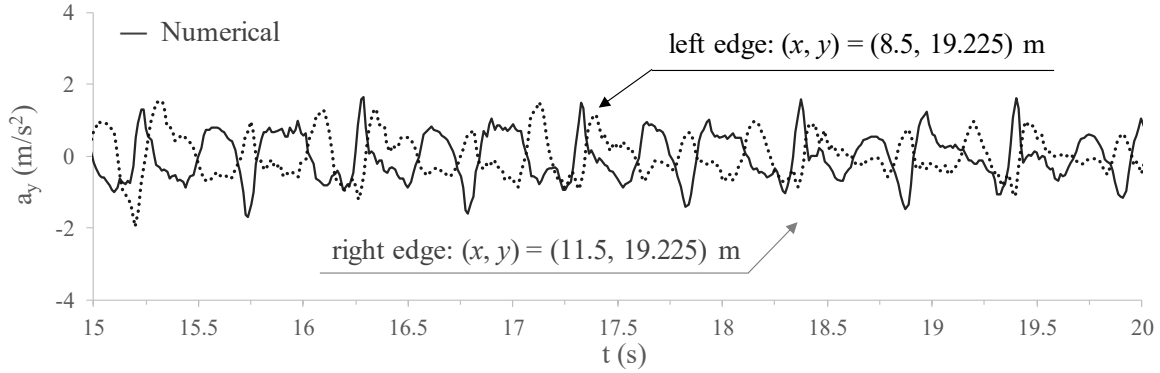

Figure F.8 – Computed vertical acceleration time-histories at the left and right top edges of the heavier shallow foundation during the period ranging from 15 s to 20 s for CM-A.

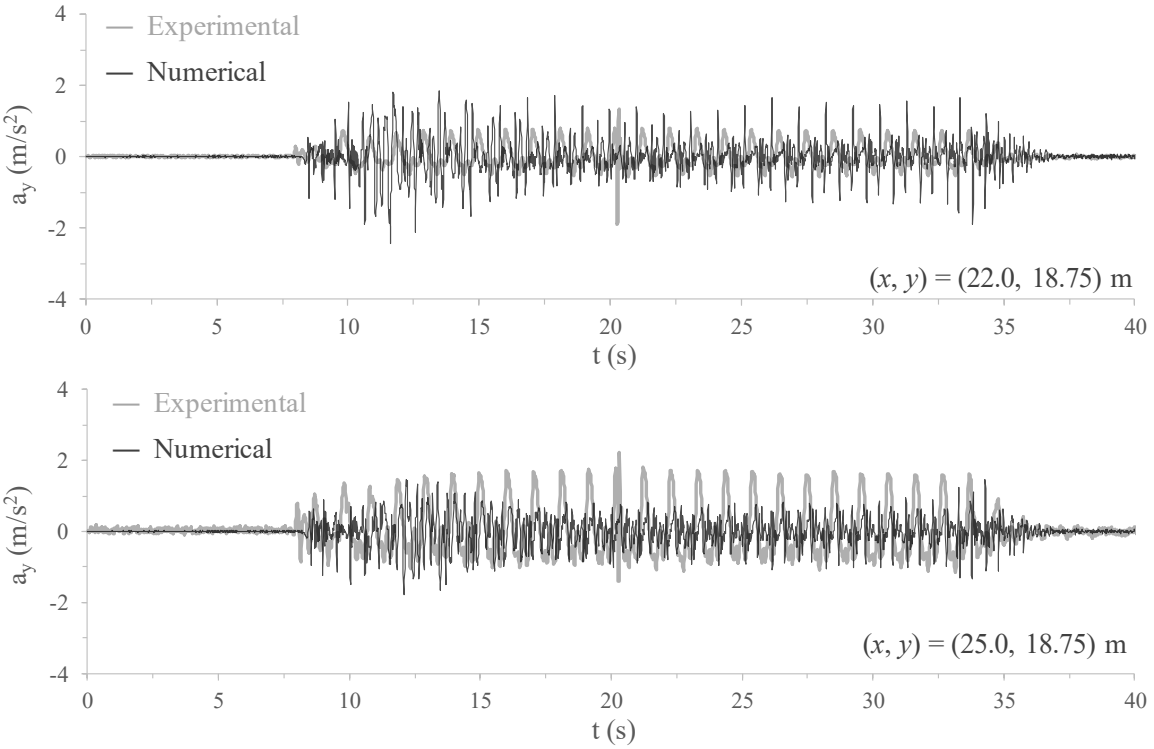

Figure F.9 – Measured and computed vertical acceleration time-histories at the left and right top edges of the lighter shallow foundation for CM-A.

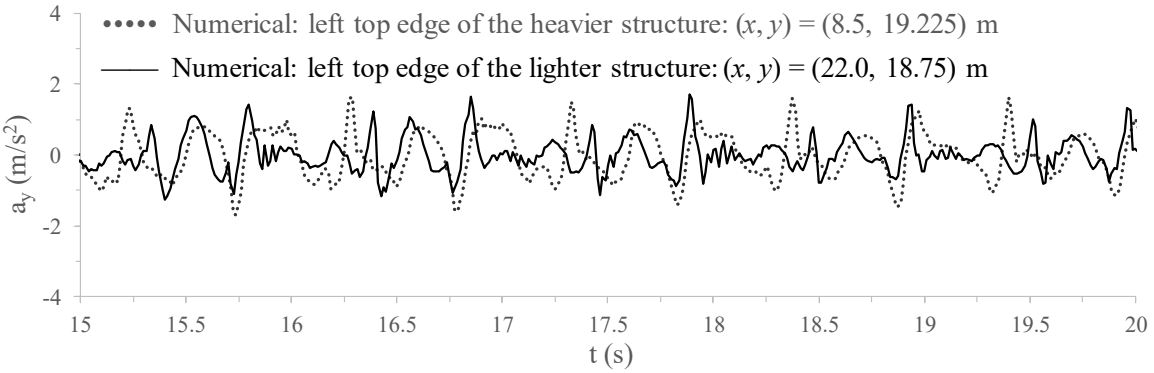

Figure F.10 – Computed vertical acceleration time-histories at the left edges of the heavier and lighter shallow foundations during the period ranging from 15 s to 20 s for CM-A.

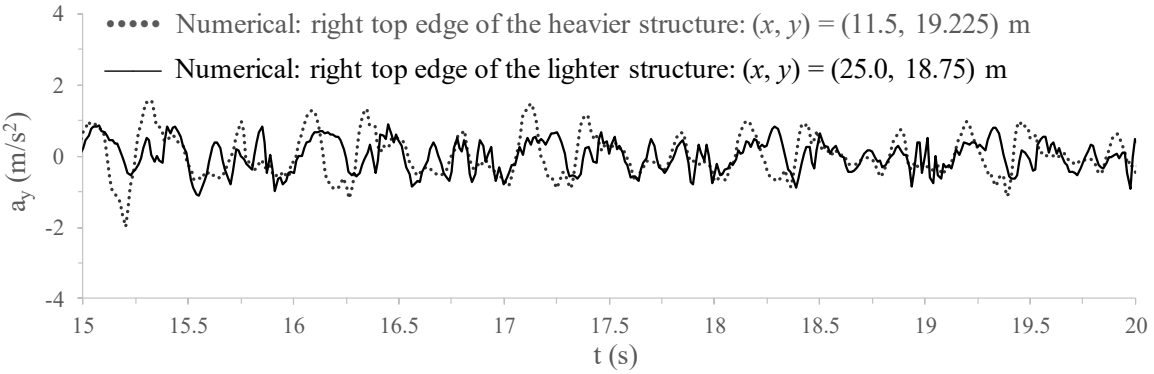

Figure F.11 – Computed vertical acceleration time-histories at the right edges of the heavier and lighter shallow foundations during the period ranging from 15 s to 20 s for CM-A.

F.2.3 Excess pore pressures

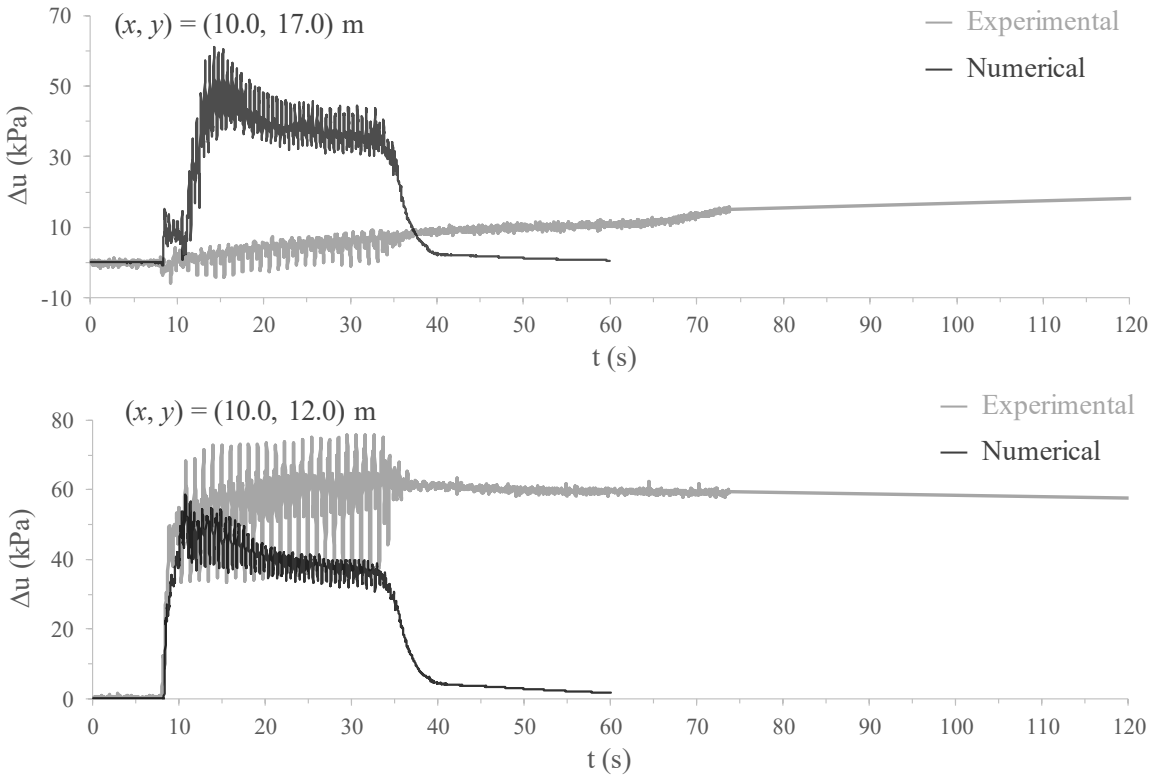

Figure F.12 – Computed and measured excess pore pressure build-up at two different positions located along a vertical alignment coincident with the axis of the heavier shallow foundation for CM-A.

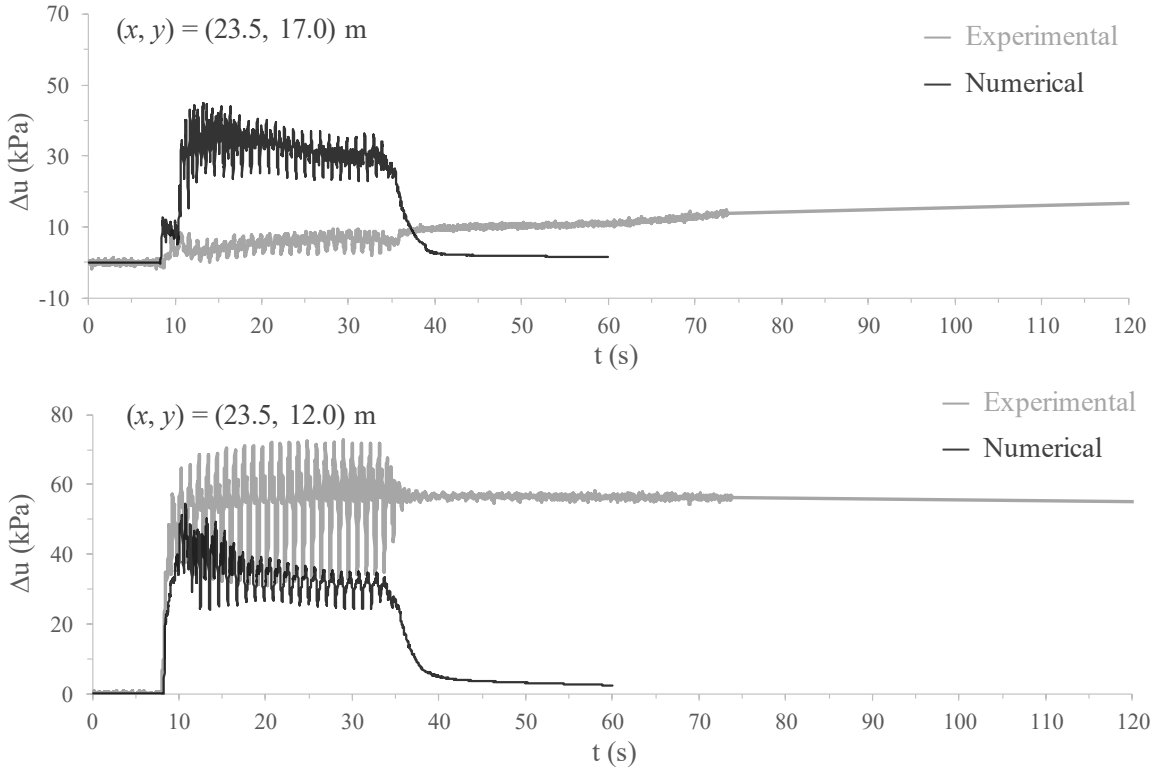

Figure F.13 – Computed and measured excess pore pressure build-up at two different positions located along a vertical alignment coincident with the axis of the lighter shallow foundation for CM-A.

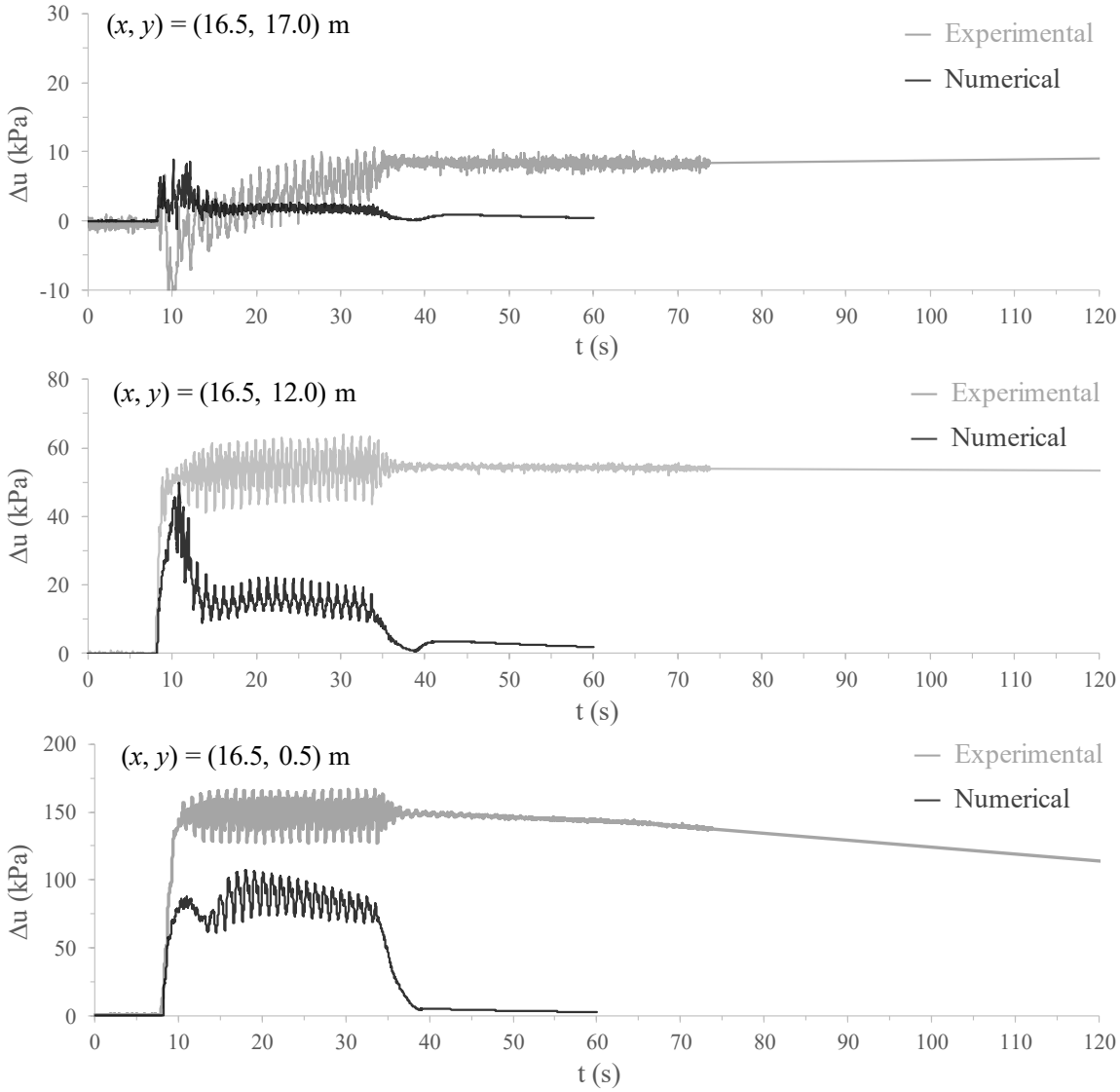

Figure F.14 – Computed and measured excess pore pressure build-up at three different positions located along a vertical alignment coincident with the middle of the model for CM-A.

F.2.4 Settlements

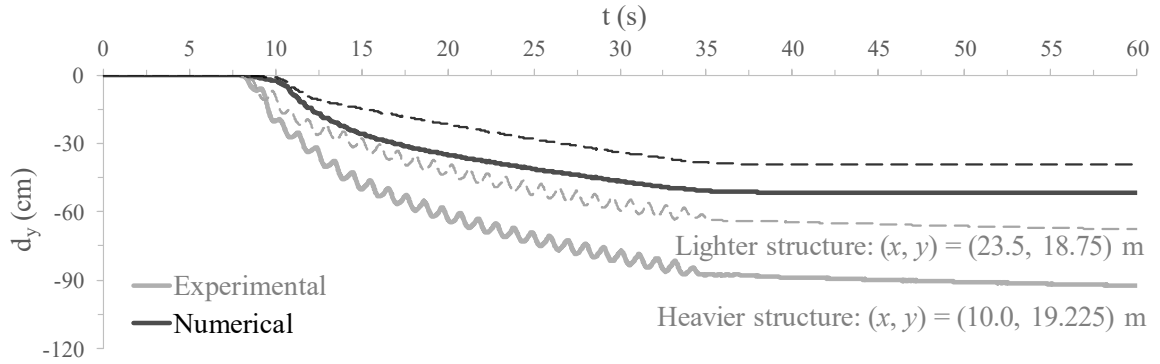

Figure F.15 – Computed and measured settlements at the top of the heavier and lighter shallow foundations during shaking and shortly after its end for CM-A.

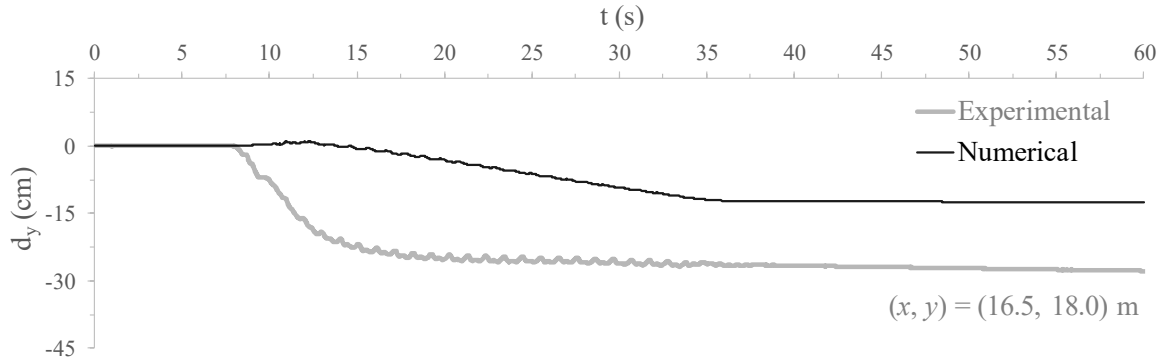

Figure F.16 – Computed and measured settlements at the ground surface in between the two shallow foundations during shaking and shortly after its end for CM-A.

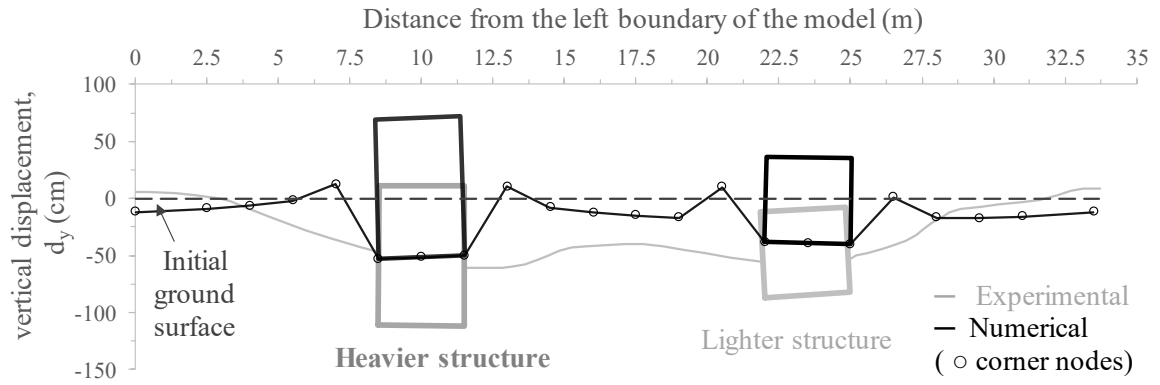

Figure F.17 – Computed and measured ground settlement profile after the complete dissipation of excess pore pressures for CM-A.